Degradation Studies of Microcrystalline Cellulose Reinforced Polylactic Acid Composites

Ainun Najwa Borhan[1*], Ming Meng Pang, Albert Tshai Kim Yeow[2]

[1]*School of Engineering, Taylor's University, Malaysia*

[2]*Department of Mechanical, Materials and Manufacturing Engineering, University of Nottingham, Malaysia*

[*]ainunnajwaborhan@sd.taylors.edu.my

Abstract

Polylactic lactic acid (PLA), a biodegradable aliphatic polyester was filled with microcrystalline cellulose (MCC), a partially depolymerised cellulose with three different compositions ranging from 10wt% to 30wt% to form a PLA composite. MCC is used as a reinforcing agent due to its good binding property and low density. The objective of this research is to prepare the polymer sheets via melt blending method and compare different composition of PLA/MCC biocomposites in order to investigate their biodegradation and hygrothermal degradation behaviour. The degradation behaviour of the polymer sheets was evaluated via hygrothermal test for 14 days and soil burial test for 58 days. The former test required the samples to be immersed in a water bath at temperature of 58 ℃ while the later test involved burying the samples in the soil at a depth of 10 cm at room temperature. In order to evaluate the physical and chemical changes of the polymers upon degradation, scanning electron microscopy (SEM) test and differential scanning calorimetry (DSC) analysis were carried out. From the weight loss data, 30% MCC composites showed the highest weight loss percentage with 21.7% for soil burial test and 23.5% for hygrothermal test when compare to 20% MCC and 10% MCC composites. This indicated that the higher the MCC content in the polymer matrix, the faster the degradation rate. The biocomposites also underwent much faster weight loss under prolong heating (hygrothermal test). Holes and voids with some microorganism attached on the surface of the samples can be seen in the SEM images of soil burial specimen. From the DSC analysis, the glass transition temperature, T_g of pure PLA samples shifted from 64.8 ℃ to lower temperature which is 63.7 ℃ after soil burial test and 57.3 ℃ after hygrothermal test. The addition of 30% MCC reduced the T_g to 62.7 ℃. It is further shifted to 61.9 ℃ after soil burial test and 55.5 ℃ after hygrothermal test. It can be concluded that the incorporation of MCC into PLA matrix enhanced its degradability thus can be used in the industry in order to preserve the environment.

Keywords : polylactic acid, microcrytalline cellulose, soil burial, hygrothermal, degradation

1. Introduction

Synthetic polymers are one of the well known useful materials to the humankind in this modern sciences and technology era. Polymeric materials are currently used in almost all sectors such as in packaging, food industry, agricultural industry, medical appliances and many more due to its wide range of application. Numerous efforts have been done by the engineers and scientists to improve the stability of polymers since their first development due to their environmental influences. However, in the past decade, polymeric materials have caused a serious environmental pollution and has become industrial waste products especially the plastic packaging [1]. The difficulties in disposing the polymer based waste have generated enormous attention and increased awareness among the public [2]. Therefore, the development of biobased and biodegradable polymers as an alternative to the existing petroleum based polymers is necessary as an effort to conserve the environment.

Degradability of polymers is chemical and physical deterioration or in other words it can be defined as the molecular mass loss. A complete degradation is achieved when the polymers are completely converted into salts or gaseous product or when there is no residue remains [2]. The production of the existing synthetic plastics such as polypropylene (PP), poly ethylene (PE), polystyrene (PS) and polyvinyl chloride (PVC) reaches 140 million tonnes worldwide per year [3]. However, due to their lack of biodegradability, several types of biodegradable polymers have been introduced into the market since the past decade which includes polylcatic acid (PLA), polycaprolactone (PCL), polyglycolic acid (PGA)and many others [4]. The high efficiency in production of lactic acid by fermentation of renewable resources which include starch and sugars has increased the attention among the researchers towards PLA. PLA is a semi-crystalline polymer that exhibits similar mechanical properties as of polystyrene and polyethylene. Besides that, it also has reasonably good properties such as high tensile strength, high melting point which is about 174°C - 184°C, low elongation and high transparency. These properties results in wide usage of PLA in medical appliances and packaging industry.

Microcrystalline cellulose (MCC) is widely used in pharmaceutical industry, paper making industry and composite manufacturing industry. It is a partially depolymerise cellulose discovered by Battista and Smith in 1955 which can be prepared by treating alpha cellulose from fibrous plant. It has amorphous region which is prone to hydrolysis and is a good binder [5]. Therefore, it is chosen to bind with PLA to produce a degradable composite. It has a good thermal stability up to 300℃. A lot of studies have been done regarding MCC filed PE and PS. However the information regarding MCC filled PLA is still lacking. This research is conducted to gain more information regarding this type of polymer in term of degradability [6].

This paper involves producing polylactic acid composite which is incorporated with three different compositions of microcrystalline cellulose to be compared with the pure polylactic acid composite. The polymers undergo degradation test such as soil burial test, and hygrothermal test in order to study their degradation behavior. Characterization tests such as scanning electron microscopy (SEM) and differential scanning calorimetry (DSC) are carried out to evaluate the physical and chemical alteration of the polymers upon degradation.

For soil burial test, the depth of the burying of the samples varies for different researcher. Bayerl et al. put the sample of PLA/flax composite at a depth of 20 cm in the compost soil [7]. Fortunati et al. buried PLA sample into an organic substrate placed in a perforated container at 4 to 6 cm depth [8]. The soil was regularly watered to keep it moist [9]. The degradation rate is independent of the burying depth. Instead, it depends on the presence of the microorganism in that particular area. According to a study done by Fukusima et al, pure PLA sheets does not show any weight loss and were not broken for the first 39 weeks. The reason behind this is that no assimilation between the microorganism and the sheets were found. Weng et al. wrote that neat PLA sample started to break 30 days after being buried. After 160 days, the sample turned into debris [9]. As of now, only limited degradation studies on the synthetic MCC filled PLA composites have been reported, particularly for soil burial test.

Hygrothermal ageing investigates the changes of PLA composite towards the environmental exposure which are heat and water. The suitable method to investigate the hygrothermal behaviour is to measure the water uptake because water usually initiates the deterioration of polymer composite. PLA hardly shows any degradation property at 25℃. As the temperature increases to 37℃, it starts to show a little degradation property. 58℃ is the best onset degradation temperature. This is because a lot of studies show that this temperature causes PLA to degrade faster since it is closer to its glass transition temperature which is between 60 ℃ to 65 ℃ [10]. Rapid degradation occurs as the temperature increases towards the glass transition. Besides that, higher temperature is not suitable because the crystalline configuration of PLA will change. PLA is said to have a better water absorption when compare to polypropene and polyethylene [11]. Berthé et al. stated that the water uptake increases with ageing time due to osmotic cracking [12].

The main objective to be achieved is to prepare and compare different loading of microcrystalline cellulose filled polylactic acid by using melt blending method. Besides that, it is also aimed to investigate the biodegradation and hygrothermal degradation behavior of microcrystalline cellulose filled polylactic acid composite. At the end if this research, it can be known whether the incorporation of MCC into PLA will enhance the degradation of the polymer sheet or vice versa. Should MCC enhance the degradability, the best formulation of the polymer composite can be known based on its degradation rate.

2. Experimental

2.1 Materials

Polylactic acid grade 3015D with density of 12.5 g/cm^3 was obtained from Nature Works. Microcrystalline cellulose was purchased from R&M Chemicals with pH of 5.5 to 7 and degree of polymerization ranging from 210 to 270.

2.2 Material processing

2.2.1 Preparation of the Composites

Three different compositions of PLA/MCC polymer sheets with one pure PLA sheet were prepared. The formulation used is tabulated in Table 1 :

Table 1. The formulation of the polymer sheets

No	Remarks	Weight of PLA (g)	Weight of MCC (g)
1	Pure PLA	100	-
2	10wt% MCC	10	90
3	20wt% MCC	20	80
4	30wt% MCC	30	70

These formulations were chosen simply based on the literature review. Lower dosage of MCC shows insignificant improvement in its mechanical properties whereas high dosage will cause difficulties in dispersing MCC in PLA matrix [13]. So, the range of 10% to 30% was suitable to be used to compare which formulation will give the best degradation property.

2.2.2 Melt Blending

In order to remove moisture, PLA 3501D was dried in an oven at 80 ℃ for 15 minutes prior to melt blending process [14]. In melt blending process, MCC was compounded with PLA by using a twin screw extruder or internal mixer (Model: Haake Polylab System E93) at the speed of 50 rpm since this is the regular speed used in producing most of fibre reinforce PLA composites [9]. The twin screw extruder was preheated first to 180 ℃ to ensure the mixture is thoroughly mixed before putting in the materials [15]. This mixing process took 7 to 8 minutes to ensure even heating. Pure PLA was melted in the same condition in order to act as a reference material. Upon mixing, the mixture was taken out for compression moulding process.

2.2.3 Compression Moulding

Compression moulding process was carried out in order to produce a 12cm × 13cm rectangular polymer sheet with 0.1 cm thickness. This size was chosen since this was the thinnest available mould. Thin sample can be cut easily. The mixture was distributed in between the mould. It was then being compressed by a hot press machine (Model: Moore E53) at temperature of 185℃ to ensure that the mixture was melted and can be shaped into the given mould. The machine was preheated for 5 minute before it underwent pressing stage for 8 minutes at 150 bar. Then, the cooling process took place until the temperature reaches 60℃ for the polymer to be harden and be ready in shape [16]. The polymer sheet was then ready to be taken out. A pure PLA sheet also was prepared under the same pressure and temperature.

2.2.4 Cutting

The rectangular sheet was cut into the size of 2 cm x 2 cm for testing purpose later by using a cutter. The square shape samples were used for soil burial test and hygrothermal test.

2.3 Degradation Test

2.3.1 Soil Burial Test

To investigate the degradability of the incorporation of MCC in PLA composite, soil burial test was carried out. In order to ensure a good water and air circulation, moist soil was placed into a perforated container [17]. Three pieces of the sample of each formulation were weighed to get the initial weight, $W_0$and buried in the soil at a depth of 10 cm with horizontal distance in between the sample of 3 cm at room temperature [18]. Three pieces of the sample were used in order to get the average reading. The medium was sprayed with water to keep the compost in moist condition for a better microbial activity [19]. The samples were weighed at eight different intervals which were on the 1st, 3rd, 5th, 7th, 14th, 21st, 28th and 58th day in order to investigate the degradation rate. Before that, the samples were wiped to remove any leftover soil dirt and dried to constant weight in the oven for 4 hours at temperature of 70℃ to remove moisture [14]. The average weight of the samples were calculated in order to calculate the percentage of weight loss by using Eq. (1) [14]:

$$Percentage\ of\ weight\ loss\ (\%) = \frac{W_0 - W_t}{W_0} \times 100\% \quad (1)$$

where W_0 is the initial weight of the samples in g and W_t is the final weight in g.

2.3.2 Hygrothermal Test

The samples were immersed in a water bath at a temperature of 58℃ [11]. This temperature was chosen because PLA shows strong degradation behaviour at this temperature. The initial weight of the sample was taken prior to the test. The samples then were weighed at six different intervals which were on the 1st, 3rd, 5th, 7th, 10th, 14th day in order to investigate the degradation rate. The physical alteration of the samples was observed as well as their weight loss. By using the data collected, percentage of weight loss was calculated by using Eq. (1).

2.4 Characterization

2.4.1 Scanning Electron Microscopy (SEM)

To study the morphology of the polymer sheets after degradation, SEM can be carried out by observing each of the samples under a scanning electron microscope (Model : Quanta 400 FEG). In order to improve the conductivity, the samples were coated with gold by using the vacuum sputter-coater. The microscope was operated at 20 kV and the images were taken at magnification of 1500x, 500x and 200x [20]. The morphology evolution was observed to confirm the degradability of the polymer sheets.

2.4.2 Differential Scanning Calorimetry (DSC)

The melting temperature of PLA/MCC polymer sheets were studied by using a differential scanning calorimeter (Model: Perkin Elmer DSC 8500) which was equipped with refrigerant cooling system. The samples were weight to approximately 10 mg before being heated at the temperature range of 40 to 200 ℃ and cooled back to 40 ℃ at rate of 10 $℃/min$. The samples were sealed into aluminum pans. An empty aluminum pan was used as a reference sample. Melting point temperature, T_m and glass transition temperature, T_g were determined from the heating cycle.

3. Results and discussions

Soil burial test is carried out to test the biodegradability or compost degradation of the polymer sheets towards microorganism. Compost degradation can be divided into two processes. The first process involves the hydrolyzation of the high molecular weight of PLA to lower molecular weight which can be affected by moisture and temperature. Then, the ester group can turn into alcohol and acid once the microorganisms catalyze the degradation. The lower molecular chain will be converted into water, carbon dioxide and humus [18].

The degradation due to hygrothermal causes by the osmotic cracking which will generate holes on the sheets. This will create a path for water diffusion. Besides that, carboxyl group possesses a strong water affinity causing it be more readily to be degraded when exposed to water [11]. While being immersed in water, the polymer will be penetrated by the water molecules. Hydrolytic degradation causes the long polymer chain to break into shorter water soluble fragments.

3.1 Weight loss

Fig. 1 indicates the percentage of weight loss (%) as a function of time in days for soil burial test. The sample of 30% MCC has the highest weight loss with 21.7% followed by 20% MCC and 10% MCC. The weight loss is a factor that determines the biodegradability. The addition of MCC filler into PLA matrix allows the penetration of microorganisms and water through the filler/matrix interface which subsequently caused the breakdown of low molecular weight fragment. Pure PLA has the lowest percentage with only 4.3% which can be concluded as almost no weight loss due to its slows rate of hydrolysis at ambient temprature [21]. The first 28 days shows that the degradation rate increases faster than the last 30 days. After 58 days of degradation, the colour of the samples gradually fades from dark brown to light brown. However, the transparent sheet of pure PLA remains the same. This proves that the addition of MCC into PLA matrix enhance its biodegradability. Theoretically, there are two stages involved with the first one called the depolymerization. The macromolecules will break down into shorter chain which usually occurs at the outer part of the organism. The edge of sample started to rupture at the end of the first month. However, the difference of the sheets after degradation is still insignificant for this test. It might require longer period for the sample to fully degrade.

Fig. 2 indicates the percentage of weight loss (%) as a function of time in days for hygrothermal test at 58 ℃. The sample of 30% MCC has the highest weight loss with 23.5% followed by 20% MCC and 10% MCC. Pure PLA has the lowest percentage with only 4.9% which is more or less the same as soil burial test. The degradation rate increases linearly with time. The percentage weight loss for this test is higher than the

soil burial test. The samples became brittle after just 3 days. The brittleness increases with time. At the end of the second week, the samples are broken into pieces. For this test, the colour of the samples also faded. However, in contrast with the result obtained for soil burial, pure PLA sample turned to white opaque sheet instead of staying transparent. This is due to the exposure of the prolong heat.

From the degradation test, it is reported that the samples of 30% MCC shows the best degradation property. Thus, these samples together with the pure PLA samples are chosen for further analysis

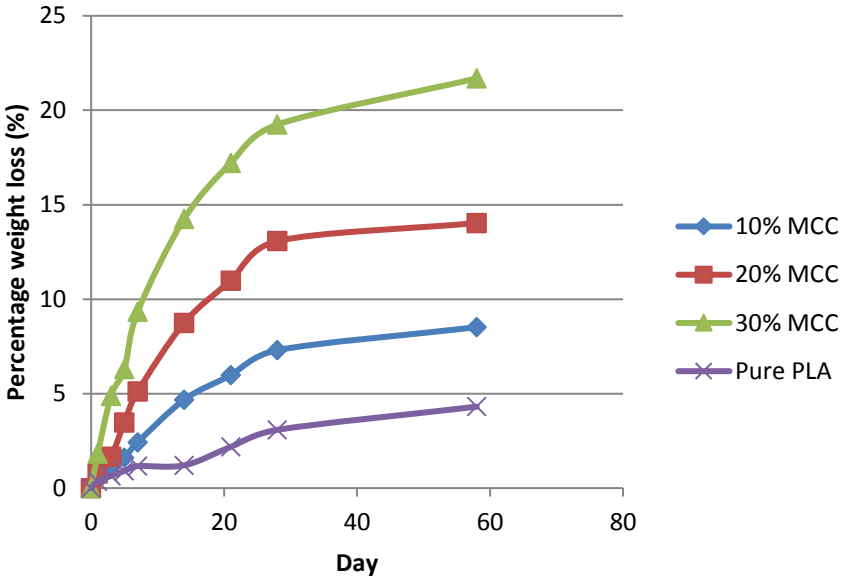


Figure 1. The percentage weight loss for soil burial test

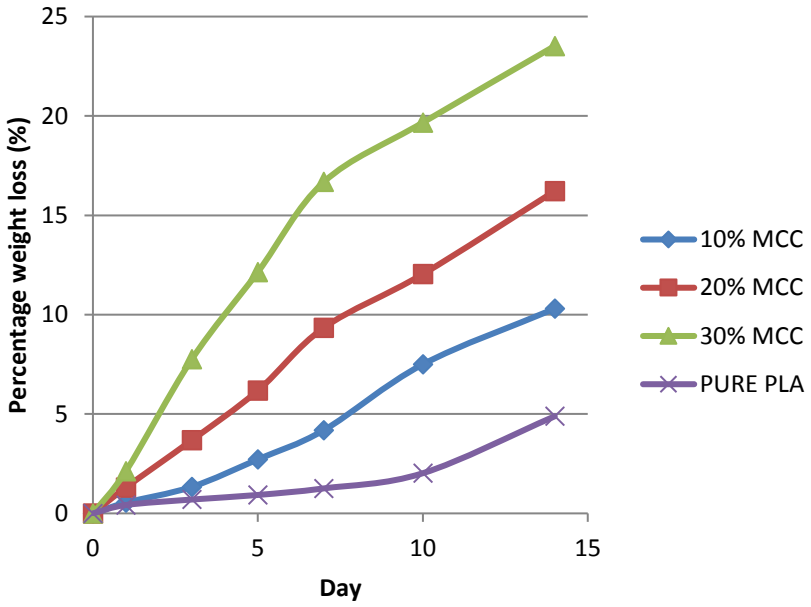


Figure 2. The percentage weight loss for hygrothermal test

3.2. SEM Analysis

SEM is carried out in order to observe the morphology of the samples after degradation takes place. At a certain magnification and resolution, SEM gives a clear image on how a polymer would be like when it undergoes physical changes.

Fig. 3 shows the SEM images of the surface of the pure PLA sheet and 30% MCC sample where as Fig. 4 is the cross sectional of both types of sample. (A) shows the PLA sample SEM image before degradation takes place. It can be seen that the surface is quite smooth with no void and crack. (B) is the image of PLA sheet after 58^{th} days of soil burial test. The surface of the sample becomes rough. The cross sectional image shows some microorganisms embedded on the top left. (C) shows the sample image after hygrothermal test. There are holes and water void presence on the sample. (D) shows the 30% MCC sample before degradation. The dispersion of MCC onto PLA can be clearly seen. There is also no hole formed which shows that it is a homogenous mixture. The image of 30% MCC after soil burial test is portrayed in (E) whereas (F) shows the 30% MCC after hygrothermal test. A few tiny holes are formed on both sheets. The cross sectional image shows that the matrix is disintegrated on the top left.

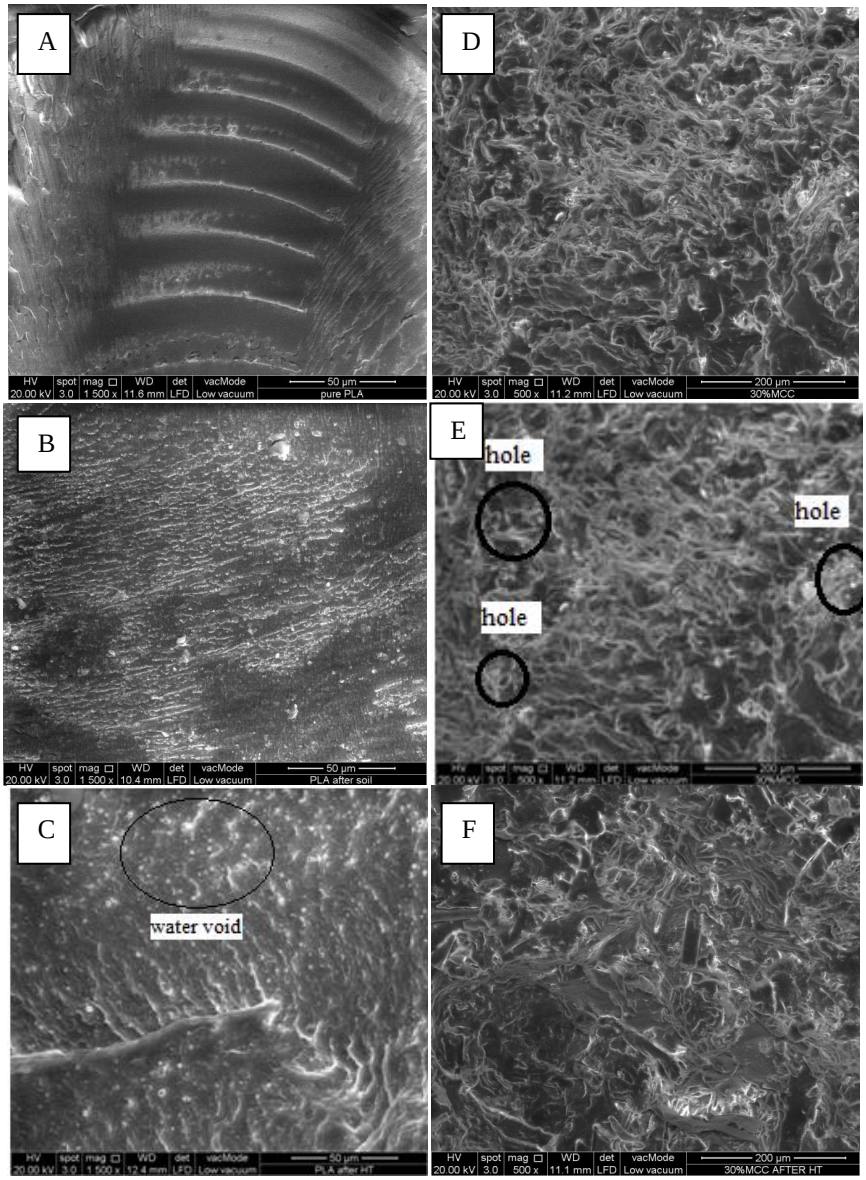


Figure 3. SEM images of the surface of the samples of (A) pure PLA sample before degradation, (B) pure PLA sample after soil burial test, (C) pure PLA sample after hygrothermal test, (D) 30% MCC sample before degradation, (E) 30% MCC sample after soil burial test and (F) 30% MCC sample after hygrothermal test

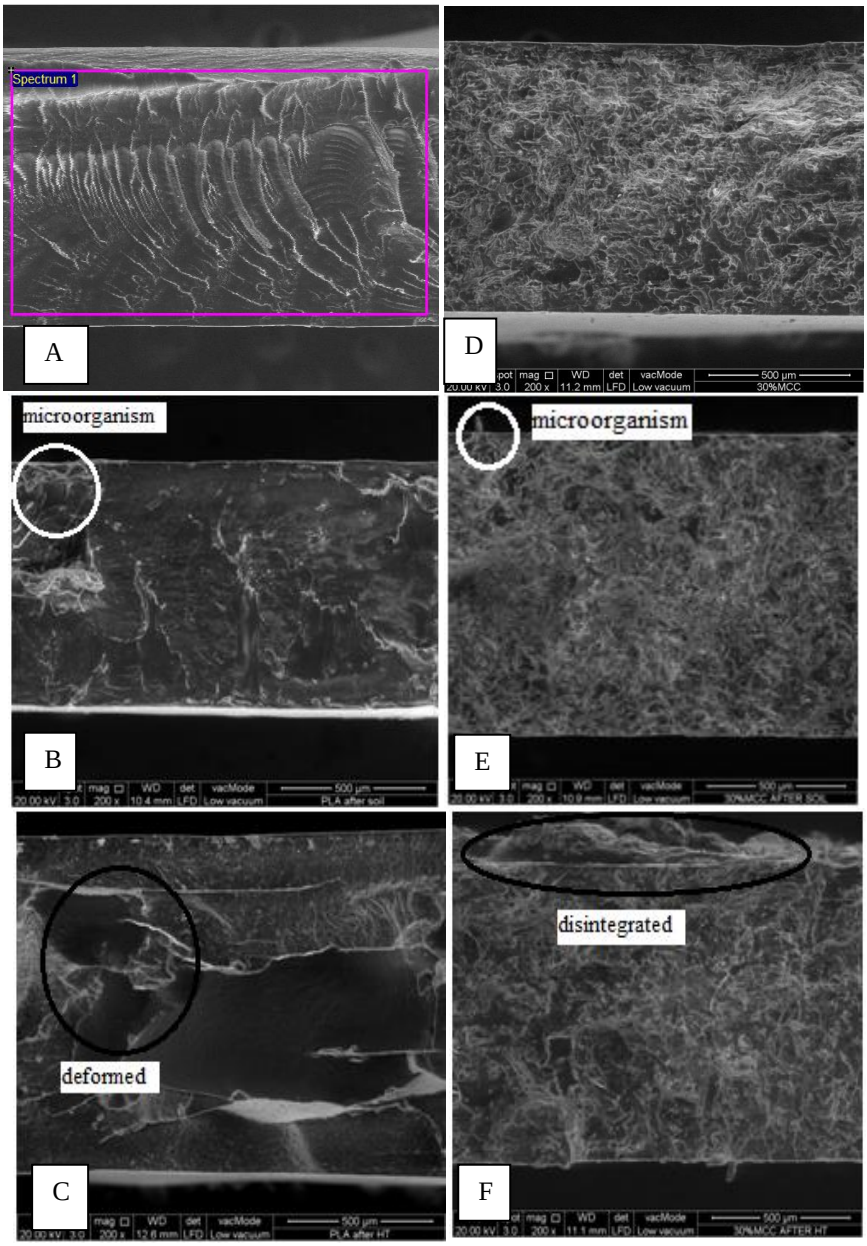


Figure 4. SEM images of the cross section of the samples of (A) pure PLA sample before degradation, (B) pure PLA sample after soil burial test, (C) pure PLA sample after hygrothermal test, (D) 30% MCC sample before degradation, (E) 30% MCC sample after soil burial test and (F) 30% MCC sample after hygrothermal test

3.3 DSC Analysis

Differential scanning calorimetry (DSC) analysis is used to study the melting and crystallization behaviours of PLA and PLA/MCC composites. 10 mg of samples were heated at temperature range of 40 to 200 ℃. Fig. 6 shows the DSC thermogram for pure PLA where as Fig. 7 is the DSC thermogram for 30% MCC. It shows the peak that indicates the glass transition temperature, T_g of the samples. T_g depends on a few factors such as intermolecular interactions, the molecular weight, steric effects, the chain flexibility, the cross linking density and the branching [22]. Theoretically, the T_g of PLA is around 60 ℃ [23]. From Figure 6, T_g of PLA before degradation is 64.8℃.

Upon degradation, the T_g has shifted to lower temperature. The shifting for hygrothermal test is greater than the soil burial test. This again proves that PLA are prone to degrade under prolong heating when compare to biodegradation. The incorporation of MCC into PLA does not give significant changes to its T_g. This is reported by previous research conducted in which the addition of MCC hardly affects the T_g value of PLA [24]. The $T_g$of 30% MCC sample is 62.7 ℃. It shifted to much lower temperature after degradation. Tg is one of the indication of the chain mobility. In this study, Tg is shifted to lower temperature after degradation, could be attributed to the hydrolysis of the polymer chain, leading to a decrease in molecular weight. Another possible reason in the deduction of Tg, is the penetration of moisture from the surrounding into the PLA composite. Water moisture can bring plasticizing effect and softening of polymer matrix. Table 2 shows the summary of the T_g for each sample.

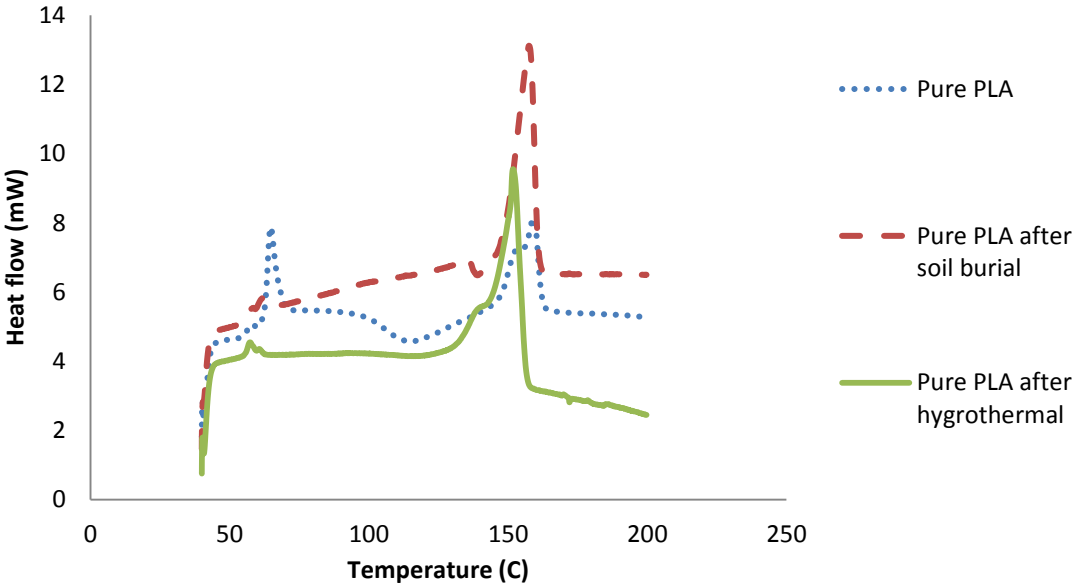


Figure 6. DSC analysis of pure PLA

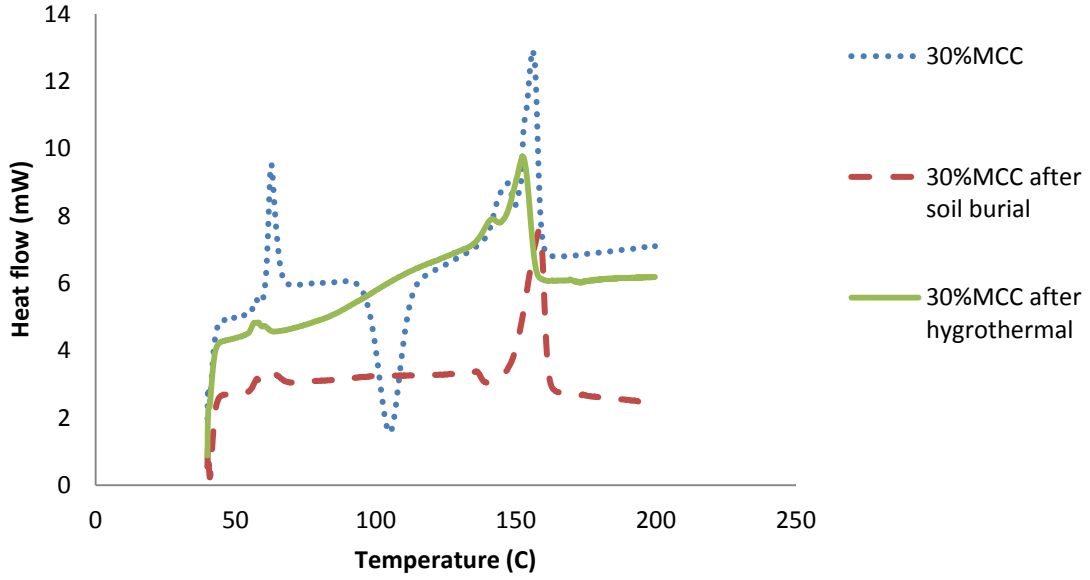


Figure 7. DSC analysis of 30% MCC

Table 2. T_g of the samples before and after degradation

Sample	Glass transition temperature, T_g (℃)
Pure PLA	64.8
Pure PLA after soil burial	63.7
Pure PLA after hygrothermal	57.3
30% MCC	62.7
30% MCC after soil burial	61.9
30% MCC after hygrothermal	55.5

4. Conclusions

The biodegradation and hygrothermal degradation behavior of microcrystalline cellulose filled polylactic acid composite have been successfully evaluated. The incorporation of MCC into PLA indeed helps to enhance the degradation. From the weight loss data, 30% MCC composites showed the highest weight loss percentage with 21.7% for soil burial test and 23.5% for hygrothermal test when compare to 20% MCC composites and 10% MCC composites. This indicated that the higher the MCC content in the polymer matrix the faster the degradation rate. The biocomposites also undergo much faster weight loss under prolong heating (hygrothermal test). Holes and voids with some microorganism attached on the surface of the samples can be seen in the soil burial SEM images. Besides that, the outer layer of the samples was disintegrated upon degradation. From the DSC analysis, the glass transition temperature, T_g of pure PLA samples shifted from 64.8 ℃ to lower temperature which is 63.7 ℃ after soil burial test and 57.3 ℃ after hygrothermal test. The addition of 30% MCC reduced the T_g to 62.7 ℃. It is further shifted to 61.9 ℃ after soil burial test and 55.5 ℃ after hygrothermal test. It can be concluded that the incorporation of MCC into PLA matrix enhanced its degradability thus can be used in the industry in order to preserve the environment.

Acknowledgements

I would like to take this opportunity to express my profound gratitude to my supervisor, Dr. Pang Ming Meng for her constant encouragement, helpful advices and guidance while carrying out this research. I would also like to thank Miss Lithnes Kalaivani and Miss Fariha from School of Engineering Lab and also Miss Sharon from School of Pharmacy Lab for their help in completing the experiments. Not to forget to Mr. Albert Tshai Kim Yeow from Nottingham University for the SEM analysis. Last but not least, I am also grateful for the chance given by Taylor's University for me to complete this research.

References

[1] K. Madhavan Nampoothiri, N. R. Nair, and R. P. John, "An overview of the recent developments in polylactide (PLA) research," *Bioresour. Technol.*, vol. 101, no. 22, pp. 8493–8501, 2010.
[2] G. E. Luckachan and C. K. S. Pillai, "Biodegradable Polymers- A Review on

Recent Trends and Emerging Perspectives," *J. Polym. Environ.*, vol. 19, no. 3, pp. 637–676, 2011.

[3] M. Shimao, "Biodegradation of plastics.," *Curr. Opin. Biotechnol.*, vol. 12, no. 3, pp. 242–7, 2001.

[4] A. A. Shah, F. Hasan, A. Hameed, and S. Ahmed, "Biological degradation of plastics: A comprehensive review," *Biotechnol. Adv.*, vol. 26, no. 3, pp. 246–265, 2008.

[5] G. Thoorens, F. Krier, B. Leclercq, B. Carlin, and B. Evrard, "Microcrystalline cellulose, a direct compression binder in a quality by design environment-A review.," *Int. J. Pharm.*, vol. 473, no. 1–2, pp. 64–72, 2014.

[6] Y. Tokiwa and B. P. Calabia, "Biodegradability and biodegradation of poly(lactide)," *Appl. Microbiol. Biotechnol.*, vol. 72, no. 2, pp. 244–251, 2006.

[7] T. Bayerl, M. Geith, A. a. Somashekar, and D. Bhattacharyya, "Influence of fibre architecture on the biodegradability of FLAX/PLA composites," *Int. Biodeterior. Biodegradation*, vol. 96, pp. 18–25, 2014.

[8] E. Fortunati, D. Puglia, J. M. Kenny, M. Minhaz-Ul Haque, and M. Pracella, "Effect of ethylene-co-vinyl acetate-glycidylmethacrylate and cellulose microfibers on the thermal, rheological and biodegradation properties of poly(lactic acid) based systems," *Polym. Degrad. Stab.*, vol. 98, no. 12, pp. 2742–2751, 2013.

[9] Y. X. Weng, Y. J. Jin, Q. Y. Meng, L. Wang, M. Zhang, and Y. Z. Wang, "Biodegradation behavior of poly(butylene adipate-co-terephthalate) (PBAT), poly(lactic acid) (PLA), and their blend under soil conditions," *Polym. Test.*, vol. 32, no. 5, pp. 918–926, 2013.

[10] P. Stloukal, A. Kalendova, H. Mattausch, S. Laske, C. Holzer, and M. Koutny, "The influence of a hydrolysis-inhibiting additive on the degradation and biodegradation of PLA and its nanocomposites," *Polym. Test.*, vol. 41, pp. 124–132, 2015.

[11] M. Deroiné, A. Le Duigou, Y.-M. Corre, P.-Y. Le Gac, P. Davies, G. César, and S. Bruzaud, "Accelerated ageing of polylactide in aqueous environments: Comparative study between distilled water and seawater," *Polym. Degrad. Stab.*, vol. 108, no. October, pp. 319–329, 2014.

[12] V. Berthé, L. Ferry, J. C. Bénézet, and a. Bergeret, "Ageing of different biodegradable polyesters blends mechanical and hygrothermal behavior," *Polym. Degrad. Stab.*, vol. 95, no. 3, pp. 262–269, 2010.

[13] R. M. Rasal, A. V. Janorkar, and D. E. Hirt, "Poly(lactic acid) modifications," *Prog. Polym. Sci.*, vol. 35, no. 3, pp. 338–356, 2010.

[14] Y. Dong, A. Ghataura, H. Takagi, H. J. Haroosh, A. N. Nakagaito, and K.-T. Lau, "Polylactic acid (PLA) biocomposites reinforced with coir fibres: Evaluation of mechanical performance and multifunctional properties," *Compos. Part A Appl. Sci. Manuf.*, vol. 63, pp. 76–84, 2014.

[15] K. Oksman, M. Skrifvars, and J. F. Selin, "Natural fibres as reinforcement in polylactic acid (PLA) composites," *Compos. Sci. Technol.*, vol. 63, no. 9, pp. 1317–1324, 2003.

[16] A. N. Frone, S. Berlioz, J.-F. Chailan, and D. M. Panaitescu, "Morphology and thermal properties of PLA–cellulose nanofibers composites," *Carbohydr. Polym.*, vol. 91, no. 1, pp. 377–384, 2013.

[17] H. C. Obasi, I. O. Igwe, and I. C. Madufor, "Effect of Soil Burial on Tensile Properties of Polypropylene / Plasticized Cassava Starch Blends," vol. 2013, pp. 14–18, 2013.

[18] K. Fukushima, C. Abbate, D. Tabuani, M. Gennari, and G. Camino, "Biodegradation of poly(lactic acid) and its nanocomposites," *Polym. Degrad. Stab.*, vol. 94, no. 10, pp. 1646–1655, 2009.
[19] M. Karamanlioglu, A. Houlden, and G. D. Robson, "Isolation and characterisation of fungal communities associated with degradation and growth on the surface of poly(lactic) acid (PLA) in soil and compost," *Int. Biodeterior. Biodegradation*, vol. 95, pp. 301–310, 2014.
[20] L. Yu, Z.-X. Chen, X. Tong, K. Li, and W.-W. Li, "Anaerobic degradation of microcrystalline cellulose: Kinetics and micro-scale structure evolution," *Chemosphere*, vol. 86, no. 4, pp. 348–353, 2012.
[21] G. Gorrasi and R. Pantani, "Effect of PLA grades and morphologies on hydrolytic degradation at composting temperature: Assessment of structural modification and kinetic parameters," *Polym. Degrad. Stab.*, vol. 98, no. 5, pp. 1006–1014, 2013.
[22] O. P. Ek, "Influence of different types of commercially available microcrystalline cellulose on degradation of perindopril erbumine and enalapril maleate in binary mixtures," vol. 62, pp. 515–528, 2012.
[23] D. Shen, R. Xiao, S. Gu, and H. Zhang, "The Overview of Thermal Decomposition of Cellulose in Lignocellulosic Biomass," 2013.
[24] S. Joseph, E. Deenadayalan, and P. A. Mahanwar, "Studies on Melt Processable Biocomposites of Polylactic Acid."

Extraction of High Quality Silica and Carbon from Rice Husk

Aisyah Fadhilah Mahmood Azmy[1*], Ting Lee[1], Wong Wai Yin[1]

School of Engineering, Taylor's University, Malaysia

*aisyahazmy@hotmail.com

Abstract

Utilisation of rice husk waste helps to solve the disposal and pollution problems in the rice milling industry. Rice husk was brought into attention because it can be found abundant and easily obtain since Malaysia is one of the rice producing countries. In this study, rice husk was used as a raw material for the production of silica and carbon. Combustion of rice husk produced rice husk ash, which highly consists with silica. Process continued with sodium hydroxide extraction and followed by hydrochloric acid precipitation to obtain purer silica. The byproduct from this method is carbon which further examine its surface area and adsorption capacity by using Brunuer-Emmet-Teller (BET) surface area and N_2 adsorption isotherms respectively. Silica obtained was characterised in terms of silica content and crystallise phase change by energy dispersive X-ray (EDX) spectrometer and X-ray difrractometer (XRD) respectively. It was found that silica obtained is amorphous silica and EDX analysis showed silica contents was 30% Si atomic**.** Carbon obtained is mesoprous with BET surface area 30 m^2/g.

Keywords: Rice husk, Rice husk ash, Combustion, Alkaline extraction, Silica, Carbon

1. Introduction

Globally, 1.2 billion tonnes of rice husk is produced and in Malaysia, there are about 470,000 tonnes per year [1,2]. Generally, the abundant rice husk wastes are decomposed and burned in open fields resulting the waste product called rice husk ash. The major components of rice husk are hemicellulose, cellulose and lignin, which are all organic materials. But after combustion the white ash obtained and it contains 61% of silica and, 10-40% carbon and minor other mineral composition [3]. Consequently, the weak disposal practices promote the emission of greenhouse gas and ash formed from burning is inevitable. The high emission rates of various gasses and fine airborne particulate matter would deteriorate air quality and exert impact on public health.

Since the major component in rice husk ash is amorphous silica, many authors have concluded that rice husk is an excellent source of silica and it can be economically viable raw material [4]. Most study has reported that the ash properties make it possible to use as an alternative source in the production of silicates and silica [5]. Silica produced by rice husk ash is widely used in the glass, ceramics, and cement as a major component and in pharmaceuticals, cosmetics, and detergents industries as a bonding and adhesive agents [3,6,7]. Silica also has been used as a major precursor for a variety of inorganic and organometallic materials, which have applications in synthetic chemistry as catalysts, and in thin films, or coatings for electronic and optical materials [3,8]. Hence, rice husk can be value added from low cost raw biomass to high quality silica with good commercial value.

There are various of methods to produce silica from rice husk ash such as combustion, microwave hydrothermal processes, flame synthesis and micro emulsion methods, which are capable of producing in highly porous and amorphous silica [9,10]. Besides, many authors have concluded that at temperature 500 to 1400 °C white ash can be obtained approximately 92 – 97 wt% silica and left with carbon residue [6,11]. By undergo thermal treatment it proved to be effective to remove most of the minerals and metallic impurities. Further the step with acid or alkaline leaching, purer silica can be obtained [3,5,12-13]. Based on U. Kalapathy study, he discovered a decade ago a method to extract silica and the method had successfully produced 91% silica by using alkaline extraction. He continued the process with acid precipitation and produced silica xerogels which has 93% silica content [5]. As his production method at simple low energy chemical method and could be done at laboratory level, his method had been a referenced in this study as a subsequent step to produce purer silica after combustion of rice husk. The byproduct of alkaline extraction method after silica is obtained is carbon biochar which mainly contains carbon and unburnt components prior to combustion. Hence additional investigation required to analyse the property of the carbon and discuss its potential for commercial application.

Hence, by extracting silica from RHA, it will contribute as one of the alternative strategies for sustainable development due to the conversion of biomass-derived into a useful chemical. Therefore, the utilisation of biomass waste would strive for environmental preservation and potentially could avoid excess amount of RHA produced globally. In the present study, the production of high quality silica and carbon simultaneously using combustion and alkaline extraction method were discussed targeted for application that fit their characterisation. Therefore, the main objectives of this study are:

I. To study the effect of combustion temperature on the yield of silica and carbon.
II. To investigate on the physical properties of silica and carbon extracted from rice husk.

2. Experimental

2.1 Rice husk ash preparation

Rice husk was collected from Chantika Kilang Beras Sdn. Bhd., Kedah, Malaysia, followed by washing with distilled water to remove dust. Only the floated rice husk on the water surface was collected as dirt and dust were settled at the bottom. After washing, the clean rice husk was dried in air oven at 110 °C for 24 hours. The

dried rice husk was ground into a powder within the size of 0.5 mm to increase rice husk surface area for better heat distribution for combustion process. The 100 g of rice husk powder was weighed and placed into flat alumina crucibles for combustion process. Combustion of rice husk powder was conducted in muffle furnace in the presence of air at four different temperature, 400 °C, 600 °C , and 800 °C for 2 hours and heat rate 10 °C min^{-1}. Upon combustion process the colour changes and weight loss were recorded. The three different temperatures representing three different samples named with RHA 400, RHA 600 and RHA 800 respectively. Rice husk and all RHA samples were analysed using energy dispersive X-ray (EDX) spectrometer.

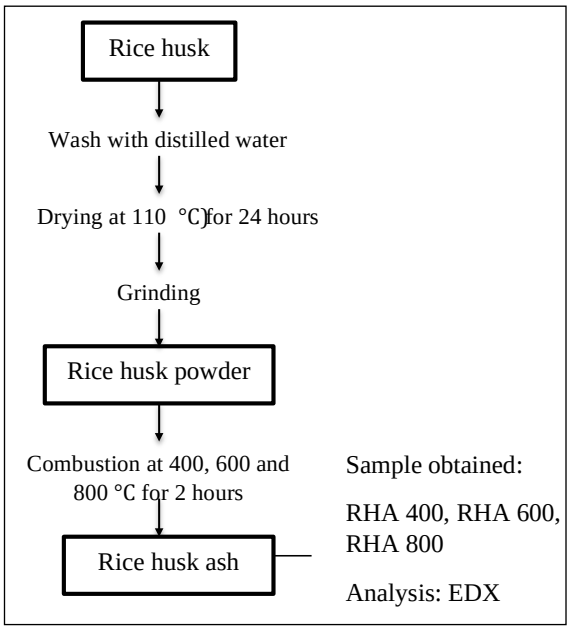


Figure 1. Flow chart for preparation of RHA samples.

2.2 Extraction of silica and carbon

For each sample, 60 mL of 1M NaOH was added to 10 g of RHA in a flask and boiled for 1 h with constant stirring at 500 rpm using hotplate stirrer. This step will dissolve silica with the alkaline and produce sodium silicate solution. After that, the solution was filtered through Whatman No. 41 ashless filter paper and separate silica filtrates (liquid form) and carbon residues (solid form). The carbon residue was washed with 100 ml of boiling water, filtered and clean carbon residue was dried in the oven at 80 °C for 12 hours. Carbon obtained was named with C 400, C 600 and C 800. All the carbon sample was characterised by Brunuer-Emmet-Teller (BET) surface area, pore volume and pore diameter. The measurement of the pore characteristics was carried out using N_2 adsorption.

Proceed with silica filtrate, which was then titrated with 1M HCl to pH 7 with constant stirring. Gels were started to form when it reached pH 10 and when it reached pH 7, the silica gels were allowed to age for 18 hours. After aging process, deionsed water was added and gels were broken to produce slurry. Slurries were then centrifuge at 2500 rpm for 15 min, and clear supernatants were removed. Gel washing was repeated and silica gels were dried at 80 °C for 12 hours. Upon this step, silica xerogel was produced and washing step was repeated with 50 mL deionised water. After that,

the solution was filtered through Whatman No. 41 ashless filter paper and separates silica xerogel and water. Finally silica xerogel was dried at same temperature and solid purified silica was produced. The silica obtained was named with Si 400, Si 600 and Si 800. The silicon content of the Si 800 samples was analysed using energy dispersive X-ray (EDX) and compared with commercial silica that was purchased containing 98% silica purity. The commercial silica that used in this project was Sebangun's silica sand which originated Sarawak, East Malaysia. This sand is now reputed to be one of the most sought-after raw materials by glass producers. Furthermore, the crystalline structure of Si 800 was examined by X-ray difrractometer (XRD) which performed at radiation speed 2 ° min^{-1} from 10 to 90 ° at range of 2Θ with step time of 0.5 seconds.

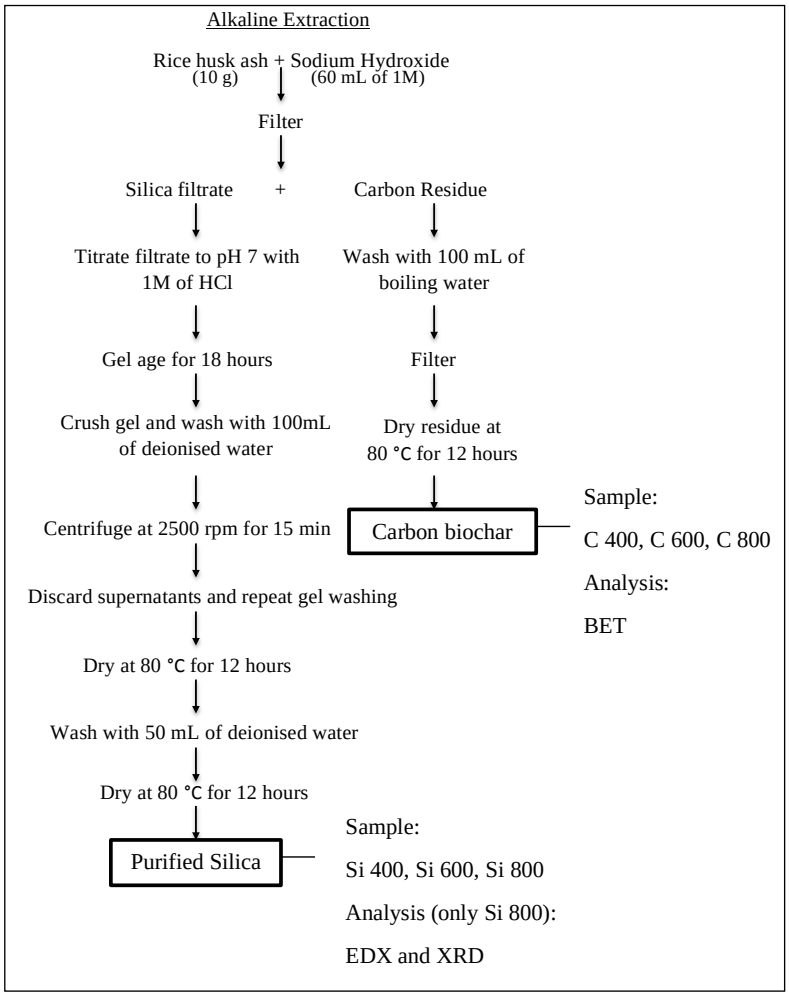


Figure 2. Flow diagram method to extract silica and carbon from RHA.

3. Results and Discussion

3.1 Stage I: Combustion of rice husk

3.1.1 Visual analysis of rice husk ash (RHA)

Grinded rice husk was combusted at different temperatures with fix initial amount of rice husk and fix soaking times in the muffle furnace. Table 1 shows the physical observation of rice husk after combustion in terms of its particle morphologies

and ash colour. From the observation, it can be clearly seen that to produce white ash RHA, high combustion temperature was required. Hence, for RHA 400 sample which combusted at lowest temperature set in this study had produced most black ash. The black colour was caused by the incomplete combustion and ash was mostly carbon residual. In contrast with RHA 800 sample which combusted at 800 °C and the soaking time at 2 h were sufficient to produce pinkish white ash. To produce pinkish white RHA was important at this initial stage of this study, as it was the first indicator that visually verifies the RHA sample contains mainly silica. Besides, it also indicates that the muffle furnace had function well with good air circulation in a way to supply oxygen to the rice husk sample and complete combustion could be achieved.

Table 1. Visual analysis of RHA particle after combustion.

Sample	Combustion temperature (°C)	Rice husk ash	Observation
RHA 400	400		• Coarse powder • Black char scattered amongst white ash • Incomplete combustion
RHA 600	600		• Finer powder than RHA 400 • White ash and char homogeneously mixed
RHA 800	800		• Finer powder than RHA 600 • Pinkish white ash

3.1.2 RHA yield after combustion

Figure 3 shows the weight losses percentage of rice husk against temperatures. When the combustion temperature was increased from 400 to 800 °C, it can significantly produced different amount of RHA. As the initial weight of raw rice husk was 100 g, it was recorded that only 12, 10 and 9 g produced after combustion. Higher combustion temperature causing increasing of weight loss hence produced lower amount of RHA. Generally only 10% to 13% of RHA was found after the combustion indicating that remaining organic compounds had combusted. At temperature 400, 600 and 800 °C, the total weight loss of 81, 85 and 86% were recorded respectively. At this stage, decomposition of biochar had occurred and RHA obtained were constituted of 15% silica and metallic impurities. The amount of RHA produced agreed well with the reviewed from literature of the thermogravimetric analysis (TGA) of rice husk [14–16] with the description as follows.

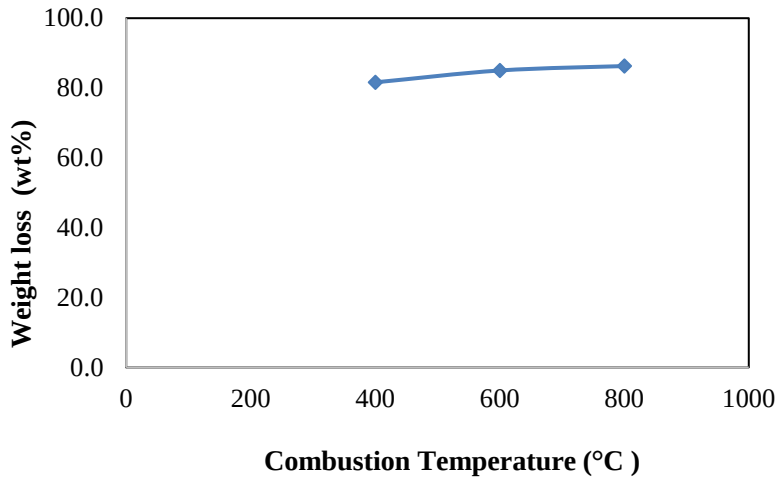


Figure 3. RHA weight loss wt% at different combustion temperatures.

Thermal degradation of rice husk sample can be generally categorized into three main regions that are dehydration of water vapor, degradation of hemicellulose and cellulose, decomposition of lignin and char. At the temperature of 100 to 150 °C removal of water vapor will occur within the husk pore structure. At approximately 200 to 400 °C, subsequent degradation of hemicellulose and cellulose of rice husk occurred. At this stage the presence of residual carbon was the highest due to the incomplete combustion of organic compounds and had converted into volatile matters. At the temperature of 400 to 600 °C, thermal degradation of lignin occurred but still had some unburnt carbonious material. Finally at the range of 600 to 1000°C, decomposition of biochar occurred and silica content was the highest. The RHA obtained generally amorphous silica and its white in colour. For this reason the combustion temperature of rice husk was set at 400, 600, and 800 °C in this study and demonstrated that amount of silica and carbon were strongly dependent on the combustion temperature.

3.2 Stage II: Alkaline extraction

3.2.1 Visual analysis of Silica and Carbon

The alkaline extraction of RHA to produce purified silica and carbon, the weight analysis of these end products were studied. Figure 4 shows that increasing combustion temperature significantly increased the silica yield and decreased the carbon yield. The increased of silica yield from 400 °C to 800 °C was 40% (from 11% to 51%) and the decreased of carbon yield was 41% (from 89% to 48%). At combustion temperature of 400 °C, it can be seen that amount of carbon was the highest at 89% (6.4 g) whereby at 800 °C the amount of silica was the highest at 51% (2.5 g).

Table 2. Visual analysis of silica and carbon after alkaline extraction

Sample	Weight	Silica	Observation	Sample	Weight	Carbon	Observation
Si 400	0.8 g		• Yellowish particle colour	C 400	6.4 g		• Black carbon • Semi-fine powder • Highest amount of carbon obtained compared to other samples
Si 600	1.2 g		• Whiter particle colour than Si 400	C 600	4.3 g		• Greyish-white carbon • Finer powder than C 400
Si 800	2.5 g		• Pinkish particle colour • Highest amount of silica obtained compared to other samples	C 800	2.3 g		• Whiter carbon and finer powder than C 800

3.2.2 Silica and Carbon yield

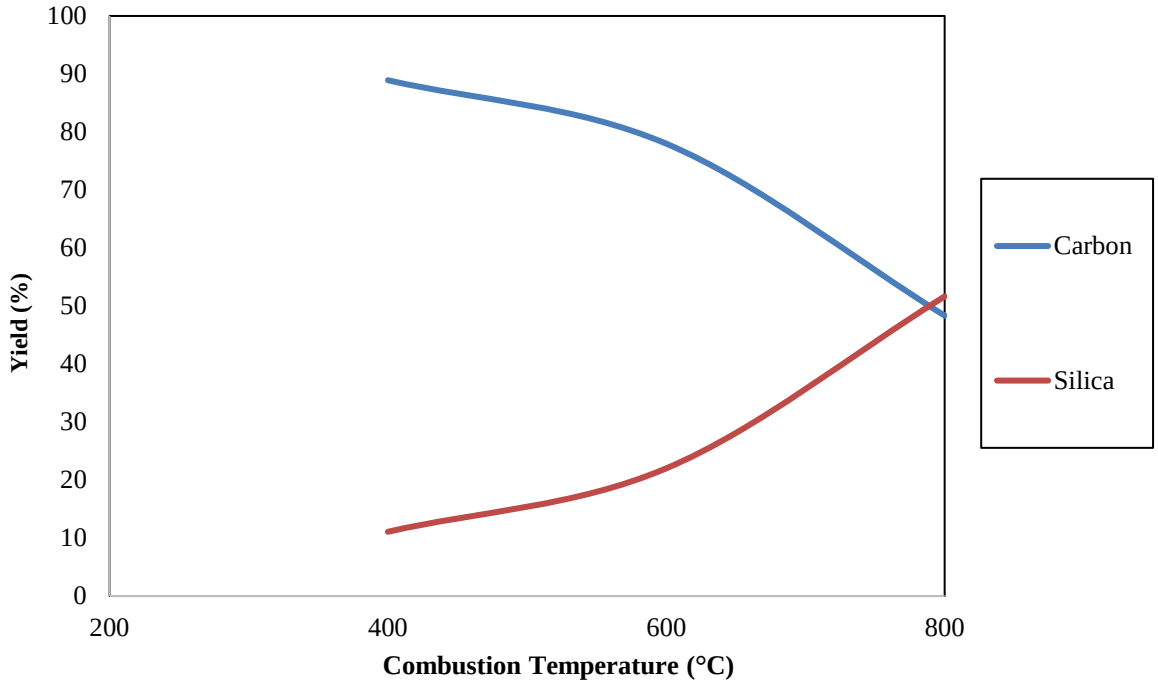


Figure 4. Silica and carbon yield% at different combustion temperature

3.3 RHA and silica extract composition

Prior to visual analysis that indicated that RHA 800 contains high silica as pinkish white ash produced and with alkaline extraction which Si 800 sample produced the highest silica yield, these were not yet a strong verification of its silica content. Hence, the silica content in sample rice husk ash and extracted silica (Raw rice husk, RHA 400, RHA 600, RHA 800 and Si 800) were estimated from the EDX spectrum based on assumption that the entire silicon element was in the form of silica. From figure 5 to 10 data showed major element silicon (Si) and minor element of carbon (C) with some metallic impurities. The silica and carbon content in each sample were depicting in a graph to demonstrate a clearer trend of its weight percent (wt%) changes with temperature and comparison with commercial silica could be made.

Figure 4 show that increasing combustion temperature significantly increased the silica content. The increment of silica content from a raw rice husk to RHA 800 was 14.3 wt% and further increment achieved after alkaline extraction with additional 0.9 wt%. Hence, this confirmed that silica extraction via alkaline extraction method was succeeded to extract out silica from the ash. The extracted silica sample, Si 800 contained 29.7 wt% silica was compared with commercial silica that had 36 wt%. The difference of 6.3% was the proof of the silica quality produced in this study compare with the commercial one which contain ~98% silica purity. The differed of the silica contain in Si 800 required for further study hence improvement of its quality and similarity silica content could be achieved. Apart from that, the silica produced in this study seems to be attractive resource of silica as only a small differ of its silica content compared to the commercial one. Application that requires less silica purity like, in concrete making would be an interesting option [4] .

In contrast with silica trend, a carbon composition reduced when increasing the combustion temperature. Hence, these result data support the fact that more volatile matter had combusted when increasing the temperature and left with silica component. RHA weight had reduced but resulting high amount of silica [14] .

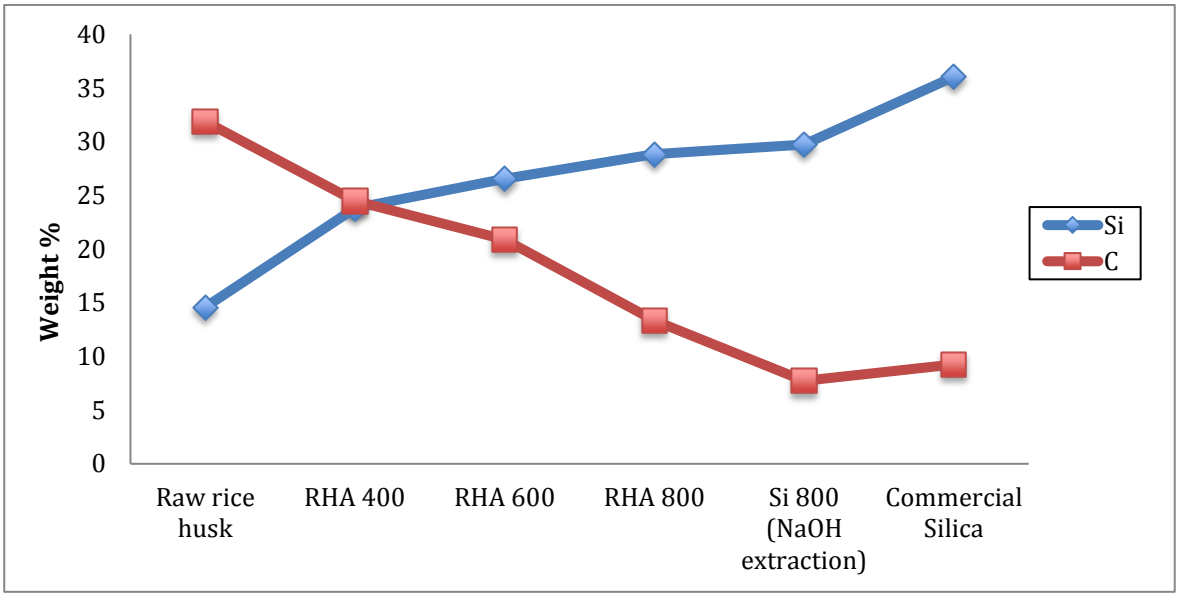


Figure 4. Silica and carbon weight wt% by RHA samples, extracted silica and commercial silica.

Table 3. EDX wt% composition of components in RHA samples and Si 800.

Sample	Si	C	O	K, Al	Na	Cl
Raw rice husk	14.59	31.87	53.3	0.24	-	-
RHA 400	25.65	24.5	51.35	0.35	-	-
RHA 600	26.53	20.88	51.04	1.25	-	-
RHA 800	28.84	13.35	57.24	0.57	-	-
Si 800	29.95	7.87	54.75	0.17	3.92	3.69
Commercial Silica	36.04	9.26	54.7	-	-	-

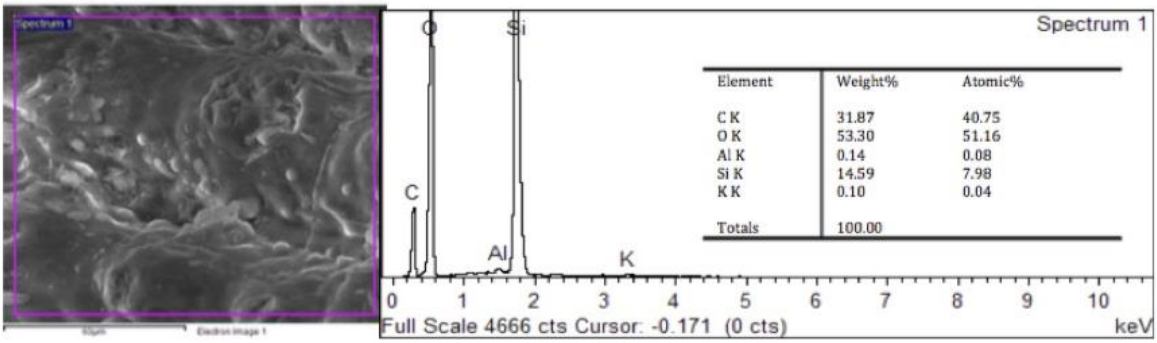


Figure 5. EDX spectrum of RH.

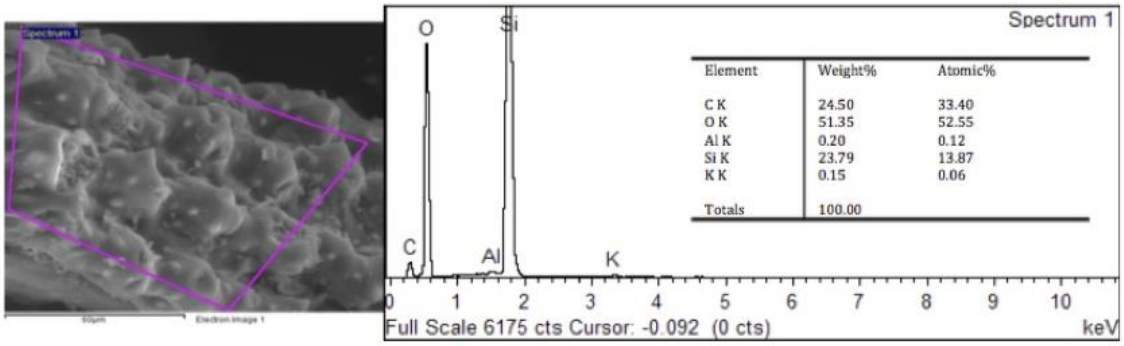


Figure 6. EDX spectrum of RHA 400.

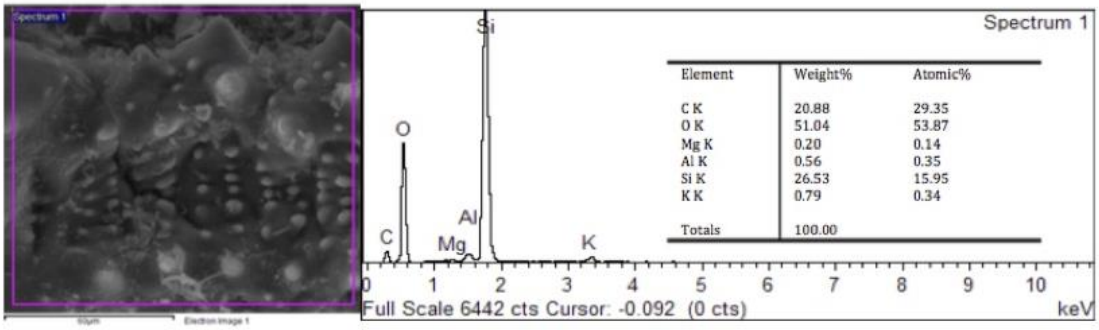


Figure 7. EDX spectrum of RHA 600.

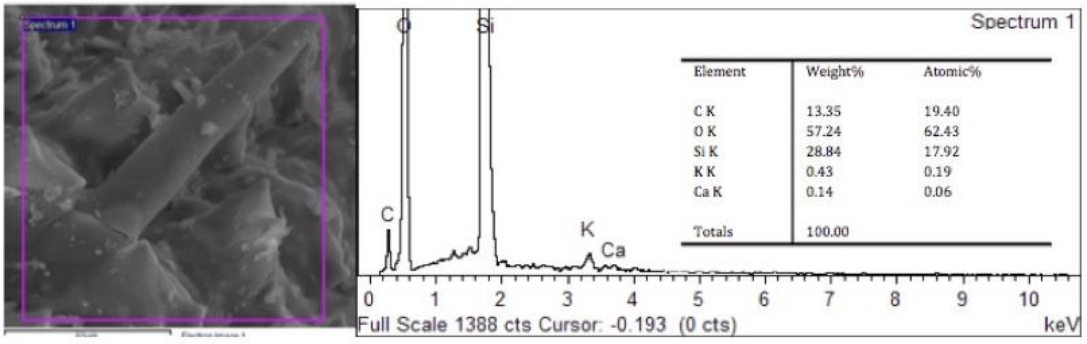


Figure 8. EDX spectrum of RHA 800.

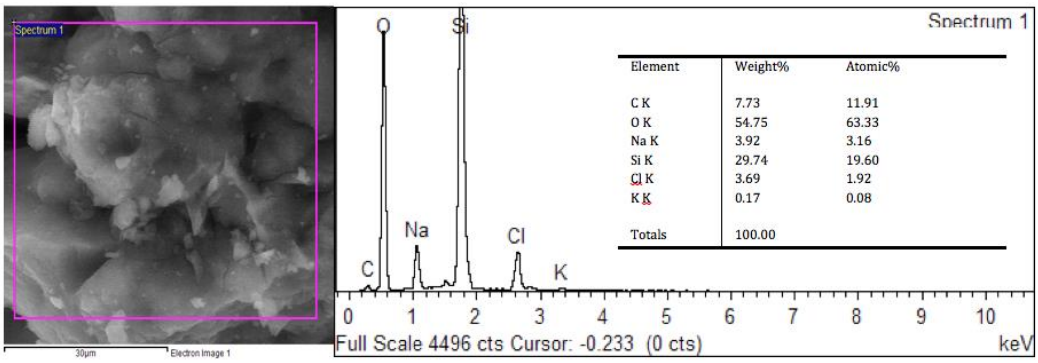


Figure 9. EDX spectrum of Si 800.

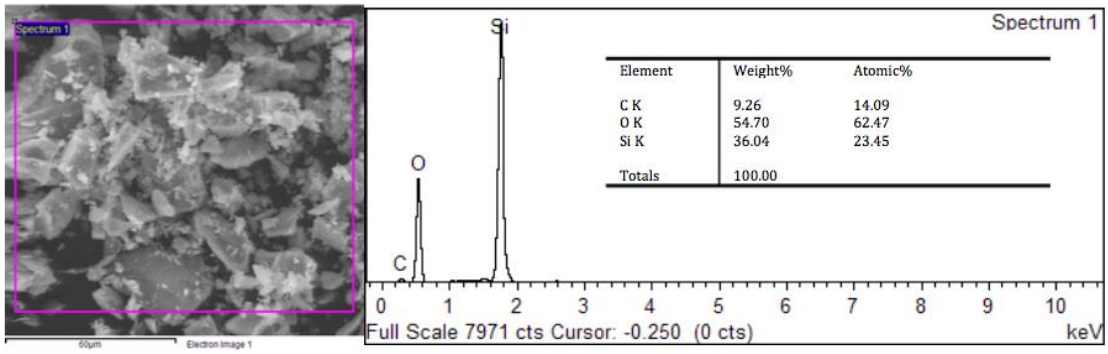


Figure 10. EDX spectrum of commercial silica.

3.4 Silica physical properties

The highest silica composition sample obtained in this study (Si 800) was further characterised by X-ray difrractometer (XRD) to examine its crystalline structure. It was essential to verify it, in a way to understand its physical and chemical properties. Hence, silica produced could accurately fulfill various of application needs. Figure 11 shows the XRD patterns of Si 800 and broad diffused peaks with the maximum intensity at 2Θ = 21.5 was observed, indicating the structure of silica present in the Si 800 remained amorphous. These results agree well with those obtained by other studies [11,12,17].

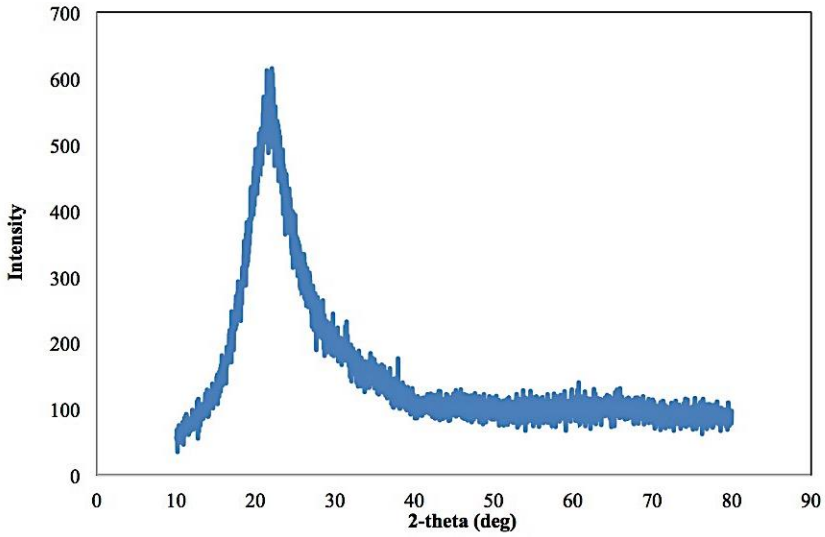


Figure 11. XRD diagram of Si 800.

3.5 Carbon pore structures

The BET surface area, pore diameter and pore volume of carbon were given in Table 4. C 800 had a maximum BET surface area and pore volume compared to other carbon samples which were at 30.2 m^2/g and 0.118 cm^3/g respectively. This indicates that combustion at 600 °C had effectively combusted hemicellulose and cellulose and decomposition of carbon was at maximum. Hence, the decomposition was leaving a high porous structure and high pore volume. In the other hand, the surface area was attributed to the amount of pore structure had been destroyed [13,19]. Besides, sample C 400 exhibited the highest pore diameter at 31.88 nm followed by sample C 800 at 23.56 nm. It was note worthy that when the pore diameter increases, the surface area and pore volume were reduced. From table also shows that all samples exhibited mesoporous as all the mesoporous values were higher than microporous values. This mesoporous property also supported by the evidence of N_2 adsorption isotherms shown in Figure 12.

The nitrogen adsorption isotherms of carbon samples were shown in Figure 12. For samples it can be seen that all samples isotherms were type IV according to IUPAC classification. This kind of behavior was associated with mesoporous materials [11,20]. Besides, according to the adsorption isotherms graph, the C 600 displayed larger amount of adsorption compared to other samples. However not much different of the adsorption capacity found among the carbon samples as no physical or chemical activation which may help to improve its adsorption capacity.

Table 4. Textual properties of carbon samples.

Textual Properties	C 400	C 600	C 800
BET surface area (m^2/g)	15.211	30.167	15.286
Micropore area (m^2/g)	5.691	3.011	4.685
External surface area (m^2/g)	9.520	27.156	10.765
Total pore volume (cm^3/g)	0.121	0.118	0.091
Micropore volume (cm^3/g)	0.003	0.001	0.002
Mesopore volume (cm^3/g)	0.119	0.117	0.089
Average pore diameter (nm)	31.88	15.71	23.56

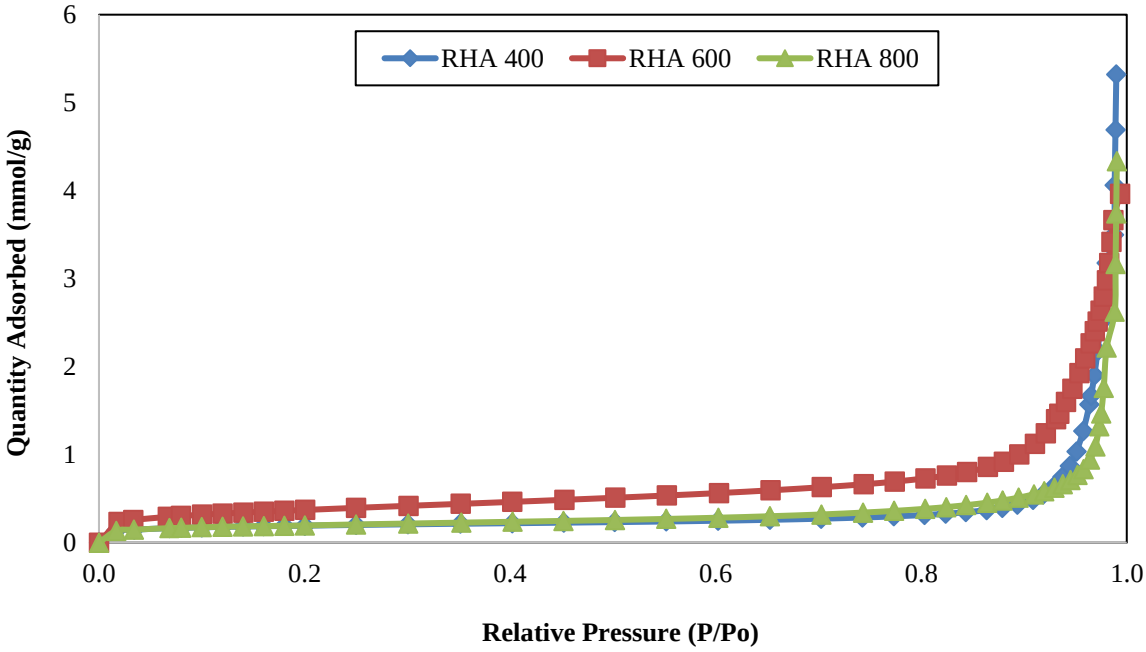


Figure 12. N_2 adsorption isotherms of carbon samples.

4. Conclusion

To conclude, combustion at low temperature had impressively produced amorphous RHA that rich in silica. The highest firing temperature at 800 °C, sample RHA 800 shows finer powder than other samples and pinkish white ash was obtained indicating ash is amorphous and rich in silica. Besides, it demonstrated highest percentage weight loss but it produced highest yield of silica due to total carbon burnout. In contrast with 400 °C, RHA 400 produced most carbon and least amount silica due the incomplete combustion. Hence, by set up combustion temperature at 400 to 800 °C, it revealed the stages of changes of silica and carbon yield due to thermal degradation of rice husk. Proceed with alkaline extraction the silica obtained as a solid silica by NaOH extraction was composed of high purity, mesoprous particles that had an amorphous structure. As increasing combustion temperature significantly increased the silica content so does with alkaline etxratcion. The increment of silica content from a raw rice husk to RHA 800 was 14.3 wt% and further increment achieved after alkaline extraction with additional 0.9 wt%. Hence, this confirmed that silica extraction via

alkaline extraction method was succeeded to extract out silica from the ash. The extracted silica sample, Si 800 contained 29.7 wt% silica was compared with commercial silica that had 36 wt%. The difference of 6.3% was the proof of the silica quality produced in this study compatible with the commercial one which contain ~96% silica purity. Therefore, extraction of silica and carbon from rice husk will contribute as one of the alternative strategies for sustainable development due to the conversion of biomass-derived into a useful high value silica. Therefore, the utilisation of biomass waste would strive for environmental preservation and potentially could avoid excess amount of rice husk produced globally.

Furthermore, silica appeared to be amorphous which is suitable in the cement and construction industries. Silica can be chemically reacted with calcium hydroxide to form compounds possessing cementitious properties. The ultrafine size of the amorphous silica makes it excellent filler which improve the strength to the concrete [4]. In the future work, to study the amorphous property of silica affect the mechanical property of the concrete is interesting area of study subsequent after this research finding. Besides, extracted carbon pore structures trend could perceive among carbon samples but in terms of their adsorption capacity the trend was almost the same. In the future work, additional process required to improve carbon adsorption capacity.

References

[1] M. K. Baharuddin (2014) "Paddy Production Survey Report Malaysia," Department of Agriculture Pennisular Malaysia.

[2] K. Baldwin and N. Childs (2015) "Rice Outlook," Departmenet of Agriculture of United States.

[3] D. An, Y. Guo, B. Zou, Y. Zhu, and Z. Wang, "A study on the consecutive preparation of silica powders and active carbon from rice husk ash," *Biomass and Bioenergy*, vol. 35, no. 3, pp. 1227–1234, 2011.

[4] N. Soltani, A. Bahrami, M. I. Pech-Canul, and L. a. González, "Review on the physicochemical treatments of rice husk for production of advanced materials," *Chem. Eng. J.*, vol. 264, pp. 899–935, 2015.

[5] U. Kalapathy, A. Proctor, and J. Shultz, "A simple method for production of pure silica from rice hull ash," *Fuel Energy Abstr.*, vol. 42, no. 1, p. 45, 2001.

[6] U. Kalapathy, a. Proctor, and J. Shultz, "An improved method for production of silica from rice hull ash," *Bioresour. Technol.*, vol. 85, no. 3, pp. 285–289, 2002.

[7] F. Adam and J. H. Chua, "The adsorption of palmytic acid on rice husk ash chemically modified with Al(III) ion using the sol-gel technique," *J. Colloid Interface Sci.*, vol. 280, no. 1, pp. 55–61, 2004.

[8] R. Ghosh, "A Review Study on Precipitated Silica and Activated Carbon from Rice Husk," *J. Chem. Eng. Process Technol.*, vol. 04, no. 04, 2013.

[9] Y. Hsieh, Y. Du, F. Jin, Z. Zhou, and H. Enomoto, "Alkaline pre-treatment of rice hulls for hydrothermal production of acetic acid," *Chem. Eng. Res. Des.*, vol. 87, no. 1, pp. 13–18, 2009.

[10] A. a. Alshatwi, J. Athinarayanan, and V. S. Periasamy, "Biocompatibility assessment of rice husk-derived biogenic silica nanoparticles for biomedical applications," *Mater. Sci. Eng. C*, vol. 47, pp. 8–16, 2015.

[11] Y. Cheng, M. Lu, J. Li, X. Su, S. Pan, C. Jiao, and M. Feng, "Synthesis of MCM-22 zeolite using rice husk as a silica source under varying-temperature conditions," *J. Colloid Interface Sci.*, vol. 369, no. 1, pp. 388–394, 2012.

[12] N. Yalçin and V. Sevinç, "Studies on silica obtained from rice husk," *Ceram. Int.*, vol. 27, no. 2, pp. 219–224, 2001.

[13] Y. Shen, P. Zhao, and Q. Shao, "Porous silica and carbon derived materials from rice husk pyrolysis char," *Microporous Mesoporous Mater.*, vol. 188, pp. 46–76, 2014.

[14] T. Lee, R. Othman, and F. Y. Yeoh, "Development of photoluminescent glass derived from rice husk," *Biomass and Bioenergy*, vol. 59, pp. 380–392, 2013.

[15] J. P. Nayak, S. Kumar, and J. Bera, "Sol-gel synthesis of bioglass-ceramics using rice husk ash as a source for silica and its characterization," *J. Non. Cryst. Solids*, vol. 356, no. 28–30, pp. 1447–1451, 2010.

[16] V. B. Carmona, R. M. Oliveira, W. T. L. Silva, L. H. C. Mattoso, and J. M. Marconcini, "Nanosilica from rice husk: Extraction and characterization," *Ind. Crops Prod.*, vol. 43, no. 1, pp. 291–296, 2013.

[17] S. Gu, J. Zhou, C. Yu, Z. Luo, Q. Wang, and Z. Shi, "A novel two-staged thermal synthesis method of generating nanosilica from rice husk via pre-pyrolysis combined with calcination," *Ind. Crop. Prod.*, vol. 65, pp. 1–6, 2015.

[18] S. Gu, J. Zhou, Z. Luo, Q. Wang, and M. Ni, "A detailed study of the effects of pyrolysis temperature and feedstock particle size on the preparation of nanosilica from rice husk," *Ind. Crops Prod.*, vol. 50, pp. 540–549, 2013.

[19] Y. Liu, Y. Guo, W. Gao, Z. Wang, Y. Ma, and Z. Wang, "Simultaneous preparation of silica and activated carbon from rice husk ash," *J. Clean. Prod.*, vol. 32, pp. 204–209, 2012.

[20] N. S. C. Zulkifli, I. Ab Rahman, D. Mohamad, and A. Husein, "A green sol-gel route for the synthesis of structurally controlled silica particles from rice husk for dental composite filler," *Ceram. Int.*, vol. 39, no. 4, pp. 4559–4567, 2013.

Effect of Pre-Washing on Odour of Empty Palm Fruit Bunch (EPFB) Fibre

Sie Kian, Ang[1], Xiao Yien, Lim[2*], Ren Yu Teh[3]

[1]*School of Engineering, Taylor's University, Malaysia*

[2] *School of Engineering, Taylor's University, Malaysia*

[3]*Furniu Fibre Sdn. Bhd, Malaysia*

[*]Xiao Yien.Lim@taylors.edu.my

Abstract

The objective of this study is to determine the potential of pre-washing to suppress the odour of the EPFB fibre. The pungent odour of EPFB fibre arise due to the biodegradation process by microbes and led to the release of malodorous compounds. Pre-washing with hot water at 90°C and the addition of antimicrobial agents was employed for microbe elimination in this work. Antimicrobial agents employed in this work were sodium hypochlorite, carvacrol and oregano with parameters of concentration and exposure time its main focus. Samples HW, SHC-3, SHC-4 and Car-4 provided the best microbe elimination efficiency with the achievement of total microbe eradication. These four (4) samples experienced minimal degradation degree of 4-9% while the unwashed fibre sample experienced approximately 28% after 4 weeks storage period. However, total microbe eradication from the four (4) samples was not achieved when applied with dip and spray washing. Statistics from odour survey reviewed that fibre pre-washed with hot water (HW) and sodium hypochlorite (SHC-4) produced the most satisfactory odour suppression. Implementing pre-washing stage in the production of EPFB fibre can provide a potential solution for odour suppression.

Keywords: EPFB fibre, Odour, Biodegradation, Pre-washing, Microbe elimination.

1. Introduction

The palm oil industries have been growing globally with the increasing world population to supply the increasing demands in the F&B industry as well as the production of chemical derivatives in the oleochemical industry [1]. With the increasing production of palm oil to meet the needs, a large amount of waste of 17.4 million tonne of Empty Palm Fruit Bunch (EPFB) and 53.1 million tonne of Palm Oil Mill Effluent (POME) are generated annually during palm oil extraction process [2]. EPFB have been utilised in the form of EPFB fibre in the manufacturing of furniture such a mattress,

cushion and etc. [3]. However, a drawback of palm fibre was that it is subjected to microbe biodegradation over a period of time which results in the unpleasant odour and weakening of the EPFB fibre which prohibit the production of higher value products [4].

Physical and chemical technique have been employed in the inhibition and elimination of microbe [5]. Hot water washing is a very common approach applied in industries for surface sterilisation [6]. The chemical technique involves the addition of antimicrobial agents which either inhibits or eliminate the microorganism [7]. Antimicrobial agents further classified as chemical and natural antimicrobial agents. Chemical antimicrobial of sodium hypochlorite (NaOCl) and Chlorhexidine (CHX) have been intensively studied for their antimicrobial properties and working mechanism, where both exhibit potential for microbe inhibition as well as elimination [8, 9]. Natural antimicrobial agents such as essential oil (EO) from various plants extract are known to show antimicrobial potentials due to the active compounds in the EOs [10]. Carvacrol, Thymol and Eugenol are the phenolic compounds in the EOs that exhibit strong antimicrobial properties [10]. The effectiveness of the antimicrobial agents is associated with various factors, but concentration and duration of exposure are two factors of significant impact [11, 12].

The aim of this study is to suppress EPFB fibre odour, with the focus on microbe elimination on the EPFB fibre in order to prevent or minimise biodegradation. The microbe elimination, odour and biodegradation activity suppression of EPFB fibres after washing with hot water washing or addition of antimicrobial agents include sodium hypochlorite, carvacrol and oregano were evaluated. Disc agar cultivation method was employed for microbe elimination analysis, which enables the evaluation of the effectiveness of the washing conditions. Ideally, total eradication of microbe on the EPFB fibre is desired. FTIR analysis was performed to investigate the biodegradation activity of the EPFB fibre. Lastly, odour survey was conducted through simple survey, which provided a significant review on the odour suppression from pre-washing of EFPB fibre. Results are discussed and comparison of the pre-washing methods are evaluated based on their potential in microbe elimination, biodegradation activity and odour suppression.Method

2.1 Sample collection

The EPFB fibre sample was collected from Furniu Fibre Sdn. Bhd., Ipoh, Perak, Malaysia. The fibre samples are in the form of loose fibre with characteristic length of 100-150 mm and the moisture content of 12-15%.

2.2 Washing with hot water

The raw EPFB fibre was rinsed with 2000 ml distilled water to wash off the excessive dirt and sands on the fibre surface. Rinsing the fibre also removed shorter fibre strands, therefore giving the consistency of longer strands on the sample. 20 g of EPFB fibre was prepared and used for each set of experiment. Duplicate samples are produced for each set of experiment. The fibre was washed by gentle stirring the fibre in water for 2 minutes with a glass rod [13]. Fibre samples are soaked in 1000 ml of water. Hot water at 90°C was investigated for washing [5, 6].

2.3 Washing with antimicrobial agents at various concentration

Antimicrobial agents were added to water at 25°C to investigate the performance in microbe elimination on the surface of the fibre. Fibres were also washed by gentle stirring in 1000 ml of washing solution. Three (3) types of antimicrobial agents were used for this experiment. The chemical antimicrobial agents used is sodium hypochlorite (NaOCl) and natural antimicrobial agents were carvacrol and oregano. NaOCl was added at three (3) different concentration of 0.1%, 2% and 5% for 2 minutes and one with 2% for 5 minutes [14]. Carvacrol was added with concentration of 0.1 and 2% for 2 minutes and 5 minutes washing respectively [12]. Oregano was added at concentration of 0.1% and 2% for 2 minutes washing [12], plus oregano at concentration of 2% and 5% with 5 minutes washing were also executed.

2.4 Apply dipping and spraying washing technique

Washing technique of dipping and spraying were investigated for hot water and 5% NaOCl. Dipping technique was carried out by dipping the fibre in water for a short time period of 40 s in 1000 ml of washing solution. [15]. Spray washing was carried out by spraying the fibre samples with a fine mist of hot water and 5% NaOCl. The total volume used for spraying was 500 ml. Spraying was performed with spraying bottles. The results from dipping and spraying were compared with stir washing to evaluate the suitable employment technique on reducing EPFB odour.

Table 1. Labelling of samples

Pre-washing method		Sample ID
None	No treatment	N
Processed	No treatment	P
Hot water	Hot water 2 minutes	HW
Washing with NaOCl	0.1% NaOCl 2 minutes	SHC-1
	2% NaOCl 2 minutes	SHC-2
	5% NaOCl 2 minutes	SHC-3
	2% NaOCl 5 minutes	SHC-4
Washing with carvacrol	0.1% Carvacrol 2 minutes	Car-1
	2% Carvacrol 2 minutes	Car-2
	0.1% Carvacrol 5 minutes	Car-3
	2% Carvacrol 5 minutes	Car-4
Washing with Oregano	0.1% Oregano 2 minutes	Ore-1
	2% Oregano 2 minutes	Ore-2
	2% Oregano 5 minutes	Ore-3
	5% Oregano 5 minutes	Ore-4
Dip washing	Hot water dip 40 seconds	HW-Dip
	5% NaOCl dip 40 seconds	SHC-3 Dip
Spray washing	Hot water spray	HW-Spray
	5% NaOCl spray	SHC-3 Spray

There were 19 samples produced in total from this work. For consistency, unwashed and all washed samples produced from the method described above were labelled according to Table 1.

2.5 Drying of the washed EPFB fibre

After every set of experiment, wetted fibre samples are dried in the laboratory oven with a temperature of 105.5°C overnight to completely remove moisture from the wetted fibre [16].

2.6 Microbe elimination analysis on washed and unwashed fibre

Microbe elimination analysis was performed by identifying the microbe growth on a nutrient rich medium of Nutrient Agar (NA) in a petri dish. NA is a general purpose medium for microbial cultivation [17]. NA is also a nutritive media which support a wide range of microorganism, non-selective meaning no inhibition of specific organisms and non-differential which do not distinguish organism by colour visibility [18]. Small samples of EPFB fibre were soaked in 10 ml of sterile water to produce a microbe suspended solution. To the suspended solution, 10, 100 and 1000 times dilution are performed and microbe cultivation was carried out for each dilution. Based on the colony growth on the agar plate, the dilution which provides suitable growth was selected for analysis. The whole procedure was done aseptically to minimise the risk of contamination [19]. Each sample was incubated for 7 days and the resulting growth of the colonies was evaluated to provide a qualitative analysis on microbial elimination for each pre-washing condition.

2.7 Fourier Transform Infrared Spectroscopy (FTIR) Analysis

Proceeding with the FTIR analysis, small samples of the washed and unwashed fibre were cut into fine short pieces. The short pieces were then grinded into slightly powdery samples with the mortar and pestle. Approximately 2 grams of samples were prepared for each fibre samples.

The FTIR spectra for the fibre sample were recorded with an FTIR spectrometer (Perkin Elmer Spectrum 100) equipped with attenuated total reflectance (ATR) unit. Each spectrum was measured using transmittance range from 4000 to 650 cm^{-1} with 16 ATR unit scans and resolution of 4 cm^{-1}. All sample spectra were baseline corrected and the transmittance value was normalised with the range of 0 to 100%. FTIR analysis was employed to evaluate the biodegradation activity of the pre-washed fibres. The spectra at wavelength 1340 cm^{-1} were selected to provide a respective comparison of the biodegradation activity [20]. A duration of 2 weeks was allowed for each analysis on the fibre samples.

2.8 Odour survey for washed and unwashed fibre

The odour of washed fibres was compared with unwashed fibre to determine the performance of the washings on suppression of odour through an odour survey. The odour survey involved the participation of candidates which will grade the odour of washed and unwashed fibres. The candidates consisted of student, lecturers, project supervisor, industrial collaborator as well as personnel from palm oil industries. The grading of the EPFB fibre odour was conducted through a survey form. Odour level was graded from scale 0 to 4, where 0 indicating no odour while 4 indicating extremely unpleasant.

Samples are reviewed to the panellist by the sample ID of A,B, C and so on. For every round of odour test, the samples are randomised. Four (4) rounds of odour survey were conducted with the duration of two (2) weeks between rounds. The odour testing will follow some guideline established by St. Croix Sensory, Inc. [21]. Data acquired from the survey results were generated into a statistical analysis report in the form of a bar chart. From this report, the effectiveness of the pre-washing method on odour suppression was evaluated based on the grading by the panellist. Statistical analysis was also used to determine the variance of the pre-washing method.

2. Results and Discussion

3.1 Microbe elimination analysis

Disc agar cultivation was used to qualify the efficiency of each pre-washing treatment on microbe elimination. Colony of microorganism on the agar are physically characterised by several parameters such as size, shape, colour, surface, margin, elevation and texture of the colony [22]. Three (3) parameters have been selected to characterise the colony growth which was the shape, surface and colour of the colony. Table 2 and

Table **3** tabulated the indication of microbe growth for a period of 7 days. Samples which have negative growth for 1000 times dilution will be tested for 10 times dilution. This was done as 1000 times dilution may be too diluted.

Table 2. Microbe growth indication for 1000 times dilution

Sample ID	Microbe growth						
	Day 1	Day 2	Day 3	Day 4	Day 5	Day 6	Day 7
N		X					
P	-	-	-	-	-	-	-
HW	-	-	-	-	-	-	-
SHC-1	-	-	-	-	-	-	-
SHC-2	-	-	-	-	-	-	-
SHC-3	-	-	-	-	-	-	-
SHC-4	-	-	-	-	-	-	-
Car-1	-	-	-	-	-	-	-
Car-2	-	-	-	-	-	-	-
Car-3	-	-	-	-	-	-	-
Car-4	-	-	-	-	-	-	-
Ore-1	-	-	-	-	-	-	-
Ore-2	-	-	-	-	-	-	-
Ore-3	-	-	-	-	-	-	-
Ore-4	-	-	-	-	-	-	-
HW-Dip	-	-	-	-	-	-	-
HW-Spray	-	-	-	-	-	-	-
SHC-3 Dip	-	-	-	-	-	-	-
SHC-3 Spray	-	-	-	-	-	-	-

* - represent no growth and X represent growth

Table 3. Microbe growth indication for 10 times dilution

Sample ID	Microbe growth						
	Day 1	Day 2	Day 3	Day 4	Day 5	Day 6	Day 7
P	X						
HW	-	-	-	-	-	-	-
SHC-1	X						
SHC-2	X						
SHC-3	-	-	-	-	-	-	-
SHC-4	-	-	-	-	-	-	-
Car-1	X						
Car-2	X						
Car-3	X						
Car-4	-	-	-	-	-	-	-
Ore-1	X						
Ore-2	X						
Ore-3	X						
Ore-4	X						
HW-Dip	X						
HW-Spray	X						
SHC-3 Dip	X						
SHC-3 Spray	X						

* - represent no growth and X represent growth

3.2 Microbe colonies on unwashed fibre

The results from the disc agar cultivation have deduced that sample N contains multiple microbe colonies as illustrated in Figure 1. However, the precise number of colony could not be accurately defined as some colony growth are overlapping each other. Approximately 6 (six) different microbes colony can be identified from Figure 1 [23].

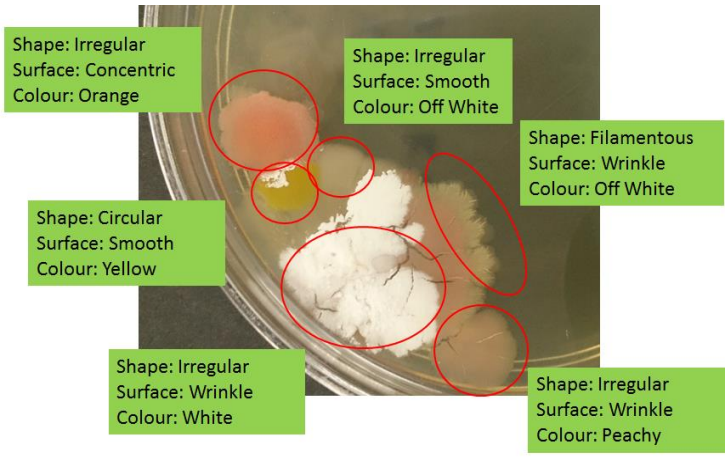


Figure 1. Microbe colony for sample N on day 7

3.3 Hot water washing on microbial elimination

The results from disc agar cultivation revealed that pre-washing condition of sample HW is effective to sterilise the EPFB fibre as no growth is present after the period of cultivation. This outcome is in agreement with other works performed on sterilisation with the similar parameters [5, 6]. This also indicates that the microbe presence on the fibre was not resistant towards higher temperature, therefore introducing high temperature provides an unfavourable condition which the microbe could not sustain themselves [15].

3.4 Chemical antimicrobial washing on microbe elimination

From

Table **3** sample SHC-1 and SHC-2 shows microbe growth, which indicate that the parameters for this treatment were ineffective for total eradication of the microbe present on the fibre [14, 24].

Figure 2 shows the microbe colony on day 7 for sample SHC-1. Observing the morphology of microbes' growth, there was two (2) colonies present that is similar to that of the unwashed samples. Figure 3 shows the microbe colonies on day 7 for sample SHC-2. The colony morphology for the sample SHC-2 solution is totally different from that of the sample N and SHC-1.

As the type of microbe colony is not the scope of study in this research, the results from sample SHC-1 and SHC-2 are only to indicate that washing with 0.1% and 2% NaOCl solution for 2 minutes could eliminate microbes to some extent but not total eradication of microbes on the EPFB fibre surface. The colonies that have microbe growth implies that these colonies are resistance towards this washing parameters and therefore not eliminated [7]. There are also colonies of different morphology to that of the unwashed samples. These colonies may not be absent in the unwashed samples, but due to the overlapping of the colonies growth, it renders the comparison.

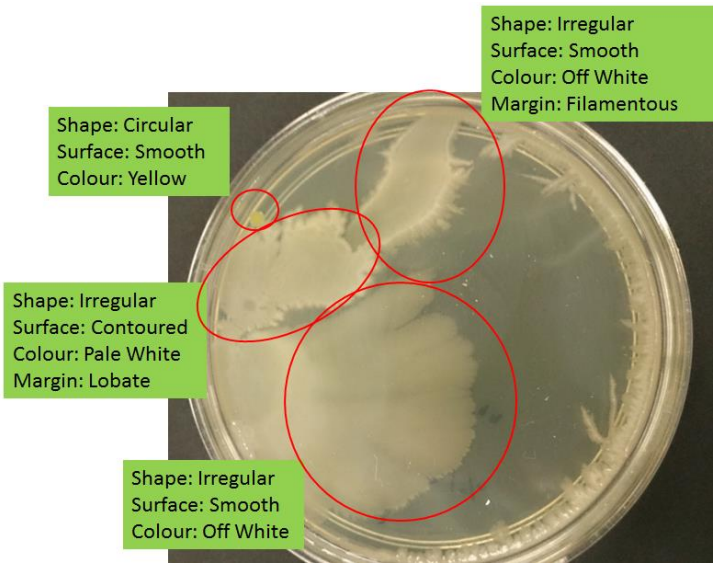


Figure 2. Microbe colony for sample SHC-1 on day 7

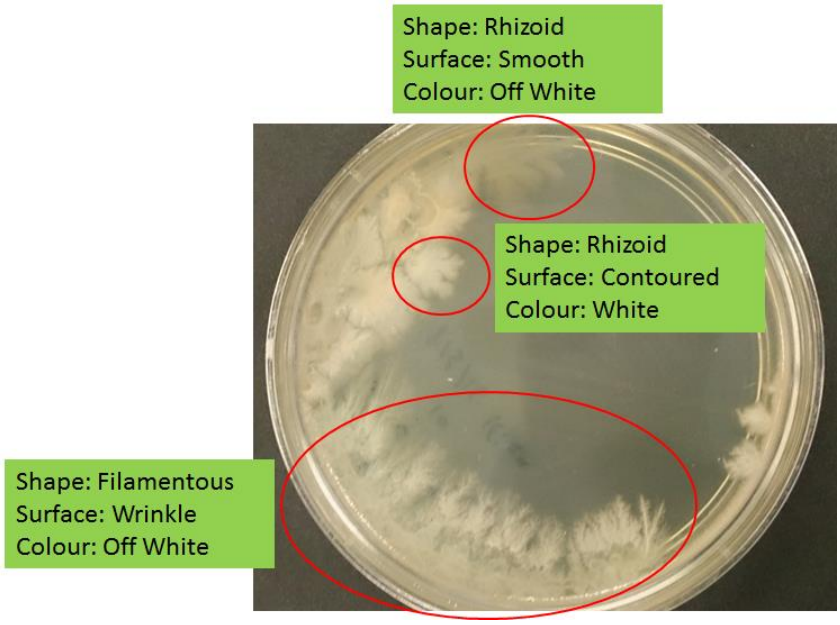


Figure 3. Microbe colony sample SHC-2 on day 7

Sample SHC-3 and SHC-4, on the other hand, provided total eradication of microbe on the EPFB fibre surface as no indication of microbe growth is recorded after the period of cultivation [14]. Concentration and duration of exposure of antimicrobial agent have a significant impact on the antimicrobial efficiency [7].

The achievement of total eradication for these parameters of NaOCl can be explained via their antimicrobial mechanism. When dissolved in water, NaOCl breaks down into hypochlorous acid ($HOCl^{-1}$) and further break into hypochlorite ions (OCl^{-1}) along with sodium, hydrogen and hydroxyl ions [25]. The hypochlorite ion, specifically the chlorine is a strong oxidant. It is responsible for the antimicrobial action by inhibiting the microbes' enzyme metabolism [25]. With longer duration of exposure, the microbes are deprived of the essential needs due to inhibition of their metabolism

for a prolonged time and eventually die. Upon the increased in NaOCl concentration, the amount of hydroxyl ions increases leading to high pH of the solution, this interferes with the cytoplasmic membrane integrity and later phospholipid degradation (rupture of the cell wall) of the microbes further causing the death of the microbes [25]. This explains why the washing condition in sample SHC-1 and SHC-2 was ineffective because the washing condition of the samples does not provide sufficient exposure time and high enough concentration to eliminate the more resistant microbes.

With the increased in antimicrobial concentration to 5% NaOCl for the same duration of exposure of 2 minutes, total eradication of microbe was achieved. Besides that, increasing the duration of exposure of NaOCl to 5 minutes with concentration of 2%, total eradication of microbe was also achieved. These findings indicate that the concentration and exposure time of antimicrobial agent have a significant contribution to the effectiveness of microbe elimination as established by other works [24, 25].

3.5 Natural antimicrobial washing on microbe elimination

Sample Car-1 and Car-2 shows microbe growth as indicated in

Table **3**. As discussed for the antimicrobial of NaOCl, concentration and duration of exposure of antimicrobial agents have significant attributes to their effectiveness. From the agar cultivation, it is deduced that washing with 0.1% and 2% for 2 minutes is not sufficient for total eradication of the microbes on the surface of the fibre. These parameters of washing with carvacrol could not achieve total eradication as some of the microbes is resistant either towards the concentration and duration of exposure of the antimicrobial agent [7].

The sample Car-3 shows colony growth while sample Car-4 did not as indicated in

Table **3**.The absent of colony growth on the agar plate for sample Car-4 implies that these parameters of washing were able to achieve total eradication of microbes on the surface of the fibre [26]. The mode of action of carvacrol is inducing disturbance to the cytoplasm membrane and causes leakage of ions from the cell which ultimately leads to the destruction of the microbes. Relating this to the exposure time of carvacrol during washing of fibre, longer duration of exposure would have allowed the disruption of all the microbes on the fibre surface compared to washing for 2 minutes. A minimum time was required to create a concentration gradient across the cell membrane that leads to the leakage of ions, where different cells have a distinctive characteristic of cytoplasm membrane, thus varies in the minimum time required. The exposure time of 2 minutes simply was not sufficient for some of the microbes.

Fibre samples of Ore-1 to Ore-4 are observed to have microbes growth on day 1 indicated in

Table **3**. Sample Ore-1 and Ore-2 both have microbe growth, this indicates that washing conditions in Ore-1 and Ore-2 were not effective for total microbe elimination.

It was speculated that the concentration and/or the duration of exposure in Ore-1 and Ore-2 were insufficient [27].

Additionally, conditions of Ore-3 and Ore-4 were investigated to determine the potential of total microbe eradication at higher concentration and longer duration of exposure, but total microbe eradication was not achieved as well. Comparing the antimicrobial efficiency of oregano essential oil with pure carvacrol, carvacrol is at least two to four fold more effective than oregano [12, 28]. This was due to carvacrol compound in oregano essential oil is approximately 25-80% in composition depending on the species of oregano plant as well [10]. The antimicrobial potential of oregano oil highly dependent on the composition of the phenolic compound carvarcol [29]. Other works have characterised that some species of oregano plant exhibit low carvacrol content [29]. Since the plant species of the oregano oil was not specified by the supplier, thus the oregano used in this research was highly speculated to exhibit low carvacrol content which attributes to the poor antimicrobial efficiency. With the establishment that even washing condition of Ore-4 could not provide total eradication of microbe, washing with oregano did not proceed with higher concentration and exposure duration as the minimum use of antimicrobial concentrations as well as minimum washing time were desired.

3.6 Effect of different washing technique on microbe elimination

Dip and spray washing technique were carried out only for HW and SHC which achieve total eradication as tabulated in

Table **3** with the exception of sample SHC-3. For sample HW-Dip and HW-Spray, total eradication of microbe was not achieved because of the decrease in exposure time with the dipping and spraying washing technique [13].

As for the NaOCl, only the concentration of 5% was conducted it has already been evidence that sample SHC-2 did not achieve total eradication; where the application of dip and spray washing will provide a duration of exposure less than 2 minutes. Fibre sample SHC-3 Dip and SHC-3 Spray did not bring about total eradication of microbe as well. These findings further support that duration of exposure of antimicrobial agent contributes to the effectiveness in microbe elimination.

From the previous experiment with carvacrol, only fibre samples Car-4 provide total eradication; since dipping and spraying technique attribute to a shorter duration of exposure, no further investigation was executed for carvacrol,

3.7 Effect of pre-washing on biodegradation activity on EPFB fibre

Fourier Transform Infrared Spectroscopy (FTIR) analysis is used to provide qualitative analysis on the biodegradation of lignocellulose of the fibre samples. Qualitative analysis is done by comparing the transmittance value of the fibre samples to its respective reference [30]. Cellulose and hemicellulose are analysed instead of lignin because they are more easily degraded by microbes due to their structure being

weak polysaccharides and microbes utilise the carbohydrates in it to sustain themselves [31]. The FTIR analysis was performed on sample N and samples which gave no colony growth on the disc agar cultivation, this enables the comparison of the biodegradation activities. Degradation degree of the cellulose and hemicellulose of each analysed sample was calculated to provide a quantitative evaluation [30].

Table 4 shows the spectra of sample N at different durations. As degradation becomes more severe, the resulting transmittance gradually increases [30]. From Table 4, the increase in transmittance of the spectra from week 0 to week 4 reveals that there was a reduction of lignocellulose contents due to microbes attack [30]. This finding is in agreement with the microbe elimination analysis as numerous colony growth was observed for sample N. The bands between 1300 and 1380 cm^{-1} are assigned to the CH bonds, CH_2 bonds and OH bonds of cellulose and hemicellulose; these spectra shows higher transmittance for degraded sample on week 2 and 4 [20]. The presence of degradation of EPFB fibre by microbes have contributed to the foul odour due to the release of malodourous metabolites [32]. After a period of 4 weeks, degradation degree of sample N reaches approximately 28% as tabulated in Table 4.

Table 4. Degradation degree of sample N after 4 weeks

Data	Week 0	Week 2	Week 4
Transmittance (%)	64.1241	66.6347	82.3957
Δ Transmittance (%)	0.0000	2.5106	17.8759
Degradation degree (%)	0.0000	3.9152	27.88

Table 5 shows the spectra of sample HW at different duration, the spectra shows that the transmittance is approximately the same for all durations. This indicates that there is very minimal degradation over the period of 4 weeks [30]. This is in alignment with microbe elimination test as no colony was cultivated for fibre sample HW. From Table 5, the degradation degree of sample HW is only at a minimal value of 4.8965%.

Table 5. Degradation degree of sample HW after 4 weeks

Data	Week 0	Week 2	Week 4
Transmittance (%)	81.2619	84.9535	85.2409
Δ Transmittance (%)	0	3.6916	3.979
Degradation degree (%)	0	4.5428	4.8965

Table 6 shows the spectra of sample SHC-4 at different duration. Analysis of the results shows that transmittance is approximately the same for all durations. This indicates that the biodegradation activity over the period of 4 weeks is very minimal [30]. Degradation degree of sample SHC-4 after 4 weeks is approximately 4% as indicated in Table 6. This result was in agreement with the microbe elimination analysis for sample SHC-4 as well.

Table 6. Degradation degree of sample SHC-4 after 4 weeks

Data	Week 0	Week 2	Week 4

Transmittance (%)	82.4315	83.3046	85.7470
Δ Transmittance (%)	0	0.8731	3.3155
Degradation degree (%)	0	1.0592	4.022

Another sample which achieved total eradication was sample Car-4. Table 7 shows the spectra of sample Car-4 experienced a slight increase in transmittance over the 4 week duration. This trend of the spectra implies that there are some extent of biodegradation activity on the fibre sample [30]. Table 7 tabulated the degradation degree of sample Car-4 with a value of 8.95%. The small percentage of degradation from samples HW, SHC-4 and Car-4 is attributed from non-biological parameters such as humidity and solar radiations [33].

Table 7. Degradation degree of sample Car-4 after 4 weeks

Data	Week 0	Week 2	Week 4
Transmittance (%)	73.5425	75.8742	80.1225
Δ Transmittance (%)	0	2.3317	6.58
Degradation degree (%)	0	3.1705	8.95

3.8 Odour of EPFB fibre after pre-washing

Odour survey was performed to acquire the resulting odour of the EPFB fibre samples. Figure 4 illustrate the statistic of the odour survey. Analysis on the statistic shows that over 80% of the candidates rated sample N unpleasant and higher. This is expected since the microbe elimination analysis shows abundant colony growth as well as high biodegradation activity obtained by FTIR analysis. Odour survey was also performed for the processed fibre, which is the end product from the EPFB fibre production factory. More than 70% rated the processed fibre to have an unpleasant odour and higher, additionally, remarks given by candidates was the presence of sourish (rancid) smell from the processed fibre.

The washed fibre samples of HW, SHC-2, SHC-4, Car-2 and Car-4 all have achieved the aim of the project which was to suppress the odour of the of the EPFB fibre. Sample HW received the most positive rating with approximately 50% rated it no odour and another 40% rated it pleasant. The odour ratings for sample SHC-2 and SHC-4 shows much similarity which more than 30% have rated no odour and approximately 50% have rated pleasant for both samples.

About 20% of the candidate rated sample Car-2 to have no odour and approximately 45% rated it to have a pleasant odour. For sample Car-4, 25% rated it no odour and 35% rated it pleasant, but a higher percentage of 40% rated it unpleasant and higher. A common conception provided by the candidates regarding the odour for Car-2 and Car-4 was that they were unfamiliar with the odour and thus leading some of them to rate it unpleasant and higher.

Based on the odour survey results, the best washing condition for odour suppression of EPFB fibre is pre-washing with NaOCl, the SHC-2 and SHC-4. NaOCl is a common antimicrobial agent used in disinfectants and sterilisation [7], thus, it is cheap and easy to acquire. Although both sample SHC-2 and SHC-4 received almost

similar odour ratings, implementing pre-washing with condition SHC-4 is much preferable as it achieved total eradication of microbe as shown in **Error! Reference source not found.**. Despite the fact that pre-washing with hot water provided a more satisfactory odour ratings, the complexity and energy requirement for implementation would be its disadvantage.

Relating the results acquired from microbe elimination analysis, FTIR analysis and the odour survey, they all have shown appropriate alignment. Microbes have contributed to the pungent odour of the EPFB fibre due to the release of volatile malodourous compounds during the biodegradation activities on the biomass as evident by sample N [4, 32]. The elimination of microbes on the EPFB fibre have minimised the biodegradation activities which ultimately suppressed the EPFB fibre pungent odour by preventing the formation of the malodourous compounds. The research question in section 1.2 was answered where pre-washing with HW, SHC-2, SHC-4, Car-2 and Car-4 have suppressed the odour of EPFB fibre to a tolerable level.

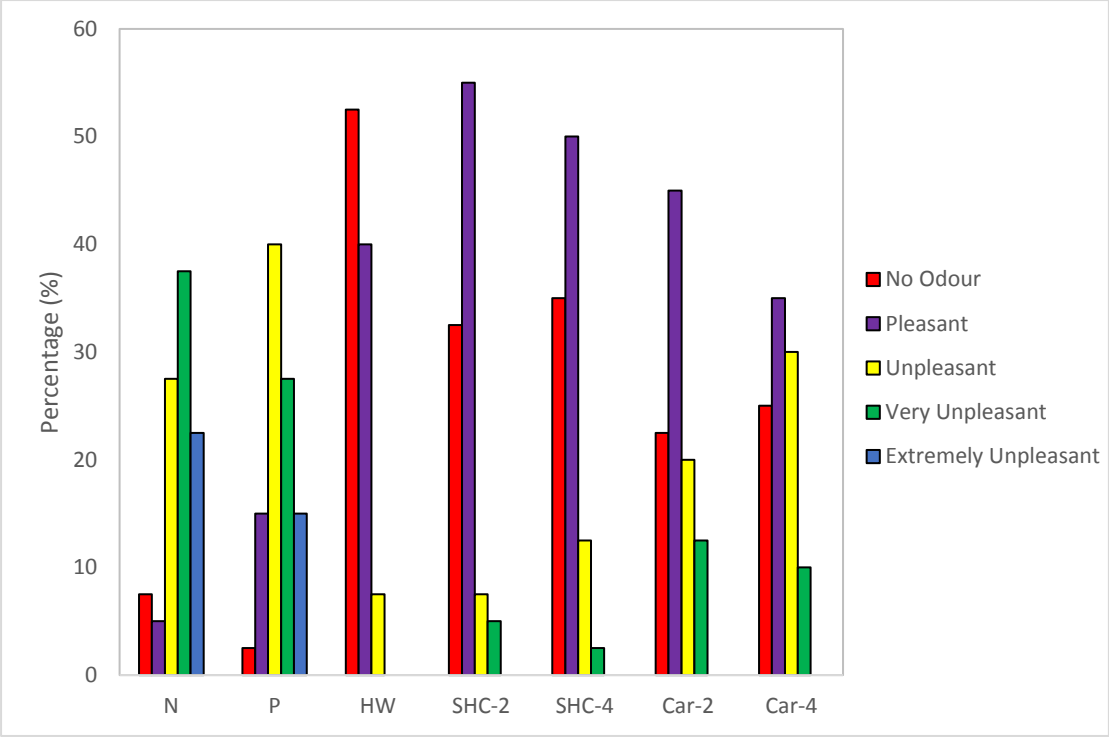


Figure 4. Odour survey bar chart

3. Conclusion

The results have demonstrated that application of pre-washing was able to suppress the odour of EPFB fibre. Microbe elimination analysis displayed that through pre-washing of EPFB fibre, microbe on the fibre surface was reduced while some achieved total eradication. Spectra obtained from FTIR analysis have demonstrated that samples which achieved total eradications of microbe show minimal biodegradation activity compared to the unwashed fibre. Lastly, statistics from odour survey shows appropriate alignment with both the microbe elimination and FTIR analysis where the

elimination of microbe yielded minimal biodegradation activity and thus contributed to the suppression of the odour.

Reference

[1] SimeDarby Plantation, "Palm Oil Facts & Figures," 2013.
[2] N. Ali, A. N. M. Tabi, F. A. Zakil, W. N. F. Mohd Fauzai, and O. Hassan, "The usage of empty fruit bunch (EFB) and palm pressed fibre (PPF) as substrates for the cultivation of Pleurotus Ostreatus," *J. Teknol. (Sciences Eng.*, vol. 64, no. 1, pp. 93–99, 2013.
[3] Hoong Chan Trading, "Resourceful on Oil Palm Fibre Related Product," 2009. [Online]. Available: http://www.hoongchan.com/oil_palm_fibre.htm. [Accessed: 25-Sep-2015].
[4] N. Qamaruz-Zaman, Y. Kun, and R.-N. Rosli, "Preliminary observation on the effect of baking soda volume on controlling odour from discarded organic waste," *Waste Manag.*, vol. 35, pp. 187–190, 2015.
[5] S. J. Hauge, M. Wahlgren, O. J. Røtterud, and T. Nesbakken, "Hot water surface pasteurisation of lamb carcasses: Microbial effects and cost-benefit considerations," *Int. J. Food Microbiol.*, vol. 146, no. 1, pp. 69–75, 2011.
[6] D. Nei, M. L. Bari, and K. Enomoto, "Validation of hot water and chlorine treatments to inactivate pathogens inoculated on mung bean seeds: Influence of the seed production area," *Food Control*, vol. 32, no. 1, pp. 186–189, 2013.
[7] F. Dazzo, "MMG 301 Dr . Frank Dazzo Control of Microbial Growth : Chemical Antimicrobials Many factors influence the effectiveness of an antimicrobial agent : • microbial population size • microbial population and community composition • microbial encasement within," 2015.
[8] Y. Chen, R. W. K. Wong, C. J. Seneviratne, U. Hägg, C. McGrath, and L. P. Samaranayake, "Comparison of the antimicrobial activity of Listerine and Corsodyl on orthodontic brackets in vitro," *Am. J. Orthod. Dentofac. Orthop.*, vol. 140, no. 4, pp. 537–542, 2011.
[9] F. J. de Souza-Filho, A. D. J. Soares, M. E. Vianna, A. A. Zaia, C. C. R. Ferraz, and B. P. F. D. A. Gomes, "Antimicrobial effect and pH of chlorhexidine gel and calcium hydroxide alone and associated with other materials," *Braz. Dent. J.*, vol. 19, no. 1, pp. 28–33, 2008.
[10] S. Burt, "Essential oils: their antibacterial properties and potential applications in foods--a review.," *Int. J. Food Microbiol.*, vol. 94, no. 3, pp. 223–53, 2004.
[11] H. & A. Russell, *Russell, Hugo & Ayliffe's Principles and Practice of Disinfection, Preservation & Sterilization*. John Wiley & Sons, 2008.
[12] A. Nostro, A. S. Roccaro, G. Bisignano, A. Marino, M. A. Cannatelli, F. C. Pizzimenti, P. L. Cioni, F. Procopio, and A. R. Blanco, "Effects of oregano , carvacrol and thymol on Staphylococcus aureus and Staphylococcus epidermidis biofilms," no. 2007, pp. 519–523, 2016.
[13] J. E. a Somner, N. Stone, A. Koukkoulli, K. M. Scott, a. R. Field, and J. Zygmunt, "Surgical scrubbing: can we clean up our carbon footprints by washing our hands?," *J. Hosp. Infect.*, vol. 70, no. 3, pp. 212–215, 2008.
[14] J. Ma, Z. Tong, J. Ling, H. Liu, and X. Wei, "The effects of sodium hypochlorite and chlorhexidine irrigants on the antibacterial activities of alkaline media against Enterococcus faecalis," *Arch. Oral Biol.*, vol. 60, no. 7, pp. 1075–1081, 2015.
[15] H. Özdemir, Y. Yildirim, Ö.¨Küplülü, A. Koluman, M. Göncüoğlu, and G. Inat, "Effects of lactic acid and hot water treatments on Salmonella Typhimurium and

Listeria monocytogenes on beef," *Food Control*, vol. 17, no. 4, pp. 299–303, 2006.
[16] S. Kim, J. M. Park, J.-W. Seo, and C. H. Kim, "Sequential acid-/alkali-pretreatment of empty palm fruit bunch fiber," *Bioresour. Technol.*, vol. 109, pp. 229–233, 2012.
[17] Becton-Dickinson and Company, "INSTRUCTIONS FOR USE – PARTIALLY COMPLETED BD Tryptic Soy Agar INTENDED USE," no. August, pp. 1–5, 2003.
[18] Georgia Highlands College, "Use of selective and differential media," 2013. [Online]. Available: http://www.highlands.edu/academics/divisions/scipe/biology/labs/rome/selective differential.htm. [Accessed: 07-Nov-2015].
[19] S. L. Tan, H. Y. Lee, and N. A. Mahyudin, "Antimicrobial resistance of Escherichia coli and Staphylococcus aureus isolated from food handler's hands," *Food Control*, vol. 44, pp. 203–207, Oct. 2014.
[20] J. Gelbrich, C. Mai, and H. Militz, "Evaluation of bacterial wood degradation by Fourier Transform Infrared (FTIR) measurements," *J. Cult. Herit.*, vol. 13, no. 3, pp. S135–S138, 2012.
[21] C. M. Mcginley, M. a Mcginley, and D. L. Mcginley, "Odor Basics, understanding and using odor testing, St. Croix, Inc.," no. The 22nd Annual Hawaii Water Environment Association Conference, pp. 1–16, 2000.
[22] E. W. Koneman, *Koneman's Color Atlas and Textbook of Diagnostic Microbiology*. Lippincott Williams & Wilkins, 2006.
[23] J. Jackman, "The Microbe : The Basics of Structure , Morphology , and Physiology as They Relate to Microbial Characterization and Attribution," pp. 13–35, 2012.
[24] R. E. Tirali, "In vitro antimicrobial activity of several concentrations of NaOCl and Octenisept in elimination of endodontic pathogens," *YMOE*, vol. 108, no. 5, pp. e117–e120, 2009.
[25] Z. Mohammadi, "Sodium hypochlorite in endodontics : an update review," pp. 329–341, 2008.
[26] A. Nosrat, B. Bolhari, M. Reza, and Sharifian, "The effect of Carvacrol on Enterococcus faecalis as a final irrigant," vol. 4, no. 3, pp. 96–100, 2009.
[27] J. Wu, S. Ge, H. Liu, S. Wang, S. Chen, J. Wang, J. Li, and Q. Zhang, "Properties and antimicrobial activity of silver carp (Hypophthalmichthys molitrix) skin gelatin-chitosan films incorporated with oregano essential oil for fish preservation," *Food Packag. Shelf Life*, vol. 2, no. 1, pp. 7–16, 2014.
[28] J. F. Martucci, L. B. Gende, L. M. Neira, and R. a. Ruseckaite, "Oregano and lavender essential oils as antioxidant and antimicrobial additives of biogenic gelatin films," *Ind. Crops Prod.*, vol. 71, pp. 205–213, 2015.
[29] C. M. Asensio, N. R. Grosso, and H. R. Juliani, "Quality characters, chemical composition and biological activities of oregano (Origanum spp.) Essential oils from Central and Southern Argentina," *Ind. Crops Prod.*, vol. 63, pp. 203–213, 2015.
[30] Y. Liu, T. Hu, Z. Wu, G. Zeng, D. Huang, X. He, and M. Lai, "Study on biodegradation process of lignin by FTIR and DSC," vol. 21, no. 24, pp. 14004–14013, 2014.
[31] W. Aizuddin, A. Samsu, A. Tarmezee, A. Sulaiman, M. N. Naim, and Y. Shirai, "Degradation of oil palm empty fruit bunches (opefb) fibre during composting process using in-vessel composter," vol. 7, no. 2010, pp. 4786–4805, 2012.
[32] M. C. Lemfack, J. Nickel, M. Dunkel, R. Preissner, and B. Piechulla, "mVOC: a database of microbial volatiles.," *Nucleic Acids Res.*, vol. 42, no. Database issue,

pp. D744–8, Jan. 2014.
[33] X. Colom, F. Carrillo, F. Nogués, and P. Garriga, “Structural analysis of photodegraded wood by means of FTIR spectroscopy,” *Polym. Degrad. Stab.*, vol. 80, no. 3, pp. 543–549, 2003.

Investigation on Treatment Technique to Reduce the Odour of the Empty Palm Fruit Bunch (EPFB) Fibre

Sie Kiong, Ang[1], Xiao Yien, Lim[2*], Ren Yu, Teh[3]

[1] *School of Engineering, Taylor's University, Malaysia*

[2] *School of Engineering, Taylor's University, Malaysia*

[3]*Furniu Fibre Sdn Bhd, Malaysia*

[*]XiaoYien.Lim@taylors.edu.my

Abstract

Empty palm fruit bunch (EPFB) fibre being hydrophilic in nature absorbed much of the atmospheric moisture which provided a favourable environment for the entry of microbes that gradually biodegrade the fibre and hydrolysed its residual oil in the process. Biodegradation of the fibre led to the emission of unpleasant odour restricted the marketing potential of the EPFB fibre for the production of value-added products. The hemicellulose in this lignocellulosic biomass contributed to the majority of its hydrophilicity. In this novel study, the EPFB fibre is treated chemically and thermally to lower the amount of the hemicellulose in order to reduce the moisture content of the biomass. The lower moisture around the fibre could minimise the biomass degradation in the effort to reduce its inherent odour. The EPFB fibre is treated chemically with dilute acid and alkali in a one-step and two-step process with H_2SO_4 and NaOH at elevated temperature. Whereas thermal treatment was performed by torrefaction at 200 and 260°C. From the experiment, both chemical and thermal treated resulted in the removal of hemicellulose and also reduce the moisture content of the EPFB fibre. Out of all treatment techniques, the two-step treatment with 4% w/v NaOH followed by 4% v/v H_2SO_4 sequence resulted in the highest removal of hemicellulose which also received the most satisfactory odour performance from the odour survey panel with the Net Promoter Score (NPS) of 70%. Resting on these results, the removal of hemicellulose have managed to lower the moisture content and bring about the odour reduction of the EPFB fibre.

Keywords: EPFB fibre, Odour, Hemicellulose, Dilute alkali/acid treatment, Torrefaction.

1. Introduction

Malaysia with its abundant of oil palm plantation is one of the leading palm oil exporter of the global oils and fats market [1]. When the oils are extracted from the oil palm fruit, abundant of lignocellulose solid biomass waste are generated, which included the kernel shell, mesocarp fibre and empty palm fruit bunch (EPFB). In this research, the area of interest focused on the EPFB waste. The biomass waste generated is four times of the amount of oil processed in the mill, and one-third of these waste is solely EPFB [2]. With the ever increasing demand of the global palm oil, even larger amount EPFB waste is generated which amounted to about 17.4 million tonne annually [3]. EPFB itself generally has a low commercial value which is either disposed into landfill or burned for steam generation at the mill. This is not a sustainable solution to handle the EPFB waste in the long run because burning large amount of this waste contributed to the ever increasing air pollution and dumping the EPFB into a landfill will only contribute more to the existing waste management issues.

On the other hand, EPFB has been utilised in the form of EPFB fibre for the production of value-added products such as fibreboard, cushion, mattress and composite materials. Utilising the EPFB waste in this manner have provided a positive impact on the economic and environmental aspects. In the aspects of economics, the disposal cost of the EPFB waste can be reduced which at the same time giving rise to the commercial value of EPFB. In terms of environmental aspects, reduced burning of this biomass can lower the contamination of the environment, plus the waste management of the EPFB waste can also be eased.

However, the presence of high atmospheric moisture has subjected the EPFB fibre to biodegradation over a period of time which resulted in the unpleasant odour of the fibre [4]. The high moisture on the EPFB fibre provided a favourable living environment for the entry of microbes, where they began to degrade and weaken the fibre. Additionally, microbial action will also degrade the residual oil found in the EPFB fibre as well, which is by enzymatic hydrolysis of the long-chained fatty acid into shorter-chained free fatty acid that is unpleasant in odour [5, 6]. This rendered the potential of EPFB fibre for the production of value-added products. Hence, the challenge encountered when utilising EPFB fibre as feedstock is to investigate the methods to reduce the unpleasant odour, which brought about the scope of this research.

Due to the high atmospheric moisture, the moisture content of the EPFB fibre can amount to as high as 50% of its dry weight [7]. Adding to this, the hydrophilicity of the EPFB fibre arises from the moisture absorbing tendency of the lignocellulosic biomass [4, 8]. With that said, EPFB fibre has a general lignocellulose composition of 40-50% cellulose, 20-30% hemicellulose and 20-30% lignin [9]. Among these three major components of the lignocellulose, hemicellulose developed the most hydrophilic behaviour that contributed to most of the atmospheric moisture absorption of the EPFB fibre [9]. Thus, it is hypothesised in this research that lowering the moisture content from the removal of hemicellulose could lead to the odour reduction of EPFB fibre, as the lower hemicellulose fraction would impart a more hydrophobic EPFB fibre.

Hemicellulose removal from lignocellulose biomass can be achieved through physical, chemical and thermal treatment. In this research, chemical and thermal treatment is the targeted area of study because physical treatment led to the change in

the size of the fibre which is not desired to be utilised for manufacturing value-added products.

For chemical treatment, acid and alkali such as dilute H_2SO_4 and NaOH treatment are the more effective and extensively used reagent for lignocellulose biomass treatment to extract the hemicellulose under elevated temperature [10–14]. In the acid treatment of the biomass, the hydrogen ions from the acid breakdown the forces of attraction between the lignocellulose components, where the main target are to solubilise and release the hemicellulose under the elevated temperature [11, 13, 15]. As for alkali treatment, it destroys the ester bonds between lignin and hemicellulose through hydrolysis of the bond, which is the α-ether link [11, 16]. Besides that, further investigation has also been conducted on evaluating the effect of combined dilute acid and alkali treatment. The study showed that treatment sequence with alkali followed by acid gives better hemicellulose removal than the treatment sequence of acid followed by alkali. This suggested that alkali should be the primary effector in the combined treatment to improve the hemicellulose extraction process [11, 13].

As for thermal treatment, torrefaction is a mild pyrolysis process where the biomass is heated in an inert atmosphere between 200-300°C, where this condition degrades majority of the hemicellulose without having a large impact on the cellulose and lignin in the EPFB fibre [17, 18]. Chen and Kuo have also narrowed out that torrefaction carried out between 240-260°C is the most suitable range for high amount of hemicellulose removal from EPFB fibre [17, 18]. With the removal of hemicellulose through these treatments, the moisture content of the fibre could be lowered, where the biodegradation could be prevented or minimised for the odour reduction [4].

Thus, in this study, a comparison of the odour reduction of the EPFB fibre was carried out between the chemical and heat treatment. Furthermore, a comprehensive discussion on the effect of different treatment of the EPFB fibre in relating to the moisture content after the removal of hemicellulose was also presented.

2. Methods

2.1 Collection of EPFB Fibre

The untreated EPFB (UF) samples were collected as loose fibres from Furniu Fibre Sdn Bhd., Ipoh, Perak, Malaysia after the screening stage where the desired long fibres are separated from the shorter fibres and dirt particles. These fibres average length is between 50-150 mm. The processed EPFB (PF) fibres are the end product from Furniu Fibre's production line. Both fibre samples are delivered fresh from the day of production. Sample PF was also collected from Furniu Fibre Sdn Bhd in this research for analytical comparison with the treated EPFB fibres. Sample PF was also used to as a reference sample to evaluate if the treatment could reduce the odour of the EPFB fibre.

2.2 One-Step NaOH and H_2SO_4 Treatment

The EPFB fibre samples are weighted to 10 g using an electronic balance and are pre-washed with distilled water to rinse off the dirt and sand from the surface of the

fibre. The one-step chemical treatment using NaOH and H_2SO_4 incorporated the work of Si et al. [13], Ying et al. [12] and Kim et al. [10] with some modifications.

For the NaOH treatment, the EPFB fibre is treated with NaOH at concentrations of 0.5, 2 and 4% w/v (weight/volume = g/ml) respectively with liquid to solid ratio of 5:1 for an hour at 120°C. The treatment was conducted at atmospheric condition using a hot plate. For the H_2SO_4 treatment, the EPFB fibre is treated with H_2SO_4 at concentrations of 2, 4 and 8% v/v (volume/volume) respectively with liquid to solid ratio of 5:1 for an hour at 120°C.

All the EPFB fibre-solution mixtures are filtered. The NaOH and H_2SO_4 treated EPFB fibre samples are collected and washed with distilled water until neutral condition before drying in the oven (Memmert U75) overnight at 105°C. The dried treated EPFB fibre samples were stored further analysis. The liquid effluent NaOH and H_2SO_4 was stored for HPLC analysis. Each experiment is performed in duplicates.

2.3 Two-Step Treatment with NaOH and H_2SO_4

The two-step treatment using alkali and acid follows the work of Si et al. [13], Ying et al. [12] and Kim et al. [10] with some modifications. For the two-step treatment, the EPFB fibre is treated with 4% w/v NaOH followed by 4% v/v H_2SO_4 as well as the opposite sequence of 4% v/v H_2SO_4 followed by 4% w/v NaOH.

The two-step treatment was carried out with the similar condition as described in Section 2.2, which is the one-step treatment above. The samples treated from the first step was washed thoroughly until neutral condition to minimise the reaction between the NaOH and H_2SO_4 during the second step treatment. After the second step treatment, the EPFB fibre samples are collected and washed with distilled water until neutral condition before drying in the oven (Memmert U75) overnight at 105°C. The dried treated EPFB fibre samples were stored further analysis. The liquid effluent from the second step treatment was stored for HPLC analysis. Each experiment was performed in duplicates.

2.4 Torrefaction

The torrefaction of the EPFB fibre sample was performed using the horizontal tube furnace (Carbolite HST 12/400). 10 g of the EPFB fibre was placed in a crucible before inserting it into the middle of the horizontal tube. Nitrogen with a flowrate of 0.6 L/min was used during the torrefaction. The torrefaction temperatures were set at 200°C and 260°C respectively with a heating rate of 10°C/min and residence time of 30 minutes. The samples were stored for further analysis. Each experiment was performed in duplicates.

2.5 Sample Identification

All the EPFB fibre samples from the treatment described above in Section 2.2 to 2.4 was assigned with their respective identification (ID) as tabulated in Table 1. The assigned ID is used to represent the respective sample from this point onwards in this paper.

Table 1. Sample identification of EPFB fibre

Treatment method		Sample ID
Untreated EPFB fibre		UF
Processed EPFB fibre		PF
One-step NaOH treatment	0.5% NaOH	ALK 1
	2% NaOH	ALK 2
	4% NaOH	ALK 3
One-step H_2SO_4 treatment	2% H_2SO_4	ACD 1
	4% H_2SO_4	ACD 2
	8% H_2SO_4	ACD 3
Two-step NaOH and H_2SO_4 treatment	4% H_2SO_4 followed by 4% NaOH	ACD/ALK
	4% NaOH followed by 4% H_2SO_4	ALK/ACD
Heat treatment with torrefaction	200°C	TF 1
	260°C	TF 2

2.6 Moisture Analysis

The moisture content of EPFB fibre samples was measured using the moisture analyser (Precisa XM50). About 0.5 g of EPFB fibre samples from each treatment are subjected to the moisture analysis. The moisture content is measured in terms of percentage moisture. The drying temperature of the anlyser was set at 105°C to remove the free and trapped moisture from the samples until the sample weigh is constant.

2.7 FTIR Analysis

The FTIR spectra (transmittance, %T) of all the EPFB fibre samples was recorded on FTIR spectrometer (Perkin Elmer Spectrum 100) based on attenuated total reflectance (ATR). Each spectrum was measured over the range of 4000 to 650 cm-1 with 16 ATR scans and resolution of 4 cm^{-1}. The spectra were baseline corrected and the transmittance was normalised from 0 to 100%.

2.8 HPLC Analysis

The liquid effluent extracted from the one-step and two-step chemical treatment was analysed using HPLC to determine the xylose. HPLC-grade D-xylose was used as the standard to measure the concentration of hemicellulose in the liquid effluent [12]. The HPLC system (Agilent 1220 infinity LC) was equipped with Hi-Plex H column (7.7 × 300 nm, 8μm) and refractive index detector (55°C). 0.005 M H_2SO_4 was used as mobile phase with the flow rate of 0.7 ml/min under isocratic conditions. The temperature and pressure of the column were 60°C and 46 bars respectively. Prior to injection, the chemical solutions were filtered with 0.2 μm syringe. Next, 20 μl of sample was loaded for analysis with a runtime of 15 minutes [12]. Standard curves were generated for D-xylose (99% purity) with R^2 value of 0.99. Under these operating conditions, xylose was detected at retention time of 8.86 minutes.

2.9 Odour Survey of Treated EPFB Fibre

The purpose of this survey is to determine which treatment techniques provided better odour reduction on the EPFB fibres. The odour level of the treated samples was graded by a panel of 30 pax that consist of random students and staff from Taylor's University, project supervisor and the industrial collaborator of this research. Random panel is involved to avoid any means of biassed opinion. The odour of the EPFB fibres was compared and graded through a survey form. The odour level was classified from scale 0 to 4 (see Table 2). The scale of 0 indicates no odour while 4 indicating very unpleasant.

There are 5 samples in total that were presented to the panel for odour grading, only the best sample (based on FTIR and HPLC analysis) from one-step and two-step chemical treatment (ALK 3, ACD 2 and ALK/ACD) was presented for the odour evaluation besides sample UF and PF.

During odour grading, all EPFB fibre samples presented to the panel was labelled as arbitrary sample with assigned identification (ID) to avoid any prejudice opinion, only the author knows the identity of the samples. The odour testing followed some basic guidelines from St. Croix Sensory, Inc., especially for the panel [19]. From this odour survey, a Net Promoter Score (NPS) analysis was used to identify the treatment technique that gives the most satisfactory odour level of the EPFB fibre samples.

Table 2. Classification of odour level of EPFB fibre

Scale	Odour level
0	No odour
1	Pleasant
2	Slightly unpleasant
3	Unpleasant
4	Very unpleasant

3. Results and Discussion

3.1 Effect of Treatment Techniques on Moisture Content

The moisture content of the EPFB fibre samples is as tabulated in Table 3. The purpose of conducting the moisture analysis is to evaluate the moisture content of the treated fibre after the chemical and heat treatment.

Based on the results in Table 3, it was clearly shown that both chemical and heat treatment managed to reduce the moisture content of the EPFB fibre compared to the sample PF. It is believed that the removal of the hemicellulose from the chemical and heat treatment could have contributed to the lower moisture content of the treated samples.

For the treatment with NaOH, sample ALK 3 have the lowest moisture content, but no result trends can be observed for increasing NaOH concentrations from ALK 1 to 3. As for the treatment with H_2SO_4, a result trend can be observed where increasing

H_2SO_4 concentration from sample ACD 1 to 3 are seen to gradually reduce the moisture content of the treated EPFB fibres. Between the two-step treated samples, sample ALK/ACD have lower moisture content than ACD/ALK. For the case of torrefaction, higher treatment temperature (sample TF 2) showed lower moisture content of the EPFB fibre. The results of this analysis demonstrated that these treatments managed to reduce the moisture content of the treated EPFB fibres.

Between the one-step chemical treatments, the H_2SO_4 treated samples showed lower moisture content compared to the NaOH treated samples. Based on this observation, it was speculated that the acid treatment would have remove higher amount of hemicellulose since the working mechanism of the acid in the treatment is mainly to solubilise the hemicellulose compared to that of an alkaline treatment [11].

Table 3. Moisture content of EPFB fibre samples

Sample	Moisture content (%)
UF	39.96
PF	18.99
ALK1	12.47
ALK2	13.18
ALK3	10.87
ACD1	12.51
ACD2	10.45
ACD3	7.31
ACD/ALK	10.59
ALK/ACD	8.60
TF1	13.63
TF2	10.69

3.2 Effect of Treatment Techniques on the EPFB Fibre Structure

The structural changes of the EPFB fibres were compared and analysed based on the ATR-FTIR spectra of the all the EPFB fibre samples. The FTIR spectra for all the treatments including sample PF are subtracted with the FTIR spectra of sample UF. The positive value for the Δ%T implied that the transmittance of that particular sample is higher than sample UF, which means the stretching of the bond is lower than that of sample UF. The four zones of wavelengths (band positions) that are of interest in this research are as tabulated in Table 4. The interpretation of the bond stretching as shown in Table 4 is well-studied by various researchers for lignocellulosic biomass [20–23].

Table 4. FTIR absorption wavelengths and bond stretching

Wavelengths (cm^{-1})	Zone	Bond stretching	Functional group name	Interpretation
3600 – 3100	A	O-H	Phenols Alcohols	Intermolecular and intramolecular OH bonds in cellulose OH vibration in cellulose, hemicellulose and lignin.

3000 -2800	B	H-C-H asymmetric & symmetric	Alkanes	Hydrocarbon straight chain or side chain of cellulose and hemicellulose.
1750 - 1625	C	C=O	Esters Carboxylic acids Ketones Aldehydes	Esters bond between lignin and hemicellulose. The C=O vibration in hemicellulose.
1300 - 1000	D	C-O C-O-C	Esters Alcohols	Esters bond between lignin and hemicellulose. The C-O or C-O-C vibration in cellulose, hemicellulose or lignin

Figure 1 represents the FTIR spectra for NaOH treatment on the EPFB fibre. It can be seen in Figure 1 that sample ALK 1 to ALK 3 yielded positive value of Δ%T in Zone A showed that the O-H stretching is lower than sample UF. This confirmed the removal of hemicellulose, cellulose and lignin since all three components have the common OH group in its structure [23, 24]. It can also be seen in Figure 1 that PF samples also have a small degree of lignocellulose removal in Zone A. By comparing the effect of the NaOH concentration on Zone A, it appeared that sample ALK 1 has higher removal of the OH groups compared to sample ALK 2 and 3.

Moving on to Zone B which represents the hydrocarbon stretching, it can be observed in Figure 1 that NaOH treatment have increased intensity of the C-H stretching peak as seen by the negative Δ%T, suggesting that the amount of C-H bonds is higher after the treatment even though the reaction of the alkali on the lignocellulose would also affect the C-H bonding in the EPFB fibre. A similar observation on the C-H stretching was also seen on the NaOH treated sisal fibre, where the hydrocarbon chains (polysaccharides) are broken into shorter chains that could contribute to an increased in C-H vibration during the FTIR analysis [20, 25, 26]. Another possible explanation can also be due to the loss of amorphous structure (such as hemicellulose) from the treatment that increases the crystallinity fraction (higher cellulose fraction) of the fibre which resulted in denser C-H stretching [27].

Zone C and D mainly reflects on the ester bond that holds the hemicellulose and lignin which is the α-ether link [11]. This two zone also represent the C-O and C=O stretching in cellulose, hemicellulose and lignin. Based on Figure 1, it was shown that sample ALK 3 has the least C-O or C=O vibration indicated by the overall positive Δ%T at Zone C and D compared to sample ALK 1 and 2. Sample ALK 2 also showed positive Δ%T towards the end of Zone D, but nevertheless, sample ALK 3 still showed dominating results of C=O or C=O bond removal across Zone C and D. This provided a qualitative indication that the 4% NaOH treatment was able to remove more hemicellulose and cellulose than the lower NaOH concentrations [20]. In both Zone C and D, a result trend can be observed that increasing the concentration of NaOH lead to the higher removal of hemicellulose and cellulose in the EPFB fibre.

Based on the FTIR analysis of one-step NaOH treatment on the EPFB fibres, spectra at different zones provided trends that do not display uniform pattern whereby no similar Δ%T trend can be observed across each zone for increasing NaOH

concentrations. However, by overall consideration across all the four zones of FTIR spectra, it was observed that sample ALK 3 has the most hemicellulose removal for the one-step NaOH treatment, so the 4% NaOH concentration would be the best one-step alkali treatment for this research.

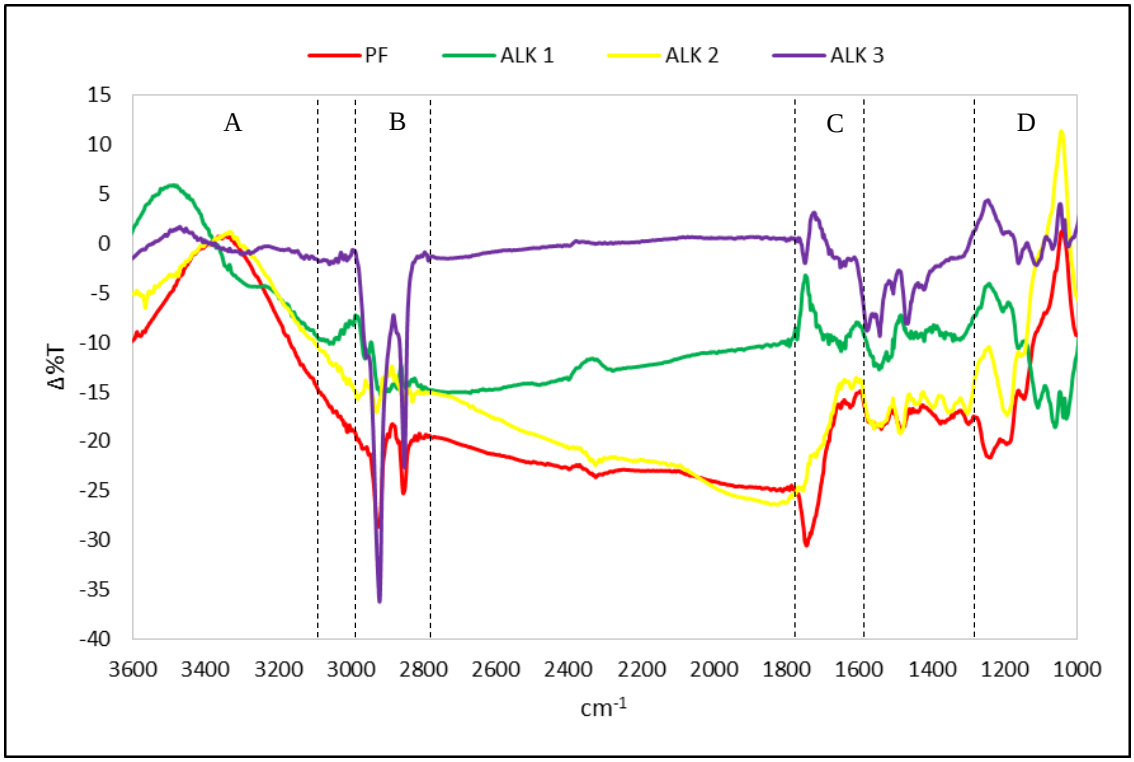


Figure 1. FTIR spectra difference between sample UF and NaOH treated samples

Figure 2 showed the FTIR spectra for the H_2SO_4 treatment on the EPFB fibre. When comparing between Figure 1 and 2, the shape of the FTIR spectra for H_2SO_4 treated samples have uniform pattern across all the zones, unlike the NaOH treated samples that have a rather random pattern when analysing from one zone to the other.

For the H_2SO_4 treatment, a clear difference can be seen for the O-H stretching in Zone A compared to NaOH treatment as the concentration of the acid increases. Based solely on Zone A, it was shown that increasing the concentration of the H_2SO_4 from sample ACD 1 to 2 resulted in an increase in the Δ%T for the O-H stretching. However, increasing the concentration of H_2SO_4 beyond that of sample ACD 2 causes diminishing results in terms of the removal of OH group in the EPFB fibre. So with Δ%T of sample ACD 2 being the most positive among the acid treatment samples, it indicated the highest removal of cellulose and hemicellulose when focused on Zone A [24]. As for Zone B, the similar observation as NaOH treatment can also be seen for H_2SO_4 treatment where the intensity of C-H stretching seems to also be higher after the acid treatment (see Figure 2) with the same reason as discussed previously for NaOH treatment.

In Zone C of Figure 2, the negative Δ%T for the spectra of the H_2SO_4 treated samples representing that the acid has no effect at this zone where it mostly represents the ester bonds in the lignocellulose. However, the working mechanicsm of the acid

treatment is not to destroy the ester bonds, but is to solubilise the hemicellulose [11]. And with that said, it can be seen that there are positive Δ%T in Zone D which indicate the removal of hemicellulose and cellulose [20]. In this zone, it can be observed that the peak of the Δ%T for sample ACD 1 and 2 are very similar implying that both 2 and 4% H_2SO_4 treatment have the comparable effect on the C-O or C-O-C of the EPFB fibre.

In terms of the effect of H_2SO_4 concentration on the treatment of the EPFB fibre, a uniform pattern of the spectra can be seen across all the zones where increasing the acid concentration from 2 to 4% improved the hemicellulose and cellulose removal but further increment to 8% lead to diminishing effect. By evaluating mainly Zone A and D between each sample, it can be observed that ACD 2 has most hemicellulose removal, implying that the 4% H_2SO_4 concentration is the best for the one-step H_2SO_4 treatment in this research.

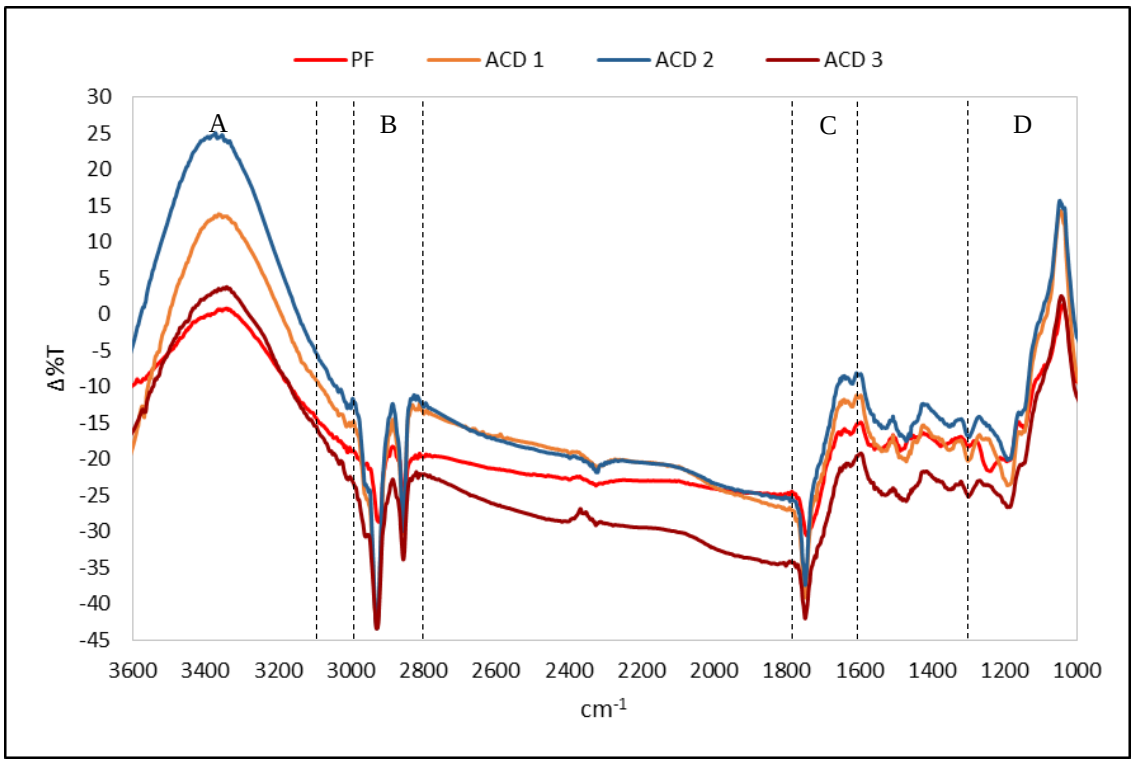


Figure 2. FTIR spectra difference between sample UF and H_2SO_4 treated samples

Figure 3 shown is the FTIR spectra for the two-step NaOH and H_2SO_4 treatment. In Figure 3, the positive Δ%T for the O-H stretching in Zone A for both sample ALK/ACD and ACD/ALK indicated removal of cellulose and hemicellulose from the combined treatment [24]. For Zone B, the results differ from the spectra of the one-step treatment and whereby there shown to have reduction of the C-H stretching when two-step treatment was applied. In Zone C and D, the ester linkage between the hemicellulose and lignin more heavily affected as compared to the one-step treatment, and at the same time also displaying the removal of hemicellulose and cellulose.

Based on Figure 3, the spectra for both ALK/ACD and ACD/ALK sample have a similar pattern, but the overall Δ%T for sample ALK/ACD is much higher than ACD/ALK when moving across all four zones. This results also verified the proposal

from Palamae et al. that NaOH should be the primary effector to improve the extraction process [11]. This is because the NaOH will not only destroy the ester link between the lignocellulose components but also causes the EPFB fibre to swell and enhance the entry of the subsequent H_2SO_4 treatment for the sample ALK/ACD where the hemicellulose can be hydrolysed more effectively [11].



Figure 3. FTIR spectra difference between sample UF and two-step NaOH and H_2SO_4 treated samples

As for torrefaction in Figure 4, the elevated temperature causes the decomposition of the lignocellulose where hemicellulose degrade in between 200 to 300°C [17]. The O-H stretching peak for sample TF 2 yielded positive Δ%T in Zone A of Figure 4 which confirmed the hemicellulose removal at 260°C. The C-H stretching at Zone B for the torrefied samples also have the similar observation again as the one-step chemical treatment. As for Zone C, the negative Δ%T can be observed for both sample TF 1 and 2. It implied that perhaps torrefaction at temperatures of 200 and 260°C did not degrade the ester bonds of the lignocellulose. While in Zone D, positive Δ%T for sample TF 1 and TF 2 confirmed the removal of hemicellulose. However, it can be seen that the peak for sample TF 1 is more positive than TF 2 in this zone. Based on the observation from Zone A and D, sample TF 2 have the most hemicellulose removal, showing that higher torrefaction temperature of 260°C can degrade greater amount of hemicellulose than at 200°C [18].

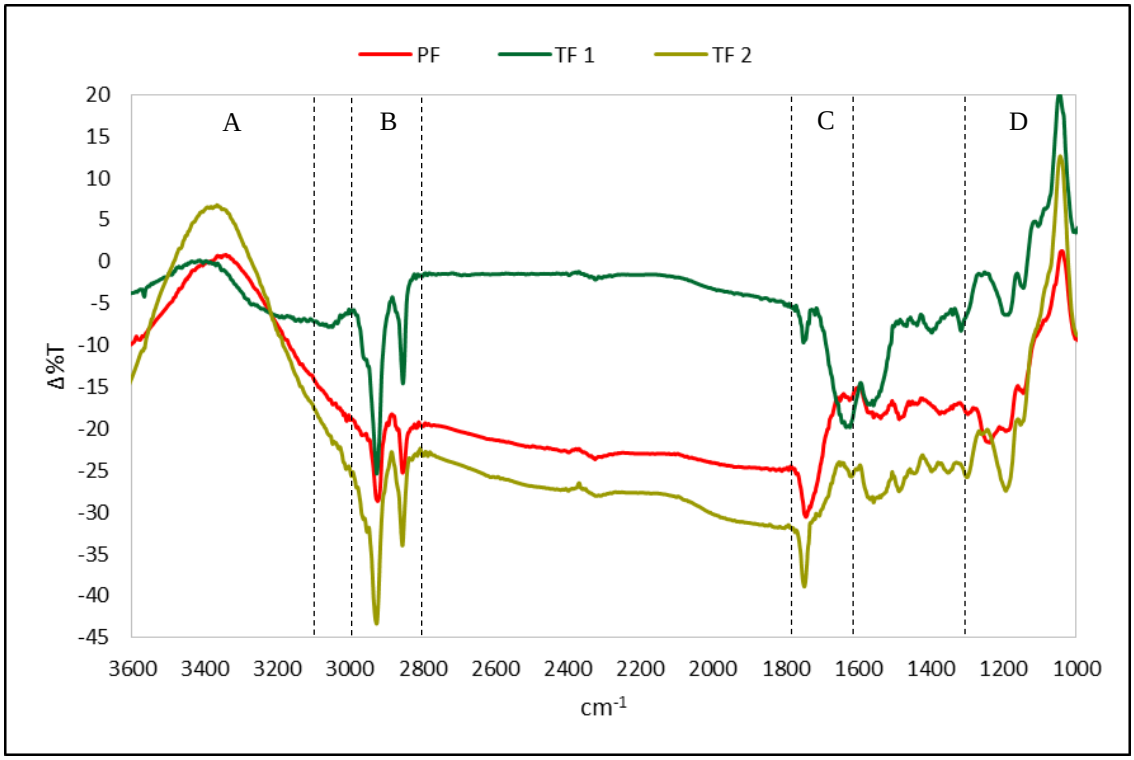


Figure 4. FTIR spectra difference between sample UF and torrefied samples

3.3 Effect of Hemicellulose Extractions from Chemical Treatment

The concentration of hemicellulose extracted was measured based on the HPLC analysis which is represented by the concentration of D-xylose detected in the liquid effluent from the chemical treatment. Table 5 shows the effect of the chemical treatment on the extraction of hemicellulose from the EPFB fibre.

Table 5. Effect of chemical treatment on the hemicellulose extraction

Type of treatment	Liquor sample	Xylose concentration (mg/ml)
One-step NaOH	ALK 1	8×10^{-3}
	ALK 2	14×10^{-3}
	ALK 3	8×10^{-3}
One-step H_2SO_2	ACD 1	26×10^{-3}
	ACD 2	32×10^{-3}
	ACD 3	30×10^{-3}
Two-step NaOH and H_2SO_4	ACD/ALK	40×10^{-3}
	ALK/ACD	87×10^{-3}

The result from HPLC analysis showed that ALK 3 has the greatest removal of hemicellulose for the alkali treatment, which also supported by the similar observation made from the FTIR analysis at Section 3.2. In the one-step NaOH treatment, the concentration of hemicellulose extracted from the EPFB fibre increases with increasing concentration of NaOH from sample ALK 1 to ALK 3 which suggest that increasing NaOH concentration improved the removal of hemicellulose from the fibre. A similar trend of result can also be compared to the NaOH treatment for another lignocellulose biomass, *Mischantus* species [13].

As for the one-step H_2SO_4 treatment, the concentration of hemicellulose extracted from the EPFB fibre increases from sample ACD 1 to ACD 2, but further increase in H_2SO_4 concentration from ACD 2 to ACD 3 showed a decline in extraction performance of the hemicellulose from the biomass. This result was supported by the work of Si et. al. where they investigated on acid and alkali treatments on the *Mischantus* species [13]. In their investigation, they have also observed that there is an optimum concentration for acid treatment of the biomass. In this analysis, sample ACD 2 showed the greatest hemicellulose removal between the acid treated samples, which also strengthen by the similar observation from the FTIR analysis.

Under the one-step NaOH and H_2SO_4 treatment, it was shown that hemicellulose can be extracted more readily under the acid medium than alkaline medium at elevated temperature. A similar observation can also be seen in the work of Ying et. al. [12]. This phenomenon is because the mechanism of the acid in the treatment is mainly to solubilise the hemicellulose fraction in the biomass as opposed to the alkali that destroys the ester bond that holds the components of the lignocellulose [11].

The combined acid and alkali treatment showed remarkable improvement in the hemicellulose extraction. In two-step treatment with NaOH and H_2SO_4, the hemicellulose extraction for sample ALK/ACD suppresses that of sample ACD/ALK. This has once again proven the results of the FTIR analysis that having alkali as the primary step in the combined treatment should be the treatment sequence for improving the hemicellulose extraction from the EPFB fibre.

3.4 Odour Survey Analysis from EPFB Fibre Treatments

Based on the odour survey, the chemically treated EPFB samples have shown to possess odour improvement compared to sample PF from the present EPFB fibre production process. Both the one-step and two-step chemical treatment on the EPFB fibre received good odour level score whereby majority of the panel classified these samples being either pleasant or no odour. Net Promoter Score (NPS) method is implemented to determine the extent of odour satisfaction from the panel.

Table 6 tabulated the NPS for the five samples presented to the panel for odour testing throughout the three batches of survey. The NPS is calculated based on the difference between the % promoters and % detractors. The % promoters and % detractors are classified based on the odour level of the EPFB fibre as indicated in Table 2 of Section 2.9. All the treated sample (ALK 3, ACD 2 and ALK/ACD) received positive NPS above 50% showing that majority of the panel are satisfied with the odour of the treated EPFB fibre. In this statistical analysis, sample ALK/ACD received the highest NPS mainly because majority of the panel identified that this sample has no odour.

The NPS of the chemically treated EPFB fibre are in the order of ALK 3 < ACD 2 < ALK/ACD. Having said that, the concentration of hemicellulose removal are also in the order of ALK 3 < ACD 2 < ALK/ACD. Hence, these results showed that increasing the removal of hemicellulose have managed to contribute to the odour improvement of the EPFB fibre.

Table 6. Odour satisfaction of treated EPFB fibres based on NPS analysis

Sample	% Promoters (A)	% Passives (B)	% Detractors (C)	NPS = A - C
	Odour level 0-1	Odour level 2	Odour level 3-4	
UF	13	20	67	- 54 %
PF	17	23	60	- 43 %
ALK 3	70	13	17	+ 53 %
ACD 2	60	13	3	+ 57 %
ALK/ACD	77	17	7	+ 70 %

4. Conclusions

Based on the outcomes of this research, the EPFB fibre has exhibited better odour with the removal of hemicellulose. Resting on the results from FTIR and HPLC, higher removal of hemicellulose have seemed to be able to provide higher NPS for the EPFB fibre. Besides that, the removal of hemicellulose from the treatment have also shown a reduction in moisture content in the fibre. Taken all together, the lower moisture content of the EPFB fibre from the hemicellulose removal have shown to exhibit odour improvement from the current processed EPFB fibre. Thus, this satisfied the proposed hypothesis of the research.

Reference

[1] Malaysian Palm Oil Council (MPOC), "Malaysian Palm Oil Industry," 2012. [Online]. Available: http://www.mpoc.org.my/Malaysian_Palm_Oil_Industry.aspx. [Accessed: 30-Oct-2015].

[2] S. X. Chin, C. H. Chia, S. Zakaria, Z. Fang, and S. Ahmad, "Ball milling pretreatment and diluted acid hydrolysis of oil palm empty fruit bunch (EFB) fibres for the production of levulinic acid," *J. Taiwan Inst. Chem. Eng.*, vol. 52, pp. 85–92, Jul. 2015.

[3] N. Ali, A. N. M. Tabi, F. A. Zakil, W. N. F. Mohd Fauzai, and O. Hassan, "The usage of empty fruit bunch (EFB) and palm pressed fibre (PPF) as substrates for the cultivation of pleurotus ostreatus," *Sci. Eng.*, vol. 64, no. 1, pp. 93–99, 2013.

[4] K. Anbukarasi and S. Kalaiselvam, "Study of effect of fibre volume and dimension on mechanical, thermal, and water absorption behaviour of luffa reinforced epoxy composites," *Mater. Des.*, vol. 66, pp. 321–330, 2015.

[5] A. Viswas and K. Tewari, *A Textbook Of Organic Chemistry, 3E*, vol. 1. Vikas Publishing House Pvt Ltd, 2009.

[6] B. K. Sharma, *Industrial Chemistry*. Krishna Prakashan Media, 1991.

[7] M. H. Lim, "A case study on palm empty fruit bunch as energy feedstock," *SEGi Rev.*, vol. 3, no. 2, pp. 3–15, 2010.

[8] S. Manna, P. Saha, D. Roy, R. Sen, B. Adhikari, and S. Das, "Enhanced biodegradation resistance of biomodified jute fibers.," *Carbohydr. Polym.*, vol. 93, no. 2, pp. 597–603, 2013.

[9] A. Hassan, A. A. Salema, F. N. Ani, and A. A. Bakar, "A review on oil palm empty fruit bunch (OPEFB) fiber reinforced polymer composite materials | Dr. Arshad Adam Salema - Academia.edu," *Polymers and Polymer Composites*, 2010. .

[10] S. Kim, J. M. Park, J.-W. Seo, and C. H. Kim, "Sequential acid-/alkali-

pretreatment of empty palm fruit bunch fiber.," *Bioresour. Technol.*, vol. 109, pp. 229–33, Apr. 2012.

[11] S. Palamae, W. Palachum, Y. Chisti, and W. Choorit, "Retention of hemicellulose during delignification of oil palm empty fruit bunch (EFB) fiber with peracetic acid and alkaline peroxide," *Biomass and Bioenergy*, vol. 66, pp. 240–248, 2014.

[12] T. Y. Ying, L. K. Teong, W. N. W. Abdullah, and L. C. Peng, "The Effect of Various Pretreatment Methods on Oil Palm Empty Fruit Bunch (EFB) and Kenaf Core Fibers for Sugar Production," *Procedia Environ. Sci.*, vol. 20, pp. 328–335, 2014.

[13] S. Si, Y. Chen, C. Fan, H. Hu, Y. Li, J. Huang, H. Liao, B. Hao, Q. Li, L. Peng, and Y. Tu, "Lignin extraction distinctively enhances biomass enzymatic saccharification in hemicelluloses-rich Miscanthus species under various alkali and acid pretreatments," *Bioresour. Technol.*, vol. 183, pp. 248–254, 2015.

[14] J. Li, Y. Liu, C. Duan, H. Zhang, and Y. Ni, "Mechanical pretreatment improving hemicelluloses removal from cellulosic fibers during cold caustic extraction," *Bioresour. Technol.*, vol. 192, pp. 501–506, 2015.

[15] A. Kristiani, H. Abimanyu, A. H. Setiawan, and F. Aulia, "Effect of Pretreatment Process by Using Diluted Acid to Characteristic of oil Palm's Frond," *Energy Procedia*, vol. 32, pp. 183–189, 2013.

[16] G. Brodeur, E. Yau, K. Badal, J. Collier, K. B. Ramachandran, and S. Ramakrishnan, "Chemical and physicochemical pretreatment of lignocellulosic biomass: a review.," *Enzyme Res.*, vol. 2011, p. 787532, 2011.

[17] W.-H. Chen and P.-C. Kuo, "A study on torrefaction of various biomass materials and its impact on lignocellulosic structure simulated by a thermogravimetry," *Energy*, vol. 35, no. 6, pp. 2580–2586, 2010.

[18] W.-H. Chen and P.-C. Kuo, "Torrefaction and co-torrefaction characterization of hemicellulose, cellulose and lignin as well as torrefaction of some basic constituents in biomass," *Energy*, vol. 36, no. 2, pp. 803–811, 2011.

[19] C. M. Mcginley, M. a Mcginley, and D. L. Mcginley, "Odor Basics, understanding and using odor testing, St. Croix Sensory, Inc.," no. The 22nd Annual Hawaii Water Environment Association Conference, pp. 1–16, 2000.

[20] Z. L. and B. Fei, "Characteristics of Moso Bamboo with Chemical Pretreatment," in *Sustainable Degradation of Lignocellulose - Technique, Applications and Commercialization*, A. Chandel, Ed. InTech, 2013.

[21] S. L. Sun, J. L. Wen, M. G. Ma, and R. C. Sun, "Successive alkali extraction and structural characterization of hemicelluloses from sweet sorghum stem," *Carbohydr. Polym.*, vol. 92, no. 2, pp. 2224–2231, 2013.

[22] H.-Y. Li, S.-N. Sun, X. Zhou, F. Peng, and R.-C. Sun, "Structural characterization of hemicelluloses and topochemical changes in Eucalyptus cell wall during alkali ethanol treatment," *Carbohydr. Polym.*, vol. 123, pp. 17–26, 2015.

[23] Q. Luo, H. Peng, M. Zhou, D. Lin, R. Ruan, Y. Wan, J. Zhang, and Y. Liu, "Alkali extraction and physicochemical characterization of hemicelluloses form young bamboo (Phyllostachys pubescens Mazel)," *BioResources*, vol. 7, no. 4, pp. 5817–5828, 2012.

[24] Isroi, M. M. Ishola, R. Millati, S. Syamsiah, M. N. Cahyanto, C. Niklasson, and M. J. Taherzadeh, "Structural changes of oil palm empty fruit bunch (OPEFB) after fungal and phosphoric acid pretreatment.," *Molecules*, vol. 17, no. 12, pp. 14995–5002, 2012.

[25] T. Milne, A. H. Brennan, and B. H. Glenn, *Sourcebook of Methods of Analysis for Biomass and Biomass Conversion Processes*. Springer Science & Business Media,

1990.
[26] N. Mokaloba and R. Batane, "The effects of mercerization and acetylation treatments on the properties of sisal fiber and its interfacial adhesion characteristics on polypropylene," vol. 6, no. 4, pp. 83–97, 2014.
[27] R. Maryana, D. Ma'rifatun, A. I. Wheni, K. W. Satriyo, and W. A. Rizal, "Alkaline Pretreatment on Sugarcane Bagasse for Bioethanol Production," *Energy Procedia*, vol. 47, pp. 250–254, 2014.

eureca 2016 – Conference Paper
Paper Number 2CE5

Ultrasonic Extraction and Antioxidant Activity from *Labisia Pumila* Leaves

Archana Aravinthen[1*], Rajesh Nithyanandam[2]

[1]School of Engineering, Taylor's University Lakeside Campus, No 1 Jalan Taylor's 47500, Subang Jaya, Selangor DE, Malaysia

[2]Faculty of Engineering, Taylor's University University Lakeside Campus, No 1 Jalan Taylor's 47500, Subang Jaya, Selangor DE, Malaysia

[*]archanaaravinthen@sd.taylors.edu.my

Abstract
Labisia Pumila or commonly named Kacip Fatimah is well known for the ease of childbirth and for its postpartum rejuvenating properties. Its compound contains great photochemical constituents which results into a higher antioxidant and medicinal value. In this study, dried plant extracts were being extracted with ethanol at different time and temperature using ultrasonic water bath to further study its antioxidant capacity. Several non-enzymatic methods were utilized to determine the antioxidant capacity, which include total phenolic content, total flavonoid content and 2, 2-diphenyl-1-picrylhydrazyl (DPPH) radical scavenging assay. The total phenolic and flavonoid content reveals that sample 16 recorded the highest amount which is 40.32 GAE mg/g and sample 10 with 16.8 RE mg/g respectively whereas sample 19 reveals the lowest of 6.16 GAE mg/g and sample 18 of 2.4 RE mg/g respectively. As for DPPH assay, sample 6 records 90.1 % of inhibitor activity compared to sample 2 of 49.5 %. Hence, sample 9 was being subjected into freeze and spray drying due to the highest inhibitory activity to study the effect of encapsulation of bioactive components of each method. It is expected that freeze dried samples (encapsulated) increases the total phenolic and flavonoid content along with DPPH inhibitory activity compared to spray drying.
Keywords**:** *Labisia Pumila*, Kacip Fatimah, Ultrasonic extraction, Antioxidant, free radicals

1. Introduction

During the ancient years, plants which contain high potential of medicinal value that can treat diseases and enhances the growth of well-being were used. Despite the current development in medicinal value, herbal medicines have similar potent ingredients such as modern medicines,

hence it's being extracted and the active ingredients are being modified for further purposes. Based on World Health Organization (WHO), there is about 80% of people worldwide relying on herbal medicines as their dominant health care [1].Geographically, Malaysia has its potential for various habitations of floras due to the tropical climate throughout year. This favours to different types of plant from the Plantae kingdom which can be beneficial for different purposes due to the complexity of the land itself. The similarity incorporated in all the plants are its availability of antioxidant potential present. Antioxidant plays a vital role in neutralizing chemicals which are commonly referred as unstable molecules (free radicals) produced during oxidation that prevents injurious diseases or even fatality [2]. They are known as secondary metabolites produced to defend against oxidative damage [3] by free radicals. Diseases such as cancer, diabetes, cardiovascular diseases and ageing are caused mainly by those free radicals [4].

For this study, is it concluded that Kacip Fatimah or scientifically named *Labisia Pumila* has been chosen to determine its potential antioxidant activity. Kacip Fatimah has been used by the Malay community for a very long time for medicinal purposes. It is small, woody and classified under the family of*Myrsinaceae* that can be extensively found in the tropical areas around the Southeast Asia Region. In Malaysia, *Labisia Pumila* is distributed in eight different varieties and some of them are studied [5]. *Labisia Pumila* has the potential to induce and facilitate childbirth as well as post-partum for about decades now. It does not only contain few other antioxidant compounds but also bioactive photochemical constituents composed of phenolic and flavanoid [6].

Abbreviations

GAE	Gallic Acid equivalent
RE	Rutin equivalence
DPPH	2, 2 diphenyl-picrylhydrazyl
UAE	Ultrasonic extraction
ANOVA	Analysis of variance
TFC	Total Flavanoid Content
TPC	Total Phenolic Content
UV	Ultraviolet
w/v	weight by volume
Superb 6	Samples 3, 4, 7,15,16,20

For extraction of extract, either methanol or ethanol is used commonly. Usually in determining antioxidant component and activity, methanol extraction is said to be a better choice compared to aqueous or ethanol extraction [7]. But as for DPPH it evidently proofs that aqueous extraction shows higher inhibition activity compared to methanol and ethanol. As for this study, *Labisia Pumila* will be extracted using ethanol to study how the time and temperature affects the antioxidant activity. Extraction methods are divided into two groups which are conventional and non-conventional methods.After further research being done, it is safe to say non-conventional extraction method has shown the most efficient result on determining its antioxidant activity specifically for the total phenolic content. Although the method has a shorter extraction time but major challenge is high cost requirement [8].As for UAE, an ultrasonic system with working

frequency fixed at 37 kHz was used for determining the total of phenolic compounds. The time and temperature were optimized into different variations. The temperature was controlled by circulating cold water using an external cold-water bath. The use of power ultrasound can improve the extraction of organic compounds contained within the body of plants and seeds by a solvent [9].

Phenolic compounds are divided into two main groups –flavonoid and non-flavonoids [11]. It has been proven that to antagonize radiation or infection, plants produces more flavanoe or flavanol [12].Hence this proves the amount of flavonoid in a plant plays a vital role for resistance of potential threats which are capability to dodge free radicals [12]. However information on *Labisia Pumila* antioxidant capacities is very limited. In order to hasten the development of *Labisia Pumila*it is persistent to establish the technical knowledge of its medicinal properties by studying its chemical constituents present. Hence the objectives of this research are to study the effect of extraction time, temperature and solvent by optimizing its optimum condition using ultrasonic extraction solvent to study plant's antioxidant component and activity. Last but not least is,to execute the characterization study of total phenolic content, total flavanoid content and DPPH scavenging radical activity

2. Research Methodology

2.1 Material and Method

2.1.1 *Plant Materials*. *Labisia Pumila* plants were collected from Forest Research Institute Malaysia (FRIM), Kepong Kuala Lumpur. Several plants were chosen randomly without defects from shaded house for the experiment.

2.1.2 *Chemicals*. 2, 2- Diphenyl-1-picrylhydrazyl (DPPH), trihydroxybenzoic acid (Gallic acid), Rutin hydrate were purchased from Chemolab Supplies. (Seri Kembangan, Selangor). Ethanol, sodium nitrite, aluminium chloride, sodium carbonate, sodium hydroxide and FolinCiocalteu phenol reagent were obtained from Taylor's University College Engineering Lab. (Puchong, Selangor). Chemicals and reagents used were in analytical grade.

2.1.3 *Apparatus.*

Ultrasonic water bath (ELMA® ELMASONIC P), Whatman no.1 filter paper, Beaker, Aluminium foil, Universal bottles (to store samples), 10ml, 50ml, 100 ml and 500 ml measuring cylinders.

2.1.4 Sample Preparation.

The roots, stems and leaves were separated from each other and placed into three different storage containers. All were subjected into an oven drying at 40℃ for approximately 2-3 days. Moisture content of plant extracts were recorded to ensure there is no water content present. Upon drying, the dried extracts were blended thoroughly until small finely powder were obtained. Weigh 1g of plant extract for each samples and it is being extracted using ultrasonic water bath

(ELMA®ELMASONIC) with 40ml of ethanol at different concentrations at various time and temperature with a fixed working frequency of 37 kHz and filtered using Whatman filter paper number 1. After extraction, plant extracts were being centrifuged for 15minutes at a speed of 4000rpm to obtain a supernatant sample. Samples were prepared by optimization using Design Expert (Version 7).

2.2 Phytochemical content

2.2.1 Total phenolic content

Total phenolic content of the plant extracts was determined using FolinCiocalteu (FC) assay which was described by Pushpanathan&Nithyanandam et al. [13]. 200µL plant extract were pipette into 50ml sample bottles. Then, 400 µL of FolinCiocalteu reagent were added following with 4ml of distilled water. After 3 minutes, 1ml of 20% sodium carbonate were added into the mixture and kept incubated at room temperature for and hr before absorbance being measured at 765nm using UV-VIS spectrometer (Thermo Scientific, (GENESYS 10S UV-Vis). Blank sample was prepared similarly as above expect by replacing the plant extract with distilled water. A calibration curve of gallic acid was prepared at different concentrations (0.2, 0.4, 0.6, 0.8, 1.0 mg/ml). Total phenolic content were expressed in terms of mg/ml per 100g dried weight.

Total Phenolic Content = GAE ×V/M

Where GAE is attained from the standard curve, V and M are total volume and mass used respectively during assay.

2.2.2 Total flavonoid content

Total Flavanoid Content (TFC). Total flavonoid content of plant extract was carried out according to the assay developed by Zhishen,Mengcheng, &Jianming et al. [14]. 500µL plant extracts was diluted into 2.5ml distilled water with 75µL of (5% w/v sodium nitrite) using pipette. The mixture was incubated at room temperature for 6 minutes. 0.3ml of (10% w/v aluminium chloride) was added following with 500µL of sodium hydroxide and 0.55ml of distilled water. The absorbance of the samples were measured at 570nm using UV-Vis spectrometer (Thermo Scientific, GENESYS 10S UV-Vis). Blank sample was prepared similarly as above expect by replacing the plant extract with distilled water. A calibration curve of rutin was prepared at different concentration (0.3, 0.5, 0.7 mg/ml). Total flavonoid content was expressed in terms of mg/ml per 100g dried weight.

Total Flavanoid Content = RE ×V/M

Where RE is attained from the standard curve, V and M are total volume and mass used respectively during assay.

2.2.3 DPPH radical scavenging activity

The scavenging activity was evaluated using DPPH radical based on method described by Pushpanathan&Nithyanandam et al. [13]. 200μL of plant extract was added with 4ml of ethanolic DPPH (60×10^{-5}M). The mixture was kept in the dark for about 30 minutes before absorbance being measured using UV-Vis spectrometer (Thermo Scientific, GENESYS 10S UV-Vis) at 517nm. This is done to block UV light as it triggers the free radicals SAHA et al. [15]. Due to the reaction, samples will change colour from deep violet to light yellow/orange.Blank sample was prepared similarly as above expect by replacing the plant extract with distilled water. Radical scavenging activity was calculated using equation below;

$$(\%)\ Inhibition = \frac{A_{blank\ sample} - A_{extract}}{A_{blank\ sample}} \ldots\ldots\ldots \text{(Eq. 1)}$$

3.0 Discussion

3.1 Response Surface Models

Table 1. Experimental Matrix and Values of the Observed Response

Run	EC[a] (%)	T[b] (min)	T[c] (℃)	TPC(mg/g)	TFC(mg/g)	DPPH (%)
1	40	100	60	23.24	5.44	69.5
2	70	70	40	26.6	10.08	49.5
3	70	70	40	26.6	10.08	49.5
4	70	70	40	26.6	10.08	49.5
5	70	70	73.64	26.6	6.44	68.4
6	40	100	30	15.2	4.0	90.1
7	100	100	60	31.2	15.88	63.8
8	40	40	30	15.2	4.0	75.5
9	40	19.55	40	23.24	10.64	63.8
10	100	40	60	38.0	16.40	85.6
11	70	70	6.36	20.0	4.0	80
12	100	100	30	38.4	15.6	67.4
13	70	70	40	26.6	10.08	49.5
14	100	40	30	37.2	12.8	72.7
15	40	40	60	14.4	6.4	56.63
16	120	70	40	40.32	16.8	78.93

17	70	70	40	26.6	10.08	49.5
18	70	70	40	6.16	2.4	64.9
19	70	70	40	26.6	10.08	49.5
20	70	120.45	40	24.08	9.24	70.7

EC^a = Ethanol concentration
T^b = Extraction time
T^c = Extraction temperature

Table 1 above indicated the amount of chemical constituents present in the plant. The highest amount of phenolic content was found in sample 16 with an amount of 40.32 GAE mg/g and the lowest was found in sample 18 with 6.16 GAE mg/g. Both samples were carried out at the same point of time and extraction temperature. Moving on, for TFC the highest content was discovered in sample 10 and the lowest in sample 18. Both flavonoid and phenolic content was found lowest at sample 18. As for DPPH activity, sample 6 inhibits the highest inhibitory activity of 90.1% compared to sample 2 which records 49.5% only. The suitability of the response was analysed by ANOVA for this project. Table 2, 3 and 4 below shows the calculated statically parameters obtained from each response Model equations for relationship between ethanol concentration, TPC and TFC and independent variables were obtained by applying multiple regression analysis.

Table 2. Analysis of variance for TPC Response Surface Linear Model

Sum of Squares	**DF**	**Mean square**	**F value**	**p-value**
1472.60	3	490.87	12.99	0.0001
1318.92	1	1318.92	34.90	< 0.0001
1.59	1	1.59	0.042	0.8403
152.10	1	152.10	4.02	0.0621
604.72	16	37.80		
604.72	11	54.97		
0.00	5	0.00		
2077.33	19			

Table 3. Analysis of variance for TFC Response Surface Linear Model

Source	**Sum of Squares**	**DF**	**Mean square**	**F value**	**p-value**
Model	399.96	9	44.44	15.25	0.0001
A-Concentration	309.92	1	309.92	106.37	<0.0001
B -Time	0.078	1	0.078	0.027	0.8730
C-Temperature	25.20	1	25.20	8.65	0.0148

AB	1.31	1	1.31	0.45	0.5174
AC	2E-004	1	2E-004	6.864E-005	0.9936
BC	2.29	1	2.29	0.79	0.3962
A^2	2.14	1	2.14	0.73	0.4117
B^2	3.68	1	3.68	1.26	0.2873
C^2	50.42	1	50.42	17.30	0.0019
Residual	29.14	10	2.91		
Lack of Fit	29.14	5	5.83		
Pure Error	0.000	5	0.000		
Cor Total	429.10	19			

Table 4. Analysis of variance for DPPH Response Surface Linear Model

Source	**Sum of Squares**	**DF**	**Mean square**	**F value**	**p-value**
Model	4225.18	9	472.80	1.76	0.1962
A-Concentration	33.43	1	33.43	0.12	0.7318
B -Time	10.50	1	10.50	0.039	0.8474
C- Temperature	527.35	1	527.35	1.96	0.1918
AB	372.24	1	372.24	1.38	0.2668
AC	297.31	1	297.31	1.10	0.3179
BC	41.54	1	41.54	0.15	0.7026
A^2	1729.77	1	1729.77	6.43	0.0296
B^2	1248.16	1	1248.16	4.64	0.0567
C^2	81.53	1	81.53	0.30	0.5941
Residual	2690.73	10	269.07		
Lack of Fit	2690.73	5	538.15		
Pure Error	0.000	5	0.000		
Cor Total	6945.91	19			

3.2 Effect of Temperature, Ethanol concentration and extraction time on investigated response

In case of model equation, temperature and ethanol concentration have significant influence. A positive influence is inhibited by extraction temperature causes the softening of the plant tissues due to temperature influence. Based on Table 4-8, TPC and TFC value was discovered lowest at the same point of extraction temperature, 70℃. As the temperature increases, it reduces the solvents viscosity and surface tension which promotes extraction of soluble compounds [31]. Besides that, the lower yield of phenolic and flavonoid occurred at a higher temperature can be also due to degradation of extractable compounds which leads to aggregation. As for ethanol concentration, increases value in concentration inhibits a lower antioxidant activity indicating that 40% of ethanol concentration is a good solvent for the *labisia pumila* antioxidants. As for extraction time for antioxidant activity it does not have any significant influence on it.

Figure 1, 2 and 3 are 3D response surface plots which represents regression equations in graphical. It visualizes the relationship between responses and experimental level of each variable. Figure 1A shows phenolic contents increases as the ethanol concentration increases. On the other hand, the temperature has a slight influence on the phenolic content in Figure 1B but the yield increases as the time passes both cases. Based on all the figures, extraction of phenolic compounds influence different variables such as temperature and contact time. These variables are selected to influence the recovery and show conflicting results of degradation of phytochemical [32]. Hence, increasing extraction solvent with increasing temperature enhances the TPC content. This is because the solubility increases as the mass transfer improves the emergences of solvent into the plant matrix.

Moving on to Figure 2A, antioxidant activity of the plant increases when extraction temperature decreases. This is because a higher temperature may degrade the cause the antioxidant thermally unstable due to elevated temperature. As for this case, extraction time has no significant effect on the antioxidant activity based on Figure 2B and 2C. Besides that, rise in temperature may produce undesirable effects such as modifying chemical compounds or structures present in plant extract [33].

As for TFC contents, figure 3A shows similar pattern as figure 1A. The total flavonoid content of the plant increases as the concentration increases. As for the extraction temperature, the TFC value decreases as the temperature decreases. It is proven that positive effect of temperature-ethanol concentration presents an interactive influence between variables where temperature improves solvent properties and increases affinity to desirable group of compounds [39]. Extraction time does not have any effect on the yield of flavonoid as well. The effect of extraction time confirmed the deceleration in the extraction yield, as Fick's second law of diffusion predicts a final equilibrium between the solute concentrations in the solid matrix and in the bulk solution after a certain time [33].

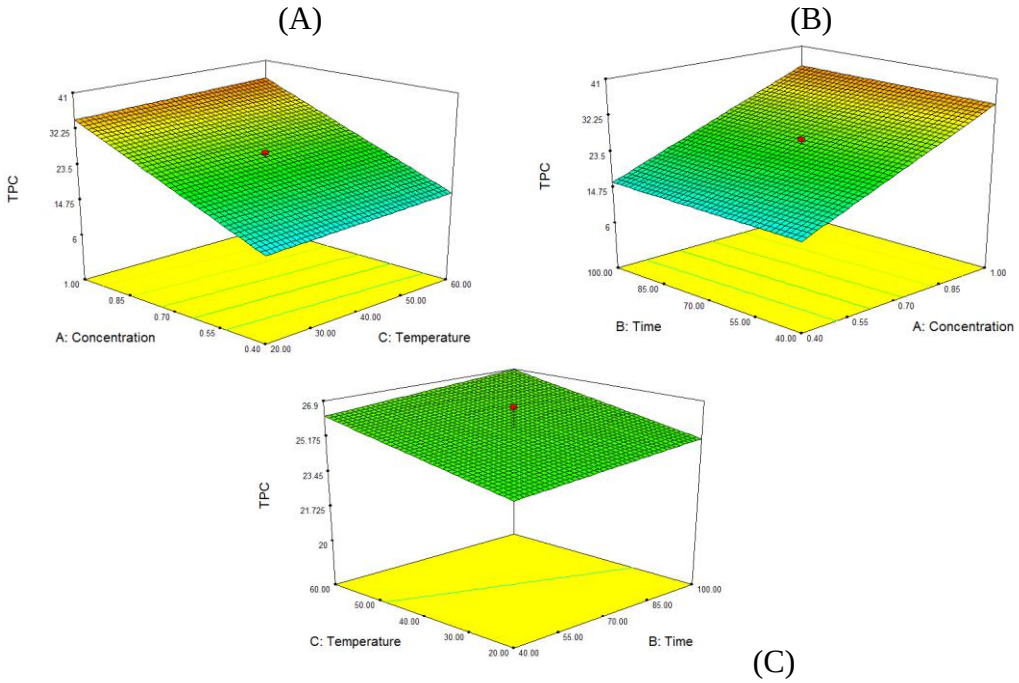
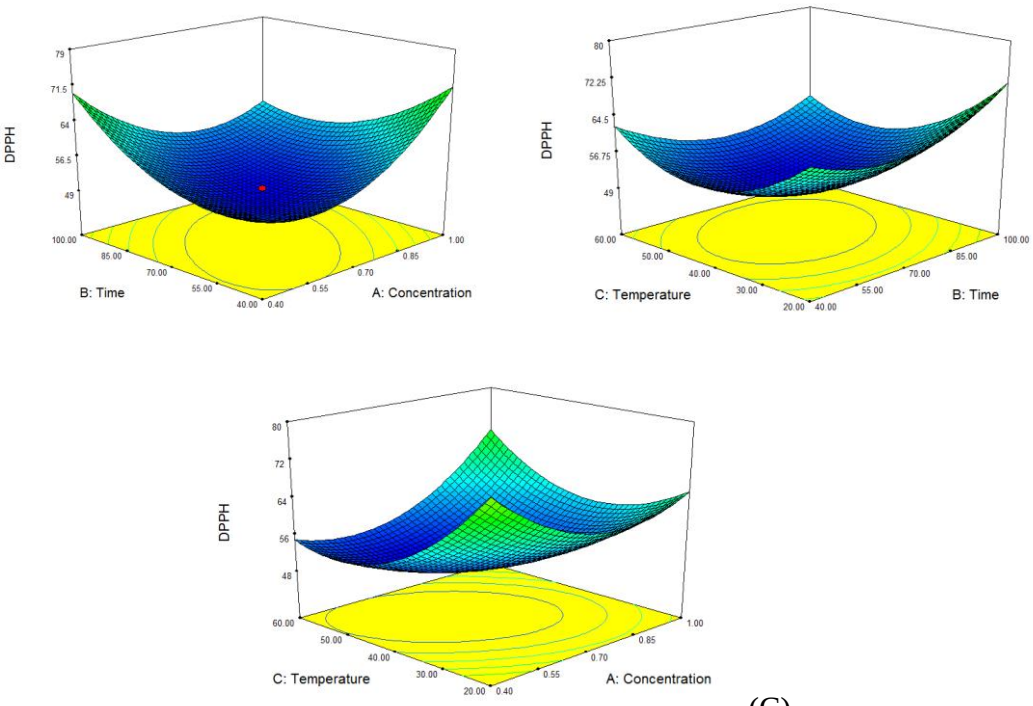
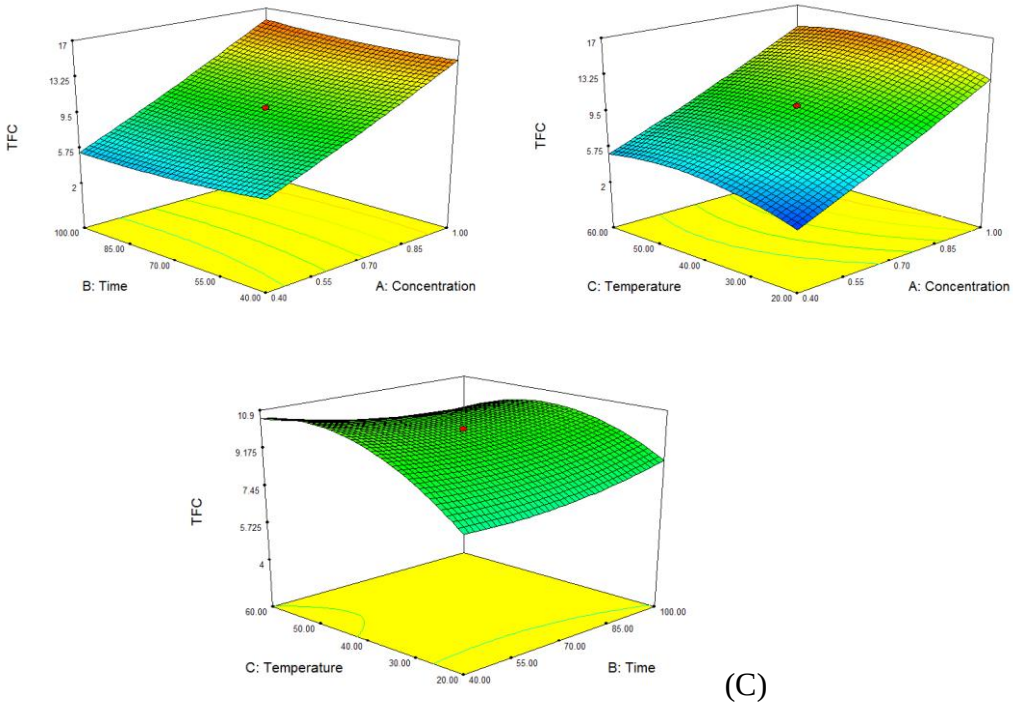


Figure 1: Response surface plot showing effects of TPC with investigated parameters A –time vs. concentration B –temperature vs. concentration C- temperature vs. time



(A)
(B)
(C)

Figure 2. Response surface plot showing effects of DPPH with investigated parameters A – time vs. concentration B – temperature vs. concentration C – temperature vs. time



(A)
(B)
(C)

Figure 3. Response surface plot showing effects of TFC with investigated parameters A – time vs. concentration B – temperature vs. concentration C – temperature vs. time

3. Conclusion

High antioxidant activity was observed in sample 6 compared to other samples. The extraction time and temperature plays a vital role in determining the total phenolic and flavonoid content. As for Sample 6, the optimum conditions were 40% of diluted ethanol carried out at 30℃ for 100 minutes. As for total phenolic and flavonoid content, sample 16 records the highest amount with a higher temperature of 40℃ for 70 minutes. As for determining phytochemical constituents, higher extraction time and optimum temperature ranging from 40℃ - 50℃, increases the flavonoid yield.

References

[1] University of Maryland Medical Centre, (2015). Herbal Medicine. [online] Available at: 1. https://umm.edu/health/medical/altmed/treatment/herbal-medicine [Accessed 28 Sep. 2015].

[2] Better Health Channel, (n.d.). *Antioxidants*. [online] Available at: 2. http://www.betterhealth.vic.gov.au/bhcv2/bhcarticles.nsf/pages/antioxidants [Accessed 28 Sep. 2015].

[3] T. LIM, Y. LIM and C. YULE, "Evaluation of antioxidant, antibacterial and anti-tyrosinase activities of four Macaranga species", Food Chemistry, vol. 114, no. 2, pp. 594-599, 2009.

[4] B. Subhasree, R. Baskar, R. LaxmiKeerthana, R. Lijina Susan and P. Rajasekaran, "Evaluation of antioxidant potential in selected green leafy vegetables", Food Chemistry, vol. 115, no. 4, pp. 1213-1220, 2009.

[5] Sunarno, B. (2005). Revision of the Genus Labisia (Myrsinaceae).*Blum - J Plant Tax and Plant Geog*, 50(3), pp.579-597.

[6] Chua, L., Lee, S., Abdullah, N. and Sarmidi, M. (2012). Review on Labisia pumila (Kacip Fatimah): Bioactive phytochemicals and skin collagen synthesis promoting herb. *Fitoterapia*, 83(8), pp.1322-1335.

[7] D. Krishnaiah, R. Sarbatly and R. Nithyanandam, "A review of the antioxidant potential of medicinal plant species", Food and Bioproducts Processing, vol. 89, no. 3, pp. 217-233, 2011.

[8] Azmir, J., Zaidul, I., Rahman, M., Sharif, K., Mohamed, A., Sahena, F., Jahurul, M., Ghafoor, K., Norulaini, N. and Omar, A. (2013). Techniques for extraction of bioactive compounds from plant materials: A review. Journal of Food Engineering, 117(4), pp.426-436.

[9] B. Liu, Y. Ma, Y. Liu, Z. Yang and L. Zhang, "Ultrasonic-Assisted Extraction and Antioxidant Activity of Flavonoids from Adinandranitida Leaves", Tropical Journal of Pharmaceutical Research, vol. 12, no. 6, p. 1045, 2014.

[10]J. Vuthijumnok, "Effect of freeze-drying and extraction solvents on the total phenolic contents, total flavonoids and antioxidant activity of different Rabbiteye blueberry genotypes grown in New Zealand", IOSR-JPBS, vol. 8, no. 1, pp. 42-48, 2013.

[11] C. Sulaiman and I. Balachandran, "Total phenolics and total flavonoids in selected Indian medicinal plants", Indian Journal of Pharmaceutical Sciences, vol. 74, no. 3, p. 258, 2012.

[12] J. Harborne and C. Williams, "Advances in flavonoid research since 1992", Phytochemistry, vol. 55, no. 6, pp. 481-504, 2000.

[13] Pushpanathan, K. &Nithyanandam, R. (2015). ANTIOXIDANT POTENTIAL OF MALAYSIAN MEDICINAL PLANT.ResearchGate. Retrieved 11 May 2016,fromhttps://www.researchgate.net/publication/282559225_ANTIOXIDANT_POTENTIAL_OF_MALAYSIAN_MEDICINAL_PLANT?ev=prf_pub

[14] Zhishen, J., Mengcheng, T., &Jianming, W. (1999). The determination of flavonoid contents in mulberry and their scavenging effects on superoxide radicals. Food Chemistry, 64(4), 555-559. http://dx.doi.org/10.1016/s0308-8146(98)00102-2

[15] SAHA, K. (2004). Evaluation of antioxidant and nitric oxide inhibitory activities of selected Malaysian medicinal plants. Journal OfEthnopharmacology, 92(2-3), 263-267. http://dx.doi.org/10.1016/s0378-8741(04)00109-6

[16] P. Nariya, N. Jirankalgikar and S. De, "Free Radical Scavenging Potential of Selected Medicinal Plants: Quantitative Evaluation by a Novel Online HPTLC-DPPH Method", Journal of Herbs, Spices & Medicinal Plants, vol. 20, no. 4, pp. 386-393, 2014

[17] E. Abdel-Hameed, "Total phenolic contents and free radical scavenging activity of certain Egyptian Ficus species leaf samples", Food Chemistry, vol. 114, no. 4, pp. 1271-1277, 2009.

[18] M. Stankovic, "Antioxidant activity, total phenol and flavonoid contents of Sideritismontana L. from Serbia", Planta Med, vol. 76, no. 12, 2010.

[19] V. Krishnan, S. Ahmad and M. Mahmood, "Antioxidant Potential in Different Parts and Callus ofGynuraprocumbensand Different Parts ofGynurabicolor", BioMed Research International, vol. 2015, pp. 1-7, 2015.

[20] A. Kumaran and R. Joel Karunakaran, "In vitro antioxidant activities of methanol extracts of five Phyllanthus species from India", LWT - Food Science and Technology, vol. 40, no. 2, pp. 344-352, 2007.

[21] B. Subhasree, R. Baskar, R. LaxmiKeerthana, R. Lijina Susan and P. Rajasekaran, "Evaluation of antioxidant potential in selected green leafy vegetables", Food Chemistry, vol. 115, no. 4, pp. 1213-1220, 2009.

[22] Dai and R. Mumper, "Plant Phenolics: Extraction, Analysis and Their Antioxidant and Anticancer Properties", Molecules, vol. 15, no. 10, pp. 7313-7352, 2010.

[23] G. Tu, T. Bui, T. Tran, N. Ton and V. Le, "Comparison of Enzymatic and Ultrasonic Extraction of Albumin from Defatted Pumpkin (Cucurbitapepo) Seed Powder", Food Technology and Biotechnology, vol. 53, 2015.

[24]N. Rahman, S. Tumin and R. Tajuddin, "Optimization of Ultrasonic Extraction Method of Natural Dyes from XylocarpusMoluccensis", IJBBB, pp. 53-55, 2013.

[25] Ahmed, M., Akter, M., Lee, J. and Eun, J. (2010). Encapsulation by spray drying of bioactive components, physicochemical and morphological properties from purple sweet potato.*LWT - Food Science and Technology*, 43(9), pp.1307-1312.

[26] Tarakemeh, A. and Abutalebi, A. (2012). Effect of Drying Method on the Essential Oil Quantity of Basil (Ocimumbasilicum L.). *Journal of Essential Oil Bearing Plants*, 15(3), pp.503-505.

[27] Nguyen, V., Van Vuong, Q., Bowyer, M., Van Altena, I. and Scarlett, C. (2014). Effects of Different Drying Methods on Bioactive Compound Yield and

Antioxidant Capacity of Phyllanthusamarus. Drying Technology, 33(8), pp.1006-1017.

[28] Salehi, F. and Kashaninejad, M. (2014). Effect of Different Drying Methods on Rheological and Textural Properties of Balangu Seed Gum.*Drying Technology*, 32(6), pp.720-727.

[29] Ma, L., Chen, H., Zhu, W. and Wang, Z. (2013). Effect of different drying methods on physicochemical properties and antioxidant activities of polysaccharides extracted from mushroom Inonotusobliquus. *Food Research International*, 50(2), pp.633-640

[30] Ma, L., Chen, H., Zhu, W. and Wang, Z. (2013). Effect of different drying methods on physicochemical properties and antioxidant activities of polysaccharides extracted from mushroom Inonotusobliquus. *Food Research International*, 50(2), pp.633-640.

[31] Juntachote, T., Berghofer, E., Bauer, F., and Siebenhandl S., 2006, The application of response surface methodology to the production of phenolic extracts of lemon grass, galangal, holy basil and rosemary, International Journal of Food Science and Technology, 41, 121–133.

[32] K. Robards, "Strategies for the determination of bioactive phenols in plants, fruit and vegetables", Journal of Chromatography A, vol. 1000, no. 1-2, pp. 657-691, 2003.

[33] Z. Zekovic, A. Cvetanovic, B. Pavlic, J. Svarc-Gajic and M. Radojkovic, "The optimization of the extraction process of flavonoids from fermented chamomile ligulate flowers", Savremenetehnologije, vol. 4, no. 1, pp. 54-63, 2015.

Ultrasound Assisted Extraction of Total Phenolic Compound from Carica Papaya Leaves

Chia Wei Qian, Chien Hwa Chong*

Jalan Taylors, Subang Jaya, 47500 Subang Jaya, Selangor, Malaysia

*Corresponding author: Chienhwa.Chong@taylors.edu.my

Abstract

In this paper, extraction of the bioactive compounds from the leaves of *C. papaya* using methanol was studied in specific temperature range in both presence and absence of ultrasound. Ultrasound assisted extraction has been studied to give better extraction yield defined in terms of total phenolic contents with lower extraction temperature and shorter extraction duration compared to maceration. The effect of extraction temperature on total phenolic content over time duration was studied by using a phenomenological model. This phenomenological model is to study the kinetic of the total phenolic contents in response to different temperature in extraction process which includes the two mechanisms, washing and diffusion in extraction process. For phenomenological model, the kinetics and coefficients of total phenolic contents washed and diffusion only identified by using curve fitting by using TableCurve 2D software. To perform this research, the 1g of leaves sampled with adding methanol and experimented in ultrasonic water bath. Identification of total phenolic content of extracts were using Folin-Ciocalteu method which using ultraviolet visible spectrophotometer compare with Gallic acid. Based on the results, the extraction kinetic of total phenolic contents performed by developing phenomenological model of the extraction yield with extraction temperature and extraction time as variables. The curve fitting of phenomenological model in compare to experimental data with both presence and absence of ultrasound were analyzed in determination coefficient (R^2), mean square error (MSE) and mean relative percent deviation (MRPD) to assess the performance of the model. In this paper, model is well fitted to the experimental data which have R^2 0.982 to 0.922 and MRPD 0.0263% to 5.186%. After curve fitting, the kinetic coefficients of washing and diffusion (k_1 and k_2), washing coefficient (f) and saturation extraction yield (y_{sat}) for each condition are defined.

Keywords: *C. papaya*, Ultrasound assisted extraction, Phenomenological model, total phenolic contents.

1. Introduction

C. papaya has a high potential on medical uses and the medical properties of bioactive compound have been studied in some researches [1]. *C. papaya* belong with with family of *Caricaceae* is founded in most of the tropical countries such as Nigeria, Mexico, Thailand, Malaysia and other South-East Asia Countries [2]. Fresh leaves of *C. papaya* are traditionally used in the various treatment of fever, pyrexia, diabetes, gonorrhea, syphilis, septic wounds and most popular on treatment of dengue fever [2], [3]. Furthermore, dried leaves and fruits also commonly used as one of the raw material in soap production.

The fruit, leaves, stems, seeds root especially leaves of *C. papaya* is rich in carpains such as alkaloids, carpain pseudocarpain, dehydrocarpaine I and II, choline and carposide [4]. These carpains endopeptidases contributed as phenolic compounds and flavonoid compounds, consist of the antibacterial, anti-sickling, antioxidant, reversible male infertility, anti-inflammatory, reduce blood sugar level and anticancer activity. In *vitro* antimicrobial activity against bacteria, fungi and yeast has been claimed by extraction of the *C. papaya*'s stems and leaves [1]. Isolated carpains from leaves and fruits showed antibacterial and antifungal properties [2]. Isolated papain from *C. papaya* plant has been claimed that main constituents for antifungal properties [3]. The leaves also has been claimed that having the higher total phenolic contents by methanolic extract compare to standard ascorbic acid [5].

An effective method and time efficient for extraction of phenolic compounds from *C.papaya* leaves is important and considered in industrial application to improve the potential of commercial production. There are some conventional methods, *i.e.*, maceration, Soxhlet, LLE, commonly used in phenolic compounds extraction from different plant materials. But these methods are mostly developed in lab scale for research purpose and time consuming. These methods also performed low extraction yield of phenolic compounds from different types of fruits, flower, leaves and *etc*. High operating temperature during extraction may reduce extraction time duration but may cause damage or degradation of phenolic compounds. The ultrasound assisted extraction (UAE) was introduced as an alternative method to enhance the extraction efficiency without any notable side effects [6]. UAE using ultrasonic wave causes cavitation and bubble collapses in liquid medium to enhance cell wall disruption in solvent extraction [6]. UAE is the most feasible compare to other conventional methods and Accelerated Solvent Extraction (ASE) because of the lowest extraction time duration compare to others. The time duration for the UAE method is about 5 to 20 mins on the extraction of the same amount of phenolic compound from the plant compare to maceration take highest time duration up to 24 h followed by Soxhlet (up to 6 h) and ASE (up to 20 mins). UAE for 30 mins shows similar performance compare to the Soxhlet extraction for 6hr on extracting essential oil from grape seed [7], [8]. Limited literatures on phenolic compounds extraction performed by UAE from *Carica Papaya* leaves.

This work aimed to investigate and analysed the UAE for phenolic compounds from *C. papaya* leaves with combined effects of operational variables, including extraction times and extraction temperatures, on the kinetic of extraction yields of phenolic compounds were developed using phenomenological modelling. The process was also compared with presence and absence of ultrasonic supply. The total phenolic

compounds of extracts were identified by using Folin-Ciocalteu method. The extracts with the Folin & Ciocalteu's reagent were identified by comparing with standard Gallic acid ultraviolet visible spectrophotometer.

2. Materials and methods

2.1 Chemical and reagents

Solid Sodium Carbonate Monohydates, Na_2CO_3 purchased from R&M Chemicals, Evergainful Enterprise Sdn Bhd (Petaling Jaya, Selangor Darul Ehsan), methanol purchased from Friendemann Schmidt (Germany), Folin & Ciocalteu's reagent purchased from Chemsolv Inc (Roanoke, VA), deionized water, Standard Gallic acid purchased from Merck Millipore Sdn Bhd (Bandar Sunway, Selangor)

2.2 Plant Material

Fresh leaves of *papaya* leaves were collected in February 2016 from Chemor, Perak. The leaves were removed from the plant and kept in sealed plastic bag before use in a chiller at 7 ^oC.

2.3 Ultrasound Assisted Extraction of phenolic compounds

C. Papaya leaves samples were extracted using ultrasound-assisted extraction method (UAE). Using an ultrasonic water bath (Sonica Ultrasonic Cleaner 3200 EP, 180W) operating at 180 W and 40 kHz frequency as ultrasonic irradiation apparatus. The dimension of the bath is 300 mm x 240 mm x 100 mm. 1g of leaves and samples added with 20 ml of methanol. In this case the solute-solvent ratio was at 1:20 g/ml. Each experiments of the both leaf samples with solvent were extracted with sonication for range of 10 to 60 mins as 10 mins interval. Several researches claimed that extraction yield of bioactive compounds such as papain from *papaya* leaves reaching maximum extraction yield start within 60 mins to 70 mins. The extraction process has been extracted in range of temperature 30 to 60^oC (maximum temperature for ultrasonic bath). The experiment repeated without ultrasound to represent maceration.

2.4 Total phenolic content (TPC) analysis

Total phenolic content (TPC) of extracts from leaf samples were identified by using the Folin-Ciocalteu method. The procedure of the TPC analysis had been refered by Yingngam et al [9]. The 1 ml of extracts, 5 ml of distilled water and 0.5 ml Folin-Ciocalteu's reagent were placed into test tube and well mixed by vortex shaker. 1.5 ml of 20% Na_2CO_3 solution is then added into the mixture and volume filled up to 10ml with distilled water [10]. The mixture kept at room temperature for 2 hrs. The mixture as the absorbance was measured at 725 nm using ultraviolet visible spectrophotometer (Shimadzu, UV-2401 PC; Japan). Gallic acid is used as standard phenolic compound. The TPC of the samples are expressed as gallic acid equivalent (mg GAE/g) with calibration equation with $R^2 = 0.99$

2.5 Data Modelling

The modelling of extraction amount like TPC at different temperatures is not covered through all these assisted extraction researches. Suggestion could be made that

using ultrasound-assisted extraction in different condition such as temperature and time. The modelling of the extraction was to study the extraction in response to different variables and shows the kinetic of both extraction mechanisms (washing and diffusion). Washing is the mechanism of the rapid external solute with high rate of transfer by convection.

According to *Milić et al.*, phenomenological modelling is used to model extraction yield in response to extraction time on both washing and diffusion processes. The two processes are assumed to occur simultaneously and the norm is generally exponential, the model is using as [11]

$$y = y_{\infty} [1- f \exp(-k_1 t) – (1-f) \exp(-k_2 t)] \quad (1)$$

Where y and y_{∞} are the extraction yield and saturation extraction yield by g/g GAE equivalent of samples. f is fraction of extracts washed. The rate constant of both washing and diffusion of extraction process are defined by Arrhenius equation:

$$k = A \exp\left(\frac{Ea}{RT}\right) \quad (2)$$

2.6 Error Analysis

The performance of the phenomenological modeling and second-order polynomial model are assessed by the coefficient of determination (R^2), mean square error (MSE) and mean relative percent deviation (MRPD) and the calculation are using equation.

$$R^2 = \frac{\sum_{i=1}^{n}(y_{a,i}-y_{p,i})^2}{\sum_{i=1}^{n}(y_{p,i}-y_m)^2} \quad (3)$$

$$MSE = \frac{1}{n}\sum_{i=1}^{n}(y_{a,i} - y_{p,i})^2 \quad (4)$$

$$MRPD = \frac{100}{n} \sum_{i=1}^{n} \left|\frac{y_{p,i} - y_{a,i}}{y_{a,i}}\right| \quad (5)$$

Where $y_{p,i}$ and $y_{a,I}$ are the predicted and actual values of the total phenolic compound yield and y_m is the mean value of total phenolic compound yield, and n is the number of experiment runs.

3. Result and discussion

3.1 Comparison of TPC between the UAE and maceration

The total phenolic contents (TPC) of *C. papaya* leaves using UAE and maceration extraction method has been shown in Figure 1. From Figure 1, it is clearly showed that the UAE extraction method has overall higher TPC extraction yield based on Folin-Ciocaltue assay compare to maceration. The TPC yield from UAE method was in range of 0.0714 mg GAE/g to 0.2729 mg GAE/g from 10 mins to 60 mins at 30^{o}C. Increasing the temperature of UAE improved the performance of extraction which TPC of extract increased to in range of 0.1681 mg GAE/g to 0.3547 mg GAE/g from 10 mins to 60 mins at 60^{o}C.

For maceration method, it was similarly increasing compare to UAE by increasing extraction time. But the TPC yield was lower compare to UAE in range of 0.0364 mg GAE/g to 0.1011 mg GAE/g from 10 mins to 60 mins at 30^{o}C. 0.0739 mg GAE/g to 0.1898 mg GAE/g from 10 mins to 60 mins at 60^{o}C. The TPC yield from UAE was greater than maceration which caused by the acoustic energy from the ultrasonic wave to improve surface mass transfer. This phenomenon was also reported from other sample such as grape seeds, P. *lentiscus* L. leaves and *Galium mollugo* L [7], [8], [11].

The ultrasound also known as ultrasonic wave was kinetic sound wave produce acoustic energy which transferrable on contacting medium. Ultrasonic wave consisted expansion cycle (rarefaction) caused negative pressure to force liquid molecules moving apart and compression cycle caused positive pressure to increase the compression between molecules [12]. When the expansion caused by ultrasound exceed tensile strength of liquid in rarefaction region, cavitation bubbles were formed [12]. The cavitation bubbles of the solvent becomes driven force to disrupt the cell wall and tissue causing the improvement of the mass transfer of solvent [11]. The compressed molecules during compression cycle improve the diffusion between the two bulk surface which is solvent and extracts due to higher pressure of solvent penetrate through the medium. It is theoretically proving that the extraction yield is improved by the presence of ultrasonic wave.

Figure 3 shows that there was no decreasing of TPC yield from in range of 30^{o}C to 60^{o}C UAE and maceration. This behavior also claimed by *Vuong et al* which extraction of dried *C. papaya* leaf using maceration from 50^{o}C to 100^{o}C [13]. The TPC yield increased from 50^{o}C till 70^{o}C then start decreasing onward [13].

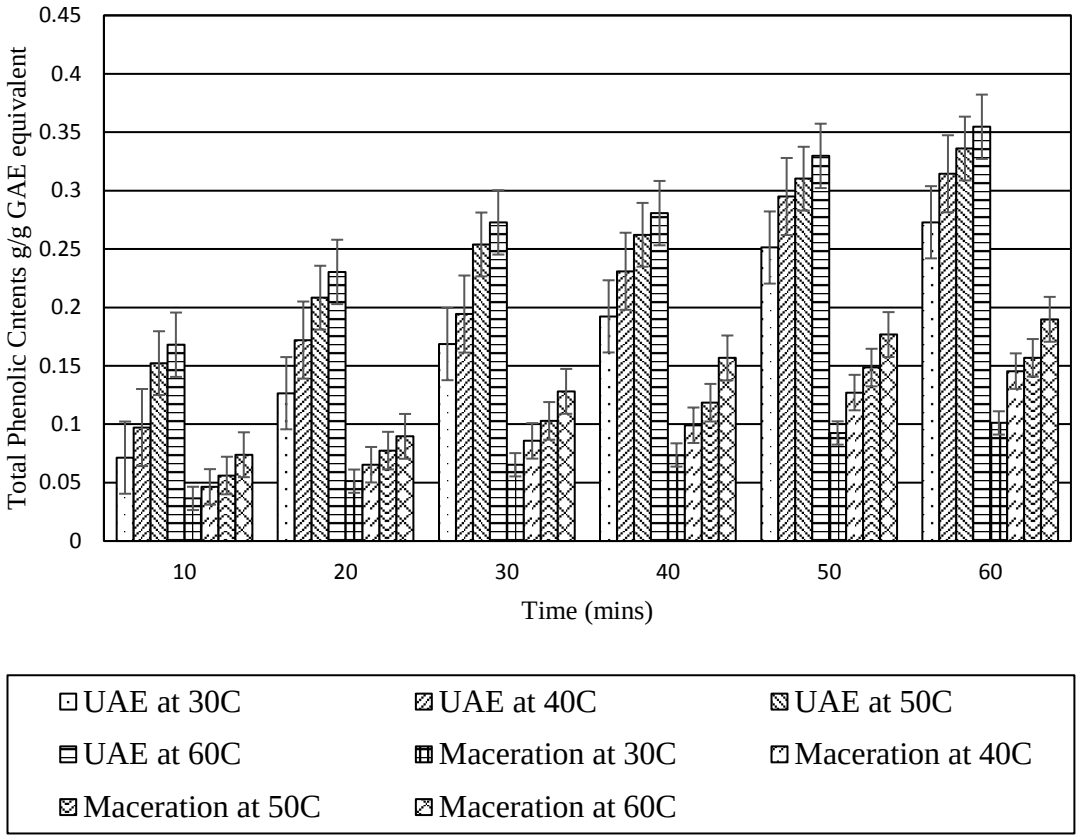


Figure 1. The Total Phenolic Contents (TPC) of *C. papaya* leaves at different temperature in range of 10 mins to 60 mins for UAE (left) and maceration (right)

3.2 Total phenolic contents in response to ultrasound-assisted extraction method

The total phenolic contents (TPC) at several extraction time at different temperatures by using UAE method was investigated. In UAE of *C. papaya* leaves, mostly researches claims that might not exceed 60 mins to 70 mins [13], [14]. Further extraction time with sonication claimed to be reached equilibrium from 60 mins and start decreasing after 70 mins [13], [14]. The parameters were set as follows: ratio of sample to solvent of 1:20 g/mL, ultrasonic input power at 100% and extraction temperature in range of 30ºC to 60ºC. Based on Figure 2, both four different temperatures condition showed the same response that the decreasing rate of TPC yield from 20 mins to 40 mins, start increasing rate of TPC yield from 40 mins to 60 mins.

There were several facts may possible causing this behavior of TPC yield along the extraction time duration. Based on the research according to *Canini et al* about *C. papaya leaves* identification of the phenolic compounds by using Gas Chromatography-Mass Spectrometry analysis, the phenolic compounds from the *C. papaya leaves* majorly consist of Protocatechuic acid (0.11 mg/g), *p*-Coumaric acid (0.33 mg/g) and Caffeic acid (0.25mg/g) [15]. *Xie et al* claims that Protocatechuic acid can extracted efficiently from fruit juices which considered as fast process [16]. It is due to Protocatechuic acid is a type of benzoic acid which has low molecular weight compare to others. Lower molecular weight compound is easier to penetrate through the plant matrices and extracted by solvent.

The research found that the extraction of the Protocatechuic acid can be reached optimum yield and equilibrium from 40 mins. This behavior can be used to explain decreasing rate of the TPC yield until 40 mins because of Protocatechuic acid extraction yield may reached equilibrium from 40 mins. Another possible cause is the degradation of Protocatechuic acid due to enzyme activity of papain and chymopapain. Papain and chymopapain are proteolytic enzyme enhance the oxidation of Protocatechuic acid into β-ketoadipate, carbon dioxide and water [17]. Some research findings prove that oxidation of Protocatechuic acid is sensitive with the presence of proteolytic enzyme such as Papain and chymopapain [18]. *p*-Coumaric acid and Caffeic acid are both classified as Cinnamic acids. The *p*-Coumaric acid and Caffeic acid has high molecular weight, 164.16 g/mol and 180.16 g/mol.

Based on the Graham's Law of diffusion, the rate of diffusion is inversely proportional to the square root of the molecular weight of compounds [19]. The lower rate of diffusion required longer time for the compounds diffuse. *p*-Coumaric acid and Caffeic acid may take longer time to start diffuse through the cell wall and membranes and to be extracted. This can explain the increasing of TPC yield after 40 mins. Both Protocatechuic acid, *p*-Coumaric acid and Caffeic acid are both having methoxyl, carboxyl, hydroxyl and ethylene groups [20]. These groups are both polar and nonpolar covalent bonds which are very weak and highly oxidizing.

Some research also reported that ultrasonic wave may promote the catalytic activity when enzyme is presence in extracts [21]. The cavitation bubbles from ultrasonic wave to solvent generates energy for both chemical and mechanical effects [22]. Each of these bubbles are called as 'hot spot' like a micro-reactor because of each bubbles consist of very high temperature and pressure. For chemical effects, some chemical compound such as containing carboxylic group in certain amount are easily enter to the cavity which is the 'hot spot' [22], [23]. In the extreme condition of the 'hot spot', the chemical compounds are easily oxidized. But most of the chemical compounds stay in bulk media which surrounding the cavities. For mechanical effect, the high temperature of the 'hot spot' vaporizing the liquid medium in the cavities. The vaporization causes the increasing of the vapor pressure which negatively correlate with cavitation intensity. Lesser cavitation bubble cause lesser performance of extraction assisted by ultrasound over time when vapor pressure increasing.

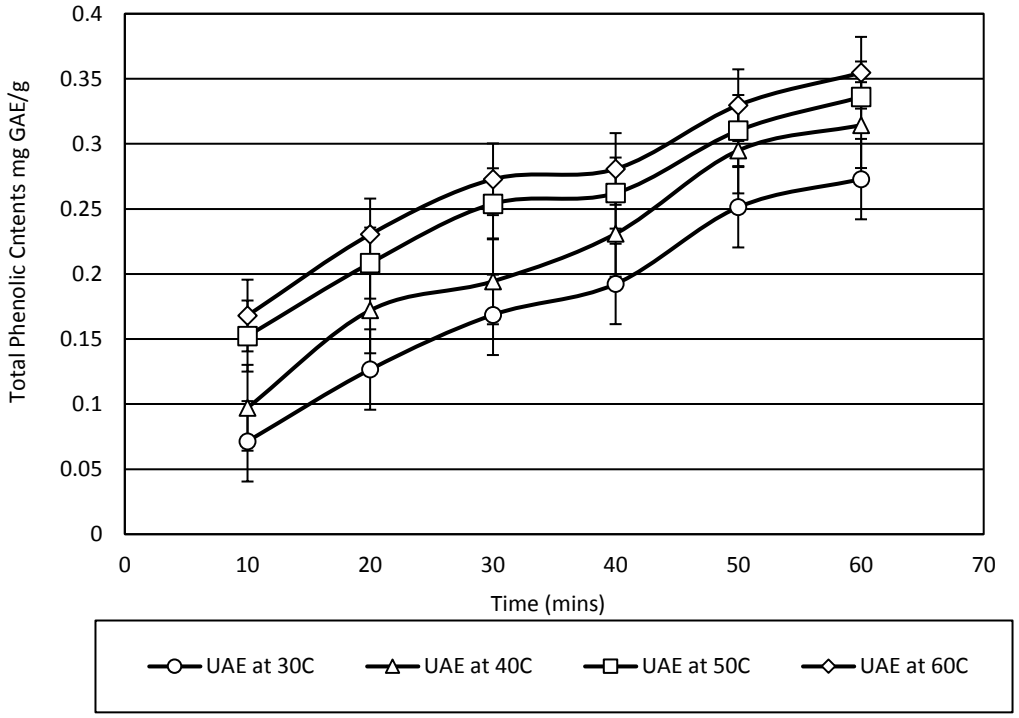


Figure 2. The Total Phenolic Contents (TPC) of *C. papaya* leaves at temperature of 30^{o}C, 40^{o}C, 50^{o}C and 60^{o}C in range of 10 mins to 60 mins for UAE

3.3 Total phenolic contents in response to maceration method

The Total Phenolic Contents (TPC) at several extraction time at different temperatures by using maceration method was investigated. In the maceration process, it is generally required longer extraction time to reach optimum TPC yield. According experiment conducted by *Milic et al* which extracting white lady's bedstraw with maceration and UAE, the extraction time to reach optimum TPC yield is 250 mins for maceration and 80 mins for UAE [11]. The design experiment for maceration is only from 10 mins to 60 mins because of comparing the performance of two extraction methods at same condition. The parameters were set as follows: ratio of sample to solvent of 1:20 g/mL, absence of ultrasound and extraction temperature in range of 30^{o}C to 60^{o}C.

Based on Figure 3, temperatures 30^{o}C, 40^{o}C and 60^{o}C shows the same behavior that the decreasing rate of TPC yield from 30 mins to 40 mins, then start increasing rate of TPC yield from 40 mins to 60 mins. The behavior of TPC yield at 60^{o}C is gradually increase from 10 mins to 60 mins. Based on the research according to *Canini et al* about *C. papaya leaves* identification of the phenolic compounds by using Gas chromatography-mass spectrometry analysis, the phenolic compounds from the *C. papaya leaves* majorly consist of Protocatechuic acid (0.11 mg/g), *p*-Coumaric acid (0.33 mg/g) and Caffeic acid (0.25mg/g) [15]. For maceration at temperatures 30^{o}C, 40^{o}C and 60^{o}C, it may have occurred because of Protocatechuic acid (PCA) reach equilibrium at 40 mins *Xie et al* claims that Protocatechuic acid can extracted efficiently from fruit juices which considered as fast process [16].

Protocatechuic acid is a type of benzoic acid which has low molecular weight compare to others. The research found that the extraction of the Protocatechuic acid can

be reached optimum yield and equilibrium from 40 mins. This behavior can be used to explain decreasing rate of the TPC yield until 40 mins because of Protocatechuic acid extraction yield may reached equilibrium from 40 mins. Higher molecular weight for *p*-Coumaric acid and Caffeic acid. has lower rate of diffusion according to Graham's Law of diffusion. The rate of diffusion is inversely proportional to the square root of the molecular weight of compounds [19]. The lower rate of diffusion required longer time for the compounds diffuse. *p*-Coumaric acid and Caffeic acid may take longer time to start diffuse through the cell wall and membranes and to be extracted. This can explain the increasing of TPC yield after 40 mins.

For the maceration at 60^{o}C, high temperature improves the rate of diffusion due to improving the kinetic energy and potential energy. High temperature overcome the delay of the diffusion of *p*-Coumaric acid and Caffeic acid.

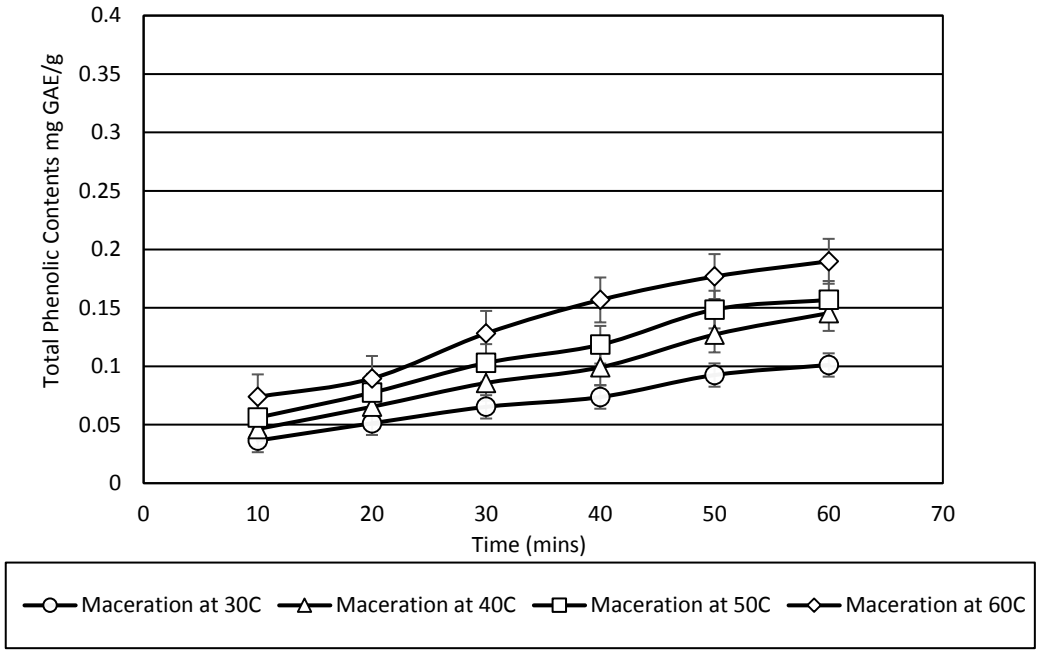


Figure 3. The Total Phenolic Contents (TPC) of *C. papaya* leaves at temperature of 30^{o}C, 40^{o}C, 50^{o}C and 60^{o}C in range of 10 mins to 60 mins for maceration.

3.4 Fitting of extraction curve

The total phenolic contents observed at the extraction experiment for both UAE method and maceration were fitted to the phenomenological model listed in Table 1. The comparison criteria used to evaluate the goodness of fit by using error analysis including R^2, MRPD and MSE by using Equations 3-5. The highest R^2 and lowest for MRPD and MSE obtained from phenomenological model within the extraction time for each temperature conditions. The R^2, MRPD and MSE changed from 30^{o}C to 60^{o}C for UAE were 0.984 to 0.992, 0.0263% to 5.1862%, 1.756E-5 to 9.706E-5. As a result, the predicted values from modelling is fitted well to the experimental values.

According to Figure 4 for UAE and Figure 5 for maceration, it showed the variations of experimental and predicted TPC yield changed with extraction time at four

different temperature conditions. From the graph, it showed that the model had a good fitting between the data. It is proven by Figure 6 & 7 as it showed a good fit between the experimental and predicted data with a R^2 of 0.9823 for UAE and 0.9792 for maceration.

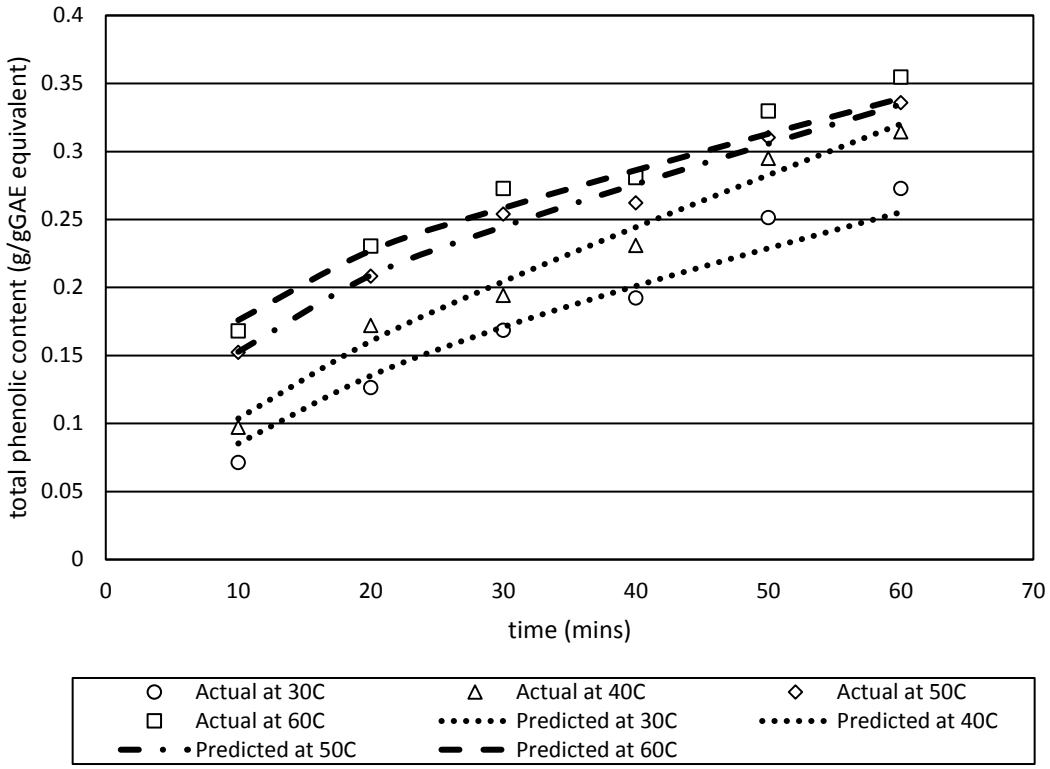


Figure 4. TPC curve of the phenomenological model equation data and experimental data for UAE

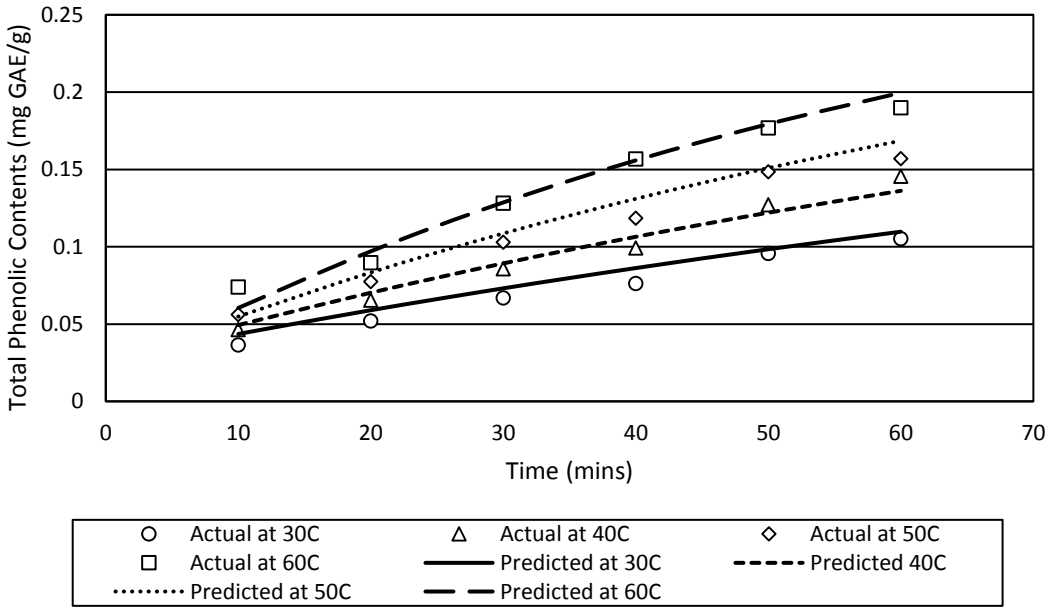


Figure 5. TPC curve of the phenomenological model equation data and experimental data for maceration

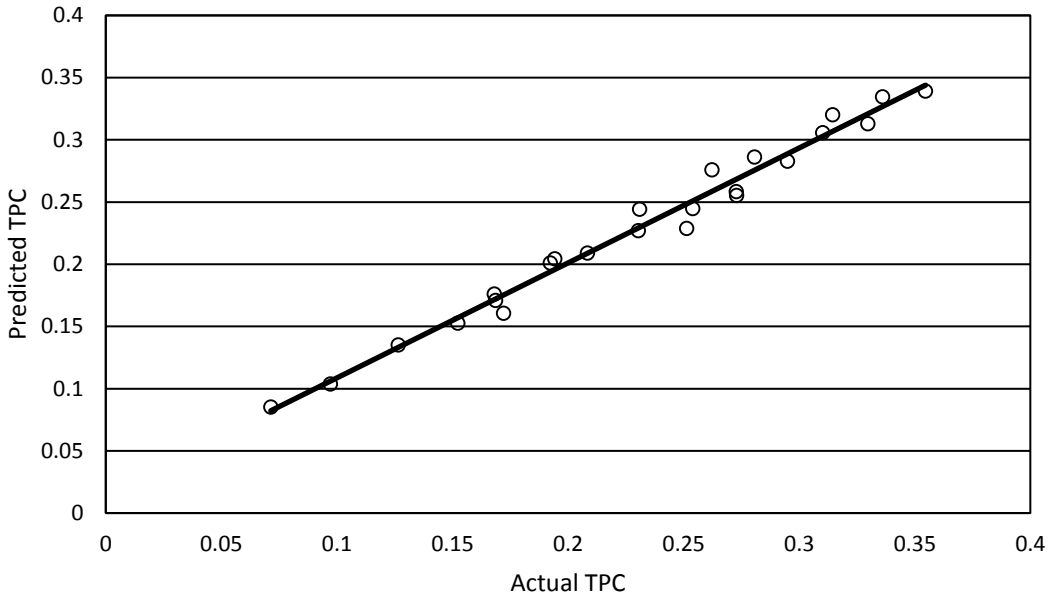


Figure 6. Comparison of predicted and experimental TPC for UAE with phenomenological model

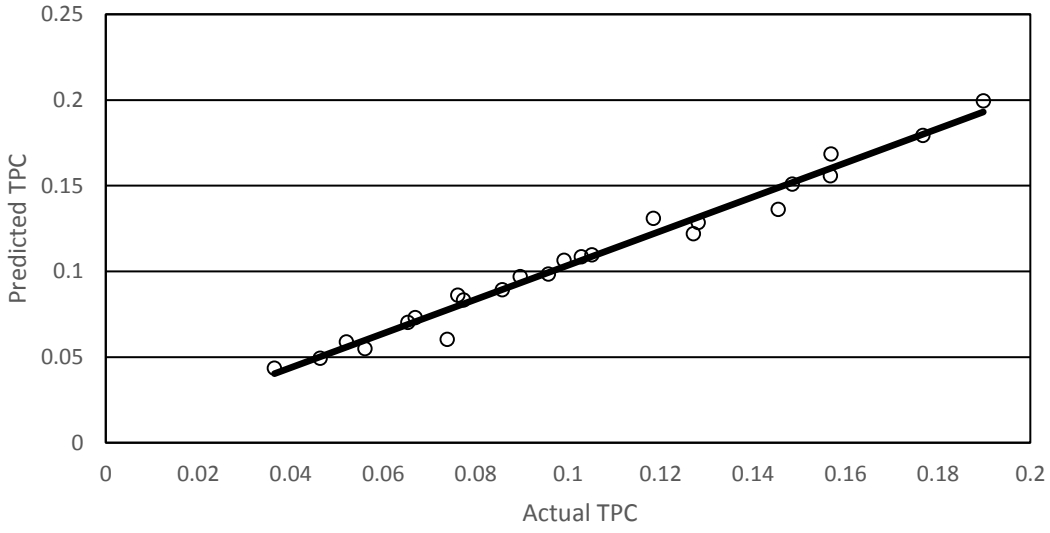


Figure 7. Comparison of predicted and experimental TPC for UAE with phenomenological model

Solvent extraction is the mass transfer between bioactive compounds and solvent passing through thin film. This application is refer to the Fick's law of diffusion and thin film theory [24][25]. Some researches claim that only one mechanism (diffusion) couldn't explain the extraction amount in response to any extraction factors especially extraction time [11], [24], [26], [27]. As some other factors affecting the extraction process, all these factors cause another mechanism such as high temperature heating of biological solid to destroy cell membranes and facilitate solute release and ultrasonic wave to reduce particle size and cavitation bubble to generate pressure difference causing disrupt cell wall matrix [24], [26], [27], [28]. This mechanism is called washing. This phenomenological model is two simultaneous processes which are washing and diffusion mechanism which proposed by *Patricelli et al*. Washing is the

rapid external solute with high rate of transfer by convection [24], [27]. Some bioactive compounds can wash out easily when the disruption of cell wall and cell membrane occurred. Diffusion is the solute with low rate of transfer by molecular diffusion from interior of plant tissue [24], [27]. Both two mechanisms were expressed by the two different kinetic coefficients. The portion of washing mechanism and the portion of diffusion mechanism is equal to one which portion of washing mechanism is represented as washing coefficient. Thus the portion of diffusion is represented as one subtracted to washing coefficient. Table 2 showed the kinetics coefficient, washing coefficient and saturation extraction yield for each temperature conditions in UAE and maceration.

Table 2. The constants and coefficients of each model fitting at different temperatures and methods.

Sample	k_1	k_2	f	y_{sat} (mg/g)	R^2	MRPD (%)	MSE
UAE at 30ºC	1.733E-3	0.0956	0.9470	1.744	0.988	3.968	9.706E-5
UAE at 40ºC	1.821E-3	0.1327	0.9638	2.355	0.981	0.715	5.317E-5
UAE at 50ºC	2.035E-3	0.1583	0.9128	1.742	0.987	0.0263	2.470E-5
UAE at 60ºC	2.258E-3	0.1873	0.8828	1.480	0.986	0.791	6.950E-5
Mac at 30ºC	7.422E-3	0.5191	0.8934	0.2565	0.992	5.186	2.210E-5
Mac at 40ºC	9.776E-3	0.8670	0.9040	0.2739	0.984	2.983	1.756E-5
UAE at 50ºC	1.095E-2	1.2015	0.9359	0.3077	0.982	2.923	3.090E-5
UAE at 60ºC	1.483E-2	2.1001	0.9450	0.3262	0.9835	2.839	2.830E-5

UAE, ultrasound-assisted extraction, Mac, maceration

Referring to Table 2, the saturation TPC yield, y_{sat} of the UAE is within 1.480 mg/g to 2.355 mg/g much higher compare to TPC yield of the maceration which within 0.2565 mg/g to 0.3262 mg/g. It is proved that the ultrasonic wave contributing better extraction efficiency in a single extraction process compare to absence of ultrasonic wave. As it explained before, the ultrasonic wave generates both acoustic energy and cavitation bubbles to increase the molecular activities in both solvent, cell, membrane, cell wall and phenolic compounds to enhance the mass transfer during extraction. Based on the data of phenomenological model in Table 2, the saturation TPC yield, y_{sat} for the UAE method and maceration can be expressed in Equation 6 and Equation 7 in change of temperatures with R^2 of 0.999 and 0.984.

$$y = 0.003T^3 - 0.0376T^2 + 1.7225T - 23.171 \quad (6)$$

$$y = 0.0039\exp(0.0219T) \quad (7)$$

The increasing of temperature in maceration extraction process causing the increasing of the saturation TPC yield, y_{sat}. This can be explained that the temperature heating causing few phenomena such as disruption the cell wall matrix, increase the rapidness motion of molecules by increasing their kinetic energy and increase the solubility to the solvent [24], [26], [27]. The decreasing of the saturation TPC yield, y_{sat} is observed after 40^{o}C by using UAE method extraction. It is because of the degradation of the phenolic compounds caused by ultrasonic wave in term of sonochemistry. In UAE, ultrasonic wave application is generating acoustic cavity of the solvent liquid to form cavitation bubble in order to disrupt the cell wall and membrane to increase the amount of freebie mass transfer (washing) of phenolic compounds. In sonochemistry, ultrasonic wave also causes cavitation of the phenolic liquid compounds to perform degradation of the phenolic compounds which claimed by *Chowdhury et al* [21]. *Chowdhury et al* reported that 17% degradation of phenolic compounds using 20 kHz power ultrasound in time 60 mins in waste water treatment application [21]. The acoustic cavities implying existence of extremely high temperature changes which has rate of vicinities up to 1010 K/s and maximum 5000 K in 487 kHz high frequency ultrasound [21]. The sonochemical reaction of phenolic compounds occurred to enhance the release of OH radical causing the degradation of phenolic compounds [21]. As the increasing of the saturation TPC yield, y_{sat} from 30^{o}C to 40^{o}C, it can be assumed the acoustic energy is not transfer to the phenolic compounds inside the cell wall matrix so acoustic cavitation is not occurred in phenolic compounds. At higher temperature after 40^{o}C, the cell wall matrix can membrane may be partially disrupted in a short time and the acoustic energy has transferred to the phenolic liquid compounds and cause cavitation of the phenolic compounds. Thus, the phenolic compounds start to be degraded.

Based on the data of phenomenological model in Table 2, The kinetic coefficient of washing, k_1 and kinetic coefficient of diffusion, k_2 for the UAE in change of temperatures method can be expressed in Equation 8 and Equation 9 with R^2 of 0.996 and 0.999, Equation 10 and Equation 11 for maceration with R^2 of 0.974 and 0.991.

$$k_1 = 3E\text{-}07T^2 - 1E\text{-}05T + 0.0018 \quad (8)$$

$$k_2 = 0.003T + 0.083 \quad (9)$$

$$k_1 = 0.0039\exp(0.0219T) \quad (10)$$

$$k_2 = 0.1351\exp(0.0453T) \quad (11)$$

The kinetic coefficient of washing, k_1 and kinetic coefficient of diffusion, k_2 for both UAE and maceration expressed in Arrhenius equation in Equation 12 in order to identify the activation energy for both washing and diffusion which shown in Table 3.

$$k = k_0\exp(\frac{E_a}{RT}) \quad (12)$$

Table 3. kinetic data for washing and diffusion coefficient of both ultrasound-assisted extraction and maceration.

Sample	k_0 (min^{-1})	E_a (kJ/mol)	R^2
UAE, k_1	3.145E-2	7.561	0.968
UAE, k_2	152.283	18.483	0.978
Mac, k_1	11.215	18.360	0.972
Mac, k_2	1.840E6	37.900	0.989

Referring to Table 3, the activation energy of washing and diffusion for UAE are lower than maceration. According to Arrhenius law, activation energy is the minimum energy required to overcome in order to perform forward reaction. It is mean that the lower activation energy required lower kinetic energy to perform washing and diffusion in extraction process. It clearly shown that the lower kinetic energy required for UAE perform washing and diffusion compare to maceration.

4.0 Conclusion

In conclusion, the present research outlines the total phenolic contents (TPC) response to extraction time at different temperatures from the *C. papaya* leaf. Phenomenological model was used as standard model for modelling and curve fitting to the experimental data. The result shows that the phenomenological model is well fitted to the experimental data for both UAE method and maceration in each temperature conditions which have R^2 0.982 to 0.922 and MRPD 0.0263% to 5.186%. The kinetic coefficient of washing and diffusion mechanisms, the washing coefficient and saturation of extraction in each condition are defined. However, there is potential improvement of the curve fitting which require development of the new model. Studies has shown lack of identification of phenolic compounds and their characteristics during the extraction process. It might not be sufficient to develop a new model which best fit to the experimental data.

References

[1] N. Otsuki, N. H. Dang, E. Kumagai, A. Kondo, S. Iwata, and C. Morimoto, “Aqueous extract of Carica papaya leaves exhibits anti-tumor activity and immunomodulatory effects,” *J. Ethnopharmacol.*, vol. 127, pp. 760–767, 2010.

[2] F. Yunita, E. Hanani, and J. Kristianto, “The effect of Carica papaya L . leaves extract capsules on platelets count and hematocrit level in dengue fever patient,” vol. 2, no. 4, pp. 573–578, 2012.

[3] N. Ahmad, H. Fazal, M. Ayaz, B. H. Abbasi, I. Mohammad, and L. Fazal, “Dengue fever treatment with Carica papaya leaves extracts,” *Asian Pac. J. Trop. Biomed.*, vol. 1, no. 4, pp. 330–333, 2011.

[4] K. L. Krishna, M. Paridhavi, and J. A. Patel, “Review on nutritional , medicinal and pharmacological properties of Papaya (Carica papaya Linn .),” vol. 7, no. 4, pp. 364–373, 2008.

[5] S. De, V. Segalen, U. F. R. S. Pharmaceutiques, and C. De Leysotte,

"Comparative Study of Antioxidant Properties and Total Phenolic Content of 30 Plant Extracts of Industrial Interest Using DPPH , ABTS , FRAP , SOD , and ORAC Assays," pp. 1768–1774, 2009.

[6] C. Corbin, T. Fidel, E. a. Leclerc, E. Barakzoy, N. Sagot, A. Falguiéres, S. Renouard, J.-P. Blondeau, C. Ferroud, J. Doussot, E. Lainé, and C. Hano, "Development and validation of an efficient ultrasound assisted extraction of phenolic compounds from flax (Linum usitatissimum L.) seeds," *Ultrason. Sonochem.*, vol. 26, pp. 176–185, 2015.

[7] C. Da Porto, E. Porretto, and D. Decorti, "Comparison of ultrasound-assisted extraction with conventional extraction methods of oil and polyphenols from grape (Vitis vinifera L.) seeds," *Ultrason. Sonochem.*, vol. 20, no. 4, pp. 1076–1080, 2013.

[8] F. Dahmoune, H. Remini, S. Dairi, O. Aoun, K. Moussi, N. Bouaoudia-Madi, N. Adjeroud, N. Kadri, K. Lefsih, L. Boughani, L. Mouni, B. Nayak, and K. Madani, "Ultrasound assisted extraction of phenolic compounds from P. lentiscus L. leaves: Comparative study of artificial neural network (ANN) versus degree of experiment for prediction ability of phenolic compounds recovery," *Ind. Crops Prod.*, vol. 77, pp. 251–261, 2015.

[9] B. Yingngam, N. Supaka, and W. Rungseevijitprapa, "Optimization of process parameters for phenolics extraction of Cratoxylum formosum ssp. formosum leaves by response surface methodology," *J. Food Sci. Technol.*, vol. 52, no. 1, pp. 129–140, 2015.

[10] S. Kamtekar, V. Keer, and V. Patil, "Estimation of Phenolic content , Flavonoid content , Antioxidant and Alpha amylase Inhibitory Activity of Marketed Polyherbal Formulation," vol. 4, no. 09, pp. 61–65, 2014.

[11] P. S. Milić, K. M. Rajković, O. S. Stamenković, and V. B. Veljković, "Kinetic modeling and optimization of maceration and ultrasound-extraction of resinoid from the aerial parts of white lady's bedstraw (Galium mollugo L.)," *Ultrason. Sonochem.*, vol. 20, no. 1, pp. 525–534, 2013.

[12] T. Y. Wu, N. Guo, C. Y. Teh, and J. X. W. Hay, *Advances in Ultrasound Technology for Environmental Remediation*. 2013.

[13] P. D. Roach, M. Bowyer, and P. A. Phillips, "Effect of extraction conditions on total phenolic compounds and antioxidant activities of Carica papaya leaf aqueous extracts Effect of extraction conditions on total phenolic compounds and antioxidant activities of Carica papaya leaf aqueous," no. September 2013, 2016.

[14] N. Di. B. Nordin, "THE EXTRACTION OF PAPAIN FROM PAPAYA LEAVES," Universiti Malaysia Pahang, 2010.

[15] A. Canini, D. Alesiani, G. D. Arcangelo, and P. Tagliatesta, "ARTICLE IN PRESS Gas chromatography – mass spectrometry analysis of phenolic compounds from Carica papaya L . leaf," vol. 20, pp. 584–590, 2007.

[16] L. Xie, J. Guo, Y. Zhang, and S. Shi, "Efficient Determination of Protocatechuic Acid in Fruit Juices by Selective and Rapid Magnetic Molecular Imprinted Solid Phase Extraction Coupled with HPLC," *J. Agric. Food Chem.*, vol. 62, pp. 8221–8228, 2014.

[17] M. Wojtas-Wasilwerska, J. Trojanowski, and J. Luterek, "Aromatic Ring Cleavage of Protocatechuic Scid by the White-Rod Fungus," *Acta Biochim. Pol.*, vol. 30, no. 3/4, pp. 291–302, 1983.

[18] K. Kon and M. Roi, *Microbiology for Surgical Infections*, 1st ed. 2014.

[19] J. N. Spencer, G. M. Bodner, and L. H. Rickard, *Chemistry Structure &*

Dynamics, 5th ed. 2012.

[20] L. Qiao, X. Ye, Y. Sun, J. Ying, Y. Shen, and J. Chen, "Ultrasonics Sonochemistry Sonochemical effects on free phenolic acids under ultrasound treatment in a model system," *Ultrason. - Sonochemistry*, vol. 20, no. 4, pp. 1017–1025, 2013.

[21] P. Chowdhury and T. Viraraghavan, "Sonochemical degradation of chlorinated organic compounds , phenolic compounds and organic dyes – A review," *Sci. Total Environ.*, vol. 407, no. 8, pp. 2474–2492, 2009.

[22] T. J. Mason, "Ultrasound in synthetic organic chemistry," *Chem. Soc. Rev.*, vol. 26, pp. 443–451, 1997.

[23] C. Vassilakis, A. Pantidou, E. Psillakis, N. Kalogerakis, and D. Mantzavinos, "Sonolysis of natural phenolic compounds in aqueous solutions : degradation pathways and biodegradability," *Water Res.*, vol. 38, pp. 3110–3118, 2004.

[24] G. C. So and D. G. Macdonald, "Kinetics of Oil Extraction from Canola (Rapeseed)," vol. 64, no. February, 1986.

[25] V. B. Veljkovic, "Kinetics of ultrasonic extraction of extractive substances from garden (Salvia officinalis L .) and glutinous (Salvia glutinosa L .) sage ˇ kovic," *Ultrason. Sonochem.*, vol. 13, pp. 150–156, 2006.

[26] E. Vorobiev and K. El-belghiti, "Modelling of Solute Aqueous Extraction from Carrots subjected to a Pulsed Electric Field Pre-treatment," vol. 90, no. 3, pp. 289–294, 2005.

[27] Y. Tao and D. Sun, "Kinetic modeling of ultrasound-assisted extraction of phenolic compounds from grape marc : Influence of acoustic energy density and temperature," *Ultrason. Sonochem.*, vol. 21, pp. 1461–1469, 2014.

[28] M. Pinelo, B. Zornoza, and A. S. Meyer, "Selective release of phenols from apple skin : Mass transfer kinetics during solvent and enzyme-assisted extraction," *Sep. Purif. Technol.*, vol. 63, pp. 620–627, 2008.

Development of nanosilica in cement based materials from rice husk

W.R. Chin[1*], Ting Lee[2], W.Y. Wong[3]

[1]*School of Engineering, Taylor's University, Malaysia.*

[*]WaiYin.Wong@taylors.edu.my

Abstract

Silica sand is the primary structural component in a wide variety of cement based materials. The commonly used commercial silica is obtained from the natural occurring sand in the environment through weathering process. Rice husk ash (RHA) is another suitable alternative silica source derived from the combustion of the rice husk (RH) which treats as an agricultural waste. The pure silica content can be further extracted by the alkaline extraction method. This study was carried out to investigate the optimum conditions to produce the highest silica content RHA and the viability of RHA used as an alternative of commercial silica sand in the concrete making. Combustion temperatures of 400, 600 and 800°C were carried out on the RH followed by alkaline extraction method. From Energy Dispersive X-ray analysis, the optimum combustion temperature to produce the rice husk ash with the silica content as high as 83% was found to be 800°C for 2 hours. Further extraction of 84% purity silica can be achieved from alkaline extraction. Brinell hardness testing was then performed to compare the hardness of the high performance concretes derived from three different silica sources, i.e., commercial silica sand as the control sample, RHA and the extracted silica from RHA. The concrete derived from RHA was found to have the highest hardness of 0.978 HB value which is mainly due to the nanoporous size distribution as shown from Brunauer-Emmett-Teller analysis. This has proven the viability of using RHA as an alternative silica source in concrete making. As a result from this study, a sustainable alternative in producing a "green" concrete is achieved whereby it is applicable in different types of structural component in the construction industry such as beams, columns, slabs and foundations.

Keywords: Green concrete, Sustainable, High performance concrete, Nanosilica.

1. Introduction

Rice husk (RH) is known as one of the common agricultural waste that can be obtained from rice mill production activity. They are normally either being burnt or dumped as waste everywhere around the world due to its economic value in the market [1]. It does not have any considerable commercial value and also caused several

problems being dumped as a waste. One of the main issue is that it harms the environment because the product particles might contain crystalline silica such as quartz and cristobalite that may be a possible threat to the health problems [2, 3]. Therefore, it encourage us to utilise the rice husk in the best possible way effectively with the current available technology. This will prevent further disposal of rice husk in the open field and also reduces the waste generation which lead to a sustainable development for better future preservation.

Based on Kalapathy et al. [4], the rice husk can be converted from a low cost waste to a valuable high content silica rice husk ash (RHA) with a good commercial by simple combustion method. The ash contains 87%-97% of silica and other constituents such as K_2O, Al_2O_3, CaO, MgO, Na_2O and Fe_2O in less than 1% respectively [5]. From the ash, the silica in the RHA can be further extracted with nano-size pore by alkaline extraction method [6]. The quality of RHA depends on the temperature and duration of combustion of the rice husk as it undergoes structural transformation at different conditions [7]. By utilising the rice husk effectively, it can turn from a priceless agricultural waste to a high content silica with a good commercial value in the market. This can also be the solution to the current environmental issue caused by the disposal of RH.

The high content silica ash is widely used in many different applications in the industry such as, fuel source in the power plant, production of glass, production of steel, and also in the cement and construction industries [5]. However, for this project, it is mainly focused on the application of silica in the cement and construction industries. Currently, the silica source applied in the cement industry comes from silica sand. This research was carried out to produce a high quality concrete by studying the parameters to produce a high quality RHA from RH for the cement-based application. The characteristics of the RHA was analysed by different types of analysis method such as Fourier Transform Infrared (FTIR) spectrometer, Energy Dispersive X-ray (EDX), Brunauer-Emmett-Teller (BET) analysis and burn-off analysis [8].

Previously, many researchers have conducted studies on different methods of high RHA silica production from RH and the contribution of it in the cement application. Studies have also been carried out on the silica content based on different conditions such as combustion temperature and duration [4, 7–11]. However, limited studies have been conducted to find which method is the effective and lower cost to produce the desired RHA that can be further apply in concrete making. The mechanical properties of the concrete derived from different silica source was carried out and compared by the Brinell hardness testing. This is to determine whether the silica source derived from RHA improves the hardness of the concrete. This research was carried out to produce "green" cement with high quality and low production cost that is derived from agricultural waste. The idea is to fully utilise the RH waste material and replaced with current cement produced from silica source derived from silica sand.

Nomenclatures

D	diameter of ball, mm
d	diameter of indentation, mm
F	force applied, N
HB	Brinell Hardness number

HCl	hydrochloric acid
NaOH	sodium hydroxide

Abbreviations

RH	Rice Husk
RHA	Rice Husk Ash
RHP	Rice Husk Powder
EDX	Energy Dispersive X-Ray
FTIR	Fourier Transform Infrared
BET	Brunauer Emmett Teller

2. Methodology

2.1 Preparation of rice husk ash (RHA)

The RH was collected in bulk from a local rice milling plant located in Chantika Kelang Beras Sdn. Bhd., Kedah, Malaysia and stored in Taylor's University laboratory for the RHA samples preparation. The RH was first pre-treated by screening to remove any undesirable substances such as soil, rice straw and particles to prevent any contamination which degrades the quality of the RHA. It is then further rinsed and washed with water to remove any remaining impurities smaller in size that will settle down to the bottom of the container. The clean RH that floats on the upper section of the container was collected using a sieve. Place the RH equally distributed on a tray covered with aluminum foil to prevent the sample from further contaminated by other impurities in the drying stage. Few holes are opened on the aluminum foil to ensure the water vapour to pass through. This will prevent moisture environment inside the tray as they will escape through the holes once they are evaporated. The tray containing the RH samples were placed in an oven for the drying process which was set at 110°C for 24 hours (ASTM D2867-09). After the drying process, the RH was ground into 0.5 mm powdered form particles using a grinder. Weight 50 g of the grounded RHP and place them onto 5 different flat alumina crucibles with 10 g each for equal distribution and allow sufficient air circulation during the combustion process. Before the combustion, the flat cruciles containing RHP were placed directly into a muffle furnace. Three different sets of combustion temperature (400, 600 and 800°C) with the absence of external gas supply were carried out for the combustion process to determine which temperature produces the highest silica content RHA. The heating and cooling profile for the furnace was set at 10°C/min heating rate and 2 hours soaking time. After 2 hours of soaking, it was allowed to cool until it reaches the room temperature. The different combustion temperatures carried out for this experiment and the furnace setting is tabulated as shown in **Table** 1. The weight of the RHA sample combusted at different temperatures were recorded to carry out the burn-off analysis using **Equation 1** shown below. Different types of analysis such as Energy Dispersive X-ray (EDX), Fourier transform infrared (FTIR) and Brunauer-Emmett-Teller (BET) analysis were also provided to determine the characteristics of the RHA and raw RH.

$$Burn\ off\ \% = \frac{Weight\ of\ initial\ rice\ husk - final\ weight\ of\ RHA\ after\ combustion}{Weight\ of\ initial\ rice\ husk} \times 100 \quad (1)$$

Table 1. Combustion temperatures and furnace settings for RHP.

Component	Combustion temperature (°C)	Soaking duration (hr)	Heating rate (°C/min)	Cooling rate (°C/min)
Rice husk powder	400	2	10	10
	600	2	10	10
	800	2	10	10

2.2 Preparation of extracted silica

Alkaline extraction method with the Sodium Hydroxide (NaOH) and Hydrochloric acid (HCl) was treated on the RHA with the highest silica content that was found from the EDX analysis to extract the silica from it. The first step in this method is to prepare 1N Sodium Hydroxide (NaOH) solution by mixing 20 g of NaOH pellets in 500 ml of distilled water in a 1000 ml beaker. Measure 60ml of 1N NaOH using a 150 ml measuring cylinder and add to the 10 g RHA samples in a 150 ml beaker. Stir the mixture constantly under boiling condition to synthesis the silica for 1 hr using a hotplate stirrer. Then, filter the solution through a Whatman No. 41 ashless filter paper and allow the filtrate to cool to room temperature. During cooling, prepare 1N Hydrochloric acid (HCl) by mixing 18g of HCl pellets with 500ml of distilled water in a 1000 ml beaker.Titrate the filtrate using the 1N HCl with constant stiring until the pH reaches 7 to allow the silica gels to precipitate and check the pH of the solution using a pH meter. Allow the silica gels to aged for 18 hrs in a 150ml beaker by covering it with aluminium foil to prevent any contamination.Wash the silica gels by adding 100ml of distilled water to the silica gels to break them up into a slurry form followed by centrifuging the slurries at 2500 rpm for 15 minutes and remove the supernatants. Repeat washing to further reduce the sodium content that is absorbed on the surface of micropores in the silica gel and dry the gels at 80°C for 12 hr to produce xerogels. Provide additional washing and further drying at 80°C for 12 hr to produce silica. The Energy Dispersive X-ray (EDX), Fourier transform infrared (FTIR) and Brunauer-Emmett-Teller (BET) analysis were performed to determine the characteristics of the extracted silica.

2.3 Mechanical testing process

The extracted silica and RHA samples was compared with commercial silica sand in cement based application. The comparison was carried out on the hardness of the concrete samples derived from different silica sources by Brinell hardness testing.

2.3.1 Preparation of concrete samples

Prepare the ingredients required for the production of high performance concrete based on the proportions shown in **Table 2** below [12]. Mix the coarsest constituent (crushed limestone) with the finest one (silica) followed by next coarsest (sand) and next finest one (cement) on a flat surface for 2 minutes before each addition. Add half of the water to the dry mixtures prepared and mix them for 2 minutes. Repeat the addition of water process for about 10 minutes until all the water is added. After the mixing process, transfer the concrete mixtures into small containers to mold them into a shape that fits the hardness testing equipment. Dry the concrete samples in an oven at

120°C for 7 days. Once the concrete samples are dried, carry out Brinell hardness testing to test and compare the strength of the different concretes.

Table 2. Proportions to produce different concrete samples in 50g basis [12].

Samples	Constituents	Amount required in gram
Commercial silica concrete	Cement	10.08
	Commercial silica sand	1.11
	Crushed limestone < 10 mm	22.27
	Sand < 2 mm	13.30
	Water	3.24
RHA silica concrete	Cement	10.08
	RHA	1.11
	Crushed limestone < 10 mm	22.27
	Sand < 2 mm	13.30
	Water	3.24
Extracted silica concrete	Cement	10.08
	Extracted silica	1.11
	Crushed limestone < 10 mm	22.27
	Sand < 2 mm	13.30
	Water	3.24

2.3.2 Brinell hardness testing

The Gunt Universal Testing Machine WP 300 was used in this test together with a Vernier caliper and stopwatch. Before conducting the experiment, surface of the concrete sample are cleaned and loaded onto Gunt Universal Testing Machine WP 300. Apply 200 N of force onto the concrete sample and start the stopwatch. Remove the concrete sample from the applied force after 30s. The impression diameter is measured using a Vernier caliper because it is more accurate with error percentage of 0.05mm. 4 different sets of readings are recorded at different spot and an average is calculated from the results in order to minimise the error. Repeat the experiments for all the concrete samples and calculate the Brinell hardness number, HB, using **Equation 2** below [13]. The HB determines the hardness of the concrete. Therefore, the hardness for the concrete samples derived from different silica source can be compared.

$$HB = \frac{0.102 \times F}{0.5\pi D\left(D - \sqrt{D^2 - d^2}\right)} \quad (2)$$

Where,
D = diameter of ball (10 mm)
d = diameter of indentation, mm
F = force applied, N

3. Results and Discussion

3.1 Physical examine of rice husk ash after combustion

The raw RHP was subjected to different combustion temperatures with a fixed initial weight of 50 g in 5 different flat crucibles with each carrying 10 g. The furnace

setting was fixed at 2 hr soaking time and also the heating and cooling rate to be 10 °C/min. The RHA produced was observed to have different colour changes as shown in **Table 3**. Based on the results obtained, the completely burned RH can be observed in grey to white colour, while partially burnt RHA is blackish due to carbon content. The higher combustion temperature (800 – 1000°C) at constant soaking time (2 hours) produces better quality of RHA with higher silica. Also, the size and shape of the crucible must be taken into consideration as they affects the quality of RHA significantly. A large flat surface with low edge crucible should be used instead of small surface with high edge crucible. This is to ensure the equal distribution of the RHA to allow good air circulation for sufficient supply of oxygen during the combustion process.

The range of combustion temperature was chosen according to TGA results from other studies. The combustion temperatures at 400, 600 and 800°C were set mainly to determine the temperature at which the carbon starts to deteriorates. At 355°C, pyrolysis is achieved whereby there is change of chemical composition and physical phase due to thermal decomposition of hemicellulose and cellulose of the RH in the absence of oxygen. At 530°C, combustion occurs to remove the carbon from the RH with the presence of oxygen [8, 13, 14]. Achieving the RHA with highest silica content is important for the concrete making process because the silica percentage affects the mechanical properties of the concrete. In this case, the RHA combusted at 800°C will be used as the sample for silica extraction and further incorporate both the RHA and extracted silica samples into concrete making.

Table 3. Physical observation of RHA after combustion

Initial weight (g)	**Combustion temperature (°C)**	**Rice husk ash**	**Observation**
50	400		• Rough powder • Blackish-grey in colour • Incomplete combustion
50	600		• Fine powder • Yellowish-white in colour • Semi-complete combustion
50	800		• Fine powder • Greyish-white in colour • Complete combustion

3.2 Characterisation of raw materials

There are 4 samples to be analysed in this experiment. Each of them are subjected to different types of analysis as shown in **Table 4** below.

Table 4. Identification of samples for different analysis.

Sample Name	Sample Details	Analysis
RHP_Raw	Untreated rice husk powder	FTIR
RHA_800	Rice husk ash combusted at 800°C	FTIR, BET, EDX, Burn-off
Si_C	Commercial silica sand	FTIR, BET, EDX
Si_P	Extracted silica from RHA_800	FTIR, EDX

3.2.1 Burn-off analysis

This analysis was carried out to determine the percentage of carbon being removed from the RHP. The weight loss during the combustion process to produce the RHA with high silica content is calculated based on the burn off percentage. A firing temperature of 800°C with a fixed soaking time of 2 hours were carried out for the study of the burn-off analysis as shown in **Table 5**. The carbon burn-off percentage from the RHA can be calculated by using **Equation 1** above. From the results obtained, the carbon burn-off percentage was as high as 86.3%. This shows that a complete combustion is not achieved as there are still traces of carbon found in the ash. To achieve complete combustion, the combustion temperature has to be increased.

Table 5. Burn-off analysis for RHA_800.

Sample	Initial weight (g)	Final weight (g)	Burn-off percentage (%)
RHP	50	6.85	86.3

3.2.2 Fourier Transform Infrared (FTIR) analysis

According to the **Figure 1** below which shows the FTIR spectra for the samples, the RHP_Raw has no significant peaks that can be observed as compared to the other three samples. The other three samples have spectra with similar peaks in the similar positions. The most significant band can be seen at 1080 cm^{-1} followed by a medium band at 790 cm^{-1} and small band for Si_C at 680 cm^{-1}. The first and most significant band at 1080 cm^{-1} shows the Si-O-Si asymmetric vibration as a result of the strong ionic character of Si-O group. As for the second band at 790 cm^{-1}, it corresponds to the symmetric stretching vibrations of internal tetrahedral as well as external linkages of SiO_4. The weakest band at 680 cm^{-1} determines the nature phase of the silica and this shows that the Si_C is in the crystalline form [8, 15]. It is observed that there are slight differences in the peak for the three different samples at 1080 cm^{-1}. The samples produced from this experiment has broader band as compared to the Si_C. Theoretically, sharper peaks will have higher purity of silica particles as shown from EDX results. Therefore, the observation from FTIR results is not fully supported by the EDX results. The broader band of the experimental samples were caused by the presence of organic compound in the samples.

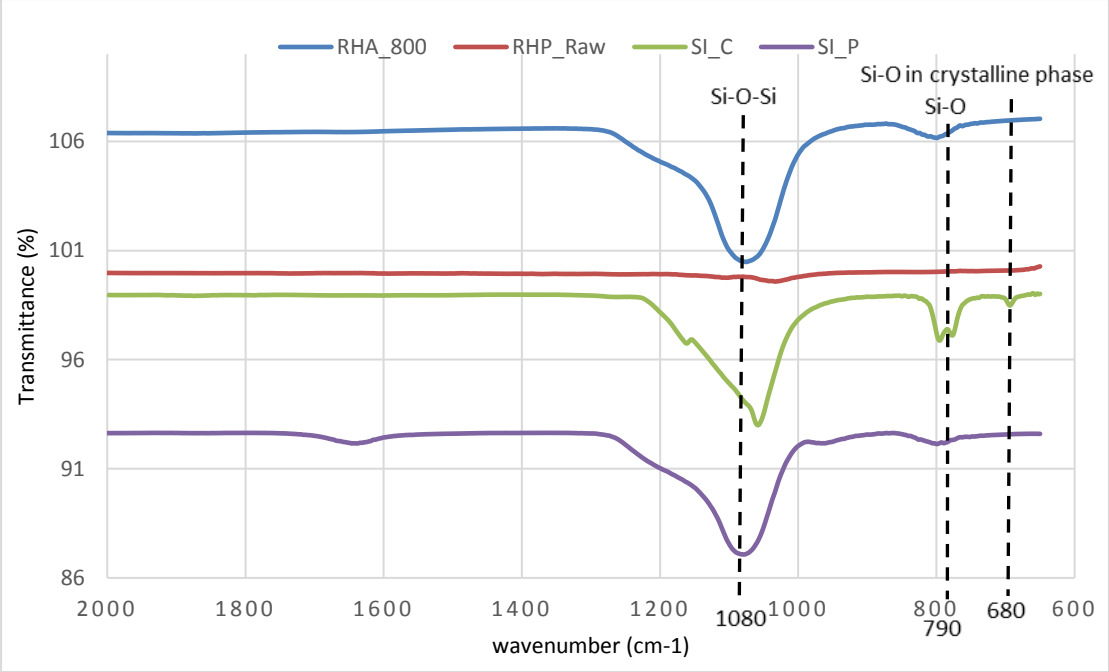


Figure 1. FTIR spectra of the samples used for concrete making: (a) RHA_800; (b) RHP_Raw; (c) Si_C; (d) Si_P.

3.2.3 Brunaur-Emmett-Teller (BET) analysis

This analysis was carried out to determine the pore characteristics of the RHA_800 and Si_C sample by the physical adsorption of gas molecules onto the samples surface. The gas used as the absorbate is non-corrosive, nitrogen gas. From **Figure 2** shows the nitrogen adsorption at constant temperature for the samples. However, the results for the Si_P sample were not included as they are contaminated during the storage which affects the results for this analysis. The adsorption isotherm for the RHA_800 and Si_C sample falls under the Type III category isotherm by referring to the IUPAC classification of physisorption isotherm [16, 17]. In the Type III isotherm, the presence of macro-pores (> 50 nm) is expected and the adsorbent-adsorbate interactions play an important role [18]. Based on the results obtained, the quantity of absorption increases at higher relative pressure and remains finite at saturation pressure (P/P_o = 1). The RHA_800 and Si_C sample indicated a rapid nitrogen intake in the range of relative pressure 0.8 – 1. This indicates that the adsorbent-adsorbate interactions are relatively weak and no monolayer formation can be identified due to the molecular clustering around the most attracted sites on the surface of the macro-porous solid [17, 18].

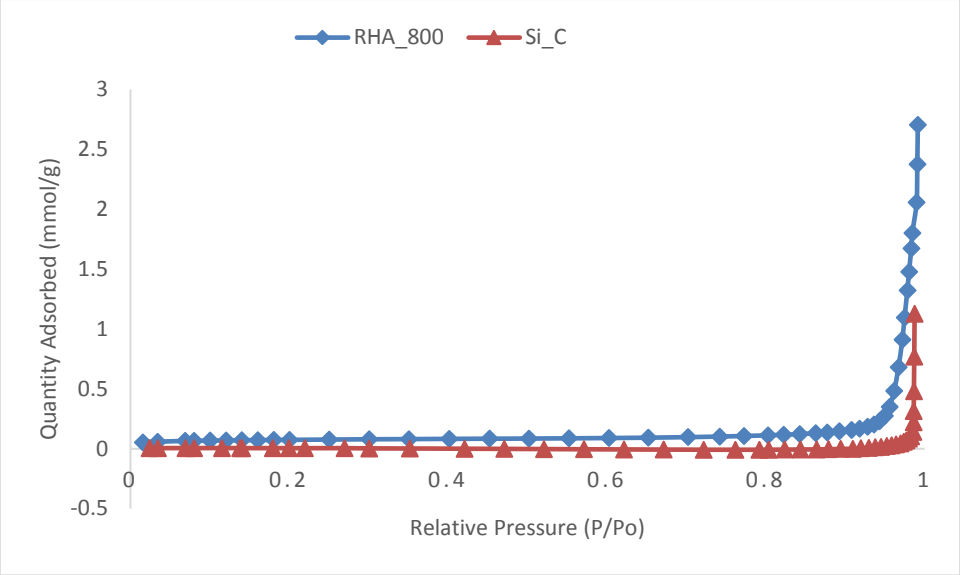


Figure 2. Nitrogen adsorption linear plot of the samples.

As for the BET surface area, pore volume and the pore diameter, the results are presented in **Table 6**. Based on the results obtained, the pore diameter of the Si_C sample is in the range of macro-pore (> 50 nm). As for the RHA_800 sample, it is in the range of micro-pore (2 nm < pore width < 50 nm). Significant difference can be observed for the pore volume and surface area as well. The surface area to volume ratio for RHA_800 is higher as compared to Si_C. This increases the pozzolanic reactivity of RHA_800 to form cementitious properties which will result in better quality of concrete produced. However, these results obtained from the nitrogen adsorption are not entirely accurate due to the quadrupolar nature of the nitrogen molecule. It affects the orientation of the adsorbed nitrogen molecule on the adsorbent surface and also affects the micro-pore filling pressure. Furthermore, there are also problems related with pre-adsorbed nitrogen molecules as well. This will result in the pore filling pressure not clearly correlated to the pore size as the pre-adsorbed nitrogen blocks the entrance of the narrow micro-pores. In order to produce an accurate result, the operational temperature and choice of adsorptive should be considered [17, 18].

Table 6. Pore Characteristics of the samples.

Sample	Surface Area (m^2/g)	Pore Volume (cm^3/g)	Pore Diameter (nm)
RHA_800	5.785	0.0624	43.169
Si_C	0.341	0.0077	90.530

3.2.4 Energy Dispersive X-ray (EDX) analysis

Three of the samples (RHA_800, Si_C and Si_P) are required to perform EDX analysis in this experiment to determine the silica composition of the samples. The visual images of the samples are shown in **Figure 3-5** below. According to the results

obtained, it is observed that the extracted silica (Si_P) contain the highest silica content of 84.15% followed by RHA (RHA_800) and commercial silica sand (Si_C) with the silica content of 75.03% and 70.62% respectively [8]. The other elements found in the samples are basically the metal impurities that are either failed to remove or contaminated during the storage of the samples. In this experiment, the alkaline extraction method carried out has the ability of extracting 84% purity of silica as shown from the EDX result. Furthermore, the carbon content in RHA_800 are reduced from 24.38% to 11.53% after extraction. Hence, instead of increasing the combustion temperature which will be more costly in terms of energy can production cost, the alkaline extraction method can be used as an alternative way to produce high silica content samples for the concrete making. This will benefits the user in terms of economically as well as environmentally. However, further analysis are required to check whether by incorporating the RHA and extracted silica in the concrete making will improve its mechanical properties or remained the same as compared to commercial silica sand.

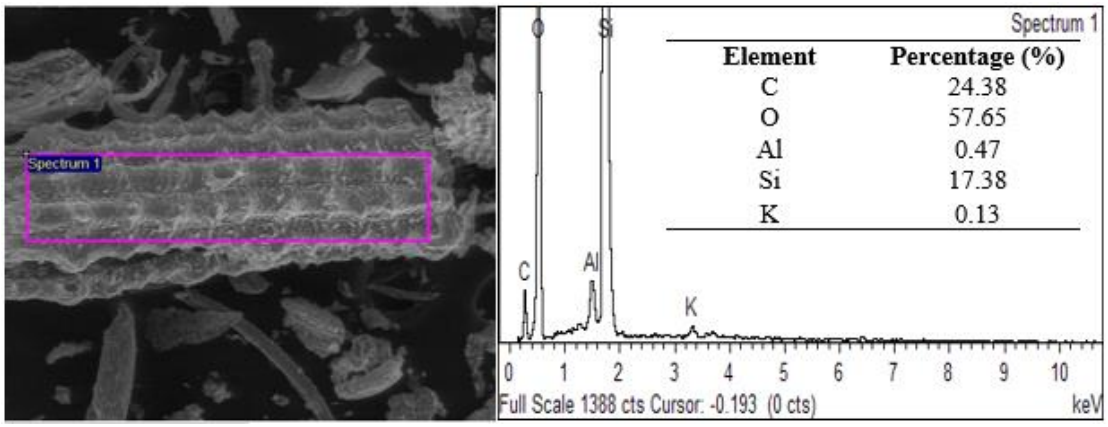


Figure 3. EDX spectrum of RHA (RHA_800).

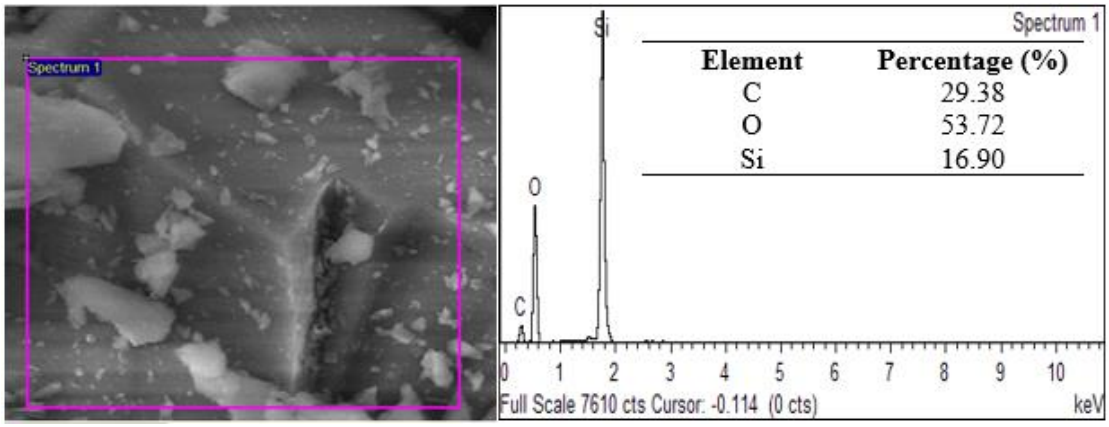


Figure 4. EDX spectrum of Commercial silica sand (Si_C).

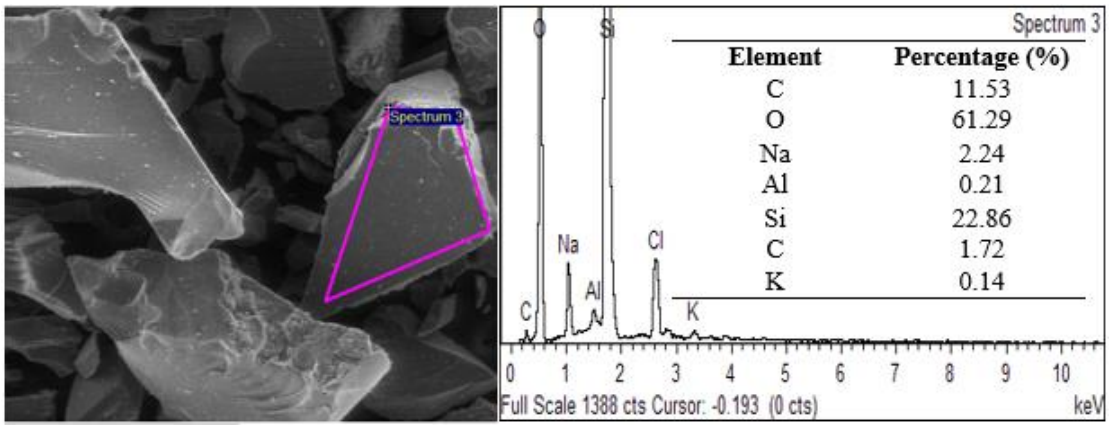


Figure 5. EDX spectrum of extracted silica (Si_P).

3.3 Indentation Hardness testing

The indentation diameter of the concrete samples and the Brinell hardness number, HB, is calculated from **Equation 3**. The results are recorded and tabulated as shown in **Table 7**. The concrete derived from the commercial silica sand (Si_C) will act as a control sample which means the concrete derived from the RHA (RHA_800) and extracted silica (Si_P) will be benchmarking with commercial silica concrete as a reference. Based on the results obtained, the RHA concrete has the highest HB value of 0.978 followed by extracted silica concrete and commercial silica concrete with the HB value as 0.969 and 0.804 respectively. It can be observed that the RHA and extracted silica concrete have better hardness compared to the commercial silica concrete (control sample). Theoretically, if the silica content affects the hardness of the concrete, the extract silica concrete will have the highest HB value. In this case, the RHA concrete has the highest HB value and this is mainly due to the size of the silica. The size of the silica derived from RHA appears to be lowest 43.169 nm as shown from BET analysis. According to ISO/TS 80004-1:2010, the term "nano-porous" refers to the silica particles with size distribution < 100 nm and they are known as nanosilica. Incorporation of nanosilica in the concrete mixture will result in higher packed density which leads to lower water demand of the mixture and eventually improves the strength due to reduced capillary porosity [19–21]. Furthermore, it also increases the reaction with calcium hydroxide and water to form compounds with cementitious properties which improves the pozzolanic reactivity. As a result, the size of the silica is the contributing factor to the hardness of the concrete.

Table 7. Indentation diameter and HB value of the samples with 200 N force applied.

Samples	**Diameter (mm)**					**HB Value**
	d_1	**d_2**	**d_3**	**d_4**	**$\bar{d}$**	
Si_P	5.40	5.40	5.42	5.39	5.40	0.969
Si_C	5.45	5.44	5.47	5.45	5.45	0.804
RHA_800	4.94	5.00	5.02	4.96	4.98	0.978

4. Conclusion

Rice husk can be considered as a valuable natural resources obtained from agricultural waste if utilised effectively. It is suitable for the cement based materials application such as concrete due to its high silica content ash. The ash can be produced by combusting at different temperatures and it is the contributing factor to producing high silica content of ash. This is due to the higher carbon removal at temperature 400 °C and above. Also, the silica has low solubility which makes it to be able to further purify by the alkaline extraction method. With the alkaline extraction method, around 84% of silica can be purified for the concrete making as well. The hardness of the concrete derived from the ash and extracted silica has shown to be acceptable through comparison with the concrete derived from commercial silica in this study. This has proven the viability of using RH as the silica source for concrete making instead of commercial silica. Therefore, it will be more economical by replacing the commercial silica with the RH in concrete making and this will further add value to the agricultural RH waste. Further improvements can be made in the future such as improving the quality of RHA used for the concrete making. This can be achieved by firing at higher temperature around 900 °C with a large flat surface and low edge crucible. Furthermore, other mechanical testing methods can be provided such as the compression, impact, and uniaxial testing to further determine the mechanical properties. Besides that, the durability of the concretes can also be tested such as its resistance to water penetration, carbonation, chloride penetration and seawater attack. This is to ensure the quality of the concrete derived from RH silica source is acceptable in different aspects of application in the construction industry.

References

[1] R. Bayuaji and M. F. Nuruddin (2014). Influence of Microwave Incinerated Rice Husk Ash on Hydration of Foamed Concrete, vol. 2014.

[2] E. J. Siqueira, I. V. P. Yoshida, L. C. Pardini, and M. a. Schiavon (2009). Preparation and characterization of ceramic composites derived from rice husk ash and polysiloxane, *Ceram. Int.*, vol. 35, no. 1, pp. 213–220.

[3] K. Kordatos, S. Gavela, a. Ntziouni, K. N. Pistiolas, a. Kyritsi, and V. Kasselouri-Rigopoulou (2008). Synthesis of highly siliceous ZSM-5 zeolite using silica from rice husk ash, *Microporous Mesoporous Mater.*, vol. 115, no. 1–2, pp. 189–196.

[4] U. Kalapathy, a. Proctor, and J. Shultz (2002). An improved method for production of silica from rice hull ash, *Bioresour. Technol.*, vol. 85, no. 3, pp. 285–289.

[5] M. Rozainee, S. Ngo, a Salema, K. Tan, M. Ariffin, and Z. Zainura (2008). Effect of fluidising velocity on the combustion of rice husk in a bench-scale fluidised bed combustor for the production of amorphous rice husk ash, *Bioresour. Technol.*, vol. 99, no. 4, pp. 703–713.

[6] V. B. Carmona, R. M. Oliveira, W. T. L. Silva, L. H. C. Mattoso, and J. M. Marconcini (2013). Nanosilica from rice husk: Extraction and characterization, *Ind. Crops Prod.*, vol. 43, pp. 291–296.

[7] K. Mohanta, D. Kumar, and O. Parkash (2012). Properties and Industrial Applications of Rice husk : A review, *Inernational J. Emerg. Technol. Adv. Eng.*, vol. 2, no. 10, pp. 86–90.

[8] T. Lee, R. Othman, and F. Y. Yeoh (2013). Development of photoluminescent glass derived from rice husk, *Biomass and Bioenergy*, vol. 59, pp. 380–392.

[9] A. Bakar (2012). Malaysian Rice Husk Ash – Improving the Durability and Corrosion Resistance of Concrete : Pre-review, *Concr. Res. Lett.*, vol. 1, no. 1, pp. 6–13.
[10] A. W. C. Farah, H. A. B. Badorul, A. M. J. Megat, and P. J. Ramadhansyah (2011). Properties of concrete block containing rice husk ash subjected to GIRHA, *Analysis*, vol. 8, no. July, pp. 57–64.
[11] L. P. Singh, S. R. Karade, S. K. Bhattacharyya, M. M. Yousuf, and S. Ahalawat (2013). Beneficial role of nanosilica in cement based materials – A review, *Constr. Build. Mater.*, vol. 47, no. OCTOBER, pp. 1069–1077.
[12] R. Deeb, a. Ghanbari, and B. L. Karihaloo (2012). Development of self-compacting high and ultra high performance concretes with and without steel fibres, *Cem. Concr. Compos.*, vol. 34, no. 2, pp. 185–190.
[13] G. Leyi, Z. Wei, Z. Jing, and H. Songling (2011). Mechanics analysis and simulation of material Brinell hardness measurement, *Meas. J. Int. Meas. Confed.*, vol. 44, no. 10, pp. 2129–2137.
[14] Q. Zhao, B. Zhang, H. Quan, R. C. M. Yam, R. K. K. Yuen, and R. K. Y. Li (2009). Flame retardancy of rice husk-filled high-density polyethylene ecocomposites, *Compos. Sci. Technol.*, vol. 69, no. 15–16, pp. 2675–2681.
[15] K. G. Mansaray and a. E. Ghaly (1999). Determination of kinetic parameters of rice husks in oxygen using thermogravimetric analysis, *Biomass and Bioenergy*, vol. 17, no. 1, pp. 19–31.
[16] R. Das, S. Ghosh, and M. K. Naskar (2014). Notes Synthesis of single crystal zeolite L rods with high aspect ratio using rice husk ash as silica source, vol. 53, no. July, pp. 816–819.
[17] Balbuenat P.B. & Gubbins K.E. (1993). Theoretical Interpretation of Adsorption Behavior of Simple Fluids in Slit Pores, *Langmuir*, vol. 9, no. 7, pp. 1801–1814.
[18] K. S. W. Sing, D. H. Everett, R. A. W. Haul, L. Moscou, L. A. Pierotti, J. Rouquerol, and T. Siemieniewska (1985). International union of pure and applied chemistry physical chemistry division reporting physisorption data for gas/soils systems with special reference to the determination of surface area and porosity, *Pure Appl. Chem.*, vol. 57, no. 4, pp. 603–619.
[19] M. Thommes, K. Kaneko, A. V. Neimark, J. P. Olivier, F. Rodriguez-Reinoso, J. Rouquerol, and K. S. W. Sing (2015). Physisorption of gases, with special reference to the evaluation of surface area and pore size distribution (IUPAC Technical Report), *Pure Appl. Chem.*, vol. 87, no. 9–10, pp. 1051–1069.
[20] M. Choolaei, A. M. Rashidi, M. Ardjmand, A. Yadegari, and H. Soltanian (2012). The effect of nanosilica on the physical properties of oil well cement, *Mater. Sci. Eng. A*, vol. 538, pp. 288–294.
[21] L. E. Zapata, G. Portela, O. M. Suárez, and O. Carrasquillo (2013). Rheological performance and compressive strength of superplasticized cementitious mixtures with micro/nano-SiO2 additions, *Constr. Build. Mater.*, vol. 41, pp. 708–716.
[22] P. Hou, S. Kawashima, D. Kong, D. J. Corr, J. Qian, and S. P. Shah (2013). Modification effects of colloidal nanoSiO2 on cement hydration and its gel property, *Compos. Part B Eng.*, vol. 45, no. 1, pp. 440–448.

Removal of Congo red by Using Hibiscus Sabdariffa for Coagulation and Flocculation Process

Chin Yong Yao*, Nurhazwani Ismail

chinyongyao92@gmail.com

Abstract
Congo red is one of the most common synthetic dyes found in the industrial effluents such as textile and cosmetics industry. The untreated or poorly treated industrial dye effluents can cause significant impact to the mankind and environment. Coagulation/flocculation is known as the feasible method for dye wastewater treatment. In this study, Hibiscus sabdariffa seed have been proposed as an alternative natural coagulant to treat Congo red in wastewater. The jar test experiment is used to investigate the four important factors that influence coagulation/flocculation process, which are the initial dye concentration, pH, coagulant dosage and flocculants dosage. The colour intensity and turbidity are the measures of Congo red removal. Respond Surface Methodology (RSM) is used to determine the optimum working conditions for the coagulation/flocculation. The regression and variance analysis are determined by using a statistical software, Minitab 16.0 to evaluate the accuracy of the model. This study also compare the ability of Hibiscus sabdariffa as natural coagulant/flocculant with alum and polyacrylamide as chemical coagulant and flocculant. The analysis shows the pH and initial dye concentration have significant effect on the turbidity and colour removal. The optimum working conditions for coagulation/flocculation using Hibiscus sabdariffa in Congo red removal are pH 2, initial dye concentration of 229 ppm, coagulant dosage of 709 mg/l and flocculant dosage of 7.2 mg/l. At these optimized conditions, the Congo red removal for natural coagulant/flocculant is comparable and more efficient than the chemical treatment, at which the turbidity removal and the colour removal are 80% and 97.3% for Hibiscus sabdariffa and 68% and 90% for chemical treatment. The result obtained is similar to the predicted result from RSM. Therefore, Hibiscus sabdariffa is an ideal alternative for the chemical coagulant in term of Congo red removal.

Keywords: Congo red; Coagulation/flocculation; Natural coagulant; Hibiscus sabdariffa

1. Introduction

Dyes are the most widely used synthetic chemicals in various industries, which are ranging from textile, cosmetics, pharmaceutical, plastic to food industry [1]. The statistics according to [2] shows that there are approximately ten thousands of different commercial dyes and pigments exist, and the production of dyes annually is reported to be more than 700,000 tons worldwide. An estimation of 10 – 15% of the synthetic dyes produced are released as effluents to the environment during the dyeing process. This phenomena has caused significant impact to the mankind and environment because most of the dyes are toxic, mutagenic and carcinogenic [3].

Most of the dyes are synthetic chemical compounds that cause damage to aquatic life and human being because of its complex aromatic structure. Congo red (CR) is one of the most common dyes that is found in the effluents from textiles, printing, dyeing, paper, rubber and plastics industries. CR is a benzidine-based anionic diazo dye and it is difficult to biodegrade due to its structural stability in nature [1]. The discharge of coloured wastewater into the natural stream or river prevent the sunlight diffusion into the water and hence limiting the photosynthesis process of the aquatic plant [4]. This will threaten the aquatic life because of the insufficient oxygen in water. The present of dyes also cause human's health on the risk of waterborne diseases. The body's immune system could not break down the dyes and thus gastrointestinal symptoms occur such as nausea, vomiting and diarrhea. Therefore, many researches related to removal of CR are ongoing throughout the years. Different methods of CR removal have been established in order to identify the most effective and feasible one [1].

The current technologies available in treating or removing dyes consist of CR are ozonation, membrane separation, adsorption by activated carbon and coagulation/flocculation. Each treatment has its merits and limitation in application [3]. In recent decades, physicochemical methods such as coagulation and flocculation has drawn much attention from the researchers due to its feasibility for dye wastewater treatment. However, research shows that conventional coagulation produces aluminum residual in treated water has been related to serious health issues such as the development of Alzheimer disease [5]. Hence, studies on the use of natural coagulants for CR removal are conducted to overcome this issue. The naturally prepared coagulants for colour removal gained much development over the years [2]. Despite chemical cost saving, the natural coagulants would improve the characteristic of produced sludge for safe utilizing or disposal [6].

Natural coagulants extracted from microorganisms, animals and plants are used as ideal alternative for coagulation/flocculation. The natural coagulant from plants are Moringa oleifera seed, Common bean and Nirmali seed [7]. The presence of positively or negatively charged polymers in plants contribute to their coagulating property. For example, the presence of water soluble cationic coagulant protein in Moringa oleifera seed, anionic polyelectrolyte in Nirmali seed and the crude extracts of common bean are the contributing factors to exhibit coagulating characteristic of plants [7].

In this study, the use of Hibiscus sabdariffa seed in CR removal through coagulation/flocculation process is extensively studied. The significant factors that affect the performance of Hibiscus sabdariffa seed in CR removal are investigated. The optimum working conditions for Hibiscus sabdariffa is studied by using Minitab 16.0. A comparison of the CR removal is carried out by using natural coagulant and chemical coagulant to compare their effectiveness of CR removal.

2. Material and methods

2.1. Preparation of natural coagulant

The raw Hibiscus sabdariffa flower was purchased from the Kubah Ria market in Kuching, Sarawak, Malaysia. The petals were removed and capsule containing the seed was collected. The seed of Hibiscus sabdariffa was removed from its capsule and was dried in the oven under 60 ^{o}C. The active coagulating agents in the seed powder was extracted using sodium chloride solvent, NaCl. In this experiment, 1 g of Hibiscus sabdariffa seed was added into 100 ml of 0.5M of NaCl solution to produce 1% w/v of natural coagulant [8]. The mixture solution was blended using an ordinary food blender for 2 min [9], then the aqueous solution (filtrate) was filtered out [10]. The filtrate was readily used as the natural coagulant. Theoretically, the concentration of coagulant is 10,000 mg/l. In order to achieve optimum result, the coagulant was prepared each time before the experiment to avoid degradation [9].

2.2. Congo red dye

The anion dye, CR was supplied by "Systerm Chemical Company" with the concentration of 0.1% at reagent grade (1000 ppm). The synthetic wastewater was prepared by diluting the dye with the appropriate amount of distilled water. The initial dye concentration of CR solution used in the experiment was between 40 and 400 ppm [11]. The pH of the solution was manipulated using 1 M of hydrochloride acid or 1 M of sodium hydroxide ([2], [9]).

2.3. Experimental Design

Beaker tests was used in conducting the experiment. The experiment was carried out in batches which involve rapid mixing, slow mixing and sedimentation. The coagulation/flocculation process was done by using Hibiscus sabdariffa seed extract as the coagulant and flocculants. The beakers was initially filled with 500 ml of synthetic dye solution prepared earlier with desired pH [9]. The coagulants was added to the beakers right before the 1 minute of rapid mixing at 95-100 rpm [12]. This was followed by a slow mixing at 45-50 rpm for 20 minutes after the flocculants was added [13]. The impeller was removed and the flocs formed was allowed to settle and stabilize for 60 min [14].

The two responses measured in the experiment are turbidity removal and colour removal. The colour removal of the synthetic dye wastewater was analyzed using a UV-

spectrophotometer with the wavelength of CR is 500 nm [3]. The turbidity removal was measured using a hand-held turbidimeter [1], [15].

The percentage of removal of parameter was calculated using the formula below [10]:

$$\text{Removal of parameter in percentage} = 100 \text{ X } (C_i - C_f)/C_i \quad (1)$$

Where C_i is the parameter before treating; C_f is the parameter after treating

2.4. Response surface methodology

RSM is a mathematical and statistical analysis technique to describe the behavior of a data set based on the fit of a polynomial equation to the data. RSM is useful when a response or a set of responses of interest are influenced by several variables. The best system performance can be obtained by optimizing the levels of these variables [16]. In this experiment, the four independent variables (factors) are pH of the synthetic dye, initial dye concentration, dosage of coagulant and dosage of flocculants while the two responses (parameters) are colour removal and turbidity removal. In consideration of the large number of variables and responses in the experiment, RSM is used in the optimization. From the previous study, Box-Behnken design has been used to investigate the optimum working conditions of cactus Opuntia ficus-indica in coagulation/flocculation of textile effluents [8].

Box-Behnken is a type of response surface design that consist of combinations at the midpoints and edges of the experiment. This design method was employed in the study. This quadratic response surface design ensures all the design points (experiment runs) fall within the safe operating zone. Besides that, it consists of fewer design points compare to other designs such as central composite design at the same number of factors. In this case, the design is known as three-level, four-variable Box-Behnken design in order establish empirical relationships between the two responses and the four factors. The real value of each variable is transformed into coordinates within a scale with dimensionless coded values from -1 to 1, where -1 is low, 0 is central and 1 is high as shown in **Error! Reference source not found.**1 [17]. For three-level, four-variable Box-Behnken design in this study, the number of experiment required is 27 runs including three replicates at the centre point,0. The experiments was conducted in a random order.

Table 1: Levels of each independent variable for RSM

Factor	Low (-1)	Central (0)	High (1)
pH, x_1	2	7	12
Initial dye concentration, x_2 (mg/l)	40	220	400
Coagulant dosage, x_3 (mg/l)	300	1050	1800
Flocculants dosage, x_4 (mg/l)	1	8	15

The coded values of each level and polynomial equation model are obtained by using equation below [8]:

$$x_i = \frac{X_1 - X_0}{X_i} \quad (2)$$

$$y = \beta_0 + \sum_{i=1}^{a} \beta_i x_i + \sum_{i=1}^{a} \beta_{ii} x_i^2 + \sum_{i=1}^{2} \sum_{j=i+1}^{a} \beta_{ij} x_i x_j \quad (3)$$

Where x_i is the coded value for each factor, $X_1$is the actual value of each factor, X_0 is the actual value of each factor at the central point, $X_i$is the different between the level of factor, $\beta_0, \beta_i, \beta_{ii}, \beta_{ij}$ are the regression coefficients and y is the response value predicted by the model.

The regression and variance analysis of the data was carried out using Minitab 16.0, which is a statistical software [17]. The fitness of the models was evaluated using ANOVA and the determination coefficient, R^2. The t-test was conducted to determine the significant of the parameters for the model [8].

2.5. Comparison of optimized natural coagulant with chemical coagulant

Aluminum sulphate (alum) and polyacrylamide were used as the chemical coagulant and flocculant respectively. According to the finding from [18], the optimum conditions for chemical coagulant and flocculation are pH 5.3 and alum dosage of 200 mg/l and polyacrylamide dosage of 1mg/l [19]. The optimum conditions for Hibiscus sabdariffa were obtained from the RSM optimization and comparison was performed between the two coagulation/ flocculation processes.

3. Result and Discussion

3.1. Model Fitting

The quadratic regression coefficient is used to predict the quadratic polynomial models for the percentage of turbidity removal (Y_1) and colour removal (Y_2) [20]. The regression coefficient for the turbidity and colour removal are obtained by least squares

method technique using statistical software, Minitab 16.0. The coefficients are shown in Table 2 and Table 3 respectively.

Table 2: Predicted Regression coefficient of the polynomial model for turbidity removal

Independent Variables	Regression coefficient	Standard error	t – Value	p – Value	Significant level
Constant	191.534	455.639	0.420	0.682	
Linear					
X_1	-46.633	56.564	-0.824	0.426	
X_2	0.438	1.503	0.292	0.776	
X_3	-0.006	0.377	-0.017	0.987	
X_4	-7.767	37.919	-0.205	0.841	
Square					
X_1^2	-2.908	2.958	-0.983	0.345	
X_2^2	-0.003	0.002	-1.442	0.175	
X_3^2	0.000	0.000	0.131	0.898	
X_4^2	0.994	1.509	0.659	0.523	
interaction					
$X_1 X_2$	0.281	0.095	2.957	0.012	**
$X_1 X_3$	-0.001	0.023	-0.044	0.965	
$X_1 X_4$	-0.051	2.439	-0.021	0.984	
$X_2 X_3$	0.000	0.001	-0.124	0.904	
$X_2 X_4$	-0.031	0.068	-0.459	0.655	
$X_3 X_4$	0.001	0.016	0.043	0.967	

** $p < 0.05$; *** $p < 0.01$

Table 3: Predicted Regression coefficient of the polynomial model for colour removal

Independent Variables	Regression coefficient	Standard error	t – Value	p – Value	Significant level
Constant	130.104	15.2379	8.538	0.000	***
Linear					
X_1	-28.377	1.8916	-15.001	0.000	***
X_2	0.118	0.0503	2.339	0.037	**
X_3	0.019	0.0126	1.477	0.165	
X_4	-0.620	1.2681	-0.489	0.634	
Square					
X_1^2	1.560	0.0989	15.776	0.000	***
X_2^2	-0.0001	0.0001	-2.494	0.028	**
X_3^2	0.000	0.0000	-0.699	0.498	
X_4^2	0.023	0.0505	0.465	0.651	
interaction					
$X_1 X_2$	-0.008	0.0032	-2.380	0.035	**
$X_1 X_3$	0.000	0.0008	0.447	0.663	
$X_1 X_4$	-0.005	0.0816	-0.059	0.954	
$X_2 X_3$	0.000	0.0000	-1.581	0.140	
$X_2 X_4$	0.000	0.0023	0.135	0.895	

X_3 X_4	0.000	0.0005	0.122	0.905

** $p < 0.05$; *** $p < 0.01$

The regression coefficient is tested with t-test and the p-Value with less than 0.05 is significant while p-Value with less than 0.01 is highly significant [20]. For the turbidity removal, the interaction between the pH and the initial dye concentration is significant ($P < 0.05$). On the other hand, for the colour removal, the linear and square term of pH (X_1) are highly significant ($P < 0.01$). The linear and square term of initial dye concentration are tested to be significant ($P < 0.05$). The interaction between pH and initial dye concentration is significant for the response of the colour removal ($P < 0.05$). The quadratic polynomial models for turbidity removal (Y_1) and colour removal (Y_2) are generated based on the coefficients as shown below [16]:

$$Y_1 = 0.281X_1X_2 \quad (4)$$

$$Y_2 = 130.104 - 28.377X_1 + 0.118X_2 + 1.560X_1^2 - 0.0001X_2^2 - 0.008X_1X_2 \quad (5)$$

3.2. Diagnostic checking of the fitted models: Analysis of Variance (ANOVA)

ANOVAs are carried out for the two models, Y_1 and Y_2 on the significant error between the independence variables [20]. The results are summarized in Table 4 and Table 5.

The ANOVA test in Table 4 shows that the regression model for the data on the turbidity removal is not significant ($p > 0.05$) and there is significant lack-of-fit for the turbidity removal ($p < 0.01$). The pure error for the model's ANOVA is small (4%). The ANNOVA result indicates that the empirical model, equation (4) is not able to accurately represent the actual relationships for turbidity removal at certain situation. Thus, the interaction of the variables for turbidity removal is not considered.

Table 4: ANOVA of the effect of the variable as linear, square and interaction on the turbidity removal

Source	Degree of freedom	Sum of squares	Mean square	F ratio	P
Regression	14	768888	54921	1.88	0.139
Linear	4	373717	7777	0.27	0.894
Square	4	133467	33367	1.14	0.382
Interaction	6	261704	43617	1.50	0.260
Residue error	12	349879	29157		
Lack-of-fit	10	349875	34988	18656.92	0.000
Pure error	2	4	4		
Total	26	1118767			

The ANOVA test in Table 5 shows that regression model for the data on the colour removal is highly significant ($p < 0.01$). The lack-of-fit of the model is not significant ($p > 0.01$) and the pure error for the model's ANOVA is very small (1.7%). These indicate that the empirical model, equation (5) is able to represent the actual relationships among the variables for colour removal. Therefore, the interaction between variables for colour removal is discussed.

Table 5: ANOVA of the effect of the variable as linear, square and interaction on the colour removal

Source	Degree of freedom	Sum of squares	Mean square	F ratio	P
Regression	14	31454.7	2246.76	68.90	0.000
Linear	4	20056.1	2601.84	79.79	0.000
Square	4	11124.6	2781.16	85.29	0.000
Interaction	6	273.9	45.66	1.40	0.291
Residue error	12	391.3	32.61		
Lack-of-fit	10	389.6	38.96	44.87	0.022
Pure error	2	1.7	1.7		
Total	26	31864.0			

3.3. Respond Surface Plotting and Optimization

From the regression analysis, the significant interaction variables in the fitted models are the pH of the solution, X_1 and the initial dye concentration, X_2 for colour removal. The relationship can be clearly shown in the three-dimensional response surfaces plots and contour plots from Figure 1 to Figure 3 [20].

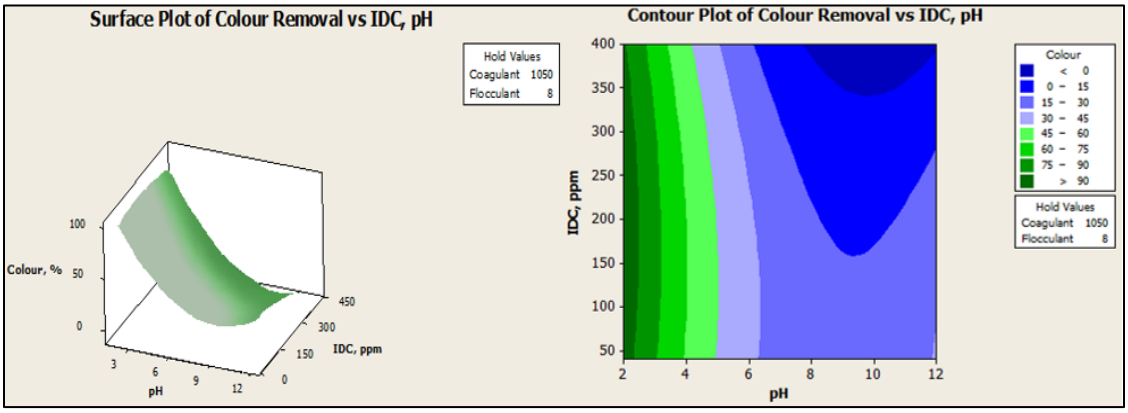


Figure 1: Response surface and contour plots of the colour removal against initial dye concentration and pH

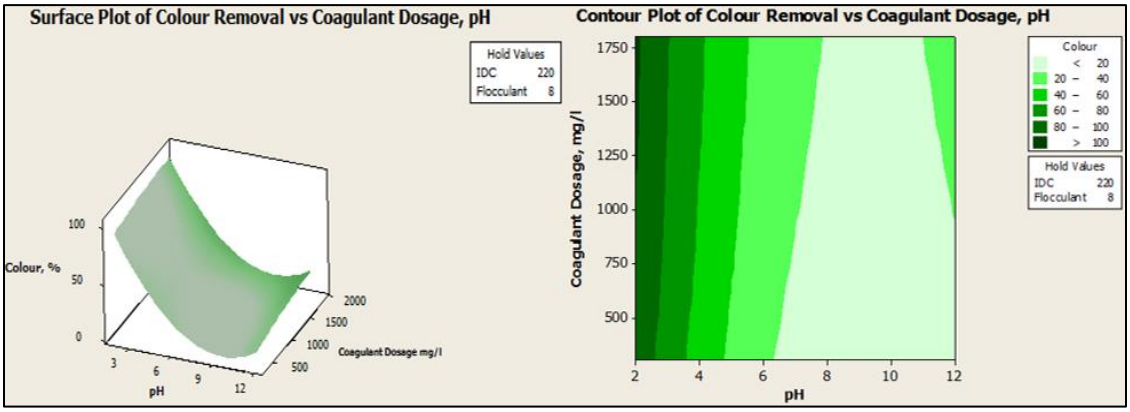


Figure 2: Response surface and contour plots of the colour removal against coagulant dosage and pH

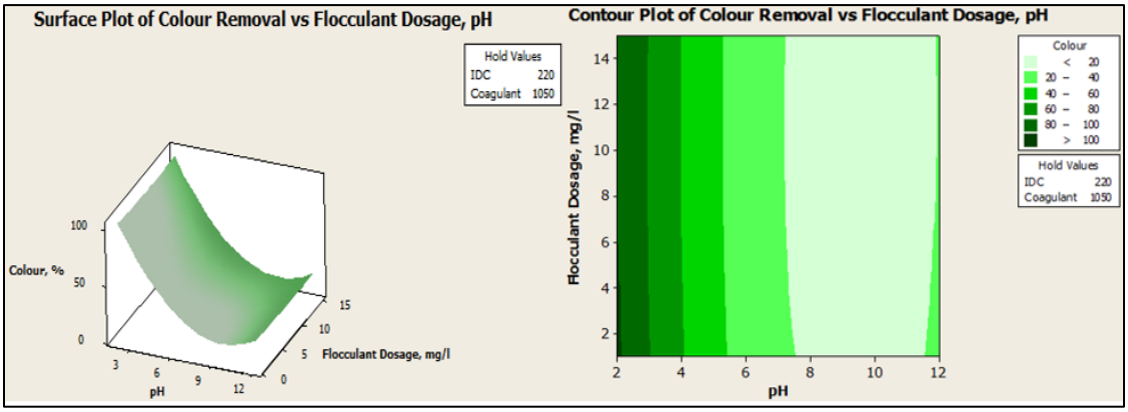


Figure 3: Response surface and contour plots of the colour removal against flocculant dosage and pH

The response surface and contour plots from Figure 1 to Figure 3 show that the colour removal is favourable at low pH regardless of the other factors. In general, the percentage of colour removal is greater than 90% at below pH 3. The percentage of colour removal drops drastically as the pH increases from 3 to 9 while it experiences slight increment from pH 9 to 12. The effect of initial dye concentration on the colour removal, range from 40 to 400 ppm, can be observed from the response surface plot in Figure 1. The moderate initial dye concentration has given the highest colour removal. Figure 2 shows the response surface plot for colour removal against the pH and coagulant dosage. An increasing trend of colour removal is observed as the coagulant dosage increases until a maximum colour removal is achieved. The colour removal drops slightly beyond the maximum coagulant dosage. The response surface plot of colour removal against flocculant dosage and pH is shown in Figure 3. From the graph, the change in flocculant dosage does not cause major effect on the colour removal. The highest percentage of colour removal achieved is at flocculant dosage of 11 mg/l.

The optimization of the factors is analyzed by using Minitab 16.0. The optimum conditions for both turbidity removal and colour removal are pH 2, initial dye concentration of 229 ppm, coagulant dosage of 709 mg/l and flocculant dosage of 7.2 mg/l. The optimum working factors have taken into consideration of all the relationship between the independent variables discussed. With these optimum conditions, the predicted turbidity removal is 80.0% and the predicted colour removal is 97.3%. On the other hand, the experimental result of the optimum conditions has 75% turbidity removal and 98% of colour removal. These results further strengthen the predicted result from the optimization.

3.4. Comparison of Natural and Chemical Coagulant/ Flocculant

The coagulation/ flocculation process was performed by using chemicals, the alum and polyacrylamide. The result obtained from this experiment can be used to compare the CR removal capability using chemical and natural coagulant/ flocculant. Figure 4 shows the result of the CR removal of both natural and chemical coagulant/flocculant. The chemical coagulant/ flocculant result in turbidity removal of 68% and colour removal of 90%. On the other hand, natural coagulant/ flocculant, Hibiscus sabdariffa shows a better result of 75% of turbidity removal and 98% of colour removal. From this experiment, Hibiscus sabdariffa is more efficient than chemical coagulant/flocculant. Therefore, Hibiscus sabdariffa is considered an ideal alternative for chemical coagulant in term of the CR removal performance.

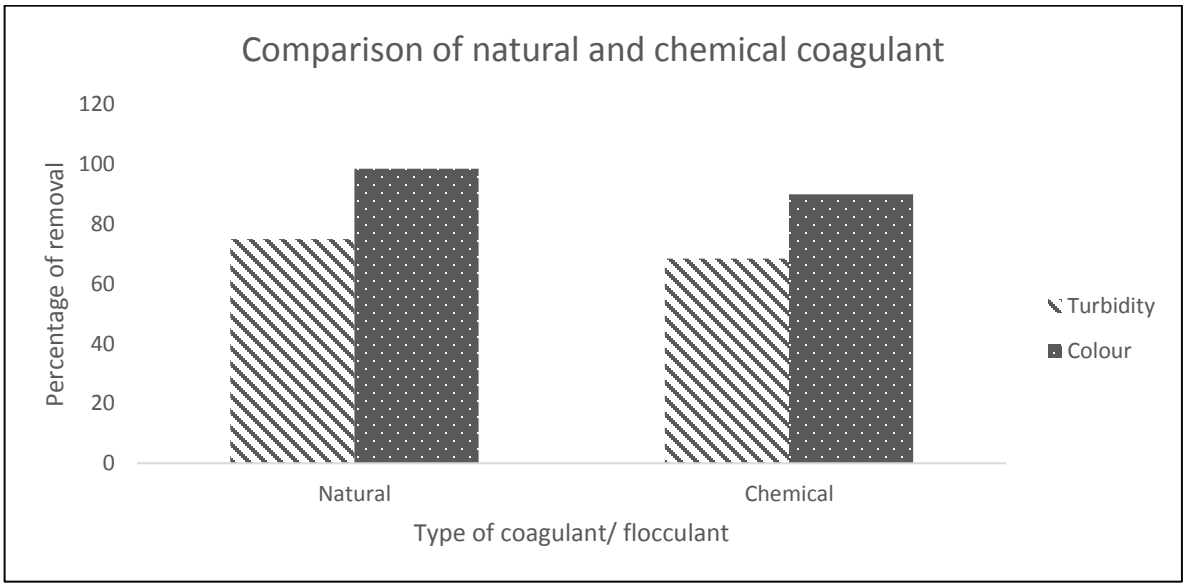


Figure 4: Congo red removal of natural coagulant and chemical coagulant

3.5. pH

The pH plays important role in the coagulation and flocculation processes. The important of pH can be shown in the high significant level from the regression and ANOVA as well as the previous studies [11]. The pH for the experiment is manipulated between 2 to 12. From the result in Figure 2, the percentage of colour removal fall drastically when

the pH increase from 3 to 9. This phenomena can be explained by the electrostatic charges around the coagulating agents [2]. The coagulating agent extracted from the Hibiscus sabdariffa seed consist of cationic amino group such as glutamic acid and aspartic acid [21]. Therefore, acidic solution is favourable to protonate the cationic amino group. The result also shows slight increment in the percentage of colour removal from pH 9 to 12. This is because the coagulating agents consist of a small amount of anionic amino group which is favour for alkali condition. For example arginine act as the anionic amino group in the coagulating agent.

3.6. Initial dye concentration

The initial dye concentration is also one of the most important factors that will affect the percentage of colour removal. The initial dye concentration is tested between the ranges of 40 ppm to 400 ppm. From the result analysis in Figure 1, the percentage of colour removal increases with the initial dye concentration until maximum at 220 ppm. Beyond 220 ppm, the percentage of colour removal drops as the dye concentration increases. These result can be explained by the particle-polymer-particle complex formation theory [12]. The coagulating agent acts as the polymer molecule with sites for the colloid particles. When the dye concentration is saturated (220ppm), there is no more polymer with available site for the colloid particle. Thus, the percentage of removal drops beyond the saturation point.

3.7. Coagulant dosage

From the experiment, the range of coagulant dosage is tested from 300 mg/l to 1800 mg/l [22]. The optimum coagulant dosage of hibiscus sabdariffa is determined from the experiment as 709 mg/l. The coagulation process may not have sufficient charges for effective homogeneous removal at low coagulant dosage. Thus higher coagulant dosage will increase the removal. On the other hand, re-stabilization or re-dispersion may occur at high coagulant dosage [14]. The formed flocs is dissolved into the solution and cause inefficient removal. Therefore, an optimum dosage of coagulant is desirable for coagulation/ flocculation process.

3.8. Flocculant dosage

The flocculant dosage test in the experiment is from 1 mg/l to 15 mg/l. The optimum flocculant dosage determined from the experiment is 7.2 mg/l. From the result of the experiment in Figure 3, the change in flocculant dosage does not affect much on the colour removal of the Congo red. Flocculant promotes higher aggregation between colliding particles. However, overdose of flocculant will cause re-dispersion [14]. Therefore, the flocculant dosage beyond 7 mg/l is not favourable.

4. Conclusions

In conclusion, the study shows that Hibiscus sabdariffa is an ideal alternative for the Congo red removal in dye wastewater treatment. The factors that have significant effect

on the CR removal are pH and initial dye concentration. At optimum working conditions of pH 2, initial dye concentration of 229 ppm, coagulant dosage of 709 mg/l and flocculant dosage of 7.2 mg/l, the turbidity removal and colour removal are 80% and 97.3%. The comparison of Hibiscus sabdariffa with chemical coagulant also shows Hibiscus sabdariffa has the better CR removal ability than chemical coagulant. This indicates that Hibiscus sabdariffa is able to perform as alternative toward the chemical coagulant. The use of Hibiscus sabdariffa in dyes industries would definitely lower the cost of the wastewater treatment. Besides that, human's health is protected from the hazardous chemical residue such as alum found in the treated water. From the research, there are future studies that could enhance the development of Hibiscus sabdariffa as natural coagulant/ flocculant. For example future studies could focus on the real industrial dyes wastewater rather than synthetic wastewater for more industrial-based study. Besides that, the settling time of the flocs can be studied in the future work because it would potentially affect the flocculant dosage.

References

[1] V. S. Mane and P. V. V. Babu, "Evaluation of performance of Coagulation / Flocculation method for the removal of dyes from aqueous solutions," no. 1, pp. 8–10, 2011.

[2] H. Patel and R. T. Vashi, "Removal of Congo Red dye from its aqueous solution using natural coagulants," *J. Saudi Chem. Soc.*, vol. 16, no. 2, pp. 131–136, 2012.

[3] F. A. Pavan, S. L. P. Dias, E. C. Lima, and E. V. Benvenutti, "Removal of Congo red from aqueous solution by anilinepropylsilica xerogel," *Dye. Pigment.*, vol. 76, no. 1, pp. 64–69, 2008.

[4] S. Coruh, G. Dogan, and U. Coruh, "Adsorption Efficiency for the Removal Congo Red by Seafood Shell Using Ann," no. September, pp. 1–10, 2010.

[5] M. H. Mehdinejad, B. Bina, M. Nikaeen, and H. M. Attar, "Effectiveness of chitosan as natural coagulant aid in removal of turbidity and bacteria from turbid waters," *J. Food, Agric. Environ.*, vol. 7, no. 3–4, pp. 845–850, 2009.

[6] A M. Abdelaal, "Using a Natural Coagulant for Treating Wastewater," *Eighth Int. Water Technol. Conf.*, pp. 781–792, 2004.

[7] G. Muthuraman, S. Sasikala, and N. Prakash, "Proteins from Natural Coagulant for Potential Application of Turbidity Removal in Water," *Ijeit*, vol. 3, no. 1, pp. 278–283, 2013.

[8] M. T. F. De Souza, E. Ambrosio, C. A. De Almeida, T. K. F. De Souza Freitas, L. B. Santos, V. De Cinque Almeida, and J. C. Garcia, "The use of a natural coagulant (Opuntia ficus-indica) in the removal for organic materials of textile effluents," *Environ. Monit. Assess.*, vol. 186, no. 8, pp. 5261–5271, 2014.

[9] Z. Z. Abidin, N. S. Mohd Shamsudin, N. Madehi, and S. Sobri, "Optimisation of a method to extract the active coagulant agent from Jatropha curcas seeds for use in turbidity removal," *Ind. Crops Prod.*, vol. 41, pp. 319–323, 2013.

[10] Y. Alima, E. Irma, C. P. Agbangnan, A. Y. Koudoro, C. A. Dèdjiho, M. P. Aïna, D. Mama, D. Codjo, and K. Sohounhloué, "Evaluation of the Opuntia dillenii as Natural Coagulant in Water Clarification : Case of Treatment of Highly Turbid Surface Water," vol. 2013, no. December, pp. 1242–1246, 2013.

[11] J. Beltrán-Heredia, J. Sánchez-Martín, a. Delgado-Regalado, and C. Jurado-Bustos, "Removal of Alizarin Violet 3R (anthraquinonic dye) from aqueous solutions by natural coagulants," *J. Hazard. Mater.*, vol. 170, pp. 43–50, 2009.

[12] A. Mishra and M. Bajpai, "Flocculation behaviour of model textile wastewater treated with a food grade polysaccharide," *J. Hazard. Mater.*, vol. 118, no. 1–3, pp. 213–217, 2005.

[13] R. Sanghi, B. Bhattacharya, A. Dixit, and V. Singh, "Ipomoea dasysperma seed gum: An effective natural coagulant for the decolorization of textile dye solutions," *J. Environ. Manage.*, vol. 81, no. 1, pp. 36–41, 2006.

[14] T. K. F. S. Freitas, V. M. Oliveira, M. T. F. de Souza, H. C. L. Geraldino, V. C. Almeida, S. L. Fávaro, and J. C. Garcia, "Optimization of coagulation-flocculation process for treatment of industrial textile wastewater using okra (A. esculentus) mucilage as natural coagulant," *Ind. Crops Prod.*, vol. 76, pp. 538–544, 2015.

[15] M. Pritchard, T. Craven, T. Mkandawire, A. S. Edmondson, and J. G. O'Neill, "A comparison between Moringa oleifera and chemical coagulants in the purification of drinking water – An alternative sustainable solution for developing countries," *Phys. Chem. Earth, Parts A/B/C*, vol. 35, no. 13–14, pp. 798–805, 2010.

[16] M. A. Bezerra, R. E. Santelli, E. P. Oliveira, L. S. Villar, and L. a. Escaleira, "Response surface methodology (RSM) as a tool for optimization in analytical chemistry," *Talanta*, vol. 76, no. 5, pp. 965–977, 2008.

[17] S. Ö. Gönen, M. Erol Taygun, and S. Küçükbayrak, "Evaluation of the factors influencing the resultant diameter of the electrospun gelatin/sodium alginate nanofibers via Box-Behnken design.," *Mater. Sci. Eng. C. Mater. Biol. Appl.*, vol. 58, pp. 709–23, Jan. 2015.

[18] A. K. Verma, R. R. Dash, and P. Bhunia, "A review on chemical coagulation/flocculation technologies for removal of colour from textile wastewaters," *J. Environ. Manage.*, vol. 93, no. 1, pp. 154–168, 2012.

[19] F. El-Gohary and A. Tawfik, "Decolorization and COD reduction of disperse and reactive dyes wastewater using chemical-coagulation followed by sequential batch reactor (SBR) process," *Desalination*, vol. 249, no. 3, pp. 1159–1164, 2009.

[20] M. Wu, H. Ding, S. Wang, and S. Xu, "Optimizing conditions for the purification of linoleic acid from sunflower oil by urea complex fractionation," *Jaocs, J. Am. Oil Chem. Soc.*, vol. 85, no. 7, pp. 677–684, 2008.

[21] Mohamed A. Shaheen, "Roselle (Hibiscus sabdariffa L.) seeds as unconventional nutritional source," *African J. Biotechnol.*, vol. 11, no. 41, pp. 9821–9824, 2012.

[22] M. Chethana, S. L. Gayatri, B. V. M, R. V. V, and S. Raja, "tetragonus (Triangle Cactus) In Dye Wastewater Treatment," vol. 9, no. 3, pp. 813–821, 2015.

Antioxidant Potential of Malaysian Fruit Extract (Myristica Fragrans)

Dianne Priya A/P Lawrence*, Rajesh Nithyanandam, Dr Pin Kar (FRIM)

School of Engineering, Taylor's Univeristy, Taylor's Lakeside Campus, No. 1 Jalan Taylor's, 47500, Subang Jaya, Selangor DE, Malaysia

*Corresponding Author:
diannepriyalawrence.thangathurai@sd.taylors.edu.my

Abstract
The aim of this experiment is to study the phytochemical content of Malaysian fruit *(Myristica Fragrans)* commonly known as Nutmeg. This study also includes the optimization of extraction conditions for both Soxhlet and Ultrasonic Extraction to yield the highest Total Phenolic Content, Total Flavonoid Content and DPPH Scavenging Activity of Nutmegs using Response Surface Methodology (RSM). Soxhlet Extraction was carried out with different extraction time and type of solvent. However, Ultrasonic Assisted Extraction is carried out with different extraction time, Concentration of Solvent and temperature of Ultrasonic Waterbath. It was shown that the optimum value TPC, TFC and DPPH Scavenging activity of Soxhlet Extraction on Nutmegs are 12.290 mg GAE/100g DW, 17.09 mg QE/100 g DW and 95.837% respectively with a desirability of 0.671. The optimum condition for Soxhlet extraction of Nutmegs to obtain optimum yield of TPC, TFC and DPPH Scavenging are by using Methanol as the extracting solvent at 184 min extraction time. However, for the optimization value of TPC, TFC and DPPH Scavenging activity for Ultrasonic Assisted Extraction of nutmegs are 28.722 GAE/100g DW, 46.600 QE/100 g DW and 98.565% respectively with a desirability of 0.977. The optimum condition for Ultrasonic Assisted extraction of Nutmegs to obtain optimum yield of TPC, TFC and DPPH Scavenging are by extracting Nutmeg at 40.512 minutes at 49.99 ℃ and at 40% ethanol concentration

Keywords: *Myristica Fragrans*, phytochemical content, Soxhlet Extraction Ultrasonic Assisted Extraction, Response Surface Methodology

1. Introduction

Fruits and vegetables are known to be a part of a healthy diet. A diet rich in vegetables and fruits can reduce blood pressure, risk of heart disease and stroke. Research have also proven that fruits and vegetables can prevent some types of cancer, reduce the risk of eye and digestive problems. It also have a positive effect upon blood sugar which can aid keep appetite in check [1]. These health benefits is studied to be associated with high antioxidant activity which inhibits the activity of reactive oxygen species(ROS) which can be found in fruits and vegetables[2]. Antioxidants protect cells against free radical damage which damages cells by preventing or delaying oxidative damage of lipids, proteins and nucleic acid caused by ROS[3]. Examples of antioxidant that protect against these diseases are beta-carotene, lutein, lycopene, vitamin A, vitamin C and vitamin E[4].

Polyphenols are the most lavish antioxidant in the diet of fruits and vegetables compared to other classes of phytochemicals due to their ability to neutralize free radicals. Besides that polyphenols also delay or strengthens many enzymes. Phenolic compounds such as flavonoids and caretonoids from fruits and vegetables has major health benefits such as anti-bacterial and anti-inflammatory actions. For an example, this antioxidant improve cell survival and as prooxidants induce apoptosis and prevent growth of tumor. However flavonoid, are phenolic substance that has the ability to reduce free radical formation. Flavonoids are also known to reduce chances of cardovascular diseases and to impede lipid peroxidation and platelet aggregation.

Extraction is defined as separation of active portions of plant from the inactive or inert components by using selective solvents in standard extraction methods. The extract obtained are commonly used as medicinal agents. Therefore it is important to stnadardize and optimize extraction procedures as it contributes tremendously to the final quality of the outcome [5]. The most commonly used extraction method is maceration, however, it is time consuming. Modern extraction methods have been developed to increases the efficiency of extraction of organic compound such as Ultrasonic Extraction and Soxhlet Extraction. The Ultrasonic Extraction is a modified maceration method facilitated by the use of ultrasound [6]. It increases the permeability of cell walls and produces cavitation [5]. The cellular breakdown increases the solubization of metabolites in the solvent and improves extraction yields.[6] Soxhlet Extraction is defined as a refluxing solvent repeatedly washes the solid extracting a desired compound into the flask [7]. It is a continuous process which can be extracted in a large amount with smaller quantity of solvent. It is economical in terms of time, energy and financially [5].

Other than that, parameters manipulated through the extraction methods are also important to standardize and optimize extraction procedures such as type of solvent used for extraction process. Alcoholic solvents are generally used to extract phenolics from natural sources because although they are not highly selective to phenols, they give a high yield of total extract. Mixtures of solvent and water is to be more competent in extracting phenolic constituents than the mono-component solvent system as it concerns its polarity. Research stated that antioxidant compound can be most effectively extracted in ethanol solvent [8]. Extraction time also plays a vital role in the optimization of extraction process. Extract increases with increasing time,

however, due to the exposure to unfavourable environment aspects like temperature, light and oxygen, extended extraction time increases the chance of decomposition and oxidation of phenolic compound [9]. Lastly, increase in temperature increases the effectiveness of extraction process as the temperature increases, the solvent viscosity decreases, an increase of solubility and diffusion coefficients of phenolics, also enhancing mass transfer and penetration of solvent into plant matrix. However an increases in temperature can also weaken the phenol-protein and phenol polysaccharide interaction in plant material resulting to decomposition of antioxidants [9].

Several studies has showed that Nutmegs (*Myristica Fragrans*) is associated with various health benefits. It has many applications in culinary, pharmaceutical and cosmetic industries. This fruit can be easily found in the islands near Indonesia, Malaysia, Caribbean and tropical areas of the world such as Southern India. These fully grown trees can reach about 50 to 60 feet in height and is the source of nutmeg and mace. Nutmeg is a delicate, slightly sweet spice which is used as spice and flvouring agent in the food industry. This fruit consist of four parts which are the skin, fruit, mace and seed. The fruit is a drupe which up on ripening splits-up to reveal ingle centrally situated oval shaped kernel known as nutmeg spice. The sed kernel enwrapped by crimson-red, lacy or thread like arils known as mace [10]. The nutmeg tree is also popularly known for its essential oils that are originated from the tree and leaves. These essential oils of nutmeg extract are very beneficial to health and are vastly used as alternative and herbal medicine.



Figure 1 Myristica Fragrans (Nutmeg)[12]

As mentioned above, nutmeg due to its nutritive content of vitamins, minerals and organic compounds has many health benefits. These benefits also includes dietary fibre, manganese, vitamin B6 etc. Nutmeg has a natural pain-relieving characteristics. It can reduce associated pain from wounds, injuries, strains and chronic inflammation such as arthritis. Other than that, according to research nutmeg stimulates the digestive

process by promoting peristaltic motion in the smooth muscle of intestine. It also reduces the discomfort of constipation and other intestinal issue as fiber content in nutmeg can bulk up the bowel movements. Nutmeg are very well known as the king of spicies when it came to oral heallth because it helps conditions such as halitosis, known as bad breath. This is due to the active antibacterial components of nutmeg kills the bacteria that causes this condition and boosts the immunity of gums and teeth. Among the health benefits attained by nutmeg is the potential use against cancerous cells. Research has shown that a methanolic compound in nutmeg and its essential oil can induce cell death in leukimia cells, which stops the spread of cancer. Lastly the mineral content of nutmeg is known to maintain organ function. Among them are potassium which relaxes blood vessels therefore reducing blood pressure and lowering cardiovascular diseases [11].

2. Research Methodology

2.1. Material and Method

2.1.1. *Fruit Material*

Nutmeg (*Myristica Fragrans*) was purchased from a fruit supplier in Penang, Malaysia. Nutmegs were washed with tap water followed by distilled water and then peeled. The fruits were cut into small pieces and the seed was disposed. Then the fruits were dried in a hot air oven at 60℃ for 36 hours. A mixer grinder was used to pulverize the fruit.

2.1.2 Chemicals

Ethanol, methanol, ethyl acetate,2,2-diphenyl picryl hydrazyl(DPPH), Folin Ciocalteau reagent, Sodium Carbonate, Gallic acid Aluminium Trichloride, Sodium nitrite, Sodium Hydroxide and Quercetin. All solvent were purchased from Syntertec Enterprise.

2.1.3 Apparatus

Waterbath, Soxhlet extractor, Ultrasonic cleaner, Centrifudger, UV-Vis Spectrophotometer, centrifudge tubes, beakers, measuring cylinder, Whatman No. 1 filter paper, Aluminium foil, Micropipettes.

2.1.4 Extraction

The two different extraction processes are investigated to obtain optimum extraction condition are ultrasonic extraction and Soxhlet extraction. Extraction condition are varied according to respective process. Solid to solvent ratio used is 1:20 for both extraction process.

2.1.5 Soxhlet Extraction

Grinded fruit were placed into the thimble. It is then filled with 150 ml of solvent. The soxhlet extractor is placed in a water bath. The variables varied for this process are extraction time which are 180, 210 and 240 minutes and type of solvent which are

methanol, ethanol and ethyl acetate. The temperature of waterbath is maintained at boiling point of each solvent for respective sample.

2.1.6 Ultrasonic Extraction

Grinded fruit were placed into beakers labelled with respective condition. Beaker is then filled with 150 ml of solvent. Ethanol is used as solvent for this extraction process. The beakers are then placed in the ultrasonic cleaner. The variables varied for this process are extraction time which are 40, 60 and 80 minutes, temperature of condition which were 30, 40 and 50 ℃ and solvent concentraion which are 40%, 50% and 60%. Frequency is maintained at 100% for optimum extraction of all samples. After extraction, the samples were centrifudged and filtered by Whatman No 1 filter paper to separate the supernatant from the residue.

2.2 Phytochemical content

2.2.1 Total phenolic Content

Determination of total phenolic content using the Folin Ciocalteau method [13]. 0.1 ml of sample after extraction process is added with 0.2ml Folin Ciocalteau reagent. The mixture is then added with 2 ml of distilled water. The mixture is left to rest for 3 minutes at room temperature. 1 ml of 20% sodium carbonate is added into mixture. The mixture is then left for an hour to be incubated at room temperature. The absorbance will be measured at 765 nm using a UV-Vis Spectrophotometer. Blank sample was prepared as explained above by replacing plant extract with distilled water. Gallic acid is used to produce a calibration curve. The results were expressed in term of milligrams of gallic acid per 100g dried weight (mg GAE/100 g DW) which was calculated using equation [13]:

Total phenolic content (mg GAE/100 g DW) = GAE x $\frac{V}{M}$ x 100
GAE = gallic acid equivalent (mg/ml) obtained from calibration curve
V = Volume of solvent used during the assay (ml)
M = Mass of plant used during the assay

Preparation of standard curve for total phenolic content

Different concentrations of gallic acid (0.2, 0.4, 0.6, 0.8 and 1.0 mg/ml) were prepared. 0.2 ml of FolinCiocalteu reagent is added to 0.1 ml of the gallic acid solution. 2 ml of distilled water is added to the mixture. Then, mixture is added with 1 ml of 20% sodium carbonate. The mixture is left to be incubated at room temperature for an hour. Using an UV-Vis Spectrophotometer the absorbance of the mixture was measured at 765 nm. Blank sample was prepared as explained above by replacing plant extract with distilled water. The standard calibration curve is plotted with absorbance values of gallic acid represented as y-axis and the concentration of the gallic acid represented as x-axis [13]. The callibrated equation obtained from standard curve is y = 1.0921x

2.2.2 Total Flavonoid content

Total flavonoid content was measured using the Ozsoy method [13]. 0.25 ml of plant extracts were mixed with 1.25 ml distilled water. The mixture is then added with 0.075 ml of 5% (w/v) of sodium nitrite solution. The mixture was incubated for 6 minutes at room temperature. Then the mixture is added with 0.15ml of 10% (w/v) aluminium chloride. 1M of sodium hydroxide (0.5 ml) was added to the mixture followed by 0.275 ml of distilled water. Using a UV-Vis Spectrophotometer the absorbance is be measured at 510 nm. Blank sample was prepared as explained above by replacing plant extract with distilled water. Quercetin is used to produce a calibration curve. The results were expressed in term of milligrams of Quercetin per 100g dried weight (QE mg /100 g DW) which was calculated using equation [13]:

Total phenolic content (mg QE/100 g DW) = QE x $\frac{V}{M}$ x 100

QE = Quercetin equivalent (mg/ml) obtained from calibration curve
V = Volume of solvent used during the assay (ml)
M = Mass of plant used during the assay

Preparation of standard curve for total flavonoid content

Quercetin with different concentrations (0.1, 0.3, 0.5 and 0.7 mg/ml) were prepared. 0.25 ml of Quercetin solution were mixed with 1.25 ml distilled water. The mixture is then added with 0.075 ml of 5% (w/v) of sodium nitrite solution. The mixture was incubated for 6 minutes at room temperature. Then the mixture is added with 0.15ml of 10% (w/v) aluminium chloride. 1M of sodium hydroxide (0.5 ml) was added to the mixture followed by 0.275 ml of distilled water. Using a UV-Vis Spectrophotometer the absorbance is be measured at 510 nm. Blank sample was prepared as explained above by replacing plant extract with distilled water. The standard calibration curve is plotted with absorbance values of Quercetin as y-axis and concentration of the Quercetin as x-axis[13]. The callibrated equation obtained from standard curve is y = 0.3709x

2.2.3 DPPH scavenging activity

DPPH Radical Scavenging activity of the extract will be determined using 2,2-diphenyl picryl hydrazyl(DPPH) assay [13]. 0.1 ml of plant extracts is added with 3.9 ml of ethanolic DPPH (0.025g/L). To block UV light the mixture is left in a dark condition in room temperature for 30 minutes. This reaction would distrupt the results of the experiment as UV light would trigger free radicals. Using a UV-Vis Spectrophotometer the absorbance is be measured at 517 nm. The colour of the sample will change from deep violet to light yellow[13].

DPPH scavenging activity(%) is calculated using the following formula:

$$\frac{Absorbance\ control - Absorbance\ sample}{Absorbance\ control}\ x\ 100$$

2.3 Statistical Analysis

Response surface methodology (RSM) was used to determine the optimal conditions of both Soxhlet and Ultrasonic Assisted extraction respectively. RSM was conducted using Design Expert Software (Version 10.0.3). A d-Optimal design was used to investigate the effects of two independent variables (Extraction time and Type of Solvent) for Soxhlet Extraction and three independent variables (Extraction time, Extraction temperature, and concentration of ethanol solvent) on the dependent variables (TPC, TFC, DDPH scavenging activity). A quadratic model was used to model the treatment effects and treatment interactions. The complete design using Soxhlet Extraction consisted of 14 experimental runs with 2 replications of the center point and Ultrasonic Assisted Extraction consisted of 17 experimental runs with 2 replications of the center point.

3 Results and Discussion

The results are shown from **Table 4.1** to **Table 4.6** and **Figure 4.1** to **Figure 4.8** it can be seen that sample from the Ultrasonic Assisted Extraction shows a higher Total Phenolic Content, Total Flavanoid Content when compared to the sample from the Soxhlet Extraction. DPPH scavenging Activity from the Ultrasonic Assisted Extraction is higher compared to Soxhlet Extraction. **Table 4.1** to **Figure 4.3 and Figure 4.1** to **Figure 4.4** shows the results of phytochemical content from Soxhlet Extraction, the effect of extraction time and the effect of solvent used for extraction. However **Table 4.4** to **Figure 4.6** and **Figure 4.5** to **Figure 4.8** shows the results of phytochemical content from Ultrasonic Assisted Extraction, the effect of temperture on extraction process , the effect of concentration of solvent used for extraction and the effect of time of extraction. Therefore, it is concluded that Ultrasonic Assisted Extraction yields higher values for Phytochemical content. This is due to the cavitation from the ultrasonic waves created in the water medium collapses near the beaker sending shock waves to the cell. The phenomena ruptures the cell wall of the fruit sample which releases the phytochemical content of cell more than fruit sample from Soxhlet Extraction. However, Soxhlet Extraction is less effective because cell wall which is mainly made of cellulose is tough to decompose as cellulose decomposes at 500℃. The temperature used during Soxhlet Extraction is not high enough to rupture the cell wall.

3.1 Soxhlet Extraction

Analysis of variance (ANOVA) procedure of the Design-Expert Software Version 10.0.3 was used to statistically analyze the means of triplicate experiments. ANOVA were used to determine the significance of the model and the interaction of the independent variables on the responses.

Table 4.1: Analysis of variance (ANOVA) for TPC of Soxhlet Extraction of Nutmegs.

Source	Sum of Squares	Degree of Freedom	Mean Square	*F*-value	*p*-value Prob>*F*
Model	136.85	6	22.81	2.23	0.1587
X_1	7.983E-003	1	7.983E-003	7.812E-004	0.9785
X_2	96.52	2	48.26	4.72	0.0491
X_1X_2	20.43	2	10.21	1.00	0.4151
X_1^2	3.86	1	3.86	0.38	0.5581
Residual	71.53	7	10.22		
Lack of Fit	66.96	5	13.39	5.85	0.1523
Pure Error	4.58	2	2.29		
Cor Total	208.38	13			

Table 4.2: Analysis of variance (ANOVA) for TFC of Soxhlet Extraction of Nutmegs.

Source	Sum of Squares	Degree of Freedom	Mean Square	*F*-value	*p*-value Prob>*F*
Model	651.38	6	108.56	4.31	0.0386
X_1	8.79	1	8.79	0.35	0.5733
X_2	573.30	2	286.65	11.37	0.0063
X_1X_2	18.04	2	9.02	0.36	0.7112
X_1^2	0.60	1	0.60	0.024	0.8815
Residual	176.40	7	25.20		
Lack of Fit	170.20	5	34.04	10.97	0.0856
Pure Error	6.21	2	3.10		
Cor Total	827.78	13			

Table 4.3: Analysis of variance (ANOVA) for DPPH scavenging activity of Soxhlet Extraction of Nutmegs.

Source	Sum of Squares	Degree of Freedom	Mean Square	*F*-value	*p*-value Prob>*F*
Model	72.73	6	12.12	2.42	0.1368
X_1	7.26	1	7.26	1.45	0.2680
X_2	33.70	2	16.85	3.36	0.0949
X_1X_2	19.28	2	9.64	1.92	0.2162
X_1^2	4.48	1	4.48	0.89	0.3763
Residual	35.12	7	5.02		
Lack of Fit	31.43	5	6.29	3.41	0.2423
Pure Error	3.69	2	1.84		
Cor Total	107.84	13			

The results for Soxhlet Extraction on Total Phenolic Content is p=0.1587 (p>0.05) proving that model does not affect the quantity of phytochemical content in extract. The p-values (Prob>*F*) of X_1 (Extraction time) and X_2 (Type of solvent) for TPC were 0.9785 and 0.0491 respectively. It is proven that the extraction time was not a huge influencing factor of TPC. However, type of solvent is proven to be an influence to the yield of TPC. As for Total Flavonoid Content is p=0.0386 (p<0.05) proving that model do effect the quantity of phytochemical content in extract [44]. The p-values (Prob>*F*) of X_1 (Extraction time) and X_2 (Type of solvent) for TFC were 0.5733 and 0.0063 respectively. It is proven that the extraction time was not a huge influencing

factor of TFC. However, type of solvent is proven to be a great influence to the yield of TFC. Lastly, for DPPH scavenging activity is p=0.1386 (p>0.05) thus concluding model does not affect the DPPH scavenging activity of fruit extract. The p-values (Prob>*F*) of X_1 (Extraction time) and X_2 (Type of solvent) for DPPH scavenging activity were 0.2680 and 0.00949 respectively. It is concluded that the extraction time and type of solvent were not a huge influencing factor of DPPH scavenging activity because of the high *p*-value (>0.05)

A mathematical equation was developed in **Equation 4.1, Equation 4.2 and Equation 4.3** to explain the effects of the two independent variables, which are Type of extraction solvent (X_1) and Extraction time (X_2) on the Total Phenolic Content (Y_1), Total Flavonoid Content(Y_2) and DPPH Scavenging activity(Y_3) of Soxhlet Extraction of Nutmegs respectively. The coefficients of regression equation were calculated using the Design Expert software.

$$Y_1=8.70-0.084X_1+3.64X_2-1.45X_2^2-2.21X_1X_2+0.60X_1X_2^2-1.25X_1^2 \quad \textbf{(Equation 4.1)}$$
$$Y_2=15.71-1.15X_1-1.04X_2-7.77X_2^2—1.84X_1X_2+1.78X_1X_2^2-0.49X_1^2 \quad \textbf{(Equation 4.2)}$$
$$Y_3=93.93-0.82X_1+2.18X_2-0.54X_2^2-1.83X_1X_2+1.89X_1X_2^2-1.35X_1^2 \quad \textbf{(Equation 4.3)}$$

Extraction condition of Soxhlet extraction was based on the TPC, TFC and DPPH Scavenging activity of the Nutmegs. The optimum values of the variables were obtain using **Equation 4.1, Equation 4.2 and Equation 4.3** obtained using Design Expert software. **Figure 4.1** shows the desirability developed from optimum points through numerical optimization. For the optimization value of TPC, TFC and DPPH Scavenging activity are 12.290 mg GAE/100g DW, 17.09 mg QE/100 g DW and 95.837% respectively with a desirability of 0.671. **Figure 4.2, Figure 4.3 and Figure 4.4** shows the effects interaction of the independent variables Time of Extraction and Type of Solvent on TPC, TFC and DPPH Scavenging Activity of Soxhlet Extraction of Nutmegs

From this research, it was shown that the optimum condition for Soxhlet extraction of Nutmegs to obtain optimum yield of TPC, TFC and DPPH Scavenging are by using Methanol as the extracting solvent at 184 min extraction time

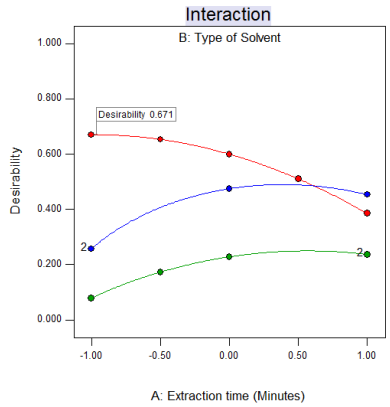


Figure 4.1 Desirability of Soxhlet Extraction Model

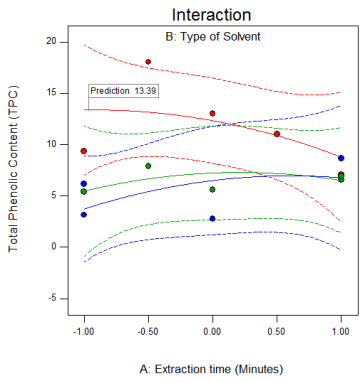


Figure 4.2 Effects of the interaction on TPC

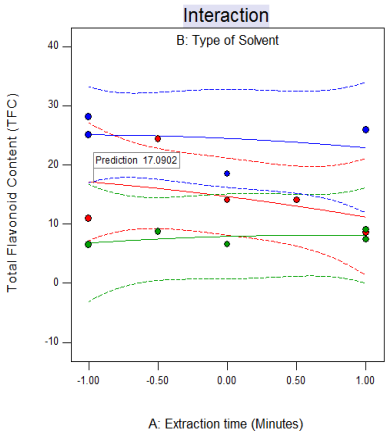


Figure 4.3 Effects of interaction on TFC

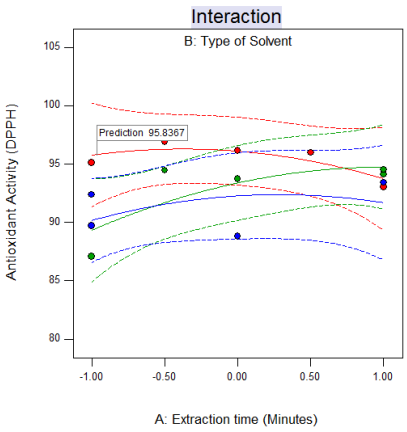


Figure 4.4 Effects of interaction on Scavenging activity

Effect of Type of Solvent on Soxhlet Extraction

Level 1- Methanol
Level 2- Ethanol
Level 3- Ethyl Acetate

3.2 Ultrasonic Assisted Extraction

Table 4.4: Analysis of variance (ANOVA) for TPC of Ultrasonic Assisted Extraction of Nutmegs.

Source	**Sum of Squares**	**Degree of Freedom**	**Mean Square**	***F*-value**	***p*-value Prob>*F***
Mode	506.04	9	56.23	5.41	0.0184
X_1	58.73	1	58.73	5.65	0.0491
X_2	253.35	1	253.35	24.37	0.0017
X_3	14.55	1	14.55	1.40	0.2754
$X_1 X_2$	89.76	1	89.76	8.64	0.0218
$X_1 X_3$	12.41	1	12.41	1.19	0.3107
$X_2 X_3$	34.43	1	34.43	3.31	0.1116
X_1^2	60.80	1	60.80	5.85	0.0462
X_2^2	8.13	1	8.13	0.78	0.4058
X_3^2	8.44	1	8.44	0.81	0.3974
Residual	72.76	7	10.39		
Lack of Fit	35.72	5	7.14	0.39	0.8311
Pure Error	37.04	2	18.52		
Cor Total	578.80	16			

Table 4.5: Analysis of variance (ANOVA) for TFC of Ultrasonic Assisted Extraction of Nutmegs.

Source	Sum of Squares	Degree of Freedom	Mean Square	*F*-value	*p*-value Prob>*F*
Model	1627.86	9	180.87	7.92	0.0062
X_1	164.06	1	164.06	7.18	0.0315
X_2	853.66	1	853.66	37.39	0.0005
X_3	107.50	1	107.50	4.71	0.0666
$X_1 X_2$	214.96	1	214.96	9.41	0.0181
$X_1 X_3$	35.86	1	35.86	1.57	0.2504
$X_2 X_3$	74.72	1	74.72	3.27	0.1134
X_1^2	273.18	1	273.18	11.96	0.0106
X_2^2	32.76	1	32.76	1.43	0.2700
X_3^2	28.49	1	28.49	1.25	0.3009
Residual	159.84	7	22.83		
Lack of Fit	89.80	5	17.96	0.51	0.7634
Pure Error	70.04	2	35.02		
Cor Total	1787.70	16			

Table 4.6: Analysis of variance (ANOVA) for DPPH scavenging activity of Ultrasonic Assisted Extraction of Nutmegs.

Source	Sum of Squares	Degree of Freedom	Mean Square	*F*-value	*p*-value Prob>*F*
Model	33.41	9	3.71	0.56	0.7941
X_1	0.28	1	0.28	0.042	0.8433
X_2	13.23	1	13.23	2.00	0.2004
X_3	4.46	1	4.46	0.67	0.4387
$X_1 X_2$	1.52	1	1.52	0.23	0.6468
$X_1 X_3$	7.396E-003	1	7.396×10^3	1.117×10^3	0.9743
$X_2 X_3$	0.72	1	0.72	0.11	0.7507
X_1^2	0.18	1	0.18	0.027	0.8747
X_2^2	1.98	1	1.98	0.30	0.6012
X_3^2	2.60	1	2.60	0.39	0.5510
Residual	46.34	7	6.62		
Lack of Fit	43.68	5	8.74	6.59	0.1371
Pure Error	2.65	2	1.33		
Cor Total	79.75	16			

The results for Ultrasonic Assisted Extraction on Total Phenolic Content is p=0.0184 (p<0.05) proving that model does affect the quantity of phytochemical content in extract. The p-values (Prob>*F*) of X_1 (Extraction time), X_2 (Extraction Temperature) and X_3 (Solvent Concentration) for TPC were 0.0491, 0.0017 and 0.2754 respectively. It is proven that the Solvent concentration was not a huge influencing factor of TPC. However, time and temperature of extraction were proven to be influences to the yield of TPC. As for Total Flavonoid Content is p=0.0062 (p<0.05) proving that model do effect the quantity of phytochemical content in extract. The p-values (Prob>*F*) of X_1 (Extraction time), X_2 (Extraction Temperature) and X_3 (Solvent Concentration) for TFC were 0.0315, 0.0005 and 0.0666 respectively. It is proven that the extraction time, Extraction temperature and Solvent concentration to be great influences to the yield of TFC. Lastly, for DPPH scavenging activity is p=0.7941

(p>0.05) thus concluding model does not affect the DPPH scavenging activity of fruit extract. The p-values (Prob>*F*) of X_1 (Extraction time), X_2 (Extraction Temperature) and X_3 (Solvent Concentration) for DPPH scavenging activity were 0.8433, 0.2004 and 0.4387 respectively. It is concluded that the extraction time, Extraction temperature and Solvent concentration were not huge influencing factors of DPPH scavenging activity because of the high *p*-value (>0.05)

A mathematical equation was developed in **Equation 4.4, Equation 4.5, Equation 4.6** to explain the effects of the two independent variables, which are Time of Extraction (X_1), Temperature of Extraction (X_2) and Concentration of Solvent of Extraction(X_3) on the Total Phenolic Content (Y_1), Total Flavonoid Content(Y_2) and DPPH Scavenging activity(Y_3) of Ultrasonic Assisted Extraction of Nutmegs. The coefficients of regression equation were calculated using the Design Expert software.

$$Y1=8.70-0.084X_1+3.64X_2-1.45X_2^2-2.21X_1X_2+0.60X_1X_2^2-1.25X_1^2 \quad \textbf{(Equation 4.4)}$$
$$Y2=15.71-1.15X_1-1.04X_2-7.77X_2^2—1.84X_1X_2+1.78X_1X_2^2-0.49X_1^2 \quad \textbf{(Equation 4.5)}$$
$$Y3=93.93-0.82X_1+2.18X_2-0.54X_2^2-1.83X_1X_2+1.89X_1X_2^2-1.35X_1^2 \quad \textbf{(Equation 4.6)}$$

Extraction condition of Ultrasonic Assisted extraction was based on the TPC,TFC and DPPH Scavenging activity of the Nutmegs. The optimum values of the variables were obtain using **Equation 4.4, Equation 4.5, Equation 4.6** obtained using Design Expert software. **Figure 4.5** shows the desirability developed from optimum points through numerical optimization. For the optimization value of TPC, TFC and DPPH Scavenging activity are 28.722 GAE/100g DW, 46.600 QE/100 g DW and 98.565% respectively with a desirability of 0.977. **Figure 4.6, Figure 4.7 and Figure 4.8** shows the effects of interaction of the independent variables Time of Extraction, Temperature of Extraction and Concentration of Ethanoic Solvent on TPC, TFC and DPPH Scavenging Activity of Ultrasonic Assisted Extraction of Nutmegs

From this research, it was shown that the optimum condition for Ultrasonic Assisted extraction of Nutmegs to obtain optimum yield of TPC, TFC and DPPH Scavenging are by extracting Nutmeg at 40.512 minutes at 49.99 ℃ and at 40% ethanol concentration.

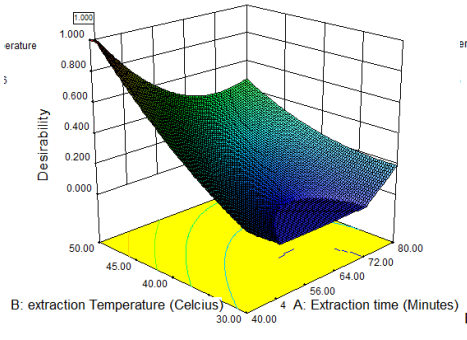


Figure 4.5 Desirability of Ultrasonic Extraction Model

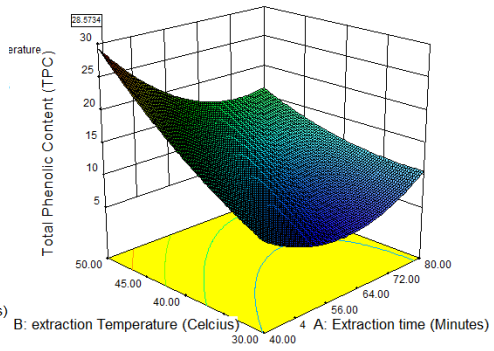


Figure 4.6 Effects of interaction on TPC

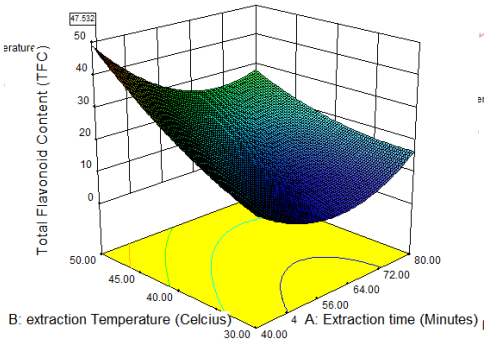


Figure 4.7 The effects of interaction on TFC

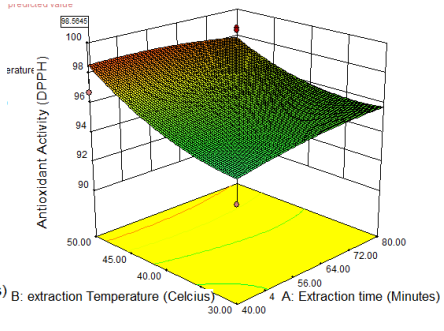


Figure 4.8 Effects of interaction on DPPH Scavenging Activity

4 Conclusion

The aim of this research is to calculate optimized values of extraction conditions for both Soxhlet and Ultrasonic Assisted Extraction to yield the highest Total Phenolic Content, Total Flavonoid Content and DPPH Scavenging Activity of Nutmegs using Response Surface Methodology (RSM). It is concluded that the optimum condition for Soxhlet extraction of Nutmegs to obtain optimum yield of TPC, TFC and DPPH Scavenging are by using Methanol as the extracting solvent at 184 min extraction time. However, the optimum condition for Ultrasonic Assisted extraction of Nutmegs to obtain optimum yield of TPC, TFC and DPPH Scavenging are by extracting nutmeg at 40.512 minutes at 49.99 ℃ and at 40% ethanol concentration. It is also concluded that Ultrasonic Assisted Extraction Process yields a consistent value of Total Phenolic Content, Total Flavonoid Content and DPPH Scavenging Activity of Nutmegs compared to Soxhlet Extraction Process. This is due to errors that were identified during conduct of experiment.

The finding from this study would be useful as the comparison is done for Nutmegs on two different method of extractions. The extraction conditions of both extraction process are also different. By using proper method of extraction and suitable extraction conditions, the pharmaceutical industry can maxime the extraction of the leaves thus increasing theTPC, TFC and subsequently increasing the scavenging ability of the nutmeg.

There are a few recommendation for the future work of this study. Extraction should be conducted in more closed environment to avoid the effect of surrounding on the extract. Parallax error should be avoided to improve significance of are of study. Equipment used for analysis should be calibrated for accuracy of experimental results. Lastly Experiment should be done consistently to maintain consistency of results.

References

[1]"Vegetables and Fruits – The Nutrition Source – Harvard T.H. Chan School of Public Health", *Hsph.harvard.edu*, 2016. [Online]. Available: http://www.hsph.harvard.edu/nutritionsource/what-should-you-eat/vegetables-and-fruits/. [Accessed: 25- May- 2016].

[2]A. Rohman, R. Sugeng and Y. Che Man, 'Characterizaton of red fruit (Pandanus conoideus Lam) oil', *International FOod Research Journal*, vol. 19, no. 2, pp. 563-567, 2012.

[3]L. Yan, L. Teng and T. Jhi, 'Antioxidant Properties of Guava Fruit: Comparison with some local Fruit', *Sunway Academic Journal*, vol. 3, pp. 9-20, 2006.

[4]N. DeVault, "High Antioxidant Fruits & Vegetables", *LIVESTRONG.COM*, 2014. [Online]. Available: http://www.livestrong.com/article/261278-high-antioxidant-fruits-vegetables/. [Accessed: 25- May- 2016].

[5]"Extraction Techniques of Medicinal Plants", 2016. [Online]. Available: http://agritech.tnau.ac.in/horticulture/extraction_techniques%20_medicinal_plants.pdf. [Accessed: 25- May- 2016].

[6]"Methods of extraction", *Fkog.uu.se*, 2016. [Online]. Available: http://www.fkog.uu.se/course/a/biolakt/biolakt-archive/BiolAkt%202010-2/StudentpresentationerHT2010%20(kopia)/BiolAktHT2010_ExtraktionNatProd_Yassir_Suzan/Extraction%20of%20natural%20products_files/Page470.htm. [Accessed: 25- May- 2016].

[7]"Soxhlet Extraction", *Chem-ilp.net*, 2016. [Online]. Available: http://www.chem-ilp.net/labTechniques/SoxhletExtraction.htm. [Accessed: 25- May- 2016].

[8]G. Spigno, L. Tramelli and D. De Faveri, 'Effects of extraction time, temperature and solvent on concentration and antioxidant activity of grape marc phenolics', *Journal of Food Engineering*, vol. 81, no. 1, pp. 200-208, 2007.

[9]T. M.C., T. C.P. and H. C.W, 'Effects of extraction solvent system, time and temperature on total phenolic content of henna (Lawsonia inermis) stems', *International Food Research Journal*, vol. 20, no. 6, pp. 3117-3123, 2013.

[10]U. Rudrappa, "Nutmeg nutrition facts, medicinal properties and health benefits", *Nutrition And You.com*, 2016. [Online]. Available: http://www.nutrition-and-you.com/nutmeg.html. [Accessed: 25- May- 2016].

[11]"Health Benefits of Nutmeg | Organic Facts", *Organic Facts*, 2013. [Online]. Available: http://www.organicfacts.net/health-benefits/herbs-and-spices/nutmeg.html. [Accessed: 25- May- 2016].

[12]"Nutmeg - The Epicentre", *The Epicentre*, 2016. [Online]. Available: http://theepicentre.com/spice/nutmeg/. [Accessed: 25- May- 2016].

[13]K. PUSHPANATHAN and R. NITHYANANDAM, 'Antioxidant Potential of Malaysian Medicinal Plant', *Journal of Engineering Science and Technology*, vol. 2014, no. 2015, pp. 138-150, 2015.

eureca 2016 – Conference Paper
Paper Number 2CE11

Reduction of Antibiotic by Fenton Oxidation Process

Hastheesudabye Puddoo*, Rajesh Nithyanandam

School of Engineering, Taylor's University, Taylor's Lakeside Campus
No. 1 Jalan Taylor's, 47500, Subang Jaya, Selangor DE, Malaysia

*hastheesudabye.Puddoo@sd.taylors.edu.my

Abstract
Fenton oxidation process is used to degrade the recalcitrant pharmaceutical product Ceftriaxone (CF), a commonly-used antibiotic in Malaysia. An artificial effluent having an initial Chemical oxygen demand (COD) and Total suspended solids (TSS) of 944 mg/L and 280 mg/L respectively is prepared to be treated. Physical and chemical treatment methods are employed to find the optimal concentration of Fenton reagent which is needed to degrade the antibiotic to a safe disposal level to the environment. Physical treatment include the variation of temperatures (37°C, 42°C, 47°C, 50°C) and pH variation (pH 2.6, pH 5.2, pH 6.1, pH 10). The molar concentration of Fenton reagent is varied as follows; 0.1M, 0.2M, 0.3M, 0.35M and 0.4M. The mole ratio of ferrous ions (Fe^{2+}) to hydrogen peroxide ions (H_2O_2) in Fenton reagent is varied as per order of 1:2, 1:4, 1:8 and 1:10. The optimum condition for maximum reduction in COD level is 0.4M of Fenton reagent at a Fe^{2+}/H_2O_2 ratio of 1:8, reaching a reduction percentage of 84.6% within 30 minutes of reaction. The experiment is carried out at ambient temperature of 28°C and at atmospheric pressure. Further investigation is made on the reduction percentage of the optimum sample by varying the pH and temperature of the sample to be treated. Findings reveal that maximum decrease in COD level occurs at 47°C and pH of 5.2. However, reduction percentage is 76.5 %. Total suspended solids investigations revealed that maximum reduction of 93% occurred at 0.4 M of Fenton reagent having the ratio of Fe^{2+}/H_2O_2 of 1:2. Furthermore, 8 intermediates were identified from the degradation products obtained in the LC/MS analysis carried out.

Keywords: Fenton process, Ceftriaxone antibiotic, Fe/hydrogen peroxide variation

1. Introduction

A large amount of antibiotic chemical is used as pharmaceutical products in the world reaching to an estimation of 100 000 to 200 000 tons per year [1]. The purpose of antibiotics is to treat diseases in human and also to promote growth in the agricultural industry [2]. Despite its vital importance in our daily life, antibiotics seem to raise

concern as a persistent water contaminant [3]. The occurrence of the antibiotic has been reported around the world in rivers in Europe [4,5], water surfaces in America [6,7], water streams in Australia [8] and rivers of Asia [9,10].

Antibiotics, once administered, are metabolised and excreted through urine and faeces which eventually reach sewage whereby water is treated. However, it was noticed that the antibiotic compounds were still present after treatment confirming its inability to degrade (recalcitrant) through conventional waste water treatment. Similarly, the effluent waste water from pharmaceutical manufacturing industries still contains antibiotic traces after treatment [11].

Since conventional waste water treatment does not fully remove recalcitrant pharmaceutics, an approach of additional advanced treatment technology is required. There are different advanced technologies which have been studied recently for the purpose of disintegrating non-biodegradable products. Those technologies are chemical oxidation using ozone and ozone/hydrogen peroxide [12,13], activated carbon as sorption processes [13,14] and membrane filtration such as nanofiltration and reverse osmosis [15]. The limitations of treating furthermore the concentrate from membrane filtration and sorption processes drives the interest towards further exploring and optimising chemical oxidation process. Below is a list of advanced chemical oxidation processes [12]:

1. Ozone/ Hydrogen peroxide, O_3/H_2O_2
2. Ozone/Ultraviolet, O_3/UV
3. Ozone/Hydrogen peroxide/Ultraviolet, O_3/ H_2O_2/UV
4. Hydrogen peroxide/Ultraviolet, H_2O_2/UV
5. Fenton, $Fe^{2+/}$ H_2O_2
6. Photo/electron Fenton
7. Chelating agent assisted Fenton/photo-Fenton
8. Heterogeneous photo-oxidation using titanium dioxide, TiO_2/hv
9. γ-radiolysis and sonolysis.

Advanced oxidant processes (AOPs) are based on the generation of free hydroxyl radicals ($^{\cdot}OH$). Free hydroxyl radicals are highly reactive due to their un-stability in configuration of energy shell and are non-selective oxidizing agents. The radicals are able to degrade organic pollutants by hydrogen atom abstraction reaction as shown in Eq (1), followed by electron transfer Eq (2) or electrophilic addition to π systems as shown in Eq (3).

$$\mathbf{RH} + {}^{\cdot}\mathbf{OH} \rightarrow \mathbf{R}^{\cdot} + \mathbf{H_2O} \quad \text{Eq (1)}$$

$$\mathbf{RX} + {}^{\cdot}\mathbf{OH} \rightarrow \mathbf{RX}^{\cdot} + \mathbf{OH}^{-} \quad \text{Eq (2)}$$

$$\mathbf{ArX} + {}^{\cdot}\mathbf{OH} \rightarrow \mathbf{OHArX}^{\cdot} \quad \text{Eq (3)}$$

Fenton reagent consists of ferrous ions and hydrogen peroxide. Different results are obtained by varying the molar ratio of ferrous to hydrogen peroxide in the Fenton reagent [16]. Other parameters such as pH and temperature also affects the process. An analytical way to compare results is to verify the Chemical Oxygen Demand (COD) level and Total Suspended Solids (TSS) level before the oxidation process and after the treatment.

Abbreviations

CF	Ceftriaxone
COD	Chemical Oxygen Demand
TSS	Total Suspended Solids
M	Molar
w/w	weight by weight
UV	Ultraviolet
H_2O_2	Hydrogen peroxide

To carry out research, an artificial effluent is produced. It was also found that few studies were carried out on the Fenton effect of oxidation on Ceftriaxone despite being commonly used in Malaysia. There is no literature on degradation of Ceftriaxone by Fenton process, nor any publication on the intermediates produced by AOP degradation of the antibiotic [24]. Therefore, Ceftriaxone is chosen to be studied to close this research gap. Contribution to knowledge includes the identification of intermdiates formed during degradation of Ceftriaxone by AOP.

Ceftriaxone, as shown in Fig 1., is an antibiotic used for bacterial infection such as pneumonia, ear infections and skin infection and is mostly used when organisms are resistant to other commonly used antibiotics such as amoxicillin and penicillin. Ceftriaxone is available in tablet form as well as solvent form for injection. The most common way to administer ceftriaxone into human beings is by injection; intravenous or intramuscular.

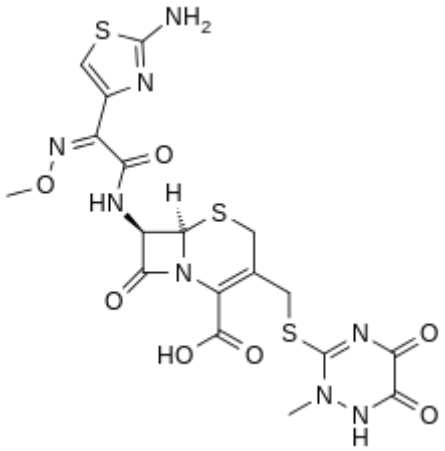


Figure 1. Skeletal structure of Ceftriaxone antibiotic.

The main objective of this research is to (1) find out the degradation efficiency of Ceftriaxone antibiotic using Fenton oxidation process by varying different concentrations and mole ratio of Fe^{2+}/H_2O_2 of Fenton reagent. Further investigation is made on that particular optimum ratio which has been found, (2) to study the effect of temperature and pH on the degradation in term of COD/TSS level reduction. Finally, (3) LC/MS technology is used to determine the degradation products obtained in the treated sample.

2. Materials and Methods

2.1 Chemicals and antibiotic

Ferrous sulphate heptahydrate ($FeSO_4.7H_2O$) and hydrogen peroxide (30% w/w) are purchased from SYSTERM, sulphuric acid 98% Grade AR and Sodium hydroxide pellets are purchased from SCHMIDT CHEMICAL, HPLC grade methanol (99.9%) is obtained from Merck, Ceftriaxone Sodium 1g was generously obtained from Kapar Klinik from Unocef.

2.2 Analytical methods

2.2.1 Physical and Chemical Treatment.

Chemical Oxygen Demand (COD, mg/L) is measured using Standard method 410 (Titrimetric, Mid-level) and digestion solution of dichromate. Concentrated sulphuric acid is used as a strong oxidizing agent. Ferrous Ammonium Sulphate solution is used as standard stock to titrate against the digested sample. The digestion solution and the treated sample are kept under closed reflux at 150ºC for 2 hours. Ferroin solution is used as indicator.

Total Suspended Solids (TSS, mg/L) is measured using Standard method 2540D. A glass microfiber filter grade GM F, 47mm is placed onto a vacuum filter set-up after oven drying for 2 hours at 105°C and weighed using analytical balance. The sample is filtered and washed with Milli-Q ultrapure water before drying into the oven at 105ºC for 2 hours. The filter paper is weighed again and TSS value can be calculated.

The pH of each sample is measured using an electronic pH meter with pH probe, Hanna GLP pH meter HI 111.

2.2.2 Qualitative Analysis

LC MS Q TOF is used to carry out the degradation analysis. The equipment is an Agilent Series Model G6550A. The sample is quenched with HPLC grade methanol. The quenched sample is then filtered through 0.45µm membranes. The analysis is carried out in negative ionisation mode, using HPLC(Agilent series 1100) equipped with a 3 X 150 mm C18 Column, 5 µm particle size (Zorbax). The mobile phases are acetonitrile and water with 0.1% formic acid at a flow rate of 0.4 mL per minute. The injection volume is 20 µL. A linear gradient progressed from 10% A to 100% A in 30 minutes.

2.3 Artificial Effluent

Ceftriaxone sodium is not purified further before use. 500mg of Ceftriaxone sodium is measured and diluted in 1000 ml of distilled water to prepare an artifial effluent concentration of 500mg/L. The room temperature and pH of solution is recorded immediately. The room temperature showed 28ºC and the artificial effluent has a pH of 5.9.The artificial effluent is kept refrigerated at 4ºC and in the dark to avoid any degradation.

2.4 Fenton Oxidation Experiment

2.4.1 Fenton Reagent Preparation

Fenton reagent is prepared by mixing an amount of ferrous sulphate to a volume of hydrogen peroxide and the mixture is further diluted to desired concentration with distilled water. Several Fenton reagent solutions are prepared where the mole concentration is varied (0.1M, 0.2M, 0.3M, 0.35M and 0.4M) and the mole ratio of Fe^{2+}/H_2O_2 of each concentration of Fenton reagent is varied (1:2, 1:4, 1:8, 1:10). The reaction is extremely exothermic and reactive. Foam is generated as the hydrogen concentration increases.

2.4.2 Fenton Oxidation Process

20 ml of synthetic effluent is poured into four 50ml beakers. The pH of the effluent is adjusted by adding a few drops of 0.05M of sulphuric acid (H_2SO_4). 10 ml of 0.1 M Fenton reagent with mole ratio of Fe^{2+}/H_2O_2 of 1:2, is pipetted into the antibiotic effluent. A stopwatch is started as the Fenton reagent comes into contact with the antibiotic. After 30 minutes of reaction, the sample is tested for COD (mg/L) level and TSS (mg/L). A blank (untreated) sample is kept and the COD (mg/L) and TSS (mg/L) is measured without any oxidation reagent and pH adjustment. A blank sample is needed to find the initial COD and TSS of the antibiotic.

2.5 Variation of pH and Temperature

100 ml of synthetic effluent is taken and the desired pH of 5 is adjusted by a few drops of diluted sulphuric acid (0.001M). 20 ml of the untreated sample is distributed into 4 different 50 ml beakers and heated up to 37°C, 42°C, 47°C and 50°C respectively using a hot plate magnetic stirrer for 45 minutes. 10 ml of the optimum molar concentration and mole ratio of ferrous to hydrogen peroxide Fenton reagent is quickly added to the sample to be treated. COD (mg/L) level is quickly tested for each sample. Similar procedure is repeated for pH 2.6, pH 6.1. to achieve a pH of 10.1, 0.05N solution of sodium hydroxide is prepared by dissolving the pellets into distilled water. After adjustment of pH, the treated samples which have been degraded at different temperatures are tested for COD (mg/L).

3. Results and Discussion

3.1 Chemical Oxygen Demand variation for different Molar ratio of Fenton reagent of Fe^{2+}/H_2O_2

The chemical treatment results for COD (mg/L) obtained from the treated artificial effluent are displayed in Fig 2 and Fig 3. The 5 different trends are separated into 2 charts in order to have a clear picture of the difference in their behaviour as the degradation process proceeds.

At 0.1 M of Fenton reagent, a gradual decrease in COD (mg/L) level is observed as the molar ratio of hydrogen peroxide increases. This indicates that a higher amount of hydrogen peroxide generates a higher number of hydroxyl radicals and thus, more carbon atoms may be oxidised. The percentage reduction of COD (mg/L) level varies from a maximum of 64.6% (displayed at a $Fe^{2}+/H_2O_2$ of 1:10) to a minimum of 56.9%

(displayed at Fe^{2+}/H_2O_2 of 1:2) within 30 minutes of degradation reaction. The efficiency of the oxidation process is not desirable because approximately 40% of the recalcitrant antibiotic i.e organic compound is still present in the treated sample. The organic compounds which did not degrade may be accounted by the overall insufficient supply of hydroxyl radicals [17].

At 0.2 M of Fenton reagent, degradation efficiency is higher than 0.1M with a maximum degradation 67.4% (displayed at Fe^{2+}/H_2O_2 ratio of 1:8). The minimum decrease in COD (mg/L) of 61.5% is observed at a ferrous to hydrogen peroxide ratio of 1:2. The degradation detention time was maintained to be 30 minutes. This implies that a higher concentration of Fenton reagent leads to a higher decrease in COD (mg/L) level of treated sample. The oxidation efficiency is not desirable as a significant amount of approximately 40% of recalcitrant products is still present in the treated sample and requires more time for degradation process. At Fe^{2+}/H_2O_2 of 1:10, the decrease in COD (mg/L) level is 63 % which is lower than the degradation efficiency observed at Fe^{2+}/H_2O_2 of 1:4 and 1:8. This slight increase in COD (mg/L) level is accounted by a phenomenon which happens when a sudden higher amount of hydroxyl radical is generated within a short period of time causing the diminution of dissolved oxygen [17].

At higher molar concentration of 0.3M of Fenton reagent, maximum reduction in COD (mg/L) is as high as 81.8%. 1:2 mole ratio of $Fe^{2+/}H_2O_2$ shows the lowest COD reduction of 65.7%, which is still more efficient than previous 0.1 M and 0.2M concentration of Fenton reagent. At Fe^{2+}/H_2O_2 of 1:10, the degradation reaction was less compared to all other samples. The excessive amount of hydrogen peroxide interferes in the experiment by reacting with •OH and hence, reducing the efficiency of the treatment [18]. Similar results are observed during Fenton reagent study on pharmaceutical sludge by

At 0.35M concentration of Fenton reagent, maximum COD (mg/L) level reduction of 73.7% is observed. 0.3M concentration shows lower efficiency than 0.3M concentration. This may be related to the reaction kinetics during the degradation process [19]. The minimum reduction is 31.4% at mole ratio of Fe^{2+}/H_2O_2 of 1:10.

The most efficient and promising efficiency occurs at 0.4M. All the samples showed high reduction within a range of 72% to 84% within 30 minutes of reaction. The highest peak of 84.6% is recorded at mole ratio of Fe^{2+}/H_2O_2 of 1:8. Since that particular sample shows the maximum percentage of reduction and hence, high efficiency, it is considered as the optimum Fe^{2+}/H_2O_2 ratio and conditions for degradation of the antibiotic Ceftriaxone. A pH of 2-3 is maintained and ambient temperature of 28ºC. It is observed that there is not much difference between the efficiency of 0.3M and 0.4M of Fenton reagent. A study showed that threshold values for optimisation of Fenton reaction are around pH 2-3 and mole ratio Fe^{2+}/H_2O_2 greater than 1:5, a reagent concentration of 0.3 and above [20].

The antibiotic may has high potential to reach mineralisation level if the hydroxyl radicals are allowed to react for longer period of time. Mineralisation is the complete degradation of the organic compound i,e water (H_2O) and carbon dioxide (CO_2). From the findings so far, it seems feasible to implement this oxidation process after secondary treatment in pharmaceutical industrial wastewater plants.

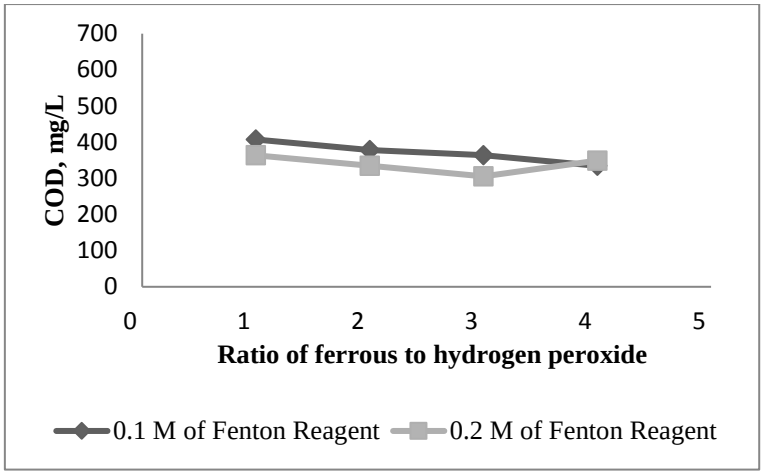


Figure 2. COD reduction for different variation in ratio of Fe^{2+}/H_2O_2 at molar ratio of 0.1M and 0.2M.

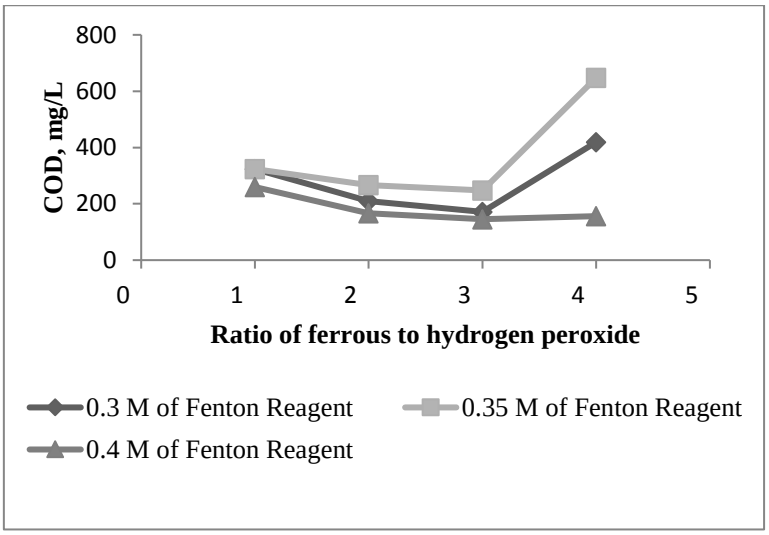


Figure 3. COD reduction for different variation in ratio of Fe^{2+}/H_2O_2 at molar ratio of 0.3M and 0.35M and 0.4M.

3.2 Total Suspended Solids variation for different Molar ratio of Fenton reagent of Fe^{2+}/H_2O_2.

The highest efficiency of Total Suspended Solids (TSS) is 93% at 0.4M of Fenton reagent and mole ratio of Fe^{2+}/H_2O_2 of 1:2. The lowest efficiency observed is only 16% at Fenton reagent concentration of 0.35M and mole ratio of Fe^{2+}/H_2O_2 of 1:8. Similar concentration of 0.35M did not prove to be efficient as shown by COD (mg/L) variation charts. The same reason might be because of the reaction kinetics. It can be seen that the mole ratio of Fe^{2+}/H_2O_2 directly affects the amount of TSS (mg/L) in the treated samples. The ratios which give the lowest TSS (mg/L) is at 1:2 and 1:8. The hydroxyl radical attack indicates that bonds do not break in an orderly manner but rather depending on concentration of radicals present during the reaction and the kinetic rate of each reaction.

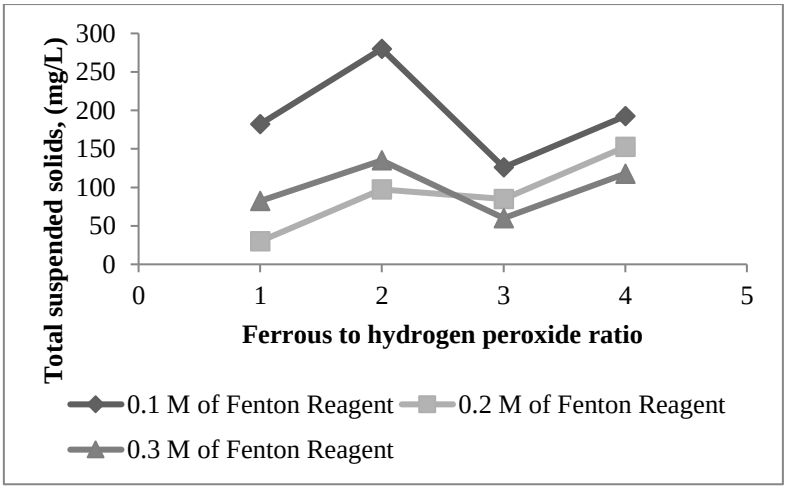


Figure 4. Total Suspended Solids variation different Molar ratio of Fenton reagent of Fe^{2+}/H_2O_2 at molar ratio of 0.1M, 0.2M and 0.3M

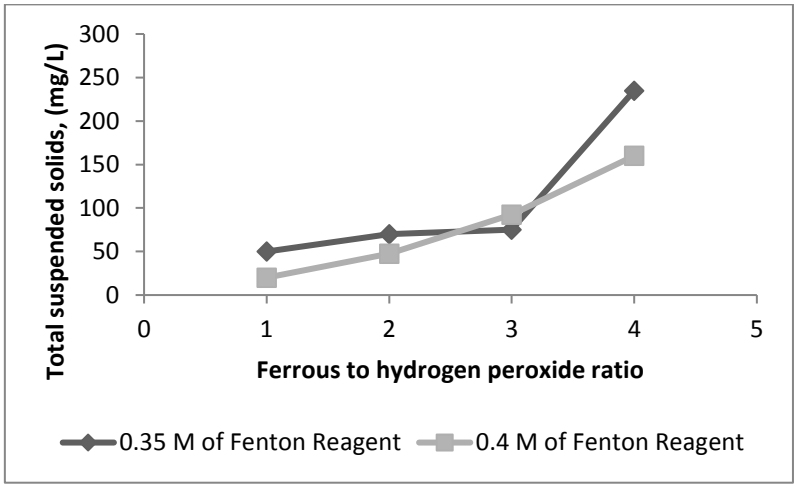


Figure 5. Total Suspended Solids variation different Molar ratio of Fenton reagent of Fe^{2+}/H_2O_2 at molar ratio of 0.35M and 0.4M

A high reduction is TSS level indicates that the organic compounds found in the antibiotic effluent have been reduced in terms of their molecular structures. As the radicals attack the bonds in between the carbon and hydrogen atoms, some carbon atoms are detached from the big molecular compound of the antibiotic to smaller functional groups like thiozale and carboxylic acid groups [21].

3.3 Chemical Oxygen Demand variation by varying pH and Temperature

From the above result, it can be deduced that the Fenton reagent works best within a pH of 2-3 as previously reviewed from many literature. Generation of hydroxyl radical depends largely on the pH value of the solution in which the radicals are generated. As the pH increases more than 4, lower number of radicals are formed and thus, degradation efficiency is reduced. Less radicals being formed may be due to the fact that there is a decrease in dissolved iron[17]. A decrease in dissolved iron causes the catalytic properties of the iron to decrease as well. Maximum reduction in COD was however recorded at pH 5.2 and temperature of 47°C. pH 6.1 shows that COD level can

be reduced furthermore compared to other pH values, however, an increase in temperature does not seem to affect the process significantly.

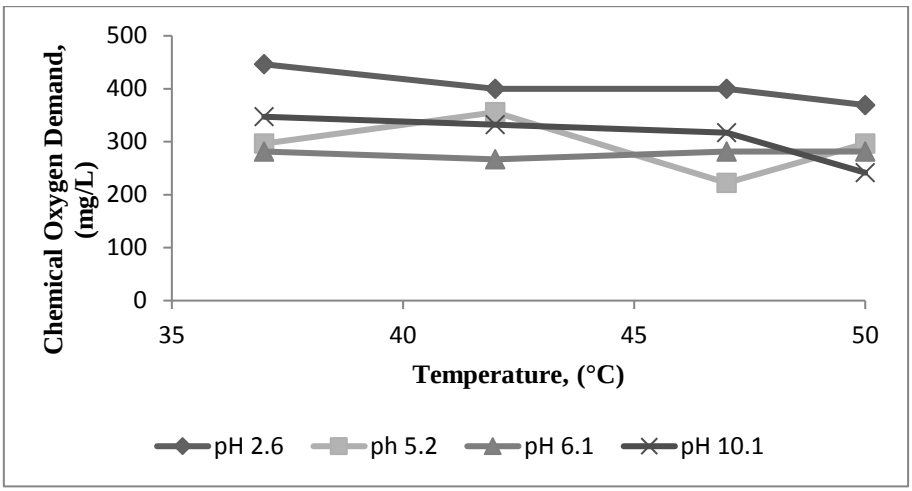


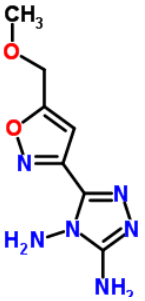
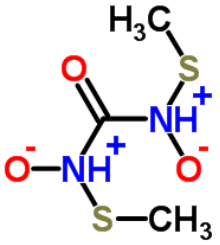
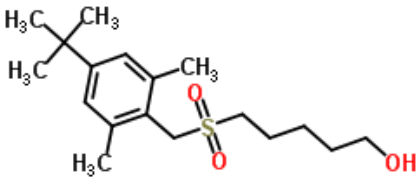
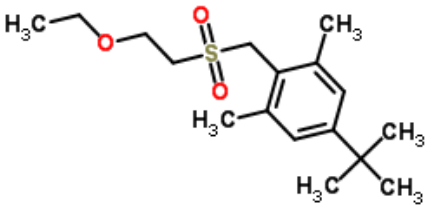
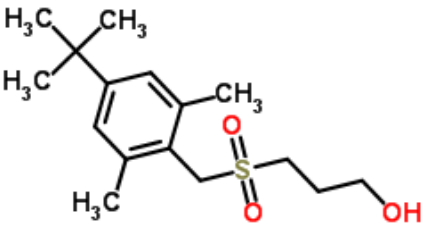
Figure 6. COD (mg/L) variation by varying the pH and Temperature (37ºC, 42ºC, 47ºC, 50ºC)

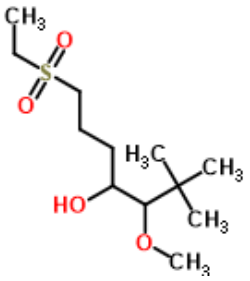
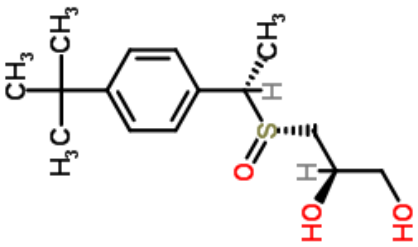
A considerate reduction in antibiotic component has been achieved. However, mineralisation of the ceftriaxone antibiotic results into water and carbon dioxide. Carbon dioxide is not a water pollutant but is a greenhouse gas. It is well-known that greenhouse gases are causing a major climate change. By solving the problem of antibiotics present in water streams, the method should not rise other issues for the environment. Further procedures should be employed such as carbon capture technologies for re-use of carbon dioxide more efficiently rather than just releasing in the air. Simple procedure such as passing the gas through calcium carbonate can be explored. The procedure also uses acidic conditions to operate. Neutralisation should be done after treatment by addition of alkali-based products such as sodium hydroxide. By using the Fenton reagent, some precipitation of Fe^{3+} will occur after 2 hours of treatment. The precipitation may be removed by the addition of sodium hydroxide which will result into Fe(OH) salt.

3.4 Identification of Degradation Product Intermediates.

The following table represents the 8 main compounds that have been identified from the 54 components detected from the chromatogram graph obtained in LC/MS Q TOF analysis.

Table 3.4 Identification of degradation products from LC/MS Q TOF analysis.

Molecular formula	Molecular Mass	Structural Formula	Name
$C_{11}H_{12}N_6O_4S_2$	356.381		5-Thiazolecarboxylic acid
$C_7H_{10}N_6O_2$	210.08		5-[5-(Methoxymethyl)-1,2-oxazol-3-yl]-4H-1,2,4-triazole-3(,4-diamine
$C_3H_8N_2O_3S_2$	183.99		Methanone, bis[(methylthio)oxidoamino]
$C_{18}H_{30}O_3S$	326.494		5-{[2,6-Dimethyl-4-(2-methyl-2-propanyl)benzyl]sulfonyl}-1-pentanol
$C_{17}H_{28}O_3S$	312.46		Benzene, 5-(1,1-dimethylethyl)-2-[[(2-ethoxyethyl)sulfonyl]methyl]-1,3-dimethyl
$C_{16}H_{26}O_3S$	298.44		3-{[2,6-Dimethyl-4-(2-methyl-2-propanyl)benzyl]sulfonyl}-1-propanol

$C_{12}H_{26}O_4S$	266.39		4-Heptanol, 1-(ethylsulfonyl)-5-methoxy-6,6-dimethyl-(
$C_{15}H_{24}O_3S$	284.14		2R)-3-[(S)-{(1S)-1-[4-(2-Methyl-2-propanyl)phenyl]ethyl}sulfinyl]-1,2-propanediol

The degradation of cephalosporins is highly dependent on the side chain C7 and the C3 atoms. the leaving group at C3 facilitates the expulsion of 3'-substituent by concerted event due to hydrolysis of C-N bond of b-lactam nucleus. As it can be seen from Table 4.2, there has no beta-lactam ring present even in the highest carbon containing molecule C18 identified (5-{[2,6-Dimethyl-4-(2-methyl-2-propanyl)benzyl]sulfonyl}-1-pentanol) at peak mass of 326 and C17 molecule (identified as Benzene, 5-(1,1-dimethylethyl)-2-[[(2-ethoxyethyl)sulfonyl]methyl]-1,3-dimethyl) giving clue that the beta-lactam ring got attacked in the first stages of degradation. Normally, authors point out that, hydroxylation takes places first at early stage of degradation [22].

The 3rd generation cephalosporin is isomerized to its 2nd generation isomer, leads the antibiotic material to be more stable. The authors suggested that chemical degradation of Cephalosporin leads to 7ACA and further degradation leads to thiazole-4-carboxylic acid. The presence of the thiazole-carboxyl group is present in the first intermediate found, leading to conclude that the hypothesis is valid.

Further degradation is observed in intermediates following the 5-thizole carboxylic acid with elimination of side methyl groups as it can be seen in the C7 molecule 5-[5-(Methoxymethyl)-1,2-oxazol-3-yl]-4H-1,2,4-triazole-3(,4-diamine. The role of iron as catalyst acts in such a way that mercaptide group is formed. This is confirmed in the C11, C3 and C15 intermediate. There is the presence of the sulphur atom rendering the component mercaptide. [22].

It is quite hard to assign the exact location of substitute or leaving functional groups of the complex parent molecule simply by looking at the molecules. The LC/MS analysis is not able to provide such information. A further study on bond-forming and bond-breaking has to be made to be more accurate in concluding. However, Trovo et al. used similar methods to degrade similar forms of antibiotic suggests that, there is approximately 3 degradation pathways which can be determined.

From the parent molecule, Trovo et al. also suggest that hydroxylation occurs first and results to thiazolidine ring (confirmed by C11 intermediate). Later, the next attack is most probable on electrophilic nature i.e benzoic ring as shown in C16, C17 and C18 intermediate. There is opening of the benzoic ring from C16 intermediate to C12 intermediate. While another pathway suggest the side methyl groups can gradually be eliminated as shown from C17 to C15 intermediate. [23]

Another pathway that Trovo et al suggest is the direct opening of the lactam ring to stereo isomers of penoilloic acid and a series of derivatives (C7, C18, C16). Further decarboxylation is the removal of carboxylic functional group. This is shown through the intermediates C7, C3 and C12. Decarboxylation is produced by hydrolysis. [18].

4. Conclusions

The antibiotic Ceftriaxone has been successfully degraded by 84.6% within 30 minutes of degradation. The total suspended solids level has reduced by 93% after the Fenton treatment. It can be concluded that parameters such as pH and temperature affects the degradation process. The optimum operating conditions at ambient temperature are reflected at pH 2.6, Fenton reagent concentration of 0.4 M and Fe^{2+}/H_2O_2 mole ratio of 1:8. From the identified degradation products, Ceftriaxone complex C_{18}-molecular structure has been reduced till C_3-molecular structure. Further treatment includes neutralisation of treated sample by use of sodium hydroxide and application of carbon capture methods to reduce the emission of Carbon dioxide gas.

References

[1] K. Kummerer. (2003). "Significance of antibiotics in the environment", *Journal of Antimicrobial Chemotherapy*, vol. 52, no. 1, pp. 5-7.

[2] A. Hollis and Z. Ahmed. (2013). "Preserving Antibiotics, Rationally", *New England Journal of Medicine*, vol. 369, no. 26, pp. 2474-2476.

[3] M. Bailón-Pérez, A. García-Campaña, C. Cruces-Blanco and M. del Olmo Iruela. (2008). "Trace determination of β-lactam antibiotics in environmental aqueous samples using off-line and on-line preconcentration in capillary electrophoresis", *Journal of Chromatography A*, vol. 1185, no. 2, pp. 273-280.

[4] Q. Tuc Dinh, F. Alliot, E. Moreau-Guigon, J. Eurin, M. Chevreuil and P. Labadie. (2011). "Measurement of trace levels of antibiotics in river water using on-line enrichment and triple-quadrupole LC–MS/MS", *Talanta*, vol. 85, no. 3, pp. 1238-1245.

[5] M. Al Aukidy, P. Verlicchi, A. Jelic, M. Petrovic and D. Barcelò. (2012). "Monitoring release of pharmaceutical compounds: Occurrence and environmental risk assessment of two WWTP effluents and their receiving bodies in the Po Valley, Italy", Science of The Total Environment, vol. 438, pp. 15-25.

[6] Cha, S. Yang and K. Carlson. (2006)."Trace determination of β-lactam antibiotics in surface water and urban wastewater using liquid chromatography combined with electrospray tandem mass spectrometry", *Journal of Chromatography A*, vol. 1115, no. 1-2, pp. 46-57.

[7] C. Wang, H. Shi, C. Adams, S. Gamagedara, I. Stayton, T. Timmons and Y. Ma. (2011). "Investigation of pharmaceuticals in Missouri natural and drinking water

using high performance liquid chromatography-tandem mass spectrometry", *Water Research*, vol. 45, no. 4, pp. 1818-1828.

[8] A. Watkinson, E. Murby, D. Kolpin and S. Costanzo. (2009). "The occurrence of antibiotics in an urban watershed: From wastewater to drinking water", *Science of The Total Environment*, vol. 407, no. 8, pp. 2711-2723.

[9] S. Zou, W. Xu, R. Zhang, J. Tang, Y. Chen and G. Zhang. (2011). "Occurrence and distribution of antibiotics in coastal water of the Bohai Bay, China: Impacts of river discharge and aquaculture activities",*Environmental Pollution*, vol. 159, no. 10, pp. 2913-2920.

[10] A. Shimizu, H. Takada, T. Koike, A. Takeshita, M. Saha, Rinawati, N. Nakada, A. Murata, T. Suzuki, S. Suzuki, N. Chiem, B. Tuyen, P. Viet, M. Siringan, C. Kwan, M. Zakaria and A. Reungsang. (2013). "Ubiquitous occurrence of sulfonamides in tropical Asian waters", *Science of The Total Environment*, vol. 452-453, pp. 108-115.

[11] B. Halling-Sørensen, S. Nors Nielsen, P. Lanzky, F. Ingerslev, H. Holten Lützhøft and S. Jørgensen. (1998). "Occurrence, fate and effects of pharmaceutical substances in the environment- A review",Chemosphere, vol. 36, no. 2, pp. 357-393.

[12] C. Zwiener. (2000). "Oxidative treatment of pharmaceuticals in water", Water Research, vol. 34, no. 6, pp. 1881-1885.

[13] T. Ternes, M. Meisenheimer, D. McDowell, F. Sacher, H. Brauch, B. Haist-Gulde, G. Preuss, U. Wilme and N. Zulei-Seibert. (2002). "Removal of Pharmaceuticals during Drinking Water Treatment",*Environmental Science & Technology*, vol. 36, no. 17, pp. 3855-3863.

[14] C. Hartig, M. Ernst and M. Jekel. (2001). "Membrane filtration of two sulphonamides in tertiary effluents and subsequent adsorption on activated carbon", *Water Research*, vol. 35, no. 16, pp. 3998-4003.

[15] M. Petrovic. (2003)."Analysis and removal of emerging contaminants in wastewater and drinking water", *TrAC Trends in Analytical Chemistry*, vol. 22, no. 10, pp. 685-696.

[16] I. Arslan-Alaton and F. Gurses. (2004). "Photo-Fenton-like and photo-fenton-like oxidation of Procaine Penicillin G formulation effluent", *Journal of Photochemistry and Photobiology A: Chemistry*, vol. 165, no. 1-3, pp. 165-175.

[17] R. Nithyanandam and R. Saravanane. (2013). "Treatment of Pharmaceutical Sludge by Fenton Oxidation Process", *International Journal of Chemical Engineering and Applications*, pp. 359-364.

[18] D. Moon, T. Maruyama, K. Osakada and T. Yamamoto. (1991). "Chemical Oxidation of Polyaniline by Radical Generating Reagents, O2, H2O2-FeCl3 Catalyst, and Dibenzoyl Peroxide.", *Chem. Lett.*, no. 9, pp. 1633-1636.

[19] A. Giri and A. Golder. (2014)"Ciprofloxacin degradation from aqueous solution by Fenton oxidation: reaction kinetics and degradation mechanisms", *RSC Advances*, vol. 4, no. 13, p. 6738.

[20] C. Zanta and C. Martínez-Huitle. (2009). "Degradation of 2-hydroxybenzoic acid by advanced oxidation processes", *Brazilian Journal of Chemical Engineering*, vol. 26, no. 3, pp. 503-513.

[21] M. Su, H. Sun, Y. Zhao, A. Lu, X. Cao and J. Wang. (2016). "Degradation Kinetics and Mechanism of a β-Lactam Antibiotic Intermediate, 6-Aminopenicillanic Acid, in a New Integrated Production Process", *Journal of Pharmaceutical Sciences*, vol. 105, no. 1, pp. 139-146.

[22] A. Deshpande, K. Baheti and N. Chatterjee.(2004). "Degradation of beta-lactam antibiotics", *Current Science*, vol. 87, no. 12, p. 16841695.

[23] A. Trovó, R. Pupo Nogueira, A. Agüera, A. Fernandez-Alba and S. Malato. (2011). "Degradation of the antibiotic amoxicillin by photo-Fenton process – Chemical and toxicological assessment", *Water Research*, vol. 45, no. 3, pp. 1394-1402.

[24] G. Quand-Meme, A. Thiery Auguste, L. Marie Hélène, B. Mohamed, S. Placide, I. Sanogo and , Ouattara. (2016). "Electrooxidation of Ceftriaxone in Its Commercial Formulation on Boron Doped Diamond Anode", *Journal of Advanced Electrochemistry*, vol. 2, no. 2, pp. 85-88.

eureca 2016 – Conference Paper
Paper Number 2CE12

Creatinine adsorption by activated carbon fibre (ACF) derived from empty fruit bunch (EFB) fibre

Ivan V.K. Chai[1*], Ting Lee[1], Xiao Yien Lim[1]

[1]*School of Engineering, Taylor's University, Malaysia*

[*] ivanchaivoonkian@sd.taylors.edu.my

Abstract

Adsorption is an important process in the haemodialysis treatment to treat patients with kidney failure. Adsorption membranes in haemodialysis systems are usually made of synthetic polymers but these membranes do not have high efficiency in removing uremic toxins such as urea, uric acid and creatinine. Thus, it is suggested to replace the current membranes with a new material that has high adsorption capability as well as being lightweight and low cost. This study suggests that activated carbon may be a potential replacement of current haemodialysis membranes as they are widely used in various adsorption applications. Activated carbon fibre (ACF) is chosen due to their better adsorptive characteristics compared to granular and powder activated carbon. Empty fruit bunch (EFB) fibre is chosen to produce ACF because it is easily available in abundance throughout the year and has low commercial value. Currently, there is not much information available on creatinine adsorption using ACF derived from EFB fibre. However, research on urea adsorption using ACF has been done by Ooi and co-workers and the data obtained is compared with creatinine adsorption. Cleaned EFB fibre is impregnated with 4 different chemicals; sodium hydroxide (NaOH), potassium hydroxide (KOH), sulphuric acid (H_2SO_4) and phosphoric acid (H_3PO_4) at an acid/alkali to fibre ratio of 3:4 (ml:g) in the pathway of producing ACF. The effects of these chemical treatments on the pore characteristics and physiochemical properties are studied. ACF samples are produced via pre-carbonisation chemical treatment followed up by carbonisation at 400 °C and activation at 900 °C. Samples produced in this work are of Type I isotherm which indicates the presence of micro and mesoporous structure. The sample treated with H_3PO_4 has the highest BET surface area of 1493 m^2/g and pore volume of 0.782 cm^3/g compared to other samples. Carbon burn-off of ACF sample treated with H_3PO_4 proved to be 86% which is the highest among all samples despite having the best adsorbing capability. This work has shown that ACF treated with H_3PO_4 has the potential in replacing the current membrane used in the current haemodialysis system with creatinine removal of 70% and urea removal of 68% which is higher than the conventional haemodialysis membrane.

Keywords: Creatinine, Adsorption, Activated carbon fibre, Empty fruit bunch fibre

1. Introduction

Kidney failure is a syndrome where the kidneys could not fulfil their tasks in filtering blood. This kind of syndrome leads to an accumulation of molecules; called uremic toxins which are normally eliminated by healthy kidneys. People that have kidney failure is unable to separate these uremic toxins such as urea, uric acid and creatinine and has to be treated by the haemodialysis technique [1]. The haemodialysis process is where two liquids are separated by a semi-permeable membrane that enables an exchange of molecules small enough to diffuse through the pores. When blood is in contact with one of the sides of the semi-permeable membrane, substances such as body waste and inorganic salts pass through into a sterile solution called the dialysate. However, this method of treatment is not efficient as patients have to go through the treatment 3 to 4 times a week where each session lasts up to 4 hours [2].

Research and development towards the improvement of the haemodialysis system has been done throughout the years. The invention of hollow fibre dialysers have helped in increasing the efficiency in uremic toxin removal as well as new discovery of different materials to help in uremic toxin removal. However, the efficiency is not high and the haemodialysis machine is rather not portable. Artificial kidney is one of the methods suggested by Hakim and Lumley to increase the functionality of the body to remove uremic toxins [3]. The vision of this artificial kidney is to be able to remove uremic toxins efficiently, light weight and low cost. This may be solved if the membrane of the haemodialysis treatment in removing uremic toxins is upgraded to a more effective and low cost adsorbent [4].

Activated carbon may be the solution to this as the usage of activated carbon can be seen in wastewater treatment and air purification applications due to the high effectiveness in adsorption [5]. Activated carbon is defined as a solid and porous carbonaceous material with high porosity and large surface area [6]. Activated carbon can found in 3 forms; powdered, granular and fibre [7]. Among these 3 forms, activated carbon fibre (ACF) has the highest adsorbing capability. There are many materials that can be made into activated carbon such as tea and coffee waste, peanut shells and wheat wastes which are of low cost materials [8].

This study has chosen empty fruit bunch (EFB) fibre to produce ACF as it is an agricultural waste generated from the oil palm industry, which is available in abundance throughout the year and has very low commercial value. It is naturally in a fibrous shape which makes it suitable to be made into ACF. ACF has a higher commercial value compared to other activated carbon types due to its higher adsorptive characteristics [9].

ACF or common activated carbons can be produced by involving a 2-step process; carbonisation and activation. Carbonisation can be done using combustion or pyrolysis [10]. The purpose of the carbonisation step is to remove any volatile compounds in the EFB fibre which will give rise to the number of pores in the fibre which is responsible for its adsorptive characteristics. Carbonisation is typically done at 400-600 °C. However, carbonisation done at an elevated temperature not only increases the carbon content but the ash content as well. This is due to greater decomposition of biomass at higher temperatures [11]. Comparison between combustion and pyrolysis was done and it showed that carbon content in biomass

samples decreases at 400 °C and samples undergone pyrolysis has more carbon content compared to samples undergone combustion [7]. The activation step is to increase the pore diameter and volume to enhance the porosity of the activated carbon. It can be separated into chemical activation and physical activation. Chemical activation involves the impregnation of the precursor of the activated carbon with chemical activating agents. The commonly used activating agents are sodium hydroxide (NaOH), potassium hydroxide (KOH), sulphuric acid (H_2SO_4) and phosphoric acid (H_3PO_4) [11–14]. Physical activation is commonly done by heating the carbon at a range of 800 to 1000 °C [10]. Physical activation requires the carbon sample to be carbonised in an inert atmosphere and subsequent activation is done with oxidising gases such as carbon dioxide (CO_2), steam or air. In this work, carbonisation is done at 400 °C and activation at 900 °C as these conditions are the optimum conditions in synthesis of ACF according to the work of Ooi and co-workers [7].

This study work focuses on the comparison between different chemical-treated EFB fibres in their ability in adsorbing creatinine as a possible method to apply these material into the current haemodialysis treatment. The performance of the EFB fibre derived ACF in adsorbing creatinine is evaluated based on the composition and pore characteristics of each different chemical-treated EFB fibre derived ACF. The adsorbing performance of the ACF samples produced is also compared between creatinine adsorption and urea adsorption.

2. Methodology

2.1 Materials

EFB fibre is collected from United Palm Oil Mill Sdn. Bhd. Nibong Tebal, Penang, Malaysia to be used as raw material. The EFB fibre is then cleaned with 5% nitric acid (HNO_3) and rinsed with distilled water until the pH reaches approximately 5. The cleaned EFB fibre is then dried in an oven overnight at 105 °C which is in accordance to the ASTM D2867-09 standard for moisture removal [16]. Sodium hydroxide (NaOH), potassium hydroxide (KOH), sulphuric acid (H_2SO_4) and phosphoric acid (H_3PO_4) are used as activating agents.

2.2 Sample Preparation

4 sets of 12 g of cleaned EFB fibre is impregnated with concentrated NaOH, KOH, H_2SO_4 and H_3PO_4 (85 %) at an acid/alkali-to-fibre ratio of 3:4 (ml:g). An oxygen deficient atmosphere during pyrolysis is created by allowing a flow of nitrogen (N_2) gas at a flow rate of 100 ml per minute. The samples are then pyrolysed separately at 400 °C for 1 hour at a heating rate of 10 °C per minute. After pyrolysis, the samples are then left to cool to room temperature. The char after pyrolysis is then weighed prior to the activation step. The furnace temperature during the activation process is set at 900 °C at a heating rate of 10 °C per minute and the flow of N_2 gas is set at 100 ml per minute. At 900 °C, the flow of N_2 gas is stopped and changed to CO_2 gas at a flow rate of 100 ml per minute for 1 hour. After 1 hour, the flow of CO_2 gas is stopped and changed back to N_2 gas at a flow rate of 100 ml per minute. The sample is then cooled down to room temperature in the N_2 gas flow [9]. After activation, weight of each

sample is measure and recorded again for the carbon burn-off analysis. Each sample is assign with sample codes as tabulated in Table 1.

Table 1. Samples identification

Sample Code	Remarks
ACF_PA	EFB fibre derived ACF treated with H_3PO_4 (85%)
ACF_SA	EFB fibre derived ACF treated with H_2SO_4 (85%)
ACF_PH	EFB fibre derived ACF treated with KOH (85%)
ACF_SH	EFB fibre derived ACF treated with NaOH (85%)

2.3 Sample Characterisation

By using the data of the weight measure before carbonisation, after carbonisation and after activation, the carbon burn-off, Θ (%) for the ACF can be calculated using the formula below:

$$\Theta = \frac{(w_0 - w)}{w_0} X\ 100\% \quad (1)$$

Where, w_o is the initial weight of the raw EFB fibre (g) and w is the final weight of the ACF (g). Nitrogen adsorption isotherm at 77 K is done using Micromeritics Instrument system after a gas pre-treatment at 300 °C for 5 hours. Pore characteristics such as surface area, micropore volume and pore size distribution are determined from the nitrogen adsorption isotherms utilising Branauer-Emmett-Teller (BET) model. Nitrogen adsorption on the samples are carried out from relative pressure (P/P_o) of 0.01 to 0.99 [17]. The crystalline structure of the produced ACF is determined using the X-Ray Diffraction (XRD) analysis which included a scan range of 10° to 90° with a step size of 0.02° and step time of 0.05 seconds. The surface chemistry of the produced ACF samples is determined using the Fourier Transform Infrared Spectroscopy (FTIR) at a wavenumber ranging from 650 to 4000 cm^{-1} for 16 cycles.

2.4 Creatinine Adsorption Test

A creatinine solution with a concentration of 2 mg/dL is prepared to simulate the minimum concentration of creatinine concentration in the blood before undergoing haemodialysis [18]. A standard calibration curve was developed by measuring the UV-Vis absorbance intensity of a series of creatinine solutions with known concentration using the UV-Vis spectrophotometer at a wavelength of 510 nm [19]. Creatinine adsorption is conducted for all ACF samples and the intensities of the creatinine samples at various time intervals are measured using the UV-Vis spectrophotometer. The intensities of the solution are then compared with the calibration curve to determine the adsorption amount by each ACF sample.

2.5 Urea Adsorption Test

A urea solution with a concentration of 120 mg/dL is prepared to simulate the average concentration of urea concentration in the blood of patients before undergoing haemodialysis [20]. A standard calibration curve was developed by measuring the UV-Vis absorbance intensity of a series of urea solutions with known concentration using the UV-Vis spectrophotometer at a wavelength of 200 nm [7]. Urea adsorption is conducted for all ACF samples and the intensities of the urea samples at various time

intervals are measured using the UV-Vis spectrophotometer. The intensities of the solution are then compared with the calibration curve to determine the adsorption amount by each ACF sample.

3. Results and Discussion

3.1 Carbon Burn-Off

Carbon burn-off is a commonly used guideline to determine the yield of activated carbon. The higher the carbon burn-off, the lower the yield percentage [21]. Burn-off means the degree of carbon loss during the production of activated carbon. A higher carbon burn-off also means that there is a need to use more materials to produce the desired activated carbon which will lead to increase in cost for production. The carbon burn-off results shown in Table 2 proves the quality of the ACF produced in this work.

All samples were pre-treated with different chemicals (NaOH, KOH, H_2SO_4 and H_3PO_4). As an overall, the carbon burn-off for the sample ACF_PA is highest among all the samples produced. Addition of H_3PO_4 into the raw fibre samples may have facilitated in the conversion of aliphatic compounds, such as cellulose and hemicellulose to aromatic compounds [22]. The higher percentage in the overall carbon burn-off may also mean that more volatile compounds are removed due to the H_3PO_4 treatment. As compared to the ACF_SA sample, ACF_SA has a higher carbon burn-off at the post-carbonisation stage. This is due to the removal of water from cellulose and this would result in a higher weight loss, causing a higher carbon-burn off [23]. H_2SO_4 is distributed among the cellulose microfibrils then the H_2SO_4 would extract water from the cellulose and water would be removed from the surface of the fibres. The total carbon burn-off of the acid-treated ACF in this study falls in the region of 75-85% which is considered to be comparable to other works on oil palm empty fruit bunch which have a carbon burn-off percentage of approximately 72-96% [21-22].

Table 2. Carbon burn-off percentage of ACF samples

Sample	Initial Weight (g)	Post-Carbonisation Weight (g)	Post- CO_2 Activation Weight (g)	Total Carbon Burn-Off (%)
ACF_PA	12	11.03	1.64	86
ACF_SA	12	5.16	3.04	75
ACF_PH	12	10.2	NA*	NA*
ACF_SH	12	10.2	NA*	NA*

*NA-Not available

The carbon burn-off analysis for both alkali treatments are not available due to the fact that the concentration of the alkali used is too high. Metal ion in alkali solutions are usually in the form of aquo ions. These aquo ions are most likely to enter the crystallisation region of the cellulose of the fibre samples. A concentration of 15-20% would start to cause swelling at the crystalline region [26]. Thus, a concentration used at this work which is 80% would have already destroyed the crystalline structure of the fibre samples, causing the whole structure of the sample to disintegrate. This would

explain the unavailable data for the carbon burn-off and further analysis done in this work.

3.2 Structure and Pore Development of Activated Carbon Fibre

Nitrogen adsorption is carried out to determine the effect of different chemical treatment on the pore characteristics of the produced ACF samples. Figure 1 shows the nitrogen adsorption isotherm at 77 K for the ACF sample for different acid treatment. The data for alkali treatment is unavailable due to the fact that the crystalline structure of the EFB fibre sample has been destroyed due to high concentration of alkali used. The isotherm for the acid-treated ACF samples pertain to type I isotherm of the referred IPUAC classification of physisorption isotherms [27]. Type I isotherm is indicative to the presence of micropores in the sample [17].

The amount of adsorption increases over higher relative pressure (P/Po) which indicates that more pores are being formed. For the ACF_SA sample, nitrogen uptake amount increase rapidly up to a relative pressure of approximately 0.06. This large amount of nitrogen uptake at a low relative pressure is due to the enhancement of the adsorbent-adsorbate interactions in narrow micropores [27]. Due to the formation of micropores, the adsorption potential of the pore increases hence filling the pores at a low relative pressure. At high relative pressure, there would be little or no adsorption because the pores are filled with the adsorbed adsorbate. As for the ACF_PA sample, it has shown a “knee” isotherm type I at low relative pressure. This variation of Type I isotherm where it shows that ACF_PA samples have a pore size distribution over a broad range where it includes the wider micropores and possibly narrow mesopores.

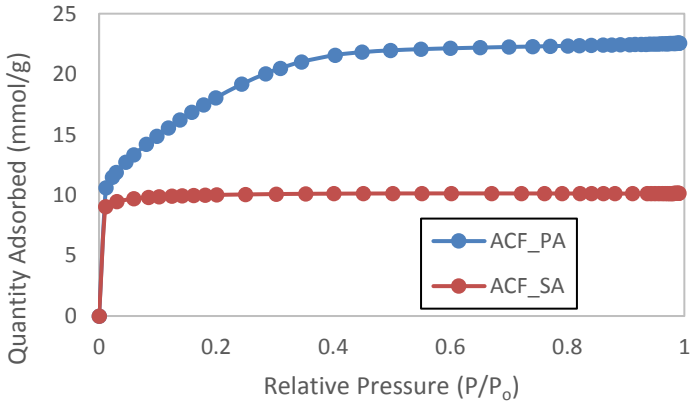


Figure 1. Nitrogen adsorption isotherm of ACF samples

The BET surface area, total pore volume as well as the average pore diameter are presented in Table 3. Based on the data obtained, the average pore diameter of ACF_PA sample is well between the range of micropore (<2 nm) and mesopore (2 nm < pore width <50 nm). This would further prove that the ACF_PA consists of both micropores and mesopores. Whereas for the ACF_SA sample, the average pore is well within the micropore range of less than 2 nm. There is a significant difference between the 2 samples where ACF_PA has almost doubled the total pore volume and BET surface area of ACF_SA. This could be due to the excess water vaporisation via H_2SO_4 dehydration which resulted in over gasification of the sample. Thus, it reduces the BET surface area as well as the pore volume [7]. The high total pore volume is also comparable to activated carbons produced from plum kernels and kenaf biomass. [14, 28].

Table 3. Pore Characteristics of ACF samples

Sample	BET Surface Area (m^2/g)	Total Pore Volume (cm^3/g)	Average Pore Diameter (nm)
ACF_PA	1493	0.782	2
ACF_SA	737	0.352	1.9

In combination with pore characterisation via nitrogen adsorption, X-ray Diffraction (XRD) was also incorporated to measure the crystalline structure of the ACF samples. The XRD patterns of the samples are shown in Figure 2. The figure shows that 2Θ had two graphitic diffraction peaks at 23° and 44° which are assigned to the disordered 002 plane and the 10 plane [17]. Based on Figure 2, the profiles of both ACF samples are rather similar. The peaks at 23° and 44° proves that the samples produced are made of carbon. However, there is a small peak at 72° where it corresponds to the presence of silicon in the fibre [29]. This may be possible due to the fact that the raw material of EFB fibre contains a small percentage of silica or silicon substrates [9]. The presence of silica in the ACF sample may be due to the change of silica percentage after the activation and carbonisation process. The firing of biomass may increase the silica content from 30% up to 96% [30].

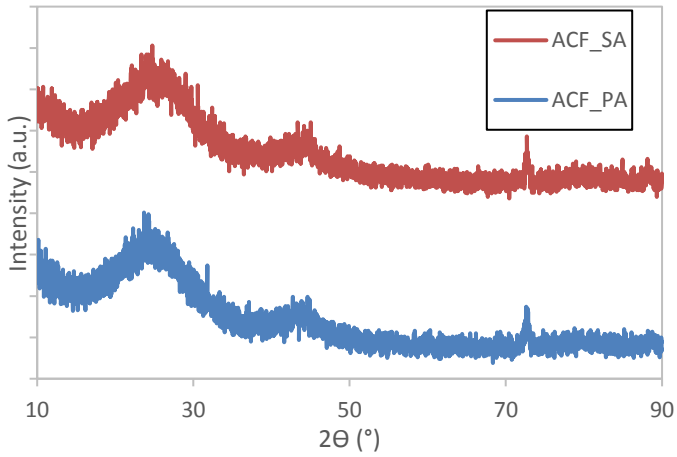


Figure 2. X-ray diffraction patterns of ACF samples

3.3 Surface Chemistry of Activated Carbon Fibre

Figure 3 shows the FTIR spectra of raw EFB fibre and ACF samples with different chemical treatment. The FTIR spectra of the produced ACF samples show some similarity and differences as compared to the raw EFB fibre. The peak intensity at the absorption band from 4000 cm^{-1} to 3200 cm^{-1} of raw EFB fibre is relatively higher than the ACF samples due to higher moisture content in the raw EFB fibre. Moisture removal is done during carbonisation and activation process. Thus, ACF samples have a lower peak intensity compared to the raw EFB fibre. The peak at 1748 cm^{-1} in the indicated the presence of C=O stretching of the acetyl group [31]. This acetyl group exists in the hemicellulose and lignin. The decrease of intensity of this peak in ACF samples shows the removal of cellulose, hemicellulose and lignin after chemical treatment, carbonisation and activation process. The C=C stretching vibrations of aromatic rings at 1450 cm^{-1}[32] in the ACF _SH intensified as compared to the raw EFB fibre and the intensity in ACF_SH has decreased as compared to the raw EFB

fibre. The stretching of the C-O-C group is observed at 1048 cm^{-1} which is linked to the pyranoside linkage structures coming from cellulose. The presence of the P-O group at 1087 cm^{-1} represents the ionised linkage of acid phosphate esters [33].

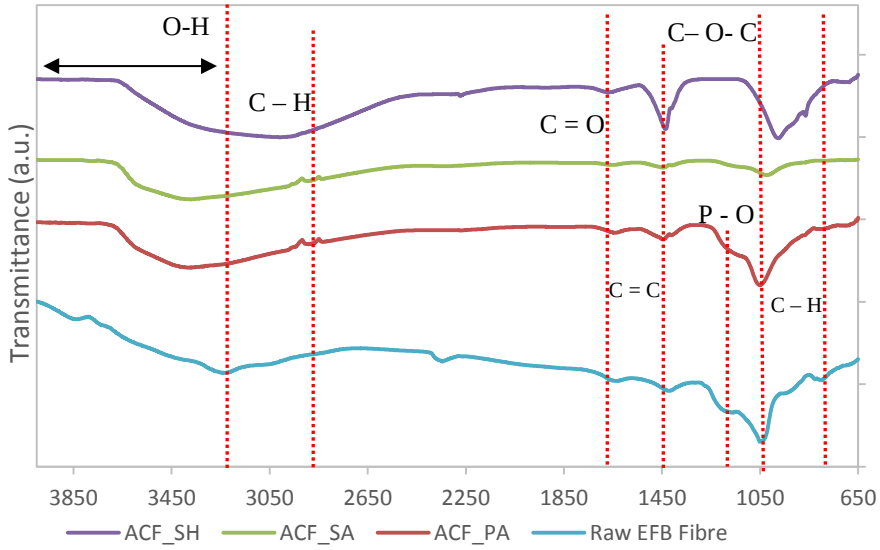


Figure 3. FTIR spectra of ACF samples and raw EFB fibre

3.4 Liquid Phase Adsorption

Urea adsorption by ACF derived from EFB fibre has already been researched on by Ooi and co-workers [7]. However, currently there is still no study done on creatinine adsorption. Thus, the creatinine adsorption done in this work is compared to urea adsorption to evaluate the effectiveness of the ACF sample in removing both creatinine and urea. These two components are among the uremic toxins filtered out during haemodialysis.

The results of creatinine removal by the ACF samples are presented in Figure 4 and Table 4 respectively. Creatinine removal is more effective using the ACF_PA sample as the removal of creatinine is approximately 70% compared to 54% of the ACF_SA. This is very much comparable or even better than the conventional haemodialysis system in creatinine removal. Conventional haemodialysis membrane can remove approximately 42% of the initial creatinine level of patients [20]. Higher degrees of creatinine adsorption can be an indication towards higher surface area and presence of micro and mesopore structures [34]. Creatinine adsorption in this work shows that both ACF samples need the same amount of time to reach equilibrium which is around 20 minutes shown in Figure 4 and Table 4. The equilibrium constant for ACF_PA and ACF_SA are 0.696 and 0.535 respectively. The higher equilibrium constant for ACF_PA indicates that the treatment using H_3PO_4 has affected and improved creatinine adsorption. Creatinine adsorption can also be governed by the BET surface area as well as the surface chemistry of the ACF sample. The higher BET surface area allows ACF_PA to adsorb more of creatinine molecules.

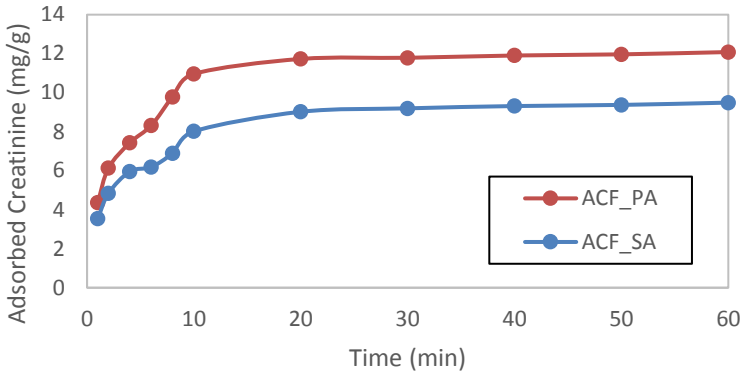


Figure 4. Creatinine adsorption by ACF samples

Table 4. Equilibrium time, amount of creatinine adsorbed during equilibrium and equilibrium constant for ACF samples

Sample	Time to achieve equilibrium, t (min)	Initial Creatinine concentration, Q_o (µmol/g)	Adsorbed Creatinine concentration when equilibrium first reached, Q_{eq} (µmol/g)	Equilibrium constant , K (Q_{eq}/Q_o)
ACF_PA	20	149.01	103.69	0.696
ACF_SA	20	149.01	79.73	0.535

The results of urea adsorption by samples ACF_PA and ACF_SA are presented in Figure 5 and Table 5. In comparison with urea adsorption, creatinine adsorption has a longer time to reach equilibrium. The smaller molecular size of urea with 60 Daltons compared with 113 Daltons of creatinine causes it to move faster [20]. Thus, the time to achieve equilibrium of 10 minutes is shorter compared to creatinine with a time of 20 minutes. The trend in urea adsorption is similar to of creatinine adsorption where sample ACF_PA is able to adsorb more urea molecules compared to sample ACF_SA with an equilibrium constant of 0.68 compared to 0.23 of sample ACF_SA. Thus, the sample ACF_PA is better in adsorbing both urea and creatinine molecules. In comparison with conventional haemodialysis membranes, the ACF_PA sample is able to remove up to 68% of urea compared to the conventional membrane removal rate of approximately 34% in average [20]. However, ACF_SA samples has proven that treatment of EFB fibre treated with H_2SO_4 could not be compared to the conventional haemodialysis membrane as the removal rate of 23.4% is lower than the conventional haemodialysis membranes.

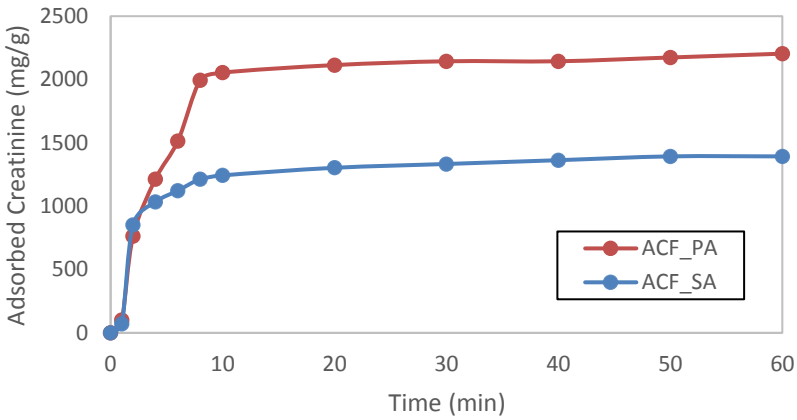


Figure 5. Urea adsorption by ACF samples

Table 5. Equilibrium time, amount of urea adsorbed during equilibrium and equilibrium constant for ACF samples

Sample	Time to achieve equilibrium, t (min)	Initial Urea concentration (μmol/g)	Adsorbed urea concentration when equilibrium first reached, Q_{eq} (μmol/g)	Equilibrium constant , K (Q_{eq}/Q_o)
ACF_PA	10	50000.00	34200.05	0.684
ACF_SA	10	50000.00	11700.00	0.234

4. Conclusion

ACF samples was successfully produced by acid impregnation using H_2SO_4 (ACF_SA) and H_3PO_4 (ACF_PA). ACF samples using KOH (ACF_PH) and NaOH (ACF_SH) impregnation was not successful due to high concentrations of alkali destroying the crystalline structure of EFB fibre. This study highlights that ACF_PA proved to be better at creatinine and urea adsorption compared to ACF_SA despite having a high carbon burn-off. Combination of micro and mesopores proved to be a better option in creatinine adsorption. Both successful ACF samples perform better than conventional haemodialysis membranes in terms of creatinine and urea adsorption proving that ACF produced from EFB fibre can be used as a potential replacement for the haemodialysis membrane. Activated carbon fibre produced using H_3PO_4 showed that it has potential in future haemodialysis adsorption applications. The data produced in this study would be very beneficial for the future development of a replacement of the conventional haemodialysis membrane.

References

[1] V. Wernert, O. Schäf, H. Ghobarkar, and R. Denoyel, “Adsorption properties of zeolites for artificial kidney applications,” *Microporous and Mesoporous Materials*, vol. 83, no. 1–3, pp. 101–113, Sep. 2005.

[2] N. T. T. Hmwe, P. Subramanian, L. P. Tan, and W. K. Chong, "The effects of acupressure on depression, anxiety and stress in patients with hemodialysis: a randomized controlled trial.," *International journal of nursing studies*, vol. 52, no. 2, pp. 509–18, Mar. 2015.
[3] N. Hakim and J. S. . Lumley, *Artificial Organs*, vol. 27, no. 12. 2009.
[4] V. Gura, A. Davenport, M. Beizai, C. Ezon, and C. Ronco, "Beta2-microglobulin and phosphate clearances using a wearable artificial kidney: a pilot study.," *American journal of kidney diseases : the official journal of the National Kidney Foundation*, vol. 54, no. 1, pp. 104–11, Jul. 2009.
[5] P. Chingombe, B. Saha, and R. J. Wakeman, "Surface modification and characterisation of a coal-based activated carbon," *Carbon*, vol. 43, no. 15, pp. 3132–3143, Dec. 2005.
[6] R. C. B. and M. Goyal, *Activated Carbon Adsorption*. CRC Press, 2005.
[7] C. Ooi, C. Ang, and F. Yeoh, "The Properties of Activated Carbon Fiber derived from Direct Activation from Oil Palm Empty Fruit Bunch Fiber," vol. 686, no. APRIL 2013, pp. 109–117, 2013.
[8] A. Bhatnagar and M. Sillanpää, "Utilization of agro-industrial and municipal waste materials as potential adsorbents for water treatment—A review," *Chemical Engineering Journal*, vol. 157, no. 2–3, pp. 277–296, Mar. 2010.
[9] T. Lee, Z. Ahmad, F. Jamil, A. Matsumoto, and F. Yeoh, "Combustion and pyrolysis of activated carbon fibre from oil palm empty fruit bunch fibre assisted through chemical activation with acid treatment," *Journal of Analytical and Applied Pyrolysis*, vol. 110, pp. 408–418, 2014.
[10] G. K. Parshetti, S. Kent Hoekman, and R. Balasubramanian, "Chemical, structural and combustion characteristics of carbonaceous products obtained by hydrothermal carbonization of palm empty fruit bunches.," *Bioresource technology*, vol. 135, pp. 683–9, May 2013.
[11] O. Ioannidou and A. Zabaniotou, "Agricultural residues as precursors for activated carbon production—A review," *Renewable and Sustainable Energy Reviews*, vol. 11, no. 9, pp. 1966–2005, Dec. 2007.
[12] Suhas, P. J. M. Carrott, and M. M. L. Ribeiro Carrott, "Lignin--from natural adsorbent to activated carbon: a review.," *Bioresource technology*, vol. 98, no. 12, pp. 2301–12, Sep. 2007.
[13] B. Viswanathan, P. Neel, and T. Varadarajan, "Methods of activation and specific applications of carbon materials," *Journal for Catalysis Research, Indian Institute of Technology Madras*, 2009.
[14] R.-L. Tseng, "Physical and chemical properties and adsorption type of activated carbon prepared from plum kernels by NaOH activation.," *Journal of hazardous materials*, vol. 147, no. 3, pp. 1020–7, Aug. 2007.
[15] W. C. Lim, C. Srinivasakannan, and N. Balasubramanian, "Activation of palm shells by phosphoric acid impregnation for high yielding activated carbon," *Journal of Analytical and Applied Pyrolysis*, vol. 88, no. 2, pp. 181–186, Jul. 2010.
[16] ASTM International, "ASTM D2867-09(2014)," *Standard Test Methods for Moisture in Activated Carbon*, 2014.
[17] W. Liu and G. Zhang, "Effect of Temperature and Time on Microstructure and Surface Functional Groups of Activated Carbon Fibers Prepared From Liquefied Wood," vol. 7, pp. 5552–5567, 2012.
[18] R. Bellomo, J. A. Kellum, and C. Ronco, "Acute kidney injury.," *Lancet (London, England)*, vol. 380, no. 9843, pp. 756–66, 2012.

[19] S. Upstone, "Ultraviolet/visible light absorption spectrophotometry in clinical chemistry," *Encyclopedia of Analytical Chemistry*, pp. 1699–1714, 2000.
[20] N. Amin, R. T. Mahmood, M. J. Asad, M. Zafar, and A. M. Raja, "Evaluating Urea and Creatinine Levels in Chronic Renal Failure Pre and Post Dialysis : A Prospective Study," *Journal of Cardiovascular Disease*, vol. 2, no. 2, pp. 2–5, 2014.
[21] J. S. Aznar, "Characterization of activated carbon produced from coffee residues by chemical and physical activation," no. March, 2011.
[22] D. Chandramohan, J. Bharanichandar, and T. Nadu, "Carbon – Science and Technology," vol. 3, pp. 314–320, 2013.
[23] D. Y. Kim, Y. Nishiyama, M. Wada, and S. Kuga, "High-yield carbonization of cellulose by sulfuric acid impregnation," *Cellulose*, vol. 8, no. 1, pp. 29–33, 2001.
[24] M. Auta, M. Jibril, P. B. L. Tamuno, A. Alechenu, and A. International, "Preparation of activated carbon from oil palm fruit bunch for the adsorption of Acid Red 1 using optimized Response surface methodology," vol. 2, no. 3, pp. 1805–1815, 2012.
[25] B. H. Hameed, I. A. W. Tan, and A. L. Ahmad, "Preparation of oil palm empty fruit bunch-based activated carbon for removal of 2,4,6-trichlorophenol: optimization using response surface methodology.," *Journal of hazardous materials*, vol. 164, no. 2–3, pp. 1316–24, May 2009.
[26] H. Chen, *Biotechnology of Lignocellulose*. 2014.
[27] M. Thommes, K. Kaneko, A. V. Neimark, J. P. Olivier, F. Rodriguez-Reinoso, J. Rouquerol, and K. S. W. Sing, "Physisorption of gases, with special reference to the evaluation of surface area and pore size distribution (IUPAC Technical Report)," *Pure and Applied Chemistry*, vol. 87, no. 9–10, pp. 1051–1069, 2015.
[28] B. Meryemoglu, S. Irmak, and A. Hasanoglu, "Production of activated carbon materials from kenaf biomass to be used as catalyst support in aqueous-phase reforming process," *Fuel Processing Technology*, vol. 151, pp. 59–63, 2016.
[29] G. N. Chaudhari, "Structural and Electrical Characterization of GaN Thin Films on Si(100)," *American Journal of Analytical Chemistry*, vol. 02, no. December, pp. 984–988, 2011.
[30] T. Lee, R. Othman, and F. Y. Yeoh, "Development of photoluminescent glass derived from rice husk," *Biomass and Bioenergy*, vol. 59, pp. 380–392, 2013.
[31] C.-H. Weng, Y.-T. Lin, and T.-W. Tzeng, "Removal of methylene blue from aqueous solution by adsorption onto pineapple leaf powder.," *Journal of hazardous materials*, vol. 170, no. 1, pp. 417–24, Oct. 2009.
[32] B. H. Stuart, *Infrared Spectroscopy: Fundamentals and Applications*, vol. 8. 2004.
[33] C. Sim, S. R. Majid, and N. Z. Mahmood, "Electrochemical Performance of Activated Carbon Derived from Treated Food-Waste," vol. 10, pp. 10157–10172, 2015.
[34] K.Gergova, N.Petrov, and Minkova, "Comparison of adsorption characteristics of various activated carbons," *Journal of Chemical Technology & Biotechnology*, vol. 56, no. 1, pp. 77–82, 2007.

Synthesis of Zinc Oxide Nanoparticles using Liquid-Phase Laser Ablation and its Antibacterial Activity

Janice Jie-Ni Low[1*], Wai Yin Wong[1], Rashmi G. Walvekar[1], A. B. Mohamad[2, 3], A. A. H. Kadhum[2, 3]

[1]*Chemical Engineering Programme, School of Engineering, Taylor's University Malaysia, No.1 Jalan Taylors, 47500, Subang Jaya, Selangor Darul Ehsan, Malaysia.*

[2]*Fuel Cell Institute, Universiti Kebangsaan Malaysia (UKM), 43600 Bangi, Selangor, Malaysia.*

[3]*Department of Chemical and Process Engineering, Faculty of Engineering and Built Environment, Universiti Kebangsaan Malaysia (UKM), 43600 Bangi, Selangor, Malaysia.*

[*]janicejieni.low@sd.taylors.edu.my

Abstract

The potential of zinc nanoparticles in various fields such as drug delivery, cancer treatment and food packaging has drawn great interest to researchers in order to search for alternative production method with simpler set up. Antibacterial activities of zinc oxide nanoparticles were shown promising owing to its antibacterial properties over a wide range of bacteria strains and non-toxicity. In recent years, liquid-phase laser ablation was introduced as a modified method from conventional laser ablation with the advantage of providing a rapid quenching effect on the ablated metal surface, concurrently enable the ease of collection of metal nanoparticles ablated from the metal surface in the liquid medium. In most of the literature studies, the type of laser used for liquid-phase laser ablation of metal is Nd:YAG laser. For the first attempt, ytterbium fibre laser was used in this study for the liquid-phase laser ablation on zinc target to produce zinc oxide nanoparticles and its antibacterial activity was investigated. In this study, the ablation parameters of laser power, frequency and ablation period were optimised to achieve zinc oxide with nano size. The nanoparticles were investigated on their particle size distribution using Zeta Sizer, morphology using TEM analysis, concentration using AAS analysis and antibacterial properties using agar disc diffusion with the presence of *E. coli*. The results show ZnO nanoparticles ranged 100-150 nm were synthesised from ytterbium fibre laser ablation using the optimised range of laser power, frequency and ablation period determined from this present work. ZnO nanoparticles revealed to be amorphous nano-sheets structures based on TEM analysis and they are in extreme low concentration based on AAS analysis (2-6 mg/L). Relatively small inhibition zones observed from antibacterial analysis due to the morphology and extreme low concentration of ZnO nanoparticles.

Keywords: Ytterbium fiber laser, Liquid-phase laser ablation, Zinc oxide nanoparticles, Antibacterial activity.

1. Introduction

In recent years, nanoparticles are being explored broadly since the invention of nanotechnology as nanoparticles possess extraordinary properties, such as physic-chemical, optical and biological properties compared to their bulk material properties [1]. Their properties changes are due to contribution of the quantum effect as the size decrease to near atomic level. According to Parak et al. [2], the discovery of nanoparticles is an important finding in medical field owing to that the biological processes can occur at nanoscale, and the nanoparticles show the ability to amend the biological functionality of certain cells, especially bacteria strains. Gram-positive and Gram-negative bacteria strains cause human diseases. Examples of bacterial diseases are food poisoning, which is caused by *Escherichia coli*, as well as bloodstream infections and pneumonia which caused by *Staphylococcus* aureus. Currently, metallic nanoparticles are being explored intensively as potential antibacterial agents [1]. It is known that silver and copper metals are commonly used in the antibacterial applications such as wound treatment and water treatment respectively since centuries ago. Other than medical field, metallic nanoparticles have potential applications in food industries, textile fabrics and water purification [1]. Zinc oxide (ZnO) nanoparticles, on the other hand, have raised considerable interest in many recent studies due to its ability of exhibiting significant antibacterial properties over a wide range of bacteria strains. It is also reported in a few studies that ZnO is safe and non-toxic to human by the U.S. Food and Drug administration (21CFR182.8991) [3, 4]. Hence, it is foresee that ZnO nanoparticles possess a huge potential in medical field such as drug delivery and cancer treatment, as well as in process food industries where they are incorporated into food packaging materials in order to inhibit the growth of food pathogens [3, 4].

Liquid-phase laser ablation was introduced as a modified method from conventional laser ablation with the advantage of providing a rapid quenching effect on the ablated metal surface, concurrently enable the ease of collection of metal nanoparticles ablated from the metal surface in the liquid medium. Liquid-phase laser ablation was first introduced in 1987, where pulsed laser was used to produce iron oxides with metastable phases from pure iron metal which was submerged in water [5]. It is a method of laser ablation in which a solid target is immersed in a liquid medium and the high power laser beam is directed through the liquid medium onto the surface of the solid target. According to the study performed by Yang L. [5], the species from the target solid are ejected from the surface at large kinetic energy when the laser beam in contact with the target surface. The species then formed a dense region, which also known as plasma at the solid-liquid interface. Unlike the conventional laser ablation, in liquid-phase laser ablation, the plasma in the liquid expands adiabatically at high velocity which creates extra pressure as it passes through the liquid. This high pressure results in the increase of temperature in the plasma. On the other hand, due to high temperature, some liquid is vaporized to form bubbles in the liquid. As more solid is vaporised, the bubbles tend to expand until they burst at certain critical temperature and pressure. It is believed that the formation of nanocrystals or nanostructures of target is formed due to the extreme high temperature and pressure released by the collapse of the ‘cavitation’ bubbles.

Conventionally, methods for nanoparticles synthesis are solvothermal, sol-gel, water-oil microemulsion and hydrothermal [8]. Conventional methods synthesize large quantity of nanoparticles in shorter time and require chemicals as capping agents to maintain the stability of nanoparticles [6]. However, the chemicals used are harmful to environment and tend to contaminate the nanoparticles. Liquid laser ablation is a much simpler method of synthesizing nanoparticles as it does not require the usage of chemicals. Besides that, liquid laser ablation is able to produce smaller size of nanoparticles with narrower distribution and weak agglomeration, hence it is suitable for metal nanoparticles synthesis [7].

Based on the literature review, there are several areas related to liquid-phase laser ablation using fibre laser to produce nanoparticles that are yet to be explored. Most of the studies related to liquid-phase laser ablation have been done using Nd: YAG laser [8-14], instead, ytterbium fibre laser, which was used in this present work is still lacking in the same field of study. The research regarding the use of ytterbium fibre laser in synthesizing nanoparticles was found limited, but several recent studies showed that fibre laser has potential to produce comparative results with the commonly used Nd:YAG laser [7, 15]. There are various factors affecting the ZnO nanoparticles size distribution, which includes the type of liquid medium, energy fluence, wavelength, frequency, pulse duration and ablation period. Since this present study is a preliminary study of the usage of ytterbium fibre laser in synthesizing ZnO nanoparticles, only three factors: laser power, frequency and ablation period were selected based on the limitation of the specifications of fibre laser used. Studies had been done to show the effect of energy fluence of laser on the particles size and surface morphology and all are done using Nd:YAG laser [10, 12, 14]. The relationship between the energy fluence and particle size ablated is uncertain as the conclusion made by different authors do not have the same agreement. Furthermore, there is yet any study performed on the effect of laser frequency and ablation period on the particles size distribution. ZnO nanoparticles is being investigated extensively on their antibacterial properties in more recent days as compared to silver and copper which are already known with their excellent antibacterial activity [1]. However, all studies related to the antibacterial properties of ZnO nanoparticles use either chemical or biological method to synthesis zinc oxide nanoparticles [3, 6, 16]. Hence, the objectives of this present work are to optimise the laser parameters for ZnO nanoparticles synthesis using ytterbium fibre laser and to investigate the morphology and the antibacterial activity of the ZnO nanoparticles synthesised using ytterbium fibre laser.

2. Experimental Work

2.1 Synthesis and characterisation of ZnO nanoparticles

ZnO nanoparticles were synthesised by laser ablation on zinc metal with purity of 99.99% in sterilised distilled water at room temperature. The zinc metal was placed on the metal holder in the beaker. Sterilised water was poured into the beaker until the water level is 5 mm above the metal target, which was approximate 95 mL of water. ZnO nanoparticles solution were obtained by the irradiation of zinc metal with Ytterbium fibre laser (IPG Laser: YLP-1-100-20-20-HC) which operated at 1064 nm wavelength, 100 ns pulse duration and 1050 mm/s scanning speed at room temperature.

Three laser parameters were varied in this work, which are the laser power, laser frequency and ablation period. In the first or preliminary stage of experiment, 4-level laser power (2 W, 6 W, 10 W, 14 W), 2-level laser frequency (20 kHz, 100 kHz) and 3-level ablation period (1 min, 3 min, 5 min) were applied to obtained 24 samples of ZnO nanoparticles solution. In the second or revision stage, the factors were revised by increasing the range of power to maximum (20 W), ablation period (7 min) as well as the frequency (60 kHz, 150 kHz, 200 kHz). This stage was only carried out with the higher power region which is 14 W and 20 W. A total of 42 samples were collected from the laser ablation. The solution contained ZnO nanoparticles was turned into brown colour right after the laser ablation and turned colourless after a few hours left unstirred, as shown Fig. 1.

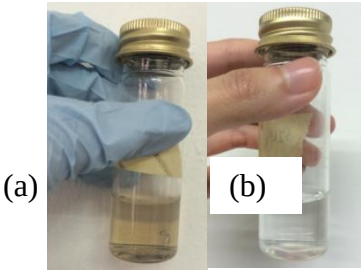


Figure 1. Colour of the solution turned from brown (a) to colourless (b) few hours without stirring after the laser ablation

The particle size distribution of the samples of ZnO nanoparticles solution obtained from laser ablation was investigated by Zetasizer (Malvern Nano ZS ZEN 3600). This analysis was conducted in triplicates and the average value was recorded. The sample with the best result (the smallest average size of ZnO nanoparticles) was selected for morphology analysis using TEM (Hitachi HT-7700) at 120 kV. Before undergoing TEM analysis, the sample was sonicated for 15 mins at room temperature. Then, a drop of sample is placed on a meshcopper grid support and it is dried in an oven at 50 ºC for 10 mins. The concentration of the best five results of ZnO nanoparticles obtained from laser ablation was analysed by AAS (PerkinElmer AAnalyst 400) using zinc lamp.

2.2 Bacterial strains

All the procedures involving bacteria strains were conducted in the Laminar Flow Cabinet. *E. coli* strains were obtained from laboratory of School of Engineering, Taylor's University. The bacteria strains kept in the freezer were defrosted for re-culture. 100 µL of *E. coli* strains were added into 100 mL of nutrient broth. The broth with bacteria strains was incubated in the Orbital Shaker Incubator (LM-400D) for overnight at 37 ºC and 100 rpm. After incubation, bacteria streaking on agar plates were done in order to obtain the isolated colony of bacteria strains. The agar plates with bacteria strains were incubated overnight at 37 ºC.

2.3 Antibacterial assay

Antibacterial activities of the best five results of ZnO nanoparticles were determined using the agar disc diffusion assay. The agar plates prepared for

antibacterial assay were incubated overnight to ensure there is no contamination occurs. The isolated colony of *E. coli* was obtained from the agar plates and it was added into 100 mL of nutrient broth. The bacteria suspension was incubated in the Orbital Shaker Incubator for overnight at 37 ºC and 100 rpm. The concentration of bacteria suspension was adjusted to match the absorbance value of 0.5 McFarland turbidity standards using UV-vis spectrophotometer (Genesys 10S) with 625 nm wavelength, which the concentration of bacteria suspension is 1.5 x 10^8 colony-forming units (CFU) / mL when the absorbance value is between 0.08 to 0.1 using 625 nm wavelength. 100 µL of bacteria suspension was inoculated on the surface of nutrient agar using a sterilised glass spreaders 90º bend. Three layers of sterile filter papers with 6 mm diameter were dipped into the ZnO nanoparticles samples in order to adsorb the ZnO nanoparticles onto the filter paper and they were placed on the nutrient agar with bacteria inoculated. The plates with bacteria and ZnO nanoparticles were incubated at 37 ºC for 48 hours. The inhibition zones of each sample were observed and the diameter of each inhibition zone was measured using a meter ruler. This antibacterial assay was conducted in triplicates and the average value was recorded.

3. Results and discussion

3.1 Zinc oxide nanoparticles formation

According to previous studies [12, 13, 18, 19], ZnO nanostructures formation by liquid-phase laser ablation is divided into two types of reactions: physical and chemical reactions. When laser beam is ablated onto the zinc metal surface, a dense zinc plasma region is produced on the liquid-solid interface. The presence of liquid medium, which is distilled water in this work, creates extra pressure on the plasma and restricts the expansion of plasma hence making it denser when compared to the plasma produced by conventional laser ablation (without liquid).

The plasma expands adiabatically at high velocity until the plasma extinguished and hence zinc clusters are formed. After the disappearance of plasma, cavitation bubble is formed and expanded with time until it collapses at its maximum size. The collapse of cavitation bubble releases high temperature and pressure to the surrounding, hence it is believed that this phenomena contributes to the formation of ZnO nanoparticles. At the same time, the zinc clusters produced from plasma react with the surrounding water medium to form zinc hydroxide, $Zn(OH)_2$ and $Zn(OH)_2$ will further decompose to form ZnO. The chemical equations of the formation of $Zn(OH)_2$ and followed by formation of ZnO are shown in Eq. 1 and 2 respectively:

$$Zn + 2H_2O \rightarrow Zn(OH)_2 + H_2 \qquad \text{Eq. (1)}$$

$$Zn(OH)_2 \rightarrow ZnO + H_2O \qquad \text{Eq. (2)}$$

The physical and chemical reactions happened simultaneously and continuously as the laser ablation continues.

The presence of ZnO nanoparticles in distilled water was justified by the colour change of the solution right after the laser ablation and few hours later, as shown in Fig. 1. The colour of solution turns brown right after the laser ablation, as shown in Fig. 1 (a) and it became colourless solution few hours later, as shown in Fig. (b). This colour change is due to the extreme high temperature and pressure released from the plume

produced by the large kinetic energy of the laser beam onto the metal surface [5]. The beaker containing the solution is warm when touched right after the laser ablation indicating the occurrence of the liquid-phase laser ablation mechanism. This observation is in agreement with Solati E., et al. [14]. At high temperature, ZnO nanoparticles formed brownish in solution and it turned into colourless after it is cooled down to room temperature.

3.2 Particle size distribution

Fig. 2 shows the relationship between the average particle size of ZnO and the laser power at different frequencies with a constant ablation period of 1 min (a), 5 min (b) and 7 min (c). Fig. 3 shows the relationship between the average particle size of ZnO and the laser frequency at different ablation period with a constant power of 14 W (a) and 20 W (b). Fig. 4 shows the relationship between the average particle size of ZnO and the ablation period at different power with a constant frequency of 20 kHz (a), 60 kHz (b) and 100 kHz (c).

There is no general trend observed from the relationship between laser power, laser frequency and ablation time with the ZnO particle size based on the graphs shown in Fig. 2, Fig. 3 and Fig. 4. However, the factors are interconnected with each other in order to obtain the desirable particle size of ZnO nanoparticles. In Fig. 2, most samples with desirable particle size, which is below 200 nm are obtained in the higher power region, 14 W to 20 W although there is no similar trend for different frequencies and ablation periods. In Fig. 2 (a), the desirable particle sizes are observed at 10 W and 14 W at 20 kHz. At higher frequency which is 100 kHz, the particle sizes at any power are undesirable at 1 min ablation period. In Fig. 2 (b), the desirable particle sizes are observed at 14 W at both 20 kHz and 100 kHz, as well as at 20 W at 100 kHz. This shows that the increase in frequency and ablation period leads to desirable particle size at higher power region. However, the further increase of frequency does not lead to further reduction of particle size, as shown in Fig. 2 (c). This phenomena is clearly shown in Fig. 3, where the desirable particle sizes are obtained in the lower frequency region, 20 kHz to 100 kHz although there is no similar trend for different ablation periods and powers. In both Fig. 3 (a) and (b), the desirable particle sizes are obtained mostly from 20 kHz, 60 kHz and 100 kHz at higher power region, which is 14 W (a) and 20 W (b). It is also observed that desirable particle size is obtained at 150 kHz, 14 W but turned undesirable at the same frequency with higher power, 20W. Hence, at lower power, higher frequency can be applied in order to obtain the desirable particle size. In Fig. 4, the desirable particles sizes are obtained in the higher ablation period, 5 min to 7 min. The desirable sizes are obtained mostly from 5 min and 7 min at lower frequency region, which is 20 kHz (a), 60 kHz (b) and 100 kHz (c). In Fig. 4 (a), the desirable particle sizes are obtained in longer ablation time (5 min and 7 min) and higher laser power (14 W and 20 W), which matches the statement concluded based on the graphs in Fig. 2. In Fig 4 (c), the desirable particle sizes are obtained from only 5 min and become undesirable at 7 min due to the higher frequency applied, 100 kHz, compared to the frequency applied in Fig. 4 (a) and (b).

Solati E., et al. [14] reported that the increase in laser energy fluence leads to the decrease in ZnO nanoparticles. Guillen G.G. et al. [12] reported no conclusion on the trend of ZnO nanoparticles against the laser energy fluencies. In this present work, overall, it can be concluded that the increase in laser power leads to decrease in ZnO

nanoparticles, however it is strongly influenced by the other parameters: laser frequency and ablation period. In conclusion, in order to obtain the desirable ZnO particle size which is less than 200 nm, the power of the ytterbium fibre laser applied should be at higher region (14 W to 20 W), lower region (60 kHz to 100 kHz) for laser frequency and higher region (5 min to 7 min) for ablation period.

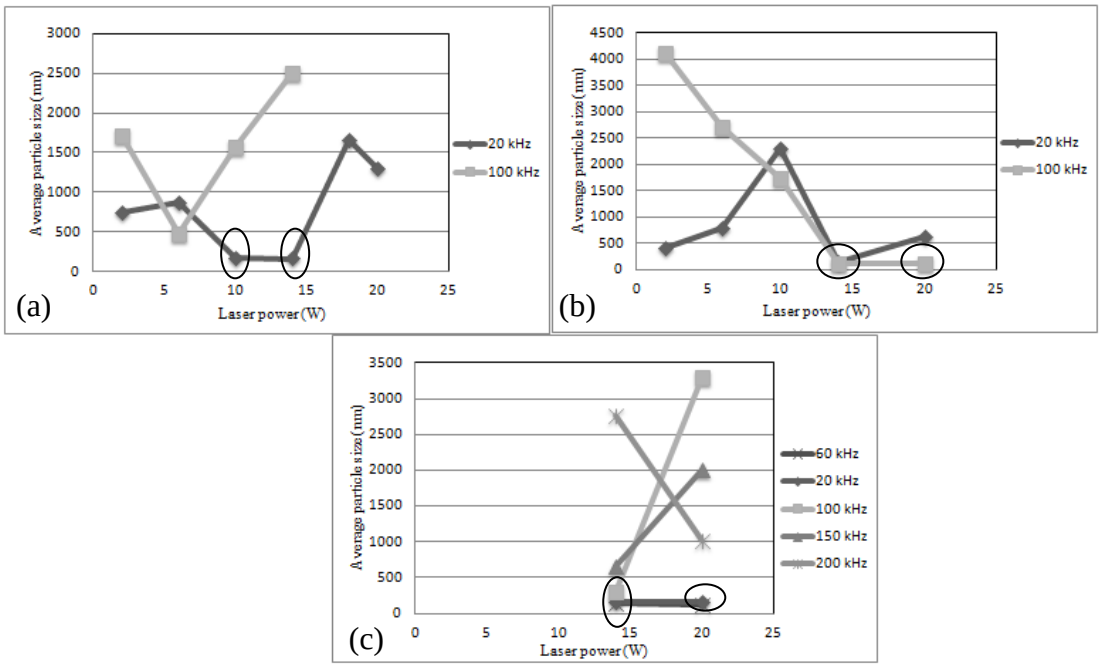


Figure 2. Graph of average ZnO particle size against laser power at constant 1 min (a), 5 min (b) and 7 min (c) ablation period.

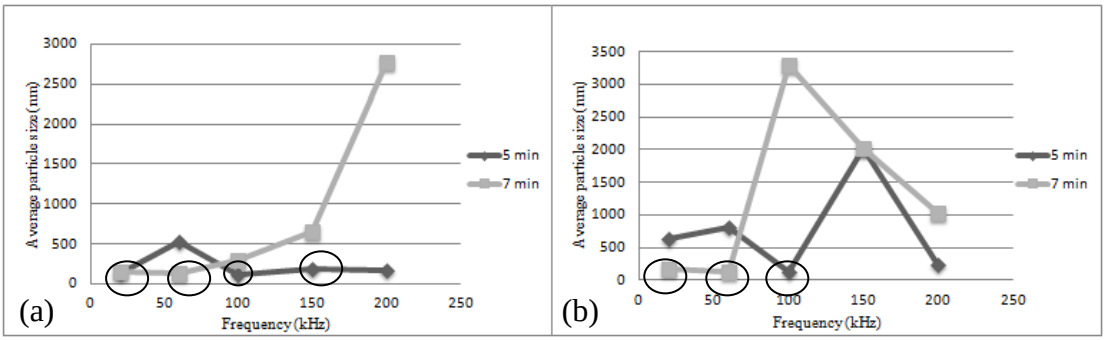


Figure 3. Graph of average ZnO particle size against laser frequency at constant 14 W (a) and 20 W (b) power.

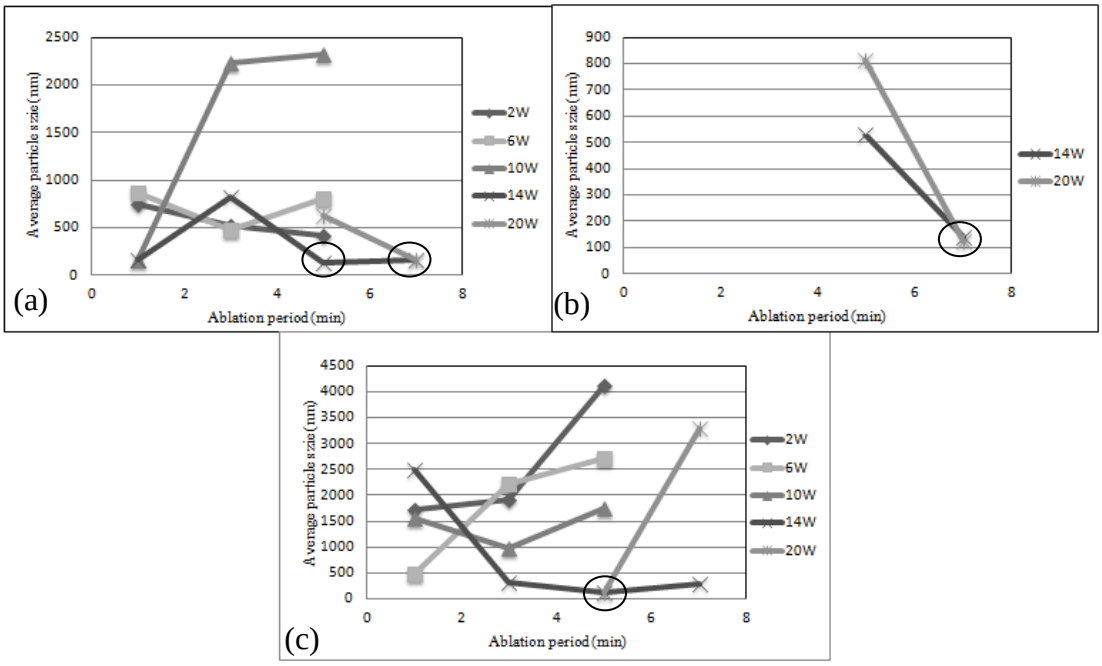


Figure 4. Graph of average ZnO particle size against ablation period at constant 20 kHz (a), 60 kHz (b) and 100 kHz (c) frequency.

Out of 42 samples in total, the five samples with the lowest ZnO particle size obtained from ytterbium fibre laser ablation are selected for further analysis. Table 1 shows the best five results of ZnO nanoparticles with their respective particle sizes and laser parameters. The power, frequency and ablation period ranges in Table 1 are matched with the conclusion made previously based on the graphs in Fig. 2, 3 and 4. Fig. 5 shows the particle size distribution (based on volume percentage) of the five samples obtained from the Zetasizer. Although the average particle size of all the samples are above 100 nm, the greatest volume percentage of all the samples are in the range of 60-80 nm based on the graphs in Fig. 5, showing that most of the ZnO particles are in nanosize. Sample S1 and S2 even showed significant amount of nanoparticles ranged 15-40 nm. Hence, these results proved that ytterbium fibre laser can be used to synthesise ZnO particles in nanosize.

Table 1. The five lowest average particle size of ZnO samples obtained from laser ablation with their respective laser parameters used

Sample	Power (W)	Frequency (kHz)	Ablation period (min)	Average particle size (nm)
S1	14	100	5	116.4
S2	20	100	5	118.4
S3	20	60	7	123.2
S4	14	20	5	135.6
S5	14	60	7	139

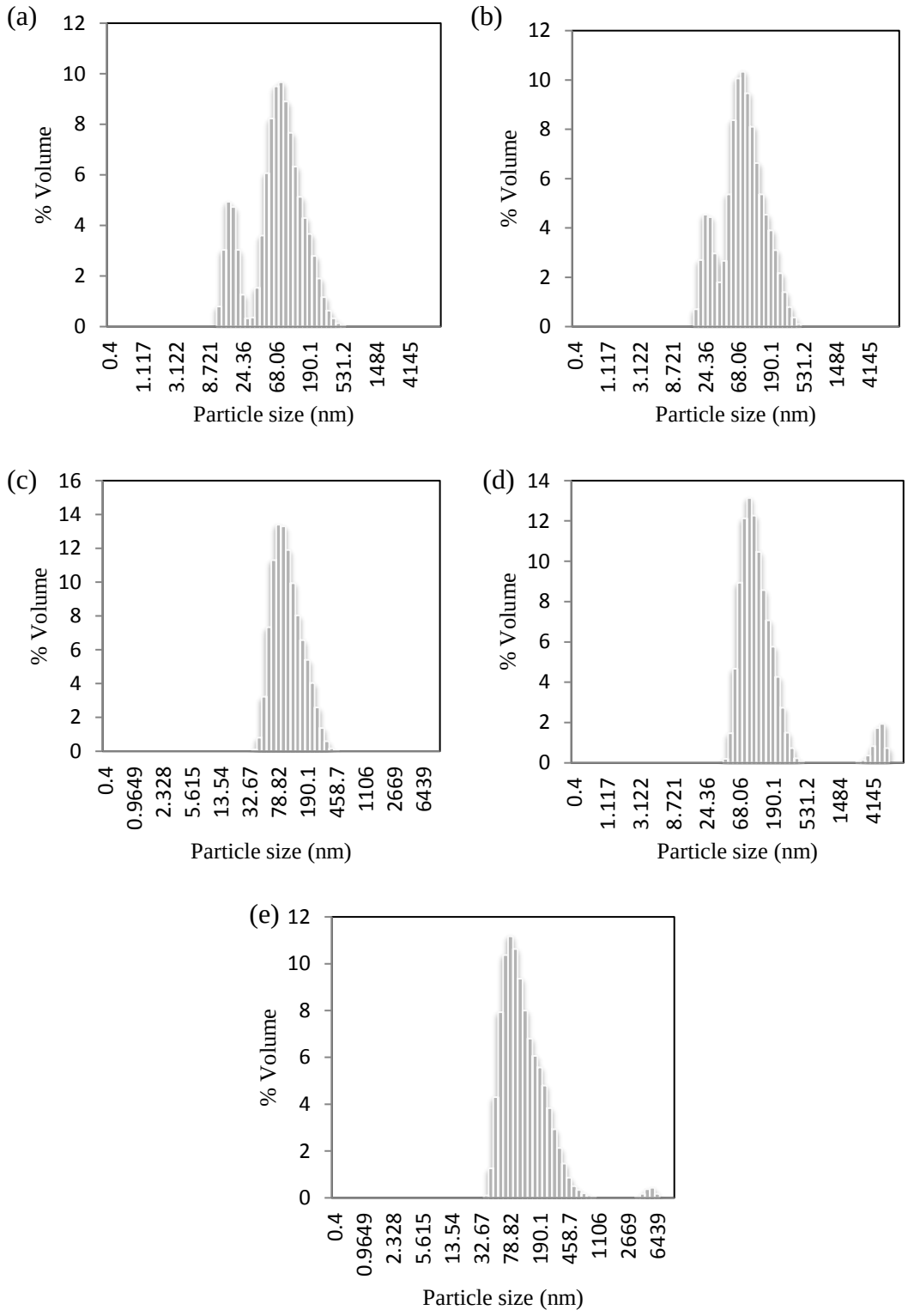


Figure 5. Particle size distribution of the five best samples of ZnO nanoparticles obtained from ytterbium fibre laser ablation in distilled water: sample S1 (a), S2 (b), S3 (c), S4 (d) and S5 (e).

3.2 Transmission electron microscopy (TEM) analysis

Fig. 6 (a) and (b) show the TEM images of ZnO nanoparticles synthesized by laser ablation in distilled water. These images revealed that ZnO nanoparticles synthesised in this work are in amorphous structures. In other words, they consist of several layers nano-sheets structures attached together, which is shown by the light and dark grey region based on the TEM images. The dark grey region show denser area where more nano-sheets layers attached together, while the light grey region show less dense area where only single or a few layers of nano-sheets attached. The ZnO nanostructures obtained from ytterbium fibre laser is different from the ZnO nanostructures obtained from Nd: YAG laser in the previous studies [12-14, 20] where most of the ZnO nanoparticles produced were either spherical or flakes in shape. Furthermore, unlike the spherical ZnO which has crystalline structure, ZnO obtained from present work does not have crystalline structure with no specific shape. It is suspected that the formation of amorphous ZnO structure is due to the relatively low laser power of the ytterbium fibre laser compared to Nd: YAG laser. As lower laser power is used, a lower plasma temperature and pressure is induced during laser ablation and hence producing weaker plasma with shorter lifetime [21]. Shorter plasma lifetime leads to shorter nucleation and growth time of ZnO particles, thus forming irregular nanosheets without crystalline structure. During the formation of ZnO, the nucleation of Zn is induced by the reduction of Gibbs free energy [22]. The reduction of Gibbs free energy is necessary in order to achieve the solubility or supersaturation equilibrium of the solute in a solution as solute above solubility equilibrium posses high Gibbs free energy. In order to lower the Gibbs free energy, solute will aggregate themselves from the solution and form a new solid phase [22]. In this case, it was observed that layers of ZnO nanosheets segregate and assemble together to reduce the free surface energy in order to reach its equilibrium state.

Fig. 6 (a) shows one of the ZnO nanoparticles contained in sample S1. This quasi-spherical nano-sheet structure has approximate 77.6 nm in diameter, which is in agreement with the particle size distribution obtained from Zetasizer. Fig. 6 (b) shows the close-up image of one of the ZnO nanoparticles in sample S1. Porous structures were observed from the close-up image where it is in agreement with the study done by Li S., et al.. [17], where they showed that the ZnO which is also obtained from pulsed laser ablation using deionised water are in porous nano-sheets structures. Fig. 6 (c) show the overview TEM image from one of the mesh grids, which only two particles (in red circles) were seen on a mesh grid. This shows that the concentration of ZnO nanoparticles obtained from laser ablation is very low, compared to studies done by Li S., et al. [17] and Solati E., et al. [14]. The concentration of ZnO nanoparticles obtained was further analysed using AAS which is discussed in the following section.

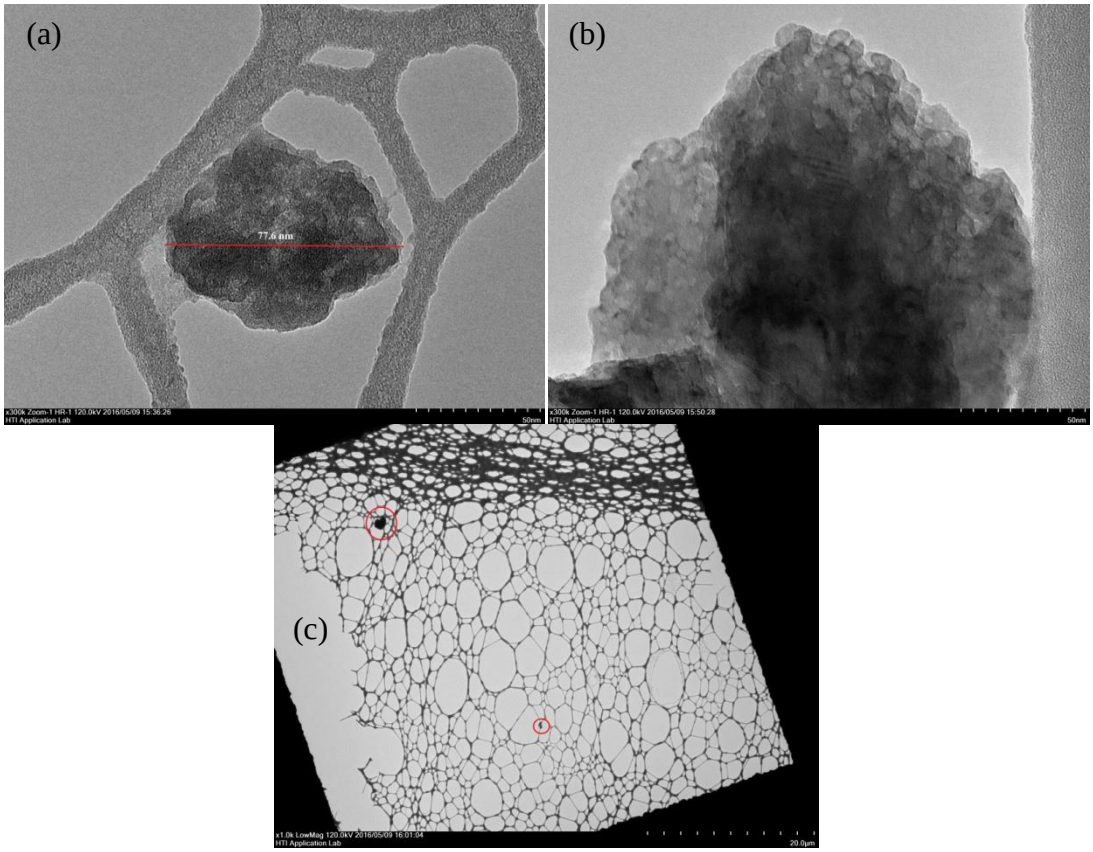


Figure 6. TEM images of ZnO nanoparticle from sample S1 (a), close-up image of ZnO nanoparticle (b) and overview in a mesh copper grid (c).

3.3 Atomic absorption spectroscopy (AAS) analysis

Table 2 shows the concentration of the five best results of ZnO nanoparticles obtained from ytterbium fibre laser ablation. These results reveal that the concentration of ZnO nanoparticles is ranged from 2 mg/L to 6 mg/L. Samples S3, S4 and S5 have relatively higher concentration than the samples S1 and S2. Since the power and ablation period used in these five samples are in small range, which is 14 W and 20 W for power as well as 5 min and 7 min ablation period, this may due to the lower frequency used in sample S3, S4 and S5, which is 60 kHz, 20 kHz and 60 kHz resepectively, while the frequency used in S1 and S2 are both 100 kHz. Compared to the studies by Ismail R. A. et al. [8] and Zimbone M. et al. [9], where the concentration of iron oxide nanoparticles by [8] and titanium oxide nanoparticles by [9] used for antibacterial analysis is 4000-4250 mg/L and 25-100 mg/L respectively, the concentration of ZnO nanoparticles obtained from ytterbium fibre laser is extremely low It is suspected that the rate of formation of ZnO nanoparticles using ytterbium fibre laser is lower than using Nd:YAG laser due to its relatively low laser power of ytterbium fibre laser.

Table 2. Concentration of the five best results of ZnO nanoparticles obtained using various laser parameters

Sample	Concentration (mg/L)
S1	2.795
S2	2.894
S3	6.086
S4	5.665
S5	5.522

3.4 Antibacterial activity

Fig. 7 shows the inhibition zones obtained from samples S1, S2 and S3 after 48 hours of incubation. The inhibition zones were indicated by relatively transparent zone surrounded the filter paper immersed with ZnO nanoparticles, as shown in black circles in Fig. 7. At nano-size scale, ZnO exhibits significant antibacterial properties compared to its bulk material properties [1]. Small particle size increases the surface area of the particles, hence they have the ability to amend the biological functionality of certain cells, especially bacteria strains [2]. It is believed that the mechanism on bacterial cell destruction of ZnO is the generation of hydrogen peroxide from ZnO surface which inhibits the bacterial growth [1, 4]. Small inhibition zones were observed in each sample with the diameter of 1-2 mm each. Compared to studies done by Suresh D. et al. [16], Anbuvannan M. et al. [6], the inhibition zones obtained from this work is relatively small due to the extreme low concentration of ZnO nanoparticles. The antibacterial activity of nanoparticles is significantly affected by the nanoparticles concentration and the initial bacterial concentration [8]. Hence, the nanoparticles concentration is the major factor of their antibacterial activity in this present study. The decrease in particle size leads to increase in antibacterial activity of the nanoparticles due to the increase in large surface area of nanoparticles and hence its membrane permeability [8]. In this present study, ZnO nanoparticles in the range of 115-140 nm size are used for their antibacterial activity. Similar inhibition zones and antibacterial activities were observed which may due to the small difference between their particle sizes. On the other hand, according to a study performed by Jaiswal et al., the antibacterial activity of ZnO nanoparticles is dependent on their morphology structures [23]. Previous studies [6, 24] reported that ZnO nanoparticles in spherical shape exhibit excellent antibacterial properties. There is yet any study performed to study the antibacterial activity of ZnO nanoparticles synthesised by ytterbium fibre laser. Therefore, it was suspected the amorphous structure of ZnO nanoparticles produced from ytterbium fibre laser showed no significant effect on its antibacterial activity towards *E. coli* bacteria strains.

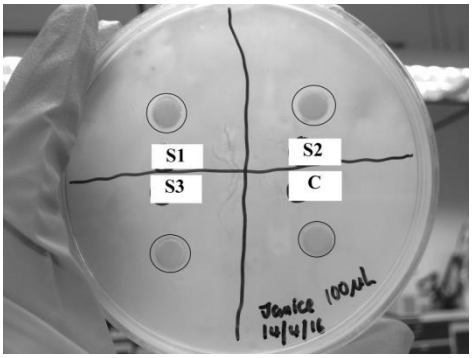


Figure 7. Inhibition zones induced by ZnO nanoparticles in samples S1, S2 and S3 against *E. coli*.

4. Conclusion

This study revealed that zinc oxide nanoparticles were successfully produced using ytterbium fibre laser ablation in distilled water. Based on the results obtained from this present work, the most desirable ZnO average particle size, which is between 100 and 150 nm, are be synthesised using higher power region (14-20 W), lower frequency region (20-100 kHz) and longer ablation period (5-7 min). The ZnO nanoparticles are in amorphous structures, and mostly contained several layers of irregular nano-sheets structures attached together. The formation of amorphous ZnO nanostructures is suspected due to the relatively low laser power of ytterbium fibre laser compared to the commonly used Nd: YAG laser. Both TEM and AAS analysis revealed that the concentration of ZnO particles is only 2-6 mg/L, which is extremely low. The extreme low concentration of ZnO obtained from ytterbium fibre laser is also suspected due to the relatively low laser power of fibre laser used. Besides that, no significant antibacterial activity was observed from ZnO nanoparticles synthesised from ytterbium fibre laser, which may be due to the extreme low concentration of ZnO nanoparticles and the morphological dependency.

In future work to further study the feasibility of using ZnO nanoparticles produced from this method as antibacterial agent, the ablation process will be repeated in the same liquid medium using the combination of parameters obtained in this study to achieve the desired concentrations (c.a. 100 mg/L) prior to the antibacterial testing. Furthermore, to further study on other potential applications of the ZnO nanoparticles produced from this method, the ablation process will be repeated using different liquid medium using the combination of parameters obtained from this study to study on the morphological structure of nanoparticles produced and its potential application.

References

[1] Vittal R.R. et al. (2011). Nanoparticles and their potential application as antimicrobials, *Science against microbial pathogens: communicating current research and technological advances*, 197-209.
[2] Parak W.J. et al. (2003). Biological applications of colloidal nanocrystals, *Nanotechnology*, 14, 15-27.
[3] Pati R. et al. (2014). Topical application of zinc oxide nanoparticles reduces bacterial skin infection in mice and exhibits antibacterial activity by inducing

oxidative stress response and cell membrane disintegration in macrophages, *Nanomedicine: Nanotechnology, Biology, and Medicine*, 10, 1195-1208.

[4] Sirelkhatim A. et al. (2015). Review on Zinc Oxide Nanoparticles: Antibacterial Activity and Toxicity Mechanism, *Nano-Micro Letters*, 7, 219-242.

[5] Yang L. (2007). *Chapter 2: Liquid-Phase Pulsed Laser Ablation,* Self-Assembly and Ordering Nanomaterials by Liquid-Phase Pulsed Laser Ablation, Univeristy of Bristol, 33-47.

[6] Anbuvannan M. et al. (2015). Anisochilus carnosus leaf extract mediated synthesis of zinc oxide nanoparticles for antibacterial and photocatalytic activities, *Materials Science in Semiconductor Processing*, 39, 621-628.

[7] Boutinguiza M. et al. (2014). Palladium nanoparticles produced by CW and pulsed laser ablation in water, *Applied Surface Science*, 302, 19-23.

[8] Ismail R.A. et al. (2015). Antibacterial activity of magnetic iron oxide nanoparticles synthesized by laser ablation in liquid, *Materials Science and Engineering C*, 53, 286-297.

[9] Zimbone M. et al. (2014). Photocatalytical and antibacterial activity of TiO_2 nanoparticles obtained by laser ablation in water, *Applied Catalysis B: Environmental*, 165, 487-494.

[10] Mahdieh M.H. et al. (2014). Size properties of colloidal nanoparticles produced by nanosecond pulsed laser ablation and studying the effects of liquid medium and laser fluence, *Applied Surface Science*, 329, 47-57.

[11] Gondal M.A. et al. (2013). Effects of oxidizing medium on the composition, morphology and optical properties of copper oxide nanoparticles produced by laser ablation, *Applied Surface Science*, 286, 149-155.

[12] Guillen G.G. et al. (2015). Structure and morphologies of ZnO nanoparticles synthesized by pulsed laser ablation in liquid: Effects of temperature and energy fluence, *Materials Chemistry and Physics*, 162, 561-570.

[13] Thareja R.K. et al. (2007). Synthesis and characterisation of zinc oxide nanoparticles by laser ablation of zinc in liquid, *Applied Surface Science*, 253, 8889-8895.

[14] Solati E., Dejam L., Dorranian D. (2013). Effect of laser pulse energy and wavelength on the structure, morphology and optical properties of ZnO nanoparticles, *Optics & Laser Technology*, 58, 26-32.

[15] Boutinguiza M. et al. (2013). Synthesis of titanium oxide nanoparticles by Ytterbium fiber laser ablation, *Physics Procedia*, 41, 787-793.

[16] Suresh D. et al. (2015). Green synthesis of multifunctional zinc oxide (ZnO) nanoparticles using Cassia fistula plant extract and their photodegradative, antioxidant and antibacterial activities, *Materials Science in Semiconductor Processing*, 31, 446-454.

[17] Li S., Chen M., Liu X. D. (2014). Zinc oxide porous nano-cages fabricated by ablation of Zn in ammonium hydroxide, *Optics Express*, 22 (15), 18707-18714.

[18] Sasaki K. (2009). Liquid-phase laser ablation, *19th International Symposium on Plasma Chemistry*, Bochum, 1-4.

[19] Chang W. et al. (2015). Bifunctional Zinc Oxide Nanoburger Aggregates as the Dye-Adsorption and Light-Scattering Layer for Dye-Sensitized Solar Cells, *Electrochimica Acta*, 169, 456-461.

[20] Fazio E. et al. (2012). ZnO nanostructures produced by laser ablation in water: Optical and structural properties, *Applied Surface Science*, 272, 30-35.

[21] Zhang X. et al. (2008). Laser power effect on morphology and photoluminescence of ZnO nanostructures by laser ablation in water, *Materials Letters*, 63, 191-193.

[22] Cao G. (2005) 3.2.1. Fundamentals of Homogenous Nucleation, University of Washington [Online] Available: http://depts.washington.edu/solgel/documents/class_docs/MSE502/Ch_3_Section_3.2.1-3.2.5.3.pdf

[23] Jaiswal P. et al. (2015). Morphological dependence of ZnO nanostructures on antibacterial activity , *J Biotechnical Biomatter*, 2015.

[24] Rajamanickam U. et al. (2012). Biosynthesis of Zinc Nanoparticles Using Actinomycetes for Antibacterial Food Packaging, *International Conference on Nutrition and Food Sciences IPCBEE*, 39, 195-199.

Starch polymers with water exchanging properties to improve soil suitability for landscaping purposes

Jason Low Wai Kit*, Dr Chong Chien Hwa
School of Engineering, Taylor's University

jlow_916@hotmail.com

Abstract
A series of starch based biodegradable polymers crosslinked with varying concentration (0.1-1 g) of citric acid (CA) and glycerol was solution casted at 150 °C subsequent to a preheating of 80°C. The effect concentration of (CA) the samples was evaluated by studying the moisture content, swelling degree, weight loss of samples at varying temperatures (35- 50°C) and biodegradability of samples based on macroscopic appearance. Increasing concentration of CA results in decreasing swelling degree of the samples with the minimum and maximum swelling degree of 55.8±2.5 % and 143.2±5.1 % occurring at 1.0 g and 0 g of CA respectively. Greater concentration of CA also cause a decrease in moisture content of samples with minimum and maximum moisture content of 5.1±0.5 % and 20.3±1.2 % occurring at 0 g and 1.0 g of CA respectively. Consequently, weight loss of polymers increases gradually with time. Samples with no CA experience the greatest weight loss with time at all temperatures. 0.3 g CA is determined as the optimum concentration of CA for starch polymers in improving soil suitability due to the least weight loss of samples with time indicating that water is gradually released with time. All samples displayed significant biodegradation at the end of the 28 day study with the sample without CA showing the highest rate of biodegradation and samples with 1.0 g of CA showing the least rate of biodegradation based on macroscopic appearance.

Keywords: Polymer, starch, citric acid, glycerol, moisture content

1. Introduction

Research of biodegradable polymers and its applications in various industries has been rapidly increasing in recent years. Biodegradable polymers plays a major role in the effort of conserving the environment especially in its applications in medicinal, packaging and also agricultural industries. Besides the well-known fact that biodegradable polymers are able to be broken down or dissociate after its intended purpose is fulfilled, it is also widely used in the industries as mentioned above due to the polymers being able to transport specific objects such as drugs or enzymes to their

desired destination. Furthermore, biodegradable polymers are increasingly applied in medicinal and agricultural properties due to specific properties such as having low or no-toxicity, being able to maintain mechanical and structural stability before degradation as well as ability of control-release of substances being transported.

Hence, polymers are widely used in this industry with the main purpose of improving soil suitability for agricultural and landscaping purposes to achieve a higher production rate. Development of super absorbents polymers and composites are also used in places facing long period of droughts, hot climates as well as low availability of souce of water. Super absorbent polymers are known to improve soil properties by increasing their water retention capacity, reduce frequency of irrigation, increase soil permeability as well as to ensure a constant supply of water even throughout dry seasons or drought where water availability is scarce [1]. However, super absorbent polymers and composites are often made of materials that are not completely biodegradable and these degraded materials causes harm to soil and crops over a long period of time.

In order to overcome this problem of biodegradability, starch is chosen as one of the main material to synthesise the biodegradable polymer. This is because the polysaccharide region of starch is completely biodegradable. Starch is also one of the most abundant and cheap polysaccharides, consisting of an average of 70% amylopectin and 30% amylose. Thus, mass production at a bigger scale would be easier and cost beneficial with a cheap and easily available material. Starch based polymers are hydrophillic in nature with the molecular formula of (St-OH) which enhances the ability of the hydrophilic group to form intramolecular hydrogen bond with water molecules, thus increasing the water absorption of polymers [2], [3]. Furthermore, starch provides a greater oxygen permeability when it is being consumed by microorganisms and also biodegrades faster than synthetic polymer [4]. The biodegradable characteristic of starch combined with the low cost and easy availability are the main reasons starch was chosen as the main material to synthesise the biodegradable polymer. But starch polymers are also brittle with low tensile strength, high water sensitivity and have poor moisture barrier properties.

One of the approach of overcoming the weaknesses of starch polymers relative to their structural and hygroscopic properties is through crosslinking. Examples of cross-linking reagents are boric acid [5], epichlorohydrin [6] and glutaraldehyde [7]; where those cross-linkers involves radiation [8], and photo-cross-linking [9]. Citric acid (CA) which is the main organic acid found in citrus food consist of three carboxyl and hydroxyl group. Due to the multi-carboyxylic structure of CA, esterification can take place between the carboxyl group of CA and hydroxyl group on starch, thus improving mechanical strength and structure. Furthermore, CA is proven to be harmless to the body and is non-toxic. CA has been approved by U.S. Food and Drug Administration (FDA) for use in human and can potentially be applied in biomedical and food packing industry.

A starch based polymer synthesised only with CA as cross-linking agent will result in a polymer that is less flexible and brittle. Glycerol which acts as a plasticizer is able to overcome this problem when added to the system by increasing plasticity. Some authors such as Reddy and Young, Shi as well as Menzel have studied on CA-

glycerol-starch system where the authors mentioned that the addition of glycerol to the system increased the plasticity and reduced the brittleness of the polymer [10],[11],[12].

In this work, the effect of concentration of CA on the moisture content, degree of swelling, weight loss of polymers at varying temperatures (35 °C to 50 °C) and biodegradability of polymer in soil is studied to identify the optimum concentration of CA in starch polymers which helps to improve the soil suitability for landscaping purposes.

2. Experimental

2.1. Materials

Soluble potato starch (AR) was purchased from Synertec Enterprise (Kuala Lumpur, Malaysia) which composed of 25% amylose and 75% amylopectin. Glycerol anhydrous (purity: 99.8%) Citric acid anhydrous (99.5% BP) was purchased from Synertec Enterprise (Kuala Lumpur, Malaysia). Effective microorganisms (EM-1) was purchased from Ace Hardware (Kuala Lumpur Malaysia).

2.2. Preparation of starch polymer

The starch polymer was prepared using solution casting method. First, the starch mixture was prepared by dissolving 10 g of starch, 1 g of glycerol, 150 of g distilled water and different concentrations of CA (0 g, 0.1 g, 0.3 g, 0.5 g and 1 g) in a 250 ml beaker. The composition of the starch mixture is shown in Table 1. The starch mixture was then heated at 80 °C for 45 minutes using a magnetic stirrer with the agitation set at 350 rpm. The starch mixture was then further heated at 150 °C for another 45 minutes with the same agitation as before. After that, the solution was casted in plastic molds and heated in the oven at 60 °C for 48 hours.

Table 1. Materials' abbreviations and their sample compositions

Abbreviations	Samples Starch (g)	Glycerol (g)	Distilled water (g)	CA (g)
SGD	10	1	150	0
SGDC0.1	10	1	150	0.1
SGDC0.3	10	1	150	0.3
SGDC0.5	10	1	150	0.5
SGDC1.0	10	1	150	1.0

2.3 Degree of swelling

The swelling degree of samples was carried out at room temperature which is at 25 °C with rounded samples of 3 cm diameter placed in deionized water for 48 hours. The swollen samples were then dried using a wire mesh of 100 mm to remove excess surface moisture. The swelling degree of samples was determined by measuring the weight gain of samples in 500 ml water as shown in the eq. 1,

$$Swelling\ degree\ (\%) = \frac{M_w - M_d}{M_d} \times 100 \quad (1)$$

Where M_w is the wet mass of samples after swelling for a fixed period of time and M_d is the dry mass of samples before swelling. The reported results are the average results of five samples in each case.

2.4 Moisture content

Moisture content of samples were determined by cutting the samples to small pieces with a total of 1 g and drying the samples in an oven at 105 °C for 24 hours. The percentage of moisture content was calculated using eq. 2:

$$Moisture\ content\ (\%) = \frac{M_o - M_d}{M_o} \times 100 \quad (2)$$

Where M_o is the mass of samples before drying and M_d is the mass of samples after drying. The reported results are the average results of five samples in each case.

2.5 Weight loss of samples at different temperatures

The samples were immersed in deionised water for 48 hours beforehand. The swollen samples were then dried using a wire mesh of 100 mm to remove excess surface moisture. The swollen samples are then cut into small pieces with a total of 1g and dried at 35 °C, 40 °C, 45 °C and 50 °C in a moisture analyser until a constant mass is obtained. The reported results are the average results of five samples in each case.

2.6 Biodegradability test

The samples were cut in round pieces of 3 cm diameter. Vegetable compost which was used as sol was sifted to remove large clumps and unwanted materials before being poured into a plastic box with a thickness of 8 cm. The samples were buried 4 cm below the soil and was left at humidity conditions of 75% and room temperature of about 25 °C. The samples and soil were watered twice daily to maintain the moisture level and prevent the soil and samples from drying out. Efficient microorganisms (EM-1) is mixed along with the water used to water the soil and samples with a ratio of 1 part per 500 part to increase the rate of biodegradation. The samples are then removed at different times and dried in a vacuum oven at 50 °C for 24 hours.

3. Result and discussion

3.1 The effect of citric acid concentrations on the degree of swelling

The water absorption capacity is a very important property in improving soil suitability. According to Shi et al. (2008), the polymer reaches swelling equilibrium in 24 hours. Hence, the selected time for swelling is 48 hour which is longer than the equilibrium time reported by Shi et al. (2008), to ensure equilibrium swelling takes place. Some authors such as Yoon, Chough & Park used CA as plasticizers and esterification agent where the temperature of polymer synthesis is set at 50 °C [13], [14]. However esterification only occurs at a high temperature which results in changes of structural and physical properties. Hence the moulding temperature for this starch polymer crosslinked with CA and glycerol was set at 80 °C and 150 °C to ensure

esterification process takes places. Residual-free CA in the starch polymer may act as a plasticizer, along with glycerol to form strong hydrogen bonds with the hydroxyl groups on the starch polymer. This helps in improving the interaction between molecules and increase mechanical strength and structure. However, the increase in crosslinking and esterification causes the swelling degree of polymer to decrease [15],[16].

The swelling degree of samples after being immersed in 500 ml of deionised water for 48 hours are shown in Table 2. Generally, it can be observed that the swelling degree of samples decreases when the CA concentration increases which is consistent with the results reported by Zou and Borredon [15], [16]. However, the decrease in swelling degree is more significant in SGDC1.0 compared to SGDC0.1 and SGDC0.3. This is because the small amount of CA did not cause any significant changes to the swelling degree of the samples. However, according Shi, the swelling degree of polyvinyl alcohol starch films cross linked with CA and glycerol has a maximum swelling of 31% without any addition of CA and a minimum swelling of 19.6% with 20 wt% of CA [11]. From Table 2, it can be observed that the maximum swelling degree of 143.2% occurs with SGD which is the control and a minimum swelling degree of 55.8% with SGDC1.0. This proves that starch polymer cross linked with CA and glycerol has a higher swelling degree than polyvinyl alcohol starch films cross linked with CA and glycerol. However the process temperature also plays a vital role in the swelling degree as different process temperature results in polymers with different swelling degrees in water.

It can also be noted that the addition of 1.0 g of CA to the system is not in excess as the swelling degree of SGDC1.0 decreases when compared to SGDC0.5. According to Zou et al., Borredon and Shi et al., increase in CA content will also cause a decrease in the swelling degree of polymer [15], [16]. This is due to the cross-linking of CA with starch macromolecules which forms covalent bonds to supplement the intermolecular hydrogen bonds and increase the resistibility of water. According to Ghanbarzadeh et al, further increase in CA content from 10% to 19% did not affect the water absorption of the films. However, when the CA content was increased to 20%, the water absorption of the starch films increased to 33.97 % and this is due to the plasticization effect of residual free CA. The residual-free CA fits into the polymer chains resulting in an increase in the space chain mobility and inter-chain which promotes water vapor diffusivity through the starch film and increases water vapor transmission through the films. Therefore the swelling degree increases when CA is added in excess to the system. In this research the swelling degree of samples decreases from SGD to SGDC1.0 indicating that CA is not yet in excess hence no plasticizing effect takes place.

Table 2: The effect of CA on the degree of swelling after 48 hours swelling

Samples	SGD	SGDC0.1	SGDC0.3	SGDC0.5	SGDC1.0
Swelling degree (%)	143.2±5.1	113.6±3.5	101.9±2.2	73.45±1.7	55.8±2.5

3.2 The effect of citric acid on moisture content

The moisture content of the polymer is based on the amount of moisture in the polymer at that respective time. Table 3 shows the moisture content of the samples after drying in an oven at 105 °C for 24 hours. The drying temperature is set at 105 °C to ensure that all moisture are fully removed to obtain the bone dry weight of the samples. From Table 3 it can be observed that the moisture content of samples decreases when the concentration of CA increases. SGDC1.0 has the least moisture content of 5.1% and SGD which is the control has the highest moisture content of 20.3%. This further supports the theory mentioned earlier where the increase in crosslinking due to increase in concentration of CA results in lesser amount of free hydroxyl group to be bonded with the water molecules which leads to lower moisture content. It can also be observed from Table 3 that SGDC0.5 and SGDC1.0 has lesser decrease in moisture content compared to SGDC0.1 and SGDC0.3. The moisture content of the control without any addition of CA is 20.3 % and is similar to the research of Seligra et al., where the moisture content of the control of biodegradable starch films crosslinked with glycerol without the addition of citric acid has a moisture content of 20 %.

Table 3: The effect of CA concentration on the moisture content of samples after drying at 105 °C for 24 hours

Samples	SGD	SGDC0.1	SGDC0.3	SGDC0.5	SGDC1.0
Moisture content (%)	20.3±1.2	14.1±0.8	7.4±0.3	5.5±0.7	5.1±0.5

3.3 The effect of citric acid on weight loss of samples at different temperatures

The weight loss of samples is measured relatively to time and the results are as shown in Figure 1. Generally, it can be observed from Figure 1 that the weight of polymer decreases gradually with time. The temperature chosen to conduct this test was 35 °C, 40 °C, 45 °C and 50 °C which represents the surrounding temperature of tropical countries such as Malaysia. The weight loss of polymer at the temperatures mentioned indicates the weight of moisture lost to surrounding at that specific temperature. According to Shi, starch films only exhibits a two-step decomposition pattern with the first step beginning only at 200 °C followed by 382 °C [11]. The first step of decomposition is due to the loss of loosely bounded water whereas the second step was caused by heat decomposition of the molecules. This further proves that at low temperatures from 35 °C to 50 °C, the starch polymer does not experience any thermal degradation hence the weight loss of polymer is attributed to the moisture lost to surrounding. From Figure 1 to Figure 4, it can also be observed that SGD which is the control has the highest weight loss of polymer for each temperature indicating that SGD has the highest WVP due to moisture lost to surrounding in the form of weight loss of polymer. Olivato reported that higher concentration of CA results in lower water vapour permeability [17]. This is due to crosslinking occurs at a higher degree with increasing concentration of CA resulting in increasing difficulty of water to diffuse through the film matrix and structure. However very few studies and research have been conducted on studying the rate of moisture lost to surrounding at different temperatures. Based on Figure 1 to Figure 4, it can also be noted that at 35 °C, 45 °C and 50 °C; SGDC0.3 has the least weight loss of polymer with time. SGDC0.3 is determined to be the optimum

CA concentration in increasing soil suitability as the swollen polymer samples experience a gradual but least release of water along with time. This is important in improving soil suitability as in dry conditions, polymers containing water who gradually release small amount of water with time is able to sustain plant life for a longer period of time. Even though SGD which is the control releases the most amount of moisture in the form of weight loss of polymer over time, however to improve soil suitability in dry conditions, polymers that can control release water gradually over a long period of time is more useful in sustaining plant life as the plant receives minimal amount of water over a longer period of time. SGDC0.3 also has stronger structural properties compared to SGD. According to Olivato, the tensile strength of the starch films were increased but the elongation property of the films decreased with increasing CA content. This is because the carboxyl and ester groups added to the system gives more reactive points for crosslinking reactions to take place , thus boosting the compatibility between the polymeric molecules and producing stronger resistant films [17]. This is important for biodegradable polymers applied in landscaping purposes as the samples buried below the ground might not be able to support the stress from the soil and hence a minimal tensile strength is needed for the polymer to withstand the stress from being buried in the soil. From figure 1 to figure 4, it can also be observed that even though the heating temperature increases from 35 °C to 50 °C, the difference in weight of polymer loss over time is very low for each samples with different temperatures. This proves that the small temperature difference between 35 °C to 50 °C does not affect the rate of moisture release of polymers.

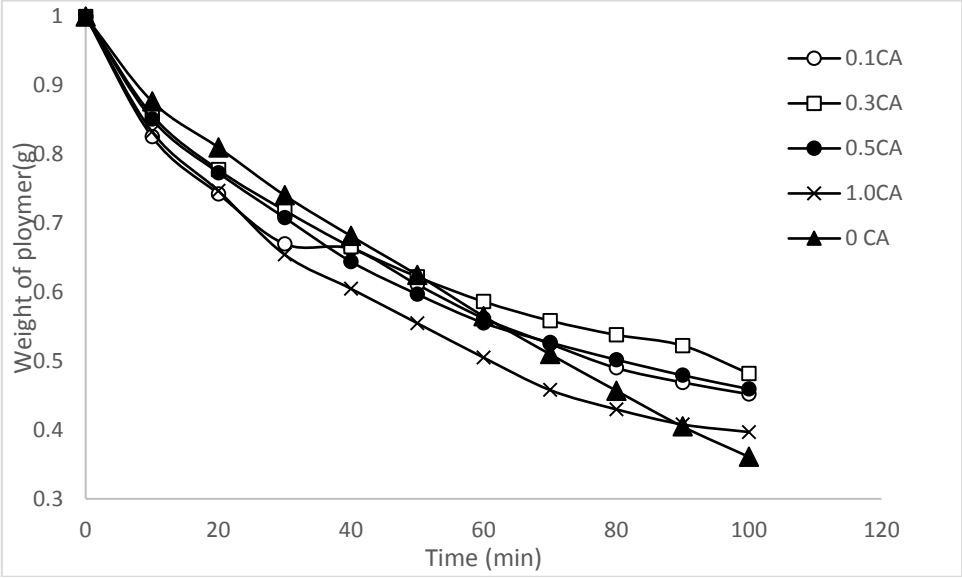


Figure 1: Change of weight of polymer with time at 35 °C

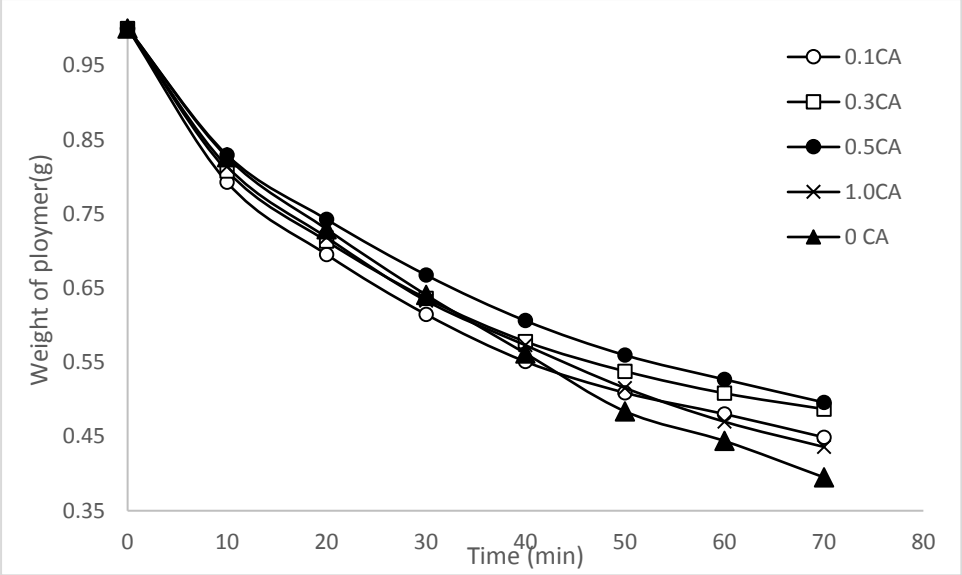


Figure 2: Change of weight of polymer with time at 40 °C

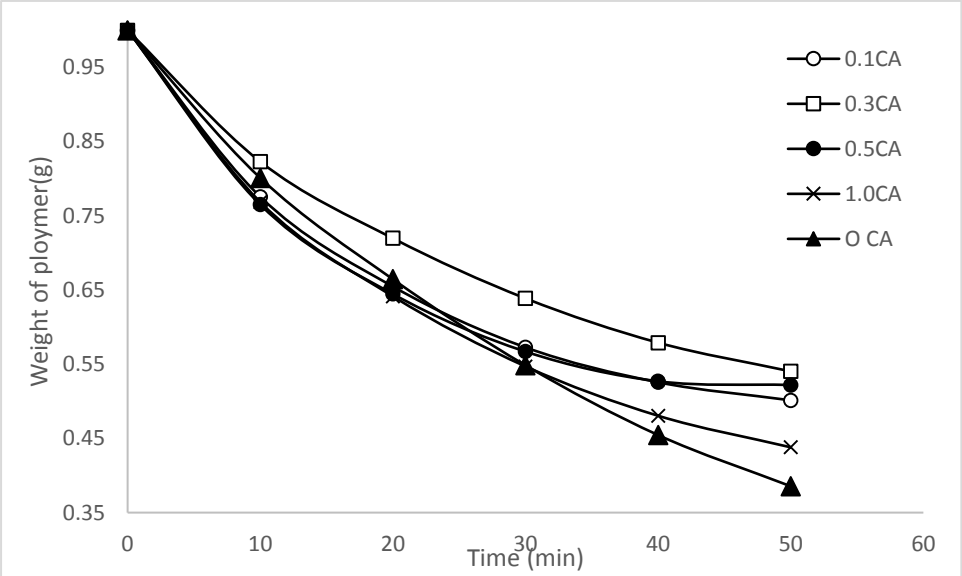


Figure 3: Change of weight of polymer with time at 45 °C

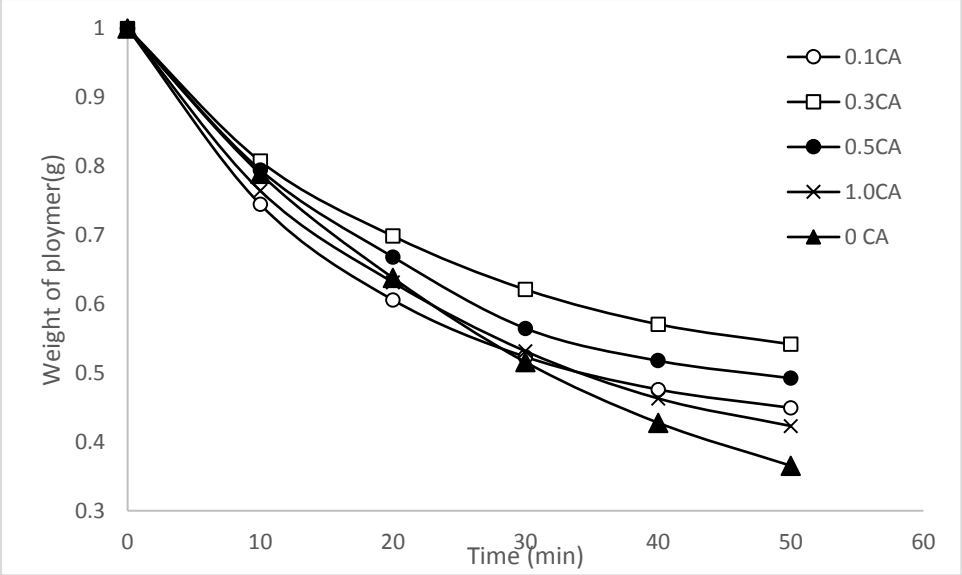


Figure 4: Change of weight of polymer with time at 50 °C

3.4 The effect of citric acid on the biodegradability of samples

Figure 5 shows the macroscopic appearance of the polymers as a function of time buried in vegetable compost. It can be observed that SGD, SGDC0.1, SGDC0.3 and SGDC0.5 showed significant degradation by the change of tonality and the formation of pores indicating the beginning of degradation at 7 days whereas SGDC 1.0 only showed significant degradation after 14 days. When the samples are buried in soil, water diffuses into the polymer which causes swelling. However, the presence of water in the polymers also promotes the growth of microorganisms and the increase of microbial attack which breaks down the structure of the polymer and increase the rate of biodegradation of polymers. Regardless of the content of CA in the samples, all samples displayed significant biodegradation at the end of the 28 day study with SGD showing the highest rate of biodegradation and SGDC 1.0 showing the least rate of biodegradation. This is due to the crosslinking of CA with starch macromolecules which forms covalent bonds to supplement the intermolecular hydrogen bonds and increase the resistibility of water.

The decrease of water vapour permeability of the polymer results in a decrease of water entering the polymer which leads to lesser microbial attack by microorganism found in the soil. According to Maiti et al., the starch PVA films shows a 69% weight loss after 30 days of degradation, however according to Figure 5, it is clear that all samples shows more weight loss based on their macroscopic appearance after a 28 day period of degradation. The usage of effective microorganisms (EM-1) also proved to have increased the rate of biodegradation of polymers. EM-1 is made up of lactic acid bacteria which has a strong fermenting effect, yeast that produces vitamins and minerals as well as phototropic bacteria. The combination of these microorganisms produces a composting effect and along with the replacement of vegetable compost as soil, the composting and biodegradation rate is increased. The ambient temperature of 25 °C with a relative humidity of 75 % is also promotes the growth of soil microorganisms for the biodegradation of samples buried in soil. The samples and soil are also watered twice daily to ensure that the moisture level in the samples and soil are maintained which is crucial for the growth of soil microorganisms and the microbial attack of

samples for biodegradation of samples to take place. The usage of chemicals used in the synthesis of the biodegradable polymer is also vital as the main chemicals which are CA, glycerol and starch are known for being organic chemicals and can biodegrade over a certain period of time.

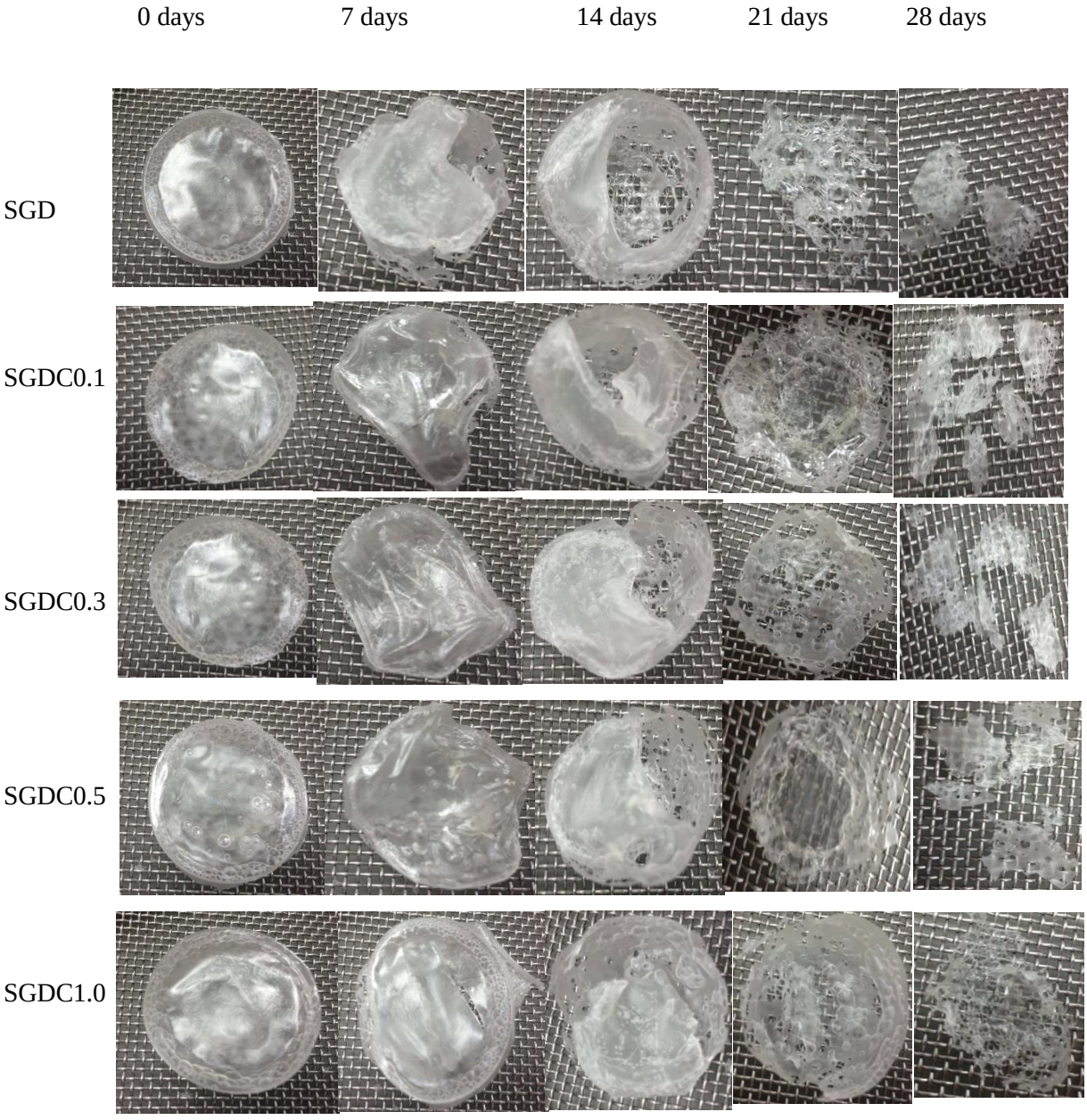


Figure 5 : Macroscopic appearance of biodegradable polymers after biodegradation test

4. Conclusions

In this research, starch based polymer was crosslinked with citric acid to study the effect of citric acid on the various properties of the polymer. The data was gathered experimentally and also compared with the results obtained from other research and literature to determine the validity of the results. SGD which is the control has the highest swelling degree of 143.2% whereas SGD1.0 has the lowest swelling degree of 55.8%. The swelling degree of samples decreases with increasing CA content. This is

due to the cross-linking of CA with starch macromolecules which forms covalent bonds to supplement the intermolecular hydrogen bonds and increase the resistibility of water. Regarding the effects of CA on the moisture content of polymer, SGDC1.0 has the least moisture content of 5.1% and SGD which is the control has the highest moisture content of 20.3%. This further supports the theory mentioned earlier where the increase in crosslinking due to increase in concentration of CA results in lesser amount of free hydroxyl group to be bonded with the water molecules which leads to lower moisture content. The effect of CA on the release of moisture from the polymer was also studied where the rate of release of moisture was assumed to be the rate of weight loss of polymer samples where no thermal degradation takes place. At temperatures of 35 °C, 45 °C and 50 °C; SGDC0.3 has the least weight loss of polymer with time. SGDC0.3 is determined to be the optimum CA concentration in increasing soil suitability as the swollen polymer samples experience a gradual but least release of water along with time. SGD which is the control has the highest release of water over time and agrees with the theory proposed by other researchers that the without the addition of CA, no crosslinking occurs within the structure of the polymer and hence water vapour permeability is highest in SGD. The effects of CA on the biodegradability of the polymer was also studied where all samples displayed significant biodegradation at the end of the 28 day study with SGD showing the highest rate of biodegradation and SGDC 1.0 showing the least rate of biodegradation based on macroscopic appearance. This is due to the crosslinking of CA with starch macromolecules which forms covalent bonds to supplement the intermolecular hydrogen bonds and increase the resistibility of water. The decrease of water vapour permeability of the polymer results in a decrease of water entering the polymer which leads to lesser microbial attack by microorganism found in the soil.

It can be concluded that the crosslinking of CA with starch based polymers help to improve soil suitability as it has a better control release of water where minimal water is gradually release over a period of time. Furthermore, the addition of CA gives structural strength to the biodegradable polymer which is essential to withstand stress from being buried beneath the ground when used in landscaping purposes. Despite the fact that crosslinking of CA with the polymer decreases the rate of biodegradation, however all samples showed significant biodegradation at the end of the 28 day study indicating that the starch based biodegradable polymer crosslinked with CA and glycerol is completely biodegradable based on macroscopic appearance.

Future work includes carrying out tests and experiments on samples in the soil with plant life to observe how the starch polymers improve the soil suitability in real case scenarios.

References

[1] Ekebafe, L.O., Ogbeifun, D.E. & Okieimen, F.E., 2011. Polymer Applications in Agriculture. *Biokemistri*, 23(2), pp.81–89.

[2] Galdeano, M. C., Mali, S., Grossmann, M. V. E., Yamashita, F., & García, M. A. (2009). Effects of plasticizers on the properties of oat starch films. Materials Science and Engineering C, 29, 532–538.

[3] Mali, S., Sakanaka, L. S., Yamashita, F., & Grossmann, M. V. E. (2005). Water sorption and mechanical properties of cassava starch films and their relation to plasticizing effect. Carbohydrate Polymers, 60, 283–289

[4] Sagar A.D., Merille E.W. Properties of fatty-acid esters of starch. J Appl Polymer Sci. 58, 1647, 1995.

[5] Yin, Y., Li, J., Liu, Y., & Li, Z. (2005). Starch crosslinked with poly(vinyl alcohol) by boric acid. Journal of Applied Polymer Science, 96, 1394–1397.

[6] Sreedhar, B., Chattopadhyay, D. K., Karunakar, M. S. H., & Sastry, A. R. K. (2006). Thermal and surface characterization of plasticized starch polyvinyl alcohol blends crosslinked with epichlorohydrin. Journal of Applied Polymer Science, 101, 25–34.

[7] Ramaraj, B. (2007). Crosslinked poly(vinyl alcohol) and starch composite films. II. Physicomechanical, thermal properties and swelling studies. Journal of Applied Polymer Science, 103, 909–916.

[8] Zhai, M., Yoshii, F., & Kume, T. (2003). Radiation modification of starch-based plastic sheets. Carbohydrate Polymers, 52, 311–317

[9] Follain, N., Joly, C., Dole, W. P., & Bliard, S. H. C. (2005). Properties of starch based blends. Part 2: Influence of poly vinyl alcohol addition and photocrosslinking on starch based materials mechanical properties. Carbohydrate Polymers, 60, 185–192.

[10] Reddy, N. & Yang, Y., 2010. Citric acid cross-linking of starch films. *Food Chemistry*, 118(3), pp.702–711.

[11] Shi, R. et al., 2008. The effect of citric acid on the structural properties and cytotoxicity of the polyvinyl alcohol / starch films when molding at high temperature. , 74, pp.763–770.

[12] Menzel, C. et al., 2013. Molecular structure of citric acid cross-linked starch films. *Carbohydrate Polymers*, 96(1), pp.270–276.

[13] Yoon, S. D., Chough, S. H., & Park, H. R. (2006a). Properties of starch-based blend films using citric acid as additive. Journal of Applied Polymer Science, 100, 2554–2560.

[14] Yoon, S. D., Chough, S. H., & Park, H. R. (2006b). Effects of additives with different functional groups on the physical properties of starch/PVA blend film. Journal of Applied Polymer Science, 100, 3733–3740.

[15] Borredon, E., Bikiaris, D., Prinos, J., & Panayiotou, C. (1997). Properties of fatty-acid esters of starch and their blends with LDPE. Journal of Applied Polymer Science, 65, 705–721.

[16] Zou, G. X., Qu, J. P., & Zou, X. L. (2007). Optimization of water absorption of starch/ PVA composites. Polymer Composites, 28, 674–679

[17] Olivato, J.B. et al., 2012. Effect of organic acids as additives on the performance of thermoplastic starch / polyester blown films. *Carbohydrate Polymers*, 90(1), pp.159–164.

eureca 2016 – Conference Paper
Paper Number 2CE15

DRYING CHARACTERISTICS AND PRODUCT QUALITY OF *CASSIA ALATA* (CA)

Wei Chuen Khaw[1], ChienHwa Chong[1]*, Jap Meng Jee[2]
School of Engineering, Taylor's University, Taylor's Lakeside Campus,
School of Biosciences, Taylor's University, Taylor's Lakeside Campus,
No. 1 Jalan Taylor's, 47500, Subang Jaya, Selangor DE, Malaysia

*Corresponding Author: ChienHwa.Chong@taylors.edu.my

Abstract

The objective of this study was to study the drying behaviour of *Cassia alata* leaves and colour change of dried leaves in terms of chlorophyll contents. This involved the investigation of drying rates, visual attributes, and effect of bioactive compounds toward chlorophyll retention. The colour attributes were compared in regard to the dried sample in three different drying temperatures using convective drying method. In addition, the experimental data was used to compare with the predicted data from six semi-theoretical thin-layer drying models to determine the goodness of fit in terms of determination coefficient (R^2), chi-square (X^2), and root mean square error (RMSE). It was found that in this study, the using of convective drying method on *Cassia alata* leaves with higher temperature enhance moisture diffusion in the falling rate period. However, air velocity and relative humidity of the surrounding are the dominant factor on moisture reduction during initial transient period. Moreover, Midilli-Kucuk model was found to be the suitable model that best fitted to the experiment data. Judging from the quality findings on chlorophyll contents in dehydrated samples at different drying temperature, it was found that enzymatic reaction is the major reason that causes colour change of leaves samples. In addition, aloe-emodin is found to be the bioactive compounds that improve the colour retention of *Cassia alata* leaves.

Keywords: *Cassia alata*, Aloe-emodin, herb drying, colour attributes, peroxidase

1.Introduction

Cassia alata L. Roxb. (or *Senna alata (L.) Roxb.*), also known as candle tree or ringworm is a medical herbal plant that belonging to the plant family of Fabaceae. *Cassia alata* is reported to show positive result for antibacterial activity, antifungal activity, anti-inflammatory activity, and antipyretic activity. Few patent applications for the use of different

parts of *Cassia alata* have been made that claiming anti-ageing [1] properties and treatment of beriberi and athlete's food [2].

Drying is one of the oldest method to preserve fruits, meats, and vegetables which ensure microbial safety of biological product due to the fact that microbial spoilage and deterioration reactions are minimized after moisture content is lowered [5]. In addition, drying process is also crucial in industrial production as the tissue of dried material will be brittle and results in rapid cell wall breakdown which is easy for grinding and homogenizing for extraction process [6]. By understand the drying behaviour of different types of materials, it can helps to improve the drying process through shorten the drying time or operate at the optimum conditions to assure highest amount of bioactive compounds are preserved.

Convective drying (CD) is consider the most popular method to reduce moisture content of fruits, vegetables, and herbs. However, few disadvantages of this drying method such as long drying times and high temperatures operating condition cause degradation of important nutritional substances and colour alteration [3]. Sun drying (SD) gives a product rich in colour and translucent appearance but time-consuming and greatly expose to environmental contamination [4]. Microwave drying (MD) has inherent advantages over conventional drying in terms of drying time and bioactive compounds loss. Previous study reported microwave drying is both cost-effective and feasible [5][6]. However, the inhomogeneity of a microwave field along with the heterogenic structure of dried material will result in occurrence of hot spots that lead to overheating [7]. Mathematical modelling of the drying processes and equipment allow operator to optimize the operation condition based on the prediction of the process parameters (drying rate, moisture ration, air velocity, etc) as a function of time during drying process in order to preserve the highest amount of bioactive compounds in the product [8].

Drying behaviour of various types of materials is unable to be predicted and must be determined by experimentally. The data obtained from the drying process (weight, moisture content, etc) are later converted into the rate-of-drying curve as drying rate versus free moisture content. The experimental drying curve then compare with Van Meel's model (Figure 1.) to explain the drying behaviour of the specific material. . The model assumed that for any sample moisture content, that is a corresponding specific drying rate that independent of the external drying conditions and relative to the initial unhindered drying rate. In unhindered region, the surface of the material is initially wet with a continuous film of unbound water present on the drying surface. For porous material, most of the water molecules evaporated from the interior of the material and surface temperature is approximately the same as wet bulb temperature [7]. At the critical point, the material surface is no longer wetted due to insufficient water molecules and the wetted area decreases gradually until completely dry and reaches first falling rate region. Follow by that, the vaporized water slowly move through the material into air. The time taken for water removed in falling rate region is relatively long [26]. On the other hand, vacuum drying is able to drive moisture toward the material surfaces by reduce boiling point of water and decreasing the external pressure that simulate the high-temperature effect [10]. This helps to reduce the drying time and avoid dried material damaged from overheat. Apart of that, freeze drying involved sublimation drying (primary drying) and desorption drying (secondary drying) that control the residual moisture final (RMF) at 5% generally [11]. For microwave drying, water and other polarized molecules are heated by microwave radiation, no heat transfer occur and temperature of the center of material is immediately increased thus quickly reach the sublimation process. The temperature of the dried layer (center layer of the sample) is not

affected by the temperature difference between the material surface layer and dried layer which helps to maintain high temperature inside the sample during drying process [11].

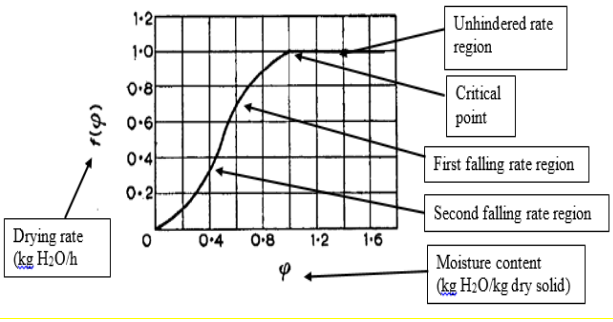


Figure 1. Dimensionless rate curve of Van Meel's model with remarks

The typical structure of leaf consists of guard cells underlying the epidermis, outer layer of leaf. Guard cell control the transportation of water vapor and carbon dioxide through close and open the stomata. Nutrients and water store inside the cells also loaded with chloroplast which hold the most abundant pigments in leaf, chlorophyll. The chlorophyll, a and b, are produced for photosynthesis process and control the absorbance of light as source of energy for the plant. The amount of chlorophyll inside the cell determines the colour of leaf and show the biochemical information of the plant. Leaf colour change occur during the loss of chlorophyll and the production of other pigment such as anthocyanins, or the remaining pigment is reveal such as carotenoids [12]. The microscopic image of internal cell structure in fresh *Cassia alata* leaf has been shown in Figure 2. The pigment degradation kinetics is one of the major factor to determine the dried product quality. Given that pigment influence the colour of the product and has considerable psychological influence toward consumer, it is crucial to operate the drying process at the optimal condition. There was a studies related to the chlorophyll degradation in peel and flesh of the apples under freeze-drying process, the result concluded that apple peel store the highest amount of chlorophyll than flesh of apple [13]. Moreover, a recent study shows that microwave heat process (1000w, 34s) integrated with pasteurisation gives a better preservation of chlorophyll and maintain natural colour of kiwifruit in comparison with conventional heat process [14]. Similar study was carried out on seasoning herb, dill (*Anethum graveolens)*, by using hot air dryer, low-humidity dryer, infrared and hot air dryer, and radiofrequency dryer. The result shows that low humidity air dryer (50℃, 28-30% RH) able to gives highest chlorophyll retention and exhibited greater greenness in comparison with other drying methods [15]. There are many other chlorophyll degradation during drying process studies on vegetables [16-17] and dried seed [18].



(a) (b) (c)

Figure 2. Microscopic image of internal cell structure of fresh *Cassia alata* leaf: *(a)* x4, *(b)* x10, *(c)* x40, stomata are shown in the red circles.

Although there are studies on the medicinal and physico-chemical properties of *Cassia alata*, chlorophyll loss with respect to drying process has not been investigated. Apart from that, it is not clear that what temperature and drying method is the optimum condition for *Cassia alata* dehydrated by convective drying method. Hence, with references to the findings and research gap, the objective of this study is aims to (1) Select a semi-theoretical model that best suited the drying kinetics of *Cassia alata* leaf, (2) Study the stability of chlorophyll during convective drying and by assessing the amount of chlorophyll in the dried product under different drying temperatures.

2. Material and methods

2.1.Sample preparation

Cassia alata plants were purchased from a local herbal plant supplier (Klang, Selangor, Malaysia). Leaves of herbs were extracted and dirt were cleaned off from the surface of the leaves. The initial moisture content of fresh samples was measured 7.84 g H_2O/g DM (dry mass). The initial moisture content of fresh samples was determined using an infrared moisture analyser (Precisa, XM50, Switzerland) with an accuracy of 52 ± 0.001 g at 105℃. The samples of *Cassia alata* leaves weighing about 5g with an average thickness of 0.9 cm underwent bone drying by using a drying oven (Memmert, UN75, Germany). The operating condition is 105℃ for 24 hours duration according to ASTM standard (D1348-94) to obtain the bone dry weight [19].

2.2. Drying procedure

The *Cassia alata* leaf samples were dried in a drying oven (Memmert, UN75, Germany) at 60℃, 70℃, and 80℃ hot air temperatures. Hot air temperature were measured by a thermal sensor attached inside the oven with an accuracy of 0.1℃. The relative humidity of hot air were measured by using a digital hygrometer (ShaShinKi, ETP101, Malaysia) and measured as 50-60% RH with an accuracy of ±1%. The air velocity approaching the samples was measured by an anemometer (Rotronic, D5-U-2, USA) and average velocity was 1.4 ± 0.01 m/s. 5g of the sample leaves was used for each test and a single layer of samples was spread evenly on the trays.

The weight loss of the samples was measured by using an analytical balance (A&D, HR250AZ, USA) with a range of 0-252 g with error of ±0.0001 g. The measurement was carried out at an interval of 15 min for the first 60 min of drying, and continue by hourly interval until the moisture content in dried samples decreased to approximately 1.00 g H_2O/g DM.

2.3 Drying models

The moisture content ratio, M_R was determined from Eq. (1):

$$M_R = \frac{M_t - M_e}{M_o - M_e} \quad (1)$$

where M_t denotes moisture content at specific drying time (g H_2O/g DM), M_e denotes the equilibrium moisture content (g H_2O/g DM), and M_o denotes the initial moisture content (g H_2O/g DM). The equilibrium moisture content was calculated at the final stage of drying process as an asymptotic value of the function fit to the experimental point using Microsoft Excel Solver (Microsoft Office, USA).

The moisture content of dried sample can be expressed in Eq. (2):

$$M = \frac{W_o - W_f}{W_f} \quad (2)$$

where W_o is the initial weight of the sample (g) and W_f is the bone dry weight (g).

Follow by Fick's second law of diffusion, the effective diffusivity can be calculated in the following equation [20]:

$$M_R = \frac{8}{\pi^2}\left(e^{D_{eff}t(\frac{\pi}{2l})^2}\right) \quad (3)$$

Taking logs and express the equation as:

$$\ln M_R = \ln\frac{8}{\pi^2} - D_{eff}\left(\frac{\pi}{2l}\right)^2 t \quad (4)$$

The slope of the line from $\ln M_R$ against t is shown as:

$$\text{Slope} = -D_{eff}\left(\frac{\pi}{4l}\right)^2 \quad (5)$$

The effective diffusivity, D_{eff} can also be determined by the following equation (3) [21]:

$$D_{eff} = D_o \exp\left(-\frac{E_a}{T_a R}\right) \quad (6)$$

where E_a is activation energy of the moisture diffusion (kJ/mol), D_o is the Arrhenius factor (m^2/s), R is the universal gas constant, and T_a is the ambient temperature of the surrounding drying environment (K). The activation energy is determined by plotting a ln (D_{eff}) versus $1/T_a$ diagram using regression analysis techniques.

The drying rate of the samples can be calculated using the following equation:

$$D_R = \frac{M_t - M_{t+\Delta t}}{\Delta t} \quad (7)$$

where D_R is drying rate (g H_2O/ g DM)

2.4 Extraction of chlorophyll and estimation of chlorophyll a/b

Extraction of chlorophyll and estimation of chlorophyll a/b concentrations were carried out following by the simple one-step method of Arnon [22]. The adsorption of leaf pigment was strongly correlated with chlorophyll a/b concentration [23], thus this method is proved to be useful for monitoring chlorophyll concentration in *Cassia alata* leaf. The fresh and dried samples were weighted 0.17g, major veins or fibrous tissue were removed and the samples were macerated with 80% acetone (10ml) in a pestle and mortar. The tissue was pulverized completely and becomes leaf homogenate. The leaf homogenate was filtered with filter paper and filtrate was collected in a test tube. The filtrate was transfer into a clean cuvette for spectrophotometric analysis using a spectrophotometer (Shimadzu, UV-2401, Japan). Configure the wavelengths to 663 nm and 645 nm and recorded the absorbance values. The absorbance values were inserted into the Arnon's simultaneous equation (equation 5-7) for the assay of chlorophyll a and b. All determination were performed in triplicated (n=3).

$$[\text{Chlorophyll a}]\ (\text{mg Chl a/g leaf tissue}) = [(12.7 \times A_{663}) - (2.6 \times A_{645})] \times \text{ml acetone/mg leaf tissue} \quad (8)$$

$$[\text{Chlorophyll b}]\ (\text{mg Chl b/g leaf tissue}) = [(22.9 \times A_{645}) - (4.68 \times A_{663})] \times \text{ml acetone/mg leaf tissue} \quad (9)$$

$$\text{Total chlorophyll} = [\text{Chlorophyll a}] + [\text{Chlorophyll b}] \quad (10)$$

2.5 Mathematical modelling

The thin-layer drying curve models are used for estimation of drying time and generalize drying curve of a specific product based on the changes of moisture content of the

product at certain relative humidity and temperatures. The thin-layer drying curve models used in the drying experiment consists of semi-theoretical and empirical types. Semi-theoretical model is derived from modified Fick's second law or Newton's law of cooling with fewer assumptions and constants. The empirical models is similar to semi-theoretical model which strongly depend on the specific experimental conditions and can be easily applied in drying simulation.

The semi-theoretical and empirical models listed in Table 1. are reported to be suitable for various agricultural products [24] and widely used by researchers for thin-layer drying experiment. In addition, a new model developed recently [25] is used for modelling in comparison with the traditional models. Evaluation criteria such as determination coefficient (R^2), chi-square (X^2), and root mean square error (RMSE) were used to evaluate the goodness of fit in order to choose the best thin-layer drying curve equation for *Cassia alata* leaves under this drying methods and conditions. The equations of the evaluations criteria have been shown in Eq. (11), (12), and (13).

Table 1. Thin-layer drying curve equations

Eq. No.	Model name	Model equation	References
1	Lewis/Newton	$MR = exp\ (-kt)$	[26]
2	Henderson & Pabis	$MR = a\ exp\ (-kt)$	[27]
3	Wang & Singh	$MR = 1 + at + bt^2$	[28]
4	Page	$MR = exp\ (-kt^n)$	[29]
5	Midilli-Kucuk	$MR = a\ exp(\ kt^n) + bt$	[30]
6	New model	$MR = a\ exp\ (-kt^n) + c\ exp(\ -gt^n)$	[25]

a,b,c drying coefficients, *k,g,n* drying constants, *MR* moisture ratio, *t* drying time

Commented [CCH1]: Elaborate more about the models selected

$$R^2 = \frac{\sum_{i=1}^{n}(MR_i - MR_{pre,i})\ x\ (\sum_{i=1}^{n}(MR_i - MR_{exp,i})}{\sqrt{\left[\sum_{i=1}^{n}(MR_i - MR_{pre,i})^2\right] x \left[\sum_{i=1}^{n}(MR_i - MR_{exp,i})^2\right]}} \quad (11)$$

$$X^2 = \frac{\sum_{i=1}^{n}(MR_{exp,i} - MR_{pre,i})^2}{N-n} \quad (12)$$

$$RMSE = \left[\frac{1}{N}\sum_{i=1}^{N}(MR_{pre,i} - MR_{exp,i})^2\right]^{1/2} \quad (13)$$

where $MR_{exp,I}$ is the experimentally observed moisture ratio, $MR_{pre,I}$ is the *i*-th predicted moisture ratio, N the number of observations and n is the number of constants.

2.6 Statistical analysis

One-way analysis of variance (ANOVA) analysis was conducted using SPSS Statistic version 21.0 (IBM Inc, USA) to compare the means of chlorophyll content of *Cassia alata*

leaves. Significance was defined at p = 0.05 and Turkey High Significant Difference (Turkey's HSD) test was used to separate the mean differences. The experiments were carried out with three repetitions and results were presented as mean ± standard deviation. The coefficients and constants from the thin-layer drying model equations in Table 1 were determined using non-linear least square regression with Table Curve 2D Window v5.01 (Jandel Scientific Software, USA). The correlation coefficient (R^2), root mean square error (RMSE), and chi-square (X^2) were used to determine the goodness of fit of predicted and experimental data.

3. Result and discussion

3.1 Drying kinetics

The drying curve of *Cassia alata* leaves dehydrated by convective drying has been shown in Figure 3. The subsequent measurement of the weight of the leaf samples showed that its equilibrium moisture content was obtained within 2 h of convective drying. The equilibrium moisture content of the samples at 80℃ amounting to 0.024 g H_2O/ g DM was much lower than dried samples at 60-70℃ amounting to 0.144 and 0.241 g H_2O/ g DM respectively. The drying rates for each temperatures (60, 70, and 80℃) were recorded within the range of 0.0017-0.00028 g H_2O/ g DM, 0.0023-0.00027 g H_2O/ g DM, and 0.0016-0.00029 g H_2O/g DM respectively. The range of drying rates at 70℃ (0.0023 g H_2O/ g DM) was larger than 80℃ (0.0016 g H_2O/g DM) at the beginning which may cause by the water residual on the surface of leaf samples. This phenomena was also reported from other sample such as *Moringa Oleifera* leaf [31]. The higher drying rates were observed in the following drying process at 80℃ than other temperatures owing to greater temperature difference which drives out the water molecules from the leaf samples [32]. According to the drying curve, it showed a rapid loss of moisture content in initial transient period (85-61% moisture loss) for three different temperatures due to the air flow accelerates unbound water on the wetted surface uptake by air. When the moisture contents of three different temperature reached the critical points (0.2-0.5 g H_2O/ g DM), it showed that high drying temperature (80℃) had lower moisture content (0.219 g H_2O/ g DM) than low drying temperatures (60 and 70℃; 0.557 and 0.362 g H_2O/ g DM respectively). Following by the falling rate period, the moisture content loss and changes of drying rate were slowed and controlled by diffusion from the interior of the leaf tissue. In this period, the internal resistance to moisture diffusion was high due to various factors such as structure deformation (shrinkage, crust formation) and water potential difference [33]. Moreover, the rapid removal of surface moisture create a dried surface on the sample and drying process enter into a constant diffusion rate period [34]. Based on the observation from the results, it showed that air velocity and relative humidity are the major factors on the drying efficiency at the early stage of drying process while the moisture content is high and air temperature play a dominant role at the end of drying process.

The moisture ratio versus drying time is plotted in Figure 4. From the graph, it was found that moisture loss in initial transient period is rapid in correspond to an exponential decrement in moisture ratio for convective drying. It was observed that convective drying at 70℃ reduced the drying time by approximately 50 and 40% in comparison with 60 and 80℃ respectively in order to reach the moisture ratio of 0.05 at the initial transient period. The results is in agreement with the observation from Figure 3 and proved that air temperature is not a predominant factor in the early stage of drying process. Apart from that, it also showed that higher moisture content and less structural deformation improve the drying efficiency of

convective drying method. Once the drying time reached the critical point, it showed that the gap of drying time was lesser and becomes constant.

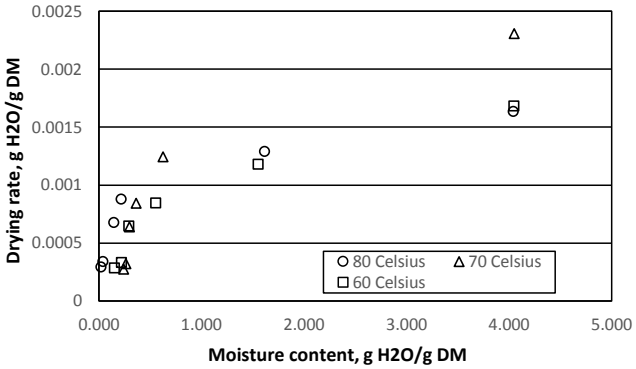


Figure 3. Drying rate as a function of moisture content for hot air drying of *Cassia alata*

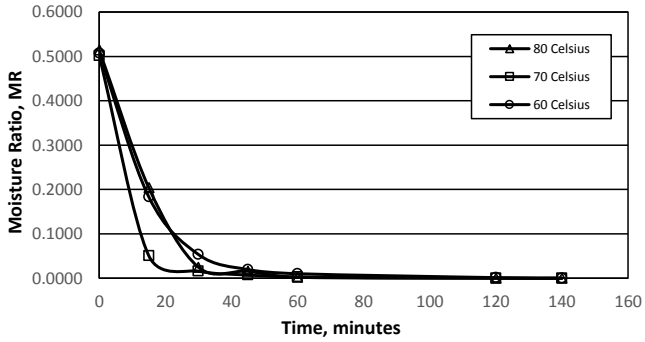


Figure 4. Moisture ratio as a function of time for hot air drying of *Cassia alata*.

The effective diffusivities (D_{eff}) characterized the moisture diffusion property that involves vapour diffusion, liquid diffusion, molecular diffusion, and so on [35]. It has a major influence toward the drying rate in the falling rate period and higher effective diffusivity results in lower internal resistance to moisture diffusion in the dried surface [36]. The slope of dried leaves at 60, 70, and 80℃ obtained from the gradient of the graph shown in Figure 5 were 3.43, 3.79, and 4.38 h^{-1}, respectively. The coefficient of determination (R^2) for each straight lines were 0.956, 0.964, and 0.976 respectively. Hence, the effective diffusivities from Eq. (5) for 60, 70, and 80℃ were 1.39 x 10^{-4}, 1.54 x 10^{-4}, and 1.78 x 10^{-4} m^2/s, respectively. The result showed that the effective diffusivities increased with temperature due to high evaporation of water molecules from the interior of leaf sample until it reach the maximum value [35]. The effective diffusivities of *Cassia alata* leaf samples were found to be higher than fruit and vegetable such as apple (15.3-3.22 x 10^{-9} m^2/s) [37], carrot (9.0 x 10^{-10} to 3.3 x 10^{-9} m^2/s) [32],

and Rambutan (1.34-4.36 x 10^{-10} m^2/s) [38]. In comparison with the literature results, it showed that outer surface texture for leaf is more porous than the selected fruit and vegetables which promoted the high capillary force that result in greater water diffusion [39].

The activation energy (E_a) and diffusivity constant (D_o) obtained from Figure 6 were 12.05 kJ/mol and 0.011 m^2/s, respectively. According to the diffusion model governed by Fick's law, the average amount of required thermal energy (Q) for this drying process can be calculated in the following equation [40]:

$$Q = (0.6\ m/\mu)E_a \quad (14)$$

where μ is the molecular mass of water (18 g/mol) and E_a is activation energy of the sample (kJ/mol). Thus, the energy required for drying 1000 g/1 kg of *Cassia alata* leaves was approximately 4.02 x 10^5 J.

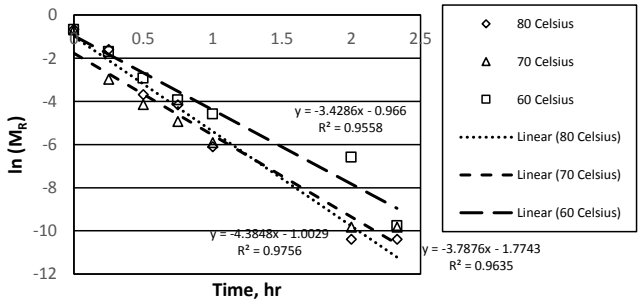


Figure 5. Experimental moisture ratio at 80℃, 70℃, and 60℃ drying temperatures

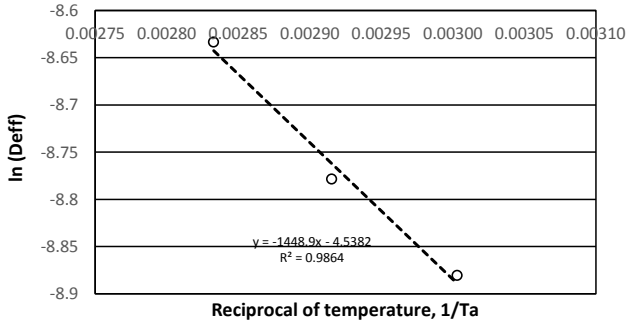


Figure 6. Correlation between effective diffusivity and drying temperatures

3.2 Fitting of drying curves

The experimental moisture ratio observed at the drying experiment were fitted to the semi-theoretical thin layer drying models listed in Table 1. The comparison criteria used to evaluate the goodness of fit are namely R^2, RMSE, and X^2 by using equations 10-12. The highest R^2 and lowest RMSE and X^2 were obtained from Midili-Kucuk model within different temperatures. The R^2, root mean square error (RMSE), and chi-square (X^2) values changed from 80 to 60℃ were 0.9992 to 0.9998, 0.0053 to 0.0025, 0.0045 to 0.0023, respectively. As a result, Midilli-Kucuk model was selected as the suitable model to express the thin-layer drying behaviour of *Cassia alata* leaf.

According to Figure 7, it showed the variations of experimental and predicted moisture ratio changes with drying time at three operating temperatures. From the graph, it showed that the model had a good conformity between the data. As a result, it suggested that the proposed model was able to describe the drying behaviour of *Cassia alata* leaf in convective drying method. The drying variables of the Midili-Kucuk model such as constant (k/min^{-1}, n) and coefficients (a,b) were regressed against the drying temperature. The multiple combinations of different parameters with highest R^2 were used in the model. The equation for the coefficient and constants were as follow:

$$a = -0.0024T^2 + 0.3678T - 13.272 \text{ , } b = 0.0025T^2 - 0.3808T - 14.216 \quad (15)$$

$$k = -0.0045T^2 - 0.6220T - 21.222 \text{ , } n = 0.0079T^2 - 1.0815T + 37.479$$

Figure 8 indicated the comparison of the predicted and experimental moisture ratio values with R^2 value of 0.9978. This showed that the predicted data from the established model was in agreement with the experimental data.

The drying constant (k) on Midilli-Kucuk model is important to describe the drying behaviour of the drying sample. The drying constant value increased with the increased in drying temperature. Therefore, it showed that higher k value improve the drying rates through higher moisture diffusion rates during the falling rate period [29]. The coefficient a and b from the model are critical moisture ratio and constant drying rate with reference to time, respectively [41]. The moisture ratio decreased with the increased of b value per minutes, and the coefficient a value is the critical point between first and second falling rate periods. The n value is the power order of drying time that increased with drying temperature.

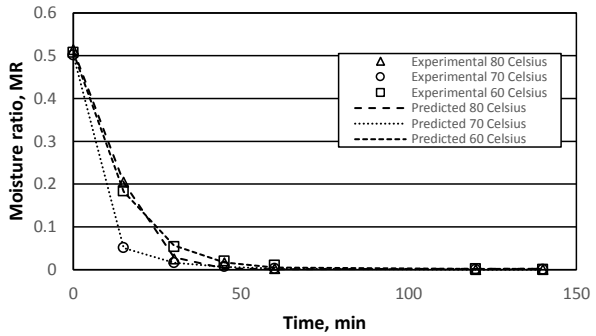


Figure 7. Drying curve of the Midili-Kucuk model equation data and experimental data

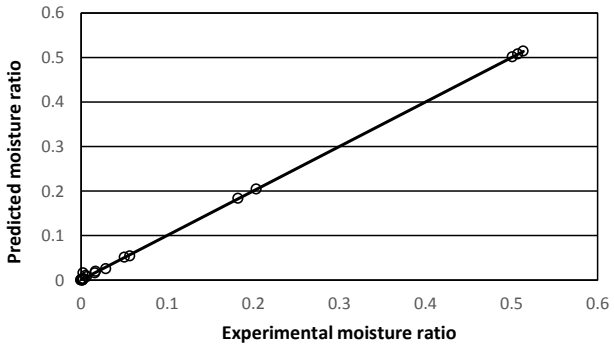


Figure 8. Comparison of predicted and experimental moisture ratio with Midili-Kucuk model

3.3 Effect of different drying temperatures on colour of dehydrated leaves

The images of fresh and dehydrated using different drying temperatures have been shown in Figure 9. The visual observation of dried leaves at 80℃ appear darker in comparison with the lower drying temperatures. The visual observation was in corresponded with the measurement chlorophyll content that listed in Table 3. According to the data in Table 3, it showed that chlorophyll a and b in *Cassia alata* leaves range from 0.98 to 1.38 mg/mg leaf to 0.58 to 2.32 mg/mg leaf, respectively. Moreover, the total chlorophyll of the sample (combination of chlorophyll a and b) fall in a range of 1.56 to 3.70 mg/ mg leaves.

A one-way between group analysis of variance (ANOVA) was carried out in order to investigate the impact of temperature had on the chlorophyll contents in the samples. Inspection of the skewness, kurtosis, and Shapiro-Wilk statistics indicates the assumption of homogeneity of variance was not violated. The ANOVA proved that was significant difference between groups, thus indicated that the chlorophyll contents was under influence of the temperatures. The Post-hoc analyses with Turkey's HSD (with a significant level of 0.05) showed that

chlorophyll a in fresh samples was significantly lower than the dried samples. However, there was no significant difference between chlorophyll b in fresh sample and dried sample at 80℃, nor between the total chlorophyll. Moreover, the results also showed that there were no significant difference between dried samples at 70 and 60℃ in terms of three different factors.

Chlorophyll is the most abundant pigment and consider the basic pigment that contribute to the green colour appearance of leaf. Chlorophyll is a lipophilic compounds which synthesized and accumulated in chloroplasts and chromoplasts within the plant cells [42]. It is known that chlorophyll is susceptible to acids, temperature, light, oxygen, and enzymes which contribute to the degradation process [36]. Degradation of chlorophyll in thermal process has been reported as a result of formation of pheophytins and pyropheophytins. During the thermal process, the magnesium in the chlorophyll ring is replace by two hydrogen ions and converted into olive brown pheophytins in acidic medium. Further heating will convert pheophytins into pyropheophytins by losing carbomethoxy group from pheophytins and enhance the colour intensity [43]. However, previous work also suggested that pheophytins can also be formed under condition other than thermal processing under long storage time at room temperature (25℃) [44].

Enzyme chlorophyllase (chlorophyll-chlorophyllide hydrolase; EC 3.1.1.14) is the catalyst for the hydrolysis of chlorophyll a/b (more rapid in the conversion of chlorophyll a) into chlorophyllides and phytol under temperature of 65-75℃ and pH 7.5. Studies showed that chlorophyllase (particularly gene GbCLH) is high in green leaves and reduce during the yellowing process, thus suggested chlorophyllase had significant impact on the homeostasis rather than the de-greening process [45]. In contrast, enzyme peroxidase was reported as one of the enzyme that contribute to the degradation of chlorophyll and de-greening process under peroxidase-hydrogen peroxide system. Peroxidase activity was reported increased in yellowing process of leaves and consider as a major factor in de-greening process of leaves. Peroxidase requires flavonoid for oxidation to degrade chlorophyll and L-ascorbic acid and β-carotene (located in chloroplast) which believed to be the protective layer on chlorophyll through inhibiting the peroxidase-hydrogen peroxide system with its antioxidants properties [46]. In addition, the β-carotene was reported decreased with the increased with ethylene from the experiment.

According to Table 3, the fresh samples showed the lowest chlorophyll contents in comparison with the dried samples. The observation indicated that unbound water and moisture inside the leaves had reduced the adsorption of chlorophyll compounds in UV-irradiation test. The observation was supported by the fact that water provide a protective effect toward chlorophyll which avoid the chlorophyll compounds from releasing to the surrounding [47]. The results in Table 3 showed that the total chlorophyll contents had significantly reduced from 60 to 80℃. This observation was also supported by the visual attributes from Figure 9. The relationship between colour change of leaves and chlorophyll contents can be related to the plant hormone response to abiotic stress from environment. In this case, phytohormone abscisic acid (ABA) was believed to be released to prevent water loss under high drying temperature, thus caused the inhibition of chlorophyllase activity and prevent homeostasis to occur. Moreover, the abscisic acid also helped to promote an acidic medium for the formation of pheophytins. Apart from that, it was also believed that the increased of ethylene in respond to

the increased of abscisic acid [48] had brokedown β-carotene and reduced its contents inside the dried leaves. Therefore, kaempferol-3-O-gentiobioside (a major flavonoids found in *Cassia alata* leaves [49] which is stable under high temperature condition [50]) was believed to be involved in the oxidation to degrade chlorophyll with enzyme peroxidase. However, the results in Table 3 also showed that the total chlorophyll contents remained similar within 60-70℃ without significant colour change (Figure 9). This observation could be related to a major anthraquinone found in *Cassia alata* leaves [51], aloe-emodin. According to the literatures, it was reported that aloe-emodin having the antioxidative effects [52] and insoluble in water [53]. It was assumed that aloe-emodin is able to inhibit the peroxidase activity due to antioxidant properties, thus prevent the degradation of L-ascorbic acid and β-carotene. Therefore, it could be concluded that aloe-emodin was able improve the retention of chlorophyll compounds within 60-70℃. A further studies on the comparison of leaves with and without aloe-emodin will helps to verify the hypothesis given from this experiment.

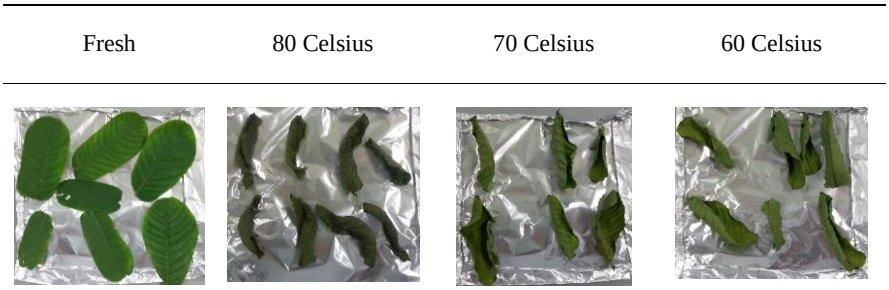


Figure 9. Images of fresh samples and convective drying (CD) dried *Cassia alata* leaves at different temperatures.

Table 3. Changes in chlorophyll contents of fresh and dried *Cassia alata* leaves

Sample	Chlorophyll a (mg Chl a/leaf tissue)	Chlorophyll b (mg Chl b/leaf tissue)	Total Chlorophyll (mg Chl b/leaf tissue)
Fresh	0.98 ± 0.20^{a}	0.58 ± 0.10^{a}	1.56 ± 0.10^{a}
CD (80℃)	1.32 ± 0.03^{b}	0.86 ± 0.01^{a}	2.19 ± 0.61^{a}
CD (70℃)	1.55 ± 0.07^{b}	1.89 ± 0.68^{b}	3.44 ± 0.61^{b}
CD (60℃)	1.38 ± 0.10^{b}	2.32 ± 0.31^{b}	3.70 ± 0.22^{b}

The values indicate mean ± standard deviation from three replications. Value within the same column with different letters denote statistically significant difference ($P<0.05$).
CD, convective drying method

4. Conclusion

Drying characteristics is an important criteria for engineer to design and select the best drying parameters to avoid major loss of active compounds and provide the best visual aspects in terms of colour attributes. It was found that in this study that the using convective drying method on *Cassia alata* leaves with higher temperature has enhance the moisture diffusion from the interior of the leaves in comparison with low temperatures during falling rate period. On the other hand, it was also found that air velocity and relative humidity are the major factors on reduction of moisture content in the early stage of drying process. The non-linear regression analysis found that Midilli-Kucuk model is the best model to describe the drying behaviour of *Cassia alata* leaves using convective drying method in comparison with five others semi-theoretical thin-layer drying models. With reference to retention of total chlorophyll contents in the dehydrated leaves, it is learned that the effective drying methods on the retention of pigments is highly depending on peroxidase activity. If the leaves contains aloe-emodin, a mild drying temperature followed by rapid drying (such as intermittent drying method) is suitable to maximise the retention of chlorophyll. The study revealed that enzymatic reaction determine the colour change of leaves during drying process.

References

[1] Y.W. Xiao, Z. Gao, H. Lin, "Air impringment drying characteristics and quality of carrot cubes," *J. Food Process Eng.*, vol. 33, pp. 899–918, 2010.

[2] J.W.R Chan., C.H. Chong, A. Malek, C.H. Khek, A. Figiel and A. Wojdylo, "Processing of Foods, Vegetables and Fruits: Recent advances," 1st ed., A. S. Hii, C.L., Jangam, S.V., Ong, S.P., Show, P.L., Mujumdar, Ed. Selangor, Malaysia: 3rd International Symposium on Processing of Foods, Vegetables and Fruits (ISPDFVF), 2015, pp. 87–100.

[3] A. Figiel, "Drying kinetics and quality of beetroots dehydrated by combination of convective and vacuum-microwave methods," *J. Food Eng.*, vol. 98, no. 4, pp. 461–470, 2010.

[4] D. Arslan and M. M. Özcan, "Study the effect of sun, oven and microwave drying on quality of onion slices," *LWT - Food Sci. Technol.*, vol. 43, no. 7, pp. 1121–1127, 2010.

[5] S. K. Giri and S. Prasad, "Drying kinetics and rehydration characteristics of microwave-vacuum and convective hot-air dried mushrooms," *J. Food Eng.*, vol. 78, no. 2, pp. 512–521, 2007.

[6] C. I. Nindo, T. Sun, S.W. Wang, J. Tang, and J.R. Powers, "Evaluation of drying technologies for retention of physical quality and antioxidants in asparagus (*Asparagus officinalis, L.*)," *LWT - Food Sci. Technol.*, vol. 36, no. 5, pp. 507–516, 2003.

[7] E. Holtz, L. Ahrné, M. Rittenauer, and A. Rasmuson, "Influence of dielectric and sorption properties on drying behaviour and energy efficiency during microwave convective drying of selected food and non-food inorganic materials," *J. Food Eng.*, vol. 97, no. 2, pp. 144–153, 2010.

[8] E. K. Akpinar, "Drying of mint leaves in a solar dryer and under open sun : Modelling , performance analyses," *Energy Convers. Manag.*, vol. 51, no. 12, pp. 2407–2418, 2010.

[9] C. J. Geankoplis, *Transport Processes & Separation Process Principles (Includes Unit Operations)*, Fourth. USA: Prentice Hall, 2014.

[10] E. T. and A. S. Mujumdar, *Modern Drying Technology: Computational Tools at Different Scales*, First. Federal Republic of Germany: Willey-VCH, 2007.

[11] B.L. Liu, H. Zhang and T.C. Hua, *Freeze-drying of pharaceutical and food products*, First. Beijing, China: Woodhead Publishing Limited, 2010.
[12] *Analysis of Leaf Pigment*, pp. 1–3, 2016.
[13] Delgado-Pelayo,Gallardo-Guerrero, and Hornero-Menndez, "Chlorophyll and carotenoid pigments in the peel and flesh of commercial apple fruit varieties," *Food Res. Int.*, vol. 65, no. PB, pp. 272–281, 2014.
[14] M. Benlloch-tinoco, A. Kaulmann, J. Corte-real, D. Rodrigo, N. Martínez-navarrete, and T. Bohn, "Chlorophylls and carotenoids of kiwifruit puree are affected similarly or less by microwave than by conventional heat processing and storage," *Food Chem.*, vol. 187, pp. 254–262, 2015.
[15] M. Madhava Naidu, M. Vedashree, P. Satapathy, H. Khanum, R. Ramsamy, and H. U. Hebbar, "Effect of drying methods on the quality characteristics of dill (*Anethum graveolens*) greens," *Food Chem.*, vol. 192, pp. 849–856, 2016.
[16] C. Sanchez, A. B. Baranda, and I. M. De Maranon, "The effect of High Pressure and High Temperature processing on carotenoids and chlorophylls content in some vegetables," *Food Chem.*, vol. 163, pp. 37–45, 2014.
[17] V. An-Erl King, C. F. Liu, and Y. J. Liu, "Chlorophyll stability in spinach dehydrated by freeze-drying and controlled low-temperature vacuum dehydration," *Food Res. Int.*, vol. 34, no. 2–3, pp. 167–175, 2001.
[18] G. Pumilia, M. J. Cichon, J. L. Cooperstone, D. Giuffrida, G. Dugo, and S. J. Schwartz, "Changes in chlorophylls, chlorophyll degradation products and lutein in pistachio kernels (*Pistacia vera L.*) during roasting," *Food Res. Int.*, vol. 65, no. PB, pp. 193–198, 2014.
[19] ASTM Standard D1348-94, "Standard test methods for moisture in Cellulose," ASTM International, West Conshohocken, PA, 2003.
[20] R. S. Aware and B. N. Thorat, "Garlic Under Various Drying Study and Its Impact on Allicin Retention," *Drying Tech*, pp. 1510–1518, 2011.
[21] A. Kaya and O. Aydın, "An experimental study on drying kinetics of some herbal leaves," *Energy Convers. Manag.*, vol. 50, no. 1, pp. 118–124, 2009.
[22] R. J. Porra, "The chequered history of the development and use of simultaneous equations for the accurate determination of chlorophylls a and b," *Photosynth. Res.*, vol. 73, no. 1–3, pp. 149–156, 2002.
[23] T. M. Cate and T. D. Perkins, "Chlorophyll content monitoring in sugar maple (Acer saccharum).," *Tree Physiol.*, vol. 23, no. 15, pp. 1077–1079, 2003.
[24] D. S. Jayas, S. Cenkowski, S. Pabis and W. E. Muir, "Review of Thin-Layer Drying and Wetting Equations," *Drying Tech*, vol. 9, no. 3, pp. 551-588 1991.
[25] C. L. Hii, C. L. Law, and M. Cloke, "Modelling of thin layer drying kinetics of cocoa beans during artificial and natural drying". *J. Eng Sci &* Tech, vol. 3, no. 1, pp. 1–10, 2008.
[26] W. Pereira, C. M. D. P. S. Silva, and F. J. A. Gama, "Mathematical models to describe thin-layer drying and to determine drying rate of whole bananas," *J. Saudi Soc. Agric. Sci.*, vol. 13, no. 1, pp. 67–74, 2014.
[27] A. Taheri-garavand, S. Rafiee, and A. Keyhani, "Mathematical Modeling of Thin Layer Drying Kinetics of Tomato Influence of Air Dryer Conditions," vol. 2, no. 2, pp. 147–160, 2011.
[28] A. Zhu and X. Shen, "International Journal of Heat and Mass Transfer The model and mass transfer characteristics of convection drying of peach slices," *Int. J. Heat Mass Transf.*, vol. 72, pp. 345–351, 2014.

[29] D. Evin, "Food and Bioproducts Processing Thin layer drying kinetics of *Gundelia tournefortii L .*," *Food Bioprod. Process.*, vol. 90, no. 2, pp. 323–332, 2011.
[30] A. Midilli, H. Kucuk, and Z. Yapar, " A new model for sing-layer drying," *Drying Tech: An International Journal*, vol. 20, no. 7, pp. 37–41, 2007.
[31] M. A. Ali, Y. A. Yusof, N. L. Chin, M. N. Ibrahim, and S. M. a. Basra, "Drying Kinetics and Colour Analysis of *Moringa Oleifera* Leaves," *Agric. Agric. Sci. Procedia*, vol. 2, pp. 394–400, 2014.
[32] C. H. Chong, C. L. Law, M. Cloke, C. L. Hii, L. C. Abdullah, and W. R. W. Daud, "Drying kinetics and product quality of dried Chempedak," *J. Food Eng.*, vol. 88, no. 4, pp. 522–527, 2008.
[33] P. Udomkun, D. Argyropoulos, M. Nagle, B. Mahayothee, S. Janjai, and J. Müller, "Single layer drying kinetics of papaya amidst vertical and horizontal air flow," *LWT - Food Sci. Technol.*, vol. 64, no. 1, pp. 67–73, 2015.
[34] S. P. Ong and C. L. Law, "Drying Kinetics and Antioxidant Phytochemicals Retention of Salak Fruit under Different Drying and Pretreatment Conditions," *Drying Tech*, Vol. 29, pp. 429–441, 2011.
[35] Q. Chen, J. Bi, X. Wu, J. Yi, L. Zhou, and Y. Zhou, "Drying kinetics and quality attributes of jujube (*Zizyphus jujuba Miller*) slices dried by hot-air and short- and medium-wave infrared radiation," *LWT - Food Sci. Technol.*, vol. 64, no. 2, pp. 759–766, 2015.
[36] M. M. Naidu, M. Vedashree, P. Satapathy, H. Khanum, R. Ramsamy, and H. U. Hebbar, "Effect of drying methods on the quality characteristics of dill (*Anethum graveolens*) greens," *Food Chem.*, vol. 192, pp. 849–856, 2016.
[37] A. Vega-gálvez, K. Ah-hen, M. Chacana, J. Vergara, J. Martínez-monzó, P. García-segovia, R. Lemus-mondaca, and K. Di, "Effect of temperature and air velocity on drying kinetics , antioxidant capacity , total phenolic content , colour , texture and microstructure of apple (var . *Granny Smith*) slices," *Food Chem*, vol. 132, pp. 51–59, 2012.
[38] S. N. F. S. A. Rahman, R. Wahid, and N. A. Rahman, "Drying Kinetics of *Nephelium Lappaceum* (Rambutan) in a Drying Oven," *Procedia - Soc. Behav. Sci.*, vol. 195, pp. 2734–2741, 2015.
[39] A. Borah, K. Hazarika, and S. M. Khayer, "Drying kinetics of whole and sliced turmeric rhizomes (*Curcuma longa L.*) in a solar conduction dryer," *Inf. Process. Agric.*, vol. 2, no. 2, pp. 85–92, 2015.
[40] A. S. Kholmanskiy, A. Z. Tilov, and E. Y. Sorokina, "Drying kinetics of plant products : Dependence on chemical composition," *J. Food Eng.*, vol. 117, pp. 378–382, 2013.
[41] C. H. Chong, A. Figiel, C. L. Law, and A. Wojdylo, "Combined Drying of Apple Cubes by Using of Heat Pump, Vacuum-Microwave, and Intermittent Techniques," *Food Bioprocess Technol.*, vol. 7, no. 4, pp. 975–989, 2014.
[42] R. Delgado-pelayo, L. Gallardo-guerrero, and D. Hornero-méndez, "Chlorophyll and carotenoid pigments in the peel and flesh of commercial apple fruit varieties," *FRIN*, vol. 65, pp. 272–281, 2014.
[43] H. S. Erge, F. Karadeniz, N. Koca, and Y. Soyer, "Effect of heat treatment on chlorophyll degradation and color loss in green peas," *GIDA*, vol. 33, pp. 225–233, 2008.
[44] G. Pumilia, M. J. Cichon, J. L. Cooperstone, D. Giuffrida, G. Dugo, and S. J. Schwartz, "Changes in chlorophylls, chlorophyll degradation products and lutein in pistachio kernels (*Pistacia vera L .*) during roasting," *FRIN*, vol. 65, no. 2014, pp. 193–198, 2015.

[45] A. Okazawa, L. Tang, Y. Itoh, E. Fukusaki, and A. Kobayashi, "Characterization and subcellular localization of chlorophyllase from Ginkgo biloba," *Zeitschrift fur Naturforsch. - Sect. C J. Biosci.*, vol. 61, no. 1–2, pp. 111–117, 2006.

[46] B. P. Eddy and M. Ingram, "Ascorbic Acid and β-carotene affect the chlorophyll degradation in stored spinach (*Spinacia oleraea L.*)," *Food Preserv. Sci.*, vol. 17, no. 2. 1953.

[47] Y. Tao, P. Wang, Y. Wang, S. U. Kadam, Y. Han, and J. Wang, "Ultrasonics Sonochemistry Power ultrasound as a pretreatment to convective drying of mulberry (Morus alba L .) leaves : Impact on drying kinetics and selected quality properties," *Ultrason. Sonochem.*, vol. 31, pp. 310–318, 2016.

[48] B. Silvestre, N. De Setta, D. Rosado, J. Almeida, L. Freschi, and M. Rossi, "Plant degreening : evolution and expression of tomato (Solanum lycopersicum) dephytylation enzymes," *Gene*, vol. 546, no. 2, pp. 359–366, 2014.

[49] T. Hennebelle, B. Weniger, H. Joseph, S. Sahpaz, and F. Bailleul, "Fitoterapia Senna alata," *Fitoterapia*, vol. 80, no. 7, pp. 385–393, 2009.

[50] H. Moriyama, T. Iizuka, and M. Nagai, "A stabilized flavonoid glycoside in heat-treated Cassia alata leaves and its structural elucidation," *Yakugaku Zasshi*, vol. 121, no. 11, pp. 817–20, 2001.

[51] W. Gritsanapan and P. Mangmeesri,"Standardized *Senna alata* leaf extract," *J. Health Res*, vol. 23, no. 2, pp. 59-64, 2009.

[52] S. Kumar and J. P. Yadav, "Ethnobotanical and pharmacological properties of Aloe vera : A review," *J. Medicinal Plant Research*, vol. 8, no. 48, pp. 1387–1398, 2014.

[53] Y. Cheng, X. Wang, W. Liu, D. Wang, and L. Chen, "Experimental measurement and correlation of the solubility of aloe-emodin in seven pure solvents," *J. Chem. Thermodyn.*, pp. 1-16, 2016.

eureca 2016 – Conference Paper
Paper Number 2CE16

Antioxidant activity determination and optimization of the isolated compounds from the roots of *Chlorophytum borivilianum* (safed musli)

Khoo Chang Jian[1*], Chua Bee Lin[2]

[1,2]*School of Engineering, Taylor's University*

[*]changjian.khoo@sd.taylors.edu.my

Abstract

Traditional herbal medicines play a crucial role to the human body. These herbs contain many diffirent types of compounds. In this research, the plant *Chlorophytum borivilianum* (safed musli) and its compounds saponins were studied. Extraction and quantification of saponins from the roots of *C. borivilianum* (safed musli) were conducted by incorporating the ultrasonic–assisted extraction (UAE) and vanillin–sulfuric acid assay respectively. The effects of extraction parameters: extraction time and extraction temperature with their respective conditions were investigated by optimization using response surface methodology (RSM). The optimal ranges of extraction parameters were identified through a single factor experimental design. Futher optimization of the optimal ranges of extraction parameters was conducted using RSM incorporated with central composite design (CCD). A second order polynomial function was fitted to the data according to the analysis obtained from ANOVA. The experimental values obtained from ANOVA were significant with 89.77% of total variation. The results show that the optimum conditions at extraction time of 46.35 minutes and extraction temperature of 55.18℃ provided the optimum extraction yield of saponins of 9.5768 mg/mL. Validation of model was conducted to compare the predicted and actual extraction yield of saponins. The relative error obtained between the two values was 8.371%. Therefore, it was proven that the developed second order polynomial model by RSM optimization was reliable. The antioxidant activity of the samples was studied using 2,2–diphenyl–1–picrylhydrazyl (DPPH). The results reveal that the samples possesed a very high antioxidant with scavenging activty of 88.58%.

Keywords: saponins, ultrasonic–assisted extraction, optimization, central composite design, antioxidant activity.

1. Introduction

Traditional herbal medicines are plant derived–substances in which they occur naturally without undergoing any industrial processing. Many years ago, plants have been used as medicinal purposes. Eventhough herbal medicines have been introduced in the early history, until today, they play a crucial role in the global community. According to a bulletin from World Health Organization (WHO), many countries have been undergoing thorough research investments in traditional herbal medicines. Herbal medicines have been used in treating diseases such as SARS [1]. Eversince herbal medicines have been introduced, the number of cases of this disease has been gradually decreasing. Hence, in this research project, a plant that was originated from India known as *Chlorophytum borivilianum* (safed musli) was studied.

C. borivilianum can be found in tropical rainforests in the peninsular region of India. It is known as "safed musli" or in other words "white tubers" in Hindi [2]. Studies have shown that the root tubers of the plant are used as a drug to treat diseases, sickness disorder and many other health related issues since the 11th century [3]. The roots of the plant serve as a tonic to reduce sexual dysfunction in males. In addition, the roots promote benefits to pregnant females where the roots serve as a tonic to replenish lost of fluids during post – partem [4]. Consider that the roots bring several medicinal benefits to the global community, hence, it is essential to study the roots of the herb. Apart from that, *C. borivilianum* contains a number of pharmacological properties such as antioxidant, anti-inflammatory and many more. There are several phytochemicals that exist in the roots of the plant. They are alkaloids, flavonoids, phenolic acids as well as saponins [5]. The plant contains 42% carbohydrate, 8–9% protein, 3–4% fibres and 2–17% saponins [6]. Among all the phytochemicals, it is reported that saponin is inevitably one of the primary constituents of a number of folk medicines, herbal drugs and pharmacological properties [7].

Extraction was done to ensure that the inert materials were eliminated using a suitable solvent [8]. The most common solvents used are methanol and ethanol with a concentration of 80% for extracting complex structures of total saponins with different polarities [9]. Methanol was used as the solvent for extraction because it has a low boiling point than ethanol and it will not damage the plant extract at low temperatures. In this research, ultrasonic asssisted extraction (UAE) was selected. Studies have shown that UAE has provided quantification studies that could bring up a reference on its capability and efficacy in obtaining a prominent yield of saponins [10]. UAE involves ultrasound where ultrasound frequency more than 20 kHz is able to facilitate in extractions by increasing the mass transfer betweent the solvent and the plant [11, 12] UAE is efficient and is able to extract three times faster than traditional extraction method [13]. Vanillin–sulfuric acid assay has been used widely for the quantification of saponins. This method is fast, inexpensive and easy to operate [10]. Various researches have been using a temperature range of 60℃–70℃ and time range of 10–30 minutes to obtain full colour development [10].

Optimization of extraction parameters usually is carried out by the traditional method which is one variable at a time (OVAT). However, the number of experiments required is high, tedious and high in cost. In addition, this method is unable to provide information on the interactions between different variables [14]. To overcome this issue, response surface methodology (RSM) was selected as the tool for optimization [15].

Among the many different classes of RSM designs, central composite design (CCD) is one of the most popular methods to carry out optimization due to its simplicity and efficiency [16].

Therefore, the objectives of this research were to quantify saponins from the roots of *C. borivilianum* through vanillin–sulfuric acid assay, to extract saponins from the roots of *C. borivilianum* through UAE using extraction time and extraction temperature as the extraction parameters as well as to optimize extraction parameters through single factor experimental design and RSM incorporated with CCD to obtain optimum yield of saponins. In addition, the antioxidant determination was conducted using DPPH. Results here may provide an explanation of antioxidant activity determination and optimization as well as to contribute new applications of *C. borivilianum* in further studies.

2. Materials and methods

2.1 Chemical reagents

Vanillin and diosgenin were purchased from Sigma–Aldrich (St. Louis, MO, U.S.A.). 2,2–diphenyl–1–picrylhydrazyl (DPPH), methanol and sulfuric acid were from Friendemann Schmidt Chemicals. All other solvents and reagents used in the analysis were of analytical grade.

2.2 Preparation and pretreatment of plant material

Fresh roots of *C. borivilianum* (safed musli) were obtained from Universiti Putra Malaysia (UPM). Preparation and pretreatment of *C. borivilianum* was conducted based on the methods presented by Chua [17]. The roots of the plant were thoroughly washed and dried in a drying oven (Model UFE-800, Memmert, Germany). The dried roots were cut into slices followed by grounding them into coarse powder using a cutting mill (Model SM–100, Retsch, Germany). The powder form of the roots were then passed through a standard sieve of 0.250 mm at designated sieve of mesh no. 60 to obtain a uniform particle size. The powder form of the roots was sealed in a plastic container and stored at room temperature for further usage. The roots were kept in Herbal Technology Centre located in FRIM.

2.3 Standard calibration curve of saponins

The preparation of standard calibration curve was modified based on Makkar [18]. 10 mg/mL of diosgenin was prepared and diluted to 6 different concentrations at 0, 2, 4, 6, 8 and 10 mg/mL to give a final volume of 250 μL with 80% aqueous methanol. 0.25 mL of 8% vanillin reagent was added into the test tubes followed by adding 2.5 mL of 72% sulfuric acid slowly on the inner side of the wall. The solution was well mixed in a vortex shaker and placed in an ultrasonic bath at 60℃ for 10 minutes. The test tubes were set aside to cool in an ice−cold water bath for approximately 3 to 4 minutes. The absorbance of each sample was measured at 544 nm using an UV−vis spectrophotometer (Model Genesys 10S, Massachusetts, United States) against a blank solution that contains 80% aqeuous methanol. By measuring the absorbance, the standard calibration curve was obtained.

2.4 Single factor experimental design

Effect of extraction time was conducted based on Jovanovic [20] with minimal modifications. Using 80% aqueous methanol as the solvent and at a solid to solvent ratio (g/mL) of 1:10, the samples were extracted at a range from 20 to 60 minutes while maintaining the extraction temperature at 40℃. The most suitable extraction time was identified based on the highest extraction yield of saponins.

Effect of extraction temperature was conducted based on Jovanovic [20] with minimal modifications. Using 80% aqueous methanol as the solvent and at a solid to solvent ratio (g/mL) of 1:10, the samples were extracted at a range from 20 to 60℃ while maintaining the extraction time at 40 minutes. The most suitable extraction temperature was identified based on the highest extraction yield of saponins.

2.4.1 Experimental range of extraction of saponins

The extraction time and extraction temperature were plotted individually by selecting one parameter while maintaining the other parameter. The parameter that will be maintained was selected from the centre points in each experiment. The experimental range of the single experimental design was shown as follows:

Table 1: Experimental range of single factor experimental design

Extraction Parameters	Parameter Levels				
	1	2	3	4	5
Extraction Time (minutes), X_1	20	30	40	50	60
Extraction Temperature (℃), X_2	20	30	40	50	60

2.5 Extraction of saponins

Extraction of saponins was conducted by employing the ultrasonic–assisted extraction (UAE). The samples were extracted from the roots of *C. borivilianum* using 80% aqeuous methanol at a solid to solvent (g/mL) ratio of 1:10. The extracted samples were placed in a universal bottle and conducted in an ultrasonic bath (Elmasonic Model P120H, Singen, Germany) operating at ultrasonic input power of 70% and frequency of 37 kHz. Once extraction was completed, the samples were filtered using Whatman filter paper no. 1 in an evaporating flask to obtain the supernatants of the sample. The supernatants were dried in a rotary vacuum evaporator (Heidolph Model Hei−VAP Precision (HL), Schwabach, Germany) at 40℃ until crude extracts were observed. The crude extracts were weighed and then quantified.

2.6 Quantification of saponins

Quantification of saponins was conducted based on Ncube [19] with minimal modifications. The crude saponin extracts were dissolved in 80% aqueous methanol to a concentration of 10 mg/mL. From this aliquots of 250 μL in triplicates of each sample

were transferred into test tubes in which 0.25 mL of 8% vanillin reagent was added into the test tube followed by 2.5 mL of 72% sulfuric acid. The solution was well mixed using a vortex shaker and placed in an ultrasonic bath at 60℃ for 10 minutes. The test tubes were set aside to cool in an ice–cold water bath for approximately 3 to 4 minutes. The absorbance of each sample was measured at 544 nm using an UV–vis spectrophotometer against a blank solution that contains 80% aqueous methanol. The saponin concentrations were expressed as diosgenin equivalents (DE) calculated from the calibration curve.

2.7 Optimization of extraction parameters using RSM

Optimization of extraction parameters on the maximum yield of saponins was carried out using response surface methodology (RSM) incorporated with central composite design (CCD) [14, 21]. Two factors and five–level face–centred cube design that require a total of 13 experiments were conducted. The independent variables studied were extraction time and extraction temperature. Each of the independent variable was studied at five coded levels ($-\alpha$, -1, 0, $+1$, $+\alpha$). Each of the value was represented in codes where extraction time and extraction temperature were coded as X_1 and X_2 respectively. The second order polynomial function to express the extraction yield of saponins was used to fit the response of the independent variables [21]. The model is shown as follows:

$$Y_1 = \beta_o + \sum_i \beta_i X_i + \sum_{ii} \beta_{ii} {X_i}^2 + \sum_{i<j} \sum_j \beta_{ij} X_i X_j \quad (1)$$

where, β_o represents the intercept, β_i represents the coefficient for the linear terms, X_i, β_{ii} represents the coefficient for the quadratic terms, ${X_i}^2$ and β_{ij} represents the coefficient for the interacting terms of X_i and X_j. Analysis of variance (ANOVA) was analysed in coded levels to study the effects of the independent variables. 2–D and 3–D response surface plots were generated to study visually on the effects of the significant independent variables as well as to determine the maximum extraction yield of saponins. RSM optimization was conducted using Design Expert Software Version 8.0.7.1 trial program.

2.8 Validation of model

The optimum conditions for the extraction yield of saponins depended on extraction time and extraction temperature were obtained from RSM optimization. The experimental and predicted values obtained from RSM optimization were compared to determine the validity of the model based on the relative error.

2.9 DPPH radical scavenging activity

DPPH radical scavenging activity was performed by the method of Zhao [22, 23] with minimal modifications. 0.004% of DPPH solution was prepared. 5 mL of the prepared DPPH solution was added into the plant extracts. The mixture was left in a dark room at room temperature for 30 minutes. The absorbance was measured at 517 nm using an UV–vis spectrophotometer. A decrease in the absorbance of the DPPH radical was due to high free radical scavenging activity during hydrogen donation [24]. It can be observed that a colour change from purple to yellow will occur. The effect of radical scavenging activity can be calculated based on the equation as follows [24]:

$$Scavenging\ Activity\ (\%) = \frac{A_o - A_1}{A_o} \times 100\% \quad (2)$$

where A_o is the absorbance of the control reaction which is DPPH in methanol and A_1 is the absorbance of the sample of extracts in DPPH solution.

3. Results and discussion

3.1 Single factor experimental design

3.1.1 Effect of extraction time on the extraction yield of saponins

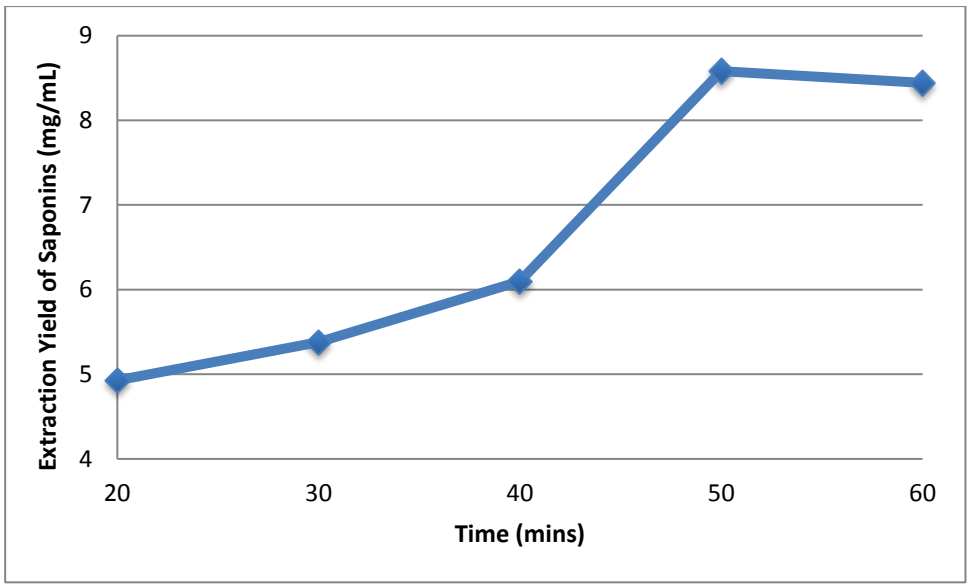


Figure 1: Effect of extraction time on the extraction yield of saponins

Effect of extraction time on the extraction yield of saponins was investigated. In the extraction of saponins, most researchers were able to extract saponins at 30 minutes and 60 minutes [10]. Hence, the extraction time of 20, 30, 40, 50 and 60 minutes were investigated while other parameters were set as follows: ratio of solid to solvent of 1:10 g/mL, ultrasonic input power of 70% and extraction temperature of 40℃. It can be seen from Figure 1, the extraction yield of saponins gradually increases from 20 minutes to 40 minutes. The extraction yield of saponins rapidly increases from 40 minutes to 50 minutes. There is a possibility that most of the saponins in broken cells were released and diffused into the solvent during this time. Besides that, ultrasound promotes the saponins inside the roots release to exterior solvent [25]. That is because ultrasonic could enhance the mass transfer of the saponins into the solvent [22]. Thus, at 50 minutes, the optimum yield of the saponins was obtained. The extraction yield of saponins decreases from 50 minutes onwards. Further increase of the ultrasonic time would cause a degradation and damage in the saponins [25] as well as through the internal diffusivity along increased turbulence within pore volumes [26] due to heating effect of overexposure to the ultrasonic treatment [27] thus obtaining a lower extraction yield. Based on the results obtained, the optimum range between 40 minutes to 60 minutes was selected.

3.1.2 Effect of extraction temperature on the extraction yield of saponins

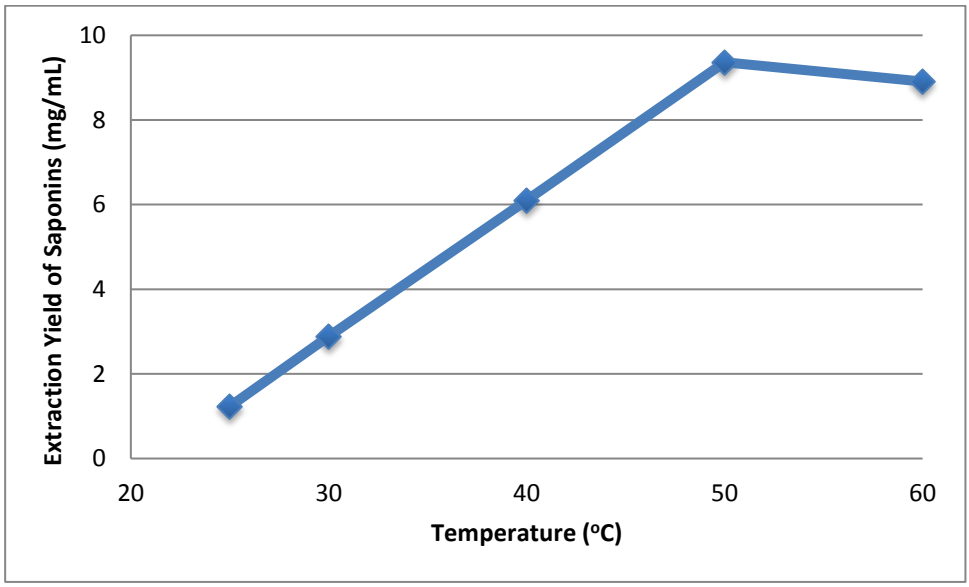


Figure 2: Effect of extraction temperature on the extraction yield of saponins

Effect of extraction temperature on the extraction yield of saponins was investigated. Research has shown that as temperature approaches to the boiling point of the solvent, the performance of the ultrasonication will decrease due to the decrease in the surface tension as well as increasing vapor pressure which will eventually cause damping in the ultrasonic wave [28, 29]. Thus, the temperature range for the extraction temperature should be less than the boiling point of methanol. Hence, the extraction temperature of 25 (room temperature), 30, 40, 50 and 60℃ were investigated while other parameters were set as follows: ratio of solid to solvent ratio of 1:10 g/mL, ultrasonic input power of 70% and extraction time of 40 minutes. It can be seen from Figure 2, the extraction yield of saponins increases linearly until 50℃. This shows that as the temperature increases, the solubility of the components increases, thus, reducing the solvent viscosity. This is because a high solubility of saponins in the solvent at a high temperature promotes a high diffusion rate [30]. Due to this phenomenon, the mass transfer increases [29]. Besides that, the combined action of acoustic cavitation as well as thermal effect could give significant results to the extraction yield [31]. Thus, at 50℃, the optimum yield of saponins was obtained. However, the extraction yield of saponins began to decrease from 50℃ onwards. This could be due to a degradation of the saponins as the temperature is further increased. Based on the results obtained, the optimum range between 40℃ to 60℃ was selected.

3.2 Quantification of saponins

The saponin concentrations equivalent to the diosgenin equivalents (DE) were expressed from the calibration curve. The equation to the calibration curve was shown as follows:

$$X = \frac{A-3.4493}{0.1574} \quad (3)$$

where X is the concentration of saponins (mg/mL) and A is the absorbance of the sample. Equation 3 was utilized in determining the concentration of saponins based on different conditions of the extraction parameters listed in the single factor experimental design.

3.3 Optimization of extraction parameters using response surface methodology

The purpose of conducting this study was to optimize the most significant extraction parameters that would give the highest extraction yield of saponins. The extraction parameters were selected based on the optimal range of the extraction parameters obtained from the single factor experimental design. In this study, RSM using CCD was applied.

3.3.1 Central composite design on the extraction yield of saponins

The extraction time and extraction temperature were selected for optimization on the extraction from the roots *C. borivilianum*. A total of 13 experiments inclusive of 5 replications were generated from Design Expert Software Version 8.0.7.1. Table 2 shows the experimental results of CCD on the extraction yield of saponins.

Table 2: Experimental results on the extraction yield of saponins using central composite design

Run	Extraction Parameters		Response
	Extraction Time (mins)	Extraction Temperature (℃)	Yield of Saponins, Y_1 (mg/mL)
1	40	40	3.5877 ± 0.0437
2	50	35	4.0896 ± 0.1158
3	35	50	3.9435 ± 0.0137
4	50	50	9.7122 ± 0.0312
5	50	50	9.3183 ± 0.0176
6	50	50	9.4771 ± 0.0387
7	50	60	8.4606 ± 0.0431
8	60	60	3.2954 ± 0.0368
9	60	40	8.4416 ± 0.1784
10	50	50	9.2611 ± 0.0636
11	60	50	4.3247 ± 0.0318
12	50	50	9.7122 ± 0.0454
13	40	60	8.9053 ± 0.0139

The results obtained from Table 2 shows that at experiment 4 with extraction time of 50 minutes and extraction temperature of 50℃ provided the highest extraction yield of saponins of 9.7122 ± 0.0312 mg/mL. However, experiment 8 with extraction time of 60 minutes and extraction temperature of 60℃ provided the lowest extraction yield of saponins of 3.2954 ± 0.0368 mg/mL.

3.3.2 Analysis of variance (ANOVA) on the quadratic polynomial model

Statistical analysis of ANOVA was analysed from Design Expert Software 8.0.7.1. Table 3 shows the analysis of variance for the response on the extraction yield of saponins.

Table 3: ANOVA for response surface quadratic model on the extraction yield of saponins

Source	Sum of Squares	Degree of Freedom	Mean Square	F Value	p-value Prob > F
Model	80.19	5	16.04	12.28	0.0024
X_1 – Extraction Time	1.76	1	1.76	1.35	0.2835
X_2 – Extraction Temperature	1.77	1	1.77	1.35	0.2829
X_1X_2	27.37	1	27.37	20.96	0.0025
${X_1}^2$	35.68	1	35.68	27.32	0.0012
${X_2}^2$	10.98	1	10.98	8.40	0.0230
Residual	9.14	7	1.31		
Pure Error	0.18	4	0.045		
Cor Total	89.33	12			

Based on the analysis from ANOVA from Table 3, the p value obtained for model was 0.0024. This indicates that there is a 0.24% chance of the "Model F–Value" which is this large can occur due to noise. Besides that, the "Model F–Value" of 12.28 indicates that the model is significant. The values of p–value (Prob > F) that are less than 0.05 indicate that the model terms are significant. In this case, X_1X_2 (0.0025), ${X_1}^2$ (0.0012) and ${X_2}^2$ (0.0230) are model terms that are significant. This results show that the interaction between the two independent variables were likely to give influence to the extraction yield of saponins. However, values that are greater than 0.1 indicate that the model terms are not significant. In this case, X_1 (0.2835) and X_2 (0.2829) are model terms that are no significant. This result show that the independent variables itself do not bring much influence on the extraction yield of saponins since the p−values were more than 0.05.

3.3.3 Fitting of Polynomial Model

Table 4: Statistical analysis for the extraction yield of saponins

Model Terms	Values
Standard Deviation	1.14
Mean	7.12
Coefficient Variation (%)	16.06
PRESS	75.02
R−squared	0.8977
Adjusted R−squared	0.8246
Predicted R−squared	0.1602
Adequate Precision	8.518

Based on the analysis obtained from Table 4, the predicted R−squared value of 0.1602 is not as close as the adjusted R−squared value of 0.8246. The results could be due to a large block effect or a possible issue on the model. Adequate precision

measures signal to noise ratio. A ratio greater than 4 is desirable. In this case, the adequate precision gives 8.518 which is greater than 4. Hence, this model can be used to navigate the design space. The value of R−squared of 0.8977 indicated that 89.77% of the total variation of the extraction yield of saponins was attributed to the independent variables. It was known that the model was significant for production in the range of the independent variables that were selected [14]. Therefore, the final equation in terms of the coded factors was shown as follows:

$$Y_1 = -155.97546 + 3.82681X_1 + 2.786X_2 - 0.02616X_1X_2 - 0.02571{X_1}^2 - 0.014258{X_2}^2 \quad (4)$$

where Y_1 represents the extraction yield of saponins, X_1 represents the extraction time and X_2 represents the extraction temperature.

3.3.4 Response surface plot

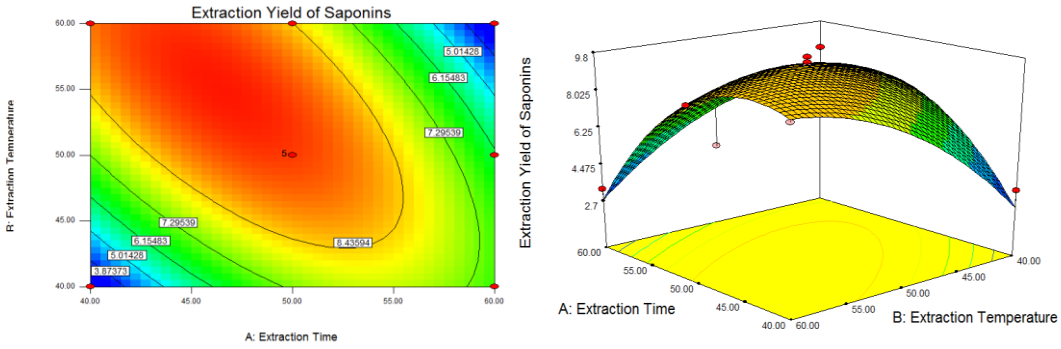


Figure 3: 2−D and 3−D response surface plots on the effect of extraction time and extraction temperature on the extraction yield of saponins

The 2−D and 3−D response surface plots generated in Figure 3 were designed based on the final equation to study the interactions between the two independent variables. Besides that, the response surface plot was also utilized to obtain the optimum extraction parameters that would give the maximum extraction yield of saponins. In both the 2−D and 3−D response surface plots, when both the extraction time and extraction temperature increases, the extraction yield of saponins achieved its optimum values of 9.5768 mg/mL at extraction time of 46.35 minutes and extraction temperature of 55.18℃. However, a further increase of both the extraction parameters would favour a decrease in the extraction yield of saponins.

3.4 Validation of model

Validation was conducted to check the adequacy as well as the realibility of the developed second order polynomial model. Table 5 shows the optimum and modified conditions for the extraction parameters.

Table 5: Optimum and modified conditions for the extraction parameters

Extraction Parameters	Optimum Conditions	Modified Conditions
Extraction Time (mins), X_1	46.35	46
Extraction Temperature (℃), X_2	55.18	55

The experiment was repeated using the modified conditions for extraction time and extraction temperature. Results showed that the extraction time at 46 minutes and extraction temperature at 55℃ provided the optimum extraction yield of saponins at 8.7751 mg/mL. The relative error between the predicted and actual extraction yield of saponins was 8.371%. Hence, it was proven that the developed second order polynomial model by RSM optimization was reliable.

3.5 DPPH radical scavenging activity

The DPPH radical scavenging activity was performed to estimate the free radical scavenging activity of the samples. Results show that the samples possesed a high value of antioxidant activity at 88.58%. It was observed that the absorbance of the DPPH sample was low (0.147). Low absorbance was mainly due to high scavenging of radical by the hydrogen donation [24]. Besides that, an increase in the extraction temperature favoured an increase in the antioxidant activity [32]. The rate of extraction for the thermally stable antioxidants at high temperatures would be higher than the rate of decomposition of antioxidants that are less soluble [32, 33].

4. Conclusion

In conclusion, the present research outlines the antioxidant activity determination and optimization of the isolated compounds from the roots of *C. borivilianum*. The isolated compounds studied were saponins. The optimum parameters to achieve the maximum extraction yield of saponins of 9.5768 mg/mL were obtained at extraction time of 46.35 minutes and extraction temperature of 55.18℃. Validation of model was conducted between the actual and predicted values and a relative arror of 8.371% was obtained. The antioxidant activity obtained was 88.58% indicating that the samples are rich in antioxidants. Apart from saponins, there are several phytochemicals exist in *C. borivilianum* namely: alkaloids, flavanoids and phenolic acids. However, studies have shown that there is a lack of extensive chemical investigation on this herbal plant. Hence, it is essential to conduct studies regarding on other phytochemicals of the herbal plant. The extraction yield of saponins based on 2 independent variables might not be sufficient to determine the optimum extraction yield of saponins. It can be due to other significant factors such as solid to solvent ratio and power input of the ultrasonic bath. Therefore, it is essential to perform additional factors to obtain better results.

Acknowledgements

The authors would like to thank Taylor’s University for financial assistance of this project. And we are grateful to the engineering lab assistant’s of Taylor’s University for their help in the equipments used in this project.

References

[1] J. C. Tilburt and T. J. Kaptchuk, “Bulletin of the World Health Organization Herbal medicine research and global health : an ethical analysis,”, vol. 86, no. 8, pp. 577–656, 2008.

[2] Z. Khanam, O. Singh, R. Singh, and I. U. H. Bhat, "Safed musli (Chlorophytum borivilianum): A review of its botany, ethnopharmacology and phytochemistry," *J. Ethnopharmacol.*, vol. 150, no. 2, pp. 421–441, 2013.
[3] K. N. Vijaya, and P. D. Chavan, "Chlorophytum borivilianum (safed musli): A review," *Department of Botany, Shivaji University, Kolhapur – 416004 (MS) India*, vol. 3, no. 5, pp. 154–169, 2009.
[4] S. Roshan, S. Soni, D. Sourabh, K. mahaveer, and G. Raman, "Safed musli (Chlorophytum borivilianum) a unique gift of Ayurveda as Divya Aushadhi," *Asian J. Pharm. Research and Development*, vol. 1, pp. 117–124, 2013.
[5] N. P. Visavadiya, B. Soni, N. Dalwadi, and D. Madamwar, "Chlorophytum borivilianum as potential terminator of free radicals in various of in vitro oxidation systems," *J Drug Chem Toxicol*., vol. 33, no.2, pp. 173–182, 2010.
[6] Wagle, A., Kelkar, G. D., Heble, M.R. (2000). *In Biotechnology: Secondary Metabolites*. New Delhi, Oxford and IBH Publishing Co, Pvt. Ltd.
[7] S. G. Sparg, M. E. Light, and J. van Staden, "Biological activities and distribution of plant saponins," *J. Ethnopharmacol.*, vol. 94, no. 2–3, pp. 219–243, 2004.
[8] Handa, S. S. (2008). *Extraction Technologies for Medicinal and Aromatic Plants*. Trieste. International Centre for Science and Technology.
[9] W. Wang, J. Jung, E. Tomasino, and Y. Zhao, "Optimization of solvent and ultrasound-assisted extraction for different anthocyanin rich fruit and their effects on anthocyanin compositions," *LWT - Food Sci. Technol.*, vol. 72, pp. 229–238, 2016.
[10] C. Y. Cheok, H. A. K. Salman, and R. Sulaiman, "Extraction and quantification of saponins: A review," *Food Res. Int.*, vol. 59, pp. 16–40, 2014.
[11] T. Mason, F. Chemat, and M. Vinatoru, "The extraction of natural products using ultrasound or microwaves," *Current Organic Chemistry*, vol. 15, no. 2, pp. 237–247, 2011.
[12] P. Garcia-Salas, A. Morales-Soto, A. Segura-Carretero, and A. Fernández-Gutiérrez, "Phenolic-Compound-Extraction Systems for Fruit and Vegetable Samples," pp. 8813–8826, 2010.
[13] A. Gupta, M. Naraniwal, and V. Kothari, "Modern extraction methods for preparation of bioactive plant extracts," *Int. J. Appl. Nat. Sci.*, vol. 1, no. 1, pp. 8–26, 2012.
[14] M. Kumar, S. Rana, V. Beniwal, and R. K. Salar, "Optimization of tannase production by a novel Klebsiella pneumoniae KP715242 using central composite design," *Biotechnol. Reports*, vol. 7, pp. 128–134, 2015.
[15] M. A. Bezerra, R. E. Santelli, E. P. Oliveira, L. S. Villar, and L. A. Escaleira, "Response surface methodology (RSM) as a tool for optimization in analytical chemistry," *Talanta*, vol. 76, no. 5, pp. 965–977, 2008.
[16] D. S. Correia, C. V. Gonçalves, S. S. Da Cunha, and V. A. Ferraresi, "Comparison between genetic algorithms and response surface methodology in GMAW welding optimization," *J. Mater. Process. Technol.*, vol. 160, no. 1, pp. 70–76, 2005.
[17] Lin, C. B. (2013). *Optimization of Production Process of Chlorophytum Borivilianum (Safed Musli) Standardized Extract.* Doctoral dissertation. Universiti Putra Malaysia, Serdang, Malaysia.
[18] Makkar, H. P. S., Siddhuraju, P, and Becker, K. (2007). *Plant Secondary Metabolites*," Humana Press, pp. 98.
[19] B. Ncube, V. N. P. Ngunge, J. F. Finnie, and J. Van Staden, "A comparative study of the antimicrobial and phytochemical properties between outdoor grown and

micropropagated Tulbaghia violacea Harv. plants," *J. Ethnopharmacol.*, vol. 134, no. 3, pp. 775–780, 2011.
[20] R. Jovanovic-Malinovska, S. Kuzmanova, and E. Winkelhausen, "Application of ultrasound for enhanced extraction of prebiotic oligosaccharides from selected fruits and vegetables," *Ultrason. Sonochem.*, vol. 22, pp. 446–453, 2015.
[21] P. Izadiyan and B. Hemmateenejad, "Multi-response optimization of factors affecting ultrasonic assisted extraction from Iranian basil using central composite design," *Food Chem.*, vol. 190, pp. 864–870, 2016.
[22] Z. Zhao, X. Xu, Q. Ye, and L. Dong, "Ultrasound extraction optimization of Acanthopanax senticosus polysaccharides and its antioxidant activity," *Int. J. Biol. Macromol.*, vol. 59, pp. 290–294, 2013.
[23] Z.-Y. Zhao, Q. Zhang, Y.-F. Li, L.-L. Dong, and S.-L. Liu, "Optimization of ultrasound extraction of Alisma orientalis polysaccharides by response surface methodology and their antioxidant activities," *Carbohydr. Polym.*, vol. 119, pp. 101–109, 2015.
[24] S. R. Ahmad, Dr. K. Pal and Dr. A . Kalam, "In vitro antioxidant properties of Chlorophytum borivilianum (Santapau & Fernandez), *J. Pharm. Pharm. Sci*.," vol. 3, no. 12, pp. 937–947, 2014.
[25] Z. Ying, X. Han, and J. Li, "Ultrasound-assisted extraction of polysaccharides from mulberry leaves," *Food Chem.*, vol. 127, no. 3, pp. 1273–1279, 2011.
[26] S. Balachandran, S. E. Kentish, R. Mawson, and M. Ashokkumar, "Ultrasonic enhancement of the supercritical extraction from ginger," vol. 13, pp. 471–479, 2006.
[27] S. Sahin, and R. Samli, "Optimization of olive leaf extract obtained by ultrasound-assisted extraction with response surface methodology," vol. 20, pp. 595–602, 2013.
[28] S. Zhao, K. Kwok, and H. Liang, "Investigation on ultrasound assisted extraction of saikosaponins from Radix Bupleuri," vol. 55, pp. 307–312, 2007.
[29] X. Fang, J. Wang, Y. Wang, X. Li, H. Zhou, and L. Zhu, "Optimization of ultrasonic-assisted extraction of wedelolactone and antioxidant polyphenols from Eclipta prostrate L using response surface methodology," vol. 138, pp. 55–64, 2014.
[30] S. H. Kim, H. K. Kim, E. S. Yang, K. Y. Lee, S. D. Kim, Y. C. Kim, and S. H. Sung, "Optimization of pressurized liquid extraction for spicatoside A in Liriope platyphylla," vol. 71, pp. 168–172, 2010.
[31] Y. Xu and S. Pan, "Effects of various factors of ultrasonic treatment on the extraction yield of all-trans-lycopene from red grapefruit (Citrus paradise Macf .)," *Ultrason. - Sonochemistry*, vol. 20, no. 4, pp. 1026–1032, 2013.
[32] K. N. Prasad, F. Abdulrahman, B. Yang, K. Weng, R. Nagasundara, A. Azlan, and A. Ismail, "Response surface optimisation for the extraction of phenolic compounds and antioxidant capacities of underutilised Mangifera pajang Kosterm . peels," *Food Chem.*, vol. 128, no. 4, pp. 1121–1127, 2011.
[33] C. Liyana–Pathirana and F. Shahidi, "Optimization of extraction of phenolic compounds from wheat using response surface methodology," vol. 93, pp. 47–56, 2005.

eureca 2016 – Conference Paper
Paper Number 2CE17

Experimental Studies on Deep Eutectic Solvents based Carbon Nanotubes Nanolubricant

Lee Pak Kee[1], Rashmi G. Walvekar[1*]

[1]*Chemical Engineering, Taylor's University Lakeside Campus, Malaysia*

[*]Corresponding Author Email: RashmiGangasa.Walvekar@taylors.edu.my

Abstract

DESs namely glyceline (glycerol + choline chloride) are explored to be developed as the base fluid of nanolubricants which are dispersed with f-MWCNTs in concentrations of 0.01, 0.05 and 0.10 wt%. The stability of synthesised nanofluids is assessed by sediment photograph capturing for duration of 2 weeks to observe the homogeneity of suspension and formation of sediments. The effect of temperature on thermal conductivity of nanofluids are measured at 25, 40 and 60℃ while viscosity of base fluids are measured at 25, 40 and 100℃ which is in accordance with ASTM standard. The thermal stability of synthesised samples are characterised by TGA. It is found that the stability of nanofluids increases with viscosity of base fluid and the loading of nanoparticles up until 0.10 wt% CNTs due to the increasing presence of functional groups which repel each other, similarly the stability of aforementioned nanofluids increases with base fluid viscosity due to reduced settling velocity. The nanofluids are found to destabilise beginning at 70℃, however homogenous suspension can be formed again if the fluids are agitated. Besides that, the enhancement in thermal conductivity increases with the concentration of CNTs whereby DES 4 based nanofluids display the largest percentage enhancement of 8.37% in thermal conductivity. The viscosity of DES 1 – DES 4 were found to decrease with increasing temperature by 93.33 – 95.03% at 100℃, similar trend is observed from increasing the concentration of the constituent salt which is explicable by the increased free volume in the liquid. DES 4 with ChCl : Glycerol molar ratio of 1:5 as the base fluid and CNTs concentration of 0.1 wt% display the highest stability and thermal conductivity enhancement. TGA shows that synthesised DESs and nanofluids are stable up to 200℃ while the presence of CNTs with concentration ranging from 0.01 – 0.1 wt% has minimal effect on the thermal stability of DESs based CNTs nanofluids. Hence the enhancement in thermal conductivity and decrease in viscosity as the effect of increasing temperature demonstrate the potential of glyceline based nanofluid to be developed as nanolubricant.

Keywords: Deep eutectic solvent, nanolubricant, functionalized carbon nanotubes, glyceline.

1. Introduction

Lubricants introduce a layer of surface between two surfaces sliding against each other, reducing friction in the process. Its wide applications range from automobile, aircrafts, industry machineries to biomedical, for instance artificial joints. Aside from providing lubrication to mechanisms, liquid lubricants, the form of lubricant most broadly used are useful in providing damping and cooling effect [1,2].

Nanofluids, a term coined in 1995 by Choi [3] are fluids made up of a base fluid with nanoparticles dispersed within. It possesses high thermal conductivity as it is affected by the properties, dimensions, shape and volume fraction of nanoparticles, thereby enhancing heat transfer [4]. Previous research has also shown that adding nanoparticles into lubricant base oil reduces friction and enhance tribological properties performance by depositing on the contacting surface [5]. Therefore, nanofluids have high potential to be developed as coolants or lubricants in automobile and electronic industries.

Despite advancing lubricant technology, the application of lubricant in specialized field where reduced pressure environments and extreme temperatures are encountered is still limited due to the unavailability of suitable lubricants. Moreover, light alloys which are replacing iron-based materials attributed to their low densities and their ability to form layers that offer corrosion protection, namely magnesium, titanium and aluminium have high reactivity towards conventional lubricants rendering them unsuitable to be used as lubricants in these cases [6].

Ionic liquids emerge as a new prospective lubricant that could be used in severe conditions thus overcoming problems faced by conventional lubricants. ILs are salts with melting points below 100^{o}C and usually composed of an asymmetric organic cation coupled with an inorganic anion. They have desirable properties like negligible volatility, thermal stability and low flammability which make them potential lubricant. Furthermore, ILs can be made from variety of anions and cations, this versatility allows them to be tuned to their own unique properties, estimated in the order of one million [7]. Nevertheless, the biggest concern in the application and synthesis of ILs remained to be their environmental acceptability and high cost of synthesis [4,6].

The discovery of deep eutectic solvents (DESs) as a new class of ILs analogues provides alternatives to overcome the disadvantages of ILs. DESs are typically formed using quaternary ammonium salts and a hydrogen-bond donor (HBD). DESs share the physiochemical characteristics of ILs such as low volatility and superior to ILs in that DESs are environmental benign, cheaper to synthesise, non-reactive with water biodegradable and low toxicity. Radošević et al found that choline chloride:glycerol DESs possess low cytotoxicity and classified as readily biodegradable considering their high degree of mineralisation. [8]. Hence, the potentials of DESs glyceline being used as the base fluid for nanolubricants have motivated this research.

2. Methodology

The research for this project was solely experimental based where properties of DES as the base fluid with nanoparticles added will be studied. The chemicals required

to perform this research were choline chloride ($C_5H_{14}ClNO$), glycerol 99.5% AR ($C_3H_8O_3$), and functionalized multi-walled carbon nanotubes (f-MWCNTs). Glycerol was obtained from Chemolab Supplies with high purity (>99.5%) and used for the synthesis of glyceline (glycerol and choline chloride) DES without further purification. f-MWCNTs with diameter of 10-20 nm is purchased from NE. Scientific with purity of >97%.

2.1 Synthesis of DES

In this research four DESs were prepared using choline chloride (ChCl) as the salt and glycerol as the HBD in different molar ratios as shown in Table 2.1, named glyceline. The mixed chemical were stirred at 300 rpm using a magnetic hot plate stirrer (Wisd Laboratory Instrument, MSH-20D) for 2 to 3 hours or until a colourless liquid is formed with temperature of 120℃ [9].

Table 2.1 Compositions of synthesised DESs with their respective abbreviations

Salt	HBD	Molar ratio (Salt : HBD)	Abbreviation
Choline Chloride	Glycerol	1:2	DES 1
		1:3	DES 2
		1:4	DES 3
		1:5	DES 4

2.2 Synthesis of CNT Nanofluid

F-MWCNTs of different weight fractions (0.01, 0.05 and 0.10 wt%) were suspended in each of the synthesised DESs respectively as shown in Table 2.2. The suspensions were then homogenised using water bath sonicator (Elma, Elmasonic P) at room temperature for 4 hours, this method is known as two-step method and it is popular due to its simplicity [10].

Table 2.2 Compositions of nanofluids with their respective abbreviations

DES	*Concentration (wt%)*	*Abbreviation*
1	0.01	NF 1
	0.05	NF 2
	0.10	NF 3
2	0.01	NF 4
	0.05	NF 5
	0.10	NF 6
3	0.01	NF 7
	0.05	NF 8
	0.10	NF 9
4	0.01	NF 10
	0.05	NF 11
	0.10	NF 12

2.3 Stability Analysis

The stability of each sample was determined by observing the homogeneity of the synthesised nanofluids and the amount of sediments. The sample remained high homogeneity and with least sediment would be the most stable compound. Photographs of nanofluids at day 0, 4, 7 and 14 after water bath sonication were taken to determine the sample with highest stability.

2.4 Thermal Conductivity Measurements

The thermal conductivity of nanofluids and DESs were measured at different temperatures of 25 – 60ºC using KD2 Pro Thermal Properties Analyzer (Decagon Devices, Pullman WA, USA). A probe of 6 cm long, 1.3 mm diameter (KS-1) was used for glycerol based fluids since KS-1 is well suited for high viscosity fluids like glycerol or oil based fluids with accuracy of ±5%. All readings were taken with the samples being immersed in silicon oil bath to heat and maintain the temperatures of nanofluids at 25, 40 and 60ºC. The instrument was set to record readings in interval of 15 minutes. 5 readings, if the readings were constant or more were taken to reduce errors for every sample measured at different temperature.

2.5 Viscosity Measurements

Viscosity of DESs were measured by Harkee MARS III Rheometer with spindle plate size P35TiL coupled with lower plate TMP 35 at temperature of 25, 40 and 100℃, which was in accordance with ASTM standard for kinematic viscosity of liquids. All measurements were done with the same shear rate of 10 s^{-1}. For calibration purpose, the spindle was allowed to autozero prior to every reading taken for 1 ml of each sample.

2.6 Thermogravimetric Analysis (TGA)

The thermal stability of DESs and nanofluids were assessed by TGA, using instrument from Perkin Elmer STA6000. The samples were heated from room temperature to 600℃ with nitrogen flow as the inert gas at heating rate of 10℃/min.

3. Results and Discussion

3.1 Stability Analysis

Photographs of sonicated nanofluids at day 0, 4, 7 and 14 were captured and shown as Figure 1, 2, 3 and 4 where the sequence of arrangement represent DES 1, DES 2, DES 3 and DES 4 based nanofluids from left to right. The nanofluids were arranged in such a way that the concentration of CNTs increases from left to right for each DES. Figure 1 indicates that well-dispersed, homogenous nanofluids were obtained after sonication as the functionalisation of CNTs surface attached functional groups such as carboxylic groups onto CNTs surface, which possess polar properties, increasing its solubility in polar solvents [11].

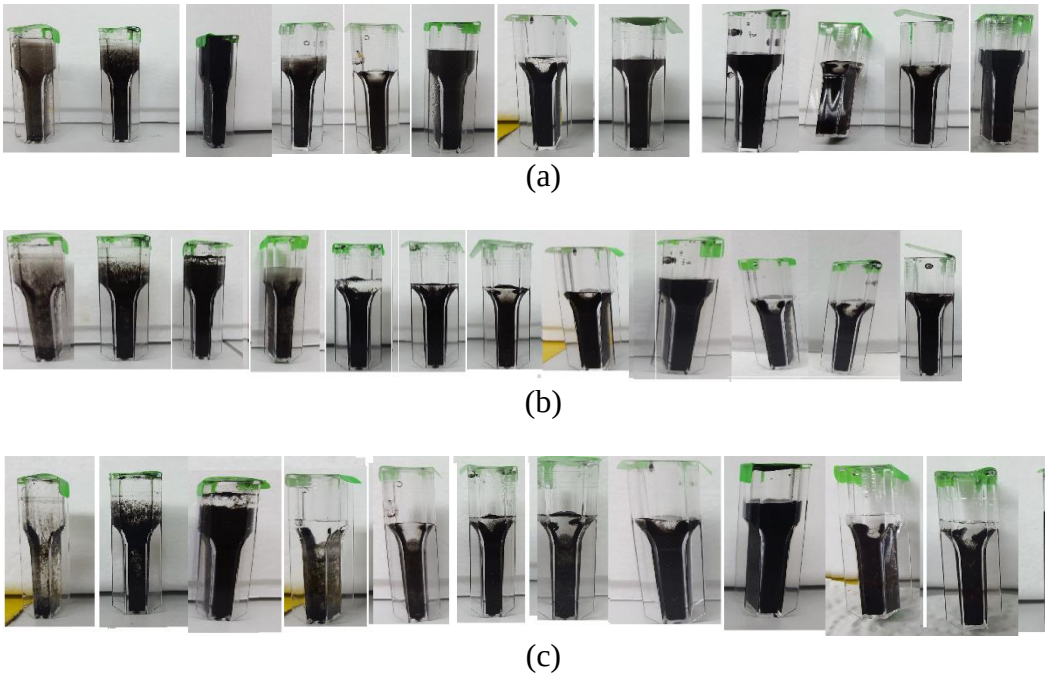


Figure 1: From left, NF1-12 on the fourth day.

Figure 2 indicates that nanofluids with higher loading of functionalized carbon nanotubes displayed higher stability relative to nanofluids with lower loading of nanoparticles. This is consistent with the results reported by Lamas et al [12]. The increased in nanoparticles concentration and aspect ratio reduce the settling velocity of f-CNTs based nanofluids due to hindered settling, an interaction between particles. The number of functional groups repelling each other increased as a result of increase in nanoparticles concentration thus nullifying the attractive force between nanoparticles and gravitational force.

It should also be noted that the stability of nanofluids increase as the viscosity of base fluid increase. This results is again in close agreement to the one obtained by Lamas et al. This could be explained by the expression of settling velocity, Equation (1) verified by Stokes [13], in which the settling velocity of a sphere is inversely proportional to the fluid viscosity, μ.

$$v_s = \frac{g(\rho_p - \rho){d_p}^2}{18\mu} \tag{1}$$



(a)

(b)

(c)

Figure 4: From left, NF1-12 on day (a) zero (b) seventh and (c) fourteenth.

It can be observed that nanofluids began to destabilise upon heating to temperature above 60℃. Nanoparticles began to form agglomerates followed by sedimentation. This observation can be explain by a surge in settling velocity due to a sharp reduction of viscosity of base fluid after heat addition. However, it is worth to mention that a homogenous fluid can be formed again if the agglomerated nanofluid was given sufficient agitation. Hence if the nanofluids are to be used as lubricant, it should be circulated between the parts which requires lubrication and an agitator or mixing region.



Figure 3: Nanofluids heated up to 70℃ (left) and return to homogenous phase after agitated (right)

3.2 Thermal Conductivity

Generally, as the molar ratio of ChCl to HBD decreased, an increase in thermal conductivity was observed, partly due to the increased weight fraction of glycerol in the DES, as glycerol contains higher thermal conductivity compared to the synthesised glyceline in different molar ratios. The thermal conductivities of nanofluids were analysed through their percentage of enhancement in thermal conductivity from that of their base fluid, using Equation (2).

$$Percentage\ Enhancement, \% = \frac{k_{nanofluid} - k_{base\ fluid}}{k_{base\ fluid}} \times 100 \quad (2)$$

It can be seen that all of the nanofluids displayed a trend of increase in percentage enhancements as the concentration of MWCNT increases. This is consistent with the results reported by Rashmi et al [14], in which the increase in thermal conductivity can be attributed to the intrinsic heat conducting ability of carbon nanotubes. Similar results were obtained by Kumaresan and Velraj [15], which stated that the transfer of heat through carbon nanotubes is more effective owing to the enhanced straightness ratio. The greatest thermal conductivity enhancement of 8.37% was seen in NF12, which is DES 4 based, at temperature of 60℃ and 0.10 wt% of MWCNT while the lowest enhancement was seen in NF7, which is DES 3 based, at temperature of 60℃ and 0.01 wt% of MWCNT, with merely 0.41% of enhancement.

Based on Figure 4, another trend was noticed whereby the percentage of enhancement in thermal conductivity at higher temperature was significantly higher for DES 4 based nanofluid. On the other end of the spectrum, DES 1 based nanofluids displayed significantly higher thermal conductivity enhancement at lower temperature. The exact mechanism behind this phenomena is yet to be known and further studies would be conducted to observe the size of clusters of nanoparticles formed at different temperature in order to determine the effect of cluster size to the enhancement of thermal conductivity.

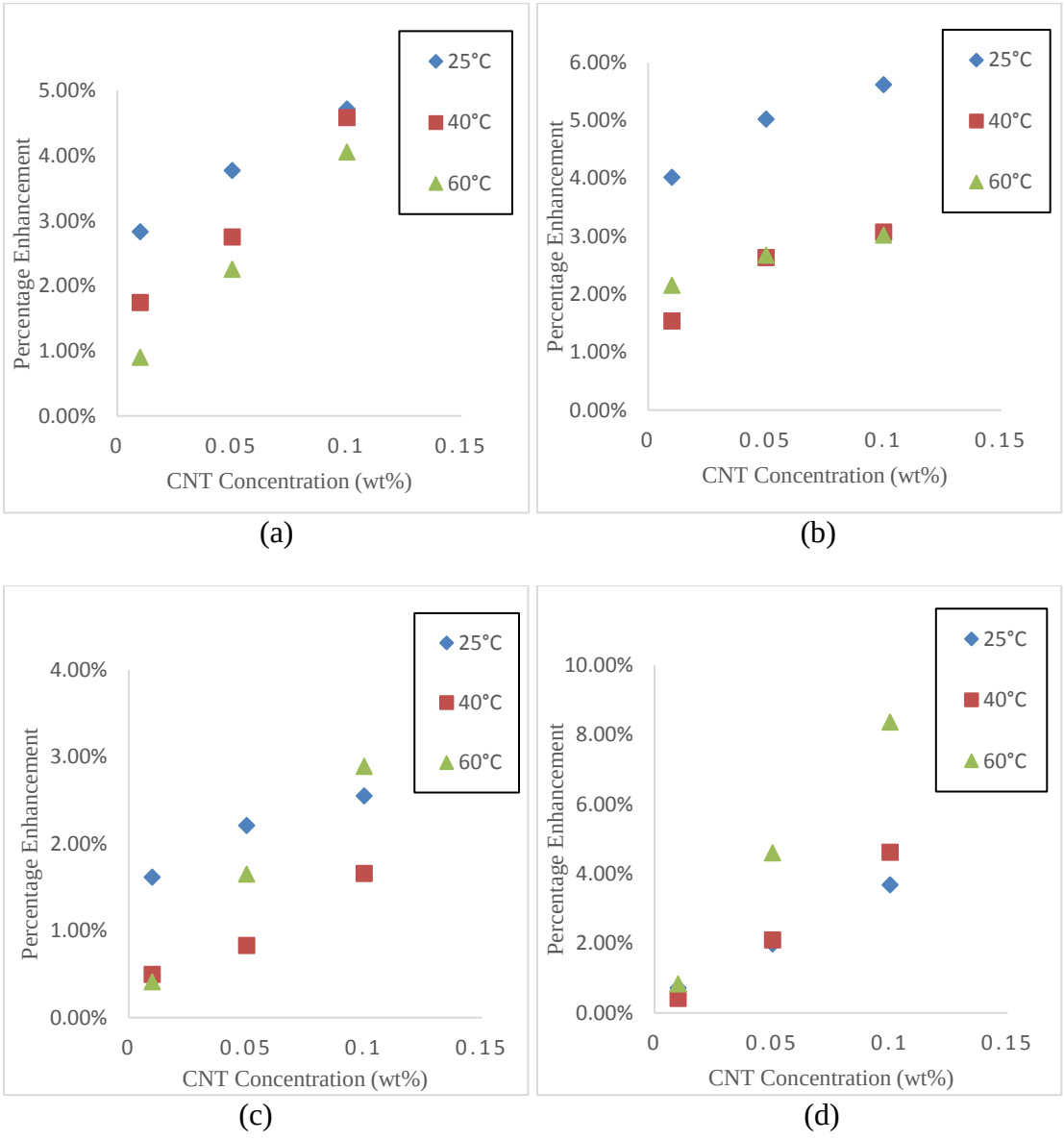


Figure 4: Percentage enhancement in thermal conductivity as a function of MWCNT concentration at different temperature for (a) DES 1 based nanofluids, (b) DES 2 based nanofluids, (c) DES 3 based nanofluids and (d) DES 4 based nanofluids.

3.3 Viscosity of DESs

Figure 5 shows a common trend of reduction in viscosity of DESs as the temperature increased from 25 to 100℃. The viscosity of the DES 1 – DES 4 were reduce by 93.33 – 95.03% at 100℃. This could be explained by the weakening of interactions strength between cations and anions at elevated temperature [16]. Similar behaviour were reported by D'Agostino et al [17] which showed that other ChCl based DESs displayed large reduction in viscosity with temperature.

As it can be seen from the pattern of viscosity as a function of temperature, the viscosity of DESs decreased in the order of DES 4, DES 3, DES 2 followed by DES 1 due to the decreasing concentration of glycerol, which has the higher viscosity compared to the glyceline synthesised. Besides, it has been reported that the increase in viscosity with decreasing ChCl concentration is consistent with the behaviour of density of glycerol-ChCl mixtures [18]. Another theory known as hole theory relates viscosity to the free volume and availability of holes in the fluid which permit the movement of ions. The type of salts would affect the size of holes distribution, and it is inferred that more viscous fluids contain smaller holes [19]. Hence the viscosity can also be closely related to the size of ions. Addition of salt into glycerol broke its three dimensionally hydrogen bonded liquid by complexing the hydroxide (OH) moieties to the anion of the salt, which lead to a decrease in surface tension, increasing the free volume of liquid hence permitting better movement of the ionic species [18].

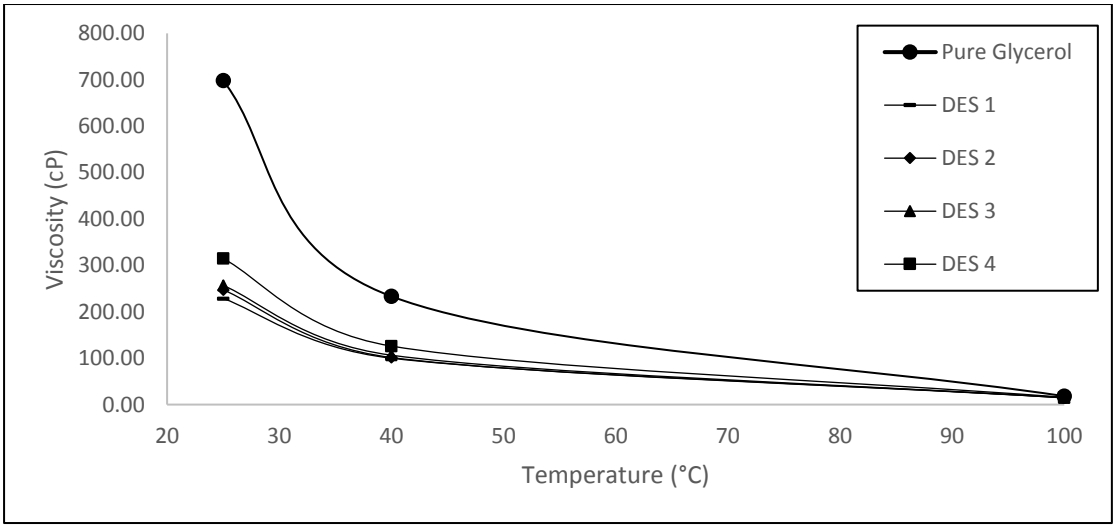


Figure 5: Effect of temperature on viscosity of pure glycerol and DES 1 – DES 4.

3.4 Thermogravimetric Analysis (TGA)

TGA is usually conducted to determine the thermal stabilities, otherwise known as decomposition temperatures for substances [76]. As it can be seen from the Figure 4.4.1-4.4.3, all of the samples are stable up to approximately 200℃. The decomposition temperature of all the samples fall within the range of 200 - 250℃. The decomposition temperature of DES glyceline produced in this research closely resembles to that of Zhao et al. [77], in which the decomposition temperature of glyceline with salt to HBD

molar ratio of 1:2 fall between 205 - 216℃. Hence this range of temperature define the upper boundary in which the application of synthesised nanofluids in this research as nanolubricants. In addition, a trend is observed for the TGA where presence of higher amount of constituent salt delays the thermal composition of sample. In other words, the higher the composition of salt in DESs, the higher the decomposition temperature. Furthermore, since all of the samples decompose within the same range of temperature, it can be assumed that the presence of nanoparticles CNTs with concentration of 0.01 - 0.1 wt% has minimal effect on the decomposition temperature of DESs based CNTs nanofluids.

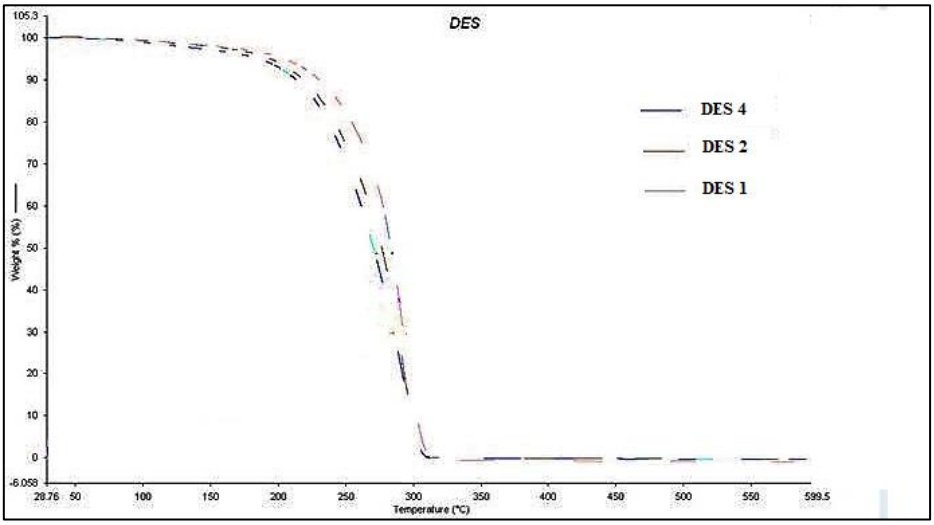


Figure 6: Thermogravimetric analysis of DESs.

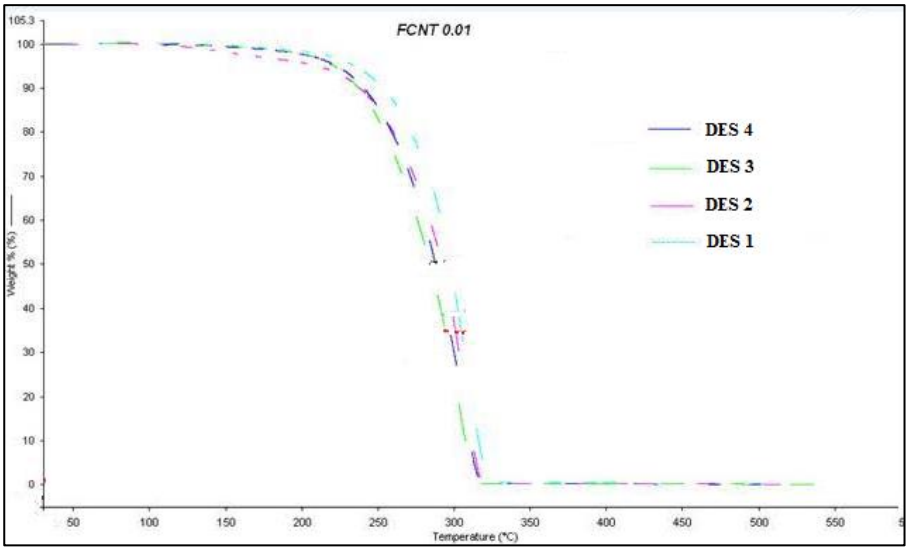


Figure 7: Thermogravimetric analysis of nanofluids with CNTs concentration of 0.01 wt%.

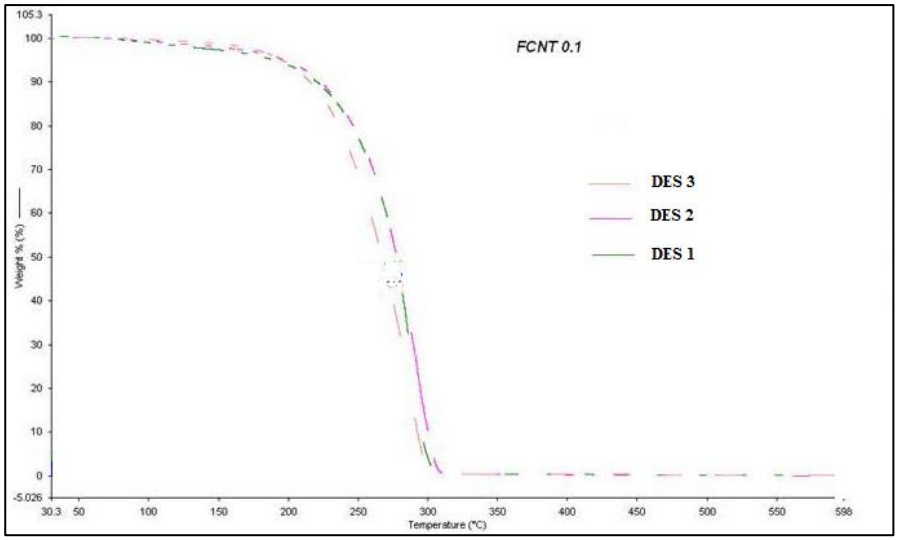


Figure 8: Thermogravimetric analysis of nanofluids with CNTs concentration of 0.1 wt%.

4. Conclusion

The prospect of DES glycerine-based carbon nanotubes nanolubricants is explored in this research and it is found that a stable and homogenous nanofluid can be formed. The stability of f-MWCNT nanofluids increases with the weight fraction of CNTs up until concentration of 0.10 wt% of CNTs due to the increasing presence of functional groups which repel each other, similarly the stability of aforementioned nanofluids increases with base fluid viscosity due to reduced settling velocity. Although the nanofluids begin to destabilise at 70℃, homogenous suspension can be formed again if the fluid is agitated. Besides that, the enhancement in thermal conductivity increases with the concentration of CNTs whereby DES 4 based nanofluids display the largest percentage enhancement in thermal conductivity. The the viscosity of DES 1 – DES 4 were found to decrease with increasing temperature by 93.33 – 95.03% at 100℃, similar trend is observed from increasing the concentration of the constituent salt which is explicable by the increased free volume in the liquid. Thermogravimetric analysis shows that synthesised DESs and nanofluids are stable up to 200℃ while the presence of higher amount of constituent salt of DESs increases the decomposition temperature. In addition, the presence of CNTs with concentration ranging from 0.01 – 0.1 wt% has minimal effect on the thermal stability of DESs based CNTs nanofluids. DES 4 with ChCl : Glycerol molar ratio of 1:5 as the base fluid and CNTs concentration of 0.1 wt% display the highest stability and thermal conductivity enhancement.

References

[1] M. H. S. Elmunafi, D. Kurniawan, and M. Y. Noordin, "Use of Castor Oil as Cutting Fluid in Machining of Hardened Stainless Steel with Minimum Quantity of Lubricant," *Procedia CIRP*, vol. 26, no. 12th Global Conference on Sustainable Manufacturing - Emerging Potentials, pp. 408–411, Jan. 2015.

[2] Y. Shokoohi, E. Khosrojerdi, and B. h. Rassolian Shiadhi, "Machining and ecological effects of a new developed cutting fluid in combination with different cooling techniques on turning operation," *Journal of Cleaner Production*, Jan.

2015.
[3] S. U. S. Choi and J. A. Eastman, "Enhancing Thermal Conductivity of Fluids With Nanoparticles *," *Materials Science*, vol. 231, no. JANUARY 1995, pp. 99–105, 1995.
[4] Y. Xuan and Q. Li, "Heat transfer enhancement of nanofluids," *International Journal of Heat and Fluid Flow*, vol. 21, no. 1, pp. 58–64, Feb. 2000.
[5] A. Hernández Battez, R. González, J. L. Viesca, J. E. Fernández, J. M. Díaz Fernández, A. Machado, R. Chou, and J. Riba, "CuO, ZrO2 and ZnO nanoparticles as antiwear additive in oil lubricants," *Wear*, vol. 265, no. 3–4, pp. 422–428, Jul. 2008.
[6] M. D. Bermúdez, A. E. Jiménez, J. Sanes, and F. J. Carrión, "Ionic liquids as advanced lubricant fluids," *Molecules*, vol. 14, no. 8, pp. 2888–2908, 2009.
[7] N. Canter, "Evaluating ionic liquids as potential lubricants.," *Tribology & Lubrication Technology*, vol. 61, no. 9, pp. 15–17, Sep. 2005.
[8] K. Radošević, M. C. Bubalo, V. G. Srček, D. Grgas, T. L. Dragičević, and I. R. Redovniković, "Evaluation of toxicity and biodegradability of choline chloride based deep eutectic solvents.," *Ecotoxicology and environmental safety*, vol. 112, pp. 46–53, Feb. 2015.
[9] R. B. Leron and M.-H. Li, "Molar heat capacities of choline chloride-based deep eutectic solvents and their binary mixtures with water," *Thermochimica Acta*, vol. 530, pp. 52–57, Feb. 2012.
[10] A. Ghadimi, R. Saidur, and H. S. C. Metselaar, "A review of nanofluid stability properties and characterization in stationary conditions," *International Journal of Heat and Mass Transfer*, vol. 54, no. 17–18, pp. 4051–4068, Aug. 2011.
[11] H. Xie, H. Lee, W. Youn, and M. Choi, "Nanofluids containing multiwalled carbon nanotubes and their enhanced thermal conductivities," *Journal of Applied Physics*, vol. 94, no. 8, pp. 4967–4971, 2003.
[12] B. Lamas, B. Abreu, A. Fonseca, N. Martins, and M. Oliveira, "Assessing colloidal stability of long term MWCNT based nanofluids," *Journal of Colloid and Interface Science*, vol. 381, no. 1, pp. 17–23, 2012.
[13] G. G. Stokes, "On the Effect of the Internal Friction of Fluids on the Motion of Pendulums," *Transactions of the Cambridge Philosophical Society*, vol. 9, p. 8, 1851.
[14] W. Rashmi, a. F. Ismail, I. Sopyan, a. T. Jameel, F. Yusof, M. Khalid, and N. M. Mubarak, "Stability and thermal conductivity enhancement of carbon nanotube nanofluid using gum arabic," *Journal of Experimental Nanoscience*, vol. 6, no. 6, pp. 567–579, 2011.
[15] V. Kumaresan and R. Velraj, "Experimental investigation of the thermo-physical properties of water–ethylene glycol mixture based CNT nanofluids," *Thermochimica Acta*, vol. 545, pp. 180–186, Oct. 2012.
[16] A. Popescu, "Density, viscosity and electrical conductivity of three choline chloride based ionic liquids," *Bulgarian Chemical …*, vol. 46, no. 3, pp. 452–457, 2014.
[17] C. D'Agostino, R. C. Harris, A. P. Abbott, L. F. Gladden, and M. D. Mantle, "Molecular motion and ion diffusion in choline chloride based deep eutectic solvents studied by 1H pulsed field gradient NMR spectroscopy.," *Physical chemistry chemical physics : PCCP*, vol. 13, pp. 21383–21391, 2011.
[18] A. P. Abbott, R. C. Harris, and K. S. Ryder, "Application of hole theory to define ionic liquids by their transport properties," *Journal of Physical Chemistry B*, vol. 111, no. 18, pp. 4910–4913, 2007.

[19] G. Garcia, S. Aparicio, R. Ullah, and M. Atilhan, “Deep Eutectic Solvents: Physicochemical Properties and Gas Separation Applications,” *Energy & Fuels*, vol. 29, pp. 2616–2644, 2015.

eureca 2016 – Conference Paper
Paper Number 2CE18

Anti-inflammatory Activity Determination and Optimization of the Isolated Compounds from the Roots of *Chlorophytum Borivilianum* (Safed musli)

Leroy Liaw Kwok Leung, Dr. Chua Bee Lin

School of Engineering, Taylor's University, Lakeside Campus
No. 1, Jalan Taylor's, 47500 Subang Jaya, Selangor, Malaysia

Abstract
Chlorophytum borivilianum (safed musli) is one of the most medicinally popular and important plant in India. Various scientific bioassay activity such as anti-stress, anti-inflammatory and many more have been documented on the compounds of *C. borivilianum.* Saponin which is the second most abundant active compound of *C. borivilianum* has been proven to have various pharmacological, bisoassay and medicinal properties. However, there is still lack of optimization study done on the extraction of saponins from the roots of *C. borivilianum.* In this research, the extraction process of saponins from the aqueous extract of the roots of *C. borivilianum* was optimized by using single experimental design and response surface methodology (RSM). Ultrasound-assisted extraction was developed for the effective extraction of saponins and the extract was quantified by spectrophotometric method. Two independent variables (extraction time and solid to solvent ratio) with a five level design were evaluated using central composite design (CCD). The range of extraction time and ratio of solid to solvent that were used in the optimization process were 20 to 40 minutes and ratio of 1:20 to 1:40 g/ml. A second-order polynomial model was developed to describe the experimental data for the total saponins content. By using the model developed by RSM, the optimised extraction parameters were obtained which were 26 minutes and 1:28 g/ml . The predicted yield of saponins by model was compared with the actual yield and had relative error of 3.78 %. Besides that, anti-inflammatory activity of the extract was assessed using inhibition of albumin denaturation method and has inhibition of 36.6%.

Keywords: Ultrasonic-assisted extraction, Anti-inflammatory, *Chlorophytum borivialianum*, Optimization

1. Introduction

Medicinal plants or better known as phytomedicine has been used long before recorded history as early as three thousand BC. Medicinal plant refer to the use of different parts of the plant such as roots, seeds, leaves or flowers for medicinal purposes. Before modern medicine exist, chemists used to extract active ingredients from plants to make medicine. Therefore, most of the pharmaceutical drugs are derived from plant's kingdom. The growth of medicinal plants market is improving dramatically over the years although in many cases chemists or scientists are still not sure about the side effect of specific ingredient from the medicinal plant. One of the reasons that medicinal plants have becoming more popular over the years is because of the increasing interest in self-care of patients. Consumers prefer to use medicinal plants which are normally labelled as 'natural' rather than modern drugs which are known as 'synthetic' [1]. Some of the commonly used medicinal plants include *Kava* that has been linked to cure liver toxicity, *Ginkgo* that has been widely use to improve memory, *Chlorophytum borivilianum* is proven to boost vitality and many more other plants in the previous findings.

C. borivilianum or better known as 'white gold' in Indian systems of medicine is now gaining popularity due to its celebrated aphrodisiac and immunomodulatory properties [2]. *C. borivilianum* is traditionally considered as general health promotive. Some of the common uses of this plant are for the production of hormone known as testosterone and to improve circulation of blood treating fatigue [3]. The most valuable part of the plant is its roots, which contain 42% carbohydrate, 80-89% protein, 3-4% fibre and 2-17% saponin [4]. Saponin which is one of the most abundant compounds in the root of *C. borivilianum* is made up of both polar and nonpolar groups. These groups provide saponin with strong surface-active properties that responsible for many beneficial effects. Some beneficial effects of saponins include inhibit protein degradation, improve active nutrient transport in intestine, and improvement of growth in various animal species [5]. Presently, crude extract of *C. borivilianum* has been utilized for treatment of human diseases especially in anti-inflammatory and other bioassay activity [6]. Inflammation is a natural reaction of living tissues to injury, infection or irritation. At the site of infection, the number of neutrophils would increase which produce a series of oxidative burst [7]. If inflammation is severe, it could be very harmful, causing life threatening hypersensitivity reactions and lastly organs damage [8].

Among the latest extraction methods, ultrasound-assisted extraction (UAE) is the most selected method because it shows more promising results in term of capability and efficacy in obtaining significant saponin yields [9]. In addition of that, UAE method is preferable to be carried out using ultrasonic bath instead of using a sonicator probe horn for direct sonication because ultrasonic bath is commonly available, easy to handle and economically advantageous [10]. UAE is known as green extraction technologies which involve less hazardous chemical, less energy consumption and more environmental friendly compared to conventional extractions such as maceration and Soxhlet extraction [11]. The working principle of UAE is by creating cavitation bubbles in the solvent by acting as a micro jet to denature the plant cell wall when the bubbles collapse resulted in a greater yield. Overall, UAE is a very good extraction method to separate and isolate saponins for analysis and quantifying purpose. The procedure for UAE is also rather simple and fast for complete extraction with average of 20 minutes

duration. One of the downside of UAE is that, filtration and rinsing after extraction is mandatory which involve longer time and have danger of contaminating the extract during the process [11]. In order to get a comparable result, several specimens should be run simultaneously to obtain average data. In addition of that, UAE is advisable for thermolabile analysis such as extraction of saponin from plants [12].

RSM is an effective statistical technique and was initially introduced by Box and Wilson in year 1951 within the ambit of chemical engineering in an attempt to assess the interactive effect of process variables and build a numerical model that precisely describes the entire process with a minimum experimental effort [13]. In order to overcome the disadvantage of single factor experimental design, response surface methodology (RSM) is introduced for further optimisation purpose. Single factor experimental design approach will lead to increase of time and costs if the manipulated variables of the research increases as it is an empirical method and known as one-factor-at-a-time approach, in which one factor is varied at a time, while keeping all the other factors constant [14]. RSM takes into account of the interaction effects between the variables and able to provide the optimal extraction parameters to gives the best yield of extraction [15]. RSM is used in many instances to minimum experimental trials needed with a goal to evaluate multiple manipulated variables and their interactions in order to obtain highest output. The use of RSM has been successfully utilized for optimization of extraction parameters includes serine protease from kesinai (*Streblusasper*) leaves [16], crude polysaccharides from *Citrus medica L. var. sarcodactylis* [17] and betacyanin and betaxanthin from *Opuntia ficus-indica* [18].

Previously, many researchers have done the studies on extraction of saponins from various plants including *C. borivilianum*. The methods of extraction used also varies from conventional method up to green technology extraction method such as ultrasonic-assisted extraction [19]-[25] However, limited studies have been done to optimise the extraction process to maximise the yield of saponin which have been proven to contain various pharmacological activity which are beneficial to us. In this study, optimisation process was carried out to maximise the extraction yield of valuable saponins from the roots of *C. borivilianum* while ensuring that the saponins does not lose its anti-inflammatory properties using single factor experimental design and RSM. Extraction parameters that were optimized in this study include ratio of solid to solvent and extraction time. Lastly, the parameters found in the experiment was used in the extraction process to validate the mathematical model form. Best to our knowledge, there have been no previous study done on the optimisation of the extraction of saponins from the roots of *C. borivilianum* using ultrasonic-assisted extraction method.

2. Materials and Methods

2.1 Materials

The main material used in this experiment the root of *C. borivilianum* was obtained from University Teknologi Malaysia (UTM) and prepared based on the methods presented by Chua [26]. The root of this plant has much higher economic value compared to other parts of the plant. The root of *C. borivilianum* was washed and dried in oven (Model UFE-800, Memmert, Germany) at 40 ^{o}C before being cut and ground into powder to increase the surface area to volume ratio. The powder was being sieved through 60-mesh sieve to get uniform size. This is to ensure that the powder dissolve

uniformly during extraction process. Lastly, the powder sample was packed in polyethylene bag and kept at room temperature until needed for further analysis.

2.2 Chemicals and Reagents

Diosgenin and vanillin were purchased from Sigma Aldrich (St. Louis, MO, U.S.A.); Methanol AR, Ethanol and Sulfuric acid 95%-97% were purchased from Friendemann Schmidt Chemicals. All chemicals and reagents used were of analytical reagent grade.

2.3 Extraction Procedure

Extraction was carried out based on method presented by Guo [22] with slight modification made. The dried and powdered sample (1 g) of *C. borivilianum* were mixed with different volumes (10 to 50 ml) of 80% methanol. The samples were then inserted into a sonicator (Model 5300 EP, Soltec, USA) with pulses of 20kHz incorporated with a temperature controller set at 25 ^{o}C for varying amount of time (20 to 60 min). The ratio of solid to solvent and extraction time for optimization process was based on the experimental design generated by Design-Expert Software after obtaining the optimal experimental range from single factor experiment. The extract was then filtered using whatman No. 1 filter paper and evaporated to dryness using rotary evaporator (Hei-VAP, Heidolph, Germany). All experiments were carried out in triplicates and the results is shown as mean values $\pm$ standard deviations.

2.4 Identification and Quantification of Saponins in the *C. Borivilianum* Extract

In order to ensure that saponins exist in the extract, a simple froth test was carried out based on method presented by Ncube [23]. The dried extract was dissolved in 10 ml of distilled water. Then the solution was shaken vigorously for 20 seconds before left standing in a upright position. The solution was observed for over a period of 45 minutes and a thick froth layer was formed on the surface of the liquid confirming the presence of saponins in the crude extract.

Vanillin-sulfuric acid colorimetric test was carried out to determine the concentration of saponins in the extracts following the methods published by Hiai et al. [24]. The chemical reagents required for this test include vanillin reagent, 72% (v/v) sulfuric acid, standard saponin solution and 80% aqueous methanol. Vanillin reagent was prepared by dissolving 800 mg of vanillin in 10 ml of analytical grade ethanol. 72% (v/v) sulfuric acid was prepared by adding 72 ml of sulfuric acid (analytical grade, 95%, w/w) to 28 ml of distilled water. 80% aqueous methanol was prepared by adding 80 ml of analytical grade methanol to 20 ml of distilled water.

A standard saponin curve was prepared using diosgenin as standard based on method presented by Makkar [5]. 10 mg of diosgenin was dissolved in 16 ml of methanol before adding 4 ml of distilled water. The final concentration of diosgenin in the standard saponin solution samples was 0.5 mg/ml in 80% aqueous methanol. The standard sample were immediately diluted to respective concentration by adding 0, 0.05, 0.10, 0.15, 0.20, 0.25 ml in test tubes and the volume were made up to 0.25 ml with 80% aqueous methanol. Then, 0.25 ml of vanillin reagents were added before adding 2.5 ml of 72% sulfuric acid into the respective test tubes slowly on the inner side of the

wall. The solutions were mixed well using a vortex shaker (QL-866, China) before being transferred to a water bath adjusted to 60^{o}C. After 10 minutes, the test tubes were cooled in ice-cold water for 4 minutes. Lastly, the absorbance of the standard samples were measured using UV-VIS spectrophotometer (Genesys 10S, Thermo Scientific, USA) at 544 nm. A standard curve was obtained by plotting the absorbance value (Au) against the concentration of the standard saponin solution (mg/ml).

Dried extract was dissolved in 80% aqueous methanol give a final of 10 mg/ml. After that, 0.25 ml of the extract solution was mixed with 0.25 ml of vanillin reagent and 2.5 ml of 72% sulfuric acid in test tubes. The solution was mixed well using a vortex shaker before being transferred to a water bath that was adjusted to 60 ^{o}C. After 10 minutes, the test tube was cooled in ice-cold water for 4 minutes. Lastly, the absorbance of the extract solution was measured using UV-VIS spectrophotometer at 544 nm against blank reagent. All experiments were carried out in triplicates to obtain the average absorbance values. The extraction yield of saponin was quantified based on the developed calibration curve.

2.5 Single Factor Experimental Design

Single factor experiment was being carried out to determine the experimental range of the extraction time and the ratio of solid to solvent ratio based on the highest yield extraction of saponin in the crude extract. A two factor-five level single factor experimental design was employed in this study. The experimental range of the single factor experimental design is shown in (Table 1).

Table 1. Experimental range of the single factor experimental design

Extraction parameters	Parameters levels				
	1	2	3	4	5
Ratio of solid to solvent (g/ml)	1:10	1:20	1:30	1:40	1:50
Extraction time (min)	20	30	40	50	60

2.6 RSM Experimental Design

The range of response surface methodology (RSM) was determined using single factor experiment. RSM was carried out to optimize the extraction of saponins. RSM was used to optimize the ratio of solid to solvent and extraction time. A two-level-two-factor, Central Composite Design (CCD) consist of total 13 experimental runs were carried out [25]. Variables which include the ratio of solid to solvent and extraction time were coded at two level (-1, 1) representing lower and higher value.

Design-Expert Software Version 7.0.0 trial program (Stat-Ease Inc. Minneapolis, USA) was used for experimental design of RSM. In order to establish the optimum conditions for the yield of saponin from *C. borivilianum*, analytical steps taken were regression analysis to obtain quadratic models, analysis of variance (ANOVA) and 3D response surface plot [26]. The fitness of the model to responses were estimated using coefficient of determination (R^2).

2.7 Bioassay Test of *in-vitro* Anti-inflammatory Activity of the Extracts

Bioassay test was carried out on the optimised saponins extract to prove that the saponins obtained from the roots of C. borivilianum has anti-inflammatory activity. The test was carried out according to Sigma protocol with minimum modification made [27]. The test sample was in kept at 37 ^{o}C in DMSO for 10 minutes before tested. Firstly, the assay medium which was made up of 80U hyaluronidase in 100 µL 20 mM sodium phosphate buffer was incubated with 25 µL of test sample After that, the 100 µL of hyaluronic acid was added to the mixture before being incubated for 45 minutes at 37 ^{o}C. Then, the mixture was precipitated with 1mL of acid albumin solution. After 10 minutes, the absorbance value of the sample was recorded at 600 nm. Each experiment will be carried out in triplicate and the mean absorbance is obtained. The percentage of inhibition of the extract was determined on a percentage basis relative to reference compound using Eq. (1).

$$Percentage\ of\ inhibition = \frac{Absorbance\ of\ extract}{Absorbance\ of\ reference\ compound} \times 100 \quad (1)$$

3. Results and Discussion

3.1 Quantification of Saponins in the *C. Borivilianum* Extract

Pure diosgenin was used as the standard for the calibration curve over a range of 5 different concentrations in 80% aqueous methanol. The curve shows linear relationship between the absorbance value and concentration of standard saponins solution. The accuracy and reliability of the graph is determined by the coefficient of determination (R^2). The determination of coefficient of the calibration curve is 0.965 which indicate satisfying linearity and the curve is able to define up to 96.5% variability of the feedback. The equation of straight line obtained from the calibration curve is shown in Eq. (2).

$$Y = 39.841X + 0.0676 \quad (2)$$

where absorbance value and concentration of the saponin (mg/ml) were express as Y and X respectively. The extraction yield of saponins in this study is expressed in term of diosgenin in mg/ml.

Eq. (2) was rearranged to obtain Eq. (3) which is used to quantify the extraction yield of saponins.

$$X = \frac{Y-0.00676}{39.841} \quad (3)$$

3.3 Single Factor Experimental Design

The extraction parameters which include solid to solvent ratio and extraction time were studied by single factor experimental design before central composite design (CCD) was introduced to further optimize the experimental parameters. Single factor experimental design was carried out by manipulating one factor at a time while keeping the other factors at their center point in each set of experiment [28].

3.3.1 Effect of Extraction Time on Extraction Yield of Saponins

The longer the extraction time, the better the extraction yield [22] but optimum extraction time should be use so that the process will be economical to be carried out [29]. Extended period of extraction time required large amount of extraction solvent and may led to the decline of extraction yield [30]. Extraction time that were being studied range from 20 to 60 minutes with 10 minutes interval each. While manipulating the extraction time, the solid to solvent ratio was kept at 1:30 g/ml.The effect of extraction time on extraction yield of saponins is shown in (Fig. 1).

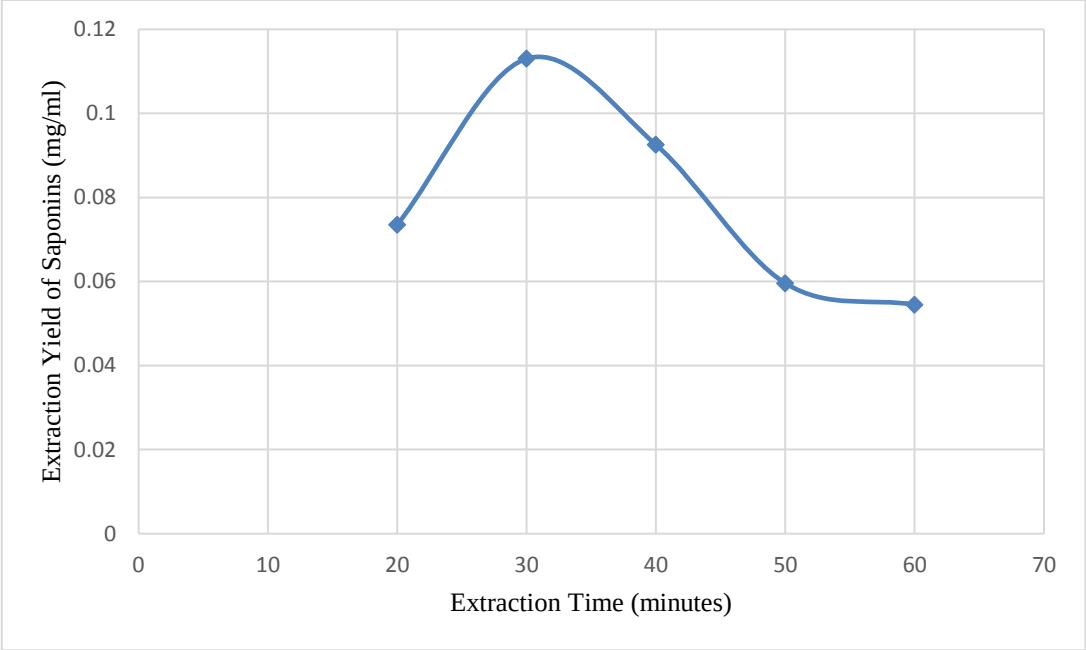


Figure 1. Effect of extraction time on the extraction yield of saponins

The result shown in (Fig. 1) shows that the extraction yield of saponins increases steadily with extraction time before decreasing significantly after extraction time exceed 40 minutes. From 20 to 30 minutes, the yield of saponins increases rapidly from 0.0735 mg/ml to 0.1130 mg/ml. Further increase in extraction time after 40 minutes decreases the extraction yield of saponins which may due to decomposition of saponin compound [31]. In addition of that, prolonged extraction time may cause readsorption of saponins on the plant particles due to the large surface areas form by prolonged extraction process [32]. Therefore, the range of extraction time chosen to be further optimize by using RSM was 20-40 minutes.

3.3.2 Effect of Solid to Solvent Ratio on Extraction Yield of Saponins

The second extraction parameter that was being studied was solid to solvent ratio. The main driving force of extraction process is the concentration gradient where lower solid to solvent ratio is preferable as it results in higher diffusion rate [33]. However, optimum volume of solvent should be used to achieve low solid to solvent ratio without compromising the extraction yield. This to minimize the waste of solvent

and reducing the cost of extraction process. Solid to solvent ratio that were being studied range from 1:10 to 1:50 g/ml minutes with 10 ml difference each. While manipulating the solid to solvent ratio, the extraction time was kept constant at 40 minutes. The effect of solid to solvent ratio on extraction yield of saponins is shown in (Fig. 2).

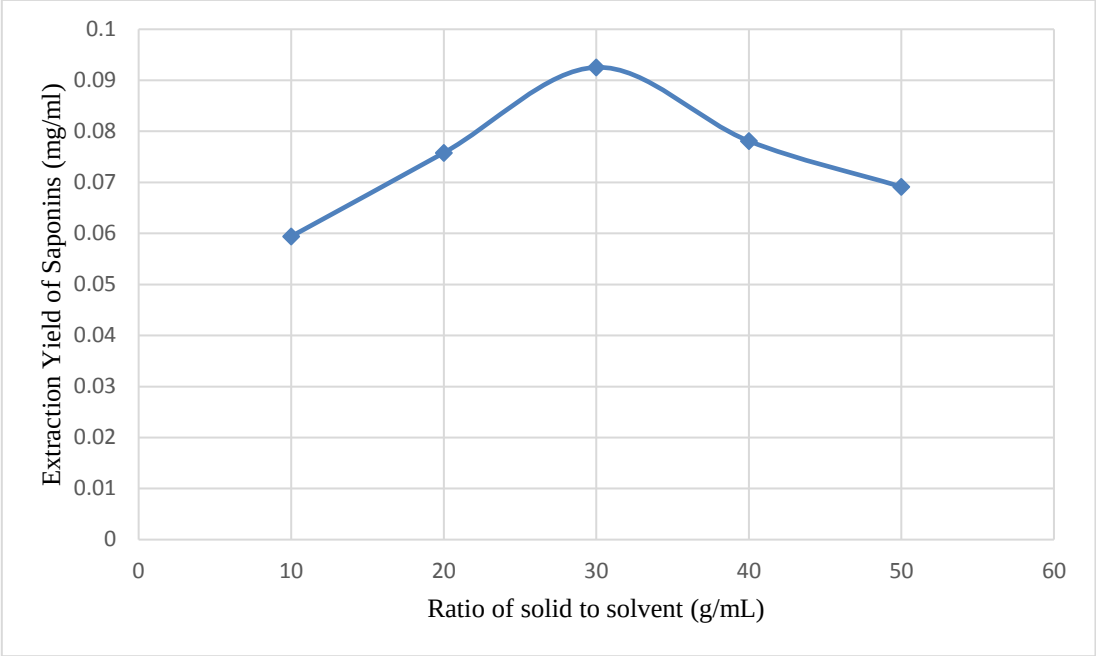


Figure 2. Effect of solid to solvent ratio on the extraction yield of saponins

According to (Fig. 3), overall result shows that solid to solvent ratio did not significantly affect the extraction yield of saponins. The extraction yield of saponins increases steadily as solid to solvent ratio decreases from 1:10 to 1:30 g/ml where extraction yield of saponins peak at 1:30 g/ml with 0.0925 mg/ml of saponins extracted. Further decrease of solid to solvent ratio decreases the extraction yield of saponins. This may be due to the saturation of saponins as the extract saponin has fully dissolve in the solvent [34]. Therefore, the range of solid to solvent ratio chosen to be further optimize by using RSM was 1:20 to 1:40 g/ml.

3.4 Optimization of Response Surface Methodology (RSM)

Results obtained from single factor experimental design were used to further optimized the extraction parameters by RSM using central composite design (CCD). The objective of the optimization process was to maximize the extraction yield of saponins and crude extract from root of *C. borivilianum.* Two variables which were chosen to be optimized were ratio of solid to solvent (X_1) and extraction time (X_2) while the response of the experiment was saponin yield (Y_1). The design matrix was generated by Design-Expert Software Version 7.0.0 program as shown in (Table 2). All the experiments were carried out in triplicate and are expressed as mean values as tabulated in (Table 2).

Table 2. Experimental results of central composite design (CCD) of saponin yield

Run	Extraction parameters		Response
	Ratio of solid to solvent (g/ml), X_1	Extraction time (min), X_2	Y_1 (mg/ml)
1	1:16	30	0.0739±0.0080
2	1:30	16	0.0814±0.0052
3	1:40	20	0.0855±0.0080
4	1:30	30	0.1130±0.0019
5	1:30	30	0.1104±0.0039
6	1:20	20	0.1179±0.0017
7	1:30	30	0.1078±0.0010
8	1:30	30	0.1054±0.0027
9	1:20	40	0.0668±0.0052
10	1:30	30	0.1154±0.0039
11	1:44	30	0.0733±0.0035
12	1:30	44	0.0748±0.0036
13	1:40	40	0.0781±0.0022

Experimental results show that the extraction yield of saponins range from 0.0668 to 0.1179 mg/ml. Experiment run number 6 with extraction parameter of 1:20 g/ml and 20 minutes yield the highest saponins of 0.1179±0.0017 mg/ml.

3.5 Analysis of Variance (ANOVA) for the Quadratic Polynomial Model

Based on the analysis done using Design-Expert Software Version 7.0.0 program, quadratic was the suggested model for this study. The results of ANOVA for the response surface quadratic polynomial model for the extraction yield of saponins was summarized in (Table 3). The extraction parameters were ratio of solid to solvent and extraction time which were denoted as X_1 and X_2 respectively.

Table 3. ANOVA for response surface quadratic polynomial model

Source	Sum of Squares	Degree of Freedom	Mean Square	*F*-value	*p*-value Prob > F
Model	5.850	5	1.170	7.49	0.0099
X_1	0.096	1	0.096	0.62	0.4582
X_2	0.920	1	0.920	5.89	0.0456
X_1X_2	0.760	1	0.760	4.86	0.0632
X_1^2	2.640	1	2.640	16.87	0.0045
X_2^2	1.920	1	1.920	12.30	0.0099
Residual	1.090	7	0.160		
Lack of Fit	0.990	3	0.330	13.27	0.1510
Pure Error	0.100	4	0.025		
Cor Total	6.950	12			

ANOVA results showed that the model was significant with *p*-value less than 0.05. The lower the *p*-value, the more the significance the source. In this case, almost

all the sources were statistically significant with *p*-value less than 0.05 except ratio of solid to solvent which has *p*-value greater than 0.05. These showed that extraction time was the main factor affecting the extraction yield of saponins. The model *F*-value of 7.49 implies the model was significant. There was only a 0.99% chance that a "Model *F*-value" this large could occur due to noise. The *F*-value of lack of fit was 13.27 but the *p*-value was greater than 0.05 showing that the lack of fit source as not significant. The results of ANOVA showed that the response surface models fit the experimental data [16].

3.6 Fitting of Polynomial Model

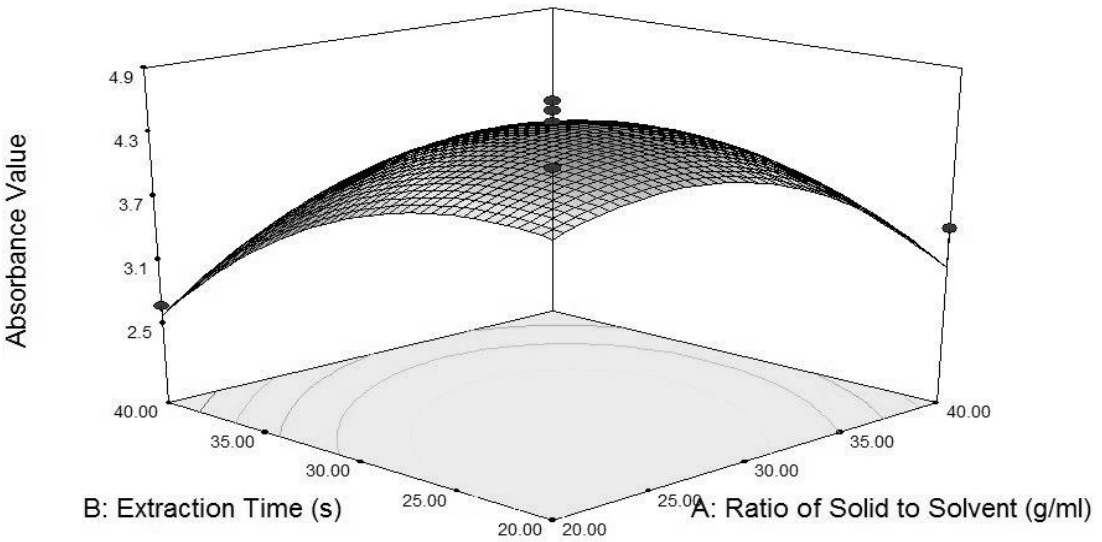
A second order polynomial model was generated by Design-Expert Software Version 7.0.0 trial program to describe the effects of the extraction parameters which include ratio of solid to solvent (X_1), extraction time (X_2) and interactions between the two parameters (X_1X_2) on the extraction yield of saponins (Y_1) from the roots of *C. borivilianum*. The second order polynomial model which fit this study is shown in Eq. (4).

$$Y_1 = -0.74235 + 0.23287X_1 + 0.15516X_2 + 0.00435885X_1X_2 - 0.00624439{X_1}^2 - 0.00533352{X_2}^2 \quad (4)$$

The higher the coefficient indicates the greater the magnitude of the extraction parameter. Whereas the positive coefficient indicates response Y_1 was proportional to the parameters while negative sign was vice versa. The fitness of the model was proven by having coefficient of determination (R^2) of 0.8425 while the adjusted R^2 was 0.7300. The R^2 showed that 84.25% of the experimental results were compatible with the results predicted by the model.

3.7 Effect of Interactive Extraction Parameters

The effect of interaction between ratio of solid to solvent and extraction time was shown in (Fig. 3) illustrated in both 3-D response surface graph and 2-D contour plot.



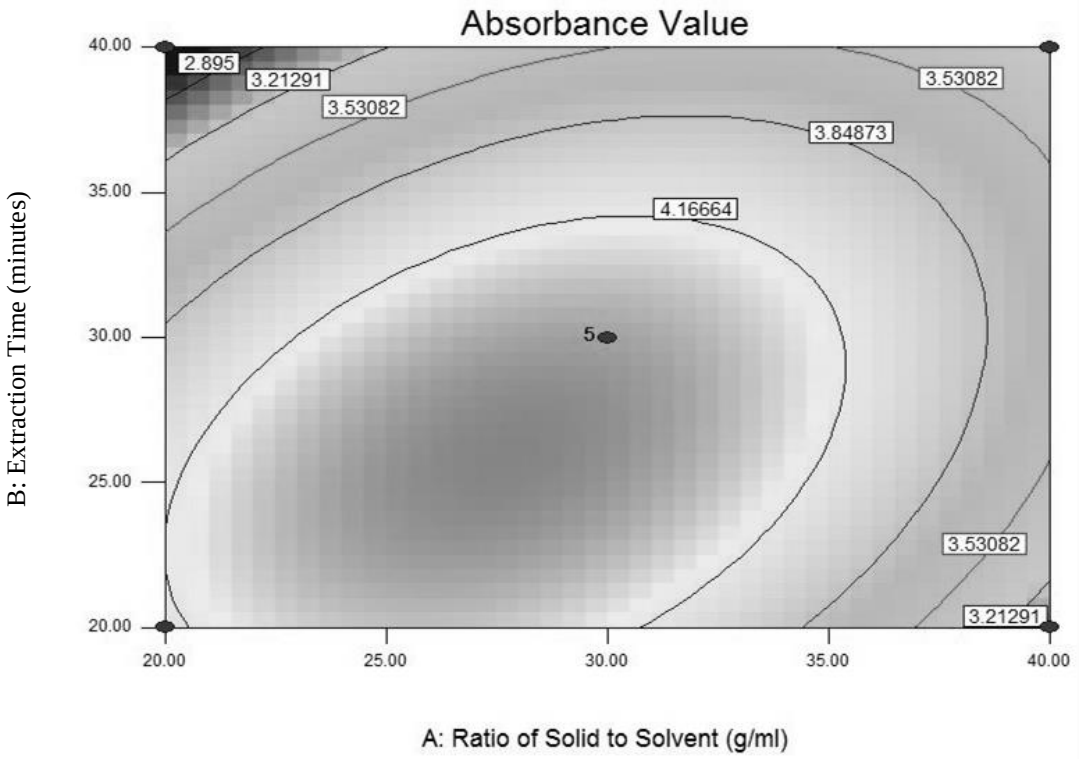


Figure 3. Corresponding 3-D response surface graph and 2-D contour plot showing the effect of interaction between extraction parameters

As shown in (Fig. 3), both extraction parameters can greatly impact the extraction yield of saponins. By increasing both ratio of solid to solvent and extraction time simultaneously could greatly increase the extraction yield of saponins which peak at around 1:30 g/ml and 30 minutes with absorbance value of 4.401 or 0.1124 mg/ml. Further increase of either parameters will lead to decrease in extraction yield.

3.8 Optimum Value of Ratio of Solid to Solvent and Extraction Time

Optimization of extraction parameters were carried out by solving the second order polynomial model generated by Design-Expert Software Version 7.0.0 trial program to obtain the highest extraction yield of saponins from the root of *C. borivilianum.* The criteria of optimization was set to have ratio of solid to solvent in range of 1:20 to 1:40 g/ml and extraction time in range of 20 to 40 minutes while maximizing the absorbance value which directly indicating the extraction yield of saponins. Results obtained was presented in (Fig. 4) below showing the corresponding 3-D response surface graph and contour plot of the optimization process.

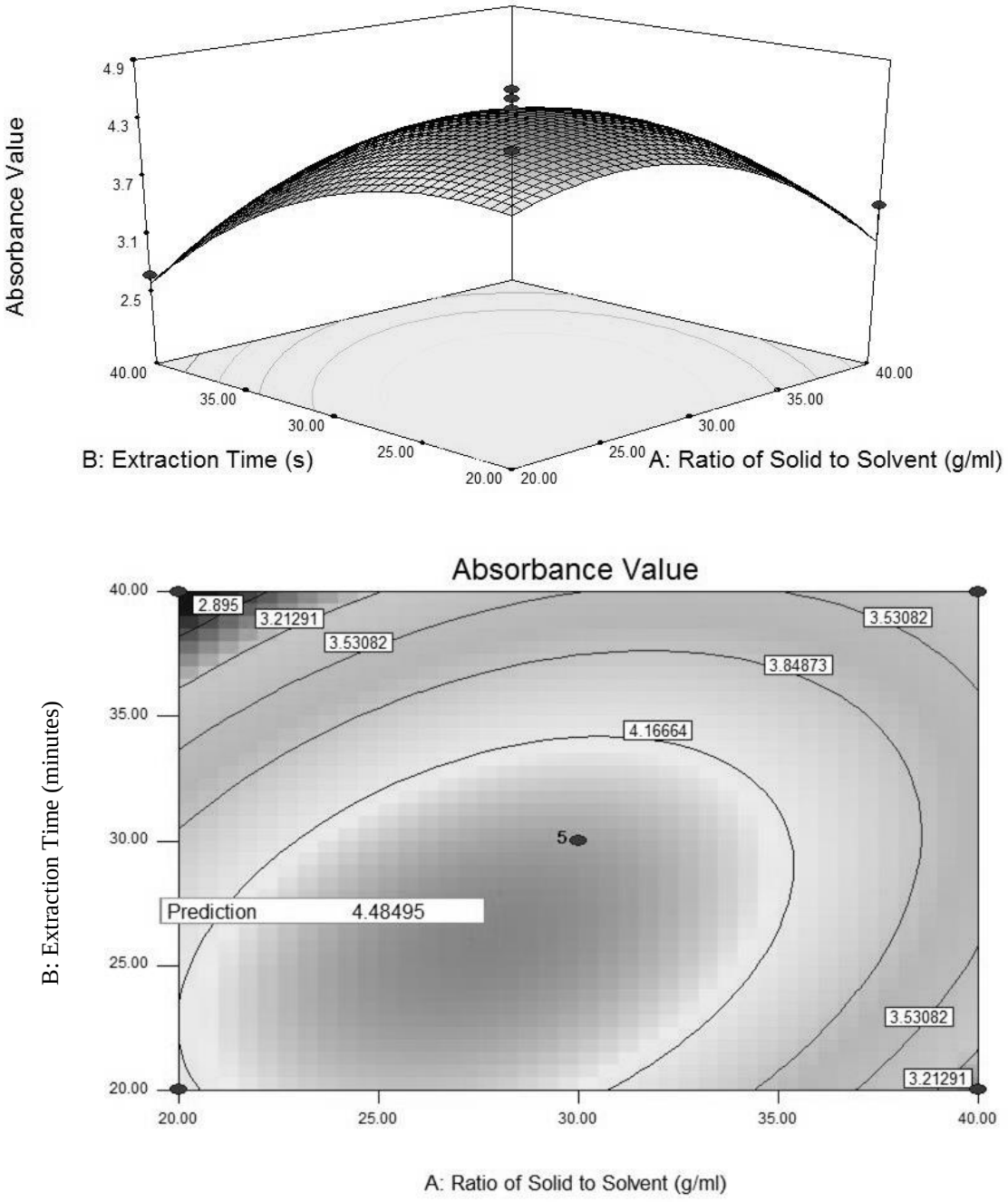


Figure 5. Corresponding 3-D response surface graph and 2-D contour plot showing the optimum extraction parameters

The optimum extraction parameters of this study were using ratio of solid to solvent of 27.68 g/ml and extraction time of 25.85 minutes which predicted to obtain 4.48495 absorbance value or 0.1124 mg/ml of saponins with desirability value of 0.892.

3.9 Validation of the Model

After obtaining the optimum extraction parameters through RSM, validation experiment was carried out to check the accuracy and reliability of the second order

quadratic equation. The optimum and adjusted extraction parameters are shown in Table 4.

Table 4. Optimum and modified extraction parameters

Extraction Parameters	Optimum Values	Modified Value
Ratio of solid to solvent, g/ml (X_1)	27.66	28
Extraction time, minutes (X_2)	25.85	26

Extractions carried out using modified extraction parameter resulted with saponin yield of 0.1081 mg/ml. The percentage of error when comparing theoretical and actual value is 3.788 %. Therefore, the polynomial model developed using RSM is confirmed reliable and able to provide solid prediction of extraction yield.

3.10 *In-vitro* Anti-inflammatory Assay of Extract Saponins

According to study done by Deore and Khadabadi [35], extract from roots of *C. borivilianum* contain convincing amount of anti-inflammatory compound. However, the exact compound which aids in the anti-inflammatory property of *C. borivilianum* has yet to be establish. In this research, anti-inflammatory assay had been carried out on saponins extracted from the roots of *C. borivilianum*. Saponins is proven to be effective in inhibiting hear induced albumin denaturation with inhibition percentage of 36.6. However, further study needs to be carried out to optimize the anti-inflammatory property of saponin extract from *C. borivilianum.*

4. Conclusions

It can be concluded that optimization process is successful using single factor experimental design and response surface methodology (RSM). The developed second order quadratic polynomial model provides satisfactory mathematical definition of optimized extraction parameters of saponins from root of *C. borivilianum* using ultrasonic-assisted extraction (UAE). This was further clarified by validating the model and obtained low relative error of 3.77% when compared with theoretical value. Optimum extraction parameters are 27.66 g/ml using 80% aqueous methanol and 25.85 minutes of extraction time using UAE set at room temperature. Extracted saponins also shows promising anti-inflammatory property. The methods of optimization can be utilized for further improvement of other extraction parameters to maximize the yield of useful compound from roots of *C. borivilianum.*

References

[1] L. Li, “Opportunity and challenge of traditional Chinese medicine in face of the entrance to WTO (World Trade Organization),” *Chin. Inform. Trad. Chin. Med.*, vol. 7, pp. 7–8, 2000.

[2] Z. Khanam, O. Singh, R. Singh, and I. U. H. Bhat, “Safed musli (Chlorophytum borivilianum): A review of its botany, ethnopharmacology and phytochemistry,” *J. Ethnopharmacol.*, vol. 150, no. 2, pp. 421–441, 2013.

[3] P. Desale, “Journal of Medicinal Plants Studies Safed Musli : Herbal Viagra for Male Impotence,” *J. Med. Plants*, no. 91, pp. 91–97, 2013.

[4] R. Sharma, T. Foods, G. Thakur, T. Foods, B. Singh, S. Rich, P. Jaiswal, and D.

Tropolite, “Conventional Method For Saponin Extraction From Chlorophytum Borivilianum Sant . et Fernand Short communication,” no. January, 2014.

[5] P. S. Metabolites, *Plant Secondary Metabolites*. Totowa, New Jersey: Humana Press, 2007.

[6] S. L. Deore, B. A. Baviskar, and A. S. Rangari, “Rapid and high yield Extraction method for Saponins from Safed musli,” *Pharmacogn. J.*, vol. 7, no. 4, pp. 210–214, 2015.

[7] S. Jalil, B. Mikhova, R. Taskova, and M. Mitova, “In vitro Anti-inflammatory Effect of Carthamus lanatus L .,” 2003.

[8] R. S. B. R. Kandikattu Karthik, Bharath Rathna Kumar P, Venu Priya R, Sunil Kumar K, “Evaluation of Anti-Inflammatory Activity of Canthium Parviflorum By in-Vitro Method,” *Indian J. Res. Pharm. Biotechnol.*, vol. 1, no. 5, pp. 729–731, 2013.

[9] C. Y. Cheok, H. A. K. Salman, and R. Sulaiman, “Extraction and quantification of saponins: A review,” *Food Res. Int.*, vol. 59, pp. 16–40, 2014.

[10] X. Fang, J. Wang, Y. Wang, X. Li, H. Zhou, and L. Zhu, “Optimization of ultrasonic-assisted extraction of wedelolactone and antioxidant polyphenols from Eclipta prostrate L using response surface methodology,” *Sep. Purif. Technol.*, vol. 138, pp. 55–64, 2014.

[11] C. Y. Cheok, H. A. K. Salman, and R. Sulaiman, “Extraction and quantification of saponins: A review,” *Food Res. Int.*, vol. 59, pp. 16–40, 2014.

[12] A. M. D. Luque, “Soxhlet extraction of solid materials : an outdated technique with a promising innovative future,” vol. 369, 1998.

[13] E. Jiménez-contreras and D. Torres-salinas, “Response Surface Methodology and its application in evaluating scientific activity .”

[14] C. B. E. E. Lin, “Optimization of Production Process of Chlorophytum Borivilianum (Safed Musli) Standardized Extract,” no. January, 2013.

[15] R. M. Banik and D. K. Pandey, “Optimizing conditions for oleanolic acid extraction from Lantana camara roots using response surface methodology,” *Ind. Crops Prod.*, vol. 27, no. 3, pp. 241–248, 2008.

[16] A. Mehrnoush, S. Mustafa, Z. I. Sarker, A. Manap, and M. Yazid, “Optimization of the Conditions for Extraction of Serine Protease from Kesinai Plant (Streblus asper) Leaves Using Response Surface Methodology,” pp. 9245–9260, 2011.

[17] I. Crops, C. Academy, and C. M. Me, “Extraction optimization , preliminary characterization , and in vitro antioxidant activities of crude polysaccharides from finger citron,” no. May, 2016.

[18] J. P. Maran and S. Manikandan, “Dyes and Pigments Response surface modeling and optimization of process parameters for aqueous extraction of pigments from prickly pear (Opuntia fi cus-indica) fruit,” *Dye. Pigment.*, vol. 95, no. 3, pp. 465–472, 2012.

[19] S. L. Deore and S. S. Khadabadi, “Isolation and characterization of

phytoconstituents from Chlorophytum borivilianum," pp. 343–350, 2011.

[20] M. Ganzera, J. Gampenrieder, R. S. Pawar, I. A. Khan, and H. Stuppner, "Separation of the major triterpenoid saponins in Bacopa monnieri by high-performance liquid chromatography," vol. 516, pp. 149–154, 2004.

[21] C. B. E. E. Lin, "Optimization Of Production Process Of Chlorophytum Borivilianum (Safed Musli) Standardized Extract," no. January, 2013.

[22] S. Guo, J. Duan, Y. Tang, Y. Qian, J. Zhao, D. Qian, S. Su, and E. Shang, "Journal of Pharmaceutical and Biomedical Analysis Simultaneous qualitative and quantitative analysis of triterpenic acids , saponins and flavonoids in the leaves of two Ziziphus species by HPLC – PDA – MS / ELSD," *J. Pharm. Biomed. Anal.*, vol. 56, no. 2, pp. 264–270, 2011.

[23] B. Ncube, V. N. P. Ngunge, J. F. Finnie, and J. Van Staden, "A comparative study of the antimicrobial and phytochemical properties between outdoor grown and micropropagated Tulbaghia violacea Harv . plants," *J. Ethnopharmacol.*, vol. 134, no. 3, pp. 775–780, 2011.

[24] Hiai; Oura; Nakajima, "Color Reaction of Some Sapogenins," *Planta Med.*, 1973.

[25] T. Belwal, P. Dhyani, I. D. Bhatt, R. Singh, and V. Pande, "Optimization extraction conditions for improving phenolic content and antioxidant activity in Berberis asiatica fruits using response surface methodology (RSM)," *Food Chem.*, vol. 207, pp. 115–124, 2016.

[26] K. Vivek, K. V Subbarao, and B. Srivastava, "Ultrasonics Sonochemistry Optimization of postharvest ultrasonic treatment of kiwifruit using RSM," *Ultrason. Sonochem.*, vol. 32, pp. 328–335, 2016.

[27] I. Nor Fariza, J. Fadzureena, A. Zunoliza, A. Luqman Chuah, K. Y. Pin, and I. Adawiah, "Anti-inflammatory activity of the major compound from methanol extract of Phaleria macrocarpa leaves," *J. Appl. Sci.*, vol. 12, no. 11, pp. 1195–1198, 2012.

[28] P. Yu and X. Chao, "Statistics-based optimization of the extraction process of kelp polysaccharide and its activities," *Carbohydr. Polym.*, vol. 91, no. 1, pp. 356–362, 2013.

[29] S. Şahin and R. Şamli, "Optimization of olive leaf extract obtained by ultrasound-assisted extraction with response surface methodology," *Ultrason. Sonochem.*, vol. 20, no. 1, pp. 595–602, 2013.

[30] X. S. Wang, Y. F. Wu, S. L. Dai, R. Chen, and Y. Shao, "Ultrasound-assisted extraction of geniposide from Gardenia jasminoides," *Ultrason. Sonochem.*, vol. 19, no. 6, pp. 1155–1159, 2012.

[31] T. Mason, "The uses of ultrasound in food technology," *Ultrason. Sonochem.*, vol. 3, no. 3, pp. S253–S260, 1996.

[32] H. Seon, K. A. Yeong, L. Ji, and E. Jo, "Optimization of ultrasonic-assisted extraction of continentalic acid from the root of Aralia continentalis by using the response surface methodology," no. Ccd, 2013.

[33] K. N. Prasad, E. Yang, C. Yi, M. Zhao, and Y. Jiang, "Effects of high pressure extraction on the extraction yield , total phenolic content and antioxidant activity

of longan fruit pericarp," *Innov. Food Sci. Emerg. Technol.*, vol. 10, no. 2, pp. 155–159, 2009.

[34] T. Sathishkumar, Baskar.R, Shanmugam.S, Rajasekaran.P, Sadasivam.S, and Manikandan.V, "Optimization of flavonoids extraction from the leaves of Tabernaemontana heyneana Wall. using L16 Orthogonal design," *Nat. Sci.*, vol. 6, no. 3, pp. 10–21, 2008.

[35] S. L. Deore and S. S. Khadabadi, "Standardisation and pharmaceutical evaluation of chlorophytum borivilianum mucilage," *Rasayan J. Chem.*, vol. 1, no. 4, pp. 887–892, 2008.

eureca 2016 – Conference Paper
Paper Number 2CE19

Comparison of Adsorption and Coagulation processes in treating heavy metals from wastewater

T. W. Leong, Rajesh Rajasekaran*

School of Engineering, Taylor's University, Malaysia

*Rajesh.Rajasekaran@taylors.edu.my

Abstract
This paper is about the theory behind the processes in wastewater treatment. In this project, the objective is to determine the efficiency of treatment of heavy metals in wastewater using the adsorption and coagulation process. This also involves the control of the pH and the usage of banana peel as the adsorbant. This project is done by preparing stock solutions and adsorbant by drying and grounding banana peels as an adsorbant. In the coagulation process, alum is added into the stock solution and the final filtrate is determined in the Atomic Adsorption Spectroscopy.

Keywords: Bio-absorption, Coagulation, Heavy metal, Wastewater

1. Introduction

Heavy metals contamination in water is a big challenge for one to solve. The major contribution to heay metal contamination are the activities of humans. Because the metals have a high solubility in the natural environment, the metals can be absorbed into the food chain [2]. This may cause a high level of accumulation of heavy metals in the human body. The intake of heavy metals into the human body above the acceptable level of concentration will cause health issues [1]. There are a few processes that can be used to treat contaminated water. A few conventional methods to remove heavy metals are adsorption, flotation, ion exchange, chemical precipitation, and electrochemical deposition. The most commonly used method is chemical precipitation where it is the less costly and more available option in terms of resources. Chemical precipitation works on the principle of chemical reaction where the metal ion is reacted and converted into an insoluble solid with a precipitate agent. Ion exchange uses the principle of exchanging the cations or anions from the surrounding materials [2]. Adsorption is the process whereby the substance in the liquid is adsorbed on an adsorbant by chemical or physical means. Some industries use the coagulation and flocculation process to be able to treat contaminated water. Coagulation uses a coagulant in order to neutralise all charges of the particle and result in precipitation.

Flocculation is when a polymer is used in order to combine all of the flocc into bigger flocc so that it is easier to remove [1].

1.1 Objectives

This project is to compare the efficiency of the adsorption and coagulation process in treating heavy metals from wastewater. To determine the factors affecting the efficiency of treating the wastewater.

2. Methodology

Stock solutions of 1000mg/L are prepared using zinc nitrate in double distilled water. Standard solutions of 20,40,60,80 and 100ppm are prepared using the dilution method $M_1V_1=M_2V_2$ [4]. Dry banana peels in the oven at 70^oC. Then, ground the peels and sieve to 60 mesh [4].

For the process coagulation, fill a 1L beaker with 500mL of 20ppm synthetic solution. The pH is adjusted to 11 using 0.1M NaOH solution and 0.1M H_2SO_4 and as the optimal pH for the coagulation. Dose in 100ppm of alum, $Al_2(SO_4)_3$. Mix the solution rapidly at a speed of 200 rpm for 60 s, the solution is slowly stirred at the speed of 60 rpm for another 30 min, followed by 30 min of settling. Filter 10mL of the final solution [3].

For the process of adsorption, fill a 1L beaker with 500mL of 20ppm synthetic solution. The pH is adjusted to 5 with the addition of 0.1M HCL. 30g/L of adsorbent is added into the solution. The solution is mixed for 20 minutes at 100rpm. Filter 10mL of the final solution [4].

The heavy metal content in the water is tested using the Atomic Absorption Spectroscopy (ASTM D1591)

3. Theoratical background

The principles of coagulation revolves around the usage of a coagulant to destabilize colloidal particles. This process has to involve the control of the pH and involve the addition of a substance called Zeolite. The coagulant will discharge the particles so that they do not repel each other and start to attract to the Zeolite. Once the particles start to combine with the Zeolite, small floccs will appear and the floccs will start to settle [1].

Table 1: Removal of heavy metal using coagulation-flocculation[1]

Species	Coagulant	Dose of coagulant	Efficiency
Zn(II)	Na_2S	100 mg/L	99.91%
Cd(II)	Na_2S	100 mg/L	99.73%
Mn(II)	Na_2S	100 mg/L	99.95%
Cu(II)	Poly-ferric sulfate	25 mg/L	99.6%
Cu(II)	Poly-acrylamide	5 mg/L	95%

Based on table 1, it can be seen that the removal of heavy metals using the coagulation and flocculation method is very efficient for all the 4 species of metal. It

can be also be observed that the type of coagulant plays a minor role in the removal of the heavy metals of about 1.6% difference in efficiency [1].

The principle of adsorption uses the transfer of ions from the liquid phase to the solid phase. The role of pH affects the selection of adsorption of different heavy metals. Previous researches showed that Cu(II) and Zn(II) are adsorbed at neutral and alkaline pH respectively. The usage of agricultural waste in the bioremediation of heavy metal ions is called bio-sorption. Some waste such as hazelnut shell, pecan shells, rice husk, jackfruit, maize cob or husk can be used as an adsorbant in the adsorbtion of heavy metals [2].

4. Conclusions

In conclusion, there is much to be done in validating the theory behind the extraction of heavy metals from wastewater. It can be seen that pH plays a vital role in the treatment of water where it will determine the metal selected by adsorption and the optimal coagulation activity.

References

[1] Kurniawan. T. A., Chan. G. Y. S., Wai-Hung. L., Babel. S., (2006), 'Physico-chemical treatment techniques for wastewater laden with heavy metals*', Chemical Engineering Journal*, vol 118, pg. 83-98.

[2] Barakat. M. A., (2011), 'New trends in removing heavy metals from industrial wastewater', *Arabian Journal of Chemistry*, vol 4, pg. 361-377.

[3] Aouji. S., Drouiche. N., Hecini. M., Ouslimane. T., Palaouane. B., (2012), 'Coagulation as a Post-Treatment Method for the Deflouridation of Photovoltaic Cell Manufacturing Wastewater', *Procedia Engineering*, vol 33, pg. 111-120.

[4] Anwar. J., Shafique. U., Waheed-uz-Zaman, Salman, M., Dar. A., Anwar. S., 2010, 'Removal of Pb(II) and Cd(II) from water by adsorption on peel of banana', *Biosource Technology*, vol 101, pg 1752-1755.

eureca 2016 – Conference Paper
Paper Number 2CE20

Life Cycle Assessment of Direct Carbon Fuel Cell Using Biomass as a Fuel Source

Merisa Gunawan[1*], Veena Doshi[2]

[1]*School of Engineering, Taylor's University*

[2] *School of Engineering, Taylor's University*

[*]merisagunawan@sd.taylors.edu.my

Abstract

Direct Carbon Fuel Cell (DCFC) has been considered as the new technology in producing electricity using solid fuel, as it has theoretical efficiency of 100%. It is also said to have 50% lower carbon dioxide emission compared to coal fired power plant. However, the environmental impacts of DCFC in terms of its full life cycle from manufacturing to disposal is still unknown, therefore the Life Cycle Assessment (LCA) is conducted. LCA study is done on DCFC system with mesocarp fibre (MF) as fuel source. The study is done to compare DCFC system with Supercritical Pulverised Coal (SCPC) power plant in terms of environmental impacts. The data collection of the DCFC and SCPC is done by conducting experiments, calculations and literature studies. Three cases are studied for DCFC system: power generation with pyrolysed MF (referred as Case 1) and power generation with acid-treated (0.5 M and 1.0 M HCl), pyrolysed MF (referred as Case 2 and Case 3, respectively). There are eight environmental impact categories considered in the study: resource depletion, global warming, ozone depletion, acidification, eutrophication, photochemical smog, human toxicity and aquatic toxicity. Comparing three cases, the pyrolysed biomass has the lowest environmental impact. Comparing three cases for DCFC system, Case 1 has the lowest Environmental Impact function (EI) value amongst all three cases. The EI values for Case 1, 2 and 3 are 1364.73, 1692.47, and 1630.28 respectively. Case 1 has the lowest EI value because of the lower emission of methane gas and no amount of acid solution used. Comparing EI values between Case 1 of DCFC system and SCPC plant, SCPC plant (EI = 31652747766.73) has much higher EI value than DCFC system, which is caused by the use of coal and emissions of ammonia, lead, mercury, nitrogen oxides and sulphur dioxide gas, which are harmful to the environment. From the results, it is seen that DCFC has potential in providing greener power industry compared to conventional power generation.

Keywords: Life Cycle Assessment, Direct Carbon Fuel Cell, Palm Oil Waste, Biomass, Environmental Impacts

1. Introduction

Fossil fuels, such as crude oil, natural gas and coal have been used as energy sources for centuries. It has been widely used for transportation fuel, paving roads, fuel for household application, and electricity and heat generation. However, fossil fuels are non-renewable energy sources, and the amount has greatly depleted over the years. Therefore, researches and investigations on renewable energy sources have been done to ensure that there will be resources left for energy use for future generations. Examples of renewable energy sources are wind, hydro, solar, biogas and biomass.

In Malaysia, one type of biomass that is abundant is palm oil mill waste, since Malaysia is one of the biggest producers of palm oil. Palm oil mill industries generate large quantities of wastes, and there have been problems in disposing it. Solid wastes generated from palm oil mill are empty fruit bunches (EFB), mesocarp fruit fibres (MF) and palm kernel shells (PKS). In order to decrease the amount of waste to be disposed, these wastes are used as fuel for steam generator. However, there are still an amount of waste unexploited, thus full utilisation of solid waste as energy generator should be done for both economic and environmental reasons [1].

Studies on biomass as fuel for power generation have been done in recent years. However, the efficiency of power generators available to convert biomass into energy is very low, with the highest efficiency of 40% for anaerobic digestion [2]. Therefore, fuel cell technology has become a solution for high efficiency power generation, since fuel cell has higher efficiency in producing electricity compared to conventional distributed energy systems such as diesel engine and wind turbine [3]. Other than that, it has simple design, is environmentally clean and makes no noise [3]. Out of different types of fuel cell existed, the only type of fuel cell that uses solid carbon as fuel to generate electricity is direct carbon fuel cell (DCFC), where it can achieve 100% theoretical efficiency [4]. Studies in using biomass as fuel in DCFC have been conducted, and results shows that it is indeed possible to do so [5].

Other than high efficiency, DCFC is also able to reduce greenhouse gas (GHG) emissions up to 50% compared to current generation coal fired power plants [6]. However, its full potential in environmental aspect is still unknown as only emission during its operation in converting solid carbon into electricity is considered. In fact, most processes in industries only considered emissions or pollution control, which is only one part of the life cycle of the said processes, causing no assurance in environment protection [7]. Therefore, in to provide the assurance that the environment is protected, an analysis of the whole life cycle of the system has to be done. This analysis can be done by doing Life Cycle Assessment (LCA).

1.1 LCA Studies

LCA is known as a tool in quantifying and evaluating inputs, outputs, and the potential environmental impacts of a product, process or activity throughout its life cycle [8]. It uses a ‘cradle-to-grave’ approach, where the analysis is done starting from raw materials’ extraction from the ground until the wastes are disposed back to the ground. Based on the results, the impacts of each part of the life cycle or overall system to the environment can be identified and evaluated, and a conclusion and improvements of the evaluated product, process or activity can be drawn. Examples of environmental

impacts that can be evaluated by using LCA are global warming, acidification, and ozone depletion [7].

Several LCA studies on coal power plant and biomass power plant has been conducted by several authors. For coal-fired power plant, the analysis done by [9] shows that the highest emissions comes from combustion process, and the second highest comes from methane leakage during mining operation. The study concludes that by applying Carbon Capture and Storage (CCS) system, the emissions from combustion will be reduced. The given statement by [9] about CCS system is proven true by [10], as the LCA study conducted on coal-fired power plant with CCS system shows that the emission from combustion decreases. However, though CCS system helped in reducing GWP, other impact categories such as EP, human toxicology and AP value increased due to increasing concentration of other pollutants. This shows that pollution control does not actually reduces the environmental impacts of the particular system.

Another LCA study is also conducted on power plant with mixture of biomass and coal used as fuel [11, 12]. Both studies concluded that by using mixture of biomass and coal as fuel for power generation, the environmental impacts can be reduced. Study by [12] also compared treated and untreated biomass, and the results shows that the treated biomass has higher impacts than untreated ones as there are more processes needed to treat it.

1.2 DCFC Studies

Direct carbon fuel cell is the only fuel cell that uses solid fuel to generate power. The fuel for DCFC is solid carbon, with operating temperature at 500-900°C, and efficiency of almost 100% [6]. The high efficiency is because of easy separation of fuel (solid) and product (gas). A DCFC consisted of an anode, cathode, and electrolyte where fuel is introduced at anode side and air introduced on cathode side for electrochemical reactions to take place. For DCFC to operate at its maximum efficiency, the overall cell reaction must be:

$$C + O_2 \rightarrow CO_2 \quad (1)$$

Where the reactions for anode (Eq. 2) and cathode (Eq. 3) being:

$$2O^{2-} + C \rightarrow CO_2 + 4e^- \quad (2)$$

$$O_2 + 4e^- \rightarrow 2O^{2-} \quad (3)$$

Other than high efficiency, variety of fuels can be used for DCFC, such as coal and biomass, making it a favourable alternative for power generation [13]. However, the fuel has to be treated first as DCFC is vulnerable to impurities such as ash and volatile matter since it can cause blockage in DCFC [5]. The treatment done by most researchers for biomass is pyrolysis, which decompose and convert biomass into biochar. A study on brown coal by Jewulski et. al. showed that by doing pyrolysis, the elemental carbon content increased by 11.3% and volatile matter content reduced by 38.57%, however the ash content increased to 34.9% [14].

As pyrolysis only reduced the volatile matter content, another treatment has to be done to decrease the ash content in the biomass. A treatment done by using acid solution was done by Rady et. al. to demineralise the biomass. HNO_3 solution was used on biomass before pyrolysis process, and the results showed that ash content reduced from 2.6 to 0.8% [15].

2. Methodology

The methodology of this study is based on ISO 14040:2006 which gives the principles and framework for LCA. In the given standard, the LCA methodology generally consists of four main phases: goal and scope definition, inventory analysis, impact assessment, and interpretation phase. The details for each phases is explained at sub-sections below.

2.1 Goal and Scope Definition

The aim of this study is to quantify and analyse the environmental impacts of DCFC using biomass as a fuel source, and to compare it with the conventional power generation by using LCA methodology. The LCA study uses cradle-to-gate approach, where the life cycle studied (with its boundaries) is shown in Fig. 1. Only Fuel Production stage and DCFC System Operation stage is considered in this study. The functional unit (FU) chosen for this study is 1 kWh of electricity generated. The conventional power generation to be compared with is coal-fired power plant without CCS system.

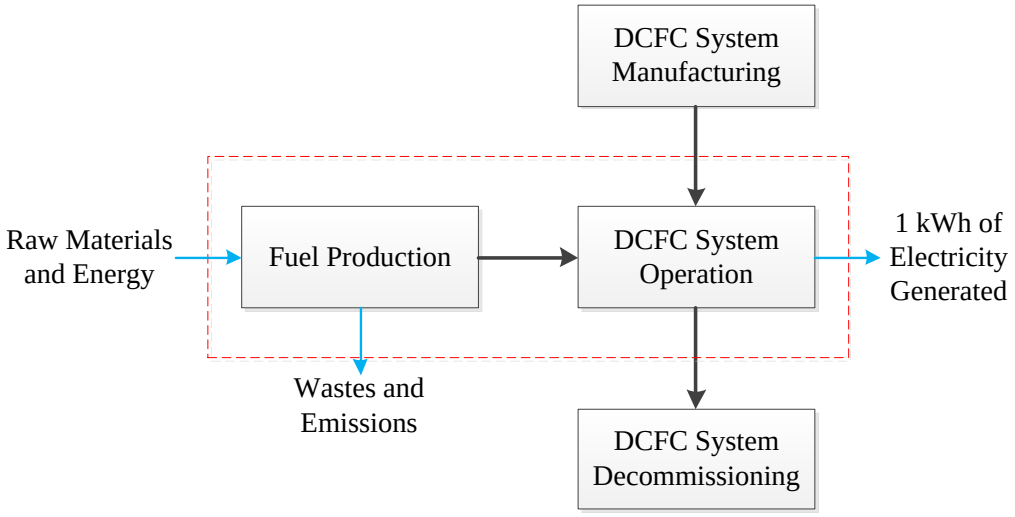


Figure 1. Life cycle of DCFC with its boundaries (dashed line)

The biomass chosen for this study is MF, with different case scenarios considered in preparing it for DCFC operation: MF that is pyrolysed without any pre-treatment (referred as Case 1), MF that is acid-washed with 0.5 M of hydrochloric acid before being pyrolysed (referred as Case 2), and MF that is acid-washed with 1.0 M of hydrochloric acid before being pyrolysed (referred as Case 3). The detailed processes for each case are compiled and shown in Fig. 2. In this study, the transportation of the raw material (MF) is not included as it is assumed that all processes are conducted at the palm oil mill, where the biomass is generated. All the processes are done in batches.

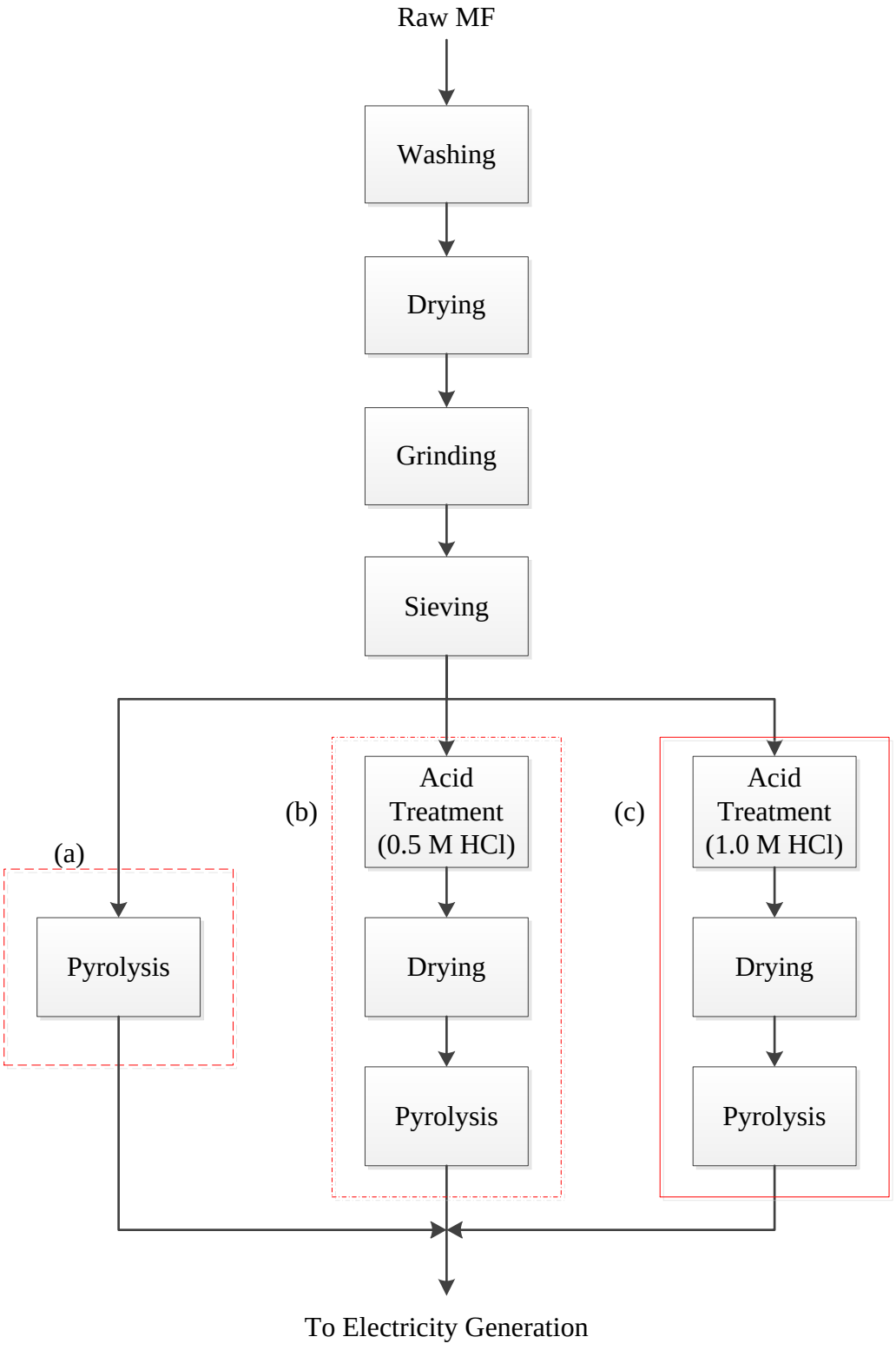


Figure 2. Processes for Fuel Production Stage: (a) Case 1, (b) Case 2, (c) Case 3

The data for the life cycle of DCFC system using MF as fuel is gathered by conducting lab-scale experiments. For data that is unable to be collected by means of experiments, literature studies with some adjustment and assumptions stated are used.

The details of the experiments is explained at the next section. For conventional power generation, the data for coal-fired power plant without CCS system (referred as CP) is taken from previous work done by other authors.

2.2 Inventory Analysis

The inventory analysis is done based on the boundary chosen which is shown in Fig. 1 and Fig. 2. The data collection for some processes, namely washing, drying, grinding, sieving, acid treatment and pyrolysis is conducted by doing lab-scale experiments. For DCFC operation stage, the data collection is done by applying assumptions and calculations with given fuel analysis results. Other data that is unable to be obtained during experiments is collected from works done by other authors. The details for each processes is shown at sub-sections below.

2.2.1 Fuel Production: Washing, Drying, Grinding and Sieving

The MF that is gathered from the upstream processes is first undergoes washing to clean the impurities that is present in MF. Once cleaned, the MF is dried for 24 hours at the temperature of 105°C to fully remove the moisture present in the fibre. The oven used for the drying process is PROTECH® Model FAC-350, which has heater power of 2 kW and able to fit up to 1 kg of MF per batch.

After it is dried, the fibre is grinded to smaller particles and sieved to the size of 0.5-2 mm. The grinder used for the process is JKI® Model JK-SG-160 that has output of 3-6 kg/h and motor power of 1.5 kW. The siever used is a sieve shaker W.S. Tyler® Model RX-812-1 with power of 0.506 kW. All the mass lost during each process, the resources used, and the time used to do each process are recorded for analysis.

2.2.2 Fuel Production: Acid Treatment and Pyrolysis

Three different scenarios (Case 1, 2 and 3) are applied for the acid treatment and pyrolysis process. The acid used for the treatment is hydrochloric acid (HCl), with concentration of 0.5 M and 1.0 M. The acid treatment is done by stirring 15 gr of sieved MF in 150 ml of 0.5 M or 1.0 M HCl solution for 6 hours. The stirrer used is DAIHAN-brand® Model SMHS-3, which has three plates to be used and total stirring power of 1.2 kW. After stirring is done, the acid-treated MF is neutralised using distilled water until it reaches the distilled water's pH value.

The untreated MF, 0.5 M HCl treated MF, and 1.0 M HCl treated MF are then undergone pyrolysis process. The furnace used for pyrolysis is CARBOLITE Model HST 12/400 with maximum power consumption of 2 kW and holding power of 0.9 kW. The furnace can fit 3 crucibles, where each crucible can fit up to 20 gr of MF. The pyrolysis are conducted with the following parameters: operating temperature of 600°C with heating rate of 10°C/min, holding time of 1 hour, and nitrogen gas flowed through the furnace with flow rate of 1 L/min. The mass lost during the acid treatment, and the mass before and after the pyrolysis are recorded.

The pyrolysis process produces not only biochar which is the desired product in this system, but also bio-oil and gas. However, the current setup does not allow the data recording of bio-oil and gas to be done due to unavailability of the instruments needed,

therefore the data for the said by-products are to be taken from literatures available. Carbon, hydrogen, nitrogen and sulphur (CHNS) analysis is also conducted on raw MF, untreated MF, and acid treated MF (0.5 M and 1.0 M HCl) to observe the effect of each processes conducted on the composition of the biomass.

The percentage of the bio-oil, biochar and gases produced from pyrolysis process taken from [16] are 43.87%, 29.80% and 26.33% respectively. The values is adjusted accordingly to the yield of biochar produced by experiments. The bio-oil produced in this study is considered as by-product and it is going to be used for other application (not considered in this study), and the gas is considered as emissions. For the gases, the composition values are taken from [17] for Case 1 to Case 3 with adjustments, assuming that all processes are the same. The composition of the gas is shown at Table 1.

Table 1. Composition of Gas Emitted from Pyrolysis [17]

Components	Case 1	Case 2	Case 3
CO	43.85	39.60	48.24
CO_2	37.87	35.97	31.76
CH_4	13.29	21.45	15.29
C_2	0.33	0.99	0.78
H_2	4.65	1.98	3.92

2.2.3 DCFC Operation Stage

The biochar produced from pyrolysis process is put into DCFC equipment for the electricity production. The DCFC equipment consisted of a button cell supported on ceramic tube, and put in a furnace. The furnace used the same type used for pyrolysis. The anode chamber is connected to nitrogen gas supply to create inert atmosphere, and the cathode chamber is connected to air supply. A total of 0.1 gram of biochar is able to be put in the anode chamber for one time operation. The operating temperature is 800°C, which is the best operating condition for the given button cell. The heating rate is assumed to be 10°C/min for the furnace used.

As the DCFC equipment used is unable to give good results for unknown reasons, the electricity production is calculated by using the higher heating value (HHV) of the biochar and assuming that only carbon in the fuel is reacted during the electrochemical reaction. It is assumed that only carbon dioxide is emitted from DCFC operation, and the efficiency is assumed to be 80% [6]. The HHV for all biochars produced in this study is calculated by using Eq. (4) by GIVEN (1986) [18]:

$$HHV = 78.3\,C + 339.1\,H - 33.0\,O + 22.1\,S + 152 \quad (4)$$

Where HHV is in kcal/kg, and C, H, O and S is the composition of biochar taken from ultimate analysis results in percentage value. Other phenomena that might happen inside the DCFC during its operation is neglected due to insufficient data available.

2.3 Impact Assessment and Interpretation

After all the data gathered is compiled and normalised with respect to functional unit, the impact assessment is done to know the environmental impacts of the system. The impact assessment analysis is conducted based on a book section about LCA by Azapagic [7], where the environmental impacts considered are non-renewable resource depletion, global warming, ozone depletion, acidification, eutrophication, photochemical oxidant formation, human toxicity, and aquatic toxicity. The classification factors for each component in inventory data for impact assessment calculations is given at Table 2. RD stands for Resource Depletion, GWP stands for Global Warming Potential, AP for Acidification Potential, EP for Eutrophication Potential, POCP for Photochemical Smog Potential, HT for Human Toxicity and AT for Aquatic Toxicity.

Table 2. Classification factors for Selected Inventory Data in this Study [7]

Component	RD	GWP	ODP	AP	EP	POCP	HT	AT
CO							0.012	
CO_2		1						
CH_4		21				0.007		
HCl			0.88					
NH_3				1.88			0.02	
Pb							0.0029	3.45E+08
Hg							120	
Other VOCs		11	0.005			0.007		
NO_X					0.13			
SO_2				1			1.2	
Coal	8.72E+07							

The calculations are done at the given order: first, the environmental impact categories is calculated by using Eq. (5):

$$E_k = \sum_{j=1}^{j} ec_{k,j} B_j \quad (5)$$

Where E_k is a category of environmental impact, and $ec_{k,j}$ is the relative contribution of burden B_j to impact E_k. The calculated environmental impact categories are then used to calculate environmental impact function which is given at Eq. (6):

$$EI = \sum_{k=1}^{k} w_k E_k \quad (6)$$

Where EI is the environmental impact function, and w_k is the relative importance of impact E_k.

In the interpretation phase, each results attained and analysed to know which processes gives high impact to the environment, the explanations for the given statements, and to see whether DCFC has lower EI value compared to conventional power generation or not.

3. Results and Discussion

3.1 DCFC Life Cycle Inventory Data and Impact Assessment

From the experiments conducted, the mass loss data for Fuel Preparation stage is known. The data is tabulated at Table 3. From the results, it is seen that out of 1 kg of raw MF, the amount of biochar produced is around 40 to 50 g or 4-5% of the initial mass. Out of all processes in Fuel Preparation stage, pyrolysis process shows the largest value of mass loss which is more than 70%. For pyrolysis process, the biochar yield for Case 1, 2 and 3 are 26.45%, 28.62% and 28.44% respectively. This shows that pyrolysis on acid-treated MF gives higher biochar yield compared to the untreated MF, and the lower concentration of acid used for the treatment gives only slightly better result than the higher concentration.

Table 3. Mass Lost Data for Fuel Preparation Stage

Process	Mass in (g)	Mass out (g)	% Mass Lost
Washing + Drying	1000.00	518.83	48.12
Grinding + Sieving	518.83	187.44	63.87
Pyrolysis (Case 1)	187.44	49.57	73.55
Acid Treatment (0.5 M HCl) + Drying (Case 2)	187.44	148.45	20.80
Pyrolysis (Case 2)	148.45	42.49	71.38
Acid Treatment (1.0 M HCl) + Drying (Case 3)	187.44	139.70	25.47
Pyrolysis (Case 3)	139.70	39.74	71.56

The CHNS analysis is conducted on the raw MF and biochars produced and the results is shown at Table 4. From the CHNS analysis, the HHV for each biochar produced can be calculated by using Eq. (4) and the calculated values are compiled together at Table 4. CHNS analysis result shows the increase of carbon content in the biochar after pyrolysis process up to 31% compared to the raw MF. Comparing three biochars produced, the untreated biochar (Case 1) has slightly lower carbon content compared to acid-treated biochar (Case 2 and 3) and also lower hydrogen and nitrogen content. The calculated HHV value shows that the HHV of MF increase after pyrolysis process and acid-treated biochar has higher HHV than untreated biochar.

Table 4. CHNS Analysis and Calculated HHV Results for Fuels Studied

Components	Raw MF	Case 1	Case 2	Case 3
C (%)	47.348	77.403	78.994	78.824
H (%)	6.560	1.970	2.034	2.049
N (%)	4.503	2.959	5.140	2.966
S (%)	0.322	0.236	0.213	0.162
O (%) (by difference)	41.267	17.432	13.619	15.999
HHV (kcal/kg)	4729.15	6310.64	6582.24	6494.35

The pyrolysis process produces not only biochar, but also bio-oil and bio-gas as by-products. Based on product's distribution results from [16], the yield of bio-oil for all cases is assumed, and the yield of bio-gas is calculated from the stated values. The

bio-gas yield value is then used to calculate the mass of each component in the gas using the values listed in Table 1. The results for gas emissions during pyrolysis process will be shown at the normalised data section. The product distribution from pyrolysis process (in percentage) is tabulated at Table 5 below.

Table 5. Product Distribution from Pyrolysis Process

Yield (%)	Case 1	Case 2	Case 3
Biochar	26.45	28.62	28.44
Bio-oil (assumed) [16]	45.55	44.46	44.55
Bio-gas	28.00	26.92	27.01

In DCFC Operation stage, it is assumed that only the carbon content present in the fuel burned in DCFC is converted to electricity with 80% efficiency, and only CO_2 gas is produced from the process. The amount of CO2 gas produced during DCFC operation is calculated based on Eq. (1), and the amount of electricity produced is based on the mass of fuel reacted in DCFC and the fuel's HHV. The data for DCFC operation stage is tabulated at Table 6. From the Table, it is seen that Case 1 has the highest amount of electricity and CO_2 gas produced, followed with Case 2 and Case 3. This is mainly because the mass of fuel processed for Case 1 is higher compared with other cases.

Table 6. Data for DCFC Operation Stage

Parameter (Unit)	Case 1	Case 2	Case 3
Mass of fuel to be processed in DCFC (g)	49.57	42.49	39.74
Carbon content in fuel (%)	77.403	78.994	78.824
Mass of fuel reacted in DCFC (g)	38.37	33.57	31.32
Amount of CO_2 produced (g)	140.69	123.07	114.85
Mass of unreacted fuel (g)	11.20	8.93	8.41
Electricity produced (kWh) (80% efficiency)	0.2252	0.2055	0.1892

The data shown at Table 3, 5, and 6 is based on 1 kg of raw MF. And it is seen that for Case 1, 1 kg of raw MF produces 0.2252 kWh of electricity, Case 2 is 0.2055 kWh, and Case 3 is 0.1892 kWh. These results are then normalised to 1 kWh of electricity produced, which is the FU for this LCA study. The normalised mass loss data for each Case are shown at Table 7 to 9. To produce 1 kWh of electricity, 4.4 kg of raw MF is needed for Case 1, 4.9 kg for Case 2 and 5.3 kg for Case 3. More amount of raw MF is needed for Case 2 and Case 3 as the mass loss for each process is higher compared to Case 1, and additional mass loss in acid treatment process also contributes to the higher mass loss.

Table 7. Mass Lost Data for Each Process with Respect to FU (Case 1)

Process	Mass in (g)	Mass out (g)	% Mass Lost
Washing + Drying	4439.95	2303.57	48.12
Grinding + Sieving	2303.57	832.22	63.87
Pyrolysis	832.22	220.09	73.55
DCFC Operation	220.09	49.73	77.40

Table 8. Mass Lost Data for Each Process with Respect to FU (Case 2)

Process	Mass in (g)	Mass out (g)	% Mass Lost
Washing + Drying	4866.00	2524.62	48.12
Grinding + Sieving	2524.62	912.08	63.87
Acid Treatment (0.5 M HCl) + Drying	912.08	722.37	20.80
Pyrolysis	722.37	206.76	71.38
DCFC Operation	206.76	43.43	78.99

Table 9. Mass Lost Data for Each Process with Respect to FU (Case 3)

Process	Mass in (g)	Mass out (g)	% Mass Lost
Washing + Drying	5284.98	2742.00	48.12
Grinding + Sieving	2742.00	990.61	63.87
Acid Treatment (1.0 M HCl) + Drying	990.61	738.34	25.47
Pyrolysis	738.34	210.01	71.56
DCFC Operation	210.01	44.47	78.82

Based on the normalised mass loss data and data from Table 1, 5 and 6, the amount of HCl used, emissions from pyrolysis process and DCFC operation stage can be calculated. The acid used and emission data for DCFC system for 1 kWh of electricity generated is compiled at Table 10. From the table, it is seen that the amount of HCl used for Case 3 is more than Case 2 as the molarity or the concentration for Case 3 is twice of Case 2. The CO_2 and CO emissions for Case 1 are the highest, while for CH_4 the highest emission comes from Case 2.

Table 10. Acid Used and Emission Data from DCFC System with Respect to FU

Components	Case 1	Case 2	Case 3
From Acid Treatment			
Mass treated (g)	-	912.08	990.61
Mass of HCl used (g)	-	166.45	361.57
From Pyrolysis			
Mass before pyrolysis (g)	832.22	722.37	738.34
Bio-gas produced (g)	233.05	194.44	199.40
CO gas produced (g)	102.20	77.01	96.18
CO_2 gas produced (g)	88.27	69.95	63.34
CH_4 gas produced (g)	30.97	41.71	30.50
C_2 gas produced (g)	0.77	0.65	0.65
H_2 gas produced (g)	10.84	9.04	9.27
From DCFC Operation			
Mass reacted in DCFC (g)	170.36	163.33	165.54
CO_2 gas produced (g)	624.64	598.87	606.97

From the data above, the inventory data for DCFC system is then compiled to be used for Impact Assessment. The important resources and emissions to be considered for Impact Assessment are the amount of HCl used and the amount of CO, CO_2 and

CH_4 gas emitted, as these components contribute some impacts to the environment. The compiled inventory data is shown at Table 11. These values are the environmental burden as the values are based on the FU of the LCA study [7].

Table 11. Inventory Data for Impact Assessment of DCFC System with Respect to FU

Burdens	Case 1	Case 2	Case 3
Emission to Atmosphere			
CO (g)	102.20	77.01	96.18
CO_2 (g)	712.91	668.82	670.31
CH_4 (g)	30.97	41.71	30.50
Resources Used (which contributes to environmental impact)			
HCl (g) (disposed in waste water)	-	166.45	361.57

The impact assessment calculations started by calculating the environmental impact of each category by using Eq. (5) explained in Methodology section. The classification factors for each burden in DCFC system which is needed for the calculation are given at Table 2. Out of 8 environmental impact categories considered in this study, only 4 is related to DCFC system, which are global warming, ozone depletion, photochemical smog, and HT. The calculated environmental impact value for each category is then used to calculate the environmental impact function EI by using Eq. (6). In this study, all environmental impact categories are assumed equally important to each other, therefore the EI value is calculated by the summation of all environmental impact category values. The values for each case are tabulated at Table 12.

From the results, it is concluded that the Case 1 has the lowest environmental impact, with EI value of 1364.73. This is mainly caused by the emission of methane for Case 1 is lower compared to Case 2, and there is no acid used for Case 1 compared to other cases. Comparing each category, the GWP value for Case 3 is the lowest among all three cases, as Case 3 emits the least CH4 gas. However, the high amount of acid used for Case causes the ODP value to increase, causing the EI value to increase. As Case 1 has the lowest EI value, Case 1 is going to be used for comparison with conventional power generation at the next sub-section.

Table 12. Compiled Environmental Impact Category and EI Values for DCFC System

Environmental Impact Category	Case 1	Case 2	Case 3
RD	0	0	0
GWP 100 years (CO_2 equivalent)	1363.29	1544.77	1310.73
ODP (CFC-11 equivalent)	0	146.48	318.18
AP (SO_2 equivalent)	0	0	0
EP (PO_4^{3-} equivalent)	0	0	0
POCP (ethylene equivalent)	0.22	0.29	0.21
HT	1.23	0.92	1.15
AT	0	0	0
EI	1364.73	1692.47	1630.28

3.2 Comparison with Conventional Power Generation

For the conventional power generation, the LCA data by [18] for normal coal-fired power plant (CP) is used. The inventory data with respect to FU in this LCA study is given at Table 13 below. From the inventory data, to produce 1 kWh of electricity, only 0.4 kg of coal is needed, which is much less compared to the amount of raw MF needed to produce 1 kWh of electricity in DCFC (4.4 kg for Case 1).

Table 13. Inventory Data for Impact Assessment of CP Plant with Respect to FU

Burdens	CP
Emission to Atmosphere	
CO (g)	4.86×10^{-2}
CO_2 (g)	1020.51
CH_4 (g)	2.81
NH_3 (g)	4.93×10^{-4}
Pb (g)	5.29×10^{-5}
Hg (g)	5.36×10^{-6}
Other VOCs (g)	4.02×10^{-3}
NO_X (g)	0.37
SO_2 (g)	0.46
Resources Used (which contributes to environmental impact)	
Coal (g)	361.57

Based on the inventory data, the impact assessment is conducted using the same method as DCFC system. The calculated environmental impact for each category and its EI value are compared with DCFC system's results in Table 14. From the calculation it is concluded that DCFC system has lower environmental impact compared to conventional power generation as it has lower EI value. SCPC plant has higher EI value than DCFC system (EI for SCPC = 3.17E+10, EI for DCFC = 1364.73) because the values for RD, HT and AT for SCPC plant are much larger than DCFC system. The GWP for DCFC system, however, is higher than SCPC plant, which is caused by the amount of CH4 gas emitted (30.97 g/kWh for DCFC system and 2.81 g/kWh for SCPC plant) and the fact that CH_4 gas is 21 times more impactful than CO_2 gas [7]. The POCP for DCFC system is also higher than SCPC plant since the amount of CH_4 gas emitted for DCFC system is higher than SCPC plant.

Table 14. Compiled Environmental Impact Category and EI Values for DCFC System (Case 1) and CP Plant

Environmental Impact Category	DCFC (Case 1)	CP
RD	0	3.17E+10
GWP 100 years (CO_2 equivalent)	1363.29	1079.56
ODP (CFC-11 equivalent)	0	0
AP (SO_2 equivalent)	0	0.72
EP (PO_4^{3-} equivalent)	0	0.05
POCP (ethylene equivalent)	0.22	0.02
HT	1.23	435.88
AT	0	18250.50
EI	1364.73	31652747766.73

4. Conclusions

From the LCA study, it is seen that DCFC system has lower environmental impact compared to conventional power generation (coal-fired power plant). In the DCFC system itself, using pyrolysed MF as fuel for power generation gives lower impact compared to doing acid treatments. However, in this study, there are many values that are assumed and/or calculated using literature review, and thus lower the accuracy of the analysis itself. Therefore, for future study, it is recommended to first fully study on each processes involved in DCFC system, including its manufacturing and disposal, to provide a better insights on how DCFC is better than conventional power generation.

References

[1] N. Abdullah and F. Sulaiman, "The Oil Palm Wastes in Malaysia," in *Biomass Now – Sustainable Growth and Use*, M. D. Matovic, Ed., InTech, 2013, pp. 75-100.

[2] S. Shafie, T. Mahlia, H. Masjuki and A. Ahmad-Yazid, "A review on electricity generation based on biomass residue in Malaysia," *Renewable and Sustainable Energy Reviews,* vol. 16, no. 8, pp. 5879-5889, 2012.

[3] S. Mekhilefa, R. Saidurb and A. Safari, "Comparative study of different fuel cell technologies," *Renewable and Sustainable Energy Reviews,* vol. 16, no. 1, pp. 981-989, 2012.

[4] Y. Gong and K. Huang, "Study of a renewable biomass fueled SOFC: The effect of catalysts," *International Journal of Hydrogen Energy,* vol. 38, no. 36, pp. 16518-16523, 2013.

[5] C. Munnings, A. Kulkarni, S. Giddey and S. Badwal, "Biomass to power conversion in a direct carbon fuel cell," *International Journal of Hydrogen Energy,* vol. 39, no. 23, pp. 12377-12385, 2014.

[6] S. Giddey, S. Badwal, A. Kulkarni and C. Munnings, "A comprehensive review of direct carbon fuel cell technology," *Progress in Energy and Combustion Science,* vol. 38, no. 3, pp. 360-399, 2012.

[7] A. Azapagic, "Appendix: Life Cycle Thinking and Life Cycle Assessment (LCA)," in *Sustainable Development in Practice: Case Studies for Engineers and Scientists*, A. Azapagic, S. Perdan and R. Clift, Eds., Chichester, John Wiley & Sons Inc., 2004, pp. 426-437.

[8] ISO, "ISO 14040:2006 Environmental management — Life cycle assessment — Principles and framework," ISO, Geneva, 2006.

[9] N. A. Odeh and T. T. Cockerill, "Life cycle analysis of UK coal fired power plants," *Energy Conversion and Management,* vol. 49, no. 2, pp. 212-220, 2008.

[10] N. A. Odeh and T. T. Cockerill, "Life cycle GHG assessment of fossil fuel power plants with carbon capture and storage," *Energy Policy,* vol. 36, no. 1, p. 367–380, 2008.

[11] F. Sebastián, J. Royo and M. Gómez, "Cofiring versus biomass-fired power plants: GHG (Greenhouse Gas) emissions savings comparison by means of LCA (Life Cycle Assessment) methodology," *Energy,* vol. 36, no. 4, pp. 2029-2037, 2011.

[12] C. Strazza, A. D. Borghi, P. Costamagna, A. Traverso and M. Santin, "Comparative LCA on methanol-fuelled SOFCs as auxiliary power systems on-board ships," *Applied Energy,* vol. 87, no. 5, pp. 1670-1678, 2010.

[13] W. Hao, X. He and Y. Mi, "Achieving high performance in intermediate temperature direct carbon fuel cells with renewable carbon as a fuel source," *Applied Energy*, vol. 135, pp. 174-181, 2014.
[14] J. Jewulski, M. Skrzypkiewicz, M. Struzik and I. Lubarska-Radziejewska, "Lignite as a fuel for direct carbon fuel cell," *International Journal of Hydrogen Energy*, vol. 39, no. 36, pp. 21778-21785, 2014.
[15] A. C. Rady, S. Giddey, A. Kulkarni, S. P. Badwal and S. Bhattacharya, "Direct Carbon Fuel Cell Operation on Brown Coal with a Ni-GDC-YSZ Anode," *Electrochimica Acta*, vol. 178, pp. 721-731, 2015.
[16] F. Abnisa, A. Arami-Niya, W. M. A. W. Daud and J. N. Sahu, "Characterization of Bio-oil and Bio-char from Pyrolysis of Palm Oil Wastes," *Bioenergy Resources*, vol. 6, pp. 830-840, 2013.
[17] H. Tan and S. Wang, "Experimental study of the effect of acid-washing pretreatment on biomass pyrolysis," *Journal of Fuel Chemistry and Technology*, vol. 37, no. 6, pp. 668-672, 2009.
[18] J. Koornneef, T. V. Keulen, A. Faaij, and W. Turkenburg, "Life cycle assessment of a pulverized coal power plant with post-combustion capture, transport and storage of CO_2," *International Journal of Greenhouse Gas Control 2*, vol 2, pp. 448-467, 2008.
[19] D. W. V. Krevelen, Coal: topology, chemistry, physics, constitution, 3rd ed., Amsterdam: Elsevier, 1993.

Optimization of Bioactive Compounds from Garlic, Oregano, and Parsley Using Response Surface Methodology

Romilda Anne[1*], Rajesh Nithyanandam[1], Mohamed Nassir[1]

[1]*Chemical Engineering, Taylor's University Lakeside Campus, Malaysia*

[*]Corresponding Author Email: Rajesh.Rajasekaran@taylors.edu.my

Abstract

Antioxidants are bioactive components used to relieve the detrimental effects of oxidative stress caused by the presence of free radicals. These valuable compounds are naturally available in medicinal plants. The present study aims to investigate the influence of two independent variables, namely temperature (^{o}C) and time (hours) on the extraction yield of phenolic compounds, flavonoids and antioxidant activity from garlic, oregano, and parsley. The optimized conditions for the extraction of bioactive components from medicinal plants were determined using two-factor central composite design (CCD) combined with response surface methodology (RSM). The order of experiments was completely randomized using central composite design with five (5) centre points. All experimental data was analyzed using "Design Expert" software (Design- Expert 7.0.0 Trial, State-Ease Inc., Minneapolis MN, USA). A second-order polynomial model proposed for predicting the responses. Major factors affecting the yield of bioactive components from the extracts of garlic, oregano, and parsley were determined using one-way analysis of variance (ANOVA). Results were analyzed using a significant level of 95%. The antioxidant activity decreases from: oregano > parsley > garlic. ANOVA analysis indicated that all experimental data were in close agreement with that of the predicted data hence indicating the reliability of the experimental data and the suitability of the proposed quadratic model. The optimum conditions proposed by ANOVA were 47.1^{o}C, 6hours for extraction using maceration method.

Keywords: Medicinal plants, Antioxidants, Total antioxidant activity, Optimization, Response surface methodology (RSM).

1 Introduction

For centuries, medicinal plants have been proven to exhibit potential medicinal properties which include anti-fungal, anti-inflammatory, antioxidant, anti-carcinogenic, anti-diabetic, and anti-depressant [1]. Contemporary, science has acknowledged the active actions of medicinal plants; hence prompting a significant increase in the study on medicinal plants as a remedy for various forms of diseases and disorders [2, 3]. The synthetic drugs lead to various forms of side effects and due to their high toxicity level, the demand is on the rise for traditional medication for primary health care [4]. The medicinal plants chosen for the present study, which included garlic, oregano, and parsley, belong to the families of *Allium*, *Lamiacea*, and *Apiaceae*.

Garlic, oregano, and parsley, just like any other medicinal plants, are rich in antioxidant constituents such as phenolics and flavonoids [6, 7]. Antioxidants are substances use to relief disorders related to oxidative stress caused by large amounts of free radicals. Free radicals are highly reactive substances which are produced naturally in the human body as a by-product of cellular processes or as a result of unhealthy lifestyle [7]. Antioxidants function to interact with free radicals hence terminating the chain reaction before severe damages occur on vital organs [5]. On a separate note, there are reports indicating an increasing demand for natural antioxidants in the food industry as an alternative to synthetic preservatives [2, 5, 9]. The effectiveness of anti-oxidative properties varies according to the chemical characteristics as well as its physical location of the plant [5].

Phenolic compounds are the most common phytochemical substances that are found in all parts of a plant, which includes bulb, leaves, flowers, and stems [9]. These substances can be divided into two main categories namely; phenols and flavonoids [9]. The main active constituents of garlic is allicin [10], oregano are carvacrol and thymol [11], and parsley are apiin and malonyl-apiin [12].

The present study therefore was conducted to optimize the process parameters (temperature and time) for the extraction of bioactive compounds from garlic, oregano, and parsley using maceration method with the aid of response surface methodology. The effects of these parameters on the total anti-oxidative properties were evaluated. In this study, ethanol was chosen as the extraction solvent because it is a strong polar solvent [13], it has low toxicity level [14] and is commonly used in conventional extraction [18, 19].

The extracts were analysed for their phenolic and flavonoid content using Folin-Ciocalteu assay and aluminium chloride colorimetric assay. The antioxidant activity was measured using 2,2-diphenyl-1-picrylhydrazyl (DPPH) scavenging assay. All in all, this paper demonstrates a different perspective on antioxidants in hopes to stimulate the interest of future researchers to indulge further into this field of study.

2 Methodology

2.1 Chemicals

Ethanol 95% (Denatured) (ChemSoln). Gallic acid (MERCK), Sodium carbonate anhydrous, analytical grade (Fisher Scientific), Sodium nitrite (R&M Chemicals),

Aluminium chloride (Systerm), Folin & Ciocateu's Phenol Reagent, [AR Grade] (ChemSoln), Quercetin (Sigma-Aldrich), and 2,2-Diphenyl-1-Picrylhdrazyl (DPPH) (Riendemann Schidt), Sodium hydroxide, [AR Grade] (Riendemann Schidt).

2.2 Sample Preparation

For this study, fresh garlic, oregano and parsley leaves were purchased from Giant Hypermarket, Subang Jaya, Selangor. Prior to extraction, all medicinal plants were oven-dried (Memmert model UN75) at 50^{o}C until constant weight (72 hours). The dried plant materials were then grind using a blender (PENTEC model TAC-383E), sieved and stored in a cool dry place till analyses.

2.3 Maceration

Dried plants weighing about 5 g was placed into a 250ml conical flask along with the ethanol solvent. The mouth of the flask was sealed with aluminum foil to prevent the evaporation of solvent. The flask were placed into an orbital incubator shaker (LM-400D) and left for the extraction process to take place according to the experimental design proposed by central composite design (CCD). The solid-to-solvent ratio of 1:30g/ml was selected and remained constant for all the experiments. This parameter was fixed based on the findings reported by Bancha *et al*. [14], which states that the relationship between the extractions yields of phenolic compound to solid-to-solvent ratios are inversely proportional. The maximum yield of phenolic compound reported was by using 1:30g/ml solid-to-solvent ratio. Extracts were filtered using Whatman No.1 filter paper. All analyses were performed on the same day of extraction.

2.4 Determination of Total Phenolic Content

Total phenolic content of each medicinal plant were determined by spectrometry using Folin-Ciocalteu reagent assay suggested by Kamtekar *et al*. [17] with some modifications. A calibration curve was developed at gallic acid concentrations of (10, 20, 40, 60, 80, 100 µg/ml). Gallic acid was used as a standard for the calibration curve. For the determination of phenolic content, 0.5ml of Folin Ciocalteu's reagent was added into 5ml of distilled water, shaken, and left to rest for 5 minutes. Then 1.5ml of 20% (w/v) sodium carbonate was added into the prepared solution and the volume was made up to 10ml by adding distilled water. The mixture was left to incubate in a cool dry place for 2 hours. An intense blue colour solution was formed. Sample absorbance was measured at 750 nm against a blank using UV-visible spectrophotometer (Model Genesys 10S) instrument. All extracts were performed in triplicates. The concentration of total phenolic content was calculated using a calibration plot ($y = 0.0141x - 0.0094$, $R^2 = 0.9996$) and expressed as gallic acid equivalent (GAE) by using the following equation:

$$\text{Total Phenolic content (mg GAE/ g)} = \frac{P \times V \times D}{W \times (100\text{-}M) \times 10} \quad (1)$$

Where:
P = Total phenolic content calculated from calibration curve (mg GAE/l)
V = Volume of extraction solvent (ml)
D = Dilution factor
W = Fresh weight of sample (g)
M = Moisture content of sample (%)

2.5 Determination of Total Flavonoid Content

Total flavonoid content was measured spectrometrically using aluminum chloride colorimetric assay proposed by Kamtekar *et al*. [17] with slight modifications. A calibration curve was developed at quercetin concentrations of (100, 200, 400, 600, 800, 1000 µg/ml). Quercetin was used as a standard for the calibration curve. For flavonoid determination, 0.3ml of 5% (w/v) of sodium nitrite solution was added into 4ml of distilled water. The solution was left to rest for 5 minutes. Then, 0.3ml of 10% (w/v) of aluminum chloride was added and the mixture was set to rest for a minute. 2ml of 1M sodium hydroxide solution was added into the mixture. An orange solution was form and the mixture is made to 10ml by adding distilled water. Sample absorbance was measured at 510 nm against a blank using UV-visible spectrophotometer (Model Genesys 10S) instrument. All extracts were performed in triplicates. The concentration of total flavonoid content was calculated from the calibration plot ($y = 0.0005x - 0.0139$, $R^2 = 0.995$ and expressed as quercetin equivalent (QE) by using the following equation:

$$\text{Total flavonoid content (mg QE/ g)} = \frac{F \times V \times D}{W \times (100\text{-}M) \times 10} \quad (2)$$

Where:
F = Total flavonoid content calculated from calibration curve (mg QE/l)
V = Volume of extraction solvent (ml)
D = Dilution factor
W = Fresh weight of sample (g)
M = Moisture content of sample (%)

2.6 Determination of DPPH Radical Scavenging Activity

The antioxidant activity of each extract was measured using the method proposed by Himaja *et al* [18] with slight modifications. (0.1mM) DPPH solution was prepared by dissolving 1.9mg of DPPH into 100ml of ethanol solution. The mixture was prepared in an amber bottle wrapped with aluminum foil to minimize light exposure. The DPPH solution was left to react for 30 minutes before used for analysis. Briefly, 1ml of extract was added into 3ml of crude extract and the sample was observed to change from purple to yellowish. The sample was prepared and left in a dark room for 30 minutes before the sample absorbance value at 517nm was measured against a blank using UV-visible spectrophotometer (Genesys 10S) instrument. The radical scavenging activity was measure using the following formula:

$$\text{DPPH scavenging activity (\%)} = \frac{Ao - As}{Ao} \times 100 \quad (3)$$

Where A_o = Absorbance reading of the control and A_s = Absorbance reading of the sample.

3 Results and Discussion

3.1 Model Analysis

The effects of extraction parameters such as temperature (30^{o}C – 50^{o}C) and time (4 hours – 6 hours) on polyphenolic compounds (phenolics and flavonoids), as well as the antioxidant potential from garlic, oregano, and parsley were investigated using response surface methodology (RSM). All experimental runs were conducted according to the central composite design (CCD) as listed in Table 1. All results were statistically analyzed by analysis of variance (ANOVA). Results are as listed in Table 2. Statistical significance was based on the confidence level of 95%. Hence, ($p<0.05$) indicates that the model terms are significant on the response variable. ANOVA analysis suggested quadratic models to represent all experimental data. On the whole, the coefficients of determination are reliable, with R^2 values generally above 80%. Based on previous studies, R^2 value less than 80% indicates that the model does not very well explain the relationship between the experimental variables [19]. On contrary, an R^2 value above 80% indicates that the model closely fit the regression line. For clear demonstration of the effects of extraction parameters on the extract of antioxidant compounds and potential, response surface plot was generated for all responses.

Table 1: Experimental values for the extraction yield of bioactive compounds from garlic, oregano, and parsley

Runs	Extraction Temprature, °C	Extraction Time, Hours	Garlic		Oregano		Parsley	
			TPC (mg GAE/g)	TFC (mg QE/g)	TPC (mg GAE/g)	TFC (mg QE/g)	TPC (mg GAE/g)	TFC (mg QE/g)
12	40	4	0.140 ± 0.001	0.612 ± 0.010	17.755 ± 0.009	25.222 ± 0.226	4.079 ± 0.009	13.426 ± 0.000
10	47.1	4	0.245 ± 0.002	0.931 ± 0.026	19.615 ± 0.049	32.361 ± 0.237	6.270 ± 0.165	12.835 ± 0.000
11	32.9	4	0.094 ± 0.001	0.925 ± 0.029	17.711 ± 0.024	27.223 ± 3.002	4.376 ± 0.006	10.923 ± 0.049
1	30	5	0.161 ± 0.002	1.216 ± 0.019	10.770 ± 0.033	22.235 ± 0.237	3.311 ± 0.008	9.038 ± 0.000
2	40	5	0.149 ± 0.001	2.784 ± 0.019	15.499 ± 0.018	23.967 ± 0.052	4.003 ± 0.005	11.823 ± 0.000
4	40	5	0.154 ± 0.001	2.621 ± 0.017	15.018 ± 0.097	24.266 ± 0.288	4.219 ± 0.002	12.639 ± 0.049
6	50	5	0.151 ± 0.003	1.278 ± 0.017	26.523 ±3.448	45.804 ± 0.091	8.321 ± 0.005	11.795 ± 0.049
8	40	5	0.143 ± 0.001	0.533 ± 0.010	15.230 ± 5.981	26.476 ± 0.315	4.994 ± 0.002	12.470 ± 0.049
7	40	5	0.187 ± 0.001	0.959 ± 0.061	14.753 ± 0.009	31.883 ± 0.103	4.121 ± 0.005	15.142 ± 0.049
9	40	5	0.145 ± 0.001	1.284 ± 0.042	15.224 ± 0.016	28.986 ± 0.274	4.325 ± 0.015	13.032 ± 0.049
3	32.9	6	0.135 ± 0.001	0.948 ± 0.019	15.722 ± 0.024	26.476 ± 0.226	4.326 ± 0.073	10.219 ± 0.000
5	47.1	6	0.243 ± 0.001	0.987 ± 0.048	27.057 ± 0.018	46.551 ± 0.288	8.501 ± 0.089	15.400 ± 0.049
13	40	6	0.136 ± 0.001	1.121 ± 0.001	17.824 ± 0.057	21.368 ± 0.186	4.467 ± 0.003	13.257 ± 0.000

Table 2. Summarized variance of analysis (ANOVA) for total phenolic content, total flavonoid content, and antioxidant activity with confidence level of 95%

Total Phenolic Content						
	Garlic		Oregano		Parsley	
R^2/ Adj R^2	0.9281/0.8768		0.9187/0.8606		0.9255/0.8724	
	COD	P value prob > f	COD	P value prob > f	COD	P value prob > f
Model		0.0007		0.0011		0.0008
Intercept	0.14		15.14		4.33	
A: Temp (°C)	0.045	<0.0001	4.44	0.0002	1.64	<0.0001
B: Time (h)	8.36E-03	0.1559	0.69	0.2907	0.34	0.1449
AB	0.016	0.0708	2.36	0.0287	0.57	0.0938
A^2	0.017	0.0206	2.2	0.0117	0.95	0.0038
B^2	0.011	0.1041	1.77	0.0295	0.18	0.456
Total Flavonoid Content						
	Garlic		Oregano		Parsley	
R^2/ Adj R^2	0.8842/0.8015		0.8252/0.7004		0.7716/0.6085	
	COD	P value prob > f	COD	P value prob > f	COD	P value prob > f
Model		0.0036		0.0139		0.033
Intercept	0.98		27.12		13.02	
A: Temp (°C)	0.63	0.0006	7.32	0.0023	1.37	0.01
B: Time (h)	0.21	0.0945	1.00	0.5447	0.2	0.6224
AB	0.38	0.0413	3.73	0.1364	0.82	0.1853
A^2	0.35	0.0183	4.58	0.0298	-1.19	0.0259
B^2	0.073	0.5496	-0.79	0.6545	0.28	0.5326
DPPH Scavenging Activity						
	Garlic		Oregano		Parsley	
R^2/ Adj R^2	0.8687/0.775		0.8683/0.7742		0.8627/0.7646	
	COD	P value prob > f	COD	P value prob > f	COD	P value prob > f
Model		0.0054		0.0055		0.0063
Intercept	5.74		93.59		19.27	
A: Temp (°C)	1.38	0.0006	0.22	0.0119	4.23	0.001
B: Time (h)	0.32	0.2180	-8.03E-03	0.9035	1.93	0.0143
AB	0.42	0.2425	0.081	0.3989	0.69	0.5475
A^2	0.68	0.0299	0.03	0.6787	2.29	0.0286
B^2	0.26	0.3344	0.40	0.0007	0.044	0.9593

COD coefficient of determination

3.2 Model Fitting

Response surface methodology was applied to optimize the extraction of bioactive components from garlic, oregano, and parsley. The summarized ANOVA results from each medicinal plant are listed in Table 2. Using the experimental data, the coefficients of the quadratic equation were calculated. The predicted responses as a function of independent variables are expressed using the second-order polynomial equation. The general mathematical expression of the equation is expressed as follow:

$$Y = \beta_0 + \sum_{i=1}^{2} \beta_i X_i + \sum_{i=1}^{2} \beta_{ii} X_i^{\,2} + \sum \sum_{i<j=1}^{2} \beta_{ij} X_i X_j \quad (4)$$

Where Y is the response of extraction yield of bioactive components or antioxidant activity, β_0, β_i, β_{ii}, β_{ij} are constant coefficients of intercept, linear, quadratic, and interaction terms, respectively while X_i and X_j are the independent variable; temperature and time. The developed mathematical expressions for all experiments are listed in Table 3 with all insignificant terms being eliminated from equation.

Table 3: Model equations in terms of coded factors (Maceration extraction)

	Garlic
TPC	$0.16 + 0.045\ X_1$
TFC	$1.03 + 0.63\ X_1 + 0.38\ X_1\ X_2 + 0.34\ X_1^2$
DPPH	$5.92 + 1.38\ X_1 + 0.64\ X_1^2$
	Oregano
TPC	$15.14 + 4.44\ X_1 + 2.36\ X_1\ X_2 + 2.20\ X_1^2 + 1.77\ X_2^2$
TFC	$26.57 + 7.32\ X_1 + 4.68\ X_1^2$
DPPH	$93.62 + 0.22\ X_1 + 0.39\ X_2^2$
	Parsley
TPC	$4.45 + 1.64\ X_1 + 0.92\ X_1^2$
TFC	$13.21 + 1.37\ X_1 - 1.22\ X_1^2$
DPPH	$19.30 + 4.23\ X_1 + 1.93\ X_2 + 2.28\ X_1^2$

X_1 extraction temperature, X_2 *extraction time*

3.3 Effect of Extraction Temperature and Time on Total Phenolic Content

The yield of phenolic extract as a function of extraction temperature and time were graphically represented in three dimensional surface plots as shown in Fig. 1. Results demonstrate that temperature has a greater impact on the extraction yield of phenolic compounds compared to that of time. It is observed that, for a given time, the yield of phenolic content gradually increases with increasing temperature. This is because raising the extraction temperature leads to a decrease in solvent viscosity hence improving the efficiency of mass transfer of polyphenolic compounds and breaking the cellular constituents of the plant cells [21–24]. The results are also in agreement with Shi *et al*. [23] who reported that an increase in temperature aids in the phenolic interactions by softening the plant tissues. Although increasing the extraction temperature generally increases the response of extraction yields of phenolic content, elevated temperatures may result to the decomposition of thermal liable components hence influencing the quantification of bioactive compounds [24].

The results represented in color coded three dimensional plots with cool blue indicting low desirability towards the response and warm yellow indicates a higher desirability. The shape of the three dimensional graphs concaves upwards indicating that the yield of phenolic contents displays an increasing trend with increasing extraction temperature and time. The effect of extraction temperature and time can be seen to be most significant in parsley and it is represented by a sharper bend in the upward direction compared to that of oregano and garlic. The optimized conditions proposed for the highest extraction of phenolic compounds were given at 47.1^{o}C, 6hours with the extraction yield of (0.243 ± 0.001 mg GAE/ g DW), (27.057 ± 0.018 mg GAE/ g DW), and (8.501 ± 0.089 mg GAE/ g DW) for garlic, oregano, and parsley respectively. The extraction of total phenolic content did not deviate much from the two suggested operating conditions. Results obtained through experimental conduct were slightly higher than the predicted values.

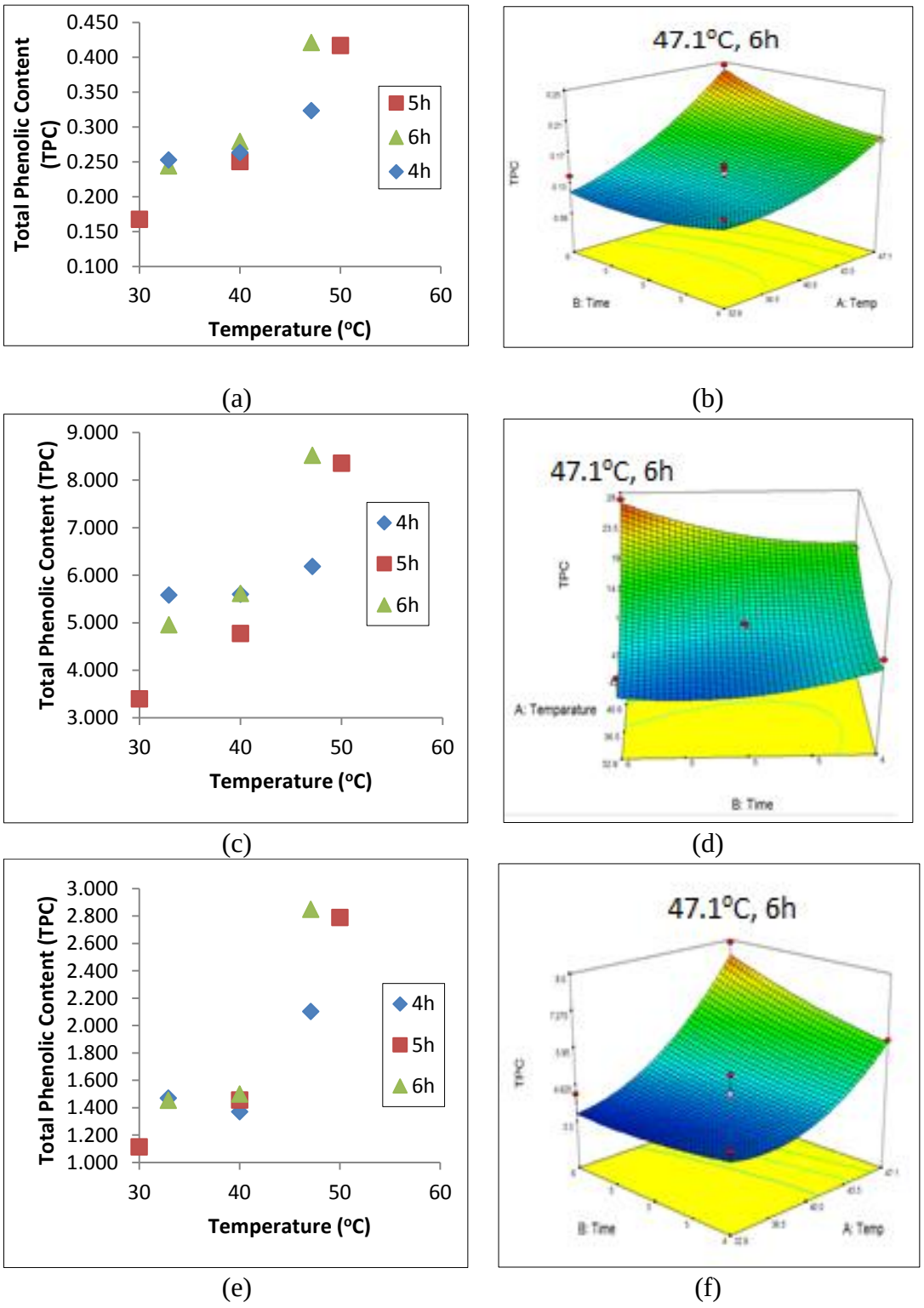


Figure 1. Effects of extraction temperature and time on total phenolic contents (TPC) of (a-b) garlic, (c-d) oregano, and (e-f) parsley

3.4 Effect of Extraction Temperature and Time on Total Flavonoid Content

The effect of extraction temperature and time on the total flavonoid content (TFC) of the three different plant extracts, using maceration method is shown in Fig. 2. It can be observed that the amount of TFC obtained increases with increasing temperature at a given time. This can be due to the findings that suggest increasing extraction temperature decreases solvent viscosity subsequently improving the efficiency of mass transfer of polyphenolic compounds [21 – 24]. However, it is interesting to note that in Fig. 2(c) the curve concaves downwards indicating that the yield of flavonoid content decreases beyond the stated temperature and time. This could be due to the reason that the flavonoid content in parsley has reached an equilibrium state with the extracting solvent. Further extracting will only leave the phenolic compounds exposed to light and oxygen which enhances the degradation process of antioxidants [25].

The proposed optimized conditions for the highest extraction of flavonoid compounds were 47.1℃, 6hours with the extraction yield of (0.987 ± 0.048 mg QE/ g DW), (46.551 mg QE/ g DW), and (15.4 ± 0.049 mg QE/ g DW) for garlic, oregano, and parsley respectively. The extraction of total flavonoid content did not deviate much from the two suggested operating conditions. Results obtained through experimental conduct were slightly higher than the predicted values.

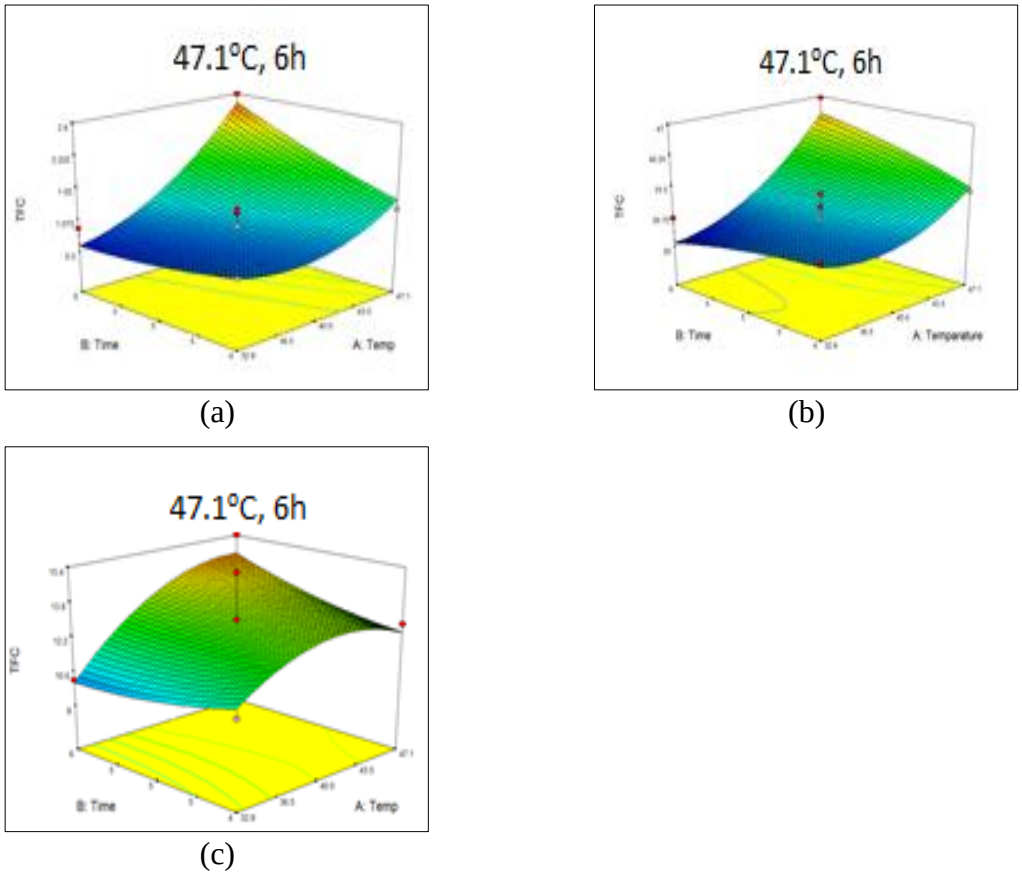


Figure 2. Effects of extraction temperature and time on total flavonoid contents (TFC) of (a) garlic, (b) oregano, and (c) parsley

3.5 Effect of Extraction Temperature and Time on DPPH Scavenging Activity

DPPH scavenging activity of different plant extracts using maceration method is shown in Fig. 3. The scavenging activity was spectrometrically measured using UV-visible spectrophotometer (Genesys 10S) instrument base on the absorbance value at wavelength 517 nm, which is indicated by the change in color of the solution from purple to yellow. The degree of decolourisation indicates the free radical scavenging activity [26]. Radical scavenging activity increases with increasing percentage of free radical scavenging inhibition. Present results depicts the scavenging activity for oregano is the highest followed by parsley and garlic. These variations can be attributed to the fact that different plant extracts have different chemical compositions [25]. There is no reported result comparing the three plants under a single experiment and at certain conditions. However, collecting data from various research data show agreement regarding the trend rather than specific numbers [12, 13, 32]. The present results demonstrate that the scavenging activity is significantly higher for the extraction of oregano compared to parsley and garlic which is the lowest. To understand this behavior, Fig. 3 shows the effect of scavenging activity as temperature changes with time. The curvature of the Temperature-Time curve along with temperature rate (dT/dt) is highest for oregano and lowest is garlic. The results explain how the T-t is approaching their optimized values.

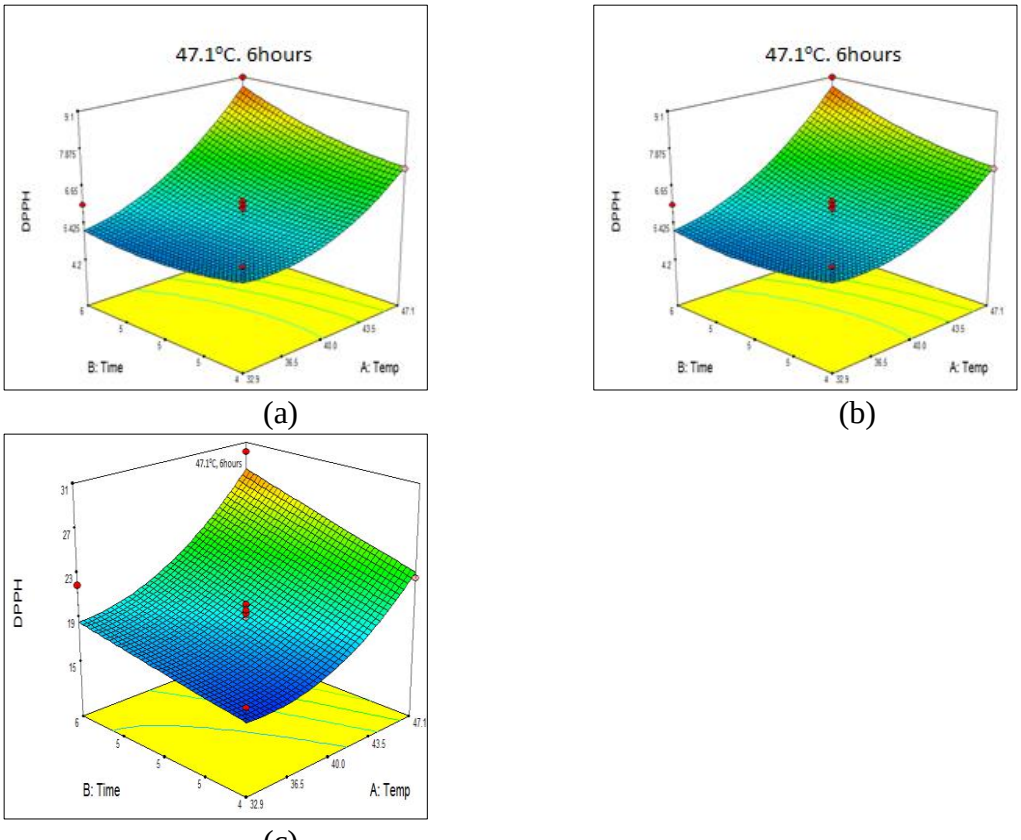


Figure 3. Effects of extraction temperature and time on the scavenging activity of (a) garlic, (b) oregano, and (c) parsley

The proposed optimized conditions were 47.1^{o}C, 6hours with 8.78%, 94.3%, and 28.46% of DPPH scavenging activity for garlic, oregano, and parsley respectively. The DPPH scavenging activity did not deviate much from the two suggested operating conditions. Results obtained through experimental conduct were slightly higher than the predicted values.

4 Conclusion

Antioxidants are substances used in medical field to relief disorders caused by large amounts of free radicals which are highly reactive substances produced as a by-product naturally in the human body. In this study, an optimization process of the extraction of bioactive compounds was achieved with the aid of mathematical software for optimization assisted by ANOVA statistics. The high correlation obtained indicates that the second-order polynomial model was suitable for the optimization of temperature and time on the extraction of bioactive components from garlic, oregano, and parsley. From the graphical representations, temperature and time significantly influence the phenolic compounds, flavonoids and antioxidant activity from the extracts of the three plants. The best suggested operating conditions to obtain the highest yield of bioactive components are at 47.1^{o}C for 6 hours using maceration. The model is said to be reliable based on the ANOVA analysis.

Reference

[1] X. Wang, R. Liu, Y. Yang, and M. Zhang, “Isolation, purification and identification of antioxidants in an aqueous aged garlic extract,” *Food Chem.*, vol. 187, pp. 37–43, 2015.

[2] A. Matkowski, P. Tasarz, and E. Szypuła, “Antioxidant activity of herb extracts from five medicinal plants from Lamiaceae , subfamily Lamioideae,” *J. Med. Plants Res.*, vol. 2, no. 11, pp. 321–330, 2008.

[3] B. B. Petrovska, “Historical review of medicinal plants’ usage.,” *Pharmacogn. Rev.*, vol. 6, no. 11, pp. 1–5, Jan. 2012.

[4] W. Z. W. N. Zahidah, a Noriham, and M. N. Zainon, “Antioxidant and antimicrobial activities of pink guava leaves and seeds,” vol. 41, no. 1, pp. 53–62, 2013.

[5] M. Oroian and I. Escriche, “Antioxidants: Characterization, natural sources, extraction and analysis,” *Food Res. Int.*, vol. 74, pp. 10–36, 2015.

[6] V. P. Nurwantoro, A. M. Bintoro, A. Legowo, A. Purnomoadi, and B. E. Setiani, “Garlic Antioxidant (Allium Sativum L.) to Prevent Meat Rancidity,” *Procedia Food Sci.*, vol. 3, pp. 137–141, 2015.

[7] M. O. Nafiu, M. O. Salawu, and M. I. Kazeem, “Antioxidant Activity of African Medicinal Plants,” *Med. Plant Res. Africa*, no. APRIL, pp. 787–803, 2013.

[8] S. E. Atawodi, “Antioxidant potential of African medicinal plants,” *J. Biotechnol.*, vol. 4, no. February, pp. 128–133, 2005.

[9] C. International and M. Asif, “Chemistry and antioxidant activity of plants containing some phenolic compounds,” vol. 1, no. 1, pp. 35–52, Jan. 2015.

[10] A. Sahebkar, C. Serban, S. Ursoniu, and M. Banach, “Effect of garlic on plasma lipoprotein(a) concentrations: A systematic review and meta-analysis of randomized controlled clinical trials,” *Nutrition*, vol. 32, no. 1, pp. 33–40, 2015.

[11] F. A. Furtado and G. L. Vieira, “Changes in Essential Oil of Origanum Vulgare L . Affected,” vol. 14, no. February, pp. 238–247, 2013.

[12] D. L. Luthria, “Influence of experimental conditions on the extraction of

phenolic compounds from parsley (Petroselinum crispum) flakes using a pressurized liquid extractor," *Food Chem.*, vol. 107, no. 2, pp. 745–752, Mar. 2008.

[13] S. Zhao and D. Zhang, "Supercritical CO2 extraction of Eucalyptus leaves oil and comparison with Soxhlet extraction and hydro-distillation methods," *Sep. Purif. Technol.*, vol. 133, pp. 443–451, 2014.

[14] B. Yingngam, M. Monschein, and A. Brantner, "Ultrasound-assisted extraction of phenolic compounds from Cratoxylum formosum ssp. formosum leaves using central composite design and evaluation of its protective ability against H2O2-induced cell death," *Asian Pac. J. Trop. Med.*, vol. 7, no. S1, pp. S497–S505, 2014.

[15] P. R. Rao and V. K. Rathod, "Rapid extraction of andrographolide from Andrographis paniculata Nees by three phase partitioning and determination of its antioxidant activity," *Biocatal. Agric. Biotechnol.*, vol. 4, no. 4, pp. 586–593, 2015.

[16] B. Sultana, F. Anwar, and M. Ashraf, "Effect of extraction solvent/technique on the antioxidant activity of selected medicinal plant extracts," *Molecules*, vol. 14, no. 6, pp. 2167–2180, 2009.

[17] S. Kamtekar, V. Keer, and V. Patil, "Estimation of phenolic content, flavonoid content, antioxidant and alpha amylase inhibitory activity of marketed polyherbal formulation," *J. Appl. Pharm. Sci.*, vol. 4, no. 9, pp. 61–65, 2014.

[18] M. Himaja, A. Ranjitha, M. V Ramana, M. Anand, and K. Asif, "Phytochemical Screening and Antioxidant Activity of Rhizome Part of Curcuma Zedoaria," *Int. J. Res. Ayurveda Pharm.*, vol. 1, no. 2, pp. 414–417, 2010.

[19] D. Krishnaiah, A. Bono, R. Sarbatly, R. Nithyanandam, and S. M. Anisuzzaman, "Optimisation of spray drying operating conditions of Morinda citrifolia L. fruit extract using response surface methodology," *J. King Saud Univ. - Eng. Sci.*, vol. 27, no. 1, pp. 26–36, 2012.

[20] M. A. Al-Farsi and C. Y. Lee, "Optimization of phenolics and dietary fibre extraction from date seeds," *Food Chem.*, vol. 108, no. 3, pp. 977–985, 2008.

[21] S. Hemwimon, P. Pavasant, and A. Shotipruk, "Microwave-assisted extraction of antioxidative anthraquinones from roots of Morinda citrifolia," *Sep. Purif. Technol.*, vol. 54, no. 1, pp. 44–50, 2007.

[22] E. M. Silva, J. N. S. Souza, H. Rogez, J. F. Rees, and Y. Larondelle, "Antioxidant activities and polyphenolic contents of fifteen selected plant species from the Amazonian region," *Food Chem.*, vol. 101, no. 3, pp. 1012–1018, 2006.

[23] Y. Shi, J., Yu, J. M., Pohorly, J., Young, C., Bryan, M. and Wu, "Optimization of the extraction of polyphenols from grape seed meal by aqueous ethanol solution.," *Food, Agric. Environ.*, vol. 1, no. 2, pp. 42–47, 2003.

[24] B. Abad-García, L. A. Berrueta, D. M. López-Márquez, I. Crespo-Ferrer, B. Gallo, and F. Vicente, "Optimization and validation of a methodology based on solvent extraction and liquid chromatography for the simultaneous determination of several polyphenolic families in fruit juices," *J. Chromatogr. A*, vol. 1154, no. 1–2, pp. 87–96, 2007.

[25] P. F. Woo, H. S. Yim, H. E. Khoo, C. M. Sia, and Y. K. Ang, "Effects of extraction conditions on antioxidant properties of sapodilla fruit (Manilkara zapota)," *Int. Food Res. J.*, vol. 20, no. 5, pp. 2065–2072, 2013.

[26] P. Kalita, T. K. Barman, T. K. Pal, and R. Kalita, "Estimation of Total Flavonoids Content (TFC) and Antioxidant Activities of Methanolic Whole Plant Extract of Biophytum Sensitivum Linn," *J. Drug Deliv. Ther.*, vol. 3, no.

4, pp. 33–37, 2013.
[27] N. W. Rahman, M. M, Fazlic, V, Saad, "Antioxidant properties of raw garlic (Allium sativum) extract," *Int. Food Res. J.*, vol. 19, no. 2, pp. 589–591, 2012.

Thermophysical and electrical properties of SiO_2-graphene/transformer oil nanofluid

Hui Qing Soo[1*], Rashmi W[1], Khalid M[2], Gupta TCMS[3], Mohsen N[1]

[1]*Taylor's University Malaysia*

[2]*University of Nottingham Malaysia Campus, Malaysia*

[3]*Apar Industries Pvt Ltd, Mumbai, India*

[*]soohuiqing@sd.taylors.edu.my

Abstract

In the present study, hybrid SiO_2-graphene nanoparticles were synthesised by sol gel centrifugation under four different pH level ranging from 9 to 12. Stability, thermal conductivity and electrical conductivity of hybrid SiO_2-graphene and pristine graphene nanofluids were investigated for three concentrations (0.01, 0.04 and 0.08 wt %) within the temperature range from 20°C to 100°C. Field emission **s**canning electron microscopy image and X-ray spectroscopy show the successful coating of SiO_2 on graphene surface. The growth units and sizes of SiO_2 nanoparticles increase with increase in pH level. Presence of SiO_2 improve the dispersion behaviour of nanosuspensions as confirmed by visual observation and UV-Vis studies. Hybrid nanofluids at pH 11 are most stable due to its optimum amount and size of SiO2 coated on graphene surface while at pH 12 show least stability due to precipitation. Thermal conductivity measured using KD-2 pro analyser further show that SiO_2 coated graphene boosts up the thermal conductivity with enhancement of 80% at pH 9. Electrical conductivity of hybrid SiO_2-graphene nanofluids shows a significant suppression of electrical conductivity enhancement in base fluid from 557% to 97% due to insulating behaviour of SiO_2.

Keywords:Hybrid SiO_2-graphene, Sol gel centrifugation, Thermal conductivity, Electrical conductivity, Stability, Surface morphology

1. Introduction

In the industry of power generation and distribution, transformer is one of the important components which helps to interconnect all stages of power systems by adjusting voltage of alternating current in the power network. Thermal management of transformer is very essential as high temperature in the system due to heat released and overloading to windings may degrade its life span and cause thermal destruction in transformer [1]. Transformer oil plays an important role to dissipate heat generated and electrically isolate the components in the transformer. Therefore, the thermal and

electrical properties of transformer oil are key aspects which directly affect the performance of transformer.

However, thermal conductivity of transformer oil is not high to efficiently dissipate the heat generated and leads to unexpected failure of transformer. In the last decades, numerous investigations were carried out on dispersion of nanoparticles which possess high thermal conductivity in a base fluid in order to enhance its thermal performance. Huminic *et al.* [2] evaluated the thermal conductivity of water with addition of FeC nanoparticles which showed a maximum enhancement of 24.1% with 1 wt% of nanoparticles. Pang *et al.* [3] also showed improvement of thermal conductivity up to 10.74% and 14.29% for addition of Al_2O_3 and SiO_2 in methanol. Similar trend was also showed by Azadeh and Fatemeh [4] with 10.95% enhancement for addition of silver decorated silica based nanofluid. Carbon based nanostructure materials such as carbon black, carbon nanotube and graphene receive high attention due to their excellent thermal properties. Especially graphene nanoparticles (GNP), it has excellent thermal conductivity which is up to 5000 W/mK, high resistance to structural damage at high temperature and high chemical stability. Many researchers have reported the improvement of thermal conductivity for various types of base fluids containing GNP such as water, ethylene glycol, and paraffin which strongly justify the capability of GNP to improve thermal performance of base fluids [5]–[7].

However, GNP is highly electrically conductive that contradicts with insulating properties of transformer oil. Therefore, researchers look into modifying the properties of GNP by coating with other nanoparticles, which is also named as hybrid nanoparticles. SiO_2 is considered as suitable nanoparticles for coating on graphene surface to improve its insulating properties due to the fact that this semiconductor nanoparticles can act as electron traps to reduce the mobility of electrons which thus increasing the electrical resistivity in the medium. H. Jin *et al.* [8] presented the enhancement of dielectric breakdown voltage up to 79% at 0.1 wt% of SiO_2 nanoparticles in mineral oil. Rafiq *et al.* [9] also studied the breakdown strength of SiO_2 /transformer oil nanofluid that showed 1.11 times higher than base oil.

Synthesis of SiO_2 nanoparticles on surface of graphene can be performed by sol-gel process, a process that consists of hydrolysis and polycondensation to convert tetraethyl orthosilicate (TEOS) into SiO_2 under acidic or base condition. pH during sol gel centrifugation is one of the important factors that affects the morphology of SiO_2 such as size and number of growth units. Not all researchers come to a good agreement regarding the effect of pH on size of nanoparticles synthesised. For instance, Alias *et al.* [10] presented largest size of ZnO nanoparticles (25.36nm) occurs at pH 9 and smallest size (18.27nm) occurs at pH 11. However, Ikono *et al.* [11] presented that increasing pH leads to increase in particle size of ZnO nanoparticles during sol gel process. Rac *et al.* [12] also studied that when pH increases, the chains of polymer will attach on each SnO_2 nanoparticles and form clusters which thus increasing particle size. This conclusion was also presented by Jayalakshimil *et al.* [13] who showed that particle size of gold nanoparticles decreases from 151.8nm to 10.2 nm when pH of solution is reduced. The contradiction of current literature indicates that this area of topic is worth investigating which arises as one of the objectives of present paper.

Studies on properties of transformer oil based nanofluids are limited and still yet to be studied intensively, especially electrical properties that is strongly related to

the performance of transformer. Thus, it opens a good opportunity to investigate the properties of transformer oil with addition of nanoparticles as well.

Therefore, due to excellent insulating properties of SiO_2 nanoparticles, little work performed on transformer oil based nanofluid and contradiction between current literature on effect of pH, this work aims to compare the hybrid SiO_2-graphene nanoparticles and pure graphene nanoparticles on enhancement of thermophysical and electrical properties of transformer oil respect to temperature and nanoparticle concentration. Study includes stability, thermal conductivity and electrical conductivity measurement and also to investigate the effect of pH on morphology of SiO_2 nanoparticles synthesised during sol gel process.

2. Experimental

2.1 Materials

The materials needed for synthesis of hybrid nanoparticles are graphene nanoparticles (size: 12nm, specific surface area: 80m/g^2, purity: 99.2%) was purchased from Graphene supermarket, USA., naphtha based transformer oil was obtained from Apar Industries, Mumbai India, Tetraethyl orthosilicate (TEOS) with purity of 98%, isopropyl alcohol (99.8% AR grade), ammonium hydroxide solution (25% AR grade) were purchased from Chemolab Supplies.

2.1 Synthesis of hybrid SiO_2-graphene nanoparticles

Synthesis method follow the methodology of Jin *et al.* [14]. Four sets of hybrid nanoparticles were synthesised with varying pH values. 0.15 g of graphene powders was dispersed in 600 ml of isopropyl alcohol with continuous sonication for about 30 min to ensure well dispersion. 100 ml of deionized water was added into graphene suspension, followed by dripping of ammonium hydroxide solution until reaching desired pH value (9, 10, 11 and 12). 5 ml of TEOS was then added with constant flow rate of 500µl/min with the aid of flow pump. The graphene suspension was stirred for 24h at room temperature to allow complete reaction for formation of SiO_2 on graphene surface. Centrifugation was then carried out in order to separate suspension, followed by washing with deionized water for more than three times to ensure complete removal of uncoated SiO_2 nanoparticles. Lastly, the precipitate was dried in oven at 70^{o}C for 12h. Dry hybrid SiO_2-graphene nanoparticles was collected.

2.2 Synthesis of GTNF

Graphene based transformer oil nanofluid (GTNF) were prepared with two-step method by dispersing pure graphene and hybrid SiO_2-graphene nanoparticles with pH values of 9, 10, 11 and 12 in transformer oil for 3 different concentrations (0.01 wt%, 0.04wt% and 0.08 wt%). The total weight of each nanofluid was 20g. The suspensions were sonicated for 4h using an ultrasonic cleaner (Elmasonic P, Elma Schmidbauer GmbH, Singen, Germany) at 37 kHz and room temperature.

2.3 Characterisation of nanoparticles

Field emission **s**canning electron microscopy (Ultra 55 FESEM, Zeiss, Chicago, USA) was employed to observe and compare the surface morphology of pure graphene and hybrid nanoparticles, whose accelerating voltage was 20V. EDX analysis was also carried out by using energy dispersive X-ray spectroscopy (EDX, Zeiss Supra 35VP) to determine the composition in the samples. Charaterisation of particle sizes were analysed too using a particle size analyser (Zetasizer nano, Malvern Instruments Ltd, Malvern, UK).

2.4 Stability studies of GTNF

Stability of those nanofluids with respective concentrations were studied with visual studies and a UV-Vis spectrophotometer (UV-1800, Shimadzu Corporation, Kyoto, Japan) for a period of 2 weeks. For UV analysis, UV-Vis absorbance curve for each type of sample was firstly plotted under wavelength between 190 and 800nm to obtain the highest peak, λ_{max}. as calibration curves were obtained for each set of samples and concentration of the samples were calculated with sedimentation time using the calibration curves. Fig. 1 below shows the calibration curve of each sample. It can be observed that hybrid nanofluids at pH 9 and 12 were poorly fitted to the linear model as the R^2 developed is very low which will be explained in stability analysis.

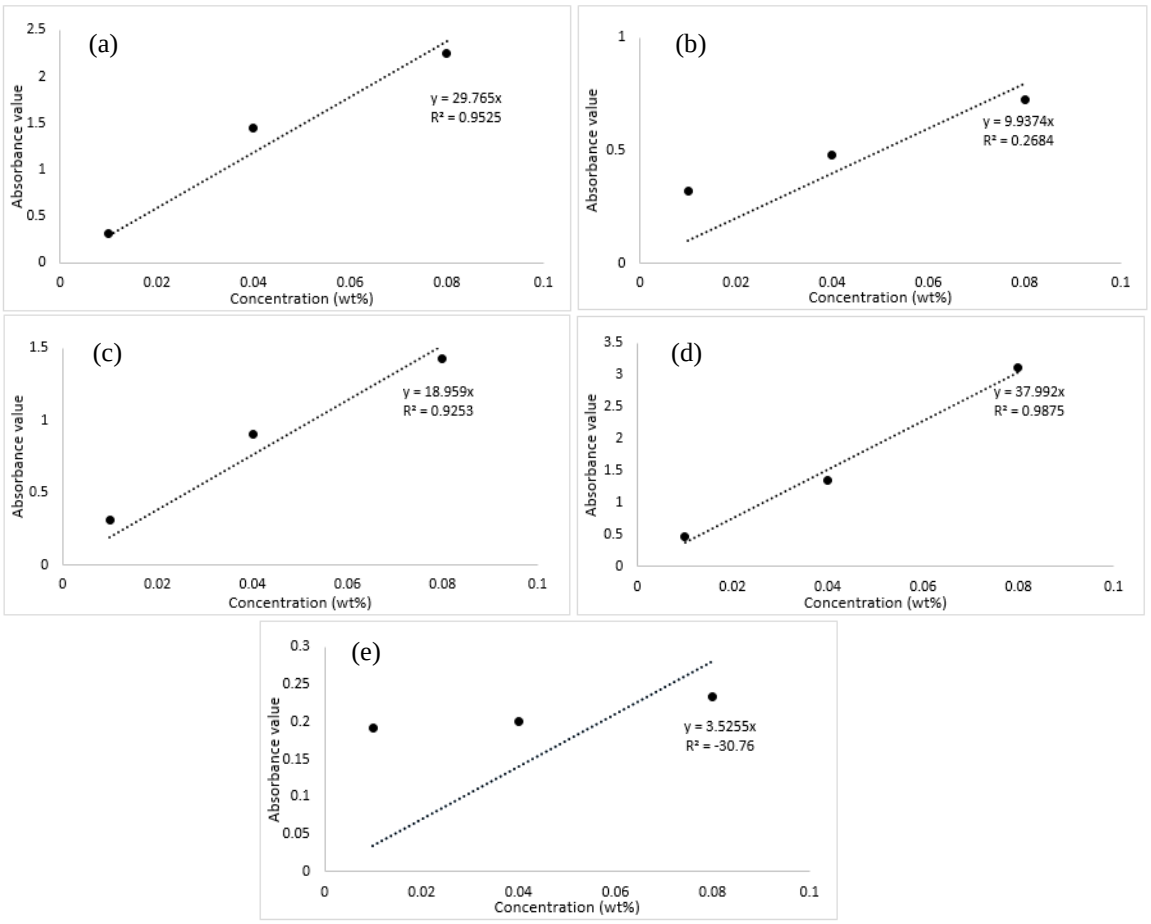


Figure 1. Calibration curve of (a) pure graphene and hybrid SiO_2-graphene synthesised at various pH values: (b) pH 9 (c) pH 10 (d) pH 11 (e) pH 12

2.5 Thermophysical and electrical properties analysis

Thermal conductivity measurement subjected to temperature ranging from 20 to 100^{o}C was carried out using a thermal property analyser (KD2 Pro, Decagon Devices Inc, Pullman, USA). The measurement was in accordance with standard ASTM D2717-95 with an accuracy of ± 5 % of full scale.

Electrical conductivity measurement was carried out at room temperature using an electrical conductivity meter (PC 700, Eutech, Landsmeer, Netherlands) which followed standard ASTM D831. Enhancement of thermal and electrical conductivity was calculated using Eq.(1).

$$\%\ Enhancement = \frac{X_{nanofluid} - X_{transformer\ oil}}{X_{transformer\ oil}} * 100\% \quad (1)$$

3. Result and discussion

3.1 Surface morphology and composition analysis

3.1.1 Field emission scanning electron microscopy

Surface morphologies of all samples were observed with FESEM as shown in Fig. 2. Fig. 2a displayed the surface of pure graphene which was very smooth and clean due to the organized structure of graphene. Graphene is a two-dimensional sheet of carbon atoms that are arranged perfectly in a honeycomb lattice. Some of the graphene were overlapped with uneven thickness. Fig.(2b-2e) showed the successful coating of SiO_2 nanoparticles on graphene surface. It could be observed that the spherical shape of SiO_2 nanoparticles were well decorated on the graphene sheet and the size of SiO_2 nanoparticles increased with increase in pH values. Under FESEM images, it was clear to discern that the sizes of coated SiO_2 nanoparticles at pH 12 (Fig. 2e) were largest compared with other nanoparticles in lower pH condition.

Chemical composition of all samples were studied using EDX which were shown in Fig. 3. Pure graphene was mainly composed of C and O. Minimal amount of oxygen was found in pure graphene (Fig.3a) due to adsorption of oxygen molecules on graphene surface which was inevitable [15]. EDX result showed that the growth units of SiO_2 were proportional with the increase in pH values. The higher the pH condition, the more the growth of silica on graphene surface.

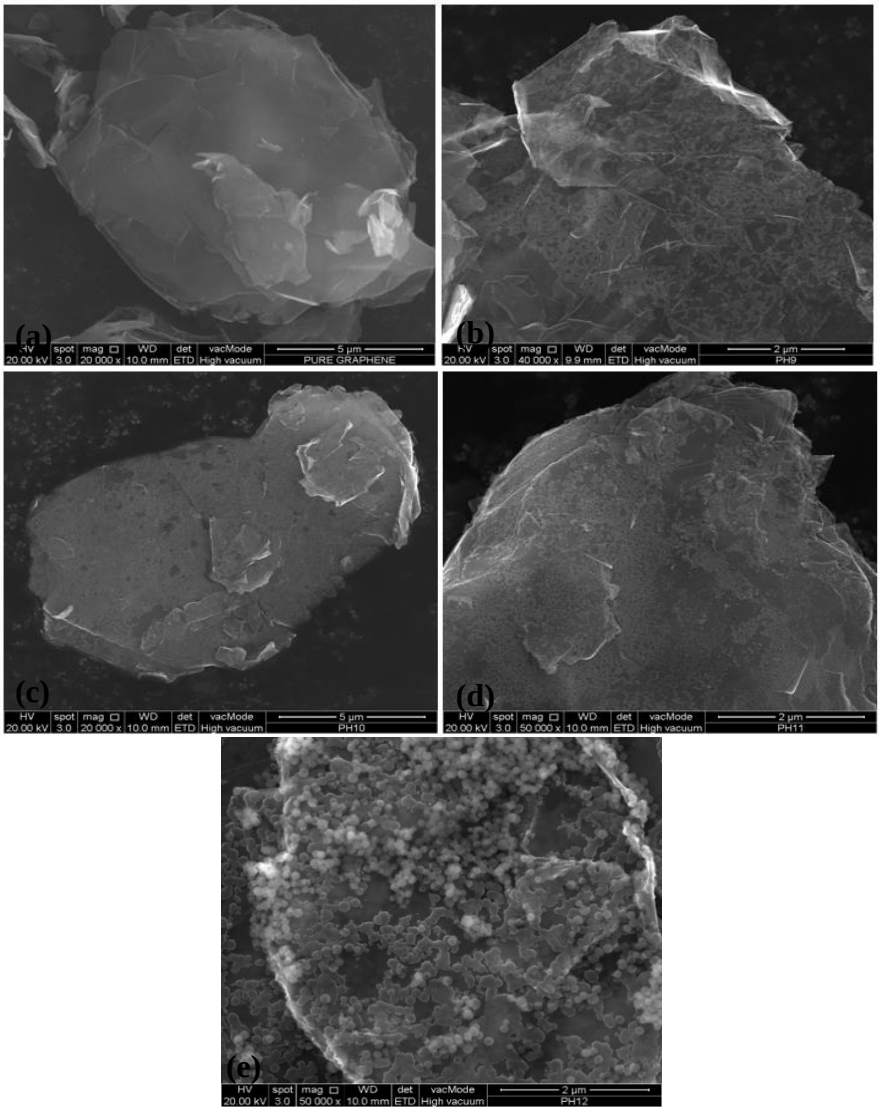


Figure 2. FESEM images of (a) pure graphene and hybrid SiO_2-graphene synthesised at various pH values: (b) pH 9 (c) pH 10 (d) pH 11 (e) pH 12

3.1.2 X-ray spectroscopy analysis

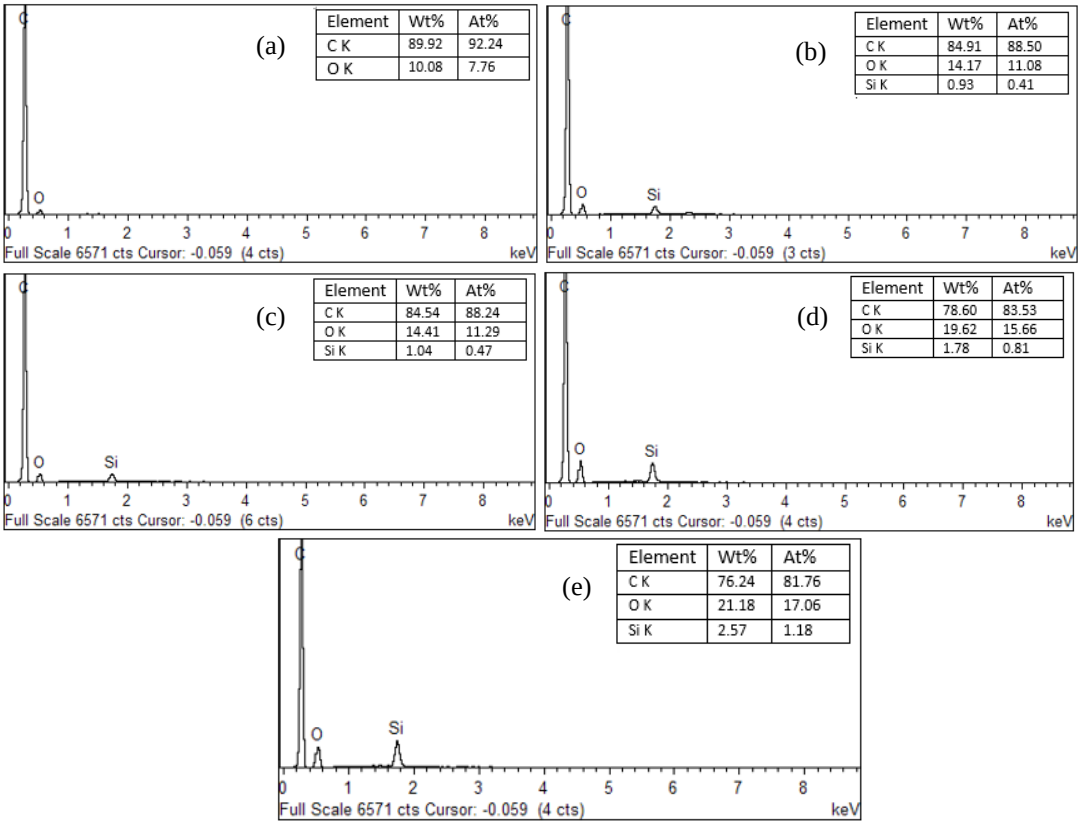


Figure 3. EDX of (a) pure graphene and hybrid SiO_2-graphene synthesised at various pH values: (b) pH 9 (c) pH 10 (d) pH 11 (e) pH 12

This phenomenon was explained by the mechanism of SiO_2 growth during sol gel process. Sol gel process consists of (i) hydrolysis reaction which replaces the alkoxide group (-OR) with hydroxyl group (-OH) and releases ROH alcohol molecules and (ii) polycondensation reaction which having silanol groups (Si-OH) to produce siloxane group (Si-O-Si) with producing water and alcohol as by products. Eq. (2) represents hydrolysis process whereas Eq. (3) and Eq. (4) represent water condensation and alcohol condensation [16].

$$\equiv Si-O-R + H_2O \rightarrow \equiv Si-OH + ROH \quad (2)$$

$$\equiv Si-OH + \rightarrow \equiv Si-OH \leftrightarrow \equiv Si-O-Si\equiv + H_2O \quad (3)$$

$$\equiv Si-OH + \equiv Si-OR \leftrightarrow \equiv Si-O-Si\equiv + ROH \quad (4)$$

Where $R=C_2H_5$

Sol gel process can be sped up under acidic or alkali condition with the aid of catalyst. In alkali-catalysed reaction, condensation rate is dominant that favors the growth of SiO_2. Therefore, with the increasing of amount of ammonia solution to increase pH condition, the rate of producing SiO_2 nanoparticles increases continuously[16].

3.1.3 Comparison between particle sizes

Comparison between lateral dimensions of all samples was carried out as tabulated in Table 1. Coating of SiO_2 on graphene surface led to higher particle sizes compared to naked graphene. The lateral dimensions of hybrid nanoparticles were ranging from 1776 to 8426nm. This result was consistent with FESEM images which showed the largest particle size was obtained at pH 12 whereas the smallest size was obtained at pH 9. Increase in size of nanoparticles with pH values was mainly contributed by the higher concentration of ammonia solution. OH^- from ammonia solution caused the silicon atoms to be negatively charged and promoted the reaction rate for formation of Si-O-Si chain. Si-O-Si chains cross-linked with each other continuously which eventually formed larger particles [17].

Table 1: Comparison between lateral dimension of pure and hybrid nanoparticles

Nanoparticles	Lateral dimension (nm)
Pure graphene	1619
Hybrid SiO_2-graphene (pH 9)	1776
Hybrid SiO_2-graphene (pH 10)	2279
Hybrid SiO_2-graphene (pH 11)	2725
Hybrid SiO_2-graphene (pH 12)	8426

3.2 Stability analysis of nanofluids

Fig.4 showed the sediment images of samples right after sonication and after two weeks. Samples with less sediments and more suspended nanomaterials indicated nanofluids with better suspension stability. Sediments were easily noticed in pristine graphene nanofluid after two weeks which showed the pure graphene nanoparticles poorly dispersed in transformer oil. By comparing the other four hybrid nanofluids, it could be noticed that hybrid nanofluids synthesised at pH 9 and pH12 have poor stability too as most of the nanomaterials settled at the bottom whereas hybrid nanofluids at pH 10 and 11 were more stable.

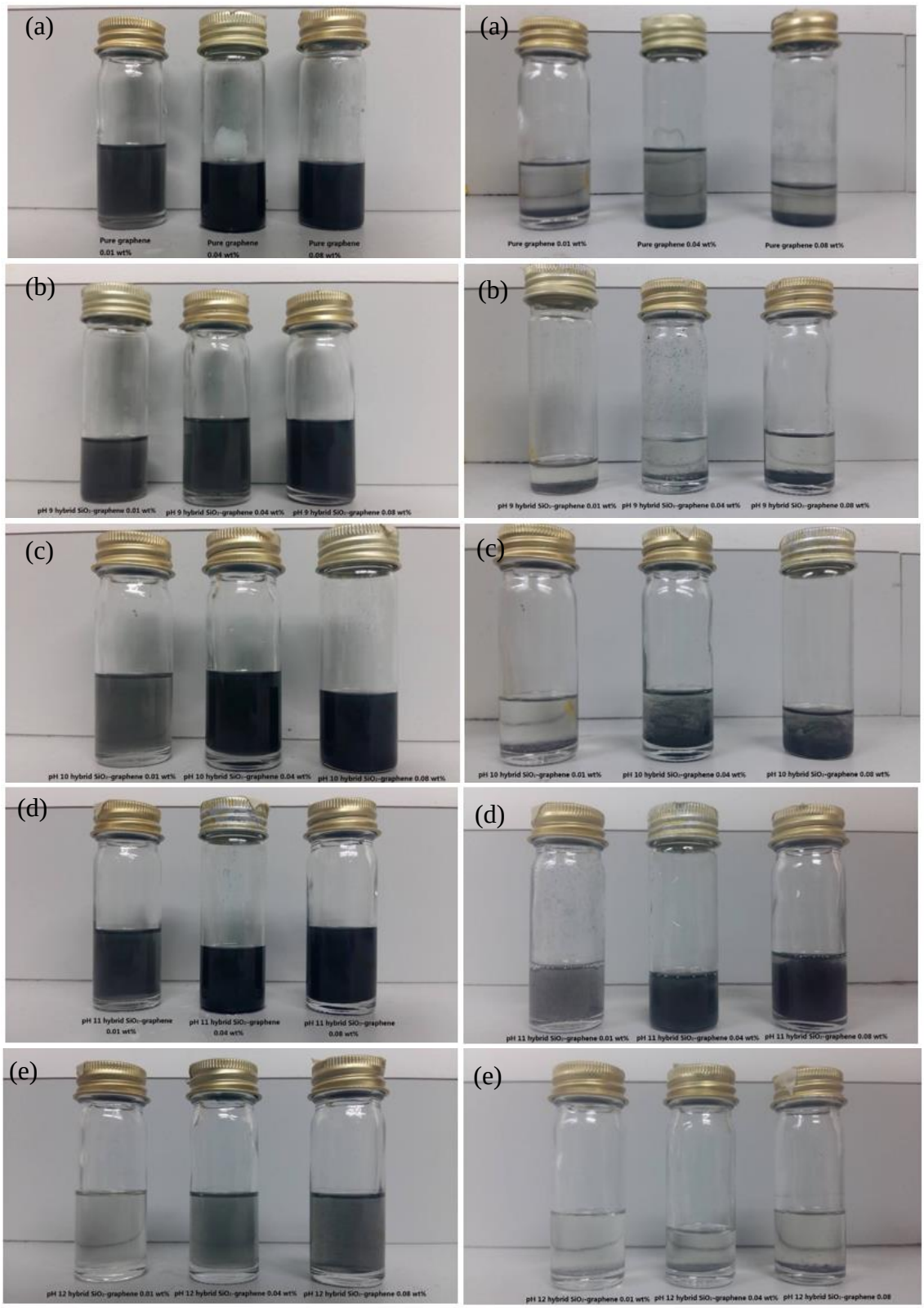


Figure 4. Sediment images of samples after sonication (left) and after two weeks (right) with three different concentrations (0.01 wt%, 0.04 wt%, 0.08 wt %)

UV-Vis analysis was carried out as shown in Fig. 5 to verify the visual studies of samples. Each type of sample was measured under different wavelength as the absorption value of λ_{max} was varied with type of samples (pristine graphene: 366nm, hybrid pH 9: 367nm, hybrid pH 10: 368nm, hybrid pH 11:368nm, hybrid pH 12:365nm). The result shown in Fig.5 was consistent with sediment images which showed the decreasing suspension stability in pure graphene and nanofluids (pH 9 and 12) over the time. Especially hybrid nanofluids at pH12, it was very unstable as the concentration of nanofluids fluctuated significantly over the time. Besides that, although sediments in hybrid nanofluids (pH 10) were not easily observed under naked eyes, UV result verified that the concentrations of this nanofluid also decreased marginally which indicated its poor stability. It was also observed that higher concentrations of nanofluids (0.08wt %) have steeper decreasing trend as it was well accepted that more nanoparticles in the fluid per unit volume have higher tendency to agglomerate and form sediments. Among all hybrid nanofluids, hybrid nanofluid at pH 11 had highest colloidal stability as its concentration was very consistent over the two weeks.

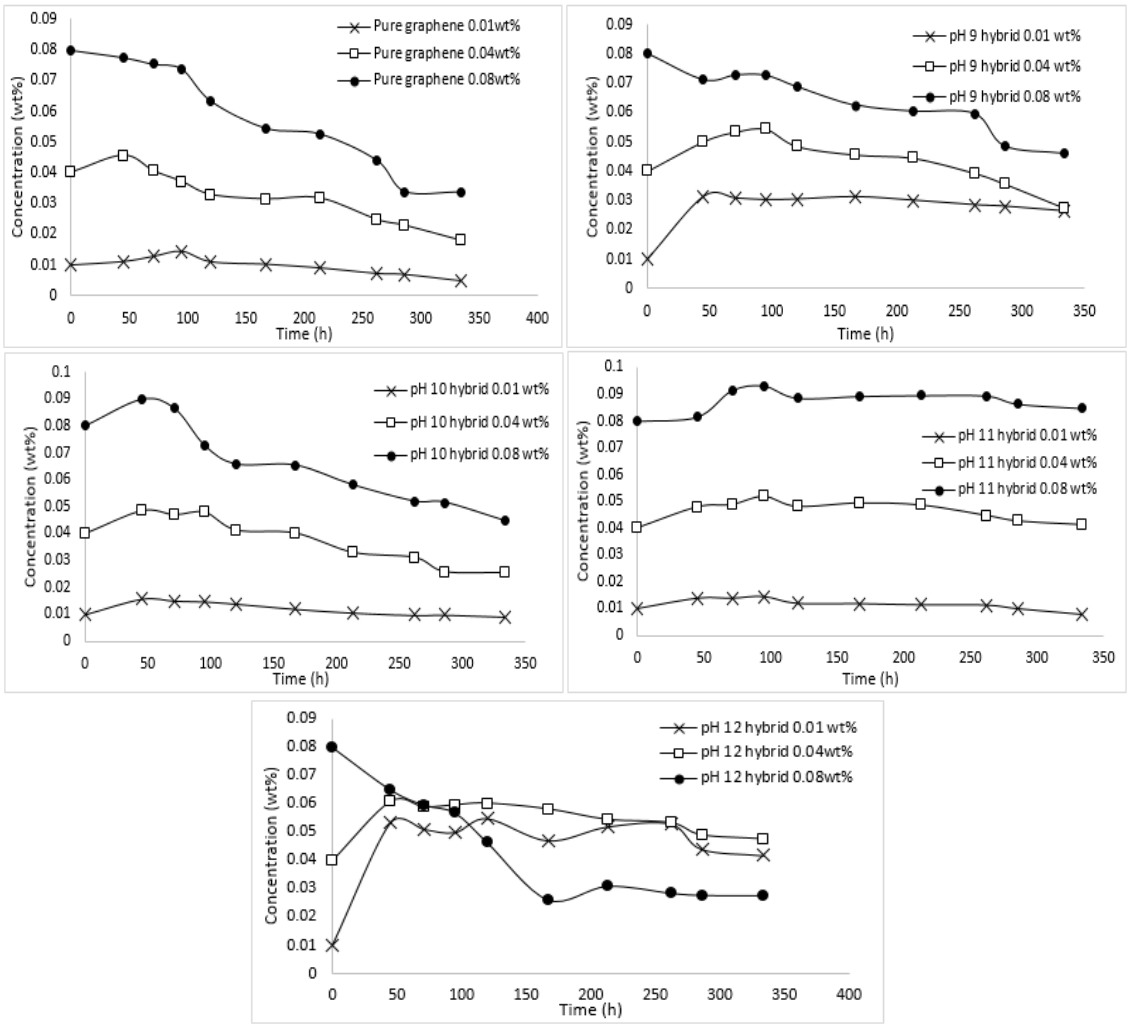


Figure 5. Changes of concentrations respect to time for all nanofluids

Pristine graphene dispersed poorly in most solvents as the interaction between graphene sheets was very strong as the nanoparticles tend to agglomerate and form clusters [18]. It was suggested that the SiO_2 coating has helped to improve the stability of graphene by increasing the repulsive electrostatic forces to keep the graphene nanoparticles from aggregating and increase the surface area between nanoparticles and transformer oil [19]. Hence, the dispersion of nanoparticles in transformer oil is enhanced. As justified in surface morphology and composition analysis, the size and growth units of SiO_2 nanoparticles on graphene surface increased with pH level. Therefore, the poor stability of hybrid nanofluids at pH 9 and 10 could be explained that the nanoparticle size and amount of coated silica nanoparticles were too little that failed to overcome the attractive Van der Waals forces and thus leading to agglomeration of nanoparticles. On the other hand, the particle sizes in hybrid nanofluids at pH 12 may be too large and precipitation took place in the nanofluid.

The unusual changes of concentrations for hybrid nanofluids at pH 9 and 12 could also be noticed which increased over the time. This error was due to their calibration curves that were poorly fitted to the linear model as shown in Fig. 1.The absorbance values of both nanofluids in calibration curve were very low indicated the nanofluids were very unstable even right after sonication. Furthermore, their absorbance values in calibration curves were very similar regardless of concentrations which caused the experimental data poorly fitted to linear model. This phenomenon could be explained by the formation of clusters in nanofluids that led to low absorption of light even at higher concentration of nanofluids. Hence, the concentrations calculated for these both nanofluids were differ from usual trend.

Due to significant instability in hybrid nanofluids at pH 12, it was justified that the nanofluid at pH 12 were not suitable to be further analysed for thermophysical and electrical properties as it may lead to inaccuracy of result.

3.3 Thermal conductivity analysis

3.3.1 Effect of GNP and coated silica

GNP is popular with its high thermal conductivity which is up to 5000 W/mK. Therefore from Fig. 6**,** it could be seen that addition of graphene nanoparticles could always enhance the thermal conductivity of its base fluid. The enhancement in thermal conductivity also increased with GNP concentration. This may due to more particles per unit volume contact with each other and enhance heat transport efficiency. It could also be observed that enhancement in thermal conductivity is much greater when the GNP was coated with silica. The highest enhancement in thermal conductivity for hybrid SiO_2-graphene nanofluid could reach 80% (0.04wt%, pH 9, at 100^oC) whereas highest enhancement in pure graphene nanofluid was only 29 % (0.08wt%, at 100^oC). By synthesizing both graphene and silica nanoparticles together, the thermal conductivity of nanofluids have been boosted up due to the contribution from thermal properties of silica. Besides that, improved stability of hybrid nanoparticles in base fluid could assist in enhancing thermal conductivity as SiO_2 coating helped to enhance dispersion of graphene nanoparticles and improve the contact between the hybrid nanoparticles in transformer oil [20].

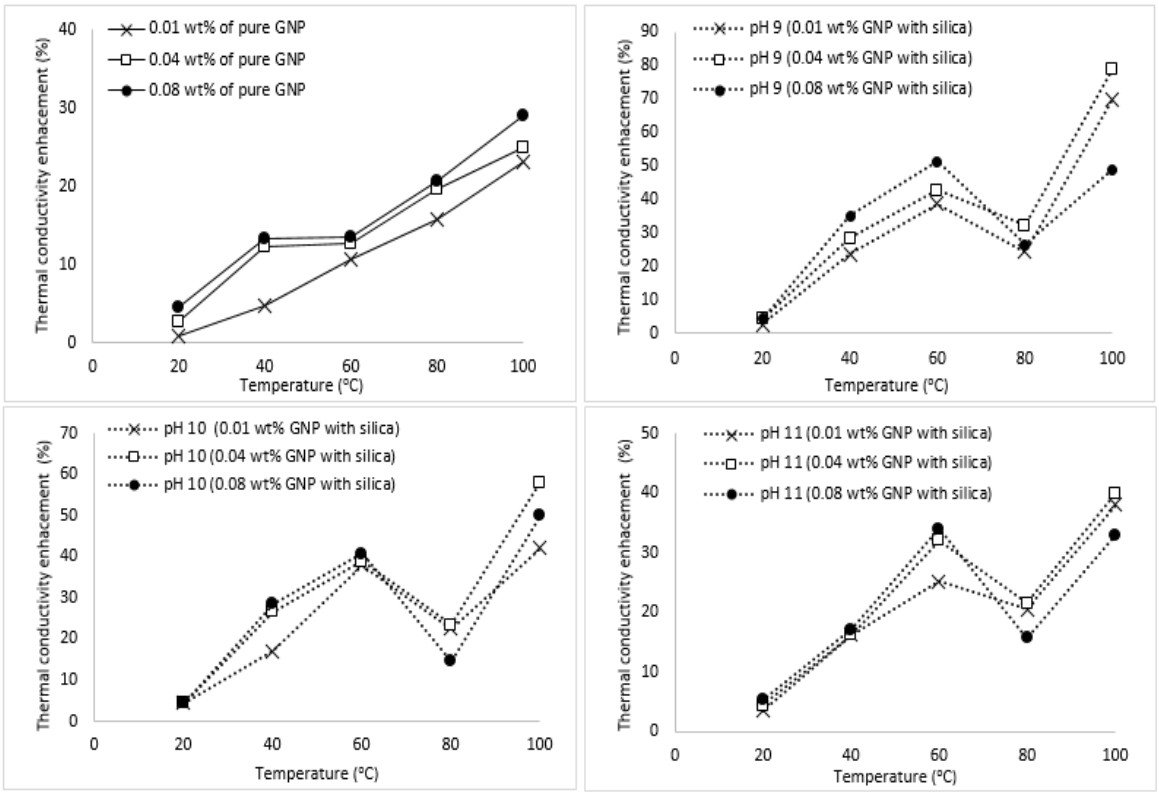


Figure 6. Thermal conductivity of pure and hybrid nanofluids

3.3.2 Effect of temperature

Fig. 6 also showed that hybrid SiO_2-graphene and pure graphene nanofluids increase significantly with temperature. Increasing trend of thermal conductivity with temperature was mainly due to increased Brownian motion of nanoparticles with temperature which resulted better local mixing and collision between nanoparticles. However, the result was not conclusive that a noticeable decrease in enhancement of thermal conductivity could be observed at 80°C for hybrid nanofluids except pure graphene. This could be explained by the natural behaviour of the transformer oil where its thermal conductivity deteriorated with temperature surpassed the effect of Brownian motion at 80°C and caused a sudden drop in enhancement of thermal conductivity [21]. The further increase in thermal conductivity after 80°C may due to stronger effect of Brownian motion of nanoparticles that successfully overtook the nature of transformer oil. Another similarity among three types of hybrid nanofluids (pH 9 to 11) was the greatest drop in enhancement of thermal conductivity at 80°C occur in 0.08 wt% of nanofluid. This may be explained that higher concentration of nanofluid was prone to agglomeration and had poorer stability which were more susceptible to the natural behaviour of transformer oil.

3.3.3 Effect of pH level and particle sizes

Furthermore, it could be noticed that enhancement of thermal conductivity for hybrid nanofluids in pH 9 and 10 were very similar before 80°C whereas a slightly lower enhancement was observed for pH 11. Possible explanation of this trend was lower pH value indicated presence of smaller particle size in fluid resulted in greater

enhancement of thermal conductivity. According to Brownian theory, particles with smaller sizes were able to collide with each other faster due to higher kinetic energy and enhanced thermal transport efficiency between nanoparticles and fluids. Besides particle sizes, pH of nanofluids also influenced the surface charges of nanoparticles and directly affected the enhancement of thermal conductivity [22]. When the pH value of nanofluids approached it optimised value (a value that diverged from the isoelectric point which was pH 2.2 for silica), the surface charges of nanoparticles increased too. The increased surface charges resulted to increased electrostatic repulsion forces between particles and improved nanomixing which ultimately enhanced the heat transport of fluid. The surface charges was contributed by hydroxyl group from ammonia solution during synthesis of hybrid nanoparticles. However, there was a range for the optimised pH value as if the pH was getting larger, higher concentration of ammonia solution caused compression of the electrical double layer and thus leading to decrease in electrostatic repulsion forces and lower enhancement of thermal conductivity of fluid [23].

3.4 Electrical properties analysis

3.4.1 Effect of GNP and coated silica

Fig. 7 showed the enhancement of electrical conductivity respect to concentrations of nanofluids at room temperature. The highest enhancement of electrical conductivity in base fluid after adding pristine graphene could reach up to 557 % which strongly justified the excellent electrical properties of graphene. It was an established fact that graphene has superior electrical conductivity due to its lamellar lattice that offers minimal resistance to electrons. Further increase in enhancement with graphene concentration could also be noticed in most of the samples as more conductive graphene nanoparticles carried electrons with high mobility in the fluid. It was clear to discern that hybrid nanofluids (pH 10 and 11) have successfully supressed the enhancement of electrical conductivity. Especially hybrid SiO_2-graphene that were synthesised at pH 11, the enhancement of electrical conductivity could be supressed until 97%. This trend was explained due to the insulating behaviour of silica which was a wide band gap insulator that hardly allowed the transfer of electrons to the conduction band. Moreover, studies have shown that conductivity in silica could only be found at very high temperature which was above 500 K [24]. Therefore, it ruled out the possibilities of conduction in coated silica in present work.

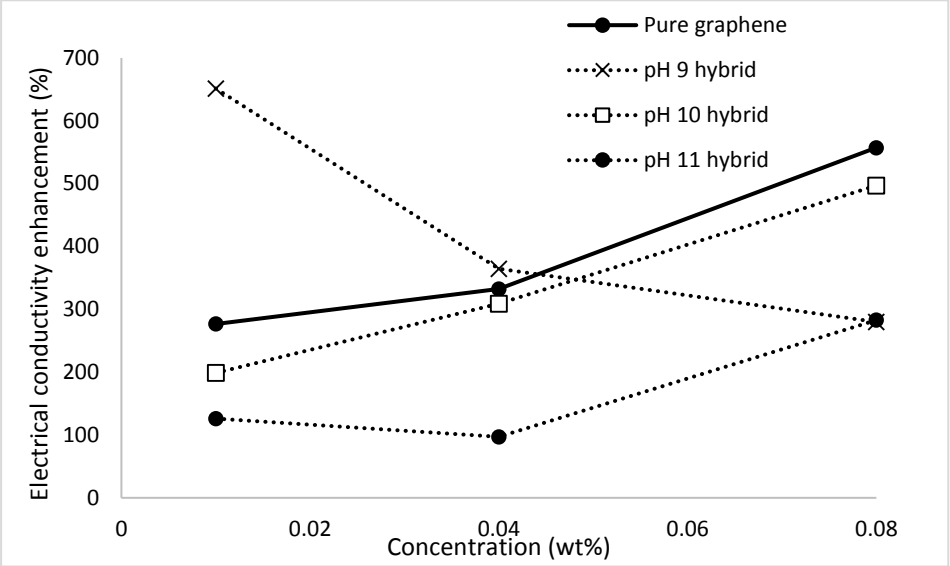


Figure 7. Electrical conductivity enhancement of pure and hybrid nanofluids

3.4.2 Effect of pH level and particle sizes

The variation in pH level was closely related to the growth units and sizes of coated silica on graphene surface as stated in characterisation analysis. As the amount of coated silica nanoparticles increased with pH level, the capability of insulating silica to oppose the enhancement of electrical conductivity was the highest at pH 11. Similarly, excellent suppression of electrical conductivity in hybrid nanofluids pH 11 was also due to its largest particle size among all other hybrid nanoparticles. When the particle sizes increased, the mobility of charged nanoparticles were limited too and slowed down the transfer of electrons in fluid [24].

3.4.3 Effect of agglomerates

However, an opposing trend could be observed for hybrid nanofluids at pH 9 which surprisingly have the greatest enhancement in electrical conductivity among all of the nanofluids, up to 651% at only 0.01wt% of concentration. It was suggested that the agglomeration of nanoparticles have strongly affected the electrical properties of hybrid nanofluid at pH 9. When large amount of clusters were formed, the clusters often attained a self-preserving size distribution (SPSD). This SPSD restrained the movement of particles into a small area and thus highly enhancing the collision of particles [25]. Therefore, transfer of electrons was improved too with higher collision frequency among nanoparticles. However, electrical conductivity decreased significantly until only 280% with increase in concentration of graphene. This phenomenon could be explained that there was a limiting value for the SPSD effect and further increase in agglomerates could strongly hinder the movement of those charged nanoparticles.

4. Conclusions

In this study, sol gel centrifugation was used to decorate SiO_2 nanoparticles on graphene surface. Coating of SiO_2 nanoparticles on graphene surface successfully inhibit the electrical conductivity of graphene in base fluid due to its insulating

behaviour while maintaining excellent thermal properties of graphene. Increasing pH level during sol gel centrifugation increase the growth of silica which result to larger particle sizes. Hybrid nanofluid at pH 11 is most stable as the optimum amount of silica and sizes are able to improve the dispersion of nanoparticles in transformer oil.

Thermal conductivity of nanofluids increase with temperature and graphene concentration. However, fluctuation of thermal conductivity enhancement happens at 80^{o}C due to the influence of natural behaviour of transformer oil which deteriorates with increase in temperature. There is an optimum range of pH level for highest thermal conductivity enhancement as if the pH level is too high, the electrostatic repulsion force will be compressed and reduce the heat transport efficiency between nanoparticles. Coated silica successfully suppresses the electrical conductivity enhancement of graphene and increasing pH level improves the hindrance of electrical conductivity. However, agglomerates may also help to enhance electrical conductivity which happens in hybrid nanofluids pH 9 until it reaching a limiting value. It can be inferred that silica nanoparticles could be a useful material in for insulation and heat transfer applications. A future plan in this study is to improve the stability of hybrid SiO_2-graphene nanofluid and investigate other parameters that affect the growth of coated silica during sol gel centrifugation.

References

[1] Yatsevsky V. A.. (2014). Hydrodynamics and heat transfer in cooling channels of oil-filled power transformers with multicoil windings. *Appl. Therm. Eng*., 63(1), 347-353.

[2] Huminic A. et al. (2015). Thermal conductivity, viscosity and surface tension of nanofluids based on FeC nanoparticles. *Powder Technol.*, 284, 78-84 vol. 284.

[3] Pang C. et al. (2012). Thermal conductivity measurement of methanol-based nanofluids with Al_2O_3 and SiO_2 nanoparticles. *Int. J. Heat Mass Transf.*, 55(21), 5597–5602.

[4] Tadjarodi A. and Zabihi F. (2013). Thermal conductivity studies of novel nanofluids based on metallic silver decorated mesoporous silica nanoparticles. *Mater. Res. Bull.*, 48(10), 4150–4156.

[5] Maruyama S. et al. (2013). Thermal conductivity enhancement of liquid and solid with single-walled carbon nanotubes. Ph.D. thesis, Dept. Mechanical Eng., Tokyo Univ., Tokyo, Japan.

[6] Baby T. and Ramaprabhu S. (2011). Enhanced convective heat transfer using graphene dispersed nanofluids. *Nanoscale Res. Lett.*, 6(1), 289-298.

[7] Mehrali M. et al. (2014). Investigation of thermal conductivity and rheological properties of nanofluids containing graphene nanoplatelets. *Nanoscale Res. Lett.*, 9(1), 15-28.

[8] Jin H. et al. (2012). AC breakdown voltage and viscosity of mineral oil based SiO2 nanofluids. *Annu. Rep. - Conf. Electr. Insul. Dielectr. Phenomena, CEIDP*, 902–905.

[9] Rafiq M. (2015). Insulating Properties of Transformer Oil-based Silica Nanofluids. *Electr. Power Syst. Res.*, 201-205.

[10] Alias S. S. et al. (2010). Effect of pH on ZnO nanoparticle properties synthesized by sol-gel centrifugation. *J. Alloys Compd.*, 499(2) , 231-237.

[11] Ikono R. et al. (2012). Effect of PH Variation on Particle Size and Purity of Nano Zinc Oxide Synthesized by Sol-Gel Method. *Internal Journal of Engineering &*

Technology, 6, 10-14.
[12]Rac O. et al. (2014). Influence of stabilising agents and pH on the size of SnO_2 nanoparticles. *Beilstein J. Nanotechnol.*, 5, 2192–2201.
[13]Jayalakshmi K. et al. (2014). Effect of pH on the Size of Gold Nanoparticles. *Int. J. Electron. Electr. Eng.*, 7(2), 159–164.
[14]Sadri R. et al. (2014). An experimental study on thermal conductivity and viscosity of nanofluids containing carbon nanotubes. *Nanoscale Res. Lett.*, 9(1) 151-167.
[15]Jeon I. Y. et al. (2013). Facile, scalable synthesis of edge-halogenated graphene nanoplatelets as efficient metal-free eletrocatalysts for oxygen reduction reaction.. *Sci. Rep.*, 3, 1810-1817.
[16] Milea C. and Bogatu C. (2011). The Influence of Parameters in Silica Sol-Gel Process. *Bull. Transilv. Univ. Brasov Eng. Sci.*, 4(1), 59–66.
[17]Matsoukas T. and Gulari E. (1988). Dynamics of growth of silica particles from ammonia-catalyzed hydrolysis of tetra-ethyl-orthosilicate. *J. Colloid Interface Sci.*, 124(1), 252–261.
[18]Johnson D. W. et al. (2015). A manufacturing perspective on graphene dispersions. *Curr. Opin. Colloid Interface Sci.*, 20(5), 367–382.
[19]Li J. et al. (2014). The situ preparation of silica nanoparticles on the surface of functionalized graphene nanoplatelets. *Nanoscale Res. Lett.*, 9(1), 172-181.
[20]Li X. et al. (2014). Effect of surface modification on the stability and thermal conductivity of water-based SiO_2-coated graphene nanofluid. *Thermochim. Acta*, 5, 6-10.
[21]Wanga G. P. W. et al. (2014). Thermal Conductivity of Transformer Oil From 253 K to 363 K. *Pet. Sci. Technol.*, 32(17), 150-159.
[22]Jang S. P.and Choi S. U. S. (2004). Role of Brownian motion in the enhanced thermal conductivity of nanofluids. *Appl. Phys. Lett.*, 84(21), 4316–4318.
[23]Xian-ju W. and Xin-fang L. I. (2009). Influence of pH on Nanofluids' Viscosity and Thermal Conductivity Influence of pH on Nanofluids' Viscosity and Thermal Conductivity. *Chin. Phys. Lett.*, 26(5), 122-127.
[24]Dutta K. and De S. K. (2007). Electrical conductivity and dielectric properties of SiO2 nanoparticles dispersed in conducting polymer matrix. *J. Nanoparticle Res.*, 9(4), 631–638.
[25]M. L. Eggersdorfer. (2012). Nanoparticle Agglomerates and Aggregates in Aerosols by Coagulation and Sintering. Ph.D. thesis, Dept. of Science, Minnesota Univ., Zurich, Germany.

eureka 2016 – Conference Paper
Paper Number 2CE23

Performance of Mesocarp Fibre as a Fuel Source in Direct Carbon Fuel Cell

She-Reen Tan[1], Doshi Veena[1*]

[1]*School of Engineering, Taylor's University, Malaysia*

[*]VeenaADoshi.ArunKumarDoshi@taylors.edu.my

Abstract
The rising demand of electricity resulted from increase of human population drives more research and development on alternative fuel source and methods of producing energy to ensure a continuous supply of electricity for many generations to come in near future. A direct carbon fuel cell (DCFC) is believed to be one of the alternative technology to the current conventional coal-fired power plants due to a higher conversion efficiency in power generation by using biomass as fuel source. This research studies the performance of a direct carbon fuel cell (DCFC) with yttria-stabilized zirconia (YSZ) as electrolyte operated with biochar derived from mesocarp fibre (palm oil biomass) at temperature ranging from 600°C to 900°C. During the fuel cell test, the untreated and dimineraslised mesosocarp fibre shows similar trend in increasing open circuit voltage when the operating temperature of DCFC increases from 600°C to 750°C. As the temperature continue to rise 900°C, the voltage decreases, indicating that the best performance of DCFC is at the optimum temperature between 750°C to 800°C. Based on the findings of this research, untreated biochar has a better potential as a carbon fuel for the DCFC compared to acid treated biochar, producing a maximum open circuit voltage of 0.88V at 750°C. Acid treatment on the mesocarp fibre was believed to enhance the thermal stability of the biochar, observed through the decomposition temperature of raw, untreated and acid treated mesocarp fibre. Pyrolysis and acid treatment has also proven to increase the carbon content of the biochar by 60% when compared to the raw mesocarp fibre biomass.

Keywords: Direct Carbon Fuel Cell, biochar, biomass, mesocarp fibre, pyrolysis

1. Introduction

The rapid growth of today's modern technology had led to many concerns over the fossil fuel consumption for the past decades. The world consumption of coal increased from 1000 to 2500 million tons in 1950 to 2000 [1]. In fact, the demand and consumption of coal is expected to continue rising for the upcoming decades. This has led to questions whether the remaining fossil fuel on earth are sufficient enough to keep

up with the rising demand and human population growth. Coal is commonly known as a fossil fuel which is consumed to produce around 40% of the world's electricity [2]. A normal coal plant generate about 3.5 million tons of CO_2 every year, leading the world's top source of carbon emission, also the primary source of climate change due to global warming [3]. In order to overcome the depletion of fossil fuel and global climate change, an alternative to the current source of energy has to be discovered and utilised. As such, this research focus on using mesocarp fibre biomass from palm oil waste as an alternative renewable energy and fuel source in a direct carbon fuel cell (DCFC).

In Malaysia, the oil palm industry is one the major agricultural crops grown which contributes about 34.56% of the country's agricultural sector [4]. Moreover, the two largest producers of palm oil, which account for roughly 85% of the world palm oil production are from Malaysia and Indonesia [5]. According to Basiron and Chan, the oil extraction rate from the palm oil production is only about 10% whereas the remaining of 90% are left as biomass [6]. Similarly, another statistics has shown that 4 kg of dry biomass is generated for every kg of palm oil extracted, of which one third of it can be found in the fresh fruit bunch (FFB) and the remaining two third is represented by oil palm frond (OPF) and oil palm trunk (OPT) inside the plantation estates (Sulaiman et al. 2011). The dry by-products in the FFB consists of empty fruit bunch (EFB), palm kernel shell (PKS) and mesocarp fibre (MF) [5]. The availability of each biomass from palm oil waste in 2005 is shown in Table 1 [7]. It is reported that mesocarp fibre has an availability of 9.6 million tonnes during that year.

Table 1. Oil palm biomass collected in 2005 [7].

Biomass Component	Quantity available (million tonnes)
Empty fruit brunches	17.00
Fibre	9.60
Shell	5.92
Fronds and trunks	21.10
Palm kernel	2.11
Total	55.73

Currently, many research has been done to develop valuable products from the FFB biomass, mainly focusing on the empty fruit bunch (EFB). For example, production of paper pulp from EFB, organic fertilizers from EFB and palm oil mill effluent (POME), bioethanol from EFB and OPT and furniture from OPT [8-11]. On the other hand, the current technologies and practices of the palm oil mills in Malaysia uses biomass such as MF and PKS as a source of fuel to generate electricity and steam from the boiler for palm oil extraction [12]. In this case, EBF is widely refrained in palm oil mills as fuel source due to its high moisture content of more than 65%, which will require more energy for drying prior to combustion, hence reducing the overall energy efficiency [13]. Besides using MF as fuel source, there are currently limited research on utilizing the biomass in other application fields such as biochar production.

The utilisation of this biomass waste does not only promote renewable energy sources, oil palm biomass can achieve sustainability with the rise in human population of the world. In terms of environmental friendly option, biomass is a good carbon

replacement fuel compared to coal as it reduces the CO_2 emission due to a lower carbon content in the biomass [14]. However, it could not be fed directly into the DCFC due to the content of impurities in the biomass. Hence, the biomass would need to go through pre-treatment to form biochar before being fed into the DCFC.

Acid treatment also known as "dimineralisation" of biomass is believed to reduce the ash content in the treated biomass and increase the yield of biochar. According to Clarke, ash is commonly referred to the non-combustible content in biomass [15]. It is also stated that ash with high potassium (K) content results to lower melting temperature of ash which forms "clinkers" that can obstruct the furnace elements [15]. Another finding from Julien et al. claimed that by using sulphuric acid, (H_2SO_4) and hydrochloric acid (HCl) in acid pre-treatment resulted in the incorporation of inorganic ions which increases the biochar and water yields while reducing the bio-oil during pyrolysis [16]. In a research done by Piskorz et al., the authors found a significant reduction in alkaline earth metal (Na and Ca) and ash content in treated biomass after pyrolysis [17].

A fuel cell is a mechanism that generates electricity by electrochemical reaction. The common fuel source used are hydrogen and oxygen (usually air) to be oxidise or reduced at the electrodes (anode and cathode) through a medium known as electrolyte to transfer the electrons in the cell and hence producing electricity. Fuel cells can vary from tiny devices generating only few watts of electricity to large fuel cell power plant producing megawatts [18]. A fuel cell is believed to have a higher efficiency in power generation, eliminating the consumption of fossil fuel and hence, reducing the greenhouse gases emission to the atmosphere. The types of fuel cells can be divided according to the respective operating temperatures. Fuel cells having operating temperature below 80°C are polymer electrolyte membrane (PEMFC), direct (DMFC) or indirect methanol (IMFC) and alkaline (AFC), while phosphoric acid fuel cell (PAFC) with intermediate operating temperature ranging from 200 – 215°C and high temperature fuels such as molten carbonate (MCFC), solid oxide (SOFC) and direct carbon (DCFC) with operating temperatures above 500°C [14].

As most of the fuel cell uses gaseous or liquid fuels, the direct carbon fuel cell (DCFC) had recently gained interest in researchers as it uses solid fuel (carbon) to produce electricity through its direct participation in the fuel cell and electrochemical oxidation [14]. Instead of using coal, biomass waste can also be fed into the DCFC as the solid fuel to generate electricity due to its high content of carbon. The biochar fuel utilisation in DCFC can achieve 100% compared to most of the other fuel cells with only 85% that uses gaseous or liquid fuels [14]. Moreover, the DCFC received much attention in the power generation field due to its promising potential of generating electric current with an electrical efficiency above 70%, almost twice of the conventional coal-fired power plants [14, 19]. At the same time, carbon dioxide emission from DCFC is reduced by 50% compared to coal-fired power plant.

Since DCFC is categorised under high temperature fuel cells, the operating temperature ranges from 600 - 900°C. The chemical energy in the carbon fuel is converted and utilised directly to electricity without the need of gasification. The overall fuel cell reaction for oxidation of fine (submicron) particles in the DCFC are [14]:

$$O_{2\ (air)} + 4e^- = 2O^{2-} \quad (1)$$

$$C + 2O^{2-} = CO_2 + 4e^- \quad (2)$$

In this research, pre-treated mesocarp fiber (MF) biomass from palm oil is used as the solid carbon fuel in the DCFC. The objectives of this research are as follow:

1. To study the electrochemical performance of Direct Carbon Fuel Cell (DCFC) with biochar derived from mesocarp fiber.
2. To optimize the performance of biochar in DCFC by varying the operating temperature of the fuel cell.
3. To study and compare the performance of DCFC with chemically treated and untreated biochar derived from pyrolysis of mesocarp fibre.

2. Methodology

In this research, three types of biochar derived from mesocarp fibre biomass are used as a fuel source in the DCFC. The biochars are distinguished by the pre-treatment methods during the fuel preparation, herein known as untreated mesocarp fibre (UMF) and dimineralised mesocarp fibre with HCl concentrations of 0.5 and 1.0 mol/L (DMF0.5 and DMF1.0)

2.1 Fuel Preparation

The raw biomass (mesocarp fibre) obtained from Seri Ulu Langat Palm Oil Mill was initially screened and washed with distilled water to remove the solid impurities. The raw biomass was then dried according to the ASTM D2867-09 standard, where sample was left in the oven under atmospheric pressure for 24 hours at a temperature of 105°C in order to remove the moisture content. The dried biomass is then grounded and sieved into sizes of 0.5 – 2 mm.

To produce dimineralised mesocarp fibre, 150 ml of 0.5 and 1.0 mol/L HCl acid were prepared in separate beakers, each mixed with 15g of dried and sieved biomass with a magnetic stirrer at 200 rpm for 6 hours. The samples were then rinsed with distilled water until a constant pH > 4.0 is obtained. The samples were left to dry according to the ASTM D2867-09 standards again before undergoing pyrolysis in a split tube furnace, programmed at a heating rate of 10°C/min to achieve 600°C in 60 minutes and held for an hour before cooling to room temperature. The pyrolysis was carried out in atmospheric pressure condition, purged with 99.99% of N_2. As for UMF, the biochar was prepared without any pre-treatment, undergoing the same pyrolysis conditions as DMF from the dried and sieved biomass.

2.2 Fuel Characterisation and Analysis

2.2.1 Proximate and Ultimate Analysis

Proximate analysis was done in this research to determine the ash and moisture content of each biochar sample prepared.

i. Moisture content determination ASTM E 190-87
The weight of crucible with 0.1g of biochar is recorded before placing in the oven to be heated at 110°C for 1 hour. After removing the sample from the oven, the weight of crucible together with the biochar is measured again. The moisture content is obtained by subtracting the final weight from the initial weight.

ii. Ash content determination ASTM E 897-88
The dried biochar obtained after the moisture analysis is used for ash determination. The sample is heated in the muffle furnace at 750°C for 1 hour, where the operating atmosphere is set to the oxidizing temperature. The sample is weighed once removed from the muffle furnace, and subtracted with the crucible weight to obtain the ash content.

Ultimate Analysis was done to on vario MACRO cube (Elementar, Germany) to obtain the C, H, N and S elements of the mesocarp fibre samples.

2.2.2 Thermogravimetry Analysis (TGA)

The Thermogravimetry analysis was done to study the weight loss of sample as the temperature increases. This analysis was carried out on a Perkin Elmer STA6000. Each sample (5 – 10 mg) was heated from 30 to 900°C with heating rate of 10°C/min, with a constant nitrogen (99.99%) flow rate of 20 ml/min.

2.2.3 Fourier Transform Infrared Spectroscopy (FTIR)

The FTIR analysis was done to understand and examine the functional groups compositions of the biochar by generating infrared (IR) spectra of the samples with a Perkin Elmer FTIR spectrometer (Spectrum 100)

2.3 Direct Carbon Fuel Cell Testing

The apparatus used to perform the fuel cell testing consist of a DCFC, furnace and an electrochemical workstation (Gamry Reference 600 Potenstiotat). The fuel cell is made with ceramic tubes, assembled within a furnace system as shown in Figure 1. The biochar (0.1g) are placed on the button cell which is fabricated with Nickel-yttria stabilized zirconia (Ni-YSZ) on the anode, Lanthanum strontium manganite (LSM) on the cathode and Yttria-stabilized zirconia (YSZ) as the cell electrolyte.

The voltage performance test on the mesocarp fibre biochar were carried out at different temperatures: 600°C, 750°C and 900°C. The DCFC was heated with a heating rate of 10°C min to the desired operating temperature. Once the desired temperature is

reached, the voltage reading produced from the fuel cell is measure and recorded for 300s. During the test, the anode chamber is purged with N2 (99.99%) to eliminate the presence of O_2 which may oxidise the fuel, whereas purified air, O_2 (99.99%) was continuously fed into the cathode side.

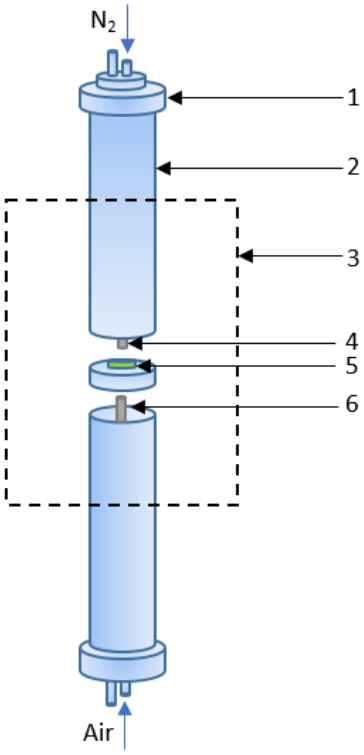


Figure 1. Exploded view of Direct Carbon Fuel Cell. 1: flange, 2: ceramic tube, 3: furnace, 4: anode current collector, 5: fuel placed on top of button cell, 6: cathode current collector.

3. Results and Discussion

3.1 Fuel Analysis

3.1.1 Proximate and Ultimate Analysis

The results obtained from the proximate and ultimate analysis of mesocarp fibre samples are tabulated in Table 2. The proximate analysis done give the moisture and ash content of each samples. It was found that the acid treatment managed to reduce the moisture but not the ash content in the mesocarp fibre biomass.

The ultimate analysis showed that the raw mesocarp fibre has a moderate carbon and oxygen content. With only pyrolysis done on the mesocarp fibre (UMF), the carbon content increases, whereas the hydrogen and oxygen content in the sample decreases. It is noticed that the acid treatment on the samples (DMF 0.5 and DMF1.0) do not give any significant changes in the composition of biomass compared to the UMF, except for the slight increase in carbon content. However, by comparing only the acid treated samples, washing the acid with a higher concentration is not needed as 0.5 mol/L of HCl treatment can already produce a good carbon yield.

Table 2. Proximate and ultimate analysis of mesocarp fibre biomass.

Samples	Proximate analysis (wt%)		Ultimate Analysis (wt%)				
	Moisture	Ash	C	H	N	S	O[a]
Raw	-	-	47.35	6.56	4.50	0.32	41.27
UMF	7.0	2.0	77.40	1.97	2.96	0.24	17.43
DMF0.5	2.1	2.0	78.99	2.30	5.14	0.21	13.35
DMF1.0	4.0	6.0	78.82	2.05	2.97	0.16	16.00

[a]By difference

3.1.2 Thermogravimetry Analysis (TGA)

The TGA curves of raw, untreated and acid treated samples are shown in Figure 2. Raw mesocarp fibre in Fig. 2(a) displayed three degradation steps, clearly showing the moisture, volatile matter, fixed carbon and ash content of the samples. However, the untreated and acid treated mesocarp fibre samples displayed only one degradation step as shown in Fig. 2(b), (c) and (d). This may be due to the composition of cellulose, hemicellulose and lignin in mesocarp fibre which greatly affects the thermal decomposition of the biomass during pyrolysis. Among these components, hemicellulose was believed to be the easiest to decompose due its short chains linear polymer structure [20]. Lignin, on the other hand is known for its high thermal resistant compared to cellulose and hemicellulose due to a more complex chemical composition, which allows the thermal decomposition to happen at a higher temperature [21]. The complicated structure of phenolic polymer in lignin, encasing the polysaccharides of the cell walls are used to produce strong and durable composite materials [22].

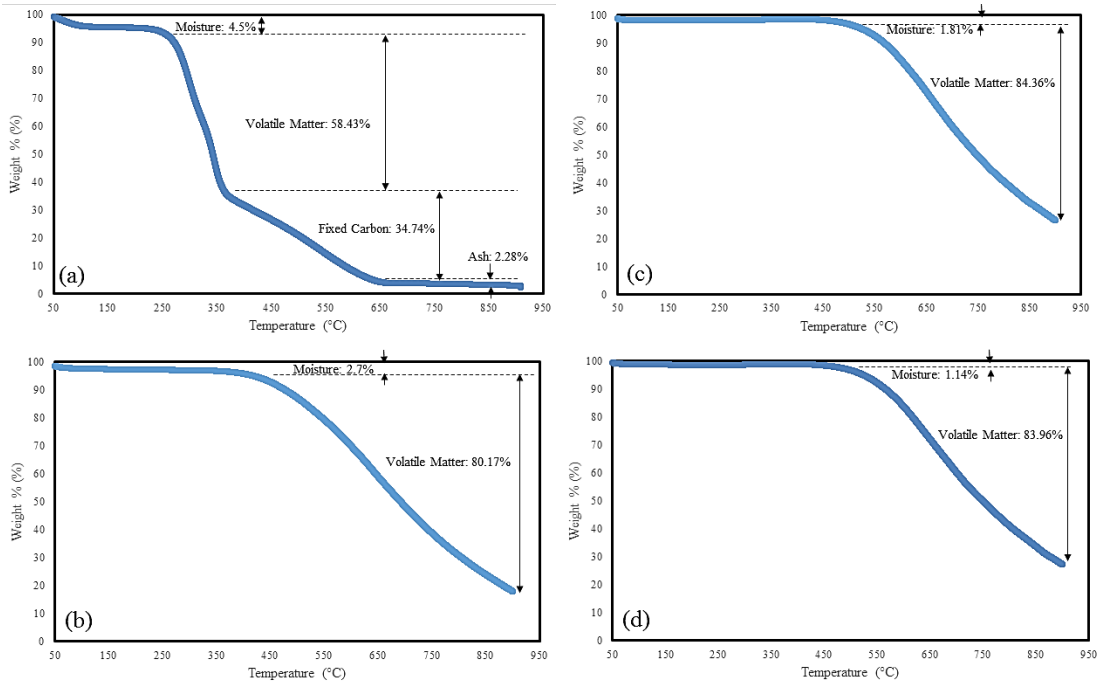


Figure 2. TGA curve for (a) Raw, (b) UMF, (c) DMF0.5 and (d) DMF1.0.

For the untreated mesocarp fibre, devolatilisation is seen to occur at the beginning of 400°C whereas a slightly increased in thermal stability is seen for the acid treated mesocarp fibre as devolatilisation begins at around 500°C. It is reported that devolatilisation is a major step among all thermochemical conversion process, where the steep slope in a TG curve between 200 to 500°C shows a significant drop in weight of samples due to the rapid thermal decomposition of hemicellulose, cellulose and some part of lignin, contributing to 50% drop in the weight of samples, except for commercial lignin samples [23]. This is because 80 wt% of biomass is produced from volatile fraction and only 20 wt% in the form of solid carbonaceous residue [24]. According to a study done by Yang et al., the decomposition temperature were 220 to 300°C, 300 to 340°C and 750 to 800°C for hemicellulose, cellulose and lignin respectively [25]. Some other studies had also reported that pyrolysis of heavier volatiles such as lignin can occur at 900°C as it possesses a higher thermal stability compared to hemicellulose and cellulose [26]. Hence, a greater presence of lignin contributes to a higher yield of char after pyrolysis.

According to Kong et al, among all the palm oil based biomass, mesocarp fibre was reported as one of the waste with highest lignin composition after palm kernel shell [27]. Table 3 shows the comparison of lignin composition in mesocarp fibre and other types of biomass used in previous studies. It is also observed that mesocarp fibre have relatively low cellulose and high lignin composition compared to other biomass. This may be one of the reason why ash content could not be determined in the single stage TG curves for untreated and acid treated mesocarp fibre as the biomass had not fully decompose even at 900°C. The acid treatment, which is believed to have also enhanced the thermal stability of the mesocarp fibre, showed a higher decomposition temperature compared to the untreated mesocarp fibre biomass.

Table 3. Composition of biomass [27-29]

Biomass	Cellulose (wt %)	Hemi-cellulose (wt %)	Lignin (wt %)
Mesocarp Fiber	33.9	26.1	27.7
Soft Wood	42	22	31
Wheat Husk	36	18	16
Rye Husk	26	16	13
Corn Cub	50.5	31	15
Coconut Shell	34	21	27

3.1.3 FTIR Analysis

The IR spectra of UMF, DMF0.5 and DMF1.0 is shown in Figure 3. It is observed that the infrared spectra of acid treated biochar (DMF 0.5 and DMF 1.0) exhibited weaker IR absorbances compared to UMF, which may be due to a lower volatile content in the samples [30]. The biochar sample spectra exhibits distinct peaks corresponding to the cellulosic, hemicellulosic and lignin components.

The characteristic of crystalline cellulose can be determined from the broad peaks between 3200 and 3600 cm^{-1}. Based on Fig. 3, the first peak occurring right after 3000 cm^{-1} are the crystalline cellulose peaks. The subsequent disappearance of these bands in the spectra is due to the loss of cellulosic content in the biochar. At the

wavelength between 1500 and 2000 cm^{-1}, the peek observed at 1580.85 cm^{-1} in Fig. 3 corresponds to the C=O vibration of the carboxylic acids in hemicellulose. According to Abnisa et al., the intensities of the bands at 1586.33 to 1571.62 cm^{-1} indicates the cracking volatiles and conversion of aliphatic compounds into aromatic compounds of the char [21]. The disappearance of the peak and appearance of a new peak at 1104.07 cm^{-1} is believed to be caused by the degradation of hemicellulose product. The degradation of lignin responds to the peak between 1500 and 1000 cm^{-1}, under the functional group of aromatic C-O stretching of methoxyl and phenyl propane structure and aromatic ring vibration.

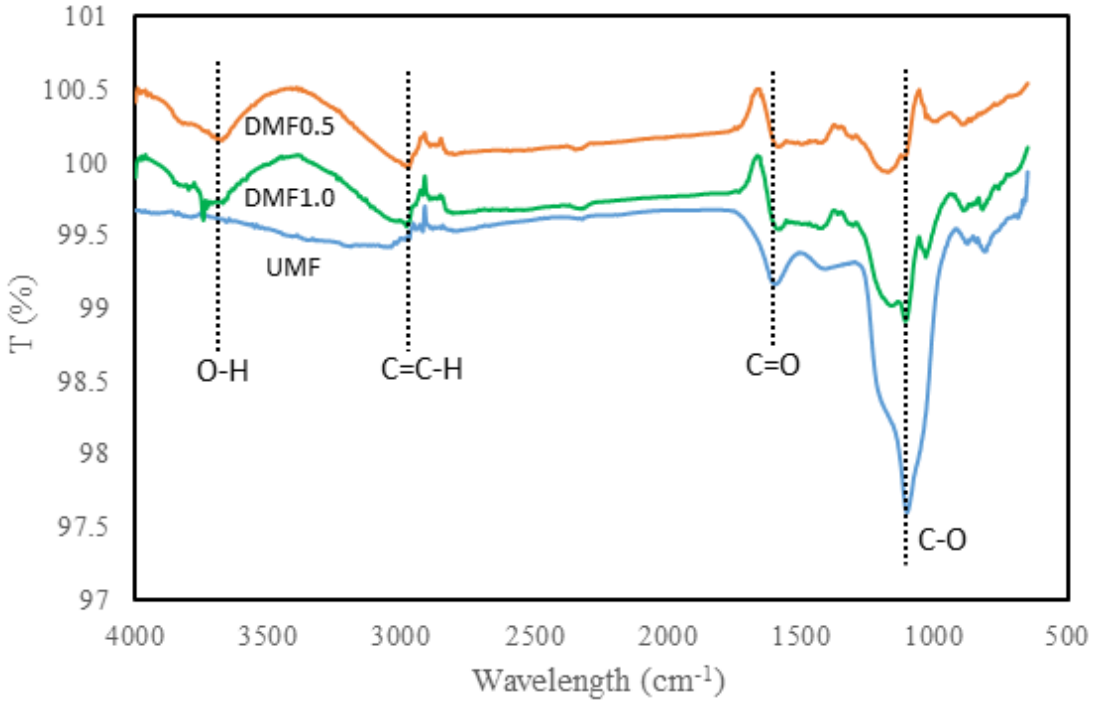


Figure 3. FTIR spectra of UMF, DMF0.5 and DMF1.0.

3.2 DCFC results

Fig. 4 shows the voltage – time graph obtained using biochar derived by mesocarp fibre biomass as solid carbon fuel source in the DCFC. The reading of open circuit voltage was measured for 5 minutes when the DCFC had reached the desired temperature of testing. There results were analysed based on the effect of temperature and acid treatment on the DCFC performance.

3.2.1 Effect of Temperature on DCFC Performance

When the DCFC was operated at 600°C, the open circuit voltage gives a range of values from 0.37 to 0.77V as shown in Fig. 4(a). As the temperature of DCFC increased to 750°C, the values of open circuit voltage measured had increased compared to 600°C, where the range begins from 0.73 to 0.88V as shown in Fig. 4(b). However, the open circuit voltage dropped to a range of 0.69 to 0.73V when DCFC was operated at 900°C. A common finding from this three cases is that the maximum open

circuit voltage values of 0.77V, 0.88V and 0.73V from 600°C, 750°C, and 900°C respectively are produced from UMF. Based on the different operating temperature, the results show that DCFC operated at 750°C achieves a higher performance compared to other operating temperatures by producing a higher range of open circuit voltage of 0.73 to 0.88V even when different pre-treated biochar was used as the carbon fuel. Some of the research on biomass fuel performance had also reported the optimum operating temperatures for maximum open circuit voltage between 700 to 750°C as shown in Table 4.

Table 4. Performance of DCFC for various biochar [31-32]

Biochar	Operating Temperature	DCFC Performance	Reference
Almond Shell	600- 750°C	Best open circuit cell potential (1.07 V) at 700°C	[31]
Corn Cub	650- 750°C	Increase in open circuit cell potential from 0.9V at 600°C to 1.05V at 750°C. Maximal power density of 185 $mWcm^{-2}$ when current density of 240 $mAcm^{-2}$ at 750°C.	[32]

3.2.2 Effect of Acid Treatment on DCFC Performance

From Fig. 4(d), the open circuit voltage produced by UMF ranges from 0.74 to 0.88V at varying operating temperatures. However, the results seen from Fig. 4(e) and (f) show that the dimineralised mesocarp fibre produces lower voltage compared to the untreated biochar. The range of voltage produced was 0.64 to 0.79V and 0.37 to 0.73V for DMF0.5 and DMF1.0 respectively. By comparing only the acid treated biochar of different concentration, the DMF0.5 (lower concentration) produces a higher voltage than DMF1.0 for all operating temperature at 600°C, 750°C, and 900°C of DCFC. This may be due to higher ash content in DMF1.0 based on the results obtained from proximate analysis. According to a research done on coconut biochar, impurities such as ash can caused blockage of electron transfers within the fuel cell [33]. Another similarity in the performance of DCFC is seen when all 3 different types of biochar generate its highest circuit voltage when DCFC was operated at 750°C.

3.2.3 Overall Performance

All 3 biochar derived from mesocarp fibre (UMF, DMF0.5 and DMF1.0) shows a similar trend in increasing open circuit voltage when the operating temperature of DCFC increases from 600°C to 750°C as shown in Fig. 5. As the temperature continue to rise 900°C, the voltage decreases, indicating that the best performance of DCFC is at the optimum temperature between 750°C to 800°C. Based on the findings of this research, untreated biochar has a better potential as a carbon fuel for the DCFC compared to acid treated biochar, producing a maximum open circuit voltage of 0.88V at 750°C.

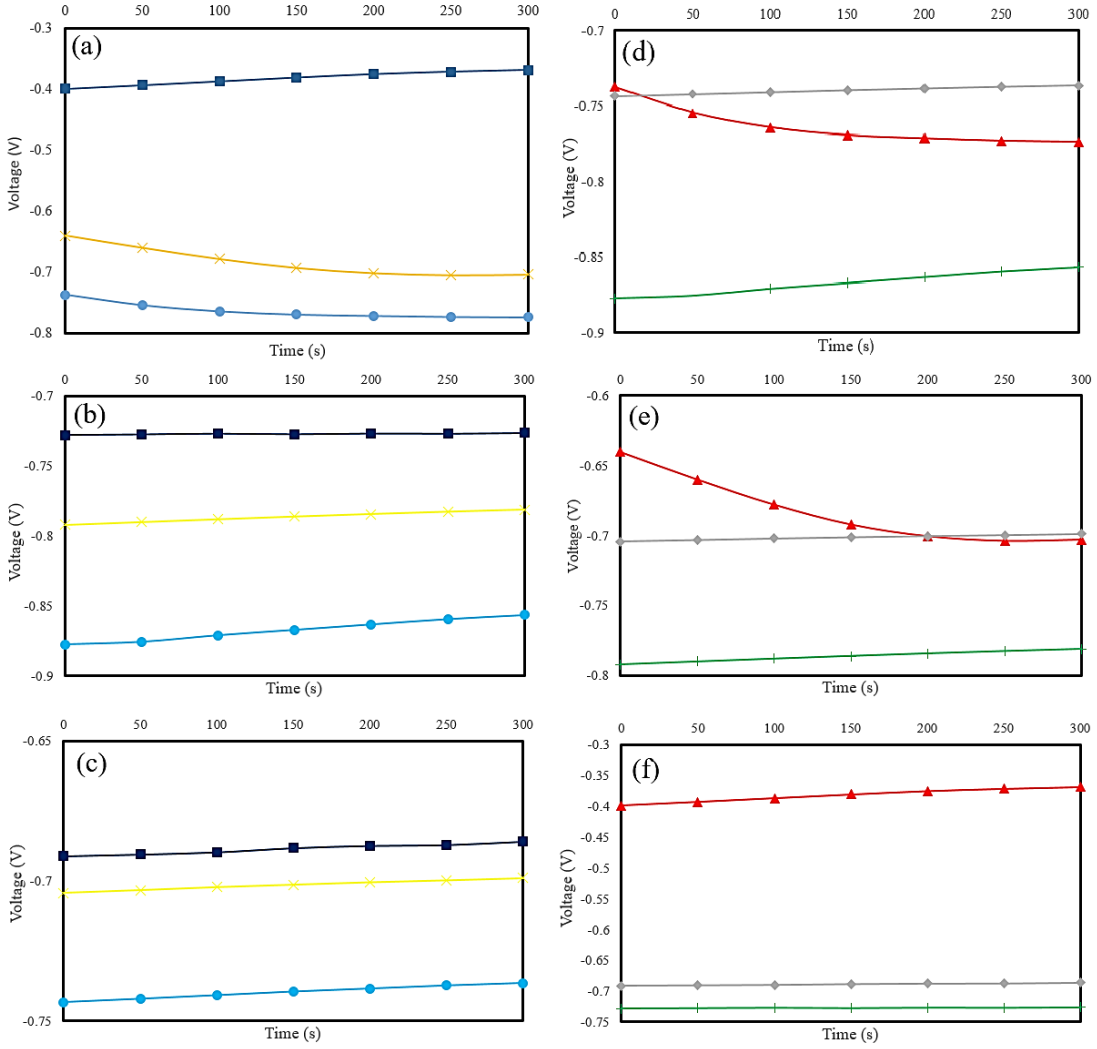


Figure 4. Voltage-Time (V-t) curves for (a) 600°C, (b) 750°C, (c) 900°C with different biochar: ● UMF, X DMF0.5, ■ DMF1.0 and (d) UMF, (e) DMF0.5 and DMF1.0 at different temperature: ▲ 600°C, + 750°C, ◆ 900°C.

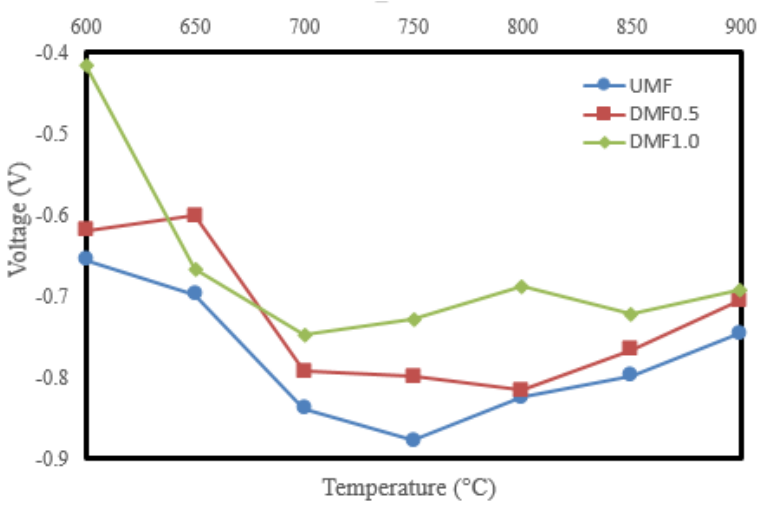


Figure 5. Voltage-Temperature (V-T) curves for carbon fuel derived from mesocarp fibre.

4. Conclusion

Mesocarp fibre biomass derived from palm oil waste was used as solid carbon fuel source in a DCFC. This research contributes to utilising biomass waste from palm oil plantation, especially in countries like Malaysia which contributes to one the largest producer of palm oil. As biochar derived from mesocarp fibre has not been tested in a DCFC, this study has proven the potential of mesocarp fibre as a fuel source in DCFC based on the characterisation analysis and the high lignin composition compared to other biomass available.

In this research, acid pre-treatment on the biomass has proven to enhance the thermal stability of the biochar, observed through the decomposition temperature of raw, untreated and acid treated mesocarp fibre. Pyrolysis and acid treatment has also proven to increase the carbon content of the biochar by 60% when compared to the raw mesocarp fibre biomass. Furthermore, acid-pretreatment was found to significantly enlarge the surface area and reduces the degree of graphitisation of the biochar compared to the untreated biochar.

During the fuel cell test, the untreated and acid treated biochar shows a similar trend in increasing open circuit voltage when the operating temperature of DCFC increases from 600°C to 750°C. However, as the operating temperature continue to rise to 900°C, the voltage decreases, indicating that the best performance of DCFC is at the optimum temperature between 750°C to 800°C. Based on the findings of this research, untreated biochar has a better potential as a carbon fuel for the DCFC compared to acid treated biochar, producing a maximum open circuit voltage of 0.88V at 750°C.

Acknowledgment

Gratitude and thanks are due to Dr. Veena Doshi, Dr. Wong Wai Yin, Ms. Nida Jafri, Ms. Lithnes Kalaivani and research partner, Merisa Gunawan for the guidance and supervisions throughout this research process.

References

[1] "Global Fossil Fuel Consumption Surges Worldwatch Institute," *Mitsubishi Heavy Industries*, 2013.
[2] O. Energy, "What is coal? - Origin Energy." 02-Mar-2015.
[3] "coal power: air pollution | Union of Concerned Scientists."
[4] S. Zafar, "Agricultural Biomass in Malaysia - BioEnergy Consult," *BioEnergy Consult*, 2015.
[5] F. Sulaiman, N. Abdullah, H. Gerhauser, and a. Shariff, "An outlook of Malaysian energy, oil palm industry and its utilization of wastes as useful resources," *Biomass and Bioenergy*, vol. 35, no. 9, pp. 3775–3786, 2011.
[6] Y. Basiron and K. W. Chan, "The oil palm and its sustainability," *J Oil Palm Res*, vol. 16, pp. 1–10, 2004.
[7] S. H. Shuit, K. T. Tan, K. T. Lee, and a. H. Kamaruddin, "Oil palm biomass as a sustainable energy source: A Malaysian case study," *Energy*, vol. 34, no. 9, pp. 1225–1235, 2009.
[8] J. Goh and K. Leong, "Development of pulp and paper products from oil palm

fiber," in *Proceedings of the international conference on oil palm biomass*, 2008.
[9] K. Haron and A. Mohammed, "Efficient use of inorganic and organic fertilizers for oil palm and potential utilization of decanter cake and boiler ash for biofertiliser production," *Natl. Semin. biofertiliser, biogas effluent Treat. oil palm Ind. waste to wealth*, pp. 21–30, 2008.
[10] T. Hilstrom, M. Mikkelsen, and B. Ahring, "Ethanol potential for empty fruit bunches pre-treated by wet-explosion," in *Proceedings of the international palm oil congress*, 2005, pp. 348–56.
[11] A. Mokhtar, K. Hassan, A. A. Abdul, and M. Wahid, "Plywood from oil palm trunks," *J Oil Palm Res*, vol. 23, pp. 1159–65, 2011.
[12] V. Subramaniam, A. MA, Y. Choo, and N. Nik Meriam, "Life cycle inventory of the production of cruide palm oil – a gate to gate case study of 12 palm oil mills," *J Oil Palm Res*, vol. 20, no. 8, pp. 484–94, 2008.
[13] Y. T. Kelly, K. Lee, A. Mohamed, and S. Bhatia, "Potential of hydrogen from oil palm biomass as a source of renewable energy worldwide," *Energy Policy*, vol. 35, no. 5, pp. 5692–701, 2007.
[14] S. P. S. Badwal and S. Giddey, "The holy grail of carbon combustion - The direct carbon fuel cell technology," *Mater. Forum*, vol. 34, pp. 181–185, 2008.
[15] S. Clarke, "Biomass Burn Characteristics," *Ontario*, 2015. [Online]. Available: http://www.omafra.gov.on.ca/english/engineer/facts/11-033.htm.
[16] S. Julien, E. Chornet, and R. P. Overend, "Influence of acid pretreatment (H2SO4, HCl, HNO3) on reaction selectivity in the vacuum pyrolysis of cellulose," *J. Anal. Appl. Pyrolysis*, vol. 21, pp. 25–43, 1993.
[17] J. Piskorz, D. Radlein, D. S. Scott, and S. Czernik, "Pretreatment of wood and cellulose for production of sugars by fast pyrolysis," *J. Anal. Appl. Pyrolysis*, vol. 16, pp. 127–142, 1989.
[18] J. Matthey, "Fuel Cell Technologies - Fuel Cell Today," 2015. [Online]. Available: http://www.fuelcelltoday.com/technologies. [Accessed: 03-Oct-2015].
[19] J. Jewulski and M. Skrzypkiewicz, "Direct carbon fuel cells based on solid oxide electrolyte technology," no. 7, pp. 268–270, 2013.
[20] S. Gaur and T. B. Reed, "Thermal data for natural and synthetic fuels," *USA Marcel Dekker, Inc.*, 1998.
[21] F. Abnisa, A. Arami-Niya, W. M. A. W. Daud, and J. N. Sahu, "Characterization of Bio-oil and Bio-char from Pyrolysis of Palm Oil Wastes," *Bioenergy Res.*, vol. 6, no. 2, pp. 830–840, 2013.
[22] W. H. Chen and P. C. Kuo, "A study on torrefaction of various biomass materials and its impact on lignocellulosic structure simulated by a thermogravimetry," *Energy*, vol. 35, pp. 2580–2586, 2010.
[23] S. Abdullah, S. Yusup, M. Ahmad, a Ramli, and L. Ismail, "Thermogravimetry Study on Pyrolysis of Various Lignocellulosic Biomass for Potential Hydrogen Production," *Int. J. Chem. Biol. Eng.*, vol. 3, no. 3, pp. 137–141, 2010.
[24] E. Osorio, M. L. I. Gomez, A. C. F. Vilela, and M. A. A. W. Kalkreuth, "Evaluation of petrology and reactivity of coal blends for use in pulverized coal injection (PCI)," *Int. J. Coal Geol.*, vol. 68, pp. 14–29, 2006.
[25] H. Yang, R. Yan, T. Chin, D. L. Tee, H. Chen, and C. Zheng, "Thermogravimetric analysis-Fourier transform infrared analysis of palm oil waste pyrolysis," *Energy Fuels*, vol. 18, no. 6, pp. 1814–1821, 2004.
[26] A. Uslu, A. P. C. Faaij, and P. C. A. Bergman, "Pre-treatment technologies and their effect on international bioenergy supply chain logistics. Techo-economic

evaluation of torrefaction, fast pyrolysis and pelletisation," *Energy*, vol. 33, pp. 1206–1223, 2008.

[27] S.-H. Kong, S.-K. Loh, R. T. Bachmann, S. A. Rahim, and J. Salimon, "Biochar from oil palm biomass: A review of its potential and challenges," *Renew. Sustain. Energy Rev.*, vol. 39, pp. 729–739, 2014.

[28] A. Mamun, "Barley husk and coconut shell reinforced polypropylene composites: The effect of fibre physical, chemical and surface properties," *Compos. Sci. Technol.*, vol. 70, pp. 840–846, 2010.

[29] A. Demirbas, "Effect of temperature and particle size on bio-char yield from pyrolysis of agricultural residues," *J. Anal. Appl. Pyrolysis*, vol. 72, pp. 243–248, 2004.

[30] H. Yang, R. Yan, H. Chen, D. H. Lee, D. T. Liang, and C. Zheng, "Mechanism of palm oil waste pyrolysis in a packed bed," *Energy Fuels*, vol. 20, no. 3, pp. 1321–1328, 2006.

[31] A. Elleuch, A. Boussetta, J. Yu, K. Halouani, and Y. Li, "Experimental investigation of direct carbon fuel cell fueled by almond shell biochar: Part I. Physico-chemical characterization of the biochar fuel and cell performance examination," *Int. J. Hydrogen Energy*, vol. 38, no. 36, pp. 16590–16604, 2013.

[32] J. Yu, Y. Zhao, and Y. Li, "Utilization of corn cob biochar in a direct carbon fuel cell," *J. Power Sources*, vol. 270, pp. 312–317, 2014.

[33] C. Munnings, a. Kulkarni, S. Giddey, and S. P. S. Badwal, "Biomass to power conversion in a direct carbon fuel cell," *Int. J. Hydrogen Energy*, vol. 39, no. 23, pp. 12377–12385, 2014.

eureca 2016 – Conference Paper
Paper Number 2CE24

Urea Release Rate Study in Starch-Derivative-Alginate Based Formulation

Woei Jiunn Tee, Siew Wei Phang, Lee Tin Sin, Dr. Soo-Tueen Bee
[1]*School of Engineering, Taylor's University*

Woeijiunn.tee@sd.taylors.edu.my

Abstract
Recently Controlled Release Fertilizers has become a very important application in agricultural field due to its ability to delay the release of fertilizing nutrients with the sequential needs of plants for nutrients. Starch-Alginate is one of the favorite coating materials for controlled release fertilizer because of its abundance, biodegradability, good water absorbency and retention. In this research the starch-alginate based controlled release fertilizers will be studied and the research questions that have been raised in this research are how the effect of starch, alginate and cross-linker content on the urea release rate in soil and water. The 4 main materials that used to synthesis the beads samples were urea, sodium alginate, calcium chloride and starch. 13 total formulations of samples were prepared in this project by using 3 factors (Starch, Sodium Alginate and Calcium Chloride) and 5 levels (very low, low, medium, high and very high) design method. The first part of this project was to immersed the fertilizer into water and measure its swelling ratio, dissolution rate and release rate while the second part was to bury the alginate beads into sandy soil inside a leaching vessel and determine its release rate. The release rate of urea was measured in terms of concentration by using UV-VIS Spectrophotometer. The whole experiment was conducted under room temperature and atmospheric pressure. Upon the completion of the project, the results have shown that when the alginate beads immersed in water for longer time, the dissolution rate of samples and urea release rate in water will be higher. Besides that, as the time was longer the swelling % of alginate beads will increase up to certain value and it will decrease again. Lastly, the composition of 3 main materials) will greatly affect the dissolution rate of samples in water, beads swelling % in water and also the urea released rate in water and soil.

Keywords: Urea Fertilizer, Controlled Released, Starch-Alginate, Hydrogel, Released Rate.

1. Introduction

The world population has now reached approximately 7.0 billion and it is expected to continue rises until 9.5 billion in 2050[1]. The development of the world

agriculture field plays a crucial role to ensure that the supply of foods around the world is sufficient for human demand. There are various types of important products that used to produce the agriculture products such as herbicides, fertilizer and many more. Fertilizer is one of the most important products among all these because it supplies the essential nutrients to the plants. Basically there are three common type of fertilizers available in the market which are Nitrogen (N), Phosphate (P_2O_5) and Potash (K_2O). Among all these fertilizers, nitrogen has the biggest market demand in the fertilizer industry because it is the most important nutrient for plants to undergo photosynthesis. Urea is the most common material used for nitrogen(N) fertilizer due to its high nitrogen content (46%)[2]. However, plant uptake of urea fertilizer is usually around 30% because of leaching losses, volatilization or other environmental effects[3]. This will cause some negative impact to the society such as economic losses, resources losses and also serious pollutions to the environment.

One method that will effectively reduce all these negative impacts is to develop the chemically or physically prepared controlled release fertilizer which is used to decrease the nutrient release rate from fertilizer[4]. Controlled release formulation (CRF) is a technology that uses the coated material to gradually release the nutrients from the products. This technology has been widely used in various pharmaceutical and agricultural products such as drugs, fungicide, herbicides, fertilizer and many more. Various researches of all these controlled release formulation applications have showed that this technology can greatly control the release of nutrients or drugs, thus it can reduce environment concern and increase the efficiency of many pharmaceutical and agricultural products.

Controlled Release Fertilizer (CRFs) is usually prepared by coating the fertilizer with materials which will reduce their dissolution rate which include sulfur, resin, polymers and phosphogypsum. Basically, the CRFs have shown many advantages over normal fertilizer such as decrease the removal rate of fertilizer from soil, supply the nutrient sustainably, reduce the frequency of application, reduce the negative impact of over dosage and toxicity[4]. The main criteria of selecting the suitable coated materials includes its environmentally friendly, the effect of materials on nutrient release rate, materials costs and many more.

Initially the most common used coating materials are sulfur and organic polymer. The first coating material for CRFs was sulfur which was developed by Tennesee Valley Authority at 1961[5]. The reason of choosing it is because it is abundant, low cost and can effectively reduce the nutrient release rate. However, sulfur based CRFs also have some disadvantages such as it is not environmental friendly because it may react with water then acidify the soil and it also may be disrupted by microorganism. Polymer coated CRFs was developed by Arthur Daniels Midland Co. (ADM) with using co polymer of Dicyclopentadiene with a glycol ester. Although this polymer has shown their ability to control the nutrient release, but it is slowly or totally not decomposed into the soil and this will lead to the accumulation of plastic residue inside the soil.

Recently, Superabsorbent polymer has caught attention and become one of the favorite CRFs coating materials due to its ability to absorb large amount of water for short period even in certain pressure[6]. This ability has helped them showing some advantages on agricultural application such as the increasing of plant growth rate,

decreasing in irrigation of water, improve nutrient retention of fertilizer, reduce the plant death rate and many more[7]. However, superabsorbent polymer is a relatively expensive materials and most of them are not environmental friendly. On the other hand, in 1970s starch also become a common coating materials for CRFs due to their low cost, renewable and complete biodegradability[8]. However, it cannot control the release of nutrient very well and it has a low water retention.

Hydrogels, which will be produced when superabsorbent materials dissolved in water and swell, are partially cross-linked hydrophilic polymers and it is a three-dimensional polymeric network which can retain large amount of water and swell without dissolve in water[9]. Hydrogels is usually coated with some biodegradable materials such as starch to increase its biodegradability and reduce its dependence on petrochemical-derived monomers[10]. Alginate beads, one of the common hydrogel, are linear unbranched natural polymers which consists of beta-D-mannuronate (M) and alpha-L-guluronate (G) residue[11]. Some characteristics of Alginate includes its biodegradability, immunogenicity and its ability to crosslink in mild condition to form gel has helped it become a common hydrogel in some controlled released application[12].

The Starch-Alginate has not been research yet in controlled release fertilizer application. Therefore, in this project the release dynamic of starch-alginate controlled released fertilizer in soil and water was studied. The main objective of this experiment is to study the effect of starch, alginate and cross-linker content on the urea release rate in soil and water. Upon the completion of this project, the starch-alginate beads will be confirmed as an appropriate material for commercialized controlled release fertilizer.

2. Research Methodology

2.1 Materials and Equipments

The Cassava Starch (CAP KAPAL ABC) was to purchase off the shelf from grocery store. Urea (>99%) was obtained from Evergreen Engineering & Resources Sdn.Bhd. Calcium Chloride anhydrous (96%) which was used as a cross-link material was purchased from Saintifik Sdn.Bhd. Sodium Alginate was obtained from Evergreen Sdn.Bhd. Sandy soil was obtained from the nursery at city of Klang. The Thermo Scientific™ GENESYS 10S UV-vis spectrophotometer was available in Taylor's University Unit Operations Lab.

2.2 Sample Preparation

First of all, dissolved sodium alginate, starch and 5g of urea into 25 mL distilled water. The mixtures were to be stirred for 15 minutes to reach homogeneous phase. Then a 1.2 mm needle size syringe was used to extract the solution into 100 ml calcium chloride solution under constant stirring. The beads were then produced in the mixture due to the crosslink of Ca^{2+} ion with alginate mixtures. The beads are collected by using strainer and rinsed it with distilled water to remove the excessive $CaCl_2$ solution. Last, the beads were oven-dried at 50˚C for 24 hours and then the starch-alginate bead samples will be obtained[13]. The samples formulations were based on 3 factors and 5 levels design methods and 13 different concentration of samples were prepared. The

factors and levels of the design method and composition for all these samples are shown in Table 1 and 2. (Note: U6 beads cannot be made, thus there is no any results for U6).

Table 1: Factors and Levels parameters of the experiment

Chemicals	Very low	Low	Medium	High	Very high
Starch (w/v%)	3	6	9	12	15
Alginate (w/v %)	0.5	1	1.5	2	2.5
Crosslinker (M)	0.1	0.2	0.3	0.4	0.5

Table 2: Composition of 13 Samples that were prepared in the project

Sample	Cassava Starch (w/v%)	Sodium Alginate (w/v%)	Calcium Chloride (M)
U1	3	1	0.1
U2	6	1	0.1
U3	9	1	0.1
U4	12	1	0.1
U5	15	1	0.1
U6	12	0.5	0.1
U7	12	1.5	0.1
U8	12	2	0.1
U9	12	2.5	0.1
U10	12	1	0.2
U11	12	1	0.3
U12	12	1	0.4
U13	12	1	0.5

2.3 Release Dynamic of Fertilizers in water

First prepared 5g of dried samples which has been prepared in the previous steps (marked as A). Then, immersed them into 100 ml of distilled water for different interval of time (1 hr, 2 hr, 4 hr, 24 hr, 48 hr, 1 week, 2 weeks and 1 month), after that sieved the beads out of the solution, removed the excessive water on the beads and measured its net weight (marked it as B). Dried them in the oven at 80˚C for 4 hours again and measured its dried weight. (marked as C). The whole experiment was conducted under room temperature and atmospheric pressure. The swelling % of samples and % of samples dissolved in water can be calculated in Equation (1) and (2).

$$\text{Swelling Ratio}\% = \frac{\mathrm{B} - \mathrm{A}}{\mathrm{A}} \times 100\% \quad (1)$$

$$\text{Dissolution Rate of Urea }\% = \frac{\mathrm{C} - \mathrm{A}}{\mathrm{A}} \times 100\% \quad (2)$$

2.4 Preparation of Soil and Leaching Vessels

The sandy soil was prepared to perform the release dynamic test of fertilizer in the soil. First, put 200 g of sandy soil into the leaching vessels. Then the alginate beads sample were inserted into a soil in a leaching vessel as shown in Figure 2. A filtered net and whatman filter paper was placed in the bottom of soil to prevent the leaking of soil. A container was placed below leaching vessel to collect the solutions that released from leaching vessels.

2.5 Release Dynamic of Fertilizer in Soil

After the soil was prepared, buried 5g of alginate beads samples into the soil (1cm below the soil surface). Distilled water is inserted into the soil regularly as a transportation media of urea inside the alginate beads. The urea will then release from the alginate bead to the soil automatically after a certain time. The release urea was then flow downward due to the gravity force and leaked out from the bottom of leaking vessels to the sample collection container. The experiment was conducted under room temperature and atmospheric pressure. The experimental set-up of this release rate testing is shown in Figure 1.

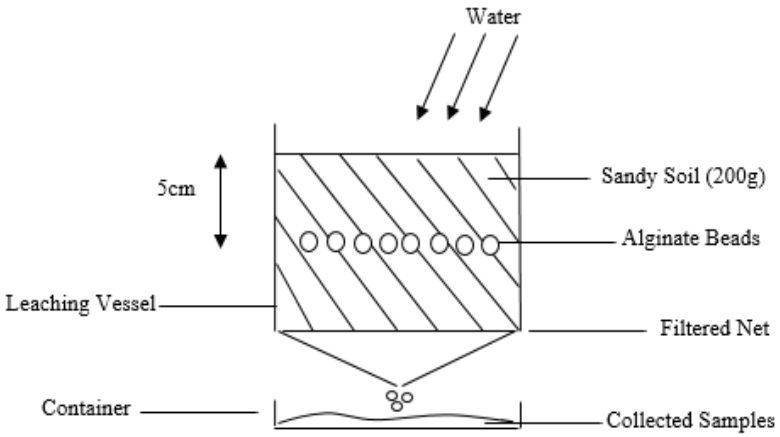


Figure 1: Experiment Set-up for Release Rate Experiment in Soil

2.6 Calibration of Urea Concentration with UV-VIS Spectrophotometer

Before the urea concentration of samples were determined by UV-VIS Spectrophotometer, it was calibrated. The calibration has been done by dissolved different amount of urea into 100ml distilled water (200 mg, 400 mg, 600 mg, 800 mg, 1g, 1.2g, 1.4g, 1.6g, 1.8g, 2g) and then measured their respective absorbance value at wavelength of 210nm. This step can be done in triplicate to improve its accuracy.

2.7 Determination of Urea concentration by UV-VIS Spectrophotometer

The samples that collected from the release test of alginate beads in water and soil was tested by using UV-VIS Spectrophotometer in Taylor's University Research Lab. The model of equipment is Thermo Scientific^{TM} GENESYS 10S UV-vis spectrophotometer. To perform the analysis, first set the wavelength of equipment to 210 nm. Then put distilled water solution into the blank solution and measured its absorbance. After that placed the samples solutions inside the equipment and tested

their relative absorbance. The actual concentration of solutions was obtained from the calibration curve which has been done in previous step.

3.0 Results and Discussion

3.1 Calibration Curve of Urea Concentration

The calibration curve of urea concentration vs its absorbance was done with UV-VIS Spectrophotometer and its results are shown in Figure 2.

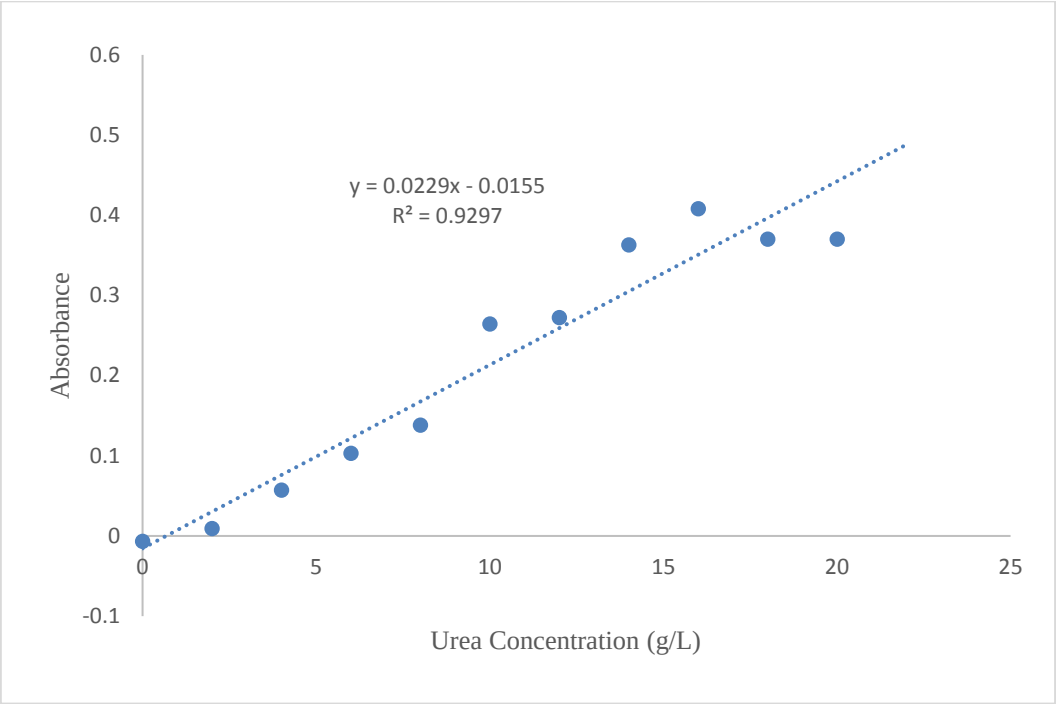


Figure 2: Calibration Chart of Urea Concentration with its Absorbance

Based on Figure 2, it clearly showed that when the urea concentration was increasing, its absorbance will increase. It is because as the urea concentration was higher, more samples light will be absorbed by the equipment. The equation of the calibration chart was y=0.0229 x -0.0155 while its R2 was 0.9297.

3.2 Release Dynamic Experiment in Water

Three analysis were analysed in this experiment which include swelling ratio, dissolution rate of samples and urea release rate. There are 7 different set of time intervals in this steps (1 hour, 2 hour, 4 hour, 24 hour, 48 hour, 1 week, 2 weeks, 1 montth).

3.2.1 Swelling Ratio of Alginate Beads

The swelling ratio testing was used to determine the water absorbing ability of alginate beads. The swelling % of all 12 alginate beads samples in distilled water was studied after different time interval and the results are shown in Figures below.

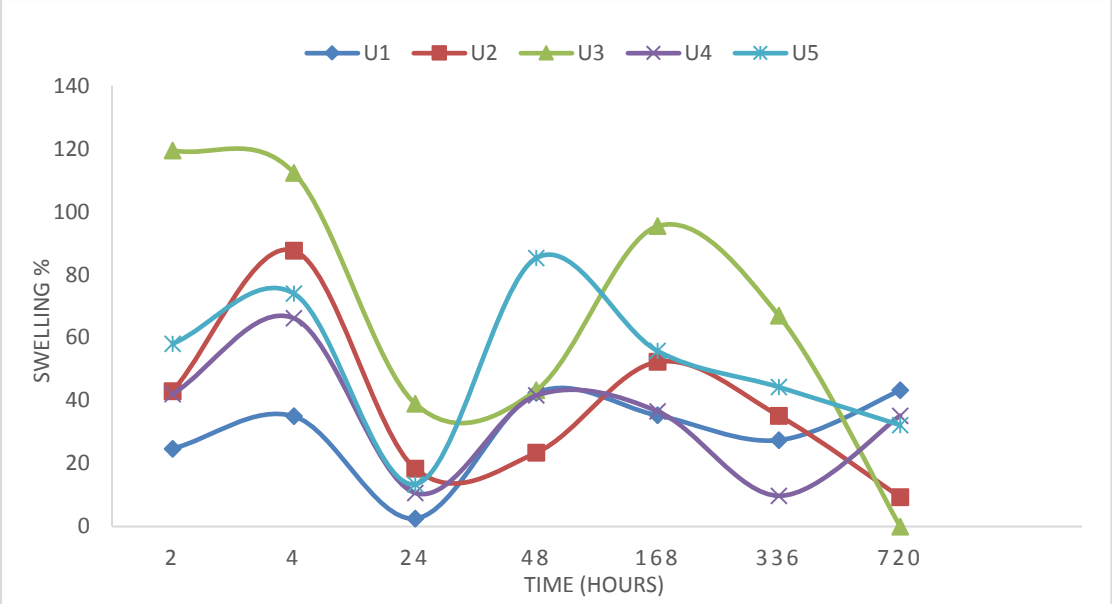


Figure 3: Swelling Ratio of Alginate Beads against Time for U1, U2, U3, U4 and U5

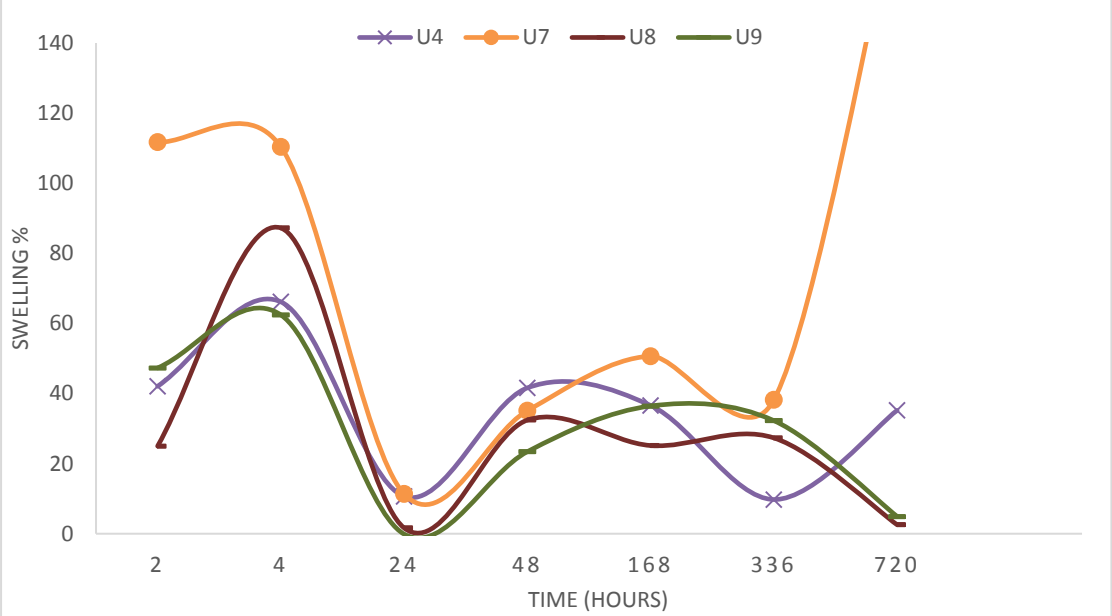


Figure 4: Swelling Ratio of Alginate Beads against Time for U4, U7, U8 and U9

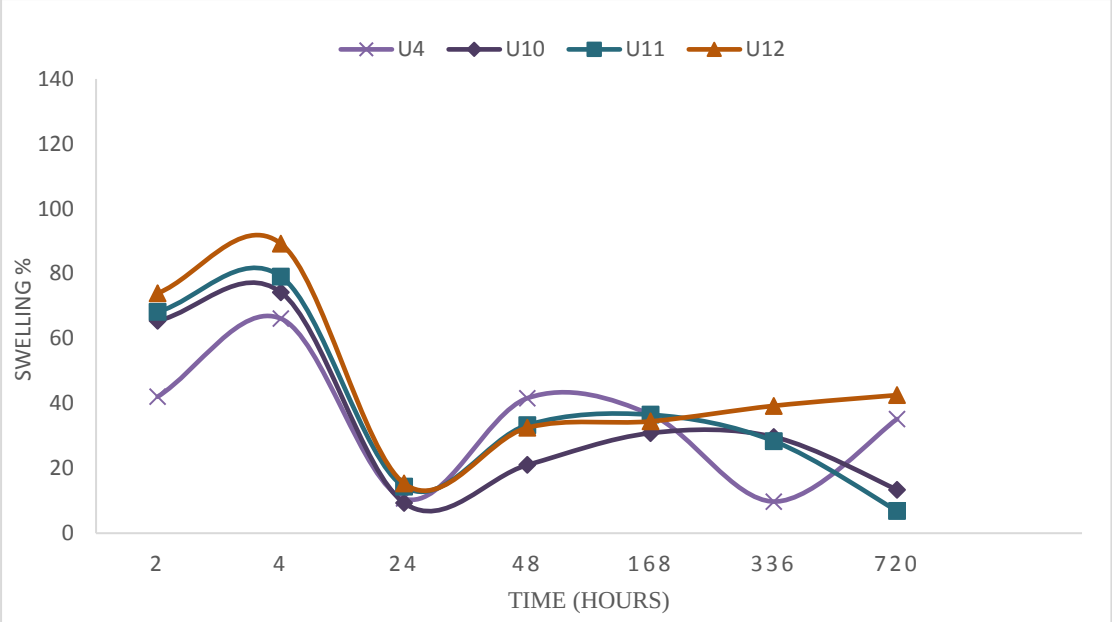


Figure 5: Swelling Ratio of Alginate Beads against Time for U4, U10, U11 and U12

Based on Figure above, it showed that the swelling % of all alginate beads were first increased from 2nd hours to 4th hours, after that it decreased from 4 hours to 24th hours and finally increased after 24th hours. The swelling % of most of the samples reached the lowest point at 24th hours while the highest point was at 4 hours. This observation showed that the water absorption of the beads has reach swelling equilibrium after 4 hours. When the alginate beads were saturated, some of its water will diffuse out from the samples itself, thus it swelling % will decrease. After most of the water was diffused out from the samples, the samples will absorb water again until they were saturated and then the water will diffuse out from the samples again. Thus, after 24 hours their swelling % was increasing up to one point and then decreased again.

On the other hand, the swelling % of U3 (9 w/v% starch) and U5 (15 w/v% starch) was a bit higher compare with U1 (3 w/v% starch) and U2 (6 w/v% starch). This indicated that the swelling % of the beads will increase when the starch contents in the beads were increasing and this may due to the hydrophilic nature of starch. As the starch amount is higher, the interaction of -OH groups in the starch with water will increase thus the beads will swell more[13]. Furthermore, comparing U7 (1.5 w/v % sodium alginate) with U8 (2.0 w/v% sodium alginate) and U9 (2.5 w/v% sodium alginate), the swelling % of U7 was the highest, second was U8 and the lowest was U9. This showed that the % swelling of beads were decreasing when the alginate content is higher. This is because the number of coordination sites provided by the increase in number of COO- will increase with the increase of alginates contents[13]. Lastly, the swelling % of beads was increasing with some irregular trend when the cross-linker content was higher and this is due to the increase of hydrogel strength.

3.2.2 Dissolution Rate of Urea

The dissolution rate testing was used to determine how many % of samples has been dissolved into water in certain time interval. In this testing, the dissolution rate of

samples for all 12 alginate beads samples in distilled water was studied after different time interval and the results are shown in Figure 8.

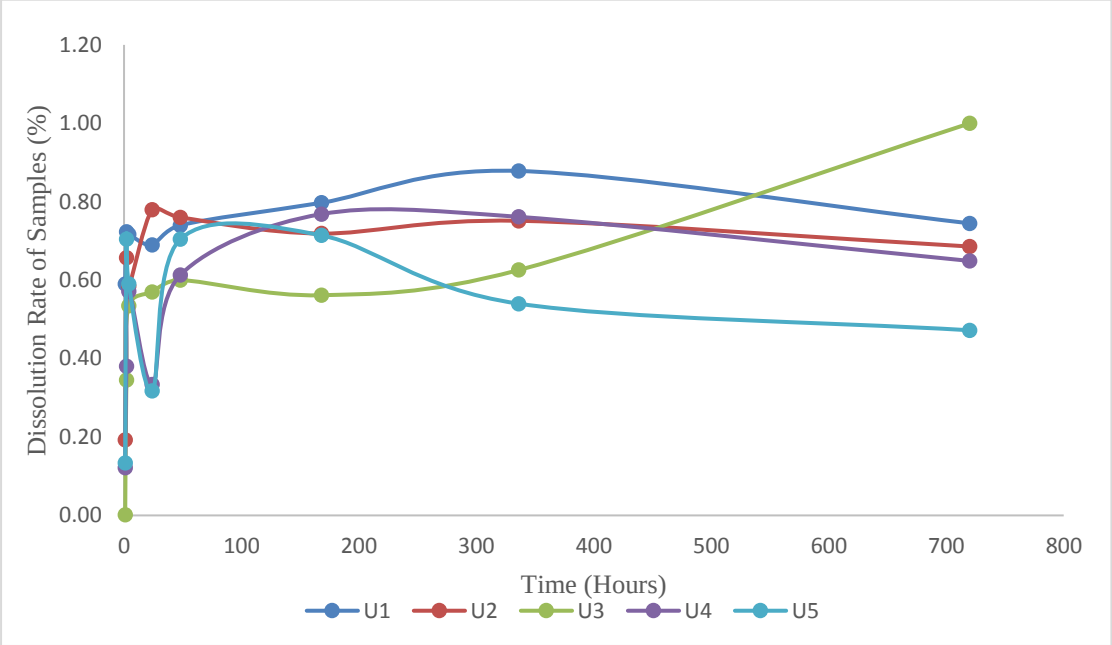


Figure 6: Dissolution Rate of Samples Against Time for U1, U2, U3, U4 and U5

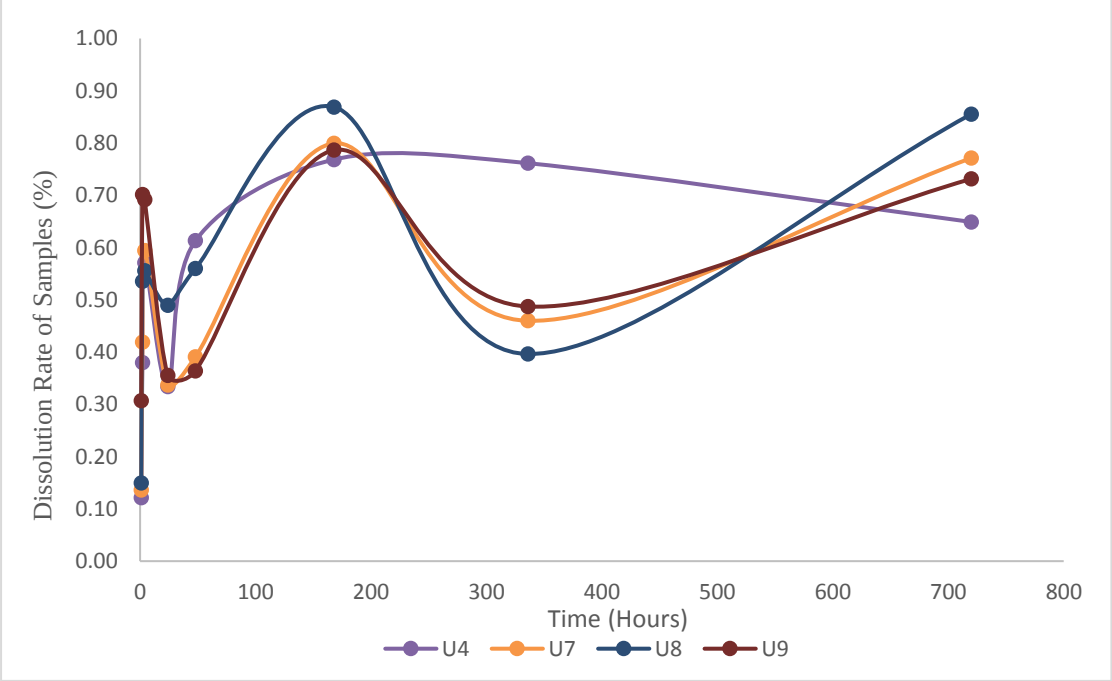


Figure 7: Dissolution Rate of Sample Against Time for U4, U7, U8 and U9

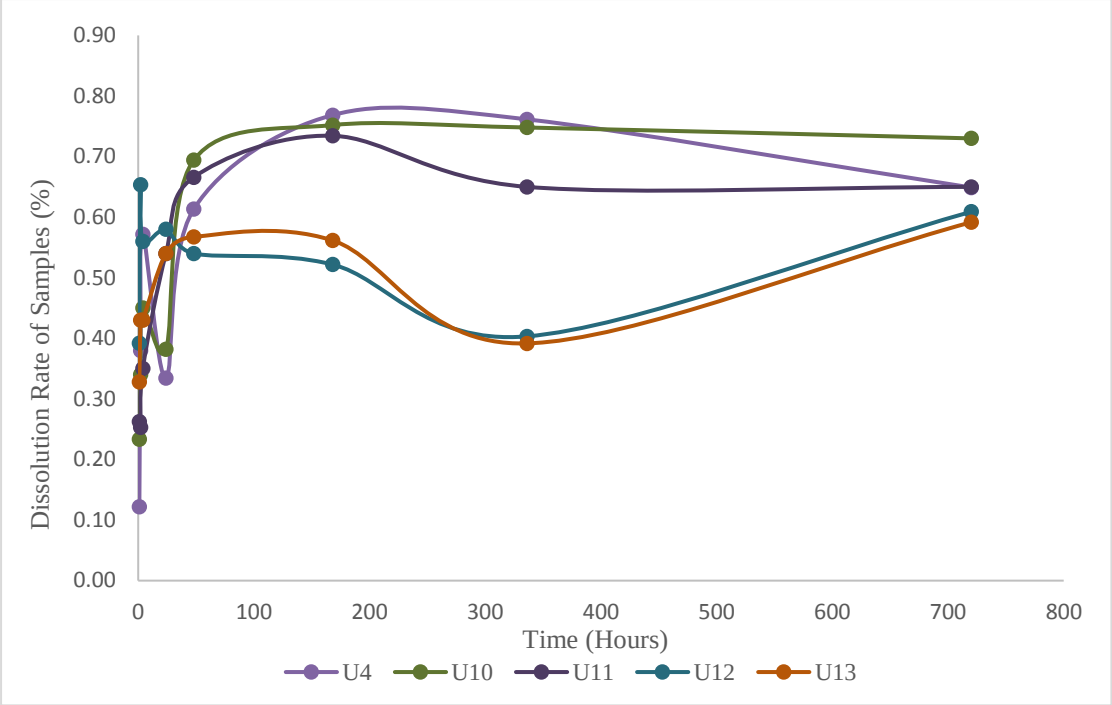


Figure 8: Dissolution Rate of Samples Against Time for U4, U10, U11, U12 and U13

Based on figure above, it showed that for most of the samples the dissolution rate of urea was increasing until it reached the highest peak as the samples immersed in water for longer time. This is because when the beads immersed into the distilled water for longer time, more urea will be diffused out of the beads until most of the urea inside the beads have been dissolve in the water. Theoretically, the dissolution rate of urea should be increased all the way when the time is longer. However according to the figure, there was also some special case in this testing where the dissolution of urea was first decrease and increase again or first increase and decrease again when the time is longer. This is because in this experiment different type of samples was using for different time, some mistakes will occur during the sample preparation and cause some errors in the results.

Next, comparing U1 with U2, U3, U4 and U5, it was not hard to observe that based on the graph, U1 have the highest dissolution rate, and the following was U2, U3, U4 and U5. This showed that the dissolution of urea was lower when the starch contents in the beads was increasing. Similar results were obtained from Suherman and Didi[14], which also showed that the greater starch concentration, the dissolution rate was decreasing. This is because the starch is act as a physical barrier, thus more starch the more physical barrier on the urea surface which will cause longer release time and dissolution rate will get smaller[14]. On the other hand, the dissolution rate of U7, U8 and U9 was different with some irregular trends. Thus, it showed that the increase of alginate contents will cause some irregular trends for the dissolution rate of urea. Lastly, for different cross-linker contents samples, U10 has the highest dissolution rate, and the following is U11, U12 and U13. This indicated that the higher the cross-linker contents, the dissolution rate of samples will be higher. This is because Calcium Chloride is high soluble in water, so the higher the cross-linker contents in the samples, the dissolution rate of samples in water will higher.

3.2.3 Release Rate of Urea in Water

The release rate of urea was the amount of urea that has been dissolved into the water in certain time. In this study, the urea release rate of all 12 alginate beads samples in distilled water was studied after different time interval and the results are shown in Figure 5.

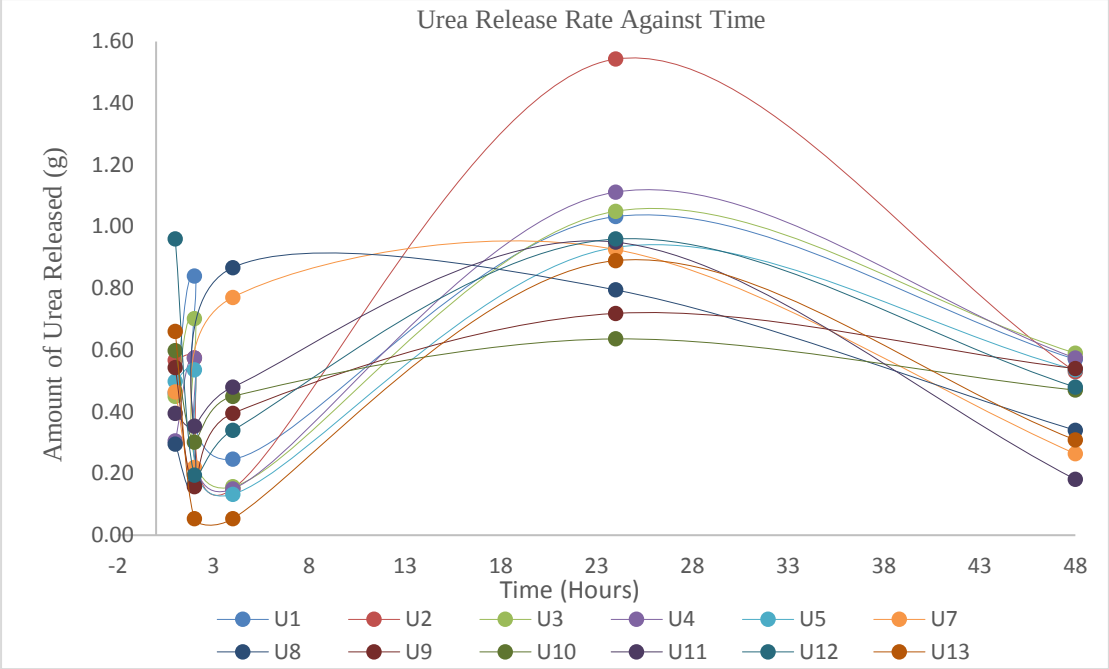


Figure 9: Amount of Urea Release from Water against Time

Based on Figure 9, initially from 1st hour to 2nd hour, the urea release for most of the alginate samples were decreasing, then they were increasing from 2nd hour to 24th hour. The urea released rate of all samples have reached at its highest peak which was at 24 hours. The highest amount of urea that was released from the sample was about 1.57g. After 24th hours, the urea released decreased. This is because after certain time some of the starch inside the beads has started to dissolved into the water, thus it will affect the absorbance value of the samples which was determined by UV-VIS Spectrophotometer. From 24th hour until one month, the graph has shown irregular trend, therefore the graph of results only shows up to 48 hours since it was meaningless to analyse irregular trend results. The effects of each material on the urea released rate will further discuss in the following sections. Based on the graph, the composition that will have the lowest release rate are 3 w/v % starch, 2.5 w/v % sodium alginate and 0.2 M crosslinker.

3.3 Release Dynamics Experiment in Soil

Figure below shows the graph of urea release rate in soil versus the time. Initially the total time cost of this experiment were 30 days, the experimental results, however, have shown that the urea released rate after 10th days has become consistent and no trend. Since it was meaningless to analyze consistent or no trend results, the discussion of this experiment was only from its 1st day until its 10th days.

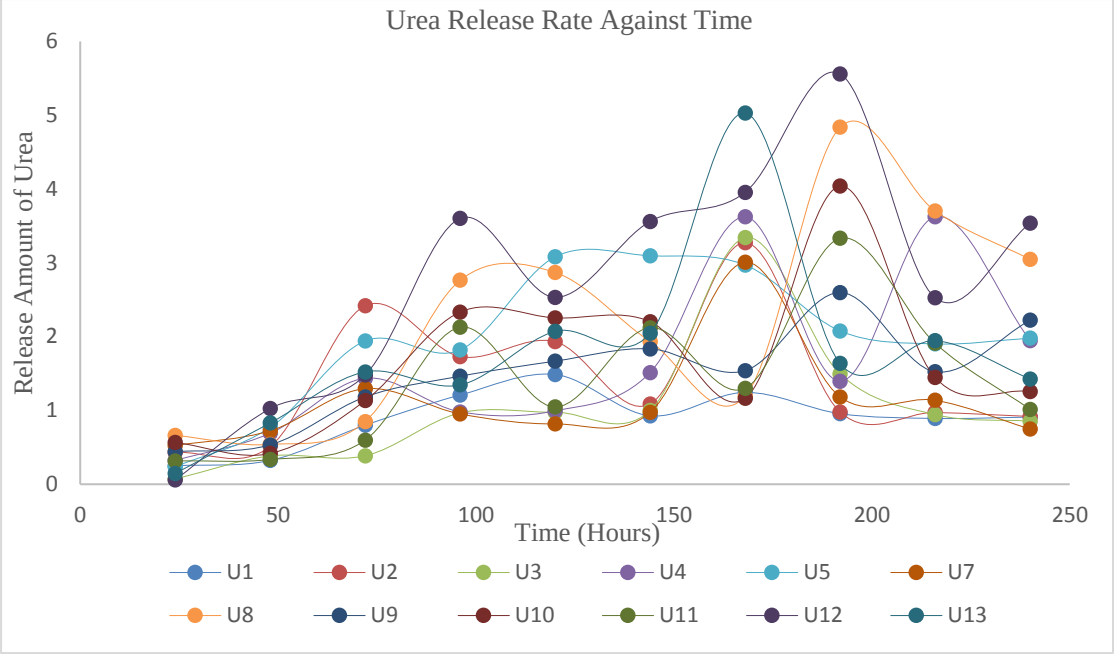


Figure 10: Amount of Urea Released from Soil against Time

Based on figure above, it shows that as the time longer, the release amount of urea will be higher. At the first two days of the experiment, the urea release for all samples were consistent and similar. However, starting from third days, their release rate become inconsistent, some of their release were decreasing while some of them were increasing. The highest release of urea for most samples were found on 7th or 8th day. After 9th day of the experiment, the urea released was decreasing until the end of the experiment, which is the 30th day. Besides that, compare the release of urea in soil with in water, it shows that the amount of urea release in soil was very large compare with in water. This is because the soil itself may contained some nutrients, thus when the solutions leak out from soil, some nutrients also will leak out following. The effects of each material on the release rate will be further discussed in the following sections. Based on the graph, the materials composition that will have the lowest release are 3 w/v% starch, 1.5 w/v% Alginate and 0.3 M crosslinker.

4.0 Conclusions

In conclusion, the swelling ratio of alginate beads are dependent on the time for samples immersed in the distilled water. The swelling % of the samples reached highest during 4th hours and lowest and 24th hours. Thus, the time taken for the alginate beads to reach its maximum swelling is around 4 hours. When the alginate beads reach maximum swelling, the water will diffuse from samples until a certain value and then it will absorb water again. Furthermore, the dissolution rate of samples was increasing as the time was longer. This is because more urea will diffuse into the water when the samples immersed into water for longer time. The urea released rate results was similar to dissolution testing until 24th hours. After 24th hours, some starch will dissolve in the water thus the results after that were not accurate. Lastly, the composition of starch, alginate and calcium chloride(cross-linker) have great impact on the swelling%, dissolution rate of samples and the urea release rate in water.

References

[1] B. Azeem, K. KuShaari, Z. B. Man, A. Basit, and T. H. Thanh, “Review on materials & methods to produce controlled release coated urea fertilizer,” *J. Control. Release*, vol. 181, pp. 11–21, 2014.

[2] K. R. Mohd Ibrahim, F. Eghbali Babadi, and R. Yunus, “Comparative performance of different urea coating materials for slow release,” *Particuology*, vol. 17, pp. 165–172, 2014.

[3] T. H. Trinh, K. Kushaari, A. S. Shuib, L. Ismail, and B. Azeem, “Modelling the release of nitrogen from controlled release fertiliser: Constant and decay release,” *Biosyst. Eng.*, vol. 130, pp. 34–42, 2015.

[4] M. Tomaszewska and A. Jarosiewicz, “Use of polysulfone in controlled-release NPK fertilizer formulations,” *J. Agric. Food Chem.*, vol. 50, pp. 4634–4639, 2002.

[5] A. Jarosiewicz and M. Tomaszewska, “Controlled-release NPK fertilizer encapsulated by polymeric membranes,” *J. Agric. Food Chem.*, vol. 51, pp. 413–417, 2003.

[6] X. Li, Q. Li, Y. Su, Q. Yue, B. Gao, and Y. Su, “A novel wheat straw cellulose-based semi-IPNs superabsorbent with integration of water-retaining and controlled-release fertilizers,” *J. Taiwan Inst. Chem. Eng.*, vol. 000, pp. 1–10, 2015.

[7] M. Y. Guo, M. Z. Liu, F. L. Zhan, and L. Wu, “Preparation and properties of a slow-release membrane-encapsulated urea fertilizer with superabsorbent and moisture preservation,” *Ind. Eng. Chem. Res.*, vol. 44, no. 12, pp. 4206–4211, 2005.

[8] D. R. Lu, “Starch-based completely biodegradable polymer materials,” *eXPRESS Polym. Lett.*, vol. 3, no. 6, pp. 366–375, 2009.

[9] W. E. Rudzinski, A. M. Dave, U. H. Vaishnav, S. G. Kumbar, A. R. Kulkarni, and T. M. Aminabhavi, “Hydrogels as controlled release devices in agriculture.,” *Des. Monomers Polym.*, vol. 5, no. 1, pp. 39–65, 2002.

[10] A. Pourjavadi, M. Doulabi, R. Soleyman, S. Sharif, and S. A. Eghtesadi, “Synthesis and characterization of a novel (salep phosphate)-based hydrogel as a carrier matrix for fertilizer release,” *React. Funct. Polym.*, vol. 72, no. 10, pp. 667–672, 2012.

[11] I. Liakos, L. Rizzello, I. S. Bayer, P. P. Pompa, R. Cingolani, and A. Athanassiou, “Controlled antiseptic release by alginate polymer films and beads,” *Carbohydr. Polym.*, vol. 92, no. 1, pp. 176–183, 2013.

[12] A. Roy, J. Bajpai, and a. K. Bajpai, “Dynamics of controlled release of chlorpyrifos from swelling and eroding biopolymeric microspheres of calcium alginate and starch,” *Carbohydr. Polym.*, vol. 76, no. 2, pp. 222–231, 2009.

[13] B. Singh, D. K. Sharma, and A. Gupta, “A study towards release dynamics of thiram fungicide from starch-alginate beads to control environmental and health hazards,” *J. Hazard. Mater.*, vol. 161, no. 1, pp. 208–216, 2009.

[14] Suherman and D. Anggoro, “Producing slow release urea by coating with starch/acrylic acid in fluid bed spraying,” *Int. J. Eng. Technol*, vol. 11:06, no. December, pp. 62–66, 2011.

DCFC Performance Study using Rice Husk-Derived Biochar

Jun Jie Yap[1*], Wai Yin Wong[1]

[1]*School of Engineering, Taylor's University, Malaysia*

[*]corresponding email: junjie_1214@hotmail.com

Abstract

A variety of agricultural wastes such as corn cob, coconut shell and oil palm empty fruit bunch are produced every year. Proper treatment can be performed on biomasses to produce biochar that can be used in various applications such as direct carbon fuel cell (DCFC) as renewable energy source. High lignin content in rice husk has shed new light in this area due to the high possibility to produce biochar with higher carbon yield. In this research, the aim is to synthesise biochar via pyrolysis and to perform electrochemical test on the DCFC using rice husk-derived biochar. Initially, rice husk was pre-treated using NaOH with a concentration of 0.4M solution at 60°C for 24 hours. Subsequently, the pre-treated sample was pyrolysed at 500°C with a heating rate of 5°Cmin^{-1} for 1 hour. The electrochemical performance of DCFC was performed using the DCFC single cell stack connected to a potentiostat and the open circuit potential was measured. DCFC performance was studied on both alkaline pre-treated and untreated biochar at different the operating temperature (550°C, 650°C, and 750°C)). The specific surface area and the proximate content of the rice husk-derived biochar were characterised using Brunauer, Emmett and Teller analysis (BET) and thermogravimetric analysis (TGA). The BET surface area of pre-treated rice husk-derived biochar was found to be lower than untreated rice husk-derived biochar. The carbon percentage of the pre-treated biochar (70.6%), however, is higher than the untreated biochar (55.6%) while the ash content is lower. The open circuit potential of the biochar increased as temperature increased due to higher rate of utilisation of rice husk-derived biochar. The open circuit potential of pre-treated rice husk-derived biochar also showed a value higher than that of untreated rice husk-derived biochar as the pre-treated biochar has lower ash content despite the higher surface area of untreated biochar. This value obtained from rice husk-derived biochar (845 mV) around 60-70% of the OCP of carbon black (1.26V) therefore it had the potential to be utilised as fuel in DCFC.

Keywords: Rice husk, Biochar, Pyrolysis, Direct carbon fuel cell, Open circuit potential.

1. Introduction

Fuel cell is an electrochemical device that converts chemical energy of a fuel into electrical energy that is made of membrane-electrodes assembly [1]. The difference between a fuel cell and a battery is that the fuel cell can continue to function as long as the fuel is supplied while a battery's life is dependent solely on the capacity of the energy storage within itself. There are many types of fuel cells that are differentiated by the types of electrodes, electrolytes and operating temperatures, namely, polymer electrolyte membrane fuel cell (PEMFC), alkaline fuel cell (AFC), direct methanol fuel cell (DMFC), phosphoric acid fuel cell (PAFC), molten carbonate fuel cell (MCFC), solid oxide fuel cell (SOFC) and direct carbon fuel cell (DCFC) [2]. Among all, DCFC is foreseen to be one of the promising fuel cell technologies used in power plant in Malaysia or Asia, owing to its advantage of using carbon as fuel source in which its raw material is abundant. Interestingly, DCFC requires only solid carbon as direct fuel without the need of gasification that further proving its potential as one of the future electricity generation device [1, 3].

DCFC can be further distinguished by the type of electrolytes, for instance, molten hydroxide, molten carbonate and oxygen ion conducting ceramic. For the DCFC with oxygen ion conducting ceramic electrolyte, there are even further classification on the method of carbon fuel delivery, such as solid carbon, carbon mixed with molten metal and carbon mixed with molten salt [2]. For the DCFC with electrolytes of molten carbonate or molten hydroxide, degradation of the electrolyte will occur seriously and there is a risk of liquid leaking. On the other hand, DCFC with oxygen ion conducting ceramic electrolyte has no volatilisation of the electrolyte and risk of liquid leaking [4]. Comparing the fuel deliveries, the technical hurdle reported for carbon mixed with molten metal, mostly tin Sb, is the excessive anodic polarisation losses due to the use of porous ceramic separator. The function of the porous ceramic separator is to separate the tin melt from the carbon fuel. For DCFC with carbon in molten carbonate, the corrosion of nickel anode and other cell components may occur, and stability of 8YSZ electrolyte in molten carbonate environment is dropped which the lithium zirconate may be formed in presence of Li / K carbonate eutectic mixture at 700°C [2]. For DCFC with solid carbon fuel, it only produce carbon monoxide CO and carbon dioxide CO_2 which will not decrease the DCFC performance by any means and it also could produce the highest power density. Thus DCFC with oxygen ion conducting ceramic electrolyte and solid carbon fuel is the best configuration of DCFC [2, 4]. For the type of DCFC, 8YSZ is the electrolyte, Ni-YSZ is the anode and LSM-YSZ is the cathode [1, 2].

There are also a few types of DCFC structures, tubular, planar and button [5]. For planar DCFC, each cell is made into a rectangle or square, flat plate or disk. The cells are connected by interconnect plates in series. For tubular DCFC, one of the electrode is usually made into a long tube with porous wall. Outside the electrode are the electrolyte and then another electrode. Planar DCFC has advantages in ease of fabrication and higher power density. However, tubular DCFC has lower cost to fabricate and easier to seal with higher thermal stability. Planar DCFC has constraints on maximum allowable temperature and temperature gradient to prevent thermal cracking [6]. Planar DCFC and tubular DCFC are the structures of DCFC that are used in industries while button DCFC is mostly used for experimental purpose as in this research. The button DCFC is easier to use for experiments since the carbon fuels to

test can be placed directly on the anode of the button DCFC and a furnace is used to heat up the carbon fuels [1].

There are more than 2 million tonnes of agricultural wastes produced annually in Malaysia. The usage of these agricultural wastes to produce energy is very attractive as they contribute little or no carbon dioxide to the environment. The major agricultural products in Malaysia are oil palm, rubber, paddy, cocoa and tropical fruits. Among the wastes of these agricultural products, rice husk is one of the most unutilised waste with potential annual energy generation of 1.025 MMboe which is equivalent to 1.67 x 106 MWh unused [7]. The rice husk can definitely be utilised such as the conversion to biochar to replace coal which is non-renewable. DCFC is a technology that can utilise this rice husk-derived biochar or any other biochar with the advantage of high efficiency of around 80% and low emission of greenhouse gases [1, 2, 8].

Rice husk has relatively high lignin content [9]. This made rice husk to be very suitable to be utilised by converting into biochar. This is due to the fact that during charring, hemi-cellulose will first decompose followed by cellulose and lastly lignin [10, 11]. Aliphatic carbon in biomass is first converted to fused-ring aromatic carbon during charring then only the aromatic carbon will lose to volatilisation. Lignin contains more aromatic carbon than cellulose and hemi-cellulose hence biomass with higher lignin content will decompose slower and have higher carbon yield [9].

To utilise rice husk as biochar in DCFC, the factors that affect the electrochemical performances must be investigated. For biochar, high fixed carbon, high surface area, amorphous, low ash content, low sulphur content are important factors that contribute to the performance of DCFC. Previous studies showed that biochar with high fixed carbon and low ash content showed higher performance. High fixed carbon is important to ensure constant fuel supply for electrochemical reactions while low ash content can prevent the ashes from building up a barrier that prevents further oxidation of biochar [12].

It is also important that the type of fixed carbon of a biochar has is amorphous. The carbon atoms on an amorphous structure can be released more easily during electrochemical reactions which enhances the electrochemical performances. Graphitic carbon has higher thermal and electrical conductivity since the structure of graphitic carbon is more connected. However, recent studies showed that thermal and electrical conductivity may not be an important factor of DCFC performance as the reactivity of the carbon fuel has more effects on DCFC performance [8]. Another factor which is also the reason that amorphous carbon is better is high surface area. As analysed using Brunauer-Emmett-Teller (BET) surface area analysis, amorphous carbon has higher surface area compared to graphitic carbon [13, 14]. Higher surface area increases the chances of oxygen ions to react with the carbon atoms of a biochar. Some studies had concluded that surface area increases DCFC performance [8, 13]. However, study by Halouani et al. [15] on biochar derived from almond shell had showed high performances regardless of the low surface area. Sulphur may cause degradation of Ni-YSZ cermet of anode of DCFC through bulk sulfidation therefore low sulphur content of biochar is important [16].

Previous studies had carried out chemical treatments to remove ash from biomass or biochar since a high quality biochar has low ash content. A few studies by

Markovska et al. [17] and Johar et al. [18] showed that NaOH treatment on rice husk can effectively remove ash as the ashes of rice husk contain mainly silica which is react able with NaOH.

$$SiO_2 + 2NaOH \rightarrow Na_2SiO_2 + 2H_2O$$

The carbon percentages and surface areas also increased as a result of ash removal [17, 19].

The most important factor that affects DCFC performances during the operation of DCFC is temperature. Most of the researches on DCFC had investigated and showed that temperature affected DCFC performances greatly. DCFC performances increased as operation temperature increased due to higher utilisation rate of rice husk-derived biochar [20, 21].

Hence, the area investigated in this study is to utilise both untreated and pre-treated biochar derived from rice husk as fuel source for DCFC test. In this study, the properties change in the biochar due to chemical treatment will provide an insight on its effect on the DCFC performance. Also, this study will be able to provide the researchers in this area on the understanding of the effect of operating temperature of the DCFC utilising biochar derived from rice husk; that is yet investigated thus far based on our best knowledge. In a bigger picture, this research will show the potential of rice husk-derived biochar as carbon fuel in DCFC for electricity generation that is considered as one of the most promising renewable energy source in the future.

2. Methodology

2.1 Materials

Rice husk which is an agricultural waste was collected from Oblique Titi Rice Mill Co., Inc., Perak, Malaysia. NaOH was provided by Friedemann Schmidt Chemical, Malaysia.

2.2 Preparation of Rice Husk

Rice husk was washed with water for several times to remove the adhering soil and other present contaminants. The excessive water was drained off and rice husk was placed uniformly on a rectangular tray. Next, the tray with rice husk was placed into an oven (UN75, Memmert, USA) at 105ºC for 24h to remove moisture following ASTM D2867-09 standard [22]. Rice husk was grounded using a grinder (JK-SG-160, KGC Scientific) and sieved into particles of 0.5-2.0mm using a sieve shaker (RX-812-1, Tyler). The rice husk powder produced was kept in a sealed container.

2.3 Pre-treatment of Rice Husk

NaOH solution was prepared with concentration of 0.4M and volume of 150ml in a 250ml round bottom flask. Rice husk powder was weighed 15g and added into the round bottom flask. Subsequently it was soaked in the NaOH solution under stirring condition at temperature of 60ºC for 4h [23] using a hotplate stirrer (IKAC-MAG HS 7S2, Applab Saintifik). The pre-treated rice husk powder was separated from the NaOH solution by filtration and washed with distilled water around five times until pH 7 in the washed solution was obtained using a pH meter (pH211-M446321, Hanna Instruments, USA). Pre-treated rice husk powder was then dried again in the oven (UN75, Memmert,

USA) following the same ASTM D2867-09 standard at 105ºC for 24h to remove moisture [17].

2.4 Pyrolysis

A laboratory scale pyrolysis reactor was used to pyrolyse rice husk powder. The reactor is 1m length by 0.08m internal diameter with a furnace (HST 12/400, Carbolite) for heating. Two alumina crucibles were used to hold around 10-11g pre-treated rice husk powder or around 15g untreated rice husk powder [24]. The rice husk powder was pyrolysed with a heating rate of 5ºCmin^{-1} to temperature of 500ºC and held for 1h [24, 25, 26]. Pyrolysis was carried out in a non-oxidative atmosphere using nitrogen as the purge gas with a flow rate of 1Lmin^{-1}. Nitrogen was introduced into the pyrolysis reactor 10 minutes before the commencement of heating to purge away the oxygen. The biochar produced was collected after cooling.

2.5 Characterisation of Biochar

2.5.1 Elemental Composition Analysis

An elemental composition analyser (Elementar vario MACRO Cube) was used to determine the elemental composition of both pre-treated and untreated biochar derived from rice husk including carbon, hydrogen, nitrogen and sulphur. The methods used for the analysis were combustion method and Dumas method (standard method).

2.5.2 BET Surface Area Analysis

Around 0.285g of pre-treated and untreated biochar derived from rice husk were degassed at 300°C for 5h and sent to the 77K N_2 adsorption measurement using Quantasorb SI Instrument (Quantachrome, USA) [27].

2.5.3 Thermogravimetric Analysis (TGA)

Thermogravimetric analysis (TGA) was carried out in a thermogravimetric analyser (STA 6000, Perkin Elmer) to observe the weight loss of both pre-treated and untreated biochar derived from rice husk in non-oxidative atmosphere which is pure nitrogen environment with nitrogen flow rate of 0.05Lmin^{-1}. The heating of biochar was conducted from room temperature to 800ºC at a heating rate of 5ºCmin^{-1} [28].

2.6 DCFC Setup

A button cell DCFC was placed in a fuel cell stack as shown in Fig. 1 to conduct experiments to measure the electrochemical performance of biochar derived from rice husk in DCFC. The active reaction area of the button cell was 1.25cm^2. In the anode, nitrogen was used to create a non-oxidative atmosphere while in the cathode, purified air was supplied to allow electrochemical reactions to occur. Experiment was started by heating the DCFC with the biochar derived from rice husk on top of it to the desired temperature using a furnace (HST 12/400, Carbolite) with a heating rate of 10ºCmin^{-1} and held at the desired temperature for 1h to ensure the measurements could all be done. Biochar loading in the DCFC was 0.1g [1, 29].

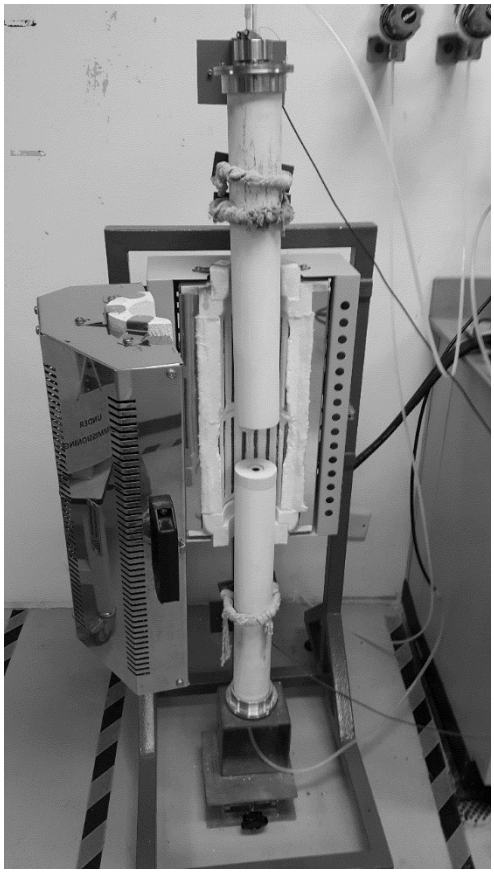


Figure 1. Fuel cell stack.

2.7 Electrochemical Characterisation

The electrochemical performance tests were conducted with 6 sets of samples and they were pre-treated (Sample A) and untreated (Sample B) biochar derived from rice husk with temperatures of 550ºC, 650ºC and 750ºC. A potentiostat (Gamry Interface 1000, Gamry Instruments, USA) was used to conduct open circuit potential measurement which measures the starting voltage of the DCFC produced by the electrochemical reactions of biochar derived from rice husk at the desired measurement temperature. Table 1 showed the experiment sets.

Table 1. Experiment sets.

Samples \ Temperature	550°C	650°C	750°C
A	A1	A2	A3
B	B1	B2	B3

3. Results and Discussions

3.1 Weight Loss

Table 2 showed the weight loss of pre-treated and untreated biochar derived from rice husk before and after NaOH treatment and pyrolysis. For NaOH treatment of rice husk, there were four runs to ensure repeatability of the study. The four runs showed that the rice husk decreased to around 10-11g from 15g after the NaOH

treatment which was around 74.52% of solid yield. This was in good agreement with the study done by McKay et al. [23] that the same NaOH treatment condition had achieved a solid yield of 79%. This also meant that the ash removed could be around 25.48%. After the treated rice husk had undergone pyrolysis, the biochar yield was found to be 35.52% which is slightly lower than 39.49% biochar yield of untreated rice husk. The biochar yield of untreated rice husk after pyrolysis, 39.49% was in good agreement with the study of Windeatt et al. [24] that the rice husk had biochar yield of 39%. This showed that as the ash was removed, the carbon structure of treated rice husk might be decomposed comparing to untreated rice husk thus reducing the biochar yield.

Table 2. Weight loss of pre-treated and untreated biochar derived from rice husk before and after NaOH treatment and pyrolysis.

Condition	Weight (g)					
	Untreated	Pre-treated				
		1	2	3	4	Average
NaOH Treatment	-	15.01	14.99	15.01	15.01	15.01
Before Pyrolysis	15.00	11.26	10.69	11.15	11.63	11.18
Solid Yield (%)	-	75.02	71.31	74.28	77.48	74.52
After Pyrolysis	5.92	3.82	3.83	4.10	4.14	3.97
Biochar Yield (%)	39.49	33.93	35.83	36.77	35.60	35.52

The ash removal efficiency was determined by knowing the ash content of the biochar produced using TGA. The solid yield of NaOH treated rice husk was 74.52%, the biochar yield was 35.52% while TGA determined that the ash content of the pre-treated biochar was 14.903%. After multiplying all the percentages together, it was shown that the ash not removed by NaOH treatment was around 3.94% of rice husk. The ash removed was around 25.48% of rice husk and this determined that the total ash was 29.42% while the ash removal efficiency was around 86.61% which was acceptable but could be further optimized as the ash removal efficiency of the research of McKay et al. [23] could reach 93%.

3.2 Elemental Composition Analysis

The results of elemental composition analysis in Table 3 showed that the carbon composition of biochar derived from rice husk increased from 55.617% to 70.632% after NaOH pre-treatment was carried out. The reason was NaOH pre-treatment had successfully removed considerably amount of ashes from rice husk and therefore the carbon composition increased [17, 23]. It could be suggested that biochar derived from rice husk might present a good carbon fuel from the results of elemental composition analysis. The hydrogen composition of pre-treated biochar derived from rice husk was also more than untreated biochar derived from rice husk. The results aligned with previous study [17, 23] that the composition of carbon and hydrogen also increased after the rice husk had been treated with NaOH.

There were several studies in the past investigated on the effect of NaOH on the nitrogen composition and sulphur composition. However, it could be seen that the composition of nitrogen and sulphur had decreased after NaOH pre-treatment. It was possible that sulphur and nitrogen were connected with ashes hence they decreased when the ashes were removed. High sulphur content could cause permanent

degradation of Ni-YSZ cermet via bulk sulfidation. The sulphur easily reacted with nickel, forming nickel sulphide with lower thermal stability [16]. It had been showed by Cherepy et al. [30] that sulfidation decreased DCFC performance as represented by decrease of carbon discharging rate and increase of cell resistance. However, generally biomass had low sulphur content [24].

Table 3. Elemental composition analysis of pre-treated and untreated biochar derived from rice husk.

Element	Composition (%)	
	Untreated	Pre-treated
Carbon	55.617	70.632
Hydrogen	2.879	3.384
Nitrogen	2.613	1.752
Sulphur	0.042	0.035

3.3 BET Surface Area Analysis

Table 4. BET surface area analysis of pre-treated and untreated biochar derived from rice husk compared with literature results.

Biochar	BET Surface Area (m^2/g)	References
Wood-chips	544	[13]
Charcoal	729	[13]
Carbo medicinalis	1249	[13]
Graphitic Carbon	39	[8]
Carbon Black	118	[8]
Activated Carbon	1241	[8]
Almond Shell	30.35	[15]
Untreated Rice Husk	21.2965	This study
Pre-treated Rice Husk	11.0523	This study

It could be seen from Table 4 that the surface area of the biochar derived from rice husk was the lowest compared to other biochar or carbons. The nearest value were seen on biochar derived from almond shell and graphitic carbon. Zhu et al. [8] had showed that graphitic carbon has lower open circuit potential compared to carbon black or activated carbon which have higher surface area. In contradiction, study by Halouani et al. [15] on biochar derived from almond shell had showed that the open circuit potential was still relatively high around 1.0-1.1V regardless of the low surface area. Comparing the surface area of untreated and pre-treated biochar derived from rice husk, it was found that the untreated biochar had higher surface area compared to pre-treated biochar. NaOH treatment should increase surface area of biochar as the ash was removed from the structure of the biochar however our experimental results showed a lower value possibly attributed to the simultaneous decomposition of biochar with ash. This was because the decomposed organic matter may blocked the pores and caused the biochar to have lower surface area [31].

3.4 Thermogravimetric Analysis (TGA)

Thermogravimetric analysis (TGA) had been conducted for both pre-treated and untreated biochar derived from rice husk in nitrogen environment. Two main stages of mass release could be observed in Fig. 2. The first stage was release of moisture from room temperature to around 150ºC [17]. It could be seen that the pre-treated biochar derived from rice husk had only 1.979% of moisture, which was lower than the moisture of untreated biochar derived from rice husk around 5.078%. This might be due to removal of some hemicellulose and cellulose which had more hydrophilic tendencies compared to hydrophobic lignin in NaOH pre-treatment together with ash which allowed the moisture in pre-treated biochar derived from rice husk to be easily released during the drying process after NaOH pre-treatment [32]. The second stage was release of volatile matters around 300-700ºC which the main structure of biochar derived from rice husk was destructed during this stage. The residue left after this stage was ash [15, 17, 33]. The composition of fixed carbon is unable to be determined in a non-oxidative atmosphere as it was released with volatile matters during the second stage [17, 33]. It was shown that pre-treated biochar derived from rice husk had only 14.92% of ashes. The ash content of untreated biochar derived from rice husk was not measurable as it did not fully decomposed before TGA was finished.

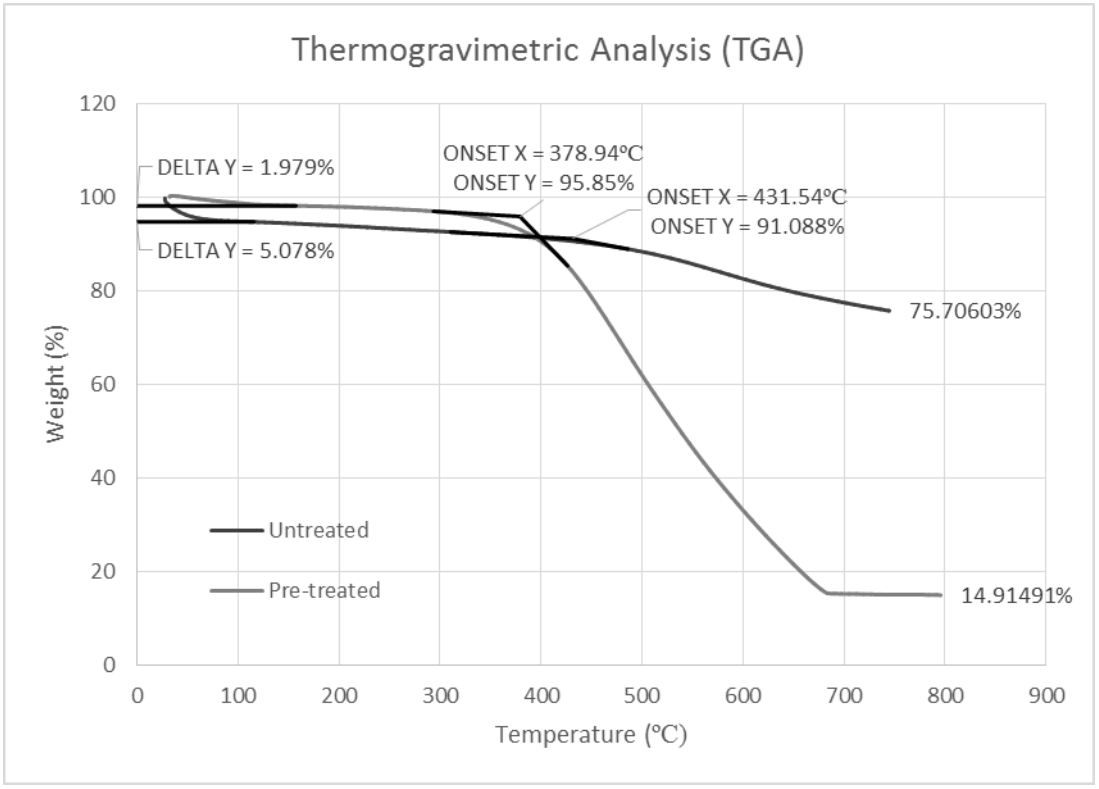


Figure 2. Thermogravimetric analysis (TGA) of pre-treated and untreated biochar derived from rice husk.

During second stage, untreated biochar derived from rice husk had a lower weight loss rate compared to pre-treated biochar derived from rice husk which the pre-treated biochar derived from rice husk started to decompose around 378.94ºC while the untreated biochar derived from rice husk started to decompose only around 431.54ºC. The phenomena may be caused by the high ash content of untreated biochar derived from rice husk which a barrier was formed by ashes on top of the biochar at early stage that prevents the biochar from further decomposition throughout TGA [12]. Markovska

et al. [17] had obtained similar results in their research. It can be also be observed from Fig. 2 that the pre-treated biochar derived from rice husk had been destructed completely before 800ºC and this justified the reason that the DCFC experimental temperatures were set at 550ºC, 650ºC and 750ºC.

Table 5. Moisture, volatile matters and ash of pre-treated and untreated biochar derived from rice husk compared with literature results.

Carbon Fuel	Moisture (%)	Volatile Matter (%)	Ash (%)	References
Graphitic Carbon	3.00	96.00	1.00	[8]
Carbon Black	3.50	96.00	0.50	[8]
Activated Carbon	6.80	93.00	0.20	[8]
Corn Cob	4.00	92.02	3.98	[21]
Almond Shell	2.50	90.50	7.00	[15]
Untreated Rice Husk	5.70	47.30	47.00	[24]
Pre-treated Rice Husk	5.08	80.01	14.91	This study
Untreated Rice Husk	1.98	-	-	This study

It was observed in Table 5 that biochar derived from rice husk had higher ash content compared to other carbon fuels. However, it was also seen that biomass has higher ash content than general carbons like carbon black. It was reasonable that the biochar derived from rice husk had such high ash content as the rice husk had high ash content around 19.6% from literature [24] and around 29.42% from this study. This was the main reason NaOH treatment must be carried out for rice husk. Although the ash content of untreated biochar derived from rice husk was undetermined in this research, the ash content of untreated biochar was determined to be 47% from literature [24] while the rice husk had lower ash content of 19.6%. With a higher ash content of 29.42% in rice husk, the pre-treated biochar had a significantly lowered ash content of only 14.91% after NaOH pre-treatment. The volatile matter percentage (including fixed carbon) of untreated biochar was only 47.30% from literature [24] which was less promising to be used in DCFC as the carbon might not be enough to have sufficiently high electrochemical performance. For pre-treated biochar in this study, the volatile matter content was quite near to other carbon fuels which might also meant electrochemical performance could be comparable.

3.5 Open Circuit Potential (OCP)

Fig. 3 displayed a graph of OCP against temperature of both pre-treated and untreated biochar derived from rice husk. OCP measured here should be in negative values which meant that the more negative the OCP value was, the better the electrochemical performance. It could be observed that OCP increased as temperature increased for both pre-treated and untreated biochar derived from rice husk. This could be explained by the fact that the reactivity of the electrodes sites increased as temperature increased thus enhancing the anodic reaction kinetics [15].

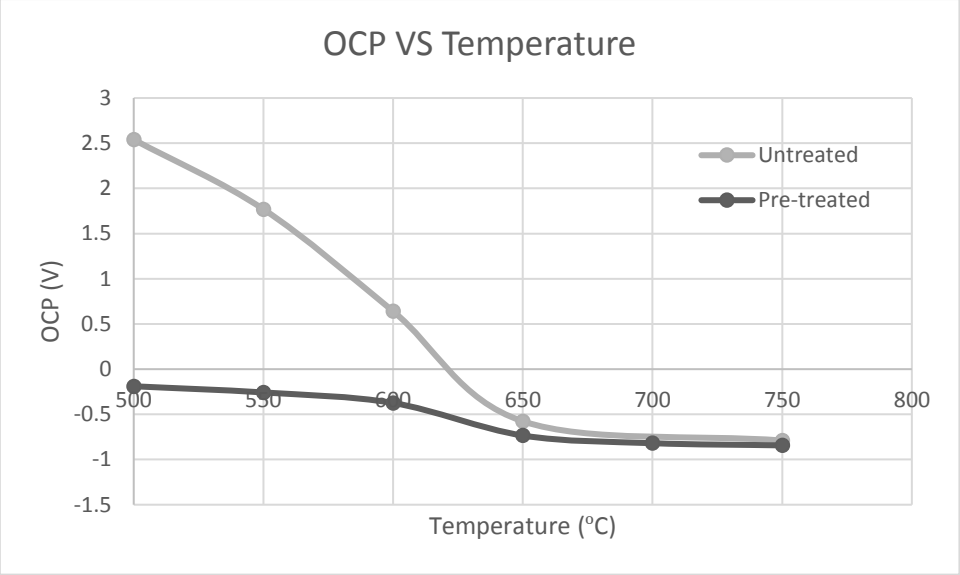


Figure 3. Open circuit potential (OCP) of pre-treated and untreated biochar derived from rice husk against temperature from 500-750ºC.

The OCP measured at desired temperatures and the weight of residue after measurements were tabulated in Table 6. The OCP values were tabulated in absolute values. This further proved that OCP increased with temperature. It could be observed that both pre-treated and untreated biochar derived from rice husk had similar OCP at high temperatures of 650-750ºC. This might showed that the surface area and ash content of biochar did not actually affect its performances in DCFC at high temperatures instead only low temperatures. Another reason might be the scale of the experiment was not large enough to observe the effects of the two factors on performances of biochar in DCFC. However, it was showed that pre-treated biochar derived from rice husk had higher OCP of 845.0mV at 750ºC compared to OCP of 806.7mV of untreated biochar derived from rice husk. The OCP of the pre-treated biochar derived from rice husk was 845.0mV, around 60-70% of the OCP of carbon black at 750ºC, 1.26V [8]. It was also quite similar to the OCP values of wood chips and corn cob biochar of 860.0mV and 900.0mV respectively [13, 21]. The residue weight of pre-treated biochar derived from rice husk had always been higher than untreated biochar derived from rice husk except for when the temperature is 750ºC. This could be explained by TGA results earlier which the pre-treated biochar derived from rice husk had completely decomposed around 700ºC therefore the residue weight was less than untreated biochar derived from rice husk at 750ºC.

OCP did not only increase as temperature increased, it also increased over time isothermally as shown in Fig. 4 and Fig. 5. As mentioned earlier, the more negative the OCP values were, the better the electrochemical performance. The reason of this phenomena was because more carbon reacted electrochemically over time and as long as the carbon did not completely reacted, the OCP continued to increase. OCP against time of pre-treated biochar derived from rice husk at 750ºC showed a decreasing trend since the pre-treated biochar derived from rice husk should have reacted completely at 750ºC as shown in TGA results earlier. OCP at 550ºC is very low even against time as the temperature of 550ºC was not enough to fully utilise the rice husk-derived biochar. The rice husk-derived biochar consisted of mostly carbons formed from lignin or some undecomposed lignin contents. Lignin decomposed more slowly at low temperatures

therefore at 550ºC, the lignin or the aromatic carbons formed by lignin may not be able to fully decompose even over a long period [34].

Table 6. OCP and residue weight of pre-treated and untreated biochar derived from rice husk at desired temperature.

Samples \ Temperature	550°C	650°C	750°C
Pre-treated OCP (V)	0.3113	0.6869	0.8450
Pre-treated Residue (g)	0.092	0.088	0.016
Untreated OCP (V)	0.3246	0.6377	0.8067
Untreated Residue (g)	0.087	0.073	0.052

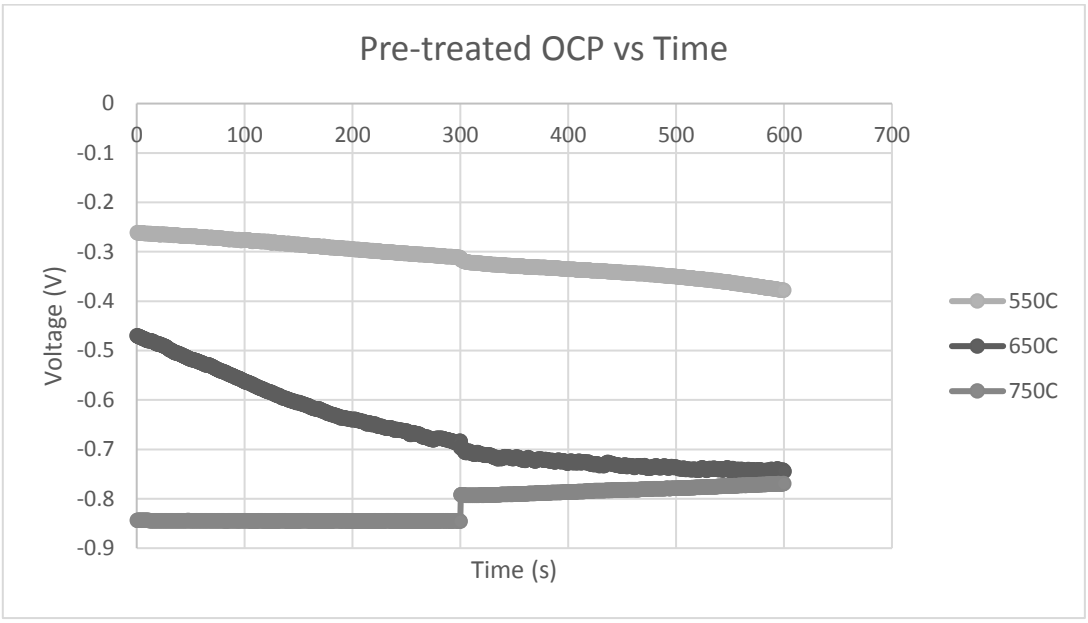


Figure 4. OCP of pre-treated biochar derived from rice husk against time at desired temperatures.

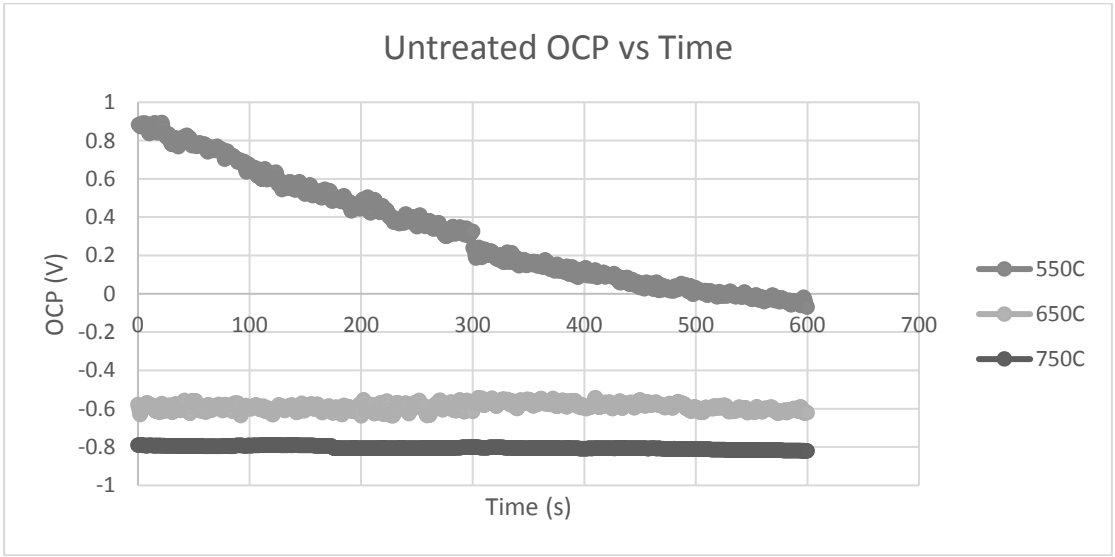


Figure 5. OCP of untreated biochar derived from rice husk against time at desired temperatures.

Table 7. Electrochemical performance of pre-treated and untreated biochar derived from rice husk compared with other carbon fuels at 750ºC.

Carbon Fuel	BET Surface Area (m^2g^{-1})	Volatile Matter (%)	Performance	References
Graphitic Carbon	39	96.00	OCP = 1.05V	[8]
Carbon Black	118	96.00	OCP = 1.26V	[8]
Activated Carbon	1241	93.00	OCP = 1.34V	[8]
Corn Cob Biochar	-	92.02	OCP = 1.05V	[21]
Almond Shell Biochar	30.35	90.50	OCP = 1.025V	[15]
Untreated Rice Husk Biochar	21.30	-	OCP = 0.8067V	This study
Pre-treated Rice Husk Biochar	11.05	80.01	OCP = 0.8450V	This study

Table 7 displayed the electrochemical performances of pre-treated and untreated biochar derived from rice husk together with other carbon fuels at 750ºC. It could be observed that activated carbon had the highest BET surface area and also highest OCP of 1.34V compared to carbon black and graphitic carbon. Corn cob and almond shell biochar had similar OCP to graphitic carbon which they may be graphitic considering the BET surface areas and OCP. Biochar derived from rice husk had the lowest OCP compared to other biochar and carbon fuels and this is explainable with the lowest surface area and volatile matter content. However, the OCP was around 60-70% of carbon black which means that it had the potential to be fuel in DCFC. The OCP results of pre-treated and untreated biochar also showed that the BET surface area may not be that important in some circumstances compared to ash content as the OCP of pre-treated biochar with lower surface area but lower ash content is higher than the OCP of untreated biochar with higher surface area but higher ash content.

4. Conclusion

This study had showed that NaOH was able to achieve 86.61% of ash removal in treatment of rice husk. However, after pyrolysis, pre-treated biochar derived from rice husk had lower biochar yield of 35.52% compared to untreated biochar with biochar yield of 39.49% due to simultaneous decomposition of biochar which the organic matter may blocked the pores. This also caused pre-treated biochar derived from rice husk to have a lower surface area compared to untreated biochar in BET surface area analysis. Elemental composition analysis had showed that the percentages of carbon and hydrogen of pre-treated biochar derived from rice husk increased after NaOH pre-treatment when compared to untreated biochar. It was observed that pre-treated biochar had ash content of 14% from TGA while the ash content of untreated biochar was undetermined in TGA due to incomplete decomposition caused possibly by ash accumulation. OCP of pre-treated and untreated biochar derived from rice husk

increased against temperature and time while the OCP of pre-treated biochar was slightly higher than untreated biochar. The OCP showed that the BET surface area might not be important in some circumstances. The OCP of biochar derived from rice husk was around 60-70% of the OCP of carbon black and this proved the potential of utilising rice husk as biochar in DCFC for the purpose of producing environmental friendly energy.

For future study, the operating conditions of pyrolysis and NaOH treatment can be further optimised to produce biochar with relatively high yield and carbon percentage. More analysis to characterise the biochar can be conducted such as scanning electron microscopy (SEM) or x-ray power diffraction (XRD) to understand the morphology, crystalline structure and atomic spacing of the biochar to give more explanations on the electrochemical performance in DCFC. The power density of biochar derived from rice husk in DCFC can be investigated besides measuring the open circuit potential (OCP). The electrochemical impedance spectroscopy (EIS) can also be conducted to understand the effect of resistances on the DCFC performance. Other factors that affect DCFC performances such as gas flow rate can also be investigated. Gas can be collected from the DCFC and measured to ensure that the concentration of carbon dioxide released in DCFC is low. The structure of DCFC, whether planar or tubular can be investigated and compared on their utilisation of biochar.

References

[1] S. Giddey et al., "A comprehensive review of direct carbon fuel cell technology," *Progress in Energy and Combustion Science*, vol. 38, no. 3, pp. 360–399, Jun. 2012.
[2] S.Giddey and S.P.S. Badwal, "The holy grail of carbon combustion – the direct carbon fuel cell technology," *Materials Forum*, vol. 34, 2010.
[3] D. Cao et al., "Direct carbon fuel cell: Fundamentals and recent developments," *Journal of Power Sources*, vol. 167, pp. 250-257, 2007.
[4] S. Wang et al., "A novel direct carbon fuel cell by approach of tubular solid oxide fuel cells," *Journal of Power Sources*, vol. 195, pp. 480-482, 2010.
[5] C. Stiller et al., "Finite-volume modeling and hybrid-cycle performance of planar and tubular solid oxide fuel cells," *Journal of Power Sources*, vol. 141, pp. 227-240, 2005.
[6] C. Zuo, M. Liu and M. Liu, "Solid oxide fuel cells," in *Sol-Gel Processing for Conventional and Alternative Energy*, New York, USA: Springer, 2012, ch. 2, pp. 1-35.
[7] R.A. Moghadam et al., "Air Gasification of Malaysia Agricultural Waste in a Fluidized Bed Gasifier: Hydrogen Production Performance," in *Sustainable Growth and Applications in Renewable Energy Sources*. Rijeka, Croatia: InTech, 2011, ch. 11, sec. 1, pp. 227-228.
[8] Z.H. Zhu et al., "Factors That Determine the Performance of Carbon Fuels in the Direct Carbon Fuel Cell," *Industrial & Engineering Chemistry Research*, vol. 47, pp. 9670-9677, Dec. 2008.
[9] C.D. Blasi, "Reactivities of some biomass chars in air," *Carbon*, vol. 37, no. 8, pp. 1227- 1238, 1999.
[10] F.J. Gonzalez-Vila et al., "Pyrolysis-GC-MS analysis of the formation and degradation stages of charred residues from lignocellulosic biomass," *Journal of Agricultural and Food Chemistry*, vol. 49, pp. 1128-1131, 2001.

[11] I. Pastorova et al., "Cellulose char structure: a combined analytical Py-GC-MS, FTIR, and NMR study," *Carbohydrate Research*, vol. 262, pp. 27-47, 1994.
[12] J.T.S. Irvine et al., "Performance of Direct Carbon Fuel Cells Operated on Coal and Effect of Operation Mode," *Journal of The Electrochemical Society*, vol. 161, no. 5, pp. F588-F593, 2014.
[13] M. Dudek et al., "Biomass Fuels for Direct Carbon Fuel Cell with Solid Oxide Electrolyte," *International Journal of Electrochemical Science*, vol. 8, pp. 3229-3253, 2013.
[14] Y. Li et al., "Preparation of carbon black from rice husk by hydrolysis, carbonization and pyrolysis," *Bioresource Technology*, vol. 102, no. 17, pp. 8220–8224, Sep. 2011.
[15] K. Halouani et al., "Experimental investigation of direct carbon fuel cell fueled by almond shell biochar: Part I. Physicochemical characterization of the biochar fuel and cell performance examination," *International Journal of Hydrogen Energy*, vol. 38, pp. 16590-16604, 2013.
[16] T.J. Schildhauer et al., "The impact of sulfur on the performance of a solid oxide fuel cell (SOFC) system operated with hydrocarboneous fuel gas," *Journal of Power Sources*, vol. 189, pp. 1127-1131, 2009.
[17] I.G. Markovska et al., "Study on the Thermochemical and Kinetic Characteristics of Alkali Treated Rice Husk," *Journal of Chinese Chemical Society*, vol. 57, no. 3A, pp. 411–416, 2010.
[18] N. Johar et al., "Extraction, preparation and characterization of cellulose fibres and nanocrystals from rice husk," *Industrial Crops and Products*, vol. 37, no. 1, pp. 93–99, May. 2012.
[19] T.N. Ang et al., "Comparative study of various pretreatment reagents on rice husk and structural changes assessment of the optimized pretreated rice husk," *Bioresource Technology*, vol. 135, pp. 116–119, 2013.
[20] Y. Li et al., "Electrochemical oxidation of catalytic grown carbon fiber in a direct carbon fuel cell using Ce0.8Sm0.2O1.9-carbonate electrolyte," *International. Journal of Hydrogen Energy*, vol. 38, pp. 16615-16622, 2013.
[21] Y. Li et al., "Utilization of corn cob biochar in a direct carbon fuel cell," *Journal of Power Sources*, vol. 270, pp. 312-317, 2014.
[22] K.J. Silgado et al., "Adsorption of chromium (VI) by activated carbon produced from oil palm endocarp," *Chemical Engineering Transactions*, vol. 37, no. VI, pp. 721–726, 2014.
[23] G. McKay et al., "Optimization of rice husk pretreatment for energy production," *Renewable Energy*, vol. 77, pp. 512–520, 2015.
[24] J.H. Windeatt, "Characteristics of biochars from crop residues: Potential for carbon sequestration and soil amendment," *Journal of Environmental Management*, vol. 146, pp. 189-197, 2014.
[25] J.W. Choi et al., "Influence of pyrolysis temperature on physicochemical properties of biochar obtained from the fast pyrolysis of pitch pine (Pinus rigida)," *Bioresource Technology*, vol. 118, pp. 158-162, 2012.
[26] P.T. Williams and Serpil Besler, "The influence of temperature and heating rate on the slow pyrolysis of biomass," *Renewable Energy*, vol. 7, no. 3, pp. 233-250, 1996.
[27] R.C. Brown et al., "Characterization of Biochar from Fast Pyrolysis and Gasification Systems," *Environmental Progress & Sustainable Energy*, vol. 28, no. 3, pp. 386–396, 2009.

[28] X. Yuan et al., "Surface characterization of rice husk bio-char produced by liquefaction and application for cationic dye (Malachite green) adsorption," *Fuel*, vol. 155, pp. 77–85, 2015.
[29] H. Yao et al., "Effect of coal based pyrolysis gases on the performance of solid oxide direct carbon fuel cells," *International Journal of Hydrogen Energy*, vol. 39, pp. 17845-17851, 2014.
[30] N.J. Cherepy et al., "Direct conversion of carbon fuels in a molten carbonate fuel cell," *Journal of Electrochemical Society*, vol. 152, no. 1, pp. A80-A87, 2005.
[31] X. Zhu et al., "A novel porous carbon derived from hydrothermal carbon for efficient adsorption of tetracycline," *Carbon*, vol. 77, pp.627-636, Oct. 2014.
[32] G. McKay et al., "The effect of alkali treatment on rice husk moisture content and drying kinetics," *Biomass and Bioenergy*, vol. 70, pp. 468–475, 2014.
[33] P.M. Stefani et al., "Nanocellulose from rice husk following alkaline treatment to remove silica," *Bioresources*, vol. 6, no.2, pp. 1440-1453, 2011.
[34] C.E. Rostad et al., "Effect of formation conditions on biochars: Compositional and structural properties of cellulose, lignin, and pine biochars," *Biomass and Bioenergy*, vol. 46, pp. 693-701, 2012.

Hardware Simulation of a New Anti-windup PI Control for Motor Speed Application

Thong Ling Chiah[1], Choon Lih Hoo[1*], Edwin Chin Yau Chung[1]

[1]*School of Engineering, Taylor's University, Malaysia*

[*]ChoonLih.Hoo@taylors.edu.my

Abstract

Proportional-Integral (PI) controller consists of both proportional and integral parameters which enable the controller to eliminate error in the response of a control system. However, PI controller always accompanied by long settling time and oscillation in its response due to the windup phenomenon. Windup occurs when the controller output transcended the limit of the system actuator and the control is under saturated state. The control system will unable to react and respond to the incoming error signal. This uncontrollable state introduces performance deterioration and even instability in the system. Many anti-windup controllers have been established to overcome windup such as the Steady-state Integral Proportional Integral Controller (SIPIC). SIPIC is a robust controller with tuning gain decoupling feature which was developed through the generic control template. The control template can be used to design any PI related controller. This research aims to develop another anti-windup PI controller that is able to lessen the theoretical treatment of the windup phenomenon from the control template. It was observed that the existing anti-windup methods tend to apply the adaptive control switching mechanism that require switching control methods between non-saturation and saturation range whereas the proposed anti-windup PI controller does not require adaptive control. The speed control performance of the proposed anti-windup PI controller is compared with the conventional PI controller through hardware simulation by using Scilab/Scicoslab version 4.4.1 software. The parameter specification was identified through system identification of a direct current motor. The proposed anti-windup PI controller shows better performance improving and eliminating the drastic high overshoot, settling time and rise time as compared to the conventional PI controller. Therefore, this research is able to contribute to the body of knowledge as the proposed anti-windup PI controller can be an alternative controller in industrial motor application.

Keywords: Anti-windup, PI controller, parameter tuning, steady state, speed control.

1. Introduction

Proportional-integral (PI) controller remain the widely used closed-loop controller among researchers in industrial application because PI controller is easy to implement and able to provide satisfying result. PI controller is able to eliminate the errors or disturbance in a system but subjected to oscillating response, tremendous overshoot and prolonged settling time [1]. This unfavorable response is due to the windup phenomenon which can even cause speed response instability besides the high overshoot and long settling time [2, 3]. Windup happened when a control system operates in a nonlinear region in which the controller output transcended the limit of the system actuator. The system will be unable to continuously detect the error signal in the system and provide necessary changes in the control when the control system falls into this saturated state. Windup phenomenon will cause physical degradation or damage to the system and soon leading to system malfunction [4].

Anti-windup was commonly used in control system to resolve system performance and stability deterioration especially for linear systems due to windup [5]. Anti-windup control works in ensuring the control output to stay within the limit of the system input. Anti-windup controller allows the control state regains its linear or non-saturated control as soon as possible when falls into the saturation region. The control system is saturated when the control output exceed the limiter range [5].

There are various type of anti-windup PI controllers proposed by control engineers. These controllers can be categorised to three main scheme type which is conditional integral (CI) scheme, tracking back calculation (TBC) scheme and integral state prediction (ISP) scheme. All controllers consist their very own mathematical equation and the construction of the components for the controller. It allows the controller to be presented in the form of a block diagram. Furthermore, the mathematical formula reduced the challenges in the theoretical treatment of the anti-windup phenomenon in PI controller.

In this paper, a new anti-windup PI controller for motor speed application is proposed. The existing anti-windup involves adaptive control which switches control operation when the control state crosses between linear range and saturation range whereas the proposed anti-windup PI controller does not require such switching mechanism. Switching in an operating system will most likely cause system instability and affect the system performance as well. The proposed anti-windup PI controller is a robust controller without the need of switching and equipped with tuning gain decoupling feature which is able to prevent the weaknesses and system instability caused by adaptive control switching.

This paper is organized in 5 sections. Section 1 is the introduction to topic. Section 2 presents the existing anti-windup controller schemes. Section 3 is the introduction to the proposed new anti-windup controller for motor speed application. Section 4 shows the simulated results of the newly proposed anti-windup controller. Section 5 is the conclusion for the research.

2. Introduction and Comparison of Existing Anti-windup Controller Schemes

Proportional-Integral (PI) controllers are widely used nowadays for motor control system due to its simplicity in application. There are consequences for PI controller where the controller can result in a higher overshoot and longer settling time which may lead to system degradation [6]. Therefore, many research on anti-windup PI controller were done in the past and three schemes of anti-windup controller that are applied most often are summarised. They are conditional integral (CI) scheme, tracking back calculation (TBC) scheme and integral state prediction (ISP) scheme. These schemes have a common behavior where they alters the integral control during saturation whereas it switches back to the conventional PI controller under non-saturation. Steady-state integral proportional integral controller (SIPIC) is a recent anti-windup controller which require no switching mechanism.

2.1 Conditional Integral (CI) scheme

A few switching method was done in the past and the most common for CI schemes is to turn off the integration mode of the controller saturation point. However, the integral action will be excluded if the control input reaches saturation together with proportional control being activated. The PI control is only effective below saturation point. Therefore, the controller input must be within the limit of saturation in order to obtain the most effective performance [7-9].

Conditional integral scheme uses the saturation range and linear range of the controller as trigger to switch the integral action on or off. It can be simplified below in equation (1) where $\dot{q}$, e, u and v denotes first derivative integral state, error signal, controller output and plant input respectively [10].

$$\dot{q} = \begin{cases} e & if\ u = v \\ 0 & if\ u \neq v \end{cases} \tag{1}$$

This method is able to produce non-overshoot performance. However, it is challenging in deciding and select the gain to fulfill performance of an anti-windup and large integral value when plant input and controller output are different [7, 10]. The block diagram of anti-windup controller using conditional integral scheme is shown in Figure 1 where ω_r^*, ω_r, s, k_p, k_i, T_L, k_T, J and B are denoted as set reference of motor rotational speed, motor rotational speed, Laplace domain, proportional gain, integral gain, external load, torque constant, moment of inertia of motor and viscous damping coefficient [8].

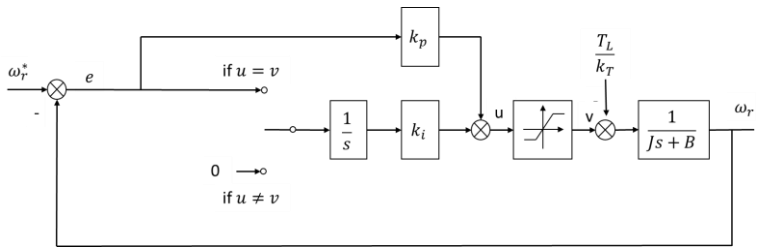


Figure 1. Conditional integral scheme anti-windup controller [8].

2.2 Tracking Back Calculation (TBC) scheme

Tracking back calculation is also a method that are widely used by the control engineers to develop anti-windup controller in the past and Figure 2 shows the block diagram of this scheme [9]. As shown in Figure 2, the difference between non-saturated and saturated signal is identified and the error is being integrated in order to provide feedback for better control in the saturation range in equation (2):

$$\dot{q} = \begin{cases} e & if\ u = v \\ e - k_a(u - v) & if\ u \neq v \end{cases} \tag{2}$$

The advantage of this scheme is that a large range of gain, k_a can be chosen as it is able to limit the integrator of the controller. However, error might occur when the chosen gain is too high and cause integrator to be reset by affecting the saturation of the controller. This scheme also bears the high risk of experiencing speed error when proportional integral (PI) is activated [9].

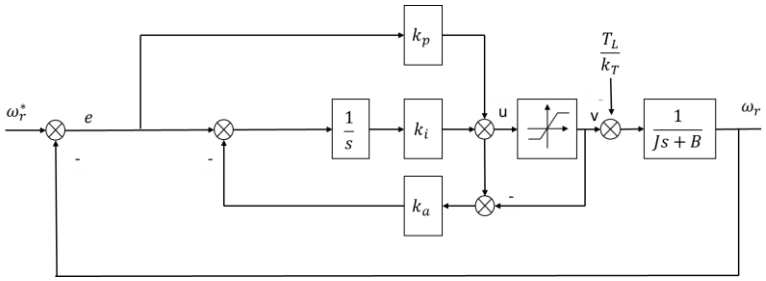


Figure 2. Tracking back calculation scheme anti-windup controller [9].

2.3 Integral State Prediction (ISP) scheme

The other anti-windup scheme is the integral state prediction (ISP) and the block diagram for its controller is shown in Figure 3 [11-12]. The integrator value of this controller is restricted using a large gain in the feedback of the control so that the controller is in linear range. This controller can function in two range which is linear and saturation range. The error from the output is connected directly to the integrator input to function as a feedback in linear range whereas integral state is reset to the steady state according to the system prediction as shown in Figure 3 at the state shown in equation (3) [10]:

$$\dot{q} = \begin{cases} e & if\ u = v \\ \omega_i(q_{ss} - q) & if\ u \neq v \end{cases} \tag{3}$$

Where ω_i, q_{ss} and τ_m denotes the potisitve parameter of the low pass filter, the integral value at steady state and time constant.

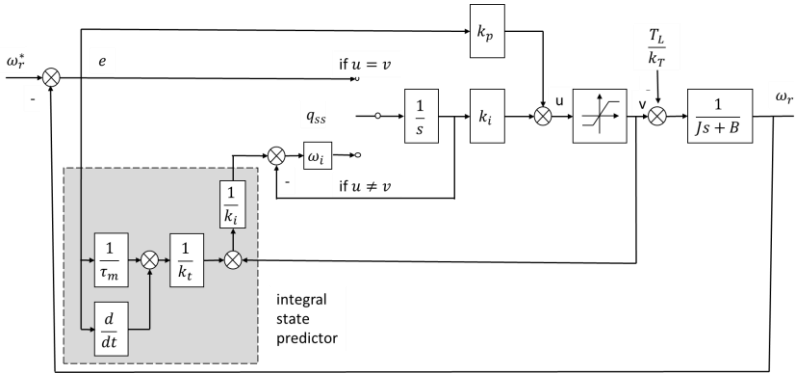


Figure 3. Integral state prediction scheme anti-windup controller [11].

Integral state loading time plays a significant role in allowing the controller to achieve a desired performance outcome. The integral state loading time is required to be a step ahead of the system dynamic so that the performance can be maintained at the top desired point [10, 12].

2.4 Comparison of Anti-windup schemes

Table 1 shows the advantages and disadvantages of the existing anti-windup schemes. The exiting anti-windup controllers have their very own integral control and it is shown in Table 2. Table 2 also shows the integral control of the controllers under different states. Based on Table 2, the existing anti-windup controller are applying the adaptive control which switches for the controller back to conventional PI controller under unsaturated state. The functionality of the existing anti-windup controllers are limited only to saturation state and switching schemes at different states will eventually cause system to be unstable.

Table 1. Comparison of anti-windup schemes.

Controller Scheme	Switching	Advantage	Disadvantage
Conditional Integration (CI)	Yes	• No overshoot speed response performance. • Effective when control input within saturation limit.	• Integral will be large when the value of controller output is different from plant output. • Difficult to choose value of gain.
Tracking Back Calculation (TBC)	Yes	• Large range of anti-windup gain alteration. • Improve overshoot.	• Error will occur if the gain is too big. • High risk of speed error.
Integral State Prediction (ISP)	Yes	• Functioning well in both linear and saturation range. • Steady state value is predicted to prevent state change.	• Integrator value is limited by feeding control back into linear state. • Derivation function is constraining the bandwidth of low-pass filter.

Table 2. Integral control comparison of the existing anti-windup schemes and conventional PI under different state.

Controller Scheme	Integral control under saturated state $u \neq v$	Integral control under unsaturated state $u = v$
Conventional PI controller	e	e
Conditional Integration (CI)	0	e
Tracking Back Calculation (TBC)	$e - k_a(u - v)$	e
Integral State Prediction (ISP)	$\omega_i(q_{ss} - q)$	e

2.5 Steady-state Integral Proportional Integral Controller (SIPIC)

SIPIC is a robust controller which is able to overcome the instability caused by the adaptive control switching mechanism of the other anti-windup controllers stated in Table 1. SIPIC has the tuning gain decoupling feature which was developed through the generic control template stated in equation (4) [13, 14].

$$\frac{q_{ss}}{s} - Q(s) = As^n f(s) + C \tag{4}$$

A and *C* indicate constant value, *f(s)* as the Laplace function, *Q(s)* as the Laplace form of integral state and *n* is a non-negative value [14].

3. Proposed Anti-windup PI Controller

A new anti-windup PI controller is proposed according to the generic control template similar to SIPIC which is able to produce a satisfying result with no overshoot. The proposed anti-windup PI controller performance are validated in motor speed control. A conventional PID controller is composed by equation (5).

$$u = k_p e + k_i q + k_d \dot{e} \tag{5}$$

Equation (5) shows a combination of proportional, integral and derivative parameters in a PID controller. u, k_p, e, k_i, q, k_d *and* $\dot{e}$ denotes controller output, proportional gain, error, integral gain, integral state, derivative gain and derivative error.

A speed motor is usually constructed by controlling the inner current where the dynamic of motor is in view of the loading effect shown in equation (6) [13]. T_l, ω_r, τ_m and v is denoted as external torque or disturbance, rotational motor speed, time constant and plant input respectively.

$$\frac{d\omega_r}{dt} = -\frac{\omega_r}{\tau_m} + k_t v - T_l \tag{6}$$

The difference between the current motor speed and the speed at set reference, $\omega_r{}^*$ shows the error in the closed loop system shown in equation (7):

$$e = \omega_r{}^* - \omega_r \tag{7}$$

The speed of motor, ω_r remain unchanged, error is excluded and plant input is $k_i q_{ss}$ at steady state where q_{ss} denotes integral state at steady state. Therefore, $\frac{d\omega_r}{dt} = 0$ which direct equation (6) to equation (8) and rearranged as equation (9) to show $k_i q_{ss}$.

$$0 = -\frac{\omega_r{}^*}{\tau_m} + k_t k_i q_{ss} - T_l \tag{8}$$

$$k_i q_{ss} = \frac{\omega_r{}^*}{\tau_m k_t} + \frac{T_l}{k_t} \tag{9}$$

According to Hoo [14], the error (e) and its first derivative ($\dot{e}$) will be zero at steady state whereas q will be at steady state, q_{ss}. The error of the system or disturbance that occurs in the system can be simplified as (10) [15-17]:

$$-\dot{e} = \left(\frac{1}{\tau_m} + k_t k_p\right) e + k_t k_i q - \frac{\omega_r{}^*}{\tau_m} - T_l \tag{10}$$

τ_m, $\omega_r{}^*$, T_l denotes the time constant, rotational speed of motor at set reference. Followed by the steady-state error shown in equation (11):

$$E(s) = \frac{e(0) + k_t k_i \left(\frac{q_{ss}}{s} - Q(s)\right)}{\left(s + \frac{1}{\tau_m} + k_t k_p\right)} \tag{11}$$

In order to eliminate windup in a control system, the steady state error should be as low as possible or it should not exist [14]. When the steady-state error is assumed to be zero, the equation is written as equation (12) by limiting $s \to 0$.

$$\lim_{s \to 0} k_t k_i s \left[\frac{q_{ss}}{s} - Q(s)\right] = 0 \tag{12}$$

The function in bracket leads to a generic form of equation (4) as proposed by Hoo [14]. The possible function for equation (4) is described in equation (13) and equation (14) shows the application of the integral component in the controller. Figure 4 shows the proposed integral component for anti-windup controller referring to equation (9). The proposed controller is shown in Figure 5 where k_t, J and B denotes the torque constant, motor's moment of inertia and viscous damping coefficient. The proposed controller was simulated using Scilab/Scicoslab version 4.4.1 and it shows satisfying result where the control can reach steady state under any circumstances and it took shorter time to reach steady state without high overshoot.

$$\frac{q_{ss}}{s} - Q(s) = \frac{(sQ(s) - q(0) + E(s))}{k_i} \tag{13}$$

$$k_i(q_{ss} - q) = \dot{q} + e \tag{14}$$

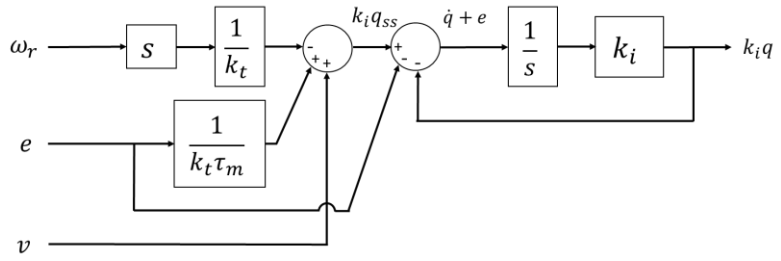


Figure 4. Proposed integral component

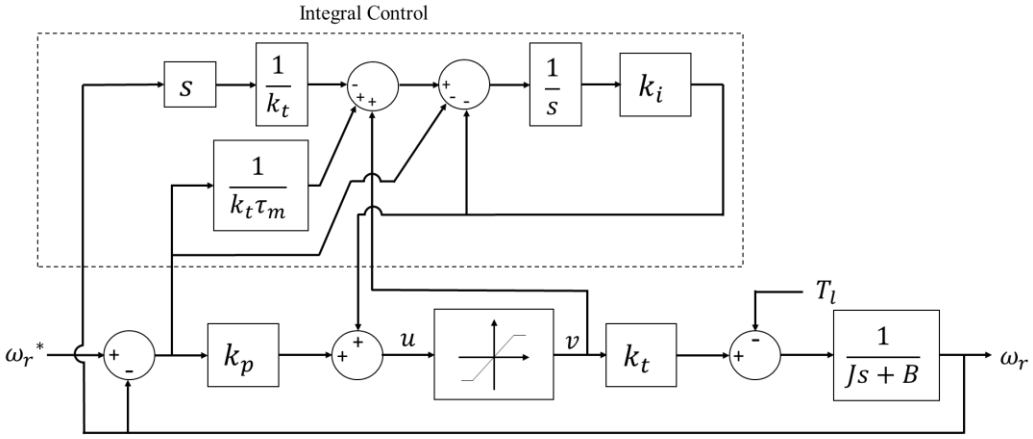


Figure 5. Block diagram of the proposed anti-windup PI controller.

3.1 Characteristic Analysis

From equation (13), the integral component of the proposed PI controller can be presented by equation (15) based on equation (13). The error equation of the proposed PI controller can be obtained by substituting equation (15) into equation (11) which leads to equation (16). The steady state error for the proposed anti-windup controller appeared to be zero when *s* approaches zero based on equation (12). The proposed PI controller does not behave like the existing anti-windup schemes which switching back to conventional PI during linear state. This allows the proposed anti-windup PI controller to be free from the disadvantageous effect of adaptive control switching mechanism.

$$Q(s) = \frac{q(0) + k_i \frac{q_{ss}}{s} - E(s)}{s + k_i} \tag{15}$$

$$E(s) = \frac{e(0)(s + k_i) + k_t k_i (q_{ss} - q(0))}{(s + k_i)\left(s + \frac{1}{\tau_m} + k_t k_p\right) - k_t k_i} \tag{16}$$

According to equation (16), the tuning parameters (k_p and k_i) are separated into distinct poles and can be tuned to desired performance with no overshoot while remaining zero steady state error. The proposed anti-windup PI controller is compared with the conventional PI controller with different tuning parameters under different speed. The results are shown in Section 4.

4. Comparison of Simulated Result for Speed Control

In order to verify the concept in the previous section, the performances of the proposed anti-windup PI controller is compared with the conventional PI controller scheme using software Scilab/Scicoslab version 4.4.1. Figure 6 illustrates the hardware simulation block diagram incorporated with the integral component in Figure 4. The hardware simulation was done with the tuning parameters stated in Table 3. The comparison of the controllers was done with different motor speed under different loading conditions. The specification for loading condition is listed in Table 4. The parameters for DC motor speed are tuned referring to the values stated in Table 5 in order to obtain a stable performance.

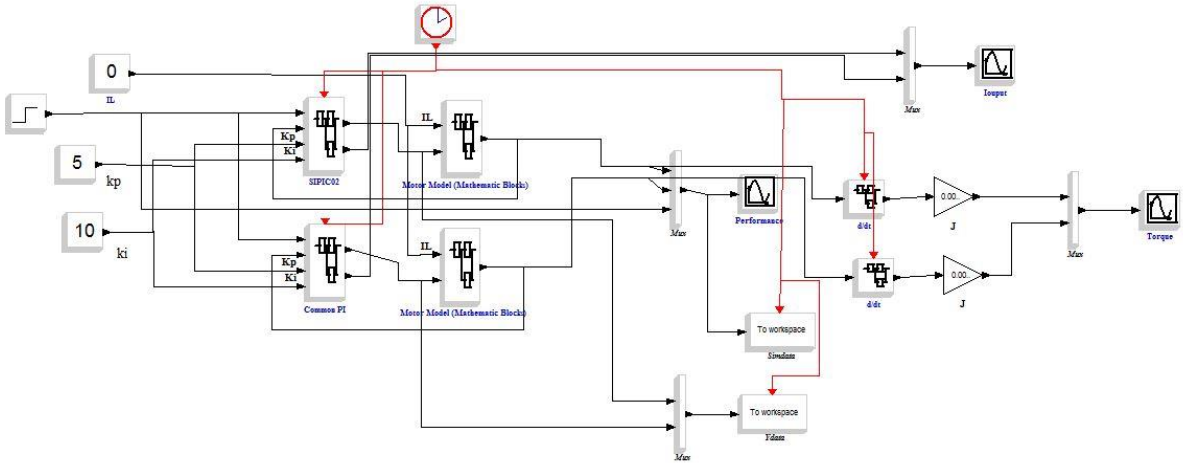


Figure 6. Block diagram for simulation in Scilab/Scicoslab software

Table 3. Tuning parameters for hardware simulation.

Speed, ω	k_p	k_i
50 rad/s	1	1
	1	5
	1	10
	5	1
	5	5
	5	10
	10	1
	10	5
	10	10
100 rad/s	1	1
	1	5
	1	10
	5	1
	5	5
	5	10
	10	1
	10	5
	10	10

Table 4. Specification for load condition.

Case	Characteristics	Values
No load	Material	-
	Moment of inertia	0 kgm^2
Load 1	Material	Mild steel black plating
	Moment of inertia	8.63×10^{-5} kgm^2
Load 2	Material	Aluminum plating
	Moment of inertia	2.83×10^{-5} kgm^2

Table 5. Parameters for DC motor speed test

Characteristics	Values
Viscous damping coefficient, B	2.12×10^{-4} kg m^2/s
Inductance, L	0.005 H
Moment of inertia of motor, J	2.14×10^{-5} kg m^2
Torque constant, k_t	0.09 Nm/A
Back-emf constant, k_m	0.09 Nm/A
Efficiency, η	0.8
Resistance, R	7.8 Ω

The hardware simulation requires a setup of DC servo motor, motor encoder and host computer with Scilab/Scicoslab 4.4.1 software and real time kernel rtai installed under Linux. The details of these setup components are stated in Table 6 to 8.

Table 6. Specification for DC servo motor.

Characteristics	Values
Maximum supply voltage	40 Vdc
Maximum continuous torque	14 Ncm
Maximum peak torque	36 Ncm
Motor voltage constant	10.3 V at 1000 rpm
Motor torque constant	9.0 Ncm/A
Mechanical time constant	20 ms
Rotor inertia	0.214 kg cm
Terminal resistance	7.8 Ohms
Rated speed	1600 rpm
No load speed	2600 rpm @ 24 Vdc
Rated torque	12 Ncm
Peak torque	27 Ncm

Table 7. Specification for motor encoder.

Characteristics	Values
Number of lines	500 lines (2000 @ quad)
Number of channel	2 channel (A, B)
Output pulse	5 Vdc
Supply voltage	± 5 Vdc

Table 8. Specification for host computer for DC motor.

Characteristics	Values
System compatibility	Windows 7 Pro 32/64 bits Linux Ubuntu Preconfigured for DUAL BOOT
Software compatibility	Open source scientific software (Scilab/Scicoslab version 4.4.1) Matlab/Simulink
Dual system support	Under same real-time environment, the system could support 2 plants at the same time provided availability of IO ports

4.1 Speed Control under No Load Condition

The conventional PI controller and the proposed anti-windup PI controller was simulated at the motor speed of 100 rad/s as shown in Figure 7. Conventional PI controller is faster integral speed as compared with the proposed anti-windup PI controller which causes overshoot phenomenon to occur in the performance. The proposed anti-windup controller has no overshoot but it has a longer settling time as compared to conventional PI controller.

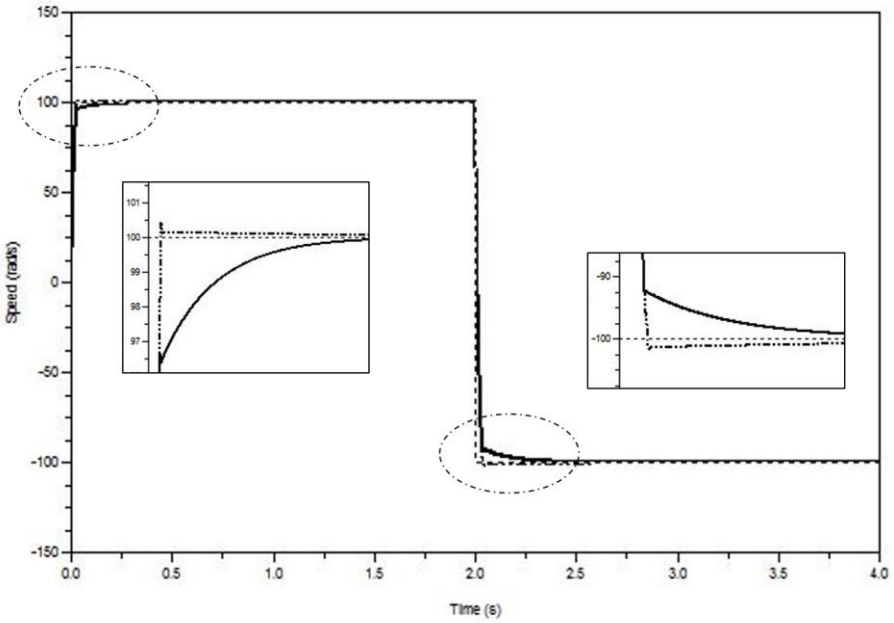


Figure 7. Comparison of speed control for conventional PI controller (dash-dot line) and proposed anti-windup PI controller (solid line) with changing step input under no load condition (speed = 100 rad/s, k_p = 5, k_i = 10).

The simulation of motor speed control was done with different set of tuning parameters as stated in Table 4. The result of the simulation was summarized in Table 9 in terms of rise time of the signal, settling time and percentage of the overshoot for conventional PI and proposed anti-windup PI controller. The comparison of conventional PI and the proposed anti-windup PI controller was made for the speed of 50 rad/s and 100 rad/s under no load condition. According to Table 9, increasing the value of parameter k_p and k_i is able to reduce the rise time and settling time for both the controllers. The rise time and settling time of the proposed anti-windup PI controller is way higher than the conventional PI controller whenever k_p is 1. Both rise time and settling time are observed to be the same as k_p and k_i increases. This is because the

performance of the controller has reached the lowest boundary of rise time and settling time when k_p is tuned to 5 for both speed of 50 rad/s and 100 rad/s. The increment of the parameter k_p and k_i is no longer giving any significant effect on rise time and settling time. However, the occurrence of overshoot still exists and the percentage of having an overshoot increases with the increment in k_i value for conventional PI controller. The proposed anti-windup PI controller does not show any overshoot performance due to the decoupling feature.

Table 9. Performance at 50 rad/s and 100 rad/s under no load condition.

Speed, ω (rad/s)	k_p	k_i	Rise Time		Settling Time		Overshoot (%)	
			PI	Proposed	PI	Proposed	PI	Proposed
50	1	1	0.012	0.521	0.742	2.427	0	0
	1	5	0.011	0.380	0.106	1.758	0	0
	1	10	0.010	0.337	0.016	1.032	0.161	0
	5	1	0.009	0.009	0.010	0.010	0	0
	5	5	0.009	0.009	0.010	0.010	0	0
	5	10	0.009	0.009	0.010	0.010	0.468	0
	10	1	0.009	0.009	0.010	0.010	0	0
	10	5	0.009	0.009	0.010	0.010	0.160	0
	10	10	0.009	0.009	0.010	0.010	0.464	0
100	1	1	0.025	0.916	0.690	2.341	0	0
	1	5	0.024	0.681	0.028	2.021	0	0
	1	10	0.023	0.567	0.026	1.262	0.635	0
	5	1	0.024	0.024	0.027	0.027	0	0
	5	5	0.024	0.024	0.026	0.026	0	0
	5	10	0.024	0.024	0.026	0.026	0.377	0
	10	1	0.024	0.024	0.027	0.027	0	0
	10	5	0.024	0.024	0.026	0.026	0	0
	10	10	0.024	0.024	0.026	0.026	0.339	0

4.2 Speed Control with Loading Condition

4.2.1 Loading with Mild Steel Plating (Loading Condition 1)

Figure 8 shows the comparison between the conventional PI controller and the proposed anti-windup PI controller at the motor speed of 100 rad/s under loading condition 1 (mild steel plating). The simulated rise time, settling time and overshoot percentage under loading condition 1 is tabulated in Table 10. The rise time and settling time for both conventional PI controller and the proposed anti-windup PI controller is longer as compared to no load condition. In addition, the overshoot percentage of the conventional PI controller increases drastically as compared to no load condition. Small percentage of overshoot is observed at low k_p and k_i values.

Conventional PI controller has faster integral speed as compared with the proposed anti-windup PI controller which causes overshoot phenomenon to occur in the performance. The proposed anti-windup controller has no overshoot but with a longer settling time as compared to conventional PI controller. The higher integral gain is the reason behind the changes which brought the system into saturation and

proportional gain could not react to correct the error immediately. The proposed anti-windup controller shows a satisfying result with no overshoot due to its decoupling feature.

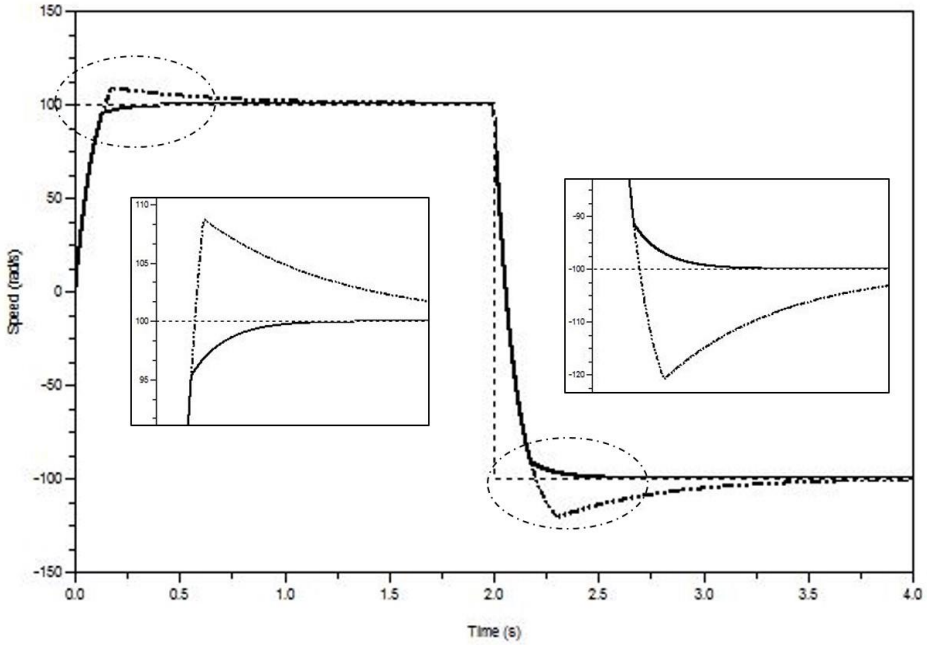


Figure 8. Comparison of speed control for conventional PI controller (dash-dot line) and proposed anti-windup PI controller (solid line) with changing step input under loading condition 1 (speed = 100 rad/s, k_p = 5, k_i = 10).

Table 10. Performance at 50 rad/s and 100 rad/s under loading condition 1.

Speed, ω (rad/s)	k_p	k_i	Rise Time		Settling Time		Overshoot (%)	
			PI	Proposed	PI	Proposed	PI	Proposed
50	1	1	0.055	1.091	0.565	2.266	0	0
	1	5	0.045	0.799	0.051	2.001	0.820	0
	1	10	0.044	0.647	0.047	1.336	9.919	0
	5	1	0.044	0.044	0.047	0.047	0	0
	5	5	0.044	0.044	0.047	0.047	0.364	0
	5	10	0.044	0.044	0.047	0.047	2.696	0
	10	1	0.044	0.044	0.047	0.047	0	0
	10	5	0.044	0.044	0.047	0.047	0.827	0
	10	10	0.044	0.044	0.047	0.047	1.965	0
100	1	1	0.118	2.001	0.160	2.287	0	0
	1	5	0.118	1.630	0.130	2.124	13.409	0
	1	10	0.120	1.141	0.130	1.830	23.939	0
	5	1	0.118	0.118	0.130	0.130	0	0
	5	5	0.118	0.118	0.130	0.130	3.405	0
	5	10	0.118	0.118	0.130	0.130	8.736	0
	10	1	0.118	0.118	0.130	0.130	0	0
	10	5	0.118	0.118	0.130	0.130	1.837	0
	10	10	0.118	0.118	0.130	0.130	4.621	0

4.2.2 Loading with Aluminum Plating (Loading Condition 2)

The comparison between the conventional PI controller and the proposed anti-windup PI controller at the motor speed of 100 rad/s under loading condition 2 (aluminum plating) is shown in Figure 9. The simulated rise time, settling time and overshoot percentage under loading condition 2 is tabulated in Table 11. The rise time, settling time and overshoot percentage is very similar to loading condition 1. The rise time and settling time for both conventional PI controller and the proposed anti-windup PI controller is shorter as compared to loading condition 1 case but longer when compared to no load condition. The overshoot percentage of the conventional PI controller increases with proportional gain and integral gain. Small percentage of overshoot is observed at low k_p and k_i values as well.

According to Table 11, the integral speed of the conventional PI controller is faster than the proposed anti-windup PI controller which leads to overshoot phenomenon. The proposed anti-windup controller has no overshoot but has a longer settling time and the simulated performance is more satisfying compared to conventional PI controller.

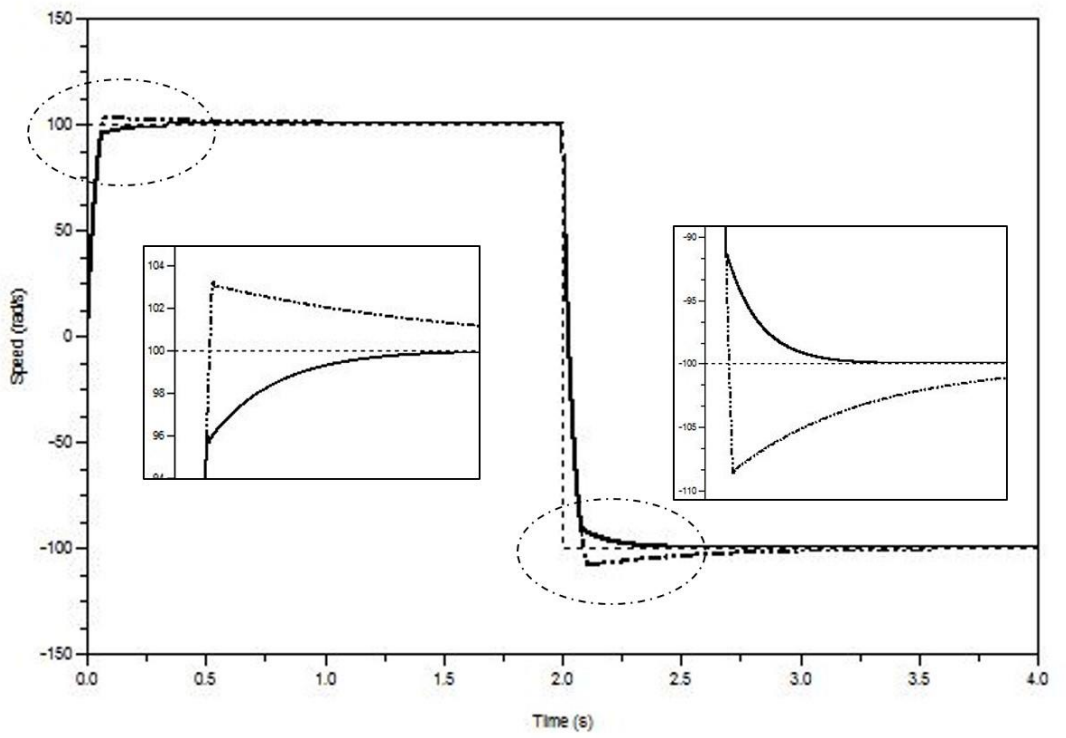


Figure 9. Comparison of speed control for conventional PI controller (dash-dot line) and proposed anti-windup PI controller (solid line) with changing step input under loading condition 2 (speed = 100 rad/s, k_p = 5, k_i = 10).

Table 11. Performance at 50 rad/s and 100 rad/s under loading condition 2.

Speed, ω (rad/s)	k_p	k_i	Rise Time		Settling Time		Overshoot (%)	
			PI	Proposed	PI	Proposed	PI	Proposed
50	1	1	0.027	0.733	0.685	2.398	0	0
	1	5	0.022	0.549	0.031	1.925	0.155	0
	1	10	0.021	0.470	0.024	1.164	1.762	0
	5	1	0.021	0.021	0.022	0.022	0	0
	5	5	0.021	0.021	0.022	0.022	0.643	0
	5	10	0.021	0.021	0.022	0.022	1.272	0
	10	1	0.021	0.021	0.022	0.022	0	0
	10	5	0.021	0.021	0.022	0.022	0.449	0
	10	10	0.021	0.021	0.022	0.022	1.272	0
100	1	1	0.055	1.578	0.574	2.174	0	0
	1	5	0.055	1.094	0.060	2.103	1.918	0
	1	10	0.055	0.840	0.060	1.533	12.633	0
	5	1	0.055	0.055	0.060	0.060	0	0
	5	5	0.055	0.055	0.060	0.060	0.752	0
	5	10	0.055	0.055	0.060	0.060	3.058	0
	10	1	0.055	0.055	0.060	0.060	0	0
	10	5	0.055	0.055	0.060	0.060	0.417	0
	10	10	0.055	0.055	0.060	0.060	1.961	0

5. Conclusion

The proposed anti-windup controller shows a promising potential to contribute to the society by serving as an anti-windup controller for better motor speed control. The proposed anti-windup PI controller shows a better result regardless of the loading condition as compared to the conventional PI controller. The performance of this controller is promising where the integral control is able to reach steady state at both saturated and non-saturated state. The proposed anti-windup controller reaches steady state without having overshoot in the speed control performance. However, the proposed anti-windup PI controller has extremely long rise time and settling time when the proportional gain, k_p is 1 as compared to the conventional PI controller. Therefore, future work will focus on reducing the rise time and settling time for low proportional gain, k_p value.

References

[1] S. M. Gadoue, D. Giaouris and J. W. Finch, "Artificial intelligence-based speed control of DTC induction motor drives - a comparative study," *Electric Power Systems Research*, vol.79, no.1, pp.210-219, 2009.

[2] K. Astrom and T. Hagglund, *PID Controllers: Theoty, Design, and Tuning*. Research Triangle Park, NC: ISA, 1995, pp. 59-92.

[3] B. Bahrani, S. Kenzelmann, and A. Rufer, "Multivariable-PI-based dq current control of voltage source converters with superior axes decoupling capability," *IEEE Trans. Ind. Electron.*, vol. 58, no. 7, pp. 3016-3026, July 2011.

[4] R. J. Wai, J. D. Lee, and K. L. Chuang, "Real-time PID control strategy for Maglev transportation system via particle Swarm optimization," *IEEE Trans. Idn. Electron.*, vol. 58, no. 2, pp. 629-646, February 2016.
[5] S. Tarbouriech and M. Turner, "Anti-windup design: An overview of some recent advances and open problems," *IET Control Theory and Application*, vol. 3, no. 1, pp. 1-19, January 2009.
[6] I. K. Al-Abbas and R. Issa, "Overshoot Elimination in Cascade Control of Separately Excited DC Motors," *European Journal of Scientific Research*, vol. 85, no. 1, pp. 98-104, 2012.
[7] R. Hanus, M. Kinnaert, and J. L. Henrotte, "Conditioning Technique, a General Anti-windup and Bumpless Transfer Method," *Automatica*, vol. 23, no. 6, pp. 729-739, 1987.
[8] J. K. Seok, K. T. Kim and D. C. Lee, "Automatic mode switching of P/PI speed control for industry servo drives using online spectrum analysis of torque command," *IEEE Trans. Ind. Electron.*, vol. 54, no. 5, pp. 2642-2647, 2007.
[9] J. W. Choi and S. C. Lee, "Antiwindup Strategy for PI-type Speed Controller," *IEEE Trans. Ind. Electron.*, vol. 56, no. 6, pp. 2039-2046, June 2009.
[10] X. L. Li, J. G. Park and H. B. Shin, "Comparison and Evaluation of Anti-Windup PI Controllers," *Journal of Power Electronics*, vol. 11, no. 1, pp. 45-50, 2011.
[11] J. G. Park, J. H. Chung and H. B. Shin, "Anti-windup integral-proportional controller for variable-speed motor drives," *Journal of Power Electronics*, vol. 2, no. 2, pp. 130-138, April 2002.
[12] K. Ohishi, E. Hayasaka, T. Nagano, M. Harakawa and T. Kanmachi, "High-performance speed servo system considering voltage saturation of a vector-controlled induction motor," *IEEE Trans. Ind. Electron.*, vol. 53, no. 3, pp. 795-802, June 2006.
[13] C. L. Hoo, S. M. Haris, Edwin. C. Y. Chung and N. A. N. Mohamed, "Steady-State Integral Controller for PI Motor Speed Controllers," *Journal of Power Electronics*, vol. 15, no. 1, pp. 177-189, January 2015.
[14] C. L. Hoo, S. M. Haris, Edwin. C. Y. Chung and N. A. N. Mohamed, "The generalization and decoupling mode of PI-based control: theoretical approach," *ICIC Express Letters*, vol. 9, no. 7, pp. 1991-1996, July 2015.
[15] C. L. Hoo, Edwin. C. Y. Chung, S. M. Haris and N. A. N. Mohamed, "Steady-state integral proportional integral controller for PI motor speed controllers: a theoretical approach," *ICIC Express Letters*, vol. 9, no. 6, pp. 1777-1782, June 2015.
[16] C. L. Hoo, Edwin. C. Y. Chung, S. M. Haris and N. A. N. Mohamed, "The boundary integral-error state, q(0)-e(0) plane for PI control," *ICIC Express Letters*, vol. 9, no. 7, pp. 1797-1802, July 2015.
[17] C. L. Hoo, S. M. Haris, Edwin. C. Y. Chung and N. A. N. Mohamed, "New Integral Antiwindup Scheme for PI Motor Speed Control," *Asian Journal of Control*, vol. 18, no. 3, pp. 1-18, May 2016.

Development of a Non-Intrusive Pressure Sensor for Sensing Pressure Inside a Fluid Pipe

Hamza Aslam, Mohsen Nabi Poor
School of Engineering, Taylor's University, Malaysia

Mohsen.NabiPoor@taylors.edu.my

Abstract
Fluid pressure is a vital parameter to be measured in common refrigeration systems, but common techniques used to measure fluid pressure include flow meters and pressure gauges, all manually installed into the pipelines. These methods have their deficiencies as they can result in leaks and drops in pressure within the pipelines. An effective non-intrusive method involves using an ultrasonic based method to measure pressure in small diameter (9.57mm) refrigeration pipes presented in this paper. To verify the theory and methods implemented in this study, water is used as a substitute to the refrigerant. The proposed technique is based on the principle that wave speed correlates with the pressure of the fluid within the pipe. Different variations of ultrasonic propagation times were recorded under different pressures: 0 Psi to 150 psi. The time difference was accurately measured to the nanosecond level using a high resolution oscilloscope. The relationship between the time difference of the propagating waves and pressure was then fed into a back propagating neural network (BPN), which was used to obtain the corresponding pressure values.

***Keywords**: Ultrasonic, Waveform, Time-delay, liquid pressure, back propagation*

1. Introduction

Fluid pressure is a vital parameter that is monitored in modern refrigeration systems. Traditional methods of obtaining the pressure inside refrigeration pipes include attaching pressure gauges by means of drilling or intruding into the sealed pipe, which can lead to possible gas leaks and drops in pressure. Hence, non-intrusive ultrasonic techniques are being researched to save time when troubleshooting and overcome the losses created when using conventional methods. Moreover, the applications of ultrasonic non-destructive testing methods include distance measurements [1], flaw detection [2], flow meters [3]–[6] , metal stress testing [7] and density measurements [8]. The advantages of using of ultrasonic waves include strong wall penetration and fast response. This has allowed ultrasonic technology to be used in measuring fluid pressure.

More work and research has been conducted in measuring pipe pressure with the use of ultrasonic waves. One of these methods includes measuring the time of travel between two sending and receiving ultrasonic transducers under different pressure values. Two ultrasonic transducers were mounted on both sides of a copper pipe. Using this method has some complications as the diameter of the pipe is less than 10mm and this can lead to superposition of the waves due to shear waves caused within the inner diameter of the pipe. Moreover, fluid temperature and placement errors of the transducers can affect the transmission characteristics of the ultrasonic waves.

Therefore, the objective of this experiment is to measure the fluid pressure in small diameter refrigeration pipes using non-intrusive ultrasonic transducers. The transducers are to be place on the outside of a pipeline, opposite to each other. The flight time of the ultrasonic wave is to be observed and the difference in time Δt, in correlation with the pressure is recorded and the data is fed into a neural for training. This paper highlights the effects of varying pressure on the time of speed of ultrasonic waves and based on measured time of flight, the corresponding pressure values are obtained.

2. Research Methodology

2.1 Overview

Ultrasound are sound waves which have frequencies ranging above 20 kHz up to 100 kHz. The speed of ultrasound is affected by the density of the medium it is travelling though. Being a mechanical wave, it depends on rarefactions and compressions to propagate though a medium, hence increase in density will result in higher wave speed. [9]. Piezoelectric ultrasonic transducers are used, where the waves are generated though piezoelectricity [10]. These transducers can also convert ultrasonic waves into electrical signals, therefore allowing the same probe to be used as a transmitter as well as a receiver.

2.2 Proposed Technique

The change in wave speed within the pipeline varies in accordance with the change in pressure of the fluid. But, wave speed cannot be obtained directly, hence the varying propagation time will be used to represent the changing wave speed [11].

It can be seen in **Fig. 1** that the flight time of the ultrasonic wave was taken from its emission from transducer UT and reception by transducer UR. As the pressure of the fluid inside the pipe is increased, the flight time is measured, and a time difference Δt is observed as compared to the fluid under no pressure. L can be considered as the distance of propagation of the ultrasonic wave and v_0 is initial velocity of propagation of the ultrasonic wave with a pressure reading of 0 psi. The time difference Δt can be written as:

$$\Delta t = \frac{L.\Delta v}{v_0(v_0+\Delta v)} \quad (1)$$

Obtaining v_0 is very difficult, the relationship between Δt and pressure P can be used to measure the pressure within the pipeline. Hence Δt can be directly obtained, and there is no need to calculate the changing ultrasonic velocity.

Moreover, the velocity of ultrasonic propagation can be defined as the function of pressure and temperature. The time difference Δt can also be written as:

$$\Delta t = \frac{L.f(P)}{v_0(v_0+f(P,T)} \quad (2)$$

Therefore we can express pressure P as the function of time difference and temperature:

$$P = g(\Delta t) \quad (3)$$

In the experimental setup, two ultrasonic transducers, defined as UT and UR, are mounted on both sides of the pipe wall, as shown in **Fig 1**. Transducer UT generates a longitudinal wave into the pipe wall, and this wave continues to spread through the fluid until it reaches transducer UR. The pressure of the fluid is being increased step by step through of pressured gas connected to the tube, and the wave propagation time is being is recorded with the corresponding pressure at each step.

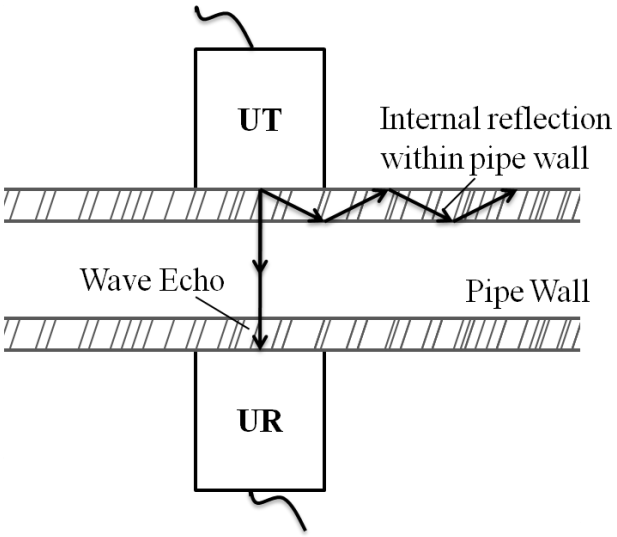


Figure 1. Schematic diagram of wave path.

In this paper a neural network method is being implemented called the back propagation network (BPN), as the function g stated above is non-linear and is very difficult to express in a mathematical expression. This technique has been applied in other researches, also in relation to non-destructive ultrasonic testing [12].

The time differenceΔt and pressure P are going to be incorporated in this BP neural network. Time difference will be the input of the network, and the pressure will be the target output value. The network will be trained and will be used to obtain the pressure inside the pipeline. A BP neural network consists of three layers: an input

layer, hidden layer and an output layer. As shown in **Fig 2**, the circles represent the neurons, which are basically the main processing units and are the building blocks of a neural network are called neurons. They are capable of communicating by transmitting signals through a number of biased weight connections. Where, as x_n is the input information, w is the weighted bias of the neurons and y is the output information.

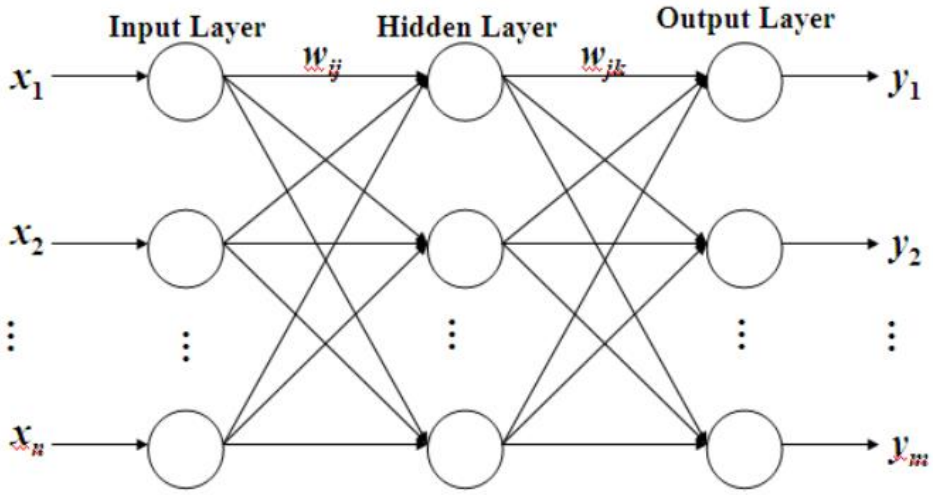


Figure 2. Topology of a basic 3 layer BP network. [13]

In a BP neural network, input data and a target output is inserted in the network algorithm [14]. The network calculated the error between the actual output and desired output by acting the input layer onto the output layer [15]. In order to minimize the error, the calculated error is back propagated, and the network then revises the weights of the connection between the nodes of the network. This ensures that the error is reduced to a set value and at this point, the network stops training and is created [16].

2.3 Experiment Set-up and Method

In order to verify the validity of the proposed method, the experiment set-up, as shown in **fig. 3** was built. It shows a schematic diagram of the experimental setup where the water in the tube is being pressurized by means of compressed air. UR represents the receiving transducer, whereas UT represents the transmitting transducer. A pressure valve and gauge allow the pressure to be monitored and regulated. As the pressure is increased, the correlating ultrasonic pulse is saved on an external memory through an oscilloscope. As time range for the measurement is in the nanosecond range, a high resolution oscilloscope is being used.

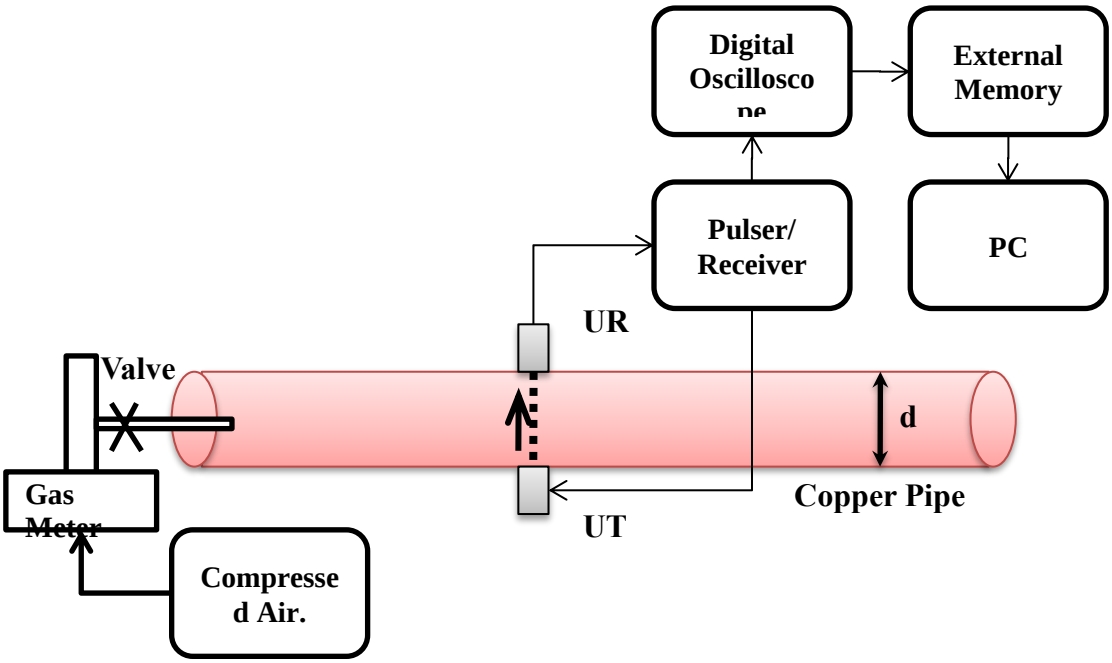


Figure 3. Schematic diagram of experiment setup.

The pipe is made of copper and has a length of 1 meter, with an internal diameter of 9.52mm. For the transmission of ultrasonic waves, Olympus transducers were used, along with a pulser and receiver, which was used to sent pulses to the transmitting probe, and receive back the signals from the receiving probe. Moreover, a high-resolution Rhode&Schwarz digital oscilloscope was used to obtain the waveforms, and eventually used to calculate the time difference. Table 1 shows the specifications of the transducers used in this research.

Table 1. Transducer specifications

Transducer type	Olympus A542S Angle Beam Transducer.
Frequency	2.25 MHz
Element size	0.25 inches

Transducer UR and UT were implemented to determine the pressure inside the pipeline. UR served as the transmitter and UT served as the receiving transmitter, and the transmitted pulse and the obtained signal can be seen in **fig. 4**. The pulser and receiver apply a voltage pulse of 5 V amplitude and 9.7 μs pulse width, to transducer UT, with a frequency of 2.25 MHz. The ultrasonic wave then propagates thought the wall of the pipe and into the medium, and is finally received by transducer UR.

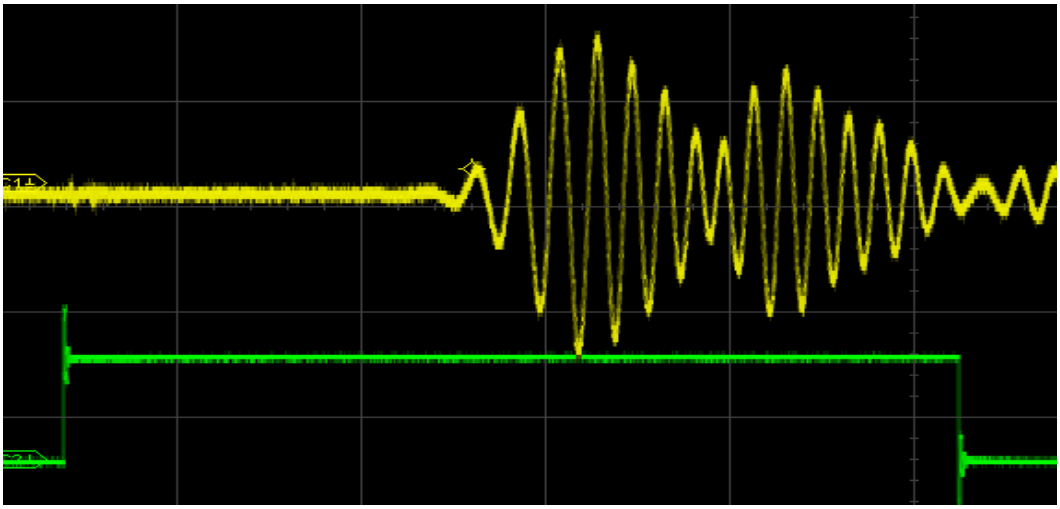


Figure 4. Waveform at receiving transducer.

Moreover, as the pressure increased step by step, it can observed that there is a shift of the ultrasonic pulse along time-axis of the received signal, as seen in **fig. 5**. As the pressure is increased, the signal shifts to the left, which indicates that there is an effect on the flight of time of the ultrasonic wave. This shift in the time-axis will be taken as the time-difference Δt, with the pulse wave under no pressure being the control. The values for the time-difference are presented in **Table 2** in section 3.

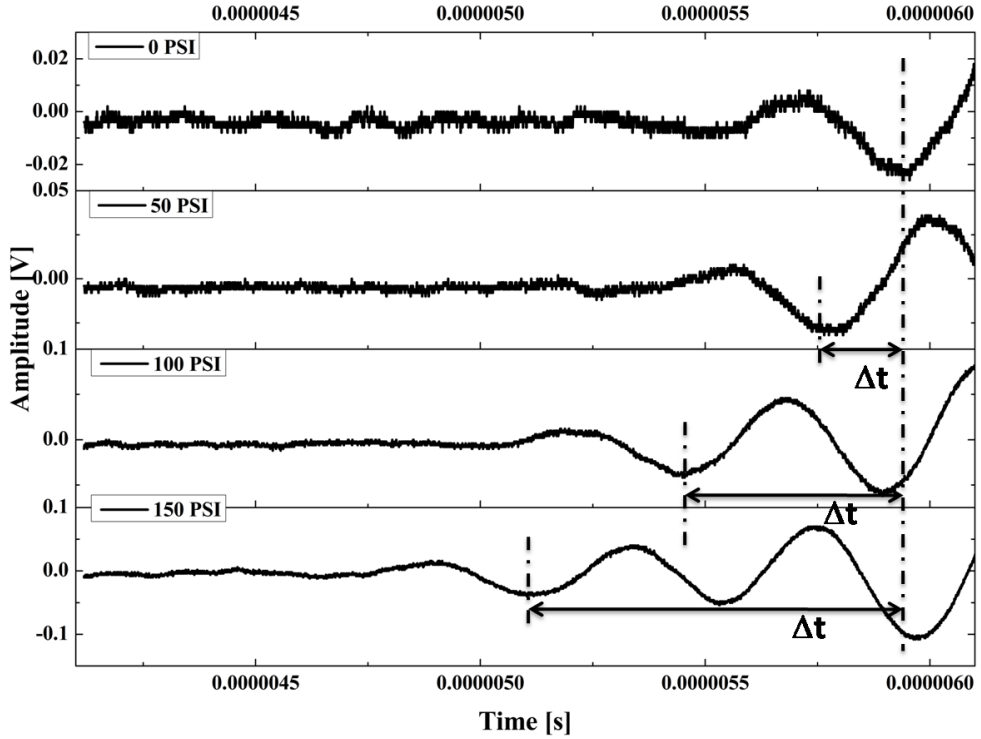


Figure 5. Comparison of ultrasonic waves with varying pressure.

3 Results and Discussion

In the BP neural network, the time difference Δt was defined as the input and the pressure 'P' was defined as the desired output. After repeated tests, the numbers of neurons in the hidden layer were chosen to be 8, as this will determine the overall performance, good fitting of data and training time of the network.

Before training the network, activation functions needed to be defined and for this BP network; Tan-Sigmoid and Log-Sigmoid functions were chosen [17]. The training error of the network can be seen in **fig. 6**, which indicates the training has stopped once it reached the set error point, as indicated in the figure.

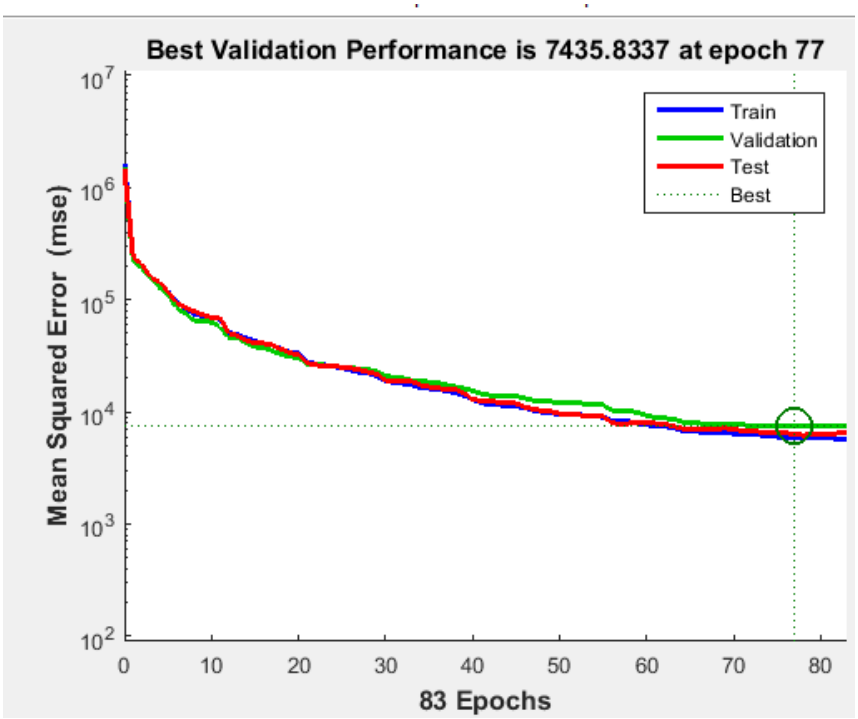


Figure 6. Training error of BPN network.

A set data was obtained by using the experimental approach explained above. This set of data was then fed into the trained neural network and the processed results can be seen in **Table 2**. The desired pressure is the data obtained using the pressure gauge and the actual pressure is defined as the result calculated using the trained BP network. It can be observed that the relative error between the desired and actual pressure is less than 5%. The time difference between 10 to 20 psi can be observed as 86.6 ns, and was measured using a high resolution oscilloscope. The sensitivity of this technique can be narrowed down to up to 10 psi; where other inconsistencies in measurement can be caused by misaligned probes, internal reflection of ultrasonic waves within the pipe walls and electromagnetic noise caused by the surroundings.

Table 2. Results from BP neural network

Δt (ns)	Desired Pressure (psi)	Actual Pressure (psi)	Relative Error (%)
0	10	9.680	-3.199
86.6	20	20.000	0.002
144.2	30	30.000	0.001
193.6	40	36.196	-9.511
254.6	50	51.056	2.112
316	60	61.159	1.932
351.4	70	69.462	-0.768
413.4	80	79.608	-0.490
460.8	90	89.985	-0.017
521.9	100	98.750	-1.250
580.1	110	109.468	-0.484
630.6	120	119.658	-0.285
688.5	130	129.970	-0.023
740.3	140	137.512	-1.777
791.3	150	145.159	-3.228

4 Conclusion

This study was conducted to measure the pressure inside small refrigerant pipelines, and for this study, water was used as substitute to the refrigerant, in order to verify the techniques and approach of the experiment. It can be observed that, the flight time of the ultrasonic wave varies with the change in pressure. By obtaining the time difference of the propagating wave, the pressure inside the pipeline can be determined. A BPN model was used, where the time difference was set as the input and the target pressure values as the output. The experimental results verify the effectiveness and the accuracy of the technique used in this study. Adding to that, the neural network also can be trained and calibrated to various pipe diameters, fluid conditions and temperatures.

Although, there is a certain percentage error in the output pressure as compared to the pressure gauge from the set up itself, but the main advantage is the non-intrusive measurement is that it mitigates the negative impacts of physically installing the pressure gauge.

References

[1] A. K. Shrivastava, A. Verma, and S. P. Singh, “E Ffect Of V Ariation Of S Eparation Between The U Ltrasonic T Ransmitter And R Eceiver,” vol. 1, no. 2, pp. 19–28, 2009.

[2] T. Faculty, M. Engineering, P. Control, J. K. Co-supervisor, and T. Stepinski, “Ultrasonic nondestructive methods in inspection of steel . mgr in ». Tomasz Š ukomski,” 2012.

[3] M. Kupnik, A. Schr, and M. Gr, “Adaptive asymmetric double-path ultrasonic transit-time gas flow meter,” *IEEE Int. Ultrason. Symp.*, pp. 2429–2432, 2006.

[4] Nel, “Good Practice Guide - An Introduction to non-invasive Ultrasonic Flow Meter,” *Tuv Nel*, pp. 1 – 23, 2010.

[5] I. J. O’Sullivan and W. M. D. Wright, “Ultrasonic measurement of gas flow using electrostatic transducers,” *Ultrasonics*, vol. 40, 1–8, pp. 407–411, 2002.

[6] W. Wright and S. Brini, “Capacitive Ultrasonic Transducers for Gas Flow Metering Applications,” *Flomeko*, 2005.

[7] Y. Kudryavtsev and J. Kleiman, “Ultrasonic Technique and Device for Residual Stress Measurement,” pp. 1–7.

[8] B. Marchetti, R. Munaretto, G. M. Revel, and E. P. Tomasini, “Non-Contact Ultrasonic Sensors for Density Measurement and Defect Detection on Wood,” *16th WCNDT 2004 - World Conf. NDT*, 2004.

[9] B. Cox, “Acoustics for Ultrasound Imaging,” January, pp. 1–20, 2013.

[10] M. W. Nygren, T. Ytterdal, and T. F. Johansen, “Finite Element Modeling of Piezoelectric Ultrasonic Transducers,” *Dep. Electron. Telecommun.*, vol. MSc, January, 2011.

[11] H. Tijdeman and A. Fokkerweg, “ON THE PROPAGATION OF SOUND . WAVES IN CYLINDRICAL TUBES National Aerospace Laboratory (NLR),” vol. 39, pp. 1–33, 1975.

[12] S. Kv and B. K. Roy, “An Intelligent Flow Measurement Technique using Ultrasonic Flow Meter with Optimized Neural Network,” vol. 5, no. 4, pp. 185–196, 2012.

[13] S. Ding, W. Jia, C. Su, X. Liu, and J. Chen, “An Improved BP Neural Network Algorithm Based on Factor Analysis,” vol. 5, no. 4, pp. 103–108, 2010.

[14] M. Cilimkovic, “Neural Networks and Back Propagation Algorithm,” *Fett.Tu-Sofia.Bg*, 2010.

[15] D. S. Touretzky, “Backpropagation Learning LMS / Widrow-Hoff Rule,” in *Artificial Neural Networks*, 2006, p. 486.

[16] R. Rojas:, “The Backpropagation Algorithm,” in *Neural Networks*, Berlin: Springer-Verlag, 1996.

[17] M. A. Wani, “Comparative Study of Back Propagation Learning Algorithms for Neural Networks,” vol. 3, no. 12, pp. 1151–1156, 2013.

eureca 2016 – Conference Paper
Paper Number 2EE3

A New High Torque Density Brushless DC Motor for Electric Vehicle Application

Heng Jing Lei[1*], Aravind CV[1*], Charles Sarimuthu[1], Suresh A[2]

[1]*School of Engineering, Taylor's University, Malaysia*

[2]*Professor, S.A. Engineering College, Chennai, India*

*aravindcv@ieee.org

Abstract

As the demands for electric vehicles grow and highly futuristic, the main challenge is to design an electric machine which could deliver high torque performance. Most modern commercial vehicles utilise the brushless permanent magnet machines as the electric motors. There are attempts made for improvement in the design of the electrical machines to improve the performance of such type of machine. Use of high density permanent magnet machines increases the torque but with increase in thermal limits. Invariably the torque density heavily depends on the air gap flux density of the machines and this motivated to have a structure with dual air gap. Hence, the resultant of air gap is the key to enhance the torque producing capability of the machine. The air gap flux linkage can be enhanced by altering the magnetic circuit of conventional machine where the air gap length of a given basic magnetic circuit is reduced. Realizing the dual air gap through two rotors adds advantage with the feasibility of both motoring and regenerating operation with independent control through electronics. In addition, the stator yoke of the conventional machine is not fully utilized. The objective of this work is to design a dual rotor machine and evaluate its improvised torque performance as applicable for the electric vehicle. In order to study the improvement, both the conventional model as used in Toyota Prius and the proposed structure are modelled, analysed and evaluated using finite element tool. Magnetic transient analysis is performed to analyse and evaluate the torque performance and magnetic flux characteristic of both the machines. The proposed machine with its position of the magnet exhibits an improvement of 51.73% of motor constant square density and 20.71% of average torque density compared to conventional machine.

Keywords: Electric Vehicle, Permanent Magnet Machine, Flux Linkage, Motor Constant Square Density, Torque Density

1. Introduction

The simplest solution towards preventing emission of excessive harmful gases is the implementation of Electric Vehicle (EV) with advanced propulsion machine to replace the generally used Internal Combustion Engine (ICE) vehicle [1]. EVs are getting popular nowadays in some countries because these vehicles are environmental friendly and energy efficiency. However, there are rooms of improvement can be made on optimizing the electric machine to increase the torque density of the electric vehicle. Generally, torque and power are the main factors towards propelling electric vehicles [2]. Thus, selection of machine is crucial in determining the torque performance of the electric system and the options are minimal at the moment.

From the manufacturer point of view, commonly used electrical machines for EV are induction, Permanent Magnet Synchronous (PMS), Switched Reluctance (SR) and the Brushless DC (BLDC) machine [3]. Induction motors are not suitable for EV because the power losses increase during high speed rotation causes the break-down torque in the constant power region which leads to decreased efficiency. The drawback of PMS machine is the excessive heat produced and armature reaction cause the demagnetization of machine.

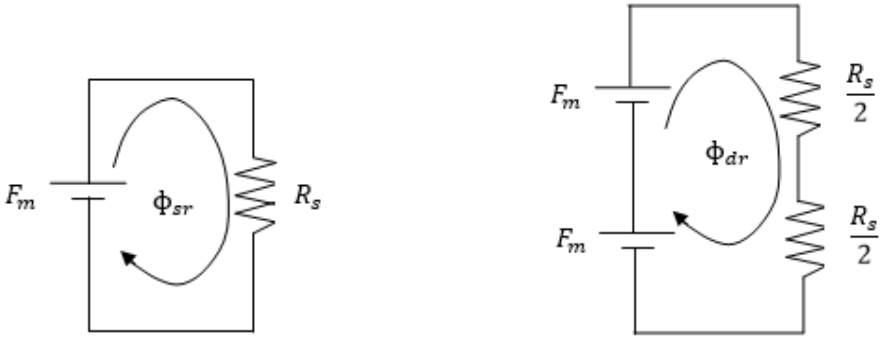
BLDC machines are mainly used for electric propulsion system for EV as these machines operate based on the amount of magnetic flux linkage produced between the electromagnet and permanent magnet forces [3]. The advanced development of permanent magnet provides high air gap flux density with significant of enhanced magnetic field properties. Hence, BLDC machines have been a popular topic recently for the development of electric vehicle [4]. BLDC machine is proposed for enhancing the torque producing capability with less heat produced for EV application.

Even though BLDC machine acquires the high torque producing capability, the generated magnetic field from the permanent magnet is fixed. The problems occurred where the fixed magnetic field fails to increase the torque producing capability by having difficulty to control the magnetic flux and thereby the issue of controlling the torque in a wide range prevails [4]. This problem is addressed by implementing flux weakening control method with the help of demagnetization of permanent magnets. However, this method would increase the production of heat from the permanent magnet which affects the properties of permanent magnet. For long term usage, the efficiency of the machine will decrease [4].

The dual air gap method is researched extensively in recent years for improvement on torque density and efficiency of various electrical machines. Higher torque density than the conventional single rotor machine without having the need to introduce field weakening control can be achieved using the above [5]. The rapid growth of electric propulsion system for EV has increased the demand of newly-developed machine for higher efficiency and performance. Hence, the development of double rotor machine has rooms for improvement on the electric propulsion system of electric vehicle [6]. Those machines are expected to be introduced in the near future. The objective of this work is to design and develop a new Double Rotor Single Stator Permanent Magnet (DRSSPM) machine based on new structure design.

2. Design Concepts

Brushless DC (BLDC) permanent magnet machines perform based on the capability of reducing the distributed opposing air gap flux linkage. The resultant air gap flux linkage of the machine is known as the torque producing point [7]. Figure 1(a) shows the equivalent magnetic circuit of the conventional BLDC machine and Figure 1(b) shows the equivalent magnetic circuit of proposed double rotor machine. The concept of double air gap flux linkage minimizes the air gap length for reducing reluctance of the air gap. Minimizing the length of air gap between the stator and rotor poles enhances the magnetic flux linkage. However, there is limitations on reducing air gap due to the cogging torque occurred from the strong repulsive force of permanent magnet during rotation [8]. The design structure of stator pole and rotor pole play an important role in affecting the torque producing capability of the machine. The design of permanent magnet structure is crucial in determining the magnetic flux flow [9]. The magnetic flux linkage equation of conventional BLDC machine is shown in Eq. (1).



(a) Single air gap magnetic circuit (b) Double air gap magnetic circuit

Figure 1 Magnetic Equivalent Circuit

Single rotor air gap flux linkage,

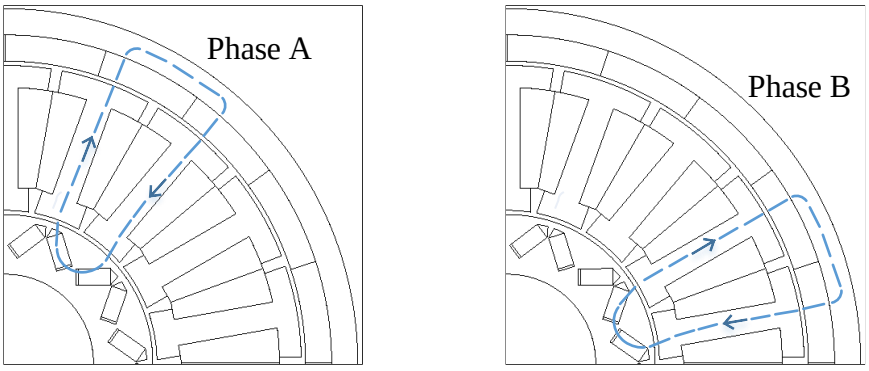
$$\Phi_{sr} = \frac{F_m}{R_s} \quad (1)$$

To enhance the torque performance of the machine, double rotor machine is proposed by introducing an inner rotor to the conventional BLDC machine. This method solves the issue of torque pulsation factor by reducing the air-gap length of the machine. The concept of reducing air-gap length provides higher torque performance and reduces the reluctance of contact flux linkage area [9]. An increase in the number of permanent magnet of rotor poles contributes to a higher torque producing capability as both machines are designed in the same size. It can be concluded that the implementation of double rotor machine has double the magnetomotive force generated from the conventional machine. Hence, the magnetic flux linkage equation for double rotor machine is derived and given in Eq. (2).

Double rotor air gap flux linkage,

$$\Phi_{dr} = \frac{F_m + F_m}{0.5R_s + 0.5R_s} = \frac{2F_m}{R_s} \quad (2)$$

Figure 2(a) and Figure 2(b) show the flux flow inside the machine as the corresponding phases are sequenced to be energized. Initially when the current is injected to the coil of the machine, the magnetic field interacts with the permanent magnet field to provide the resultant force. This makes the motion of the rotating part into action and the sequential switching of the phases through the electronic makes the continuous motion. To determine the excitation sequence the rotor position is happened to be sensed using a hall sensor [8].



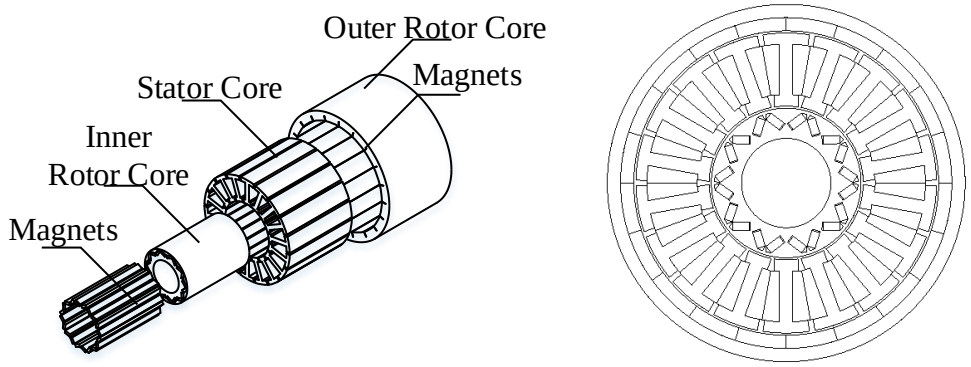
(a) Flux flow in Phase A (b) Flux flow in Phase B

Figure 2 Flux Flow inside the Machine

3. Structural Configuration

Figure 3(a) presents the exploded view of the proposed DRSSPM machine design for EV application while Figure 3(b) shows the 2D model of the proposed machine. The stator is made up of single stator core with T and T structure of stator laminations which used for coil winding of star connections and the stator core consists of 18 poles for winding configuration. Both outer and inner rotor are made up of laminated rotor cores with 20 poles configuration with each facing at the mutual axis. Permanent magnets are mounted on the surface of the outer rotor poles while the inner rotor poles are inbuilt with the similar size and properties of permanent magnet.

The double rotor design structure has more advantages than the conventional single rotor design as the design helps to fully utilize the leakage flux occurred in the stator core and solve the issue of torque pulsation occurrence [10]. Table 1 shows the dimension of the DRSSPM machine. The proposed machine is designed to maximize the flux linkage generated in the double air gap between the stator and the rotor which results in increasing the torque producing capability of the machine. Transient magnetic study and magnetic circuit analysis are performed for conventional BLDC machine and proposed machine through numerical and FEA tools.



(a) Exploded view (b) Front view

Figure 3 Proposed Machine

Table 1: Design Specifications of the Proposed Machine

Parameter	Value	Parameter	Value
All		Radius of Inner surface	50mm
Diameter of the Machine	108mm	Height of Magnet	4mm
Stack Length	32mm	Width of Magnet	15.7mm
Inner Rotor		**Stator**	
Number of Poles	20	Number of Slots	18
Pole Arc	18^o	Pole Arc	20^o
Radius of Outer surface	20mm	Radius of Outer surface	45.35mm
Radius of Inner surface	13.5mm	Radius of Inner surface	23.24mm
Height of Magnet	2.5mm	Radius of Outer coil	42mm
Width of Magnet	7.1mm	Width of Tooth (Outer)	3.35mm
Outer Rotor		Width of Tooth (Inner)	3.63mm
Number of Poles	20	Slot width Opening (Outer)	1.56mm
Pole Arc	18^o	Slot width Opening (Inner)	0.89mm
Radius of Outer surface	54mm		

4. Finite Element Analysis Method

The design structure of the machine is constructed using Finite Element Analysis (FEA) tool. The magnetic flux characteristic and torque characteristics of both machines are analyzed to determine the overall performance. Performing transient magnetic study is necessary to provide a more precise analysis of results since the performance of both machines is mostly dependent on the geometry [11]. Both conventional machine and proposed machine are designed and simulated using the same procedure shown in Figure 4. From the simulation results, the flux flow line, torque density, and magnetic flux direction of the design structure are analyzed. To obtain the numerical results, the torque characteristic and magnetic flux flow are plotted to obtain the torque value and the flux linkage. Figure 5 shows the flux linkage generated from the proposed machine at different rotational angle 0^o, 15^o, 30^o, 45^o, 60^o, and 75^o. The magnetic flux flow are distributed evenly for each slot segment.

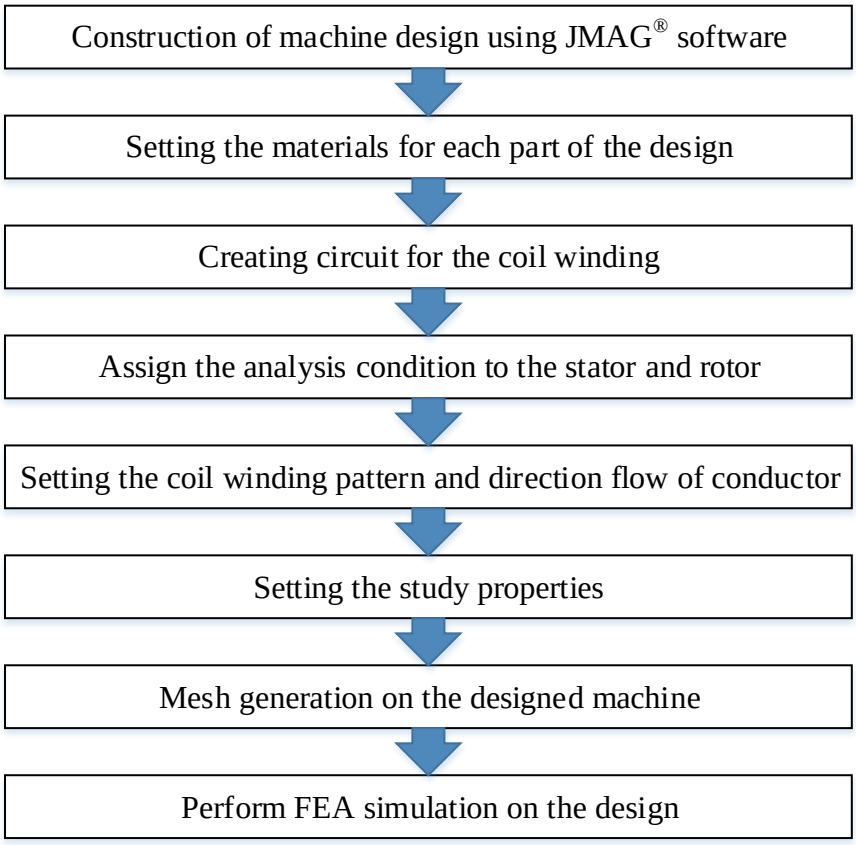


Figure 4 Flow of conducting FEA

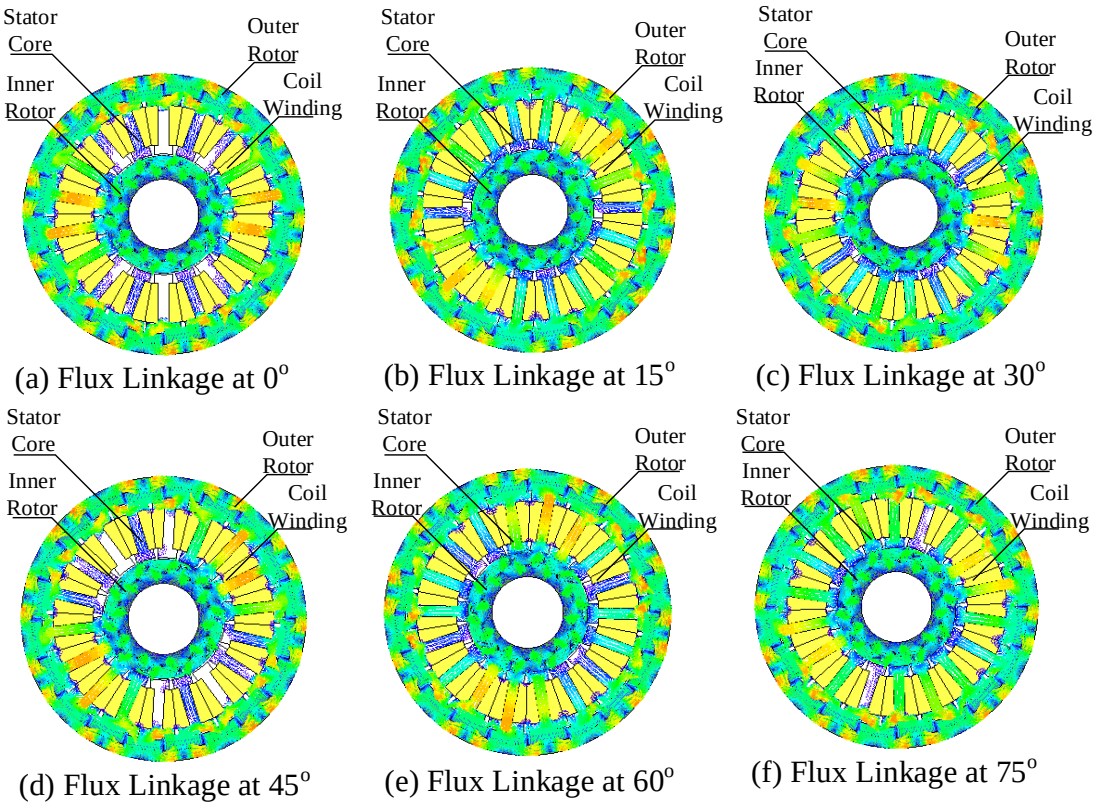


Figure 5 Flux flow for various rotational angle

5. Design Evaluation Parameters

Comparative assessment has been performed to compare the torque performance of both conventional BLDC machine and proposed machine by using parametric evaluation. Motor constant, torque constant, torque per unit volume and motor constant square density are used for determining the torque producing capability for each machine. Motor constant square density, G is very useful for determining the torque performance as the parameter includes the motor constant, volume of the machine and torque constant [12]. The formula for motor constant square density, G is given as Eq. (6). The other parametric equations are given in Eq. (3), Eq. (4) and Eq. (5).

Motor constant, $K_m = \frac{K_t}{\sqrt{I^2 R}}$ (3)

where K_t is the torque constant $[Nm/A]$, I is the maximum current injected to the machine $[A]$ and R is the resistance of coil $[\Omega]$.

Torque constant, $K_t = \frac{T_d}{I}$ (4)

where T_d is the average torque $[Nm]$, and I is the maximum current injected to the machine $[A]$.

Torque per unit volume, $T_m = \frac{T}{(\pi D^2/4)\, L_{stk}}$ (5)

where T is the average torque $[Nm]$, D is the diameter of the machine $[m]$, and L_{stk} is the stack length of the machine $[m]$.

Motor constant square density, $G = \frac{Km^2}{(\pi D^2/4)\, L_{stk}}$ (6)

where K_m denotes the capability of the machine $[Nm/A/W^{-(\frac{1}{2})}]$, D is the diameter of the machine $[m]$, and L_{stk} is the stack length of the machine $[m]$.

6. Results and Discussions

Figure 6 presents the torque produced from proposed DRSSPM machine without load when different input current of 21A and 63A are supplied to the machine. The objective is to study the relationship between the torque produced and the input current. The behavior of torque characteristic is similar at each input current. The higher the supplied input current the higher the torque producing capability of the machine. This means that the increase in current enhances the torque producing capability of the machine. However, every machine has different rated current due to the thickness of the coil winding that withstand the amount of heat. The number of winding is inversely proportional to the thickness of the armature conductor. Thus, machine with lesser coil winding can be used for thicker wire to allow larger current to flow.

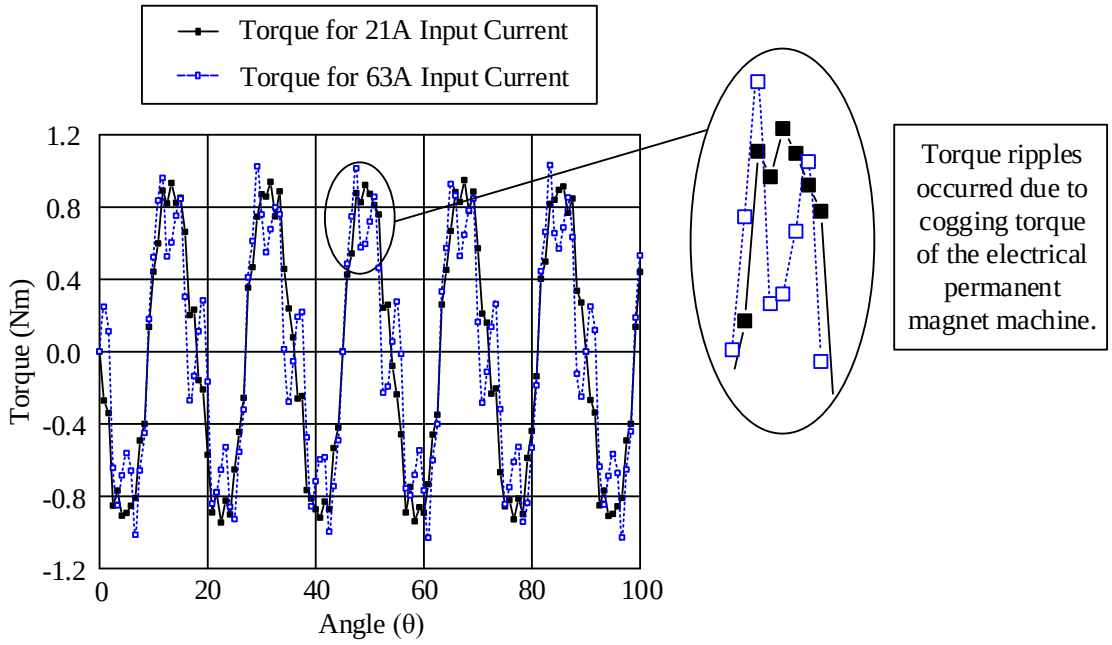


Figure 6 No-load torque for various input current

Figure 7 presents the torque characteristic determined from both conventional and proposed machines with no load from angle of 0º until 36º when three phases current is supplied to both machines. In the transient magnetic study, both machines are operating at 21A rated current while rotational speed of 300rpm is given for both machines at the frequency of 50Hz. The proposed DRSSPM machine has an average torque of 0.9484Nm which has an improvement of 20.71% in comparison to conventional SRPM machine. The dual air gap provides a better torque performance of proposed machine compared to conventional machine.

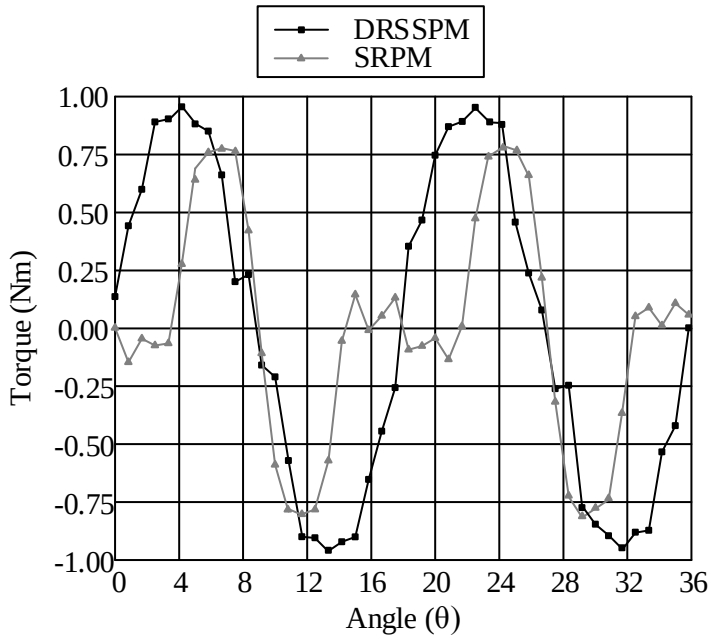


Figure 7 Static torque characteristic

Figure 8 illustrates the speed torque characteristic of the proposed DRSSPM machine. Generally, torque is inversely proportional to the speed of the output shaft. Initially, the torque is at maximum which is stall torque but the shaft is not rotating. The torque becomes constant over a wide range of speed because the torque happened in constant power region during this period. When the speed reaches the maximum, no torque is produced at this point to the motor shaft. The maximum speed occurred at this point considered as no load speed where demagnetization process occurred.

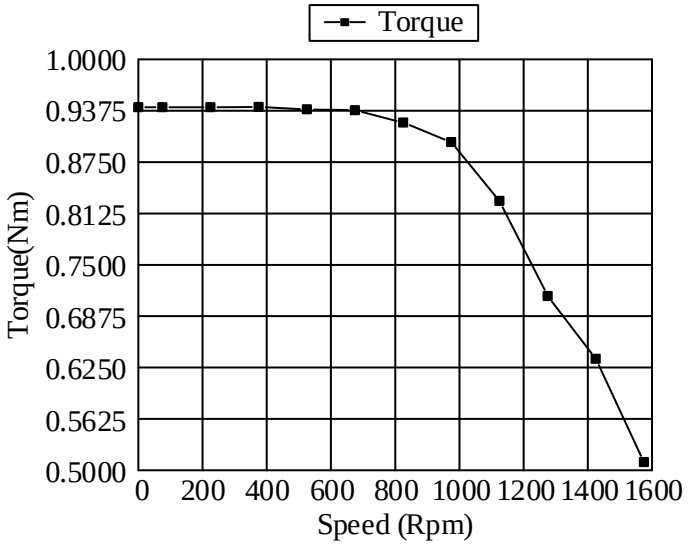


Figure 8 Torque speed characteristic

Figure 9 describes the power produced by the proposed machine when various speed is applied to the machine. During low-speed of rotation, the power required for the machine is low. The power required for machine increases during the starting of machine because large currents are needed to produce high torque. The power increases if the rotational speed increases until the power reaches the constant region. When the machine achieves a particular point of speed, the torque starts to reduce while the power becomes constant for a wide range of speed.

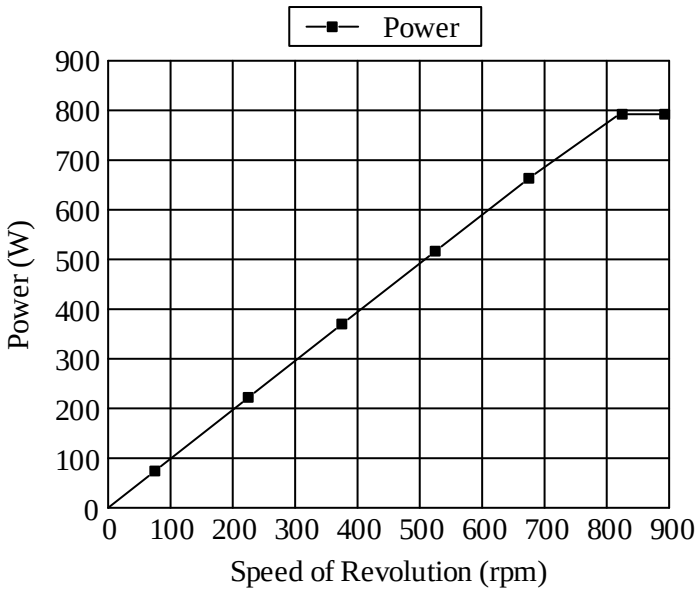


Figure 9 Power-speed characteristic

Table 2: Overall comparative evaluations

Parameter		SRPM	DRSSPM
$\boldsymbol{I}$	$[\boldsymbol{A}]$	20.83	20.83
$\boldsymbol{V}$	$[\boldsymbol{m^3}]$	2.6 x 10^{-4}	2.6 x 10^{-4}
$\boldsymbol{T_{max}}$	$[\boldsymbol{Nm}]$	0.7980	0.9832
$\boldsymbol{T_{min}}$	$[\boldsymbol{Nm}]$	0.7764	0.9595
$\boldsymbol{T_{avg}}$	$[\boldsymbol{Nm}]$	0.7857	0.9484
$\boldsymbol{T_m}$	$[\boldsymbol{Nm/m^3}]$	3069.23	3781.54
$\boldsymbol{K_t}$	$[\boldsymbol{Nm/A}]$	0.03831	0.04719
$\boldsymbol{K_m}$	$[\boldsymbol{Nm/A/W^{-(1/2)}}]$	5.8160 x 10^{-3}	7.1641 x 10^{-3}
$\boldsymbol{G}$	$[\boldsymbol{Nm^2/A^2/W/m^3}]$	0.1301	0.1974
$\boldsymbol{T_{improvement}}$		-	20.71%

Table 2 presents the overall comparative evaluation for conventional SRPM and proposed DRSSPM machines computed from the equations in design evaluation parameters. These machines are supplied with current source of 20.83A. Thus, the machines were provided with the input voltage of 12V due to the power rating, 250W of these machines. The parameters of $T_m, K_t, K_m, and\ G$ are computed based on the equations as mentioned earlier. The proposed DRSSPM machine has an improvement of 51.73% of motor constant square density compared to the conventional SRPM machine.

7. Conclusions

A new BLDC double rotor permanent magnet machine for torque improvement for electric vehicle application is presented. The introduction of inner rotor added to the conventional rotor increases the magnetic flux linkage generated from the machine. Magnetic transient study and torque analysis are conducted for both machine using FEA tools to study the characteristic. The proposed machine has an enhancement of 51.73% motor constant square density and 20.71% average torque compared to the conventional machine. Having the same volume with the conventional machine, the proposed machine improvises the torque performance for electric vehicle application.

References

[1] W. L. Soong and T. J. Miller, "Field-Weakening Performance of Brush-less Synchronous AC Motor Drives," *Proc. IEE-Elect. Power Application,* vol. 141, no. 6, pp. 331–340, Nov. 1994.

[2] C. C. Chan, K. T. Chau, and J. Z. Jiang, "Vehicles Drives for Electric Vehicles," *IEEE Trans. On Industrial Electronics*, Vol. 43, no. 2, April 1996.

[3] J. Lindstrom, "Development of an Experimental Permanent-Magnet Motor Drive," vol. Licentiate, no. 312L, 1999.

[4] J.A. Tapia, F. Leonardi, T.A. Lipo, "Consequent-Pole Permanent-Magnet Machine with Extended Field-Weakening Capability," *IEEE Trans. On Ind. Applicat.,* vol. 39, no. 6, pp. 1704–1709, Dec. 2003.

[5] X. Zhu and M. Cheng, "A Novel Stator Hybrid Excited Doubly Salient Permanent Magnet Brushless Machine for Electric Vehicles," *Journal of Electrical Engineering and Technology*, vol. 1, no. 2, pp. 185–191, 2006.

[6] N. Hashemnia and B. Asaei, "Comparative study of using different electric motors in the electric vehicles," *IEEE Trans. On Electrical Machines,* October. 2008.

[7] L. Jian and K. T. Chau, "Design and Analysis of an Integrated Halbach-magnetic-geared Permanent-magnet Motor for Electric Vehicles," *J. Asian Electr. Veh.*, vol. 7, no. 1, pp. 1213–1219, 2009.

[8] J. Choi, S. Jang, H. Park, and K. Kim, "Characteristic analysis on synchronous machine with double-side permanent magnet rotor for flywheel energy storage system in EV," pp. 1223–1227, 2012.

[9] C. Liu and K. T. Chau, "Electromagnetic Design and Analysis of Double-Rotor Flux-Modulated Permanent Magnet Machines," *Progress In Electromagnetics Research,* vol. 131, no. 1, pp. 81–97, Sep. 2012.

[10] D. G. Dorrell, S. Member, A. M. Knight, S. Member, and L. Evans, "Analysis and Design Techniques Applied to Hybrid Vehicle Drive Machines — Assessment of Alternative IPM and Induction Motor Topologies," vol. 59, no. 10, pp. 3690–3699, 2012.

[11] A. C. V, M. Norhisam, I. Aris, M. H. Marhaban, D. Ahmad and M. Nirei, "Double-Rotor Switched Reluctance Machine (DRSRM): Fundamentals and magnetic circuit analysis," *Research and Development (SCOReD), 2011 IEEE Student Conference on*, Cyberjaya, 2011, pp. 294-299. doi: 10.1109/SCOReD.2011.6148753

[12] S. Niu, S. L. Ho, and W. N. Fu, "A Novel Double-Stator Double-Rotor Brushless Electrical Continuously Variable Transmission System," vol. 49, no. 7, pp. 3909–3912, 2013.

[13] P. Xu, X. Liu, K. Shi, F. Xiao, and A. D. Topology, "Design and Analysis of a Dual-Rotor Radial Flux Permanent-Magnet Generator," pp. 669–672, 2014.

[14] R. Hariyadi, "Improvement in Torque Density of the Double Rotor Switched Reluctance Motor," ," *Taylor's University School of Engineering Thesis submission,*. December, 2014.

[15] Lam Pin Wen, "Design of a Novel Double Rotor Interior Permanent Magnet Machine for Hybrid Electric Vehicle Application," *Taylor's University School of Engineering Thesis submission*, pp. 64–70, Dec. 2014.

[16] Chong Wei Hsiung, "A New Permanent Magnet Synchronous Machine For Small Battery Operated Vehicle," *Taylor's University School of Engineering Thesis submission*, pp. 1–59, June. 2015.

eureca 2016- Conference paper
Paper Number 2EE4

A new intelligent STATCOM controller for transmission lines

Husain Ali Salman, *Charles R. Sarimuthu, Aravind C.V, K.C Fung

School of Engineering, Taylor's University Lakeside Campus, Malaysia

*CharlesRaymound.Sarimuthu@taylors.edu.my

Abstract

Power transmission lines infrastructure composes of a large group of components. Transmission lines are subjected to disturbances which hinder the efficiency of power transmission. Disturbances such as faults or component malfunctions affect the overall power quality negatively. One of the main power quality issues is voltage fluctuations. To maintain a high power quality regular active maintenance is required, which gives extra costs in order to minimize costs. Hence, it is more effective to automate the process by introducing power electronics devices in a voltage regulating system to control the amount of reactive current injection to optimize voltage magnitudes of transmission lines and load buses at a power system. Shunt Static Synchronous Compensator (STATCOM) is a Flexible AC Transmission System (FACTS) device used for voltage regulation based on the reactive power exchange concept. It needs a controller to input a control signal in order to guide STATCOM operations. The conventional controller for STATCOM uses Proportional Integral closed loop parametric gain tuning technique to produce outputs that govern STATCOM. However, it has been proved that by tuning this controller with artificial neural networks better results are achieved.

1.0 INTRODUCTION

Reactive power is the phantom power that cannot be physically sensed. It is the power sacrificed in transmission lines to provide power flow from supply to loads. The ratio of amount of power sacrificed to amount of power utilized is given by the power factor. The power factor is the ratio of real to apparent power. It is ideal at 1 power factor or also known as unity. However, in practical this factor is not possible, therefore, power factor is maintained closer to unity to achieve more efficient power flow. Power factors can be lagging or leading depending on the reactive element present in a power system or machine. Lagging power factor means that load is inductive as it consumes reactive power.

Leading power factor means that load is capacitive and is producing reactive power. Leading and Lagging factor represent the relationship between current and voltage, in

leading current leads the voltage waveform, in lagging current is late behind the voltage waveform. At unity both waveforms are on the same point [1].

Reactive power availability in a power system is proportional to voltage levels. Hence, by control of reactive power voltage levels can be controlled and regulated. A STATCOM is composed of a Voltage Source Convertor (VSC) which is a power electronic switching device. In STATCOM, VSC such as Insulated Gate Bipolar Transistor (IGBT) and Gate Turned Off Thyristor (GTO) are a bridge between the internal STATCOM DC side represented by a shunt capacitor bank to the AC power system managed. The AC side of the VSC is connected a transformer which coupled with a reactor. When the voltage at the power system is greater than nominal values, STATCOM absorbs the excess reactive power content towards it DC voltage side to charge the capacitors and also drop voltage on the power system buses. Vise-versa when the voltage at power system is lower than nominal values, the STATCOM injects reactive current to the power system to increase voltage level. The energy flow from its internal DC side through the transformer then the reactor produces equivalent reactive current to control voltage. The direction of reactive power flow between the transmission system and DC side of STATCOM along with the amplitude of reactive power exchange is determined by the VSC firing angle.

The concept of compensation for bus voltages is through the injection or absorption of reactive current when it is insufficient or exceeding limits. This affects the voltage proportionally. The compensation is triggered by the firing angle of the power electronic device. Hence, controlling the angles is implemented to balance the voltages as required [1].

2.0 RESEARCH METHODOLOGY

2.1 Scientific Approach

Current flow direction represents direction of power flow too. Current flows from the voltage point with the higher angle to that with lower angle. Therefore, by control of phase angle of voltage at the power system and STATCOM reactive power flow direction is controlled. As for the amount of reactive power exchanged which is proportional to a voltage change, it is determined by the reactive current amplitude. The reactor on the AC side of STATCOM control the amount of reactive current injected. Therefore, by controlling impedance reactive current is varied. The concept explained here is seen in Equations (1) and (2).

$$\boldsymbol{I} = \frac{\boldsymbol{V_S - V_R}}{\boldsymbol{Z}} \quad \textbf{(1)}$$

$\boldsymbol{I}$ Line Current
$\boldsymbol{V_S}$ Sending-end Voltage
$\boldsymbol{V_R}$ Receiving-end Voltage
$\boldsymbol{Z}$ Impedance

$$\boldsymbol{Q = \sqrt{3}VISin\theta} \quad \textbf{(2)}$$

$\boldsymbol{V}$ 3_{ph} L-L Voltage
$\boldsymbol{\theta}$ Phase angle

2.2 Conventional PI STATCOM construction

STATCOM's main operation is the exchange of voltage between a potential DC source coupled with a link capacitor and the transmission system. STATCOM's are connected usually in shunt to the bus most sensitive to transients and disturbance in terms of voltage change, which is usually the middle point of the transmission lines [2].

In STATCOM's, VSC are used for PWM to select the direction of flow of reactive current and its amplitude, this is achieved by varying the firing angle [2]. When the firing angle is negative the flow of reactive current is from DC source to the AC transmission system, and vise-versa when the firing angle is positive. This is feasible given that STATCOM's can alter the reactance of the reactor coupling it to the power system it is governing.

STATCOM operation starts with a measure of voltage on the power system main bus. After the measurement are obtained in 3-phase they are transformed into dq-axis reference. This is because controlling 3phase require integral-derivative equations which are quite complex in nature to model and use for control. dq0 park transformation technique, converts a 3phase signal into a 2 signal value by eliminating once of the phases. Hence, now the system deals with 2 phase dq-axis currents and voltages i_d, i_q, V_d and Vq. Those newly computed values are compared to reference values which represents the power system governed at its equilibrium value. The difference between the actual and reference values is computed. The V_{dq} values are used to output the modulation index which is proportional to the phase angle. While i_q represents the reactive power exchange factor, which is proportional to the firing angle. Modulation index and firing angles are computed by two PI control schemes internally in STATCOM.

Hence, to summarize reactive power exchange in STATCOM is provided conventional PI controllers apply proportional (Kp) and integral (Ki) closed loop gains based on dq-axis values of voltage and currents. To produce the reactive current at the maximum capabilities of the STATCOM.

To improve the performance of the STATCOM and power system measurements and control, Phasor Measurement Units (PMU) are applied. As a results, phase angles are directly provided from state estimation to state measurement. Besides that, data is provided rapidly on a synchronized sub-second basis providing high data update rate for quick computation. Lastly, it better for dynamic behavior observing and post disturbance assessment [3].

Nevertheless, it is argued that the conventional PI controllers have several problems. These problems, include failure to compensate at loading cases which differ at high margins from the original loading the power system can handle, this is due to its weak voltage stability enhancement margins. Moreover, it is suggested that even at loading cases which vary merely from the original loading case the PI controller compensation efficiency is low in comparison to more advanced controllers in terms of settling time, voltage regulation level and smoothness of response change. To examine those claims the PI controller will be tuned with artificial neural networks.

2.3 Artificial Neural Networks

Neural networks are intelligent artificial systems to find hidden gems in the data they are provided with. They can be accepted as a technique which belongs to a broader category of techniques known as data mining. Those tools are presented with inputs which lead to a certain selection of outputs, when the data is presented to neural networks they seek to find a pattern in which the target output is achieved. This is achieved through the hidden neurons in the neural networks, they fit data and predict resulting input from a given output.

Artificial Neural Networks (ANN) have the advantage over classical control schemes in terms of nonlinear relationship computation capability. ANN also works well with continuous and categorical data while some other data mining tools fail. ANN's act in the same manner as a brain of a computer, where active hidden neurons are used to process data presented [4].

There are various types of neural networks. The general construction of neural networks is made up of 3 main layers. The first layer is the input layer, the second layer consists of the number of hidden neurons selected by user, the third layer is the target output layer, while the last layer is an optional bias layer of the hidden neurons. Hidden neurons find similar characteristics in inputs, to simply and group input data into categories for faster computation of target output. All input layers are connected to all hidden neuron layers, which are also connected to all output layers [4].

From those hidden neurons, ANN can achieve "self-learning", the hidden neurons classify the signal coming from the weighted sum inputs, it is impossible for the user to fully understand the scheme in which the hidden neurons classify input data. However, it can be understood in the sense that every intermediate or output neurons has an "activation function" which is a sigmoid, to the weighted input sum. It triggers a set of neurons from binary state 0 to 1 where this neuron "fires", depending on the number of neurons fired of a system composing of several hidden neurons the target output that meets a specific input is produced after neurons recognize a pattern given. Then output signal from the neurons layer is passed to the outputs which also have activation functions [4].

To find the best set of weights sum for the inputs training techniques are used. The most commonly used method of training is back-propagation. Where weights are the links between each input and hidden layer, each hidden layer and each output. Depending on the number inputs, number of samples for each inputs, number of outputs and samples for each output for a system, the number of hidden neurons is continuously altered to find the best matching neurons that give the weighted sum with least Mean Squared Error (MSE).

Manually, this can be done by trial and error through altering the number of hidden neurons, recording the output target value and comparing it to desired output target to realize the error margin. The process is repeated with different number of hidden neurons until the most optimal number of neurons is selected. This is important because lack or excess of neurons will lead under or over fitting. After the optimal number is selected, the network can be trained.

In Matlab, data samples of inputs and outputs, is divided to 3 sections. Training, validation and testing data. The user can select the percentage from the samples allocated to each section with the training process using atleast 50% of the samples. The software allows the use to select from different algorithms to categories the data [4].

2.4 ANN execution Scheme

After studying the PI STATCOM structure. Two points of control were determined. The phase angle and the firing angle. The ANN controller was selected to control the phase angle output of the PI controller in the degree needed to regulate a specific voltage sag/swell value on the power system buses. ANN can derive the relationship from given input and output sets.

To provide samples of possible transients, active power demands at network is maintained and reactive power content at load is varied. When this happens it affects voltage levels on STATCOM buses non-linearly. Voltage at transmission lines for each reactive power variation is measured and the phase angle needed to correct this voltage is computed manually in the Simulink by trial and error. Each input and its output is a data set sample. Multiple Samples need to be fed to the ANN in order to train it to provide accurate results and relationship between inputs and output.

The ANN control plant follows a Single Input Single Output control strategy (SISO), with the voltage at the transmission point being the input and the corresponding angle to compensate the transients is output for that input. A data sheet is made up at different loading cases and fed to artificial neural networks.

2.5 ANN optimization

The neural network in the project was designed using Matlab Nerual Fiting Tool. The inputs and outputs of the ANN are fed to the fitting tool with selection of percentage of samples allocated for training, validation and testing.

It is preferred to keep the training percentage as high as possible without neglecting the other configurations. This is because a solid training is important for an effective controller. In this case 70% of samples is given for training while the other two shares the remaining percentage. Number of hidden neurons and one of the three backpropagation optimization algorithms available is selected. Before implementing the system, from the regression plot it possible to foresee the performance depending on the wellness of the fit of samples on the regression plot.

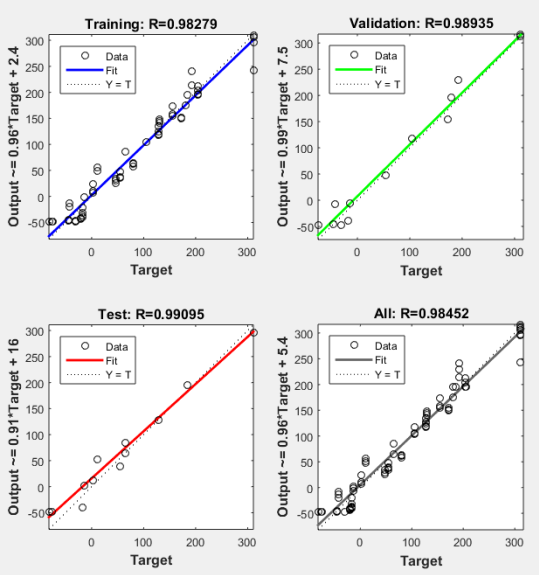


Figure 1.0 Result with small number of samples

The Bayesian regularization back propagation is selected to process the input and output data in the hidden neurons. This is because it minimizes the weight of input functions by neglecting other inputs in the calculations. Therefore, they use less number of neurons. They have the advantages of improving overall generalization of the network and to avoid overfitting by cancelling out unwanted samples. An increased percentage of error of samples plot on the regression curves results in more random output due to incapability of full input data reading and analysis.

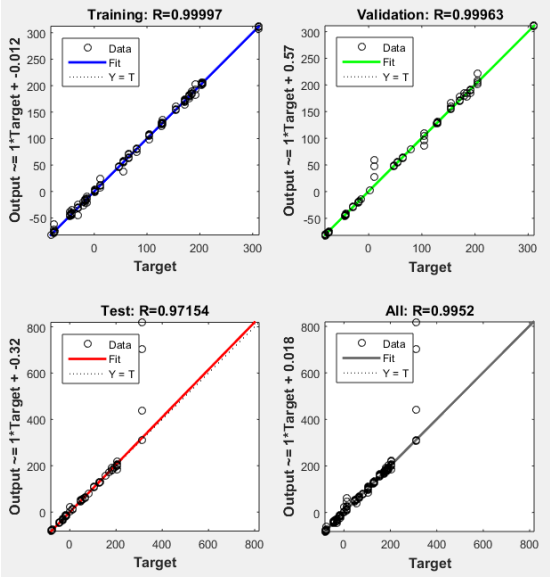


Figure 2.0 Result with more samples

2.6 Comparison scheme between PI STATCOM and ANN tuned PI STATCOM

The effectiveness of both controllers is tested on a power transmission system. The power transmission system parameters are given as following.

Generator 500KV, 700MVA
Transmission lines 300Km
Load 600MW

The optimal load the network handles is 670MW. However, when the loading changes voltage transients occur and the controller's voltage regulation response can be measured then. The power networking modelling and simulations were performed using Simulink

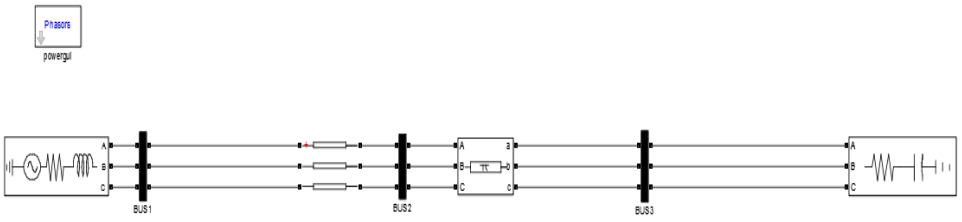
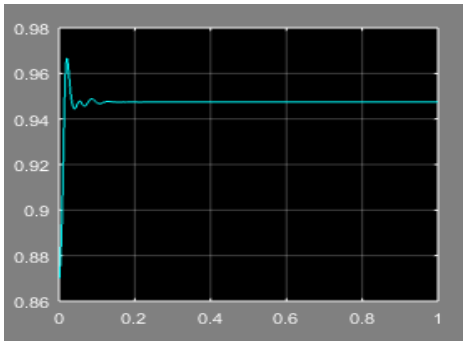


Figure 3.0 Test network assembly in Simulink

Table 1.0 ANN datasheet

Transmission line Vpu	Angle
1.7084 ~ 1.464	311°
1.464 ~ 1.45	192°
1.45 ~ 1.3996	204°
1.3996 ~ 1.3401	185°
1.3401 ~ 1.2939	205°
1.2939 ~ 1.2162	180°
1.2162 ~ 1.1816	155°
1.1816 ~ 1.1712	172°
1.1712 ~ 1.1524	130°
1.1524 ~ 1.1243	128°
1.1243 ~ 1.0889	105°
1.0889 ~ 1.048	65°
1.048 ~ 1.0383	80°
1.0383 ~ 1.0287	11°
1.0287 ~ 1.0167	55°
1.0167 ~ 1.0095	47°
1.0095 ~ 0.9953	2°
0.9953 ~ 0.9849	-14°
0.9849 ~ 0.9718	-42°
0.9718 ~ 0.9345	-17°
0.9345 ~ 0.9085	-20°
0.9085 ~ 0.8713	-45°
0.8713 ~ 0.8353	-30°
0.8353 ~ 0.8100	-76°
0.8100 ~ 0.7876	-82°
0.7876 ~ 0.765	-75°

4.0 RESULTS AND DISCUSSIONS



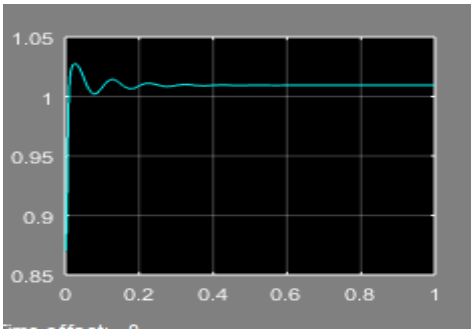
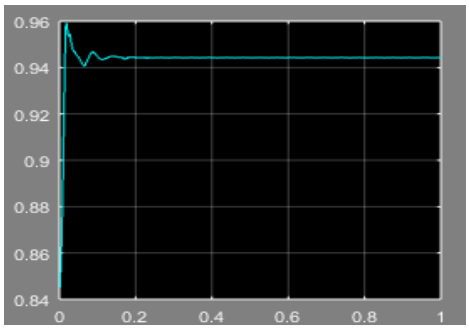


Figure 4.0-5.0 PI and ANN STATCOM response (output voltage) on 900MW+100MVar



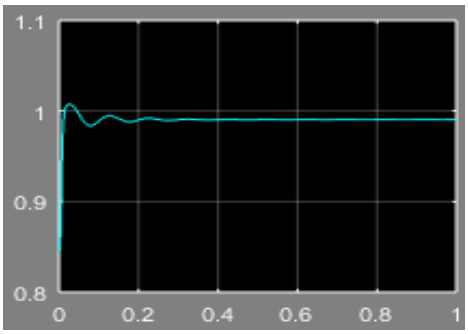
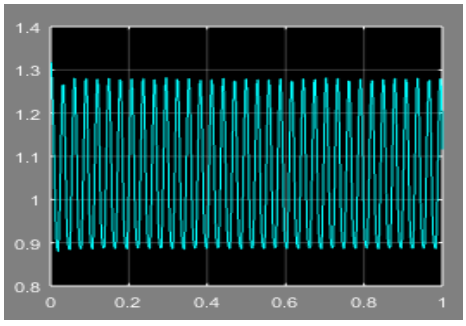


Figure 6.0-7.0 PI and ANN STATCOM response (output voltage) on 900MW+200MVar



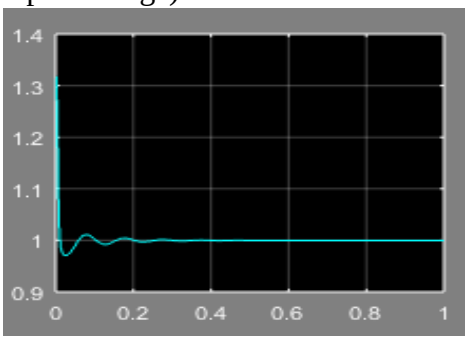
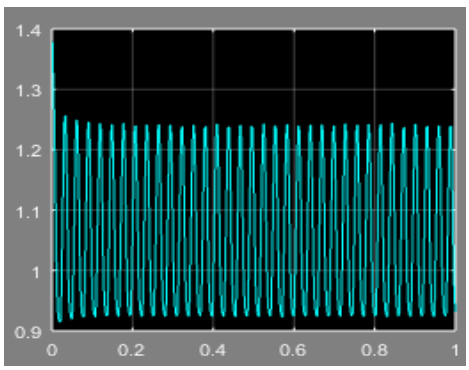


Figure 8.0-9.0 PI and ANN STATCOM response (output voltage) on 50MVar



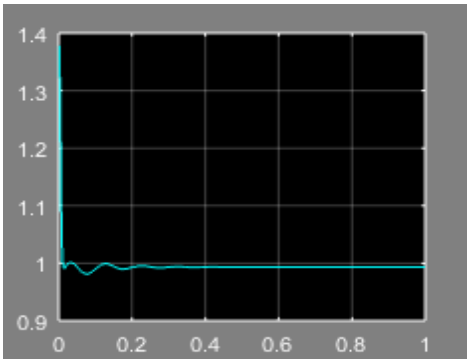


Figure 10.0-11.0 PI and ANN STATCOM response (output voltage) on 100MVar

From Figure 4.0 -11.0, it is observed that the output voltage response presented by ANN controller is better than that of the conventional PI controller in operating the STATCOM in capacitive and inductive mode.

In the capacitive modes, the ANN controller has shown the capability to provide the closest output value to the nominal value in comparison to PI controller. Whereas in the inductive modes the PI controller continued oscillating and didn't achieve an output set point, this is because it exceeds its voltage stability enhancement margin. Meanwhile with ANN control STATCOM managed to smoothly regulate transmission line voltage.

5.0 CONCLUSION

ANN can be adapted to achieve a certain target through different training techniques. The design of artificial neural network depends on the how neurons are activated. The advantage it has over other controllers is that it involves human interaction for training purposes which enables the user to detect and prevent computing errors. Furthermore, create automatic control scheme and non-linear relationship between inputs and output which enables the design of multiple, reliable and flexible control procedures.

To sum up, the performance of the conventional PI STATCOM controller is tested against ANN tuned PI controller. The voltage of the weak point in the transmission lines is the input while the target of the ANN is the phase angle to manipulate flow and amplitude of reactive current. The results have shown that the ANN controller is superior to the PI controller in performance and with training it was capable of eliminating PI controller issues and enhancing its performance.

REFERENCES

[1] Md. Arifur Kabir, Md. Nazrul Islam and Yashiro Kazushige, "Modelling of Shunt FACTS Device to Improve Voltage Dynamics", International Journal of Engineering Research & Technology (IJERT), Vol. 2 Issue 5, pp 491- 498, 2013.

[2] Giani, Annarita, Eilyan Bitar, M. A. Garcia, Miles McQueen, Pramod Khargonekar, and Kameshwar Poolla. "Smart grid data integrity attacks: characterizations and countermeasures π." In Smart Grid Communications (SmartGridComm), 2011 IEEE International Conference on, pp. 232-237. IEEE, 2011.

[3] Wang, Huai, Ke Ma, and Frede Blaabjerg. "Design for reliability of power electronic systems." In IECON 2012-38th Annual Conference on IEEE Industrial Electronics Society, pp. 33-44. IEEE, 2012.

[4] G.S.Naganathan, C.K.Babulal, " Voltage Stability Margin Assessment Using Multilayer Feed Forward Neural Network" , *Applied Mechanics and Materials Vol. 573, pp 661-667, 2014*

[5] Ch.V.Rajkumar and Srihari Dattabhimaraju.P. " ANN Controlled STATCOM for Improving Transient Stability of the Power System". International Journal of Engineering Research & Technology (IJERT), Vol. 2 Issue 2, February- 2013.

Comparison of Proportional Integral Controller with and without Neural Network for DSTATCOM Operation

Koh Chong Fung, *Charles R.Sarimuthu, Aravind C.V

School of Engineering, Taylor's University Lakeside Campus, Malaysia

CharlesRaymond.Sarimuthu@taylors.edu.my

Abstract
In power system, major industrial devices such as transformers and some other synchronous machines requires reactive power for sustaining magnetic field. Reactive power is describes as the movement of background energy within an alternating current (ac) system arise from the creation of electromagnetic field. Reactive power is necessarily needed to ensure that voltage is kept constant in order for active power transfer through the transmission lines. If there is insufficient of reactive power, voltage sags occurs and cause no power to be deliver to the load at the transmission lines. This reactive power deficiency in utility distribution network can cause major industrial loads and any other relevant commercial operations to stop functioning, resulting in huge losses to the economy. Therefore, it is important to take relevant steps in identifying the prominent concerns of power quality disturbances and hence what measures can be done to enhance the quality of power recommended. One of the ways to mitigate power quality in distribution system is the use of FACTS devices. Studies has shown that DSTATCOM proves to be the most reliable and efficient devices for distribution system. In this paper, a Neural Network based PI controller and a PI controller are designed to monitor and regulate the voltage at the load end of the distribution system. A well-trained Neural Network controller was created with a simple structure based on the number of hidden layers and number of neurons per layer used. Each controller was designed with suitable gains to ensure that the load voltage response is within a specific steady state error. By applying MATLAB simulation, both controllers were compared in term of minimal settling time on the voltage characteristics while different types of load applied. These Simulink results were obtained by performing through qualitatively and quantitatively testing. Thus, these results concluded that the Neural Network based PI controller is a better controller for DSTATCOM in distribution system because it has satisfactory compensation of voltage sag capability, better reliability and better feasibility compared with PI controller.
Keywords: Neural Network, DSTATCOM, Distribution system, Voltage control.

1. Introduction

In the current era of electrical power systems, the electrical power system structure can be mainly divided into four components: generation, transmission, distribution and utilization. However, the voltage ratings in a power system can be divided into three levels: the generation level (10kV–25kV). The power is generated at a relatively low voltage level to keep high voltages insulation of the generator armature within boundary, the transmission level (110kV–420kV), and the distribution level (10kV–72kV). Electricity is produced in generating stations which consists of large amounts of generators that supply electrical power, the transmission system then carries the electrical power from the generating station to the load station and finally the distribution system feeds electrical power to nearby cities and factories. Power is supplied to the customers at various voltage levels. Heavy industrial consumers connect from 150 kV until 10 kV voltage levels and households connected to a 0.4 kV voltage level [1]. The change in voltage levels is done by transformers.

The fast development of reliable semiconductor devices leads to new possible power electronics configuration for better power transmission and load flow control. In the society that we are living now, the society's dependence on electricity has become critical and the social impact of failing power system is beyond imagination. Power disturbances occur on every electrical system, the affectability of today's complex electronic devices make them more vulnerable on the quality of power supply. For example, a short period of disturbances can cause computer data to be hay wired, interrupted communications, and equipment failure [2]. A spike of power voltage can bring even harm to valuable equipment. Thus, engineers are responsible for ensuring that the power system supplies reliable power to its customers at rated voltage and frequency under allowable load fluctuation limit. There is a wide variety of power quality disturbances such as transient overvoltage/swells, harmonics distortion, voltage sags, voltage flickering, impulse transients and interruptions [3]. Currently, one of the most common issues faced in power systems is the occurrence of voltage sag. Voltage sag is defined as the decrease in voltage magnitude for a short period of time, caused by a fault usually within the utility system, customer's facility or the existence of large amount of increase in current in electrical devices. This fault may cause relevant sensitive equipment to trip or hinder any other motors connected to the power system, resulting in poor power quality. In an industry, voltage sag occurs frequently in the transmission and distribution system and cause major severe problems and economical loss. Power quality permeates through the electrical industry and plays a crucial role in conceiving an appropriate solution for reliable power supply worldwide. As the concept of power electronics continue to advance, semiconductor devices opens up new possible power electronics configuration to aid power transmission and load fluctuation control. One of the ways to mitigate power quality in transmission and distribution system is the use of FACTS devices. Among these devices, DSTATCOM proves to be the most reliable and efficient devices for voltage regulations [4]. Its applications are for sensitive loads that may have been affected by voltage fluctuations in the ac system. A suitable adjustment on the phase and voltage magnitude of the DSTATCOM output voltage allows satisfactory reactive power exchange between the DSTATCOM and the system.

In this paper, a Neural Network based PI controller and PID controlled are designed and simulated to control the voltage at the load end of a distribution system

as the load varies. The comparison between these two controllers is to identify the best controller that can be easily generated for the DSTATCOM. The well-trained Neural Network controller will be generated in a simple structure based on the number of hidden layers and number of neurons per layer. Both controllers will be adjusted to a suitable gain based on the feedback which contains the changes in voltage error. These gains should keep the output voltage magnitude within the minimum steady state error.

2.0 Research Methodology

2.1 Overall Methodology Process Flowchart

The simulation is done by following the process as shown on Fig. 1.

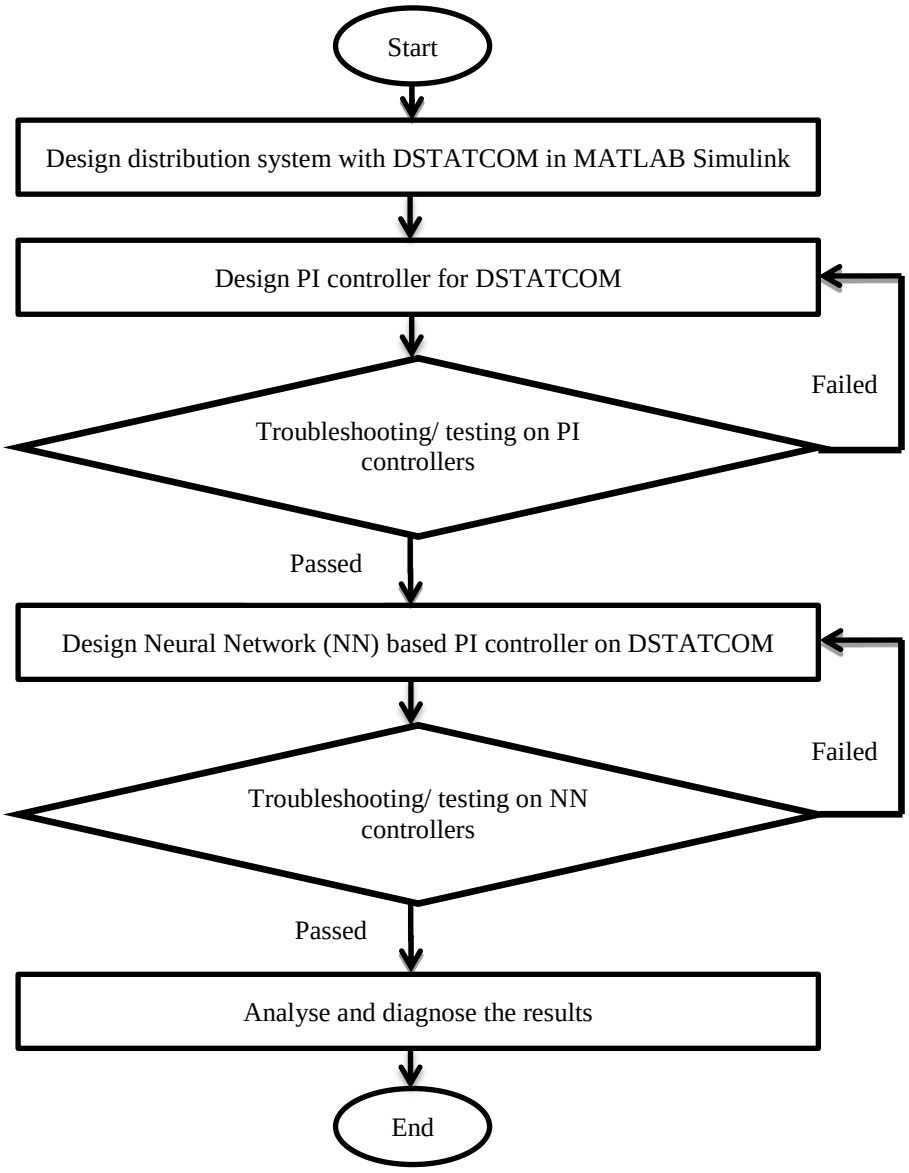


Figure 1. Flowchart for the methodology used.

In order to enhance the performance of the distribution system, the DSTATCOM will be connected to the distribution system. The DSTATCOM was

designed using MATLAB Simulink ver. 2016a. Firstly, the DSTATCOM is disconnected from the system to analyze the waveform of the output voltage with a 200kW resistive load. If voltage sags below 1 p.u, the DSTATCOM will be injected into the distribution system. The control scheme is based on the sinusoidal PWM and the DSTATCOM takes the measurement of the rms voltage at the load point. The measured rms voltage will then be compared with a reference voltage. The difference in value between these two voltage values generates the error signal and act as the controller's input. Such error will then be processed by a controller to produce out the required angle to eliminate the error to zero, which means adjusting the load rms voltage to become the reference voltage. In this paper, a well-trained Neural Network controller and PI controller will be created to test their performances under the effect of different load values of resistive loads, inductive loads and capacitive loads applied to the system. The response of the voltage control done by both controllers are obtained through MATLAB simulation.

2.1.1 Distributed Static Compensator (DSTATCOM)

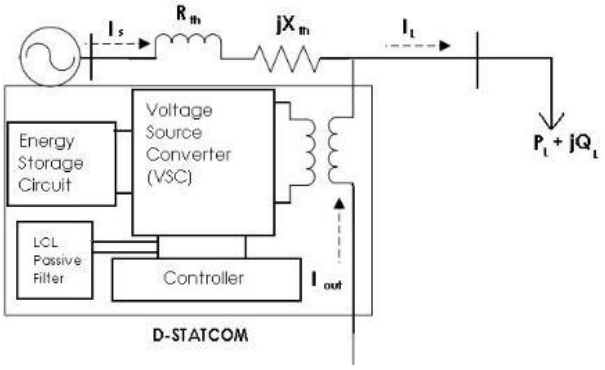


Figure 2. Schematic diagram of DSTATCOM [5].

The DSTATCOM is a custom power device utilized in power distribution system. It is low in cost, small in size, and has a quick response on dynamic load under disturbances [6]. DSTATCOM comprises of a voltage source converter (VSC), dc storage device, and a coupling transformer connected in shunt to the distribution system through the coupling transformer. The VSC changes the dc voltage across the dc storage device into a set of three phase ac output voltage. These voltages are in phase and coupled with the system through the coupling transformer's reluctance [6]. Suitable adjustments of the phase and magnitude of the DSTATCOM output voltage permits compelling control of active and reactive power exchange between DSTATCOM and the ac system. Such configuration permits the DSTATCOM to generate the injected shunt current, I_{sh} referred from Eq. (2), to correct the voltage sags by adjusting the voltage drop across the system impedance [5]. The formula for determining I_{sh} is:

$$\boldsymbol{I_{sh} = I_l - I_s = I_l - \frac{V_{th} - V_l}{Z_{th}}} \quad (1)$$

$$\boldsymbol{I_{sh} \angle \eta = I_l \angle -\theta - \frac{V_{th}}{Z_{th}} \angle (\delta - \beta) + \frac{V_l}{Z_{th}} \angle -\beta} \quad (2)$$

Where,

I_l = load current
V_l = load voltage
Z_{th} = thevenin impedance
I_s = source current
V_{th} = thevenin voltage

2.1.2 Proportional Integral (PI) controller

The purpose of the control scheme is to ensure that the voltage magnitude remains constant at the point where the sensitive load is connected when power disturbances is present. The control system measures the rms load voltage whereby reactive power measurement is not required. The VSC switching strategy depends on the sinusoidal PWM technique which offers simplicity and great response. As custom power is generally used for low power control application, the PWM technique offers more adaptive alternations compared to Fundamental Frequency Switching (FFS) strategies favored in FACTS applications. Furthermore, high switching frequencies can be utilized to enhance the efficiency of the converter without bring about major switching losses. The controller input is an error signal acquired from the reference voltage and the rms value of the terminal voltage measured. This error will be processed by the PI controller whereby the output is an angle, δ given to the PWM signal generator. It is imperative to aware that in an indirectly controlled converter, active and reactive power is exchange between DSTATCOM and the ac system simultaneously. The error signal generated by comparing the reference voltage with the rms load voltage measured. The PI controller process the error signal and produce out the required angle to eliminate the error to zero which means the rms load voltage is brought back to the reference voltage. Figure 3 shows the Simulink model of a PI controller.

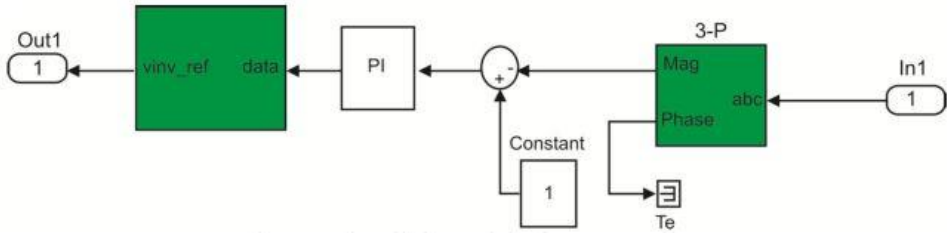


Figure 3. Simulink model of a PI controller [5].

From figure 3, the PI controller is a closed loop controller which controls the system with a weighted sum of error and integral that value. The PI controller drives the error signal to be zero for a step input.

$$Error\ signal = V_{ref} - V_{in} \quad (3)$$

Where,

V_{ref}= 1 p.u as reference voltage
V_{in}= measured load voltage in per unit value

2.1.3 Neural Network based PI controller

The artificial neural network was introduced as a set of simplified neuron. These neurons can be generally defined as simple signaling units of the nervous system of a living being in which every neuron is a discrete cell whose functionality is the same as its cell body. In 2005, Gwong Won Kim et al [7] presents an ANN based coordinated control scheme for STATCOM to maintain its output voltage at substation bus of a power system. In 2010, Aman Ganesh et al [8] designed an ANN based STATCOM to control the switching criterion of the voltage source converter so that the total harmonic distortion can be reduced by injecting line current at the Point of Common Coupling (PCC). In the following year, Amer et al [9] presents the ANN based STATCOM to improve the damping of a single machine infinite bus system and multi machine power system to compare ANN controller and PID controller on the effectiveness of both controllers in power system stabilization control.

From the literature survey mentioned earlier, network can generally be categorizes as a system with or without feedback. In the case of networks with feedback, its output value is determined by its input value. For network with no feedback, an output vector is computed from its output neurons for each input vector enters into the network [10]. Subsequently just, networks having a forward stream of data are defined as feed forward network. Another network that falls under the feed forward network category is the multi-layered feed forward back propagation network which consists of a layer of z-hidden units. One thing to take note is that the output value is always bias with the hidden units. This bias acts like weights on connection from its unit ensuring that the output is always 1. The number of hidden layers of a network can be set as desires. Figure 4 shows an illustration of a neuron network whereby the input layer is connected to the hidden layer and the hidden layer is then connected to the output layer through some sort of weights interconnection.

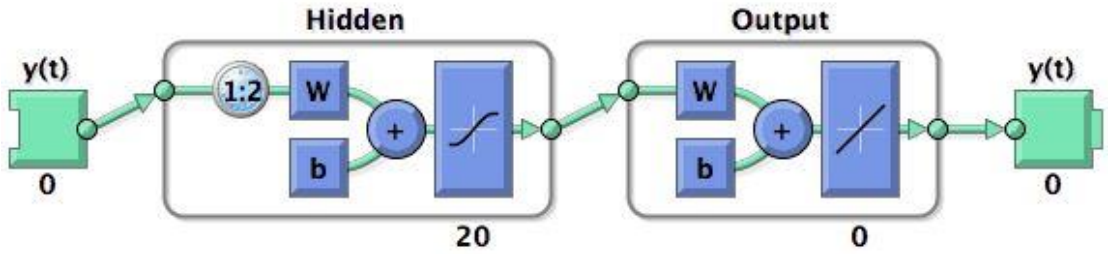


Figure 4. Illustration of a neuron network in MATLAB [11].

In this paper, the purpose of creating a neural network controller is to enhance the robustness of the conventional PI controller. A neural network based PI controller is designed with suitable gains depending on the operating condition which is the error in voltage regulation. The role of the well-trained Neural Network is to tune the PI controller with minimum mean square error. The Neural Network controller is generated in a simple structure depending on the number of hidden layer and number of neurons per layer used. In order to train the Neural Network, the input pattern is used together with the output pattern that consists of the optimal gain value which has been collected after performing several simulations of the closed PI controlled voltage at load point. These patterns are used to train the Neural Network and the output of the Neural Network is the optimal values of K_p and K_i.

3.0 Result and Discussions

In order to improve the performance of the distribution system, the DSTATCOM is connected to the distribution system. The DSTATCOM is designed using MATLAB Simulink version 2016a. Figure 5 and 6 shows the Simulink model for DSTATCOM with PI controller and Simulink model for DSTATCOM with Neural Network controller respectively.

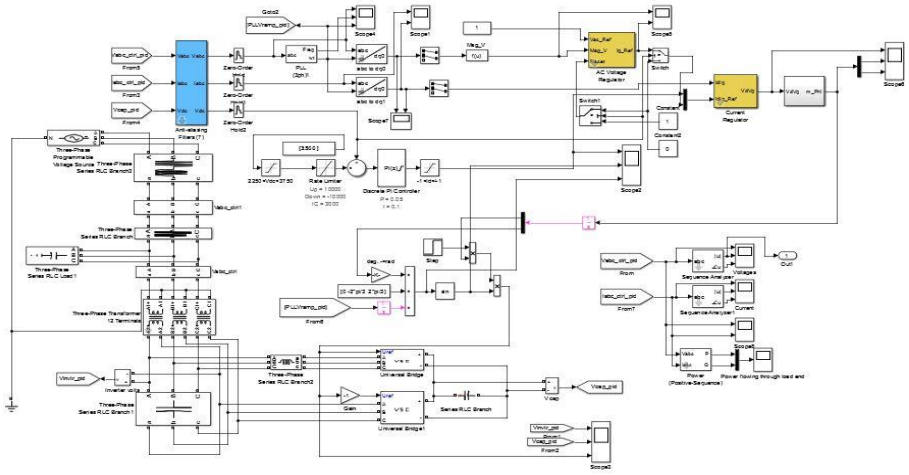


Figure 5. Simulink model for DSTATCOM with PI controller.

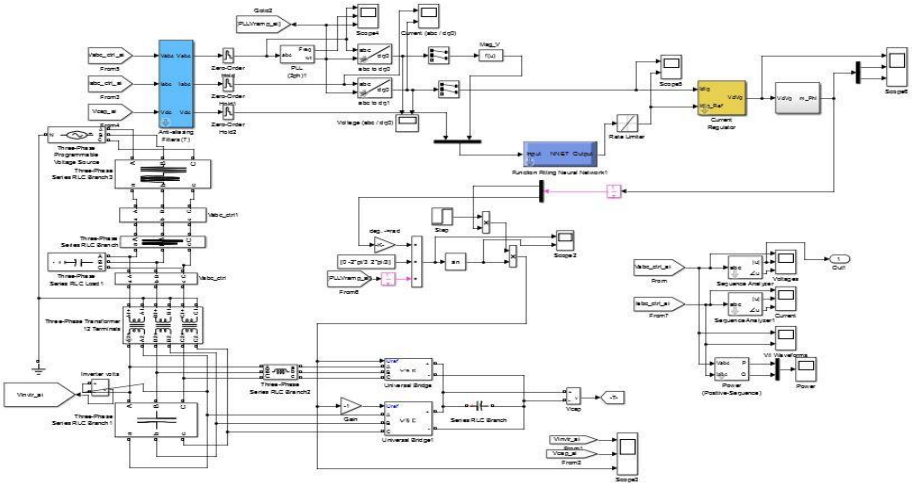


Figure 6. Simulink model for DSTATCOM with Neural Network controller.

The DSTATCOM acts as a controlled reactive power source. It consists of a Voltage Source Converter and a DC storage capacitor device, capable of absorbing or injecting reactive power to the system. The whole system was built to mitigate voltage sagging issue. However, some of the parameters are not available, so an approximate value is used during simulation. Table 1 shows the parameters selected for the system.

Table 1. Parameters of Simulink model.

No.	Parameter	Value
1	Voltage source	25kV
2	Frequency	60Hz
3	Line impedance	312.5Ω, 0.01178μH
4	DC voltage	3.5kV
5	Capacitor	3.3mF

Figure 7 illustrates the simulation done by both controllers namely PI controller and Neural Network based PI controller and also the output voltage profile with DSTATCOM disconnected from the system.

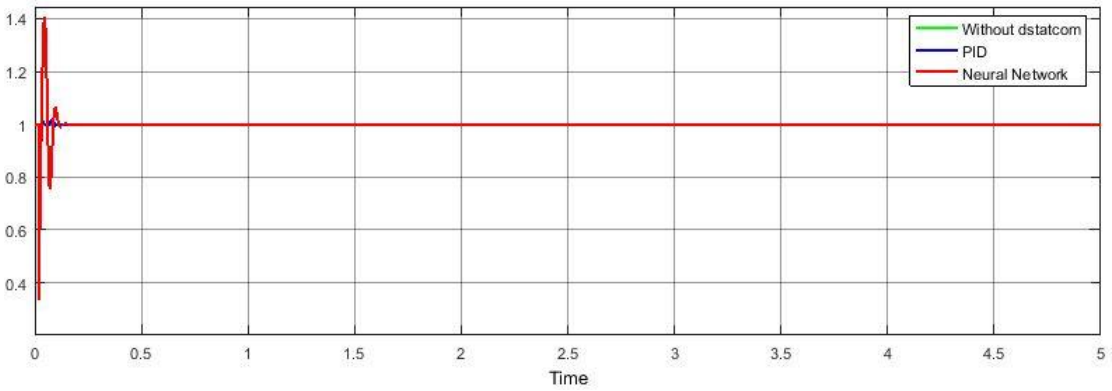


Figure 7. Load voltage profile with resistive load P=200kW.

According to figure 7, it is seen that both methods are capable of compensating voltage sag. However, the load voltage for using PI controller is 1 p.u whereas the load voltage for using Neural Network controller is 0.9965 p.u. This shows a percentage error of 0.35% between both controllers under the effect of connecting 200kW resistive load on transmission lines. Therefore, the PI controller has higher compensation rate of voltage sag compare to Neural Network method when connecting resistive load.

Figure 8 shows the comparison result between the two controlling methods, that is PI and Neural Network methods when a 200kVAR inductive load is connected to the transmission lines while the resistive load have been removed.

According to figure 8, it can now be seen a slightly notable compensating response between the two controlling methods. However, the capability of recovering voltage sag for PI controller still triumphs over Neural Network controller. The load voltage for using PI controller is still 1 pu whereas the load voltage for using Neural Network controller is 0.9922 p.u. This shows a percentage error of 0.78% between both controllers under the effect of connecting 200kVAR inductive load on transmission lines.

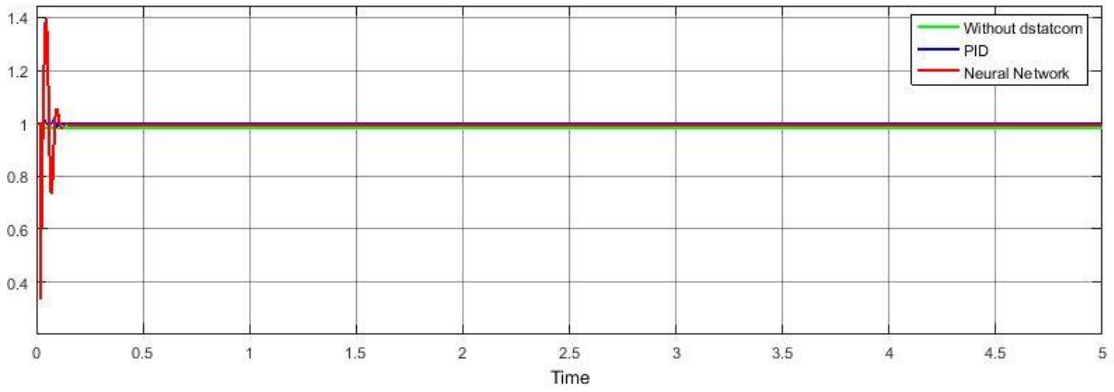


Figure 8. Load voltage profile with inductive load Q_L=200kVAR.

Figure 9 below shows the comparison result between the two controlling methods, that is PI and Neural Network methods when a 200kVAR capacitive load is connected to the transmission lines while the inductive load have been removed.

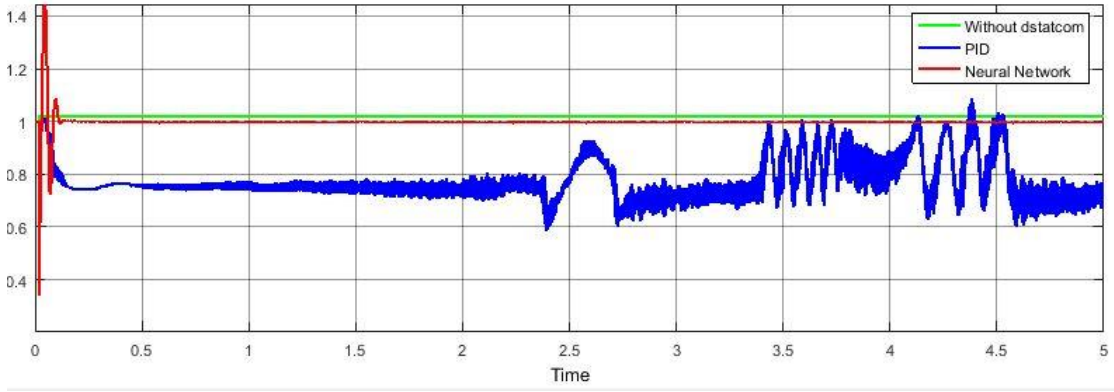


Figure 9. Load voltage profile with capacitive load Q_C=200kV_{ar}

According to figure 9, it can be seen clearly on the response between the two controlling methods. It is obvious that the PI controller is incapable of mitigating voltage sag. The load voltage for using PI controller is 0.7562 p.u whereas the load voltage for using Neural Network controller is 1 p.u. Table 2 shows the summary of results between both controllers as load value increases for different type of loads.

Table 2. Load voltage values obtained through Simulink with DSTATCOM using PI and ANN controller.

No.	Time (s)	Load value			Load voltage with DSTATCOM using PI controller (p.u)			Load voltage with DSTATCOM using ANN controller (p.u)			Error (%)		
		P (kW)	Q_L (kV_{ar})	Q_L (kV_{ar})	Resistive load	Inductive load	Capacitive load	Resistive load	Inductive load	Capacitive load	Resistive load	Inductive load	Capacitive load
1	5	200	200	200	1.0000	1.0000	0.7562	0.9965	0.9922	1.0000	0.35	0.78	-32.24
2		280	280	280	1.0000	1.0000	0.7664	0.9963	0.9900	1.0000	0.37	1.00	-30.48
3		360	360	360	1.0000	1.0000	0.9681	0.9960	0.9877	1.0000	0.40	1.23	-3.29
4		440	440	440	0.9947	0.9578	1.0000	0.9959	0.9852	1.0090	-0.12	-2.86	-0.90
5		520	520	520	0.9935	0.9505	1.0000	0.9955	0.9824	1.0120	-0.20	-3.35	-1.20
6		600	600	600	0.9923	0.9434	1.0000	0.9952	0.9795	1.0160	-0.29	-3.82	-1.60
7		680	680	680	0.9910	0.9363	1.0000	0.9950	0.9765	1.0190	-0.40	-4.29	-1.90
8		760	760	760	0.9896	0.9293	1.0000	0.9946	0.9732	1.0240	-0.51	-4.72	-2.40
9		840	840	840	0.9882	0.9225	1.0000	0.9942	0.9697	1.0280	-0.61	-5.12	-2.80
10		920	920	920	0.9868	0.9157	1.0000	0.9938	0.9661	1.0330	-0.71	-5.50	-3.30
11		1000	1000	1000	0.9853	0.9090	1.0000	0.9934	0.9798	1.0390	-0.82	-7.79	-3.90

4.0 Conclusion

This paper presents the analytical study on dynamic power control done by DTATCOM in a distribution system. The study reveals that the well-trained Neural Network can be used to predict voltage values on load bus of the transmission line on any type of load connected to the transmission system at any time. The Neural Network based PI controller is designed in a simple structure according to the number of hidden layers and number of neurons per layer used, comparing with the structure designed for a conventional PI controller. The difference in voltage control performance done by these two controllers is not much. This shows that the Neural Network based PI controller is capable of implementing for DSTATCOM with simpler hardware needed compared with the PI controller. However, the development of Artificial Neural Network technique can always be developed further for future research study.

References

[1] P. Schavemaker and L. Van der Sluis, *Electrical power system essentials*. Chichester, England: Wiley, 2008.

[2] Sulaiman, Rosli Omar, Nasrudin Abd Rahim, Marizan (2009) *Modeling and Simulation for Voltage Sags/Swells Mitigation Using Dynamic Voltage Restorer (DVR)*. Journal of Theoretical and Applied Information Technology. pp. 464-470.

[3] S. Nawaz and S. Hameed, "Mitigation of power quality problems by using DSTATCOM", *International Journal of Recent Advances in Engineering & Technology*, vol. 1, no. 3, pp. 175-179, 2013.

[4] M. Jaspreet Kaur, 'Role of DSTATCOM in Distribution Network under Various Fault Conditions', *IJAREEIE*, vol. 04, no. 07, pp. 6307-6315, 2015.

[5] S. Sivakoti, N. Kumar and D. Archana, "Power Quality Improvement In Distribution System Using D-Statcom In Transmission Lines", *International Journal of Engineering Research and Applications*, vol. 1, no. 3, pp. 748-752.

[6] H. Mohamed, M. Abdulsalam, F. Mansur and M. Anwar, "Design and Simulation Studies of D-STATCOM for MitigatingVoltage Sag Problem by Using Fuzzy Inference System, and Proportional Integral based on controlled

application", *International Journal of Advanced Research in Electrical, Electronics and Instrumentation Engineering*, vol. 3, no. 8, pp. 11414-11421, 2014.

[7] G. Kim and K. Lee, "Coordination Control of ULTC Transformer and STATCOM Based on an Artificial Neural Network", *IEEE Trans. Power Syst.*, vol. 20, no. 2, pp. 580-586, 2005.

[8] A. Ganesh, G.K. Singh and R. Dahiya, "Design and Analysis of Adaptive Neural Controller for Voltage Source Converter for STATCOM", in *Proc. of Int. Conf. on Advances in Electrical & Electronics*, India, 2010.

[9] R. A. Amer, G. A. Morsy and H. A. Yassin, "SCG Stability Enhancement Using STATCOM Based-ANN Controller", *WSEAS TRANSACTIONS on SYSTEMS and CONTROL*, vol. 6, no. 9, pp. 325-338, 2011.

[10] M. Hassan and G. Kothapali, "Comparison Between Neural Network Based PI and PID Controllers", in *2010 7th International Multi-Conference on Systems, Signals and Devices*, Edith Cowan University, 2011, pp. 1-6.

[11] "Release Notes for Neural Network Toolbox - MATLAB & Simulink", *Mathworks.com*, 2016. [Online]. Available: http://www.mathworks.com/help/nnet/release-notes.html. [Accessed: 26- May- 2016].

eurec2016 - Conference Paper
Pape Number 2EE7

Mathematical modelling simulation analysis and efficiency of a photovoltaic thermal system

Mohammed Al-Jabri, Mr.Taghi Hajibejgy

School of Engineering, Taylor's University, Malaysia

Eng.aljabri@outlook.com

Abstract

This paper analyses the heat response data collected from a Photovoltaic thermal system (PV/T) system, under normal conditions, with different heat transfer fluid water and nanofluid acting as a coolant. Experimental and simulation values were compared and analyzed in this paper. The thermal response of the PVT system depends solely on the irradiation of sunlight. Therefore, the thermal energy output of the PVT system varies according to the solar irradiation. In this experiment, the PVT thermal response was measured via Thermocouple sensors mounted in each layer of the PVT system, which included solar panel, aluminum thermal plate, and Heatsinks. A charge controller was connected to the output of the PV to regulate the charging process for a battery so that the electrical output can also be effected by the thermal response of the solar panel. The amount of solar irradiation was calculated based on the reading from the Pyranometer and the surface area of the PV. The setting of the Pyranometer and the thermocouples to measure the PV thermal value and the ambient temperature was set to ten seconds each, which was read using a data logger.

Keywords: Hybrid PV/T, Thermal energy, Heat transfer , thermal collector, photovoltaic

1.0 Introduction

Solar is one of the clean, renewable and sustainable sources of energy which has to be harvested everywhere on the earth special places which have extended the sunshine around the year like Malaysia. This source of energy can be harvested by Photovoltaic Thermal (PVT) which can contribute to the energy consumption of the household or industry [1]. In regards to utilizing the combination of thermal and photovoltaic systems, the technology has been there for a while now, but not much work has been done to improve on it. PVT's have to start to attract more interest in the solar energy sector due to increasing demands for renewable energy source [2]. A PVT can harvest both electrical and thermal energy since the PV by itself alone only can retain up to 20% maximum and the majority of the energy around 70% is wasted via thermal [3]. The low efficiency of the PV can be further improved by harvesting the thermal portion of the Sun radiation on the PV system and collected such energy in a thermal tank for the future usage. A suggested approach is to come up with a mathematical modelling of the system, simulate using MATLAB/Simulink, analyze the gathered data, evaluate the efficiency as a mean to transfer the thermal energy collected in a container under the PV and suggest improve efficiency of the system and build the best model according to the results that been approached.

Solar panels work perfectly only in certain weather condition, but since the weather is always changing and the solar panels are used in different climate all over the world, most panels do not operate under ideal conditions. Understanding how the solar panels react to these different conditions is essential for engineers to develop a solution accordingly [4]. With this knowledge, a design can be introduced to improve the efficiency of solar panels that operate in non-optimal conditions. This study was undertaken to employ water in the container as a coolant in the PVT system. PV cells when its strike with a sunlight basically generates electricity, however, silicon PV cells tend to convert only small part of the radiation to electricity while the rest result in heating of the solar panels. As PVT system, there is heat transfer from the cells to the thermal plate or tubes to the coolant underneath. The heating of the coolant reduces the temperature of the PV cells, therefore increasing their efficiency when the solar cells are exposed to a high temperature and radiation conditions. The hybrid PV/T has a pump and storage tank but in this paper. Figure1 demonstrate the general Idea of the PV/T system principle.

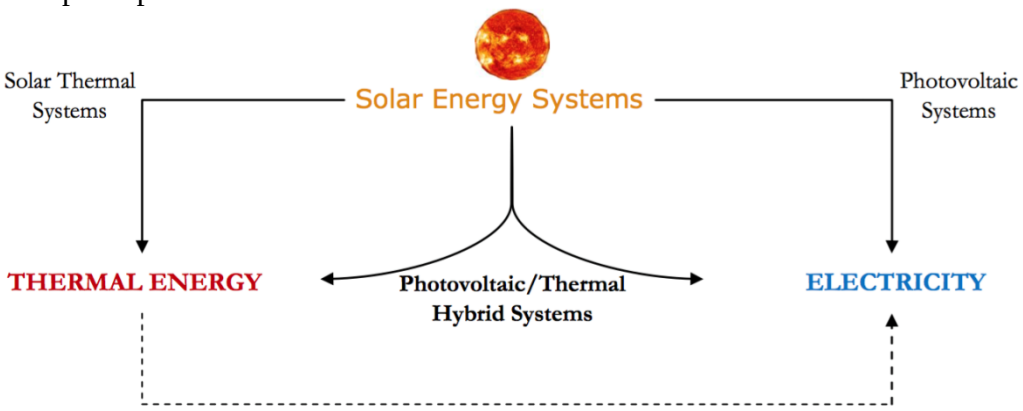


Figure 1.1: Overview of solar energy system [5].

2.0 PV/T System Description

The hybrid system has 16 PV panels that can provide 18V high current module. This has been achieved by arranging the 9 V panels in parallel and series order. The final order can be seen in Figure2.1. The thermal collector is attached to the PV panels to extract the heat from the panels. A thermal aluminum plate and Heatsinks are used for this purpose as shown in Figure 2.2.



Figure 2.1: PV panels module

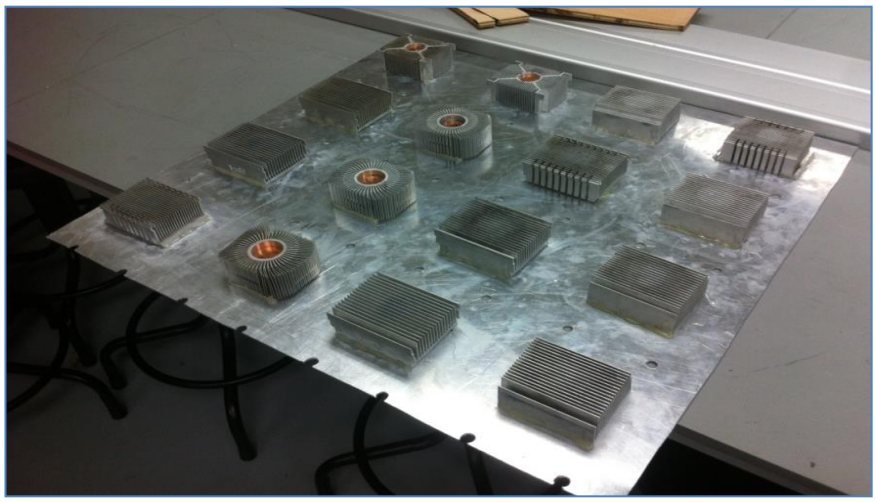


Figure 2.2: Thermal Collector Plate

However, the heat dissipated from the thermal collector plate is been transfer to low thermal conductivity container which contains water. Later on, a circulation to a heat exchanger can be done to heat up the tank water.

3.0 PV panel composition

The PV panels are the most critical part this study which is important to know the panel material because the efficiencies of various materials have changed levels of reliance on temperature [6]. Therefore, a PV system must be designed not just as indicated by the most extreme, least and normal weather conditions at different location additionally with a comprehension of the materials utilized as a part of the PV board.

The PV panel is made out of various layers relying upon the photovoltaic innovation utilized. polycrystalline PEET PV panel is under investigation in this work. There are 4 fundamental layers in this PV panel, the glass covering, an against intelligent covering (ARC), PV cells, ethylene vinyl acetic acid derivation (EVA) layer. Since its low surface area regarding the panel region negligibly affects the temperature response [7].

4.0 Experiment Verification

This experiment investigates the thermal energy transfer in the PV/T system to identify the system behavior according to the solar irradiation since the heat transfer of the system layers and calculating the total efficiency of the system by using water and nanofluid as a coolant. Also, the solar panel temperature is important to know which can affect the electrical output power and lead to reduce the efficiency [7]. However, water is employed in the thermal container without any circulation as a start in this experiment to validate the mathematical model.

The pyranometer is a device that used to measure solar irradiance on a flat surface, which can measure the solar radiation flux density (W/m2). The pyranometer is directly connected to the data logger to accurately track the solar irradiation.

Data logger is an electronic device which records data over time or in relation to a location with a sensor. The frequency of capturing data can be set from 1 sec to minutes' range. The duration of the capturing data can be set as the user desired from minutes to hours. For this particular case, the data logger was set to capture the data every 10 seconds for 3 hours. The data obtained was saved in a USB drive which was placed in the data logger and later transferred to the computer for analysis. The thermocouple is a sensor which used to measure the ambient temperature in conjunction with recording the irradiance of Sun at the same time. These data, irradiance of Sun and ambient temperature were saved on the same thumb drive and later transferred to a computer for analysis.

In this simulation, MATLAB software was employed for further analyzing the data obtained and to calculate the heat transfer of the PV/T and the efficiency in relation to the solar irradiance and ambient temperature.

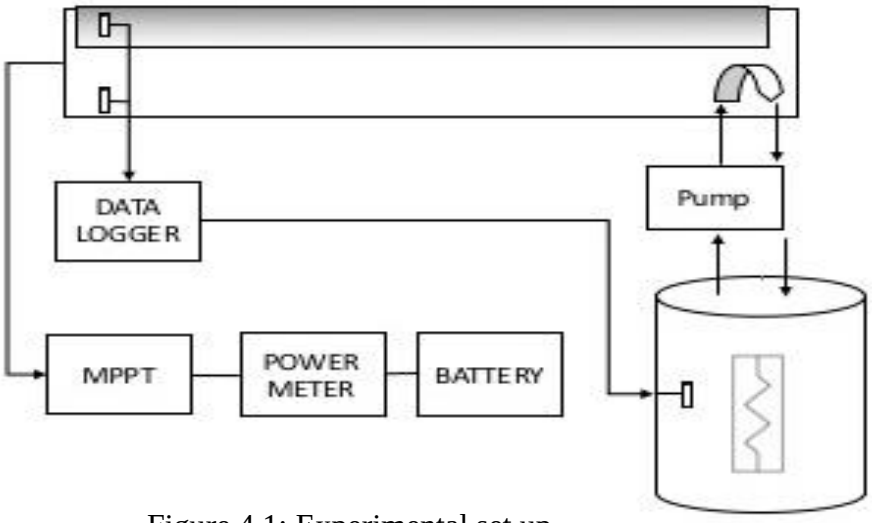


Figure 4.1: Experimental set up

Figure 4.1 elaborate more the experiment verification by showing the schematic diagram of the whole system structure. Basically placing thermocouples sensor in each layer of the collector and the tank to observe the heat transfer by recording the data in a data logger. Charge controller (MPPT) used to control the output of the PV to regulate the charging process for a battery and power meter to observe the output power by recording the output data. Heat exchanger coil has been mounted inside the tank. Moreover, the Figures below show the types of equipment used to conduct the experiments.



Figure 4.2: Thermocouple



Figure4.3: Data logger



Figure 4.4: Solar charger(MPPT)



Figure4.5: Pyranometer

location

country	Malaysia
city	Subang Jaya
GPS Coordinate	N3o 3.886’ E101o 36.995’

Time period for Experiments

Month for experiments start	January
Day of month for experiment start	23
Length of Experiments (days)	32
Time step during experiment (h)	3 to 4
Graphics display during Experiment	NO

Collector Orientation

Slop angle	0°
Azimuth	0°

Collector specifications

Area(m)	2
Emittance of absorber plate	0.86
Emittance of cover	0.92
Back insulation Conductivity (W/K.m)	0.2
Back insulation Thickness(mm)	50
Index of refraction of cover material	Glass
Absoptance of absorber Plate	0.65
Collector fin efficiency Factor	0.95
cell efficiency	0.15
PV cell type	polycrystalline
PV references temperature	25
Thickness of the cover (mm)	3
wind velocity (m/s)	1
Tank capacity	29L

Cooling fluid parameters

flow rate (L/min)	3
inlet fluid temperature(°C)	40
water heat capacity (J/kg. °C)	4181

5.0 Mathematical model illustration

For example, the table below shows some assumptions of a different parameter that has an impact on the system efficiency can give a pre-results of the system efficiency after implementing them in the mathematical model. Moreover, it can be determined how to evaluate the system and how to improve heat transfer and overall efficiency. Yet more areas can be covered that affect the efficiency but the details below only cover some.

Table5.1: System input assumptions

Parameter	Symbol	Value	Units
PV thickness	b_{pv}	0.35	mm
Emittance of cover plate	$€_{pv}$	0.89	
PV conductivity	Kpv	130	w/(m.k)
Ration of tube to spacing	d/w	0.076	
Insulation conductivity	kin	0.035	w/(m.k)
Thermal Collector Area	Acol	0.88	m^2
Thermal absorber plate thickness	b_t	0.4 0.3	mm mm
Flow rate	V_m	7	L/h
Tube diameter	d_d	8	mm
PV absorbance	α_{pv}	0.84	
Tube Spacing	w	0.15	m

How some of these variables would decide the impact of the thermal and electrical efficiency of the PVT system. This permits us to decide the parameters that have the best impact on the PVT system and to give a knowledge into what input could be made by adjusting any configuration parameter.

Maybe the conspicuous beginning stage for breaking down any heat exchanger is to look at what impact flow rate has on its efficiency. Commonly, heat exchange is controlled by the Reynolds number which is a component of flow rate; multiple flow rate was used to inspect its impact on the efficiency. In Figure 4.3 it can be seen in different flow rates there is a slight increment in the thermal efficiency. Moreover, in any case, the expansion in the Reynolds number with expanded flow rate implies that heat transfer from the PV cells is enhanced, in this manner implying that electrical efficiency increments possibly.

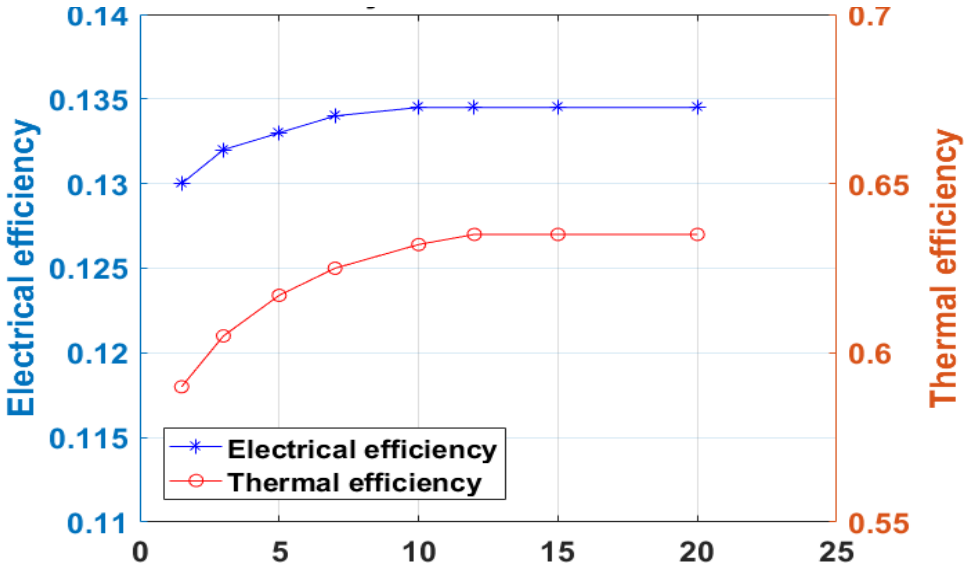


Figure 5.1: Efficiency vs fluid flow rate

It can be seen in figure 4.4 that by enhancing the thermal conductivity between the PV cells and the thermal plate there is an obvious increment in the electrical efficiency. In light of this perception, there is an important to guarantee that great thermal coupling between these materials is ensured.

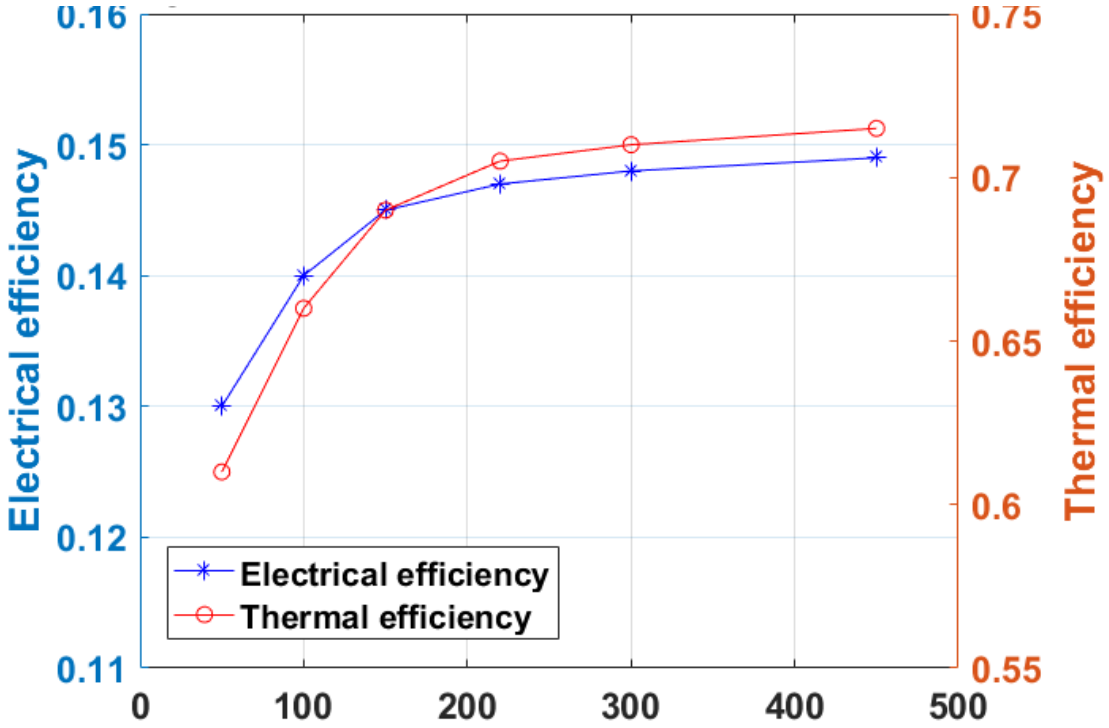


Figure 5.2: Thermal plate thermal conductivity

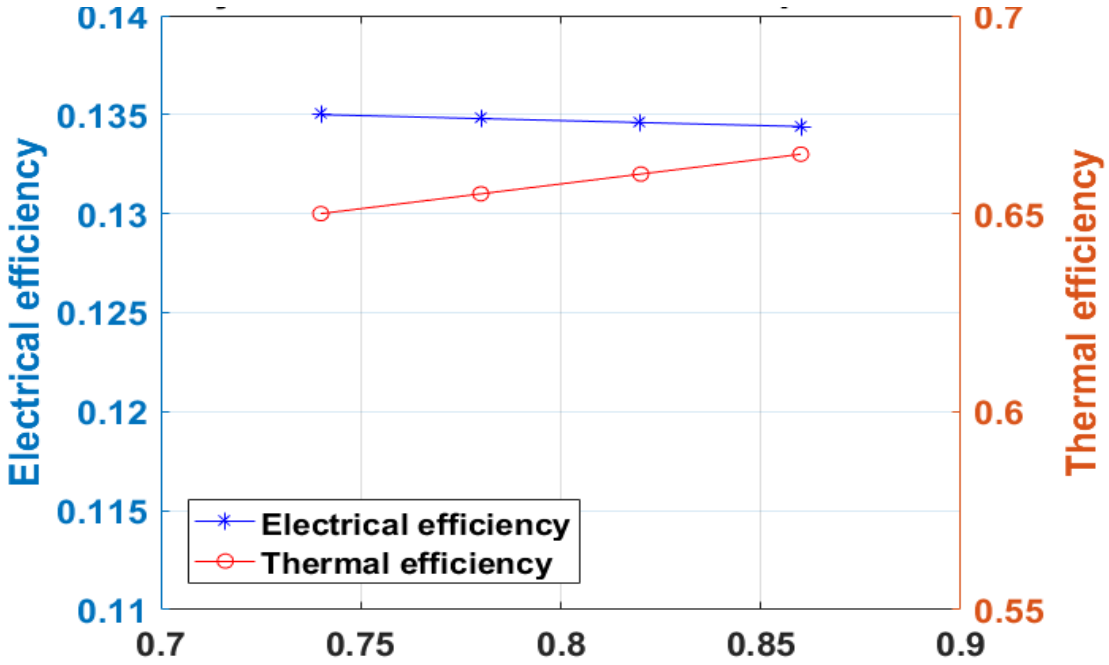


Figure 5.3 PV absorptions

From Figure 4.5 above it is obviously demonstrated that absorptions enhance the thermal efficiency. Commonly, PV cells are intended to amplify their absorption of wavelengths where the photoelectric impact jumps out at silicon cells, in the extent from 400nm up to roughly 1200nm. In any case, the solar spectrum proceeds to roughly 2500nm and these long wavelengths have a tendency to be reflected though they are consumed by the solar thermal system. The alterations One of the downsides of

expanding the absorption of longer wavelengths is that it tends to be showed in the PV cell temperature being increased hence bringing a decline in the electrical efficiency.

.

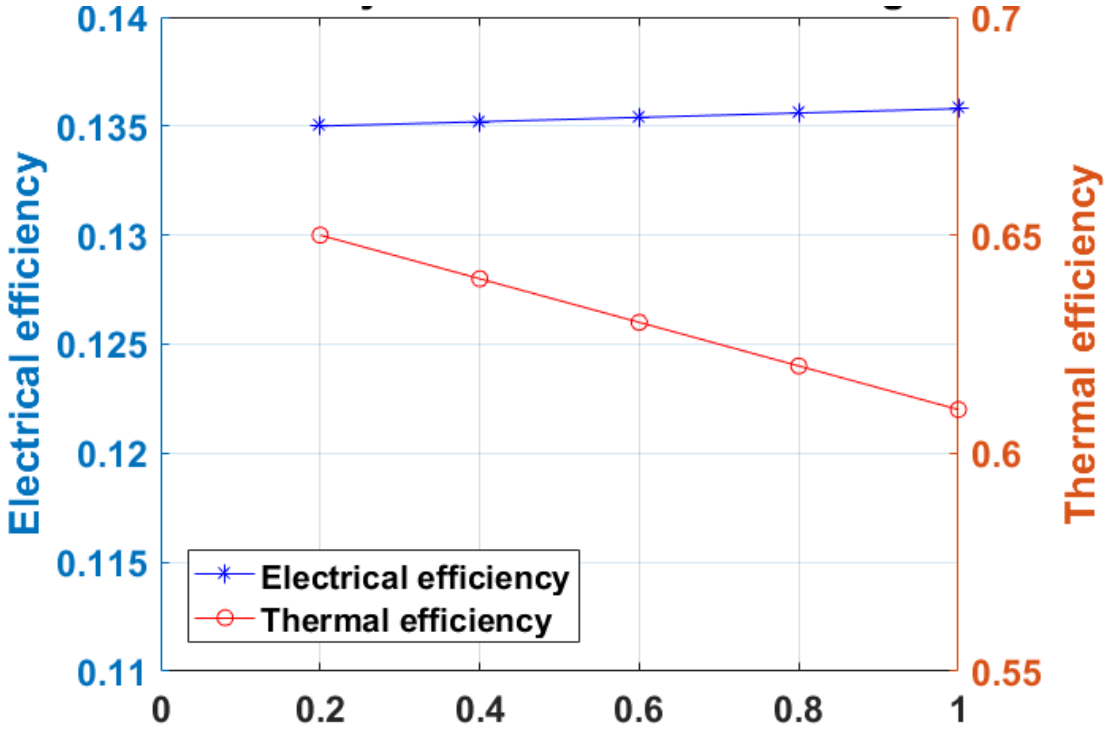


Figure 5.4:PV cell coverage

In Figure 4.6 it can be seen that expanding the range secured by PV cells results in a decrease in thermal efficiency, moreover, it additionally brings about a slight change in the electrical efficiency.

6.0 Results and discussion

The data that has been taking from the temperature sensors and the pyranometer, later on, been used by MATLAB to be further analyzed. The Figures below are the outputs of this experiment and the simulation.

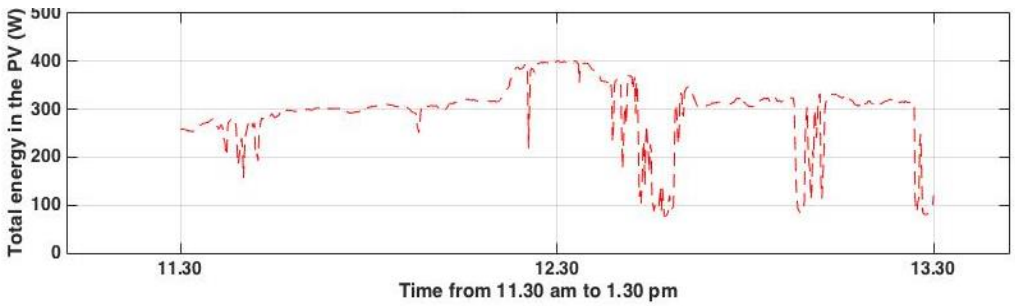


Figure 6.1: Solar radiation

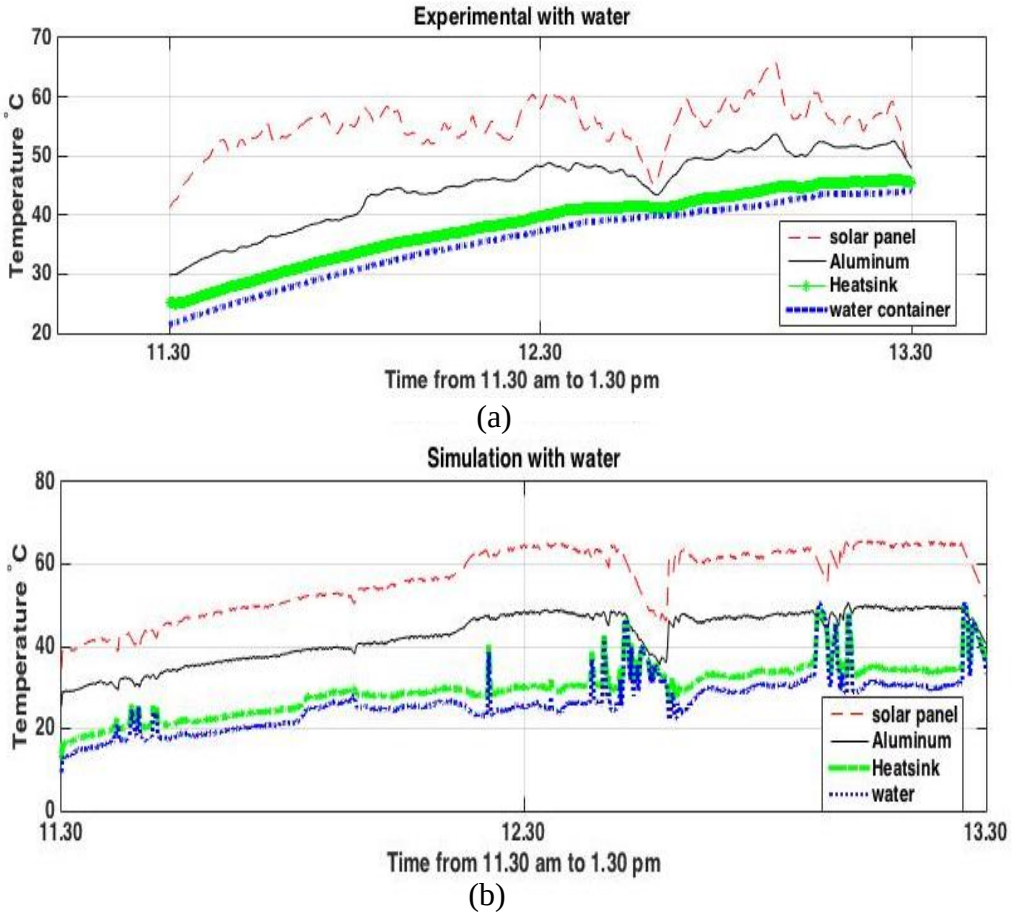
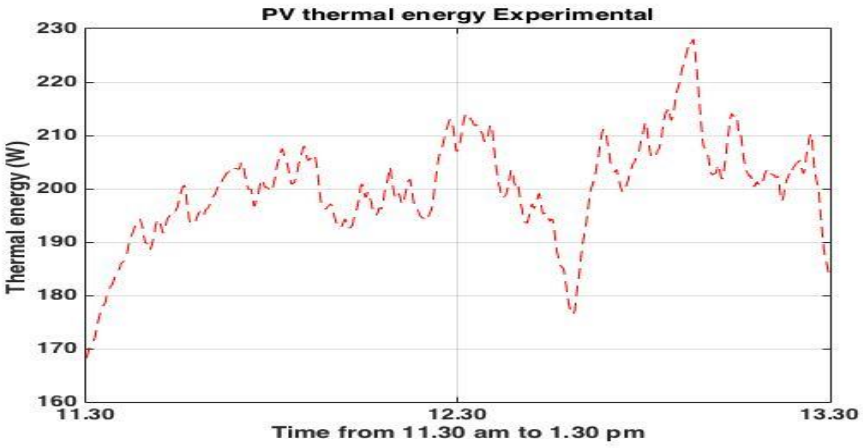


Figure 6.2: Simulation (b) and experimental(a) of PV/T layers heat transfer

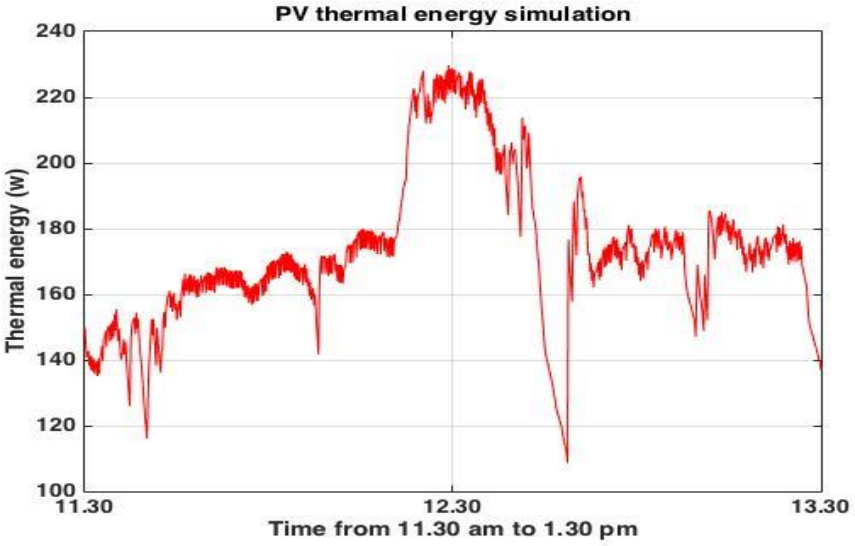
Figure 5 shows a comparison between experimental and simulation analysis of each layer's temperature in the PV/T system. The layers in sequence solar panel, aluminum thermal plate, heat sink and water in the container. Figure 4 indicates that the behavior of the temperature in each layer depending solely on the solar radiation as shown in figure1. However, the surface of the thermal aluminum plate is bent and deform because of the heat generated while welding the Heatsinks so it's not symmetry with the solar panel which leads to some heat loss also the thermal glue in between which has 2% loss and that explain the gap in between the thermal aluminum plate and the PV panel.

Heat is characterized as the type of energy that is exchanged between two systems by ideals of a temperature contrast [8]–[10] . Figure 6 shows the thermal energy been transferred by radiation from the sun to the PV. The thermal energy is rising in some points which indicate the PV is gaining energy and reached around 220W.

Noticing a drop of the thermal energy between 12 pm to 13 pm, that's can be explained as the panel cooling down by losing heat to the other layer of the PVT system which is the thermal plate.



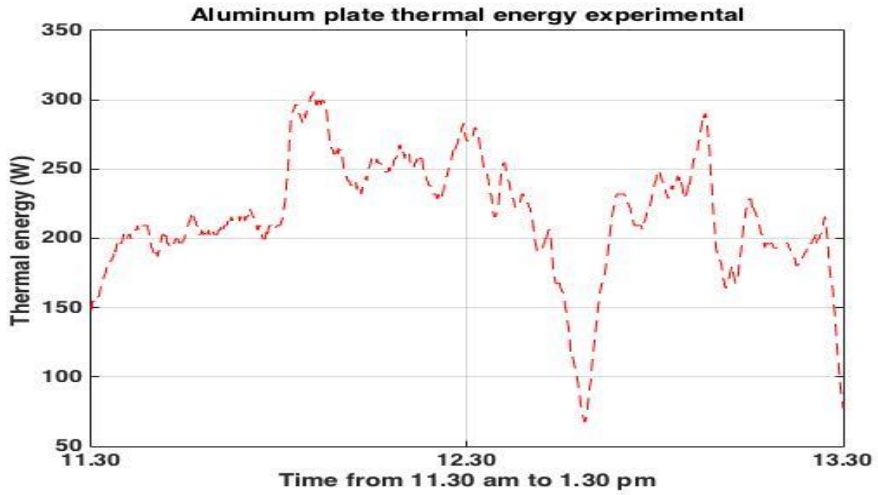
(a)



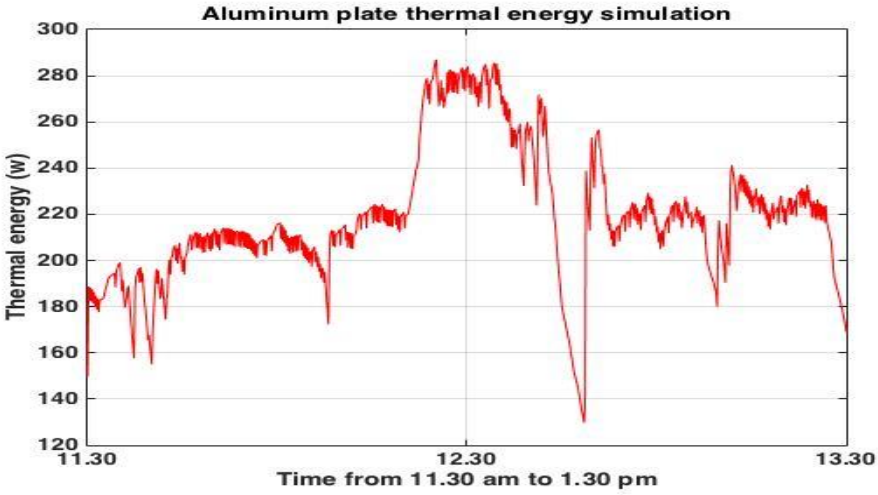
(b)

Figure 6.3: Simulation (b) and experimental (a) of thermal energy.

Moreover, the thermal plate reached a maximum energy of 300 W result of the interaction between the PV and the thermal plate. Spontaneously, heat flows from a hotter body to a colder one. This heat transfer process between the PV panel and the thermal plate called conduction since there are two plates attached to each other. The drop in some points can be explained that the thermal energy is transferred out of the plate to the heatsinks under the plate.



(a)



(b)

Figure 6.4: Simulation(b) and experimental (a) of thermal energy.

6.1 Experimental with water

Here it can notice the small gap between the heatsink and the fluid which can be improved by increasing the surface area of the heatsinks, however, some loss outside the collector can effect too. Moreover, the tank temperature reaches around 40 °C from an initial temperature of 24 °C which indicate a 16 °C gain to the water. Moreover, the PV temperature not exceeded the 60 °C like in figure 6.2 which show a reduction of 7 °C degrees after circulating the water in the container. Also, can notice the high gap between the PV panel and thermal aluminum plate also thermal aluminum plate and the heatsinks.

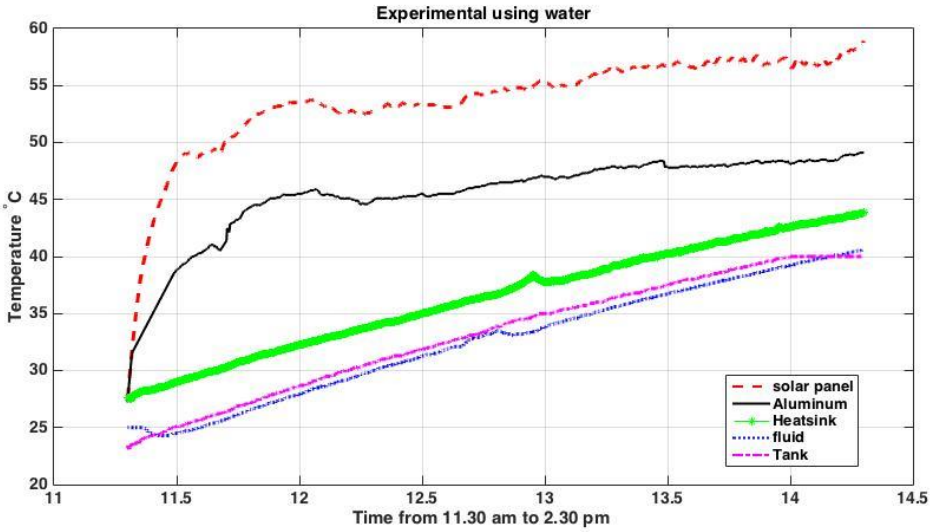


Figure 6.1.1: experimental using water for PV/T l

The thermal aluminum plate is bent and deform because of the heat generated while welding the Heatsinks so it's not symmetry with the solar panel which leads to 13% heat loss and the thermal glue in between which has 1% loss. Also, the heatsinks attached to the thermal plate in a point welding only which cause 11% loss.

6.2 Experimental with Nano fluid

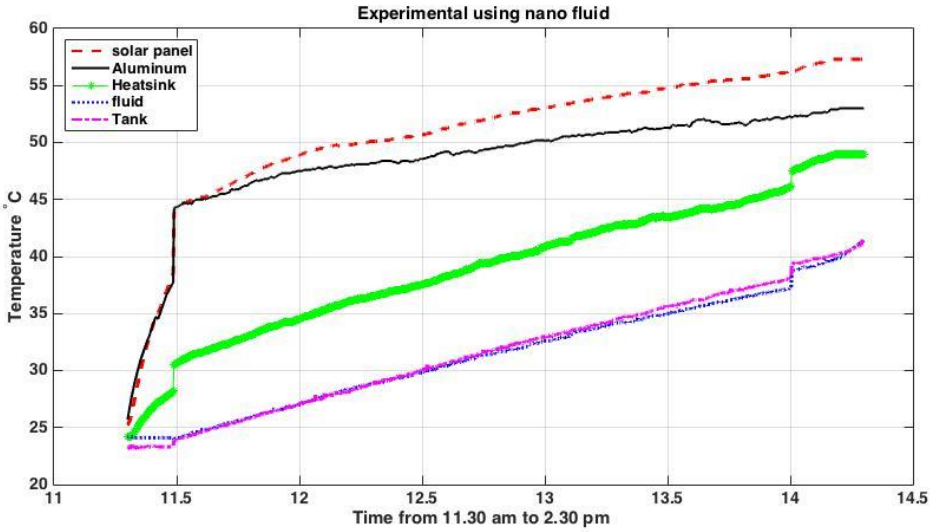


Figure6.2.1: Experimental using nanofluid for PV/T

Employing nanofluid increases the thermal transfer as shown in figure 4.3.4 to 19 °C, reaching a 42 °C were initially started from 23 °C. The nanofluid and the water in the tank both temperature almost same which show the nanofluid has a better thermal conductivity and improved the heat flow to the tank. Also having a high thermal conductivity it's mean conducting heat faster and that shows the aluminum thermal plate has a smaller gap with PV panels temperature which indicates the nanofluid absorb the heat faster. Moreover, the PV panels temperature did not exceed 60 °C due to a better heat flow.

6.3 Temperature affect

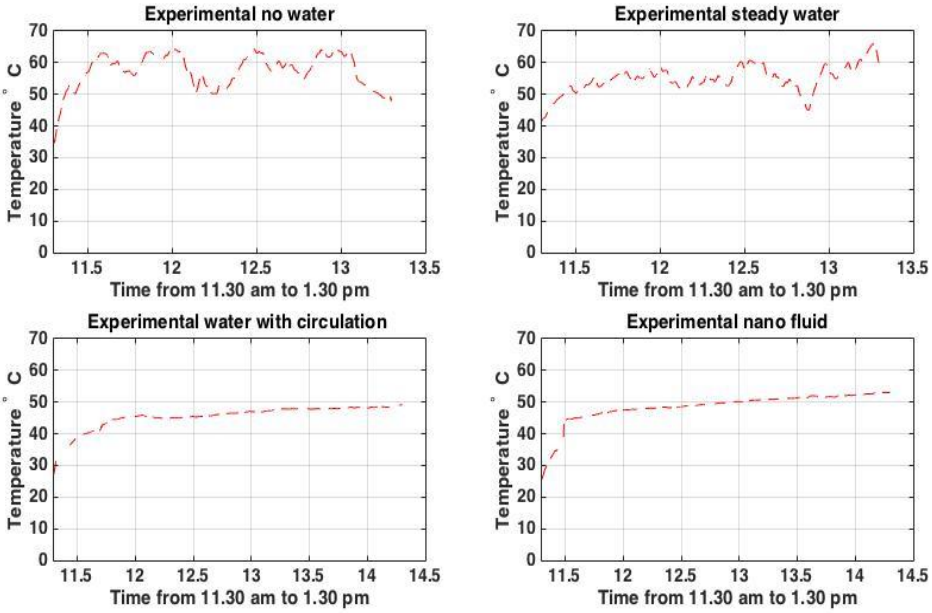


Figure 6.3.1: PV temperature

Investigate in different methods regarding the heat transfer fluid it gives an insight of PV temperature behavior. Figure 6.3.1 shows the four experiments that been conducted and how much increase in the temperature of the PV panel. In the beginning, using no heat transfer fluid shows the PV panel can reach a temperature of 65 °C, even after adding the steady water the temperature still reached 65°C. However, applying circulation to the water almost maintain the PV temperature thus, the efficiency slightly improved since the PV temperature effect the electrical Output. As can be noticed from Figure 6.3.2 each increment of 5 degrees above the optimal temperature (25°C) can decrease the output voltage about 0.5 volts. Therefore, a reduction or maintaining a lower Surface temperature on the PV panel can improve the electrical efficiency.

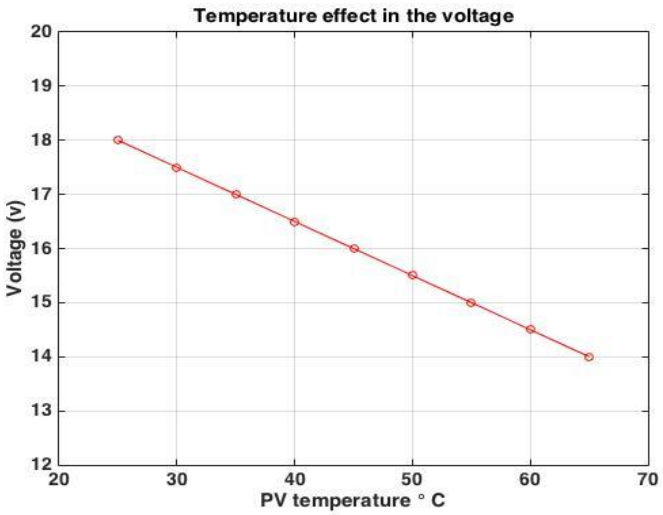
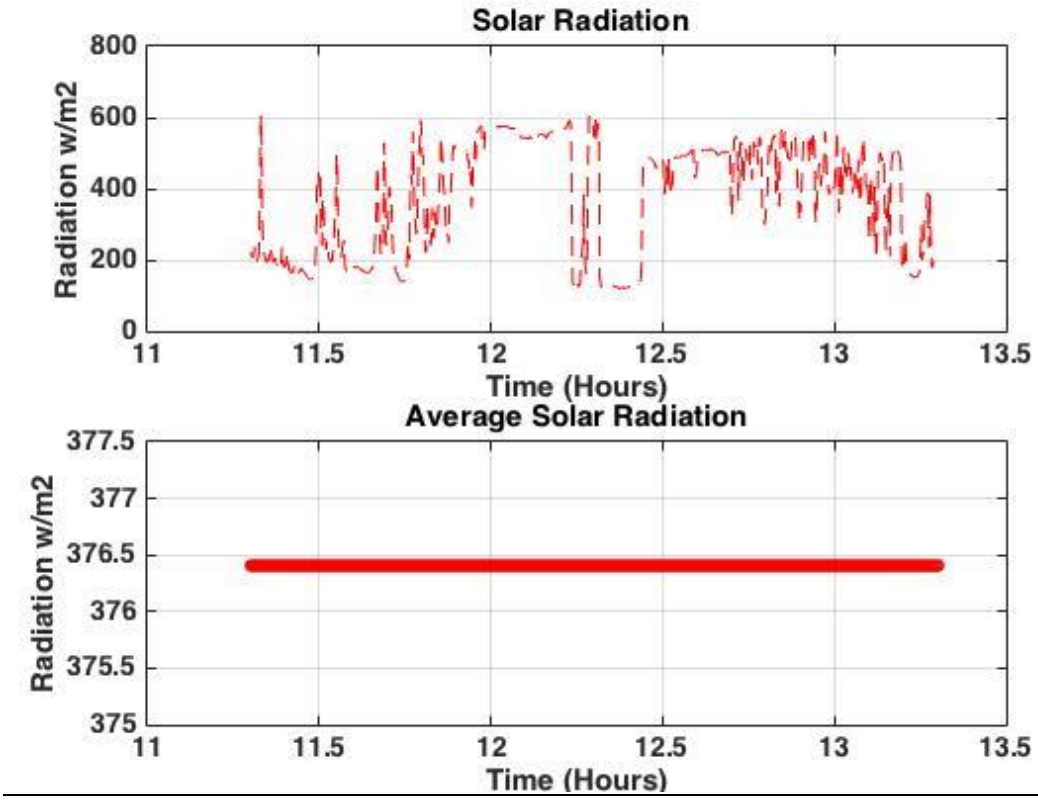


Figure 6.3.2: PV voltage vs PV temperature

6.4 Electrical Efficiency



Solar radiation for pv surface area =376.5 w

$$\text{Electrical output} = \text{Voltage} * \text{Current} \longrightarrow [10]$$
$$= 18\text{V} * 2.8\text{A} = 50\text{W}$$

$$E\text{lectrical efficiency} = \frac{\text{Electrical output}}{\text{Solar radaition}} \longrightarrow [10]$$

$$= \frac{50}{376} = 13.3\%$$

The electrical efficiency of the system is found to be 13.3% % based on average radiation.

6.5 Thermal Efficiency:

- Water as Heat Transfer Fluid:

With thermal output of 16-degree Celsius difference in 30L, the power stored:

$$\text{Thermal output} = m * C * \Delta T \longrightarrow [11]$$

$$= 27 * 4181 * 16 = 1806192\ J$$

$$E = J/s \longrightarrow [12]$$

=1806192/(time)= 1806192/ (60*60*3) =167.24 W

$$\text{Thermal efficiency} = \frac{167.24}{376} = 44.4\%\ [x]$$

- CNT Nanofluid as Heat Transfer Fluid:

With thermal output of 19 degrees' Celsius difference in 28L, the power stored:

$$\text{Thermal output} = \text{m} * \text{C} * \Delta\text{T}$$

$$= 27 * 4181 * 19 = 2144853$$

$$E = J/s$$

$$= 2144853/(\text{time}) = 2144853/ (60*60*3) = 198.59\ \text{W}$$

$$\text{Thermal efficiency} = \frac{198.59}{376} = 52.8\%$$

6.6 Total system efficiency

- Employing water 44.4% + 13.3 % = 57.7%

- Employing nanofluid 52.8%+13.3% = 66.1%

5.0. Conclusion

The sensible and viable use of solar energy is a critical way which can manage the worldwide vitality crisis at present. Photovoltaic (PV) cell, which changes over sun radiation to electricity, with no structure for mechanical thermal interlink. So the study on enhancing the productivity of solar panel is exceptionally essential. This paper showed the thermal response of the PV/T system layers and how much the solar panel can absorb heats when the temperature rises. Thermal collector and thermal tank are carefully improved. Both function well in collecting and storing thermal energy. Heat transfer fluids used are water and CNT nanofluid. The test done on the performance of the system using these two fluids showed that the CNT nanofluid (66.1 %) performed better than water (57.7%) in thermal efficiency Finding a way to make the thermal energy transfer faster in each layer can help to improve the efficiency of electrical and thermal output, hence fast heat transfer can maintain a steady temperature. with this knowledge, a design can be produced to improve the efficiency of solar panels that operate in non-optimal conditions. However, this study will be continued to employ a nanofluid to improve furthermore the heat transfer in the PV/T system.

References

[1] V. P. Sector, “Solar Photovoltaics,” vol. 1, no. 4, 2012.
[2] R. N. Schock, A. Adegbululgbe, J. Fenhann, I. Konstantinaviciute, W. Moomaw, H. B. Nimir, B. Schlamadinger, C. Turner, Y. Uchiyama, N. Wamukonya, X. Zhang, O. R. Davidson, P. R. Bosch, R. Dave, and U. Kingdom, “Energy Supply,” 2007.
[3] J. D. Nrel, P. M. Nrel, L. L. Nrel, J. B. Nrel, and D. J. Group, “Photovoltaic-Thermal New Technology Demonstration,” no. January, 2015.
[4] A. Z. Journal, “PERFORMANCE EVALUATION OF POLYCRYSTALLINE SOLAR,” vol. 9, pp. 69–81, 2013.
[5] M. Kaya, “Thermal and Electrical Performance Evaluation of PV / T Collectors in UAE,” 2013.
[6] T. International and J. Of, “Solar Power Analysis Based On Light Intensity,” pp. 1–5, 2014.
[7] D. M. Tobnaghi and R. Madatov, “The Effect of Temperature on Electrical Parameters of Solar Cells,” pp. 6404–6407, 2013.
[8] B. Zalba, “Review on thermal energy storage with phase change: materials, heat transfer analysis and applications,” *Appl. Therm. Eng.*, vol. 23, no. 3, pp. 251–283, 2003.
[9] F. P. Incropera, D. P. DeWitt, T. L. Bergman, and A. S. Lavine, *Fundamentals of Heat and Mass Transfer*, vol. 6th. John Wiley & Sons, 2007.
[10] M. A. Green, K. Emery, Y. Hishikawa, W. Warta, and E. D. Dunlop, “Solar cell efciency tables (version 46),” *Progress in Photovoltaics: Research and Applications*, vol. 23, no. 7, pp. 805– 812, 2015.
[11] J. H. Lienhard, “Heat Transfer,” *J. Heat Transfer*, vol. 82, no. 1, p. 198, 2010.
[12] ZondagHA,DeVriesDW,VanHeldenWGJ,VanZolingenRJC,VanSteenhovenAA Thethermalandelectricalyield of a PV-Thermal collector. Solar Energy 2002; 72(2): 113–128.

On the Phenomenon of Lightning Side Flashing from Trees

Nadzmi Azizi bin Jailan[1], Siow Chun Lim[2*]

School of Engineering Taylor's University

[*] *ChunLim.Siow@taylors.edu.my*

Abstract
In this paper, a research is done to estimate the critical location for a person to be standing nearby a tree in the presence of lightning. The lightning current characteristics used in this paper are those recommended by IEC standard for Negative First Stroke, Negative Return Stroke and Positive Stroke. Materials considered in the paper are tree and copper. The distance between a person and a lightning struck object varies and the computed electrical field strength distribution is around the height of 1 m to 10 m high. Based on the results discussed, there exists the point of which a side flashing to a person at a given distance is most probable. It is not advisable for a person to stay under a tree due to the enhance probability of side flashing.

Keywords: Lightning, Side Flashing, Trees

1. Introduction

Lightning is a natural phenomenon that occurs around the world and it is known to cause damage to the environment, structure, people and animals [1]. A typical lightning current carries up to 100 kA[1]. It was documented that lightning has one of the highest fatality rate towards people over the years compared to other natural disasters [2]. A proper documentation of injuries and death related to lightning is very rare to obtain even in the global scale [3]. In Malaysia, it was estimated to have 100 to 150 lightning death discovered cases per year [1]. In the year 1995, the maximum lightning ground flash density was over 38 flashes/km^2 with an average of 4.40 flashes/km^2 [4]. The table below shows some lighting related incident captured by the local news media from the year 2010 until 2014.

Table 1: Lightning related incident

Source	Location	News Title
The Star	Kota Tinggi	Lightning kills soldier during jungle training
	Kuala Lumpur	Jogger struck by lightning in Titiwangsa park
	Kuala Terengganu	Land of lightning
	Batu Pahat	Lightning strikes two dead
	Alor Setar	Lightning strike injures fisherman
	Kuala Terengganu	Lightning kills teen washing hands with rain water
News Strait Times	Kuala Terengganu	15-Year-Old boy killed, 3 others injured by lightning
	Hyderabad, India	Lightning kills 22 people
	Mexico City	Lightning strike kills 7, including 4 children
	Sandakan	Bornean sun bear struck by lightning dies
	Batu Pahat	9 –Year-Old girl struck by lightning dies
	Batu Pahat	Two dead, one injured after lightning strike
	Jasin	2 die in Merlimau lightning strike
	Butterworth	Two dies in Batu Kawan lightning strike

Lightning mostly occurs during thunderstorms, it seeks out a path, whereas the impedance is at its lowest in order for it to discharge [5]. If the path struck is not the best (have higher impedance value), a side flash might occur in order for it to reach the ground. Side flash is a term when a lightning struck an object, but due to the high impedance value of the object, it reacts by finding a shortest path to ground and jumping or ‘side flashing’ to the nearest object with a lower impedance. A tree is an example of a high impedance object as it is not a rare case to see a tree struck by lightning. The lightning and tree model is as shown in Figure 1.

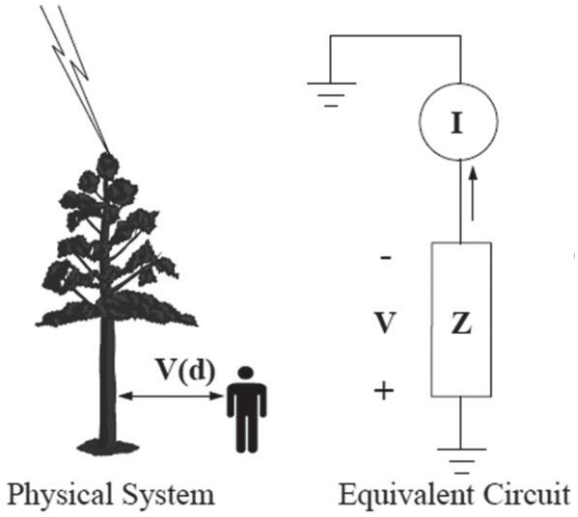


Figure 1: The lightning model and equivalent circuit [1]

As the air breakdown strength is approximate 3×10^6V/m, there is a possibility of side flashing happening if the electric field intensity develops at the object exceeds the said value. Based on the impedance of the tree as well as the lightning current that struck the tree, there is a possibility to determine whether side flash might occur and its range.

2. Methodology

At the beginning of this research, the concept of Conceive, Design, Implement and Operate was used to help produce the results for this research. In the Conceive phase, news of people getting struck by lightning while they are walking around or taking shelter were shared as unforeseen tragic event. The idea was conceive as the question that came to light was 'How does a person get struck by lightning when the initial hit was a tree?' Using this question, further study was done to understand the reasons of a person can be struck by lightning as a secondary target. 'Side Flash' a term that was used commonly by those that describe the situation.

The design phase is where the research was deepen to understand the concept and the method of simulating the situation. By doing so, a simulation can help predict and estimate the possibility of a person getting a side flash when standing under a tree. At this phase, mathematical model, existing research about lightning and trees and experiment done by researchers about it was compiled. Using MATLAB software as the base of simulation, lightning and trees were translated into mathematical model. With that, the third phase started, the Implement phase. This phase is where the simulation was data collected used for the simulation. As the necessary equipment are not there to help produce a physical experimentation as well as it being a dangerous task to handle such high voltage and current, the research proceed with simulation and numerical estimation to produce the results.

The Operate phase is where the results was compiled and discussed. By observing the results and graphs produce from the simulation, the deduction of the possibility of side flashing occurring was done. The comparison between three different object was able to produce expected outcome based on existing literature and research.

Different trees have different values of resistivity and inductance. The impedance value of each tree varies due to their age, height and moisture [6]. The

following parameters was obtained through an existing research allowing the simulation to produce the expected results [3].

E: The radial electric field at any given point of the tree
R: The resistance of the tree
L: The inductance of the tree
V_a: The potential at the topmost point of a human body
V_b: The potential at any given point of the tree
r: The distance between the topmost point of the human body to a given point of the tree
d: The distance between the human body and the object
l: The height of the point of concern of the tree

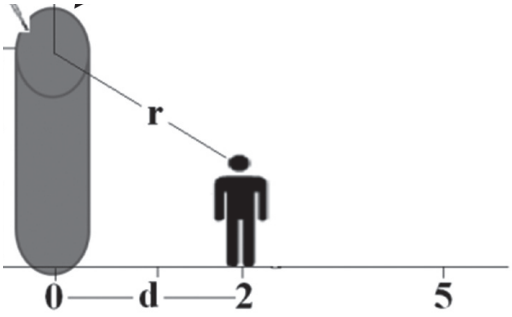


Figure 2: Configuration of lighting struck object and a person modelled for calculation [3]

$$V_b = i_{max}R + L(\frac{di}{dt})_{max} \quad (1)$$

Using the formula above, the potential along the tree is calculated. The maximum lightning current (i_{max}) and first current derivative ($\frac{di}{dt}$ max) considered in this study as recommended in IEC standard are [1]:

1. 90kA and 65kA/μs for negative first stroke (NFS)
2. 28.6kA and 161.5kA/μs for negative subsequent stroke (NSS)
3. 250 kA and 32kA/μs for positive stroke (PS)

The value for resistance, R, and inductance, L, was obtained through journal papers and articles about the electrical properties of tress as well as similar cases about lightning struck trees.

$$r = \sqrt{d^2 + (l-2)^2} \quad (2)$$

$$\Delta V = V_b - V_a \quad (3)$$

$$E = \frac{\Delta V}{r} \quad (4)$$

The height of a person is considered to be as a low impedance object at 2 m. In this research, the distance between the tree and the person is set to 3 different cases, 1 m, 2

m and 5 m away. The height of the tree is considered to be 10 m and the electric field is calculated at the height of 5 m. The simulation considered the human body to be a perfect conductor and grounded, therefore

$$V_a = 0 \quad (5)$$

3. Results and Discussion

The calculated value of resistance and inductance for both type of trees are shown in Table 2. The distance between the tree and the person is shown in Figure 3 to Figure 8 by the different colour. The distance is represented by the letter d in the figures.

Table 2: The electrical properties

Objects Struck	Resistance (Ω/m)	Inductance (H/m)
Tree A	810×10^3	3.32×10^{-19}
Tree B	650×10^3	4.17×10^{-13}
Copper Tape	3.36×10^{-4}	3.017×10^{-6}

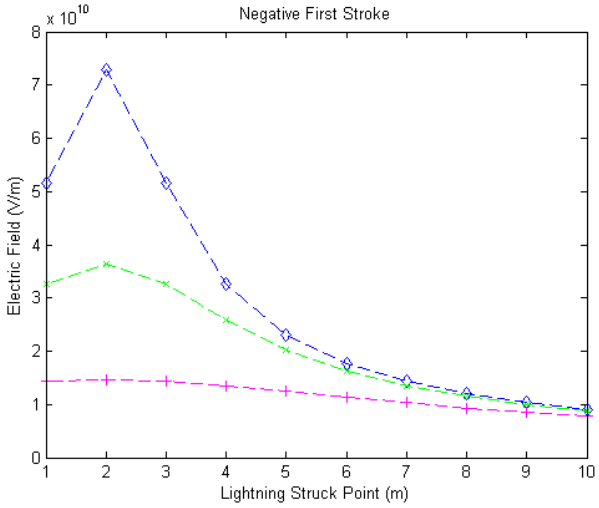


Figure 3: Negative First Stroke on Tree A

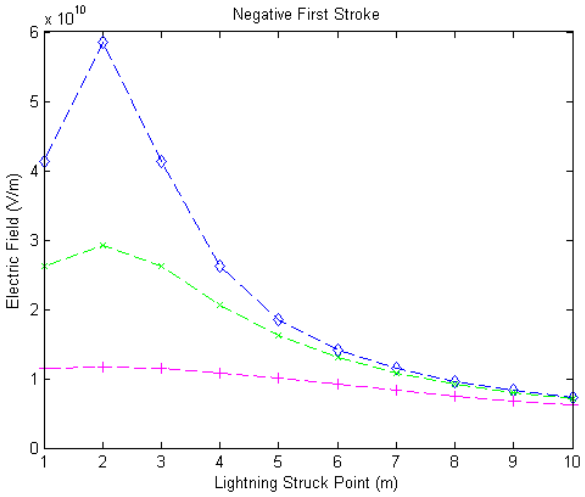


Figure 4: Negative First Stroke on Tree B

Figure 3 and Figure 4 shows the estimation of the electric field distribution against the height at the given point of the tree for Negative First Stroke. The curve shows the peak of the electric field is at 2 meters high when the person is 1 meter away from the tree. The electric field strength drops slowly as both the height and the distance between the person and the tree increases.

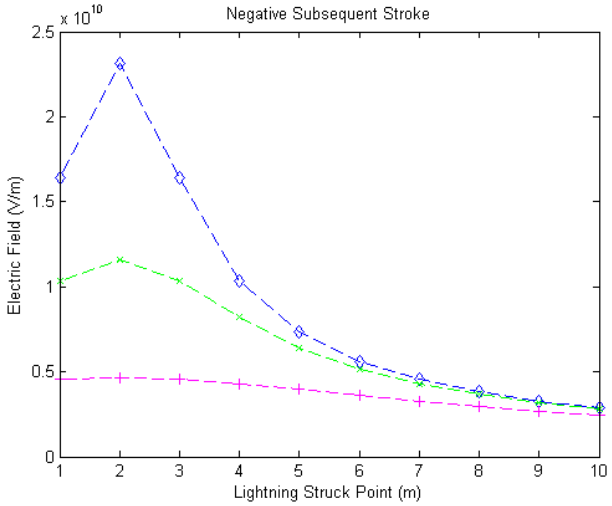


Figure 5: Negative Subsequent Stroke on Tree A

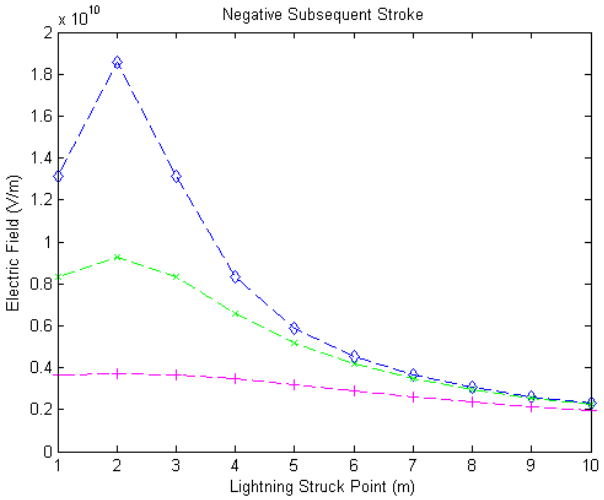


Figure 6: Negative Subsequent Stroke on Tree B

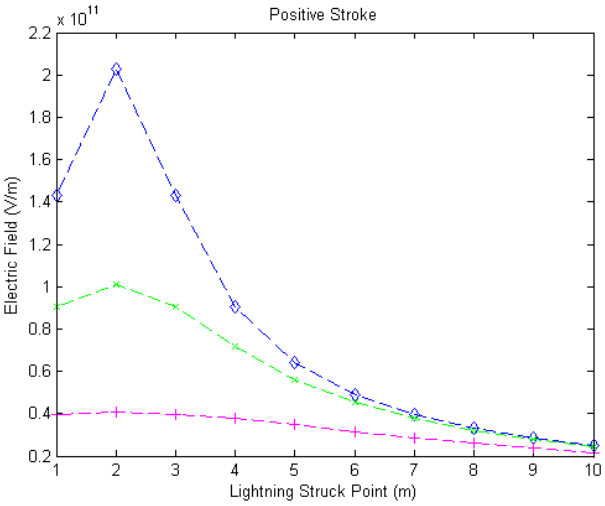


Figure 7: Positive Stroke on Tree A

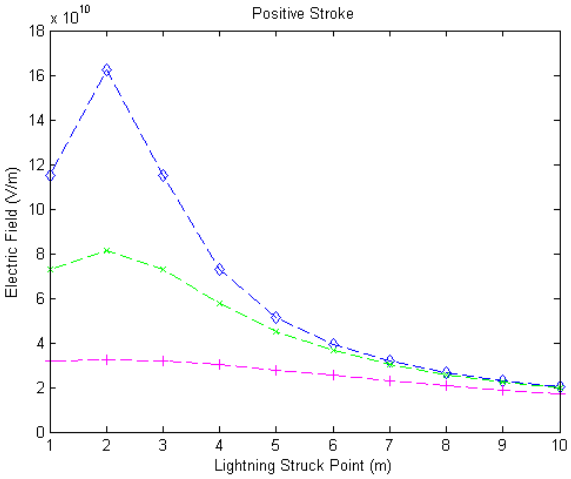


Figure 8: Positive Stoke on Tree B

Figure 5 to Figure 8 shows similar results to Figure 3 and Figure 4. Although we can see the declining in electric field strength as the distance and the height increases, the possibility of a side flashing is still high as the air breakdown strength was overcome. Figure 9 to Figure 11 shows copper used as the object struck by lightning.

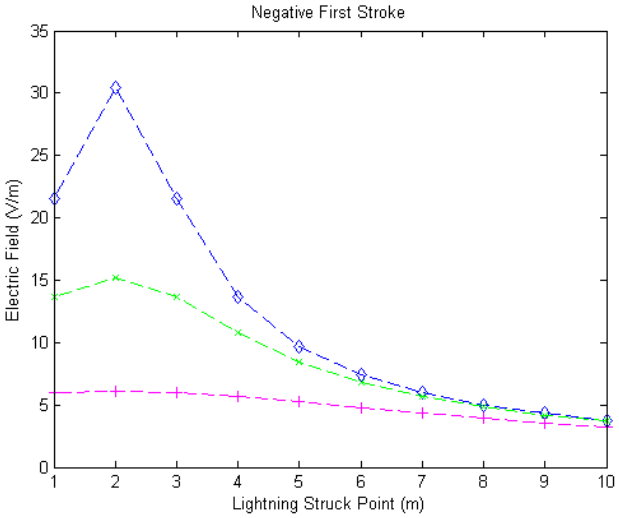


Figure 9: Negative First Stroke on Copper Tape

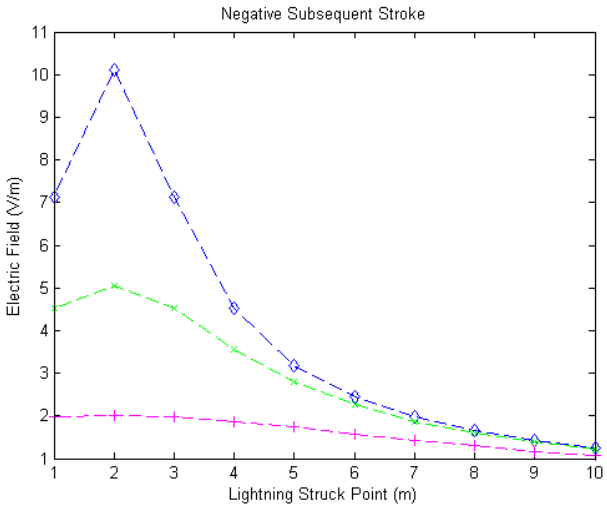


Figure 10: Negative Subsequent Stroke on Copper Tape

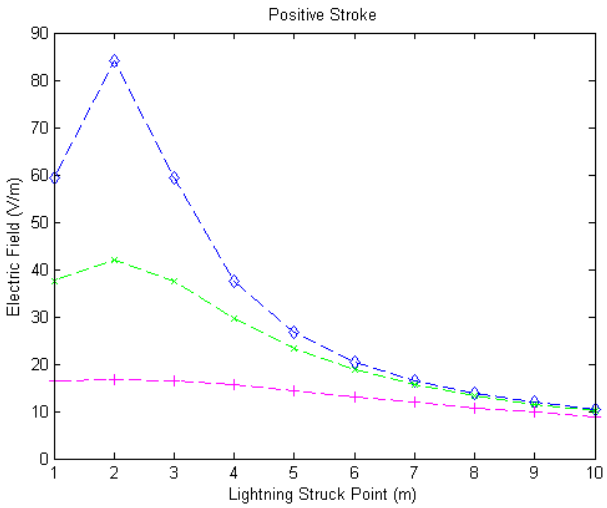


Figure 11: Positive Stroke on Copper Tape

As Figure 9 to Figure 11 shows that the difference in electric field strength is great. The possibility of a side flash when the object struck have similar electrical properties as copper tape is low. The hazard of being near a tree due to the electric field is very high as the value shown in the results exceeds the air breakdown strength greatly. However, the simulation in this paper are estimation and approximation. The possibility of side flashing is not 100%.

In real life, the height of the point which the lightning struck varies as it is difficult to predict the exact location of the struck point. It is not necessary that a person will not get struck by lightning when he is standing 10 meters away when the point struck on the tree is higher than 10 meters. There are more parameters and variables needed to compute such as the height of the person, the exact electrical properties of the trees and the amount of trees in the area. This paper goal is to determine whether the possibility of a person getting side flashing while standing at a certain distance from a tree. Therefore, it is advisable to seek shelter in an enclosure away for a tree rather than standing under it.

4. Conclusion

The possibility of a lightning to side flash to a person from a tree is based on the capability of it overcoming the air breakdown strength, $3x10^6$ V/m. The details of the simulation in identifying the possibility is discussed in the paper. There is a possibility at which the lighting side flashing to a person occurring. Further studies required in order to identify more sound results as several simplification were employed in the study to obtain the data in which the results are based on approximation.

Reference

[1] U. C. Foya, Protection of Structures against Lightning, M.Sc. thesis, Department of Electrical and Electronics Engineering, Natural and Applied Science of Middle East Technical University Jul. 2004.
[2] Hariati Azizan, 'On lightning watch', The Star: Archives, March 7, 2010
[3] Ghasem Nourirad, Chandima Gomes, Mohd Zainal Abidin Ab Kadir, Siow Chun Lim, 'Risk of Side Flashes from Lightning Struck Objects to Human Body: A Quantitative Analysis', Electrical and Electronic Engineering Department, Universiti Putra Malaysia (UPM), 2013.
[4] Zulkarnain Abdul-Malek. Recent Advances in Lightning Detection and Protection Studies, Fakulti Kejuruteraan Elektrik, 2008. UTM Skudai, Malaysia.
[5] Rita McKenzie. Trees and Lightning, Dept of Forestry & Natural Resources, Purdue University, West Lafayette.
[6] Evan M Gora, Stephan P Yanoviak, 'Electrical Properties of Temperate Forest Trees: A Review and Quantitative Comparison with Vines', Department of Biology, University of Louisville, Louisville, KY, USA NRC Research Press, 23rd October 2014
[7] Yang Cao, Tapani Repo, Raimo Silvennoinen, Tarja Lehto, Paavo Pelkonen, ' Analysis of the Willow Root System by Electrical Impedance Spectroscopy', Journal of Experiment Botany, Vol 63, No 1, pp 351-358, 2011.
[8] Ronald L. Holle. 2010. Annual Rates of Lightning Fatalities by Country. Proc. 21st International Lightning Detection Conference. 19-20 April 2010. Orlando Florida, USA.
[9] L.M. Ong, and H. Ahmad. Lightning Air Terminals Performance under Conditions without Ionization and With Ionization," Institute Of High Voltage and High Current, 2003. UTM Skudai, Malaysia.
[10] A. Kalair, N. Abas and N. Khan*. Lightning Interactions with Human and Lifelines, Department of Electrical Engineering, Journal of Lightning Research, 11-28 May 2013, COMSATS Institute of Information Technology, Park Road, Islamabad, Pakistan.
[11] Vladimir A. Rakov*. Lightning Discharge and Fundamentals of Lightning Protection, Department of Electrical & Computer Engineering, Journal of Lightning Research, 3-11 April 2012, University of Florida, Gainesville, FL, USA.
[12] DIB Djalel, Rahmani Lazhar, Iabar Hocine, A New Model of Electromagnetic Fields Radiated by Lightning, International Journal of Engineering and Innovative Technology (IJEIT), Volume 2, Issue 4, October 2012.
[13] Seyed Abbas Mosaddeghi, Electromagnetic Environment Associated with Lightning Strikes to Tall Strike Objects, Ecole Polytechnique Federale de Lausanne, 2011.
[14] Miller EK, Poggio AJ, Burke GJ. An integro-differential technique for time-domain analysis of thin wire structures. J Comput Phys 1973; 12: 24–48.
[15] R. Moini*, S.H.H. Sadeghi, B. Kordi, 'An Electromagnetic Model of Lightning Return Stroke Channel Using Electric Fields Integral Equation in Time Domain', Department of Electrical Engineering, Engineering Analysis with Boundary Elements, 27, 2003, pg 305-314.
[16] Evan M. Gora, Stephan P. Yanoviak. Electrical Properties of Temperate Forest Tree: A Review and Quantitative Comparison with Vines, Department of Biology, University of Louisville, Louisville, KY.

[17] Cheng –Jung Lin, Chih-Hsin Chung, Te-Hsin Yang, Far-Ching Lin. Detection of Electric Resistivity Tomography and Evaluation of the Sapwood-Heartwood Demarcation in Three Asia Gymnosperm Species, The Finnish Society of Forest Science, The Finnish Forest Research Institute, 13-22 March 2012, Taiwan Forestry Research Institute, Taipei Taiwan.

[18] G. I. Torgovnikov. Dielectric Properties of Wood and Wood-Based Materials. Wood Science. Springer-Verlag, 1993.

[19] Therese Sjoden, Electromagnetic Modelling for The Estimation of Wood Parameters, Vaxjo University, School of Mathematics and System Engineering, Engineering Physics, 2008.

[20] Therese Sjoden, Borje Nilsson and Sven Nordebo, Microwave Modelling and Signal Estimation for Detection of Wood Properties, Vaxjo University, School of Mathematics and System Engineering, 2008.

[21] B. Nilsson. Determination of spiral grain in trees by remote electromagnetic sensing. Submitted to Wave Motion, February 2005.

[22] Michael Adebayo Omidiora, Modeling and Experimental Investigation of Lightning Arcs and Overvoltages for Medium Voltage Distribution Lines, Department of Electrical Engineering, Doctoral Dissertations, 24 October 2011, Aalto University, Finland.

Evaluation of Magnet Size Ratio of Permanent Magnet Generator for Wind Applications

Zain Anjum Maqsood[1], Aravind CV[1,*], Dhanasekaran R[2]

[1]*Taylor's University Lakeside Campus, Malaysia*

[2] *Director-Research, Syed Ammal Engineering College, Ramanathapuram, India*

[*]aravindcv@ieee.org

Abstract

The major challenge in the wind energy generation is on the capability of the generator used as energy convertors. Permanent magnet generators are employed for many years replacing the induction generators and efforts are put-in much on the control technique to harness the energy than on the looking for viable improvised magnetic generators. In this work, the magnetic circuit inside the conventional generator used is modified based on the electro-magnetic principles. Both the conventional and the proposed machine are analyzed using finite element tool. Use of Halbach set of magnetic orientation further improves the power density of the proposed generator. Five different models of the Halbach array system are designed each with a different ratio of the magnets. The results obtained are investigated for higher power density and a model is selected out of the five models designed initially based on its power density capability. The selected model has a power density 38.64% higher than the conventional 1:1 model. The foundation of selecting the optimum design is influenced by generation of high torque alongside attaining good flow of magnetic flux in the machine and reduced effect of harmonics. The analysis is done with constant speed that correlates the power density with that of the generator constant square density to reduce the complexity in computations.

Keywords: Novel Design, Wind Energy, Permanent Magnet, Halbach Array, Finite Element Method

1. Introduction

In the power generation industry, the electromechanical conversion of energy plays a vital role. Therefore, improving the efficiency of the generators is extremely significant in order to fulfill the energy demands around the world. Usually in a system where the energy is converted, a high amount of energy is lost in conversion in terms of mechanical transmission, power loss in the wires etc. [3]. Studies show that using a permanent magnet design inside a generator or motor can improve the efficiency of the system.

With more research on this type of technology, a good design is developed solving one of the main problems faced by the power generation industry. Permanent magnets have been in the market for a very long time now but recently due to advancement in power electronics controlling the operation of the generators a good increase in permanent magnets based designs is observed. For wind turbine application, the main things to consider are high torque and efficiency on low speeds. Because the wind does not move the rotor at a high speed, it just moves the rotor at low speed therefore the torque must be high [4].

Permanent Magnet Generators are introduced in the wind turbines in the early 2000s. Ever since then the market for these types of generators is on a boom. Statistics show the increase to be from 17% to about 40% that means the future is bright for this type of technology. The main reason for the increase is that using PMGs increases the efficiency along with flexibility and reliability [5]. Many big companies are carrying out intense research on PMGs by studying the basics principles in order to make this technology as efficient as possible. To design a great generator or motor finite element method (FEM) study can be used to understand the effects of different parameters on the output.

Using wind power to generate electricity is good in terms of saving the environment because the wind energy is free and it does not require you to burn the fossil fuels. This directly effects the environment in a way that the greenhouse gases are reduced and the pollution in the environment resulting in acid rains is reduced. After researching many different types of generator designs the idea of implementing halbach array into the design looks very convincing. In a halbach array system the excitation of the magnets help the flux to flow with more stability. This implementation strenghtens the flux flow along with the magnetic field in the design. The excitiation of the magnet is changed in halbach to help the flux to flow more easily and to strenghten the flow as well.

The objective of this paper is to study and analyze the effects of different magnet ratios of a Halbach design on the power density of the model by conducting series of simulations through the application of finite element method to select the optimum design.

2. Theoretical Framework

2.1 Proposed Design

Figure 1 and Figure 2 shows the machine designed and used in this analysis. Table 1 shows the parameters computed using the standard mathematical design equations.

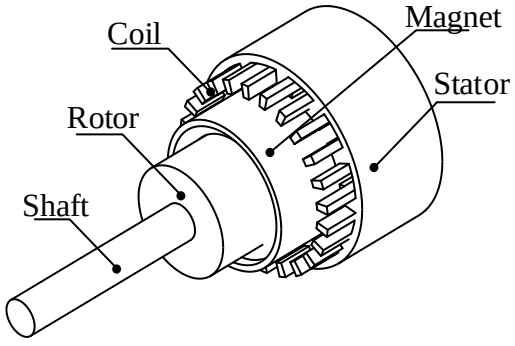


Figure 1. Exploded View

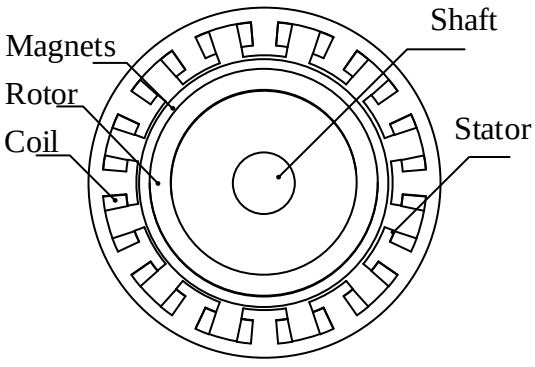


Figure 2. Front View

Table 1. Parameters of the machine designed

Parameters	Value
Machine	
Outer diameter	50 mm
Stack length	50 mm
Shaft diameter	8.8 mm
Shaft length	100 mm
Air-gap	0.5 mm
Rotor	
Number of poles	10
Outer diameter of the rotor	32.4 mm
Inner diameter of the rotor	26.4 mm
Arc length of the pole	20.024 mm
Stator	
Number of slots	12
Inner diameter of the stator	36.4 mm
Outer diameter of the stator	50 mm
Arc length of the stator	14.94 mm
Area of coil	38.52 mm^2

After doing all the analysis on the model a 12-slot 10-pole machine with Halbach array and a ratio of magnets 1:2 is chosen. Each pole is divided into two different magnets one magnet represents the north or the south pole whilst the other magnet is based on the concept of Halbach that directs the flux to flow either right or left to strengthen the flux on one particular side of the magnet.

2.2 Finite Element Method

Finite element method (FEM) is a numerical method to solve linear and non-linear partial differential equations of a given system. It starts of by constructing the

design of your desired generator in 2D or 3D depending on your needs. Moving on the material properties of the different parts inside the generator is configured along with the excitation pattern of the magnets and coils. Moving on mesh of the system is generated that breaks the given structure into very small finite elements [7]. The finite element model results are useful to understand the behavior of the constructed model. After this the results can be analyzed and compared to understand to make sure that you get the most accurate results. If these results obtained are not what is expected the model can still be modified in many different ways to reach a point where the results are extremely accurate.

3.0 Methodology

3.1 Process Flow

Figure 3 shows the approach used in this research design. The process of designing the machine starts by understanding the fundamentals of electromagnetic principles. The flux flow of a conventional generator design is studied to produce a magnetic circuit. This magnetic circuit is then analyzed and studied to be modified to a new magnetic circuit based on the understanding of the Halbach concept. The basic idea of Halbach is to double the magnetic flux on single side of the magnetic instead of distributing the flux evenly on both sides of the magnet this phenomenon actually helps the strengthen the flux on the desired side of your design. So based on this idea first model of a PMBLDC is made. In this model, the size of the north and south pole is kept equal to the Halbach magnet. Subsequently to understand the effect of different magnet ratios on the power density the size of the north pole and the Halbach are altered resulting in five different models principally based on Halbach concept. These models are then analyzed through the application of finite element method and the results are recorded. These results are then analyzed in order to choose the optimum model by comparing the generator constant square density (G). Halbach model and the optimum model that is 1:2 are analyzed again for torque production and studying the effects of harmonics on the design and the optimum model is selected. Finally, after all the analysis the finalized model is sent for fabrication.

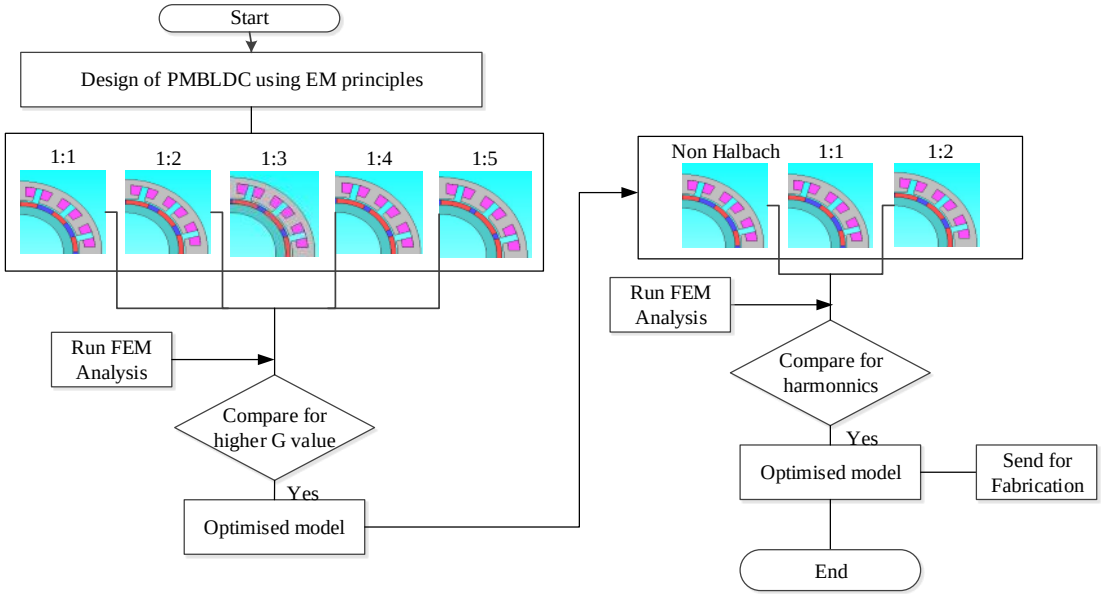


Figure 3. Analysis Flow Chart

3.2 Parameter Evaluation

The power constant is given by Equation (1).

$$P_t = \frac{T.\omega}{i} \tag{1}$$

where T is the torque in newton meters and i represent the current in the coil in Amperes.

The generator constant is given as in Equation (2).

$$K_g = \frac{Pt}{i} \tag{2}$$

The loss in the generator due to winding is given as in Equation (2).

$$P = I^2 R \tag{3}$$

where P_t is the power constant and P is the resistive power loss in watts, I is the current in the coil in amperes whilst the R represents the resistance of the coil in ohms.

The generator constant square density for the designed generator is as in Equation (4). This is used as a comparative analysis parameter as it helps to compare of any generators as the power density is compared to the volume of the machine making it as a ratio of comparison.

$$G = \frac{Pg}{V} = \frac{Kg/P}{V} \quad (4)$$

where P_m is the generator constant and V represents the volume of the machine.

4.0 Results and Discussion

4.1 Machine Characteristics

To determine the best angle of operation the machine is kept at a constant speed of 300rpm and using the case control seven different cases with an increment of 15 degrees starting from 0 to 90 degrees are generated and the simulation is run the results are recorded and analyzed by plotting the curve.

Figure 4 shows the angle for all the cases are plotter and the pattern of the plot for all the 7 cases that are studied in this research. Based on the analysis of the results 60 degrees is chosen as the most optimal supply angle.

The attraction and repulsion forces of the magnets produce torque in a machine. The magnets produce magnetic field in the machine these fields interact to make the machine to rotate resulting in the production of torque. To decide the model with best torque characteristics three different models are studied by keeping the rotational speed at 300 rpm and the supply angle to 60 degrees. The torque results from the simulation are recorded and analyzed by plotting the graphs.

Figure 5 shows the torque produced by three different models. The interpretation of the graph is the torque for Halbach with a ratio of 1:1 is giving a torque that is very low. While on the other hand the non-Halbach version of the 1:1 model gives a much higher torque but the problem is that the torque is not uniform and is fluctuating over the same time. Finally, for the 1:2 Halbach model the torque is uniform and higher flux value than the Halbach 1 by 1 hence this model is the most acceptable one for the application designed for.

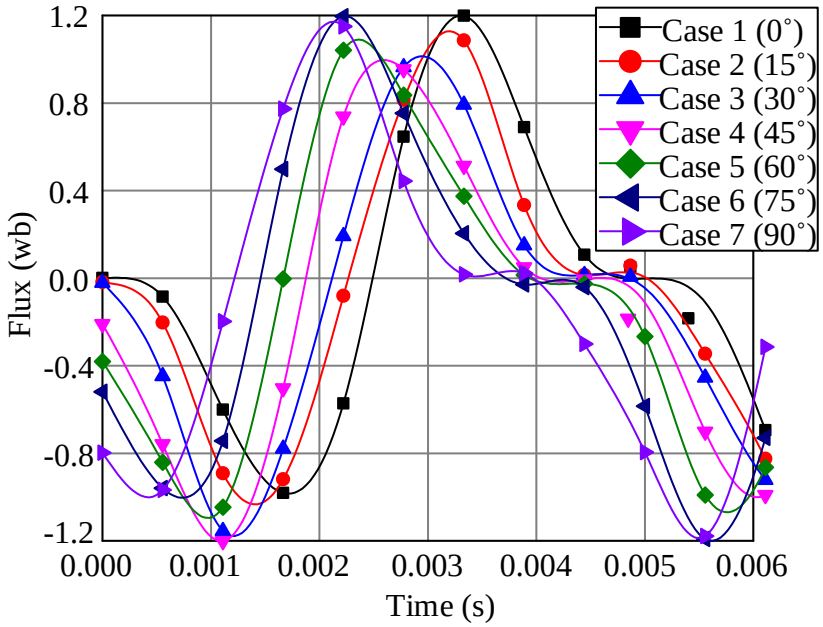


Figure 4. Plot to decide the most suitable phase angle

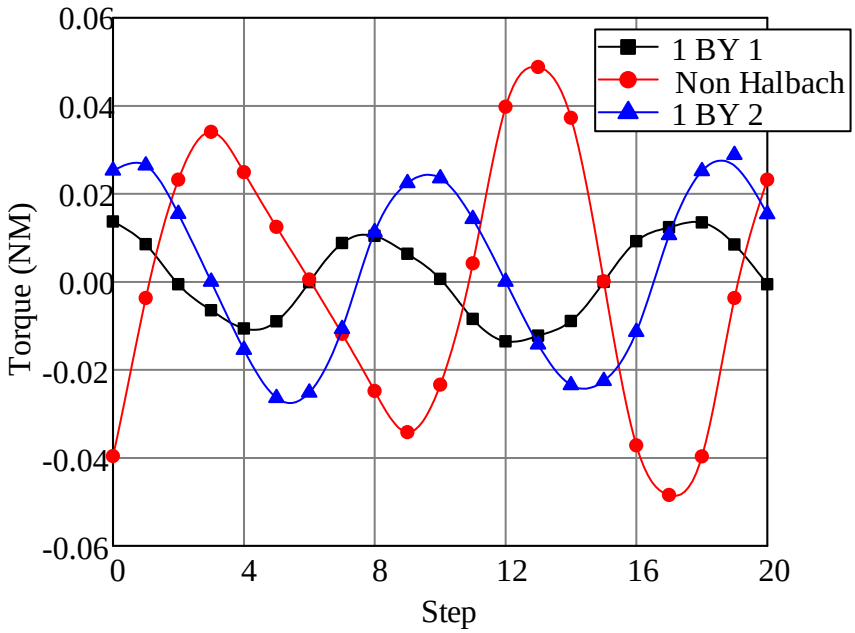


Figure 5. Torque characteristics curve

4.2 Fast Fourier Transform Analysis

Figure 6 and Figure 7 show the results of applying Fourier transform to understand the effects of magnet ratios on the third harmonic. The graphs below show that 1:1 model either Halbach or non Halbach give the same results and the 1:2 model gives different results. The second bar represents the 3rd harmonic of the system so the model with a ratio of 1:2 has a lower amplitude of the second bar than that of the 1:1 model hence the most suitable model is the 1:2 Halbach model.

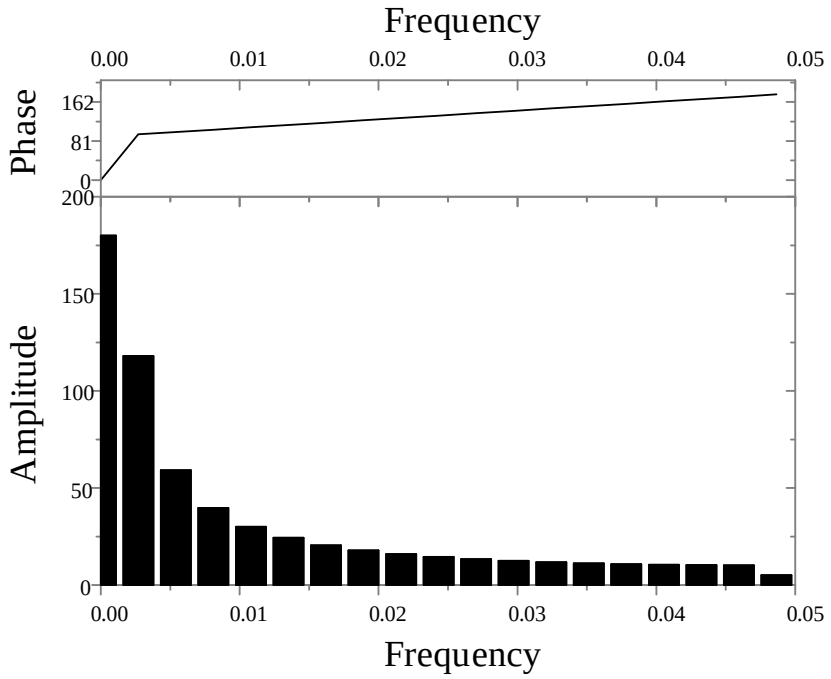


Figure 6. Fast Fourier transform results for 1:1 (Halbach & Non Halbach) model

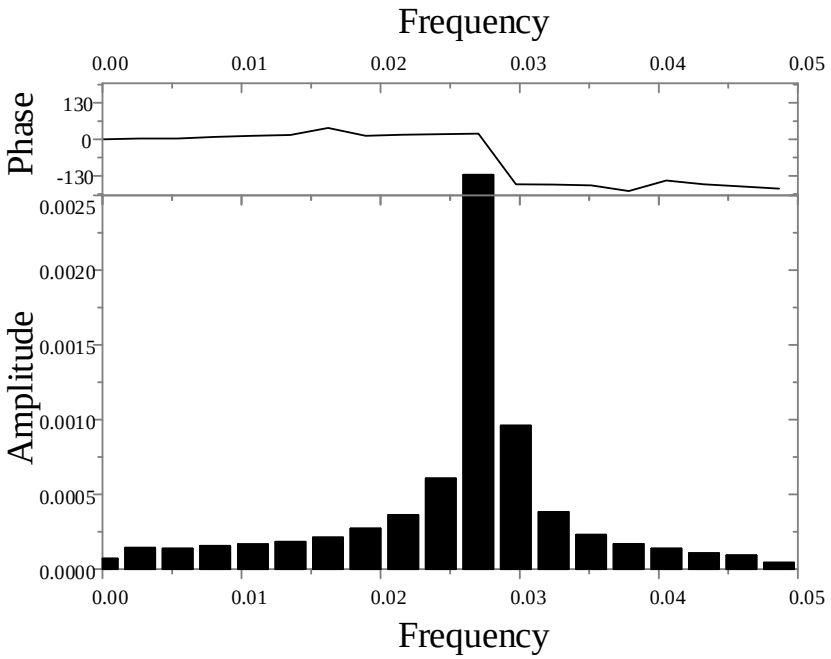


Figure 7. Fast Fourier transform results for 1:2 Halbach model

Table 2. Performance Parameters

Parameters	**1:1**	**1:2**	**1:3**	**1:4**	**1:5**
K_T (Torque Constant)	$1.9e^{-4}$	$3.1e^{-4}$	$2.7e^{-4}$	$2.4e^{-4}$	$2.4e^{-4}$
K_G (Generator Constant)	$1.3e^{-5}$	$2.7e^{-5}$	$1.76e^{-5}$	$1.76e^{-5}$	$1.76e^{-5}$

G (Generator Constant Square Density)	4848.9	7902.3	6984.6	6418.8	6145.2

In the table 2 above the torque produced by all five models is recorded from the software. The volume of the machine is calculated by multiplying the cross sectional area into the stack length. Using these values, the torque constant, generator constant and generator constant density is calculated to select the design with the highest generator constant square density. The model with 1:2 has the highest generator constant square density and is suitable for the application of design proposed, as seen in the table.

5.0 Conclusion

The design of a generator has a big impact on the electrical output of the model, minor modification in the design can make the model to operate very differently. In this paper the idea of using Halbach array into a generator design are studied along with the selection of the best ratio for the Halbach. The 1:2 model is selected as the final model as the generator constant density is the highest at about 26.341, this is a staggering 38.64% higher than the 1:1 conventional Halbach array model. Correspondingly, the torque and the fast Fourier transform results also favour the 1:2 models. For future work further optimization of the design can be achieved by carrying out analysis parameter alteration and analysing the behaviour of the model.

References

[1] O. Elbeji, M. Ben Hamed, and L. Sbita, “PMSG Wind Energy Conversion System : Modeling and Control,” no. July, pp. 88–97, 2014.

[2] F. Ben Amar and M. Elamouri, “Wind Energy Conversion Systems Adapted to the Tunisian Sites,” vol. 2013, no. February, pp. 57–68, 2013.

[3] M. Abbasian and A. H. Isfahani, “Optimal Design of a Direct-Drive Permanent Magnet Synchronous Generator for Small-Scale Wind Energy Conversion Systems,” vol. 16, no. 4, pp. 379–385, 2011.

[4] S. M. Hosseini and M. Mirzaei, “Design , Prototyping and Analysis of a Low-Cost Disk Permanent Flat-Shaped Magnets,” vol. 32, pp. 191–203, 2008.

[5] C.-Y. Hsiao, S.-N. Yeh, and J.-C. Hwang, “Design of High Performance Permanent-Magnet Synchronous Wind Generators,” *Energies*, vol. 7, no. 11, pp. 7105–7124, 2014.

[6] S. A. Khan, R. K. Rajkumar, R. K. Rajkumar, and A. Cv, “Performance analysis of 20 Pole 1.5 KW Three Phase Permanent Magnet Synchronous Generator for low Speed Vertical Axis Wind Turbine,” *Energy Power Eng.*, vol. 05, no. 04, pp. 423–428, 2013.

[7] S. Mine, “Direct - drive permanent magnet synchronous generator design for hydrokinetic energy extraction,” 2013.

Upper Limb Animation System

Ahmed Firdaus bin Ahmed Farid[1*], Dr. Leong Wai Yie[1], Mr. Jeffrey Chin[1]

[1]*School of Engineering, Taylor's University Lakeside Campus, Malaysia*

[*]firdausfarid@live.com

Abstract

The upper limb is one of the most important parts of the human body due to the fact that it promotes reach, touch, and grabbing motions which is useful for a person to perform everyday tasks. Over the years, people are exposed to many forms of illness, injuries, disabilities or even accidents that may affect the mobility of their upper limb area. These unfortunate events will affect one's productivity thus finding an effective solution is critical as to remedy the affected parts of the upper limb back to full functioning order. Therefore, the application of an upper limb tracking system is proposed in helping rehabilitating patient recover quicker. In this paper, the tracking system is made to be different than other existing tracking system where it tries to have the simplest, lowest cost and effective Upper Limb Tracking System(ULTS). Softwares such as Arduino IDE and Processing is used to unlock the latest potential together with the use of effective codes to simulate and produce reputable data for comparison and analysis purposes for the patient's progress. The codes applied were found to produce drift and noise for the motion data readings thus offset algorithms were applied into the codes. Due to the drift of the gyroscope, the accelerometer which is more stable is used to determine the upper limb motion angles. Complementary and Kalman filters were also applied in the codes to provide less noise and smooth accurate graph data. The live graphs produced allow better understanding on gyroscopes sensitivity and drift effect. The filters applied provided with a more accurate graph which is a lot smoother and easier to understand. The filters were also explain on its theory. Movement of graphs together with raw data was produced which will help provide a baseline and target value. Furthermore, an external robotized arm which runs through myoelectrics is also implemented as a solution to help patients gauge their progress visually which helps the everyday person to understand the numerical data better as it allows them multiple angle views of their arm when their own arm's movement is replicated onto the prosthetics. With the external robotized arm, the user is able to have a both an accurate motion tracking system which will help them understand their arm performance while having the simplicity of a prosthesis that gives out simple visual gauge that helps the patient or user track their progress.

Keywords: tracking system, sensors, rehabilitation, upper limb, Arduino, Processing,

1. Introduction

The human upper limb consists of parts from the human fingers until the shoulder area. Everything in between them would be classified as the upper limb region of the human body. The upper limb is one of the most important parts of the human body due to the fact that it promotes reach, touch, and grabbing motions which is useful for a person to perform everyday tasks. Over the years, people are exposed to many forms of illness, injuries, disabilities or even accidents that may affect the mobility of their upper limb area. These unfortunate events will affect one's productivity thus finding an effective solution is critical as to remedy the affected parts of the upper limb back to full functioning order. To address the problem, it is found over the years that exercise training is one of the best ways to rehabilitate the affected parts of the upper limb back into health as independent and repetitive movements during the exercise would strengthen the limb muscles and allow quicker recovery to give the patient full level of function. Based on a journal, the author agrees that strength or independent exercise training that induces resistance to the affected part of the upper limb helps with rehabilitation [1]. To achieve the best result through the rehabilitation exercise, the movements and trajectories of the limb has to be quantified and measured for progress and comparison purposes. In this case, being able to capture the motion movements and details when the patient is to perform a specific task is desirable as to give out the most accurate results of their progress and for comparison purposes.

Throughout the years, there have been many protocols developed to assess the upper limb kinematics. Most of the measurement systems rely on electromagnetic and optoelectronic principles whereby even though it is effective, the high cost, complexity and restricted field of operation prevents them from being well exposed to the general public for their rehabilitation purposes [2]. To aid the study, questions such as how an upper limb tracking system help rehabilitating patients gauge their progress and how effective is having an external robotized prosthesis help patients visually understand their progress can be stated as the study revolves around the design of a system that should help the patients progress quicker. The tracking system is made to produce angle reading datas that will be used as a gauge and the external robotized prosthesis is a simple arm that has markings to help assess the movement visually.

As the motion tracking of the human upper limb research has been done extensively through other studies, the system can be improved by trying to use new types of inertial sensors and microcontrollers together with the motorized prosthetic upper limb. The motorized prosthetic arm will be made to replicate the rehabilitation movements visually thus giving the patient better understanding of their progress. The prosthetic arm would be functioning through the use of Electromyography(EMG) sensors which converts electrical potential of the human muscle cells into a direct motion when it is paired with a microcontroller motor servos [4].

With the motion tracking of the upper limb paired together with the replication of the upper limb movement through the use of motorized prosthetics, this could be the first system that allows both advantages to limb rehabilitation and health knowledge as it would give patients the opportunity to gauge their rehabilitation progress together with the ability to visually inspect the functionality of their arm. Therefore, these two systems could eventually be a cost effective way into the limb tracking and replication study.

Therefore, our solution in this study is to overcome the unnecessary complexity and cost issues by using inertial sensor based systems whereby it is more user friendly and very cost effective thus giving the opportunity to obtain the limb motion reading for analysis purposes while the prosthetic arm incorporates visual results to compliment the quantitative data obtained. The measurements from the human limb motion can be quantified through the use of gyroscopes and accelerometers [3]. These sensors allows the motion data obtained to be connected to a base station(microcontroller) for processing which in turn produce the needed readings of the movements. The objective of the study is mainly to design the upper limb tracking system and the external robotized prosthetics. With the design ready, we can point out that the project scope is limited to the involvement of the tracking system that is made of sensors and components in a small package in which the user can wear it on their arm. Also, the data obtained from the sensor readings gives the users the opportunity to gauge their performance while the external robotized prosthetics is made to replicate the actual movement of the user's arm thus giving the patients visually easy to understand movements of the affected arm.

As for the literature review, the already available human motion tracking technology and existing upper limb studies together with a basic breakdown of the design of the external prosthetics will be discussed in this section.

1.1 Mechanical Human Motion Tracking

This method of tracking human limb motion is one of the oldest technology out of all the available systems [5]. The system is mechanical due to the linkages used to connect and link the person together with the system. It works by having fixed structures of jointed, straight plastic or metallic rods which is linked together with sensors such as potentiometers that moves at the joints of the person's body. In simple form, the links forms an exoskeleton surronding and attached the wearer thus for every movement done by the wearer, the exoskeleton system tracks every relative motion happening. This system is actually relatively accurate for a motion tracking system as it records real time data due to the linkages measuring every motion instantaneously through direct contact. Furthermore, the system is priced reasonably well to produce but does not relate to today's technology advancements as the system is rather restrictive in motion as the user is constantly restricted to the specified degree of freedom of the exoskeleton linkages thus making it not worthy for future use.

1.2 Magnetic Motion Tracking

Due to the nature of magnetic sensory devices being widely available, it is relatively inexpensive to obtain thus making it a cost effective way to create a motion tracking system. The magnetic tracking system is reasonably accurate when determining the position and orientation of a solid object. A magnetic tracker ususally consists of a source emitter and receivers which are sensors that is placed at the desired motion tracking area of the human body. The trackers detect motion through generated magnetic fields while having the ability to work without major obstruction or shadowing problems [7]. The source emitter is made out of three coils which are right angles to each other whereby when the the coils are subjected to current signals, a rotating magnetic field is produced. This will then prompt the the sensor coils which are perpendicular to each other. When this happens, the induced current in the sensor

coils will then form a nine element rotation matrix, which will then be used to compute the position and orientation of the sensor respective to the emitter [8]. Even though the magnetic tracking system seems feasible in the long term, it has its own limitations that prevent the system to be fully utilized thoroughly. Due to the nature of magnetic fields, when the distance of the magnetic tracker is put further away from the generating source, the magnetic field power decreases thus scaling and modification of the user movement should be made to simulate a larger working volume [9]. The scaling and modification of the user movement is needed as the distance of the emitter is directly proportional to the position and orientation errors in the fourth power caused by deformation of the magnetic field created [10]. This would then cause inconsistency to the accuracy of magnetic systems within the working area.

1.3 Motion Estimation Through Inertial Measurements

Author Huivu Zhou, focused on almost the same research question whereby the upper limb motions are estimated through the use of inertial measurements. However, in this study the author went with using commercial sensors such as the MTx inertial/ magnetic sensors made by Xsens from the Netherlands [13]. As stated above, magnetic sensors do provide an alternative for cheap and accurate sensor that would determine the position of the upper limb. Unfortunately, the nature of magnetic devices of having magnetic inteference and distance issue is not a desirable limitation to have as it would be affecting the sensor readings since the world is littered with magnetic objects from our daily lives. Eventhough the sensor is magnetic based, the rest of the sensor is still Inertial Measurement Unit(IMU) based whereby it uses components that is available today such as an accelerometer and gyroscopes to obtain readings. The Xsens unit definitely provides all the bells and whistle as a tracking unit system but due to the high purchase price, it is not recommended as the everyday user cannot afford the high cost [13].

1.4 Inertial Measurement Sensors

1.4.1 Gyroscopes

Gyroscope is basically a device that measures orientation and rotation. Today it is incorporated into a sensor and installed in many electronic devices. To allow tracking of the human motion a micro electromechanical system(MEMS) based gyroscope can be used. These sensors work based on the Coriolis effect principle whereby it generates a Coriolis acceleration through the result of the angular rotation produced by a vibrating MEMS structure. The sensor has various direction about a driving tranducer's axis which brings out a vibration on different axis in a detection transducer. The vibrations occured is regulated by an oscillator circuit and a signal conditioning system whereby transforming the measurements to the output which is then expressed in angular rates. This then offers an interface to the sensor [12]. MEMS gyroscopes are generally integrated as a sensor. These sensors have a relatively low power consumption but give out a little inaccuracy. The power consumption is a little more than that of an accelerometer but still considered low which is very much needed in small battery powered application. The latest designs of gyroscopes were able to give out three dimensional read outs [13].

1.4.2 Accelerometers

Accelerometers are sensors used to measure its own linear acceleration. It is usually paired with a gyroscope for its application. When a mass or substance is connected to a spring-damper link which is also fixed to the sensor's platform, the sensor can detect when it is accelerating. As the sensor is sensing acceleration, it is actually moving in a opposite direction relative to the sensor housing (Figure 4). Then the mass displacement which is proportional to the force of the spring can be determined. Here the measurement of displacement is then converted to the sensor output which is able to read in digital or analog form thus providing with the acceleration reading [13]. The principle that goes on behind the accelerometer is that it measures the forces between a mass and the housing to which the former is attached. Specific forces acting such as the acceleration is considered a discrepancy between the instantaneous acceleration and free fall due to gravity. During free fall moments, the sensor reads the measurement as zero. For a sensor to stay immobile, a specific force is needed which is pointing upwards and has a gravitational acceleration value. Only then the projection of a specific force to the sensor axes measurements can be obtained[13].

1.5 Robotized Prosthetic Arm

Prosthetics became a necessity over the years to cater to amputees which involved in either accidents, injuries or even illness to help them continue on with their daily tasks without the akwardness [7]. Over the years, many advancement has been made towards the prosthetic limbs whereby it is getting even more realistic to the point that it went from having true to life joint movement to having real live movements through the technology of robotics. Eventhough the technology is already there it is still not perfect whereby it still does not move as accurate as we want to. Today, robotics are used in various forms of application when it is applied to prosthesis. Neuro rehabilitation is one of the examples whereby robotics can be applied as it is a medical process which aims to help patients to recover or compensate their lacking mobility. Here sensor such as the electromyography(EMG) sensor can help to move the motorize robotic prosthetics by connecting the EMG sensors to any parts of the human body thus using the electrical potential of the human muscle to activate the joint movement after the digital data is sent through a microcontroller such as an Arduino [17].

According to a paper published by New Jersey's School of Engineering paper, as robotic arms such as the 3D printed ones are getting more attainable by the public, people can now obtain the design drawings from the web and start producing it. This means that compared to regular prosthetics that requires professionals to design it, the 3D printed ones are alot cheaper to produce while being more modern in design as these newer ones can be personalized with servo motors and microcontrollers which allows more features[18]. This shows that an external robotized prosthetics has alot of potential but currently it only serves one purpose which is just as a prosthesis. When paired together with a tracking system, the prosthesis can definitely be made to compliment the motion tracking system of the arm by visually defining the user's rehabilitation process.

2. Research Methodology

According to the flowchart in Figure 1., the project begins by understanding the project scope of the study. Next, there will be discussion on the components needed, assembly of the components and also the programming or coding needed to run the experimental setup. Lastly the data collected will be discussed and tabulated for further understanding of the study.

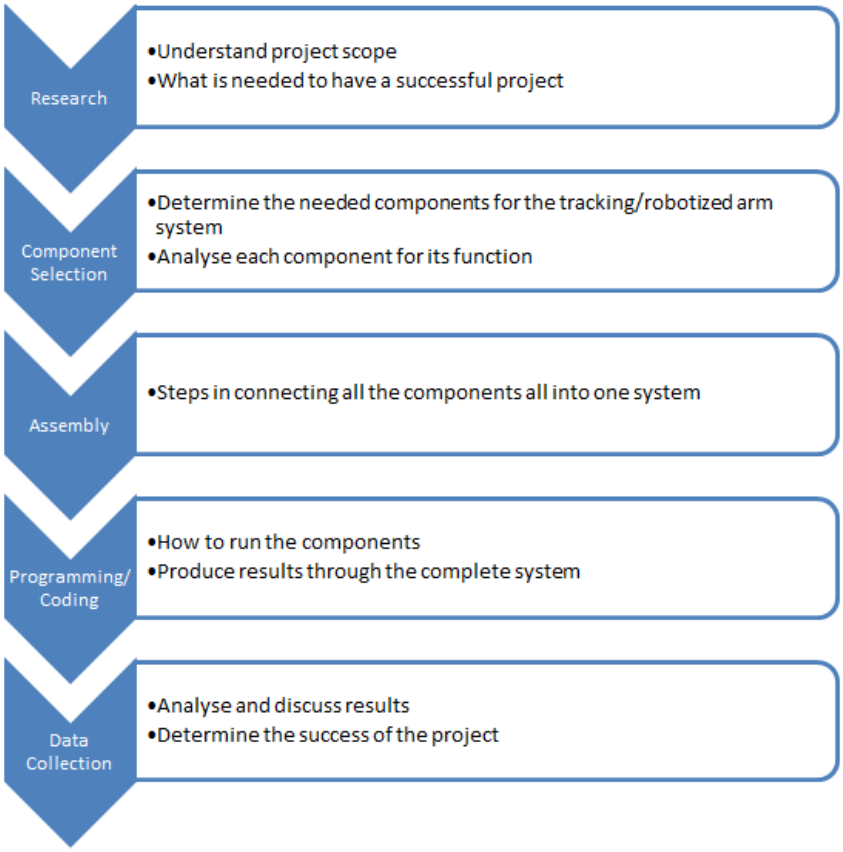


Figure 1. Methodology Basic Flow Chart

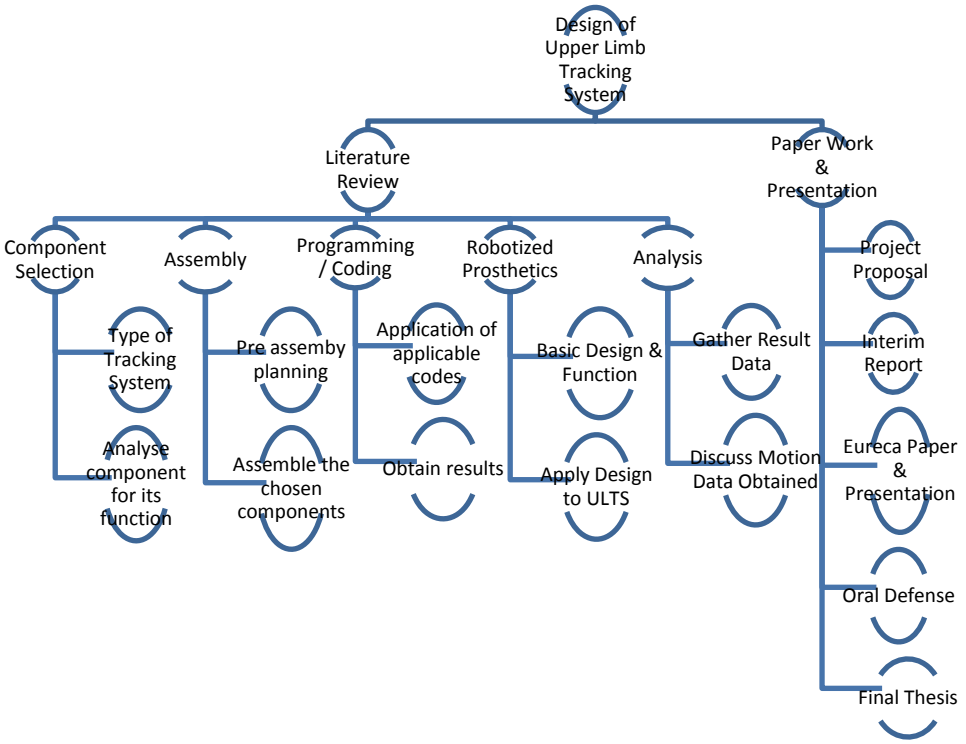


Figure 2. Work Breakdown Structure

2.1 Hardware & Equipment

2.1.1 Upper Limb Tracking System (ULTS)

A microcontroller board is basically a mini computer. It does whatever a computer can do albeit being limited by its hardware specifications thus only able to control or run one task at a time [19]. Here the Arduino Uno microcontroller was chosen as the desired microcontroller/base unit. An Arduino microcontroller was chosen due to its flexibility, support, user friendliness and having the most reasonable price compared to a Raspberry PI for example. A Raspberry PI may be a mini full blown personal computer but since this study only requires basic sensors and very little computing power, the low cost and simplicity of the Arduino Uno makes more sense[20]. The Arduino is also flexible in a way where it allows the user to purchase a basic fully built microcontroller or have the DIY version which gives the user the opportunity to assemble only the required output and input pins and components. This gives more opportunity especially to enthusiasts as the processor is the only main component that is important for processing any task. The rest of the components available on the Arduino Uno for example are there simply as a simple easy to use platform for the general public to quickly plug and play their desired sensors. Furthermore, it is also preinstalled with a boot loader which allows the user to write codes without the need of any external software thus using the default Arduino IDE Coding software [21]. With these specifications, the sensors that will be used in this study can be connected to the Arduino Uno thus having the ability to control the sensors and give out the desired results.

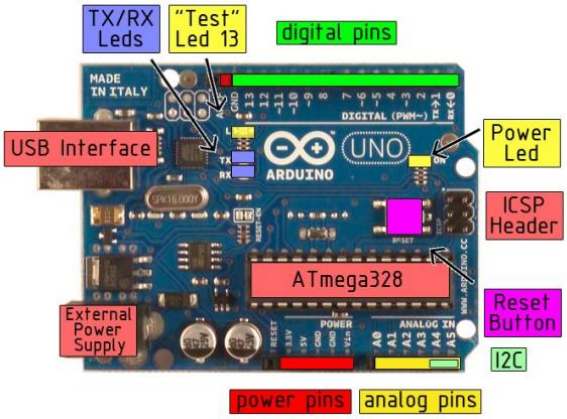


Figure 3. Arduino Uno Microcontroller

Since the system is to be wearable and wireless, the board will have its power supplied through a four 1.5 volt AA batteries connected on a battery tray thus supplying a constant 6 volts to the board. Since most sensors or devices that connects to the Arduino Uno runs on either 3.3V or 5V the 6V would not be a problem as the board has a built in voltage regulator to regulate the supplied voltage according to the pin where the sensor is connected to.

Table 1. Microcontrollers Comparison

Specifications	**Arduino Uno**	**Arduino Mega 2560**	**Iris Mote XM2110CA**
Processor	ATmega328P	ATmega2560	ATmega1281
Flash Memory	32KB	256KB	128KB
RAM	2KB	8KB	8KB
EEPROM	1KB	4KB	4KB

.

Based on a research paper done, a Memsic Iris Mote processor was used to run the same type of sensors used in this study[22]. The Iris Mote was taken as a baseline for processing capabilities thus based on the Table 1 above, an Arduino Uno may not seem to be up to par with the specifications of the Iris Mote but since balance of performance, ease of use, availability and cost is put into consideration, the Arduino Uno was chosen. The Arduino Mega would definitely run well with more RAM and FLASH memory performance but due to the large size which is unnecessary for the connection of just a few components. The Iris Mote on the other hand is not as widely available in Malaysia and requires self-assembly(ie. Soldering) of detailed parts together thus making it out of the selection list for easy to assemble components.

Next, the sensors chosen for the tracking system is the accelerometer and gyroscope. An accelerometer is a device that measures the difference in change of the gravitational acceleration. It could measure tilt and acceleration at its respective axis. The accelerometer is used so that the acceleration or tilt of the user's upper limb can be extracted for analysis. Next, the gyroscope helps in determining the orientation which

gives out the angular position around each available axis namely X,Y and Z[23]. By having this feature, the arm's pitch, yaw and roll along their respective axis can be determined. Here, a 6 degree of freedom(6DOF) MPU6050 one piece sensor made by DFRobot was chosen to determine the desired results.



Figure 4. DFRobot 6DOF MPU6050 sensor

The MPU6050 sensor has both accelerometer and gyroscope built into a single chip whereby it has 3 axis for the accelerometer and 3 axis for the gyroscope. Compared to the LPR series gyroscope and MMA series accelerometer used based on a student's paper, the MPU6050 is smaller, requires less components and easier to connect thus making it a desirable feature to have as the tracking system is better to be made as small and light as possible to allow better user comfort[22]. The components used based on the paper still does the same thing as the MPU6050 just having separate individual sensors incase the user wants to run only specific sensors only.

For easy connectivity, the Electronic Brick HC06 Bluetooth module was chosen as it one of the simplest ways to allow the ULTS system to connect and communicate with the coding/programming software(ie. Arduino IDE & Processing) thus allowing the ULTS system to operate wirelessly without any external cables for data transfer. The HC06 Bluetooth module runs on basic Bluetooth 2.0 which is also available built in most if not all laptops[24]. This gives wireless transfer of codes into the Arduino microcontroller thus reducing the hassle of needing a proprietary cable while giving the ULTS system a better visual appeal from its wireless look.

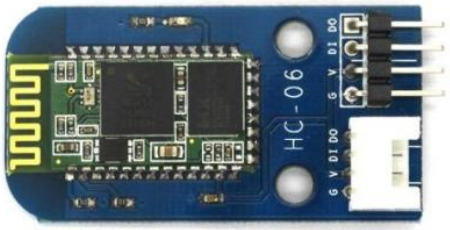


Figure 5. Electronic Brick HC-06 Bluetooth Module

2.1.2 3D Print External Prosthetic Arm

3D printing had come a long way since its early days. Today, it requires the designer to just design the desired piece through a CAD software such as Solidworks then transferring the design file to the 3D printing machine for it to build the final

product. Many practical applications have been coming out too as enthusiasts, educators or students are able to innovate through the design of others that has been put out on to the web. With such easy access, prosthetic hand models can be obtained easily through sites such as Limbitless and Thingiverse[25]. Since the arm is a side feature to compliment the ULTS, the design of the prosthetics will be obtained from a Taylor's University School of Engineering student's past project. The external robotized prosthetics as stated by the objective will act as an easy to analyse the movement of the patient which will be replicated by the robotized arm. The arm provides multiple angle of visual analysis while allowing markings to be put at the elbow join to compare before and after arm mobility. Below is the design of the prosthesis obtained from SOE student Adam Tan Zhe Xin[26]. Some minor modifications is made to cater to the project scope.

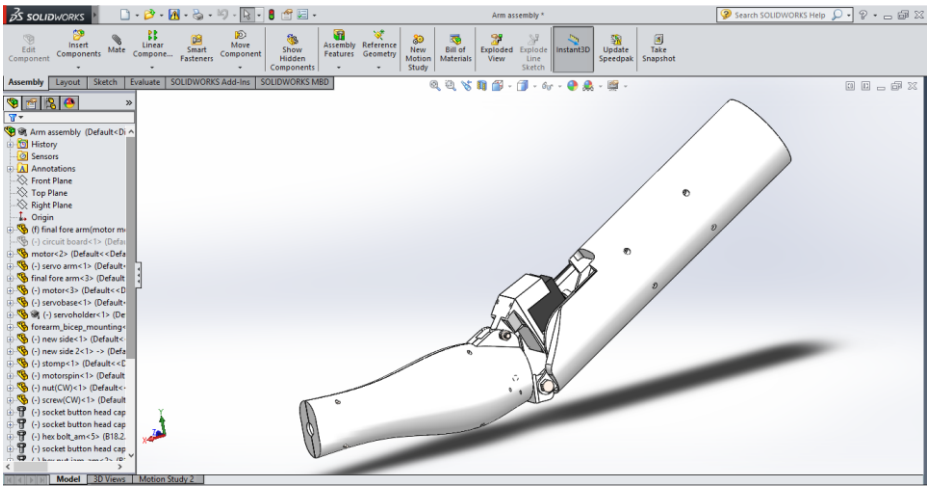


Figure 6. Robotized Prosthethics Designed through Solidworks[26]

To allow the prosthetic arm to replicate the human upper limb movement, three key components are needed. Servo motors, a microcontroller and myoelectric sensors. Servo motors are small and gives a more precise rotation comparing to regular DC motor. Unlike DC motors, servo motors are actually made up of gears (either plastic or metal). A potentiometer is connected to the output shaft and an onboard controller. This will then give the servo motor the ability to rotate to a specific angle by keeping track of its current angular position. Controlling servo motor is different from controlling DC motors. The motor will require PWM (Pulse-Width-Modulation) controlling method to align the output shaft to a certain angle, depending on the duty cycle of the signal sent to the microcontroller. Here the servo motors play a role of controlling the movement of the elbow[28]. The movements depends on the strength of the muscle nerve signal [27]. The signal will then be processed by the microcontroller and translated into the movement of the elbow. As for the microcontroller, an Arduino microcontroller is very well sufficient for the sensor and motor setup thus an Arduino Uno would be more than sufficient. An Arduino microcontroller is flexible in which is already explain previously under the Arduino microcontroller section. The microcontroller board will process the muscle signals that has been amplified by the muscle sensor(EMG), then translates it into the movement of the limb, which in our case is the movement of the elbow. An Arduino Uno should be powerful enough to run the motor servo and sensor as the setup does not require much processing power. Furthermore, the coding is the most important to make sure that the signal through the muscle(EMG) sensors are transmitted to the

motor to allow it to replicate real time movement. The codes to run the prosthetics will be obtained directly from the online open source pages for direct plug and play functionality. As for the connectivity to bridge the human arm together with the prosthetics, the potentiometer is used as the input signal from the muscle sensor to stimulate the movement of the servo motor. The muscle sensor that we will be using is called Muscle sensor v3[29]. Next, the myoelectric sensor pad will be regular EMG sensor pad that can be seen in any hospital. It will be the interface that will bridge the connection between the user and the microcontroller, so that the user will be able to control the prosthetic limb with just the flexing of muscle.

3. Experimental Setup and Discussion

3.1 Upper Limb Tracking System

3.1.1 Assembly

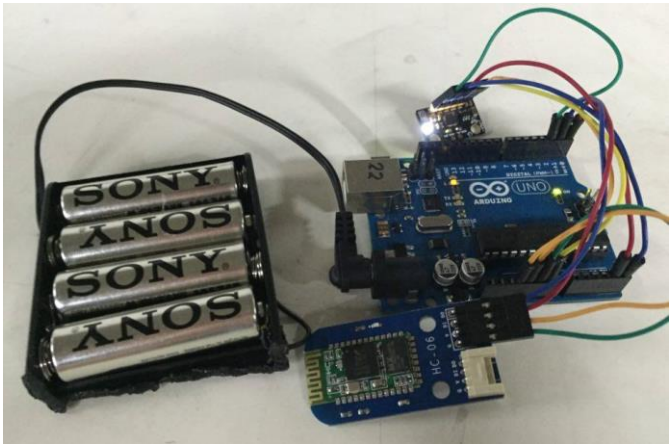


Figure 7. Upper Limb Tracking System Full Assembly

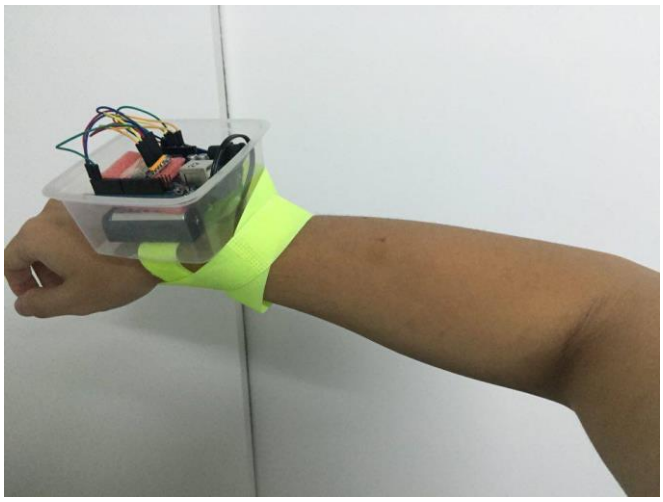


Figure 8. ULTS Experimental Setup

Most of the connections of the sockets and pins were obtained online through many open source webpages. From the respective spec sheets available the pins can be connected accordingly to allow connectivity

Table 2.Connection Table for the MPU6050 Accelerometer/Gyroscope and the Arduino Uno Microcontroller

MPU6050	Arduino Uno
VIN	5V
GND	GND
SDA	A4
SCL	A5

Table 3.Connection Table for the HC06 Bluetooth Module and the Arduino Uno Microcontroller

HC06 Bluetooth	Arduino Uno
G	GND
V	3.3V
D1	RX pin
D0	TX pin

3.1.2 Setup and Results

After the assembly of all the relatable components to form the ULTS, the associated codes were compiled and uploaded to the microcontroller board to begin initiating the sensors connected. The codes can be transferred through the traditional method of connecting the microcontroller with the proprietary cable or through Bluetooth since the ULTS has Bluetooth connectivity.

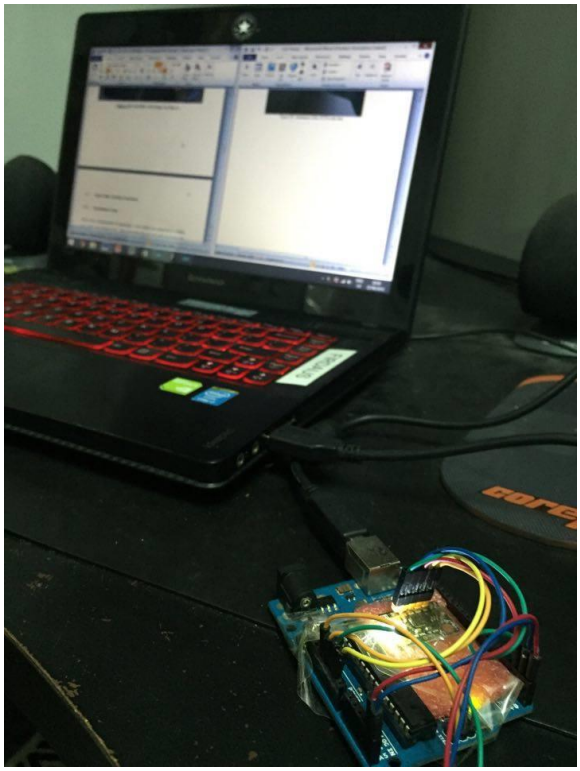


Figure 9. Transferring of Codes

The ULTS prototype was attached to the arm as shown above.

This experiment was carried out to determine the position and orientation of the upper limb. The upper limb is subjected to few types of arm movement to evaluate its performance thus giving the opportunity to analyze and compare the motion data.

During the experiment the arm movement was subjected to a few types of motion. The pitch, roll and yaw of each of their respective X, Y and Z axis of the upper limb was tested to find its motion data. The data in question is the inertial force vector which is the acceleration values of the accelerometer and the angular rates from the gyroscope. The motion data is tested up to 3 times for each of the motion being done to achieve an average result value.

The data collected from the accelerometer and gyroscope combo were filtered through the use of Kalman and Complementary filter. The filter was used to determine the actual motion data output as the raw data obtained from the sensor is exposed to interference and drift. With the filters, the comparison between theoretical and raw data can be made thus giving a more detailed comparison and result of the orientation and acceleration values. This will be discussed further in the discussion section.

Below is the type of movement the arm is subjected to obtain the motion data:

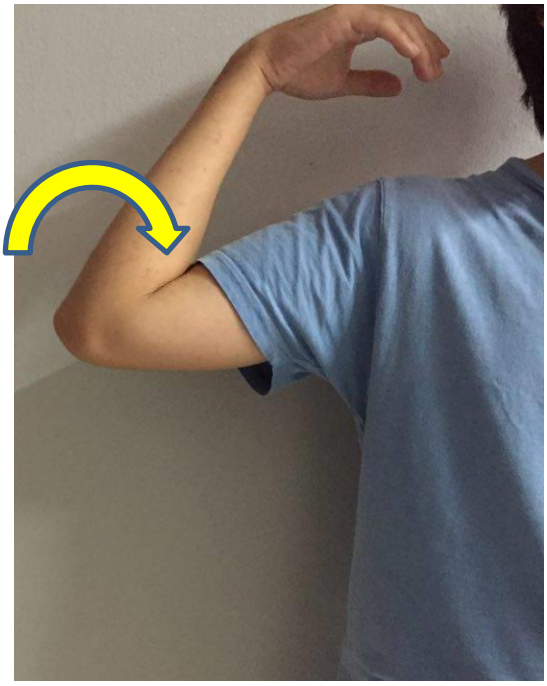


Figure 10. Forearm Pitching Upwards (A)



Figure 11. Forearm Roll Motion (B)



Figure 12. Forearm Yaw Motion (C)

Based on the experimental setup and procedures done, the values from the accelerometer and gyroscope can be obtained at all the initial static position as a baseline average value before beginning the full motion of the arm. Sensor values obtained shown below in Table 7 and 8 below are the result of having the sensor values averaged since each axis of the sensor gives out two columns of sensor values showing its maximum and minimum values for each column due to sensitivity of the system.

COM3 (Arduino/Genuino Uno)

```
The gyro scale is set to 7.63 milli Degree/s
The accel scale is set to 1.20 milli m/s^2
Calibrating gyroscope .... dont move the hardware .........
.....................................................................................................................................
gyro_x register offset = -22
gyro_y register offect = 84
gyro_z register offset = -158
Calibrating accelrometer .... dont move the hardware .........
.....................................................................................................................................
Accel_x register offset = 607
Accel_y register offect = -707
Accel_z register offset = 7743
gyro_x_scalled  gyro_y_scalled  gyro_z_scalled  accel_x_scalled accel_y_scalled accel_z_scalled angle_x_gyro    angle_y_gyro
-0.08   0.00    -0.01   -0.42   0.49    4.31    -0.00   0.00    -0.00   -5.60   -6.50   81.41   -0.28   -0.32   4.07    40.00
-0.11   -0.02   0.00    -0.21   0.25    6.97    -0.28   -0.33   4.07    -1.74   -2.03   87.33   -0.36   -0.41   8.23    40.00
-0.14   0.02    0.02    -0.12   0.13    8.25    -0.36   -0.41   8.23    -0.84   -0.89   88.78   -0.38   -0.43   12.26   40.00
-0.14   0.02    0.00    -0.06   0.06    8.99    -0.39   -0.43   12.26   -0.38   -0.38   89.47   -0.39   -0.43   16.12   40.00
-0.13   0.00    0.02    -0.03   0.02    9.35    -0.39   -0.43   16.12   -0.18   -0.15   89.78   -0.38   -0.42   19.80   40.00
-0.15   -0.02   0.03    -0.01   0.01    9.56    -0.38   -0.42   19.81   -0.06   -0.06   89.92   -0.37   -0.40   23.31   40.00
-0.12   -0.02   0.02    -0.01   0.00    9.67    -0.37   -0.40   23.31   -0.04   0.00    89.97   -0.35   -0.38   26.64   40.00
-0.13   -0.03   0.02    0.01    -0.01   9.71    -0.35   -0.38   26.64   0.04    0.04    89.96   -0.33   -0.36   29.81   40.00
-0.12   0.00    0.04    0.00    -0.01   9.75    -0.34   -0.36   29.81   0.03    0.06    89.94   -0.32   -0.34   32.82   40.00
-0.14   0.01    0.02    0.02    -0.02   9.76    -0.32   -0.34   32.82   0.09    0.09    89.88   -0.30   -0.32   35.67   40.00
-0.14   0.04    0.04    0.02    -0.01   9.78    -0.30   -0.32   35.67   0.11    0.05    89.89   -0.28   -0.30   38.38   40.00
-0.13   0.04    0.00    0.02    -0.01   9.78    -0.29   -0.30   38.38   0.11    0.05    89.88   -0.27   -0.28   40.96   40.00
-0.09   0.03    0.01    0.01    -0.01   9.78    -0.27   -0.28   40.96   0.04    0.05    89.94   -0.25   -0.26   43.41   45.00
-0.11   0.01    0.02    0.00    -0.01   9.77    -0.25   -0.26   43.41   0.01    0.07    89.94   -0.24   -0.25   45.73   40.00
-0.12   0.03    0.01    0.00    -0.01   9.77    -0.24   -0.25   45.73   0.03    0.05    89.95   -0.23   -0.23   47.94   45.00
-0.11   0.02    -0.01   0.01    -0.01   9.76    -0.23   -0.23   47.94   0.06    0.04    89.94   -0.22   -0.22   50.04   40.00
-0.12   0.01    0.01    0.01    -0.01   9.76    -0.22   -0.22   50.04   0.05    0.06    89.93   -0.21   -0.20   52.04   45.00
-0.14   0.02    -0.01   0.00    -0.01   9.79    -0.21   -0.20   52.04   0.01    0.04    89.96   -0.20   -0.19   53.93   40.00
-0.15   0.02    0.00    0.01    -0.01   9.77    -0.20   -0.19   53.93   0.06    0.06    89.92   -0.19   -0.18   55.73   40.00
-0.14   0.02    -0.02   0.00    -0.01   9.78    -0.19   -0.18   55.73   0.03    0.08    89.92   -0.18   -0.16   57.44   40.00
-0.15   0.02    0.01    0.00    -0.01   9.77    -0.18   -0.16   57.44   0.03    0.06    89.94   -0.17   -0.15   59.07   40.00
-0.15   0.00    0.02    0.01    -0.01   9.77    -0.18   -0.15   59.07   0.05    0.06    89.93   -0.16   -0.14   60.61   40.00
-0.13   -0.02   0.02    0.01    -0.01   9.78    -0.17   -0.14   60.61   0.04    0.06    89.94   -0.16   -0.13   62.08   40.00
```

Figure 13. Arduino Serial Monitor for Accelerometer and Gyroscope Motion Data Example

Table 4. Initial Baseline Readings Average

Intial Position	Gyro X axis	Gyro Y axis	Gyro Z axis	Accel X axis	Accel Y axis	Accel Z axis
Forearm Pitch (A)	- 0.2	-0.3	4.5	1.5	43.5	40
Forearm Roll (B)	- 1	0.2	-4.5	10	-17	20
Forearm Yaw (C)	1.3	- 0.45	4.5	1	38	43

Table 5. Full Motion Readings Average

Intial Position	Gyro X axis	Gyro Y axis	Gyro Z axis	Accel X axis	Accel Y axis	Accel Z axis
Forearm Pitch (A)	- 1.3	- 1.45	1	-23.5	-25	-38
Forearm Roll (B)	0.9	-1	- 5.5	21.5	-10.5	12
Forearm Yaw (C)	-1	0.1	4.5	1.2	42	43.5

- The gyroscope has a scale of 7.63 milli degree/seconds while the accelerometer has a scale of 1.2 milli meter/second^2.

Each axis values were determined through the use of codes done by Omer a fellow electronics enthusiast. The codes were uploaded onto one of the biggest open source website Github whereby normal people or developers upload their work which is already completed thus allowing people to use them for further development and analyse the results from the codes available[31]. The codes applied to obtained these motion data value can be referred to in the Appendix section. Since these codes only cater to particular sensors where in this case the MPU6050 sensor, it is actually better to refer though open source and developer webpages as they have a baseline to refer to.

To begin with, based on observation the gyroscope values of each respective X, Y and Z axis were very unstable compared to the accelerometer values. This might have happened due to the problem with gyroscopes whereby since it runs on algorithms that integrates over time, drift will occur as the system struggles to return to zero when the sensor goes back to its original position even though the codes applied is already made to help counter the errors and offsets. The motion data is still considered relatively accurate on the short term but when used for long terms, the gyroscope suffers from drift that will cause inaccuracy of the result data.

Here, it shows the importance of calibration. Calibration solves some of the inaccuracy but not completely. The codes applied for the results above helps to find the angles around each of the respective axis. When each of the axis of either the gyroscope or the accelerometer is exposed to any error or offset, the error will cause the drift effect which would produce big values that is not understandable. Thus to go around the problem, the accelerometer is made to calculate the angle and combine it with the gyroscope to combat the drift problem[32].

Each gyroscope output are given as follows whereby each axis uses the same equations. Here the axis is used as an example.

$$\text{gyro_x_scalled} = \frac{d}{dt}\theta_x^{gyro} \tag{1.0}$$

To obtain the angle for gyro_x_scalled, it must be integrated.

$$\theta_x^{gyro} = \int \text{gyro_x_scalled}\, dt \tag{1.1}$$

Euler's integration method is applied as it is the most common method used.

$$\theta_x^{gyro}(t_n) = \text{gyro_x_scalled} * T + \theta_x^{gyro}(t_{n-1}) \tag{1.2}$$

Assumption of x and y axis having their angles at 0 and z axis at 90 which gives

$$\theta_x^{gyro}(t_0) = 0^o \tag{1.3}$$
$$\theta_y^{gyro}(t_0) = 0^o \tag{1.4}$$
$$\theta_z^{gyro}(t_0) = 90^o \tag{1.5}$$

Value of T gives out a huge effect towards the accuracy of the calculated angle. Slowing of the dynamics of the application produces smaller cycle time which gives out more accurate results. In this case a measurement of 20 milliseconds was used to allow the Arduino sketch to execute every 20 milliseconds to allow the measurement samples to be taken at each timed interval[32].

Next, as the offset compensation is still not ideal the angle of both the accelerometer and gyroscope are combined. The MPU6050 sensor chip measures 1G which is 9.81m/s^2 when levelled. With the value in hand, the acceleration of X and Y axis can be made to calculate the angle of each respective axis[31].

Below is the equation to determine the angles through the accelerometer X and Y axis.

$$\theta_x^{accel} = \tan^{-1} \frac{accel\,x\,scalled}{\sqrt{accel\,y\,scalled^2 + accel\,z\,scalled^2}} \tag{1.6}$$

$$\theta_y^{accel} = \tan^{-1} \frac{accelyscalled}{\sqrt{accelxscalled^2 + accelzscalled^2}} \quad (1.7)$$

With equations 1.6 and 1.7 angle through the use of the accelerometer can be determined. Although the angle maybe reasonable to be analysed, angle calculated through the use of accelerometer are still noisy and any slight vibrations can affect the accuracy of the angle due to the nature of accelerometers reacting to every minute force acting. In this case the best method to determine an accurate result of the motion data is through the use of filters which will be discussed below.

Using equations 1.6 and 1.7 the results for the angles through the use of accelerometer gives out the following :

Table 6. Motion Angle Through the use of Accelerometer Before Movement

Intial Position	**Θ Accel X axis**	**Θ Accel Y axis**
Forearm Pitch (A)	1.45	47.38
Forearm Roll (B)	20.86	-37.24
Forearm Yaw (C)	1	41.46

Table 7. Motion Angle Through the use of Accelerometer After Movement

Intial Position	**Θ Accel X axis**	**Θ Accel Y axis**
Forearm Pitch (A)	-27.32	-29.23
Forearm Roll (B)	53.43	-23.09
Forearm Yaw (C)	1.14	43.98

With the available motion data obtained, it is reminded that the readings are of a person with full functioning upper limb motion. As the system is to track and help patients track their rehabilitating progress, their motion data values should fall within the values determined above thus giving a good baseline for the user to gauge and determine their arm performance.

To achieve an almost noise and interference free tracking through the use of gyroscopes and accelerometers, it is still best when filtering algorithms are applied. Below shows the visual result of how much a filter can help smoothen out and give a more accurate result. Each colour of the live graphs shown below represents an axis of X, Y and Z of the gyroscope or the accelerometer and the filtered result.

Table 8. Graph Colour Representation

	Gyro X axis	**Gyro Y axis**	**Accel X axis**	**Accel Y axis**	**Kalman Filter X axis**	**Kalman Filter Y axis**	**Complementary Filter X axis**	**Complementary Filter Y axis**
Colour Code	Yellow	Purple	Green	Light Blue	Red	Black	Blue	Dark Green



Figure 14. Forearm Pitching Upwards (A) Live Motion Graph

For Figure 27 above, based on observation, the yellow line representing the gyroscope's X axis deviates from its initial position when the forearm pitches upwards to the maximum position. From here it is clear that the X axis represents the pitching motion. As suspected, the gyroscope's graph deviates a lot compared to the accelerometer's of the same axis. This proves that the gyroscope is easily interrupted with noise and interference that will inherently cause the drift. With the application of a Kalman Filter algorithm into the Processing codes, as shown above, the red and blue lines which represents the Kalman and Complementary filter allows accurate and smooth reading of the moving X axis pitching motion. The algorithm for the filters will be discussed later in a different section below.



Figure 15. Forearm Roll Motion (B) Live Motion Graph

Next, the rolling motion of the forearm shows that it rolls within the Y axis based on the graph in Figure 28. Here, it is also apparent that the gyroscope suffers from the same drift issue as the gyroscope's Y axis that is represented in purple deviates so much from the actual value. The filters shows that with a minor rolling motion, the graph does not even deviates that much from the forearm initial motion.



Figure 16. Forearm Yaw Motion (C) Live Motion Graph

As for the yaw motion of the forearm, the live graph does not register any motion as each of the lines remained constant with just minor deflection due to vibration of the hand. In this case we can clearly determine that with a 6 degree of freedom IMU sensor like the MPU6050, at a leveled position even though the sensor is moving horizontally, side to side or parallel to the leveled ground the sensor could not track or register any movement due to the limited degree of freedom from the sensor used.

To discuss on the drift issue for the gyroscopes, the Kalman filter applied is one of the most widely applied filter to compensate the inaccuracy of the gyroscopes. Kalman filter is an algorithm made which runs through a few measurements that is observed over time. The measurements are what we have observed which is the noise and interference that causes the error and inaccuracy of the motion data. To overcome the issue a Complementary filter as applied into the codes above is good enough to improve the gyroscope's accuracy but a Kalman filter is always chosen due to its nature of being more accurate in smoothening and gaining the gyroscope's accuracy back to normal[33][35].

With the equations solved the Kalman filter codes can be sketched thus producing the Kalman filter line in the live graph for easy and accurate reading of motion. As for the Complementary filter, it is a simpler filter to be applied. The Complementary filter actually manages both low and high pass simultaneously whereby the low pass filters the high frequency signals at which reduces the accelerometer exposed vibrations. The low pass filters also filters the low frequency signals which is the main issue for the experiment which is the drift issue of the gyroscope. The combination of these filters provides decent and accurate readings without the complexity of the Kalman filter[36]. Based on the motion data live graph

shown above, the Complementary filter results deviates just slightly of the Kalman's thus proving it is a decent filter to implement especially on equipments that do not necessarily need high pin point accuracy.

As stated in the objective, the external robotized prosthetic was made as a side feature to compliment the ULTS. The idea is to replicate the human arm movement through the use of electromyography as explained in the methodology section. By replicating the user's arm movement it will bring a whole new experience to the user as most everyday person does not want the hassle of having to learn complex graphs and gibberish numbers. This then allows the user to simplify the ULTS by having their arm attached with the EMG pads which will then instantaneously replicate their arm movement.

As the EMG sensors feed of human muscle electrical potential, with the available codes on open source webpages, coding it is as easy as just applying and uploading the codes to the arm's microcontroller unit. With the design and application aside, since the prosthetic arm is external, the everyday person can visualize their arms limitation or performance during rehabilitation. Markings can be applied as to determine how much has the user healed over time.

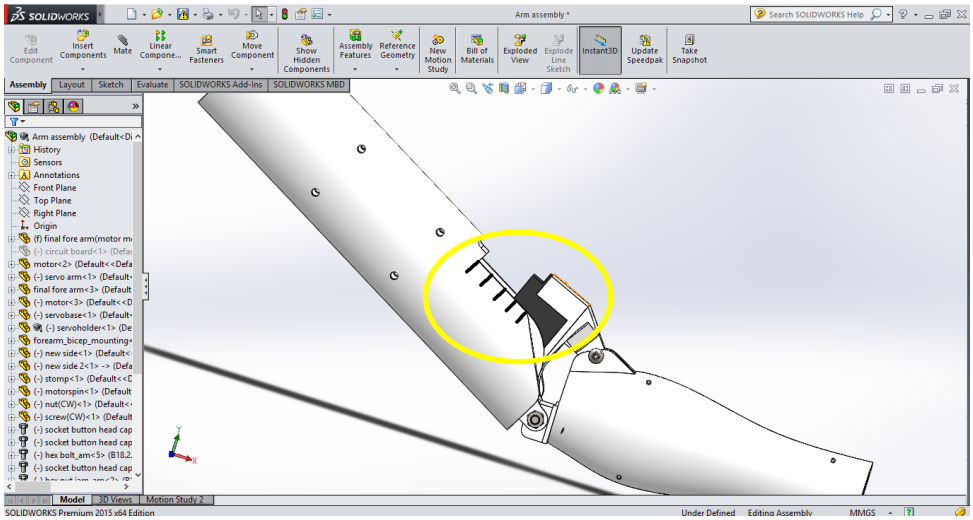


Figure 17. Simple Markings for Easy Progress Tracking

The idea of the application maybe a simple one but it cannot be dismissed as even though the tracking of the arm motion can be determined accurately through inertial sensors, having the option to let the professionals such as doctors to help with the ULTS and help analyse the data while the user is able to easily operate the robotized prosthetics at home is a good one. Simplicity and ease of use will encourage the user to keep on going for rehabilitation thus allowing them to heal faster. With the markings, the user can make simple progress achievement notes by allowing them to gauge their progress at the beginning, in the middle and till the end of the rehabilitation sessions thus making them work harder and not skip rehab sessions just to have that push to get their arm back into health.

4. Conclusion and Recommendation

This project has successfully achieved the aims and objectives stated. First, an improved, low cost, simple and portable upper limb tracking system has been further developed with the use of two in one sensors together with having an external robotized arm as a visual aid to compliment the quantitative result values.

By applying codes that counters the offset and irregularities such as noise and drift, we were able to obtain relatively accurate readings of each of the X, Y and Z axis of the accelerometer and the gyroscope. By solving the offset issue, we then found the importance of calibration as it helps reduce errors when obtaining the average readings for each type of different arm motion. Since the average readings can be obtained, the values obtained are applied into the theoretical equations which then gave the angular results for each X and Y axis respectively of the arm's motion.

Next, by applying the right codes into Processing, we were able to produce a live graph of the sensor's reading thus giving the opportunity to analyze each of the arm's motion. Through the graphs, it can be seen as observed during each of the accelerometer and gyroscopes results, the gyroscopes suffers from huge inaccuracy due to the large deviation of the tested motion axis. Filters were then applied to produce noise and drift free sensor readout which proves effective giving accurate and smooth graph shapes of the tested motion axis. This shows that filters are very important in the case of general use inertial sensors as these sensors do not come built in with the needed compensation components to counter these issues.

If the right calibration and filters are applied into these inertial measurement sensors, they show great future possibility for a cheap, simple and easy to use human motion tracking system. Also, with the aid of an external robotized arm, the everyday user has the opportunity to easily gauge their arm's performance after rehabilitation sessions through the markings available on the prosthetics. This proves that simple visual results is still relatable as it removes the need to learn and understand complex graphs and values of the tracking system.

References

[1] Harris, J. E., Eng, J. J., & Ot, P. T. (2010). Strength Training Improves Upper Limb Function in Individuals With Stroke A Meta-Analysis, 136–141. http://doi.org/10.1161/STROKEAHA.109.567438

[2] Cutti, A. G. et al., 2008. Ambulatory measurement of shoulder and elbow kinematics through inertial and magnetic sensors. *Medical&Biological Engineering & Computing*, 46(2), pp. 169-178.

[3] Luinge, H. J., Veltink, P. H. and Baten, C. T. M., 2007. Ambulatory measurement of arm orientation. *Journal of Biomechanics*, 40(1), pp. 78-85.

[4] WebMD, (2015). Electromyogram (EMG) and Nerve Conduction Studies. [online] Available at: http://www.webmd.com/brain/electromyogram-emg-and-nerve-conduction-studies [Accessed 10 Nov. 2015].

[5] Sutherland, I. E., 1968. A head-mounted three-dimensional display. *Proceedings of the Fall Joint Computer Conference*. San Francisco, California, 9-11

December, 1968. New York: Association for Computing Machinery, pp. 757-764.

[6] Burdea, G. C. and Coiffet, P., 2003. *Virtual reality technology*. 2nd ed. [e-book] New Jersey: John Wiley and Sons. Available at: Google Books <books.google.com> [Accessed 15 November 2015].

[7] [1] D. D. Quoc, J. Sun, V. N. Le, and L. Luo, "Complementary Filter Performance Enhancement through Filter Gain," vol. 8, no. 7, pp. 97–110, 2015.

[8] Raab, F. H. et al., 1979. Magnetic position and orientation tracking system. *IEEE Transactions on Aerospace and Electronics Systems*, 15(5), pp. 709-718.

[9] Molet, T. et al., 1999. Anyone for tennis. *Presence: Teleoperators and Virtual Environments*, 8(2), pp. 140-156.

[10]Nixon, M. A. et al., 1998. The effects of metals and interfering fields on electromagnetic trackers. *Presence: Teleoperators and Virtual Environments*, 7(2), pp. 204-218.

[11]Bachmann, E. R., 2000. *Inertial and magnetic tracking of limb segment orientation for inserting humans into synthetic environments.* PhD Thesis, Naval Postgraduate School. Available through University of Southern California GamePipe Laboratory website http://gamepipe.usc.edu/~zyda/Theses/EricBachmann2.pdf [Accessed 6 October 2015].

[12] Foxlin, E., Harrington, M. and Pfeifer, G., 1998. Constellation: A wide-range wireless motion-tracking system for augmented reality and virtual set applications. *Proceedings of the 25th Annual Conference on Computer Graphics and Interactive Techniques*. Orlando, Florida, 19-24 July, 1998. New York: Association for Computing Machinery, pp. 371-378.

[13]]"MTI-10-2A5G4 - XSENS - MEMS Module, 4.5 V, 34 V, Module, ± 450°/s | Farnell element14", *Uk.farnell.com*, 2016. [Online]. Available: http://uk.farnell.com/xsens/mti-10-2a5g4/imu-mems-motion-tracking-module/dp/2452306. [Accessed: 23- May- 2016].

[14] Moog Crossbow, n.d. *Theory of operation of angular rate sensors*. [pdf]. Available at: http://www.moog-crossbow.com/_Assets/Literature/Application_Notes_Papers/Theory_of_Operation_of_Rate_Sensors.pdf [Accessed 9 November 2015].

[15] Šprdlík, O., 2012. *Detection and estimation of human movement using inertial sensors: Applications in neurology*. PhD Thesis, Czech Technical University. Available through http://aa4cc.dce.fel.cvut.cz/sites/default/files/downloads/publications/diz_Sprdlik_hyperref.pdf [Accessed 10 November 2015].

[16] Soundlab.cs.princeton.edu, (2015). *3.3 Accelerometer (Analog Devices ADXL50)*. [online] Available at: http://soundlab.cs.princeton.edu/learning/tutorials/sensors/node9.html [Accessed 17 Nov. 2015].

[17] K. Talbot, "Using Arduino to Design a Myoelectric Prosthetics," 2014.

[18] Y. Wang and P. Artemiadis, "Advances in Robotics & Automation Closed-Form Inverse Kinematic Solution for Anthropomorphic Motion in Redundant Robot Arms," vol. 2, no. 3, 2013.

[19] "How Microcontrollers Work", *HowStuffWorks*, 2000. [Online]. Available: http://electronics.howstuffworks.com/microcontroller1.htm. [Accessed: 24- May- 2016].

[20] "Raspberry Pi or Arduino? One Simple Rule to Choose the Right Board | Make:", *Make: DIY Projects and Ideas for Makers*, 2015. [Online]. Available: http://makezine.com/2015/12/04/admittedly-simplistic-guide-raspberry-pi-vs-arduino/. [Accessed: 24- May- 2016].

[21] "Arduino - Software", *Arduino.cc*, 2016. [Online]. Available: https://www.arduino.cc/en/Main/Software. [Accessed: 20- Jun- 2016].

[22] H. Wen You, "Remote Upper Limb Tracking System," 2013

[23] "6 DOF Sensor-MPU6050 (SKU:SEN0142) - Robot Wiki", *Dfrobot.com*, 2016. [Online]. Available: http://www.dfrobot.com/wiki/index.php/6_DOF_Sensor-

[24] MPU6050_(SKU:SEN0142). [Accessed: 24- May- 2016] 2016. [Online]. Available: http://ftp://imall.iteadstudio.com/Electronic_Brick/IM120710006/DS_IM120710006.pdf. [Accessed: 24- May- 2016].

[25] Enabling The Future, (2014). *The Limbitless Arm*. [online] Available at: http://enablingthefuture.org/upper-limb-prosthetics/the-limbitless-arm/ [Accessed 15 Nov. 2015].

[26] T. Adam, "Artificial Prosthetic Limb," 2015

[27] V. K. Giri, "DC Motor Control using EMG Signal for Prosthesis," vol. 7109, pp. 163–166, 2011.

[28] "How Servo Motors Work", *Jameco.com*, 2016. [Online]. Available: http://www.jameco.com/jameco/workshop/howitworks/how-servo-motors-work.html. [Accessed: 20- Jun- 2016].

[29] v3, M., OpenLog, S., Arduino, S., (GT-511C3), F., Sensor, P., AD8232, S. and Kit, B. (2015). *Muscle Sensor v3 - SEN-13027 - SparkFun Electronics*. [online] Sparkfun.com. Available at: https://www.sparkfun.com/products/13027 [Accessed 17 Nov. 2015].

[30] "Overview \ Processing.org", *Processing.org*, 2016. [Online]. Available: https://processing.org/overview/. [Accessed: 20- Jun- 2016].

[31] "helscream/MPU6050_Arduino", *GitHub*, 2016. [Online]. Available: https://github.com/helscream/MPU6050_Arduino. [Accessed: 23- Jun- 2016].

[32]]"Arduino with MPU6050 and angle calculation – HobbyLogs", *Hobbylogs.me.pn*, 2014. [Online]. Available: http://hobbylogs.me.pn/?p=47. [Accessed: 25- Jun- 2016].

[33] K. Lauszus, "TKJ Electronics » A practical approach to Kalman filter and how to implement it", *Blog.tkjelectronics.dk*, 2012. [Online]. Available: http://blog.tkjelectronics.dk/2012/09/a-practical-approach-to-kalman-filter-and-how-to-implement-it/. [Accessed: 25- Jun- 2016].

[34] D. Simon, *Embedded Systems Programming - Kalman Filtering*, 1st ed. 2001, pp. 72-79.

[35] "TKJElectronics/KalmanFilter", *GitHub*, 2016. [Online]. Available: https://github.com/TKJElectronics/KalmanFilter. [Accessed: 25- Jun- 2016].

[36] W. Higgins, "A Comparison of Complementary and Kalman Filtering", *IEEE Trans. Aerosp. Electron. Syst.*, vol. -11, no. 3, pp. 321-325, 1975.

Finite Element Modelling and Calibration of Rubber Bushing for Impact Simulation Application

Aisyah Hanis Abdul Aziz[1*], Ch'ng Shiau Ying[1], Yap Kim Haw[2], Chan Yun Fai[2]

[1]*School of Engineering, Taylor's University, Malaysia*

[2]*Panasonic Appliances Air-Conditioning R&D Malaysia Sdn. Bhd.*

[*]hanis.aaziz@gmail.com

Abstract

This study is done in conjunction with Panasonic Appliances Air-Conditioning R&D Malaysia with the main focus of determining and observing the effects of impact upon rubber bushings present in air conditioning units and to validate impact simulation results with its experimental counterpart. The purpose of this study is to answer the two research questions, one of which relates to how different meshing strategies of the rubber bushing will affect the accuracy of the simulation results while the other questions how to properly simulate a rubbing bushing given its characteristics and the parameters involved to achieve accurate results. The study aims to improve how rubber bushings are modelled in finite element analysis as past studies represent them as simple multidimensional spring which negatively affects the overall accuracy of the simulation results. To achieve these objectives, a simple compression experiment will be performed on a rubber sample given material data of rubber provided by Panasonic Appliances Air-Conditioning R&D Malaysia in the form of a stress-strain graph at the compression rate of 0.01/s. The simulation counterpart to the experiment will then be validated with those experimental results using the software Hypermesh and solver RADIOSS. These tried and tested parameters will then be used in a more complex impact simulation which involves real rubber bushings, a personalized jig, and a representation of an air-conditioning compressor. By modelling and performing an accurate simulation of the rubber bushings, it is believed that cost, time and energy can be saved in regards to future workings in research and development.

Keywords: Finite Element Analysis, Rubber, Hypermesh, RADIOSS, Validation.

1. Introduction

A rubber bushing, otherwise known as a rubber isolator, is an essential and classic component as a means to isolate vibrations. These bushings are more commonly known to aid in the quality of a vehicle in terms of noise emission, vibration and ride [1]. Several studies found discuss this component, most addressing the role of rubber bushings in the automotive industry. The area of interest these studies generally focus on is how rubber bushings deform and behave upon impact. As such, most of them depict crash experiments and simulations of a vehicle and how the impact will affect the rubber bushing.

This project focuses on the interest towards how the rubber bushing acts as a damper to isolate vibrations in an air-conditioning unit due to its compressor and is a joint study under Panasonic Appliances Air-Conditioning R&D Malaysia. The main study of this project is to determine and observe the effects of impact upon these rubber bushings and to validate impact simulation results with its experimental counterpart.

This project will be separated into two stages. The first stage involves a sample rubber specimen that was modelled and a simulated to undergo a compression test. The results from this simulation will be validated via an experiment done in the lab. The purpose of this simpler simulation would be to ensure the settings for the simulation for rubber will be correct for the next stage. The continuation of the study would be to manufacture a jig for a real impact testing involving industrial rubber bushing and a representation of the compressor used in a Panasonic air-conditioning unit. A simulation can then be done and validated by the test results.

The main concern of this project was the validation of simulation results against experimental data. During the initial set up of the simulation, it would be a requirement to first find the material characteristics of the material involved which in the case of the project would be rubber. A compressive test would be done to obtain the stress experienced by the rubber sample against the time taken to compress it.

The rubber specimen used in the rubber bushings in Panasonic air-conditioning units have been sent for testing by the Panasonic R&D department to obtain the data mentioned. The engineering stress-strain curve obtained will be used in the simulation to depict its material properties and will remain unchanged throughout the course of the project. The reason for this is that the company will be using these standardized properties for future simulations or experiments.

Rubber bushings play a significant role in the quality of the vehicle in terms of noise emission, vibration and ease of ride [1]. As such, upon cases such as impact of

the vehicle against a rigid object, the rubber bushing acting as the mount would surely abstain forms of deformation that will lead to an overall effect on the vehicle and its inner workings. At high speed impact, the engine mount has an essential role in keeping the engine of the vehicle intact as compared to low speeds, at which the mount may retain its function [2].

In accordance to rapid development in the engineering industry, the role of numerical methods has increasingly become more important. Numerical methods revolve around the main idea of taking an intensive problem and reducing it into a simpler alternative [3]. These methods is used as simplification when an experiment cannot be done due to instances such as extremely large components that hinder experimentations or when no other form of solution can be made possible. Due to the simplification process, it is important to note that the results of these methods will vary from real life conditions though this method is still preferred when an approximate result within an acceptable accuracy can be obtained rather than no obtainable results [4].

Finite Element Method (FEM) involves the concept of breaking down a given area of a structure into smaller segments or pieces called finite elements which are typically linear, quadratic or cubic triangles that combine to make up the original structure [5]. This process is generally referred to as meshing, where the geometry is discretized into smaller pieces. This is done because the overall solution to an engineering problem would be deemed too complex and unpredictable by using functions across the entire domain [13]. By discretization, the solution within an element can then be approximated using relatively simpler functions such as polynomials [13]. When the concept of FEM is used in a specific area of interest to analyse and find the magnitude of a particular variable (structural stress values etc.), it is called Finite Element Analysis (FEA).

In FEA, the vertices coordinates of each element can be determined, and thus the area and centroid of each triangle can be calculated. Integrating this equation, and all the equations derived from the surrounding elements that make up the whole structure will give the area of the entire structure, similar to integrating the total outer curvature of the structure [5].

Computer-aided engineering (CAE) offers several advantages as opposed to hands on testing in terms of better insight into the structural response of the system, the ability to identify challenges faster as well as better savings in terms of time and finances [1]. Other advantages of finite element analysis would include an increase in visualization, reducing design time, reducing the number of prototypes of a system as well as testing, and achieving an optimum design [6].

Modelling, which is defined as simulating a physical structure of process through substitution into an analytical or numerical construct, requires that the problem

or situation be understood well to avoid unsuitable shapes of elements [7]. This often refers to the nodes of the elements and how the meshing quality will affect the results of the simulation.

Therefore it is important to provide a suitable meshing strategy and mesh the structure or object accordingly with the most suitable meshing method to achieve accurate results. The two meshing types that will be focused on for 3D modelling of this project are tetrahedral (tri) and hexahedral (quad) meshing. Based on the past studies done, there are varying results when the accuracy of tetrahedral and hexahedral meshing is compared which include that quadratic tetrahedral and bilinear hexahedral meshing produces the same accuracy at the same computational time [8] and that the same order of hexahedral elements trump its tetrahedral counterpart in terms of accuracy [9].

More recent study reveals that tested under different evaluation conditions, hexahedral meshing generally outperforms tetrahedral meshing both linear and quadratic in terms of accuracy [10]. Therefore for this particular project, it is important to identify which meshing strategy will yield more accurate results when validated against experimental data. Thus the question arises, how does the type of meshing for rubber bushings affect the accuracy of results in simulation?

The challenges faced would be to model the rubber bushings appropriately and setting correct material characteristics to the model. In the past, rubber bushings would be modelled in a more simplified way with multidimensional spring elements instead of a more realistic presentation due to the complexity or rubber's material characteristics [11].

For hyperelastic models like rubber, there are several hyperelastic constitutive models which include the Mooney Rivlin model and the Yeoh model which are more generally used to fit hyperelastic models in comparison the others. It is important that a hyperelastic model is defined by the strain-energy function that can be derived from the thermodynamic, symmetry and energetic considerations as well as its strain variants in the case of isotropic materials [12].

	Dependencies			
		Cauchy–Green invariants		
Material models	Principal stretches λ	I_1	I_2	Fibre direction $\vec{n}$
Mooney–Rivlin		X	X	
Yeoh		X		
Neo–Hookean		X		
Ogden	X			
Humphrey		X		
Martins	X			X
Veronda–Westmann		X	X	

Figure 1: Material model dependencies [12]

The Mooney-Rivlin material model is well-known and widely used in the study of hyperelastic materials as it is amongst the pioneers of hyperelastic material models as well as amongst its high accuracy at anticipating an isotropic rubber-like material's nonlinear behavior [12]. In the case of this material model, its strain-energy function is often seen in previous studies in the form of the equation below.

$$W = \frac{\mu_1}{2}(I_1 - 3) - \frac{\mu_2}{2}(I_2 - 3) \quad [1]$$

2. Research Methodology

2.1 Rubber Sample Modeling

The software Solidworks was used to model the rubber samples that were provided by Panasonic Appliances Air-Conditioning R&D Malaysia. This software was chosen out of other known CAD software as it was deemed that prior exposure and experience were sufficient to aid in the completion of this project. Before the 3D CAD could be produced, the rubber sample was first measured using a digital Vernier caliper to minimize any errors from occurring during the simulation that may arise from deviations in the actual dimensions.

The cylindrical rubber sample was found to have the diameter of 28.22mm and the thickness of 12.93mm. These two dimensions were sufficient to produce the model of the rubber sample in Solidworks. The completed model was then exported from Solidworks and saved in a parasolid format (.x_t). This step is taken to ensure that the

model can be imported into the pre-processing software, Hypermesh, which is used solely during the completion of this project.

2.2 Compression Simulation

2.2.1 Meshing Strategies

One of the objectives of the project is to acquire the best meshing strategy to apply to the rubber sample model. Therefore three methods were chosen to be tested, all of which are meshed as hexa elements. Once imported into Hypermesh, the rubber sample model was then meshed according to the three different meshing strategies. The first meshing strategy involved the use of the feature Automesh. This feature is listed under 2D meshing methods in the software. By selecting only the top circular surface of the rubber sample and specifying the desired element size, the software will then proceed to automatically produce a 2D meshing.

In the case of the project, the element size that was chosen was 1.0 mm. The 2D meshing was then projected downwards by selecting the feature Line Drag listed under the 3D meshing methods. A line running across the body of the model from its two adjacent surfaces is then chosen and a number or length is specified, which is 13 in the case of the project, as the sample thickness is 12.93 mm. The Automesh meshing strategy is thus completed and will be referred to as the Automesh method throughout this report.

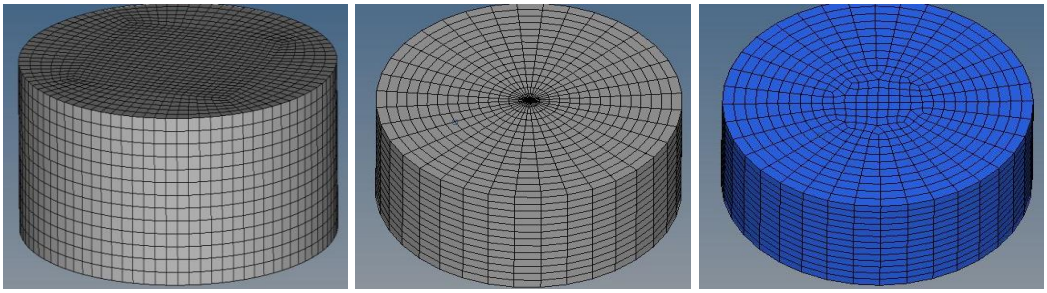


Figure 2: (l-r) Automesh Method, Spin Method, and Combination Method.

The second method used in the project is deconstructing the rubber model into one quarter of its original shape and size and selected one of the two exposed inner surfaces. Similar to the Automesh method, a 2D meshing is created onto that surface with the same element size of 1.0 mm. A point is then chosen as the origin or center of the model and the elements were then selected and spun about the Y-axis and that specified point at 360° with 36 sections using the feature Spin listed under 3D meshing methods. The second meshing strategy is then completed and will be referred to as the Spin method throughout this report.

The final method used in the project is a mixture of both the Automesh and the Spin method. This method involves separating the rubber model into two cylinders, a smaller inner cylinder and its corresponding outer, hollowed cylinder. The smaller inner cylinder will be proceeded to be meshed using the Automesh method whilst the hollowed outer cylinder will be deconstructed into one quarter its original size and then meshed using the Spin method. These two separate components are then combined to form the Combination meshing method, as it will be referred as throughout this report.

2.2.2 Setting the Material, Property and Boundary Conditions

As previously stated, the material data of rubber was introduced into the simulation software using an engineering stress vs strain graph that was provided by Panasonic Appliances Air-Conditioning R&D Malaysia. The data was plotted into the X-Y plot option in Hypermesh to produce the graph as seen in the figure below.

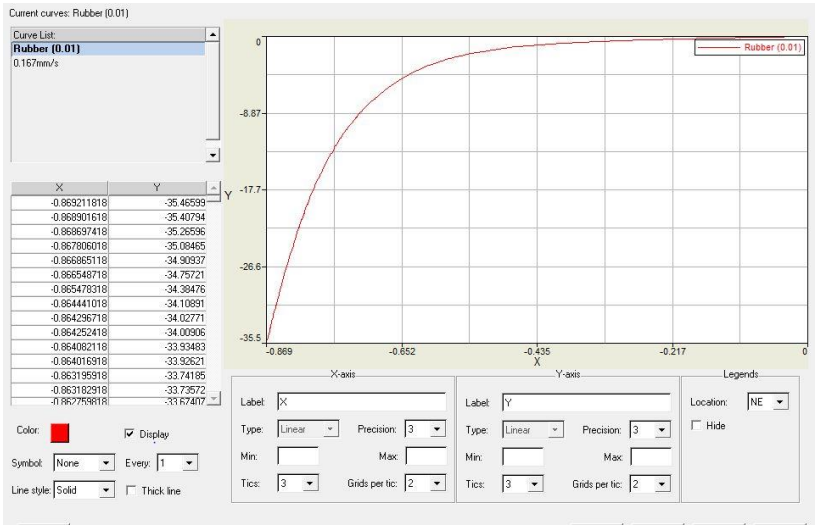


Figure 3: Plotting the stress vs strain graph for rubber in Hypermesh

To model the non-linear behavior of the rubber, the Poisson's Ratio was also specified as 0.495 as stated in the report that was provided along with the stress vs strain graph by the company. Other notable parameters that were specified in the software for the material section included the initial density of the rubber sample that was calculated with the aid of Solidworks. The material card MLAW69 was selected as it is used for tabulated input for hyperelastic material and its LAW_ID was chosen as 2, which signifies using the Mooney-Rivlin material model as opposed to Yeoh's material model. This model was selected in accordance to the stress vs strain graph that was obtained.

As for the property of the model, the card image P14_Solid was selected, and other parameters were specified in accordance to the meshed elements chosen. To simulate the compression experiment, the nodes situated on the top surface of the rubber sample were fixed in all other directions except Y, whilst the bottom nodes were fixed completely. The same upper nodes were also applied with a load that has been specified in the X-Y plot of the software as a compressive force downwards at 0.167 mm/s. Engineering cards are chosen to display the stresses in all directions, as well as specifying the frequency of which the animations would be produced by the processing

solver RADIOSS. The file is the exported in its solver format and run on the software RADIOSS.

2.3 Compression Experiment

The compression experiment was performed in one of the material testing labs located in Panasonic using the Shimadzu tensile machine. Two flat plates were attached onto the machine and the rubber sample was placed in between. The upper plate was then adjusted to touch the upper surface of the rubber sample. The software used to capture the data from this experiment was TRAPEZIUM LITE X. The rate of compression was set to 10 mm/min, or 0.167 mm/s to mimic the conditions in the simulation. The time was set at 35 s as opposed to the 30 s set for the simulation to allow more observation to be done on the specimen. Three rubber samples were used and the experiment was repeated a total of three times in order to get three readings to be compared to the simulation values in an attempt to minimize error.

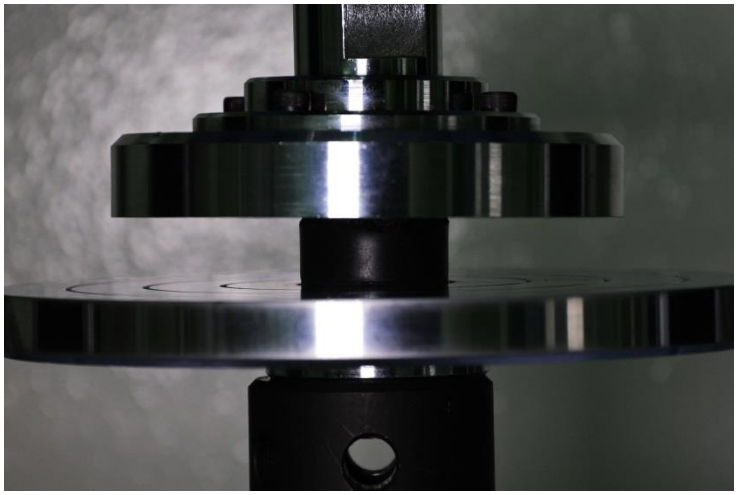


Figure 4: The compression experiment set-up

3. Results and Discussions

3.1 Meshing Strategy

As observed from the figure above, the simulations of the rubber bushing that was meshed using the Automesh method and the Combination method displays a similar result and mimics the trend of the three experimental curves. However, the Spin method results in a fairly different reading and overall trend as compared to the other two meshing methods. Therefore to further compare which method is best used to simulate the rubber sample, the time step for processing was taken into consideration.

Due to the smaller elements generated by the Spin method, most particularly in the center of the rubber sample due to the nature of the method causes the time step to be smaller, therefore increasing the overall time taken for the simulation to be resolved. The time step for the Spin method is $3.97E^{-07}$ which is the smallest when compared to the other two methods, the Automesh method at $2.27E^{-06}$ and the Combination method at 2.80^{-06} respectively.

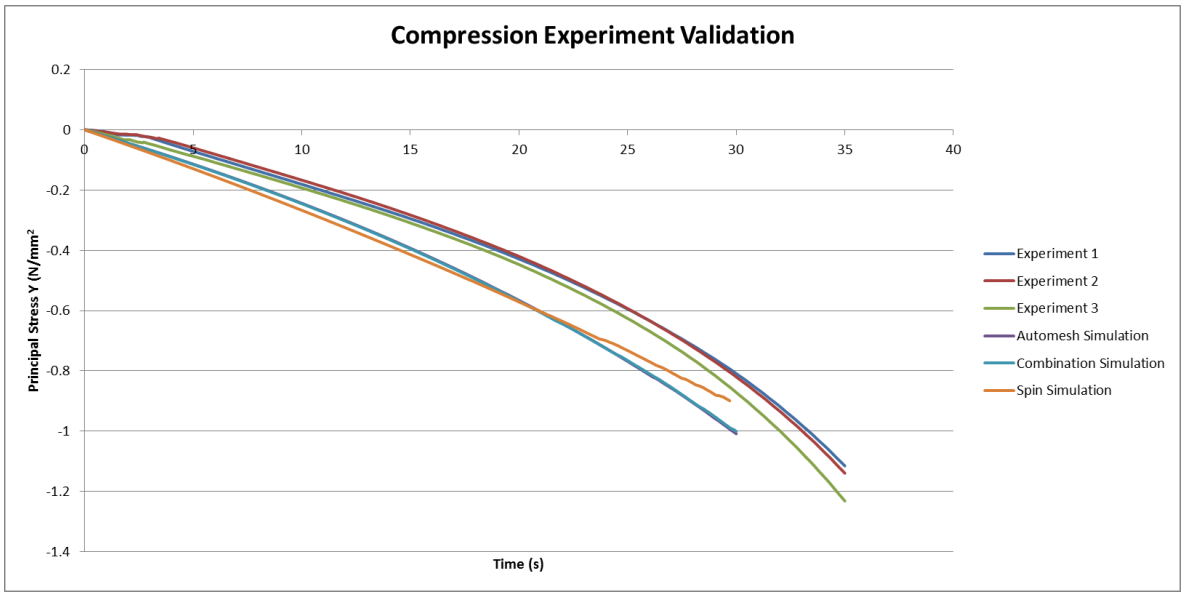


Figure 5: Graph of Stress vs Time for experiments and simulations

It is crucial to be both accurate in the results and efficient in terms of time consumed during the completion of simulations to ensure a productive work flow. Therefore it can be concluded that based on these two factors, the most suitable method of meshing between the three methods would be the third method in which two meshing strategies are combined at once to produce accurate results at a reasonable time taken to resolve the simulation.

3.2 Validation

The figure above indicates that the simulation, though has low precision as the values seem to vary from the experimental values, has a certain degree of accuracy. To validate its accuracy in numerical terms, the percentage error between the simulation and the averaged experimental values were calculated. Below is the equation that was used to calculate the percentage difference [14].

$$\%\, Difference = \frac{|E_1 - E_2|}{(\frac{E_1 + E_2}{2})} \quad (2)$$

The percentage for each set of data was calculated and was found to be ranging between the minimum values of 0.18% to a maximum value of 1.23%. It is noted that the percentage difference between the simulation and the experimental data increases with time because though the real rubber sample was compressed using two solid steel plates, the metal plates were not modeled and simulated in the simulation.

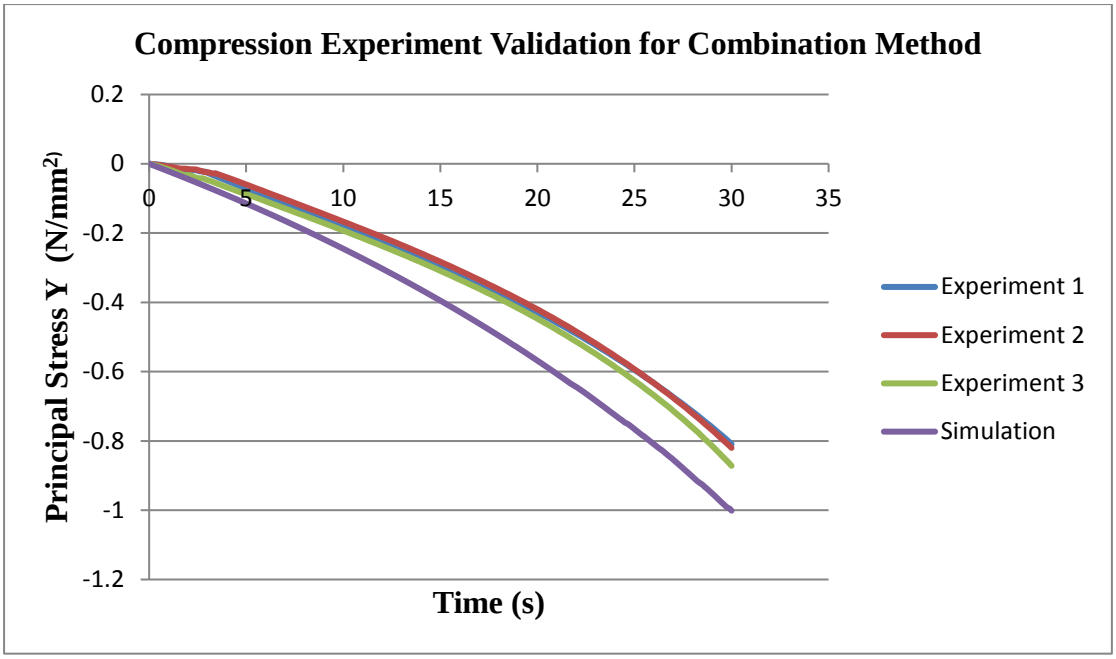


Figure 6: Graph of Stress vs Time of experiments and Combination Method

Therefore upon observation, it is apparent that towards the end of the 30 s mark, the buckling of the rubber in the simulation begins to distort upwards as there is no metal plate model keeping it in place. It can be concluded that the modeling of these flat steel plates and reassigning the boundary conditions accordingly may cause the accuracy of the simulation to increase.

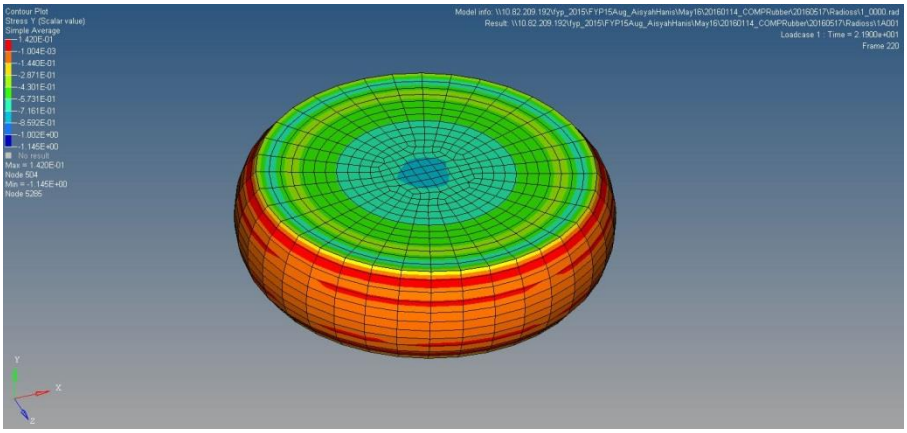


Figure 7: Distortion in Y-Direction

To address the overall lack of precision and also the deviation from the actual experimental value, a possible source would be the condition of the rubber samples itself. The samples that were procured from Panasonic were not perfectly cylindrical rubber samples as there were notable imperfections on the surface of each and every one of the samples that also deviate from one another. This was possible due to an error during production. However, as there is no possibility of modeling these imperfections accurately when creating the 3D model in Solidworks, the rubber sample model that was used in the simulations were all perfectly cylindrical. Therefore this inconsistency

in the experiment and its simulated counterpart could contribute to the cause of error between the two readings.

4. Conclusion

To conclude the findings of this project, it can be stated that the first objective was met in terms of acquiring a suitable meshing strategy to use in future simulations of the rubber sample. For the cylindrical rubber sample used in this project in particular, it was found that the best method would be to combine both the Automesh method that is more generally used in other studies and the Spin method. This was done to ensure that the Spin method does not generate too small an element towards the center of the rubber sample where the Spin occurs. The Automesh method was used to mesh the center instead to minimize the time step from becoming too small thus lengthening the time taken for the solution to be produced.

The second objective of modelling a rubber sample and assigning its material properties accurately were also met, as the simulation results were successfully validated by the experimental values. However, there are notable percentage differences between each set of data from the simulation and the averaged experimental data. The possible cause that may contribute to this percentage are the variations between the perfectly cylindrical rubber sample in the simulation and the imperfections present on the surface of the rubber samples tested during the compression test. Another possible cause of the percentage difference is the absence of the two metal plates used to compress the rubber sample in the experiment in the simulation.

Reference

[1] S. Park, M. Koka, K. Thomson and J. Robbins, 'A FE Modeling and Validation of Vehicle Rubber Mount Preloading and Impact Response', in 8th International LS-DYNA Users Conference, Dearborn, 2004, pp. 5-23.
[2] N. Dharwadkar and K. Adivi, 'Modelling of Engine Suspension Components for Crash Simulations', Masters, Chalmers University of Technology, 2011.
[3] S. Rao, The finite element method in engineering. Amsterdam: Elsevier/Butterworth Heinemann, 2005.
[4] G. Ramamurty, Applied Finite Element Analysis, 2nd ed. New Delhi: I. K. International Pvt Ltd, 2010, pp. 1-8.
[5] J. Akin, Finite element analysis concepts. Hackensack, NJ: World Scientific, 2010.
[6] N. Gokhale, S. Deshpande, S. Bedekar and A. Thite, Practical Finite Element Analysis. Pune: Finite to Infinite, 2008.
[7] R. Cook, Finite Element Modeling for Stress Analysis. California: John Wiley & Sons Inc., 2011.
[8] Cifuentes, A.O., and Kalbag, A., "A performance study of tetrahedral and hexahedral elements in 3-D finite element structural analysis," Finite Elements in Analysis and Design, 12 (1992) 313-318.
[9] Bussler, M, and Ramesh, A., "The Eight-Node Hexahedral Element in FEA of Part Designs," Foundry Management & Technology, Nov. 1993, 26-28.
[10] S. Benzley, E. Perry, K. Merkley, B. Clark and G. Sjaardama, A Comparison of All Hexagonal and All Tetrahedral Finite Element Meshes for Elastic and Elasto-plastic Analysis, 1st ed. Provo.

[11] O. Centeno G, 'Finite Element Modeling of Rubber Bushing for Crash Simulation: Experimental Tests and Validation', Masters, Lund University, 2009.

[12] Martins, P., Natal Jorge, R. and Ferreira, A. (2006). A Comparative Study of Several Material Models for Prediction of Hyperelastic Properties: Application to Silicone-Rubber and Soft Tissues. Strain, 42(3), pp.135-147.

[13] Liu, G. and Quek, S. (2003). The finite element method: A practical course. Cornwall: MPG Books Ltd, pp.5-6.

[14] John R. Taylor, An Introduction to Error Analysis: The Study of Uncertainties in Physical Measurements, 2d Edition, University Science Books, 1997.

The Development of an Optimal Aerodynamic Design for a Human Powered Vehicle

A. L. Laimon[1*], S. N. Namasivayam[1]

[1]*School of Engineering, Taylor's University Lakeside, Malaysia*

[*]alexanderlaimon.luke02@sd.taylors.edu.my

Abstract
The effects of the parameters of frontal area, surface area and the shape of the fairing on the aerodynamic drag of a HPV are researched and evaluated using CFD. The optimal aerodynamic designs for a pure speed and everyday use HPV are presented, and the design methodology of using the low drag laminar flow NACA 6 series of fairings is explained. It is found that using the k-ε turbulence model, the discrepancy between the CFD results and wind tunnel data for a benchmark model is 26.67%. However, although the absolute accuracy is low, the trends in the data can still be analysed and observed. The CFD results have shown that the boundary layer is fully turbulent in the simulations, and in the future the use of the transition SST turbulence model may be used to better capture the transition from a laminar boundary layer to turbulent. The use of C_DA as a better metric of comparison for the aerodynamic efficiency between models is illustrated, and it is shown that the pure speed HPV has a lower value of C_DA than the benchmark model, which is itself designed with pure speed in mind. In conclusion, increasing the frontal area and surface area does increase the C_DA of a HPV, however the shape of the fairing plays a more important role in determining its aerodynamic drag.
Keywords: bicycle aerodynamics, CFD, fairing, velomobile, human power.

1. Introduction

A Human Powered Vehicle (HPV) is defined as any vehicle that is propelled by human muscle power. Thus, due to the limited power that is available, a HPV must be as efficient as possible in order to reach high speeds. As HPVs generally have very little rolling resistance, aerodynamic drag is the largest retarding force acting on the HPV, becoming dominant beyond 15 km/h. By using a fairing that completely encloses the rider and chassis, the drag force can be reduced significantly, allowing well streamlined HPVs to reach speeds of over 100 km/h [1].

Generally, there are two main factors that contribute to aerodynamic drag; pressure drag and skin-friction drag [2]. Pressure drag is the result of an increase in pressure at the front of the vehicle, and a decrease in pressure in the rear as it moves

forward through the air. This pressure difference creates a net force that opposes the movement of the vehicle. Pressure drag is the dominant drag force in bluff body shaped vehicles where a large amount of flow separation occurs and is largely dependent on the frontal area. Skin-friction drag is the result of viscous shearing forces between the air and a surface. For well streamlined bodies such as airfoils that have very little flow separation, skin-friction drag is the main contributor to drag force [3] and is proportional to the wetted surface area (i.e. all external surfaces of the body exposed to the freestream). The HPVs designs in this project are streamlined bodies, thus skin-friction drag is the dominant drag force. The equation for drag force is given by equation 1.

$$F_D = \frac{1}{2}\rho V^2 A C_D \tag{1}$$

A represents the reference area, which is typically the frontal area for bluff bodies (such as automobiles) or the wetted surface area for streamlined bodies. The use of either of these reference areas however may result in misleading values of the drag coefficient C_D, which is the dimensionless drag coefficient that is dependent on the shape of the body. When C_D is used, it is possible that some bluff bodies can have a lower drag coefficient than more streamlined bodies. Therefore, the drag area, $C_D A$ is used which is the product of the drag coefficient and the reference area that was used to calculate it. It has the consequence of attaching a unit to the dimensionless drag coefficient; however it is a more consistent way to indicate the actual aerodynamic efficiency of the body [2].

The shape of the body relates to the pressure drag and skin-friction drag; it is perhaps the most important factor to consider when designing a fairing. To keep pressure drag to a minimum, the trailing edge of the fairing should be contoured so that flow separation does not occur or is kept to a minimum. Turbulent boundary layers have a higher skin-friction drag coefficient than laminar boundary layers[1], therefore the laminar flow region at the leading edge of the fairing should be preserved and extended for as much of the length of the fairing as possible. This is done by contouring the fairing in a way that produces a favorable (constant or decreasing) pressure gradient from the leading edge of the fairing up to the minimum pressure point, after which the boundary layer irreversibly transitions to turbulence.

The aim of this project is to create an optimum aerodynamic fairing for a HPV, taking into account the optimal configurations of the key parameters of frontal area, surface area and shape. However, the optimum design differs depending on the use case. There are broadly two types of HPVs that make use of fairings; pure speed HPVs that aim to break the land speed record under human power, and everyday use HPVs that aim to be a practical vehicle for daily transportation. Therefore, the objectives of this project are to conceive, design, implement and operate an optimum aerodynamic fairing for both a pure speed HPV and an everyday use HPV.

2. Fairing Design Methodology

The NACA 6 series of airfoils are an improvement over the older NACA airfoil series with the intention of maximizing laminar flow, they are designed with a large

area of favorable pressure gradient from the leading edge to achieve this, and thus have lower drag coefficients than the older airfoil series [4]. As the recumbent position for the rider is used for this project (a leaning position that minimizes frontal area), the maximum thickness of the fairing (essentially where the abdomen of the rider resides) lies towards the rear of the HPV. Therefore, the NACA 66 and 65 series of airfoils are an appropriate choice to create the shape of the fairing as their point of maximum thickness coincides with this point. The NACA 6 series nomenclature states that the second number represents the designed minimum pressure point of the airfoil; for the NACA 66 series, the minimum pressure point occurs at 60% of the chord length, and thus there is a favorable pressure gradient on the airfoil up to this point.

Due to the proximity of the HPV to the road, ground effect is a significant factor that contributes to the drag force. For a symmetrical airfoil that is close to the ground, flow is accelerated through the underside of the airfoil, thereby decreasing pressure in that region and creating negative lift, which in turn increases drag. To account for ground effect, the airfoil is cambered so that the underside is flatter, reducing the decrease in pressure in that region and thus decreasing drag. This is applied to the vertical (side view) airfoil shape, where the cambered NACA 65-415 airfoil is used for both the pure speed and everyday use HPVs. For the horizontal (top view) airfoil, the NACA 66-018 and the NACA 66-021 airfoils are used for the pure speed and everyday use HPVs respectively (the last two numbers indicate the maximum thickness of the airfoil, where the NACA 66-018 airfoil has a maximum thickness of 18% of the chord length). The fairings are created using Solidworks, and the final designs for the pure speed and everyday use HPVs are shown in figure 1. The specifications of each design are given in Table 1.

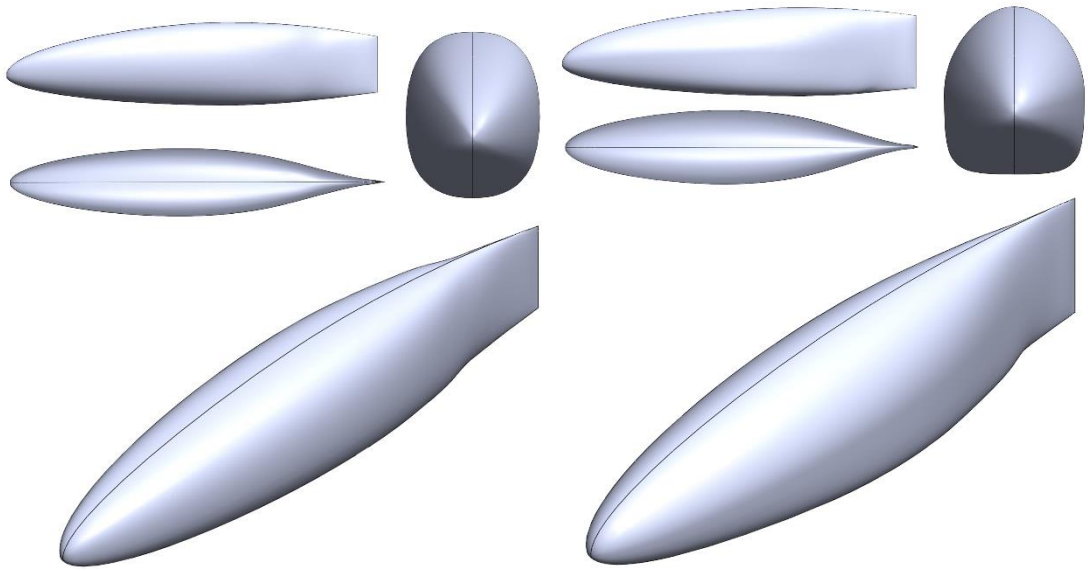


Figure 1. Pure Speed HPV (left) and Everyday Use HPV (right)

The pure speed HPV uses two inline wheels while the everyday use HPV uses the tadpole wheel configuration where there are two front wheels on either side of the rider and a single rear wheel. This is why the bottom sides of it are in a ‘box’ shape to cover the wheels.

Table 1. Pure Speed and Everyday Use HPV Specifications

Specification	Pure Speed	Everyday Use
Length (m)	2.837	3.000
Width (m)	0.509	0.626
Height (m)	0.630	0.750
Frontal Area (m^2)	0.271	0.396
Surface Area (m^2)	4.100	5.368

3. Computational Fluid Dynamics

In order to verify the CFD simulations, a benchmark model was used; the Virtual Edge HPV designed by Matt Weaver [1]. This HPV design was used because the full specifications of the HPV including frontal area and surface area are provided (and subsequently replicated in the 3D model), along with wind tunnel data shown in table 2. The 3D model compared to the actual HPV is illustrated in figure 2.

Table 2. Virtual Edge Data

Length (m)	2.840
Width (m)	0.480
Height (m)	0.850
Frontal Area (m^2)	0.316
Surface Area (m^2)	4.320
C_D (at $Re = 6 \times 10^6$)	0.0450
C_DA (m^2)	0.0142

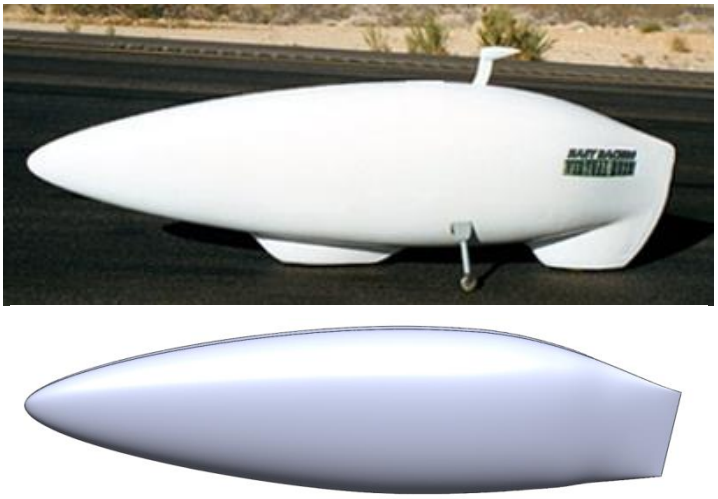


Figure 2. Virtual Edge Benchmark Model

The CFD simulation was done using ANSYS FLUENT, and the setup was adapted from several sources. Figure 3 shows the flow domain for the half model along with the named selections, where the sides and front extend to 3x HPV length, and the rear extends to 6x length [5]. Due to the sharp angles at the trailing edges of all the fairings, the meshes were highly skewed although the maximum skewness did not go above 0.95.

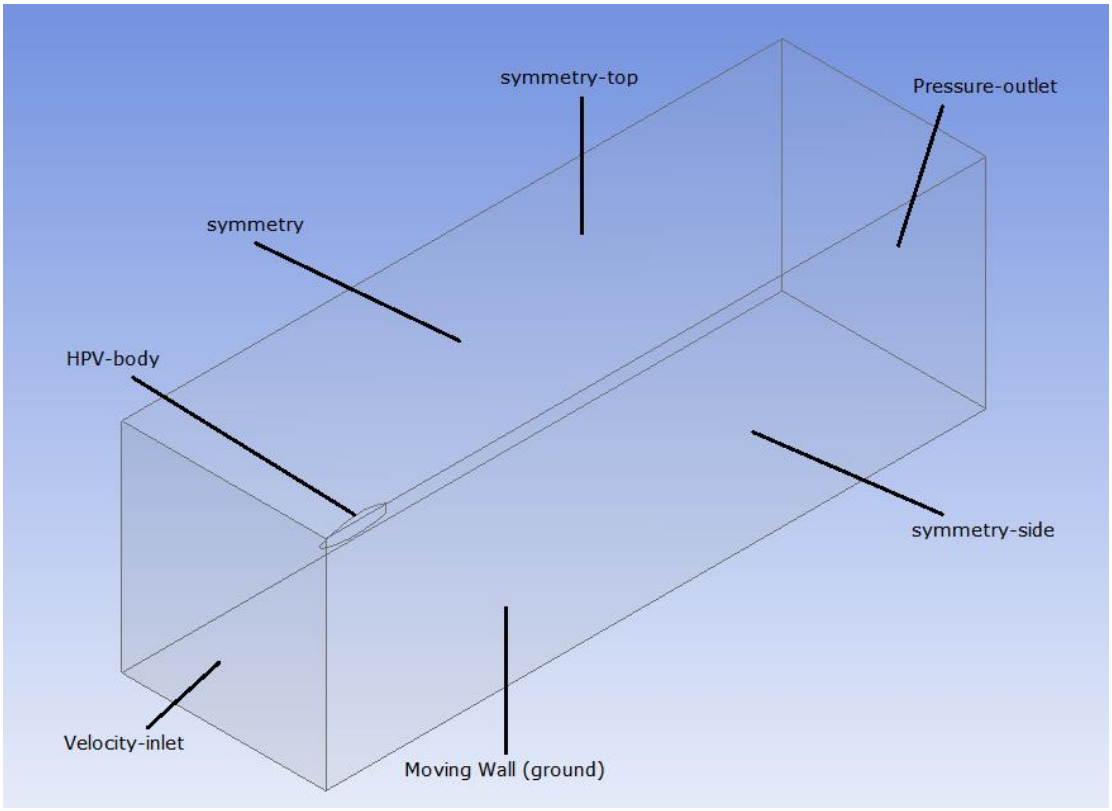


Figure 3. Flow Domain

The Realizable k-ε turbulence model was used [6] [5] [7]. In order to keep the number of mesh elements to a minimum, a wall function approach was adopted with a target y+ of above 30 (first cell height of 1mm for all designs, 20 inflation layers) [8]. Due to the changes in flow velocity around the fairing, preliminary simulations had shown that the y+ had gone below 11.225 at some areas, which is outside the relevant range for wall functions. Therefore, scalable wall functions are used as it virtually displaces these regions to a y+ of 11.225, thereby remaining within the required range for wall functions. A summary of the FLUENT solver settings is shown in Table 3. The same meshing and solver settings were used for all designs.

Table 3. FLUENT Solver Settings

Meshing	
Element Types	Tetrahedral and prisms
Number of Elements	1.5~2 million
Spatial Discretization	
Gradients	Least squares cell based
Pressure	Standard
Momentum	Second order upwind
Turbulent kinetic energy	Second order upwind
Turbulent Dissipation Rate	Second order upwind

Second order upwind is used because of its higher accuracy compared to first order. However, first order was used for the first 100 iterations in order to help convergence. The coupled pressure-velocity coupling scheme was used, and a low courant number and under relaxation factors were used due to the high skewness of the

mesh. As the Virtual Edge drag coefficient of 0.045 was done using a Reynolds number of 6×10^6, the freestream velocity at the velocity inlet was set to 30 m/s. The reference area for calculating the drag coefficient is set to the frontal area.

4. Results & Discussion

After roughly 500 iterations, the drag coefficients for all the models had converged. The y+ at convergence never went below 11.225 (due to the use of scalable wall functions), with a maximum y+ of 60 for all the models. Therefore, it falls within the range of relevancy for wall functions. Figure 5 shows the CFD results for all the models, showing the pressure, viscous and total drag coefficients for all three models.

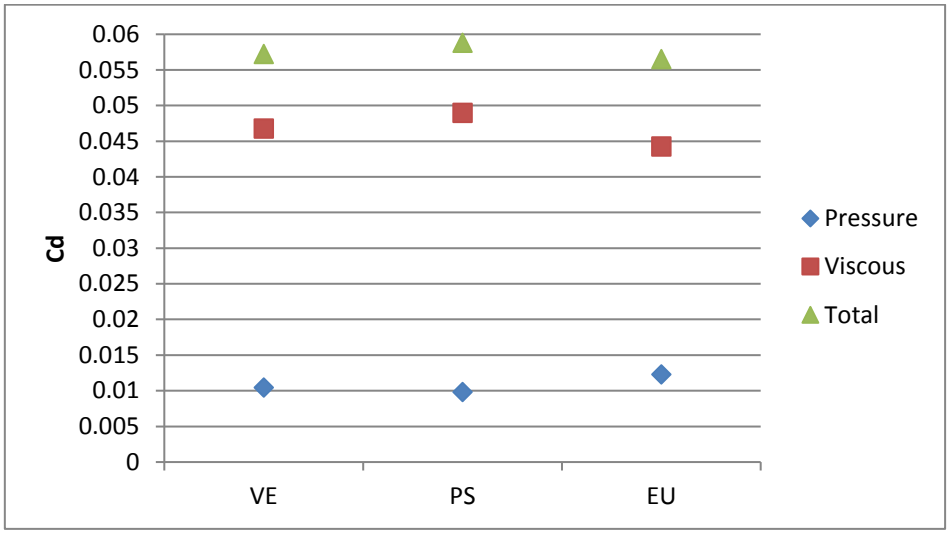


Figure 5. CFD Results for C_D

For the Virtual Edge, the total drag coefficient is 0.057, which is 26.67% higher than the wind tunnel data provided. There are several possible sources for this large difference in results. One of the references used for setting up the simulations [6] had stated that the k-ε turbulence model may give a drag coefficient value of up to 20% higher than wind tunnel data. Another reason for this discrepancy is that the 3D model of the Virtual Edge has slight differences with the actual Virtual Edge, as the exact 3D model is not publicly available and thus its exact contours could not be replicated fully. To improve these simulations in the future, a more reliable benchmark model should be chosen if possible. Also, reference [6] has shown that the Transition SST turbulence model is able to provide more accurate results (3% error) when compared to wind tunnel data, however a y+ of ~1 is required which leads to a large increase in the number of elements.

Observing figure 5, the Virtual Edge has a lower viscous drag coefficient than the pure speed HPV, while both have almost equivalent pressure drag coefficients. This leads to the Virtual Edge having a lower overall C_D. However, the everyday use HPV which has the largest values of projected frontal area and surface area has the lowest total drag coefficient of all the models (0.0565), although it does have the highest amount of pressure drag which agrees with the fact that it has the largest frontal area. Referring back to section 1, this is the reason that the drag area, C_DA is a better representation of the aerodynamic efficiency of a HPV, as the drag coefficient based on

frontal area in this case is misleading. As such, figure 6 shows the drag area of the three HPVs.

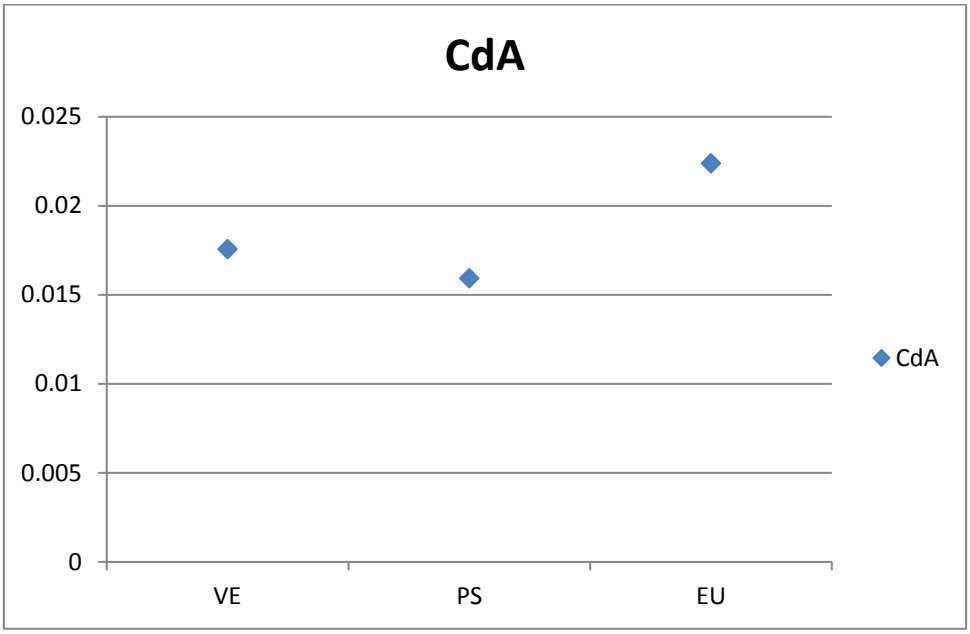


Figure 6. C_DA of the three HPVs

Using C_DA as the comparison metric, it is now shown that the pure speed model has the lowest drag area of all the models making it the most aerodynamically efficient design (i.e. for the same power input, it is able to reach higher speeds when compared to the other HPVs). It is also shown that the everyday use HPV has the highest value of C_DA, agreeing with the fact that it has the largest amount of projected frontal area and surface area. Interestingly, the C_DA value for the Virtual Edge of 0.0176 is now 24% higher than the wind tunnel data value of 0.0142.

Figure 7 shows the local skin-friction drag coefficient along the length of the Virtual Edge superimposed against the data from Kyle and Weaver [1]. The red line represents the CFD simulation data; the black squares represent the local skin-friction coefficient in a turbulent boundary layer, while the black diamonds are the local laminar skin-friction drag coefficient

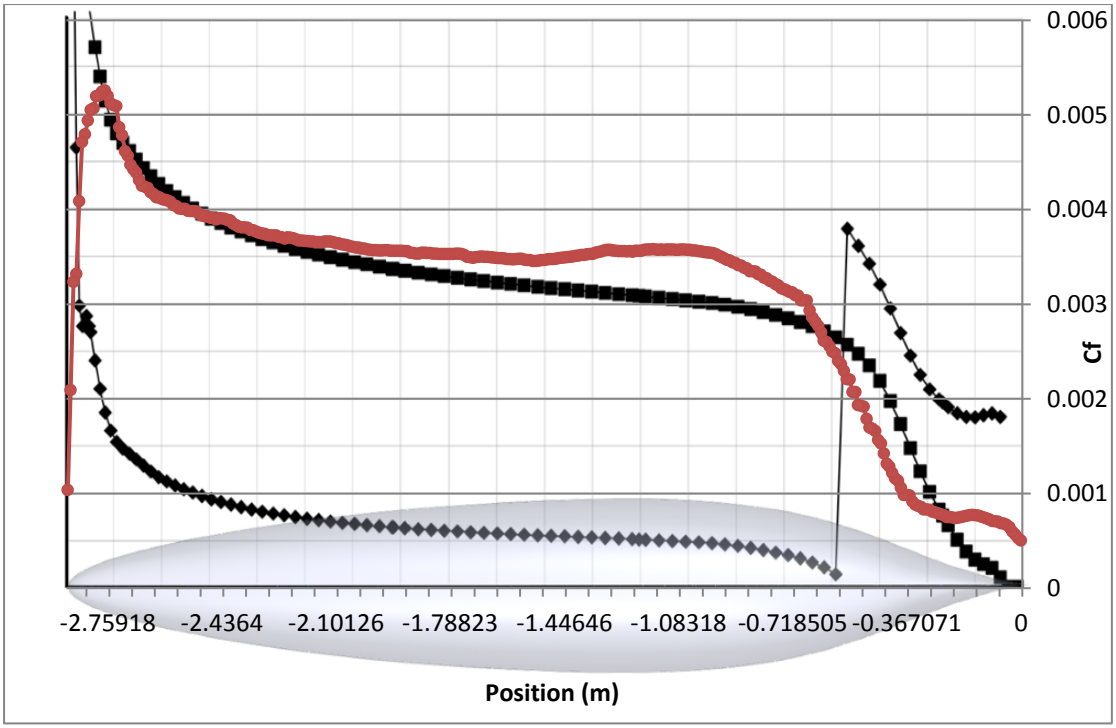


Figure 7. Graph of Local Skin-Friction Drag Coefficient Along Length

It is observed that the boundary layer across the entirety of the model is in turbulent flow (the given drag coefficient value of 0.045 is in forced turbulent flow as well). At the leading edge, the CFD data follows the data from literature very closely, before gradually deviating. This discrepancy may be one of the sources of error that contributed to the difference between the CFD results and the wind tunnel data for the Virtual Edge. However, in spite of the discrepancy between the CFD results and wind tunnel data, figure 7 shows that the trends in the data are present even though the absolute accuracy isn't, therefore the CFD results presented here may still prove to be useful in getting an idea for the flow around these HPV models.

Figure 8 shows a comparison in local skin-friction drag coefficient between all the models. The left of the graph is the leading edge of the models, and the difference in starting points is due to their different lengths. As the pure speed and everyday use HPVs both use the NACA 66 series as their horizontal profiles, they follow a very similar curve of local skin-friction coefficient.

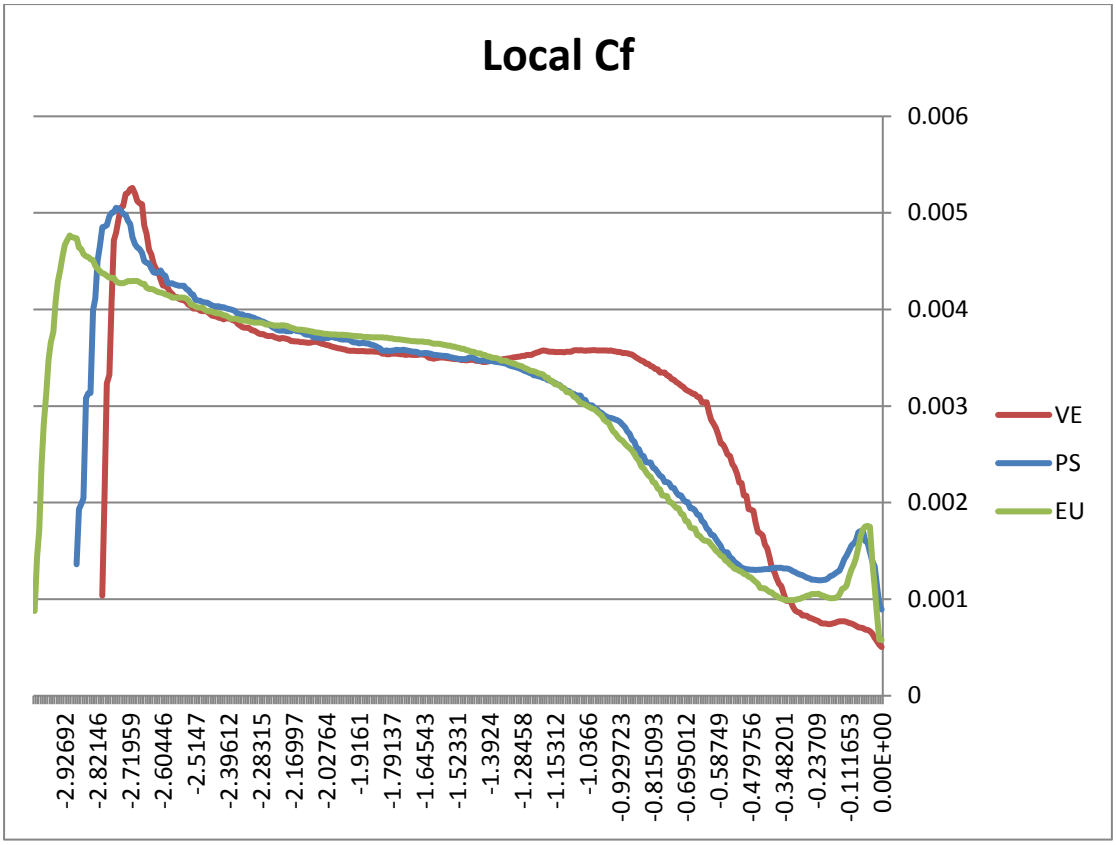


Figure 8. Comparison of Local Skin-Friction Coefficients

Figure 9 shows the pressure coefficient of each of the models along its length, where the left side of the graph is the leading edge. The extent of the decreasing pressure gradient represents the area of favorable pressure gradient at the leading edge of the model. As both the pure speed and everyday use HPVs use NACA 66 airfoils for their horizontal shape, the point of minimum pressure occurs at roughly 45% after the leading edge for both models, which is the point of maximum thickness. This falls short of the designed favorable pressure gradient for 60% of the chord length. However, that designed value assumes that the boundary layer is laminar at the leading edge before transitioning to turbulent. In the case of the CFD simulations however, the entire boundary layer flow for all the models is turbulent as shown in figure 8. A turbulent boundary layer conforms to the contours of a body much closer than a laminar boundary layer, which is why the minimum pressure point for these two fairings is at the point of maximum thickness rather than the designed transition point. Comparing against the Virtual Edge, its maximum thickness occurs further back from the leading edge than both the pure speed and everyday use HPVs. However, as the entire boundary layer is turbulent, the benefit of the designed transition point for maximizing laminar flow is not represented in the CFD simulations. The use of the transition SST turbulence model may prove to be more accurate here as it is able to simulate this transition point.

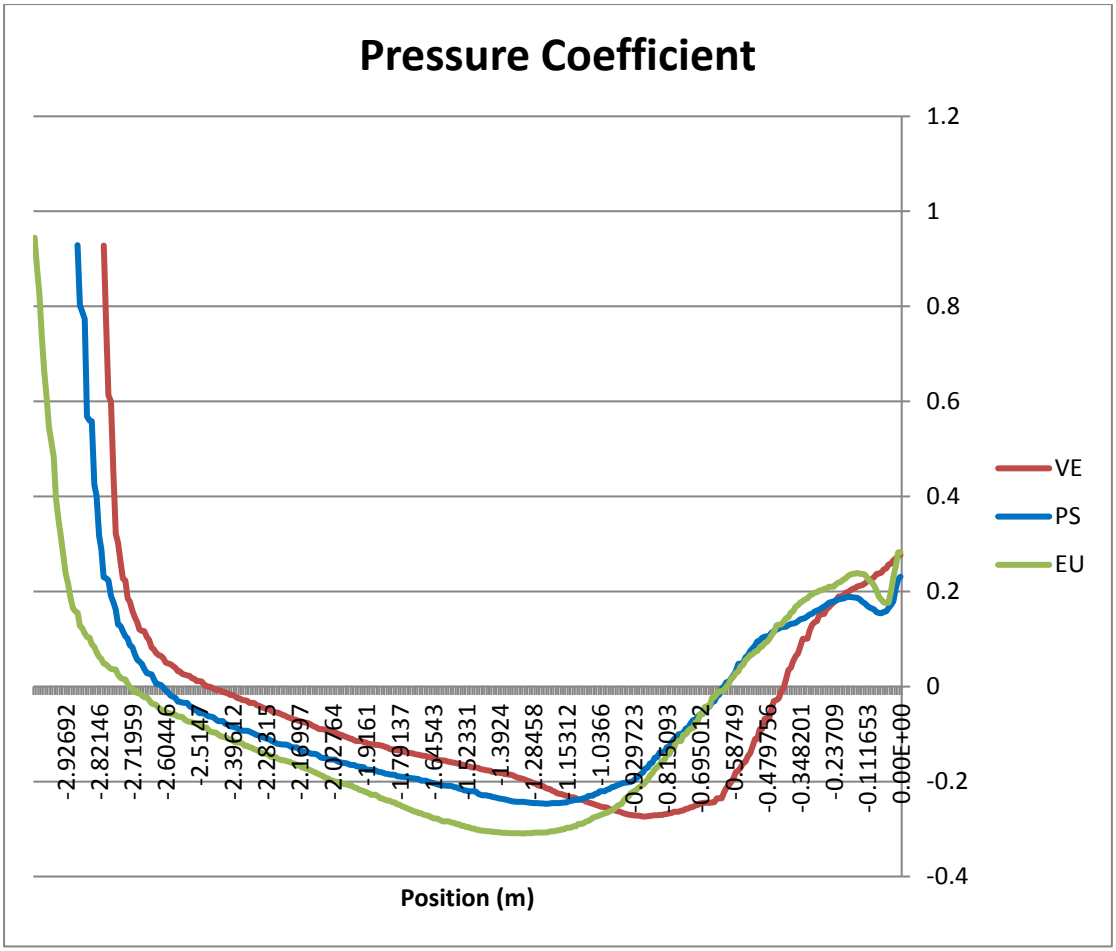


Figure 9. Pressure Coefficient Along Length

6. Conclusions & Future Work

In conclusion, the effects of the projected frontal area, wetted surface area and the shape of the vehicle on the drag of the fairing have been shown. However, they are only useful insofar as to get an idea of the flow around the fairing, as sufficient accuracy has not been achieved with the current CFD simulation method with errors of up to 26.67% different from wind tunnel data. However, the design methodology of using appropriate airfoil shapes to create the fairing has shown to produce results that are relatively similar to an existing high-performance design, judging by the trends in the data. The pure speed model has even shown to have a lower drag area than the Virtual Edge, which is itself designed with pure speed in mind.

For future work, there should be more refinement in the CFD simulations to produce results that agree better with wind tunnel data. This may involve the use of the transition SST turbulence model to more accurately capture the transition of the boundary layer from laminar to turbulent, although at the cost of increased requirement in computer resources. Similarly, a more reliable benchmark model could be used if the exact 3D model is able to be obtained or at least more accurately recreated. For the fairing designs, the airfoil shapes merely represent the first iteration of the design, as more improvements can be made to reduce the drag coefficient further.

References

[1] Kyle C. R., Weaver M. D. (2004). Aerodynamics of human powered vehciles. *IMechE*.
[2] Barnard R. H. (1996). *Road Vehicle Aerodynamic Design*. London: Addison Wesley Longman.
[3] Carrol D. R. (1997). *The Winning Solar Car*. Warrendale, PA: SAE International.
[4] Abbot I. H. (1959). *Theory of Wing Sections*. Toronto, Ontario: General Publishing Company Ltd.
[5] Lanfrit M (2005). Best practice guidelines for handling automotive external aerodynamics with FLUENT.
[6] Pachecho P. et. al. (no date). Aerodynamic Design of Solar Energy Cars for Australian and Chilean Race Competitions.
[7] Mark Darwin A/L Partap Singh, S. M. Salim, "Aerodynamic investigation of a solar car body," in EURECA Year 1, 2013
[8] Salim S., Cheah S.C. (2009). Wall y+ strategy for dealing with wall bounded turbulent flows. *IMECS*

Using $k - \varepsilon$ Models to Compare the Flow-Induced Vibration for Water Flowing in a Pipe with Orifice Plate

Azzam Syafiq Samsuddin[1*], Dr. Mohamed Nassir, Mohd Hardie Hidayat Mohyi

[1]*School of Engineering, Taylor's University, Malaysia*

[*] azzamsyafiq.samsuddin@sd.taylors.edu.my

Abstract

In industries that have operations that utilizes significant amount of flows and piping systems, it is extremely important to identify and control the flow rates of various chemical processes so that the flow operations can operate optimally with excellent safety and to minimize loss in operating performance. In order to monitor the flow rates, orifice meters are widely used due to their simplicity in operation. Orifices operate by utilizing the effects of velocity and variations in pressures caused by the reduction of the cross-sectional flow area. When the flow is throttled through the orifice, the resultant flow velocity interacts with the surrounding pipe, causing flow-induced vibration (FIV). Without proper supervision, the vibrations could inflict serious damage to the pipes over time and may even cause breakdown. The aim of this research is to study the FIV for water flowing in a pipe with an orifice plate by utilizing $\boldsymbol{k - \varepsilon}$ turbulence models in Computational Fluid Dynamics (CFD) software, by looking for the possibility of simulating FIV using $\boldsymbol{k - \varepsilon}$ turbulence models and to compare it with real-life situations. Due to the interaction between the water flow and pipe wall, this research involves fluid-structure interaction (FSI) phenomena and this can be studied from the System Coupling component in ANSYS. System Coupling connects two simulation components, Transient Structural which is for the pipe, and Fluent which simulates the fluid flow. The results will be analysed through Fast Fourier Transform function in Fluent to convert the time domain results into frequency domain. Three different aspect ratios of the orifices is used in this study, which are 0.255. 0.304 and 0.355 with inlet flow rate at 20 m^3/h. At the end of experiment, it is concluded that the $\boldsymbol{k - \varepsilon}$ turbulence models is not suitable to simulate FIV for water flowing in a pipe through an orifice plate.

Keywords: Orifice Plate, $k - \varepsilon$ turbulence models, Flow-Induced Vibration, Fluid-Structure Interaction, Computational Fluid Dynamics, Fast Fourier Transform.

1. Introduction

The significance of monitoring the flow rates in various chemical processes are huge in industries that involve fluid flows in pipes. Such industries include manufacturing plants, nuclear plants, water distribution, on-and-off-shore petroleum complexes and many others. The flows in these pipes have to be continuously monitored using flow meters, and available flow metering devices mostly operate based on pressure differential. Among the available flow meters, orifice meters are the most widely used flow measurement instrument due to the ease in construction, installation and maintenance, no moving parts, low cost, able to operate in extreme weather and able to be utilized for various forms of fluids such as liquids and gas. Orifices operate by utilizing the effects of velocity and pressure variations caused the reduction of area of cross-sectional flow area[1]. Different types of orifices exist in the market, such as the concentric orifice and eccentric orifice, however the most common type is the concentric round orifice plate.

In any fluid flow systems, the interaction between the pipe and fluid flow causes flow-induced vibration (FIV) on the pipes. The study of interaction between a movable or deformable structure with an internal or surrounding flow is known as fluid-structure interaction (FSI) and it is one of the most sophisticated subjects in computational fluid dynamics (CFD)[2]. FSI simulations are of great assistance in modeling and simulating realistic flow problems such as vortex-induced vibration of marine cables and ocean currents that affect flexible risers[3]. Vibrations have been identified by numerous agencies to be the cause of multiple mishaps in the industry. FIV is a very complex phenomenon in which to this day, there is still no widely accepted consensus for a specific theory[4]. Currently, multiple studies have been conducted to research on FIV effects on pipes and valves, however not the same can be said for orifices. As of this time of writing, there is yet any mathematical models available to describe the fluctuating pressure as excitation of random vibration, hence direct numerical calculations of FIV response is impossible[4].

One of the causes of the FIV created from flows across orifices are from the differential pressure which happens across the orifice plate. This difference in pressure causes Newtonian forces on the orifice plate and creates unbalanced forces on both sides of the plate, in which consequently, also causes swirling and back stream of the flow. These effects cause the vibrations on both the orifice plate and the surrounding pipe near the orifice. Aside from the unbalanced forces, the installation of the orifice plates also affects the FIV. Studying these vibrations are of great importance due to its possibility to reach resonance by achieving the same frequency as the natural frequency of the pipe. If the frequency of the vibrations has the same magnitude as the natural frequency of the surrounding pipes, it will severely damage the structure and could destroy the pipe[5].

There are a number of ways to study FIV, including experimental, investigation using numerical analysis, and utilizing simulation programs[5]. From the simulation approach, the current trend in researching flows of fluids is based on simulation on Navier-Stokes or Reynolds stress equations[6]. Computer simulations are utilized due to their more economical and time-saving characteristics when compared to equivalent real-life experiments and helps researchers gather a complete data on the behaviors of the flow without assembling and utilizing expensive apparatuses. The CFD simulation

techniques can be used with various mathematical models such as Kappa – Epsilon ($k-\varepsilon$) models, Kappa – Omega ($k-\omega$) models, Spalart – Allmaras model, and Reynolds Stress models (RSM). In this particular study, the FIV will be simulated by using the $k-\varepsilon$ turbulence models. It is important to note that although flows with similar properties are simulated under the same program, different research teams have acquired different results due to applying varieties of parameters to depict certain conditions and/or accuracies, as well as computational limitations[6]. FSI analysis for this study is conducted using the System Coupling function in ANSYS, which combines two separate components: Fluid Flow (Fluent) which simulates the fluid flow, and the Transient Structural which represents the pipe that encloses the flow.

$k-\varepsilon$ models are one of the most widely utilized turbulence models when performing CFD simulations. In Fluid Mechanics, the $k-\varepsilon$ models are known to be a two-equation model, in which one equation (k) represents kinetic energy which affects the energy in the turbulence and the other (ε) represents the turbulent dissipation energy due to the viscosity, which influences the scale of the turbulence. The $k-\varepsilon$ turbulence models are simple to use, most commonly validated, has exceptional performance for numerous important flows that is used in a number of industries, and needs less computational power when compared to more general Reynolds Stress models[7]. They are also widely used due to its robust feature and economy in solving relatively simple flows[8].

The orifice meters are characterized by two properties, namely the Discharge Coefficient (C_D) and its aspect ratio, β. The definition of discharge coefficient is the ratio of actual flow to the theoretical flow, and is acquired from experiments that are conducted under supervised conditions of velocity profiles that are swirl-free, undisturbed and symmetrical in the flow region after the orifice[9]. The aspect ratio β is defined as the ratio of the inner circle's diameter of the orifice to its outer body diameter $d_{orifice}/D_{pipe}$. This property has an important role in influencing the flow pattern inside the pipeline. The orifice has a circular shape with a flat cross-sectional profile and the outside diameter of the orifice is maintained throughout the period of the study.

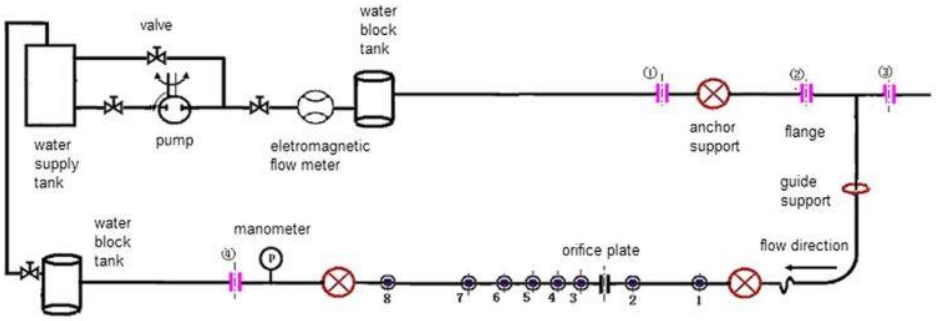


Figure 1. The test loop as arranged by Qing et al [4]

Previous studies that attempted to conduct a similar study was performed by studying the flow using physical apparatus by Qing et al [4] as shown in Figure (1). They attempted the experiment by utilizing a straight pipe made of 1Cr21Ni15Ti stainless steel in which the dimensions were 6 meters in length, 2.5 millimeters in thickness and 90 millimeters in diameter. The experiment was conducted with three values of inlet velocities: 15, 25 and 40 m^3/h and three different orifice aspect ratios:

0.255, 0.304 and 0.335. The study concluded that the orifice significantly affects the flow and increases the fluctuating pressure level. The fluctuating pressure is at a near field turbulence and the dominating energy is more concentrated at lower frequency range. Lesser energy is contained at the lower frequency range the further the flow goes from the orifice.

Sridevi et al conducted a study by using CFD to compare the flow analysis through different profile of orifices[1]. Two simulation programs were used: Fluent to solve the balance equation using control volume approach and GAMBIT to draft and mesh the geometry of the orifices. Four types of orifice profiles were chosen which were sharp-edged, borda, short-tube and rounded types as shown in Figure (2). The simulations were done in steady state with an inlet velocity of 3 m/s, with pipe dimensions of 5 millimeters thickness, 60 millimeters in diameter and 150 millimeters in length, with tetrahedron meshing. One turbulence model was used, which was $k-\varepsilon$ model and for each orifice profiles, velocity, pressure and vorticity of the flow were observed. The study concluded that the CFD results and experimental data were in good agreement hence CFD can be considered as a viable alternative and cost-effective tool for estimating mass flow rate.

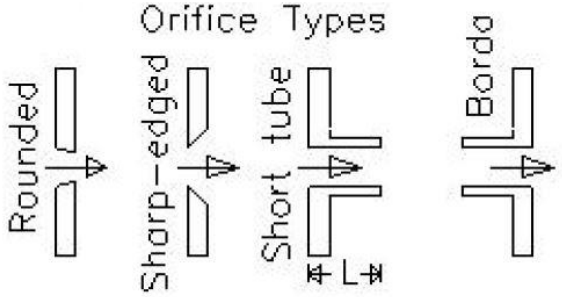


Figure 2. Cross-sectional profiles of the orifices used by Sridevi et al. [1]

Doborowski et al applied and discussed the mathematical details of the Reynolds-averaged Navier Stokes (RANS) and discussed the various turbulence models, including the three types of $k-\varepsilon$ turbulence models, which are Launder – Spalding $k-\varepsilon$ model, Renormalization Group Theory $k-\varepsilon$ model, and realizable $k-\varepsilon$ model [6]. Fluent software was again used for the simulation and the equations were solved by utilizing finite volume method (FVM) with multiple sizes of grid meshing. The calculation results were validated with the experimental data from a study by Morrison et al. Doborowski concluded that the Launder – Spalding model, when compared with the other $k-\varepsilon$ turbulence models, gives the best results and requires the lowest cost.

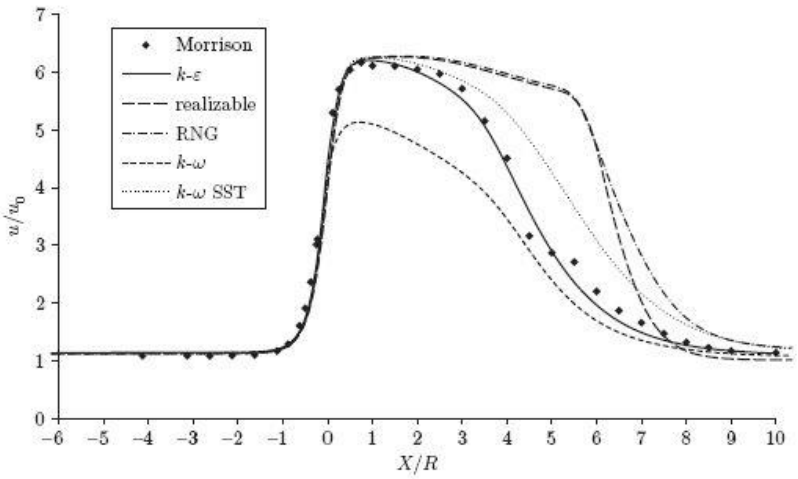


Figure 3. The results of the simulation when compared to Morrison et al. [6]

Siba et al conducted a study in which they focused on the pressure distribution and fluctuation of a flowing fluid after a circular orifice [10]. The study used computer simulation program ANSYS 14.0 to conduct the study. Navier-Stokes equations were employed to describe the velocity, pressure, stress, vorticity, strain and total deformation of the orifice. The simulation was conducted with three different Reynolds numbers (which was affected by flow velocity) 10 000, 20 000, and 30 000 and three different aspect ratios of orifice 0.2, 0.4 and 0.6. As for the turbulence model, standard $k - \varepsilon$ model was utilized. The results were that when the aspect ratio was constant, for increasing Reynolds numbers, the contour lines of the flow became denser, which indicated increase in wall pressure, in which a sudden increase was detected at the location of the orifice. Besides that, the size of the tail of the spinning flow also got larger, which indicated increased velocity. On the other hand, at constant Reynolds number and increasing aspect ratios, the contour lines became less dense which showed decrease in pressure. The study concluded that as Reynolds numbers increase, the pressure increases as well, however the maximum magnitude of axial velocity shifts slightly back.

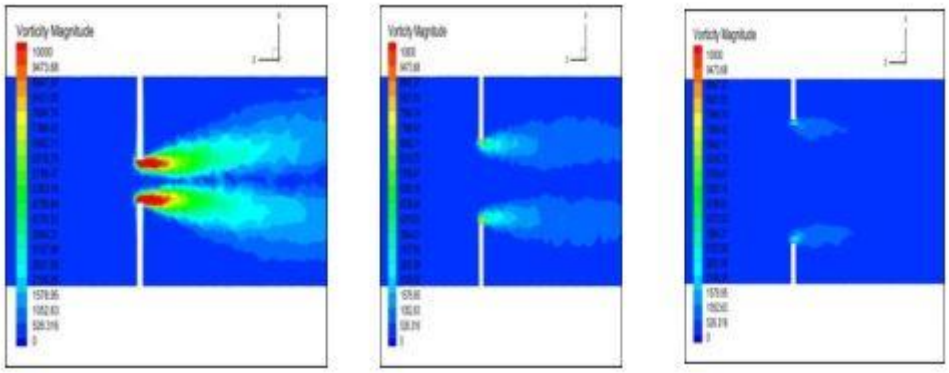


Figure 4. The vorticity at aspect ratio 0.2 for Reynolds numbers 10 000, 20 000 and 30 000 [10].

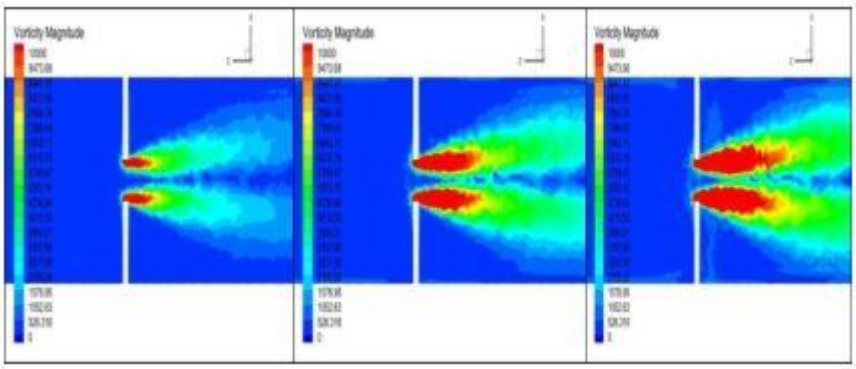


Figure 5. The vorticity at Reynolds number 10 000 for aspect ratios 0.2, 0.4 and 0.6 [10].

The $k-\varepsilon$ models are described by a set of equations called the Reynolds-averaged Navier-Stokes (RANS) equations which contain two equations, which are equations of motion,

$$\rho\mathbf{U}\nabla.\mathbf{U} = -\nabla\rho + \nabla\mu_{\text{ef}}.(\nabla\mathbf{U} + \nabla\mathbf{U}^T) + \frac{2}{3}\rho\nabla k \quad (1)$$

And equations of continuity,

$$\nabla.\mathbf{U} = 0 \quad (2)$$

Where,
U - mean velocity vector
ρ - the density of the fluid
k - kinetic energy of turbulence
$\mu_{\text{ef}} = \mu + \mu_{\text{t}}$ – the effective viscosity, where μ is molecular viscosity and μ_{t} is the turbulent viscosity.
These equations are closed by equations of the turbulence model[11],[12]. These viscosity models are used all over the world and the turbulent viscosity is treated as a scalar quantity [6].

The most widely used $k-\varepsilon$ model is the Launder-Spalding model, in which the turbulent viscosity is calculated using the following equation:

$$\mu_{\text{eff}} = \rho c_\mu \frac{k^2}{\varepsilon} \quad (3)$$

Where,
k – the distributions of kinetic energy of turbulence
ε – the dissipation rate of kinetic energy of turbulence
In which the above equation is obtained from the equation below:

$$\rho\nabla.\varepsilon\mathbf{U} = \nabla.\left(\mu + \frac{\mu_t}{\sigma_k}\right)\nabla\varepsilon + \frac{\varepsilon}{k}(c_1 G - c_2\rho\varepsilon) \quad (4)$$

The numerical coefficients σ_k,σ_ε, c_1, c_2, and c_μ are constants which are obtained from experiments, and Launder and Spalding recommend the following values: σ_k=1.00, σ_ε = 1.30, c_1 = 1.44, c_2 = 1.92 and μ = 0.09 [13].

On the other hand, the equations for RNG $k-\varepsilon$ model is derived from the Renormalization Group Theory. The equations are similar to the previous $k-\varepsilon$ model especially for k, however for ε it requires an additional component:

$$-\frac{c_\mu\eta^3(1-\frac{\eta}{\eta_0})}{1+\beta\eta^3}\frac{\varepsilon^2}{k} \quad (5)$$

$$\text{Where, } \eta = \sqrt{\frac{G}{c_\mu \rho \varepsilon}} \tag{6}$$

In which the values of the constants recommended are σ_k = 0.8, σ_ε = 1.15, c_1 = 1.42, c_2= 1.68, c_μ = 0.0865, η_0 = 4.38 and β = 0.012 [14].

In addition to the previous two models, this study also involves the Realizable $k-\varepsilon$ model. The meaning of 'realizable' is that the model satisfies certain mathematical constraints on normal stresses, in which it is consistent with the turbulent flows' physics. This model differs from the previous models by adopting a new eddy-viscosity formula involving a c_μ variable a new model equation for dissipation based on the dynamic equation of the mean-square vorticity fluctuation. The modeled transport equation for ε is as follows:

$$\rho \nabla . \varepsilon \mathbf{U} = \nabla . \left(\mu + \frac{\mu_t}{\sigma_e}\right) \nabla \varepsilon - \rho c_2 \frac{\varepsilon^2}{k + \sqrt{\frac{\mu}{\rho}\varepsilon}} \tag{7}$$

The values of the coefficients are σ_k = 1.0, σ_ε = 1.2 and c_2 = 1.9 [15].

2. Methodology

2.1 Geometry

The solid part of the FSI simulation will be the pipe that encloses the fluid, as well as the orifice that affects the whole flow. The pipe was created in SolidWorks with the dimensions of 3 meters in length, 90 millimeters in diameter and 2.5 millimeters in thickness. The orifice is positioned at the 1-meter mark from the inlet of pipe. Three different orifice aspect ratios will be chosen which are 0.255, 0.304 and 0.335. As for the thickness of the orifice, it is chosen to be 9 millimeters. These specifications are to follow the study of Qing et al so that the results of this study will have a reference for validation. The material of the pipe and orifice is specified to be stainless steel, which is available in Engineering Data Sources in ANSYS Database.

The pipe, orifice and fluid that is described in Figure (2) was first modeled in a Computer Aided Design (CAD) program, SolidWorks, and then imported to the Transient Structural component in ANSYS Workbench. Transient Structural was chosen because we need the results over a specified time, as the results will be analyzed in Fast Fourier Transform (FFT) to acquire the frequency. In ANSYS's DesignModeler, the components of the simulation need to be specified whether it is solid or fluid. Later in meshing for Transient Structural, the fluid is suppressed and only the pipe and orifice is meshed. As for the fluid, the geometry from Transient Structural was shared with Fluid Flow (Fluent). The pipe and orifice were suppressed for this component.

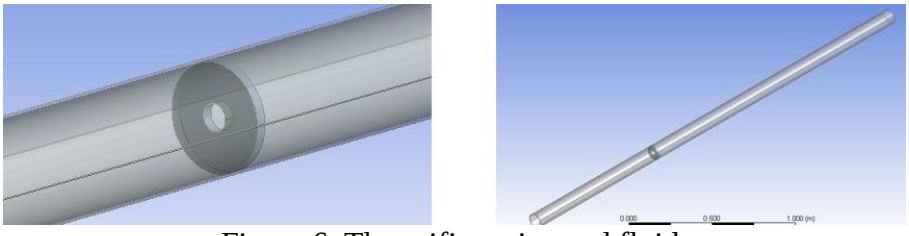


Figure 6. The orifice, pipe and fluid.

2.2 Meshing

Any simulation of geometry must went for meshing before conducting the simulation. For Transient Structural, the Meshing was conducted in Mechanical component in ANSYS. The orifice and pipe were meshed separately so that meshing will be simpler to manage. Since the mesh size was remained constant throughout the flow field models, hexahedron type meshing is used. In order to determine whether the meshing model was good or bad, two parameters were examined: skewness and orthogonal quality. Skewness was aimed to be lower than 0.8, while orthogonal quality was targeted as high as possible, which is close to 1.

For meshing fluid, the procedure is different compared to that of the solid part. First the named selections of the fluid body had to be specified, in which the inlet, outlet and pipe wall regions were defined. Inflation is added at the regions near the pipe wall. The inflation layers are useful for flows to capture the boundary layers of the fluid near the wall and orifice structure. The mesh near the inflation layers were hexahedron, unlike the rest of the fluid geometry which was in tetrahedron. The mesh metrics were assessed similar to that of solid part.

2.3 Boundary Conditions Setup

Setting up the boundary conditions for the FSI Coupled analysis required the participating simulation components to be solved independently first. For Transient Structural, the fixed supports were defined at the two ends of the pipe. No loads or forces were defined for the pipe, as the forces would come from the Fluent data transfer. For regions of the pipe that is in contact with the fluid, those regions would be defined with Fluid Solid Interface property. At these interfaces, Mechanical receives force data from, and sends the displacement data to, System Coupling. The Analysis Setting of the Transient Structural is defined for the time of the System Coupling analysis, in which the Step End Time is set to be 20 seconds. The Fluent settings were set according to the desired turbulence models, cell zone conditions and mass flow rate at the inlet. The inlet flow rate was specified to be 25 m^3/h and three $k-\varepsilon$ turbulence models as well as three orifice aspect ratios was studied: 0.255, 0.304 and 0.335

In System Coupling, the time period of the simulation was defined in End Time, which is 20 seconds. The Step Size was defined at 0.1 seconds, which means that each iteration would be equal to 0.1 second in the simulation. The coupling iterations were left at the default value of 5, which means 5 iterations would occur for each coupling step. The data transfers between Transient Structural and Fluent had to be specified as well, in which the data transfer was defined between the Fluid Solid Interfaces of the pipe and the pipe wall regions of the fluid. This two-way transfer of data would transfer force and displacement data within its participants. After the System Coupling has converged all the data transfers involved, the time-based data will be transformed into the frequency domain by using FFT function in CFD-Post.

3. Results

The velocity profile of the flows does not change much between the turbulence models. The smallest aspect ratio, 0.255 records the highest velocity at 18 m/s and as

the aspect ratio gets bigger at 0.335, the velocity decreases to about 10 m/s. This is expected as the cross-sectional area of the inner hole of the orifice becomes bigger, more space will be available for the flow to squeeze through the orifice, hence reducing the throttling effect on the flow. The distance required for the flow to return to fully turbulent flow becomes slightly longer with smaller orifices, as the distance for the flow to become fully turbulent for aspect ratio 0.255 is about 0.5 meters, while for 0.335 is about 0.3 meters. However for the same orifice aspect ratios with different $k-\varepsilon$ turbulence models, the distance is fairly similar between the models.

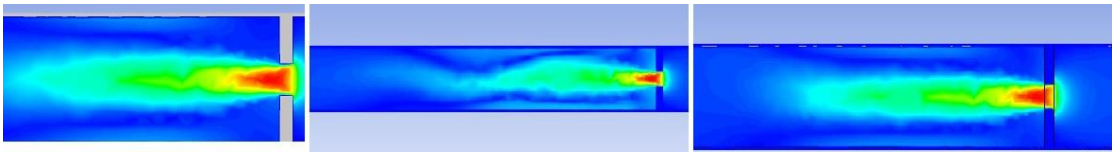


Figure 7. Velocity profile for β = 0.255. From left, Standard $k-\varepsilon$, RNG $k-\varepsilon$, and Realizable $k-\varepsilon$

According to Qing et al [4], they used vibration accelerometers and placed it at spots before and after the orifice flow region to measure the structural vibrations caused by the fluctuations in pressure of the flow. In order to obtain the frequency, the time history signal acquired throughout the period of the experiment was converted into Power Spectral Density (PSD), which is a measure of a signal's power intensity in the frequency domain, after FFT has been performed. The time-domain data that is used to convert to vibration frequency is the small displacement of the pipe wall. The results from the study by Qing et al indicated that the maximum level of pressure fluctuation was located at a distance of 1.7*D downstream from the orifice, in which D denotes the outer diameter of the orifice. In this study, the point of interest where the frequency is obtained will follow that same position as well, as shown in Figure (3).

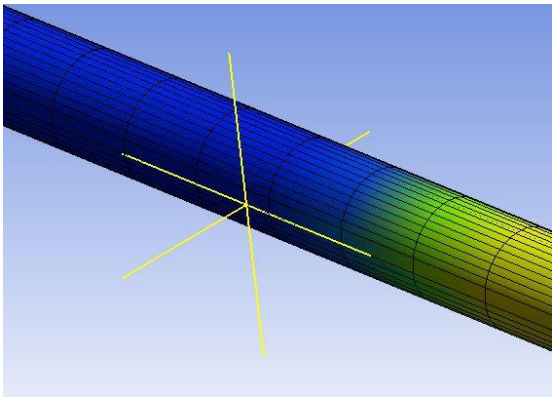


Figure 8. The location of the point of interest.

The natural frequencies of the pipe have to be obtained before simulation, so that the results can be gauged whether the frequency of FIV would reach natural frequencies or not. According to Qing et al, the frequencies in the first four peaks were 8, 24, 44 and 80 Hz respectively.

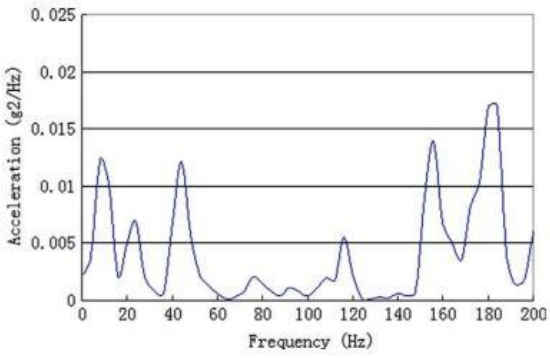


Figure 9. PSD Spectrum of the vibration accelerated response of the test section. [4]

3.1. Graphs of the Vibration

Below are the results of frequency from the simulation using Standard $k-\varepsilon$ model, RNG $k-\varepsilon$ model and Realizable $k-\varepsilon$ model from three different aspect ratios: 0.255, 0.304 and 0.335. The results from the simulation were converted using FFT to obtain results in the frequency domain.

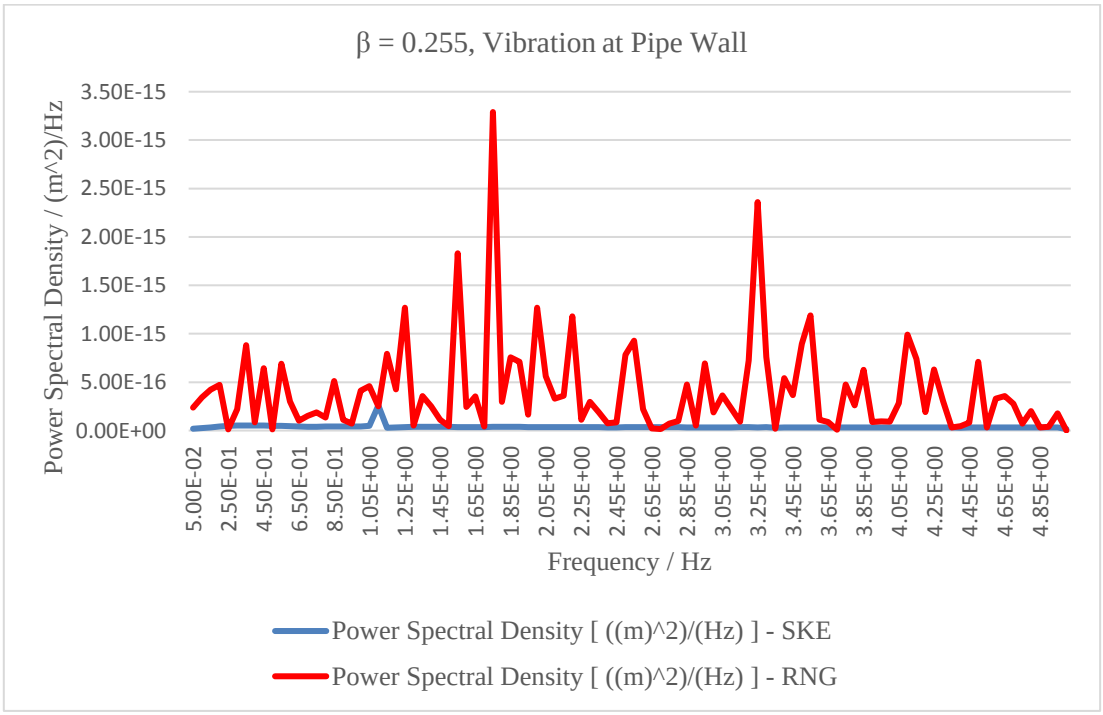


Figure 10. Frequency of FIV of the pipe wall for β = 0.255.

In this graph, the displacement in time-domain is converted to frequency domain using FFT. It can be seen that the graph of RNG turbulence model is fluctuating at a very inconsistent rate, peaking at around 1.7 Hz with the PSD value of 3.3 x 10^{-15} m^2/Hz, while the Standard model only showed very small frequency range relative to the RNG model, its highest PSD reading of 2 x 10^{-15} m^2/Hz is recorded at 1.05 Hz. The Standard model captured the flow-induced vibrations involved, however when compared to the RNG results it is very small.

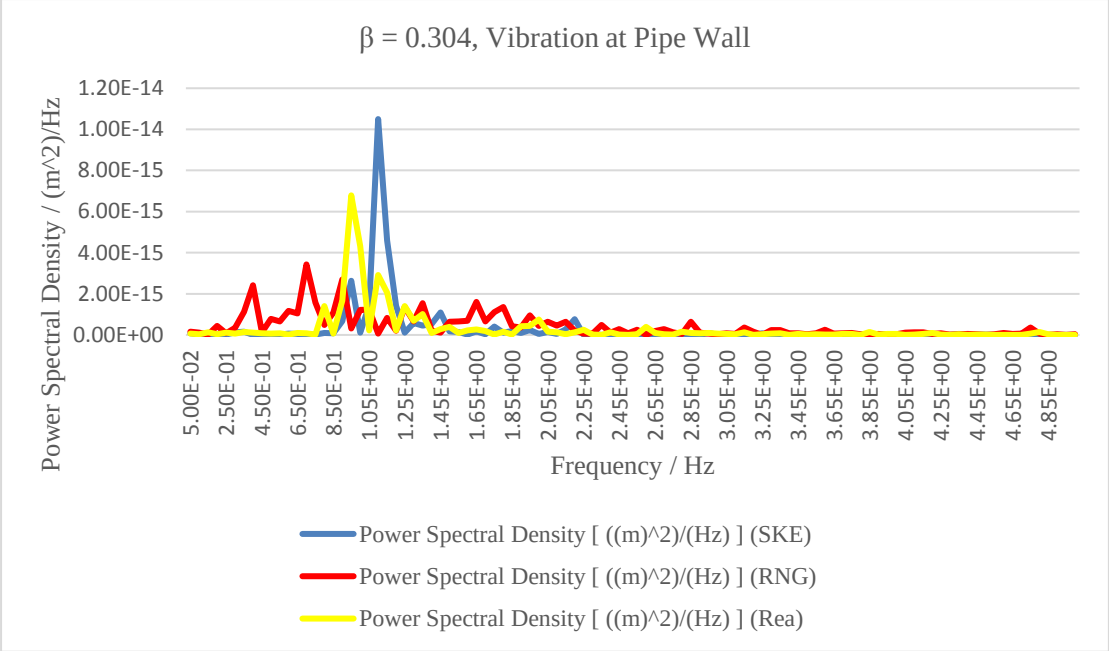


Figure 11. Frequency of FIV of the pipe wall for β = 0.304.

For aspect ratio of 0.304, the readings show a more consistent reading throughout the duration of the simulation. All three graphs for Standard, RNG and Realizable give peak frequencies around the same range, with Standard at 1.1 Hz, RNG at 0.65 Hz and Realizable's peak value at the middle between the two, at 0.9 Hz. However only Standard model gives the highest PSD value, which is at around 1 x 10^{-14} m^2/Hz.

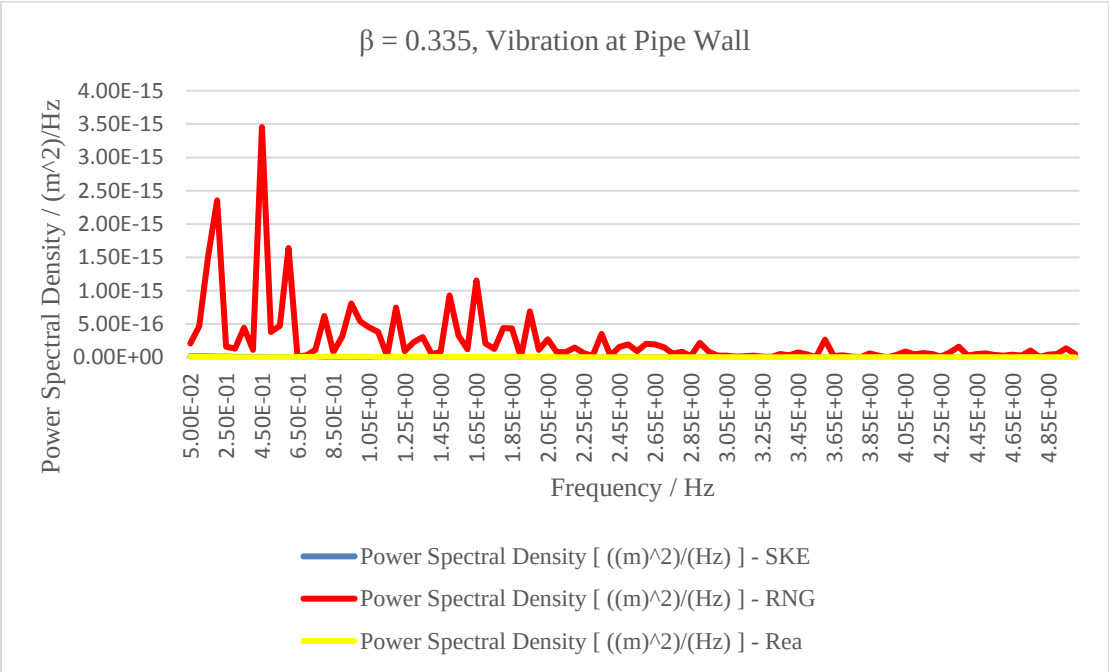


Figure 12. Frequency of FIV of the pipe wall for β = 0.335.

For aspect ratio of 0.335, the Realizable and Standard models give very low PSD values throughout the experiment. On the other hand, the RNG captures the vibration at a fluctuating level, peaking at PSD value of 3.50 x 10^{-15} m^2/Hz. However,

the frequencies are only ranging about 0 – 2.05 Hz. Besides the different $k-\varepsilon$ turbulence models, a graph is also drafted to see the effects of different aspect ratios of the flow with the same turbulence model. In this case, the results from different aspect ratios of the orifice is compared within the RNG $k-\varepsilon$ model.

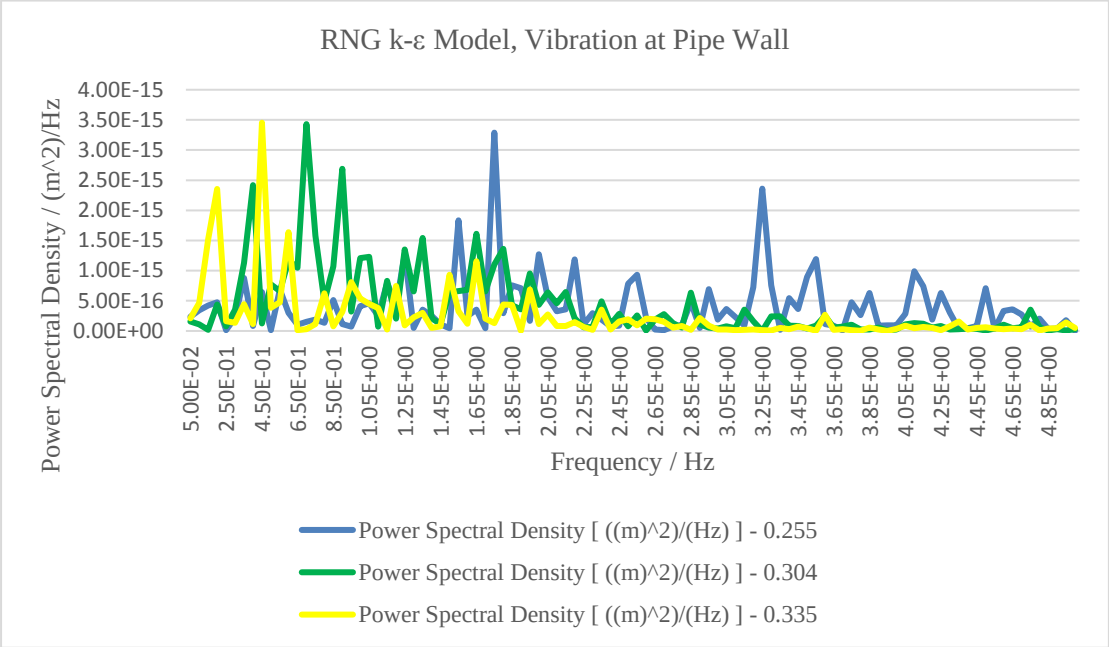


Figure 13. Frequency of FIV of the pipe wall for all aspect ratios, taken from previous RNG graphs.

For the study of frequency comparison between orifices with different geometries, RNG turbulence models is used since all three RNG results from previous three graphs provide usable graphs. It can be seen that for orifices with smaller aspect ratios, which also means smaller inner diameters, the range of peak frequencies becomes higher. For the smallest aspect ratio at 0.255, the peak frequencies range from 1.65 Hz to 3.25 Hz. At aspect ratio 0.304, the peak frequencies are at lower values, ranging from 0.25 Hz to 1.65 Hz. For the largest aspect ratio of 0.335, the peak frequencies are lowest among the three, which is at 0.05 Hz to 0.85 Hz. The increase in peak frequencies for smaller aspect ratios is because the pressure gets higher from the smaller cross-sectional area available for flow.

3.2 Comparison with Previous Study

The results of this simulation and the paper by Qing et al could not be compared exactly because of various difference in parameters. First of all, the material that was used by Qing et al was 1Cr21Ni15Ti stainless steel and the material properties for that material is not available on online resources. The closest material that could be used by the student in the simulation is stainless steel that is available in ANSYS material library.

Secondly, the simulation was done only until 20 seconds and can only achieve until frequency values of 5 Hz. The referred study managed to get readings for four modes of the pipe wall's frequency which are up to 80.0 Hz. For the simulation to generate readings of more than 5 Hz and up to 100 Hz, more computational space is

required in the hard drive and Random Access Memory (RAM) of the computer. However, from the simulation results and the referenced paper, it can be said that the flow-induced vibration from the flow rates that are set into the inlet from the experimental boundary condition is very low [4]. Hence the flow-induced will not reach the natural frequency of the pipe and destroy it due to resonance.

4. Conclusions

The results above are the first attempts at analyzing the FIV through an orifice plate by using $k - \varepsilon$ models in FSI analysis. It appeared that the PSD graphs from the simulations are significantly different compared to the PSD graph from the referenced paper. Early conclusions can be said that the $k - \varepsilon$ turbulence models are not suitable for simulating FIV for water flowing through an orifice, however due to the limitations of computational ability, that conclusion is still objectionable. Future work can be done to improve the results by using more capable computer that can meet the demands of FSI simulations.

References

[1] T. Sridevi, D. Sekhar, and V. Subrahmanyam, "COMPARISION OF FLOW ANALYSIS THROUGH A DIFFERENT GEOMETRY OF FLOWMETERS USING FLUENT SOFTWARE," pp. 141–149, 2014.

[2] T. He, "A CBS-based partitioned semi-implicit coupling algorithm for fluid–structure interaction using MCIBC method," *Comput. Methods Appl. Mech. Eng.*, vol. 298, pp. 252–278, 2016.

[3] T. He and K. Zhang, "Combined interface boundary condition method for fluid–structure interaction: Some improvements and extensions," *Ocean Eng.*, vol. 109, pp. 243–255, 2015.

[4] M. Qing, Z. Jinghui, L. Yushan, W. Haijun, and D. Quan, "Experimental studies of orifice-induced wall pressure fluctuations and pipe vibration," *Int. J. Press. Vessel. Pip.*, vol. 83, no. 7, pp. 505–511, 2006.

[5] M. Siba, W. Wanmahmood, M. Z. Nuawi, R. Rasani, and M. Nassir, "FLOW-INDUCED VIBRATION IN PIPES : CHALLENGESS AND SOLUTIONS - A REVIEW," vol. 11, no. 3, pp. 362–382, 2016.

[6] B. Dobrowolski, K. Krecisz, and A. Spyra, "Usability of Selected Turbulence Models for Simulation Flow Through a Pipe Orifice," *Task Q.*, vol. 9, no. 4, pp. 439–448, 2005.

[7] M. S. Shah, J. B. Joshi, A. S. Kalsi, C. S. R. Prasad, and D. S. Shukla, "Analysis of flow through an orifice meter: CFD simulation," *Chem. Eng. Sci.*, vol. 71, pp. 300–309, 2012.

[8] D. C. E. Migoya and A. Crespo, "Comparison of turbulence models for the computaional fluid dynamics simulation of wind turbine wakes in the atmospheric boundary layer."

[9] A. Erdal and H. . Andersson, "Numerical aspects of flow computation through orifices," *Flow Meas. Instrum.*, vol. 8, no. 1, pp. 27–37, 1997.

[10] M. A. Siba, W. Mohd, F. Wan, M. Z. Nuawi, R. Rasani, and H. Mohamed, "Wall Pressure Due to Turbulent Flow Through Orifice Plate," vol. 5167, no. 02, pp. 36–41, 2015.

[11] D. C. Wilcox, *Turbulence Modeling for CFD (Second Edition)*. 1998.

[12] S. B. Pope, *Turbulent Flows*, vol. 1. 2000.
[13] B. E. (Brian E. Launder, "Lectures in mathematical models of turbulence [by] B. E. Launder and D. B. Spalding," p. 1972, 1972.
[14] V. Yakhot and S. a. Orszag, "Renormalization-group analysis of turbulence," *Phys. Rev. Lett.*, vol. 57, no. 14, pp. 1722–1724, 1986.
[15] T.-H. Shih, W. W. Liou, A. Shabbir, Z. Yang, and J. Zhu, "A new k-ϵ eddy viscosity model for high reynolds number turbulent flows," *Comput. Fluids*, vol. 24, no. 3, pp. 227–238, 1995.

Nomenclatures

β	*Aspect ratio*
C_D	Discharge coefficient
k	Kinetic energy
ε	Turbulent dissipation energy due to the viscosity

Abbreviations

CFD	Computational Fluid Dynamics
FFT	Fast Fourier Transform
FYP	Final Year Project
FEA	Finite Element Analysis
FVM	Finite Volume Method
FIV	Flow – Induced Vibration
FSI	Fluid-structure Interaction
PSD	Power Spectral Density
RAM	Random Access Memory
RANS	Reynolds-averaged Navier-Stokes
RNG	Renormalization Group Theory
RSM	Reynolds Stress Model

Design and Analysis of an Adjustable Track Using Finite Element Method

Bhakti Venugopal[1], Jeffrey Chin Kong Leong[1]

[1]*School of Engineering, Taylor's University, Malaysia*

*bhaktivenugopal@gmail.com

Abstract
A tracked vehicle can be described as a self-propelled vehicle that moves on two continuous tracks supported by sprockets, idlers and rollers and is an alternative option to a tire with its applications varied across a myriad of different fields because of its ability to traverse harsh and rough terrain easier and more effectively than a regular tire. Soil conditions are affected by the amount of water and temperature in them at any given time. Passage of heavy vehicles with the wrong track size or orientation will compact the softer soil. Soil compaction reduces the ability of crops to grow therefore it is important to find an adjustable track that is able to change its orientation to travel across different soil conditions. This research analyses the best orientation of sprockets, idlers and rollers for different soil conditions and how it can be applied to adapt to softer soil. This is done by examining the factors of an adjustable track that affects soil pressure distribution. An increase in the number of rollers decreases the average pressure distribution on the soil. The balance of track tension must be observed as either too high or too low a value affect drawbar pull and sinkage effectively. A longer track length will help distribute the pressure more evenly. Taking these factors into consideration, the design of the adjustable track is able to change and modify its length, number rollers and track tension to suit different conditions. The frame design is then analysed for stress and total deformation by using the ANSYS software. With the data from the stress analysis, the design will be modified and improved with respect to the data analysis. The design improvements cease once the design reaches maximum efficiency with respect with performance and material. The final outcome is a design of an adjustable track that is able to change its orientation at a push of a button to accommodate softer soil conditions to lower soil compaction and its adverse effects.

Keywords: Adjustable Continuous Track , Finite Element Method, Soil Compaction

1. Introduction

1.1 Background

A tracked vehicle can be described as a self-propelled vehicle that moves on two continuous tracks supported by sprockets, idlers and rollers as can be seen in Figure 1.1. A continuous track is an alternative option to a tire and its applications are varied across a myriad of different fields. The continuous track is more compatible for use over rough and off terrain roads compared to its regular tire counterpart. The history of continuous tracks can be traced as far back as the 1700s, however it usage and popularity grew after during the turn of the century in the 1900s.

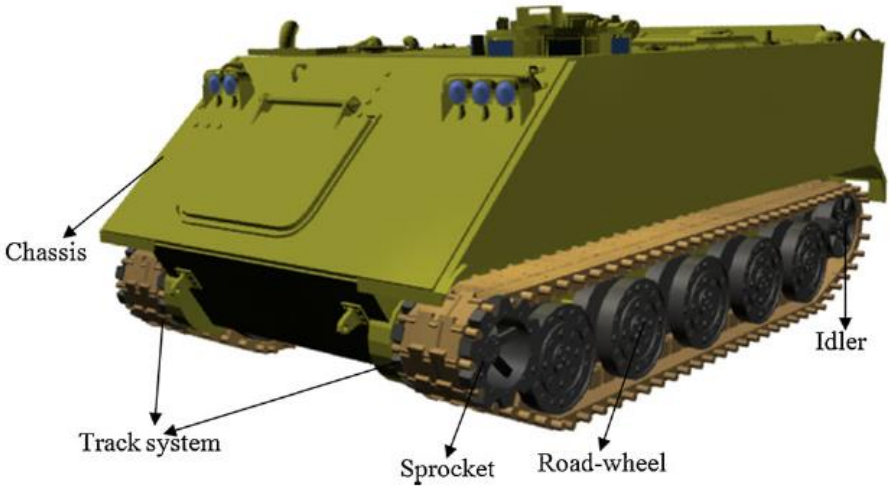


Figure 1.1: The SAMS/2000 tracked vehicle model [1].

The continuous track can be simplified into its core components of a sprocket, chain links, rollers and an idler which can be seen in Figure 1.1. The power transmission is achieved through the relationship between the sprocket and the chain links as can be seen in Figure 1.2. Each tooth of the sprocket applies a percentage of the transmitted load onto the chain link to produce torque which in turn will power the vehicle [2]. The rollers or road wheels are in place to ensure an even and constant contact between the track and the terrain [3]. This is essential so that the rollers provide an even distribution of contact force between the track and terrain instead of just a concentrated force at the sprocket and idler.

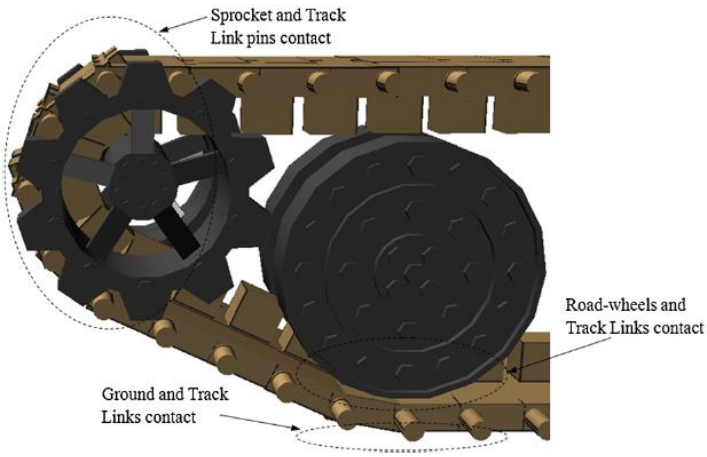


Figure 1.2: Tracked vehicle contact model [1].

There are many reasons why a continuous track is the preferred method of traction compared to the regular tire. The continuous track provides a better distribution of weight and pressure on the ground. Arvidsson in his study in 2011 came to the conclusion that while there was significant pressure from the rollers and the pressure exerted on the ground was not evenly distributed along the track, the depth and the penetration resistance exerted by the continuous track was much lower than that exerted by the wheel [4]. This is beneficial in the agricultural industry where low soil compaction have a significant impact on the ability for the crops to grow.

1.1 Soil Compaction

A study done on soil disturbance and post logging forest recovery on the bulldozer paths in Malaysia exhibited the dramatic differences between the ability for plants to grow across the path over compacted soil and non-compacted soil. The study examined and tracked the growth of plant life growing on the abandoned logging paths noticing that over the middle of the path where the soil was most compacted growth of plant life was slow while the looser and less compact soils on the side of the paths grew at a much quicker rate [5].

Different soil conditions are not simply limited to different soil types in different areas of the world but it varies with the amount of water in it any given time. Therefore, this problem is not mutually exclusive to vehicles that are to be used in different fields

for different crops but also for vehicles that only service one field and a certain type of crop. This is evident in Figure 1.3 which illustrates the different levels of precipitation experienced by a maize farm in China over three years.

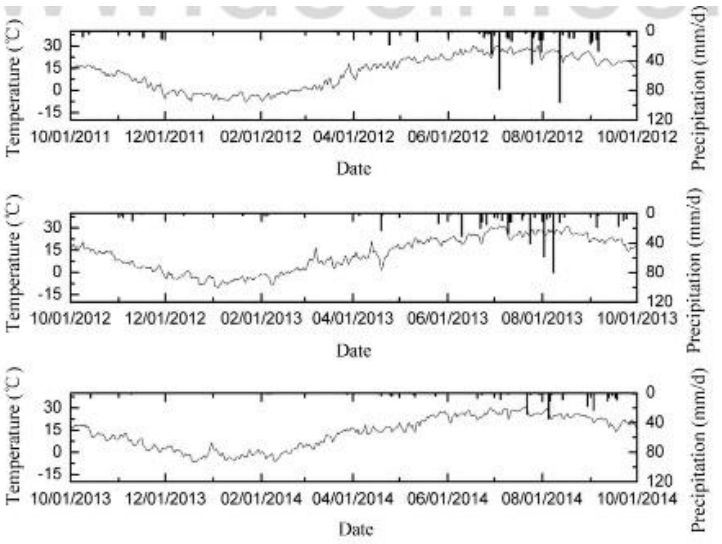


Figure 1.3: Temperature and Precipitation values across the year in maize farm in China [6].

Soil compaction has been recognised as a serious issue in mechanised agriculture as the passing of heavy vehicles over soft soil compacts the soil and reduces its porosity of the soil. In order to facilitate healthy growth of crops the soil must be able to absorb water allow to allow the transportation of nutrient to the roots [6]. Moreover if the soil is too compact, it will not inhibit the flow of water and nutrients but also the growth of roots as it has no space to grow.

Soil bulk density is one of the most comprehensive approach to measure soil compaction as it takes the weight of dry soil (M_{solids}) divided by the total soil volume (V_{soil}) [7]. The total soil volume consist of the combined volume of soil, air and water as can be seen in Figure 1.4.

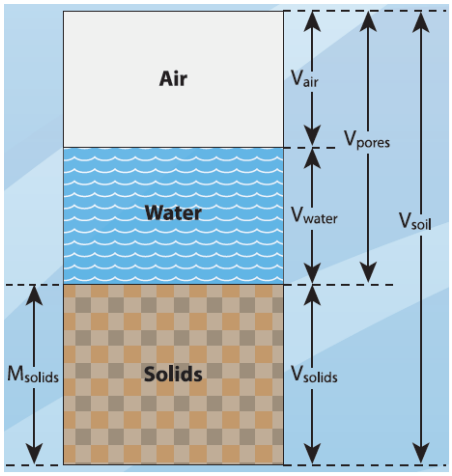


Figure 1.4: Structural composition of the soil fraction of solid, water and air [7].

1.3 Design Configurations

The objective of the project is conceive and design an adjustable continuous track that is able to change orientation of the track to suit a specific soil condition. In order to achieve this a study must be done to examine the key parameters of a tracked vehicle which include number of roller, orientation of the rollers and track tension and how each factor contributes towards soil compaction.

1.4 Number of road wheels

The first parameter to be examined is the effect of number of road wheels and the corresponding vertical stress or pressure experienced by the ground. A similar study experimented the amount of vertical stresses experienced by a construction continuous track and found that increasing the number of wheels also decreased the maximum and average pressure experienced by the ground. This phenomenon is expressed in figure 1.5

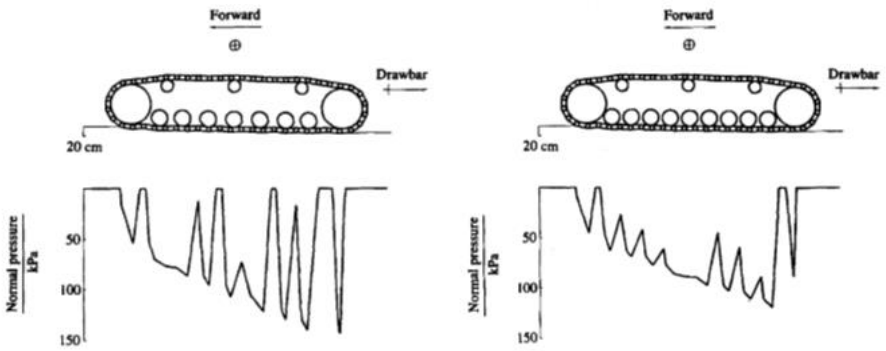


Figure 1.5: The normal pressure experienced by the ground exerted by 7 versus 9 road wheels [8].

1.4 Initial Track tension

Initial track tension determines how much the track deflects in between each of the road wheels therefore the correlation between the initial track tension and the pressure exerted on the soil must be determined. Figure 1.6 displays the graphical data obtained by experimenting with 4 different track tensions and its corresponding ground pressure. From the results the relationship that can be gleaned indicates that increasing the initial track tension will result in a lower ground pressure.

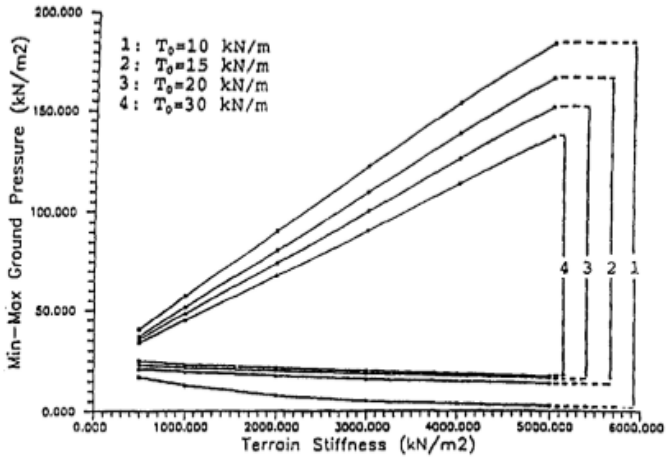


Figure 1.6: Effect of initial track tension against the min-max ground pressure [9].

1.6 Orientation of the road wheels

The orientation of the road wheels has a significant effect on the pressure distribution under the track system and the amount of sinkage that occurs. Figure 1.7 illustrates the predicted normal distribution under a track system with five rollers versus eight overlapping rollers.

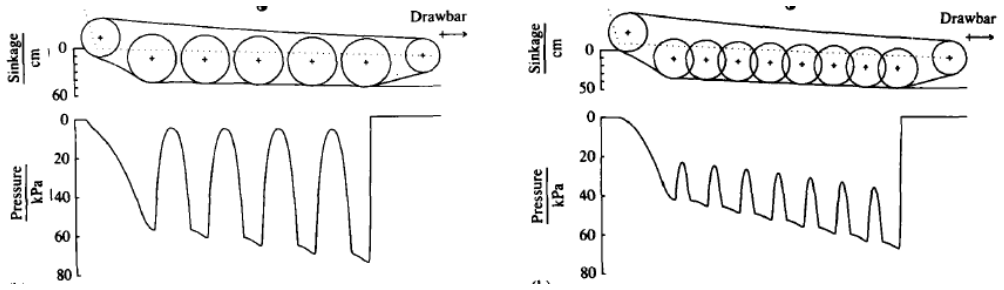


Figure 1.7: The predicted normal distribution under a track system with five rollers versus eight overlapping rollers [10].

1.6 Radius of road-wheel

The radius of the road wheels and the effect it has on the maximum pressure exerted is also analysed to help reduce the soil compaction experienced by the soil. A study conducted by J.Y. Wong in 2007 analysed the effect of size of radius on soft soil conditions. The conclusion drawn from the study indicates that a larger radius of roller is able to distribute the pressure more evenly and prevent high soil compaction [21]. In a separate study with three different radius of the road wheel at 0.28m, 0.33m and 0.38 the ground pressure is measured and tabulated on a graph as seen in figure 1.8. The conclusion drawn from the study indicates that a larger radius of roller is able

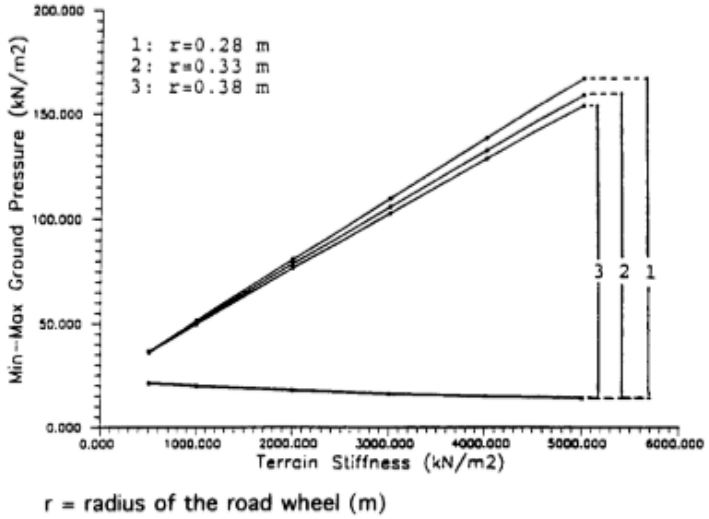


Figure 1.8: Effect of radius of the road wheel against the min-max ground pressure [9].

2. Research methodology

The research methodology follows the CDIO (Conceive Design Implement and Operate) framework as shown in Figure 2.1. In this project the implementation and operation aspect of the CDIO concept will not be considered due to time and budgetary constraints.

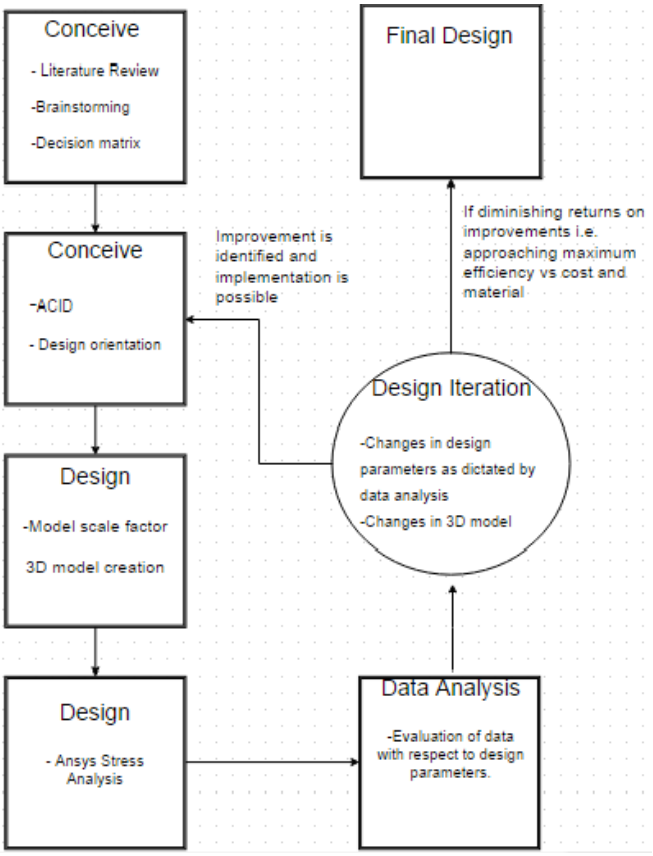


Figure 2.1: Research flowchart

The first step in designing a project is to first understand the problem that requires attention and attempt to design a solution to overcome it. From the research done in the literature review, it was clear that the continuous track used in the agricultural sector is not able to adapt itself to different soil conditions.

The tractor chosen to base the dimensions and design of the adjustable continuous track is the Challenger series MT835 as seen in figure 2.1. The major feature of the new adjustable track is the ability to change the length of the track to accommodate the extra road wheel. To do so one end of the track must be able to extend forward to increase its length. While most conventional tractor design has two axles for the driver and the idler as seen in figure 2.2 the MT 835 has a single driving axle with a drawbar axle to provide support on the other end. The drawbar axle provides support on both ends of the track frame without limiting the extension of the idler and the track.



Figure 2.2: Challenger MT835 [11].

Solidworks was used to model the individual parts and assemble to form a complete adjustable track as seen in figure 2.3. The full assembly consist of two idlers, ten road wheels, two drivers and the frame of the track. The frame of the track supports the weight of the vehicle through the driver axle and the drawbar support axle. The weight of the vehicle is then distributed through the idlers, road wheels and drivers to exert pressure on the ground

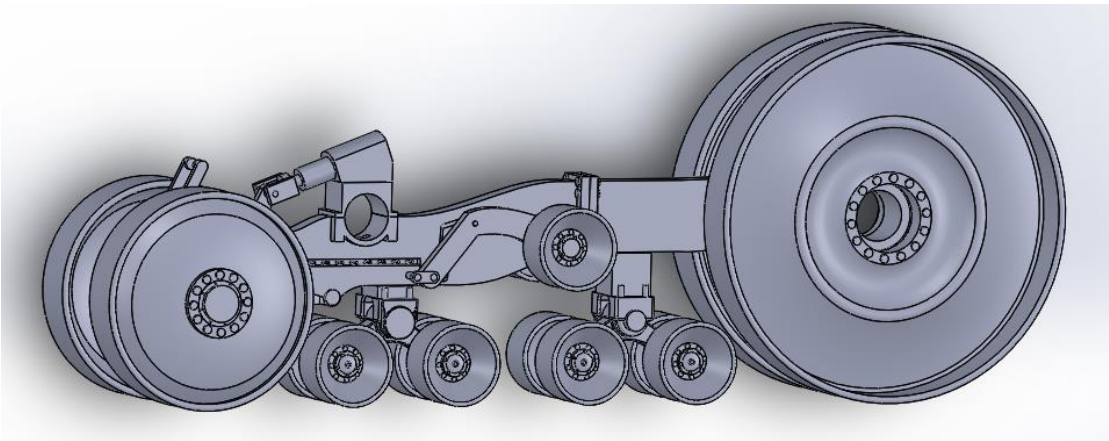


Figure 2.3: Full assembly of an adjustable continuous track.

The frame of the track is also the major component for the extension mechanism, track tension bar as well as the hydraulic cylinder. The extended and un-extended frame of the track is as seen in figure 2.4 and figure 2.5 respectively.

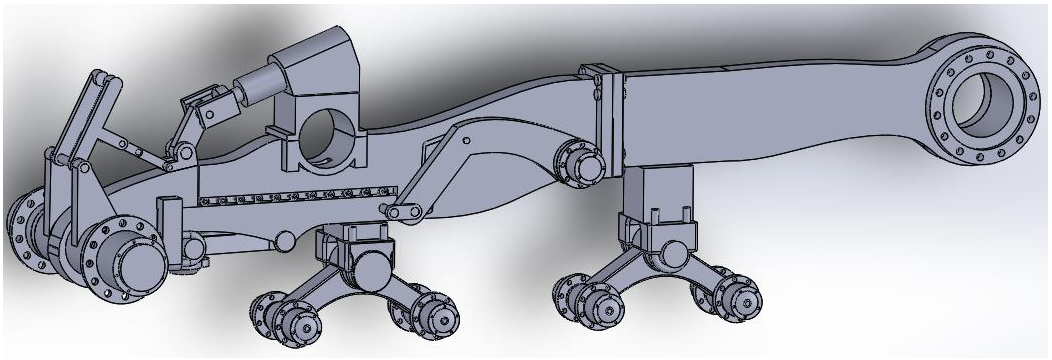


Figure 2.4: The un-extended frame of the adjustable continuous track.

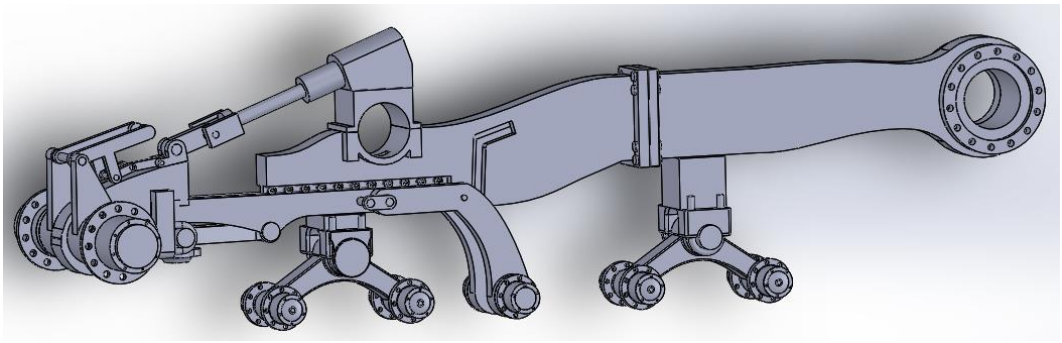


Figure 2.5: The extended frame of the adjustable continuous track.

Other than supporting the weight of the vehicle, the frame of the adjustable track is responsible for the extension mechanism, hydraulic cylinder, the drop down wheel and the track tension bar as seen in figure 2.6.

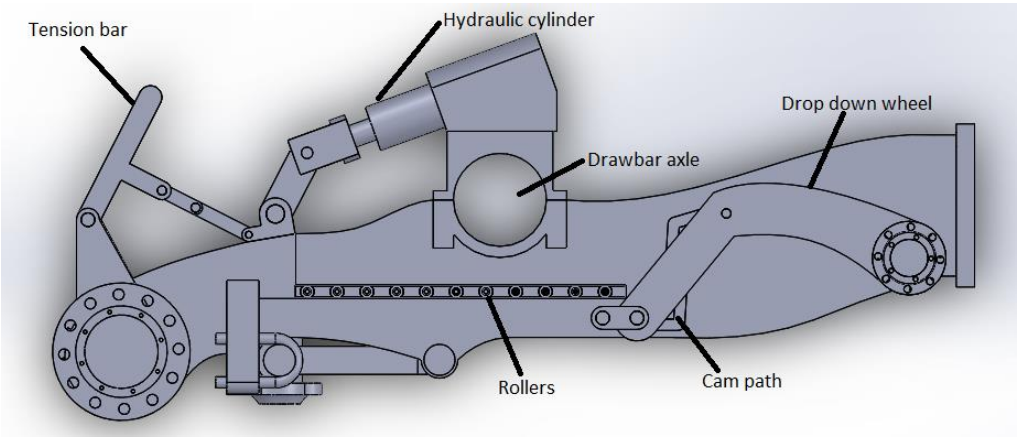


Figure 2.6: Diagram of the mechanisms of the adjustable frame

The extension mechanism consists of a fixed track supported by the drawbar axle and the extendable portion of the track which rolls forward on the support of rollers. The two separate pieces of the track are kept aligned by a fitted grove that runs

the entire length of the extendable track. The rollers are also kept in place by its own set of curved grooves and pin screws to ensure the rollers are not displaced. The force generated to push the extendable track horizontally is provided by the hydraulic cylinder which is capable of exerting pressure of up to 300bar. The base of the hydraulic cylinder is attached to the drawbar axle which provides strong support to exert the pressure required. The hydraulic cylinder is placed at an angle 25 degrees below the horizontal to run parallel to the belt track above it. Due to the difference in the angles of the linear motion of the hydraulic cylinder and the extendable frame a connector is added to facilitate the horizontal motion.

The hydraulic cylinder not only pushes the extendable track horizontally but it also provides the force necessary to bring down the drop down wheel and to lower the tension bar. The purpose of the tension bar is to provide track belt tension when the adjustable track is un-extended. The track belt fitted to the system is of an appropriate length for the track when it is fully extended, however when the adjustable track is un-extended the belt will be slack and may slip off the frame. To ensure this doesn't happen the tension bar pushes the belt upwards to compensate for the slack of the belt. As the track extends the tension bar folds inwards to a point where it lies beneath the idler as seen in figure 2.6.

The drop down wheels are also powered by the motion of the extendable track to which it is connected to via a pin joint. As the extendable portion of the track moves forward horizontally the drop down wheel and its support is pulled along a cam path which ultimately bring its level with the other road wheels. The cam path is shaped like the letter "z" as seen in figure 2.6 because the initial horizontal motion at the top moves the drop down wheel out of the collision path of the road wheel directly below it. The slanted vertical drop provides a quick descent while the final horizontal path is to lock the drop down wheel into place and ensure a strong vertical support.

3. Results and Discussion

The earlier stages were essential to prepare the research and design for this process. The geometry model is analysed for stress and total deformation whereupon the data gathered is then evaluated with respect to the design parameters and further

improved on. The idler is the first part of the adjustable track to be analysed for stress and total deformation experienced under working conditions. The stress experienced along the body of the idler is minimal with the maximum occurring at the axle as seen in figure 3.1. This maximum occurs at a point that was predicted while designing the geometry therefore in the final design the idler axle is supported by the frame that will help alleviate the amount of the stress experienced.

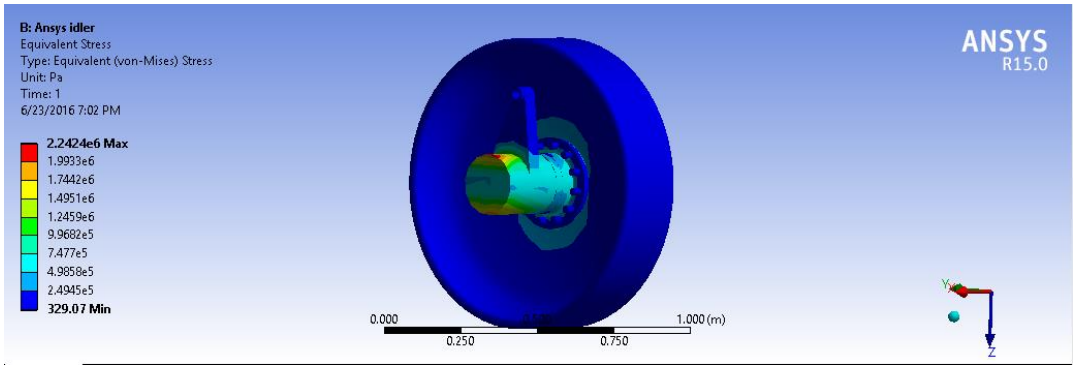


Figure 3.1: The equivalents (von-Mises) stress analysis of the idler.

The driver of the adjustable track showed significant amounts of stress in area where the two arches meet. The design was remodelled to increase the thickness as well as adjusting the curve of the arch to better fit the driver. These adjustments brought down the maximum stress experienced to 2.9333x e^5 Pa as seen in figure 3.2.

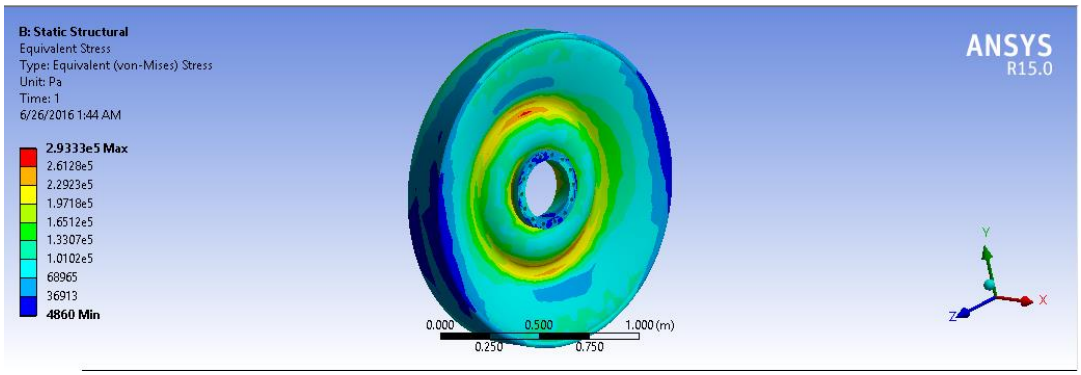


Figure 3.2: The equivalents (von-Mises) stress analysis of the driver.

While the maximum value of stress may seem large, the total deformation test indicated that the least amount of deformation occurs at this area. This would suggest that while the stress experienced at these point was high, the deformation and ultimately the potential failure at this point is low. The maximum deformation occurs at the bottom

of the driver as seen in figure 3.3. The maximum deformation occurring at the contact point with ground is expected as is with the idler. Even so the maximum deformation value is a mere 2.5154 x e^{-6} m showing no danger of massive deformation.

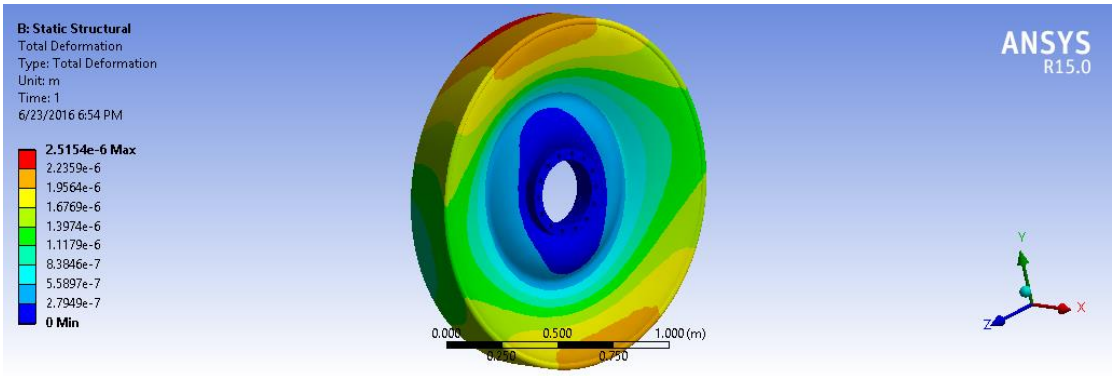


Figure 3.3: The total deformation analysis of the driver.

The road wheels are similarly tested with the highest stress occurring at the contact point between the axle and road wheel as seen in figure 3.4. More accurately the maximum stress occurs in the space surrounding the M24 bolts holes. This distribution of stress is unlike the results of the previous test run on the idler and driver. In order to reduce the maximum stress experienced the space around the holes is widened while the number of holes is decreased. Eventually the maximum stress experienced is lowered to a final value of 1.6218 x e^{6} Pa.

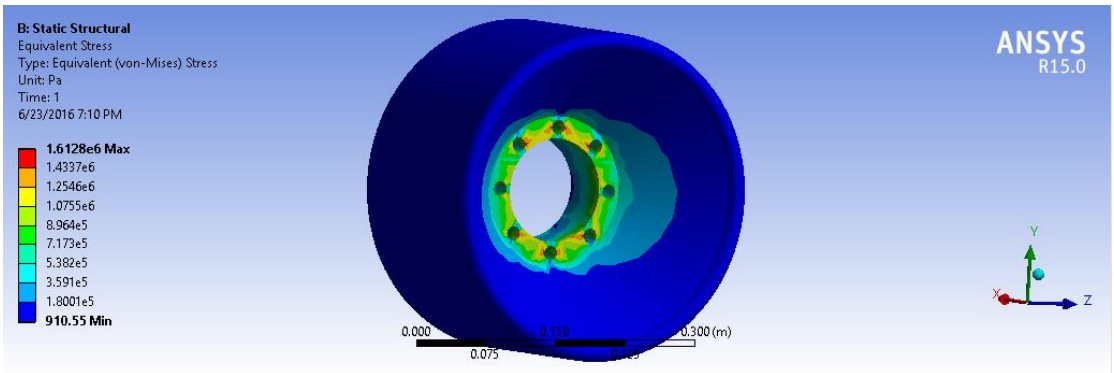


Figure 3.4: The equivalents (von-Mises) stress analysis of the road wheel (front side).

When it comes to analysing the frame of the track the maximum pressure exerted is at the point below the drawbar axle. This was expected as part of the weight of the vehicle rest at this spot. While the value of stress experienced was large as seen

in figure 3.5, the total deformation occurs at the drawbar axle where the weight of the vehicle is applied as seen in figure 3.6

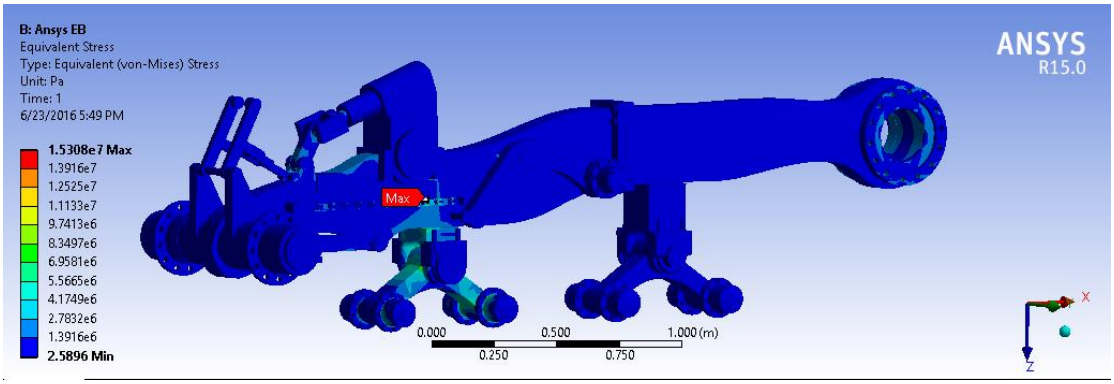


Figure 3.5: The equivalents stress analysis of the un-extended adjustable track.

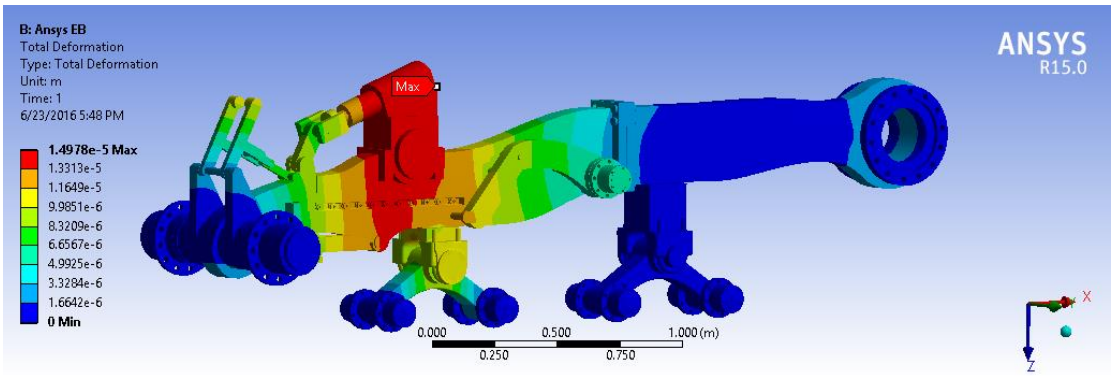


Figure 3.6: The total deformation analysis of the un-extended adjustable track.

In the case of the fully extended adjustable track, the maximum stress once again occurs at the point below the drawbar axle, however since the extendable track has moved forward the maximum stress occurs at the arm mechanism of the drop down wheel as seen in figure 3.7. The maximum stress that occurs here is 3 times larger than that of the un-extended version. The analysis of the total deformation experienced in figure 3.8 however shows that the deformation that occurs at this point is minimal.

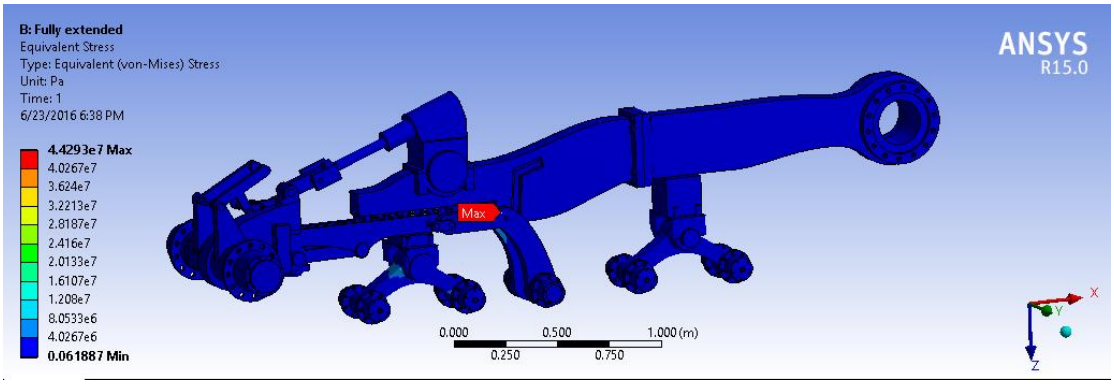


Figure 3.7: The equivalents stress analysis of the fully extended adjustable track.

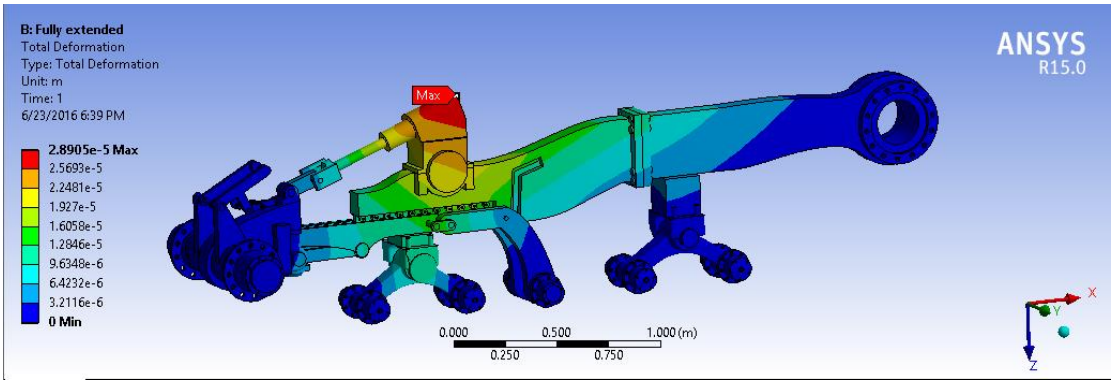


Figure 3.8: The total deformation analysis of the fully extended adjustable track

4. Conclusions

From the analysis made, the design of the adjustable track is able to change its orientation to suit softer soil conditions. The addition of the extra wheel as well as the lengthening of the continuous track has been proven to reduce the amount of soil compaction experienced. The design has been simulated under normal working conditions to test the stress and total deformation experienced. The improvement made as well as the final results indicate that the design is structurally sound.

References

[1]. Wallin, Michael et al. 'A Comparative Study Of Joint Formulations: Application To Multibody System Tracked Vehicles'. *Nonlinear Dynamics* 74.3 (2013): 783-800. Web.

[2]. Marshek, Kurt M. 'On The Analyses Of Sprocket Load Distribution'. *Mechanism and Machine Theory* 14.2 (1979): 135-139. Web.

[3]. Nakanishi, Toshikazu, and A. A. Shabana. 'Contact Forces In The Non-Linear Dynamic Analysis Of Tracked Vehicles'. *International Journal for Numerical Methods in Engineering* 37.8 (1994): 1251-1275. Web.

[4]. Arvidsson, J. et al. 'Rubber Track Systems For Conventional Tractors – Effects On Soil Compaction And Traction'. *Soil and Tillage Research* 117 (2011): 103-109. Web.

[5]. Pinard, M.A, M.G Barker, and J Tay. 'Soil Disturbance And Post-Logging Forest Recovery On Bulldozer Paths In Sabah, Malaysia'. *Forest Ecology and Management* 130.1-3 (2000): 213-225. Web.

[6]. Liu, Xiuwei et al. 'Effects Of Different Irrigation Regimes On Soil Compaction In A Winter Wheat–Summer Maize Cropping System In The North China Plain'. *CATENA* 137 (2016): 70-76. Web.

[7]. Soilquality.org.au,. 'Bulk Density - Measurement | Fact Sheets | Soilquality.Org.Au'. N.p., 2015. Web. 19 Nov. 2015.

[8]. J Y Wong. (1994). Applications of a computer aided method to parametric study of tracked vehicles with rigid links. *Mechanical and Aerospace Engineering*. 23 (3), 251-264.

[9]. J.K.Gigler. (1994). A simulation model for the prediction of the ground pressure distribution under tracked vehicles.. *Journal of terramechanics*. 30 (6), 461-469.

[10]. Wong, J Y, and J Preston-Thomas. 'Parametric Analysis Of Tracked Vehicle Performance Using An Advanced Computer Simulation Model'. *ARCHIVE: Proceedings of the Institution of Mechanical Engineers, Part D: Transport Engineering 1984-1988 (vols 198-202)* 200.24 (1986): 101-114. Web.

[11]. Park, W.Y. et al. 'Prediction Of The Tractive Performance Of A Flexible Tracked Vehicle'. *Journal of Terramechanics* 45.1-2 (2008): 13-23. Web.

eureca 2016 – Conference Paper
Paper Number 2ME6

Simulation of the Mullins Effect in Rubbers for Vibration Isolator

George Kenji Putra[1*], S.Y. Ch'ng.[1]

[1]*Taylor's University*

[*]georgekenjiputra@gmail.com

Abstract

Under cyclic loading, elastomers show complicated stress-strain behavior. This inelastic behavior can be categorized as Mullins Effect, hysteresis, and permanent set. The current project focuses on Mullins effect of elastomers. It is important to consider Mullins Effect when it comes to components design that related to elastomeric materials. Simulation using Finite Element Analysis (FEA) software about Mullins Effect on elastomeric materials were conducted in order to deepen understanding about rubber behavior during monotonic and cyclic loading. By knowing the behavior of the elastomeric material, lifetime certain item that made out of this material can be certainly predicted. Initially, the experiments about rubber behavior under monotonic and cyclic loading were conducted in order to get the appropriate data. Dumbbell specimens following ASTM standard D412-C (2mm thickness) are used for the experiments. Certain data treatment had to be done in order to simplify the data without changing the details. Simulation performed under monotonic and cyclic loading, in this case vibration will act as the cyclic loading. Harmonious result between experimental and simulation results are expected to be seen.

Keywords: Elastomers, Mullins Effect, Carbon Black

1.0 Introduction

Rubber discovered at 15th century by South American. After completed scientific study on rubber, Charles de la Condamine published his finding in the year 1745. Therefore, rubber has been used comprehensively on Western world since it was introduced there initially. As the time passes by, the study of rubber is keep going on and experienced some development [1]. Synthetic rubbers such as Styrene-Butadiene, Butyl, Nitril, and Acrylic are developed to fulfil the industrial demands [2].

In these modern industrial days, elastomers play a significant role in human life. Sport and goods, automotive, and industrial sealing are the example of elastomeric materials application in real life. Because of its unique properties combination, elastomers are one of the most versatile engineering materials. The outstanding mechanical properties, good chemical bonding, thermal and electrical insulation allow elastomers to become an important part of industry.

Usage of synthetic rubbers are become more common now in industrial area. Fillers addition and vulcanization can be done in order to modify the elastomers. The purpose of doing modification is to improve the properties and chemical compatibility of elastomers. As the properties of elastomers improved, it could lead to increases productivity and decreases the maintenance cost.

Mechanical loading is the object of elastomeric components in real application. The mechanical behaviors of elastomers (large elastic deformation, non-linearity, and cyclic property changes) make the engineering design become more challenging [3]. Large elastic deformation of elastomers shows inelastic behavior under cyclic loading. Those are permanent set, hysteresis and Mullins Effect (stress-softening). In vibration isolator applications, Mullins Effect is a big disadvantage. Thus, the understanding, characterization, modeling and simulation of Mullins effect are prerequisite for durability analysis of vibration isolators.

2.0 Experimental Program

2.1 Materials

Dumbbell specimens following ASTM standard D412-C (2mm thickness) are used for the experiments. The material is NBR filled with 25% Carbon Black. The complete dimension of specimen is provided in **Figure 1**.

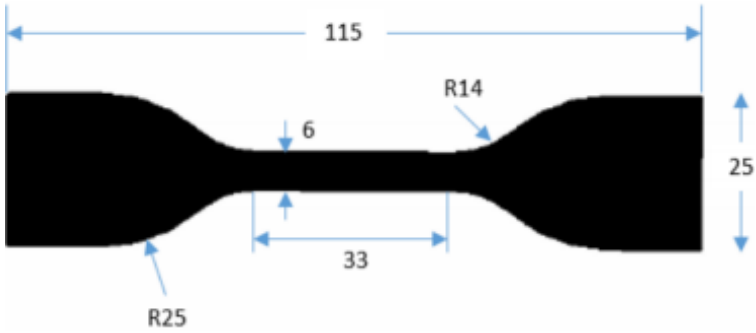


Figure 1: Dumbbell specimen referring ASTM standard D412-C

2.2 Mechanical Testing

The Dumbbell specimen clamped vertically in the tester machine (refer to **Figure 2**). Two different types of testing were carried out namely monotonic tensile

test until complete rupture and cyclic tensile test with 100% increment strain in each cycle. The purpose of the experiment is to investigate mechanical loading that rubber experienced.



Figure 2: Dumbbell specimen clamped on the testing machine

The procedure for the experiment will be as following below:

1. Clam the specimen vertically. Only one specimen is allowed at the time.
2. Set the strain rate as 0.5 per second at the computer.
3. Wait until the machine stops operating, and the data will be recorded by the computer.
4. This experiment will be conducted at least six times.

2.2.1 Monotonic Tensile Loading

Stress-strain is extremely non-linear under the absences of constant value of the elastic modulus, where the elastic modulus varies with increasing extension. Whilst the strain value is low, stress value requires to overcome secondary bonding. The high increment in the stress needed at higher strain is due to the primary covalent bonds along the molecular backbone [4].

In this section, the specimen will be stretched with strain rate of 0.5 per second until it ruptures. The purpose of this experiment is to determine the Neo-Hookean parameter (C_{10}) that will be used on the simulation.

2.2.2 Cyclic Loading with 100% Increment

Under cyclic loading, an elastomer exhibits strong inelastic responses such as hysteresis, stress-softening (Mullins effect) and permanent set. But the only concern of this project is Mullins effect or also known as softening effect of rubber. In this experiment, the specimen will be stretched by increment 100% of its total length, and

returned it to the initial position. The total cycles for this experiment are six cycles (600% of its length).

The aim of this experiment is to study and analyze Mullins effect that is happening on rubber material filled with 25% Carbon Black, as this material will be used for the Vibrator Isolator simulation.

2.3 Experimental Data Treatment

Mullins effect is the only purpose on this project. Because of that, the experimental results had to be treated so that we can determine the characteristics of it. In order to get this done, the data treatment proposed by Chagnon et al. [5] is adopted and summarized below:

1. Only unloading paths are considered and the reloading paths are assumed to coincide with them.
2. The unloading paths are horizontally shifted such that they start from zero strain (stretch=1).
3. The shifted unloading paths are extended to rejoin the monotonic primary curve.

The resulting treated experimental data are presented in **Figure 3** below and will be used to find the parameter in behalf of simulation.

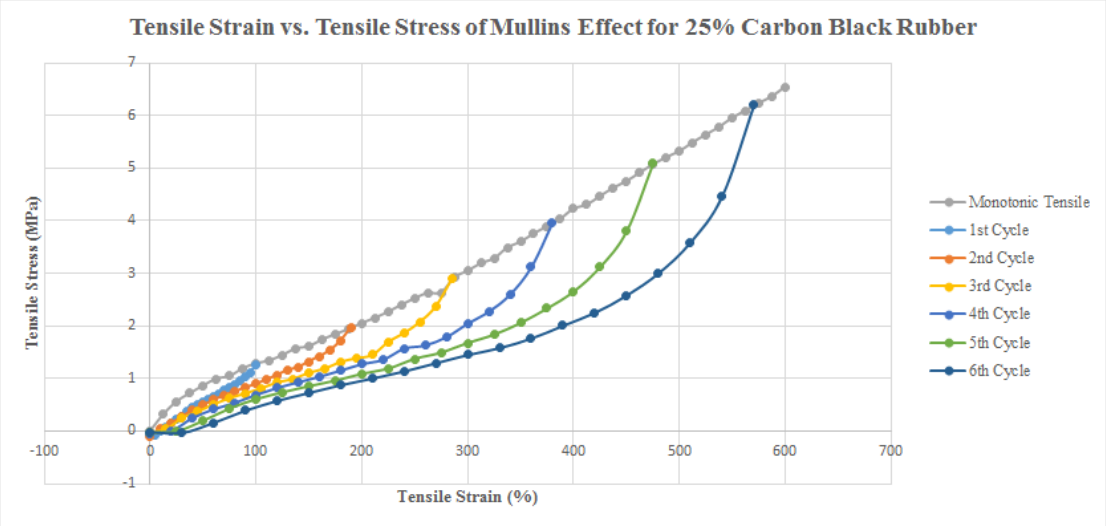


Figure 3: Treated experimental data for rubber filled with 25% Carbon Black

3.0 Material Parameters

In this topic, hypereleasticity fundamentals will be explained. There are several models for rubber out there, but Neo-Hookean model is chosen since Neo-Hookean model known for its simplicity compared to other models. Furthermore, the pseudo-elastic model of Ogden and Roxburgh [6] is considered for describing the Mullins effect.

3.1 Neo-Hookean Model

Out of numerous models available, Neo-Hookean had chosen to be the method that we are going to use due to its simplicity. Beforehand, there are some parameters that have to be determined, such as C_{10} and D_1 (Bulk Modulus).

For linear equation, $y = mx + c$, $2C_{10}$ corresponds to the gradient of the plot of P (Tensile Stress) as function of $(\lambda - \frac{1}{\lambda^2})$.

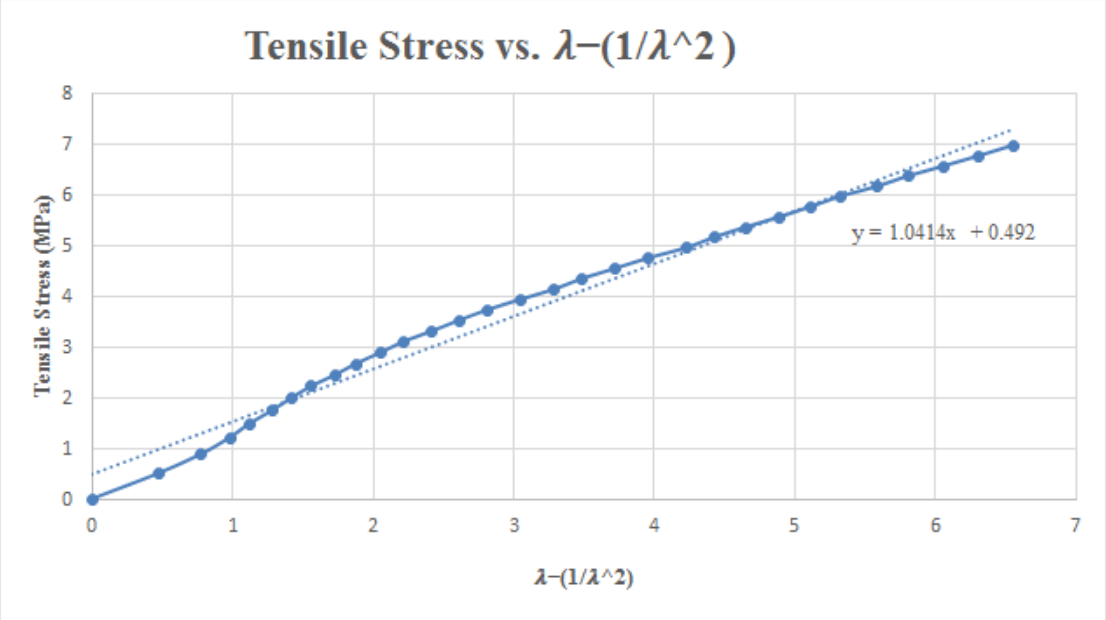


Figure 4: Tensile Stress vs. $\lambda-(1/\lambda^2)$

By referring to **Figure 4** above, we know that $y = 1.0414x + 0.492$. From that equation: $2C_{10} = 1.0414$. Hence $C_{10} = 0.5207\ MPa$.

For Bulk Modulus, that value has to be positive small number in order to maintain the material's volume while it deforms. Hence, we chose the value of D_1 as 1E-013.

3.2 Pseudo-Elastic Model for Mullins Effect

Damage depends on the maximum deformation ever experienced and the current deformation state. The higher the maximum deformation, the higher the damage. [7] The parameter $\frac{1}{r}$ is correspond to the maximum value of damage wherease $\frac{1}{m}$ is the measure of the initial slope of the damage curve [7]. According to this theory, damage, d evolved only in the unloading path and the damage is 0 during the loading path. Damage is a scalar parameter, ranging between 0 to 1 where 0 is no damage and 1 is complete damage.

Pseudo-elastic model contains two parameters, r and m. Here are the steps to determine the parameters that will be used in the simulation:

1. Firstly, input the stretch value λ_1 from experimental data and C_{10} predetermined from monotonic tensile loading graph. Then, set a starting guess values for r and m using MATLAB software. First determine value of I_1 then performed minimization method to determine the theoretical stress values. This minimization method is to minimize the error between the theoretical values and experimental values, and hence fit the most appropriate r and m values.
2. Constraint file is included, provide MATLAB the condition such that the values of r *and* m must be positive.
3. Error file is to perform normalized root mean squared error function to minimize the errors.

As shown in the **Figure 5**, the pseudo-elastic model is able to fit the experimental data well, even though there are some divergences here and there. The value r and m calculated are 1.6702 and 6.1397 respectively

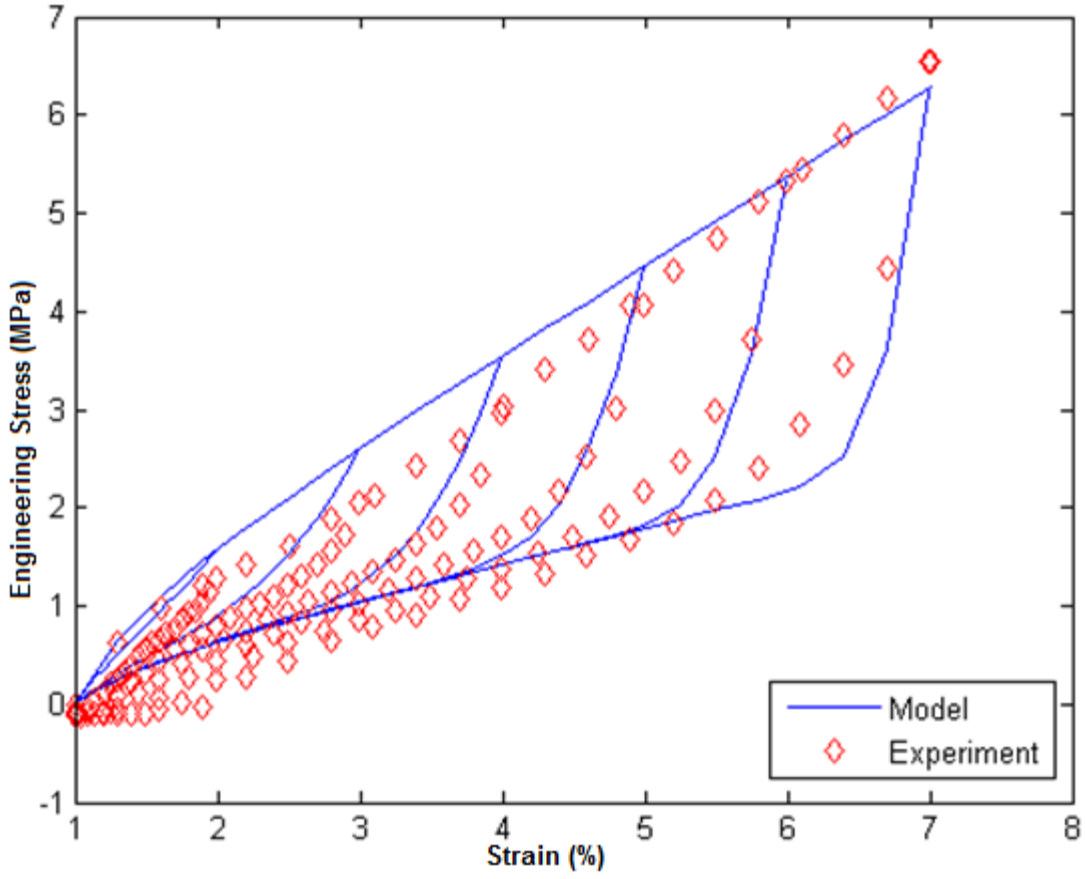


Figure 5: Comparison between Engineering stress from experimental and theoretical stress

3.3 List of Simulation Parameters

Table 1 below summarizes the parameters that will be used on both of simulations, dumbbell and vibrator isolator.

Table 1: Material parameters for simulation

No	Constant Name	Variable
Hyperelastic Neo-Hookean		
1	C10	520,700
2	D1	1E-013
Mullins Effect		
1	R	1.6702
2	M	6.1397

4.0 Simulations

4.1 Dumbbell Simulation

The simulation software used in this project is ABAQUS. The specimen is simplified into one quarter of the actual dumbbell shape to shorten the simulation time utilizing the benefit of symmetrical shape of the specimen. The model is constructed using other CAD software and imported into ABAQUS for simulation. For the material model, hyperelastic Neo-Hookean model is chosen to represent the material behavior of the specimen. In order to simulate the damage effect from cyclic loading, additional material behavior known as Mullins effect is selected in the material model.

For mesh, hex type mesh is chosen because it produces the most precise result among the other types. In order to simulate hyperelastic material, Hybrid Formulation has to be activated. Next step is to create Steps. Steps here mean the activity that will be assigned to the model. In this phase, turning on Nlgeom (Non-Linear Geometry) is a must since Elastomer indeed non-linear material. Next is to determine the Boundary Condition. Two faces to be fixed, six times stretching (100%, 200%, 300%, 400%, 500%, and 600% of dumbbell length), and six times returning (go back to initial condition).

Lastly, simulate the model with all the conditions that have been set. After the simulation is done, extract the Stress and Stress data and construct a graph Stress against Strain referring to the extracted data.

Because of software limitation, the result that we got from this simulation was not really precise. The time step for every step (from Pull 1 until Pull 6 and Return 1 until Return 6) could not be set too high, else it would give errors. The more the time step, the more data can be produced. As we can see from **Figure 6,** the curve produced from simulation result not as smooth. This is due to the lack of data produced by the software.

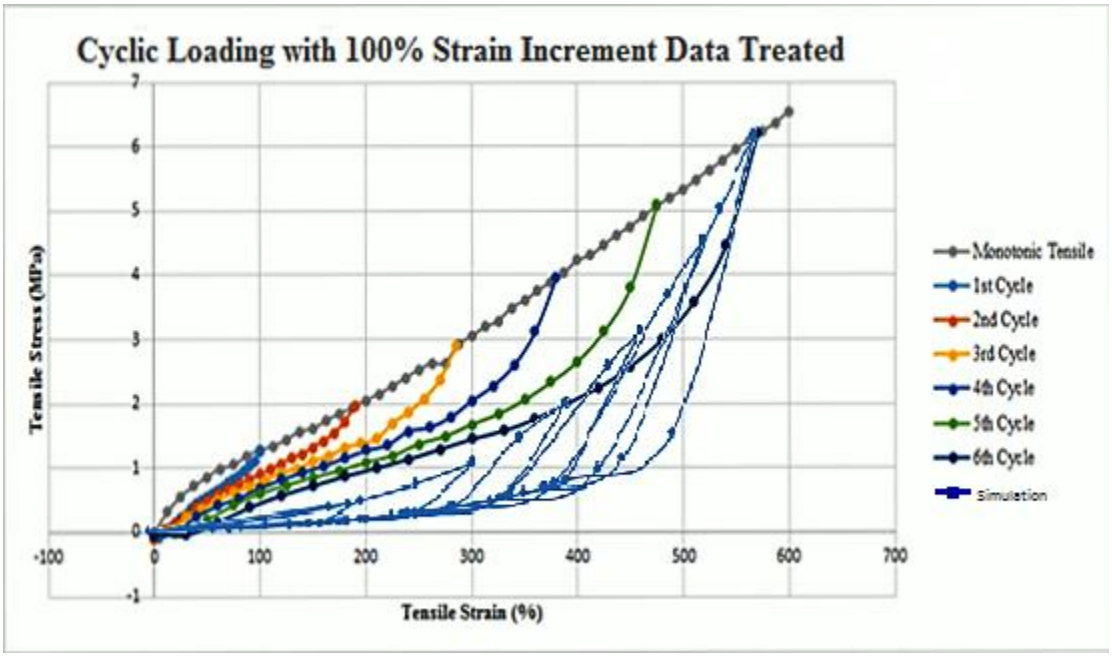


Figure 6: Comparison between experimental and simulation result

4.2 Vibration Isolator Simulation

The model for this simulation is using only the surface of the Vibrator Isolator instead using the whole model to simulate, due to time limitation. **Figure 7** shows the full model and the surface that we are using for the simulation.

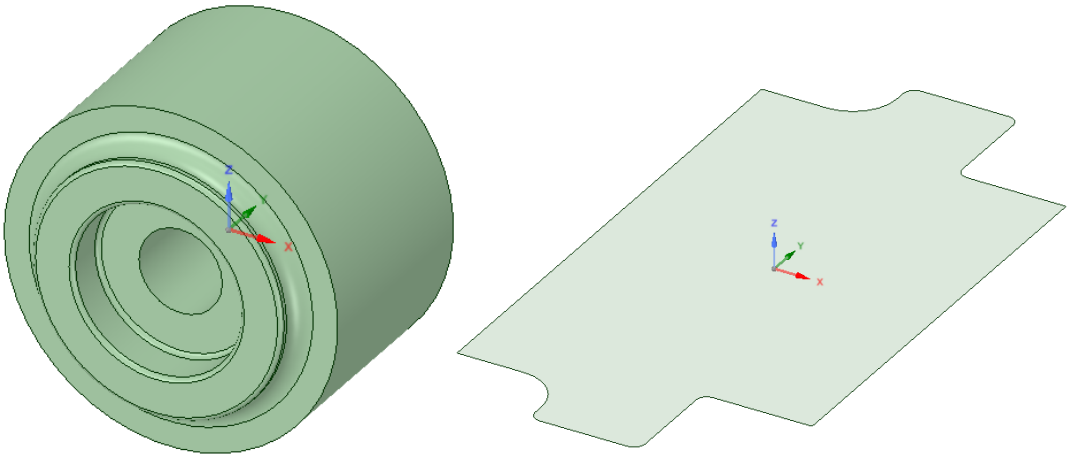


Figure 7 (from left to right): Full design of Rubber Bushing (Vibrator Isolator) and its surface

The setting for Material and Mesh will be the same as dumbbell simulation before. For Steps, compression of material is needed instead of stretching it. Since in real life case, Vibrator Isolator will be compressed on the automobile application. It compresses 10% of its total length, not to mention two edges have to be fixed. These conditions will be placed on Boundary Conditions section.

Referring to **Figure 8** below, Mullins effect for vibration isolator can be seen as expected. This means that the parameters that keyed in before worked. There are still chances that the parameters being not precise, because the parameters were taken from tensile experiment while the simulation was meant for compression. This case particularly can be the continuation for this project.

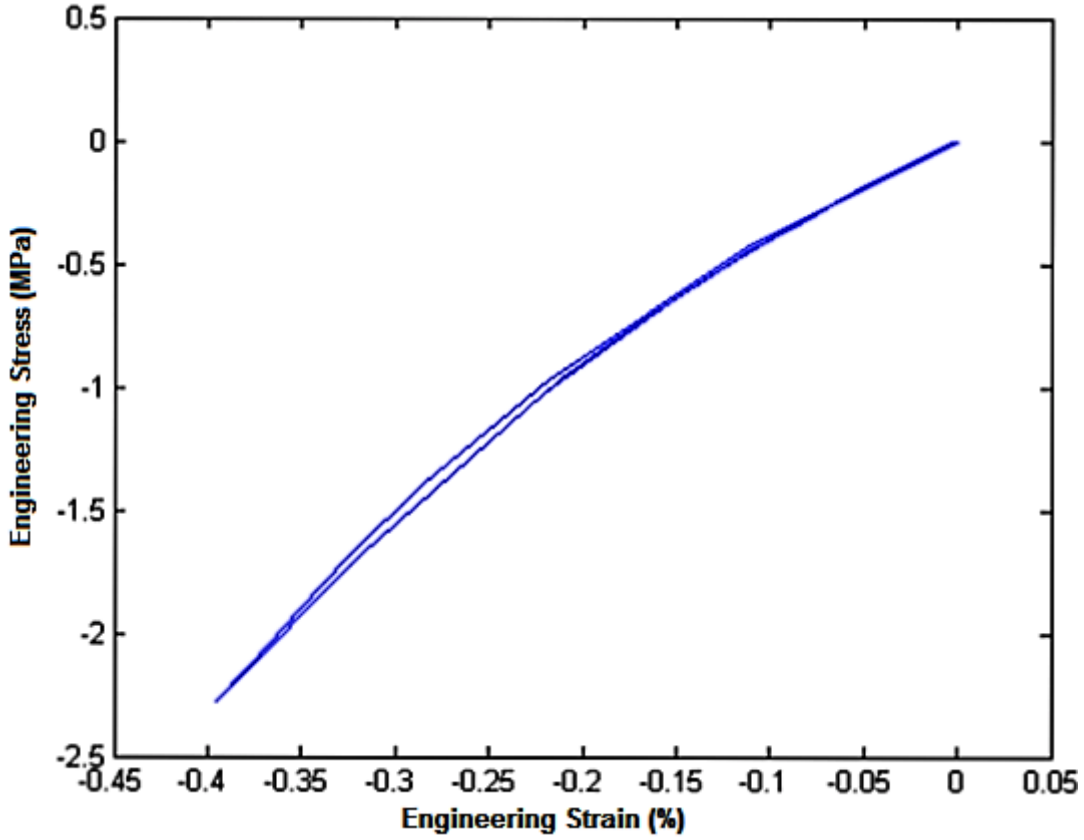


Figure 8: Graph of engineering stress vs. engineering strain for vibration isolator simulation

5.0 Conclusion

In this project, investigations about Mullins effect were addressed by doing mechanical experimental (monotonic tensile loading and cyclic loading). Material used for this experiment is rubber filled with 25% Carbon Black. The result showed inelastic responses such as hysteresis, permanent set, and softening effect. From the experimental results, we managed to obtain Hyperelastic Neo-Hookean parameters ($C_{10,}$ and D_1) and Pseudo-Elastic for Mullins Effect parameter (r, and m). These parameters, later on, will be used to run the simulation on Abaqus CEA software.

Two simulation were conducted, simulation to dumbbell specimen and simulation to rubber bushing as vibration isolator. Results showed that, the proposed model was qualitatively in good agreement with experimental observations. Hence, the parameters that obtained from mechanical experimental can be applied to real life example, in this case was vibration isolator for automobile.

References

[1] Morton, M. 1999. Natural Rubber. In: Subramanian, A. eds. 1999. Rubber Technology. Springer Netherlands, 179.

[2] Vandakudri, A. and Krishnamurthy, K. 2013. Elastomers Application for New Age Industries and Engineering Support. [E-book] Available through: http://www.itcinfotech.com/Uploads/GUI/knowledgecent re/Elastomer.pdf.

[3] Bauman, J. 2008. Fatigue, stress, and strain of Rubber Components: Guide for Design Engineers. Cincinnati: Hanser Publishers.

[4] Gent, A. N. (1992). Engineering with rubber: how to design rubber components. Carl Hanser Verlag GmbH Co KG.

[5] Chagnon, G., Verron, E., Gornet, L., Marckmann, G., & Charrier, P. (2004). J. Mech. Phys. Solids, 52(7), 1627– 1650.

[6] R.W. Ogden, D.G. Roxburgh, A pseudo-elastic model for the Mullins effect in filled rubber, Proc. Roy. Soc. A – Math. Phy. 455 (1999) 2861–2877.

[7] Loo, M., Andriyana, A., Chagnon, G. and Afifi, A. 2013. Experimental investigation of the Mullins effect in swollen elastomers. Constitutive Models for Rubber VIII, p.437.

eureca 2016 – Conference Paper
Paper Number 2ME7

Design and Analysis of Microheater for Efficient Vaporization of Liquid Propellant

Izzaz Iskandar bin Ismail*, Cheah Kean How

School of Mechanical Engineering, Taylor's University, Malaysia

*izzaziskandarismail@sd.taylors.edu.my

Abstract

The role of satellites is to support industries down on Earth. To further drive growth in these sectors, the development of nanosatellites, satellites of mass ranging from 1 – 10 kg, are being explored. These microelectromechanical-based systems (MEMS) devices have significantly lower project costs and timelines due to their minute size. As their missions get increasingly complex, more efficient miniaturization of nanosat propulsion systems is needed. The Vaporizing Liquid Microthruster (VLM) is one candidate for propulsion as it is efficient and highly reuseable. VLMs consist of a microheating element (the microheater) deposited on a thermally insulated substrate, typically silicon. Liquid propellant is heated in the vaporizing chamber and is expelled through the nozzle, creating thrust. A previous study by Cheah et al [1] was done utilizing Platinum as microheating element and Zirconia High Temperature Co-fired Ceramic (HTCC) as substrate, yielding the highest temperature achieved by a VLM in literature with 5 W of power.. This study attempts to improve heat output and solve the cracking issues faced by the previous study model, by investigating the use of lower cost materials of silver metal and Low Temperature Co-fired Ceramic (LTCC). Three Designs were made, meshed, and analysed using FEA. FEA was carried out on ANSYS, used to numerically and graphically represent the thermal temperature distribution that occurs from running the microheater at 5 W of power for a duration of time on the ceramic substrate. The substrate is then compared to the previous study microheater. The temperatures achieved by the three Designs are 313.03 °C (Design 1), 268.19 °C (Design 2), and 323.17 °C (Design 3), compared to the experimental data from the previous study, 409.1 °C. Design 3, which yielded 323.17 °C, managed to output thermal stresses of only 409.9 MPa, a significant improvement over the previous study's 9.63×10^8 MPa. However, it is still not enough as the mechanical strength of LTCC is taken to be 320 MPa. The Design and materials used are promising and are encouraged to be explored in future work.

Keywords: MEMS, LTCC, VLM, microheater, nanosatellite, thermal stress

1.0 Introduction

Satellites play a supporting role for global industries, ranging from telecommunications, medical, and financial sectors. However, the cost of sending a satellite to space is still astronomical [2]. A reduction in mass of satellites results in less launches as more can be sent with the same launch, in addition to having shorter project schedules and funding required [3]. Moreover, nanosatellites when sent en masse are able to test newer technologies that would not have been possible without the redundancy of systems that they provide. The satellite industry is still growing, and is expected to do so in the years to come as developing countries take advantage of the technology to advance their economies and quality of life [4].

Various propulsions systems exist for nanosatellites, such as solid propellant fuels and ionic propulsion [5]. The most effective one today are Vaporizing Liquid Microthrusters (VLM). They consist of a microheater, typically only millimetres in length, deposited on a thermally insulated substrate. A VLM turns liquid propellant into hot gases escape through its nozzle, propelling the craft. Controllable and reusable, VLMs are ideal for nanosatellite usage as its fuel can be stored in a light and low pressure tank [5].

The first VLM was done by Mukerjee et al., using silicon micromachined chips and wet etching of silicon, it was designed, fabricated and tested successfully, generating 0.15 mN to 0.46 mN of thrust with 5 W of power [6]. In 2011 Hwang et al. demonstrated better heat dissipation and increased heating area of microheaters deposited on poly-silicon mesh [7]. Since then, research around VLMs has been about pushing microheater designs that yield better heat outputs, as it is demonstrated by a simple analytical model of VLM carried out by Bidabadi et al. that remarkable increases in thrust is seen if the power delivered by the heater is increased. In 2015 Cheah et al fabricated and evaluated a VLM that employs high temperature co-fired ceramics (HTCC) that yielded temperatures as high as 409.1 °C using only 5 W of power. The ceramic substrate combination with platinum microheater used was able to use 21% less energy to achieve a temperature of 100 °C compared to pre-existing VLM. The limitation of this design is the cost needed, and the potential cracking of substrate when differing temperatures are located on the substrate.

In 2012 Karthikeyan et al., successfully employed for the first time to develop a VLM using low temperature co-fired ceramic (LTCC) technology [8]. The study showed that LTCCs can be used to manufacture VLMs, and that production with these types of ceramics is simple, fast, and cost efficient compared to poly-silicon VLMs. Also, silver metal was used to increase the temperature of organic light emitting diodes systems, with the use of silver wires [9].

Therefore, an opportunity presents itself to investigate the combination of silver and its temperature increasing properties with ceramic based VLM. To get a better thrust output, the microheater is required to produce more heat with a similar power consumption. Furthermore, the use of LTCC as compared to HTCC VLM done by Cheah et al is a prospect to be studied on, as it costs less.

This study aims to optimize the design of Microelectromechanical (MEMS)-based microheaters for efficient operation of VLM analysing the possibility of a VLM based on a silver microheater on an LTCC substrate. In order to properly determine performance gains or decrements, a Design of existing VLM based on Cheah et al.'s study is designed with 3D design software DesignModeler. In this study, two other Designs are also designed in order to study the effects of microheater geometry in heat distribution and temperature output. They are then analysed using finite element method, on ANSYS software, to simulate temperature outputs of the microheater using 5 W of power. In addition to calculating how much the simulated microheater improves compared to previous versions of microheater, the final hypothesis to be investigated is to determine whether the optimized design manages to reduce thermal stresses to levels that might not hinder the operation of the VLM.

The scope of study will be limited to simulation and modelling. The reason for this is because there is a lack of facilities needed in order to test designs. Since microthrusters produce very little force, the University possesses no equipment of such sensitivity to measure that data.

2.0 Research Methodology

2.1 Design of Microheater

The microheater design stage was done with a few requirements. First, it is limited to a vaporizing chamber of size 2.5 mm by 5 mm. The thickness of the microheater is set to be 5 μ which is the thickness of silver paste when deposited on the LTCC substrate using screen-printing method. The width of the microheaters is set at 150 μm. Sketching and modelling of the three microheater designs are done with DesignModeler. Design 1 was drawn to emulate the design of previous study [1] microheater. This is to ensure there is a control value for comparisons, since geometries are all similar.

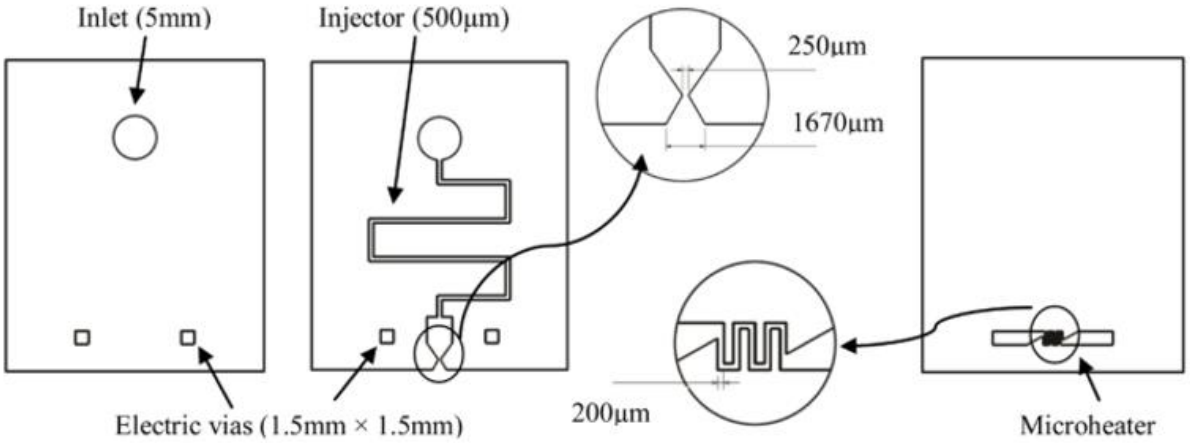


Figure 1: Previous study of microheater [1].

Design 2 was designed with more turns compared to Design 1. In addition, it is running from top to bottom of the vaporising chamber space for maximum heat

distribution without consuming too much silver paste. Design 3 was designed as a circular pattern. It is predicted that the concentric design will result in a better heat distribution as the area that the heating element covered is higher due to the tight coil wrapping. The three different microheater designs are shown in Figure 2.

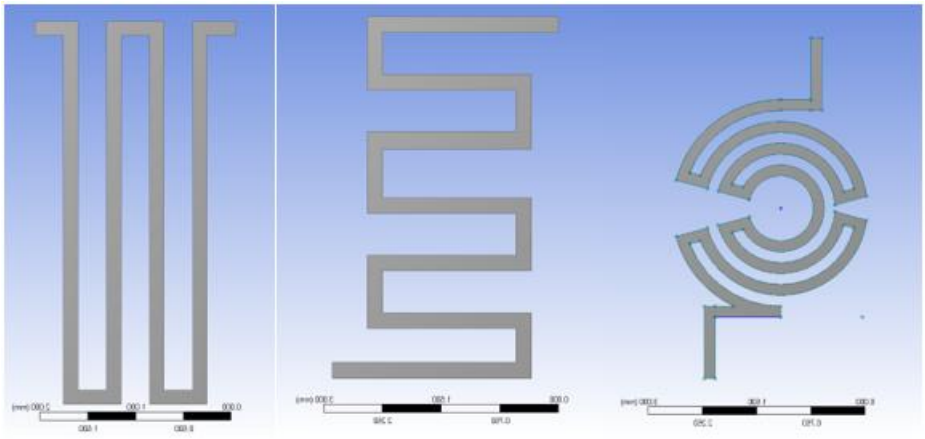


Figure 2: Designs 1, 2 and 3 of microheater designs in DesignModeler.

2.2 Numerical Analysis of Microheater

2.2.1 Construction of 3D FEA model

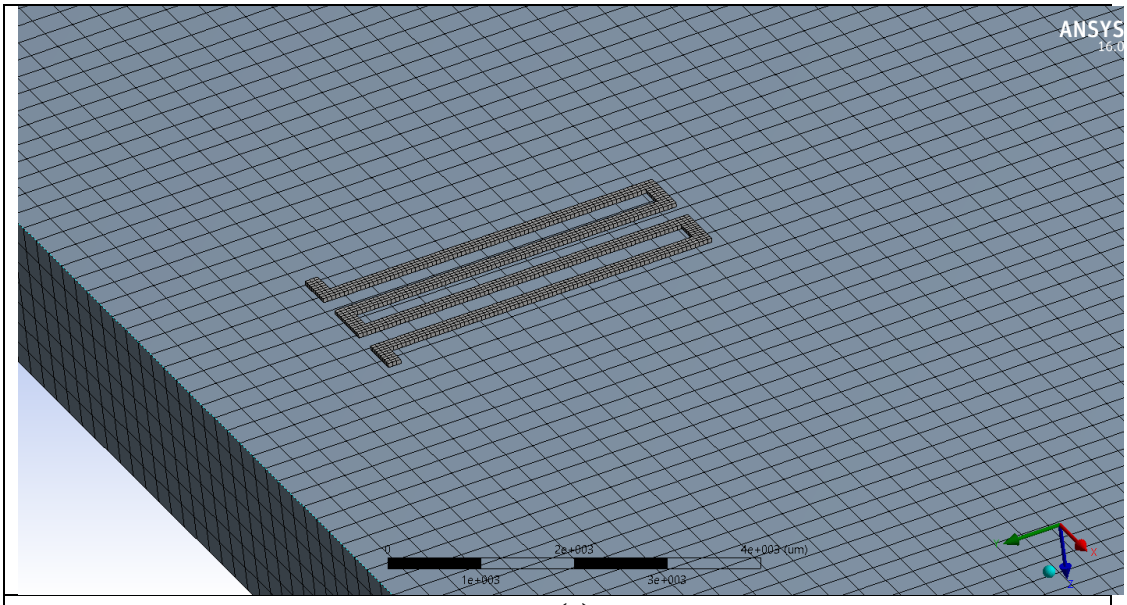
The Designs were extruded along the Z-axis after sketching to a thickness of 5 µm. The Add Material option was used. Next a surface was selected, and a rectangle was sketched to be the substrate. This was done using the Add Frozen option to facilitate material type later on in the meshing stage. The substrate was extruded to a thickness of 2 mm. For Design 3, a series of concentric circles were sketched, with intersecting lines crossing each one at a distance of the width of the microheater. Using the Trim tool, it was shaped accordingly to its final design.

2.2.2 Meshing

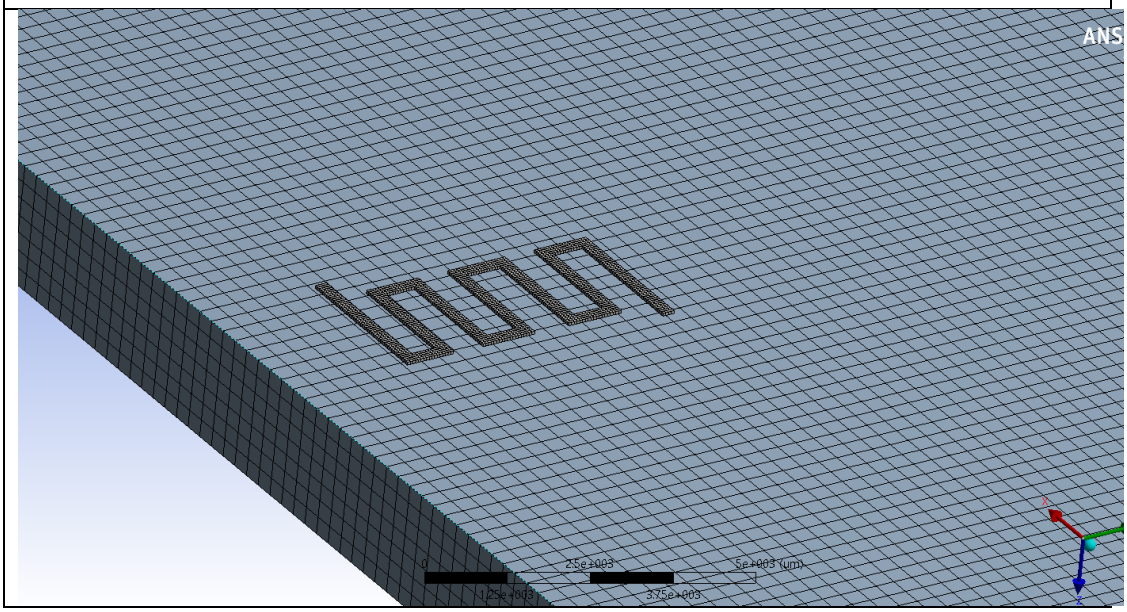
The Designs were meshed in two steps; the microheater, and the substrate. Body Sizing was used for the substrate, whereas Face Sizing was used for the microheaters. Although it is possible to have over 500 000 elements in the mesh, the computing time is too long while the improvement in accuracy is not marginal. Therefore, the optimum element size chosen a 80 000 element mesh. These sizes were both determined based on a Grid Independent Test at the end of the simulation. This step is especially important because a smaller mesh sizing results in more elements, and a higher accuracy in calculations. The skewness of the mesh was checked to ensure good quality of meshing. The mesh sizing chosen had a skewness that was near zero. A summary of the meshing for all three Designs are provided in Table 1. The 3D Designs after meshing are shown in Figure 4.

Table 1: Meshing properties for microheater Designs

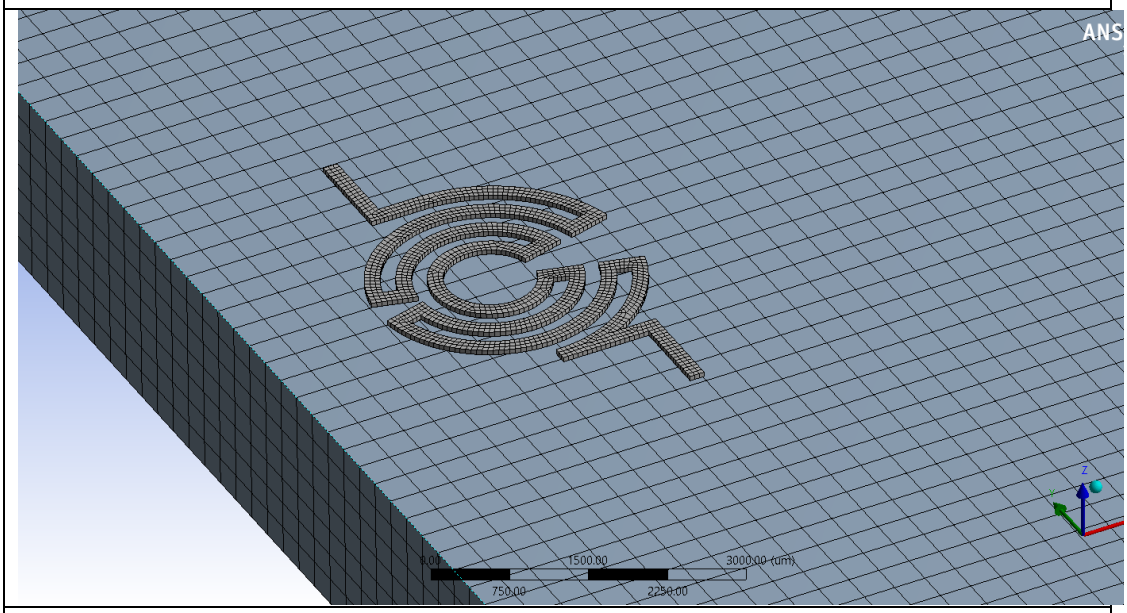
	Design *1*	Design *2*	Design *3*
Mesh element	81777	81586	80534
Skewness (Max)	0.0046927	0.05669	0.57875
Mesh type	Body sizing and face sizing		



(a)



(b)



(c)

Figure 4: The meshed designs for a) Design 1 b) Design 2 and c) Design 3.

2.2.3 Boundary conditions

After setting the contacts condition as "Bonded – solid to solid", the corresponding material properties were assigned to heating element and substrate. The material properties of silver and LTCC are shown in Table 2. The material properties of LTCC ceramic tape are extracted from Electroscience [10].

The analysis is set to Thermal Transient. Table 3 shows the analysis settings (Step Controls) that were set in the FEA. In this study, the initial temperature for all nodes are set to be 29 °C which is to simulate the room temperature. As the FEA is to simulate a dry test of the microheater (without vaporizing the propellant), convection enabled, at 100 W/(m^2.°C). A trial run showed that temperature distribution of the Designs reached to reach steady-state after 15 seconds. Thus, the time scale for transient analysis was set to 30 seconds, at a program-controlled time step. The internal heat generation was evaluated as 5 W divided by the volume of heating element. This represents the power dissipated in the form of heat as the electrical current passing through the heating element.

Table 2: Material properties of silver and LTCC

	Density (kg m^{-3})	Elasticity (GPa)	Thermal Conductivity (W $m^{-1}.°C^{-1}$)	Specific Heat (J $kg^{-1}.°C^{-1}$)
Silver	10490	83	429	233
LTCC	3160	100	3.0	660

Table 3: Analysis settings (Step Controls) for Transient Thermal

	Design 1	Design 2	Design 3
Number of Steps		1	
Current Step Number		1	
Step End Time		30 s	
Auto Time Stepping		Off	
Define By		Time	
Time Step		1 s	
Time Integration		On	
Internal Heat Generation (W/m^3)	3.81×10^{10}	2.656×10^{10}	3.120×10^{10}
Convection ($W/m^2.°C$)		100	

2.2.4 Thermal stress analysis

The output data from the Thermal Transient analysis were linked into Static Structural. The bottom surface of the substrate was set as a fixed support. The end time of analysis is the same as in the previous step. Due to the low thermal conductive properties of ceramics, there will be regions of high temperatures and regions which are low throughout the substrate. This causes some uneven expansion and induces thermal stress which can be illustrated in graphical form by ANSYS. The thermal stresses and the deformations that occur were assessed. Based on the results, further evaluation can be carried to determine whether the microheater design is efficient. The Von-Mises stress will be utilized to indicate the intensity of stress on the substrate due

to any deformation that occur. Thus, the output data gathered from ANSYS will be used to consolidate and understand the individual discrete finite element meshes.

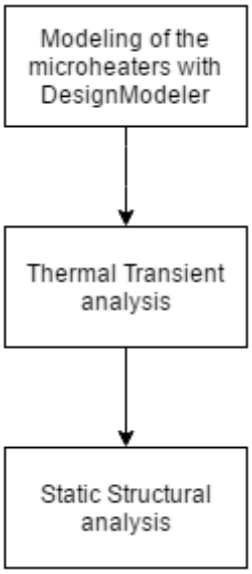


Figure 5: Flow chart of analysis methods.

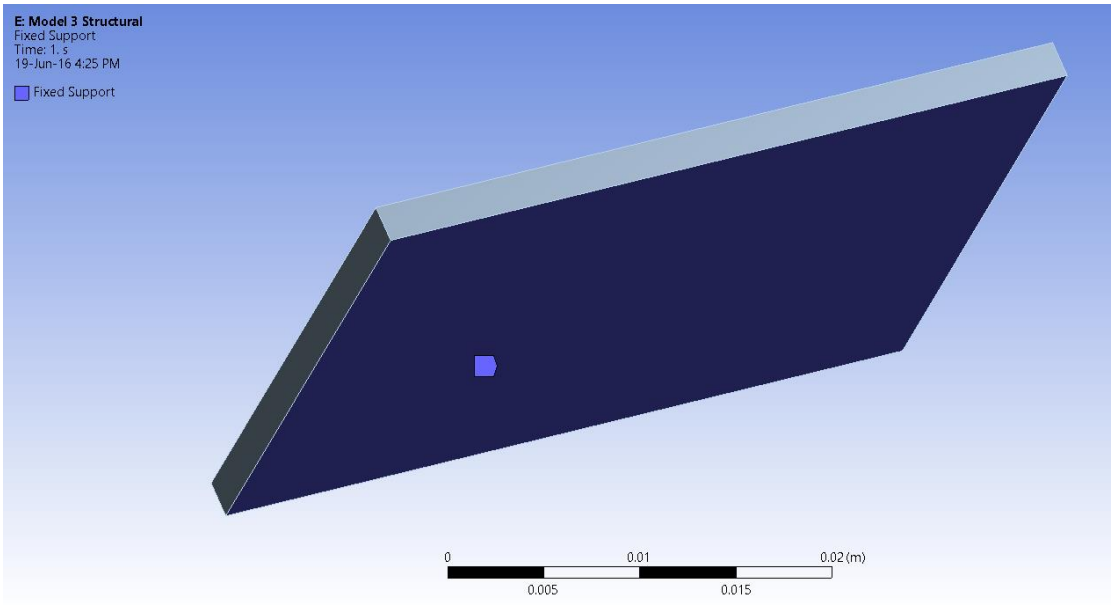


Figure 6: Location of fixed support applied on simulated designs.

3.0 Results and Discussion

3.1 Thermal Analysis

In order to validate our analysis, an FEA of the previous study microheater is done. By observing that its results are analytically similar to experimental data, we can prove/disprove the simulation. ANSYS is fed data from the properties in Table 7. Based on the simulation of the original study microheater, the difference between temperatures of the study done by Cheah et al is around 70 °C. The simulated model yielded 471.52 °C, whereas the experimental data from the study yielded 409.1 °C. The analysis settings were done similar as to what was listed in the research methodology chapter, except that the materials were now HTCC ceramic as the substrate and Platinum metal for the microheater.

Table 4: Mechanical and thermal properties of HTCC and Platinum.

	Density (kg m^{-3})	Elasticity (GPa)	Thermal Conductivity (W $m^{-1}.°C^{-1}$)	Specific Heat (J $kg^{-1}.°C^{-1}$)
Platinum	21440	91	69.1	128
HTCC	3.600	175	2.1	480

It is assumed that due to the ideal nature of the simulation, the simulated original model would yield a temperature higher than actual experimental value. In the previous study, it is stated that the microheater chip supplied cannot be heated to its final temperature immediately. The Static Structural analysis conducted after Transient Thermal confirmed this. Experimentally, the microheater failed after just a few seconds. In the FEA conducted, there was a very rapid increase in temperature within the first second of the simulation. By 3 seconds it had already reached its maximum temperature of 471.52 °C. Such rapid rise in temperature caused the previous study microheater chip to fail at a temperature of only 80 °C. This is fairly consistent with what is observed during the FEA done with this design in the study.

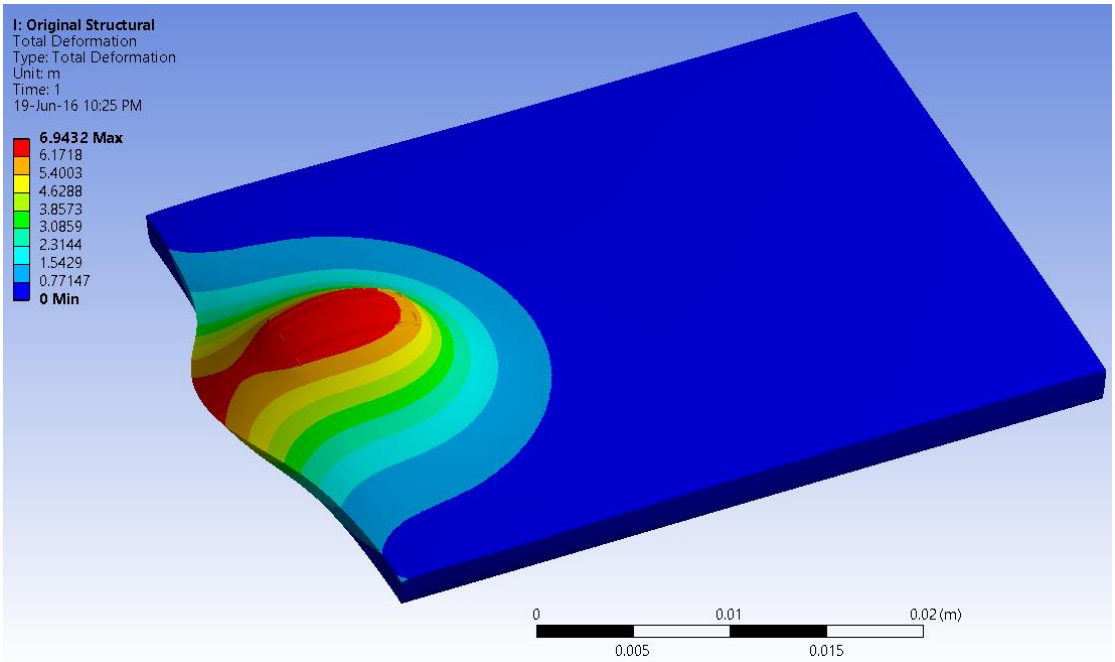
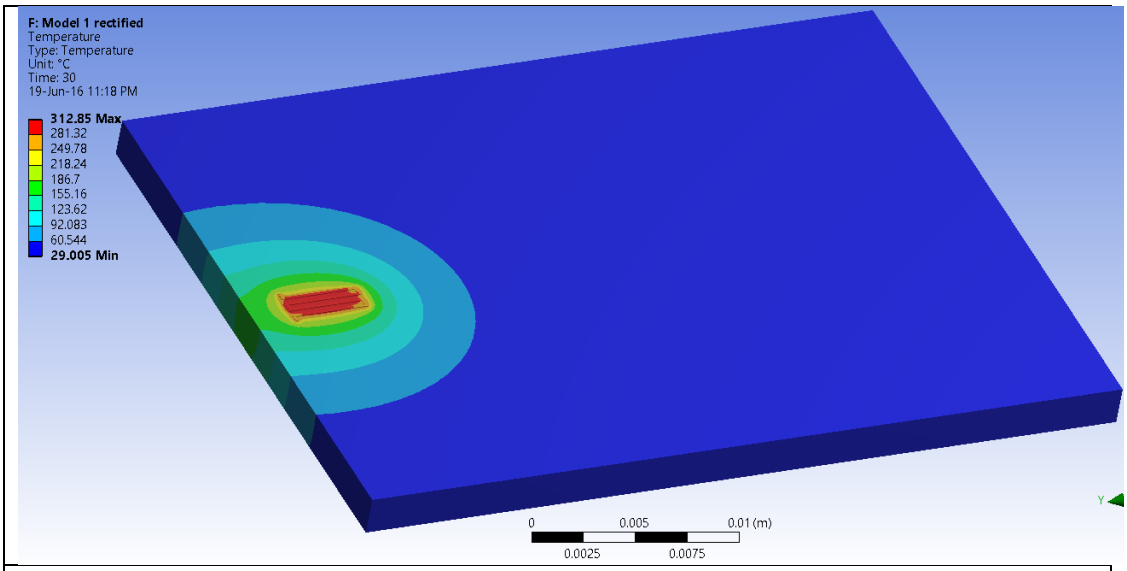


Figure 7: Deformation of the previous study microheater using FEA.

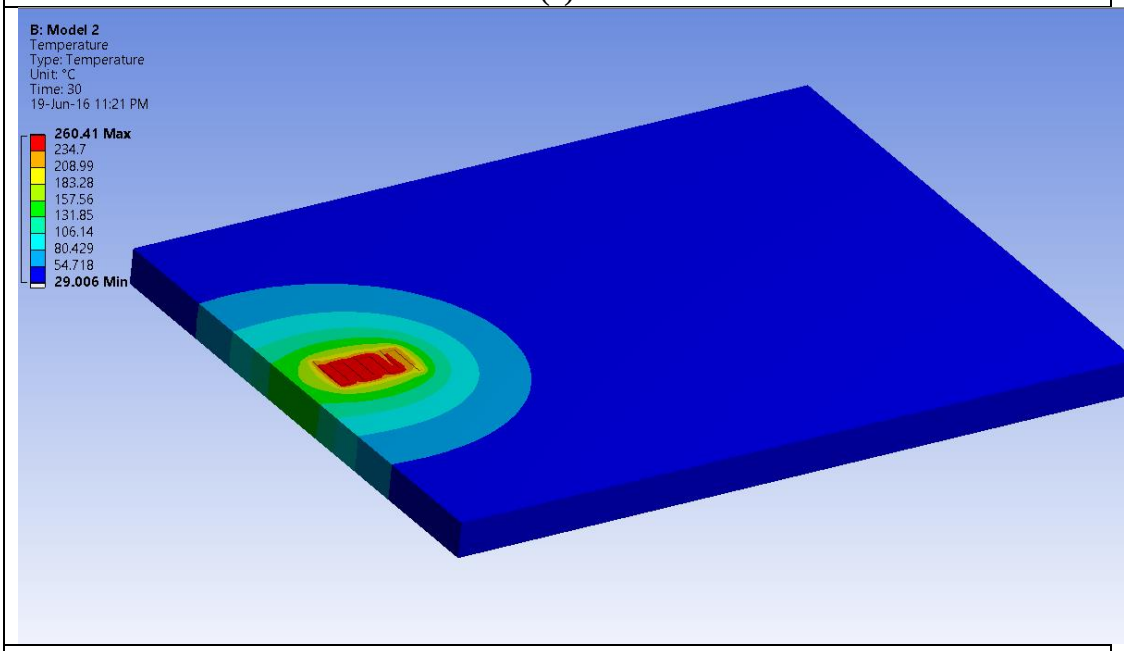
The maximum deformation achieved was in the vicinity of 6-7 meters. This is obviously a value that is too large, and extremely exceeding the mechanical properties of Zirconia HTCC. Evaluating the performance of the previous study model using the same methods of analysis for the newly designs was a key factor in being able to draw reliable conclusion from data gathered in this study. We find that the FEA results line up with the results from the previous study. Therefore, the study of the three new microheater designs with different materials can proceed.

Design 1 was put through Thermal Transient analysis first. It managed to achieve a maximum temperature of 312.85 °C after 30 seconds of operation, with 5 W of power supplied. It exhibited a sharp rise in temperature during the first 10 seconds and then the growth slowly tapered out. This behaviour is similar to those shown with Designs 2 and 3, where they exhibit the same initial rise in temperature. This behaviour is common to all heating elements and their surrounding material. Due to the very low thermal conductivity of LTCC, despite some parts of the substrate reaching excess of 300 °C, the bulk of the material remains close to the initial temperature.

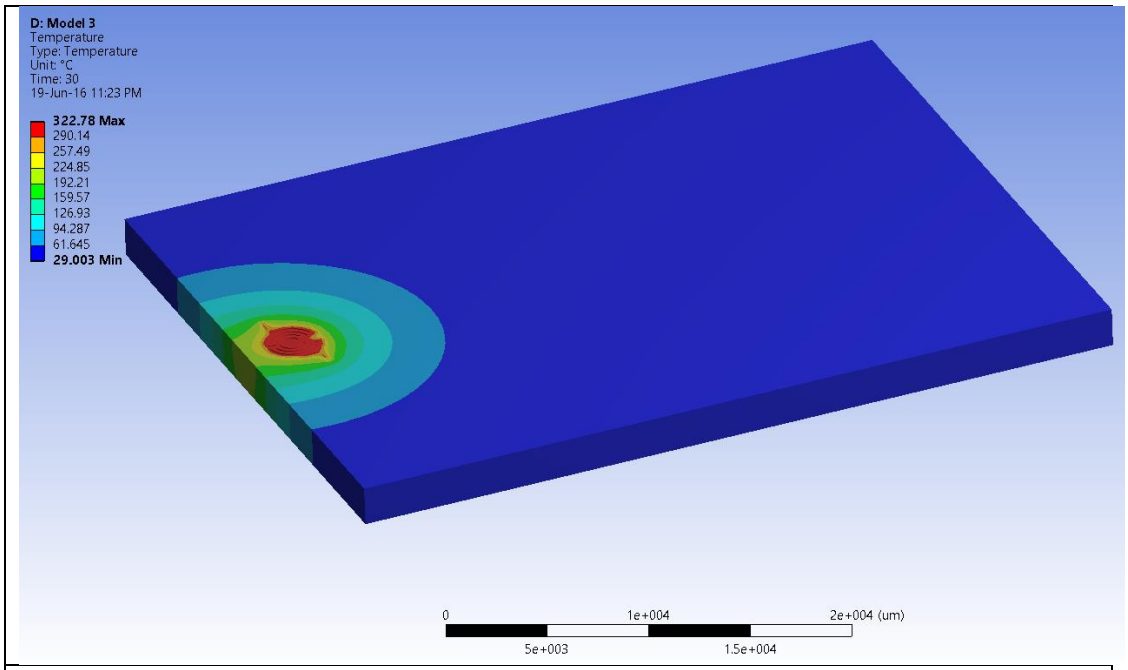
The same analysis was also done with Designs 2 and 3. Figure 8 shows the temperature achieved by each microheater Design per unit of power supplied. It appears that Design 3, with its circular arrangement, is able to generate a higher temperature than the other two designs.


F: Model 1 rectified
Temperature
Type: Temperature
Unit: °C
Time: 30
19-Jun-16 11:18 PM
312.85 Max
281.32
249.78
218.24
186.7
155.16
123.62
92.083
60.544
29.005 Min
0
0.005
0.01 (m)
0.0025
0.0075
Y

(a)


B: Model 2
Temperature
Type: Temperature
Unit: °C
Time: 30
19-Jun-16 11:21 PM
260.41 Max
234.7
208.99
183.28
157.56
131.85
106.14
80.429
54.718
29.006 Min

(b)



(c)

Figure 8: Temperature distribution results for a) Design 1, b) Design 2, and c) Design 3

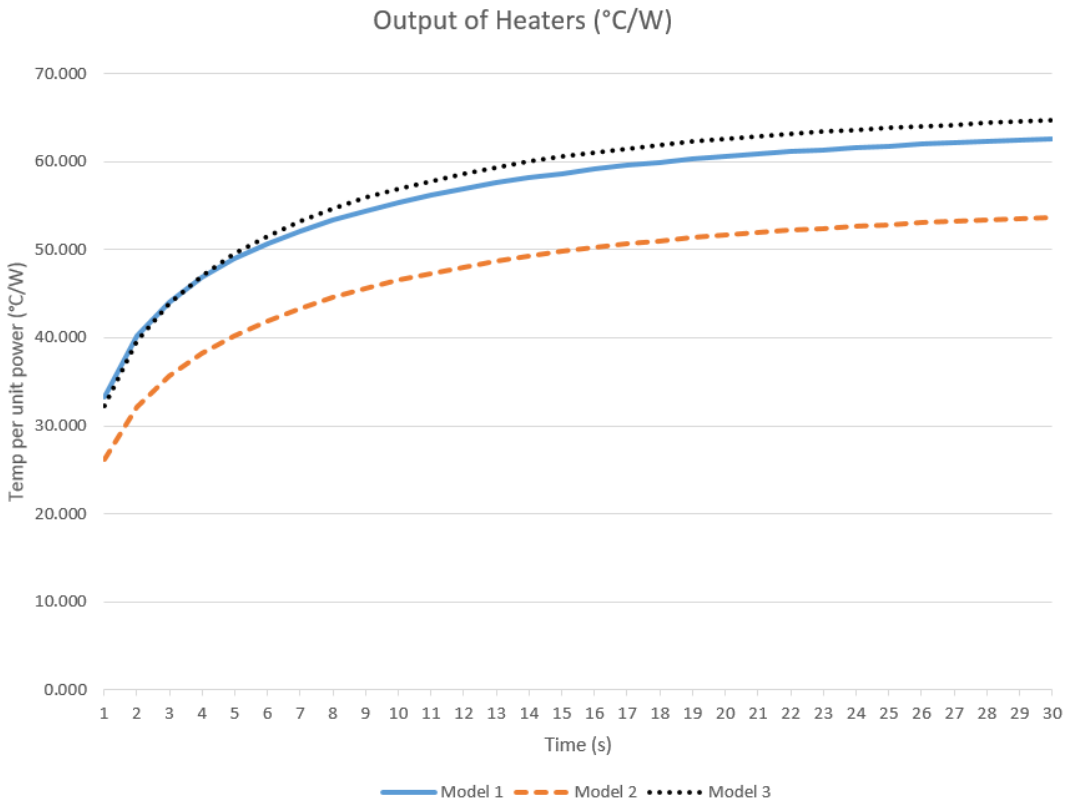


Figure 9: Output of heaters in terms of temperature over power supplied.

3.2 Stresses and Deformations

It is expected that the higher the temperature of the microheater, the greater the stresses would be on the substrate. However, Design 3 showed that its temperature was as high as Design 1, but with lower stresses, albeit a higher amount of maximum total deformation. The stresses are halved; they are 849.39 MPa and 409.9 MPa for Designs 1 and 3 respectively. Although Design 3 has a higher deformation, it is only by about half a micrometer.

Table 5: Summary of stress and deformation analysis.

Result	Design 1	Design 2	Design 3
Max Stress (MPa)	849.39	688.64	409.9
Max Deformation (μm)	4.4585	3.9525	5.088

3.3 Selection of Geometry and Materials Based on Criteria

It is decided that for the first research question, the one dealing with maximum heating efficiency in °C/W, is Design 3. Given the same amount of power supplied, it is able to bring a temperature of 322.78 °C. Moreover, the stresses that it endures are considerably less than other Designs, including the one done in the previous study.

Unfortunately, it has no improvement over the previous study model, in terms of temperature. Further investigation is needed for this. The previous model managed a maximum of 409.1 °C. However, it is not known whether Design 3 would exhibit the same behaviour as previous study model did; whereby it cannot be raised to its maximum temperature instantly. Comparing the gains in temperature of previous model and Design 3, the latter has a slower rise to steady state. This slower rise in temperature can possibly reduce the thermal stresses that occur on the microthruster chip.

Although each LTCC supplier has its own formulation, in general, their properties are considered to be similar enough to consider them having the same mechanical properties. Differences in measurement of these values can arise over test methods and preparation of said LTCC, but for simplicity and a rough indication on what sort of forces microheaters subjugate their surrounding materials to, the value of 320 MPa is taken to be the threshold in terms of stresses on the substrate. In a study done by Sandia Labs, the published mechanical strength of DuPont-produced LTCC Tape (DuPont 951) is 320 MPa [11].

Similarly, no Design managed to yield stress results of less than 320 MPa. However, it is still notable that the thermal stresses ad deformations have improved

compared to the previous study model. This can be attributed to the much slower rise in temperature of the silver microheater compared to Platinum. Further studies are encouraged to improve the Designs and materials employed.

4.0 Conclusion

The study started by the investigation of VLM for use in current-gen nanosatellites. The propulsion system has to be small, efficient, and reliable. The development of silicon-based VLMs brought about more and more efficient forms of nanosatellite propulsion to produce more thrust with less power.

Three different designs of microheater were designed. Therefore, the 3D finite element Designs were done using design software DesignModeler, which is a part of ANSYS Workbench. FEA has been chosen as the most appropriate technique to demonstrate the performance of each design in a numerical fashion. The analyses used are a two-step method, first using Thermal Transient in order to get the temperature outputs from the microheater, which is set to have 5 W of power running through them. Then, the output data is fed to Static Structural. The meshing type chosen are face meshing and body sizing due to the relatively simple structure of the designs and substrate. There are no complex curves in the designs, therefore hard behaviour of mesh is chosen. To determine the sizing needed for meshing, a grid independent test was done.

In the FEA, all three designs were tested with the same parameters or power, thickness, and initial temperature. The only difference was the geometry. The first design yielded a maximum of 312.85 °C. The second one did 268.19 °C, and the third recorded the highest, 323.17 °C. The 3rd design showed the best performance in terms of °C/W. However, even though Design 3 nor the other Designs are able to satisfy the objective of temperature improvements over previous study, there was a significant decrease in thermal stresses in the LTCC substrate.

This study is not ideal because all aspects of the LTCC and microheater production could not be included. It is a limitation of solely using FEA over actual fabrication and experimentation. The mechanical strength of LTCC materials was determined in literature to be similar to the strength of HTCC materials, like the one used in the previous study [1]. However, measurement of mechanical strength of any material is dependent on size of the sample, experimental methods, and preparation of said material. These aspects were not considered in the project. To make the study ideal, and more reliable, it is encouraged to consider them during the planning stage of any follow-up study. Even though LTCCs seem to be a technology approaching maturity, with increasingly varying uses, applications of the material are still under development. The prospective advantages of LTCC to bring about the development of high-density complex VLM modules are numerous and must continue to be explored.

References

[1] K. H. Cheah and K.-S. Low, "Fabrication and performance evaluation of a high temperature co-fired ceramic vaporizing liquid microthruster," *J. Micromechanics Microengineering*, vol. 25, no. 1, p. 015013, 2015.

[2] "How (and Why) SpaceX Will Colonize Mars - Page 3 of 5 - Wait But Why | Page 3." [Online]. Available: http://waitbutwhy.com/2015/08/how-and-why-spacex-will-colonize-mars.html/3. [Accessed: 07-Oct-2015].

[3] T. V. Trong, T. D. Quoc, A. N. Tuan, A. V. Tuan, T. P. Van, and T. D. Van, "Design and manufacture of a nanosatellite for space technology education and potential application," pp. 1–9.

[4] The Tauri Group, "State of the Satellite Industry Report," no. September, p. 33, 2014.

[5] C. Rossi, "Micropropulsion for Space-A Survey of MEMS-based Micro Thrusters and their Solid Propellant Technology," *Sensors Updat.*, vol. 10, no. 1, pp. 257–292, 2002.

[6] E. V. Mukerjee, a. P. Wallace, K. Y. Yan, D. W. Howard, R. L. Smith, and S. D. Collins, "Vaporizing liquid microthruster," *Sensors Actuators, A Phys.*, vol. 83, pp. 231–236, 2000.

[7] W.-J. Hwang, K.-S. Shin, J.-H. Roh, D.-S. Lee, and S.-H. Choa, "Development of Micro-Heaters with Optimized Temperature Compensation Design for Gas Sensors," *Sensors*, vol. 11, no. 12, pp. 2580–2591, 2011.

[8] K. Karthikeyan, S. K. Chou, L. E. Khoong, Y. M. Tan, C. W. Lu, and W. M. Yang, "Low temperature co-fired ceramic vaporizing liquid microthruster for microspacecraft applications," *Appl. Energy*, vol. 97, pp. 577–583, 2012.

[9] H. Cheong, D. Song, and J. Park, "Microelectronic Engineering Transparent film heaters with highly enhanced thermal efficiency using silver nanowires and metal / metal-oxide blankets," *Microelectron. Eng.*, vol. 146, pp. 11–18, 2015.

[10] "Ceramic Tape Systems | ESL Electroscience." [Online]. Available: http://www.electroscience.com/ceramic-tape-systems. [Accessed: 25-May-2016].

[11] F. Uribe, S. Garrett, S. Monroe, and S. Burchett, "Characterization of the Mechanical Properties of LTCC ;"Green Tape for the MC4352 MET YYTM," no. March, pp. 1–77, 2008.

Numerical Analysis of the Effect of the Number of Round Dimples on the Aerodynamics Efficiency of NACA 0012 Airfoil

Jason Sie Wei Law[1], Abdulkareem Shafiq Mahdi Al-Obaidi[1*]

[1]*School of Engineering, Taylor's University, Malaysia*

[*] Abdulkareem.Mahdi@taylors.edu.my

Abstract

Airfoil is widely used in industry as it is the basic element of all lifting surfaces such as wings for airplanes and blades for compressors or turbines. One of the most important criteria to determine a good airfoil design is the amount of lift and drag produced. A good design should provide maximum lift and minimum drag, which also known as high aerodynamic efficiency. To further improve the aerodynamic characteristics, dimples are one of the possible solutions. Based on the previous studies and for certain design conditions, it is proved that dimples decrease the drag and increase the lift. In this research, the effects of the numbers of dimples are investigated and analysed. A standard NACA0012 airfoil is considered without and with dimples. Different numbers of dimples on the airfoil are studied numerically at subsonic speeds and angles of attack from -10º to 10º. The dimples are arranged in 3 different arrangements, which are at the top surface, bottom surface and also the top and bottom surfaces of the airfoil. The airfoil with dimples is modelled and simulated in ANSYS Fluent to determine what is (are) the possible numbers of dimples which give the optimum aerodynamic efficiency. It is shown that the best configuration of dimples is adding 1 dimple at the bottom surface of the airfoil which increases the efficiency by 4.18% compared with the clean airfoil.

Keywords: Airfoil, Aerodynamic Characteristics, Dimples, Lift and Drag, Aerodynamic Efficiency

List of Symbols

P	Density	kg/m^3
ΔU	Difference at the field point	m
d_t	Distance from the point in the flow field to the trip on the wall	m
D	Distance to the closest wall	m
g	Gravity	m/s^2
Δx_t	Grid spacing along the wall	m
h	Height	m
C_l	Lift Coefficient	-
S	Magnitude of Vorticity	1/s
P	Pressure	Pa
Re	Reynold Number	-
v	Velocity	m/s
w_t	Wall vorticity	1/s

1.0 Introduction

Aerodynamics has always been a very popular topics. The theory of aerodynamics is the greatest works of a lot of individuals since early time. These all probably started with ancient humans' desire to mimic the actions of the birds and soar in the sky. Therefore, they start to question themselves, what substances and theories cause birds to fly and can human soars in the sky too? This is how this topic "Aerodynamics" became popular and interesting throughout the whole world.

In the 15th centuries, a man named Leonardo da Vinci concluded that it was the movement of the wing relative to the air and the resulting reaction that produced the lift necessary to fly [1]. Therefore, he has produced several designs of machines to copy the action of a bird's wing as shown in Figure 1.

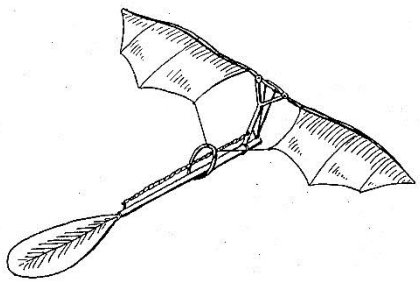


Figure 1. Ornithopter [1]

Since 18th centuries, most of the researches have started to conduct experiments to improve the aerodynamics of a certain object. One of the most carried out experiment is to study the objects with rough surfaces, also known as dimples [2]. One of the most common studied object is dimpled golf ball. Golf balls are all manufactured with dimples as shown in Figure 2 on its surface to increase the lift. Among all the ball games, golf ball is the one with the highest speed, not only because of the material and

method of hitting it, it is also influenced by the dimples on its surface [3]. In short, the main forces that acting behind all these theories are lift and drag forces.



Figure 2. Dimpled Golf Ball

When fluid flows around an object, lift and drag forces are produced by the distribution of pressure and shear stress as shown in Figure 3. To define lift and drag force, lift force is the perpendicular force to the stream velocity while drag force is the parallel force to the stream velocity. However, how lift and drag is produced? For example, an airfoil. When an airfoil is travelling over a fluid, there are differences conditions between the top and bottom surfaces of the object. The flow on the top surface will be faster than the bottom surface. According to Bernoulli's equation in equation (1), when velocity increases, pressure decreases. Hence, this results in a pressure difference between the 2 surfaces. The bottom surface will have a higher pressure than the top surface and this is the condition that generates lift for the airfoil [4]. Then, how is drag force generated? Drag force is actually produced simultaneously when the lift force is generated. Drag is generated by the interaction of a solid body with fluid.

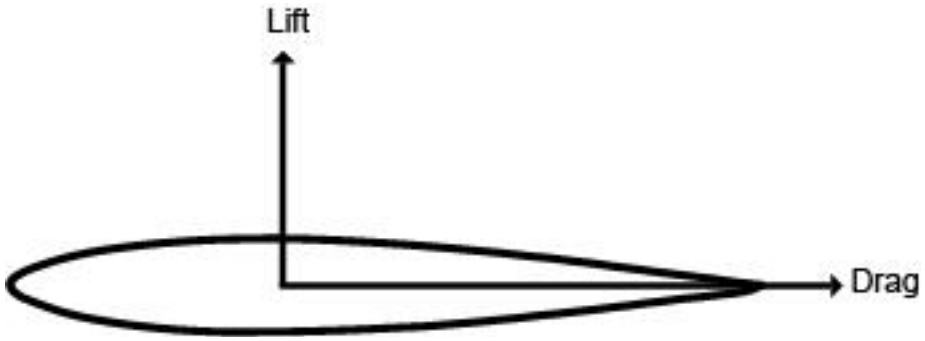


Figure 3. Lift and Drag Forces of an Airfoil

$$P_1 + \frac{1}{2}\rho {v_1}^2 + \rho g h_1 = P_2 + \frac{1}{2}\rho {v_2}^2 + \rho g h_2 \quad (1)$$

To obtain a good aerodynamic efficiency, the object has to be able to produce high lift force and low drag force. The ratio between these 2 forces give us the aerodynamics efficiency. Therefore, as mentioned above, through a lot of researches these centuries, adding dimples on the surface is a very common and effective method. For example, by comparing a smooth and dimpled golf ball. Since the laminar boundary layer around the smooth surface separates very fast, it produces a very large wake over the entire rear area as shown in Figure 4 that sketched by the author. The large wake maximizes the region of low pressure and results in maximum difference between the

front and rear pressure. Hence, a large drag is produced over the smooth surface [3]. To overcome this challenge, dimples are proposed.

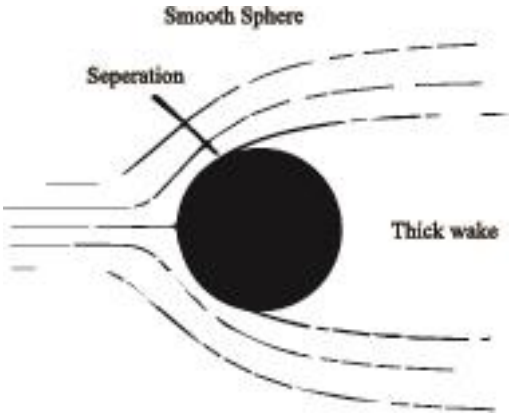


Figure 4. Thick Wake Produced by Smooth Golf

Similar condition as above, but a dimpled golf ball is used. Conversely, a thinner turbulent boundary layer of air compared to the one above clings to the surface which allows the air to flow following to the surface further around the rear area of the golf ball. This decreases the size of the wake as shown in Figure 5 that sketched by the author and thus produced lesser drag because smaller wake minimizes the region of low pressure.

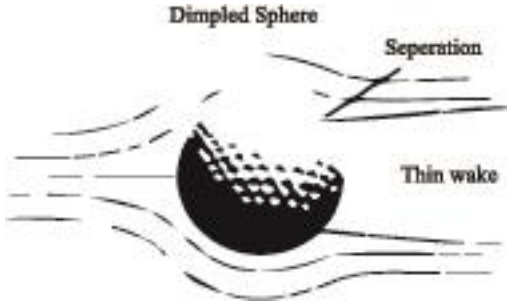


Figure 5. Thick Wake Produced by Dimpled Golf

It is actually proven that the dimples will cause the laminar boundary layers from transition to turbulence, adding momentum to the flow which assists the flow to overcome the pressure gradient and also delay the separation [5]. Apart from that, there is actually a company named as FastSkinz in USA has already utilized the technology of dimples on a lot of different famous field such as racing, outdoor billboard advertising, large commercial fleets and wind turbines [6].

The main objective of this research is to find out the effects of number of round dimples on the aerodynamics efficiency of NACA 0012 airfoil. In this research, some assumptions are made to let the project run smoothly. Firstly, the airfoil used will be assumed as fix throughout the whole project, which is NACA 0012. Besides, for the dimples, this research mainly focuses on 3 different scenarios, dimples on top surface, dimples on bottom surface and dimples on both top and bottom surfaces. All scenarios will be modelled with 4 cases, from one to four dimples on a surface with angle of attack of -10° to 10° is an interval of 5°. Furthermore, the shape and geometry of the dimples are all assumed as round dimples, the other shape and geometry are not considered. The simulations used in this project are all assumed in 2D, as 3D simulations will take too long time and too complicated for the author.

The 4 numbers behind the NACA indicates the geometry of the airfoil. The first digit determines the camber, the second digit determines the position of the camber while the last 2 digits indicates the thickness of the airfoil in percent of the chord [7]. NACA 0012 is a symmetrical airfoil without any camber.

2.0 Numerical Set Up

This research is mainly on numerical approach. ANSYS Fluent is used to run the Computational Fluid Dynamics (CFD) simulations of all different types of dimpled and clean airfoils in order to find out the airfoil with the best aerodynamics efficiency. The numerical simulation consists of two stages, first stage is for validation which only involves clean airfoil while another stage is for the main purpose of this research which is the dimpled airfoils. Besides, throughout the whole numerical set up for both stages, the model used is Spalart-Allmaras model. The governing equations of this model are stated in equation (2) to (5) [8].

$$\tilde{S} \equiv S + \frac{\tilde{\nu}}{\kappa^2 d^2}\left[1 - (\tilde{\nu}/\nu)\left[1 + \frac{(\tilde{\nu}/\nu)^4}{[(\tilde{\nu}/\nu)^3 + {C_{\nu 1}}^3]}\right]^{-1}\right] \tag{2}$$

$$f_w = \frac{\tilde{\nu}}{\tilde{S}k^2 d^2}\left[1 + C_{w2}\left(\left(\frac{\tilde{\nu}}{\tilde{S}k^2 d^2}\right)^5 - 1\right)\right]\left(1 + {C_{w3}}^6\right)^{\frac{1}{6}} \{[1 + C_{w2}((\frac{\tilde{\nu}}{\tilde{S}k^2 d^2})^5 - 1)]^6 + {C_{w3}}^6\}^{-\frac{1}{6}} \tag{3}$$

$$f_{t1} = C_{t1} g_1 \exp\left[-C_{t2}\frac{{w_t}^2}{\Delta U^2}\left(d^2 + {g_t}^2 {d_t}^2\right)\right] \tag{4}$$

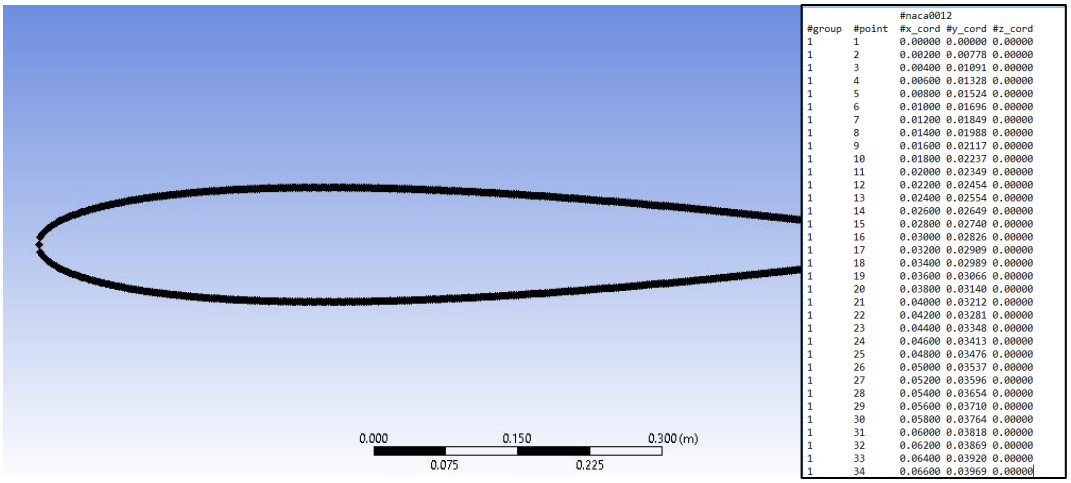
$$f_{t2} = C_{t3} \exp[-C_{t4}(\tilde{\nu}/\nu)^2] \tag{5}$$

where S is the magnitude of the vorticity, d is the distance to the closest wall, d_t is the distance from the point in the flow field to the trip on the wall, ω_t is the wall vorticity at the trip, ΔU is the difference at the field point and that at the trip, $g_t = \min(0.1, \Delta U/\omega_t \Delta x_t)$ where Δx_t is the grid spacing along the wall at the trip. The empirical constants of the Spalart-Allmaras model are: $C_{b1} = 0.1355$, $\sigma = 2/3$, $C_{b2} = 0.622$, $\kappa = 0.4187$, $C_{w1} = 3.239$, $C_{w2} = 0.3$, $C_{w3} = 2.0$, $C_{v1} = 7.1$, $C_{t1} = 1$, $C_{t2} = 0.2$, $C_{t3} = 1.2$ and $C_{t4} = 0.5$ [9].

2.1 Validation

Before the main objective of the research starts, some simulations have ran for validation purpose first. The results of this stage will be compared with the journal paper to ensure that all the settings are correct and acceptable in order to proceed with the main simulations of this research. Therefore, all the settings used here are based on the referred journal paper such as the boundary conditions and model. The validation results will be compared to a journal paper using the similar conditions.

Firstly, for the geometry of the NACA 0012 airfoil, its coordinates have to be very precise as a little flaw may come out with a very inaccurate results. Therefore, the coordinates of NACA 0012 airfoil is sourced from NASA and many data from NASA have proved that the coordinates is perfect. Using the coordinates, the airfoil will be modelled in ANSYS as shown in Figure 6. The chord length of the airfoil is set at 1 m, same with the referred journal paper.



#naca0012

#group	#point	#x_cord	#y_cord	#z_cord
1	1	0.00000	0.00000	0.00000
1	2	0.00200	0.00778	0.00000
1	3	0.00400	0.01091	0.00000
1	4	0.00600	0.01328	0.00000
1	5	0.00800	0.01524	0.00000
1	6	0.01000	0.01696	0.00000
1	7	0.01200	0.01849	0.00000
1	8	0.01400	0.01988	0.00000
1	9	0.01600	0.02117	0.00000
1	10	0.01800	0.02237	0.00000
1	11	0.02000	0.02349	0.00000
1	12	0.02200	0.02454	0.00000
1	13	0.02400	0.02554	0.00000
1	14	0.02600	0.02649	0.00000
1	15	0.02800	0.02740	0.00000
1	16	0.03000	0.02826	0.00000
1	17	0.03200	0.02909	0.00000
1	18	0.03400	0.02989	0.00000
1	19	0.03600	0.03066	0.00000
1	20	0.03800	0.03140	0.00000
1	21	0.04000	0.03212	0.00000
1	22	0.04200	0.03281	0.00000
1	23	0.04400	0.03348	0.00000
1	24	0.04600	0.03413	0.00000
1	25	0.04800	0.03476	0.00000
1	26	0.05000	0.03537	0.00000
1	27	0.05200	0.03596	0.00000
1	28	0.05400	0.03654	0.00000
1	29	0.05600	0.03710	0.00000
1	30	0.05800	0.03764	0.00000
1	31	0.06000	0.03818	0.00000
1	32	0.06200	0.03869	0.00000
1	33	0.06400	0.03920	0.00000
1	34	0.06600	0.03969	0.00000

Figure 6. Model of NACA 0012 in ANSYS

For the validation stage, only clean airfoil will be simulated. Therefore, the airfoil is then surrounded by a C domain as shown in Figure 7. The size and geometry of the C domain is modelled according to the referred journal paper in order to compare the results later on.

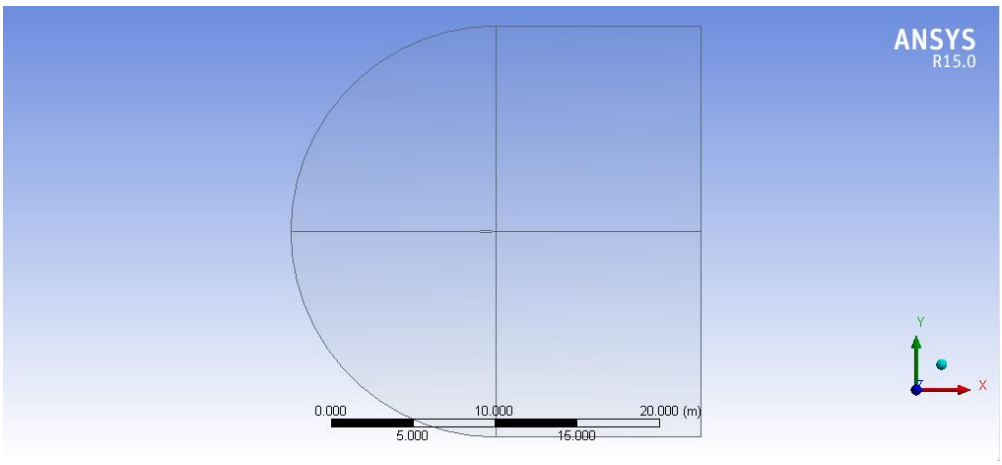


Figure 7. C Domain

After the airfoil and the C domain have been modelled, the settings shown in Table 1 below are used to mesh the model. This is to obtain a minimum mesh skewness which provides maximum skewness of 0.67 which is acceptable. Figure 8 shows the completed mesh of the C domain and also around the airfoil.

Table 1. Mesh Settings for Validation

	Overall C Domain Surface	
Mesh Control	Mapped Face Meshing	
Mesh Method	Quadrilaterals	
Constrain Boundary	No	
	C curve	Wall around airfoil
Numbers of Divisions	200	400
Behavior	Hard	Hard
Bias	No	Yes
Bias Factor	-	150

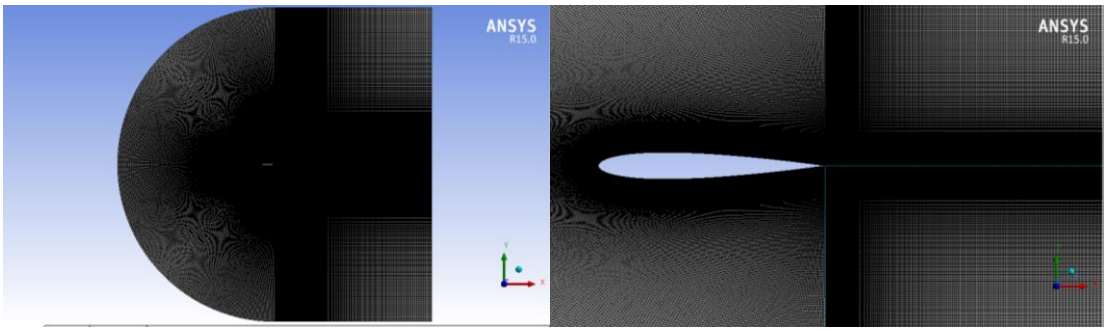


Figure 8. Meshing of Airfoil and C Domain

After meshing, the boundary conditions and the solver settings are set according to Table 2, following the settings in the journal paper in order to compare the results. After everything is well configured, the preparation for the simulation is done and ready to be run. The simulation results will then be compared with the journal paper and will be further discussed below.

Table 2. Boundary Conditions and Solver Settings for 0 Angle of Attack.

Modal	Spalart-Almaras
Inlet x-velocity	43.82m/s
Inlet y-velocity	0m/s
Outlet Gauge Pressure	0
Solution Method Scheme	SIMPLE
Solution Initialization	Standard Initialization, compute from inlet

2.2 Actual Simulations (Dimpled Airfoil)

After the simulations for validation are completed and compared with the journal paper, the settings for the simulations are then set and confirmed as the purpose of validation stage is to make sure all the settings are correct. Therefore, the set up for the actual simulations are all similar with the validation simulations. The only difference is in main simulations, the airfoil is dimpled and more work is needed for meshing. This will be further explained. Besides, as mentioned above, this research has 3 different arrangements of dimples, which are top dimpled surface, bottom dimpled surface and both top and bottom dimpled surfaces as shown in Figure 9.

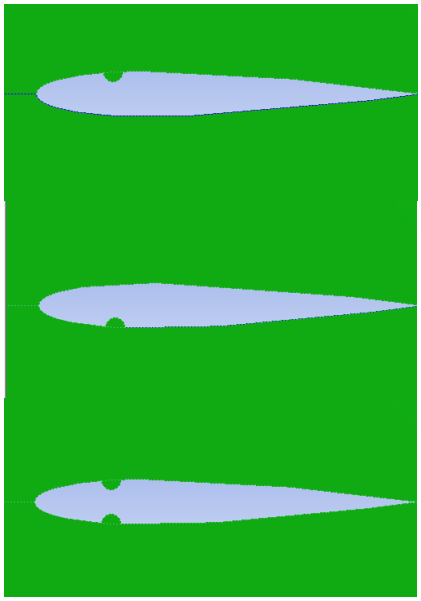


Figure 9. Top, Bottom and Both Top and Bottom Dimpled Surfaces

Besides, the geometry is slightly different in the actual simulation compared with the validation. The whole model is scaled down in a factor of 0.1 to make the airfoil has a chord of 0.1 m. After all the airfoils are modelled, the following meshing settings are applied for all the airfoils to ensure that the skewness does not exceed 0.97 as followed in the validation stage. The settings are slightly different than the validation stage as this model is scaled down. The meshing gives a skewness of 0.75. The meshed airfoil is shown in Figure 10.

Table 3. Mesh Settings for Actual Simulations

	Overall C Domain Surface		
Mesh Control		Mapped Face Meshing	
Mesh Method		Quadrilaterals	
Constrain Boundary		No	
	C curve	Wall around airfoil	Dimple
Numbers of Divisions	50	150	50
Behavior	Hard	Hard	Hard
Bias	No	Yes	No
Bias Factor	-	150	-

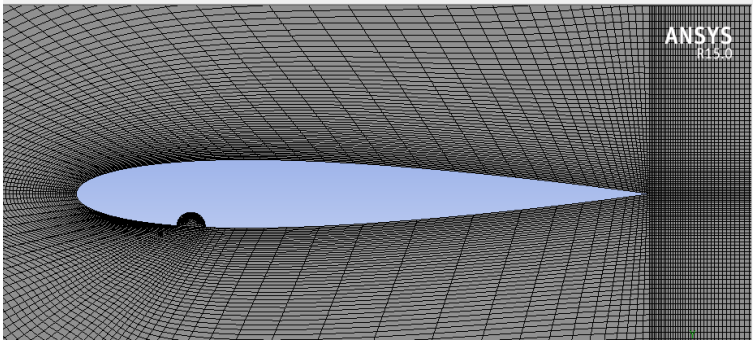


Figure 10. Meshed Dimpled Airfoil

As the model has been successfully meshed and the quality of the mesh has checked and passed, the following boundary conditions and solver settings are used to solve the model. It is slightly different with the validation stage especially the inlet velocity, instead of 43.82 m/s, 10 m/s is used for 0 angle of attack as that is within the range of the wind tunnel that will be used for future experimental testing.

Table 4. Boundary Conditions and Solver Settings for 0 Angle of Attack

Modal	Spalart-Almaras
Inlet x-velocity	10 m/s
Inlet y-velocity	0 m/s
Outlet Gauge Pressure	0
Solution Method Scheme	SIMPLE
Solution Initialization	Standard Initialization, compute from inlet

For this research, 4 conditions for each scenario (top, bottom, top and bottom surfaces) will be simulated, which are 1, 2, 3 and 4 dimples will be modelled on the airfoil. The dimples will be placed in an arrangement of 20%, 40%, 60% and 80% of the chord length as shown in Figure 11 to 13. Figure 11 shows the specific dimensions which are similar to Figure 12 and 13.

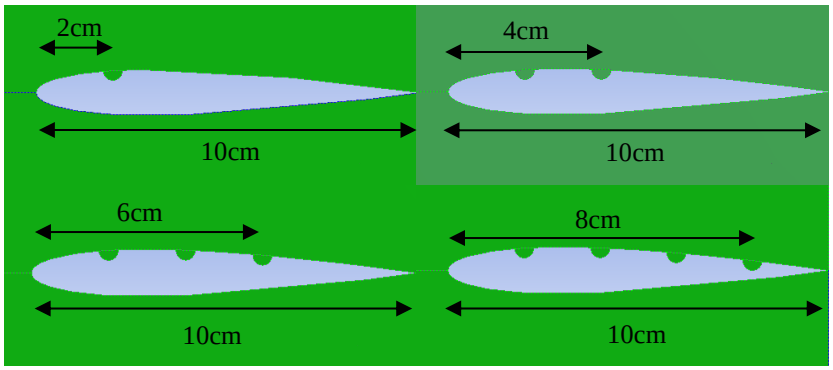


Figure 11. 4 Different Arrangements of Dimples for Top Surface Dimpled Airfoil

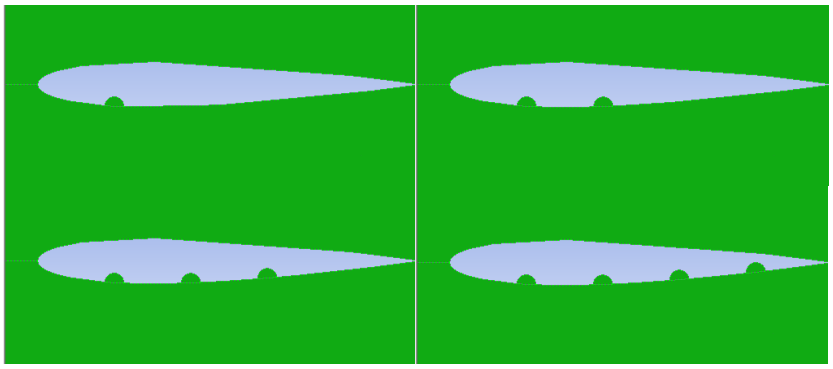


Figure 12. 4 Different Arrangements of Dimples for Bottom Surface Dimpled Airfoil

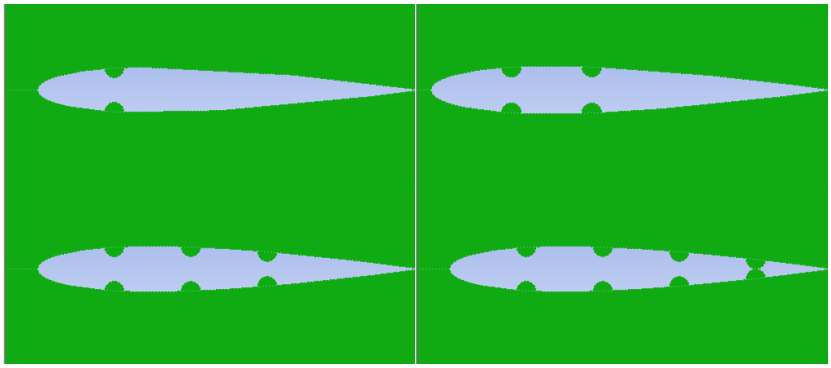


Figure 13. 4 Different Arrangements of Dimples for Top and Bottom Surfaces Dimpled Airfoil

3.0 Results and Discussions

For the validation stage, the inlet velocity used is 43.82 m/s because the results here need to be validate with the journal paper. Therefore, the Reynold number used must be the same in order to compare. To have a same Reynold number, Re, which is 3×10^8, the following equation (5) is used.

$$Re = \frac{\rho v d}{\mu} \tag{5}$$

Where ρ is the density of air, v is the inlet velocity, d is the chord length of the airfoil while μ is the dynamic viscosity of the air. The following settings as shown in Table 5 are used to calculate the Reynold number. After the calculation using equation (5), the inlet velocity used is 43.82 m/s.

Table 5. Settings to Calculate the Inlet Velocity

Reynold Number	$\mathbf{3 \times 10^8}$
Density of the Air	$1.225\ \text{kg/m}^3$
Chord Length of the Airfoil	1 m
Viscosity of the Air	$1.7894 \times 10^{-5}\ \text{kg/ms}$

As shown in Figures 12 and 13, when comparing the lift and drag coefficient with the results published in [9], there is a slight difference between the actual simulation and the published results. It shows that when the angle of attack is higher, the more the error between the actual simulation and journal paper. When the angle of attack reaches 10°, the error of percentage for lift coefficient reaches 5.34% while the drag coefficient reaches 24%. This range of errors are still acceptable as the acceptable error is below 30% as mentioned by the supervisor. According to Figures 12 and 13, both the lift and drag coefficients for actual simulation and journal paper possess the same trend, which is an increase when the angle of attack increases.

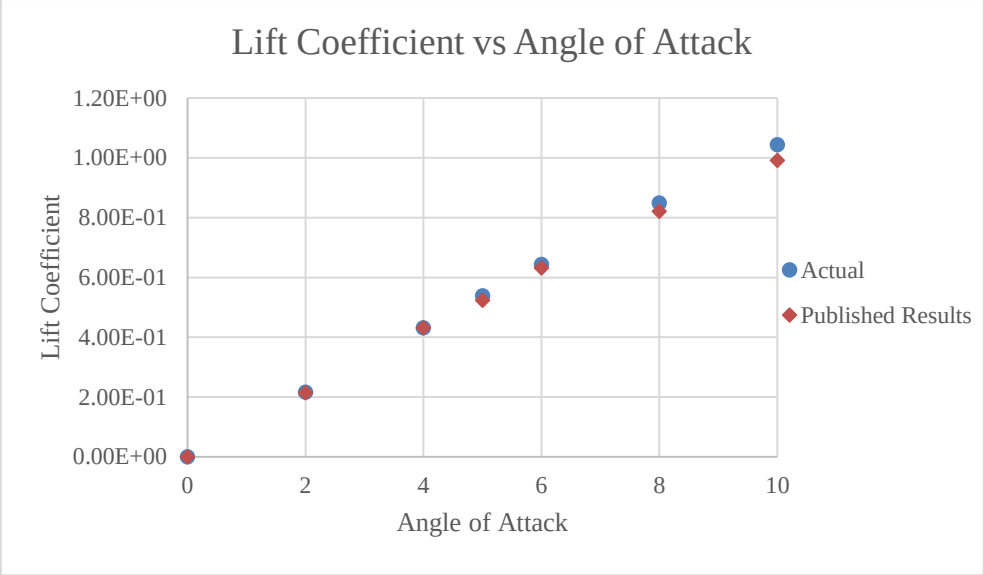


Figure 14. Comparison of Lift Coefficient between Actual Simulation and [9]

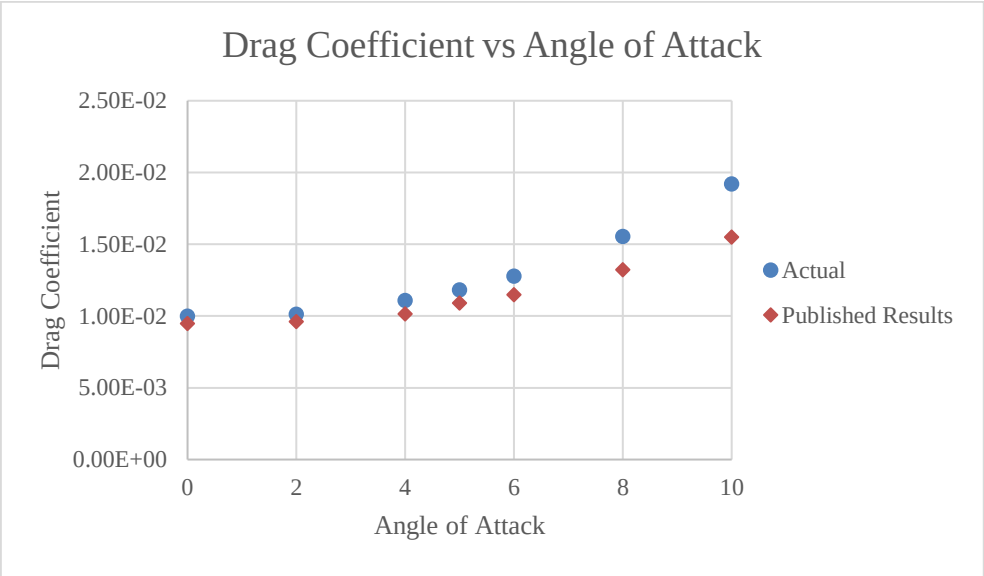


Figure 15. Comparison of Drag Coefficient between Actual Simulation and [9]

For the actual simulation, which is the dimpled airfoils, 4 types of graphs have been produced to study the effect of number of dimples on aerodynamics efficiency. The graphs are lift coefficient against angle of attack (AOA), drag coefficient against AOA, aerodynamics efficiency against AOA and lift coefficient against drag coefficient. Every types of the graphs are divided into 4 scenarios, which are single dimple, double dimples, triple dimples and quadruple dimples airfoil. The acronyms used for these 4 scenarios are tabulated in Table 6.

Referring to Figures 14, it is proven that the lift coefficient is definitely increasing when higher angle of attack is used, despite how many dimples are added. However, adding dimples do not ensure more lift coefficient is produced. Figure 14 (1) and 14 (2) show that only downside dimples will have a higher lift coefficient than the clean airfoil while Figure 14 (3) and 14 (4) show that if the number of dimples go up to

3 and 4, the lift coefficient produced will be even lower than the clean airfoil. Besides, in Figures 14, among all the upside, downside and both up and downside dimpled airfoil, the downside dimpled airfoil always give the highest lift coefficient.

Table 6. Acronyms Used in the Following Sections

Acronyms	Configurations of Dimples
UD	Upside Dimple
DD	Downside Dimple
UDD	Up and Downside Dimples

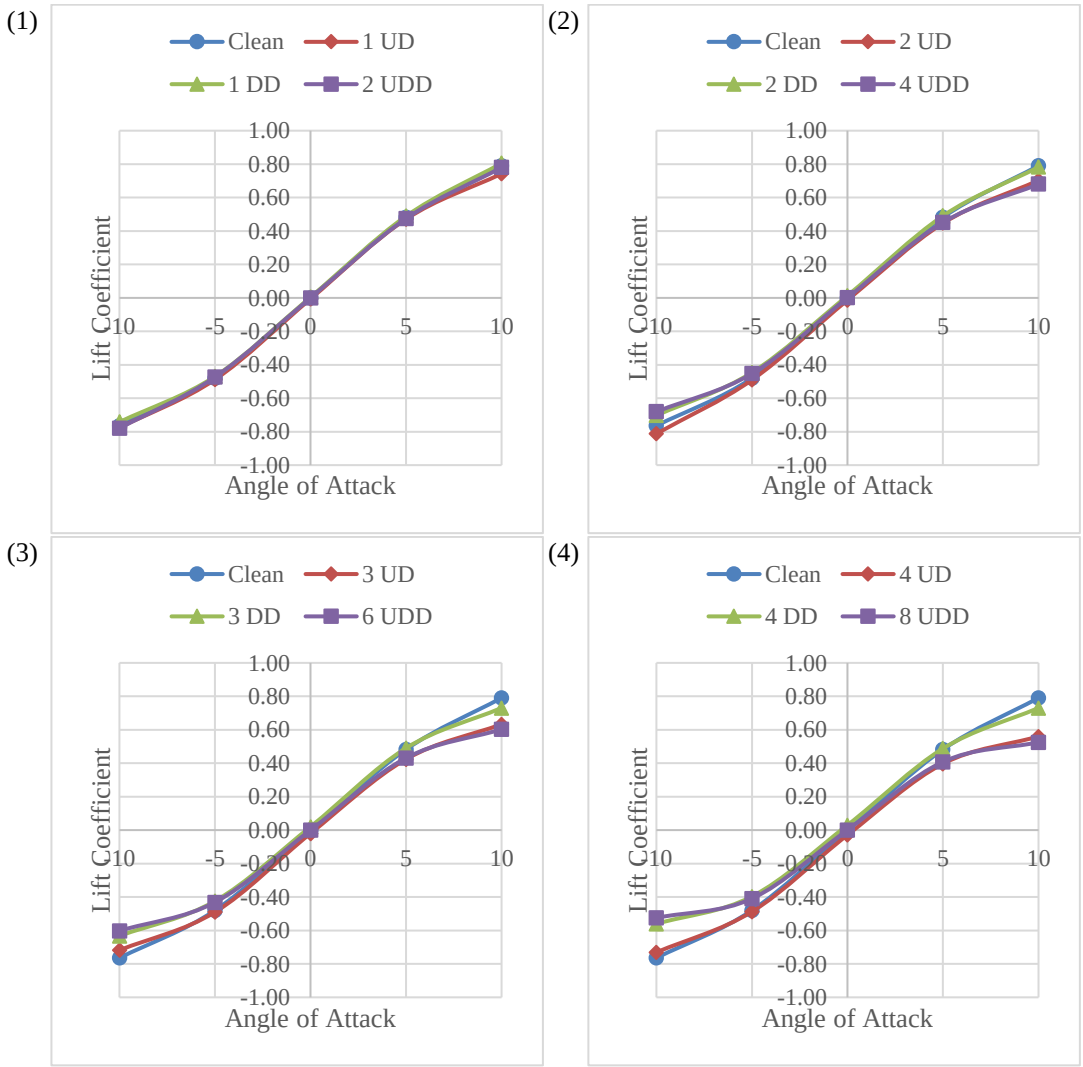


Figure 16. Lift Coefficient vs. Angle of Attack for All Scenarios

As for the drag coefficient, the trend is the same for drag coefficient against angle of attack despite how many dimples are added as shown in Figures 15. It shows that up and down dimpled airfoils have the highest drag coefficient in all cases. It can also be seen that when dimples are added on the airfoil, the drag coefficient increases.

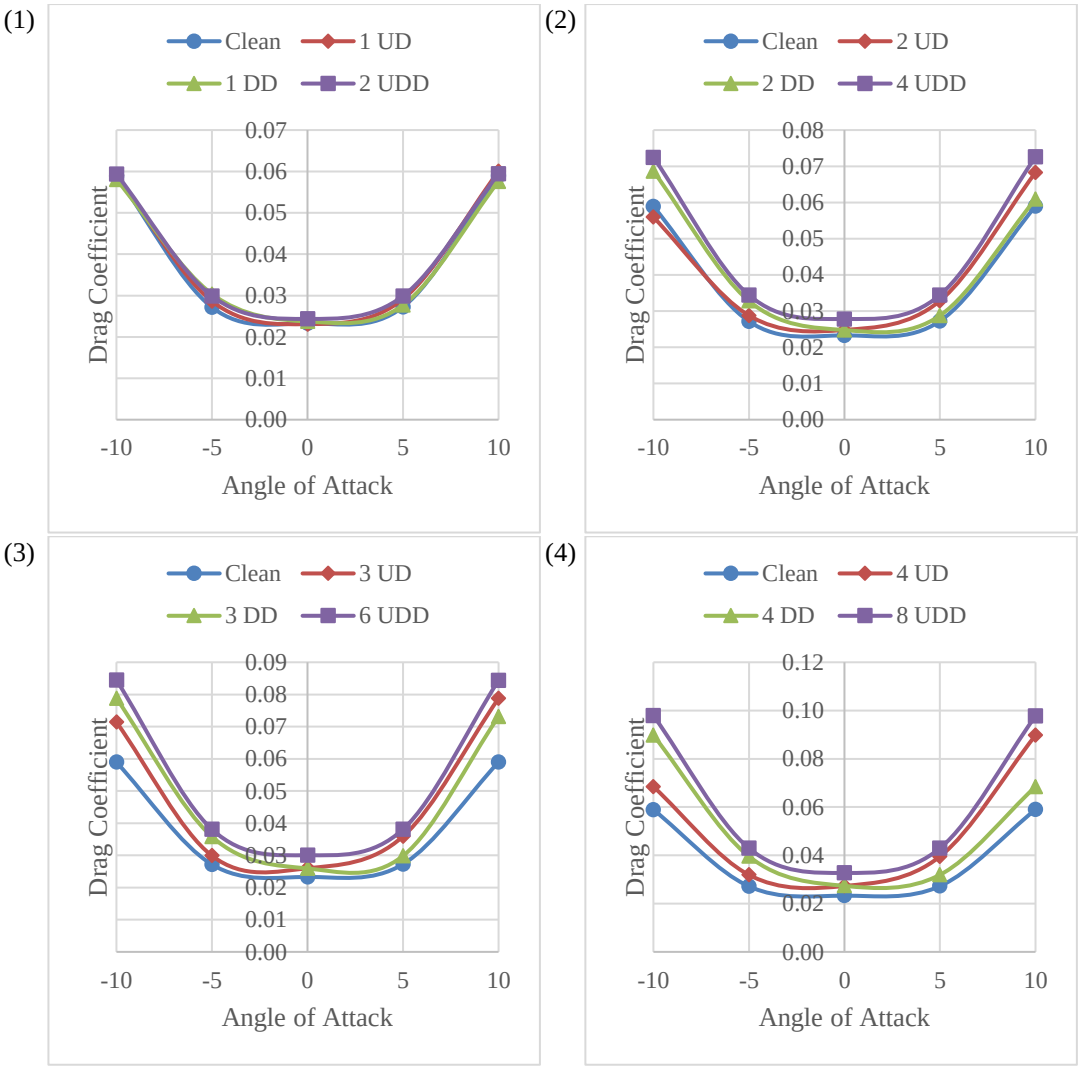


Figure 17. Drag Coefficient vs. Angle of Attack for All Scenarios

Figures 16 shows how the numbers of dimples as well as arrangements of dimples (upside, downside, up and downside) affect the aerodynamics efficiency of the airfoil, which is the main objective of this research. Figure 16 (1) shows that when 1 downside dimple is added on the airfoil, the aerodynamics efficiency increases compared with the clean airfoil while conversely, Figure 16 (2), 16 (3) and 16 (4) shows that when 2, 3 and 4 dimples are added on the airfoil despite the arrangement, the aerodynamics efficiency decreases compared with the clean airfoil. Besides, dimples on both up and down surfaces always produce the least aerodynamics efficiency compared with the others. Therefore, this arrangement is not taken into consideration.

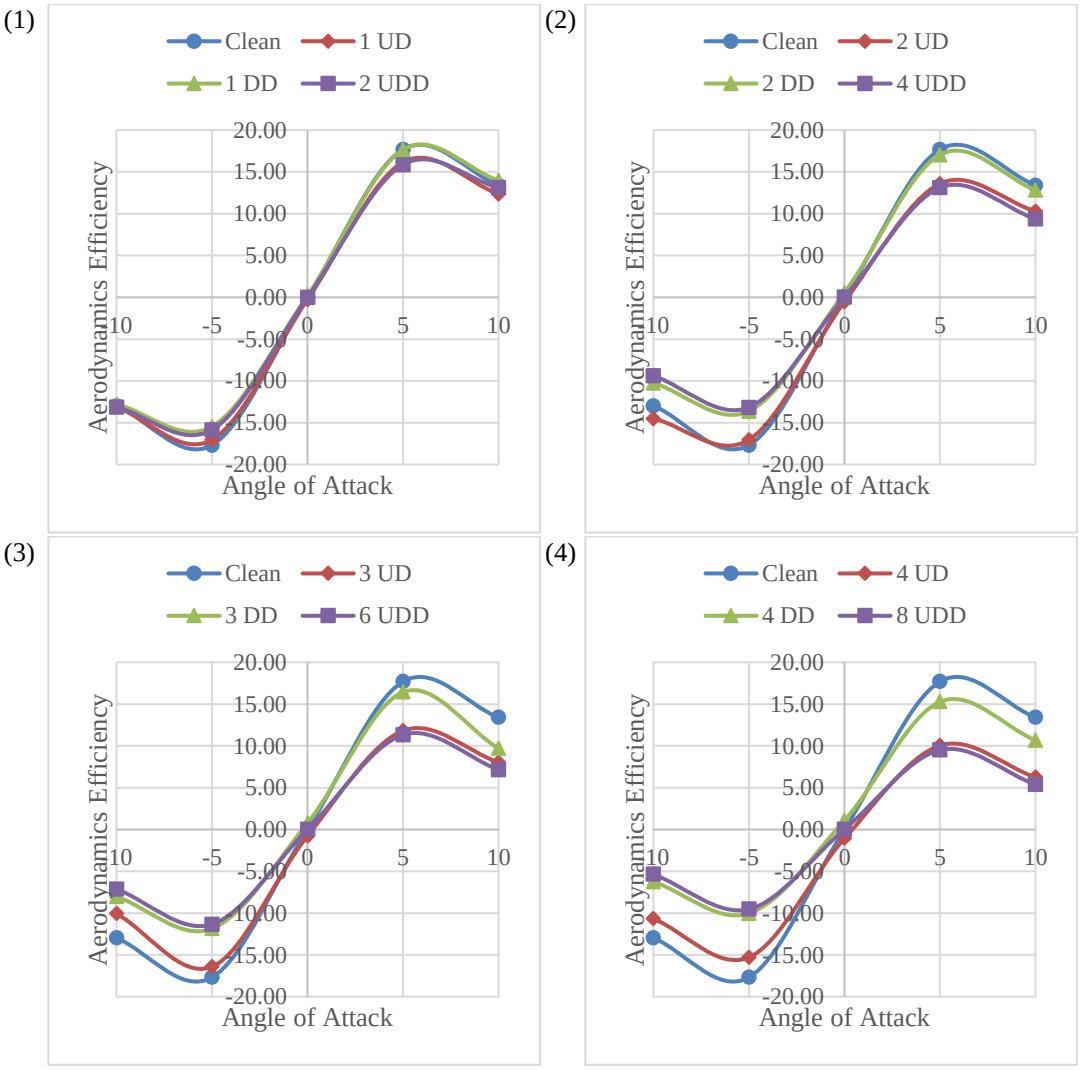


Figure 18. Aerodynamics Efficiency vs. Angle of Attack for Single Dimple

Hence, according to all the data provided and simulated in the figures above, it can be seen that adding more than 1 dimple on the airfoil will decrease the aerodynamics efficiency. Only when 1 dimple is added on the downside of the airfoil will increase the efficiency. All the data has been tabulated in Table 7 and it clearly shows that which conditions of airfoil provides the best aerodynamics efficiency.

Table 7. Tabulated Data of Aerodynamics Efficiency of Different Conditions of Airfoil

Arrangement of Dimples on Airfoil	-10º	-5 º	5 º	10 º
Clean	0	0	0	0
1 Dimple Upwards	+ 0.00%	- 3.62%	- 8.68%	- 7.74%
2 Dimples Upwards	+ 1.39%	- 3.65%	- 23.16%	- 23.26%
3 Dimples Upwards	- 11.90%	- 7.17%	- 33.25%	- 40.08%
4 Dimples Upwards	-22.45%	- 13.51%	- 43.23%	- 53.45%
1 Dimple Downwards	-1.38%	-12.55%	-0.25%	+4.20%
2 Dimples Downwards	-21.03%	-22.99%	-3.64%	- 4.28%
3 Dimples Downwards	-38.08%	-32.93%	-7.09%	- 27.63%
4 Dimples Downwards	-51.88%	-43.26%	-13.63%	- 20.42%
2 Dimple Up & Downwards	+ 1.22%	- 10.38%	- 10.34%	- 2.15%
4 Dimples Up & Downwards	- 27.59%	- 25.60%	- 25.88%	- 30.13%
6 Dimples Up & Downwards	- 45.01%	- 35.88%	- 36.00%	- 46.73%
8 Dimples Up & Downwards	- 58.68%	- 46.08%	- 46.28%	- 59.93%

4.0 Conclusion

In conclusion, using the dimple in terms of the arrangement and number as a means to improve the aerodynamic efficiency shows different results. Adding 1 dimple at the downside of the airfoil will increase the aerodynamics efficiency by 4.18% comparing with the clean airfoil. Besides, this study also found out that when the air is flowing at a higher AOA, the lift coefficient increases. However, the drag coefficient increases as well which cause the overall aerodynamics efficiency decreases. Therefore, the AOA that provides the best efficiency is 5º. However, more numerical analysis can be carried out such as adding more than 4 dimples on the airfoil might result in a different unexpected result. Other arrangements of the dimples can be carried out too such as location of the dimples, shape of the dimples and others to find out the best combination to provide the best aerodynamics efficiency. Besides, higher AOA can be simulated to find out the effect of high AOA on the aerodynamic characteristics for airfoils with dimples. Furthermore, experiment using the wind tunnel can be carried out to compare with the numerical results and confirm the trend of the results for dimpled airfoils.

References

[1] N. Sp- and T. a Talay, “NASA History Division INTRODUCTION TO THE,” *History*, 1975.

[2] E. C. Miller, “Effects on the Boundary Layer Caused by Inclusion of Dimples at Varying Depths,” *J. Aircr.*, vol. 49, no. 4, pp. 969–972, 2012.

[3] S. S. Mahamuni, “International Journal of Aerospace and Mechanical Engineering A Review on Study of Aerodynamic Characteristics of Dimple Effect on Wing International Journal of Aerospace and Mechanical Engineering,” vol. 2, no. 4, pp. 18–21, 2015.

[4] A. Chavarin and M. Rappuhn, “Experimental Comparison of Lift between a NACA 2412 Airfoil and a NACA 2412 Dimpled Airfoil Table of Contents,” 2014.

[5] N. Beratlis, A. Vizard, K. Squires, and E. Balaras, “Effects of Roughness Elements on the Sepration of Laminar Boundary Layers,” no. 2010, pp. 1–6, 2013.

[6] Fastskinz, "Fastskinz," 2009. [Online]. Available: http://fastskinz.com/. [Accessed: 01-Oct-2015].
[7] J. D. J. Anderson, *Fundamentals of Aerodynamics. Third Edition*. 2001.
[8] T. Javaherchi, "Review of Spalart-Allmaras Turbulence Model and its Modifications Spalart-Allmaras Governing Equation," pp. 1–14, 2010.
[9] Douvi C. Eleni, "Evaluation of the turbulence models for the simulation of the flow over a National Advisory Committee for Aeronautics (NACA) 0012 airfoil," *J. Mech. Eng. Res.*, vol. 4, no. 3, pp. 100–111, 2012.

Characterization of Alumina/Y-TZP Ceramic Composites

Y. K. Joshua Theah[1*], W. J. Kelvin Chew[1*], S. Ramesh[2]

[1]School of Engineering, Taylor's University, Taylor's Lakeside Campus, No. 1 Jalan Taylor's, 47500 Subang Jaya, Malaysia.

[2]Center of Advanced Manufacturing and Materials Processing, Department of Mechanical Engineering, Faculty of Engineering, University of Malaya, 50603 Kuala Lumpur, Malaysia.

[*] yoonkean93@hotmail.com; KelvinWaiJin.Chew@taylors.edu.my

Abstract

This study was carried out for the purpose of identifying the effects of different alumina content and sintering temperatures on the mechanical properties (density, hardness and fracture toughness) of the Al_2O_3/Y-TZP composites. The conduct of the experiments began at powder preparation where the powders of 3 mol% Y-TZP and Alumina (Al_2O_3) were mixed into five batches; 0, 5, 10, 20, and 30 wt% of alumina. The mixed powders were then be compacted into green bodies using cold isostatic pressing before pressurelessly sintered at 1250, 1300, 1400 and 1500°C with 2 hours holding time. Two green bodies are allocated for each temperature. After sintering, the advanced ceramics underwent X-ray diffraction (XRD) analysis for phase identification to ensure that its tetragonal phase was more than 70%. The advanced ceramic composites were then grinded and polished before its mechanical properties were determined using Archimedes' principle, Vickers indentation method and Niihara's equation. The obtained results were tabulated into graphs for a much clearer and simpler view. Relative density was found to increase as sintering temperature increases, except for the 30 wt% alumina/Y-TZP composite in which there was a spike in its relative density at temperature 1300°C. The relative density was also found to decrease in its value as alumina content increased. Hardness decreased with higher sintering temperature, with a single exception - 20 wt% Al_2O_3/Y-TZP. In addition, hardness was found to increase as alumina content in the composite increased. As for fracture toughness, it was seen that there was first an increase in the fracture toughness followed by a decrease in the fracture toughness as sintering temperature was increased.

Keywords: Zirconia, alumina, composites, XRD, mechanical properties.

1. Introduction

In the recent years, zirconia-based ceramics have gained a whole lot of attention, because of its potential in numerous applications such as hip prosthesis, cutting tool material, dental restorations and etc. Zirconia (ZrO_2) is the oxidized form of zirconium (Zr), which has 3 natural phases namely monoclinic, tetragonal and cubic that occurs at different ambient temperatures; at room temperature, above 1,170°C and above 2,370°C respectively.

The phase transformation from cubic to tetragonal and back to monoclinic causes a huge amount of stress due to significant volume expansion, which causes the zirconia (ZrO_2) to crack when it is cooling down [1]. The retention of the high temperature phases of zirconia can be made by introducing other oxides such as yttrium oxide or better known as yttria (Y_2O_3) into zirconia. Yttria acts as a stabilizer to stabilize the tetragonal or cubic phases at room temperature. A few other examples of oxides that have been proven effective as stabilizers are calcium oxide (CaO), cerium (III) oxide (Ce_2O_3) and magnesium oxide (MgO) [1]. However, even with a stabilizer, it is still possible for the tetragonal or cubic phase to revert back to its monoclinic phase at any given time if sufficient amount of stress acts on the material [1]. Y-TZP or Yttria-stabilized tetragonal zirconia polycrystals is an advanced ceramic consisting of zirconia that is completely of tetragonal phase. Different amounts of yttria stabilizer content have an impact on the mechanical properties as well as electrical properties of zirconia. For instance, tetragonal zirconia holds the highest mechanical properties whereas cubic phase has the highest electrical conductivity via ionic conduction among the 3 phases [1].

Recently, small amounts of alumina (Al_2O_3) have been found in Y-TZP with improved mechanical properties. Trace quantities of alumina have been known to help in densification, as well as enhancing tensile deformation in superplastic flow [2]. Nonetheless, the underlying mechanism in which the presence of alumina in the microstructure relates to densification and superplasticity still remains unclear. Thus, the objective of the project was to determine the effects of different alumina content and sintering temperatures on the mechanical properties of the Y-TZP ceramic composite. This study investigated the mechanical properties (density, fracture toughness and hardness) possessed by alumina/Y-TZP ceramic composites (0, 5, 10, 20 and 30 wt% alumina) at various sintering temperatures (1250, 1300, 1400, 1500°C).

2. Methodology

2.1 Powder Preparation

Powders of 3 mol% Y-TZP and alumina (Al_2O_3) was mixed to produce 4 batches; 0, 10, 20, and 30 wt% of alumina. Each batch was targeted to weigh 50 g, so calculations were first made to determine the corresponding alumina weight to the weight of the Y-TZP according to the batch ratio mentioned above. After weighing the precise amount of alumina and Y-TZP powders for each of the batches, the alumina powder was placed into a beaker, mixed with approximately 200ml of ethanol before being placed into an ultrasonic bath for 5 minutes. After 5 minutes, the Y-TZP powder was then added into the beaker and placed into the ultrasonic bath again for another 15

minutes. This was to ensure the mixing of the powders was done effectively. The mixture was then poured into an attritor mill, followed by 5 mm diameter zirconia balls for the process of ball milling which crushes the powder into fine powder and enhances the mixture of both powders. The machine was set to run at 500 rpm for 20 minutes. After the milling process, the slurry was poured into a bowl and placed into an oven to dry at 60°C for 12 hours. The dried powder was sieved using a certified fine grade laboratory sieve to ensure the powder was even finer.

2.2 Green Body Preparation

The powders were compacted into green bodies, consisting of disc-shaped ceramic pellets. Each batch of powder was compacted into 8 green samples, weighing consistently at 2.5 g each. The reason as to why 8 samples were made for each batch was because 2 samples were allocated for each targeted sintering temperature, therefore resulting in a total of 40 green bodies. The compaction was first achieved through uniaxial pressing manually followed by second press via cold isostatic press (CIP). In the manual pressing stage, the weighted 2.5g of powder was placed into a specially made cylindrical die before being placed into the hydraulic press bench. The compression pressure was set to a close approximation of 5 MPa for about 10 seconds. After each batch completed the first stage, the green bodies were labelled/marked so that it will not get mixed up. As for the cold isostatic pressing, green bodies were placed into the cold isostatic pressing machine and subjected to the pressure of 200 MPa. The CIP ensures that every side of the green body is equally compacted to further improve the density of the green samples prior to sintering.

2.3 Sintering

The green bodies went through conventional sintering using a furnace at four different temperatures; 1250, 1300, 1400 and 1500°C. Each green body was pressurelessly sintered at their respective temperatures with 10°C/min ramp rate and 2 hours of holding time. Holding time only starts after the furnace has reached its designated sintering temperature from ambient temperature.

2.4 X-ray Diffraction

After sintering, the ceramic bodies went through X-ray diffraction (XRD) for phase identification as soon as it cools down to room temperature. The XRD (Rigaku Geiger-Flex diffractometer, Japan) used had Cu-Kα as its radiation source. It was set at a scan speed of 0.5°/min and step scan of 0.02°, which worked at 40kV and 15mA. The 2-Theta range determined was from 20° to 60°. This process was done to check if the Y-TZP still remained in the tetragonal phase, because Y-TZP/ Al_2O_3 can either transform its phase back to monoclinic or even progress into the cubic phase during sintering. If the tetragonal phase was less than 70 % then the whole procedure needed to be redone, starting back at the powder preparations. Whereas, if the tetragonal phase was still above 70%, it can then proceed to the next step. The relative amount of tetragonal and monoclinic phase was determined by using Toraya's equation [3].

$$V_m = \frac{1.311 X_m}{1 + 0.311 X_m} \quad (1)$$

where,

V_m is the volume fraction of monoclinic zirconia
X_m is the integrated intensity ratio

$$X_m = \frac{I(11\bar{1})_m + I(111)_m}{I(11\bar{1})_m + I(111)_m + I(111)_t}$$

(2)

where,

I is the peak intensity and subscripts t and m denote the tetragonal and monoclinic phase respectively.

The volume fraction of (t)-ZrO_2 was determined by;

$$V_t\% = 100\% - V_m\%$$

(3)

2.5 Grinding and Polishing

Next, the advanced ceramic composites were grinded using a grinding and polishing machine. Silicon carbide (SiC) sandpapers were used, gradually from a rougher grade to a smoother one. The specific grades used were 120, 240, 600, 800 and 1200 grit. In order to obtain a mirror surface finish, the grinded samples were subsequently polished using a polishing cloth and synthetic diamond paste of 0.6 µm and 0.1 µm particle grit, in order respectively.

2.6 Mechanical Properties

2.6.1 Density

The bulk density was measured using the water immersion technique based on Archimedes principle. This method was demonstrated using a standard analytical balance (Mettler Toledo Balance AG204, Switzerland) equipped with a density kit and distilled water was used as the immersion medium. The relative density of samples was then determined by correlating its bulk density with the theoretical density of the entire mixture. The bulk density was determined using the Eq. (4) below [4].

$$\rho = \frac{W_a}{W_a - W_w}\rho_w$$

(4)

where,

ρ is the bulk density of the sample
W_a is the weight of the sample in air
W_w is the weight of the sample in water

ρ_w is the density of distilled water

2.6.2 Vickers Hardness

Hardness was determined via Vickers Indentation method, whereby a pyramidal diamond indenter was indented into the advanced ceramic with an applied load of 20 kg using a hardness testing machine (FutureTech, Japan). The load was applied slowly and held in place for 10 seconds. The accuracy and quality of the applied load were set according to ASTM E384-99 [5] and ISO 14705 [6] to obtain the most precise results. Once the indenter was removed, the impression appeared as a square with two diagonals of similar length, as shown in (Fig. 1) below. Both the diagonal impressions, namely D_1 and D_2 were measured using a filar micrometer that was attached to the microscope on the Vickers machine. The values obtained was then placed into Eq. (5) below to acquire its corresponding Vickers hardness values [7].

$$H_v = \frac{1.854P}{(D)^2} \quad (5)$$

Where;

P is the applied load

D is the average diagonals = $(D_1+D_2)/2$

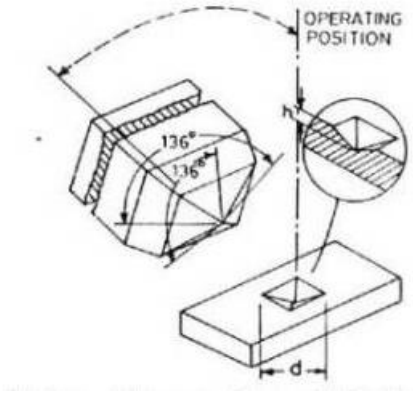


Figure 1. Vickers Indentation method [8].

2.6.3 Fracture Toughness

The fracture toughness, K_{IC} was determined using Niihara's equation [9], shown in Eq. (6) below. The micro cracks formed at the corners of the impression was measured from the same Vickers hardness indentation by using the filar micrometer. The values obtained were then applied into Niihara's equation.

$$\left(\frac{K_{Ic}\phi}{H_v a^{\frac{1}{2}}}\right)\left(\frac{H_v}{E\phi}\right)^{\frac{2}{3}} = 0.035\left(\frac{L}{a}\right)^{-\frac{1}{2}} \quad (6)$$

Where;

K_{IC} is the fracture toughness
E is the Young Modulus of the material
H is the Vickers hardness
L is the average crack length
a is the half indentation diagonal
ϕ is the constraint factor

3. Results and Discussion

The results obtained from the ceramic bodies that underwent X-ray diffraction were tabulated into (Fig. 2) below. To verify that results obtained, the results was compared to the XRD standard for tetragonal zirconia (Fig. 3). The results used here for demonstration and representation were the XRD spectra for 1400°C. It can be seen that the results do match the standard XRD spectrum for tetragonal zirconia, shown in Fig. 3 as the peak intensity occurred at 30° and the second highest intensity at 50°, followed by 60° and 35°. This finding ensured that the results were usable and that the experiment can proceed to the next step which was determining its mechanical properties.

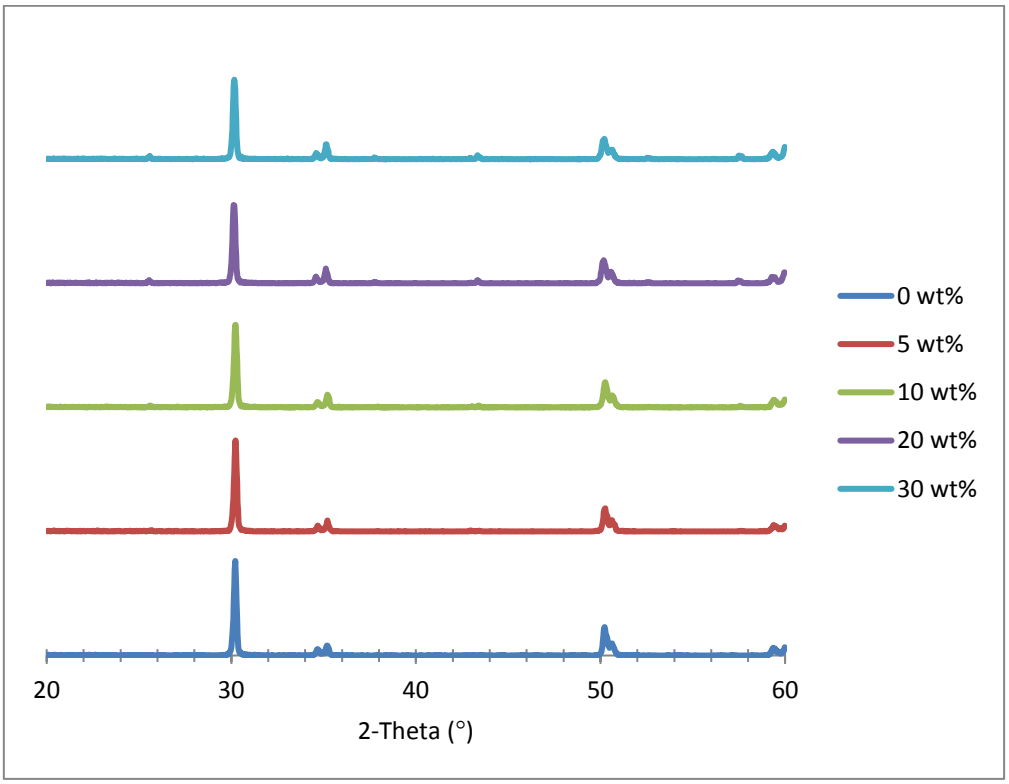


Figure 2. XRD pattern at 1400°C for the Al_2O_3/Y-TZP composites.

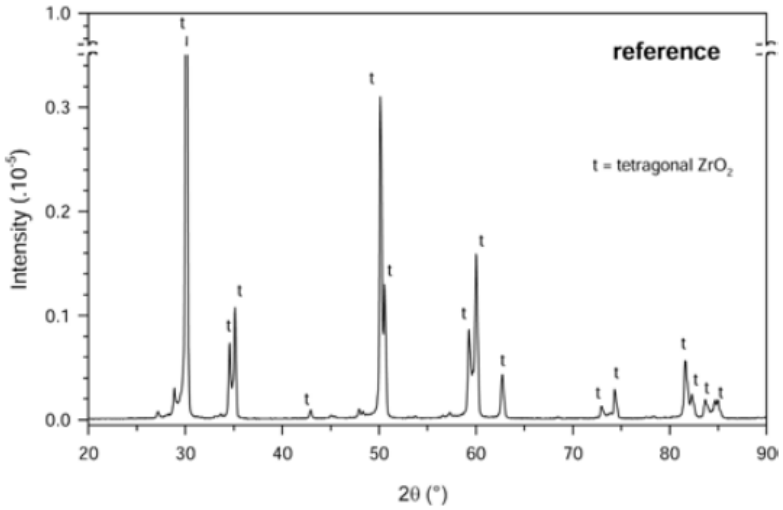


Figure 3. XRD standard spectrum for tetragonal zirconia, Y-TZP [10].

Furthermore, the reason for all the XRD spectra for the different alumina contents at 1400°C being similar was because the volume fraction of tetragonal zirconia (%) was very close and can be seen in Fig. 4. At 1400°C, it can be observed that the tetragonal zirconia phase content range from 98% to 99%. Similar content levels were also attained at the other sintering temperatures, thus the difference was so minute that it didn't affect the XRD pattern much. However, the highest volume fraction of tetragonal zirconia obtained in percentage would be for Y-TZP composite with 5 wt% alumina and sintered at1500°C.

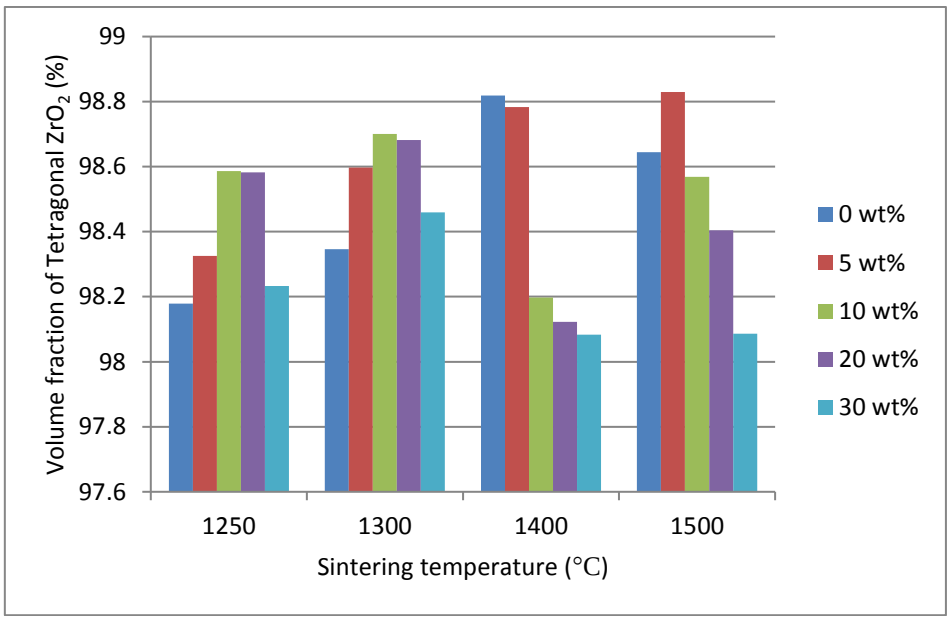


Figure 4. Volume fraction of tetragonal ZrO_2 (vol%) of different alumina/Y-TZP composites from various sintering temperatures.

Fig. 5 shows the graph plotted from the values of relative density (%) achieved for the different compositions with increasing sintering temperatures. The most apparent trend was that relative density tended to increase as sintering temperature was raised. This finding applies for all alumina contents, except for 30 wt%. For this composite, there appeared to be a spike in its relative density when sintered at 1300°C. The overall of the results however corresponds to the data found in [11]. Another pattern found was that with more alumina content, its respective relative density is seen to decrease.

As for hardness, the values obtained for the different composites at two different sintering temperatures, namely 1400 and 1500°C were plotted into (Fig. 6). It can be seen that the trend is a decrease in hardness as the sintering temperature was increased, except for 20 wt% alumina. This result can also be supported with the data from [11], whereby at 20 wt%, hardness increased as sintering temperature became higher. Another observation made here was that hardness tended to increase as the alumina content increased, before decreasing again. Hardness can be seen increasing gradually for 0 wt% to 10 wt% but can be seen to have lower values than at 10 wt% for 20 wt% and 30 wt% alumina. The highest hardness value was obtained through Y-TZP composite with 10 wt% alumina sintered at 1400°C.

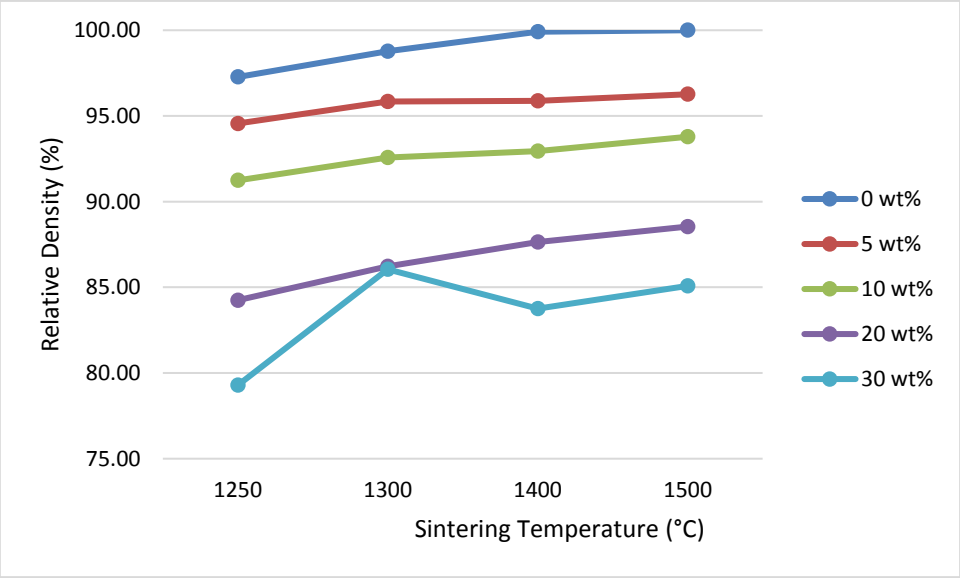


Figure 5. Relative density of the examined composites from different sintering temperatures.

.

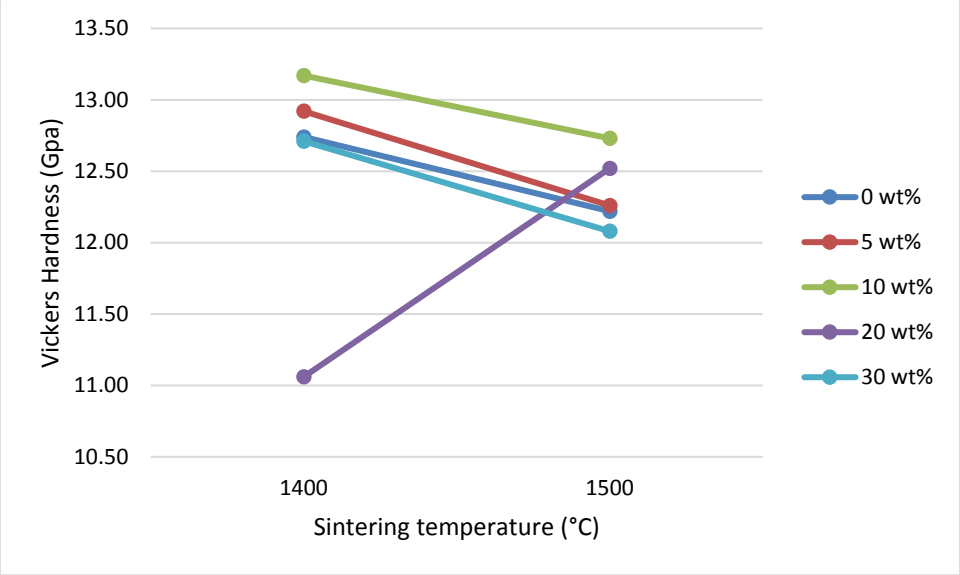


Figure 6. Vickers Hardness as function of sintering temperature for the examined Al_2O_3/Y-TZP composites.

The obtained fracture toughness data was also plotted into a graph as seen in (Fig. 7) for a clearer view. Yet again, the pattern to be seen is that fracture toughness decreases when sintering temperature increases for composites with alumina content ranging from 0 wt% to 10 wt%, whereas the fracture toughness of composites with 20 wt% and 30 wt% alumina can be seen to increase with the rise of sintering temperature. Although it may seem somewhat disordered, data from [11, 12] also suggested that fracture toughness increases with the increase in sintering temperature for both 20 and 30 wt% content of secondary phase. The highest known fracture toughness value in the study was achieved by 30 wt% Al_2O_3/Y-TZP sintered at 1500°C, followed by the zirconia composite with 10 wt% alumina that was sintered at 1400°C.

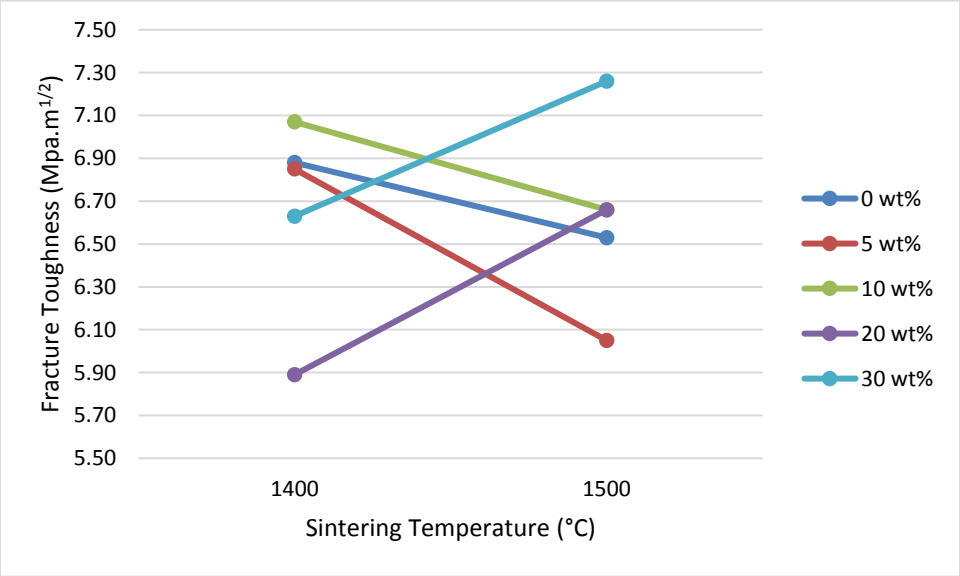


Figure 7. Fracture toughness of the examined composites against applied sintering temperatures of 1400°C and 1500°C.

4. Conclusions

To conclude this paper, there were some evident patterns surrounding the findings of the mechanical properties. First of which is the apparent trend for relative density whereby it increased as sintering temperature increased, except for the alumina-zirconia composite containing 30 wt% Al_2O_3 in which there was a spike in its relative density at temperature 1300°C. Moreover, the relative density was found to decrease in its value as alumina content increased. Regarding hardness, the trend found was that hardness decreases as sintering temperature increases, all except for one which was with the 20 wt% alumina. In addition, hardness was found to increase as alumina content in the composite increased. As for fracture toughness, it was seen that there was first an increase in the fracture toughness followed by a decrease in the fracture toughness as sintering temperature was increased. To be more specific, alumina content of 0 wt% to 10 wt% had its fracture toughness increase as sintering temperature increased, whereas 20 wt% and 30 wt% had its fracture toughness decreasing as the sintering temperature was increased.

References

[1] P. Platt, P. Frankel, M. Gass, R. Howells, and M. Preuss, "Finite element analysis of the tetragonal to monoclinic phase transformation during oxidation of zirconium alloys," *J. Nucl. Mater.*, vol. 454, no. 1–3, pp. 290–297, 2014.

[2] T. S. Suzuki, Y. Sakka, K. Morita, and K. Hiraga, "Enhanced superplasticity in a alumina-containing zirconia prepared by colloidal processing," *Scr. Mater.*, vol. 43, no. 8, pp. 705–710, 2000.

[3] F. Zhang, K. Vanmeensel, M. Inokoshi, M. Batuk, J. Hadermann, B. Van Meerbeek, I. Naert, and J. Vleugels, "Critical influence of alumina content on the low temperature degradation of 2 – 3 mol % yttria-stabilized TZP for dental restorations," *J. Eur. Ceram. Soc.*, vol. 35, no. 2, pp. 741–750, 2015.

[4] K. Dadey, T. Janecek, and A. Klaus, "Dry-bulk Density: Its uses and determination," *Proc. Ocean Drill. Program, Sci. Results*, vol. 126, pp. 551–554, 1992.

[5] M. T. Unit, "Application Note," pp. 3–4, 2003.

[6] I. Std, "International Standard," vol. 2000, 2009.

[7] Z. Roell, "Vickers Hardness Test," *Indentec Hardness Test. Mach. Ltd.*, pp. 8–9.

[8] K. P. Shah, "Hardness testing," *Pratical Maintenance*, 2011. [Online]. Available: http://practicalmaintenance.net/?p=928.

[9] Niihara, K., Morena, R. and Hasselman, D. P. H. Evaluation of KIc of brittle solids by the indentation method with low crack-to-indent ratios. J. Mater. Sci. Lett., 1982, 1, 13–16.

[10] K. Èástková, H. Hadraba, and J. Cihláø, "HYDROTHERMAL AGEING OF TETRAGONAL ZIRCONIA CERAMICS," pp. 85–92, 2004.

[11] N. a Travitzky, a Goldstein, O. Avsian, and a Singurindi, "Microwave sintering and mechanical properties of Y-TZP / 20 wt .%," *Mater. Sci. Eng. A*, vol. 286, pp. 225–229, 2000.

[12] W. Acchar, Y. B. F. Silva, and C. A. Cairo, "Mechanical properties of hot-pressed ZrO2 reinforced with (W,Ti)C and Al2O3 additions," *Mater. Sci. Eng. A*, vol. 527, no. 3, pp. 480–484, 2010.

Effect of Atmospheric Altitude on the Drag of Wing at Subsonic and Supersonic Speeds

Justin Moo Xian Yuen[*/], Abdulkareem Sh. Mahdi Al-Obaidi[/]

School of Engineering, Taylor's University, Malaysia

[*]*jusm12@hotmail.my*

Abstract

Drag produced by a wing is always aimed to be reduced or kept low. Unfavorable drag force means additional effort is required to carry out work, which generally reduces the efficiency of the wing. Three of the variables affecting the drag force generated by a wing are the condition of fluid that it is operating in, the travelling velocity and the drag coefficient which depends on the wing's aerodynamic geometry. The operational condition of missile involves rapid gain in altitude, hence the effect of altitude is expected to the most significant for missile flight compared to other aerial vehicle. Operational speed of missile ranges from subsonic to supersonic speed where the occurrence of shock wave causes a spike in overall drag coefficient, hence the drag coefficient is highly unsuitable to be considered as a constant. Study was carried out to determine the effects of altitude on the three variables which determines the drag force. Through analytically approach, the factors affecting the variables generally were caused by the changing air parameters with altitude. Atmospheric modelling is developed according to the International Standard Atmosphere which considers the earth's atmospheric layer up to 105 km above sea-level and separates them into different layers. Through calculation, it is determined that the kinematic viscosity of air affects the drag coefficient the most through Reynold's number. Whereas density of the atmospheric air contributes the most when drag is considered as a force. The effects of attitude show that the drag coefficient of wing was increased by 10.8%, 45.8% and 139.2% at 25 km, 50 km and 75 km above sea-level. The results when drag coefficient of the wing is considered as a function to altitude and Mach number were calculated based on semi-empirical formulation. The resultant drag coefficient were used to analyse for trajectory and flight performances using an in-house developed MATLAB computer program. Trajectory plot shows significance variation in trajectory compared to different consideration of drag. (Drag = 0, Drag coefficient = *f*(Altitude and Mach number) and Drag = Constant).

Keywords: Drag coefficient, atmospheric altitude, trajectory, subsonic and supersonic, wing.

Nomenclature

Λ_{LE}	Leading edge sweep angle
$R_{Specific}$	Specific gas constant (J K^{-1} kg^{-1})
μ	Dynamic viscosity (Ns/m^2)
A	Area (m^2)
AR	Aspect ratio
b	Wing span
C_D	Drag coefficient
$C_{D\ Parasite}$	Parasite drag coefficient
C_{Db}	Base drag coefficient
C_{Df}	Skin friction drag coefficient
C_{Dw}	Wave drag coefficient
C_f	Skin friction coefficient
C_p	Base pressure coefficient
c_r	Root chord
c_t	Tip chord
C_w	Theoretical wave drag parameter
h	Height (m)
Ma	Mach number
Re	Reynold's number
S_{Ref}	Referenced area (m^2)
S_{wet}	Wing wetted area (m^2)
t	Wing thickness
P	Pressure (Pa)
T	Absolute temperature (K)
g	Gravitational force (m/s^2)
m	Mass (kg)
v	Volume (m^3)
ν	Kinematic viscosity (m/s^2)
ρ	Density (kg/m^3)
ϕ	Wing sweep correction factor

1. Introduction

Air properties such as temperature, pressure and density change with altitude, hence the drag force experienced by a wing also varies with altitude [1]. This is due to the air being a form of gas, where it can be expanded and compressed depending on pressure and temperature [2]. Both temperature and pressure of the atmospheric air changes with altitude. It is determined that pressure have a dominant effect on density as compared to temperature, this is due to the greater decreasing rate of atmospheric pressure with altitude. Hence it can be said that density decreases exponentially with altitude [2]. The effects of the decreasing density and dynamic viscosity with altitude, results the increase in the drag coefficient (C_D) of the wing due to lower Reynolds number [3].

The atmosphere also contributes to the total drag force experienced by the wing. The operating Mach number of the wing effect the overall C_D of the wing. It is determined that especially during transonic speed ($0.8>Ma>1.2$) the wave drag coefficient (C_{Dw}) have a significant effect on the total C_D of the wing due to the occurrence of shock wave, hence causing a spike in C_D [4]. The travelling Mach number is the ratio of the traveling velocity of the body to the speed of sound. The speed of sound generally changes with temperature, hence we can say that the Mach number of the wing is a function to altitude as well [5].

Wing geometry effects the total C_D of the wing. Wings with large thickness for example have an increasing effect on the form drag due to the larger pressure variation around the wing [6]. According to the Prandtl-Schlichting formulation the local skin friction of an airfoil can be determined by introducing Reynold's number into consideration [7]. The Reynold's number considers the length of the wing with the consideration of its travelling speed and the air viscosity.

Studies also shows that the aspect ratio (AR) is particularly important when the wing travels through transonic speed ($Ma>0.8$). A large AR causes large hike in C_{Dw} and also AR can have significant effect even in subsonic speed due to friction drag [8] [9]. Analysis were carried out to determine C_D of a spherical body at high altitude further certifies that the change in C_D is obvious and significant at higher altitude but the actual effect on missile trajectory is unknown [10]. M. S. Selig, R. W. Deters, and G. a. Williamson [11] determines the effect of low Reynold's Number at subsonic speeds. The experiment result shows visible effect on the overall C_D which is mainly contributed by the skin friction drag at subsonic speed. Research carried out by Al-Obaidi [12] found that through semi-empirical calculation, the rate of increase of C_D have an increasing effect with altitude. The main contribution of the changing C_D is still unknown in the overall trajectory of SSM missile, hence this serves as the main motivation of this study.

Effect of Reynold's number on the trajectory of a shuttlecock was similarly determined using trajectory as a form of visualization and comparison by J. Le Personnic, F. Alam, L. Le Gendre, H. Chowdhury. The comparison of trajectory between two types of shuttlecock made of different material shows that the material which deforms under high Reynold's number at higher speed travels higher and landed further. Conclusion determines that the variation was caused by the lower drag force experienced by the more flexible shuttlecock, as the flexibility at higher speed reduces the C_D at the base of the shuttle cock, hence causing the overall C_D of the shuttlecock to be lower [13].

This shows the effect of variable C_D at affecting the overall trajectory during low subsonic speed but not in supersonic speed.

M. S. Selig, R. W. Deters, and G. a. Williamson shows the effect of Reynold's number ranging from 100,000 to 500,000 on C_D, which is seem to be more beneficial in modern day's flight setup such as Unmanned Aerial Vehicle (UAV), commercial aircraft as well as the motorsport application which only operates through subsonic speeds. Through their experimental study carried out by using the wind tunnel, it is found that Reynold's number does have an effect on the overall C_D of an airfoil. The results were compared between Reynold's number of 100,000 being the lowest, which results in the highest C_D. At higher Reynold's number of 500,000 which indicates higher operating speed, the C_D is lowest [11]. Both experiments are carried out with the same setup and experimental parameters. This study further proves the effect of Reynold's number to C_D of a wing. But this study still lacks the analysis on the actual drag force which is the aimed to be kept at a low at all times as well as on a single wedged wing designed to operate up to supersonic speeds.

Therefore, it is important to consider the factors affecting the drag force experienced by the wing which eventually results a changes in trajectory [14]. Major factors known as air parameters, wing geometry, Mach number, C_D and even gravitational forces is taken into consideration when simulating to determine its trajectory and flight performances. Mathematical models and sub-programs are developed using MATLAB to analyze the change of these factors with altitude. Actual flight setup where initial trajectory controls as well as full rocket engine modelling which simulates closely to actual engine performance was considered into the overall analysis. The results from the numerical analysis are visualized and compared with different considerations where $C_D = 0$, $C_D =$ Constant and $C_D = f$ (Altitude) through trajectory and performance plots. The motivation of this project, though it may be small but will be impactful especially in missile trajectory where the slightest variation in the trajectory may affect the result completely.

2. Methodology

Analytical method is used to determine factors affected by altitude which is numerically analysed using mathematical equations, data extraction from semi-empirical tables. Analysis were carried to closely model each of the atmospheric layers where air parameters were calculated. C_D of the wing is calculated by using part of the output from the atmospheric modelling combined with flight condition and parameters such as the Mach number. Semi-empirical data acquired through combination of theoretical and experimental data for a typical surface-to-surface missile (SSM) were used to closely estimate for C_D. The loop of calculations are carried with the aid of computer program which is able to numerically calculate each of the parameter affected by the changing altitude. Calculation includes extensive data extraction from graphs using several degree of cubic spline interpolation method based on the operating condition of the wing. These factors determined change throughout the flight time were analysed by solving basic equations of motion which analyses the 3-DOF of the body. Effects of the changing variables, due to atmospheric parameters and the aerodynamic characteristic C_D of the wing with altitude are visualized and compared with several other flight conditions to assess their individual effect on the overall trajectory. Comparison were made where drag force is not considered throughout the flight (Drag = 0), the

aerodynamic drag characteristic C_D is considered constant (C_D = constant) and lastly which is the main objective of this study where atmospheric parameter and drag characteristic of the wing as a function of altitude. ($C_D = f$ *(Altitude and Mach number)*).

2.1 Equations of motion

The trajectory analysis of the body under different consideration of drag coefficients were carried out by solving the equations of motion, which serve as the main framework of the study. The changing variables determined are the air parameters and C_D are used to calculate for the net force. Newton's second law states that the acceleration of an object is produced by a net force directly proportional to the magnitude of the net force in the same direction as the net force, and inversely proportional to the mass of the object. This further signifies the importance to closely simulate the missile'schanging mass due to fuel consumption. Although acceleration from the rocket engine will propel the body up to speed, but the effects of decreasing fuel mass is required to improve the accuracy and the realistic effect of the analysis. Displacement, velocity and the acceleration of the missile are calculated using basic equations of motion shown below [15]:

$$Acceleration = \frac{F_{net}}{mass} \tag{1}$$

$$Velocity = v_{initial} + at \tag{2}$$

$$Displacement = s_{initial} + vt + \frac{1}{2}at^2 \tag{3}$$

The acceleration and deceleration of the body throughout the flight varies, caused by the changing drag forces and mass of the missile. Hence, the resultant velocity of the missile varies throughout the flight. The drag force experienced by the missile at any moment during the flight is calculated using the equation:

$$F_{Drag} = \frac{1}{2}\rho C_D A V^2 \tag{4}$$

The equation of drag force depends on several parameter density (ρ), velocity (V) and drag coefficient (C_D) which is known to be changing throughout the flight. Hence, we can say that the drag force experienced by the body is a function of altitude.

$$F_{Drag} = f(Altitude) \tag{5}$$

$$F_{Net} = F_{Thrust} - F_{Drag} \tag{6}$$

The net force (F_{net}) exerted on the body includes the total of drag force and the thrust (F_{thrust}) which is propelling the body through the atmosphere. Hence the net acceleration at a specific moment of the missile is determined. With the combination of all these information, the analysis of the trajectory can be carried out.

2.2 Parameter setup and assumptions

In this study, only the isolated wing is considered in analysing the effects due to altitude. The consideration on wing alone eliminates the effect of missile body, wing to body interference and body to wing interference, which requires more time and knowledge

to analyse. The computer program was developed in a way which can be easily altered to make relevant adjustment and different flight consideration to be used to analyse for different flight parameter such as the wing configuration. The missile's wing configuration and design varies according to the missile's operational purposes. As for this study, a typical SSM configured wing is selected for analysis as it serves as the baseline configuration for all the SSM [16]. The SSM wing is a single wedged wing which is able to operate in subsonic and supersonic speed. The detailed aerodynamic characteristic of the wing is shown in Figure 1. Semi-empirical data for the SSM wing were obtained through the USAF DATCOM missile software [17]. These data which are usually classified and difficult to be obtained were accessible by the supervisor of this study, Al-Obaidi [12], hence the decision to use the SSM configured wing for this study. The SSM wing generally served as a medium to visualize and compare the effects of altitude on aerodynamic performances.

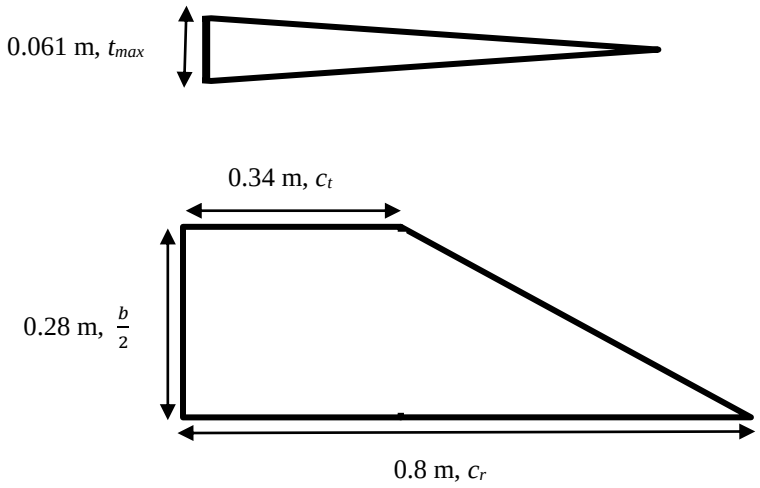


Figure 1: SSM Configured wing geometry.

Other than the wing's configuration, the atmospheric parameters also affects the aerodynamic performance of a wing. According to the latest U.S Standard Atmosphere 1976 which models the atmospheric air parameters density, pressure, temperature and viscosity of the earth's atmosphere. These mathematical models produced fundamentally based on several assumptions. The vertical pressure distribution which relates pressure, density to altitude as well as the atmospheric air as an ideal gas which relates pressure density and temperature [18]. Hence, by utilizing these assumptions for different atmospheric layers, the complete modelling of the atmosphere can be produced using computer program, the calculations were carried out based on Eqs. (7) and (8). The atmospheric model was then included into the main framework which simulates the missile flight by solving the equations of motion. As altitude increases, the gravitational force of the earth exerted on the body decreases due to the increasing radius to the centre of the earth [19]. Hence, the changing gravitational force with altitude is also taken into consideration during simulation.

$$\Delta Pressure = -\rho g \Delta h \tag{7}$$

$$Pv = mR_{Specific}T \tag{8}$$

2.3 Semi-empirical approach

Semi-empirical formulas and data are used to ensure that the simulation is carried out as realistic as possible without carrying out actual flight experiment in this study. The data used and produced are from the DATCOM missile software, and the formulation according to these data are taken from [20], [21], [22], [23] and [12]. The computer program developed for this study contains all the relevant equations and data required to determine the total C_D of the wing at different conditions such as travelling Mach number and the kinematic viscosity of atmospheric air.

The formulas developed are shown below where the total C_D is made up of 3 major component skin friction drag coefficient C_{Dfr} , wave drag coefficient (C_{Dw}) which exist at transonic and supersonic speed and lastly, base drag coefficient (C_{Db}) which is mainly affected by the wing thickness.

$$C_D = C_{Dfr} + C_{Dw} + C_{Db} \tag{9}$$

2.3.1 Skin friction drag

The skin friction drag coefficient can be calculated though the following equation with C_{Dfr} known as the skin friction coefficient of the wing. C_f is the primary skin friction factor determined using the Prandtl-Schlichting formulation which is combined with considers the factors known to manipulat the actual skin friction C_{Dfr} [7]. The consideration includes the wing thickness factor, η_t which results higher C_{Dfr} when the wing is thicker. The area of the wing wetted by the air which can be directly related to the skin friction factor, where larger area wetted by the fluid results larger skin friction [24]. This method which considers the factors of wing geometry allow accurate calculation of the skin friction drag coefficient:

$$C_{Dfr} = C_f \eta_t \frac{S_{Wet}}{S_{ref}} \tag{10}$$

2.3.2 Wave drag

The wave drag coefficient is known to occur at speed above subsonic due to shock wave, and at this speed the Mach number is known as the drag-divergence Mach number. At this point C_D of the wing becomes very large, typically increasing by a factor of 10 in some cases [25]. The spike in C_D outside subsonic speed is crucial to be considered when simulating in order to accurately and realistically determine the total drag force experienced by the body. C_w is the theoretical wave drag parameter which can be obtained from semi-empirical graphs depending on wing geometry and Mach number. Where A is the aspect ratio of the wing which is constant and depends on wing geometry, ϕ is the wing sweep correction factor and which also depends on the wing geometry. Lastly, K_{pr} is the constant factor for a given sharp-nose profile of the wing, as for the single-wedge SSM configuration wing used in this study, the K_{pr} is equal to 0.25 [20].

$$C_{Dw} = C_w A R t_{max}{}^{-2} [1 + \phi(K_{pr} - 1)] \tag{11}$$

2.3.3 Base drag

The base drag component which is only accounted for wings having a profile with base, such as single-wedge wing. At supersonic speed, the base drag coefficient C_p is known to be related to the average base thickness across the wing $\bar{t}_{base}$. The base drag coefficient can be obtained through graphs produced by [12] as a function to Mach number.

$$C_{Db} = -(C_p)\bar{t}_{base} \tag{12}$$

For calculations when Ma < 1 at subsonic, the drag components consists of pressure drag and skin friction drag only. Hence the total drag component now only consist of parasite drag which is associated with pressure and skin friction component. The parasite drag can be determined by incrementing the flat plate skin friction factor *k*. S_{wet} is the wetted surface area of the wing exposed to fluid flow and C_f skin friction coefficient which can be found through graph by [24] and Eqs. (10). Lastly the *k* factor is formulated in the equation below from a series of graph at [24] and can be calculated using formula below:

$$C_{D\,Parasite} = kC_fS_{wet} \tag{13}$$

$$k = 1 + \frac{2C(\bar{t}_{max})\,(cos\,\Lambda_{LE})^2}{\sqrt{1-Ma^2\,(cos\,\Lambda_{LE})}} + \frac{C^2\Lambda_{LE}(\bar{t}_{max})^2(1+5\,(cos\,\Lambda_{LE})^2)}{2(1-Ma^2\,(cos\,\Lambda_{LE})^2} \tag{14}$$

The coefficient *C* in the *k* factor equation can be determined by the conditions where if $M\cos\Lambda_{LE} > 1$ then $C = 0$ otherwise $C = 1.1$ [24]. Hence, by combining and relating all the equations and graphs where data are extracted through interpolation which is usually time consuming to be carried out manually were computationally determined. Furthermore, in order to increase the accuracy of the analysis, small time intervals is required which requires the entire process to be looped for more than 3000 intervals. This causes the entire process to be extremely time consuming also results significant cost to be analysed manually. The computer program developed in-house through MATLAB is designed to loop the entire calculation process until certain requirement is met where decision can made along the calculation process depending on results and parameters generated from previous loop. The process also significantly reduces the time for analysis. Various results from the calculation can be plotted easily for visualization and comparison.

2.4 Validation of semi-empirical results

The simulated results of the C_D were compared with experimental wind tunnel data for validation. The model was analysed by researcher J. Ferris for subsonic up to transonic speed ($0.6<Ma<1.20$) and by C. Babb and D. Fuller in the supersonic region ($1.5<Ma<4.63$) of a meteorological missile used for high-altitude research activity [26][27]. The geometrical shape and configuration of the missile used is similar to this study. The C_D was determined by experimenting missile with and without fins which operates at zero angle of attack (AOA). By subtracting the overall C_D of the missile with fins with the C_D of the missile without fins, the contribution of fins alone can be estimated. The design of the wing used is replicated as closely as possible according the provided technical data. The aero-dynamical properties were computed at same Mach number and at sea-level. Given the limitation of the MATLAB computer program especially at the subsonic and supersonic transition Mach number, the resultant plot is

notably different at the peak C_D during transonic. The difference in the shape of the wedged wing which is unable to be simulated using the developed program affects the drag characteristic especially at the transonic region where the simulated results produces the lower peak C_D. Overall, the C_D throughout the Mach number behaves similarly with the experimental results with close accuracy even at high Mach number. The travelling Mach number of the missile throughout the flight time is usually in subsonic or supersonic speed. Hence, it can be said that the C_D calculation by the develop program is accurate to be considered. The resultant C_D of the fins alone is plotted and shown in Figure 2.

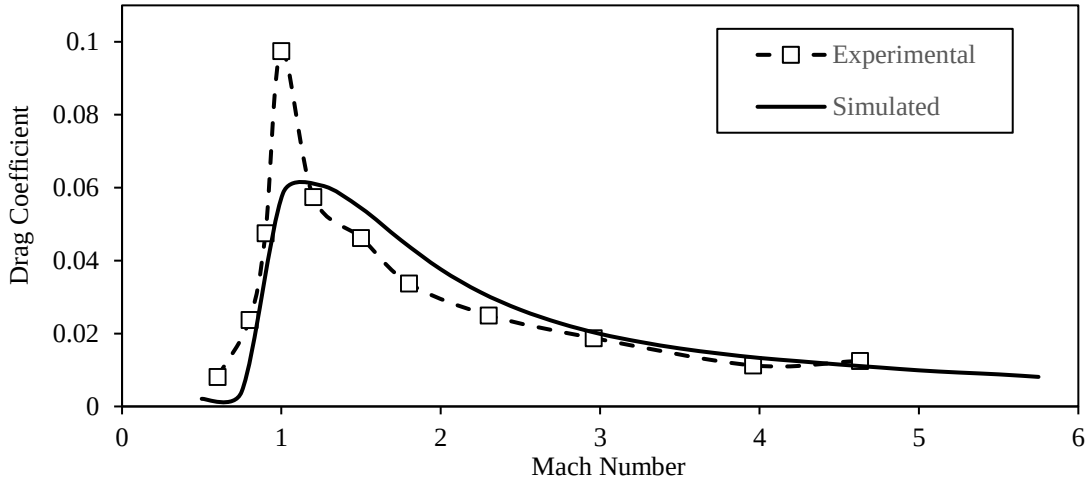


Figure 2: Experimental and simulated drag coefficient as a function to Mach number.

3. Results and discussion

The developed computer program is able to numerically determine the trajectory of the body and produce graphical plots through the output for visualization purposes. In order to make sure the program is accurate and reliable for calculation, validation through manual calculations which involves manual interpolation and table lookup is carried out repeatedly throughout the entire flight time. Then comparisons are made with the results generated by the computer program to validate the accuracy of the program.

The inputs which is required to be determined at the initial of the simulation are the wing geometry, initial launching parameters such as controlled flight angle during powered flight and the changing mass of fuel and rocket engine setup. At the end of the simulation, results shown in Figure 3 to 7 are some of the plots regarding the flight performances of the missile produced. The graph showing C_D of the wing against different Mach numbers at different altitude is determined. The resultant velocity profile of the flight and also the resultant trajectory plot of the body serves as the representation of results of the simulation.

3.1 Drag coefficient

The influence of altitude on the C_D was determined to be contributed mainly by the changing of the kinematic viscosity of the atmospheric air with altitude. Figure 3 shows the resultant drag coefficient for the SSM wing simulated at 0 km (Sea level), 25 km, 50 km and 75 km above sea level. The resulting plot shows that C_D is higher at high altitude. The increase in C_D with altitude is mainly caused by the lower Reynold's number at higher altitude. This is due to the increase in the kinematic viscosity (ν) of the atmospheric air as altitude increases. Kinematic viscosity is the ratio of dynamic viscosity (μ) to the density of the fluid. Although the overall the dynamic viscosity of the atmospheric air increases with altitude, but the rate of density decreases is significantly larger compared to dynamic viscosity. Hence, this causes the kinematic viscosity of the air to increase exponentially with altitude.

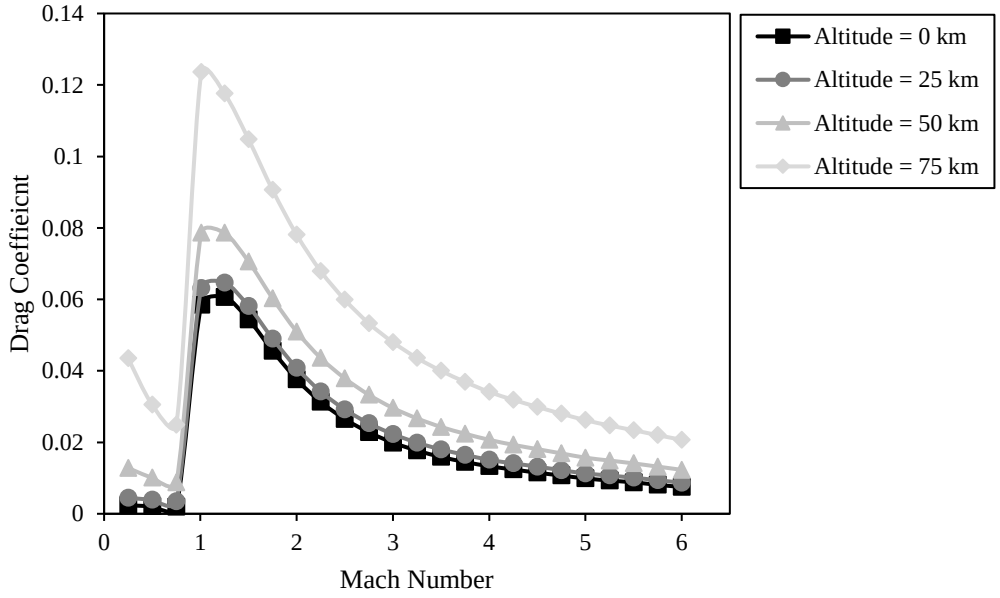


Figure 2: Drag coefficient at different altitudes of an SSM wing.

Table 1 shows the percentage difference of C_D due to altitude change. It can be seen that C_D increases by 10.83% at 25 km above sea-level, 45.8% at 50 km whereas at 75 km, C_D increases by 139.24%, which is more than doubled.

Table 1: Difference of Drag Coefficient with altitude.

Altitude (km)	**Average C_D**	**Difference (%)**
0 (Sea-level)	0.0219	0
25	0.0243	+10.83
50	0.0319	+45.80
75	0.0524	+139.24

Figure 4 shows the increase of C_D reacts exponentially with the increase of altitude. This shows that the effect of altitude on C_D seems to be drastic and is relevant to be

considered during trajectory analysis. Although C_D is affected significantly with altitude but the overall contribution to drag force is less compared to the change of air density with altitude which is more significant compared to C_D.

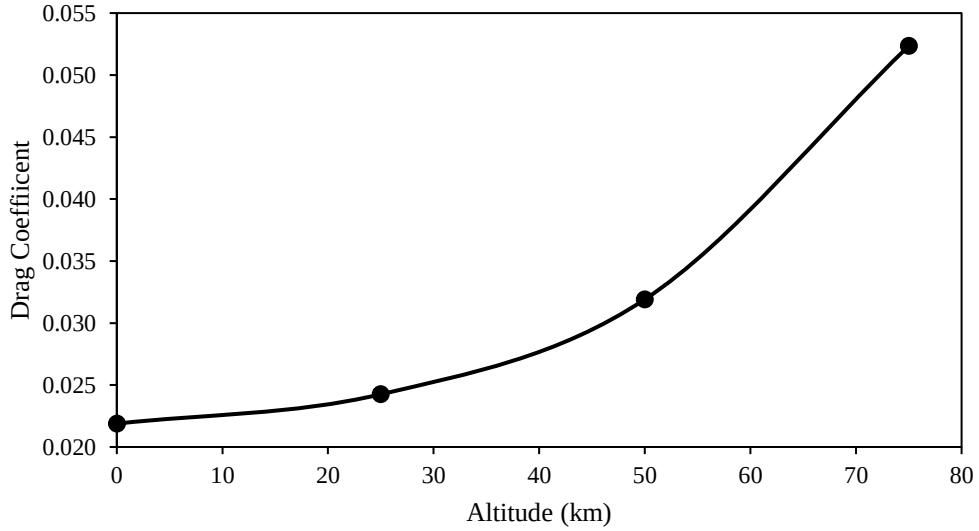


Figure 4**:** Change of drag coefficient with altitude.

3.2 Trajectory plot

Figure 5 shows the result of trajectory simulated with different assumptions of drag. The trajectory when Drag = 0 is analysed where drag caused by air resistance is assumed to be absent, the trajectory is known as the ideal trajectory. The trajectory shows that the body not only travel and land significantly further but furthest compared to the other two analysis when drag is considered. However, the results is known to be unrealistic in real life, but it serves as a visualization to show the significance of drag force in affecting the performance of missile. The other trajectory which shows the body landed the nearest to the launching location is where drag is considered as a constant value which was set at a maximum for both C_D and ρ at 0.0219 and 1.225 kg/m^3 which is usually the consideration for simple flight calculations. During flight, the body experiences constant air density set at sea level which is also the maximum in the earth's atmosphere. Hence, the trajectory resulted to travel the least with the same flight and parameters setup as previous analysis. The third trajectory shows that the body landed between the ideal trajectory and the constant drag trajectory. This trajectory is the main output of this study which is to fully analyse the effect of the changing parameters by altitude on C_D and ρ to the overall trajectory. It is clear that the body is able to travel much further compared to when C_D and ρ is considered as constant. As the body gains altitude with the applied thrust, the drag changes with time and altitude, the higher the altitude the lower the density of atmospheric air. However, previous analysis in Figure 3 shows that as altitude increase, the overall C_D of the wing increases. It may seem strange as the expected drag force at higher altitude is known to be lower hence the favourable high cruising altitude that air craft tends to operate at. It is true that drag as a force is low at higher altitude due to the effect of lower density. When drag is a coefficient C_D, it is shown to increase with altitude. This is due to the low Reynold's Number at higher altitude which indicates that skin friction drag is dominant where more energy is used mostly to overcome the skin friction factor, hence the increase in C_D [28].

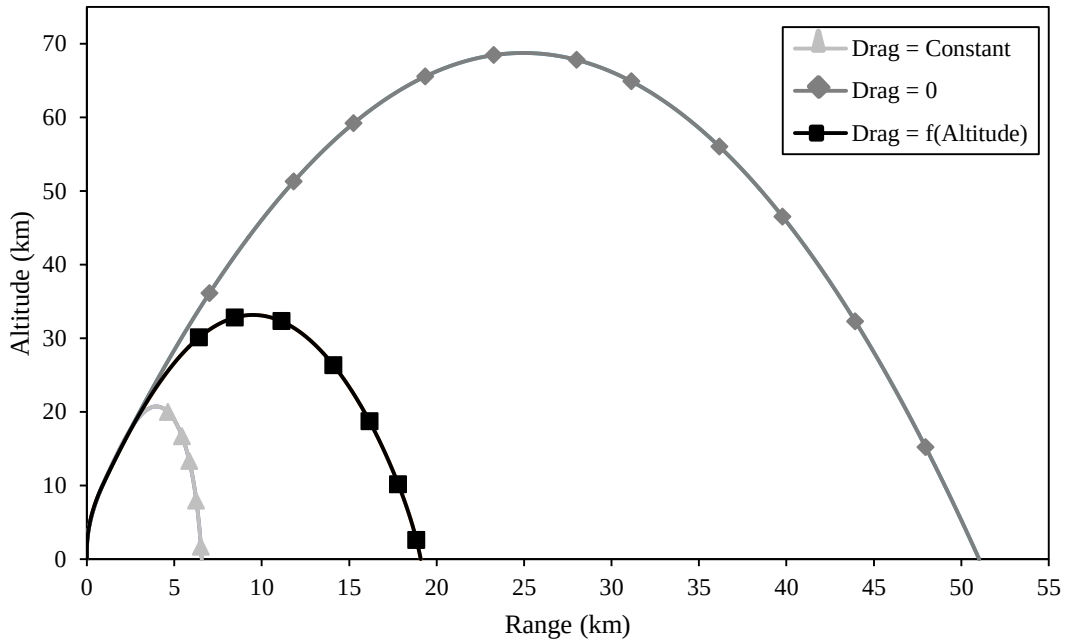


Figure 3**:** Trajectory analysis for different drag assumptions.

Figure 6 shows a detailed trajectory analysis on different assumptions on C_D and ρ. The analysis where C_D and ρ is set as a constant value based on sea-level which is also known to have the maximum air density of 1.225 kgm^{-3} and C_D of 0.0219 which were determined through the analysis carried out previously at sea-level. Hence, all these flight conditions are set to be simulated for the trajectory with identical rocket and engine setup. This analysis is carried out to show the effect of the different assumption on each C_D and ρ to the trajectory of the body. The resultant trajectory for the different cases are compared with the trajectory where density and C_D changes with altitude. This trajectory is known to be the most realistic analysis of all the flight conditions where in actual flight condition, both C_D and atmosphere where the body operates at changes with altitude.

First, the trajectory where only C_D is simulated to be changing with altitude whereas ρ is set to be constant and at a maximum value of 1.225 kg/m^3. The resulted trajectory shows that the landing distance and maximum altitude reached by this setup is to be minimum compared to the other cases. This is caused by the increase of C_D with altitude, as the body reaches higher altitude the C_D increases. With the density of the air set at sea-level condition which is also the maximum, this means that as altitude increases, $C_D$increases and ρ is predetermined at a maximum value, hence the overall drag force experienced by the body is increase with altitude. This circumstance resulted the body to travel and landed nearest and the with the shortest flight time.

The second trajectory which is analysed with the opposite assumption from the first analysis, where density is modelled to be changing with altitude and C_D is configured to be constant. C_D taken at sea-level condition which is also known to be minimum at any altitude of flight. Hence, we can see that the trajectory is shown to reach maximum altitude and have the greatest range. This assumption is also the assumption which have the nearest result to the trajectory which considers the both factors as a function to

altitude. This results is caused by the larger contributing factor of density compared to C_D on the drag force experienced by the body.

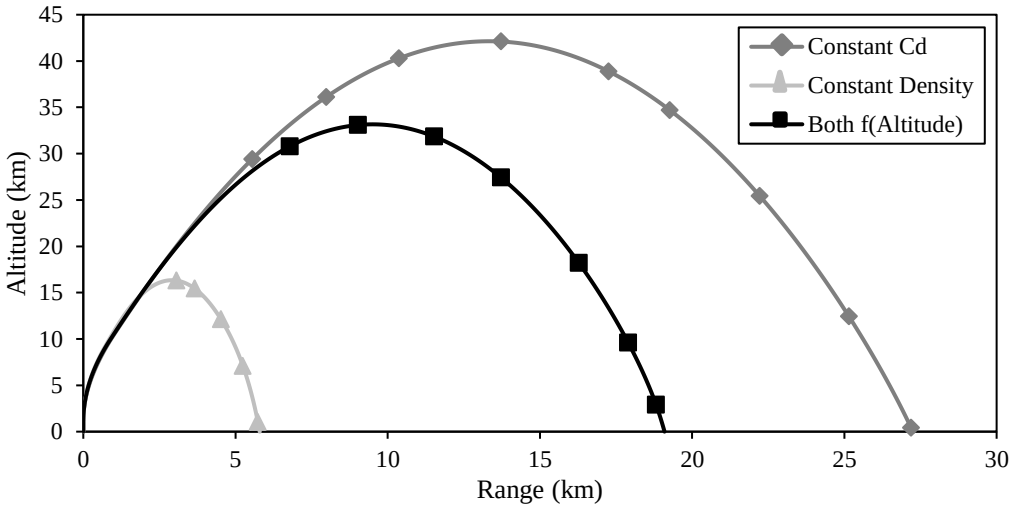


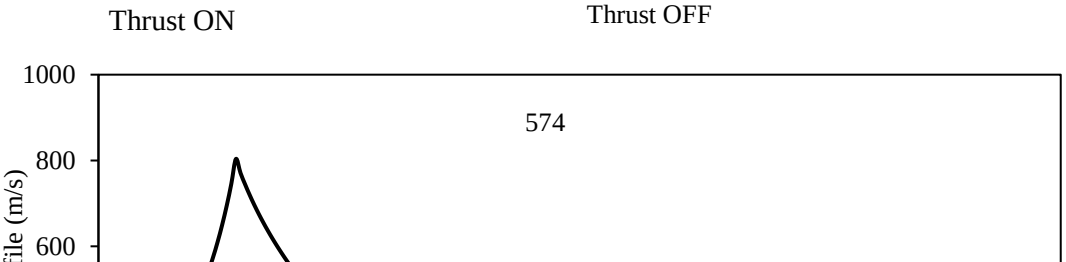
Figure 4: Trajectory for different density and drag coefficient assumptions.

3.3 Velocity profile

An example of flight performance data that can be produced by the MATLAB program is the velocity versus time graph. Figure 7 shows the velocity profile of the body at different part of the flight in detailed. This graph can be used to compare with different flight and launching simulation which allows thorough analysis and visualization on the velocity of the body. Figure 7 below shows the velocity vs. time graph of the trajectory when drag is fully considered as a function of altitude and Mach number. The resultant graph shows that during launch known as the powered flight stage, thrusters from the engine propel the body continuously until the booster runs out of fuel which causes the velocity to peak at around 840 m/s. During the thrusted flight up to 30s, it can be seen there is a slight increase in the acceleration of the body as it approaches higher altitude, this shows the combination effect due to low atmospheric air density and the increase of C_D .

At 30s into the flight time, thrust is terminated but the body continues to gain altitude due to its momentum. The velocity of the body decreases as time passes due low travelling velocity hence low drag force. Until the body reaches a velocity of 100 m/s, at this stage of flight the body's momentum no longer sufficient to gain altitude. This is where gravitational force takes over the trajectory of the body. At this stage, the missile glides back to earth purely by gravitational force and its remaining momentum.

As the body return back to earth, the velocity increases up to a point where the net force exerted on the body is zero, which means the gravitational force is almost equal to the aerodynamic drag force exerted on the body. According to *Newton's Second Law* of motion, when there is no external force exerted on the body, the body will remain stationary in this case at constant velocity. At the near end of the flight, the velocity of the missile starts to stabilize at a constant value, this is also known as the terminal velocity of an object which depends on C_D and atmospheric properties.



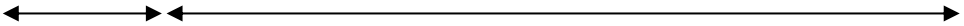


Figure 5: Velocity of the body through the flight.

4. Conclusions

The effects of atmospheric altitude on the trajectory of the missile are studied and analysed in detailed. The results show altitude not only affects the atmospheric air parameters, but also C_D of the body is determined depending on the geometrical shape, fluid conditions and Mach number. Through the analytical plotting of the trajectory, it can be said that the consideration of the changing C_D with altitude has drastic effect on the trajectory and also the flight performances, hence it is important to fully analyse and include the effects of altitude to determine the accurate drag force experienced by a body. The conclusion that can be made to this study are summarized as:

- The developed program had been able to produce graphs which show realistic flight performance data as planned.
- Results shows that C_D increases with altitude exponentially due to the effect of atmospheric air parameters which change with altitude.
- Trajectory plot which shows the consideration of the density as a function to altitude have greater effect on the overall trajectory compared to C_D.
- The consideration of C_D as a function to altitude also show obvious deviation of trajectory path compared to when C_D is consider as constant.

At high altitude, C_D of the wing increase in an exponential rate. As altitude increases, the atmospheric air parameter viscosity and density contributes the most in affecting the drag force throughout the flight. Hence, the combination effect of these factors are important to be considered when analysing for flight performance and trajectory. In order to increase the accuracy of the MATLAB program, a smaller time interval is recommended to be used which may require additional computational time.

The effect of the varying C_D and atmospheric parameters with altitude is clear and thoroughly discussed in Section 4. The results shows the importance to consider drag as a function to altitude, velocity and wing geometry, which is visualized through trajectory analysis. This also shows the importance to prioritize in minimizing drag of a moving body. The reduction of drag results direct and significant improvement to the operational efficiency and performance of the wing.

References

[1] F. S. M, A. P. Analysis, and V. D. M. V. Müller, "CHAPTER 3 Drag Force and Drag Coefficient," pp. 1–57, 2009.

[2] *Pilot's Handbook of Aeronautical Knowledge (PHAK)*. US Department of Trasnportation, Faderal Aviation Administration, 2008.

[3] D. Dr Auld, "Drag Coefficient Prediction Chapter 1," Sydney, 2013.

[4] I. Kroo, "Compressibility Drag: Introduction," *Stanford Univ.*, 2015.

[5] H. Hidayat, "Advance Thermodynamics: Compressible Flow," *Taylor's Univ.*, 2015.

[6] Nancy Hall (Glen Research Centre), "Factos That Affect Drag," *NASA*. [Online]. Available: https://www.grc.nasa.gov/www/k-12/airplane/factord.html. [Accessed: 15-Apr-2016].

[7] J. J. Bertin and R. M. Cummings, *Aerodynamics for Engineers*, 5th ed. Upper Saddle River, New Jersey 07458: Pearson Education, 2009.

[8] M. Azdi and A. S. M. Al-obaidi, "Effect of Aircraft Wing Geometry and Shape on the Lift at Low Subsonic Speeds," *EURECA*, pp. 286–302, 2014.

[9] A. Wood, "Wing Design Part 1 - Wing Area and Aspect Ratio," *L[Air]gacy.com*, 2014. [Online]. Available: http://www.lairgacy.com/2013/08/wing-design-part-1-wing-area-and-aspect.html. [Accessed: 15-Apr-2016].

[10] B. R. Bowman and K. Moe, "Drag Coefficient Variability at 175-500 km from the Orbit Decay Analyses of Spheres," *AAS/AIAA Astrodyn. Conf.*, no. 1, pp. 117–136, 2005.

[11] M. S. Selig, R. W. Deters, and G. a. Williamson, "Wind Tunnel Testing Airfoils at Low Reynolds Numbers," *49 th AIAA Aerosp. Sci. Meet.*, no. January, pp. 1–32, 2011.

[12] A. S. M. Al-Obaidi, "The Influence of Configuration Design on the Aerodynamics and Stability of SSM at Supersonic speeds," Ph.D Thesis, Al-Rasheed College of Engineering and Science, Baghdad, Iraq, 2005.

[13] J. Le Personnic, F. Alam, L. Le Gendre, H. Chowdhury, and A. Subic, "Flight Trajectory Simulation of Badminton Shuttlecocks," *Procedia Eng.*, vol. 13, pp. 344–349, 2011.

[14] C. Hamper and K. Ord, "Projectile Motion with Air Resistance," in *Higher Level Physics*, vol. 2, M. Rumble, Ed. Pearson, 2009, pp. 27–31.

[15] D. R. Knight, "Projectile Motion," in *Physics for Sceintists and Engineers*, 1st ed., B. Adam, Ed. San Fancisco, CA: Pearson Education, 2004, pp. 159–163.

[16] C. Lee and A. Al-Obaidi, "Calculation and Optimization of the Aerodynamic Drag of An Open-Wheel Race Car," *Sch. Eng. Taylor's Univ.*, pp. 1–15, 2014.

[17] R. D. Finck, *USAF Stability and Control DATCOM*, vol. 18, no. 4. Ohio, 1978.

[18] N. Sissenwine, *U.S Standard Atmosphere, 1976*, 3rd ed. Washington D.C: United States Air Force, 1976.

[19] J. Twicken, "Calculate Surface Gravity," in *Stanford University*, R. Wigand, Ed.

Stanford, CA: STAR Lab, 1998.

[20] D. E. Hoak, *USAF Stability and Control DATCOM*, Rept. 0410. Flight Control Division, Air Force Flight Dynamics Laboratory, 1972.

[21] N. F. Krasnov, *Aerodynamics. Part 2 (Methods of Aerodynamic Calculations).* Moscow: Mir Publisher, 1985.

[22] A. A. Lebedev and L. C. Chernobrovken, *Flight Dynamics of Pilotless of Flight-Vehicles (in Russian Language).* Mashen Ctroen, Moscow, 1973.

[23] S. Jankovic, *Aerodynamics of Projectiles (in Yougslavian language).* Beogradu, Belgrade: Masinski Fakultet, 1979.

[24] Z. Petrovic, *Elements of Semi-empirical Aerodynamics*. Private Communication, April 2002.

[25] J. John D. Anderson, *Fundamentals of Aerodynamics*, 4th ed. New York, NY: McGraw-Hill, 2007.

[26] C. Babb and D. Fuller, "Static Stability Investigation of a Sounding-rocket Vehicle at Mach Number 1.50 to 4.63," *NASA-TR-R-100*, 1961.

[27] J. Ferris, "Static Staility Investigation of a Single-stage Sounding Rocket at Mach Number 0.60 to 1.20," *NASA-TN-D-4013*, 1967.

[28] H. Koffeman, "The Reynolds Number," *Aero Drag*, 1992. [Online]. Available: http://www.aerodrag.com/Articles/ReynoldsNumber.htm. [Accessed: 23-May-2016].

Blended Polycaprolactone with Forsterite for the Enhancement of Hardness

Kong Ye Kai[1*], Yong Leng Chuan[2]

[1]*School of Engineering, Taylor's University, Malaysia*

[*]kongyekai@sd.taylors.edu.my

Abstract

Polycaprolactone (PCL) is a biodegradable polymer which has been widely fabricated into porous scaffolds in tissue engineering for bone tissue repair or regeneration. However, pure PCL has very poor mechanical strength and bioactive behavior to support the bone tissue regeneration process. Blending the PCL with bioceramics such as forsterite is one of the solutions to enhance the mechanical properties of the biodegradable polymer as bioceramics have good bioactive behavior and mechanical properties. This study investigates the hardness of different synthesis ratio of PCL/forsterite sample in compared to pure PCL sample which both can be used in bone tissue engineering applications. The PCL/ forsterite samples are fabricated with smaller range of forsterite content from 0wt% to 10wt% with 2wt% increment in order to obtain more specific results. DSC test was done to study the melting properties of the sample with different forsterite content. The onset temperature which is also known as melting point has ranged from 58 °C to 62 °C. The sample was then fabricated by using a 10 mm diameter and 10 mm thickness cylindrical mold and the hardness of the samples were measured by using a WP300 Universal Material Tester to find the impression diameter that caused by the load from the tester. The mechanical test results shows that the sample with highest forsterite content which is 10 wt% possessed the highest hardness number which is 5.767 and it is 87% higher than the pure PCL's hardness. Hence higher forsterite content in the blended material will result in higher hardness.

Keywords: Polycaprolactone, Forsterite, Melting properties, Forsterite content, Hardness.

1. Introduction

The usage of biomaterials in medical field is very common nowadays as it is very safe for human bodies due to its high biocompatibility and biodegrability. It is commonly used by doctor and scientists to study the cell activity in human bodies and even use it in growing, cure and even replace the damaged tissue and organ that is harmful for human body activities. [1] Other than the biocompatibility of biomaterials, mechanical properties of the biomaterial is also an important factor for the performance

of the biomaterial in carrying out different biological tasks such as biomedical implant and devices. For example, the femoral stem of a hip replacement must be able to withstand all the static and cyclic load that caused by human body weight and daily activities without mechanical failure for the lifetime of the implant. [2] Therefore choosing the most suitable mechanical properties of the biomaterials is very important before applying it into its own specific application. There are many ways in determining the mechanical properties of biomaterials which are the stress-strain graph, strain to failure, flex fatigue testing over time, compression test and also hardness test. [3]

Due to the high biocompatibility and potential in manipulating the mechanical properties, biomaterials have been widely used in bone tissue engineering to provide a way to repair or replace damaged bone tissue. [4] In bone tissue engineering, the biomaterials are normally made into 3D scaffold and implanted onto the damaged bone to provide mechanical support in the same time allows new cell to attach on it to form bone tissue. A scaffold is a three dimensional biocompatible structures that able to mimic the mechanical properties and cellular activity to provide a template for cell attachment and bone tissue regeneration. [5] Therefore, a biomaterial with suitable mechanical properties and biocompatibility should be used to fabricate a scaffold to support the cracked bone from different sources of force.

Biodegradable polymer is a type of biomaterial that has been used in tissue engineering technology in the fabrication of scaffold. Polycaprolactone (PCL) is a hydrophobic and slow-degrading polymer that has been widely used due to its potential in wide range of biomedical applications. [6] However, it possesses poor mechanical strength and bioactive behavior that needed for bone tissue regeneration hence limit its use in orthopedics. [7] One of the ways to improve its mechanical properties is to blend it with other biomaterial such as other biopolymers and bioceramic. A few studies have been done regarding the blending of PCL and other biomaterial. The study of blending PCL and Poly Lactic Acids (PLA) has increased its compressive modulus from 18.7MPa to 146.5MPa. [8] The blending method of this material is by using melt blending method. [8]. Another study is done by blending PCL with hydroxyaoatite (HA) and has increased its compressive modulus from 0.2MPa to 0.75MPa. [9]

This research has been conducted to study the enhancement in mechanical properties by blending polycaprolactone with forsterite. Forsterite (Mg_2SiO_4) is a bioceramic that provides good bioactivity and good mechanical properties. Previous research also suggests that magnesium (Mg) is one of the important elements that indirectly influence the body mineral metabolism. [4] Hence it is believed that incorporate forsterite with PCL will enhance the biodegradation, bioactivity and mechanical properties of PCL. Previous study on PCL/forsterite shows that the blending of forsterite in PCL has increases the elastic modulus from 3.1 MPa to 6.9 MPa and compressive strength from 0.0024 MPa to 0.3 MPa. [10] This research is done to determine the hardness of the PCL/forsterite material with forsterite content range from 0 wt% to 10 wt%. It is very important to determine the hardness of a material to ensure that the material will survive and perform in its specific applications. However, there is no previous study done on the hardness of PCL blending with other material. By judging from the trend from previous studies, hypothesis has been made that the higher the content of forsterite in PCL/forsterite material, the higher the hardness possessed by the material.

The project objectives are to determine the melting properties of the PCL/forsterite material with forsterite content range from 0 wt% to 10 wt% and to determine the hardness of the PCL/forsterite material with forsterite content range from 0 wt% to 10 wt%.

2. Research Methodology

The materials used in this research are polycaprolactone (PCL) with molecular weight of 10000 g/mol and 60°C melting point and forsterite powder with molecular weight of 140.6931 g/mol. The materials will be processed with different blending ratio with forsterite content from 0 wt% to 10 wt%. The processed materials will be undergoing different stages in this research methodology in order to achieve the research objectives. There are three main stages in this research which are sample preparation, hardness testing and results discussion. The summary of the research methodology is shown in the flowchart in figure 1.

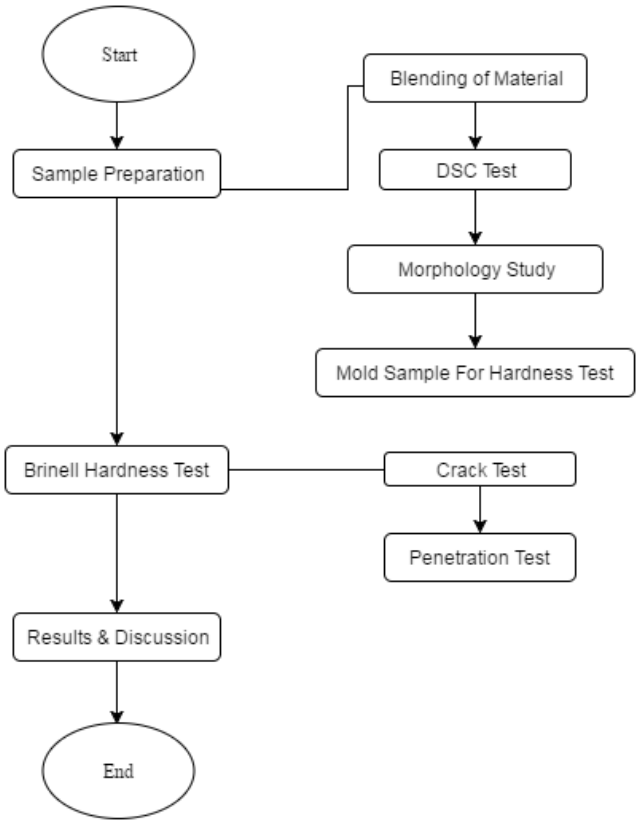


Figure 1: Research Methodology Flowchart

2.1 Sample Preparation

To prepare the sample to be used for hardness testing, the polycaprolactone is blended with desired weight percentage of forsterite. The weight percentage of forsterite is ranged from 0 wt% to 10 wt%. There are 6 different blended PCL/ forsterite to be prepared which are forsterite content 0 wt%, 2 wt%, 4 wt%, 6 wt%, 8 wt% and 10 wt%. The molecular weight of polycaprolactone and forsterite are 10000 g/mol and 140.6931 g/mol. By taking 60 g of polycaprolactone for each sample, the weight of the forsterite to be blended can be calculated with refer to Eq. (1) below:

$$Weight\ of\ Forsterite = \frac{Desired\ Percentage\ of\ Forsterite \times 140.6931}{\left(\frac{Desired\ Percentage\ of\ PCL \times 10000}{60}\right)} \quad (1)$$

By using Eq. (1), the weight of the forsterite to be blended with 60 g of polycaprolactone is shown in Table 1.

Table 1. Weight of Polycaprolactone and Forsterite with Different Weight Percentage

Weight Percentage of PCL (wt%)	Weight Percentage of Forsterite (wt%)	Weight of PCL (g)	Weight of Forsterite (g)
100	0	60	0.0000
98	2	60	0.0172
96	4	60	0.0352
94	6	60	0.0539
92	8	60	0.0734
90	10	60	0.0938

The materials are then blended together by using melt blending method by melting the polycaprolactone with hotplate in 80 °C and slowly adding the forsterite into the molten polycaprolactone for mixing purposes. The molten is then stirred and placed into a petri dish once it is blended homogenously. It is then let cooled until it becomes a wax form.

Forsterite has a melting point of 1890°C which is much higher than melting point of PCL which is 60°C. [11] Hence it is necessary to determine the effect on melting properties by blending 2 to 10 wt% of forsterite into PCL. DSC test will be able to provide quantitative and qualitative data on endothermic and exothermic processes of material that caused by phase changes, melting, glass transition and other heat related changes. [12] The DSC test will provide a DSC curve to show the information on the melting properties of the materials and the onset melting point where the materials start to melt. The amount of material needed for DSC test will be ranged from 5 mg to 10 mg per sample. The test is done by using a DSC machine and the setting of the test is as shown in Table 2.

Table 2. Settings on DSC Test

Item	Settings
Sample Properties	Thermoplastic
Scan Temperature Range (°C)	25 – 180
Expected Melting Point (°C)	150
Scan Rate (°C/min)	5
Decomposition Temperature (°C)	200

The blended materials are ready to be processed into sample for hardness testing once the DSC test and analysis on the melting properties is done. The blended materials are melted using hotplate and the molten is then poured into a cylindrical mold and let cooled to form the testing sample which is in a wax form. Sample with dimension of 10 mm diameter and 10 mm thickness is made. Each sample can be conducted with hardness test for 2 to 3 times. Hence 3 copies for each blending ratio are needed. In total there are 18 copies of samples produced for the hardness test.



Figure 2. Molded Sample for Hardness Testing

Morphology study of the blended materials was done by using Environmental Scanning Electron Microscope (ESEM) at a voltage of 20 kV and current of 60 – 90 mA. The fully hydrated samples can be imaged without deterioration for extended period, coating or other preparation. The distribution of forsterite on the sample is observed and the homogeneity of the blended material is studied.

2.2 Brinell Hardness Test

The molded samples are then tested for hardness by using Brinell Hardness Testing Method. Equipment used in this testing is WP300 Universal Tester. For Brinell Hardness Test, the load applied to the samples is done by a ball made of hardened steel. The load factor, x is referring to Table 3 provided by the WP300 Universal Material Tester manual book. According to Table 3, load factor of 0.5 is selected for the blended materials. However, the blended materials are unable to withstand the load that recommended by the manual which is 490 N. Hence, crack test is needed to determine the maximum load of the sample before it cracks. The outcome of the test will be the diameter of the impression caused by the steel ball.

Table 3 Load Factor $\boldsymbol{x = \frac{0.102\,F}{D^2}}$ depending on material [13]

Load Factor, X	30	10	5	2.5	1.25	0.5
Measurable Hardness range HB	67 … 400	22 … 315	11 … 158	6 … 78	3 … 39	1 … 15
Material	Iron Materials	Light Metals	Pure aluminum	Bearing metals	Lead, Tin, Soft solder	Soft metal at high temperature
Test Force (N)	29420	9800	4900	2450	1225	490

2.2.1 Crack Test

As there are not much hardness test was done previously on polycaprolactone, the crack test was conducted in order to find the maximum load that can be applied to the sample. One of the samples will be used for this test to find the maximum load that can be applied to the surface of the sample before it cracks inside. In order to complete

this test, load from the steel ball is applied slowly to the sample and observed until the sample is cracked inside. The maximum load is then recorded for the penetration test. For the polycaprolactone/forsterite sample, the maximum load that can be applied is approaching 300 N. Hence a force of 250 N will be used for the penetration test.

2.2.2 Penetration Test

Penetration test was conducted to find the hardness of the materials. For penetration test, load was applied to the samples slowly until it reaches 250 N. The load was applied on the sample for 60 seconds. After that, the diameter of the impression done by the steel ball which has a diameter of 10mm, D is observed. The diameter of the impression, d can be calculated by referring to Eq. (2). The test is repeated 4 times in order to get average result on the diameter of the impression. By using the diameter of the impression, the Brinell hardness of the material can be determined by referring to Eq. (3).

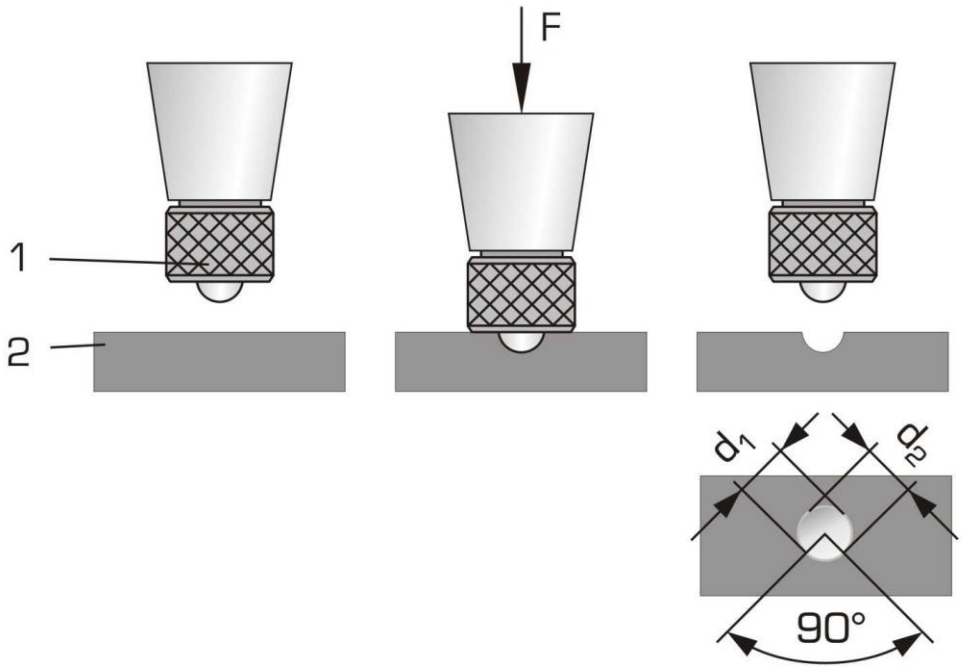


Figure 3. Hardness Testing According to Brinell [13]

$$d = \frac{d_1 + d_2}{2} \quad (2)$$

$$HB = \frac{0.102 \times F}{0.5\,\pi\,D\left(D - \sqrt{D^2 - d^2}\right)} \quad (3)$$

3. Results & Discussion

The DSC test was conducted to determine and compare the melting properties of the blended materials with different forsterite content and the hardness of the blended

materials are to be determined by using the Brinell Hardness Test. The results from both of the tests are recorded and calculated to be plotted into graphs.

3.1 DSC Test

After melt blending the polycaprolactone and forsterite together, it is necessary to conduct DSC test on the blended materials before fabricate it into the sample for mechanical test. From the DSC test, a DSC curve is produced to measure the enthalpy changes for phase transition of the blended materials without changes in mass. From the DSC curves, the melting properties of the blended materials can be determined which are the onset point and the peak point. The onset point indicates when the blended material starts to melt and the peak point is where the biggest crystal of the blended material melts completely. Both of these temperatures are extracted from the curves and recorded in Table 4.

The onset temperature and peak temperature of the blended materials are determined and recorded in Table 4. The lowest onset temperature occurred at 10 wt% of forsterite content where the highest occurred at 2 wt% forsterite content. The lowest peak temperature where the biggest crystal in the sample melted occurred at 10 wt% of forsterite content and the highest peak temperature occurred at 2 wt%. However, this can be explained as the samples are tested with different sample mass as 2 wt% of forsterite content sample has higher sample mass. By having a higher sample mass, more energy will be needed to melt the sample completely. Hence the onset and peak temperature for 2 wt% of forsterite content is higher. Comparing to the melting point of the pure polycaprolactone provided by the supplier which is 60 °C, the results obtained from DSC test shows that the range of onset temperature from 58 °C to 62 °C and the peak temperature from 61° C to 66 °C has very minor difference from the melting point provided by the supplier. Hence by blending very small amount of forsterite into polycaprolactone only affect the melting properties of the materials gradually. By using the results obtained, the minimum limit of the temperature needed in fabricating the samples for hardness test can be determined.

Table 4. Onset Temperature and Peak Temperature of PCL/Forsterite

Forsterite Content (wt%)	Sample Mass (mg)	Onset Temperature (°C)	Peak Temperature (°C)
0	7.4	60.59	62.38
2	9.8	61.30	66.02
4	7.9	60.73	63.71
6	6.7	59.80	61.87
8	5.7	59.93	62.05
10	6.1	58.47	61.26

3.2. Morphology Study

The morphology study of the PCL/ forsterite samples is conducted by using SEM. The SEM images shown in figure 4 shows the distinct differences between each sample and it is represented by the distribution of forsterite in the samples which can be seen as white particle on the dark background. From figure 4, it can be observed that as the forsterite content increases, the amount of white particles (forsterite) on the PCL surface increases as well. The difference is more obvious by comparing samples with

forsterite content 2 wt% and 10 wt%. Other than that, the distribution of forsterite is even on the surface instead of accumulating in a big pile at a corner. Hence, it is proved that the samples possessed good homogeneity during the blending process.

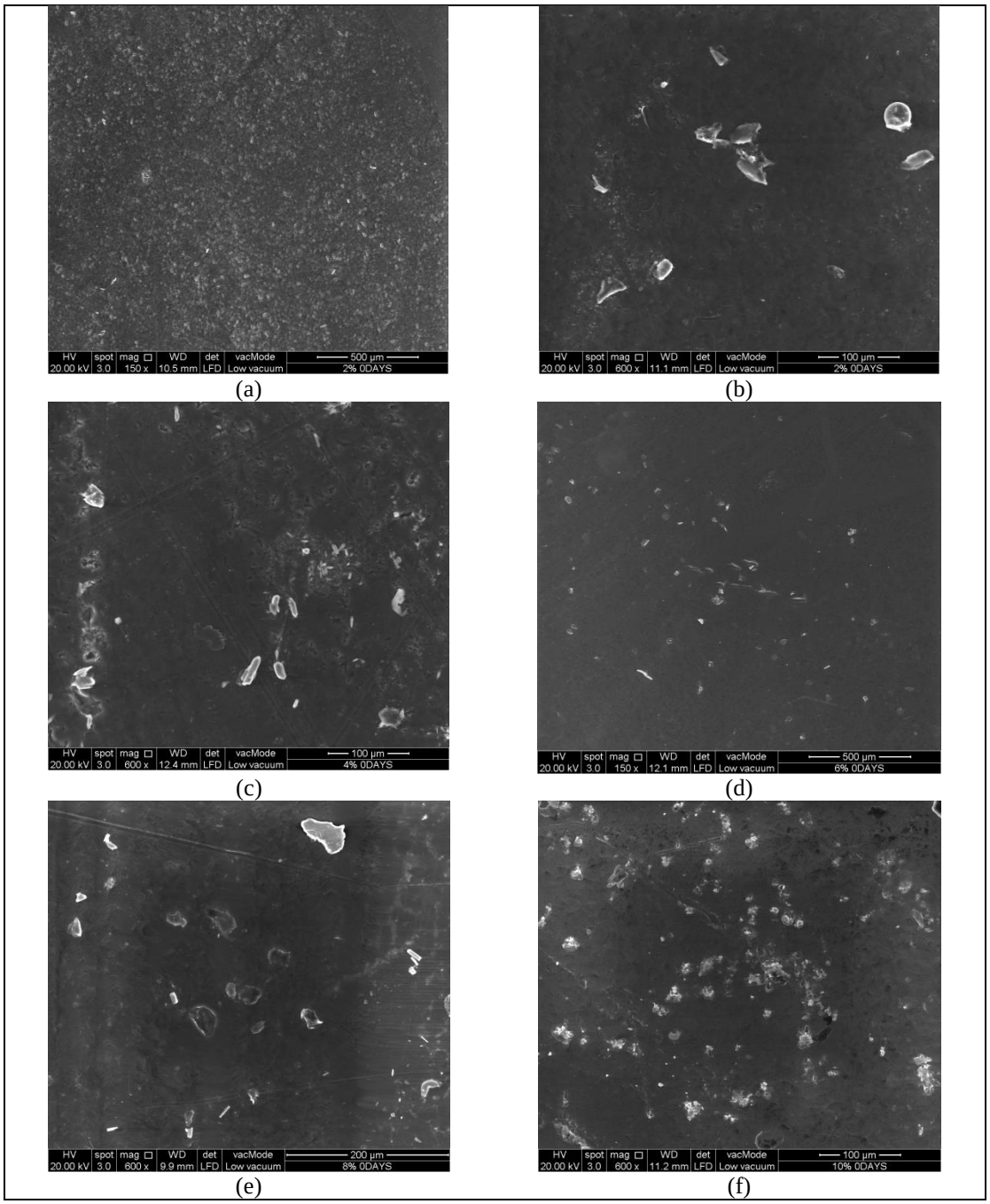


Figure 4. SEM images of the PCL/ forsterite samples with different forsterite content. (a) 0 wt%, (b) 2 wt%, (c) 4 wt%, (d) 6 wt%, (e) 8 wt%, (f) 10 wt%

3.3. Brinell Hardness Test

The Brinell Hardness Test was conducted to determine the hardness of the blended materials. From the experiment, the impression diameter caused by the load

from the steel ball on the sample is measured. The test for each sample is conducted for 5 times and the average impression diameter is calculated. The hardness of the materials is calculated by using Eq. (3). The results are shown in Table 5 and plotted into graph in figure 5.

Figure 5 shows the results obtained from the Brinell Hardness Test. According to the equation from Brinell which is Eq. (3), lower impression diameter will results in higher hardness number. From the experiment, pure PCL has an average impression diameter of 3.2 mm and hardness number of 3.087. Compared to the pure PCL, the blended material which contained forsterite and PCL has higher hardness as the hardness number is increasing according to the graph shown in figure 5. The highest hardness number is possessed by the PCL/forsterite material with forsterite content of 10 wt% which is 5.767. By blending 10 wt% of forsterite into PCL has increases the hardness of the pure PCL by about 87%.

Table 5. Impression Diameter and Hardness of Polycaprolactone/ Forsterite Sample

Forsterite	**Impression Diameter, d (mm)**						**Brinell Hardness**
Content (wt%)	**d_1**	**d_2**	**d_3**	**d_4**	**d_5**	**d_{avg}**	**Number (BHN)**
0	3.26	3.18	3.20	3.18	3.18	3.200	3.087 ± 0.0671
2	3.14	3.06	3.10	3.10	3.14	3.108	3.278 ± 0.0726
4	3.00	2.86	2.90	2.96	2.84	2.912	3.746 ± 0.1759
6	2.74	2.66	2.70	2.76	2.76	2.724	4.293 ± 0.1414
8	2.42	2.50	2.50	2.50	2.54	2.492	5.146 ± 0.1882
10	2.26	2.40	2.44	2.28	2.40	2.356	5.767 ± 0.4062

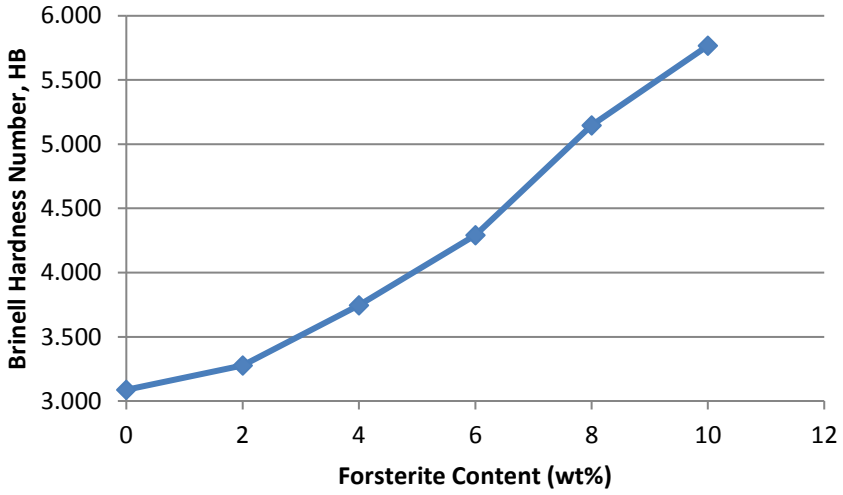


Figure 5. Graph of Hardness Number against Forsterite Content

4. Conclusions

In conclusion, the samples of PCL/forsterite biomaterial with forsterite content ranged from 0 wt% to 10 wt% has been successfully produced to be utilized for hardness test. The DSC results show that the onset temperature which is also known as melting point for the blended material is still within the 60 °C range comparing to the melting point of pure PCL which is 60 °C. Hence by blending small amount of forsterite

into PCL doesn't affect the melting properties much comparing to the pure PCL. The Brinell Hardness Test shows that the hardness is increasing following the increment of forsterite content and the highest hardness number of the PCL/ forsterite samples is possessed by the samples with highest forsterite content, 10 wt%. Hence, the higher the forsterite content, the higher the hardness number of the blended material.

For future works of this research, the forsterite content can be manipulated to study the effect of higher forsterite content in the blended materials on the mechanical properties. Besides that, other mechanical test can be conducted to find the other mechanical properties of the PCL/forsterite material such as tensile test and compression test to find the maximum tensile and compressive stress of the material. However, proper equipment and more material will be needed to be fabricated into the specimens that needed in these mechanical test. Lastly, the materials can also be used in its application which it can be fabricated into scaffold to check its flexibility to be shaped and also all the required parameters that needed in the fabrication.

Acknowledgment

Upon completing this research project, the author would like to express his appreciation to the family members, friends, lecturers and laboratory technicians of Taylor's University that provides help and support throughout the entire project.

References

[1] L. S. Nair and C. T. Laurencin, "Biodegradable polymers as biomaterials," *Prog. Polym. Sci.*, vol. 32, no. 8–9, pp. 762–798, 2007.
[2] R. Roeder, *Mechanical Characterization of Biomaterials BT - Characterization of Biomaterials*. 2013.
[3] J. R. Davis, "Overview of Biomaterials," *Mater. Med. devices*, p. 315, 2003.
[4] M. Kharaziha and M. H. Fathi, "Improvement of mechanical properties and biocompatibility of forsterite bioceramic addressed to bone tissue engineering materials," *J. Mech. Behav. Biomed. Mater.*, vol. 3, no. 7, pp. 530–537, 2010.
[5] S. Bose, S. Vahabzadeh, and A. Bandyopadhyay, "Bone tissue engineering using 3D printing," *Mater. Today*, vol. 16, no. 12, pp. 496–504, 2013.
[6] C. Sciences, "Polymers for Bone Tissue Repair," no. December, 2006.
[7] H. M. Wong, P. K. Chu, F. K. L. Leung, K. M. C. Cheung, K. D. K. Luk, and K. W. K. Yeung, "Engineered polycaprolactone–magnesium hybrid biodegradable porous scaffold for bone tissue engineering," *Prog. Nat. Sci. Mater. Int.*, vol. 24, no. 5, pp. 561–567, 2014.
[8] T. Patrício, A. Glória, and P. Bártolo, "Mechanical and biological behaviour of PCL and PCL/PLA scaffolds for tissue engineering applications," *Chem. Eng. Trans.*, vol. 32, pp. 1645–1650, 2013.
[9] M.-J. Chern, L.-Y. Yang, Y.-K. Shen, and J.-H. Hung, "3D scaffold with PCL combined biomedical ceramic materials for bone tissue regeneration," *Int. J. Precis. Eng. Manuf.*, vol. 14, no. 12, pp. 2201–2207, 2013.
[10] M. Diba, M. Kharaziha, M. H. Fathi, M. Gholipourmalekabadi, and a. Samadikuchaksaraei, "Preparation and characterization of polycaprolactone/forsterite nanocomposite porous scaffolds designed for bone tissue regeneration," *Compos. Sci. Technol.*, vol. 72, no. 6, pp. 716–723, 2012.
[11] "Olivine," no. 100, pp. 11–19.

[12] I. N. Here, “TA INSTRUMENTS DIFFERENTIAL SCANNING Operating Instructions.”
[13] G.U.N.T, “Test Instructions,” in *WP300 Universal Material Tester*, 2016.

eureca 2016 – Conference Paper
Paper Number 2ME12

Development of Torsional Thrust Stand that Resolves Micronewton Force

Lam Jiang Kai[1*], Cheah Kean How[1]

[1]*School of Engineering, Taylor's University, Malaysia*

[*]*jiangkai21@gmail.com*

Abstract

Nanosatellites are getting more developed recently. They are low cost, small in size and proven to be capable of carrying space missions. Many efforts have been spent to improve each function of nanosatellites. One of the functions is the micropropulsion system, in which microthruster is the main component. It is important for the performance of microthrusters to be evaluated before implementation. This is where the development of thrust stands become significant. Thrust stands are scientific instruments used to evaluate the performance of microthrusters based on the analysis of thrust measurements. In this project, a torsional thrust stand is to be developed. It is aimed that this thrust stand to achieve a measuring resolution at range between 30 to 50 micronewton. The components of thrust stand are mainly the structures, displacement sensor, damper, calibration system and external vibration cancelling. Critical areas studied in this project involve testing the new method of using voice coils at different diameter as the electromagnetic calibrator, as well as eliminating external vibrations. Based on the results in the end, the 51.5 mm coil is found to be suitable for the calibrator because it is able to calibrate the thrust stand to achieve resolution at approximately 40 micronewton. It also has reasonable engagement distance at 5mm for consistent and repeatable readings. Percentage error at 14.86 % can be improved by using a better sensor. The passive vibration cancelling method applied is also proved to be effective as the ambient noise is only about 2 micrometer.

Keywords: Micronewton, Thrust stand, Microthruster, Nanosatellite, Electromagnetic.

1. Introduction

Nanosatellites (1 to 10 kg) is one of the internationally most participated development in the past decade, particularly the CubeSat. It was proven that this type of low cost, small-sized system can be useful in some areas of space studies [1]. One of the major components of nanosatellites is the microthrusters which is part of the propulsion system responsible of movement around outer space. The development of microthrusters is crucial as it is the key element in providing thrust. To support this development, engineering instruments are required to test and evaluate microthrusters. This is where the significance of thrust stand comes in. A schematic of the state-of-the-art torsional thrust stand is shown in Fig. 1.

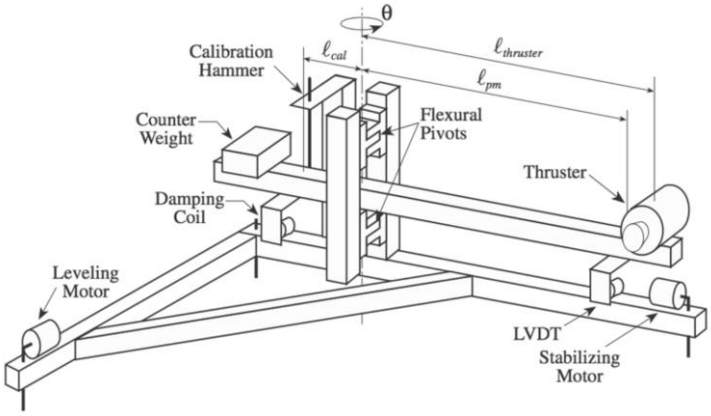


Figure 1. State-of-the-art torsional thrust stand [2].

In this project, a torsional thrust stand is to be developed. Torsional thrust stand is one of the configuration under pendulum type thrust stand. It is essentially a spring-mass-damper system. Its fundamental working principles are well defined in [3, 4]. Other configurations and their respective advantages and disadvantages are summarised in [4] as well.

There are many aspects to be covered in developing a torsional thrust stand. One of the major aspects is the displacement sensor. In some of the past studies, linear variable differential transformer (LVDT) can be considered as a type of sensor that is used quite often [5]. Besides, in the development by [3, 6], laser displacement sensors are used.

Another major component is the calibrator used to calibrate the thrust stand. Generally, calibrator can be categorised into non-contact and contact [3]. Non-contact calibrators include electrostatic fin or comb [7], gas dynamic [8] and electromagnetic [9]. On the other hand, contact calibrators include using a pulley-weight system [10], and an impact hammer or pendulum [5].

Other aspects such as the damping mechanism applied includes magnetic damping [11], and oil damping [12]. Next, external vibrations that could cause inaccuracy to the thrust stand have to be eliminated properly. In their studies, [6] installed an optical bench underneath the thrust stand for active vibration cancelling. There are also passive vibration cancelling methods with lower cost.

This project aims to design, fabricate, setup and calibrate a torsional thrust stand capable of achieving a measuring resolution in the range of 30 to 50 micronewton with appropriate external vibration cancelling. To achieve the objective, different and unique components or methods would be implemented, particularly in the area of calibrator and external vibrations elimination. In addition, it is also hoped that the studies carried out in this project could help to further reduce the cost of thrust stand development.

2. Research Methodology

2.1 Thrust Stand and Its Main Components

2.1.1 Design and Structure of Thrust Stand

This project started with the research and background study of the past developments on thrust stands. Once the aspects are covered and understood, the project then enters the design stage where the structural parts are produced in SolidWorks and suitable components are identified. For the structure of the thrust stand, as it is torsional type, a few design features are to be incorporated. One of them is to allow the platform where the microthruster is placed to oscillate about an axis (hence torsional type). Apart from that, clamps that hold the pivot bearing are also to be designed for this thrust stand. Other features include structural supports as well as mountings or connections for all the parts. Next, the thrust stand is manufactured by Infinite Tooling Sdn. Bhd. All of the parts are made of aluminium plates or sections, and assembled using fasteners.

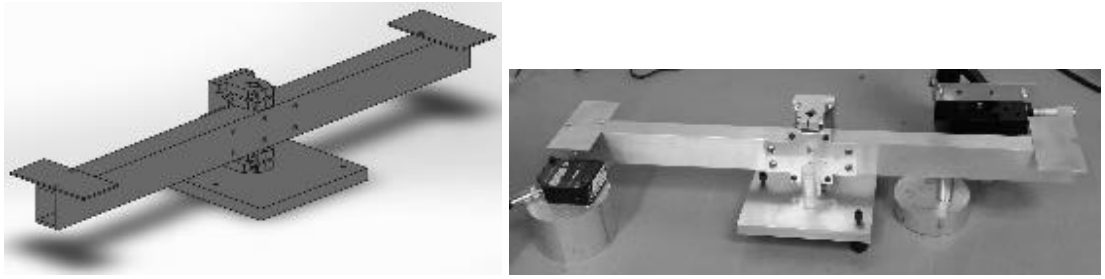


Figure 2 (a) & (b). Torsional thrust stand in SolidWorks (left) and assembled (right).

2.1.2 Pivot Bearing

In order to enable the platform to oscillate, a pivot bearing is mounted using clamps at the middle of the platform. The pivot bearing acts as a torsional spring providing the restoring force to the platform. For this project, pivot bearing model G-20 manufactured by C-Flex is used. It is single ended type and its load capacity is between 63.5 kg to 90.7 kg with a spring rate of 20.7 N/m, suitable for the development of the thrust stand. Its diameter is 1.27 cm and length is 2 cm. Fig. 3 below shows the G-20 pivot bearing that is used.



Figure 3. Pivot bearing C-Flex G-20.

2.1.3 Displacement Sensor

In the application of torsional thrust stand, a displacement sensor is required to measure the deflection of the platform when forces are exerted to it by the microthruster. Obtaining the deflection data is essential since it is directly related to resolving the forces involved. Therefore selecting the right displacement sensor is important for the thrust stand. High resolution and sampling rate are some of the key specifications among others. In this project, a type of laser displacement sensor made by Micro-Epsilon (optoNCDT series, ILD 1401) as shown in Fig. 4 is used. Laser sensors make use of the principle of optical triangulation to measure displacement of a target object. Besides, they are categorised as non-contact sensors which is ideal for the application. Key specifications of this particular ILD 1401 include resolution of 1 μm, sampling rate at 1 kHz and measuring range at 10 mm.

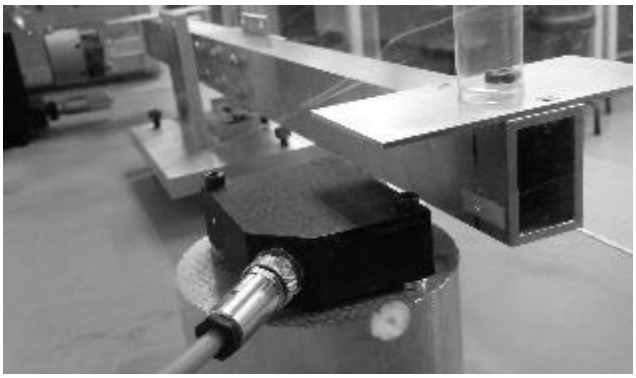


Figure 4. ILD 1410 laser displacement sensor.

2.1.4 Damping Mechanism

A damper is required for damping the oscillation of the platform when the force is applied. The concerned measurement is the deflection due to the force. By damping the oscillation, it is faster to achieve steady deflection. Typically, the damper is installed at the platform's end opposite to the end at which forces are exerted. Throughout the development of this project, the magnetic damping method is used. A strong magnet is fixed near under the platform made of aluminium. Such arrangement forms an eddy current brake. This method is suitable for this project as it is a small force application and non-contact which is ideal for accurate data measurement. Furthermore, it is a simple mechanism to be setup.

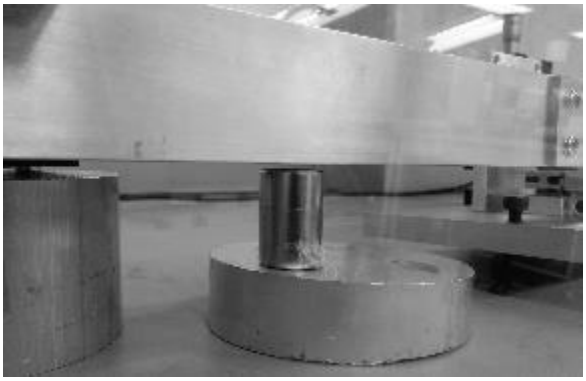


Figure 5. Magnet under the platform for damping.

2.2 Electromagnetic Calibration System

The development of the thrust stand is considered incomplete until it is calibrated for actual thrust measurement to be carried out. Calibration establishes the relationship between the deflection of platform and the force produced by microthruster. This process is done by installing a calibrator onto the thrust stand. In general, the calibrator would provide an accurately known force or impulse to be applied to the platform. Then, the displacement of the platform due to the applied forces is monitored using the laser sensor and analysed.

For this project, a type of electromagnetic calibrator is implemented. The aforementioned known force is produced electromagnetically using voice coils and permanent magnet as the plunger. Voice coils are basically solenoids with wire windings around a bobbin of certain diameters. A magnetic field would be generated when electric current passes through the coil. Depending on the amount of current *I* supplied, the magnetic field strength *B* could be manipulated. The relationship between the field strength and the current supplied follows the Ampere's Law, as shown in Eq. (1) below. As for the permanent magnet plunger, a small ferrite magnet in disk shape with weak magnetic field strength is used.

$$B = \mu NI \tag{1}$$

Both the voice coil and the plunger are configured in such a way that when current is passed through the coil, the generated magnetic field would repel the permanent magnet. This repulsive force is then measured. By supplying different amount of current, the repulsive force would be different as well based on how strong or weak the generated magnetic field is pushing away the permanent magnet plunger.



Figure 6. 51.5 mm diameter voice coil.

Challenge occurs when a very small force, at micronewton level, needs to be generated. To achieve this, experiments on voice coils of different diameters were carried out. While the size of the permanent magnet is fixed, different coil diameters give change in the gap between the permanent magnet and the voice coil. Then, the effects of the change in the gap size on the force measurement could be determined.

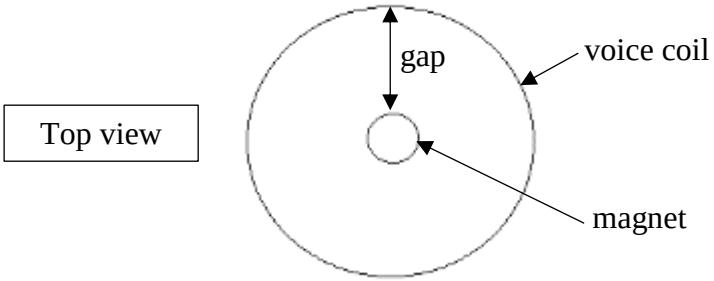


Figure 7. Gap defined as the difference between the radius of the voice coil and that of the magnet.

On the other hand, the experiments also helped to determine the engagement distance range between the voice coil and the magnet. This procedure is crucial because the calibrator needs to be able to generate consistent and repeatable known forces within a reasonable range of engagement distance.

2.2.1 Experimental Setup

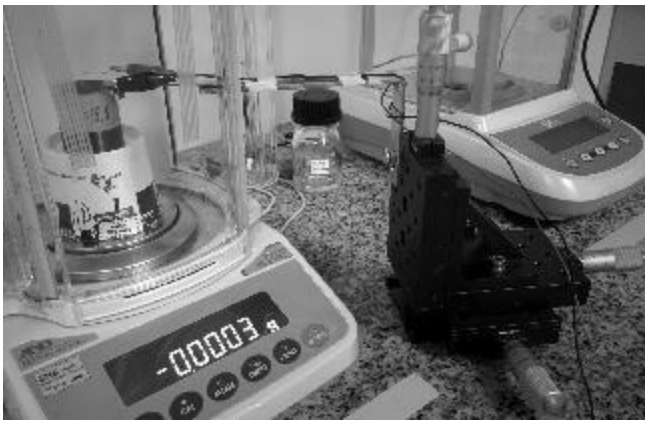


Figure 8. Experimental setup for measuring force.

Fig. 8 above shows the experimental setup for measuring the repulsive force. Here, a weighing balance with a resolution of 0.1 mg is used as the load cell to obtain the force value (1 mg = 10 μN). The permanent magnet is first levelled and fixed to a certain height using a cup, and then placed on the weighing balance. The levelling is to ensure that the magnetic property of the permanent magnet does not influence the internals of the weighing balance hence its measurement reading. Then, the voice coil is fixed and connected to a three axis mechanical stage. The mechanical stage functions as a more accurate method to bring the voice coil to the desired position. It has three knobs for adjusting the position with 0.01 mm accuracy. Next, the coil is connected to a power supply to provide current flow. This is done by adjusting the voltage from the

power supply. When connecting the coil to the power supply, it is made sure that the polarity of the coil is configured such that the generated field repels the permanent magnet. From here, the readings on the weighing balance corresponding to the voltage level adjusted can be recorded. The voltage levels range from 0.3 V to 4.8 V with 0.3 V increment. The readings obtained are in milligram unit, so conversion to force in Newton is done by multiplying the gravitational acceleration (9.81 m/s^2). This experiment is repeated using voice coil diameters of 25.5 mm, 35.5 mm, 51.5 mm and 75 mm. From the results, a graph of force against voltage can be produced.

For the engagement distance test, the setup is similar as above. The first point is set to 0 mm, where the end of the coil is at the same level as the magnet. The 0 mm distance is also used throughout the force-voltage experiments described above. Then, the distance increases (voice coil moving away from the magnet) up to 12 mm with 2 mm increment. This is done by turning the knob on the mechanical stage. For each of the voice coil diameter used, this engagement distance test is repeated at three voltage levels; 0.3 V for low-end, 2.4 V for mid-end and 4.8 V for high-end. As such, the force readings corresponding to the engagement distance at three distinct voltage levels can be obtained for each of the voice coil used. Last but not least, a graph of force against distance with three voltage levels can be plotted.

2.2.2 Implementation onto Thrust Stand

After obtaining the results from the experiments above, the electromagnetic calibrator can then be installed for calibration. The permanent magnet is fixed to one end of the platform; whereas the voice coil is mounted to the mechanical stage and wired to the power supply in similar way. They are then positioned as shown in Fig. 9 below. Switch on the power supply and the known calibration force is applied at said end. Then, the displacement caused can be recorded by the displacement sensor at the other end. By supplying different voltage levels, the corresponding displacements can be obtained and eventually a displacement-force calibration curve can be plotted.

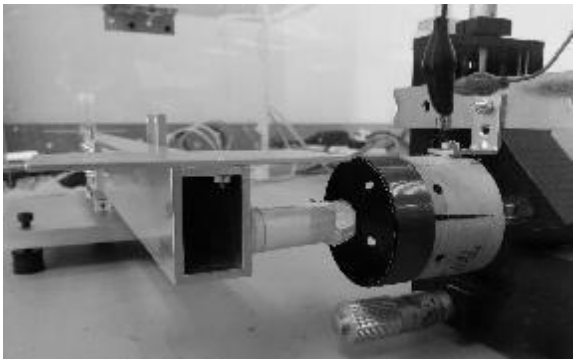


Figure 9. Application of the electromagnetic calibrator on the thrust stand.

2.3 Eliminating External Vibration

Vibrations on the oscillating platform caused by external means would affect the accuracy of the displacement data obtained. Unwanted external vibrations come from the surroundings such as air movement and the transfer of vibrational energy from the base of the thrust stand. The effects of these external vibrations become even more

significant when it comes to measurements in the micrometer range. Therefore it is crucial to isolate the thrust stand from the surroundings so that the external vibrations could be eliminated or minimised for accurate data acquisition.

2.3.1 Anti-Vibration Stud Mounts

In this project, a passive method of external vibration cancelling is used. This method consists of installing several stud mounts underneath the base plate of the thrust stand. Made of natural rubber, these stud mounts, as shown in Fig. 10 (a) have anti-vibrational properties that essentially isolate the system from vibrations around the base. Besides, they also act as excellence support and levelling foot for the thrust stand.

2.3.2 Casing

Apart from that, a casing as shown in Fig. 10 (b) is also used to enclose the entire structure to minimise the surrounding air movement. The casing is made using acrylic sheets with features such as handles for easy removal, hinged side panels for easy access to the thrust stand components, and small openings for wiring.

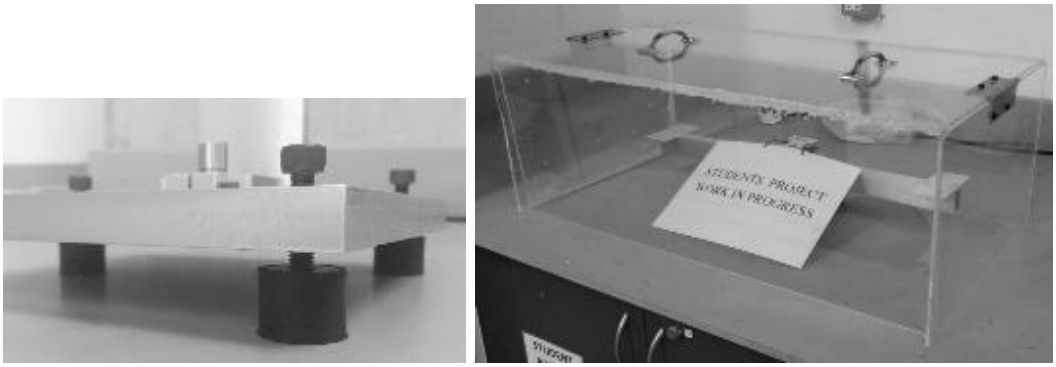


Figure 10 (a) & (b). Stud mounts (left) and casing (right).

3. Results and Discussion

3.1 Electromagnetic Force Measurement

Electromagnetic force generated by different sizes of voice coils at various voltage levels are measured. The data obtained is presented in a graph as shown in Fig. 11 below. It is found that the relationship between force generated and voltage supplied is linear for all four cases as indicated by the R-squared values which are close to 1. This proves that voice coils are suitable to be applied because the forces they generate are predictable for any voltage supplied.

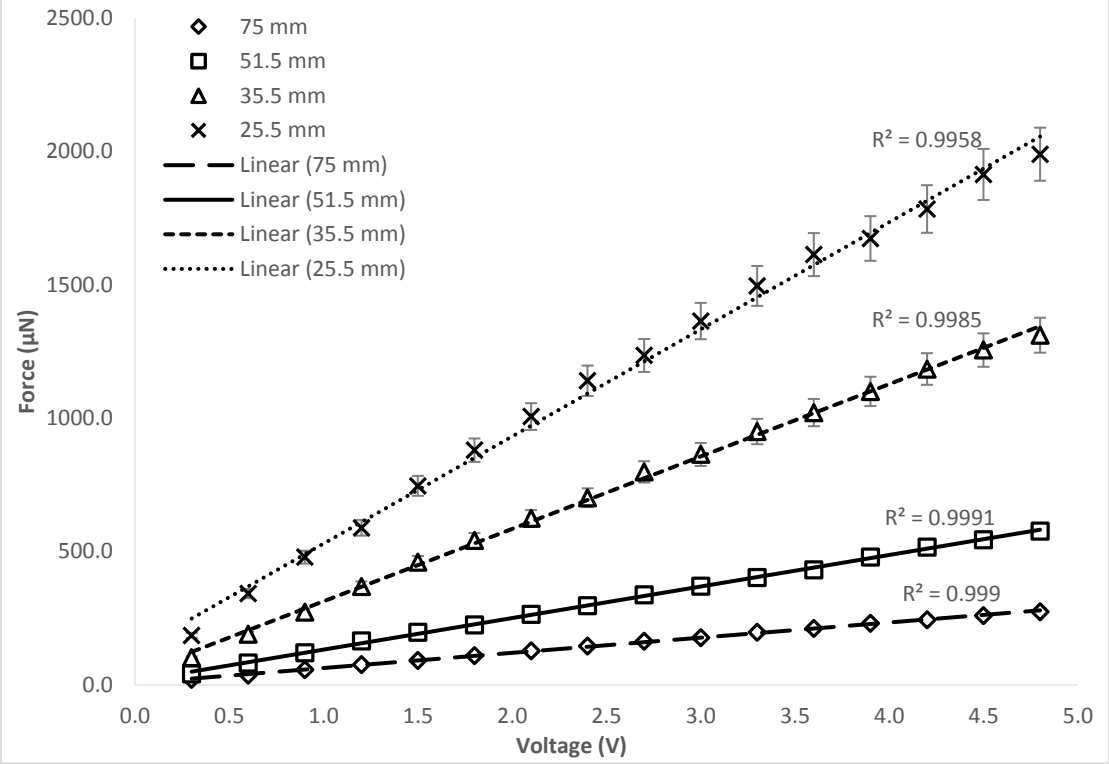


Figure 11. Electromagnetic force generated by voice coils of different diameter at various voltages. Each force measurement is repeated three times. Error bar is 5 %.

The effect of change in gap size is also determined. Results show that as the coil diameter increases, the corresponding force becomes weaker. This may be due to lesser magnetic flux interaction between the voice coil and the magnet plunger as the gap increases.

Further comparison on the minimum forces produced by each voice coil is done in order to select one that is able to provide calibration force for the thrust stand to achieve the desired measuring resolution. Table 1 summarises the minimum force generated by each voice coil diameter.

Table 1: Minimum force value produced by each voice coil diameter.

Diameter (mm)	Minimum Force (µN)
25.5	186.0
35.5	102.3
51.5	41.2
75	20.9

Based on the table, 51.5 mm coil is to be considered for the selection since its minimum force value is within the range set in project objective. The 75 mm coil, albeit able to achieve even smaller calibration force than required, its size is too big and could cause difficulty during installation.

Next, Fig. 12 to 15 shows the force generated by each voice coil corresponding to various engagement distance at three voltage levels. From the graphs, it can be observed that the forces become gradually weaker regardless of the voltage level. Such trend is expected because the repulsive force due to the magnetic interaction should be lesser as the components are pulled further apart. The 75 mm coil is the only exception whereby the forces become stronger. Further investigation will be needed.

It is also shown that for most cases, the force generated becomes inconsistent and unrepeatable at approximately 4 mm and beyond. Beyond 4 mm, the forces deviate too much from the initial value. Based on this result, it is ensured that the components are engaged within 4 mm when setting up the calibrator to the thrust stand so that the calibration force is precise.

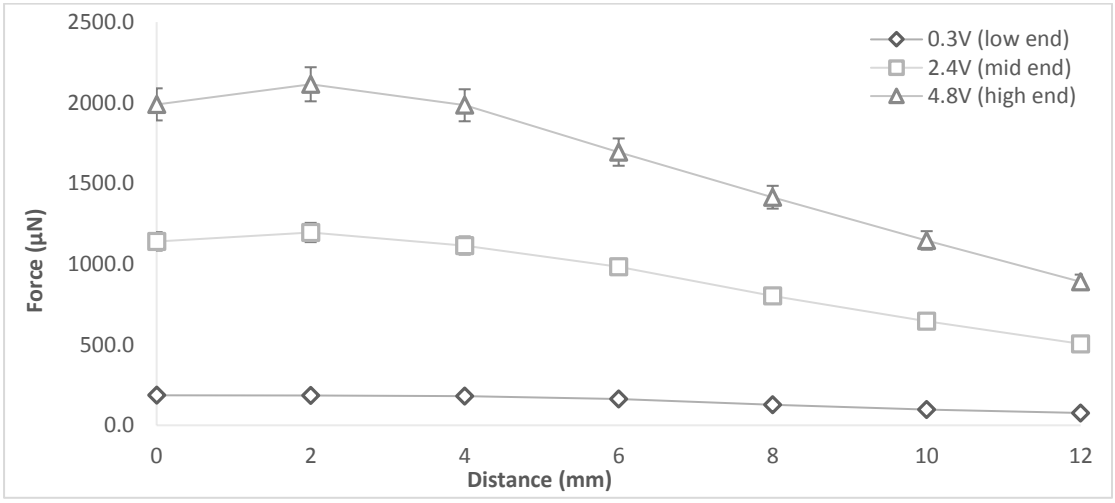


Figure 12. Electromagnetic force generated by 25.5 mm voice coil corresponding to various engagement distances at three voltages. Each force measurement is repeated three times. Error bar is 5 %.

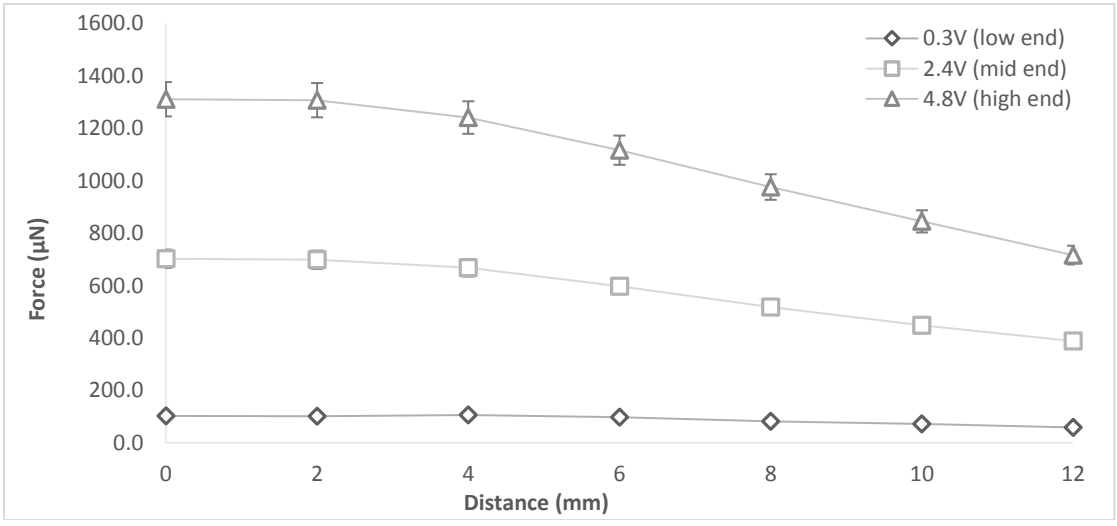


Figure 13. Electromagnetic force generated by 35.5 mm voice coil corresponding to various engagement distances at three voltages. Each force measurement is repeated three times. Error bar is 5 %.

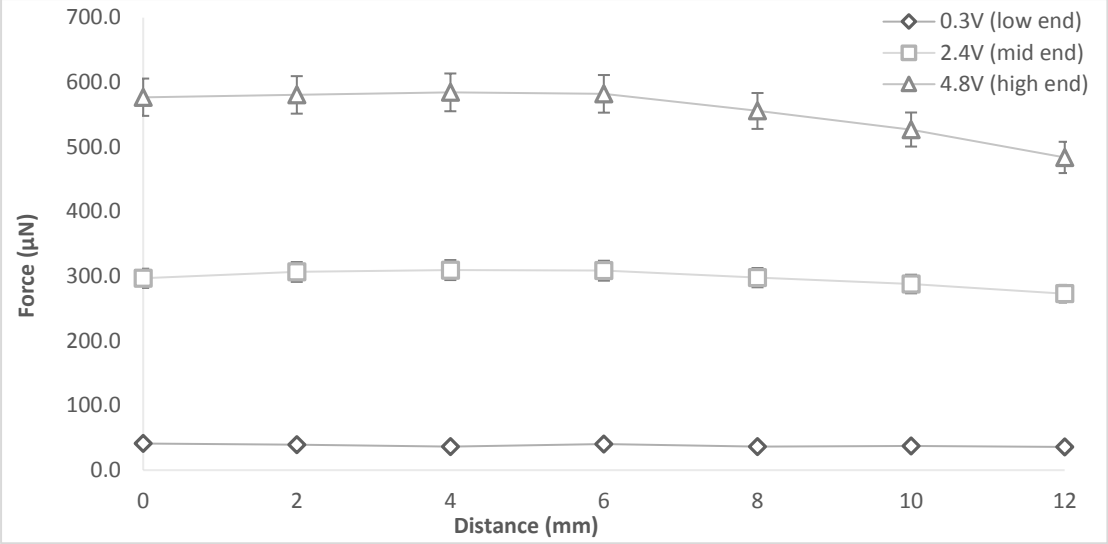


Figure 14. Electromagnetic force generated by 51.5 mm voice coil corresponding to various engagement distances at three voltages. Each force measurement is repeated three times. Error bar is 5 %.

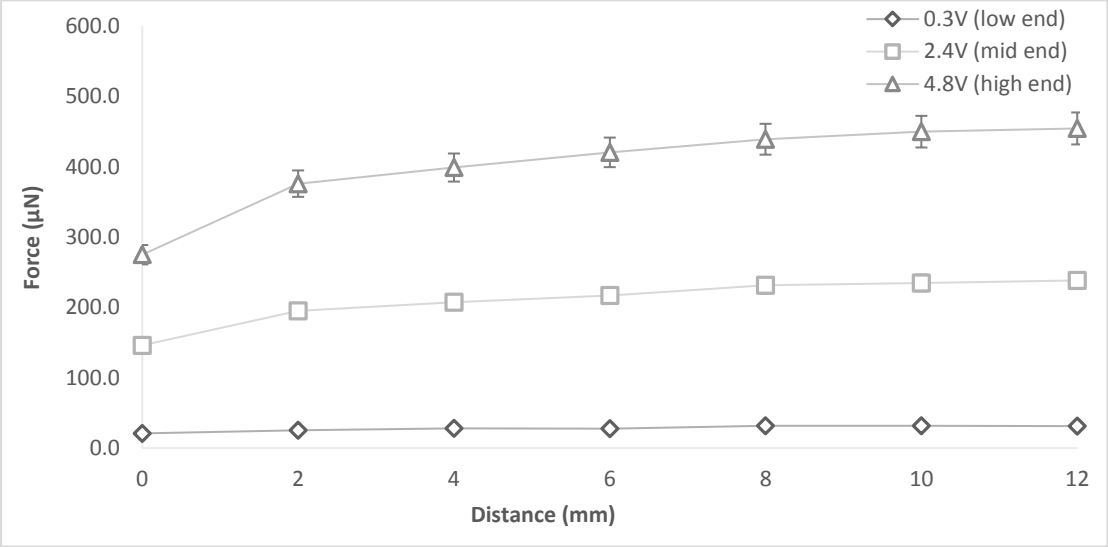


Figure 15. Electromagnetic force generated by 75 mm voice coil corresponding to various engagement distances at three voltages. Each force measurement is repeated three times. Error bar is 5 %.

Based on all the results above, the 51.5 mm coil is chosen. It shows the least inconsistency in force generated up to about 5 mm of engagement distance compared to others. More importantly, it is capable of generating forces at the required range. Upon application onto the thrust stand, the engagement distance of the calibrator is set to 3 mm.

3.2 Calibration for Constant Force Measurement

After installing the calibrator to the thrust stand, calibration process is then carried out by applying the electromagnetic calibration force to the platform. The

response is then captured by the displacement sensor. Various voltage levels (hence forces) are applied to obtain the corresponding response.

Fig. 16 below shows an example of thrust stand response to a constant calibration force generated at 2 V. As shown, the platform first oscillates sinusoidally when the calibration force is applied. The oscillation is then dampen due to the eddy current brake damper installed. Then, the steady deflection at 41 μm is obtained as indicated by the pointing arrow. Once the calibration force is withdrawn, a similar oscillation occurs. It can be observed that the steady position returns to zero, indicating that there is no drifting of the platform. It should be noted that the illustration below is only one sampling cycle. In actual, three repeated cycles were done to ensure its consistency in the deflection and also to obtain a mean deflection value.

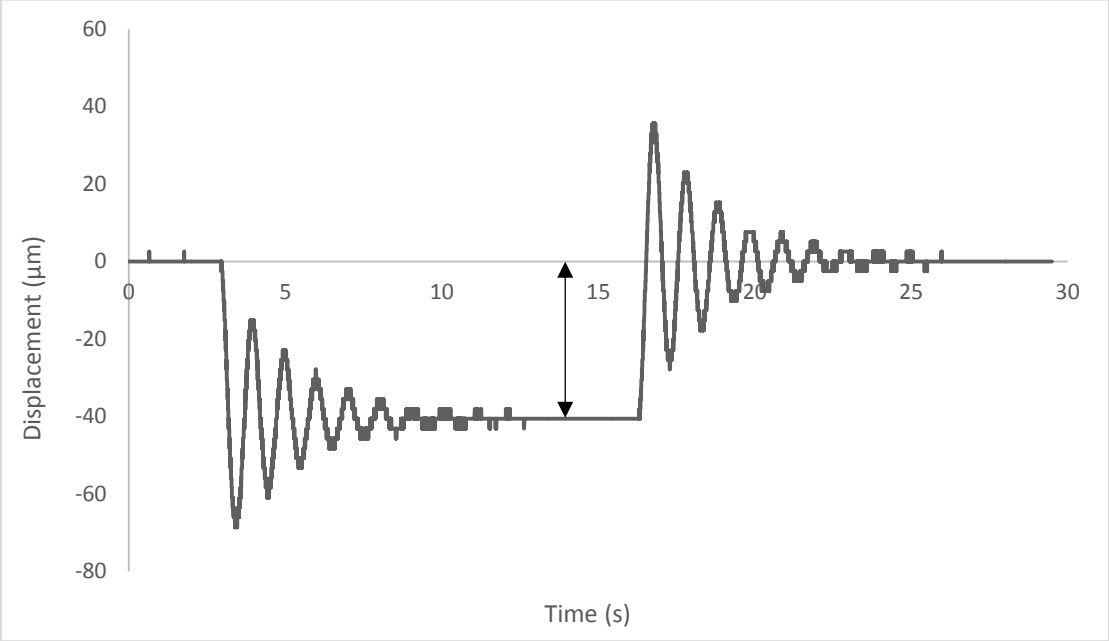


Figure 16. Thrust stand response to constant calibration force generated by 51.5 mm voice coil with 2 V supplied. Pointing arrow shows the steady deflection.

In this particular sample, some deflections of not more than 2 μm are observed at the beginning even though no force was applied. It may be caused by the ambient noise like air movements. While the casing was able to isolate the thrust stand from surrounding air movement for the most parts, such deflections indicates that the casing can be improved. On the other hand, the use of the rubber foot mounts were also proved to be effective in isolating vibrations near the base plate. This is indicated by the flatness of the graph line during steady conditions at about 14 to 16 seconds and 26 to 30 seconds.

A calibration curve is then plotted using the deflection data collected at various voltages (forces) applied. With this curve, the force produced by a microthruster can be made known based on the displacement that it causes to the platform beam as it fires.

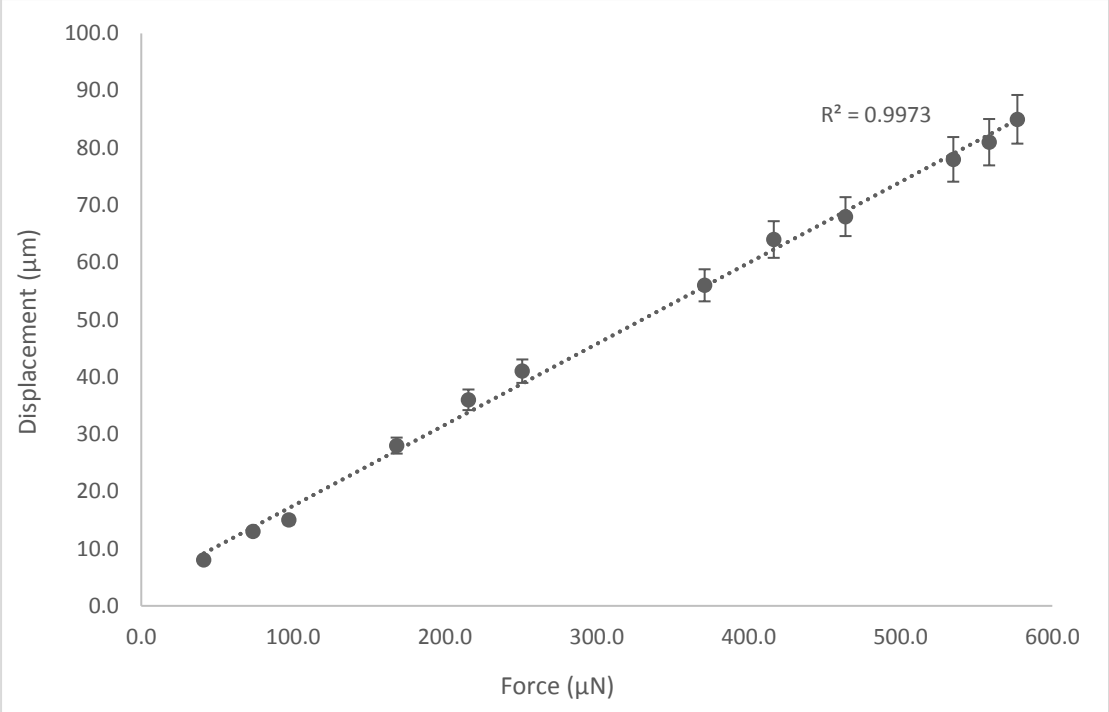


Figure 17. Calibration curve for constant force measurement.

Using the 51.5 mm coil as the electromagnetic calibrator, calibration force at two orders of magnitude that ranges from 41.2 μN to 577.0 μN was generated.

3.3 Error Analysis

Errors in measurement may come from many aspects. By applying 2 V to the calibrator, the calibration force generated is 251 μN.

Sensitivity of the thrust stand is given by:

$$sensitivity = \frac{251\ \mu N}{41\ \mu m} = 6.12\ \mu N/\mu m$$

Since the smallest calibration force produced by the calibrator is 41.2 μN, the smallest linear displacement is expected as:

$$min.\ linear\ displacement = \frac{41.2}{6.12} = 6.73\ \mu m$$

As the linear displacement sensor has a resolution of 1 μm, it gives the uncertainty error as:

$$uncertainty\ error = \frac{1}{6.73} \times 100\ \% = 14.86\ \%$$

This level of accuracy is acceptable for force measurement in the level of micronewton given the resources. It should be noted that the uncertainty error is a

function of linear displacement measured. If the displacement is larger (larger calibration force), the error will reduce accordingly.

The ambient noise that causes about 2 μm of deflection in the sample response shown could also contribute to errors in the measurements. It may occur throughout the oscillation. The errors could be reduced if a sensor with higher resolution is used. In addition, it would be better to use a sensor with higher sampling rate as well. Errors may also stem from the limitations of other equipment used like the weighing balance. Overall, improvements can be done to reduce errors provided if the budget allowed.

4. Conclusion

In conclusion, the objectives of this project are met. The torsional thrust stand is fully built and calibrated. An alternative method of using voice coils as electromagnetic calibrator is developed in this project. The thrust stand is able to be calibrated to a resolution of approximately 40 μN. The uncertainty error of 14.86 % is considered acceptable, though it can be improved by using equipment of higher caliber. Ambient noises are only at about 2 μm with very little fluctuations occurring. This proved that the passive vibration cancelling method used in this study is effective.

References

[1] W. Shiroma, L. Martin, J. Akagi, J. Akagi, B. Wolfe, B. Fewell, and A. Ohta, "CubeSats: A bright future for nanosatellites," *Cent. Eur. J. Eng.*, vol. 1, no. 1, 2011.

[2] J. K. Ziemer, "Performance Measurements Using a Sub-Micronewton Resolution Thrust Stand," in *27th International Electric Propulsion Conference*, 2001.

[3] K. H. Cheah, K. Low, Q. V. Tran, and Z. Lau, "Development of an electrostatic calibration system for a torsional micro- newton thrust stand," 2013.

[4] A. Pancotti, T. Haag, S. King, and M. Walker, "Recommended Practices in Thrust Measurements," in *33rd International Electric Propulsion Conference*, 2013.

[5] H. Koizumi, K. Komurasaki, and Y. Arakawa, "Development of thrust stand for low impulse measurement from microthrusters," *Rev. Sci. Instrum.*, vol. 75, no. 3185, 2004.

[6] J. Soni and S. Roy, "Design and characterization of a nano-Newton resolution thrust stand," *Rev. Sci. Instrum.*, vol. 84, no. 095103, 2013.

[7] A. G. Cofer, S. D. Heister, and A. Alexeenko, "Improved Design and Characterization of MicroNewton Torsional Balance Thrust Stand," in *49th AIAA/ASME/SAE/ASEE Joint Propulsion Conference*, 2013.

[8] N. P. Selden and A. D. Ketsdever, "Comparison of force balance calibration techniques for the nano-Newton range," *Rev. Sci. Instrum.*, vol. 74, no. 5249, 2003.

[9] Z. He, J. Wu, D. Zhang, G. Lu, Z. Liu, and R. Zhang, "Precision electromagnetic calibration technique for micro-Newton thrust stands Precision electromagnetic calibration technique for micro-Newton," *Rev. Sci. Instrum.*, vol. 84, no. 055107, 2013.

[10] J. R. Flores, M. Ingle, N. Robinson, and A. Choudhuri, “Development of a Torsional Thrust Balance for the performance evaluation of 100mN-5N class thrusters,” in *47th AIAA/ASME/SAE/ASEE Joint Propulsion Conference & Exhibit*, 2011.

[11] B. Seifert, A. Reissner, N. Buldrini, and F. Plesescu, “Development and Verification of a µN Thrust Balance for High Voltage Electric Propulsion Systems,” in *33rd International Electric Propulsion Conference*, 2013.

[12] C. R. Phipps, J. R. Luke, W. Helgeson, and R. Johnson, “A low-noise thrust stand for microthrusters with 25nN resolution.”

eureca 2016 – Conference Paper
Paper Number 2ME13

The Behaviour of Unsteady Turbulent Flow through an orifice at Low Aspect ratio

Lee Deng Cherng[1]

[1]*Bachelor Degree (Hons) in Mechanical Engineering*

Dengcherng_93@hotmail.com

Abstract
This paper is about the behaviour of unsteady turbulent flow through an orifice at low aspect ratio. The type of orifice used is square-edged concentric orifice plate, because this type of orifice plate is most common used. The diameter of the flow is set to 2 inch, total length of the pipe is 10 inch, orifice thickness is set to 0.2 inch according to the ISO 5167. The distance of the orifice is 2 inch away from the inlet so that can observe the turbulent occur in the downstream. The range of aspect ratio is 0.1, 0.12, 0.14, 0.16, 0.18 and 0.2, while the Reynolds number is 5000, 10000, 15000, 20000, 25000, and 3000, which means the velocity inlet will be changing as well. *K*-ε model will be used for the simulation as it is simplest complete turbulent model.

Keywords: Low aspect ratio. Turbulent. CFD. Reynolds Number. *K*-ε model.

1. Introduction

Flow measurement is essential in this modern world while most of all the companies need fluids to manufacture their product or mixing a chemical in a very small quantity. In some operations, the ability of conducting accurate flow measurements is so important that it can make difference between profits or taking loss for the company. Moreover, inaccurate flow measurement can lead to serious damage to the product. Thus, precise measurement is important.

There are three type of flow in fluid mechanics, which is laminar flow, transitional flow, and turbulent flow. First, laminar flow is type of flow that run smoothly down the stream. Turbulent is which the flow is characterized by chaotic property changes with low momentum diffusion, high convection of momentum and rapid change of pressure, while transitional flow is the mix of laminar and turbulent flow. In term of Reynolds numbers, laminar flow has the range of 2400 and below, transitional flow has the range of 2400 to 6000, and turbulent flow has the range of 6000 and above [1]. The reason why turbulent is paid more attention to other two flow motion is because as mentioned above, turbulence has developed chaotic property which is hard to predict the flow of particle compared to laminar flow. Besides, most of the flow that happen in every corner in the Earth is turbulent flow, for example, water

from hose, flow past a curved wall, air particle pass through the airfoil, volcano eruption, and so on [2]. Therefore, to understand the power of nature better, the knowledge of turbulent cannot be neglected, in fact should be strengthen.

Since this project is about flow measurement, it is worth mention that there are three type of measuring apparatus for fluid flow measurement, Venturi, Nozzle and Orifice. The entrance of venturi is a converging cone with 15^o to 20^o angle. It converges down to the throat, which is the point of minimum cross-sectional area, minimum pressure in meter and maximum velocity. A flow nozzle meter is usually consist of a short nozzle, held in place between two pipe flanges. It is simpler and less expensive than venturi. The orifice meter is the simplest among all. It is a thin circular plate with holes and installed between two pipe as well [3].

Table 1: Overall Comment on Each Type of Flow Measurements

Type of Flow Measurement	Head Loss	Discharge Coefficient	Installation	Price
Venturi	Lowest	Highest	Hard	High
Nozzle	Low	Low	Moderate	Moderate
Orifice	Highest	Lowest	Easy	Low

When a certain volume of liquid is flowing down the pipe, it requires some amount of energy. Energy difference or pressure difference is a must in order for the flow to move. Some of the energy is lost due to resistance, and it is call as head loss [4]. Discharge coefficient is the ratio of actual mass flow rate to the ideal mass flow rate. For better flow measuring system, head loss and discharge coefficient has a great impact on the result. Lowest head loss mean that the outlet is similar pressure compared to the inlet, while high discharge coefficient shows that the flow measuring system is close to the ideal method of flow. Based from head loss and discharge coefficient, venturi is no doubt the best measuring system. Comparing venturi and orifice, orifice meter has a large permanent loss of pressure due to the presence of eddies on the downstream side of the plate, venturi meter greatly reduces the pressure loss with the benefits of its geometry. On the other hand, venturi meter takes time to install as venturi is big and hard to manufacture. Therefore, venturi is often use when the flow need to recover its energy and the flow is in high pressure. Due to its material and time to build one venturi meter, these resulting the cost of venturi meter to be expensive [5]. In term of flexibility, orifice can easily be changed to accommodate widely different flow rates, whereas throat diameter of venturi is fixed, so its application is limited. Thus, all these factors make orifice the better choice for flow measurement as it is cheap, easy to install, great flexibility [3].

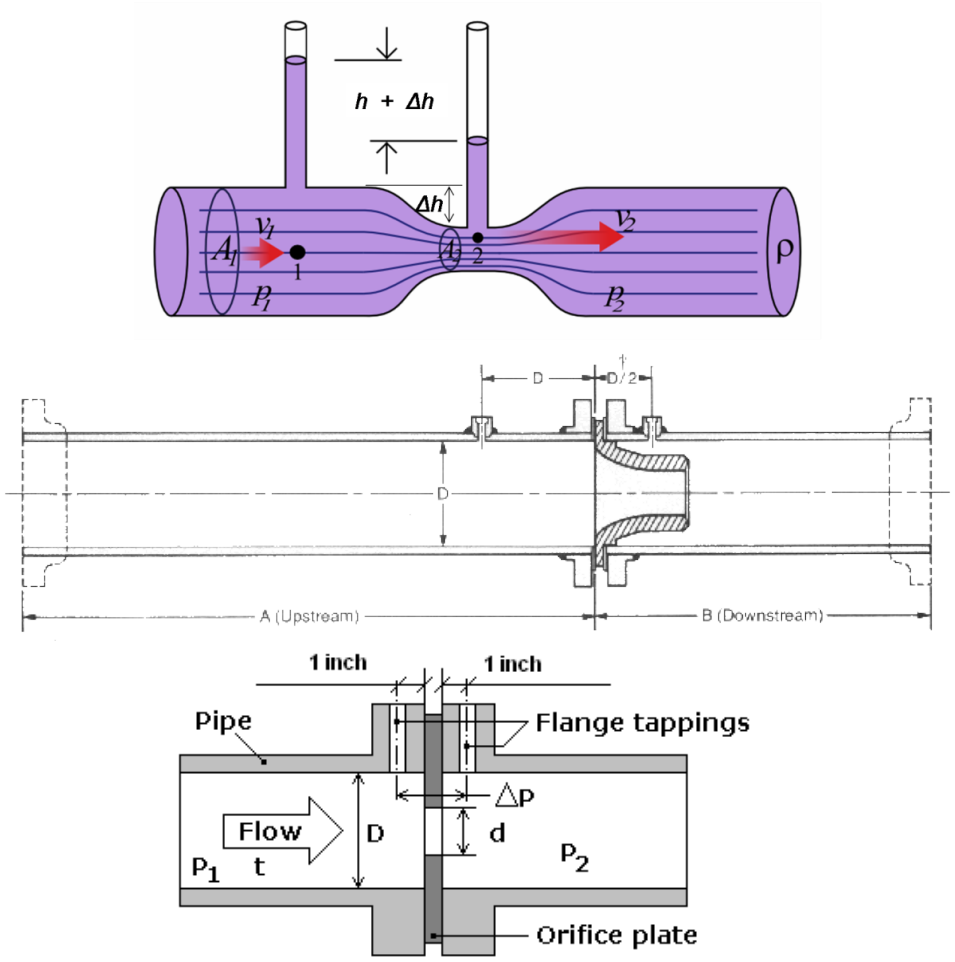


Figure 1: Venturi, Nozzle and Orifice (from top to bottom)

After mentioning different type of flow meter, orifice also can be categorized into three main groups which is concentric, eccentric and segmented. Concentric orifice plate is orifice with a full hole in its centre and is used when the application involved ideal liquid, gases and steam service. Eccentric orifice plate has a full circle that place at the bore offset from the centre point. Due to this hole position, it can minimize problems when dealing with solid containing materials. Besides, this design also able to prevents upstream damming. Therefore, it is best to use eccentric orifice plate for solid containing fluid, oil containing water and wet steam. Lastly, segmented orifice plate has hole in form of segment of a circle and it is placed concentric to the circle. Segmented orifice plate eliminate damming of foreign materials on the upstream of the pipe. The segmental section can be place either top or bottom depending on the type of fluid [6]. Basically, segmented orifice plate is used widely when measuring colloidal and slurry flow [7].

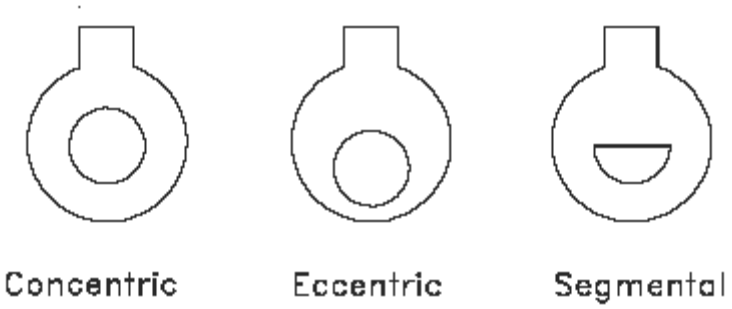


Figure 2: Type of Orifice Plate

Besides categorize as concentric, eccentric and segmented, orifice plate also has different edge. Most commonly used for flow measurement is square edged orifice plate. This type of orifice is the simplest to manufacture compared to other type of edge. This structure is simple, high accuracy and easy to be replace and install. Square edge orifice can be used regardless of flow direction due to both side of the orifice face is the same. This type of orifice is recommended for clean water, gases and steam flow with the range of Reynolds Number between 10000 to 10^7. Quadrant edge orifice plate is which the inlet edge is rounded to a quarter circle. This type of orifice is used for viscous fluids and Reynolds number with the range of 2000 to 10000. Conical entrance of orifice is another popular product. This conical entrance orifice plate are used for laminar flow, with the Reynolds Number between 80 to 2000. This orifice has predictable discharge coefficient due to the speed of fluid flow [8].

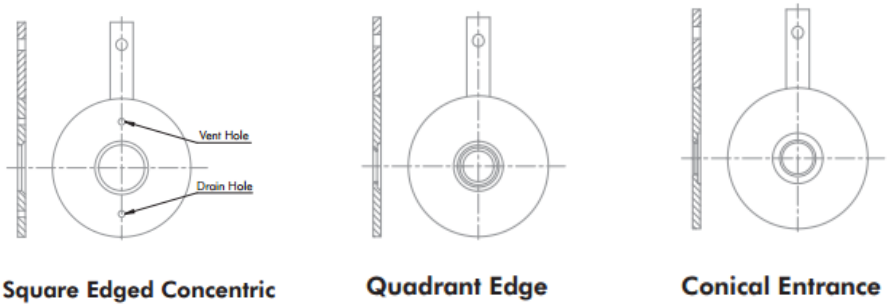


Figure 3: Different type of Orifice Edge

When dealing with flow measurement, Bernoulli Equation is referred as the formula to calculate the flow of fluid in the pipe. Assuming a horizontal flow, the Bernoulli's Equation can be written as:

$$\frac{p}{\rho g} + \frac{v^2}{2g} + h = \text{constant} \qquad \text{Eq (1)}$$

Where p is the static pressure, v is the average velocity, h is hydraulics height. The continuity equation can be expressed as:

$$\rho v A = Q = \text{constant} \qquad \text{Eq. (2)}$$

Where ρ is density, v is average velocity, and A is area.

In addition to these two basic equations, the coefficient of discharge c_d, is defined as the ratio of experimental discharge and theoretical discharge.

In order to able to study flow measurement better, experimental method and analysis method is a must to do so. ANSYS-CFD is the most common programme for simulation of fluid flow. It simulate the interaction of fluid, water or air flow with the geometry given. The simulation is based on the cell generated as known as meshing. The programme will then predict the velocity, pressure, force and other criteria in each node of the meshing. This programme predict the fluid flow, heat and mass transfer, chemical reaction and so on by solving numerically the set of governing mathematical equations, which is Conservation of mass, Conservation of momentum, Conservation of energy, Conservation of species and Effects of body forces [9]. There are many different model in ANSYS programme, when dealing with internal turbulent fluid flow, k model or Large Eddy Simulation (LES) model is often used. In turbulent flow, it is hard to determine how large the eddy is produced during the flow, but LES can resolved the eddy directly regardless of its size. Thus, LES can predict much more accurate for turbulent flow [10]. There are two type of k model, *k-ε* model, and *k-ω* model. *K-ω* model is based on Wilcox *k-ω* model which predicts free shear flow spreading rates, thus applicable to wall-bounded flow and free shear flows. *K-ε* model is the simplest complete models of turbulence, which the prediction is based on two equation. In the derivation of the *k-ε* model, the assumption is that the flow is fully turbulent and the effect of molecular viscosity are negligible. Thus this model is valid for fully turbulent flows [11]. The advantage of *k-ε* model is that it is simple turbulent model, excellent performance for industrial flows, while the pros of LES model is accurate due to yield information relating to mean flow and statistics of resolved fluctuation. The cons of LES is validation experience is limited, time taking and expensive [12].

2. Literature review

There are many works done to study about turbulent flow in the past. These contributors did the researches experimentally, theoretically and analytically in order to further contribute to the body of knowledge. With the presence of ANSYS programme, the study nowadays been carried out using computers to predict the flow.

Orifice is one of few apparatuses that are currently use for flow measurements. Venturi, nozzles, and orifice plate are the most known flow meters. All these tools are well investigated at certain conditions; however more and specific research could be very decisive in case of progressing and developing such a tool. The most important property that was investigated is the coefficient of discharge (C_d). Colter L. Hollingshead, in his Master thesis, investigated the three flow meters thoroughly. In his work, Colter L. Hollingshead considered two changing factors; namely aspect ratios of , 0.5, 0.6, 0.65, and 0.7 and the pipe length from 15.41 to 20.27 cm. Figure 4 shows the coefficient of discharge versus Reynolds number. It is clearly shown that the maximum coefficient appears at Reynolds number of about 100 which is laminar flow. As the flow is developed to turbulent, the coefficient of discharge become almost independent of Reynolds numbers. There was no explanations mentioned by the author's work, however it seemingly the issue is related to the diminishing effectiveness of the viscosity as the velocity increases rapidly based on increasing Reynolds number. The

work presented by Hollingshead is compared with other work conducted by Miller's Data (Miller, 1996) [13].

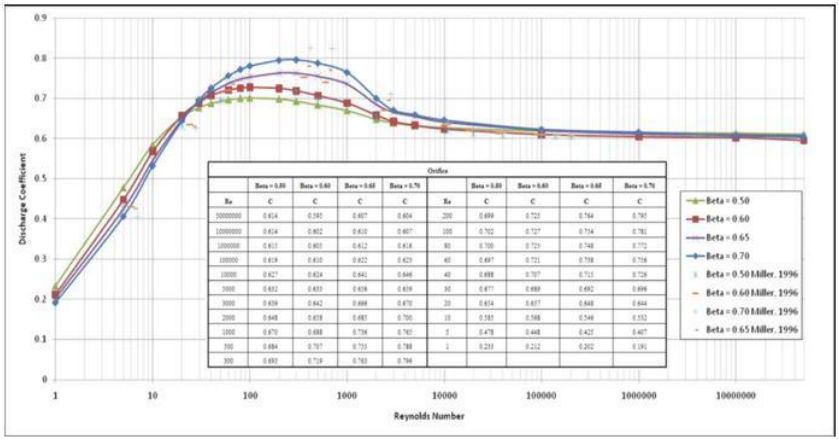


Figure 4. : Effect of the different aspect ratio of orifice on discharge coefficient

The effects of the boundary conditions and the type of fluid used in CFD simulation were the topic of a recent research performed by Shah et al. This study is comprehensive study through which the influence of the modeling, initial and boundary conditions, the structural meshing effects were discussed. Based on the thesis wrote by Manish S.Shah, JyeshtharajB.Joshi, AvtarS.Kalsi , C.S.R.Prasad, DayaS.Shukla in India in 11/Nov/2011, they studied different fluid which is water and air to pass through a beta ratio range from 0.5 to 0.8. They used *k-ε* turbulence model to run the simulation [14].

The authors showed that the turbulent flow is developed in the upstream of the orifice meter. Turbulent wakes and recirculation zones can be observed at the downstream of the orifice meter. The author also talked about Veena Contrata, which is the point of the maximum velocity. Beyond the point Veena Contrata, the velocity of the flow decrease and the energy conserved at all the points in the domain.

For the information, orifice plate come in different thickness. The thickness of the orifice does affect the flow in downstream pipe. Wu JianHua, Ai WanZheng, and Zhou Qi did their research on the thickness of orifice effect to the head loss coefficient[15]. They did the research in experimental method with set up shown in Fig. 7 with the aspect ratio, β of 0.4, 0.5, 0.6, 0.7, and 0.8 and the α, which is the ratio of orifice's thickness to the approach flow diameter or known as contraction ratio, with the range of 0.05, 0.10, 0.15, 0.20, and 0.25 for the aspect ratio of 0.7 [15]. They proved that the head loss coefficient increase when the contraction ratio decrease and when the aspect ratio decrease which is shown in Fig. 8.

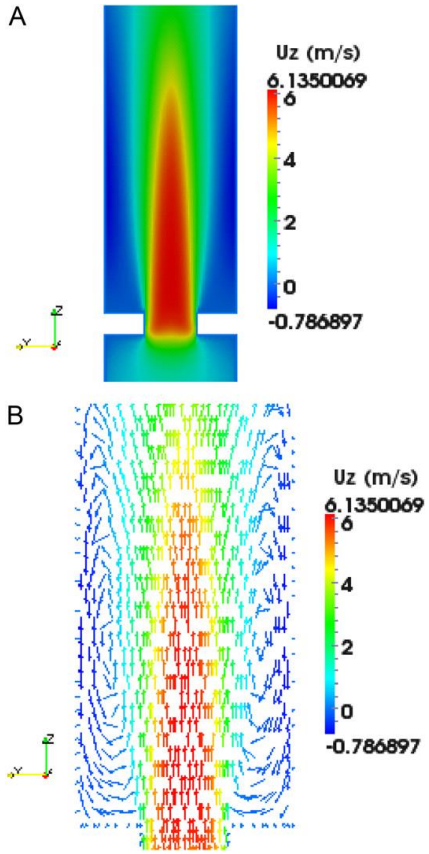


Figure 5: A) Velocity contours and B) Velocity vectors

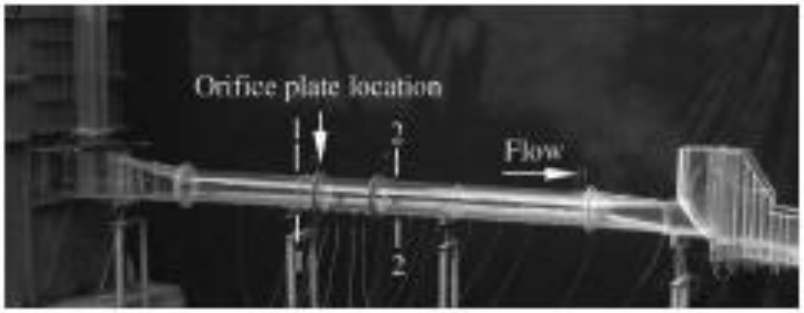


Figure 6: Experiment model

	α				
β	0.05	0.10	0.15	0.20	0.25
0.40	/	95.30	/	/	/
0.50	/	32.50	/	/	/
0.60	/	12.20	/	/	/
0.70	4.40	4.33	3.73	3.43	3.03
0.80	/	1.45	/	/	/

Figure 7: Table of Aspect ratio β, contraction ratio α and the head loss coefficient

Table 2: Summary of Literature Review

Author	Aspect ratio β	Working Fluid	Remarks
Manish S.Shah, JyeshtharajB.Joshi, AvtarS.Kalsi , C.S.R.Prasad, DayaS.Shukla	0.5 to 0.8	Water and Air	High aspect ratio is used and used two working fluid
Colter L. Hollingshead	0.5, 0.6, 0.65, and 0.7	Water	Used v-cone, orifice plate, venturi to conduct the simulation
Wu JianHua, Ai WanZheng, and Zhou Qi	0.4 to 0.8	Water	Changing of contraction ratio and aspect ratio

3. Methodology

During the early stage of the project, student was given journals about related topic. This allowed student to have better understanding on the concept of fluid flow measurement. Besides, by studying journals and did some online researches, student able to pinpoint that most researchers are dealing with the aspect ratio between 0.2 to 0.8, since student's project is studying about aspect ratio between 0.1 to 0.2, student able contribute a new knowledge to the body if success. By reviewing the past paper, student also able to understand the relation of fluid flow to different flow measurement, aspect ratio, contraction ratio and so on.

With these information, student proceeded with planning of the experiment. This project mainly using simulation with the help of ANSYS. The geometry, type of fluid flow used. Type of orifice, diameter of hole of orifice, thickness of orifice, velocity in inlet valve, and so on is determined carefully as each parameter mentioned above has a possibility of affecting the result. The type of orifice used in this project is square-edged concentric orifice as this orifice is widely used due to its flexibility. The flow diameter is 2 in while the diameter of hole or orifice is changing based on the aspect ratio with the range of 0.1, 0.12, 0.14, 0.16, 0.18, and 0.2. The thickness of orifice is calculated as 0.2 inch based on ISO 5167-2:2003, which is a standard for global orifice use. The velocity of the inlet is dependable on Reynolds Number with the formula of $R = \frac{\rho V D}{\mu}$ where R is Reynolds number, ρ is density of fluid, D is the diameter of the pipe, V is the velocity of the fluid, and μ is fluid viscosity. To avoid confusion during simulation results, student set the distance between the orifice and the inlet is 2 inch and it will remain unchanged throughout the simulations. The material of fluid flowing is set to water-liquid form. In ANSYS programme, *k-ε* model is chosen to run the simulation as it is quick and complete turbulence model.

After planning the detail of the pipe system, student draw the geometry in Workbench in 2D geometry. 3D geometry is unnecessary for this project as it is simple geometry and the result in all dimension is almost similar, so 2D geometry is faster method to achieve result. The inlet diameter is 2 inch, distance of the orifice plate in

the pipe is 2 inch, the total length of the pipe is 10 inch, thickness of the orifice is 0.2 inch. In order to have clearer result on the downstream of the pipe, orifice plate is suggested to put in front session of the pipe.

Meshing is important part for achieving a better result as ANSYS is predicting the result in each cell. Inflation from wall layer is selected for better results on the wall surface. Inflation is which the cell will grow bigger in size depend on the parameter user insert. Student let the cell grown 27 layer with the ratio of 1.05. For mesh type, quadrilateral cell is used since its 2D and it is simple geometry. The orthogonal quality of the mesh is 0.95 while the skewness is 0.1e-6 which is good enough for the simulation to run. The velocity of the inlet is calculated with the formula mentioned previously and inserted into the programme. The boundary condition of the pipe system is set for ANSYS to be able to predict the flow property. Then the simulation is run. Lastly, pressure contour, velocity profile, turbulent energy data is recorded.

4. Results and Discussion

Velocity profile and pressure profile is important because the profile shows magnitude of velocity and as well as the characteristics of the flow such as direction, shape of flow and so on. It helps to understand how the fluid behave under different situation.

Velocity increased drastically when approaching the opening of orifice plate metal, as shown in Figure 4-1. The velocity continue increased until the maximum velocity is reached. The point of maximum velocity is referred as Veena-Contracta. The magnitude of the fluid velocity decreased after passed through the point Veena-Contracta. The pressure decreased sharply before entering the domain Veena-Contracta. The pressure is in its minimum limit in Veena-Contracta, and started to recovered as the flow goes. However, in Figure 4-5, the pressure did not rise back to its inlet pressure level. The difference between the pressure is known as Head Loss, which is cannot be recovered. In the thesis done by Prajapati, C B, Singh, S N, Patel, V K, and Seshadri, V, their result for concentric orifice plate simulation proved that the low pressure zone behind the orifice plate and the pressure loss is partially recovered while the rest is permanently loss. Excellent agreement can be seen between the project wall pressure profile and the wall pressure profile done by Prajapati, C B, Singh, S N, Patel, V K, and Seshadri, V [19].

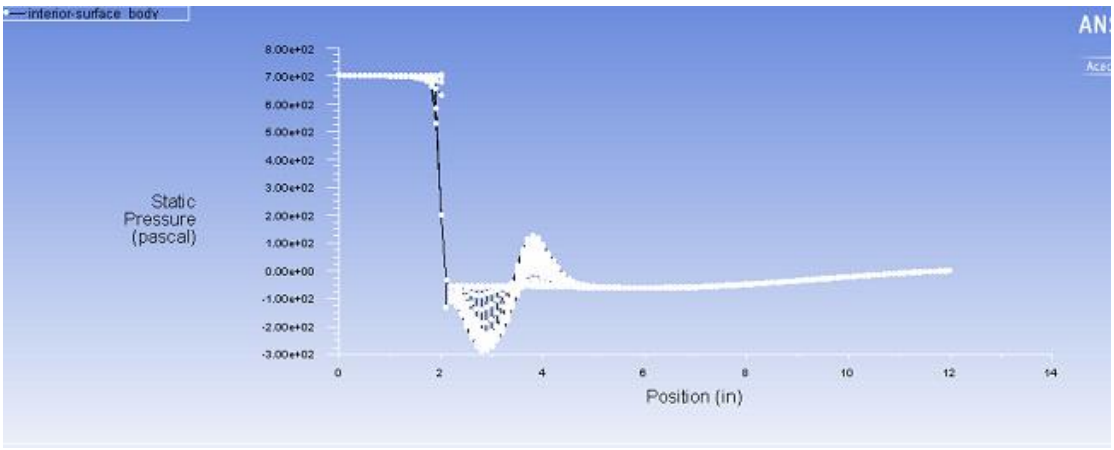


Figure 8: Wall Pressure Profile on Reynolds number 5000, Aspect Ratio 0.1

After simulation and graph plotting, it is clearer to determine the head loss of the orifice. From the graph, head loss coefficient increases when Reynolds number increases shown in Table 4-2. This is due to the sharp drop of pressure when entering orifice plate. This conclude that when the velocity inlet increase, the head loss coefficient increase as well due to higher friction on the wall surface. Besides that, the graph also shows that the head loss coefficient increases when aspect ratio of orifice plate decreases. This result matches the experimental research done by Wu JianHua, Ai WanZheng, and Zhou Qi [16].

Table 3: Pressure Loss for Aspect Ratio 0.1

Reynolds number	Pressure Inlet (Pa)	Pressure Outlet (Pa)	Permanent Pressure Loss
5000	7.00E+02	-5.00E+01	750
10000	3.00E+03	-2.50E+02	3250
15000	6.00E+03	-5.00E+02	6500
20000	1.20E+04	0.00E+00	12000
25000	1.75E+04	0.00E+00	17500
30000	2.50E+04	-2.50E+03	27500

Table 4: Pressure Loss for Reynolds number 5000

Aspect Ratio	Pressure Inlet (Pa)	Pressure Outlet (Pa)	Permanent Pressure Loss
0.1	7.00E+02	-5.00E+01	750
0.14	4.00E+02	-5.00E+01	450
0.16	2.63E+02	-2.50E+01	287.5
0.18	2.00E+02	0.00E+00	200
0.2	1.63E+02	-2.50E+01	187.5

When the fluid exiting the orifice plate, the velocity spike up. These velocity profiles shows the fluid behaviour after passing through the orifice. The centre of the orifice is at Position 1in.The magnitude of the velocity increase when the Reynolds number increase. This can be seen in Figure 4-6. Moreover the aspect ratio of the orifice plate affect the magnitude of velocity as mentioned previously. This can be seen in Figure 4-7. The result show that when the aspect ratio increase, the velocity decrease.

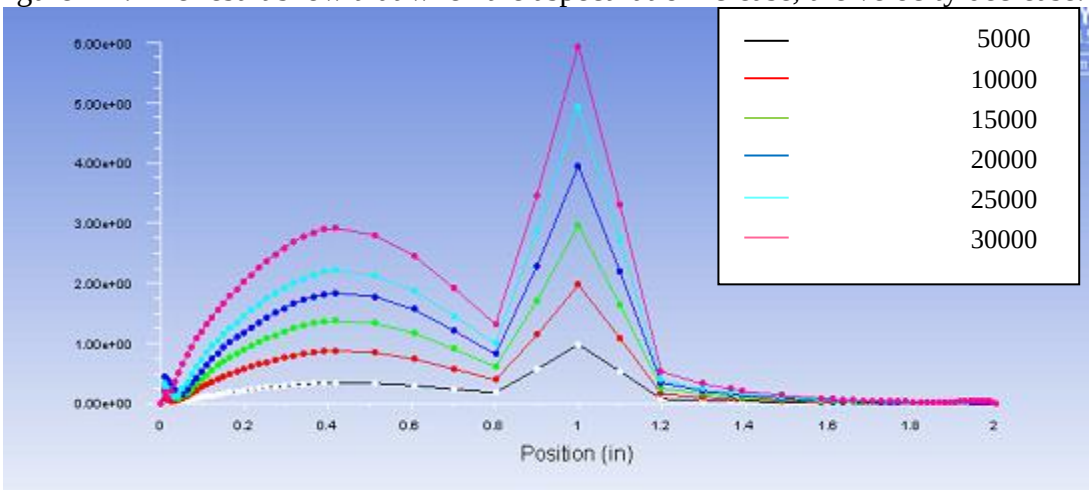


Figure 9: Velocity Profile on different Reynolds number with Aspect ratio 0.1

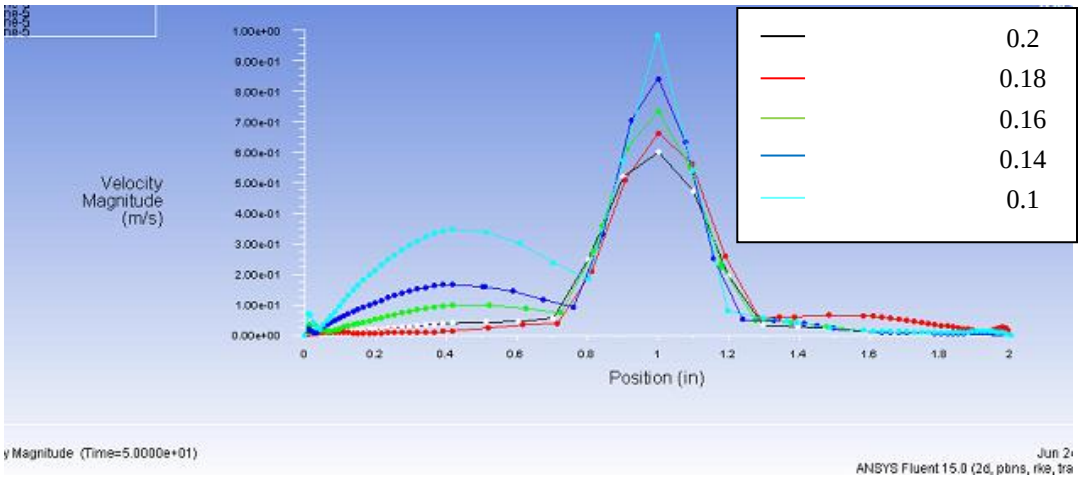


Figure 10: Velocity Profile on different Aspect Ratio with Reynolds number 5000

5. Conclusion and Future Works

The results are yet to be check whether it is correct by checking with supervisor and get numerical analysis if possible. In nutshell, this project involved 36 different simulation and student will continue the work which is the 0.12 aspect ratio simulation and others. As a result, the project's aim which is the effect of low aspect ratio to the downstream pipe will be fulfilled.

References

[1] "OMEGA ENGINEERING - Flow Control." [Online]. Available: http://www.omega.com/techref/flowcontrol.html. [Accessed: 24-May-2016].

[2] R. Ecke, "The Turbulence Problem." [Online]. Available: http://cnls.lanl.gov/External/articles/LAS_Robert_turbulence.pdf. [Accessed: 24-May-2016].

[3] H. Bengston and Lamar Stonecypher, "Pipe Flow Measurement with a Differential Pressure Flow Meter like the Orifice or Venturi Meter." [Online]. Available: http://www.brighthubengineering.com/hydraulics-civil-engineering/52906-orifice-flow-nozzle-and-venturi-meter-for-pipe-flow-measurement/. [Accessed: 24-May-2016].

[4] "Head Loss in Piping Systems - TechInfo." [Online]. Available: http://www.hydromatic.com/ResidentialPage_techinfopage_headloss.aspx. [Accessed: 24-May-2016].

[5] Olivia, "Difference Between Venturi and Orifice." [Online]. Available: http://www.differencebetween.com/difference-between-venturi-and-vs-orifice/. [Accessed: 24-May-2016].

[6] "Orifice Plate Type Flow Detector Review | Engineers Edge | www.engineersedge.com." [Online]. Available: http://www.engineersedge.com/instrumentation/orifice_plate_flow_detector.htm. [Accessed: 24-May-2016].

[7] "What are the different types of orifice plates and their uses ?" [Online]. Available:

http://iamechatronics.com/notes/process-measurement/128-what-are-the-different-types-of-orifice-plates-and-state-their-uses-. [Accessed: 24-May-2016].

[8] General, "Flow Division Catalog." [Online]. Available: http://www.fati.com/fati_esp/pdf/strumenti/Flow Division Catalogue.pdf. [Accessed: 24-May-2016].

[9] "Fluent ANSYS." [Online]. Available: http://imechanica.org/files/fluent_13.0_lecture02-intro-to-cfd.pdf. [Accessed: 24-May-2016].

[10] A. Fluent, "Turbulence Model- Additional Info_part2.pdf." .

[11] A. Fluent, "Turbulence-Model-Additional-Info_Part-1.pdf." .

[12] Lim Chin Hong, "Turbulent Modelling." 2014.

[13] Sætre and Johansen, "Discharge Coefficient Performance of Venturi, Standard Concentric Orifice Plate, V-Cone and Wedge flow Meters at Low Reynolds Numbers," *J. Pet. Sci. Eng.*, vol. 78 , pp. 559–566, 2011.

[14] M. S. Shah, J. B. Joshi, A. S. Kalsi, C. S. R. Prasad, and D. S. Shukla, "Analysis of flow through an orifice meter: CFD simulation," *Chem. Eng. Sci.*, vol. 71, pp. 300–309, 2012.

[15] and Z. Q. Wu JianHua, Ai WanZheng, "Head loss coefficient of orifice plate energy dissipator," *J. Hydraul. Res.*, vol. 49, no. 6, pp. 830–831, 2011.

Modelling the Mullins Effect in Stress-strain Behavior of Rubber

Lee Kar Fai[1*], Ch'ng Shiau Ying[2]

[1] *School of Engineering, Taylor's University, Malaysia*

[2] *School of Engineering, Taylor's University, Malaysia*

[*]karfai.lee@sd.taylors.edu.my

Abstract

The very first extension in rubber material is caused by the instant change in their mechanical properties through a process known as Mullins effect. Researches on Mullins effect have been widely studied on for the past six decades that it led to experimental evidences for stress-softening in rubbers, especially when they undergo cyclic loading. Since Mullins effect is the most noticeable loading observed in the cyclic stress-strain response, it is crucial to study the Mullins effect to prevent any undesirable failure, due to the fact that rubbers exhibit significant decrease in stress level which leads to a softer path on subsequent loading. Despite the extensive research on the rubber behavior, there has been minimal study on rubber loaded with carbon black material, which motivates the purpose of this research. This project models the Mullins effect in rubber based on neo-Hookean model using 0%, 25% and 40% of carbon black-loaded rubber. The research purpose entails two research questions; how the rubber material behaves under cyclic tensile loading, and if the developed model could predict the stress strain behavior and the damage from deformation in rubbers under cyclic loading. The methodology includes the research on Mullins effect, ensued by the tensile (cyclic loading) and stress-strain testing, both of which are repeated to study the behavior of the stress-strain for rubber under cyclic tensile loading. New model for the Mullins effect is developed using neo-Hookean model. This model takes into account the carbon black loading percentage of Mullins effect, which is not considered in other literature. Based on the experimental results, the stress-strain graphs particularly on 0%, 25% and 40% of carbon black loading are used to develop a mathematical model using MATLAB. The developed model could predict stress-strain behavior and the damage from deformation regardless of any percentage of carbon black loading applied.

Keywords: Mullins Effect, Stress, Strain, neo-Hookean, Damage.

1. Introduction

According to Bouasse and Carriere[1], the first extension in rubber materials is caused by the instant change in their mechanical properties. It is a process known as "Mullins effect". Studies for "Mullins effect" have been done for the past six decades which created the experimental evidences for stress-softening in rubbers. New models were created to investigate the mechanical behavior of rubbers which relied on the strain history. The large deformations, non-linear behavior and Mullins softening models will undergo high level of complexity and they depend heavily on phenomenological parameters. Physical experiments were conducted from, chain breakage at the interface between the rubber and the fillers, slipping of molecules, chain disentanglements, rupture of the cluster fillers in order to obtain better results and better understandings in stress-softening.

All rubber materials will show hysteresis and stress softening phenomena in the cyclic loading. The viscoelasticity is caused by the rubber's behavior [2]. During the transition from the first cycle to the second cycle, the loss in stiffness in rubber is a non-neglectable process. The loss of stiffness in rubber behaviour has become a very important factor in the prediction of fatigue lifetime [3]. A lower consecutive stress can be observed from the stress-strain response and the very first loading phase will generate the same amount of stretch caused by the stress.

There have been many researches done to propose different theories for the Mullins effect explanation. Mullins and Tobin [4] proposed that the elastomer comprised hard and soft phases, of which the hard phase would turn into soft one during the deformation process. Some other works have since validated the theory [5-8]. Simo adopted the Continuum Damage Mechanics (CDM) concept which considered Mullins effect as damaging phenomenon described by scalar damage parameter [8]. The material response is characterized by multiplying the classical hyperelastic strain energy, with the damage level represented by a reducing parameter. Contrary to the work by Miehe [9] which claimed that damage evolves when the material undergoes an applied level of deformation for the first time, Ogden and Roxburgh [10] proposed zero damage when the similar situation applies. They proposed that the Mullins effect is a result of links breakage in the material, which involves both filler matrix and chain interaction links. Chagnon et al. [11] then developed this theory by including the dangling chains effect in the network. The research claimed that the number of monomers involved in the elastic response is related to the maximum deformation as a decreasing function. The Mullins effect is considered to be a consequence of the breakage of links inside the material. Meanwhile, Diani et al. [12] concluded several observations based on materials exhibiting softening effect. It was claimed that the softening, which is characterized by lower resulting stress for the same amount of applied strain actually appears after the first load.

This research is based on two research questions, namely, "How does the rubber material behave under cyclic tensile loading?" and "Could the developed model predict the stress strain behavior and the damage from deformation in rubbers under cyclic loading?" The objectives of this research are to study the stress-strain behavior of rubber under cyclic tensile loading, and to model the Mullins effect of rubbers under cyclic loading using neo-Hookean model. Tensile test for cyclic loading and stress strain test are conducted on rubber of Nitril Butadiene Rubber (NBR) type, and the

mathematical modeling based on neo-Hookean model is developed using MATLAB. The percentage of carbon black loaded rubber analyzed are 0%, 25% and 40%.

2. Theoretical Framework

Based on the available models, neo-Hookean is chosen in this research due to its simplicity. The theoretical framework for both NBR rubber type and neo-Hookean model are explained in detail in the next section.

2.1 Nitril Butadiene Rubber (NBR)

Nitril Butadiene Rubber (NBR) is a synthetic rubber copolymer comprising acrylonitrile (ACN) and butadiene. It comprises unsaturated copolymers of 2-propenenitrile and various butadiene monomers (1,2-butadiene and 1,3-butadiene). Its molecular structure is as illustrated in Fig. 1.

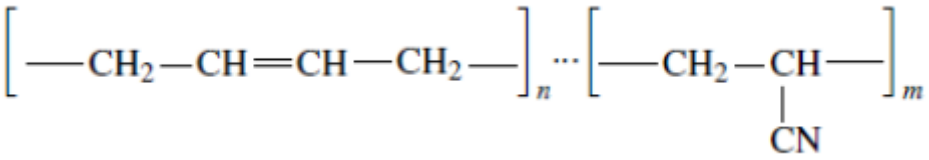


Figure 1. Molecular structure of NBR [13]

NBR is obtained by the process of emulsion polymerization using free-radical polymerization. The most crucial property which sets NBR of its advantage would be the high resistance to fuel, oil and other chemicals. The degree of resistance depends on the ratio of acrylonitrile to butadiene. Basically resistance to oil increases with the increasing content of acrylonitrile within the elastomer, but it compensates with the lower flexibility of the material, thus the unlikelihood of high composition of such content in the elastomer [13].

Another advantage of NBR includes the good elongation properties, adequate resilience, tensile and compression set. NBR is more resistant to oil and acids as compared to natural rubber, but comes with poorer strength and flexibility properties. NBR is a generally used elastomer used as a seal energizer or low pressure applications, for instance, hydraulics and pneumatics. NBR is used to make pneumatic seals, low pressure hydraulic seals, hoses, O-rings, gaskets, grommets and washer to deal with the fuel and oil in both automative and aeronautical industries. As long as oil resistance is not posing as an issue, NBR gets rarely picked as the material selections. Since NBR is generally attacked by ketones, ozones, aldehydes, chlorinated and intro hydrocarbons, it does not seem popular with applications that require weather, ozone, sunlight and flame [14].

2.2 Mechanical Responses under Cyclic Loading

Synthetic rubbers usually exhibit strong inelastic responses under cyclic loading, one of which is the stress-softening known as Mullins effect, as illustrated in Fig. 2.

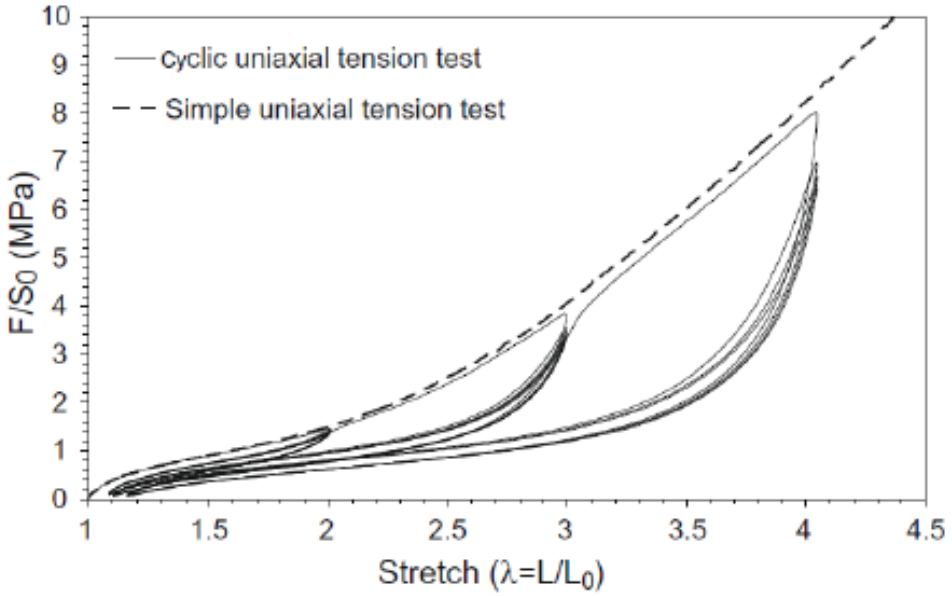


Figure 2. Stress-strain responses of SBR under simple uniaxial tension and cyclic uniaxial tension [12]

The phenomenon of stress-softening (Mullins effect) was initially observed by Bouasse and Carriére [1], after which was studied extensively by Mullins [4]. That was how the name was derived for the phenomenon. The stress-strain response conducted by Mullins is as illustrated in Fig. 3. The response was derived from a cyclic, quasi-static deformation. Based on Fig. 3, the rubber exhibits a relatively stiff response in the first loading, and eventually illustrating a significant decrease in the stress level, which is denoted by the dashed lines. The Mullins effect is characterized by the decrease of the stress level in both uploading and unloading during the first few loading cycles. This would be ensued by the stabilizing stress-strain response, which observes the subsequent loading cycles to be tracing the path of the stabilized stress-strain curve. It is therefore crucial to consider the Mullins effect for designs involving elastomer components under cyclic loading.

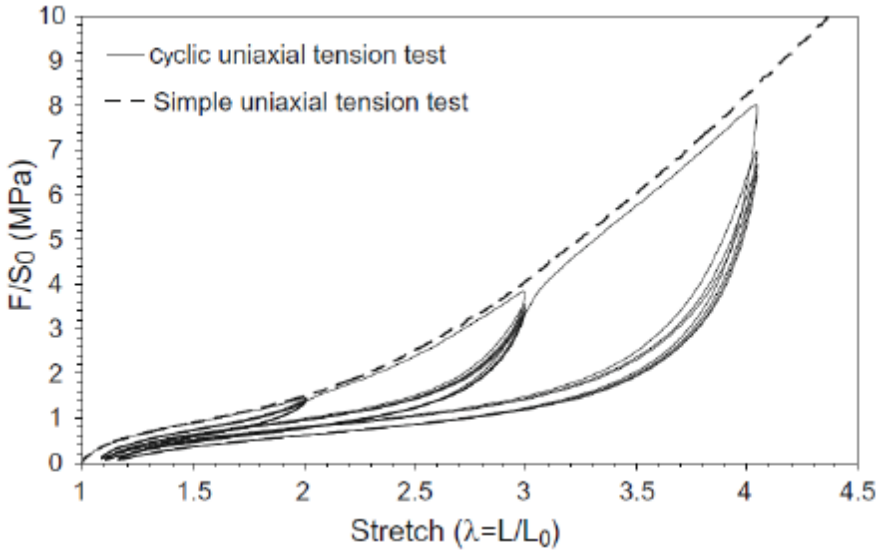


Figure 3. Softening of elastomers due to the Mullins effect [4]

While stress-softening is commonly observed in filled and unfilled crystallized rubber, no study has reported its occurrence in an unfilled uncrystallized rubber [12].

2.3 Constitutive Equation

The basics of hyperelasticity are explained in this section, from which the mathematical model in this research is developed. Assuming that the rubber material is homogenous, hyperelastic and incompressible, the rubber body occupies region Ω in its unstressed layout. When deformation takes place, the body would occupy new region Ω_d and the material point X is shifted to position x. The deformation gradient tensor, $\boldsymbol{F}$ is given by [14]

$$\boldsymbol{F} = \frac{\delta x}{\delta X} \tag{1}$$

Based on the principle of objectivity and isotropy, the strain energy function W could be expressed as function of two invariants of $\boldsymbol{B}$, given by [14]

$$\boldsymbol{W} = W(I_1, I_2) \tag{2}$$

Where

$$I_1 = tr\ \boldsymbol{B} \tag{3}$$

$$I_2 = \frac{1}{2}(I_1^2 - tr\boldsymbol{B}^2) \tag{4}$$

Based on the second law of thermodynamics, the Cauchy stress tensor is given by [15]

$$\sigma = -p\boldsymbol{I} + \mathbf{2}\left[\frac{\delta W(I_1,I_2)}{\delta I_1} + I_1\frac{\delta W(I_1,I_2)}{\delta I_2}\right]\boldsymbol{B} - \mathbf{2}\frac{\delta W(I_1,I_2)}{\delta I_2}\boldsymbol{B}^2 \quad (5)$$

Where p is a Lagrange multiplier based on the incompressibility assumption.

2.3.1 Extension of Pseudo-elastic Model to Mullins Effects in Rubbers

For rubbers, the parameters *r* and *m* depend on the deformation, and the damage function *d* is given by

$$d = d\left(\varkappa, I_{1,max} - I_1\right) = \frac{1}{r(\varkappa)}\,\mathrm{erf}\left[\frac{1}{m(\varkappa)}\left(I_{1,max} - I_1\right)\right] \quad (6)$$

Where $\varkappa$ is the dimensionless interaction parameter between rubber and solvents.

The Cauchy stress tensor in Eq. (5) during the unloading and subsequent reloading to submaximal deformation then becomes [14]

$$\sigma = -p\boldsymbol{I} + \mathbf{2}(\mathbf{1} - \boldsymbol{d})\left[\frac{\delta W(I_1,I_2)}{\delta I_1} + I_1\frac{\delta W(I_1,I_2)}{\delta I_2}\right]\boldsymbol{B} - \mathbf{2}\frac{\delta W(I_1,I_2)}{\delta I_2}\boldsymbol{B}^2 \quad (7)$$

3. Methodology

In the research methodology section, the work is divided into two parts for which are Research and Testing on rubbers (Mullins's Effect) in the first half of the research and Research and Modelling on mathematical models in the second half. Firstly, the research on the Mullins Effect is conducted, followed by tensile testing (cyclic loading) and stress-strain testing on rubber with carbon black loading of 0%, 25% and 40%. Based on the testing results, the behavior of stress-strain for rubber under cyclic tensile loading is analyzed using MATLAB. Based on the developed model from the MATLAB coding, the stress strain behavior under cyclic loading could be predicted. The developed model also is used to obtain the parameters *r* and *m* which are explained in the earlier section, after which are utilized to predict the damage function *d*. The flowchart for the research project is as illustrated in Fig. 4. The outcome is a developed model based on neo-Hookean model which could be used to predict stress strain behaviour and the damage from deformation.

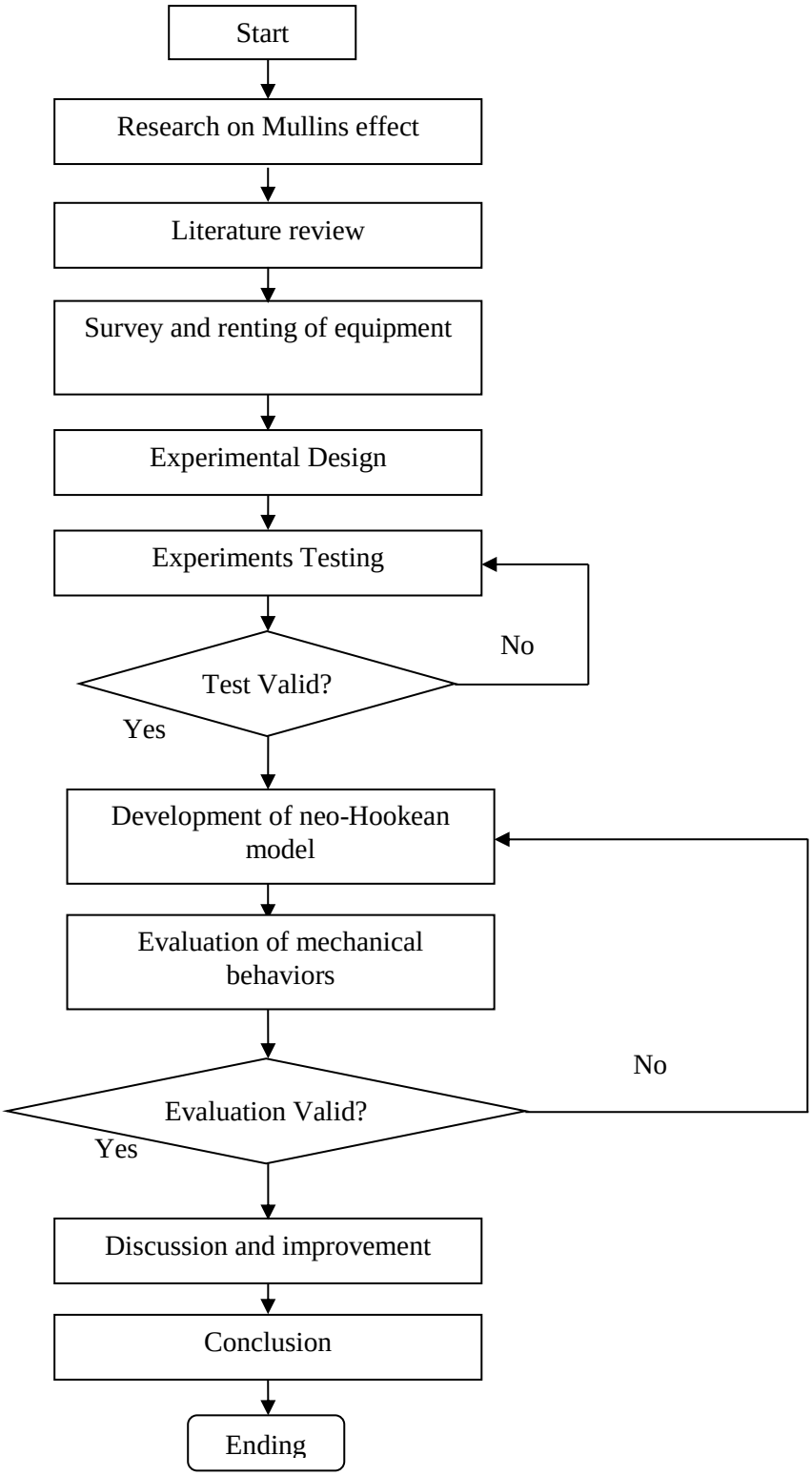


Figure 4. Flowchart of research project

4. Results and Discussion

The percentages of carbon black loading are chosen as such after thorough investigation. Other researches done are mainly of without carbon loading, therefore 0% loading. Besides, 25% carbon black loading is chosen because it is the specification commonly used commercially. 40% carbon black loading is the highest percentage that could be obtained commercially to study the behavior of Mullins effect, which would be important to serve as the benchmark for higher percentage of carbon black loading compared to that of the ones commercially available.

Based on the neo-Hookean model, the engineering stress tensor, *P* is given by

$$P = 2C_{10}(\lambda - \frac{1}{\lambda^2}) \quad (8)$$

Where C_{10} is the material constant, and

$$\lambda = \frac{\varepsilon}{100} + 1 \quad (9)$$

Where ε is the strain.

The engineering stress tensor, *P* is developed based on the data from tensile and stress testing, as illustrated in Fig. 5. The highest carbon loading of 40% has the highest gradient in the graph, followed by 25% and lastly, 0%. The gradient obtained is 2.9512, 1.0763 and 0.2644, respectively.

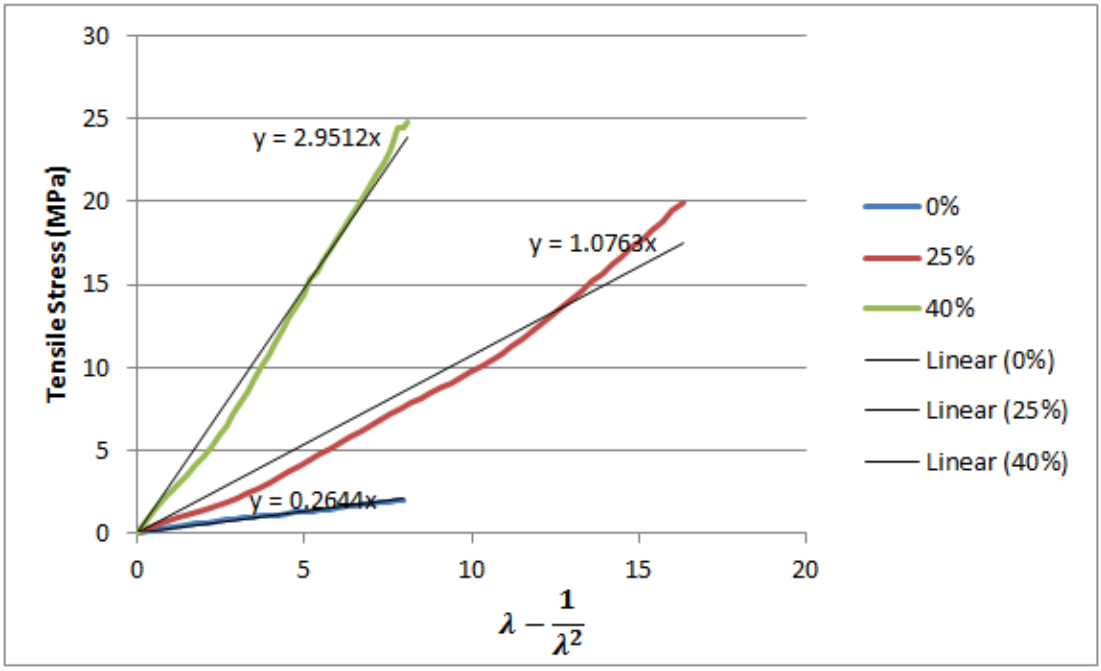


Figure 5.Tensile Stress against $\lambda - \frac{1}{\lambda^2}$.

These data are used as the material constant which are then used for the Eq. (10)

$$C = [a(CB)^2 + b(CB) + 1]C_{10}^0 \quad (10)$$

Where CB is the carbon black percentage in decimal form, and *a* and *b* are constant.

Based on Eq. (10), the normalized shear modulus, μ is plotted for the carbon black percentage of 0%, 25% and 40%, as shown in Fig. 6. The polynomial equation obtained from the graph is compared with Eq. (10) to identify the *a* and *b* constants.

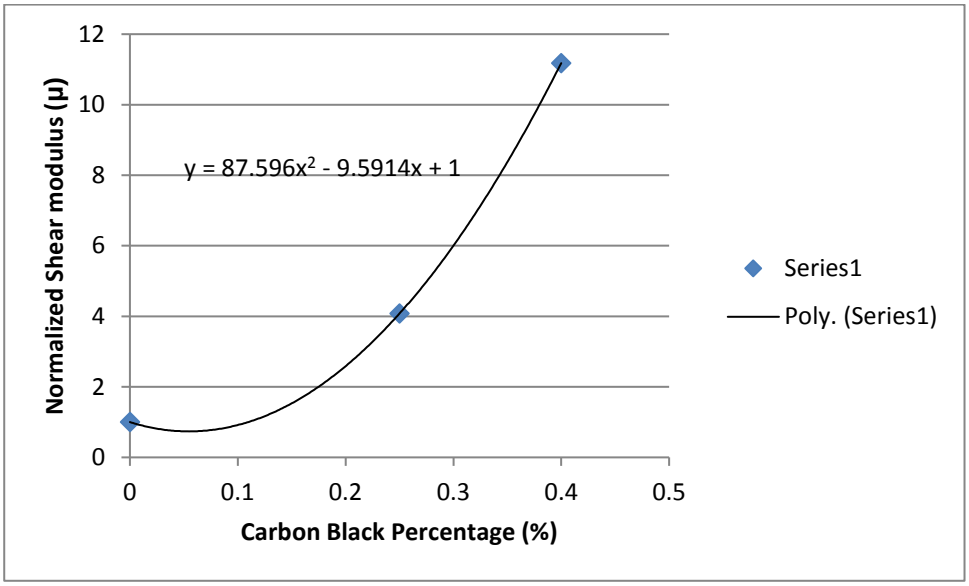


Figure 6. The normalized shear modulus against carbon black percentage.

The material constants obtained and the data from the tensile and strain testing are used in the MATLAB coding for the mathematical model. The plotting of engineering stress against engineering strain for each carbon black loading is as illustrated in Fig. 7, Fig. 8 and Fig. 9, respectively. Both theoretical and experimental results display similar patterns and have good correlation with each other which means the Mullins effect are well predicted. Similar results are obtained in [12], thus validating the research results.

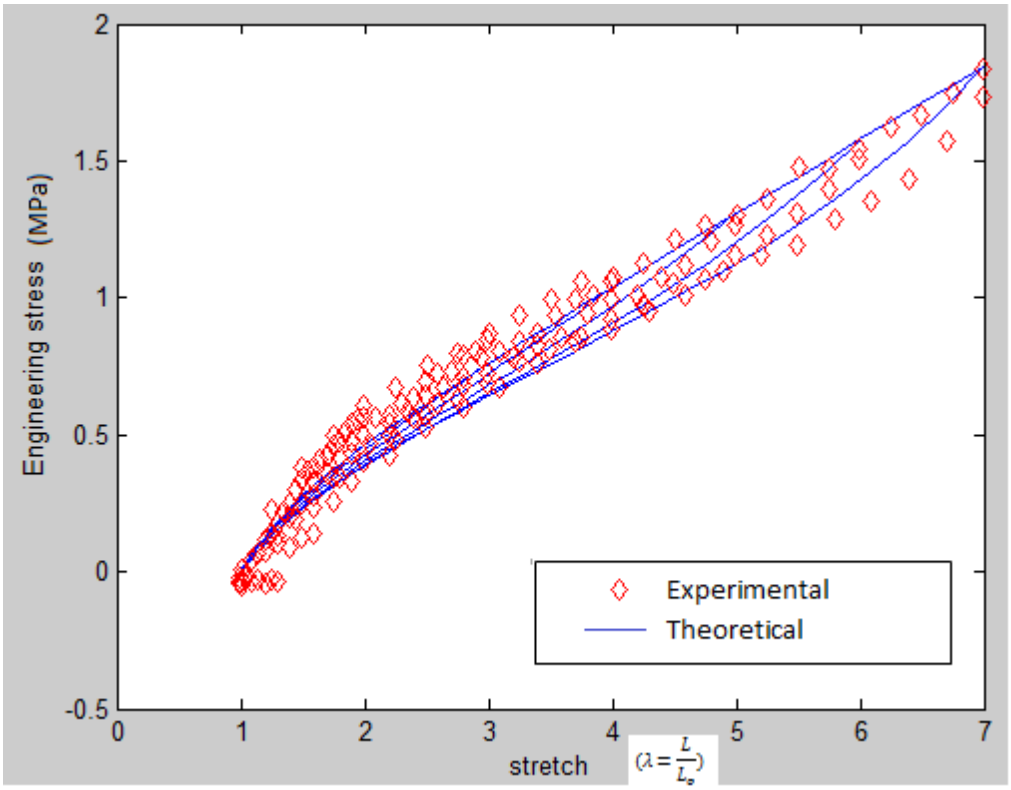


Figure 7. Engineering stress against engineering strain for 0% carbon black loading.

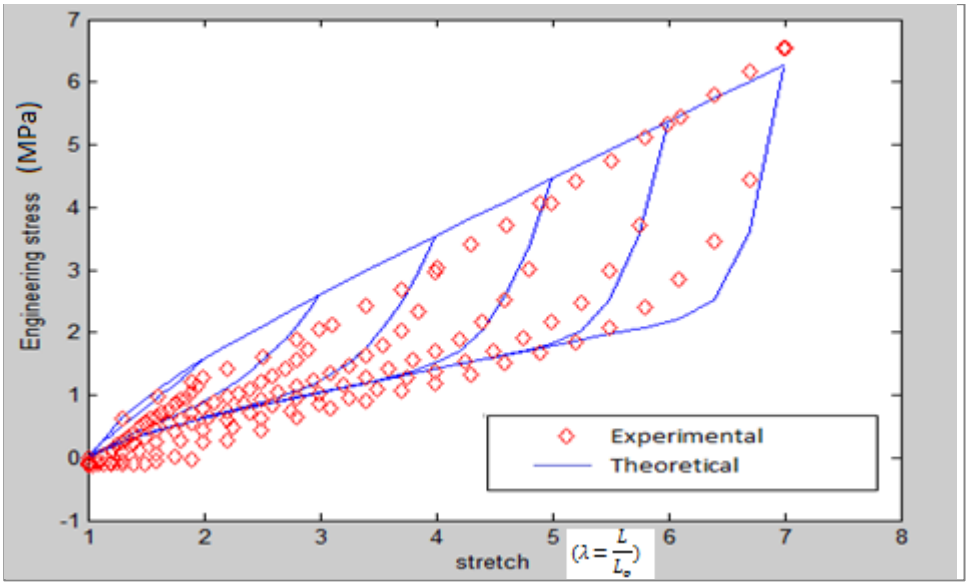


Figure 8. Engineering stress against engineering strain for 25% carbon black loading.

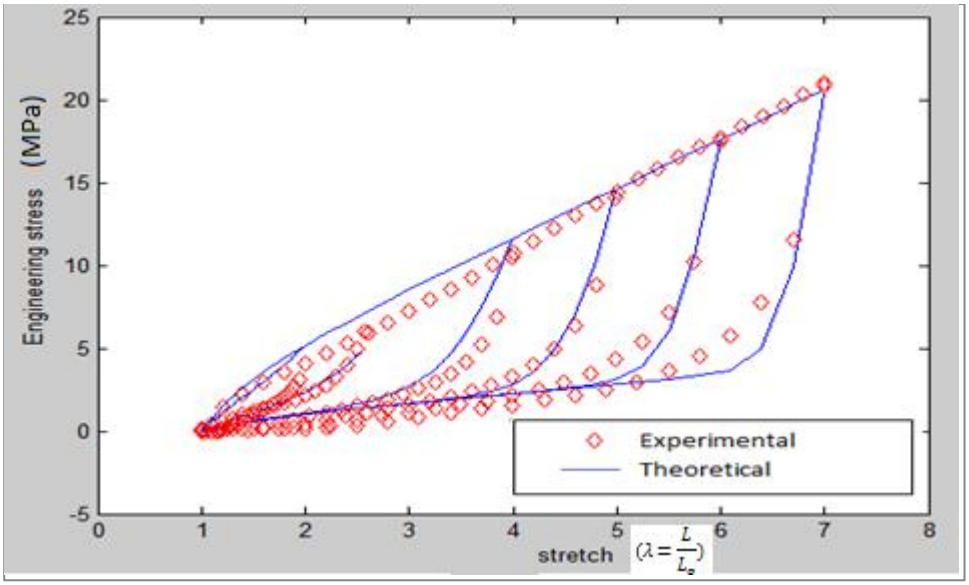


Figure 9. Engineering stress against engineering strain for 40% carbon black loading.

Based on the engineering stress and strain graphs, the parameters *r* and *m* are obtained from MATLAB. The normalized *r* value is as shown in Fig. 10. Meanwhile the normalized *m* value is as shown in Fig. 11. Both parameters are plotted against carbon black loading percentage.

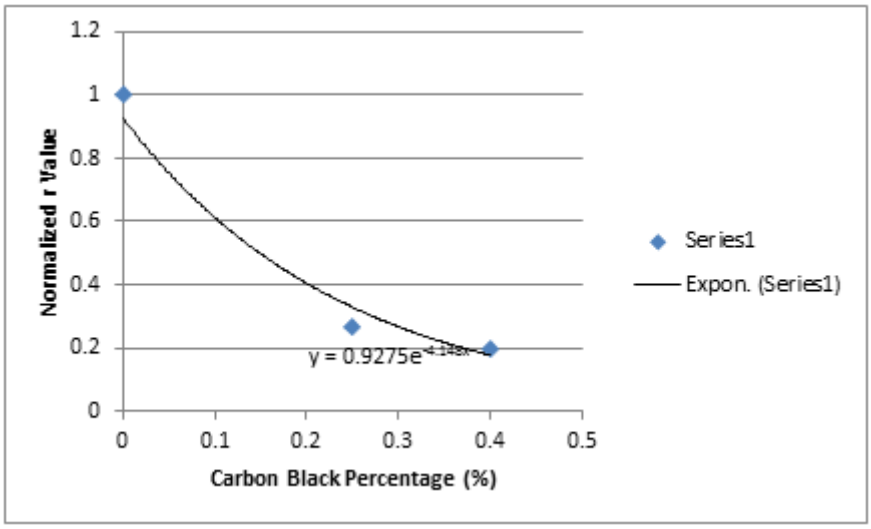


Figure 10. Normalized *r* value against carbon black percentage.

Based on Fig. 10, the equation generated from the graph is represented by Eq. (11)

$$r_x = Te^{-q(CB)}r^o \quad (11)$$

Where r^o is the *r* value for 0% carbon black loading, *CB* is the carbon black percentage in decimal form and *T* and *q* are constants.

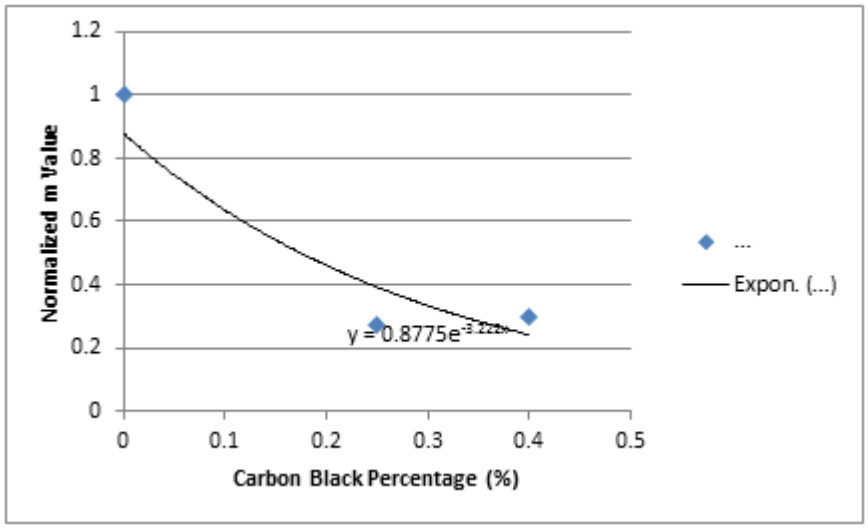


Figure 11. Normalized *m* value against carbon black percentage.

Based on Fig. 11, the equation generated from the graph is represented by Eq. (12)

$$m_x = Re^{-s(CB)}m^o \quad (12)$$

Where m^o is the *m* value for 0% carbon black loading, CB is the carbon black percentage in decimal form and *R* and *s* are constants.

Both parameters *r* and *m* obtained could be used in the damage function in Eq. (6), which are crucial to predict the damage from the deformation regardless of the percentage of carbon black loading. Eq. (11) and (12) developed would be a simple tool to predict any damage without the need of repeating the whole experiment process.

Table 1 summarizes the constant values for carbon black loading which has been discussed previously.

Table 1. Summary of constant values for carbon black loading.

Carbon Black Percentage (%)	0	25	40
C_{10}	0.2644	1.0763	2.9512
r	6.2091	1.6702	1.2424
m	22.188	6.1411	6.6722

The significance of the project includes the improvement of the model by including the effect of carbon black loading in predicting the Mullins effect of rubber under cyclic loading. Most of the literatures available do not include the carbon black loading in the research. Besides, this research develops new model based on the three different concentration of carbon black in the rubber, namely 0%, 25% and 40%. The

newly developed model could predict the damage from deformation with any % of carbon black loading without repeating the entire experimental work.

5. Conclusion

This paper analyzes the Mullins effect in rubber, particularly with carbon loading percentage of 0%, 25% and 40%. The studied rubber is of NBR type. Tensile stress testing and tensile strain testing are carried out to obtain the experimental data, after which are used for MATLAB coding to solve the unknown parameters *r* and *m* for the new model. The new model based on neo-Hookean model could be used to predict the stress-strain behavior and the damage from deformation regardless of any percentage of carbon black loading applied.

References

[1] Bouasse, H., Carriére, Z. (1903). Courbes de traction du caoutchouc vulcanise. *Annales de la Faculté des Sciences*, vol. 5, 257-283.

[2] Bergström, J. S., Boyce, M. C. (1998). Constitutive modeling of the large stain time-dependent behavior of elastomers. *J. Mech. Phys. Solids*, vol. 46, pp. 931–954.

[3] Gracia, L. A., Liarte, E., Pelegay, J. L., Calvo, B. (2010). Finite element simulation of the hysteretic behaviour of an industrial rubber. Application to design of rubber components. *Finite Elements in Analysis and Design*, vol. 46, pp. 357-368.

[4] Mullins, L., Tobin, N. R. (1965). Stress softening in rubber vulcanizates. part i. use of a strain amplification factor to describe the elastic behavior of filler-reinforced vulcanized rubber. *J. Appl. Polym. Sci*, 9(9), 2993–3009.

[5] Huntley, H. E., Wineman, A. S., Rajagopal, K. R. (1997). Stress softening, strain localization and permanent set in the circumferential shear of an incompressible elastomeric cylinder. *IMA J. Appl. Math*, 59(3), 309–338.

[6] Beatty, M., Krishnaswamy, S. (2000). A theory of stress-softening in incompressible isotropic materials. *J. Mech. Phys. Solids*, 48(9), 1931–1965.

[7] Qi, H. J., Boyce, M. C. (2004). Constitutive model for stretch-induced softening of the stress–stretch behavior of elastomeric materials. *J. Mech. Phys. Solids*, 52(10), 2187–2205.

[8] Simo, J. C. (1987). On a fully three-dimensional finite-strain viscoelastic damage model: formulation and computational aspects. *Comput. Method. Appl. M*, 60(2), 153–173.

[9] Miehe, C. (1994). Discontinuous and continuous damage evolution in ogden-type large-strain elastic Materials. *Eur. J. Mech. A-Solid*, 14(5), 697–720.

[10] Ogden, R. W., Roxburgh, D. G. (1999) A pseudo–elastic model for the mullins effect in filled rubber. *P. Roy. Soc. A-Math. Phys*, 455(1988), 2861–2877..

[11] Marckmann, G., Verron, E., Gornet, L., Chagnon, G., Charrier, P., Fort, P. (2002). A theory of network alteration for the mullins effect. *J. Mech. Phys. Solids*, 50(9), 2011–2028.

[12] Diani, J., Fayolle, B., Gilormini, E. (2009). A review on the Mullins effect. *European Polymer Journal*, 45, pp. 601-612.

[13] Patil, A. O., Coolbaugh, T. S. (2005). Elastomers: a literature review with emphasis on oil resistance. *Rubber Chem. Technol*, 78(3), 516–535.

[14] Chai, A., Verron, E., Andriyana, A., Johan, M. (2013). Mullins effect in swollen rubber: Experimental investigation and constitutive modelling. *Polymer Testing*, vol. 32, no. 4, pp. 748-759.

[15] Holzapfel, G. (2000). *Nonlinear solid mechanics*. Chichester: Wiley.

eureca 2016 – Conference Paper
Paper Number 2ME15

Characterization of Alumina-doped Y-TZP Ceramics

Y. B. Leong[1*], W. J. Kelvin Chew[1*], S. Ramesh[2]

[1]*School of Engineering, Taylor's University, Taylor's Lakeside Campus, No. 1 Jalan Taylor's, 47500 Subang Jaya, Malaysia.*

[2]*Center of Advanced Manufacturing and Materials Processing, Department of Mechanical Engineering, Faculty of Engineering, University of Malaya, 50603 Kuala Lumpur, Malaysia.*

[*]lyben1993@hotmail.com; KelvinWaiJin.Chew@taylors.edu.my

Abstract

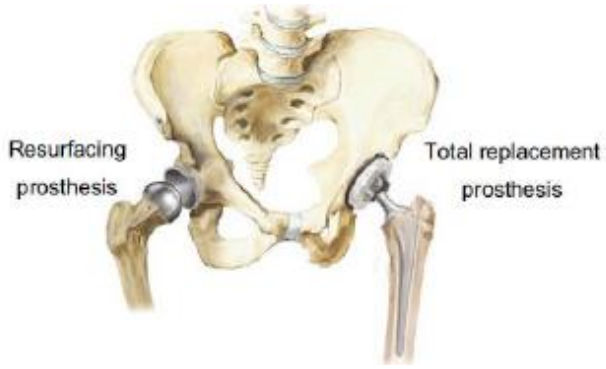
This study is to investigate the effects of alumina dopants on the mechanical properties (relative density, fracture toughness and Vickers hardness) of Y-TZP ceramics. Besides that, this study aims to determine the XRD pattern and tetragonal content percentage of alumina-doped Y-TZP after sintering. The dopant content of alumina that studied were 0, 0.1, 0.3, 0.5 and 1 wt%. Both alumina and zirconia were mixed in powder form and compressed into pellets. These pellets were then sintered in different temperature. The sintering temperatures applied were 1250, 1300, 1400 and 1500°C for 2 hours. Results showed that XRD spectra correspond with the tetragonal zirconia XRD standard's spectrum regardless of different alumina dopant contents. In addition, results showed that only small amount of tetragonal phase content transformed to monoclinic phase content after sintering based on tetragonal content percentage determined from XRD analysis. Furthermore, results showed that most of the Y-TZP ceramics with alumina dopants have the highest relative density at sintering temperature of 1400 °C and with at least 96% relative density. As for Vickers hardness, the application of sintering temperature of 1400 °C was better compared to 1500 °C for all the alumina contents studied. Regarding fracture toughness, Y-TZP with 0.3 wt% alumina dopant showed the lowest fracture toughness amongst all the alumina contents. There were not much changes from 0 wt% to 0.1 wt% alumina content. This finding indicated that additional of small amount of alumina content up to 0.1 wt% will not disrupt the tetragonal phase stability of Y-TZP for both the sintering temperatures. Sintering at 1500 °C resulted in a higher fracture toughness compared to 1400 °C for most of the alumina dopants except for 0.3 wt%.

Keywords: Zirconia, Alumina Dopant, Mechanical Properties, X-Ray Diffraction.

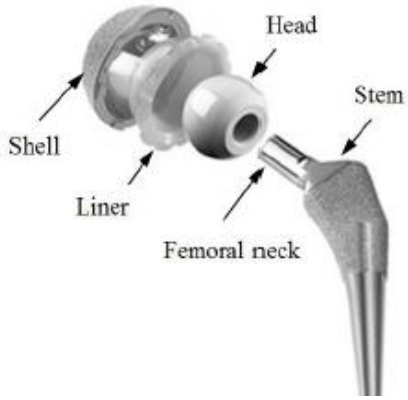
1. Introduction

Zirconia, ZrO_2, is an advanced ceramic that often used for dental and medical applications due to its good mechanical properties and biocompatibility [1, 2]. Zirconia has three well-defined phases of different crystal structure: cubic, tetragonal and monoclinic [1, 3]. Pure zirconia will be stable at different phases according to the ambient temperature. At room temperature, pure zirconia exists in the monoclinic structure and transforms into the tetragonal structure at about 1170°C and subsequently, cubic structure around 2370°C. Magnesium oxide, yttrium oxide or calcium oxide can be used to stabilize zirconia. These stabilizers will allow the zirconia to be stabilized in tetragonal or cubic phase at room temperature [1]. The reason to stabilize the zirconia in tetragonal phase is that tetragonal zirconia has significantly better mechanical properties compared to other two phases [2].

Yttria-stabilized tetragonal zirconia polycrystals or Y-TZP, consists of fully tetragonal zirconia that is stabilized with a small percentage of yttria oxide [1]. Y-TZP is among the commonly used material for medical implantation because of its high strength and toughness following its ability to undergo transformation toughening. One of the applications of Y-TZP is the hip prosthesis for an artificial hip joint as shown in Figure 1(a). This hip replacement prosthesis is use to support the whole upper body weight by joining the pelvis to the lower limb. Y-TZP is one of the candidate material for the femoral head component of the hip prosthesis as shown in Figure 1(b).



(a)



(b)

Figure 1: Diagrams indicating (a) the two main types of hip prosthesis – resurfacing and total replacement as well as (b) the mmain components in an artificial hip joint [3].

2. Methodology

In this study, zirconia in the form of Y-TZP was doped with various dopant contents to investigate its effects on the mechanical properties and tetragonal content after sintering. Alumina was chosen as the dopant for this research. A total of five alumina contents were experimented: 0, 0.1, 0.3, 0.5 and 1 wt%. Besides that, the studies include four different sintering temperatures: 1250, 1300, 1400, 1500°C.

2.1 Sample Preparation

2.1.1 Powder Preparation

Y-TZP and alumina powders were mixed to produce tetragonal zirconia ceramic five different alumina contents: 0, 0.1, 0.3, 0.5 and 1 wt%. The total weight of the powder mixture was set to 50 g, thus calculations of the Y-TZP and alumina weights were determined according to the weight percentage (wt%) of the alumina content. Alumina powder was then placed into a beaker with ethanol and placed into an ultrasonic bath for 5 mins. The Y-TZP powder then added into the beaker and continue the ultrasonic process for another 15 mins. The mixture solution was then poured into the attritor milling machine. Approximately 250 cm^3 of 5 mm diameter zirconia milling balls were added into the attritor milling machine. The mixture was mix under 500 rpm for half an hour. After this step, the mixture was then sieved to remove the milling media. The slurry was then put into the oven at 60°C for 24 hours to dry. The dried powder was then sieved using a 125 μm mesh sieve to fine and ready to press ceramic powders.

2.1.2 Green Body Preparation

The sieved powders were pressed into disc shaped samples under approximately 5 MPa force under a cylindrical die. Each sample consists of 2.5g in weight and a total of 40 samples were pressed. The uniaxially-pressed pellets were further compacted by using a cold isostatic pressing (CIP) machine. The cold isostatic pressing process was applied because it will press the powder in all direction through fluid.

2.1.3 Sintering Process

Four sintering temperatures were chosen in this experiment: 1250 °C, 1300 °C, 1400 °C and 1500 °C. All samples were sintered in a box furnace (LT Furnace, Malaysia) using a single step sintering profile with a ramp rate of 10°C/min and holding time of 2 hours.

2.1.4 Grinding and Polishing

All the samples were grinded using five different grades of silicon carbide papers: 120, 240, 600, 800 and 1200 grit. Each sample was first grinded horizontally for first grade and orientation changed by 90° for every grade after that. After grinding process, the samples were polished using 6 and 1 μm of diamond paste. The samples were polished until mirror-like surface finish was obtained.

In general, the experimental parameters applied in the present study can be summarized as per Table 1.

Table 1. General experimental parameters.

Parameter	Specifications				
Dopant					
Alumina content (wt%)	0 (undoped)	0.1	0.3	0.5	1
Sintering Profile					
Sintering Temperature (°C)	1250	1300	1400	1500	-
Ramp Rate (°C/min)			10		
Holding Time (hrs)			2		

2.2 Characterization

2.2.1 X-ray Diffraction

X-ray diffraction (XRD) instrument was used to check on the percentage of monoclinic phase and tetragonal phase in the samples. This analysis is important because the phase might change from tetragonal to monoclinic during the sintering time. Higher volume content (vol%) of monoclinic phase zirconia will result in lower mechanical properties. Thus, the samples go through the XRD with Cu-Kα radiation source with a 0.5°/min scan speed and 0.02° step scan at 40kV and 40mA. The equation that was proposed by Toraya [4] was then used to determine the monoclinic and tetragonal phase percentage.

$$V_m = \frac{1.311X_m}{1 + 0.311X_m} \quad \text{(Equation 1)}$$

where V_m is the volume fraction of monoclinic zirconia

X_m is the intergrated intensity ratio

$$X_m = \frac{I(11\bar{1})_m + I(111)_m}{I(11\bar{1})_m + I(111)_m + I(111)_t}$$

(Equation 2)

where I is the peak intensity
Subscript m represent the monoclinic phase
Subscript t represent the tetragonal phase

Equation 3 can be used to get V_t :

$$V_t\% = 100\% - V_m\%$$

(Equation 3)

2.2.2 Density

Relative densities were determined by using the water immersion technique with an analytical balance equipped with a density measurement kit (Mettler Toledo, Switzerland). Distilled water was used as the immersion medium. The weight of the samples was measured in water and subsequently, in air. The relative density was then calculated by using 6.0 g/cm^3 as the theoretical density of Y-TZP.

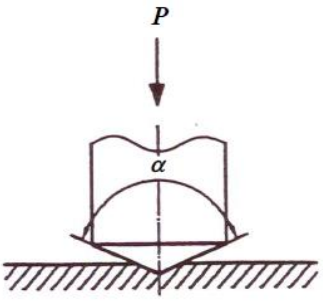
2.2.3 Vickers Hardness

In this Vickers hardness test, 20 kg applied load was applied to the samples by using a pyramidal diamond indenter, as indicated in Figure 2(a). This load was applied slowly on the sample for 10 s. A square shape appeared on the sample after the sample is removed as shown in figure 21. Diagonal lengths D_1 and D_2 as shown in Figure 2(b) were measured using a built in microscope in the Vickers hardness machine. Vickers hardness of the samples were calculated according to equation 4 [5].

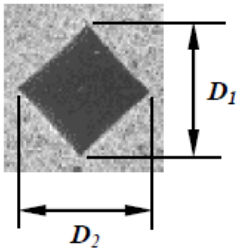
$$H_v = \frac{1.854P}{(D)^2}$$

(Equation 4)

where P is the applied load
Average diagonals, $D = (D_1 + D_2)/2$



(a)



(b)

Figure 2: Vickers hardness was measured with a pyramidal indenter as indicated in (a) with loading force P, while image (b) shows the resulting indent on the surface of sample and two diagonals (D_1 and D_2) measured.

2.2.4 Fracture Toughness

From the indentation on the surface of sample from Vickers hardness measurement, the fracture toughness of samples can be determined by using the equation proposed by Niihara et al. [6] as shown in equation 6.

$$\left(\frac{K_{Ic}\phi}{H_v a^{\frac{1}{2}}}\right)\left(\frac{H_v}{E\phi}\right)^{\frac{2}{3}} = 0.035\left(\frac{L}{a}\right)^{\frac{1}{2}}$$

(Equation 6)

Where K_{IC} is fracture toughness
H_v is Vickers hardness
E is Young's modulus
a is half of the average diagonal
L is the average of the crack length
ϕ is the constraint factor

Figure 3 is a schematic diagram of a typical Vickers indentation showing the cracks emanating from the four corners of the indent. By using the microscope on the Vickers hardness testing machine, the length of all four crack lines were measured. The average crack length was then determined and applied in equation 6 to determine the fracture toughness of the samples.

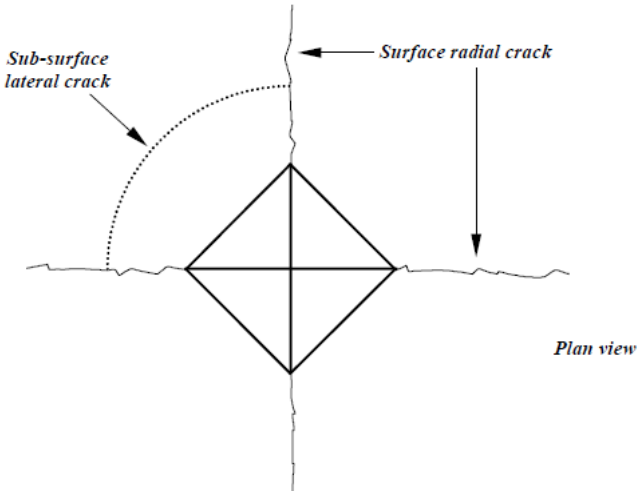


Figure 3: Plan view of a Vickers indentation with crack lines.

3. Results

3.1 XRD

Figure 4 shows the results of XRD analysis of alumina-doped Y-TZP samples. In general, all the XRD trace of Y-TZPs with different alumina contents were similar to each other. Besides that, these spectra can be compared to the tetragonal zirconia XRD standard (Fig. 5). The peaks pattern of the results were compared to the standard's pattern.

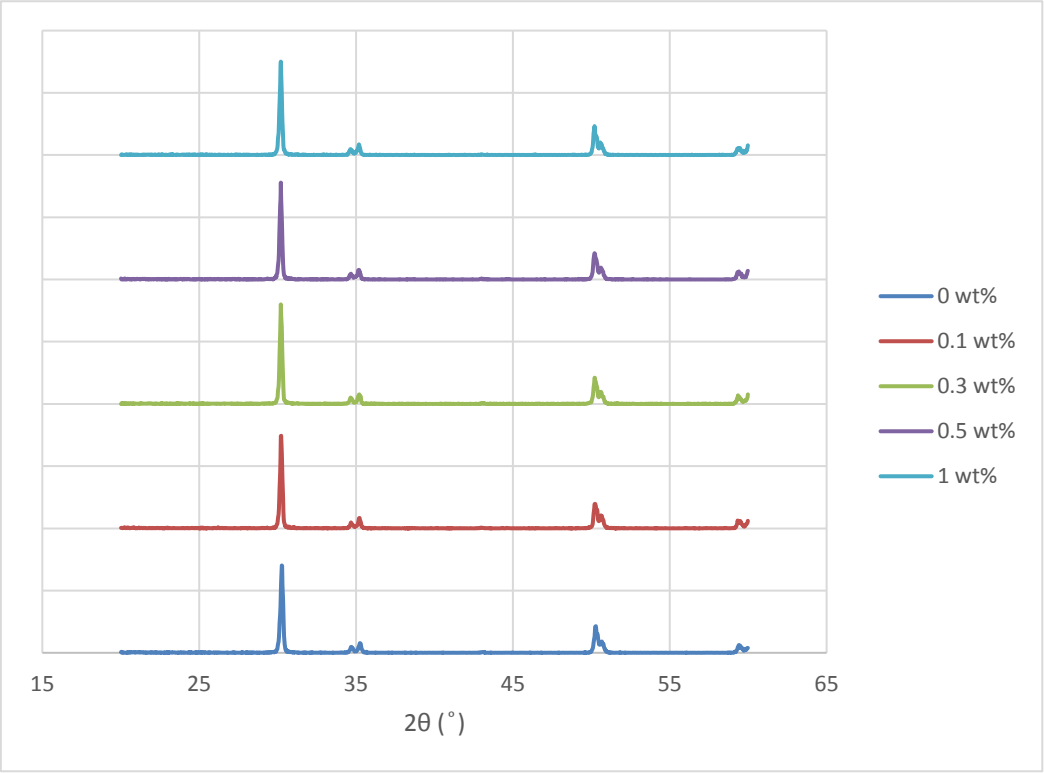


Figure 4: XRD spectra of alumina-doped Y-TZP samples sintered at 1400°C

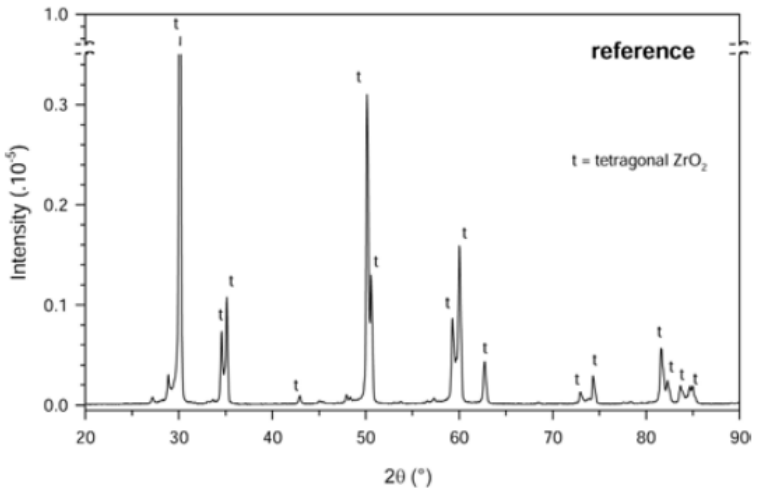


Figure 5: XRD standard spectrum for tetragonal zirconia.

Based on Figure 4, it has the highest peak at about 30°, then followed by 50°, 60° and 35°. This trend of peaks shows that the spectra for all samples matches the standard's pattern.

3.2 Tetragonal Phase Content of Zirconia

The graph of tetragonal content percentage against sintering temperature for Y-TZP with five different alumina dopant contents after sintering process is as shown in Figure 6.

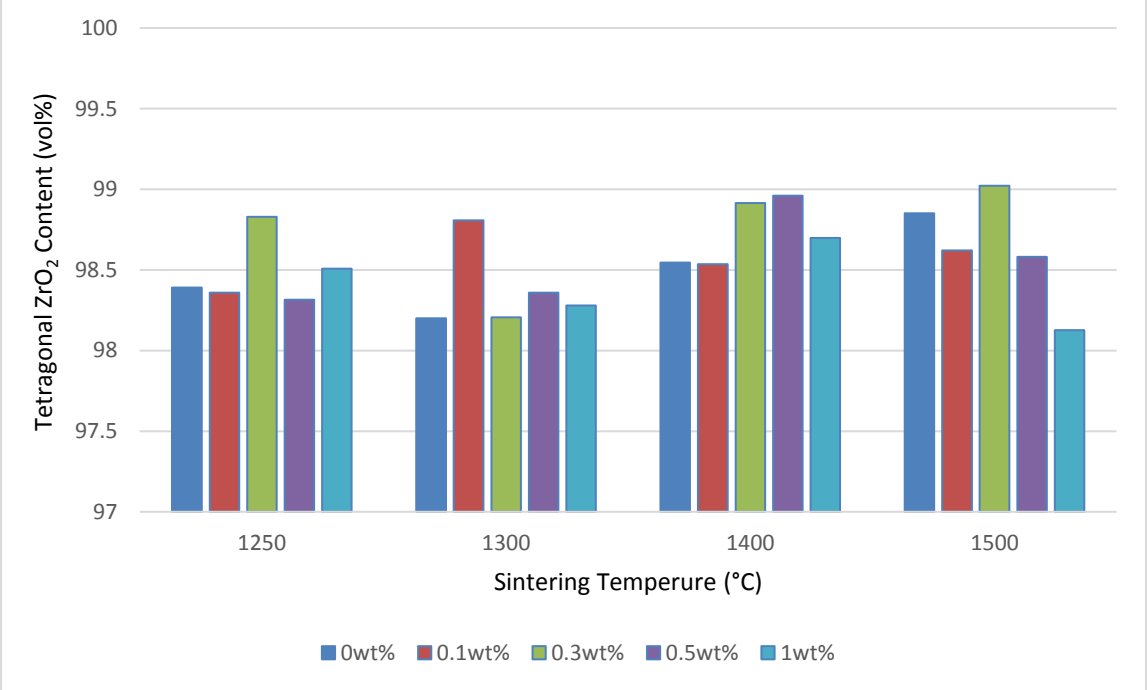


Figure 6: Graph of tetragonal zirconia content in volume percentage against different sintering temperatures.

Results showed that 0.3 wt% had the highest percentage at sintering temperature of 1250 °C and 1500°C. However, 0.1 wt% had the highest percentage at 1300 °C and 0.5 wt% had the highest percentage at 1400 °C. Overall, all the results fall in between 98% to 99.5% which means that only very small amount of tetragonal phase content transform to monoclinic phase content. This trend indicated that by using alumina as dopant did not significantly disrupt the tetragonal zirconia phase stability. In comparison with the results of Ramesh *et al*. [9] for manganese oxide as dopant which achieved tetragonal zirconia phase content between 87% and 96%, the results of the present study clearly showed that alumina dopant in the range of 0.1 to 1 wt% was less disruptive to the tetragonal zirconia phase.

3.3 Relative Density

Figure 7 is the graph of relative density against sintering temperature for 5 different alumina contents after sintering. Results show that most of the alumina contents have the highest relative density at sintering temperature of 1400°C, only 0.3 wt% has its highest relative content at sintering temperature of 1300 °C. Although the sintering temperature of 1250°C achieved relatively low relative densities, it should be noted that the addition of alumina was clearly beneficial in improving the densification of Y-TZP. In general, all compositions of Y-TZP achieved relative density beyond 96%. Furthermore, the present results corresponded well with the findings of Anastasia *et al*. [3] that higher relative density happened in between the range of 1400 °C and 1500 °C sintering temperature except for Y-TZP that was co-doped with 0.3 wt% of alumina and silica.

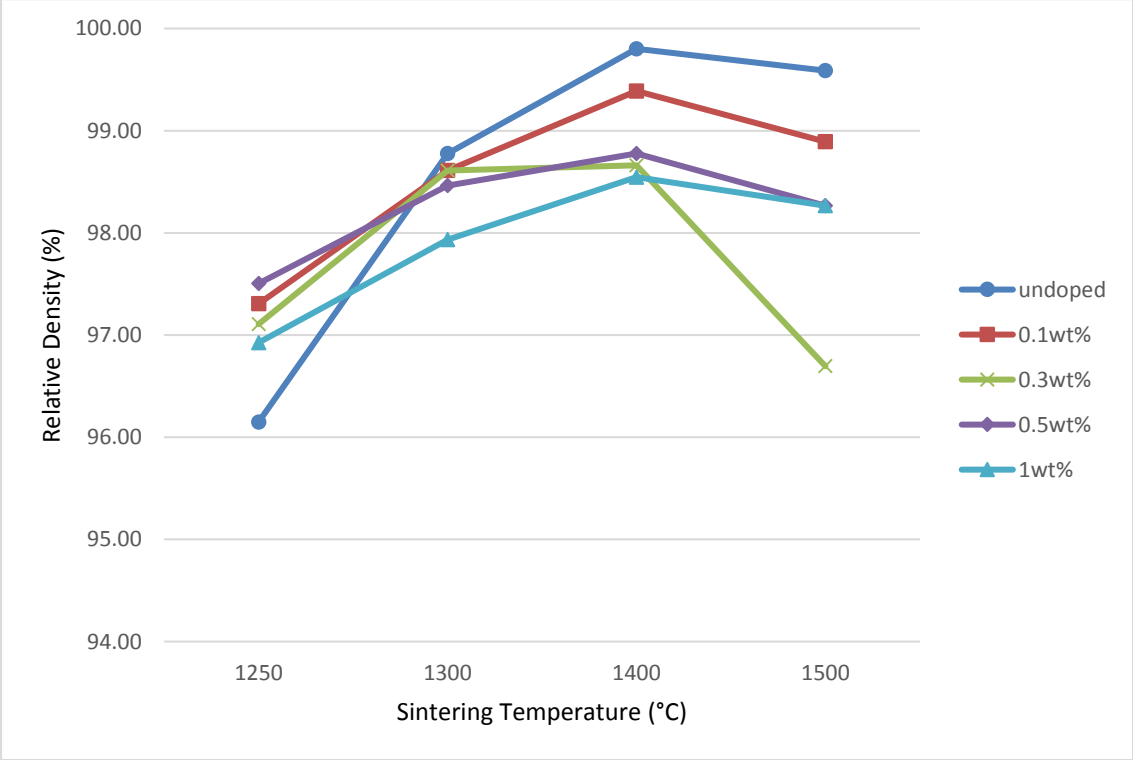


Figure 7: Graph of relative density against sintering temperature.

3.4 Vickers Hardness

Figure 8 is the graph of Vickers hardness against alumina content for sintering temperatures of 1400°C and 1500°C. The results show that Vickers hardness is better at sintering temperature of 1400 °C for all alumina contents. For 1400 °C, Vickers hardness is better at 0 wt%. However, it is better at 0.1 wt% at 1500 °C. The decreasing trend of Vickers hardness when alumina content increases is in agreement with the findings of Ramesh et al [9]. The overall reduction in hardness of samples when the sintering temperature was increased from 1400°C to 1500°C is possibly due to the lower densification as observed in Figure 7.

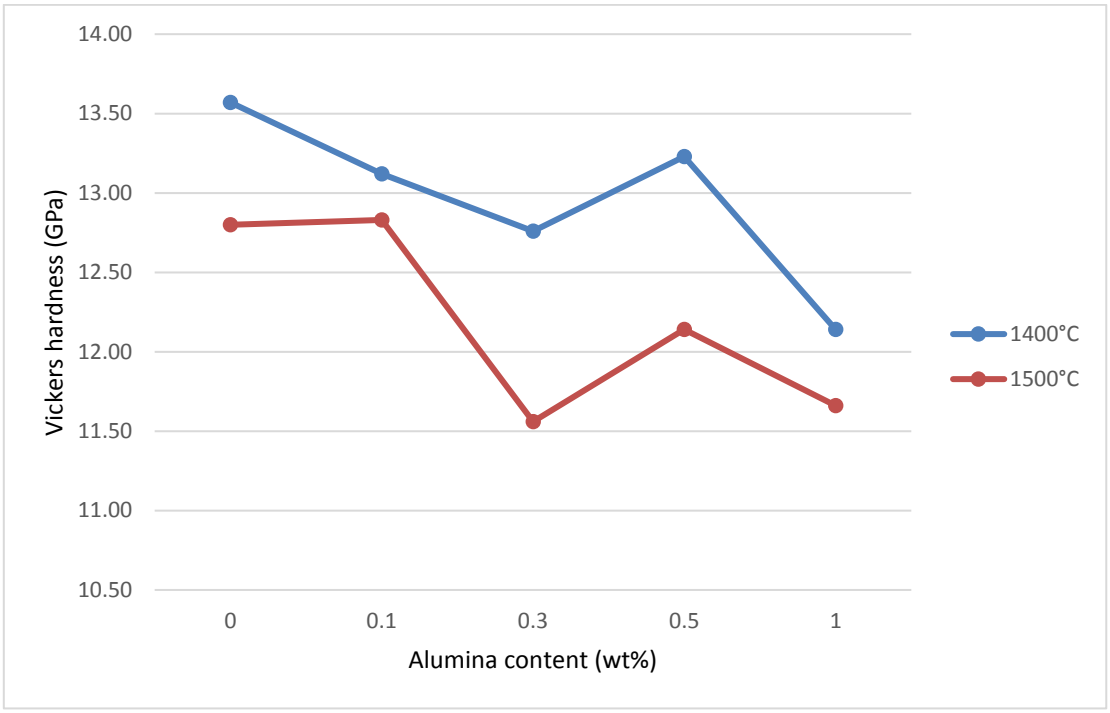


Figure 8: Graph of Vickers hardness against alumina content.

3.5 Fracture Toughness

Figure 11 shows the graph of fracture toughness against alumina content for sintering temperature of 1400 °C and 1500 °C. The results show that 0.3 wt% has the lowest fracture toughness amongst all the alumina contents. There are not much changes from 0 wt% to 0.1 wt% alumina content. This shows that additional of small amount of alumina content up to 0.1 wt% does not disrupt the tetragonal phase stability of Y-TZP for both the sintering temperature. In overall, sintering temperature of 1500 °C has a higher fracture toughness compared to 1400 °C. The present results corrincide with the results of research by Ramesh et al. [9] on manganese oxide dopants with the overall trend of small amount of dopants does not change the fracture toughness significantly.

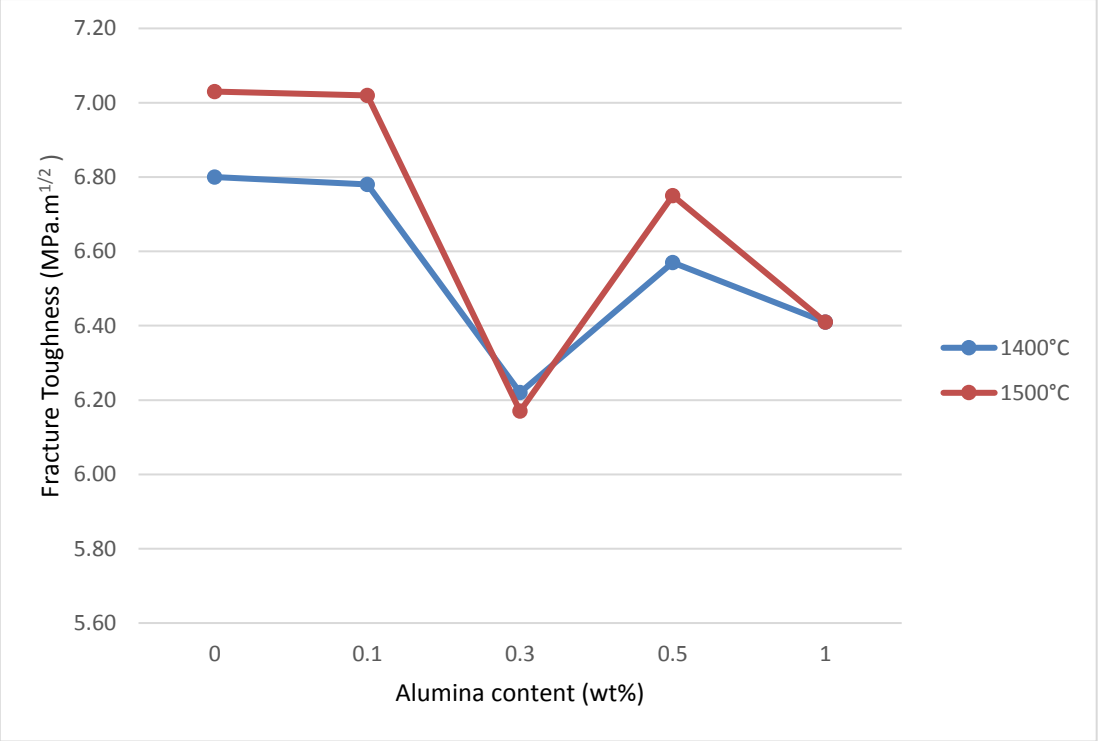


Figure 11: Graph of fracture toughness against alumina content.

4. Conclusion

In conclusion, the results of XRD spectra correspond with the tetragonal zirconia XRD standard's spectrum in spite of the addition of alumina as dopant. Besides that, the tetragonal content percentage falls in between 98% to 99.5% which means that only very small amount of tetragonal phase content transform to monoclinic phase content after sintering. This trend shows that the application of alumina as dopant has neutral effect on the tetragonal zirconia phase stability. Furthermore, results show that most of the alumina-doped Y-TZPs achieved the highest relative density at sintering temperature of 1400°C while only 0.3 wt% alumina-doped Y-TZP obtained its maximum densification at sintering temperature of 1300°C. In general, all compositions attained good densification of above 96% relative density. As for Vickers hardness, sintering temperature of 1400°C is better compared to 1500°C for all the alumina contents studied. Regarding fracture toughness, the addition 0.3 wt% alumina resulted in the lowest fracture toughness amongst all the alumina contents. No significant change in toughness was observed when the alumina content was raised from 0 wt% to 0.1 wt%. This finding may possible be due to the observation that the addition of small amount of alumina content up to 0.1 wt% did not disrupt the tetragonal phase stability of Y-TZP for both the sintering temperatures. Sintering temperature of 1500°C resulted in a higher fracture toughness compared to 1400°C for most of the alumina dopants except for 0.3 wt%.

References

[1] L. G. D.´Altoé G. M. C. F. and F. B. Cláudia Ângela Maziero Volpato, *Advances in Ceramics - Electric and Magnetic Ceramics, Bioceramics, Ceramics and Environment*. InTech, 2011.

[2] H. Tong, C. B. Tanaka, M. R. Kaizer, and Y. Zhang, "Characterization of three commercial Y-TZP ceramics produced for their high-translucency, high-strength and high-surface area," *Ceram. Int.*, 2015.

[3] A. Samodurova, A. Kocjan, M. V. Swain, and T. Kosmač, "The combined effect of alumina and silica co-doping on the ageing resistance of 3Y-TZP bioceramics," *Acta Biomater.*, vol. 11, pp. 477–487, 2015.

[4] E. Askari, P. Flores, D. Dabirrahmani, and R. Appleyard, "A review of squeaking in ceramic total hip prostheses," *Tribol. Int.*, 2015.

[5] F. Zhang, K. Vanmeensel, M. Inokoshi, M. Batuk, J. Hadermann, B. Van Meerbeek, I. Naert, and J. Vleugels, "Critical influence of alumina content on the low temperature degradation of 2–3mol% yttria-stabilized TZP for dental restorations," *J. Eur. Ceram. Soc.*, vol. 35, no. 2, pp. 741–750, 2015.

[6] Z. Roell, "Vickers Hardness Test," *Indentec Hardness Test. Mach. Ltd.*, pp. 8.

[7] K. P. Shah, "Hardness testing," *Pratical Maintenance*, 2011. [Online]. Available: http://practicalmaintenance.net/?p=928.

[9] S. Ramesh, M. Amiriyan, S. Meenaloshini, R. Tolouei, M. Hamdi, J. Pruboloksono, and W. D. Teng, "Densification behaviour and properties of manganese oxide doped Y-TZP ceramics," *Ceram. Int.*, vol. 37, no. 8, pp. 3583–3590, 2011.

eureca 2016 – Conference Paper
Paper Number 2ME16

Blended Polycaprolactone with Forsterite for the Enhancement of Biodegradability

Lim Haochuan[1*], Yong Leng Chuan[2]

[1]*School of Engineering Taylor's University, Malaysia*

[*]limhaochuan@sd.taylors.edu.my

Abstract

The blending between biomaterials to enhance the biodegradability is very common and feasible with the technology today. Polycaprolactone (PCL) is found with very good biocompatibility in human's body, and commonly in used as a base biomaterial for many synthesized biomaterial. The blending between PCL and forsterite provides the closest degradation rate to the human's regeneration rate compared to blending with other biomaterial. Although the PCL alone can be degrades well in human's body, but different age of people are suitable for different degradation rate of the biomaterial, due to various regeneration rate. Thus, this study is to investigate the biodegradability of the synthesized biomaterials, and to optimize the biodegradability of PCL by different blending ratio of forsterite. The forsterite-PCL blended biomaterial sample will be fabricated with different blending ratio, from 0 wt. % of to 10 wt. % of forsterite in the blended biomaterial. Differential scanning calorimetry (DSC) testing is used to determine the temperature required to melts down the blended biomaterial completely. The samples of blended biomaterial with different forsterite content are melt and fabricated with a cylindrical mold. Due to time constraint, the degradation only takes up to 12 days as an accelerated degradation process, and the time point to record the weight of sample is set to be 3 days. While, the biodegradation rate will based on the weight loss of the sample. During the degradation, the sample will be immersed into the Sodium hydroxide (NaOH) solution. As hypothesis, the increment of forsterite content will increase the weight loss and as well. Hence, the increment of forsterite wt. % in the blending ratio will result a faster degradation rate according to weight loss percentage.

Keywords: Polycaprolactone, forsterite, degradation rate, biodegradability, weight loss, water absorption; blending ratio

1. Introduction

Tissue engineering has now become more popular than ever, due to the solutions provided for tissue recovery. Healing, repair, or regenerate the damaged cell in human or animal's body has become handier than the past [1]. The development progress of tissue engineering is going on very well, and trying to eliminate and decrease the uses of medical drug. In addition, the safety and efficiency of medical procedure can be improved enormously with the technology of tissue engineering today [2]. Non-biological materials were used in tissue engineering for experiments and testing at the beginning. However, the results were not as good as expected, due to the incompatibility of materials in physiology condition [3]. From then on, only biomaterials were taken for the research, to prevent unnecessary study on the materials that cannot be accepted by human's body. Biocompatibility is the primary condition for any material to be classified as "biomaterial". A biomaterial should not produce any harmful substances or causing any bad influences to human's body; but to interact effectively with the damaged cell to heal it [4]. To implant any biomaterial into human's body, it has to be both biocompatible and biodegradable to the implanted part. All biomaterial are proven to be naturally degradable in the environment with any weather condition [5], which makes tissue engineering even more popular now.

There are many kind of biomaterials in tissue engineering, but this research will only focus on biopolymer and bioceramic. Both of them are having great hostile response in physiology condition and provide good mechanical strength. Two of these biomaterials are most likely to be used in bone implantation due to their good mechanical strength.

Polycaprolactone (PCL) is the chosen biopolymer for this research, because it has lower degradation rate compared to poly(lactic-co-glycolic acid) (PLGA) and polylactic acid (PLA) [6]. In addition, the degradation rate of PCL is found to be quite close to human's recovery rate [6]. However, PCL itself has hydrophobic chemical nature, which makes it to has poor surface wetting and interact with biological fluids to avoid cell adhesion [7]. In comparison with biopolymer, the degradation rate of all bioceramic is way to fast to be accepted by human body [8]. Hydroxyapatite (HA) is considered as one of the most important bioceramic in tissue engineering due to its bioactivity and degradability. But, the orthopaedic applications of hydroxyapatite ceramics has very low fracture toughness and insufficient mechanical strength to be utilized in implantation [9]. Therefore, forsterite has been introduced to represent most of the bioceramic to take place in the implantation. Both of them are able to release magnesium and silicon ions to biological medium, which are very good in the aspect of biodegradability. By comparing between these two bioceramics, forsterite has slightly better mechanical properties and fracture toughness than hydroxyapatite [10]. Yet, the degradation rate of forsterite alone is too fast, and the apatite formation ability is poor as well [9].

There are researchers found that mixing between two biomaterials are possible, and it brings positive effects too [7][5]. Biodegradability, bioactivity, and mechanical strength can all be improved or adjusted through the mixing [2]. Blending between two biomaterials can covers the shortcoming of each other and provides a better outcome. For instance, the degradation rate can be manipulated from the forsterite content that blended into PCL to achieve the desired result. Furthermore, blending between PCL

and forsterite has been done before in tissue engineering, and the number of research on this blended biomaterial is still growing rapidly until today. The forsterite-PCL synthesized biomaterial is found with good scaffold structure for bone and the degradation rate can achieve even more closer to actual regeneration rate of human bone [11]. But, if the content of forsterite in this blended biomaterial is more than 30 wt. %, it will cause inferior mechanical properties to the scaffold [2].

The optimum synthesis ratio of the blended biomaterial is yet to be confirmed. Therefore, this research will study the biodegradability of the blended biomaterial within the range of forsterite content, from 0 wt.% to 10 wt.%. Whereas, the biomaterials to be studied in this research will only be PCL and forsterite.

2. Research Methodology

To prepare the blended biomaterials sample for degradation, it has to go through few important processes which involved precise measurement, implicated testing, and organized procedure. Figure 1 shows the flowchart that consist of those important processes.

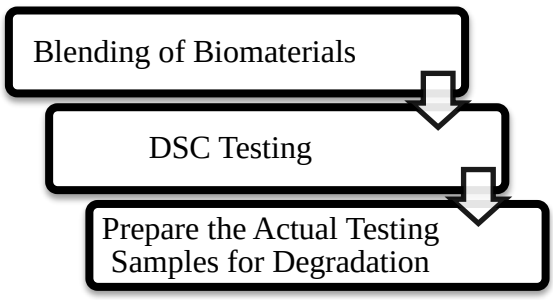


Figure 1. Flowchart of sample preparation

2.1 Materials

The biomaterials involved in this research are PCL and forsterite, which both of them are known as biocompatible in human's body [6]. The PCL is come in solid-flakes form; while the forsterite is in powder form before the blending. The molecular weight of the PCL is 10,000 g/mol with 60℃ of melting point; and the molecular weight of the forsterite is 140.6931 g/mol.

2.2 Preparation of Samples

The synthesized forsterite-PCL is prepared by using simple mixing method, where the PCL will be melted into molten state with hot plate, and then the forsterite powder will be added into the melted PCL. During the melting process of PCL, the temperature of the hot plate is increased slowly until it is just enough to melt the PCL. To make sure two of the biomaterials are blended homogenously, the mixture are constantly stirred for quite a period of time with glass stirrer. Then, the blended biomaterial is left to be cooled down until it returns back to solid form again. However, there are various specific weight percentage of forsterite to be used for blending with PCL in this research. These weight percentage are 0 wt. %, 2 wt. %, 4 wt. %, 6 wt. %, 8 wt. %, and 10 wt. %. While, the weight of PCL is fixed to be 60 grams for each sample.

The following eq. (1) can be used to determine the weight of forsterite based on the weight percentage above:

$$Weight\ of\ forsterite = \frac{Desired\ percentage\ of\ fosterite \times 140.6931}{(\frac{Desired\ percentage\ of\ PCL \times 10{,}000}{60})} \quad (1)$$

Table 1 shows the calculated value of forsterite weight for each weight percentage of forsterite.

Table 1. Weight of forsterite for different weight percentage of forsterite

Weight Percentage of PCL (wt.%)	Weight Percentage of Forsterite (wt.%)	Weight of PCL (g)	Weight of Forsterite (g)
100	0	60.00	0.0000
98	2	60.00	0.0172
96	4	60.00	0.0352
94	6	60.00	0.0539
92	8	60.00	0.0734
90	10	60.00	0.0938

The blended biomaterials are then sent for Differential Scanning Calorimetry (DSC) to test the melting properties of the blended biomaterial. The main reason of doing the DSC testing is to find out the point where the blended biomaterial started to change from one state to another. So that, the melting process of the blended biomaterial can be controlled within the suitable temperature range for each different blending ratio biomaterial. The DSC testing takes about 5 mg to 10 mg of the sample to be tested, and the parameters of the DSC testing machine is shown in Table 2.

Table 2. Parameters of DSC testing machine Setting

Sample Properties	Thermoplastic
Scan Temperature Range (℃)	25-180
Expected Melting Point (℃)	150
Scan Rate (℃)	5
Decomposition Temperature (℃)	200

The blended biomaterials are melted by using hot plate with the suitable temperature, based on the DSC results. Once the blended biomaterial is melted into molten form, it will be put into a cylindrical mold as and let to be cooled down until it returns back into solid form. Then, it will be taken out from the mold and be ready for the degradation process. Each different blending ratio will only have one sample, and there will be six samples in total to be prepared for the degradation.

2.3 Accelerated Degradation

Sodium hydroxide (NaOH) solution is used as an accelerated degradation solution in this research, with the concentration of 5 mol/L. The NaOH is come in pallet form, but it can be easily prepared by mixing the desired amount of water with the calculated mass of the NaOH pallet. The mass of the NaOH can be obtained with eq. (2) below:

$$Mass\ of\ NaOH = (Desired\ Concentration) \times (Desired\ Volume) \times (Formula\ Weight\ of\ NaOH) \quad (2)$$

Each sample is immersed in separate test tubes containing 10 mL of 5 mol/L NaOH solution. The degradation process takes up to 12 days in total, and the time point of the degradation is set to be 3 days. All the sample will be removed from the solution and rinsed with distilled water. After that, they will be dried by using clean tissues and let them sit for about an hour until they are totally dried up. Then, each sample will be weighted and returned back to the same test tubes that they were taken out. This process is repeated every 3 days, up to 12 days [12].

2.4 Weight Loss

Weight loss from each individual sample can be obtained from the difference between the initial weight of sample at the beginning and each time point (every 3 days) using an electronic weighing scale with the resolution of 1.0 mg. The following eq. (3) is used to determine the weight loss:

$$Weight\ loss\ (\%) = 100\% \times (W_0 - W_t)/W_0 \quad (3)$$

where W_0 is the starting dry weight and W_t is the dry sample weight after removal from the solution.

3.0 Results and Discussions

As above mentioned, DSC testing is used to test the melting properties of the blended biomaterials with different weight percentage of forsterite. Graphs are generated based on the tested biomaterial. Both onset temperature and peak temperature of the tested biomaterial can be determined from the graph. On the other hand, the weight of sample on each time point is recorded up to 12 days. Graph is plotted based on the weight loss percentage within the degradation period to analyze and discuss.

3.1 DSC Testing Results

Before melting the blended biomaterials with different content of forsterite and put into the mold, the melting properties of each of them have to be determined. Knowing the melting properties of each sample is very important as it can ensure the melting process is conducted under the safe condition. Whereas, the melting properties like onset temperature and peak temperature are the key purposes of the testing. The onset temperature from the DSC curve is to determine temperature when the blended biomaterial just started to melt, and the peak temperature is where all the bigger crystals of the blended biomaterial will be melted completely. Table 3 shows the mass of sample, onset temperature, and peak temperature for all sample with different weight percentage of forsterite.

Table 3. Results obtained from DSC curve

Forsterite Content (wt.%)	Mass of Sample (mg)	Onset Temperature (℃)	Peak Temperature (℃)
0	7.4	60.59	62.38
2	9.8	61.30	66.02
4	7.9	60.73	63.71
6	6.7	59.8	61.87
8	5.7	59.93	62.05
10	6.1	58.47	61.26

Based on the results from DSC curve in Table 3, it shows that the lowest onset temperature at 10 wt. % forsterite content, and the highest onset temperature at 2 wt.% forsterite content. Basically, the DSC curve is used to measure the enthalpy change for each blended biomaterial with different forsterite content without changing the mass. Thus, the actual factor that affects the onset temperature and the peak temperature of the sample is the mass. The greater the mass of sample, the higher the enthalpy is needed to melts the sample. However, the temperature required to melts the blended biomaterials completely is not much different from the pure PCL. The melting point of the pure PCL provided from the supplier is 60℃, and the melting point of the rest blended biomaterials did not reach higher than 67℃. Therefore, adding forsterite into PCL will not raise too much in the melting point. The hot plate temperature is set to be 80℃ when melting the blended biomaterial, by taking heat loss into the consideration. As long as the temperature is kept above the peak temperature for every sample, they will be melted perfectly and completely to be put into the mold.

3.2 Weight Loss Analysis

The initial weight of the samples are all taken and recorded to compare and analyze the weight loss percentage between each sample over the degradation period. The weight loss percentage for each different synthesis ratio is calculated by using eq. (3). The weight loss percentage of the samples with 0 wt.%, 2 wt.%, 4 wt.%, 6 wt.%, 8 wt.%, and 10 wt.% of forsterite content are illustrated in Table 4.

Based on the graph in Figure 2, the degradation rate of each sample is not so alike throughout the 12 days degradation, for each sample. The degradation rates of the pure PCL and PCL/forsterite (2 wt.%) sample are initially slow and then significantly faster after 6 days. It can be observed that the pure PCL degrades very slow compared to other samples that blended with forsterite. The maximum weight loss of the pure PCL is about 1.26 %, and it is occurred at day 12 of the degradation. Whereas, the PCL/forsterite (2 wt.%) only lost 1.38% of its original mass. The sample PCL/forsterite (4 wt.%) has a very uniform degradation rate, according to the graph in Figure 2. The weight loss of the sample PCL/forsterite (4 wt.%) constantly increases until end of the degradation, and the total weight loss percentage is 2.59 %. For the sample PCL/forsterite (6 wt.%), the weight loss percentage is high from the beginning to the end of the degradation. The weight loss percentage at the end of the degradation is 2.76 %, and the degradation rate is constantly increase throughout the 12 days degradation as well. In addition, the sample PCL/forsterite (6 wt.%) is also having the highest weight loss percentage among the other sample. Next, both degradation rate of sample PCL/forsterite (8 wt.%) and (10 wt.%) are having the same behavior, which is

initially fast (from 0 to 6 days), then moderate (from 6 to 9 days), and lastly the degradation rate is fast again (from 9 to 12 days).

Results show that the increment of forsterite can improve the degradation rate and weight loss during degradation. However, it is not necessary that the more the content of forsterite in the synthesized biomaterial will increase the degradation rate or weight loss percentage. The results from the degradation experiment deny the previous study which stated that the increment of forsterite in PCL/forsterite synthesized biomaterial will increase the weight loss percentage and the degradation rate [5][7] [13]. This may due to some factors that affect the degradation experiment or the structure of sample. Every sample has slight difference in structure and weight, therefore the average weight of sample is used to calculate the weight loss percentage. Nonetheless, the differences in sample structure is beyond the range of control, since the sample is fabricated manually. Furthermore, the forsterite content in each sample is measured with the scale of 0.1 mg. Error might occurred during the measurement of forsterite due to the relatively less weight. The forsterite used for blending is in powder form, even if the measurement of weight is correct, there might be some particles attached on the surface of any equipment used during the measurement. Since the amount of forsterite used is very less in weight (refer to Table 1), any losses of forsterite during the measuring process will cause serious effect on the synthesized biomaterial produced.

Table 4. Weight loss percentage of each sample

Duration (Days)		Forsterite Content (wt. %)					
		0	2	4	6	8	10
0	Average Weight (g)	0.4512	0.5572	0.5595	0.5900	0.5434	0.5464
	Weight Loss (%)	0.00	0.00	0.00	0.00	0.00	0.00
3	Average Weight (g)	0.4510	0.5567	0.5569	0.5853	0.5387	0.5425
	Weight Loss (%)	0.04	0.09	0.46	0.80	0.86	0.71
6	Average Weight (g)	0.4507	0.5560	0.5535	0.5815	0.5358	0.5400
	Weight Loss (%)	0.11	0.22	1.07	1.44	1.40	1.17
9	Average Weight (g)	0.4479	0.5537	0.5493	0.5786	0.5347	0.5389
	Weight Loss (%)	0.73	0.63	1.82	1.93	1.60	1.37
12	Average Weight (g)	0.4455	0.5495	0.5450	0.5737	0.5315	0.5344
	Weight Loss (%)	1.26	1.38	2.59	2.76	2.19	2.20

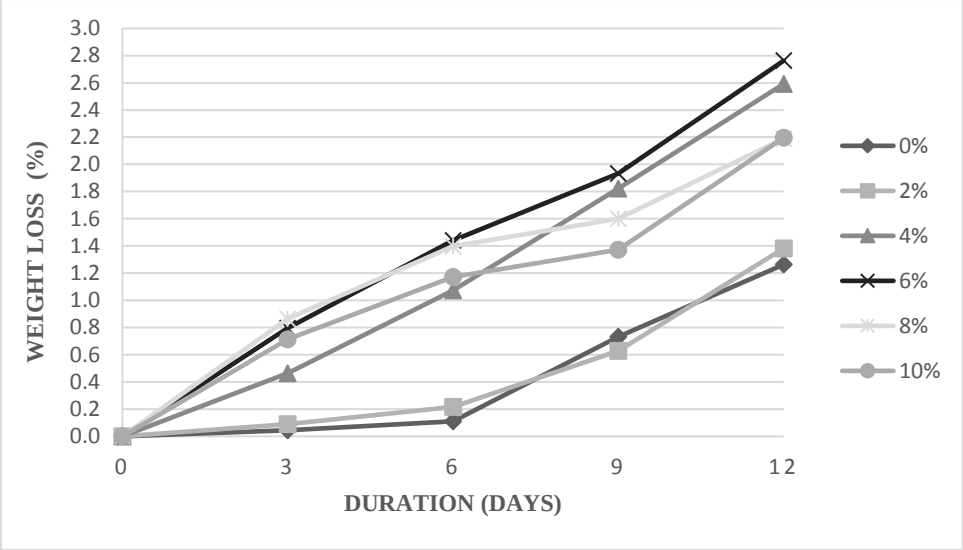


Figure 2. Weight loss percentage of blended biomaterial with different forsterite content

4.0 Conclusion

This research validates the previous work that has been done on the same blended biomaterial, forsterite-PCL synthesized biomaterial can degrades better than the pure PCL. As hypothesis of this research, the increment of forsterite content will increase the weight loss as well. However, the weight loss percentage of the blended biomaterial is very little. In future, the sample could be prepared in scaffold form to enhance the degradation process. The forsterite content can still be increased, as long as it doesn't goes over 30 wt. % to cause inferior mechanical properties to the blended biomaterial. Alternatively, the period of degradation can be increased up to the actual degradation rate instead of using accelerated degradation. So that, the results produced can be more precise and easier to be analyzed.

References

[1] M. Kharaziha and M. H. Fathi, "Improvement of mechanical properties and biocompatibility of forsterite bioceramic addressed to bone tissue engineering materials," *J. Mech. Behav. Biomed. Mater.*, vol. 3, no. 7, pp. 530–537, 2010.

[2] M. Diba, M. Kharaziha, M. H. Fathi, M. Gholipourmalekabadi, and a. Samadikuchaksaraei, "Preparation and characterization of polycaprolactone/forsterite nanocomposite porous scaffolds designed for bone tissue regeneration," *Compos. Sci. Technol.*, vol. 72, no. 6, pp. 716–723, 2012.

[3] J. M. Williams, A. Adewunmi, R. M. Schek, C. L. Flanagan, P. H. Krebsbach, S. E. Feinberg, S. J. Hollister, and S. Das, "Bone tissue engineering using polycaprolactone scaffolds fabricated via selective laser sintering," *Biomaterials*, vol. 26, no. 23, pp. 4817–4827, 2005.

[4] L. S. Nair and C. T. Laurencin, "Biodegradable polymers as biomaterials," vol. 32, pp. 762–798, 2007.

[5] K.-J. Wu, C.-S. Wu, and J.-S. Chang, "Biodegradability and mechanical properties of polycaprolactone composites encapsulating phosphate-solubilizing bacterium Bacillus sp. PG01," *Process Biochem.*, vol. 42, no. 4, pp. 669–675, 2007.

[6] H. M. Wong, S. Wu, P. K. Chu, S. H. Cheng, K. D. K. Luk, K. M. C. Cheung, and K. W. K. Yeung, "Low-modulus Mg/PCL hybrid bone substitute for osteoporotic fracture fixation," *Biomaterials*, vol. 34, no. 29, pp. 7016–7032, 2013.

[7] M. Chern, L. Yang, Y. Shen, and J. Hung, "3D Scaffold with PCL Combined Biomedical Ceramic Materials for Bone Tissue Regeneration," vol. 14, no. 12, pp. 2201–2207, 2013.

[8] H. Man, P. K. Chu, F. K. L. Leung, K. M. C. Cheung, K. D. K. Luk, and K. W. K. Yeung, "Engineered polycaprolactone – magnesium hybrid biodegradable porous scaffold for bone tissue engineering," *Prog. Nat. Sci. Mater. Int.*, vol. 24, no. 5, pp. 561–567, 2014.

[9] F. Tavangarian and R. Emadi, "Improving degradation rate and apatite formation ability of nanostructure forsterite," *Ceram. Int.*, vol. 37, no. 7, pp. 2275–2280, 2011.

[10] S. Mehdi Mirhadi, A. Abbas Nourbakhsh, N. Lotfian, and B. Hosseini, "Strength development, bioactivity and biodegradability of forsterite nanostructure scaffold," *Ceram. Int.*, vol. 41, no. 1, pp. 1361–1365, 2015.

[11] M. Diba, M. H. Fathi, and M. Kharaziha, "Novel forsterite/polycaprolactone nanocomposite scaffold for tissue engineering applications," *Mater. Lett.*, vol. 65, no. 12, pp. 1931–1934, 2011.

[12] Y. Leng Chuan, "Design and fabrication of hybrid tissue engineering scaffolds incorporating extrusion based rapid prototyping technology," University of Nottingham, 2013.

[13] M. Diba, M. Kharaziha, M. H. Fathi, M. Gholipourmalekabadi, and A. Samadikuchaksaraei, "Preparation and characterization of polycaprolactone / forsterite nanocomposite porous scaffolds designed for bone tissue regeneration," *Compos. Sci. Technol.*, vol. 72, no. 6, pp. 716–723, 2012.

eureca 2016 – Conference Paper
Paper Number 2ME17

Numerical Analysis of Aerofoil for Wind Turbine Blade

Manish kumar sing Domun[1*], Mohammad Hosseini Fouladi[2], Azadeh Ghadimi[3]

School of Engineering, Taylor's University, Malaysia.

[*]manishdomun@gmail.com

Abstract
The impacts of improving the aerodynamic performance of the aerofoil for wind turbine blade will result to an increase in the energy output efficiency produced by the wind turbine. The cyclic fatigue that is formed on the blade of the aerofoil will be reduced as the size of the blade and the static loading acting on it is reduced. This reduction in size will subsequently follow in a reduction of material and cost of the entire wind turbine system as the blade is the most critical part. The purpose of this study is to investigate the relationship of dimples shape and sizes on a S833 3D aerofoil which affect the aerodynamic performance of the aerofoil. The ratio of the coefficient of lift to that of the drag is defined as the aerodynamic performance of the aerofoil. Dimples on the surface of the aerofoil enables to reduce drag pressure as the wake region of the boundary layer of the fluid is reduced. In addition to that, the dimples cause a delay of the separation point of the boundary layer at different angle of attack of the aerofoil and also allows a smooth transition of the fluid flow from laminar to turbulent over the surface of the aerofoil. Moreover, the aerofoil is numerically analysed at different angle of attack 0^o to 20^o at a constant Reynolds number. The shape of the dimple has been determine from previous studies conducted which is round spherical dimple. Based on the result, the most suitable size of the dimple was determined which is 2 mm.

Keywords: Aerodynamic performance, 3D aerofoil, numerical analysis, wind turbine blade s833, dimples.

1. Introduction

Most wind turbine uses the principle of lift for the aerofoil blade since it is more efficient in terms of aerodynamics. [1]. Firstly, the lift and drag coefficients are related to the pressure variations along the surface of the aerofoil and secondly, to the friction between the fluid and the aerofoil. The shear stress distribution is related to the friction over the surface body of the aerofoil and is independent of the aerofoil shape [2]. On the other hand, pressure variation is related to the air velocity which is in accordance with the Bernoulli's principle. The equation is as mathematically shown below where the p is the static pressure and U is the local velocity along the aerofoil and ρ is the density of the fluid [3].

$$p + \frac{1}{2}\rho U^2 = constant \qquad (1)$$

One of the most significant problems faced in aerodynamics is the flow separation which ultimately result in the stall condition whereby there is a sudden loss of the lift. The flow separation is caused to the due shear stress by skin friction of the aerofoil surface and the fluid. This flow separation produces a phenomenon as pressure drag [2]. This sudden loss of lift can be devastating for a wind turbine whereby it uses the concept of lift for the rotation of the blade to produce electricity. The stall is the defined as the hardest point in the angle of attack to overcome whereby it comes just after the maximum lift of the aerofoil. The separation point has a great impact on the performance of the aerofoil whereby a delay in the separation of the boundary layer results in an increase of the in the lift at a high angle of attack [4].

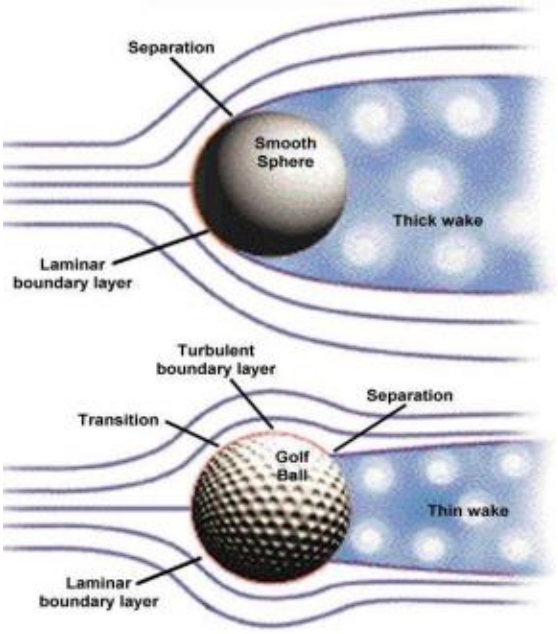


Figure 1: The effect of dimples on fluid flow [2].

Based on the concept of the dimple on the surface of a golf, past studies conducted showed that a golf ball with a dimpled surface can travel higher and further distance than a smooth surface golf ball. This is because the dimpled surface causes turbulence at low Reynolds number resulting in extra momentum and energy to the boundary layer and hence delaying the flow separation [5]. Due to the effect of delaying the separation flow of the boundary layer of the fluid, there is a reduction in the wake areas and reducing the pressure drag as shown in Figure 1. The dimples on aerofoil are significant as the angle of attack increase and function with the same principle as vortex generators [5]. Hence, a reduction in the drag results in an increase of the aerodynamic performance which is defined as the ratio of the lift to that of the drag.

2. Research Methodology

The first objective in the selection of the aerofoil for the wind turbine blade is a high lift coefficient and secondly is the low profile drag coefficient. Moreover, for a range of 1 m to 3 m diameter at variable pitch and speed for a Horizontal Axis Wind Turbine (HAWT), the aerofoil family of S833, S834 and S835 aerofoils are the most appropriate for inaudible, thick and natural-laminar flow which provide a high lift coefficient to drag ratio. [6]. The s833 aerofoil is selected to examine the impact of dimples shape, size and position on an aerofoil as shown below.

A steady state analysis is considered for the simulation of the aerofoil. Based on the calculation of the Reynolds Number as shown in equation below, the flow of the fluid over the aerofoil is assumed to be fully turbulent. Moreover, all the case studies are carried out at the same Reynolds number and the CAD model is done in Solidworks 2014 and simulations are carried in ANSYS Fluent 2014.

$$\boldsymbol{Reynold's\ Number} = \frac{\rho U l}{\mu} = \frac{1000 \times 20 \times 0.12}{1.789 \times 10^{-5}} = \mathbf{1.342 \times 10^5} \qquad \textbf{(2)}$$

2.1 Features of Dimple

3.1.1 Shape of Dimple

Based on the previous studies conducted, a circular spherical shape of the dimple has showed a better aerodynamic performance compare to other shape configurations. The result of the simulation also demonstrated that the turbulence caused at the boundary layer is due to the circular motion of the random particles of the fluid forming the vortex caused by the round dimples [7]. Furthermore, another study concluded that the spherical round dimple are shallow in depth and flat to ensure a better transitional flow from laminar over the surface of the aerofoil and the angle between the angle between the surface of the aerofoil and dimple is high which causing the shear in the fluid boundary layer [8]. A semi-circular shaped dimple compared to a squared shaped dimple produce a higher lift at a low velocity [9]. Hence, selecting a round dimple provide a better aerodynamic performance compared to other shapes.

2.1.1 Size of Dimple

The sizes of the spherical dimple that are taken into consideration range between 2 mm to 4 mm diameter since the objective is to increase the aerodynamic performance. A dimple which is too small in size will not have any effect on the aerodynamic performance as the fluid flow over the aerofoil will not be altered from laminar to turbulent and on the other hand, a dimple which is too big in dimension will cause an increase in the drag of the aerofoil by increasing the skin friction resulting in turbulence flow and thus increase the pressure drag due to viscosity.

3.1 Computational fluid domain, meshing and Boundary condition

The computational fluid domain is a C-shaped domain consist of a circular and rectangular shapes around the aerofoil and at the trailing edge respectively as shown in Figure 2. The different shapes in the C shaped domain for the aerofoil allow to mesh at a fine element size around the aerofoil for better accuracy of the results. The C domain has a dimension of 2 m radius and length of 2 m length for the rectangular shape in order to study the wake region formed and the turbulence in the flow of the fluid.

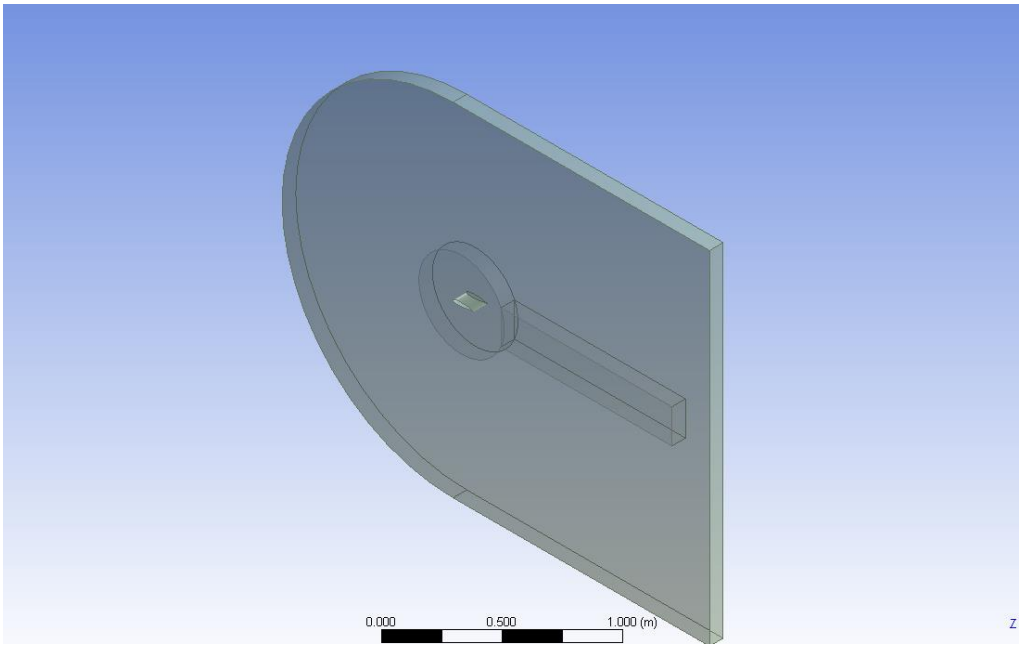


Figure 2: Computational fluid domain for aerofoil

The meshing of the computational fluid domain and the dimples are as shown below. Tetrahedral mesh are used to mesh the computational fluid domain and the mesh control is paved on the surface of the aerofoil as shown in Figure 3 and Figure 4 which form the mesh to be a hexahedral mesh on the surface of the aerofoil and surface of the dimple. The inlet is defined as velocity inlet of 20 m/s, the outlets are defined as pressure outlets and the wall of the domain is assigned as adiabatic boundary. Moreover, the solver used is the Sparlat-Allmaras since it is designed for aerofoil and based on the objective of the paper which is to study the aerodynamic performance of the aerofoil. All simulations are carried out at a constant Reynolds number with velocity 20 m/s and dynamic viscosity

of 1.78×10^{-5} Pa-s and density of air at 1.235 kg/m^3. All the aerofoil is simulated at different angle of attack of 0^o, 5^o, 10^o, 15^o and 20^o and both the lift and drag are monitored for the solution at surface of the aerofoil.

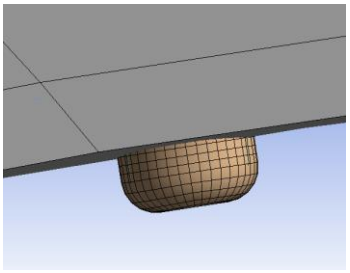


Figure 3: Meshing of dimples

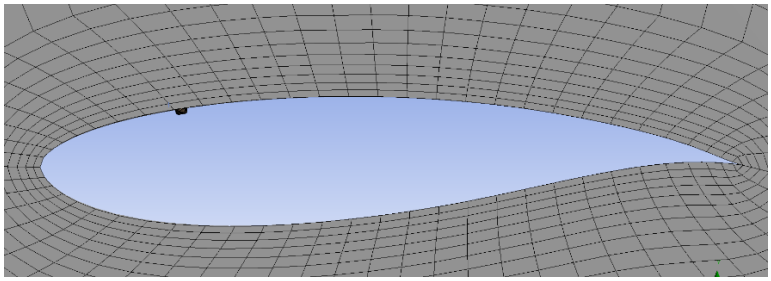


Figure 4: Meshing of aerofoil computational domain

3. Result and discussion

The graph of the coefficient of lift against the angle of attack of the s833 aerofoil for dimple sizes shows that the smooth aerofoil has a lower coefficient of lift compared to the dimpled surfaces of dimple size 2 mm to 4 mm. This is because the coefficient of lift is related to the surface of the aerofoil and to the shape of the aerofoil and whereby in this case the surface has been altered. The dimpled aerofoil cause an increase in the coefficient of lift as the boundary layer of air over the aerofoil surface is changed from laminar to turbulent, thereby increasing the velocity of fluid flow the over the convex shape at the leading edge of the aerofoil. The dimples on the surface of the aerofoil cause a decrease in the shear which is related to the viscosity at the boundary layer and the velocity of the fluid since the fluid as to over a lower shear force between the surface of the aerofoil and fluid. As the shear of the fluid is lower, the velocity travelling over the surface of the aerofoil is increase and consequently increase of the coefficient of lift. The smooth aerofoil has a lower coefficient of lift as the shear is much higher since the flow of the fluid over the surface of the aerofoil is laminar in the boundary layer and the contact between the surface of the aerofoil and the fluid wall is ‘sticky’. At high of attack the dimple has no effect since the coefficient of lift is dependent upon the shape of the aerofoil and as the aerofoil consist of a thick leading edge.

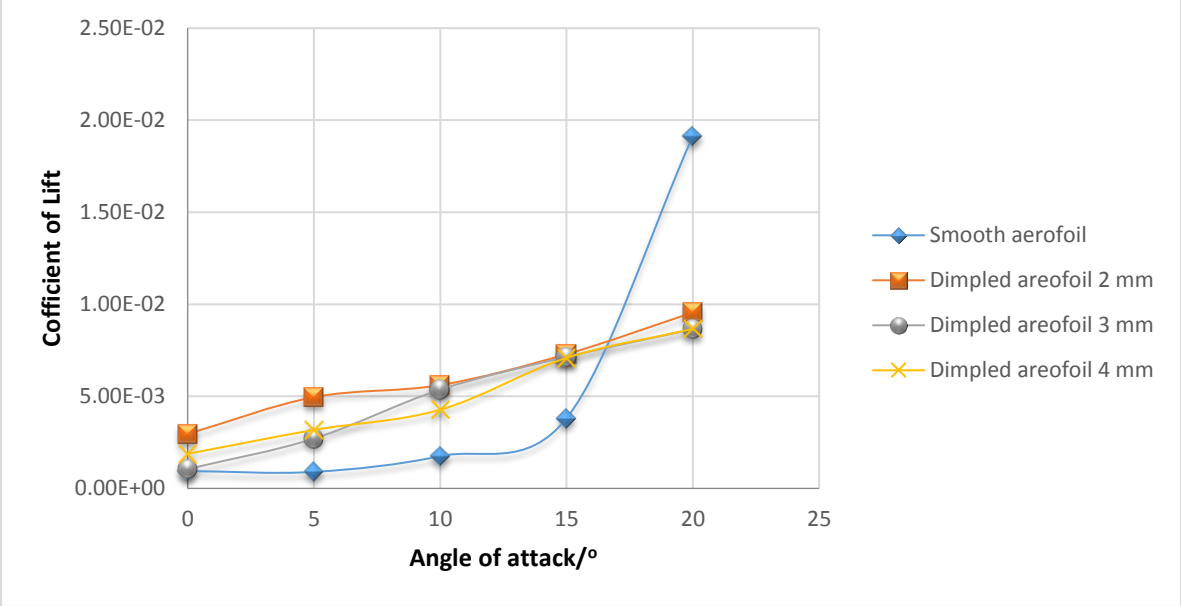


Figure 5: Graph of Coefficient of lift against the angle of attack for dimples sizes

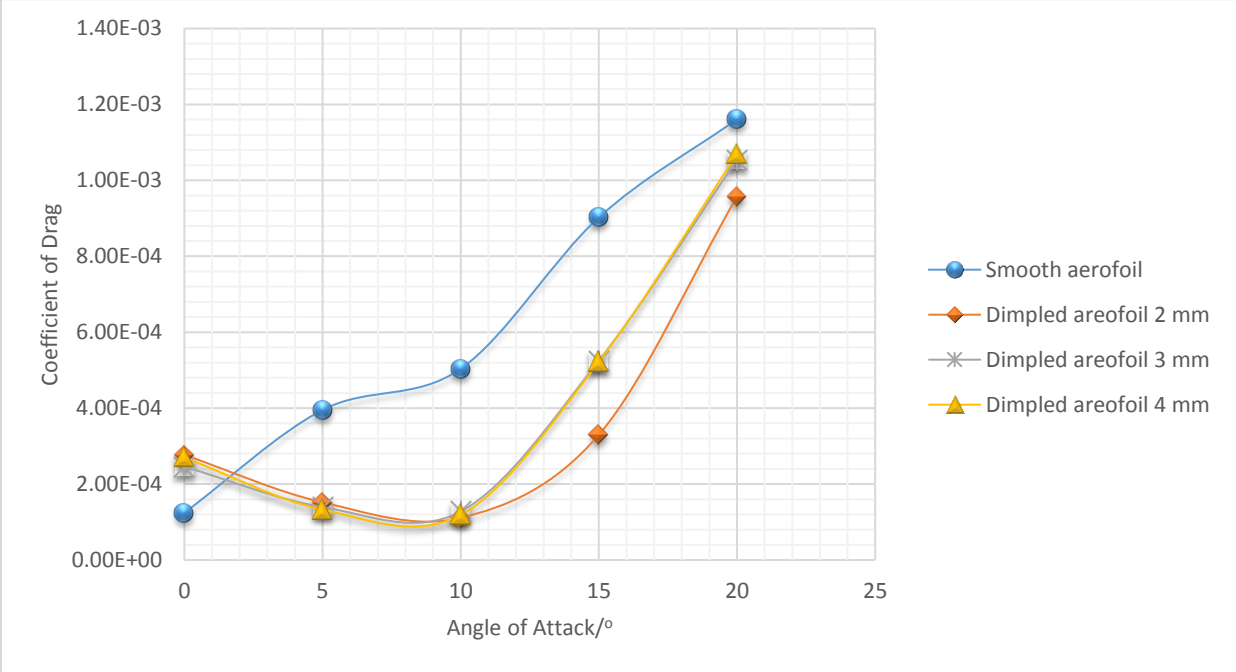


Figure 6: Graph of Coefficient of drag against Angle of attack for dimple sizes

The graph of coefficient of drag against the angle of attack for dimples sizes shows that the smooth aerofoil has a higher drag compared to the dimpled aerofoil as the angle of attack increases to 20°. The dimples on the surface of the aerofoil cause a change in the flow of the fluid from laminar to transitional and finally turbulent at the boundary layer. At angle of the attack 0°, the coefficient of drag is lower since the fluid flow over the entire surface of the aerofoil from the leading edge to the trailing edge and a laminar flow is

formed compared to the dimpled surface at 0^{o} angle of attack, the boundary layer has been alter to turbulent which cause an increase in the drag coefficient as it increase the skin friction. Furthermore, as the angle of attack increases, from 5^{o} to 15^{o}, the coefficient of drag is reduced for dimpled aerofoil compared to smooth aerofoil since the dimples delays the flow separation of the fluid at the boundary layer and cause a smaller wake region due to better recirculation of fluid at the trailing edge. The wake region is caused due to a sudden flow separation resulting in adverse pressure gradient and thus increasing drag. The turbulence formed in the boundary layer of the fluid provide a better recirculation of the fluid in the wake region. At angle of attack 20^{0}, the coefficient of drag of the dimpled aerofoil is approximately the equal to that of the smooth aerofoil as the wake region formed at the trailing edge of the aerofoil is too large and the turbulent flow formed by the dimples is not sufficient to fill in the 'vacuum space'.

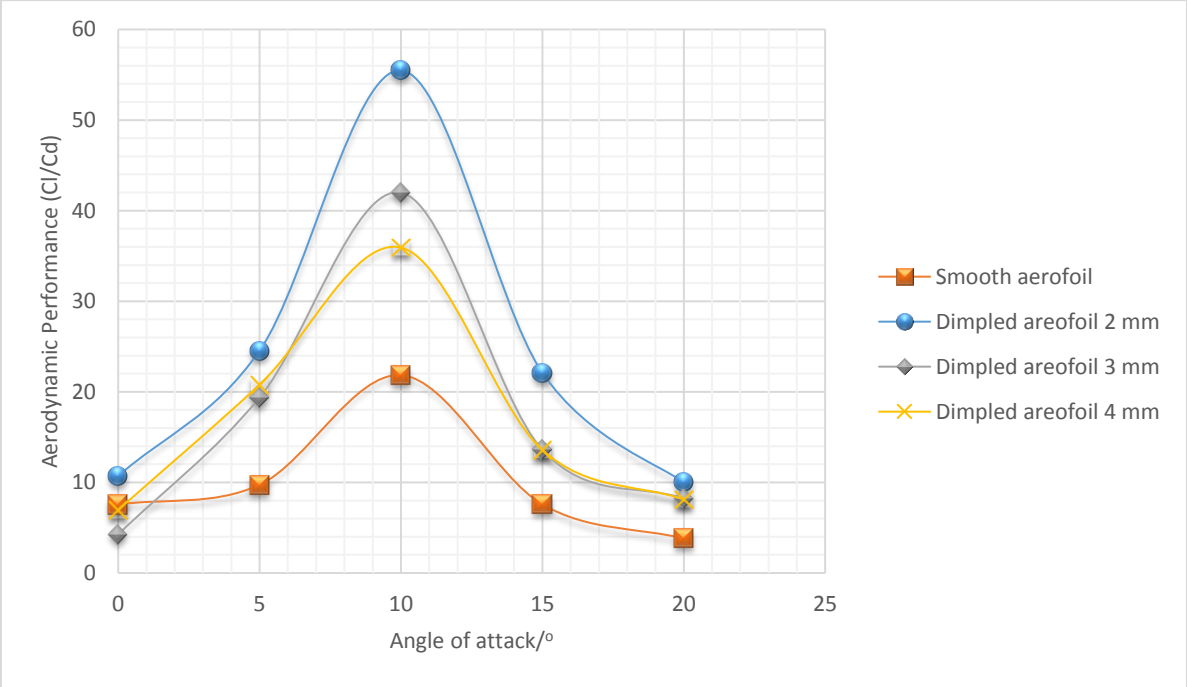


Figure 7: A graph of Aerodynamic performance against the Angle of attack for dimple size.

The graph of the aerodynamic performance against the angle of attack for dimple sizes show that the dimples of diameter 2 mm has a better aerodynamic performance compare to the other dimples sizes and the smooth aerofoil. At 0 angle of attack the aerodynamic performance of aerofoil is approximately the equal for the different dimples sizes and the smooth aerofoil. All dimpled aerofoil demonstrate a better aerodynamic performance compared to the smooth aerofoil as the angle of attack increases. As the angle of attack increase from 0 to 20, the dimples size of 2 mm diameter shows a better aerodynamic performance compared to the other dimples sizes since the change in flow of the fluid in the boundary layer from laminar to turbulent and is sufficient to accommodate for the recirculation of the fluid in the wake region decreasing the coefficient of drag. The aerodynamic performance is maximum at an angle of attack 10 since that angle of attack

the coefficient of drag is the lowest and coefficient of lift is relatively high. Furthermore, at the stall condition which occur after the an angle of attack of 10^{o} whereby there is a sudden drop in the coefficient of lift, the dimpled aerofoil of 2 mm demonstrate a better aerodynamic performance relative to the other dimples sizes and smooth aerofoil.

4. Conclusion

To conclude, the relationship of dimples shape showed by previous study that round spherical dimple increase the aerodynamic performance to other configuration due to better flow. In addition to that, the study conducted on the dimple sizes demonstrate that dimples of diameter 2 mm provide a better aerodynamic performance than other dimple dimensions. The dimple change the boundary layer from laminar to turbulent thus reducing shear and increases the velocity which produces a lower downward pressure. The drag is greatly reduced as it enables the recirculation of the fluid in the void space at the trailing edge and a smaller wake region is formed.

References

[1] A. Nelson, Wind Energy Renewable Energy and the Environment, London: CRC Press, 2009.

[2] S. S.Mahamuni, "A Review on Study of Aerodynamic Characteristics of Dimple Effect on Wing," *International Journal of Aerospace and Mechanical Engineering* , vol. Volume 2, 2015.

[3] J.F Manwell et al., WIND ENERGY EXPLAINED Theory, Design and Application, United Kingdom: John Wiley & Sons Ltd, 2010.

[4] A. Ghoddoussi, "A Conceptual Study of Airfoil Performance Enhancements Using CFD," *Department of Aerospace Engineering,* 2011.

[5] R. T. S. S. Bhadri Rajasai, "Aerodynamic effects of dimples on aircraft wings," *Institute of Research Engineers and Doctors,* 2015.

[6] D. M. Somers, "The S833, S834 and S835 Airfoils," *National Renewable Energy Laboratory,* Vols. NREL/SR-500-36340, 2005.

[7] D. Srivastav, "Flow Control over Airfoil using Different Shaped Dimples," *International Conference on Fluid Dynamics and Thermodynamics Technologies,* vol. volume 33, 2012.

[8] F. Alam, "A study of golf ball aerofodynamic drag," *5th Asia-pacific congress on sports technology (APSCT),* vol. volume 13, pp. 226-231, 2011.

[9] G. A. P. V. E. Livya, "Aerodynamic Analysis of Dimple Effect on Aircraft Wing," *International Journal of Mechanical, Aerospace, Industrial, Mechatronic and Manufacturing Engineering,* vol. 9, 2015.

eureca 2016 – Conference Paper
Paper Number 2ME18

Preparation of Graphene Oxide Nanofluid in Application of Flow Battery

Muhammad Akmal bin Zulkifli, Azadeh Ghadimi, Taghi Hajibeigy

[1]*School of Engineering, Taylor's University, Malaysia*

[*]akmalzul92@yahoo.com

Abstract

Recently, one of the new expanding areas is the Nanomaterial suspensions in liquid (nanofluid) in technology (nanotechnology). It can be applied in wide applications especially in thermal and electrical conductivity. This research project will be focused on graphene oxide nanofluid preparation and how to use it as an electrolyte of a flow battery. The research project is conducted to answer research questions of how to produce a stable and homogenous graphene oxide nanofluid and how graphene oxide nanofluid generate electricity and become a flow battery. The preparation of graphene oxide was carried out by using the simplified Hummer's method. The step taken to produce graphene oxide nanofluid from the prepared graphene oxide sheets is by the two-step preparation method.The significant factor that needs to be taken care of about nanofluid is to make it stable and homogenous throughout the application of experiment to get an accurate result. The method used to produce stable and homogenous graphene oxide nanofluid was by using ultarsasonification method and pH control method. After the preparation of the nanofluid, the nanofluid has been used as an electrolyte for a flow battery to generate electricity out of it and to measure the current and power of the battery. The result of the experiment was recorded and shows that the electric current and power depends on the volume fraction of the nanofluid.

Keywords: nanofluid, flow battery, electricity, power, graphene oxide.

1. Introduction

The technology advancement and engineering development have led to abundance of solution for challenges occurring now and in the future. Recently, one of the new expanding areas is the nanomaterial suspensions in liquid in technology. It can be applied in a wide application of technologies such as energy generation and storage, thermal management, lubrication, and biomedical. Having the unique and variety characteristics of the nanomaterials make it desirable for engineering purposes [1]. Nanofluid materials have become one of the solutions for expensive thermal management size increment acting as an effective novelty coolant to provide heat dissipation in lower cost [2].

Primarily, the term ‘nanofluid’ was found by two researchers, Choi and Eastman. It refers to fluids that contain dissipated nanosized particles with a characteristic possessing high thermal management and thermal conductivity. It will be expected to become one of the best advanced heat transfer fluids with required temperature in many applications such as heat exchanger system and solar collectors. The tiny size of the nanoparticles can have higher thermal conductivity compared to the bigger size particles at specific concentrations. The uniqueness of physical and chemical characteristic of nanofluid makes it covetable and can be used in many different applications in the industries [3]. Nanofluid is usually produced by two–step preparation method. The nanoparticles and the base fluids are prepared separately and then mixed together to produce the nanofluid. After dispersion, due to high van der Waals interaction, there are probabilities that the nanoparticles will sediment forming a two layered solution. This can be treated by few ways such as surfactants addition, surface modification and pH control are some of the methods to ensure the stability of the nanofluid [4].

Graphene oxide is a recent emerging type of nanofluid used in many applications, more specific to this research is using as electrolyte to conduct electricity [5]. Graphene is a 2D $sp2$ nanostructure material meaning that it is two dimensional and one atom thick bonded by $sp2$ hybridized orbital. Graphene is an ideal material for electrode because it has high specific surface area due to chemical stability and good conductor of heat and electricity [6]. The inferior side of graphene is the material is not very stable in water because of its hydrophobic property and usually creating two phase suspension. Graphene oxide is preferable because it is more stable in water due to its hydrophilic nature [7].

Brodie’s and Hummer’smethod can be used to oxidize graphene to become graphene oxide. The main process in Brodie’s method is potassium chlorate ($KCLO_3$)-fuming nitric acid (HNO_3) whereas Hummer’s method using graphene to react with mixture of potassium permanganate ($KMnO_4$) and concentrated sulfuric acid (H_2SO_4) [8].

Flow batteries have their own special features compared to other types of electrochemical energy storage such as Li-ion batteries, Ni-metal batteries, capacitors and super-capacitors because it fitted into the category of large-scale energy storage. They can be charged and discharged heavily. Besides, they also have a long lifetime and can be designed easily in a large scale referred to the module design. They behave differently compared to the other types of battery systems because the energy stored inside the electrolyte and the storage capacity determined by the concentration and volume of the electrolyte. Flow batteries converts chemical energy to electrical energy using electrolyte that carry one or more dissolved electro-active elements [9].There is a research finding regarding graphene oxide nanofluid that can be used as electrode to conduct electricity [7]. Thus, this project aims to represent graphene oxide nanofluid as a flow battery.

2. Research Methadology

2.1 Preparation of graphene oxide nanofluid

Initially the graphite material was treated with sulphuric acid **(**H_2SO_4) and phosphoric acid (H_3PO_4) with both having 98% concentration. The solution was stirred to make sure it dispersed evenly inside the beaker. While stirring, potassium permanganate ($KMnO_4$) with 99.9% purity was added gradually inside the beaker. Precaution step has to be taken during the addition of $KMnO_4$as the reaction may be explosive. The solution is left to stir for about three days [10].

After three days, hydrogen peroxide (H_2O_2) with 30% concentration was added to the solution. The addition need to be done in ice bath to cool down the solution as the step can give rise to temperature. After that, the solution was left to stir for 10 minutes. Next, the solution has been washed 3 times using 1 mole of hydrochloric acid and followed by distilled water until it reached natural pH which is around 6-7 pH. This step was done in centrifuge. Observation has been done as the colour of graphene oxide suspension will change from bright yellow to light brown and then dark brown. The solution also will turn from a less viscous solution to a more viscous one like jelly.

After that, the solution was dried inside an oven at 50℃ to remove water molecules inside the solution. The temperature should not be higher than 50℃ because high temperature could denature functional groups in graphene oxide and it may become reduced graphene oxide. The process will take over for 24 hours. Figure 6 shows the overall process to prepare graphene oxide [11].

Finally, the step taken to produce graphene oxide nanofluid from the prepared graphene oxide sheets is by the two-step preparation method. Graphene oxide sheets are dispersed in deionized water to produce the graphene oxide nanofluid. Then the solution is ultrasonicated for 60 minutes with 37 kHz frequency to produce a stable and homogenous nanofluid and the pH was controlled to be around 7 by adding drops of sodium hydroxide (NaOH) solution to ensure the stability of the nanofluid. Equation 1 shows the formula used to calculate volume fraction of graphene oxide nanofluid.

$$vol\% = \frac{\frac{M_{GO}}{\rho_{Go}}}{\frac{M_{Go}}{\rho_{Go}} + \frac{M_{water}}{\rho_{water}}} \times 100\% \qquad (1)$$

The density of graphene oxide used is 2.62g/cm^3 and the volume of distilled water used in the experiment was fixed to 300ml throughout the experiment. By varying the mass of graphene oxide, the desired volume fraction was prepared [12].

2.2 Creating Prototype of flow battery

Flow battery used the concept of electrochemical energy storage with the energy stored in liquid form and held separate from the actual battery cell. This device

called of flow battery has two electrolytes which is positive and negative. It works by pumping liquid electrolytes pass the membrane where a chemical reaction releases the electrons that supply power in the form of electricity. The advantage of this flow battery design is that it can be scaled up the container of the electrolyte according to how many hours of electricity need to store. The bigger the tanks the more energy it could store. The prototype of flow battery was build using PVC pipe. This materials was used because it has good chemical resistant and can store liquid without easily been leaked. Figure 1 shows the prototype build for flow battery.



Figure 1: Prototype of flow battery

The main focus of this research project which is graphene oxide nanofluid was set to be an electrolyte at the cathode part while a fixed value of 300ml of 0.5 mol of sodium chloride (NaCl) for the anode part was used throughout the study. NaCl was used as another electrolyte because of the characteristics of it which is a good conductor of electricity. There was an experiment conducted which proved that salt water could generate voltage when it flows thorough a graphene sheet showing that it could generate electricity when reacted together. It is also being used as an electrolyte in the Aluminium-air battery [13]. The ion selective membrane used was the Nafion proton exchange membrane. Nafion proton exchange membrane is normally used for electrochemical cell for ion exchange membrane including the vanadium redox flow battery. Proton exchange membrane is a semipermeable membrane which permeable to protons but does not conducting electrons [14]. Carbon felt was used as electrode for the experiment because it has good capability of transferring electron and conduct electricity [8].

2.3 Measurement of the current and power generated

The voltage was measured using digital meter by using a circuit with a 0.99 M ohm resistor. The resistor was needed to measure a small voltage passing through the circuit. Figure 2 shows how the experiment was set up.



Figure 2: Experiment set up with flow battery and circuit

The Current and power generated by the battery was calculated using equation 2 and 3 below where V is the voltage, I is current and P is the power.

$$I = \frac{V}{R} \quad (2)$$

$$P = VI \quad (3)$$

3. Results and Discussions

3.1 FTIR spectrometer Analysis

Figure 3 illustrates the result of Fourier transform infrared spectroscopy (FTIR) spectrometer of graphene oxide sheets. The result simply shows the present of oxygen and water containing functional groups in the element. The peak at 1065 cm^{-1} is due to C-O present in the lattice. The peak at 1375 cm^{-1} shows the C=O which is the carboxyl functional group. In addition, the sharp peak at 1619 cm^{-1} shows the present of C=C in the lattice. Finally the stretching peak around 3600 to 3200 cm^{-1} confirms the present of hydroxyl functional groups.

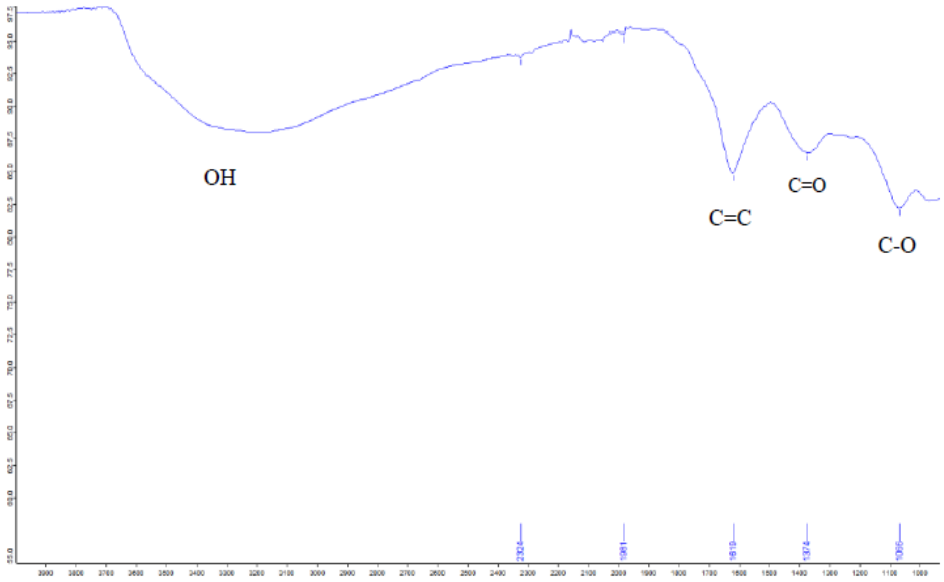


Figure 3: FTIR spectrometer Analysis of graphene oxide

3.2 Stability of Graphene Oxide

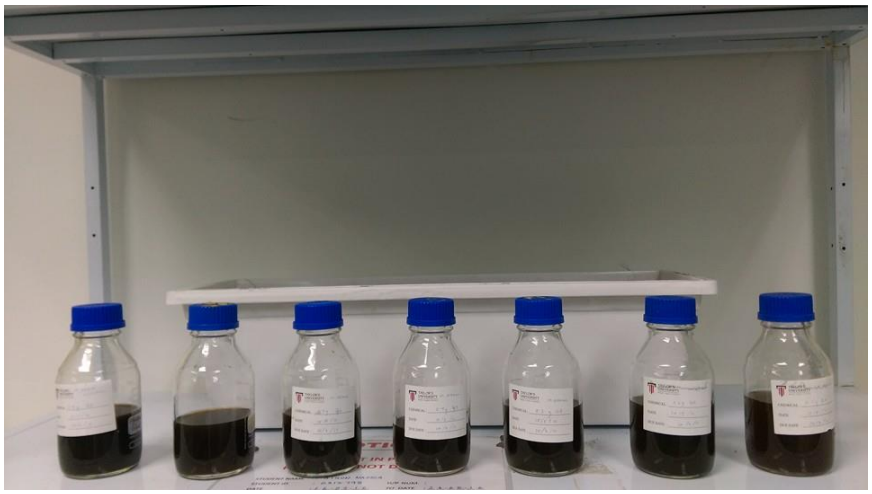
Stability of nanofluids can be determined by its zeta potential value and how far the distance from the isoelectric point (IEP). When the zeta potential value of the nanofluids is close to IEP, the electrostatic value will be less because IEP is the point where there is no net electrical charge. This will cause higher attraction forces between particles and it will bring to sedimentation. Zeta potential value is the degree of repulsion of same charged particles contained in solution. Higher zeta potential value means higher electrostatic force compare to the force of attraction between particles and this will make the nanofluids more stable in time.

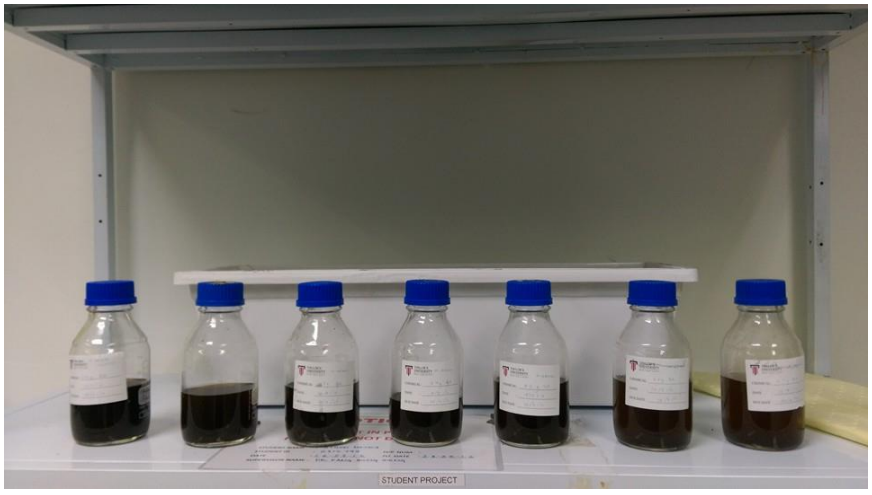
The methods used to produce a stable graphene oxide nanofluids are by controlling the pH of solution and ultrasonication. The pH of solution is adjusted to be around 7 by adding drops of low concentrated Sodium Hydroxide solution. Besides that, ultrasonication method also used to produce the nanofluids. The duration and the frequency of ultasonication can affect the production of nanofluids. Thus, 60 minutes of duration with 37 kHz of frequency are used to prepare the graphene oxide nanofluids. Table 4.1 shows the result of stability of samples.

Table 4.1 Stability of samples

Sample number	Concentration volume	Initial pH	Final pH	Stability (days)
1	0.0127	4.5	7.0	>30
2	0.0254	4.3	7.0	*>30*
3	0.0382	4.6	7.0	*>30*
4	0.0509	4.4	7.0	*>30*
5	0.0636	4.2	7.0	*>30*
6	0.0763	4.1	7.0	*>30*
7	0.089	4.4	7.0	*>30*

Based on observation from figure 4.2, no clear sedimentation occurs from all samples prepared meaning that all samples that prepared are stable but it can be seen that the color of the nanofluids have a little change from dark brown to a lighter brown through period of times. The nanofluids are considered not stable if sedimentation occurs. Before it sediments, the sample color will slowly changes from dark brown to light brown and finally solid particles will be seen clearly on the bottom of the container. By observing the samples it can be suggested that using pH of 7 and 60 minutes of 37 Hz ultrasonication can be a solution to produce a stable GO nanofluid for more than 30 days for these volume fractions.





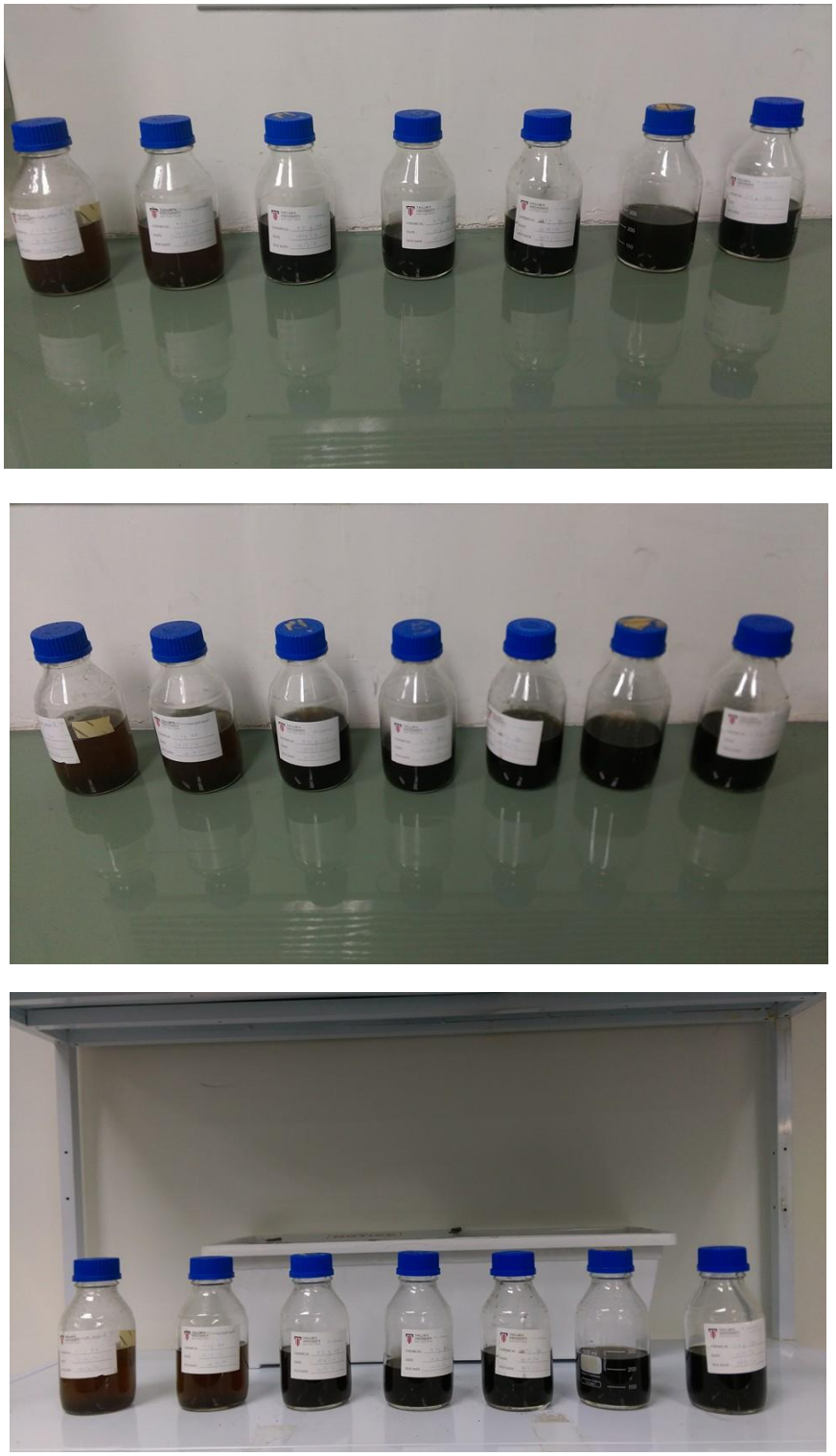


Figure 4.2 Stability monitoring of samples 1-7; from top to bottom (1 day, 7days, 14 days, 21 days, 30 days)

3.2 Electric current and power produced

The electric current generated by graphene oxide nanofluid with different volume fraction is measured on the 1st day after ultrasonication and the results are recorded. Table 4.2 and figure 4.3 show the results obtained from the experiment. The

table and the figure show that the electrical current generated by the graphene oxide nanofluid depends on the volume fraction of nanoparticles dispersed in the solution. The higher the volume fraction, the higher the electricity generated by the nanofluid. The highest value of current recorded was 0.621 µA with volume fraction of 0.089%. The lowest value recorded was 0.493 µA with volume fraction 0.0127%.

Table 4.2 Current produced by different volume fraction

Volume fraction (%)	Current (µA)
0.0127	0.493
0.0254	0.512
0.0382	0.53
0.0509	0.556
0.0636	0.585
0.0763	0.599
0.089	0.621

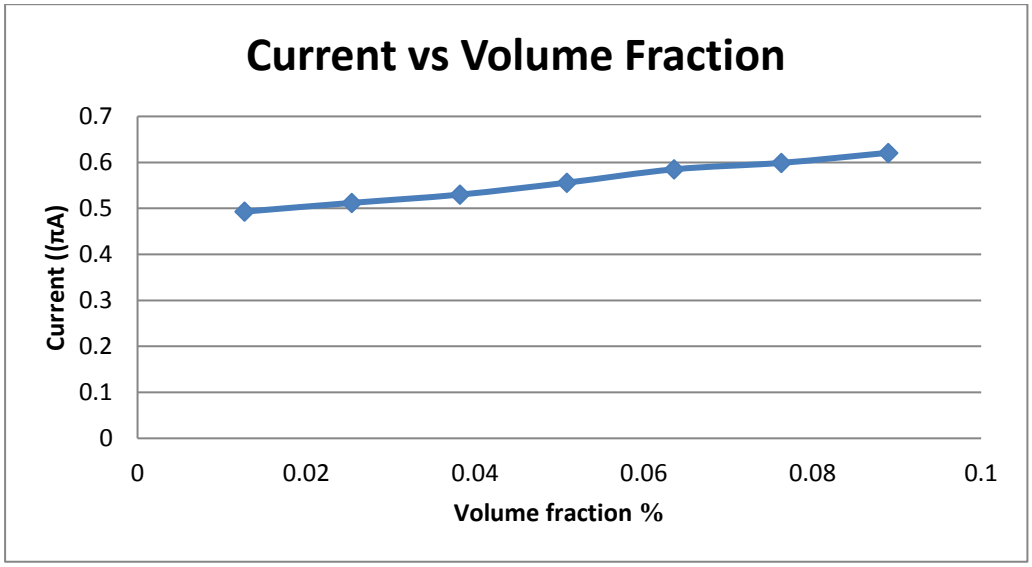


Figure 4.3 Current produced with different volume fraction

Figure 4.4 shows the same pattern of results, directly proportional between volume fraction and current produced when being tested with different period of times which is 1 day, 7 days, 14 days, 21 days, and 30 days. The test conducted to study the effect of stability on the amount of current produced. The results show that the amount of current generated was reduced when the number of days increased. From the graph plotted it appears to have bigger gap towards the end of 30 days compared to initial period. Even though the nanofluids are still considered to be stable, the amount of current generated are decreasing through period of times showing that the stability of nanofluids are slowly reduced by time. The result indicated that the highest series of result was delivered during 1st day and the lowest during the 30th day.

Table 4.3 Current produced by different volume fraction through period of times

volume fraction	current (μA)				
	1 day	7 days	14 days	21 days	30 days
0.0127	0.493	0.4778	0.455	0.43	0.385
0.0254	0.512	0.505	0.489	0.474	0.426
0.0382	0.53	0.523	0.497	0.458	0.422
0.0509	0.556	0.556	0.516	0.506	0.451
0.0636	0.585	0.544	0.576	0.558	0.49
0.0763	0.599	0.591	0.572	0.599	0.505
0.089	0.621	0.608	0.581	0.536	0.51

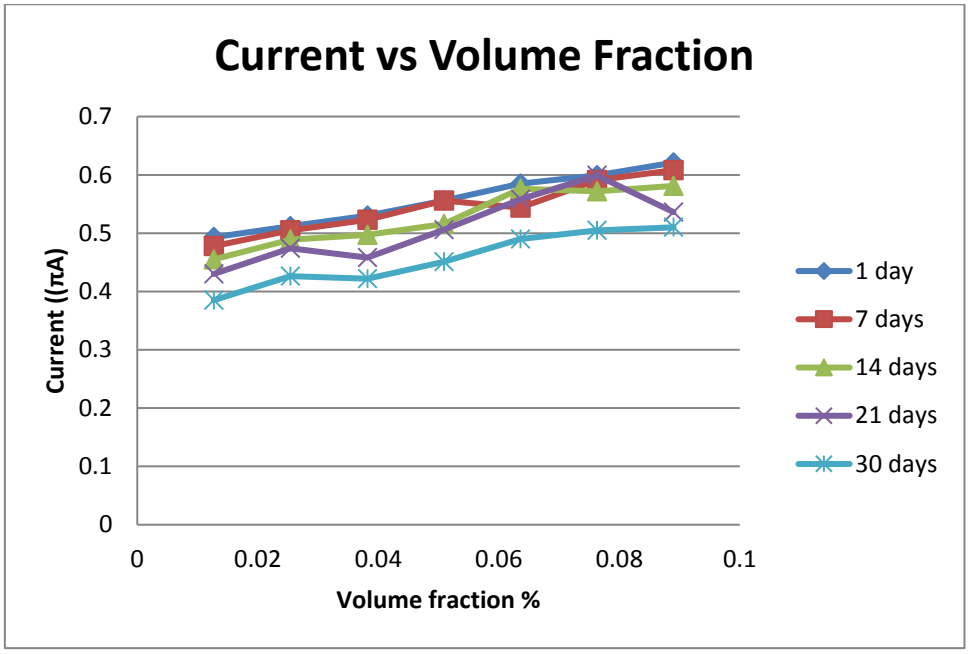


Figure 4.4 Current produced with different volume fraction through period of times

Electric power is the rate of energy transferred in an electric circuit. The power generated by the graphene oxide flow battery was calculated using the value of current and voltage. The table and figure show the results obtained from the study. Table 4.4 and figure 4.5 show that the power generated by the nanofluid battery depends on the volume fraction of the nanofluid. The higher the volume fraction of graphene oxide nanofluid, the higher the power generated. The highest power recorded in this study was 0.382 πW with 0.089% volume fraction and the lowest was 0.241πW with 0.0127% volume fraction. Figure shows the power generated by GO nanofluid measured during period of times. The results indicate the exact same trend of directly proportional same as the current result shown before.

Table 4.4 Experimental results

Volume fraction (%)	Voltage (v)	Current (μA)	Power (πW)
0.0127	0.488	0.493	0.241
0.0254	0.507	0.512	0.26
0.0382	0.525	0.53	0.278
0.0509	0.55	0.556	0.301
0.0636	0.579	0.585	0.339
0.0763	0.593	0.599	0.355
0.089	0.615	0.621	0.382

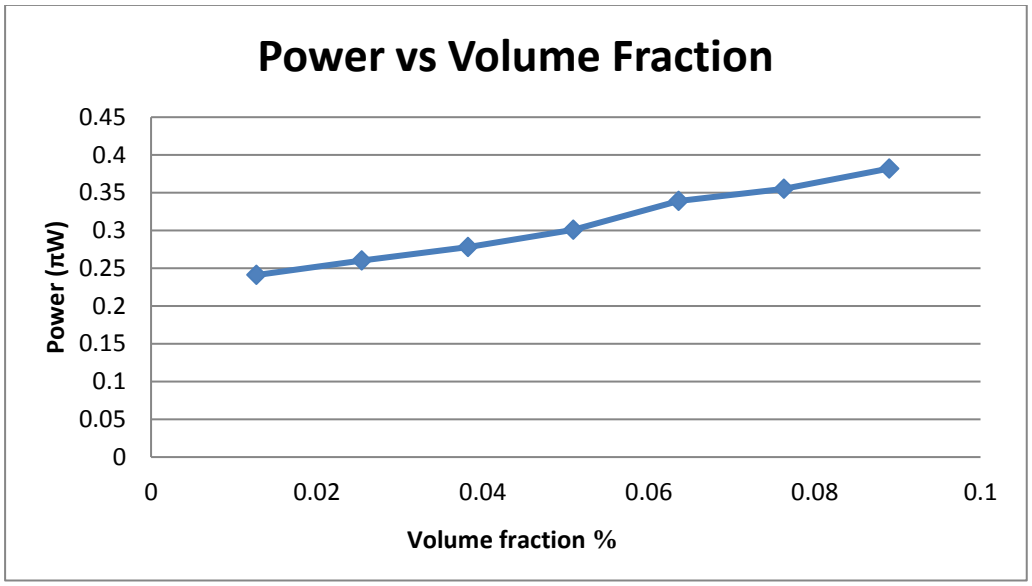


Figure 4.5 Power generated with different volume fraction

The current produced by the nanofluid battery is determined by the number of ions inside GO nanofluid and NaCl solution that reacted within the system. The voltage of the battery depends by the total difference in chemical potential between the two chemical solutions and electrolytes in the battery. Hence, the power developed by the battery is the product between the total current and total voltage delivered in the battery. Table 4.5 and figure 4.6 indicated that the power delivered by the nanofluid battery is increasing with higher volume fraction but the amount of power developed is reduced through period of times. The same pattern observed as the electric current result. The highest series of result was during the 1st day and the lowest was during the 30th of measurement.

Table 4.5 Power produced by different volume fraction through period of times

volume fraction	Power (πW)				
	1 day	7 days	14 days	21 days	30 days
0.0127	0.241	0.226	0.205	0.183	0.147
0.0254	0.26	0.253	0.237	0.222	0.18
0.0382	0.278	0.271	0.245	0.207	0.176
0.0509	0.301	0.3	0.264	0.254	0.201
0.0636	0.339	0.308	0.328	0.308	0.238
0.0763	0.355	0.346	0.324	0.318	0.253
0.089	0.382	0.366	0.335	0.293	0.258

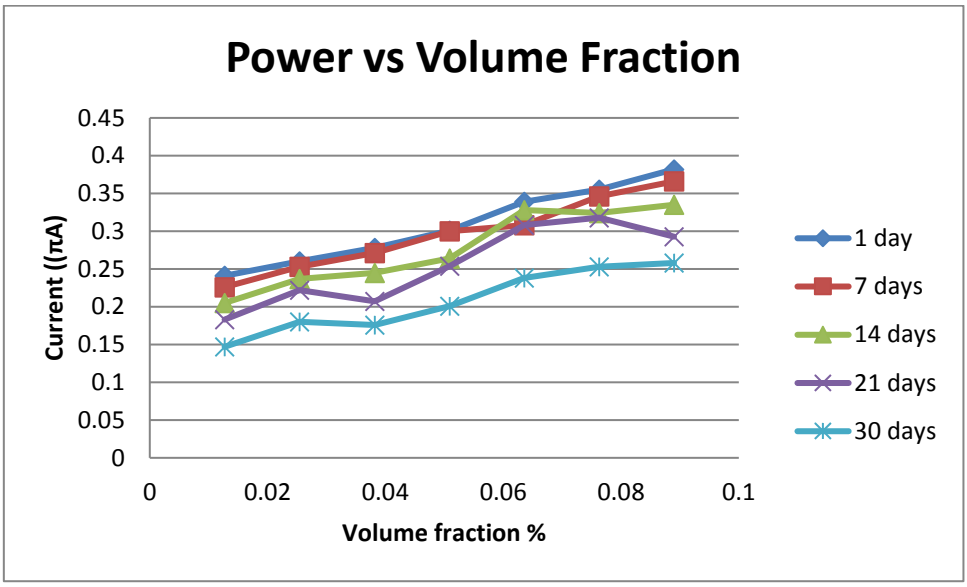


Figure 4.6 Power generated with different volume fraction through period of times

Electric current and power produced depends on the volume fraction of nanoparticles dispersed in the solution. This is because when the volume fraction increases, ionic concentration inside the solution increases giving more chance for the ions to react and carry charges thus produced greater amount of electricity.

Based on theory of colloidal suspension, the factors that affect current generation and conductivity of nanofluid are the formation of dielectric layer on the surface of particles and net electric charge of particles. Formation of EDL depends on two factors, ionic concentration of solution and volume concentration of particles [22ts. electric charge on the surface of particles will form once the nanoparticles are dispersed in solution. This electric charge will attract the oppositely charged ions to form the charged diffuse layer around the particle which is called the electrical double layer. Based on this experiment, electric charges are formed once the GO nanoparticles are dispersed in the base fluid and will be attracted by the oppositely charged particles from NaCl solution through the proton exchange membrane to form EDL. The membrane only allows charged particles to pass through it and prevent the two solutions from mixing with each other.

Besides, net electric charges also affect the formation of EDL of particles. When the amount of ions inside the solution is high, there are enough ions to compensate the electric charges of particles. Thus lower the electrical density on the particles surfaces and EDL will be formed easier.

In addition, when the nanoparticles are stable and homogenously dispersed in base fluid, it will make a better electrophoretic mobility which is better motion of dispersed particles in fluid. Better electrophoretic mobility will result in better movement of ions in the solution. This will leads to improvement of current generation and conductivity of nanofluid. This explains why the electric current and power generated by the nanofluid reduced when measured through period of times as the stability of the nanofluid also decreasing.

The main limitation in the results shown is the current and power produced by the nanofluid flow battery is still considered low compared to the commercial types of batteries. The rate current produced depends on the reaction of chemicals which is the reduction and oxidation reactions. During discharge process, oxidation reaction will release electron from anode or negative side of the flow battery. The electron will moves through circuit and then will be accepted by cathode or positive side of the battery via reduction process. In this particular experiment, the cathode side of the battery which is GO nanofluid need to reduce to be able to generate electricity. But the tendency of all GO particles to undergoes reduction process is low due to the stable and inert nature of GO. Future works can be done on the suitable method to reduce GO while measuring the electricity and without disturbing the stability of the nanofluid.

7. Conclusions

In conclusion, the results obtained from this study gave the basic knowledge regarding graphene oxide and the method suitable to produce stable and homogenous graphene oxide nanofluid. Besides that, it suggests that the electric current and power produced depends on the volume fraction of the nanofluid based on volume fraction of 0.0127-0.089 %. Even though there are still many question remain open, the findings can help in future studies regarding nanofluid flow battery especially when using graphene oxide as electrolyte. The main drawback and limitation of this study is it only covers until about 0.09% of volume fraction. Future studies can be done to know the effect of having more or less volume fraction of graphene oxide nanofluid. Besides that, future studies can be done using other type of nanofluid instead of graphene oxide conceivably it can generate higher electricity.

References

[1]D. S. E.V. Timofeeva, J.P. Katsoudas, C.U. Segre, “Rechargeable Nanofluid Electrodes for High Energy Density Flow Battery,” *Nanotech Conf.*, no. September 2015, 2013.
[2] N. A. C. Sidik, H. a. Mohammed, O. a. Alawi, and S. Samion, “A review on preparation methods and challenges of nanofluid,” Int. Commun. Heat Mass Transf., vol. 54, pp. 115–125, May 2014.

[3] M. Mehrali, E. Sadeghinezhad, S. T. Latibari, S. N. Kazi, M. Mehrali, M. N. B. M. Zubir, and H. S. C. Metselaar, "Investigation of thermal conductivity and rheological properties of nanofluid containing graphene nanoplatelets.," Nanoscale Res. Lett., vol. 9, no. 1, p. 15, 2014.
[4] Y. Li, J. Zhou, S. Tung, E. Schneider, and S. Xi, "A review on development of nanofluid preparation and characterization," *Powder Technol.*, vol. 196, no. 2, pp. 89–101, Dec. 2009.
[5] Z. Li, B. Yang, S. Zhang, and C. Zhao, "Graphene oxide with improved electrical conductivity for supercapacitor electrodes," *Appl. Surf. Sci.*, vol. 258, no. 8, pp. 3726–3731, Feb. 2012.
[6] R. K. Gupta, Z. a. Alahmed, and F. Yakuphanoglu, "Graphene oxide based low cost battery," *Mater. Lett.*, vol. 112, pp. 75–77, Dec. 2013.
[7] L. T. Le, M. H. Ervin, H. Qiu, B. E. Fuchs, and W. Y. Lee, "Graphene supercapacitor electrodes fabricated by inkjet printing and thermal reduction of graphene oxide," *Electrochem. commun.*, vol. 13, no. 4, pp. 355–358, Apr. 2011.
[8] Z. González, C. Botas, C. Blanco, R. Santamaría, M. Granda, P. Álvarez, and R. Menéndez, "Graphite oxide-based graphene materials as positive electrodes in vanadium redox flow batteries," *J. Power Sources*, vol. 241, pp. 349–354, Nov. 2013.
[9]Q. Xu and T. S. Zhao, "Fundamental models for flow batteries," vol. 49, pp. 40–58, 2015.
[10] M. Mehrali, E. Sadeghinezhad, S. Tahan Latibari, M. Mehrali, H. Togun, M. N. M. Zubir, S. N. Kazi, and H. S. C. Metselaar, "Preparation, characterization, viscosity, and thermal conductivity of nitrogen-doped graphene aqueous nanofluid," *J. Mater. Sci.*, vol. 49, no. 20, pp. 7156–7171, Jul. 2014.
[11] K. G. K. Sarojini, S. V Manoj, P. K. Singh, T. Pradeep, and S. K. Das, "Colloids and Surfaces A : Physicochemical and Engineering Aspects Electrical conductivity of ceramic and metallic nanofluid," vol. 417, pp. 39–46, 2013.
[12] G. Kucinskis, G. Bajars, and J. Kleperis, "Graphene in lithium ion battery cathode materials: A review," *J. Power Sources*, vol. 240, pp. 66–79, Oct. 2013.
[13] N. Kuzmanic, "Electrochemical properties of aluminium anodes for Al / air batteries with aqueous sodium chloride electrolyte," pp. 969–977, 2012.
[14]J. Xi, "Nafion / organic silica modified TiO2 composite membrane for vanadium redox flow battery via in situ sol – gel reactions," no. October 2015, pp. 2–8, 2009.

eureca 2016 – Conference Paper
Paper Number 2ME19

Design and Building Compressed Air Driven Engine

Naresh Jeyapalan[1*], Douglas Tong Kum Tien[1]

[1]*School of Engineering, Taylor's University Malaysia*

[*]DouglasKumTien.Tong@taylors.edu.my

Abstract

Over the past decades, engines powered by fossil fuel have been a crucial issue due to the emission of gasses such as carbon monoxide and nitrogen oxide which are very harmful to human health. Consequently, engineers have been working on identifying alternative sources of energy for engines that would lead to the reduction of air pollution. One of these alternatives involves the use of compressed air. However, compressed air engines (CAE) are still in the developmental stage as the power output generated is generally low. Nonetheless, compressed air engines are a cheaper alternative besides resulting in less pollution on the road. This study is conducted to identify the most suitable method of modifying a motorcycle single cylinder internal combustion engine (ICE) into a CAE that would operate at optimum performance. Besides, this study also aims to identify whether a CAE is able to provide similar power output as an internal combustion engine of the same size. A motorcycle single cylinder ICE would be tested on a dynamometer to obtain the engine performance characteristic curve which includes the horsepower and torque while running at different revolutions per minute (RPM). The engine would then be converted into a CAE by attaching the compressed air hose to the intake pipe. The engine would be supplied with compressed air from a pressure of 7 to 10 bars for testing. At the end of the study, it is expected that an ICE has been successfully converted into a fully functioning CAE running at optimal performance. A comparison of the performance characteristics has been made for both engines in the form of graphs and mathematical calculations. Based on the experiments conducted, the CAE is not capable of producing similar performance as the ICE for the engine that has been tested. The ICE produces 15.51 hp at 9353 RPM and torque of 12.58 Nm at 8031 RPM while the maximum CAE performance is obtained when the supply compressed air pressure is at 10 bar which is 2.71 hp and 7.03 Nm. Though the CAE performance is not significant, it would be a feasible alternative for single passenger vehicles in densely populated cities as it does not emit harmful gasses that would pollute the environment and also high powered engines are not a feasible choice to be used in cities with massive traffic congestions.

Keywords: Compressed air engine, single cylinder engine, horsepower, torque, pollution reduction

1. Introduction

Emission from engines using fossil fuel as its power source has been a crucial issue in the past few decades due to the harmful gases that are emitted by the engine. These gases cause air pollution that can be harmful to human health when inhaled. Engineers and scientists have been working hard in reducing emission from engines especially vehicle engines. Policy makers all over the globe are continuously pushing for solutions for vehicles to run on alternative sources of energy rather than petroleum.

The next possible method to reduce emissions would be creating engines that are powered by compressed air. Since this is a relatively new technology, existing ICE can be modified to be a CAE. Engineers worldwide has begun work on developing CAE as it does not produce any air or noise pollution because there is no burning of fossil fuel involved. The usage of CAE would be very beneficial for single passenger vehicles used in cities where air pollution is a major crisis.

The purpose of conducting this experiment is to identify the best approach to modify an existing ICE into a CAE that will provide optimal performance. Besides, the engine has to be converted in the most cost effective method to ensure the cost of operation and maintenance is kept to a minimum.

1.1 Engine Working Mechanism

Fig. 1 shows the basic layout of a single cylinder CAE. The engine consist of an intake valve, exhaust valve, piston head, connecting rod/link, flywheel and crankshaft. The processes that take place in a CAE are intake and exhaust only. During the intake process, the intake valve will be open when the piston reaches the top dead centre (TDC) while the exhaust valve is closed. The compressed air would flow into the cylinder during this period to push the piston to the bottom dead centre (BDC) which produces the power stroke. The exhaust valve will then be opened as soon as the piston reaches the BDC while the intake valve would close. The piston moves from the BDC to the TDC to discharge the compressed air inside the cylinder. This is possible because the pressure inside the cylinder is higher than the atmospheric air pressure. The intake process starts again when the piston reaches the top dead centre [1].

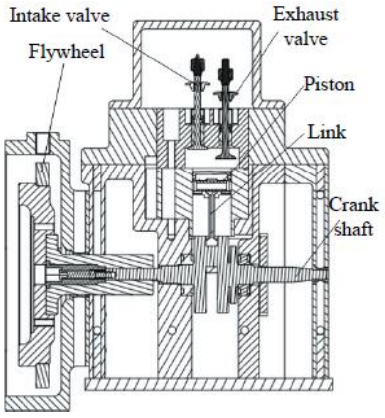


Figure 1. Basic layout of single cylinder CAE [1]

1.2. Advantages and Disadvantages of CAE

CAE are considered better than ICE because no fuel is needed. Thus it is cost efficient and do not cause any pollution. Engines which are powered by compressed air are generally powered by electricity as compressors are used to compress air and store it inside a tank. Besides, the temperature generated from CAE is relatively low compared to vehicles that are powered by ICE or electric motors. Thus, a cooling system is not needed for vehicles that are powered by CAE and this helps in reducing the cost of manufacturing the entire vehicle. Furthermore, vehicles powered by CAE take a shorter time to fill up compressed air inside the tank compared to electric vehicles which requires a few hours to recharge the batteries. The most significant advantage of CAE vehicles is its cost to run the vehicle. It is cheaper to obtain compressed air compared to petrol or charging up batteries. Every engine has its own disadvantages including the CAE. The major disadvantage of a CAE is that it uses an indirect form of energy where air needs to be compressed first before it can produce a desired output. This is because electricity is needed for a compressor to compress air and to fill up a tank. The conversion of energy that takes place will cause some losses in the form of heat and sound [2].

1.3 CAE Performance Characteristics

In a study done by Huang et al. [3], a 100cc 4 stroke single cylinder motorcycle engine produced by KYMCO was converted into a CAE and it was tested at compressed air pressure between the range of 5 to 9 bars. The engine was not tested as an internal combustion setup but based on the specification by the manufacturer; the engine produces peak power of 5.6 kW at 7500 rpm and peak torque of 7.44 Nm at 6000 rpm. The engine was modified from 4 strokes to 2 strokes using a cam mechanism which is driven by the crankshaft. This modification had caused the intake and exhaust valve lift to reduce from 5 mm to 2 mm. The reduce lift had cause a restriction of the air flow rate entering the engine and exiting the combustion chamber. In the experiment conducted by Huang, the engine produces its highest output of 0.95 kW at 9 bar and 1320 rpm. At the same pressure, the highest torque obtained is 9.99 Nm. However, this torque value was obtained when the engine is running at a speed of 465 rpm. This shows that the CAE produces less power but more torque when compared to the same engine in the internal combustion setup. The low power output of the CAE is caused by the lower engine RPM.

1.4 Camshaft and Valve Lift Timing

In a research regarding compressed air powered vehicles done by Boddapati [4], a four stroke engine was converted into a two stroke engine to be used as a CAE. The cam profile of the engine had to be modified in order for the intake and exhaust valve to open at the right timing. The valve timing of two stroke CAE engine built by Boddapati is shown on Fig. 2. For a CAE, the intake valve should be open as long as possible to allow more compressed air to enter the engine. The exhaust valve has to be open just before the piston reaches the bottom dead centre to start expelling the compressed air to enable the cycle to run continuosly. This study has shown that modifying the cam profile is a difficult task as the valve timing needs to be accurate.

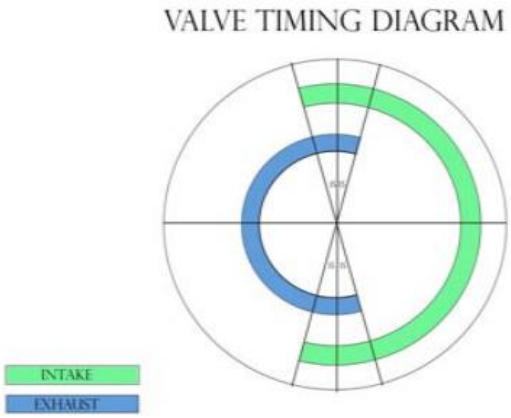


Figure 2. Valve timing of 2 stroke CAE [4]

2. Research Methodology

In this section of the paper, the method of modifying the engine and methods of testing the engine will be explained. Besides, the valve lift of the intake and exhaust valve is also discussed in this section.

2.1 Engine Technical Specification

The engine being used in this experiment is a Lifan 110cc 4 stroke engine. This engine is initially a standard ICE and was later converted to be a CAE. The engine specifications are shown on Table 1. The specifications shown is when the engine is not modified yet and still in a 4 stroke mechanism.

Table 1. Lifan 110cc engine specifications

Specification	Details
Displacement (cc)	107
Compression Ratio	9.0:1
Bore x Stroke (mm)	52.4 x 49.5
Max Power (kW/rpm)	5.2/7500
Max Torque (Nm/rpm)	6.9/5000
Idling Speed (rpm)	1500
Transmission	4 speed

2.2 Engine Conversion

Before the experiment can be conducted, the engine has to be converted from a 4 stroke to 2 stroke mechanism. This is because the compressed air has to enter and exit the combustion chamber at every cycle because no compression or combustion stage occurs in a CAE.

The modification that is done to convert the engine into a CAE is by replacing the camshaft to ensure that the engine operates in a 2 stroke mechanism. The camshaft in the engine is connected to the crankshaft by a timing chain. When the crank is undergoing rotation, the camshaft will also rotate simultaneously and the timing of the valves are maintained [5].

A 4 stroke engine has 2 cam profiles with one lobe each which controls the opening and closing of the intake and exhaust valves respectively as shown in Fig. 3. However, for a CAE to operate, both cam profiles need to have two lobes each which are symmetrical about the centre line of the camshaft. Thus, the intake valve will open when the piston travels from TDC to BDC while the exhaust valve will open when piston travels from BDC to TDC. The cam profile of the CAE with two lobes each is shown in Fig. 4.

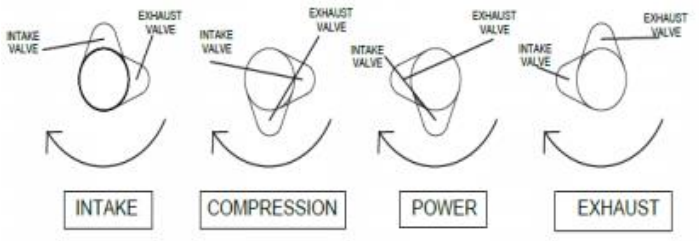


Figure 3. Cam profile of 4 stroke ICE [6]

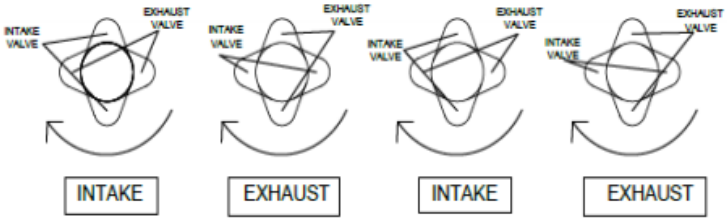


Figure 4. Cam profile of 2 stroke CAE [6]

The valve lift of the intake and exhaust of the CAE after the modifications done on the camshaft is shown on Fig. 5. Each valve will take turns to open at every 90˚ of revolution. The valve lift of the exhaust valve is made slightly higher than the intake valve to ensure that the compressed air leaves the engine as quickly as possible and also to prevent compressed air to remain in the engine just before the intake valve opens. The data used to plot the graph on Fig. 5 is obtained by measuring the cam nomenclature of the camshaft used.

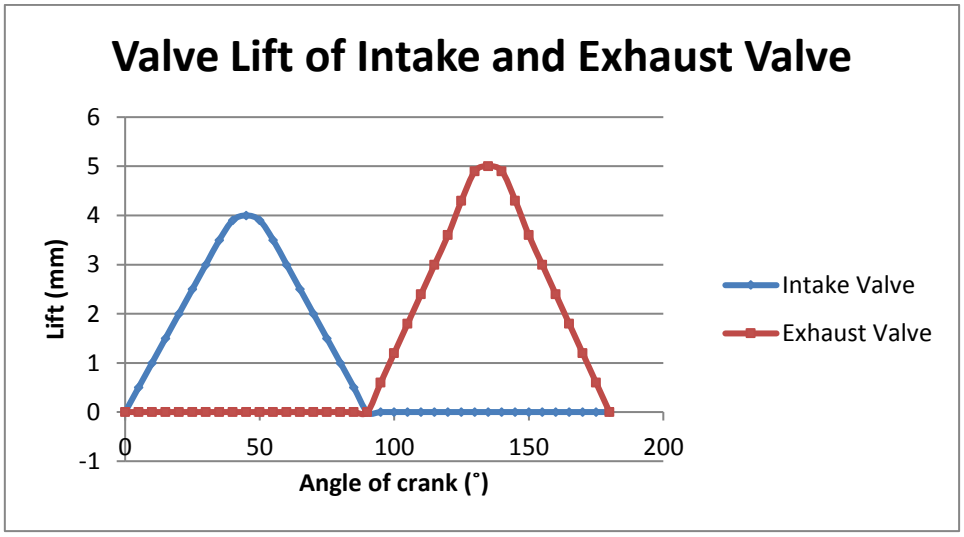


Figure 5. Graph of valve lift of intake and exhaust valve against crank angle

Once the engine had been successfully converted, it is tested by supplying compressed air through the intake pipe to identify if there are any air leaks present as shown on Fig. 6. If a leak occurs, it is mostly likely due to incorrect fitting or untightened components inside the engine. Only after no leaks were present, the engine was assembled onto a motorbike to undergo testing on a dynamometer.

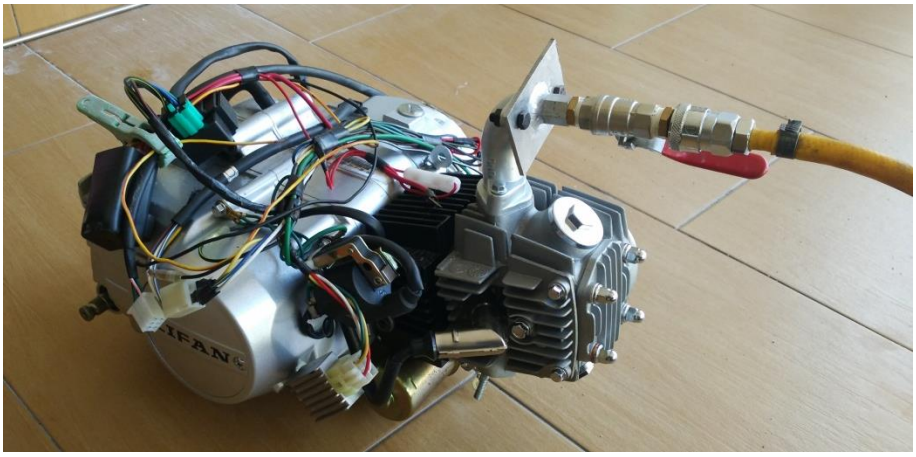


Figure 6. Testing of CAE by supplying compressed air through intake pipe

3. Results and Discussion

The modification that has been done to the engine is to covert it from 4 stroke to 2 stroke by changing to a suitable camshaft which allows a 2 stroke mechanism. The modification done allows a maximum lift of 4 mm and 5mm for the intake valve and exhaust valve respectively. The modification that has been done is shown on Fig. 7.



Figure 7. Modified camshaft for 2 stroke mechanism inside engine

After modifying the engine from 4 stroke to 2 stroke, the engine was first tested as an ICE to determine the performance figures. The engine was mounted onto a motorcycle and placed on a dynamometer to undergo testing. The motorcycle was revved from idle all the way to maximum RPM in order to get the maximum performance figures of the engine. Fig. 8 shows the dynamometer chart of the modified 2 stroke ICE engine.

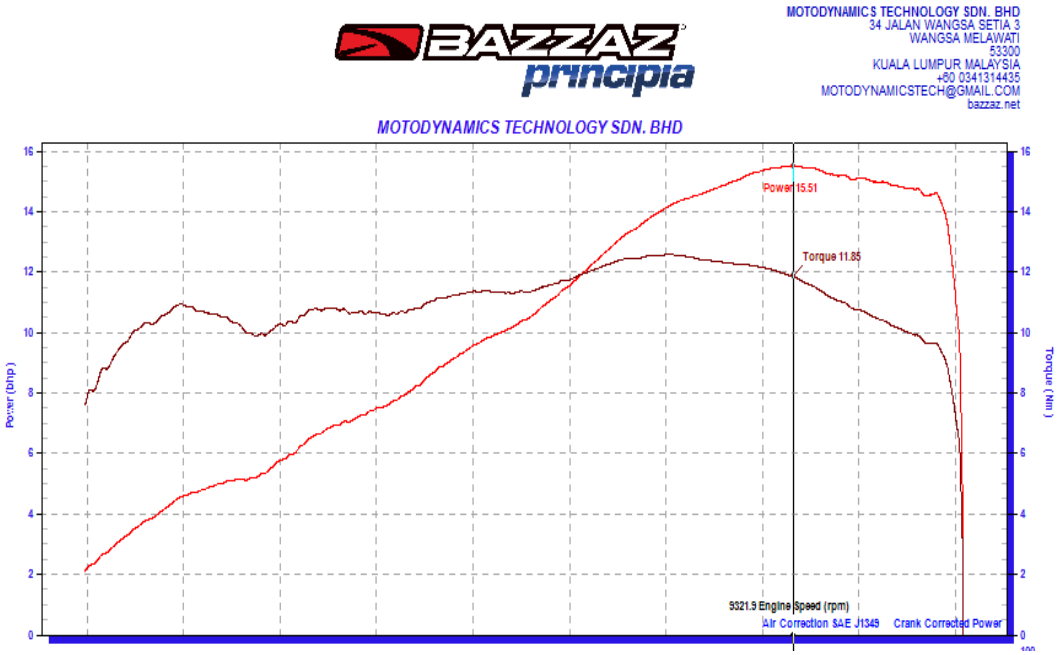


Figure 8. Performance curve of converted 2 stroke ICE engine

Based on the results shown on Fig.8, the engine shows good power delivery without any drop in performance. When the engine is tested, the ambient temperature was at 37˚C with humidity of 55%. The result shows that the maximum horsepower is 15.51 hp at 9353 RPM and maximum torque is 12.58 Nm at 8031 RPM.

The 2 stroke CAE was installed onto the motorbike but unable to undergo testing on the dynamometer. This is because the RPM of the CAE is very low and unable to provide sufficient amount of torque to move the rollers on the dynamometer. Thus the CAE was tested using a torque meter to obtain the torque values and a tachometer was used to measure the RPM. The torque meter and tachometer was placed on the crankshaft to determine the values. The horsepower of the engine is calculated based on the formula shown on Eq. (1) and Eq. (2). The overall performance of the CAE tested between the pressure ranges of 7-10 bar is shown on Table 2.

$$\omega = \frac{2\times\pi\times RPM}{60} \quad (1)$$

$$P = \tau\omega \quad (2)$$

Table 2. CAE performance figures

Pressure (bar)	RPM	Torque (Nm)	Horsepower (hp)
7	935	3.12	0.41
8	1389	4.33	0.84
9	2038	5.39	1.54
10	2746	7.03	2.71

When taking readings for the torque value, the engine is first allowed to stabilize for a few seconds to prevent any fluctuations in the readings. The results show that RPM increases when compressed air pressure increases. Higher RPM leads to higher engine torque and this eventually leads to higher horsepower. The experiment proves that the performance of CAE can be improved if the engine is provided with higher compressed air pressure. However, the CAE in this experiment is not capable to produce similar performance as ICE due to pressure limitations.

4. Conclusion

To conclude, the Lifan 110cc ICE was successfully modified into a CAE by converting it from a 4 stroke engine into a 2 stroke engine. By using the engine as a CAE, there is no start up power required to run the engine. Thus, no batteries are needed and it makes it even cheaper to run a CAE compared to an ICE. Besides, CAE do not emit any harmful exhaust fumes to the environment as no fuel is combusted during the operation. The utilization of CAE for single passenger vehicles in densely populated cities would greatly reduce air pollution and this would set a new milestone in green technology.

From the experiments conducted, it clearly shows that the performance of CAE is lower than ICE due to several factors. The main factor would be the limitation of the compressor which is only capable of supplying pressure output of 10 bar. The highest torque and horsepower obtained was when the CAE was tested with compressed air pressure of 10 bar. The results that were obtained are 2.71 hp and 7.03 Nm for horsepower and torque respectively.

References

[1] Q. Yu, M. Cai, Y. Shi, and Z. Fan, “Optimization of the Energy Efficiency of a Piston Compressed Air Engine,” *Strojniški Vestn. – J. Mech. Eng.*, vol. 60, no. 6, pp. 395–406, 2014.

[2] A. Mourya, A. Khan, D. Bajpayee, and N. Gupta, “Modified Compressed Air Engine Two stroke engine working on the design of a four stroke petrol engine,” no. 4, pp. 58–60, 2014.

[3] C. Y. Huang, C. K. Hu, C. J. Yu, and C. K. Sung, “Experimental investigation on the performance of a compressed-air driven piston engine,” *Energies*, vol. 6, no. 3, pp. 1731–1745, 2013.

[4] V. Boddapati, B. Tech, and M. Engineering, “Air Powered Vehicle -An Eco Friendly Engine,” *Int. J. IT, Eng. Appl. Sci. Res.*, vol. 4, no. 1, pp. 29–33, 2015.

[5] M. Minajagi, A. Swapnil, M. Kailas, S. Sushilkumar, and P. Tejesh, “Compressed Air Driven Vehicle,” vol. 3, no. 06, pp. 42–45, 2015.

[6] N. Parashar, S. M. Ali, S. Chauhan, and R. Saini, “Design and Analysis of Compressed Air Engine,” vol. 3, no. 6, pp. 693–696, 2014.

eureca 2016 – Conference Paper
Paper Number 2ME20

Design of a Small Scale High Torque Stirling Engine

Ng Yi Ming*, Lim Chin Hong

School of Engineering, Taylor's University, Malaysia

**yiming.taylors@gmail.com*

Abstract
Stirling engines have great potential to replace non-renewable energy sources. They are external combustion engines that mainly depend on the expansion and contraction of working fluids by the displacer piston. However, one of the problems of these engines is the relatively high heat flux from the hot-section of the displacer cylinder to the cold-section of the cylinder resulting in lower temperature difference which is undesired. This work presents the development and optimization of a Gamma-type Stirling engine where the focus of optimization is on the heat flux within the displacer cylinder in which a synthetic fluoropolymer of tetrafluoroethylene called polytetrafluoroethylene (Teflon) is implemented together with the base material of the cylinder, aluminium 6061-T6. After property and manufacturing consideration, Teflon was chosen as the heat insulator to separate the hot and cold-sections. Aluminium tubings, displacer piston and flanges will be manufactured using the computer numerical control (CNC) machine whereas the Teflon heat insulator will be manufactured by a third party source. The Teflon heat insulator portion and the aluminium portions are combined using flanges where each end of the materials are welded to the flanges and then the flanges are secured by using bolts and nuts. The expected outcome of this work is a 5-10% increase in power output of the engine which can be calculated by gathering data on revolutions per minute (RPM) of the shaft using a digital tachometer. A torque meter is used as well to measure the torque output of the shaft. By having these two values, the power output can be calculated. The experimental results obtained are then compared to theoretical values.
Keywords: Stirling engine, Heat flux, Heat insulator, Regenerator, Polytetrafluoroethylene

1. Introduction

Stirling engines were most commonly known as an economizer in the year 1816 by Robert Stirling who was the minister of the Church of Scotland . His device (economizer) was in a form of an inverted beam engine which also incorporates the phase shift difference between the power piston and displacer cylinder that is widely seen in all Stirling engines today . The economizer was only coined nearly a hundred

years later by a Dutch engineer named Rolf Meijer [1]. The special characteristic of the Stirling engine is that it is an external combustion engine and the efficiency closely approximates the theoretical maximum Carnot efficiency which is actually very high for such an engine . They are powered by the expansion and contraction of the fixed amount of gas used in the cylinder . Which in turn , leads to a cyclic process which generates power at the end . There are essentially three types of Stirling engines in which the sole difference between them is the arrangements of the components such as the pistons, cylinders and displacers. The three types are the Alpha , Beta and Gamma types. The Alpha type has two separate pistons in separate cylinders in which one is hot and the other is cold. Because it has two power pistons running , the power-to-volume ratio is very high . Also , because the hot cylinder can go up to very high temperatures , the durability of the seals are an issue. Therefore, Alpha stirling engines are mechanically more difficult than the rest [2]. The Beta type stirling engine has only one power piston arranged within the same cylinder as the displacer . When the working fluid is on the hot side , it expands and pushes the piston up and when it is on the cold side , it contracts and pulls the piston down . The Beta type avoids the problems of the hot moving seals. The Gamma type stirling engine is similar to the Beta type but the only difference is that the power piston is connected in a separate cylinder alongside the displacer cylinder, in which both of the displacer and power piston is connected to the same flywheel [2].

Stirling engines are gradually becoming more and more popular among academicians and engineers because of their complex yet simplicity of the design and the results that it produces. The Stirling engine can be powered by various working fluids that is thinner than air such as hydrogen and helium as an example, low fuel consumption, high efficiency as discussed before, clean combustion, low noise production and more. Due to the flexibility of fuel that can be used, the system can be run with ease using diesel, natural gases or even wood because the displacer cylinder only requires heat to startup the system. Different heat sources have different rates of heat transfer inputs therefore it is very flexible. Also, the life span of Stirling engines are relatively longer because the number of moving parts and components of the engine are far less as compared to internal combustion engines. The main reason why it was not very popular before this is because of the rapid development and applications of internal combustion engines. Internal combustion engines do offer way better power-to-weight ratio and they have quick response time as compared to stirling engines but the features of the stirling engine however, are more positively inclined compared to internal combustion engines and that is why this study is conducted to increase the power output of stirling engines so that it is more widely commercialized.

Chen et al [5] had fabricated a Stirling engine which incorporates a moving regenerator and has found that the engine shaft torque and power had increased by 2.3 – 2.5 folds . Chen has also found that by increasing the radius of the diplacer , hence reducing the gap between the displacer and the cylinder , the narrower gap will direct more working fluid to flow into the regenerator for heat exchange therefore increasing the regenerator effectiveness . The thermal conductivity of the aluminium 6061-T6 was found to be 167 W/mK [6] . The selection of material for the finned heat sink is quite simple , the thermal conductivity of the selected material must be higher than that of aluminium 6061-T6 in order for more heat flux through the selected material . Not only that , the melting point of the material must also be relatively high to the heat source that is used which in this case is a Bunsen burner . Below shows Table 1 of the few

important properties of a few materials that need to be taken into account before selecting the right one .

In this paper, a small scale high torque Stirling engine was built and tested and improvements to the engine would be done once the pre-testing is carried out. Improvements to the engine was pre-considered whilst building the engine and examples are using polytetrafluoroethylene (Teflon) as a separator between the hot-section and cold-section of the displacer cylinder to drastically reduce the heat flux from the hot to the cold-section. Also, this work implements a moving regenerator in the displacer piston where meshed copper wires are fitted in a perpendicular manner parallel to the streamline flow of the working fluid into the hollow displacer piston to act as a moving regenerator.

2. Theoretical Framework

2.1. Heat Transfer in Displacer Cylinder

Heat transfer rate through conduction in any given regular cylindrical shape can be given as :

$$Q_{conduction} = -Ak\frac{dT}{dr} \quad (1)$$

Where
Q_{dot} = Rate of heat transfer
A = Surface area exposed
k = Thermal conductivity of material
dT = Change in temperature ($T_2 - T_1$)
dr = Thickness of cylinder wall ($r_2 - r_1$)

Based on the formula above Eq. (1) suggested above, we can observe from simple proportions that if a low heat transfer rate is desired , the variables which needs to be minimized are the surface area exposed (A) , thermal conductivity of material (k) and the change in temperature (dT) whereas the variables which needs to be maximized is the thickness of the cylinder wall (dr) . However , the variables cannot be changed simply as such because the design parameters must also be adhered to . For example , we cannot have a very exponentially large cylinder wall thickness because that would be absurd to the design . Therefore , all variables needs to meet the design parameters to formulate the optimum heat transfer rate which also satisfies the parameters in the design which was set .

The basic theoretical diagram of thermal resistance is similar to that of electrical resistance . In electrical applications, V represents voltage, I represents current and R represents resistance. In thermal applications, T represents temperature, Q represents heat energy and k represents thermal conductivity. Both of these applications are similar in terms that the temperature is the voltage running through the supposed circuit, (in this case are materials for thermal applications) heat energy supplied is also the current supplied and lastly thermal conductivity, k is also the resistance. Based on the three main heat transfer methods, two methods are most common in the application of Stirling engines; conduction and convection. Comparing the two ways of heat transfer, conduction has a way higher heat transfer rate than convection . As a brief schematic, since the material of this project's Stirling engine is aluminium 6061-T6 , we will use

this material as our thermal conductivity factor for conduction heat transfer and also we are using air as another thermal conductivity factor for convection heat transfer. If we expose the model under heat, and taking 100% heat energy as the initial heat energy, below in Figure 1 shows the basic schematic for heat flux between aluminium and air.

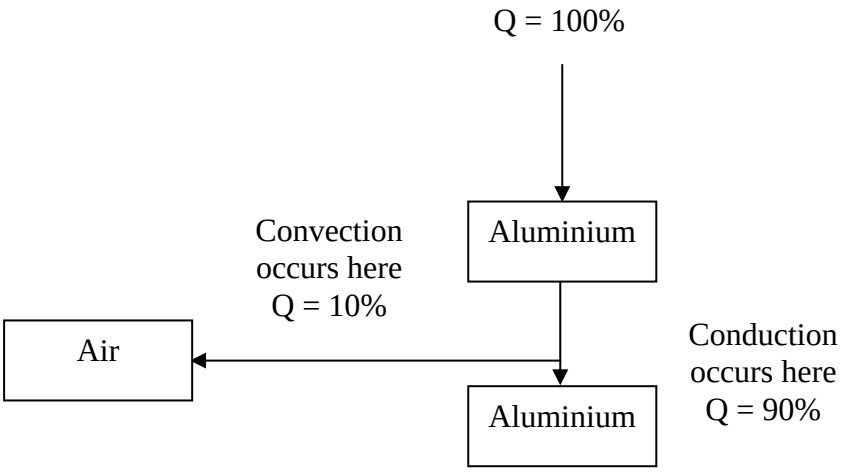


Figure 1 : Diagram of heat flux for conduction and convection.

From the Figure 1 above, we can observe that conduction heat transfer is the highest heat transfer rate. Therefore, assuming that the current input is constant, the equation that will govern the relationship between the voltage and the resistance is as shown below.

$$V = I \, . R \tag{2}$$

From the equation above Eq. (2), since assumed that the current input is constant , the voltage is then directly proportional to the resistance. Hence, it is concluded that by increasing the resistance or in this case thermal conductivity , the temperature would in fact increase because temperature difference ($T_2 – T_1$) is similar to the potential difference ($V_2 – V_1$). So, this drawback of large heat transfer rate from the hot-section to the cold-section of the displacer cylinder can be reduced by implementing two methods simultaneously into the design of the displacer cylinder and flange . Previously, the cold-section of the displacer cylinder was dependant on air and water as cooling agents or coolants and the hot side was dependant on a Bunsen burner from the laboratory as a heat source . The author suggests that the displacer cylinder can be sectioned into two parts within its length. One section will be insulated with proper and high performance heat insulators and the other section will be a finned heat sink installed so that most of the heat provided by the Bunsen burner will be transferred to the heat sink instead of flowing too much towards the cold side of the displacer cylinder which is undesired. As an example, by placing a high-performance thermal grade heat insulator between the cold side of the displacer cylinder and the hot side, heat transfer from the hot side to the cold side can be minimized drastically . This can be achieved by using microporous anorthite-based lightweight refractory which was fabricated by using aluminosilicates and calcium-based substances as raw materials and by carrying out the slip casting process which was done by Primachenko et al [3]. They successfully fabricated a microporous anorthite which yielded an ultra-low thermal conductivity of 0.25 W/mK at 650°C . For a heat insulator to withstand 650°C would

impact the Stirling engine by a big factor because this would minimize heat transfer from the cold side to the hot side drastically .

Priogov et al [4] also prepared a microporous anorthite ceramic with a thermal conductivity of 0.14 W/mK but can only withstand a temperature of 400°C by carrying out direct foaming process . Depending on the working condition of the Stirling engine , different ceramic material can be used as a heat insulator with the expense of cost structure . Other heat insulators can also be introduced but depending on individual goals. For this work, the author is implementing a high-grade polytetrafluoroethylene (Teflon).

2.2. Regenerator

A regenerator is an integral part of most Stirling engines . A regenerator primarily has two main functions which are to separate the hot-section and the cold-section of the displacer cylinder , as well as to preheat and precool the working fluid used in a Stirling engine . The working mechanism of a regenerator is the material itself . When the working fluid gets heated up in the hot-section , as it travels to the cold-section , the regenerator will ‘absorb’ some of the heat from the working fluid so that as the working fluid reaches the cold-section of the cylinder , the amount of work needed to cool down the working fluid is lesser . Vice versa when the working fluid from the cold-section is travelling towards the hot-section , as it travels , the regenerator will preheat the working fluid using the heat that was ‘absorbed’ from the hot-section . This in turn can promote the rate of expansion and contraction of the working fluid in a Stirling engine .

Table 1 : Comparison between Silver and Copper for material selection.

Properties/Materials	Silver (Ag)	Copper (Cu)
Thermal Conductivity	419 W/mK	385 W/mK
Melting Point	961.93 °C	1083.2 - 1083.6 °C
Density	10.491 g/cc	7.764 g/cc

Based on the table above, it shows that silver has a higher thermal conductivity as compared to copper but copper has a higher melting point than silver, making it able to withstand higher temperatures in case the heat source is exchanged to a higher performance heat source which provides higher temperatures at faster rates. The density of copper is lower than that of aluminium, therefore when copper is used as a heat sink , there is lesser force acting upon the displacer cylinder. However, silver is not easily obtainable and is very expensive compared to copper which is way cheaper and easily obtainable. Since budget is also a factor of selection, copper is the most suitable on top of silver hence copper will be used as the material for the regenerator. Yoshitaka et al [7] also have done a study on regenerators in low temperature differential (LTD) Stirling engines and found that the regenerator efficiency of the material mesh used which was layered in parallel to the direction of the working fluid’s travel path was

significantly lower than if the meshes were layered in normal. Timoumi et al [8] has also fabricated a Stirling engine and optimized the performance of the engine. He found that the reduction of matrix porosity and the increase in the conductivity of the regenerator material will yield an increase in the performance of the Stirling engine.

3. Methodology Framework

3.1. Design Parameters of Stirling Engine

Using a CAD (Computer Aided Designing) software called SpaceClaim, the author was able to design the Stirling engine in its entirety. All main components of the Stirling engine are present which are the displacer cylinder, power cylinder, displacer piston and power piston. The schematic diagram of the Stirling engine prototype is shown in **Figure 2** and its main components are labelled as shown**.** The engine's main design parameters are listed in **Table 2**. This Stirling engine is a double-acting Gamma configuration in which there is one power piston and one displacer piston. The term double-acting configuration defines that the engine utilizes movement from both the displacer piston and power piston to transfer working fluids from one end to the other. Also, a simple slider-crank mechanism is implemented because of its ease of manufacture and high reliability as well as to minimize the number of moving parts of the engine. As we know, the more the moving parts, the more the friction present in the engine.

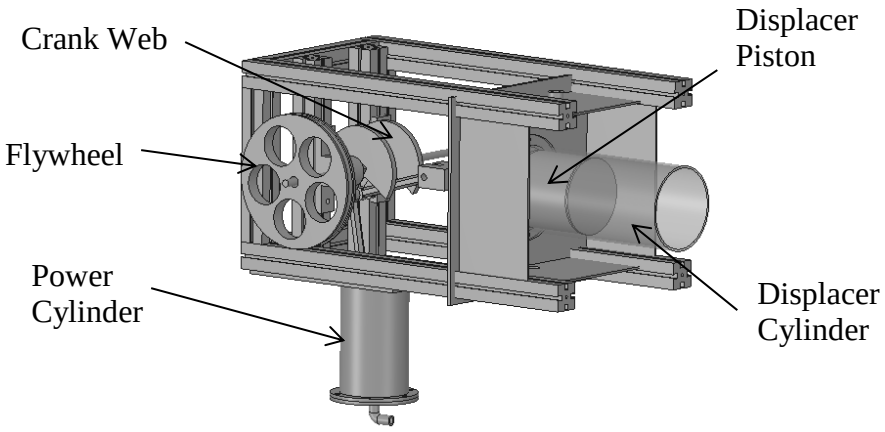


Figure 2 : Full 3D model designed from scratch using SpaceClaim.

The power piston which is placed inside the power cylinder is a power piston from a car engine with a bore of 86mm and with a stroke of 75mm. Two piston rings were also fitted to the power piston so as to ensure efficient air sealing which in turn leads to higher power output of the engine. The power cylinder itself has an internal diameter of 89mm. The power piston only has a linear motion and as it moves up and down within the cylinder, it converts the motion into rotary motion of the flywheel which is also connected to the crankshaft and this in turn would produce an output from the system. This output can be calculated in various ways, in this case being, using a digital tachometer to measure the flywheel's revolutions per minute (RPM) as well as using a torque meter to gather data on the engine's torque output. Having these two values, then power output can then be calculated using the power equation governing these two values which are shown below in Eq. (3) :

$$P = T\omega \quad (3)$$

Where T = Torque output (Nm)
ω = Radian/second (rad/s)

The displacer piston and displacer cylinder were manufactured according to the dimensions of 3.175mm and 6.350mm respectively and both are the same material which is aluminium 6061-T6. The displacer piston serves as a linearly moving piston that transfers working fluids from the hot-section to the cold-section and vice versa so the displacer piston is manufactured in a way that there is a 3mm clearance between the inner walls of the displacer cylinder and the displacer piston. The bore and stroke of the displacer piston is 114.3mm and 110mm respectively, in which the swept volume can be calculated to yield a value of 1129cc and therefore the ratio of swept volume of the displacer piston to the power piston can be approximate at 2.60.

The engine's crankshaft on the other hand is manufactured by using a linear steel shaft, a normal screw which acts as the engine's crank pin and two crank webs which are directly and linearly supported by two pillow block bearings which also allow smooth rotation within the bearing. The crank webs are designed as a semicircle shape with a small protruding middle part in such way that a 90° phase difference between the displacer piston and power piston is ensured. The pillow block bearings are very crucial so as to ensure a straight connection between the crank webs and also it reduces vibrations due to the imbalances during rotation. The crank pin on the other hand is connected both to the displacer piston and power piston's connecting rod by using male rod ends ball bearing which is very high precision ball bearings where the inner rings are made with copper alloy holders that allows very smooth and self-aligning movements during rotation. As for the connecting rods, they are made from aluminium and it is a solid shaft with a hexagonal nature and each connecting rod is connected to the displacer piston and power piston with a phase angle difference of 90°. Besides that, a flywheel was also implemented in the Stirling engine design because it is also a crucial mechanical component in the Stirling engine which is attached to one end of either crankshaft. Flywheels are implemented to deliver continuous momentum and energy due to the moment of inertia and therefore maintaining the rotational movement of the engine.



Figure 3 : CNC 3-Axis Milling Machine by HAAS used for project.

Table 2 : Stirling engine's main design parameters.

Engine Parameter	Dimensions
Configuration	Gamma-type, Double-acting
Power Piston (Bore x Stroke)	86 x 75 mm
Piston Swept Volume	465.5 cc
Displacer Piston (Bore x Stroke)	114.3 x 110 mm
Displacer Piston Swept Volume	1129 cc
Swept Volume Ratio	2.60

The displacer piston is designed in such a way that the targeted swept volume ratio for this engine is around 2. In which, the swept volume is effectively the displacer swept volume divided by the piston swept volume given by the equation Eq. (3) below.

$$V_{s,ratio} = \frac{V_{s,displacer}}{V_{s,piston}} \tag{3}$$

$$2.1 = \frac{V_{s,displacer}}{435.7}$$

$$V_{s,displacer} = 914.9cm^3$$

Therefore, the displacer piston is designed so that the swept volume should achieve a value of approximately 915cm³ - 920cm³ with a tolerance of 5cm³ in the design. The stroke of an engine is also known as the distance between the top dead center (TDC) and the bottom dead center (BDC). Stroke of an engine is an important factor in the design of engines because it directly correlates to the swept volume of an engine which in turn affects the power output. Eq. (4) below shows the equation to calculate the swept volume of the power piston.

An aluminium tube available in the university laboratory has an outer diameter of 114mm. Since the swept volume formula can be given by Eq. (4), by substituting the $V_{s,displacer}$ of 914.9cm³ with the diameter of the tube which is 11.4cm, the stroke, L of the displacer piston can be calculated to be 9cm.

$$V_s = A_c . L \tag{4}$$

Where V_s = Cylinder swept volume
A_c = Cylinder area
L = Length of stroke (TDC to BDC)

$$V_s = A_c . L$$

$$914.9cm^3 = \frac{\pi}{4}(11.4cm)^2 . (L)$$

$$Stroke, L = 9cm$$

Now that the stroke of the displacer is obtained, the cylinder can be manufactured accordingly whereby the 3mm gap clearance between the displacer piston and the displacer cylinder is ensured. Shown below is the CAD design of the displacer portion, in which the displacer cylinder is a modified cylinder where the Teflon material is implemented together in the design.

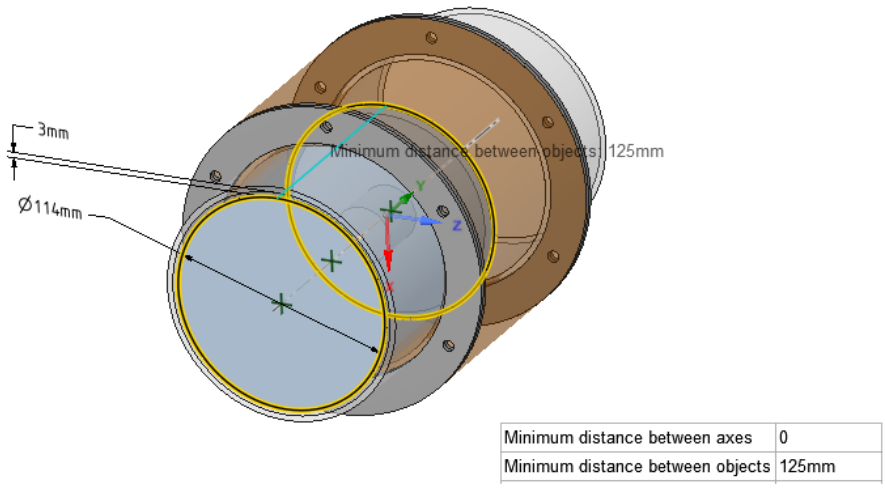


Figure 4 : Relevant dimensions on SpaceClaim.

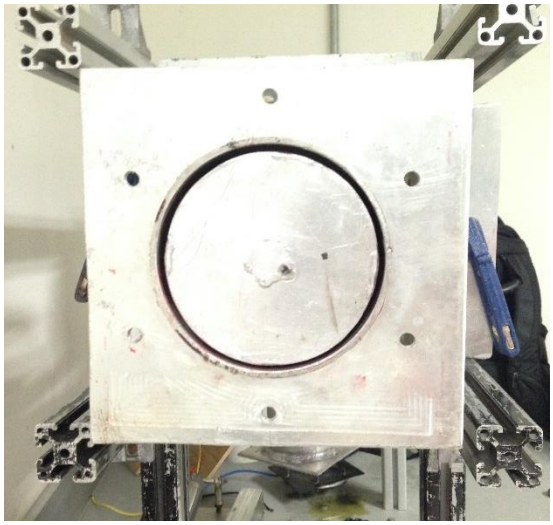


Figure 5 : Finished product of displacer piston and cylinder with 3mm gap clearance all round.

The manufacturing process of the displacer piston was begun by cutting the available aluminium tube in the laboratory to a length of 120mm using an automated hacksaw machine. After the cutting process, the author used a lathe machine to trim the front and rear ends of the tube to ensure that it is perpendicular to the ground up. Then, aluminium sheets of thickness 2.5mm were also available in the laboratory and was brought for plasma cutting using the manufacturing workshop's plasma cutter equipment as shown in **Figure 6**. The two cut aluminium sheets were of diameter 114mm to cover the cylinder on both sides and was brought to third party welding services to assist in the welding jobs. The displacer piston serves as a linearly moving piston that transfers working fluids from the hot-section to the cold-section and vice versa so the displacer piston is manufactured in a way that there is a 3mm clearance between the inner walls of the displacer cylinder and the displacer piston. The bore and stroke of the displacer piston is 114mm and 90mm respectively, in which the swept volume can be calculated to yield a value of 918.63cc and therefore the ratio of swept volume of the displacer piston to the power piston can be approximate at 2.10.



Figure 6 : Shiyo CUT70 DC Inverter and Plasma Cutter equipment.

3.2. Pre-Testing Preparation

Before conducting the actual testing of the fully built Stirling engine, preparations for the engine need to be carried out in order to avoid unnecessary troubles or unwanted random situations arising during the operation of the engine. Therefore, engine oil was sprayed into the power cylinder and power piston to reduce friction as well as grease was used to lubricate every moving component of the engine for example the crank webs, connecting joint, linear bearing and more. Thermocouples are used to measure the heat on the wall of the displacer cylinder in which one is placed on the hot-section and the other is placed on the cold-section. Digital tachometer with an accuracy of ±0.1 RPM was used to measure the revolutions per minute of the engine by detecting the rotational movement of the flywheel. Two Bunsen burners are placed beside the displacer cylinder's hot-section to provide heat energy to the engine.



Figure 7 : Experimental setup using thermocouples.

4. Results and Discussion

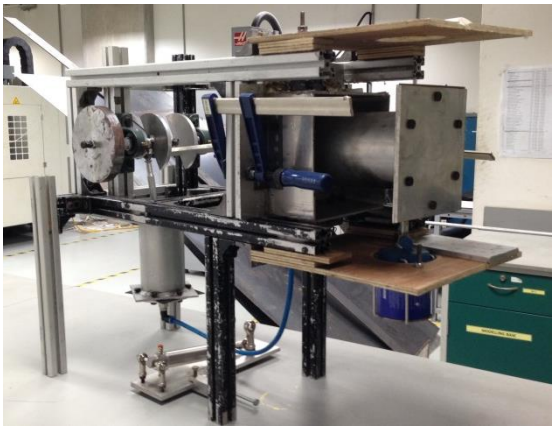


Figure 8 : Fully constructed Gamma Stirling engine.

During the actual testing of the Stirling engine prototype, the hot-section of the displacer cylinder was heated using two Bunsen burners placed on opposite sides and the temperature recorded was at 165°C. Then, an initial force was applied to the flywheel to provide a momentum for the engine to continue running. Unfortunately, the

Stirling engine prototype built had failed to perform continuous reciprocating movements. The failure of this engine prototype might be due to several factors affecting the engine itself such as technical issues, operating problems and more. These factors were observed and recorded throughout the experimentation session.

It was observed that the temperature of the cold-section of the displacer cylinder was recorded at a temperature of 70°C which is considered very high and undesirable in the operation of a Stirling engine because the as mentioned before, Stirling engines run solely by temperature difference and if the temperature difference is not high or the temperature gradient is too low, the power output could potentially be very low or the engine would not run. In this case, the engine did not run. Also, since the heat transfer from the hot-section to the cold-section was relatively high, the increased temperature and pressure in the displacer cylinder caused downward forces on the displacer piston therefore making it difficult for the flywheel to rotate smoothly which in turn led to additional forces being required to push the displacer piston from bottom-dead-centre (BDC) to top-dead-centre (TDC). Also, it was observed that there was a flaw in the manufacturing process of the Stirling engine in which the crank webs that was self-manufactured had a diameter of 85mm whereas the displacer piston had a stroke of 75mm. In all normal engine practices, the diameter of the crank web should always be the same as the stroke of the piston so that it can perform reciprocating movements properly. Besides that, it was also detected that the air being forced out from the power cylinder by the power piston during compression from TDC to BDC was very little. This could be due to two factors which are air leakages in the engine system as well as the pressure drop in the cylinder was too high due to using a small diameter elbow pipe fitting. Due to these technical problems faced, the engine could not be tested further and therefore the manufacturing of the Teflon-aluminium displacer cylinder could not be carried on until the engine can run. This is because, to make a comparison between a fully aluminium displacer cylinder and a Teflon-aluminium displacer cylinder, the fully aluminium one should be run first so as to make it a control experiment. Only then can the next step be carried on which is to manufacture the Teflon-aluminium displacer cylinder.

However, a few improvement suggestions were made based on the few issues during the first testing of the prototype. A simple cooling system should be implemented into the design of the displacer cylinder to allow cool running water to cool down the displacer's cold-section so as to increase the temperature gradient for maximum efficiency as well as rotational movement. The crank webs should also be fixed in a way that the diameter of the crank web should be the same as the stroke of the displacer piston to ensure smooth reciprocating movement. Also, another elbow pipe fitting of bigger diameter should be used to decrease the pressure drop from the power cylinder during compression. Rubber seals should also be used in between flanges and any components which can potentially have air leakages. Lastly, a counterweight can be manufactured and placed on the engine system to balance out the total mass of the engine. This can be done by weighing all moving components of the engine which are the displacer piston, connecting rods, cranks webs, nuts and power piston.

5. Conclusions

To summarize, Stirling engines are great external combustion engines which can be powered by many sources of heat as explained, ranging from renewable to non-renewable energy. The development of Stirling engines has become more innovative and have great potential due to the worsening of the environmental issues such as climate change, global warming and also the depletion of non-renewable fossil fuels. This research aims to build and test a Gamma-type Stirling engine because they are of simplified design and are able to operate under low temperature difference which makes the design more economically viable. In conclusion, it was shown that temperature gradient is very crucial in the working principle of Stirling engines. It needs to be properly monitored to ensure that the Stirling engine is able to keep running. Also, the designing phase is an important step in this project to ensure all components fit well and is similar to its 3D model. In this experiment, it can be seen that there were a few factors contributing to the failure of the engine to be run. These factors need to be addressed to ensure that the Gamma Stirling engine can be run smoothly and continuously.

References

[1] A brief stirling engine history . 2015 . [ONLINE] Available at: http://www.kontax.co.uk/docs/history.pdf. [Accessed 01 October 2015].

[2] Stirling engine - Stirling engines into three distinct types. 2015. Stirling engine - Stirling engines into three distinct types. [ONLINE] Available at: http://stirlingshop.com/html/stirlingengines_types.html. [Accessed 01 October 2015].

[3] V.V. Primachenko, V.V. Martynenko, L.A. Dergaputskaya. (2001). Anorthite lightweight material with microporous structure. *Proceedings of UNITECR'01, vol. 1, Cancun, Mexico* . 1, p193-195.

[4] A.A. Priogov, V.P. Rakina, M.M. Mirakyan, N.V. Volkov. (1970). Anorthite insulating refractory. *Refractory*. 5 (1), p36-40.

[5] Wen-Lih Chen, King-Leung Wong, Hung-En Chen. (2014). An experimental study on the performance of the moving regenerator for a c-type twin power piston Stirling engine. *Energy Conversion and Management*. 77, p118-128.

[6] MatWeb - The Online Materials Information Resource . 2015. [ONLINE] Available at: http://matweb.com/search/DataSheet.aspx?MatGUID=1b8c06d0ca7c456694c7777d9e10be5b&ckck=1. [Accessed 02 November 2015].

[7] Yoshitaka Kato, Kazunari Baba. (2014). Empirical estimation of regenerator efficiency for a low temperature differential Stirling engine. *Renewable Energy*. 62, p285-292.

[8] Youssef Timoumi, Iskander Tlili, Sassi Ben Nasrallah. (2008). Performance optimization of Stirling engines. *Renewable Energy*. 33, p2134-2144.

The Effect of Sintering Additives on the Properties of Steatite Ceramic

Ooi Chong Kiat[1], Jeffrey Chin[2]

[1] School of Engineering, Taylor's University, 47500 Subang Jaya, Malaysia

[2] Center for Advanced Manufacturing & Material Processing, Department of Mechanical Engineering, University of Malaya, 50603 Kuala Lumpur, Malaysia

*Jeffreykongleong.chin@taylors.edu.my

Abstract

The main composition of steatite ceramic is magnesium silicate. When hydrated, magnesium silicate is known as talc. There are also other minor composition inside steatite such as clay and flux to provide enough vitreous phase during firing process. By controlling the sintering process, a high quality steatite material can be produced. In this present research work, the doping of the sintering additives is believed to enhance the properties of the steatite. The specimen was doped with 20 wt% MnO_2 and 20 wt% ZnO separately and sintered it at temperature 950ºC to 1200ºC with the heating rate of 10ºC/min. The specimen undergoes two stages sintering to keep the temperature low so that no phase changes occur. At the end of the sintering process, the doped specimen is compared with the undoped. In SEM analysis, the steatite doped with sintering additives is found to have finer grains (low porosity) at low temperature compared to undoped steatite. For XRD evaluation, the presence of clinoenstatite polymorphs is detected at low temperature which proves that the sinterability is enhanced by two-stages of sintering and sintering additives. Besides that, steatite doped with ZnO has the greatest density of 2.79 g/cm^3 at 1200ºC as well as recorded the highest elasticity (Young's modulus) for 76.72 GPa. Same trend happened at the Vickers hardness testing which doping steatite exhibited a better performance.

Keywords: Steatite, Steatite ceramics, sintering, sintering additives, two-stage sintering

1. Introduction

Generally, steatite is a group of ceramic materials which mainly consists of hydrated magnesium silicate, $H_2Mg_3(SiO_3)_4$ or $Mg_3Si_4O_{10}(OH)_2$ during unfired condition. Transparentizing will happen after sintering process. Alumina can be replaced by this steatite ceramic materials because of its relatively low cost production to meet the similar performance requirements [1]. Steatite ceramics are widely found

in electronics, electrical engineering, radio electronics and others fields due to their low power losses even in the high frequency field and the capability of high dielectric resistance whether at room or high temperatures [2].

Ceramics are non-metallic solid, inorganic and crystalline materials. Steatite is one of them and it majorly consists of magnesium silicate (when hydrated is commonly known as talc), small amounts of clay and flux such as feldspar to generate sufficient vitreous phase during the sintering process. This vitreous phase is very important to control the sintering process as well as may affect the mechanical and dielectric properties of the material [3]. However, the natural and major raw material or ingredient is magnesium silicate, $MgSiO_3$ [4].

There are mainly four processes to produce steatite ceramics which is, dry pressing, extrusion, casting and semi wet pressing. The raw materials are talc (80-90%), plastic clay (5-10%) and a flux melting agent (5-10%). The presence of clay is to build up the compatibility of the mass and its fabricability while the feldspar (melting agent) carries the development of the melting phase. Normally, the mixing materials are fired at around 1400^{o}C. The final product is formed by crystallization, fusion and dissolution during vitrification [5]. After the sintering process, around 70% crystalline $MgSiO_3$ in protoenstatite phase is gained the by product is around 30% of glass phase [6].

Sintering process always take place in the existence of a liquid phase. Therefore, when after cooling, the microstructure is composed by crystalline magnesium metasilicate grains which surrounded by a vitreous matrix. There are only three possible polymorphs for magnesium metasilicate, protoenstatite, ortoenstatite and clinoenstatite [7]. Protoenstatite is the main crystalline phase in steatite ceramics as it is thermodynamically stable at high temperature up to 985^{o}C and can be stabilized by the vitreous phase. Nevertheless, once this crystalline has not been stabilized adequately, phase change might happen to room temperature polymorph, which is clinoenstatite. This is known as martensitic transformation resulting in volume change for the crystals and leads to further cracking [8]. The expansion of 2.8% in the elementary cells volume is the consequences of protoenstatite to clinoenstatite inversion [9]. The mechanical strength will become weaker when there is inherent stressed caused by the volume change. This has been the root cause of material damage during manufacturing and service for decades [10].

There are still possible ways to improve the performance of steatite by either stabilize protoenstatite form to room temperature or reinforce the ceramics with glass matrix. According to the studies nowadays, this problem can be overcome by adding some sintering aids during sintering process to increase its densification. Some examples for the aids are boron oxide, aluminum oxide, antimony oxide or magnesium ions [11]. For recent study, dense low-loss steatite ceramics are targeted to obtain at lower sintering temperature without the necessity of very fine particles through sintering additives such as zinc oxide and manganese oxide. 20 wt% composition of sintering additives were chosen because it can show the positive outcomes based on the previous researchers [12].

2. Methodology

In preparing the steatite powder, talc, kaolin (clay) and feldspar (melting agent) were used with the ratio 1: 0.5: 0.3 using wet colloidal technique. For the dopants, ZnO powder (NANOAMOR) and MnO_2 powder (BDH) are commercially available. Steatite powders are prepared in 40g to mix with different dopants that amounts 20wt%. After all, the powder and dopants were mixed with 150ml of ethanol and ball milled for 60 minutes.

The wet slurry were dried, crushed and sieved into powder form again. After that, it will be pressed uniaxially at 2.5 to 3.0 MPa into a circular disc with diameter 20mm and rectangular bars with dimensions 4x13x32mm. Next, it will be cold pressed isostatically at 200 MPa. The compacted green samples are now ready to be sintered at temperature 950-1200^{o}C. The ramp rate is 10^{o}C/min and it is two stage sintering before cooling down to room temperature.

Some measurements and calculations are carried out after the sintering process to determine the performance of the of the steatite materials, including Scanning Electron Microscope (SEM), X-ray Diffractometer (phase stability studies), Water immersion technique (bulk density), Resonant frequency method (Young's modulus) and Vickers Hardness Tester (hardness).

2.1 Materials Preparation

Table 1. Ratio and chemical composition of starting powders (based on 1g of powder)

	Ratio	Chemical Composition							
		SiO_2	Al_2O_3	K_2O	Na_2O	CaO	Fe_2O_3	MgO	TiO_2
Talc	1	32.6	0.1	0.03	0.1	0.88	0.33	38.4	0.03
Kaolin	0.5	46.6	37.8	1.43	0.1	0.05	0.82	0.1	0.16
Feldspar	0.3	65.5	18.5	11	3.5	0.5	0.08	0.03	0.01

Table 2. Steatite body composition

	Dopant (g)	Steatite (g)	Talc	Kaolin	Feldspar
Undoped	0	40	22.2	11.1	6.7
20 wt% ZnO	8	32	17.8	8.9	5.3
20 wt% MnO_2	8	32	17.8	8.9	5.3

Zinc oxide and manganese dioxide were doped with steatite as sintering additives with 20 wt% concentration to produce different batches of powder besides the undoped one.

Before that, the steatite powder were poured into a container that consists of 150ml of ethanol and undergoing ultrasonic pulses at 28-34 kHz for 6 minutes. After that, powder together with the dopants experience ultrasonic again around 20minutes to improve the dispersion and homogeneity of dopant in the powder.

The mixture is then poured into high density polyethylene (HPDE) bottles and ball milled. After that, the solutions were sieved and dried at 60^{o}C for 24 hours to allow ethanol to evaporate. Now the steatite powder is ready to pressed uniaxial 250-300 kPa into discs and rectangular bars by using hardened steel mould and die set to form a green body sample.

2.2 Sintering Process

The green body is heated in a sintering furnace below its melting point temperature so that consolidation can happen. Surface area of the sample will decrease but the compact strength will increase. When the time of high-temperature sintering is longer, the numbers of pores inside the sample is expected to reduce that brings high the densification.

For this research, two stages sintering was applied to improve the sintering performance so that more quality final product can be obtained. Conventional pressureless sintering method was applied using standard rapid heating furnace at six different temperatures. The ramp rate is 10^{o}C/min. The sintering profile is shown and the sintered samples are labelled below.

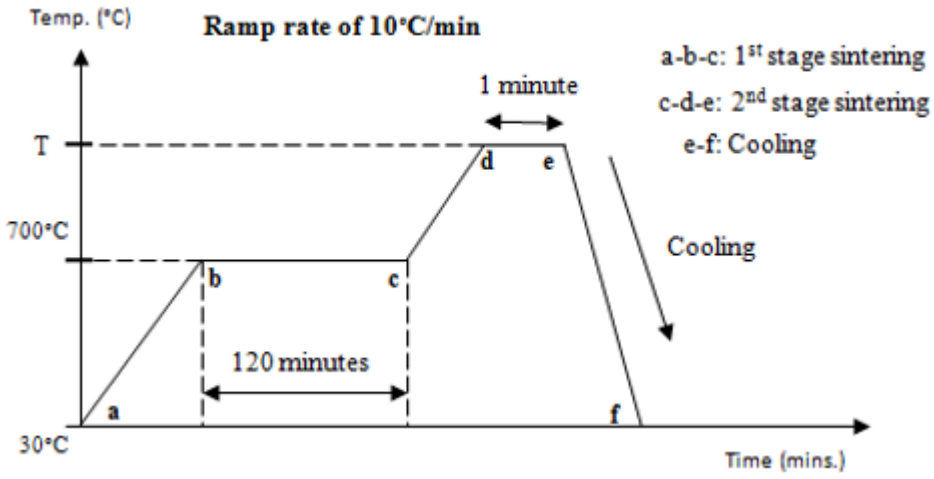


Figure 1. Sintering profile of the samples

Table 3. Samples identifications

Temperature (°C)	Undoped	20 wt% ZnO	20 wt% MnO_2
950	A1	B1	C1
1000	A2	B2	C2
1050	A3	B3	C3
1100	A4	B4	C4
1150	A5	B5	C5
1200	A6	B6	C6

2.3 Grinding and Polishing

In order to measure the density, the sintered sample have to be grounded and polished on one of the surface. Besides that, other measurements such as phase analysis, Vickers hardness testing and microstructural evaluation will be carried out to analysis the samples' performance. The surface were grinded and polished by Imtech Grinder Polisher. 600, 800 and 1200 grits were used to ground the samples before polishing it using diamond paste.

2.4 Measurements and Calculations

2.4.1 Microstructural Examination

By using scanning electron microscope (SEM), the microstructural of the steatite ceramics can be evaluated. The SEM works by focusing on the small spot of electrons and scan it using electrostatic force. The electrons emerging were then collected by an electron detector and the image will be showed on a monitor as a series of lines.

2.4.2 X-Ray Diffraction

XRD is used to identify and determine the various types of crystalline phase found in the samples. The samples were determined at room temperature with radiation source Cu-Kα ($\lambda = 0.15406$ nm) and step scan of 6°/min and 0.02° respectively, at 35 kV and 15 mA.

2.4.3 Density Measurements

Water immersion technique was used to measure the density. Based on the density table of water, the distilled water temperature was recorded to measure the density of distilled water. After that, the dry sample is weighed and recorded before

immersing it into the distilled water. The electronic balance will be calibrated to zero. Once the reading is balance, the value will be recorded. The weight of the wet sample is definitely higher as the water is penetrating the pores in the sample. Next, the sample was took out from the distilled water and the excess water is wiped out from the sample. The third reading will be taken as the weight of fluid-saturated sample. The steps above are repeated for all the samples.

$$\rho = \left(\frac{W_a}{W_{sat-W_w}}\right)\rho_w \qquad (1)$$

Where

w_a = Weight of dry sample (g)

w_{sat} = Weight of fluid-saturated sample in air (g)

w_w = Weight of sample in water (g)

ρ_w = Density of water (Refer to Appendix A for density values that vary with temperature)

2.4.4 Young's Modulus Determination

The Young's modulus or modulus of elasticity (E) is calculated as follow:

$$E = 0.9465\left(\frac{mF^2}{b}\right)\left(\frac{L}{t}\right)^3 T \qquad (2)$$

Where

E = Young's modulus (Pa)

m = Mass of bar (g)

F = Fundamental resonant frequency of the bar in flexural (Hz)

b = Width of bar (mm)

L = Length of bar (mm)

t = Thickness of bar (mm)

$$T = 1 + 6.585(1 + 0.0752\mu + 0.8109\mu^2)\left(\frac{t}{L}\right)^2 - 0.868\left(\frac{t}{L}\right)^4 - \frac{8.34(1 + 0.2023\mu + 2.173\mu^2)\left(\frac{t}{L}\right)^4}{1 + 6.338(1 + 0.1408\mu + 1.536\mu^2)\left(\frac{t}{L}\right)^2}$$

Where,

μ = Poisson's ratio taken as 0.23 for steatite body

2.4.5 Vickers Hardness Determination

This test is important to measure the hardness of the specimen by putting the loads slowly without impact to make an impression. The load is a pyramidal diamond that has 136^{o} tip with 2kg applied force. The scar were then observed to measure the diagonal length.

3. Results and Discussion

The sample is analyzed with Scanning Electron Microscope (SEM) to determine the porosity of steatite. The result showed that the steatite sintered at high temperature has less porosity compared to the one sintered at low temperature. On the other hand, the steatite doped with sintering additives is observed to contain finer grains even at low sintering temperature. It is because the dopants started to melt and provided a liquid phase to enhance the grain boundary mobility at low temperature so that sintering process is accelerated.

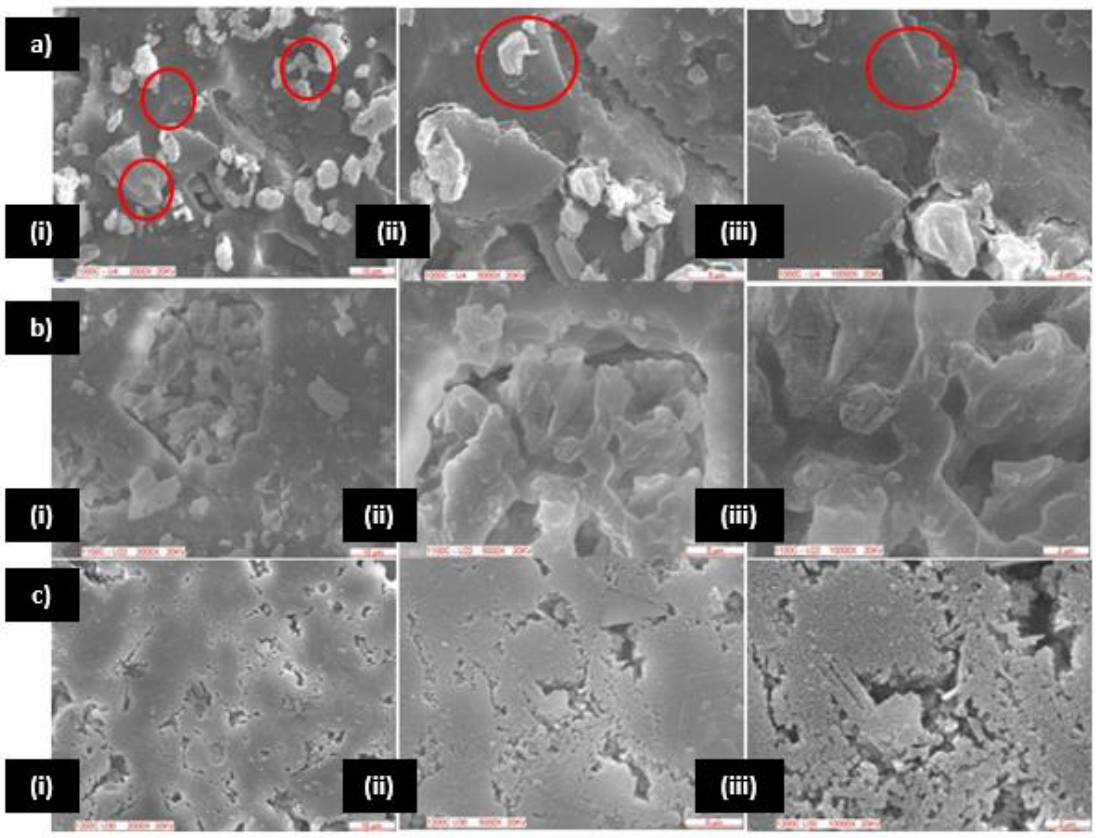


Figure 2. SEM image for microstructure of undoped steatite sintered at:
a) 1000°C – (i) Image at magnification of 2000X, (ii) Image at magnification of 5000X, and (iii) Image at magnification of 10000X
b) 1100°C – (i) Image at magnification of 2000X, (ii) Image at magnification of 5000X, and (iii) Image at magnification of 10000X

c) 1200°C – (i) Image at magnification of 2000X, (ii) Image at magnification of 5000X, and (iii) Image at magnification of 10000X

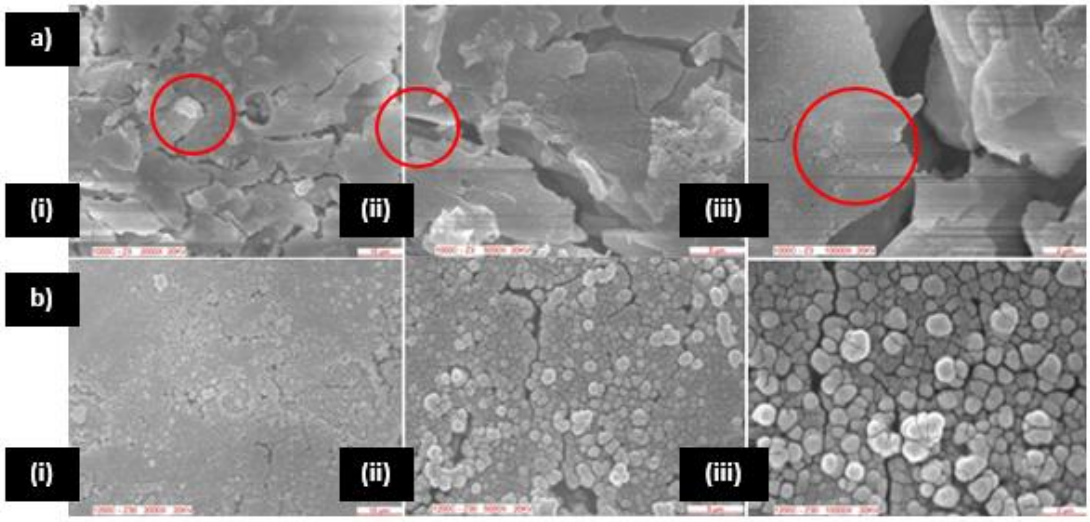


Figure 3. SEM image for microstructure of steatite doped with 20 wt% ZnO sintered at:

a) 1000°C – (i) Image at magnification of 2000X, (ii) Image at magnification of 5000X, and (iii) Image at magnification of 10000X

b) 1200°C – (i) Image at magnification of 2000X, (ii) Image at magnification of 5000X, and (iii) Image at magnification of 10000X

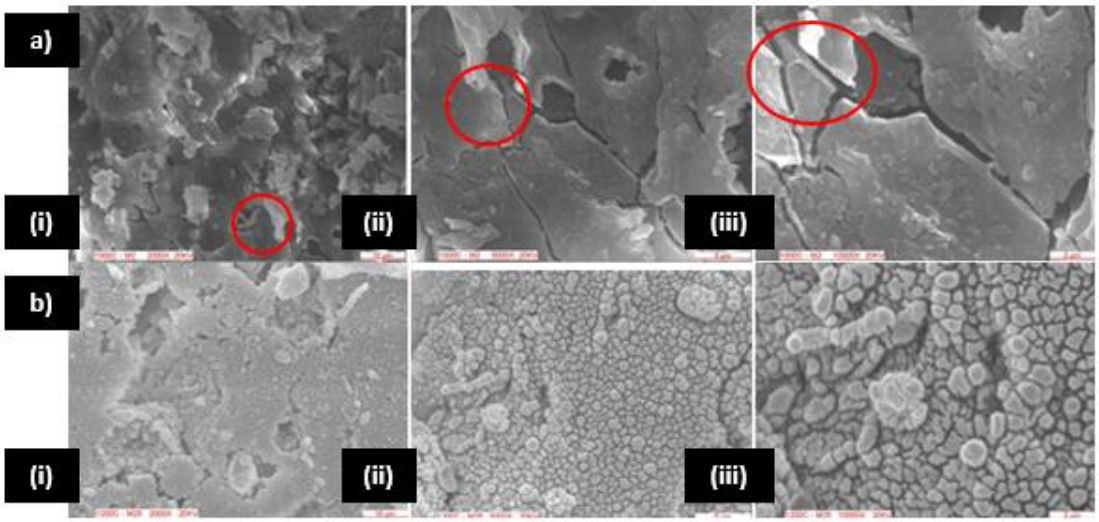


Figure 4. SEM image for microstructure of steatite doped with 20 wt% MnO_2 sintered at:

a) 1000°C – (i) Image at magnification of 2000X, (ii) Image at magnification of 5000X, and (iii) Image at magnification of 10000X,

b) 1100°C – (i) Image at magnification of 2000X, (ii) Image at magnification of 5000X, and (iii) Image at magnification of 10000X

XRD analysis has been carried out to evaluate the phase stability for sintering temperature 1000°C, 1100°C and 1200°C. The amount of protoenstatite is expected to be more than clinoenstatite as clinoenstatite phase can only be found either naturally or transform from protoenstatite at high temperature, specifically from 1250°C. However, the polymorph of clinoenstatite are found at 1000°C at the steatite materials in this research work. This clearly shows that the two stage sintering and sintering additives managed to accelerate the formation of protoenstatite at temperature below 1250°C. In the sintered body that doped with ZnO, a new phase was observed which is Willemite (Zn_2SiO_4). For the body that doped with MnO_2, the sample was bloated because of its low melting point.

Table 4. Phases present in the sintered steatite body (C = Clinoenstatite, Q = Quartz and W = Willemite (Zn_2SiO_4)

Composition / Sintering Temperature	**Undoped**	**20 wt% ZnO**	**20 wt% MnO_2**
1000°C	Q + C	Q + C + W	Q + C
1100°C	Q + C	Q + C + W	Q + C
1200°C	Q + C	Q + C + W	Bloated

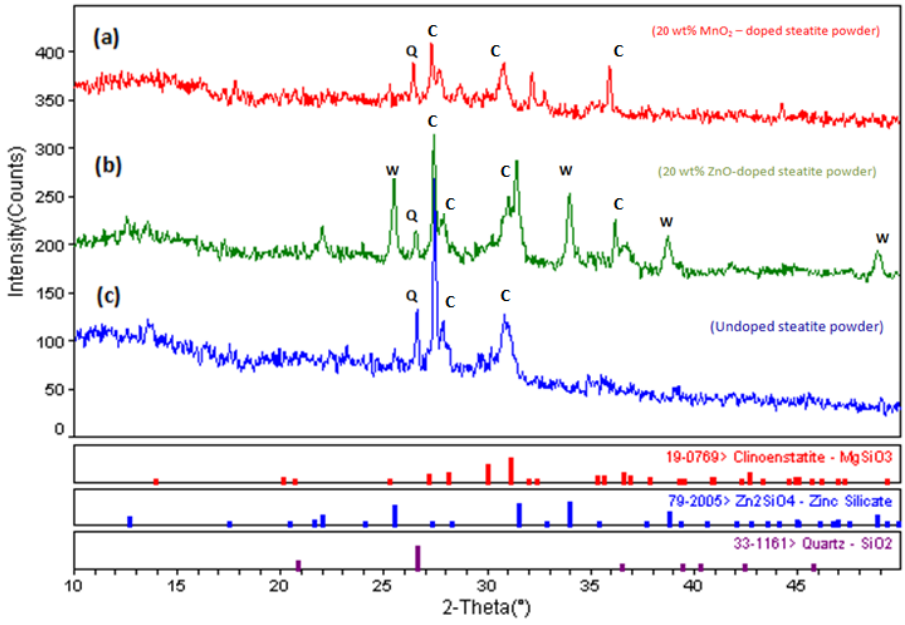


Figure 5. XRD patterns of steatite samples sintered at 1000°C: (a) 20 wt% MnO_2-doped steatite powder, (b) 20 wt% ZnO-doped steatite powder, (c) Undoped steatite

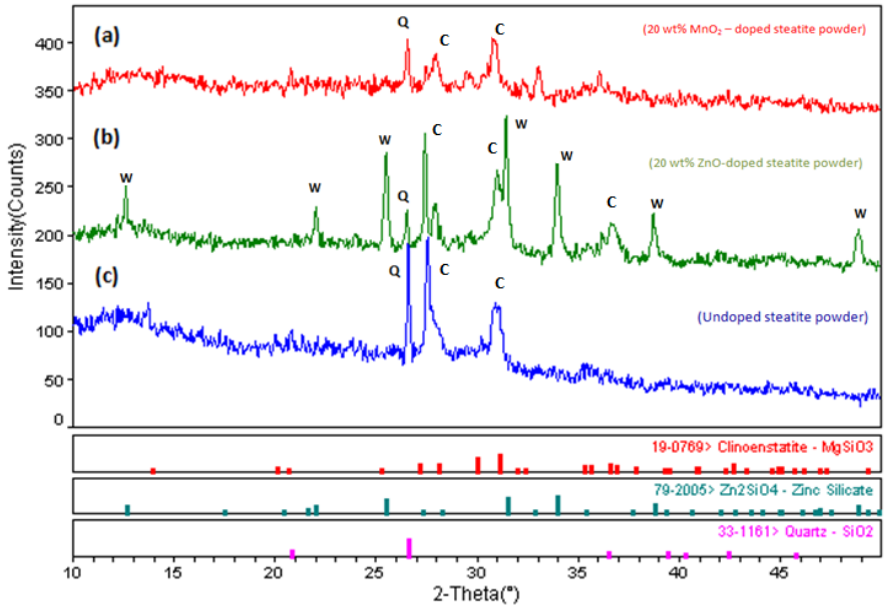


Figure 6. XRD patterns of steatite samples sintered at 1100°C: (a) 20 wt% MnO_2-doped steatite powder, (b) 20 wt% ZnO-doped steatite powder, (c) Undoped steatite

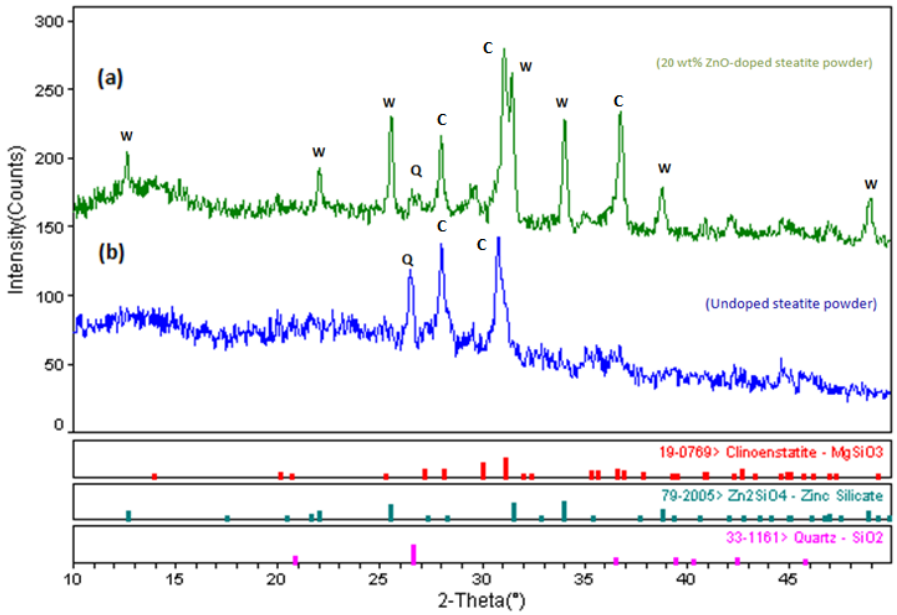


Figure 7. XRD patterns of steatite samples sintered at 1200°C: (a) 20 wt% ZnO-doped steatite powder, (b) Undoped steatite

For the bulk density, the densification of all the sintered steatite body increased with the increase of the temperature. This indicates that the two stage sintering are more efficient than conventional sintering. Furthermore, the steatite body that doped with sintering aids seem to have higher density than the undoped one at similar sintering temperature. When sintered at 950°C, the bulk density of the undoped steatite is 2.13 g/cm^3. It increases as the sintering temperature increases until 1200°C, the density is recorded at 2.31 g/cm^3 which is the maximum value for undoped steatite in this research. On the other hand, the steatite doped with 20 wt% MnO_2 has the density of 2.12 g/cm^3 at 950°C which is quite similar with undoped steatite. However, the effect of MnO_2 as a sintering additive is just about to start at sintering temperature of 1050°C. Starting from

this point, although the trend of the bulk density across the temperature is same with undoped steatite, the increment or gradient of the MnO_2 doping steatite density improve rapidly. Next, for the steatite doped with 20 wt% ZnO, the bulk density during 950°C sintering temperature is already 2.25 g/cm^3 which is higher than the other two. The density continues to rise when crossing the temperature until a maximum bulk density of 2.79 g/cm^3 is achieved. Compared to the undoped steatite, the sample doped with MnO_2 has an improvement of 5.3% at 1150°C while the sample doped with ZnO is 20.8% better under similar sintering circumstances at 1200°C.With the presence of sintering aids, polymorph of protoenstatite phase can be formed at lower temperature and stabilized. Therefore, it reduced the potential of volume expansion due to the phase transformation from protoenstatite (high temperature) to clinoenstatite (room temperature). Figure 8 shows the density of the samples at different temperatures.

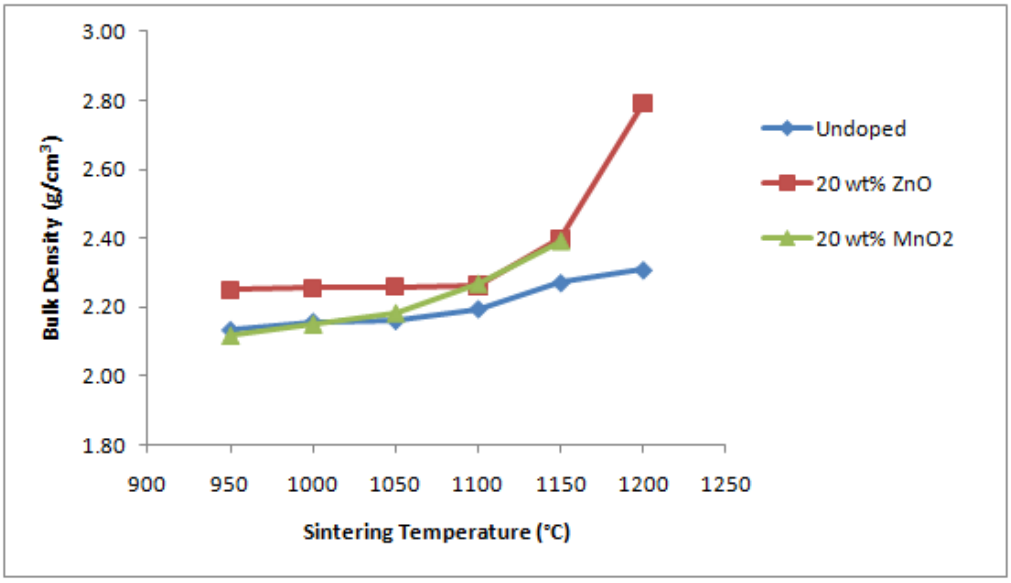


Figure 8. Bulk density of all three specimens across the sintering temperature

For the aspect of Young's modulus, all the three types of samples showed the similar trend which is increasing when the sintering temperature rises. During the sintering process at low temperature (<1050°C), all the samples had no significant improvement at modulus of elasticity. However, when the temperature goes beyond 1050°C, the modulus of elasticity values for all samples increase drastically until the maximum reading is taken at 1200°C. For the sample doped with MnO_2, the elasticity value is the highest from 1060°C to 1150°C followed by the sample doped with ZnO and lastly undoped steatite. Unfortunately, the sample the doped with MnO_2 was found bloated when it is sintered at 1200°C due to low melting point of the dopants thus no sample can be tested at that temperature. 76.72GPa is the maximum E value achieved by the sample doped with 20 wt% ZnO that sintered at 1200°C. Figure 9 shows the modulus of elasticity for each sample.

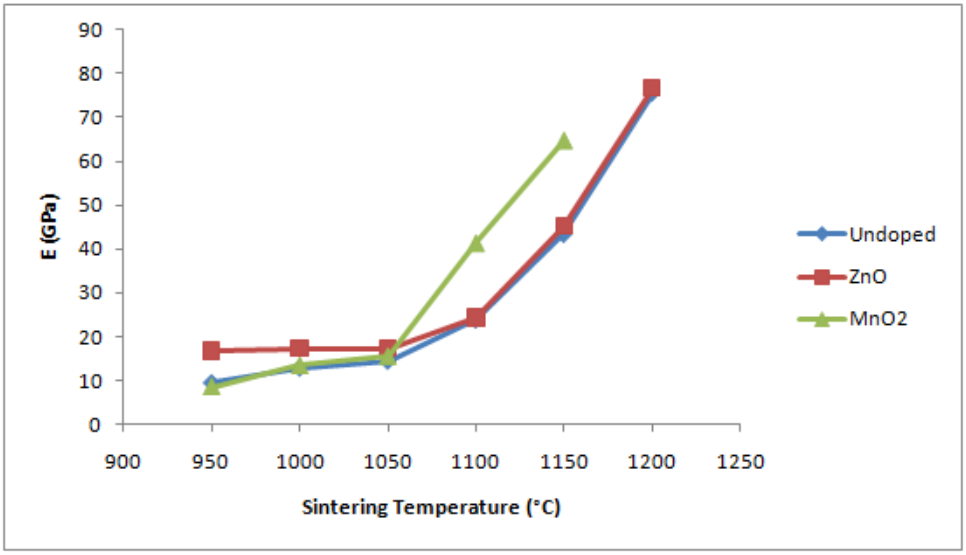


Figure 9. Young's modulus of the steatite body versus the sintering temperature

For the Vickers hardness testing, the results agreed with the trend of the bulk density and Young's modulus curve. For the undoped steatite sample sintered at 950°C, the Vickers hardness, H_v was recorded at ~0.42GPa. There is only small improvement from 950°C to 1050°C. After this point, the hardness value went up impressively until 1200°C and showed the maximum value of ~4.49GPa. Throughout this two stages sintering process, the improvement of the hardness value marked a 228% of increment which is very encouraging. Comparing to the conventional sintering process that carried out by previous researchers, the result of 1.36GPa is obtained for undoped steatite that sintered at 1100°C. On the other hand, the H_v results for the samples that doped with 20 wt% ZnO and MnO_2 exhibited the same trend as the undoped steatite which increasing with the sintering temperature. At 950°C, the sample doped with ZnO has the H_v value of ~0.56GPa while the sample doped with MnO_2 has ~0.46GPa H_v value. Both of the results are slightly higher than the undoped steatite at that temperature. Also, there are only small increment in hardness value for both doped steatite before 1050°C. After that, the sample doped with MnO_2 rise up drastically again until ~3.48GPa at 1150°C before it get bloated. Meanwhile for the sample doped with ZnO, the hardness value continues to rise in small amplitude and eventually reached the peak at ~4.06GPa at 1200°C. Figure 10 shows the Vickers hardness value of the samples.

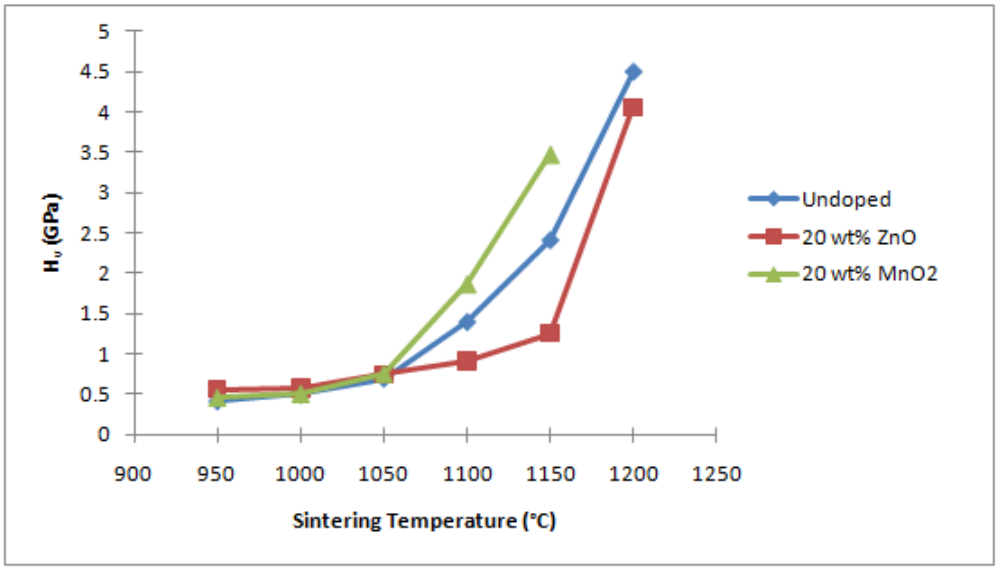


Figure 10. Vickers hardness of the steatite body versus the sintering temperature

4. Conclusion

In this research work, sintering aids had played its important role to improve the strengths and characteristics of the steatite materials after the sintering process. Bulk density, Young's modulus and Vickers hardness increase with the existence of the sintering additives across the sintering temperature. The two stage sintering managed to keep the sintering temperature low to avoid phase transformation from protoenstatite to clinoenstatite that may lead to volume expansion and finally materials cracking. Although similar results can be obtained by using conventional sintering, the sintering temperature needed to be raised until protoenstatite phase is formed. In conclusion, by using two stage sintering and doped with specific sintering aids, the strength of the steatite materials will get improved as well as the sintering process will be more cost effective because the sintering temperature needed is relatively low.

References

[1]Soykan, H.Ş. 2007. Low-temperature fabrication of steatite ceramics with boron oxide addition. *Ceramics International*. 33: 911-914.

[2] W. Mielcarek, D. Nowak-Wozny, K. Prociow, Correlation between MgSiO3 phases and mechanical durability of steatite ceramics, J. Eur. Ceram. Soc. 24 (15/16) (2004).

[3]Ctibor, P., Sedlacek, J., Neufuss, K. & Dubsky, J. 2005. Dielectric properties of plasma-sprayed silicates, *Ceram. Int*. **31** (2): 315-321.

[4]Morimoto, N., Appleman, E.D., & Evans, H.T. (2009). The crystal structures of clinoenstatite and pigeonite. Zeltschrift f. Krist. 114, 120-147.

[5]Reynard, B., Bass, J.D., & Jackson, J.M. (2008). Rapid identification of steatite-enstatite polymorphs at various temperatures. Journal of European Ceramics Society. 28, 2459-2462.

[6] Smith, J.D. and Fahrenholtz, W.G. (2008) *Refractory Oxides. Ceramics and glass materials: Structure, Properties and Processing*. Shackelford, J.F. and Doremus, R.H. (eds.). New York: Springer, 87–110.

[7]Vela, E.; Peiteado, M.; García, F.; Caballero, A.C. and Fernández, J.F. 2007. Sintering behavior of steatite materials with barium carbonate flux. *Ceramics International*. 33: 1325-1329.

[8]Bloor, E.G. (1964). Conversion in steatite ceramics. J.Br. Ceram. Soc. 63, 309-316.

[9]Thurnauer, H., & Rodriguez, A.R. (1942). Notes on the constitution of steatite. J. Am. Ceram. Soc. 25 (15) 443-445.

[10]Vereshchagin, V.I., & Gurina, V.N. (1997) Polymorphism of magnesium metasilicate and its role in the production of no aging steatite ceramics. Glass Ceram. 54 (11/12) , 365-367.

[11]Avetikov, V.G.; Borisova, A.Y.U.; and Zinko, E. 1970. Sintering Range and Viscosity of Steatite Materials. *Glass and Ceramics*. 27(5/6): 294-296.

[12]Peicang, X. and Xiayoun, Z. 1988. Mineral physical characteristics of pyroxene phase transformation and a probe into the mechanism of talc porcelain aging. *Acta Mineral. Sin.* 8: 104-112.

eureca 2016 – Conference Paper
Paper Number 2ME22

Two-Stage Sintering of Iron Oxide Doped Y-YZP Ceramics

Pang Chuan Yao[1*], Sivanesan Sivakumar.[2]

[1,2] *School of Engineering, Taylor's University, Malaysia*

[*]chuanyao.pang@sd.taylors.edu.my

Abstract
The main objective of this paper is to observe the strengthening of mechanical properties without losing the original material properties while performing two-stage sintering of a 3mol% Yttria-stabilized Tetragonal Zirconia Polycrytals ceramics(Y-TZP) doped with iron oxide. The purpose of performing this research is to expand the area of usage of zirconia ceramic in medical field applications. The challenges in this research are the observation and exploration of the development potentials and limitations of Zirconia ceramics using the process of two stages sintering of Y-TZP ceramics that doped with iron oxide. For this research, two stages of sintering process used iron oxide to analyse the effect on mechanical properties of the 3mol% of Y-TZP. The material used in this research is 3Y-TZP powder; commercially readily available. This material was subjected to different sintering schedule Temperature point 1 ranging from 1200 to 1500°C by pressurizes sintering with a holding time of few minutes using a standard heating rate of 10°C/min and left to cool down for another 6-30 hours of holding times in order to minimize the densification between both process. After the processing stage, the following up will be the process of mechanical materials testing and evaluation to obtain result from the material's properties such as hardness, fracture toughness, flexural strength and Young's modulus. The expecting outcomes of this research is two stage sintering process is able to enhance Y-TZP ceramic with high flexure strength and good fracture toughness that are able to provide stability application on medical application. The understanding of sintering ability and method of iron oxide doped sintering.

Keywords: 3Y-TZP 1, Two-Stage 2, Doped 3, Sintering 4, Densification 5.

1. Introduction

In the bio-materials research fields, Yttria-stabilized zirconia has been conducted quite an amount of research, whereby one of the materials is able to have biocompatibility. This material can be used as human implantation with a very low chance of being rejected by human body or brain signal as an artificial transplant with

high fracture toughness and low thermal conductivity. One of the challenges that engineers wanted to increase the stability of usage of Zirconia ceramics is by improving material properties. The Zirconia ceramics was checked with the hardness, Young's Modulus, resistance and strength of the materials properties. This is to find out the main limitation of ceramics for engineers to justify its application without any poor fracture toughness. The microstructural transformation design will be the major component to obtain good application ceramics, whereby ceramics with high toughness and high strength [1].

The sintering temperature of this material is one of the key components to show the densification effect after heating the material to some point of temperature. For the normal pure YSZ, it can have the sintering temperature from 1300°C or higher [2]. However, there having research proven that doped with iron oxide (Fe_2O_3) with 3Y-TZP and 8Y-TZP were found the densification rate been increased and larger grain size while comparing with undoped 3Y-TZP and 8Y-TZP by using much lower temperature than 1300°C [2].

For a material starting happened accelerated grain growth can be observe from the microstructure of the material, where the best range of percentage for the grains postpone around ρ=92%. As this is important component for maintaining pore-grain boundary through grain growth, a sintering method called two step sintering (two-stage).

From defining the material properties, phase transformation which the one of the main progress that able to observe the changes between two phase of mechanical properties. The previous research made showed the phase changes from tetragonal (T) to monoclinic (M) is the major components that help engineers to improve the usage of the Zirconia ceramic as the stability of the product, where (T) to (M) phase transformation becoming the challenge engineers faced as able to take control of the phase transformability freely where also can still remaining the ceramics still in tetragonal phase while cooling down after sintering [1]. With after sintering and control the limitation of transformation phase, another concern with transformation is the degradation of the ceramics, where also known as the degradation of properties with low temperature [2].

The concern regarding application of Y-TZP ceramics is the sensitivity of low temperature degradation (LTD) in the application of biomaterial as the access of the micro cracking and property deterioration [2].

The purpose of performing this research is to obtain experimental result that help the society an improvement understanding on material technology, and will expand the area of usage of zirconia ceramic in engineering perspective. The challenges on this research to observe and explore the potentials of development and increase range of limitation on knowledge of zirconia ceramics while preforming in a process of 2 stage sintering of Y-TZP ceramics that doped with iron oxide.

2. Pure Yttria-Tetragonal Zirconia Poly-crystal (Y-TZP)

From origin of Y-TZP with any doped materials will reach for an amount of temperature to preform phase transformation as from monoclinic (m) to cubic (c) as the Figure 1 show. Y-TZP has a tetragonal structure. This structure enables Y-TZP to have

a very high flexural strength compared to other zirconia-based compounds. As shown in the Figure 1, the structure changes accordingly to the temperature.

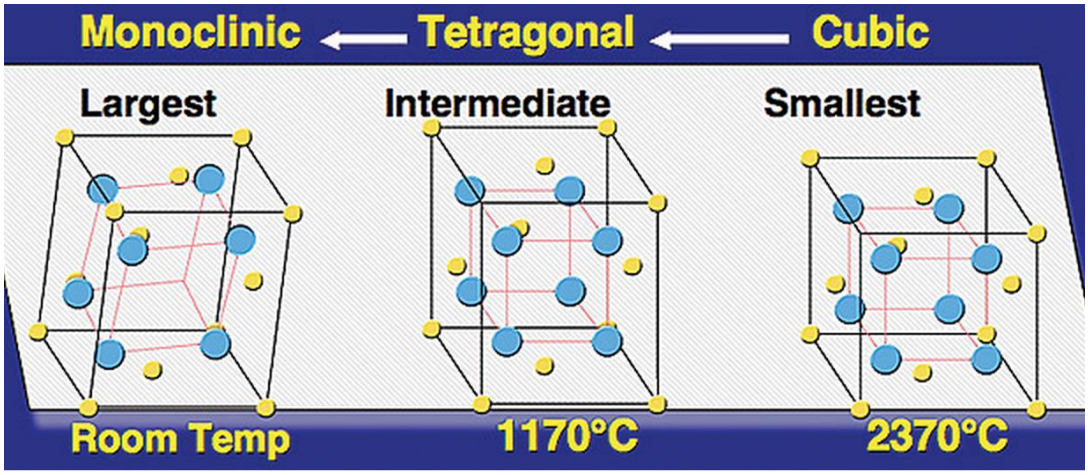


Figure 1. Zirconia Poly-crystal phase transformation [3]

Researchers will first analyze the phase transformation of the sintering process of zirconia ceramic, as the component researchers seek for is the mechanical and material properties [6]. Currently, Y-TZP is able to have flexural strength which is larger than >1 GPa and good fracture toughness from 6 to 10 $MPam^{1/2}$ [4].

The limitation that occurred on current Y-TZP ceramics is the accessibility of the phase transformation from tetragonal (t) to monoclinic (m), after the sintering process will having slow reaction on (t) to (m) transformation, under the process will lead to micro cracking on the surface on the materials [5].

2.1. Iron Oxide (Fe_2O_3) Doped

In this research, one of the aim needed is to stabilize the effectiveness of the (T) to (M) transformation while sintering doping Y-TZP ceramics and to ensure after sintering the specimens able to have good low temperature degradation which increase the life time around greater than 20 years only will interest of usage in medication application. Another interest on doping will be the effect on the grain size can less than 0.3 µm fractions of (t)-(m) phase transformation.

From a research conducted from University of Zürich to observe the effect of dopants and sintering temperature on microstructure and LTD of dental Y-TZP, in the research using iron oxide doping ceramics and sintering temperature range from 1300°C to 1450°C, with the result obtained turn out the amounts of iron oxide doping did not produce any effect on the stability of Y-TZP against LTD, the procedure of the experiment with iron oxide doped Y-TZP section having the specimens (Al_2O_3 < 0.25wt%and Fe_2O_3 < 0.15wt%) by using heating rate of 10°C/min, sintering temperature of 1500°C with 1 hours of holding time and lastly with 10°C /min of cooling rate, obtained result with an average grain size of 0.585 µm>0.3µm fractions of t-m phase transformation. The doping having aluminum oxide and iron oxide into Y-TZP ceramics to obtain result that grain size greater than 0.3 µm which the stability of this dental zirconia against LTD do not had much effect with both doping [6].

Another research conducted from University of Manchester on effect of iron oxide (Fe_2O_3) doping on sintering of Yttria-stabilized zirconia. The experiment having Fe_2O_3 doped 3mol% YSZ and 8mol%YSZ as the specimens to observe the effect made on the grain growth, and the result obtained show that the densification rate had been change from vary amount of Fe_2O_3 (0.5wt%) and the grain size had been increase while comparing with the undoped 3mol% YSZ and 8mol%YSZ as the result range for grain size do not exceed than 0.4 μm, in order to prove the doped effect can within the acceptable fractions of t-m phase transformation [7].

2.2. Two-Stage Sintering Process

In this research, sintering process is one of the key component that affects all the result, whereby the choice of normal sintering process and Two-stage sintering process can have obtained different results on grain sizes, LTD, stability and application of the materials.

From a research conducted by student from university of Pennsylvania, using two step sintering of ceramics undoped, the result given was that two step method offers a promising approach for fabrication of bulk nano grain ceramics [7-8], given that for two-step sintering able to give a good result, while in this research will be conducted of two stage sintering doped with iron oxide which can be produce better performance Y-TZP ceramic. There is another research paper of using normal sintering to see the effect while using Fe_2O_3 as doped components for Yttria- Stabilized Zirconia(YSZ). The paper concluded that the effect of 3YSZ doped with Fe_2O_3 was obtained a small grain growth while using normal sintering process the gap will increase performance of the material by changing sintering to two stage sintering [8-9].

Another research conducted from Mahasarakham University whereby two stages sintering with alumina-zirconia composites were carried out. The result obtained from the experiment showed that the sintering process able to controlled the phase formation, microstructure and mechanical properties. With the two stage sintering process, the grain growth of the material was able to control down, and with high hardness and fracture toughness [10].

For this research, the method of two stage sintering process is the main component needed to analysis and verify with the study from both research study. The temperature for T1 will be set around 1200 ^oC -1500 ^oC with using 10 ^oC/min heat rate, after reaching T1 will be having around 3 minutes to 1 hours of holding time as in order to examine intermediate microstructure as to control the level of densification. After the first holding time, the sample will rapid cooling with 50 ^oC/min down to T2 with 6 to 30 hours of holding time. The T2 will be set around 1000 ^oC.

3. Research Methodology

The first step will be construction and initiation powdering process. This powder preparation is for the experiment by imitating the powder characterization of the powder by the powder particle size, microstructure, phase purity, and temperature of sintering, preparation of iron oxide powder and etc. Next process will be doped iron oxide and sintering green body process as to thermal analysis the zirconia powders

while in the first stage. The Green Body is prepared with uniaxial pressing and cold isotactic pressing. Processing with sintering by carried out using 1200 ºC-1500 ºC to reach temperate 1, with few minutes holding time only using cooling ramp rate around 10ºC/min to temperature 2 stage with 6-30 hours of holding time. The physical and microstructure was preceded by examination and evaluation where testing the sintering samples shall be ground and polished for better surface finish, using X-ray diffraction(XRD) for phase analysis, and measurement of grain size and microstructural changing effect. After the processing, the following up will the process with mechanical materials testing and evaluation as to obtain result from the material's properties like hardness, fracture toughness, flexural strength and Young's modulus. The testing needs to be monitoring the changes of changing the crystal structure and mechanical properties.

3.1. Experiment Process

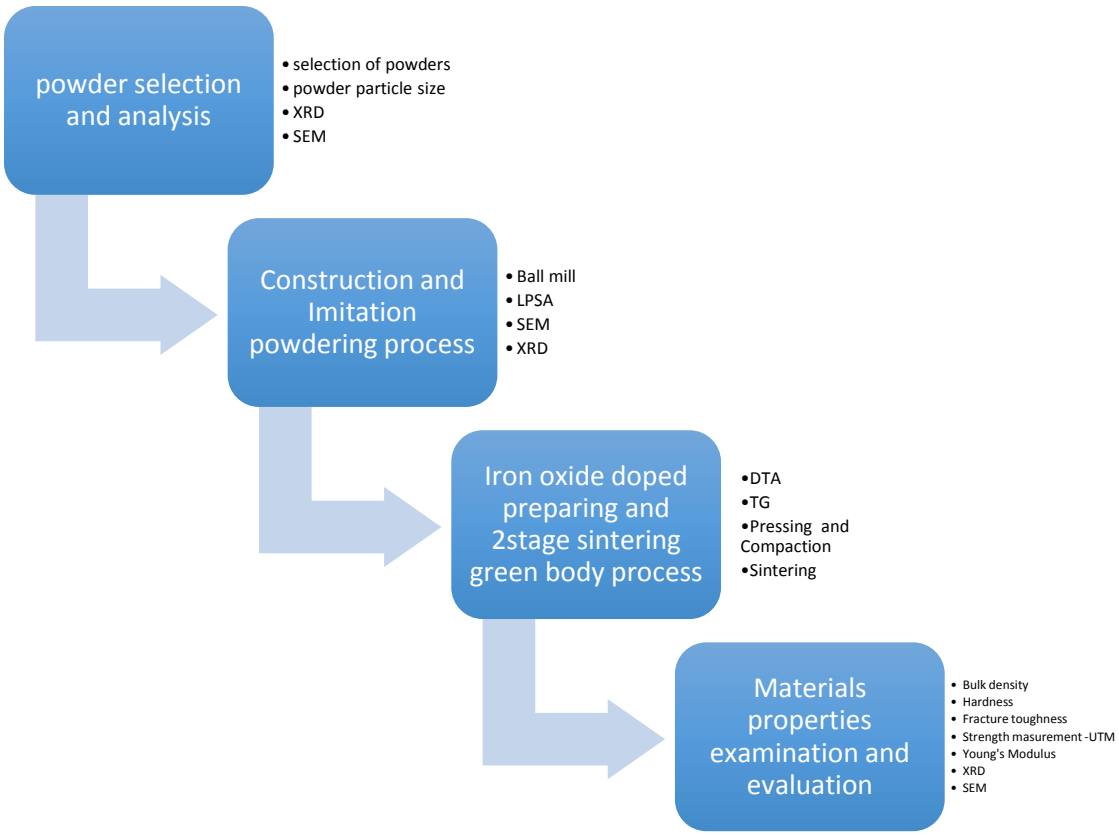


Figure 2. Process chart for the experiment

The Figure 2 show the process flow chart of the experiment, on the first process powders selection for this experiment were using 3mol% Yittria-Stablized Zirconia powder (KZ-3YF) and 0.5mol% Iron Oxide powder. Once received powders needed to perform analysis phase content and morphology using XRD and scanning electron microscope(SEM). After powder preparation, using ball mill for doping and mixing for

both powder. Before sintering, needed to perform laser particle size analyzer(LPSA) to analysis the powder particle size, and thermal analysis by differential thermal analyzer(DTA). To check the weight loss during the heating and cooling of the samples by Thermogravimetric analyzer(TG). Pressing and compaction using bench powder press and cold isostatic press, for the sintering process. After the samples done sintered, the sample need to perform physical evaluation and mechanical testing and evaluation.

3.2. Powder selection and Analysis

In this research, the experiment will be conducted with preparing the Y-TZP powder, which in this experiment using 3mol% Yittria-Stablized Zirconia powder (KZ-3YF), the powder will be prepare under spray dried, and ready to use for pressing. The powder characteristics and material properties are obtained from the manufacturer (Kyoritsu Ltd. Japan) as the Table 1 shown below

Table 1- Y-TZP Powder properties [11]

YSZ Powder properties	
Yttria (Y_2O_3)	3 mol%
Particle Diameter	0.3 µm
Bulk Destiny	6.10 g/cm³
Bending Strength	1000 MPa
Hardness	13 GPa
Fracture Toughness	4-6 MPa.m½

This research also will be using red iron oxide powder as a doping material into the Y-TZP powder; the powder characteristics and material properties show as the Table 2 below

Table 2- Iron Oxide (Fe_2O_3) Powder properties [12]

YSZ Powder properties	
Iron Oxide (Fe_2O_3)	0.5 mol%
Particle Diameter	50 nm
Bulk Destiny	5.242 g/cm³

3.3. Green Body Preparation

In this research, the YSZ powder doped with Iron Oxide (Fe_2O_3) and using a mold to form into a disc shape around 20 mm diameter, and 5 mm thickness with around 2.5 g. The specimen will be applied with a cold hard pressed (CIP) using around 200 MPa to make the specimen able to form the particle more uniformly, which help to improve densification for next procedures.

3.4. 2-Stage Sintering Process

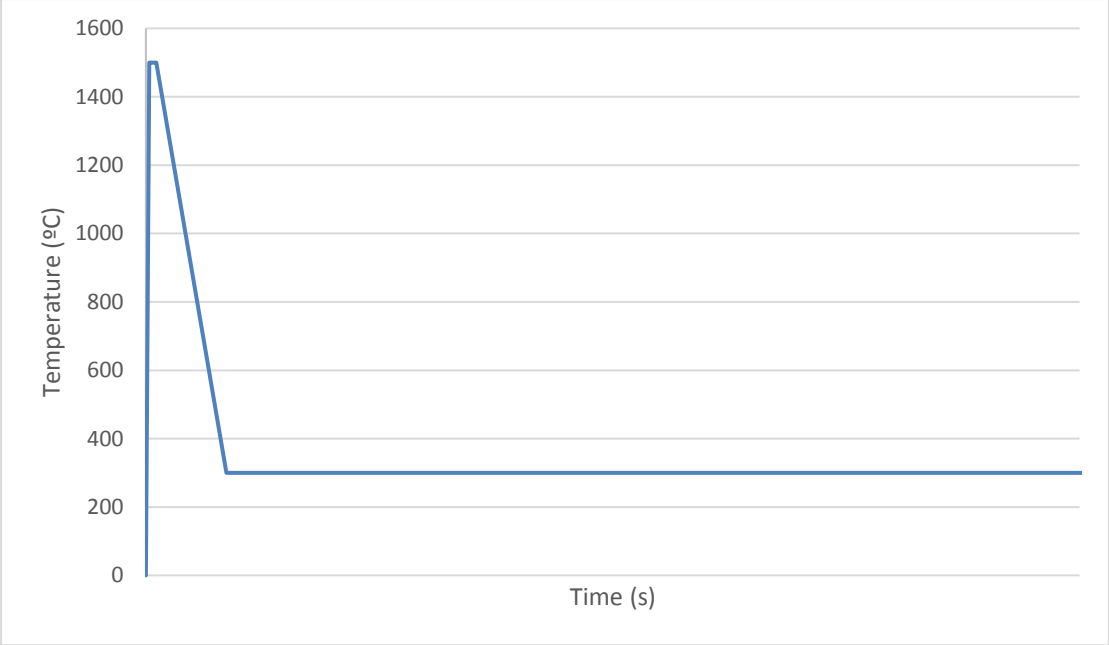


Figure 3. Temperature and time graph on two stage sintering method

After the Green Body specimen is being prepared as disc shapes, it has to be grounded and polished to ensure the specimen able to produce a good surfacing for XRD and SEM evaluation later. For this research using two stage sintering process which this method using a higher temperature T1 on first time sintering with 3,4,5 and 6 minutes of hold time, and let it to be cool down with room temperature is use to lower the temperature, after reach that temperature T2 let the specimen on hold for 10 hours. Finally let the specimen to cool down to room temperature. Two-stage sintering method can minimize densification while in both heating and cooling process.

4. Results and Discussion

4.1 Grain Sizes and Microstructure Evolution

For this research, the samples are 3Y-TZP doped iron oxide sintering temperature to 1500°C with 3 to 6 minutes of holding time using SEM for polished and thermal exposed were demonstrated in Fig 4.

Reactiveness of Yttria and pure Yttria isolation during sintering might be the reasons of the development of cubic phases which less than 10 % at sintering temperature 1500°C. Pure Yttria isolation in the grain boundaries will affect the result in terms of tetragonal transforming to cubic polymorph.

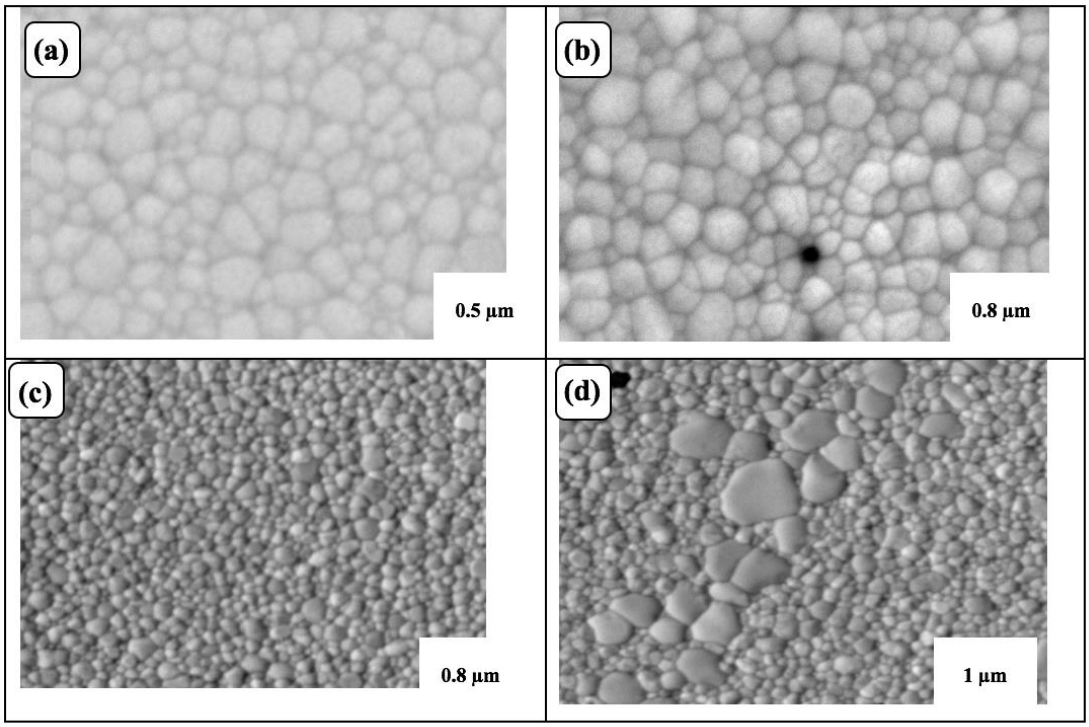


Figure 4. SEM microstructure of 3Y-TZP doped sintering temperature at 1500°C at various holding time. (a) 3 min (b) 4 min(c) 5 min and (d) 6min

4.2 Bulk Density

The bulk density of 3Y-TZP doped samples were investigated at two stage sintering process with step 1 of holding time at range 3-6 minutes at a given range of sintering temperature 1200ºC -1500ºC as show as Fig. 5. From the holding time at the 6th minute showed the effect of increasing density from temperature 1200 to 1450ºC. However, when the sintering temperature goes to 1500 ºC, the density dropped from 5.878 Mg.m^{-3} to 5.61 Mg.m^{-3}. This density decrease could be one of the attributes to the cubic phase transformation related as the sample has been sintered for 6 minutes at 1500ºC.

The sintering holding time was proven that one of main components that affects the density of the samples regardless of the sintering temperature. From the Fig 5, it showed the longer of the holding time resulted in much higher destiny obtained as result. The results showed that the density value larger than 5.5 Mg.m^{-3} linked to relative density of 90% from the hypothetical could only be obtained when sintering temperature was higher than 1350ºC. As from the results above, it showed that the greater the temperature is, the density will increase unrelatedly of the holding time.

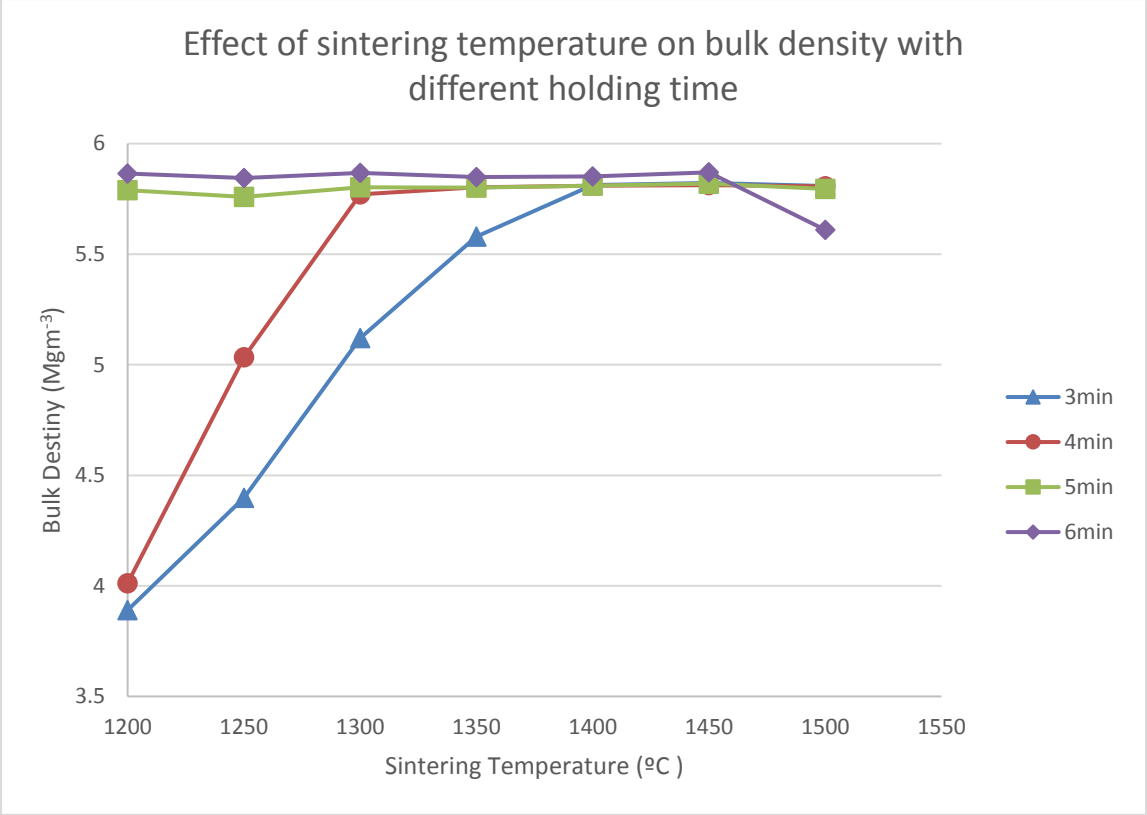


Figure 5. Effect of sintering temperature on bulk density of 3Y-TZP doped with different of holding time

4.3 Vickers Hardness

The results of effects of the different holding times and temperature against Vickers hardness are shown as Fig 6 From the result obtained shows that the longer the holding time needed for stability of samples with higher hardness. For the holding time with 3 minutes, it showed that the value suddenly increased rapidly when the sintering temperature surpassed 1250ºC. The value reached about 13 GPa when the temperature at 1400ºC; it is the maximum hardness.

However, hardness values for 4,5 and 6 minutes' samples reduced to 11.8 GPa, 12.4 GPa and 12.22 GPa when sintering continued to higher temperatures correspondingly. Commonly, the hardness of samples started to reduce when a sintering temperature of more than 1400ºC was employed without regarding of the holding time. At a certain sintering temperature, this pattern of increasing hardness until maximum can be found. The decreased in hardness was caused by two factors; increased in grain size and also decreased in the densities. The cause of this is due to hardness is closely reliant on bulk density, which diminished significantly after sintering at 1450ºC because of the presence of cubic phase.

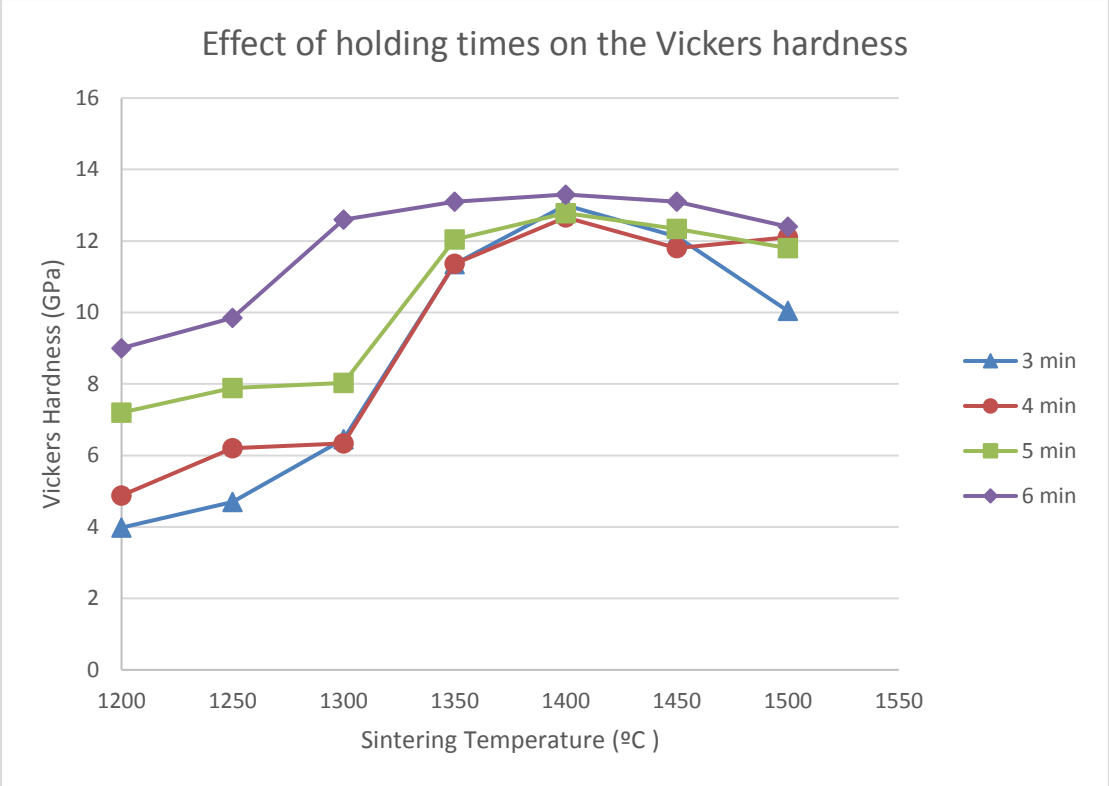


Figure 6. Effect of holding time on the Vickers hardness with 3Y-TZP doped samples.

4.4 Fracture Toughness

The results of the effects of sintering temperature and holding time on the fracture toughness (K_{Ic}) of the samples showed in Fig. 7. It showed from temperature 1200ºC -1500ºC with two stages sintering first holding time from 3-6 minutes. The fracture toughness found lesser affected by temperature below than 1350ºC with under than 5.0 $MPam^{1/2}$. This also proved the sintering temperature below than 1350ºC having minor effect on the tetragonal phase stability to the samples. From the result obtained, it shows that 6 minutes holding time was able to give the highest fracture toughness when the temperature reaching to 1500ºC which in this case that 6 minutes will be the best choice for two stage sintering. From previous result of Bulk Destiny and Vickers hardness, both result showing those 6 minutes holding producing stable bulk density and high Vickers hardness value.

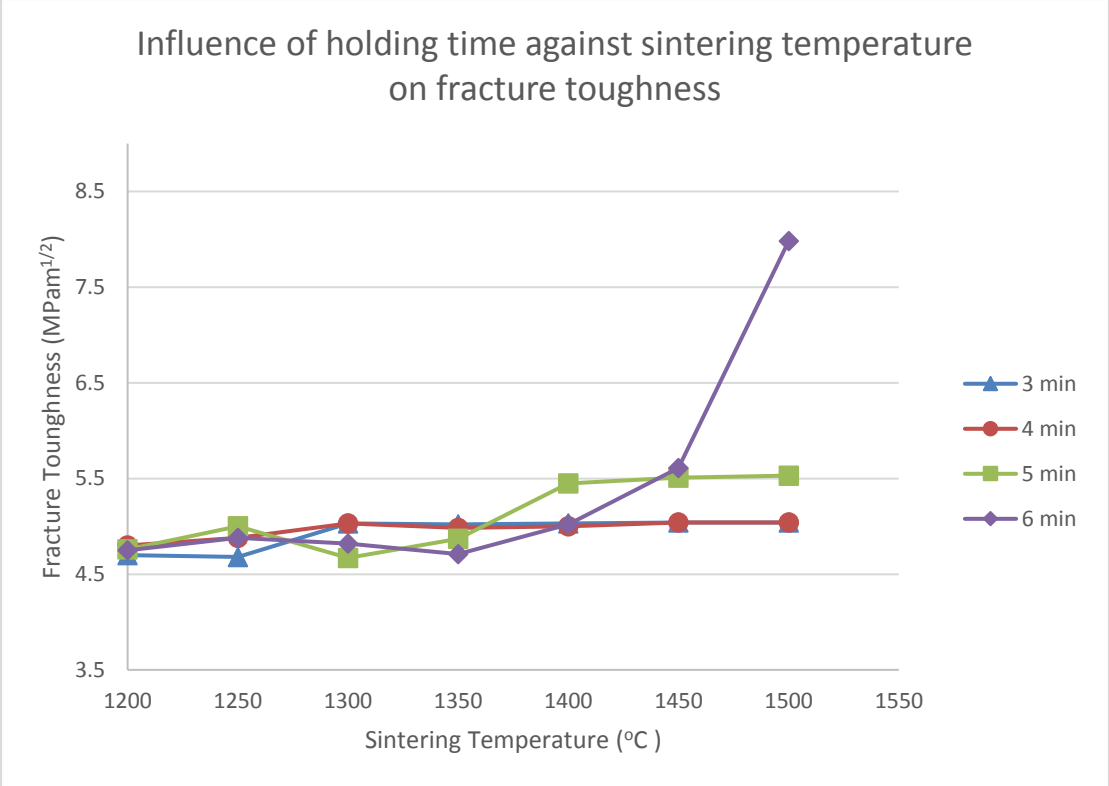


Figure 7. Influence of holding time against sintering temperature on the fracture toughness

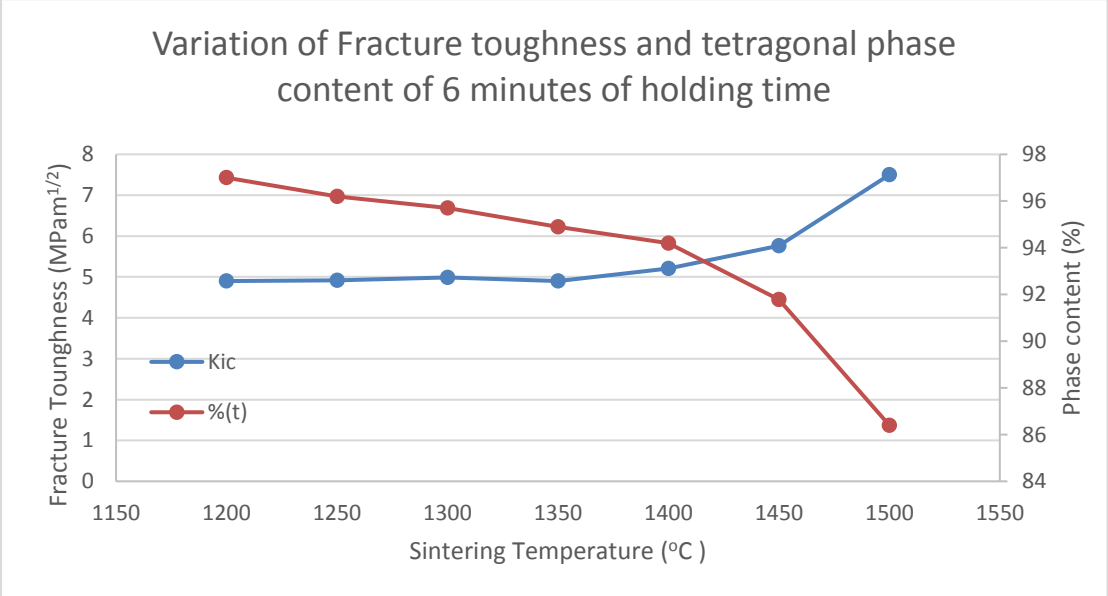


Figure 8. Variation of fracture toughness and tetragonal phase content of minutes holding time

For Fig.8 was the further analysis from 6 minutes holding to observe the effect between fracture toughness and phase content against the sintering temperature. From the result obtained, it shows that the fracture toughness increased but the phase content reached around 87% when the temperature reaches 1500ºC. Accelerated grain growth can be observed from the microstructure of the material, where the best range of

percentage for the grains postpone around ρ=92%. As this is important component for maintaining pore-grain boundary through grain growth, a sintering method called two-step sintering. This effect occurs at sintering temperature 1400ºC-1450ºC where the density in a range of 91.8%- 94.2%.

4.5 Young's Modulus

For Young's modulus analysis of 3Y-TZP doped samples, two stage sintering process with step 1 of holding time at range 3-6 minutes and given range of sintering temperature 1200ºC -1500ºC as show as Fig. 8 As the result obtained, the value of Young's modulus of the samples were increasing when the sintering temperature surpass 1300 C. Temperature above than 1350ºC, the result shows that samples starting becoming instability. From observing the result of temperature 1350ºC, the Young's modulus obtained the highest was 209 GPa with 6 minutes of holding time while minimum obtained was 195 GPa with 3 minutes of holding time.

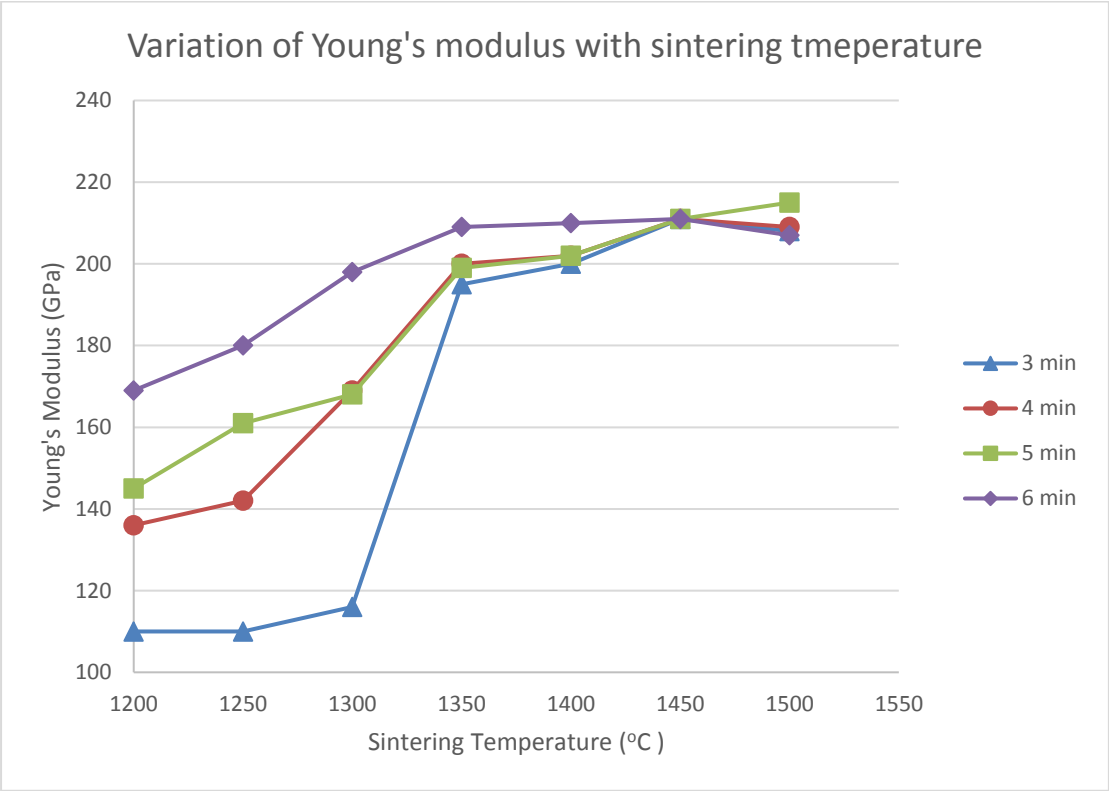


Figure 8. Variation of Young's Modulus with sintering temperature

As the value of Young's modulus of the samples, they showed temperature 1200ºC given the lowest value of 110 GPa with 3 minutes of holding time, and the highest value being observe is where the sintering temperature reaches to 1300ºC with 6 minutes of holding time. Commonly, material can go up to 200GPa or above can go up to sintering temperature above that 1350ºC with insignificant effect from the holding time. The 6 minutes holding time was providing stable and high value showed from Fig. 8. However, the temperature reaches from 1400ºC to 1500ºC, the Young's modulus was reduced from 211 GPa to 207 GPa. This can be enlightened through the cubic(c) phase transformation subsequent in a reduction that's related to Fig 4 where the bulk density also reduces when reaches to 1500ºC.

5.0 Conclusion

As for the conclusion, the study was performed to find new potentials of engineering 3Y-TZP doped with Iron Oxide ceramics with mechanical properties that were anticipated. The main parameters that were manipulated are both sintering holding time and temperature effect while in two stage sintering. Sintering temperature from 1200ºC to 1500ºC with holding time 6 minutes found to be in the cubic (c) phase. The amount of the cubic phase made the samples sintered found the amount of cubic phase while obtaining result from Young's modulus and Bulk density. The sintering time is one of the important factors governing the density of the sample, whereby it was found in the result that 6 minutes of holding time provided higher value of density (5.89 $Mg.m^{-3}$) of 98% relative density. Densification was found to accelerate without any substantial grain growth when the relative density lower than 95%. The thread of higher holding time effect applied to result of Young's modulus, Vickers hardness and Fracture toughness of the samples.

References

[1] B. Basu, 'Toughening of yttria-stabilised tetragonal zirconia ceramics',*International Materials Reviews*, vol. 50, no. 4, pp. 239-256, 2005.

[2] S. Ramesh, S. Meenaloshini, C. Tan, W. Chew and W. Teng, 'Effect of manganese oxide on the sintered properties and low temperature degradation of Y-TZP ceramics', *Ceramics International*, vol. 34, no. 7, pp. 1603-1608, 2008.

[3] Dentalaegis.com,2015. [Online]. Available: https://www.dentalaegis.com/media/11191/. [Accessed: 07- Oct- 2015].

[4] R. McMeeking, A.G. Evans, Mechanics of transformation toughening in brittle materials, J. Am. Ceram. Soc. 65 (1982) 242-246.

[5] K. Kobayashi, H. Kuwajima, T. Masaki, Phase change and mechanical properties of ZrO_2-Y_2O_3 solid electrolyte after ageing, Solid State Ionics 3/4 (1988) 489-495.

[6] L. Hallmann, P. Ulmer, E. Reusser, M. Louvel and C. Hämmerle, 'Effect of dopants and sintering temperature on microstructure and low temperature degradation of dental Y-TZP-zirconia', *Journal of the European Ceramic Society*, vol. 32, no. 16, pp. 4091-4104, 2012.

[7] F. Guo and P. Xiao, 'Effect of Fe2O3 doping on sintering of yttria-stabilized zirconia', *Journal of the European Ceramic Society*, vol. 32, no. 16, pp. 4157-4164, 2012.

[8] X. Wang, P. Chen and I. Chen, 'Two-Step Sintering of Ceramics with Constant Grain-Size, I. Y2O3', *Journal of the American Ceramic Society*, vol. 89, no. 2, pp. 431-437, 2006.

[9] P. Bowen and C. Carry, 'From powders to sintered pieces: forming, transformations and sintering of nanostructured ceramic oxides', *Powder Technology*, vol. 128, no. 2-3, pp. 248-255, 2002.

[10] A. Rittidech and N. Suekwamsue, 'Influence of yttria additives on structural, microstructural and mechanical properties of alumina–zirconia composites prepared by two-stage sintering', *Ceramics International*, vol. 41, pp. S123-S126, 2015.

[11] Kyoritsu-kcm.co.jp, 'High-Purity Zirconia / KCM Corporation', 2015. [Online]. Available: http://www.kyoritsu-kcm.co.jp/english/new_material/new_material_01.html. [Accessed: 18- Nov- 2015].

[12] Reade.com, 'Hematite Powder / Red Iron Oxide (Fe2O3) from READE', 2015. [Online]. Available: http://www.reade.com/products/35-oxides-metallic-powders/251-red-iron-oxide-ferric-oxide-fe203-iron-iii-oxide-jewelers-rouge-iron-sesquioxide-anhydrous-iron-oxide-cas-1309-37-1-red-ochre-mil-i-706a-specular-iron-english-red-mars-red-red-iron-trioxide-indian-red-. [Accessed: 18- Nov- 2015].

Numerical Modal Analysis and Design of Piezoelectric Energy Harvester

Shaun Tan Soon Xie[1*], Assoc. Prof. Dr. Mohammad Hosseini Fouladi[1]
[1]*Taylors University, No. 1 Jalan Taylor's, 47500 Subang Jaya, Selangor DE, Malaysia*

*shauntan290993@hotmail.com

Abstract
Energy is consumed all around us but we are bound to lose energy in the form of heat or vibrations; one way to alleviate these losses is to convert said energy into electricity via a process known as energy harvesting. The aim of the research is to use human movement to generate electricity and hence to design a piezoelectric energy harvester (PZH) as the power source. Since the maximum frequency of any human movement can be assumed to be about 5 Hz, the PZH as per the research has to be designed to accommodate the abovementioned target frequency range in order to produce a maximum power output; this is achieved with the aid of numerical modal analysis. Literature research is conducted and various designs have been criticized; some of which include the cantilever, the cymbal-drum structure, wafer shells and a recently identified helical structure. It is concluded that the helical structure meets the required conditions for efficient operation, which are flexibility, relatively low resonant frequency and low initial loading conditions. Designs were modelled and tested for their resonant frequencies; the best result achieved was approximately 83 Hz. Further development needs to be done to analyse its power output and further research will be done in an attempt to bring down the resonant frequency of the design.

Keywords: Piezoelectric, energy harvesting, modal analysis, energy generation

1. Introduction

Energy harvesting has been a great interest over the past decade because of the need of an alternative wireless electrical power supply whose purpose is to replace the conventional chemical battery. Most interests focus in the use of a piezoelectric device to extract, or rather to harvest the aforementioned energy from its surroundings. Piezoelectric materials generate electricity when said material is deformed by a small percentage of its original shape.

Early developments show that vibration as an energy source is successfully converted into electrical energy but is only truly efficient when the vibration source

operates at resonance; that is the efficiency of these harvesters suffers a huge drop if the input frequency does not match the natural frequency of the harvester. Hence, either the resonant frequency of the device has to be reduced or its resulting power has to be magnified. The research aims to use human movement to generate electricity and therefore to design a piezoelectric energy harvester, hereon known as PZH, as a power source for a hypothetical wireless miniature device that would operate while on the human body; some examples include a pacemaker or a battery charger installed in a shoe. Previous iterations of PZHs completed by former students have a resonant frequency of approximately 80 Hz. Since the human is assumed to only be able to produce an average frequency of about 5 Hz via any kind of movement, the PZH needs to be redesigned to harvest energy at much lower frequencies in order to be useful for this particular application.

It is hypothesized that the resonant frequency of PZHs can be reduced to that of ambient vibrations through numerical modal analysis. Through modeling and simulation software, it is possible to design a PZH that caters to specific needs, as well as avoid any additional costs that may incur from experimental methods.

Most of the literature available defines energy harvesting as the capturing of small amounts of energy from the surrounding energy sources, thereby accumulating them and storing that energy for later use. The primary intended use of this energy is to power wireless systems and other forms of microelectromechanical systems (MEMS) technology; specifically to use these harvesters as alternatives to the conventional chemical battery. While energy harvesting plants are able to generate up to kW and even MW levels of power [1], this research only is limited to the generation of mW levels, or to a lesser extent μW levels of electrical power. This literature review highlights the various ways of harvesting energy from ambient vibration using different designs. The key characteristics of each design will be summarized at the end of the review.

1.1 Cantilever Beams

The cantilever-based energy harvester as shown in Fig. 1 [2] is perhaps the most commonly researched type of piezoelectric energy harvester. Kim et al. [3] states that a cantilever type energy harvesting system has a relatively simple structure and can produce a large deformation under vibration. It consists of a cantilever beam with a piezoelectric device attached along the beam. A proof mass is also added to provide the necessary inertial force.

Depending on the overall geometry of the harvester and the mass, the beam will have a particular resonant frequency; the power output of the harvester will be at maximum only when the system is resonating. The resonant frequency of all cantilever-based energy harvesters varies with the length and width of the beam, the proof mass and the resistive load of the device.

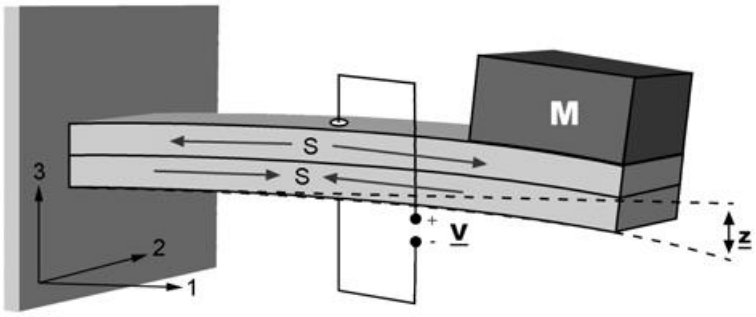


Figure 1. A two-layer beam mounted as a cantilever. [2]

The maximum power varies, but is generally in the order of μW. Due to its geometry, cantilever-based harvesters can be complex in design and yet also be useful in small-scale applications. However, it is prone to cracking and buckling as its mechanical properties are not great. Power output of cantilever-based harvesters depends on the geometry of the setup; the key parameters being the excitation frequency and initial force.

1.2 Wafer Stacks

The wafer-stack configuration as shown in Fig. 2 and Fig. 3 is one in which piezoelectric layers are placed on top of each other to create an energy harvester [4]. Energy is generated by the stack when it experiences a deformation, in this case compression. For testing purposes, a compressive harmonic force is applied on the stack. Power output varies from one design to another, but highly depends on the compressive force acting on the stack. An increase in the compressive force and input frequency results in a greater power output. This design is suitable for high-stress applications such as harvesting energy from compression in buildings [4] or absorbing compression from vehicles on traffic roads [5]. Furthermore, this design does not require a large input frequency, typically 10 Hz [4,5] as most of the power comes from the compressive forces.

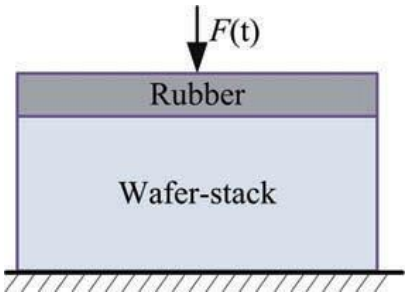


Figure 2. Construction of the piezoelectric stack. [4]

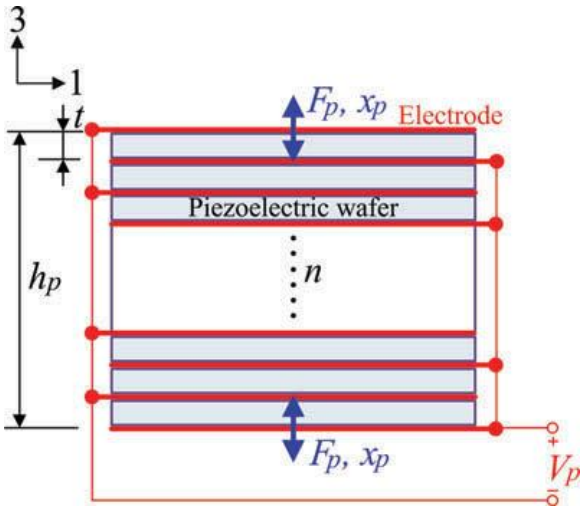


Figure 3. Longitudinal mode of the piezoelectric stack. [4]

A disadvantage specific to this research is that this design requires a large compressive force usually in the order of kN. Fig. 4 illustrates this disadvantage and shows the voltage output of a design produced by Jiang et al. [6]. Wafer stacks can produce up to 100 mW of power with the appropriate design [4-6].

1.3 Cymbal Structures

Cymbal structures as shown in Fig. 5 are structures which consist of a PZT disk fitted in between two studded metal caps and generate power under compression [7]. While similar to the wafer-stack in concept, its applications are otherwise different. The cymbal structure does not require a high pre-stress load (although a higher amount is preferred) [8] and is thus best suited towards smaller applications but however requires a high operational frequency of about 100 Hz to produce a decent power output. Larger structures can be used to accommodate greater forces such as on automobile engines. A cymbal prototype developed by Kim et al. [7] can produce up to 35 mW of power depending on the resistive load of the circuitry.

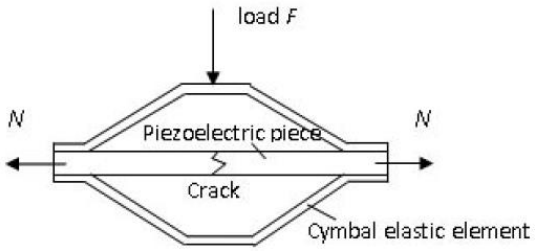


Figure 5. Cymbal structure piezoelectric energy harvester. [9]

Drums as shown in Fig. 7 are a variant of the cymbal structure where a disk is fitted between two PZT rings; the operation principle otherwise remains similar. The key difference is that the drum is mechanically stronger and can operate on very high frequencies (approx. 1 kHz) whereas power output is reduced [8].

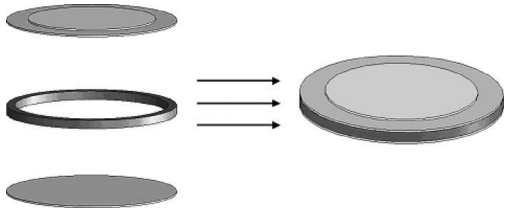


Figure 7. Schematic diagram of a piezoelectric drum transducer. [8]

1.4 Helix Structures

The helical structure as shown in Fig. 9 is a device which consists of two counter-wound helical structures around a structure made of an elastic fabric string. The inner fabric helix is used to separate the outer piezoelectric helix from the core to obtain a highly stretchable device that is to be applied on the human body. Yun et al. [10] had produced a prototype that, when stretched by 20% of its length, generated a maximum power output of 0.6 mW at an operational frequency of 4 Hz. Their prototype exhibited a general increase in power output when the input frequency and stretch amount is increased. Power output is also increased when the resistive load of the circuitry is increased, but only up to a certain point before it starts to drop. Some potential applications highlighted by them using this design include energy harvesting backpacks and even shoes from stretching and contraction.

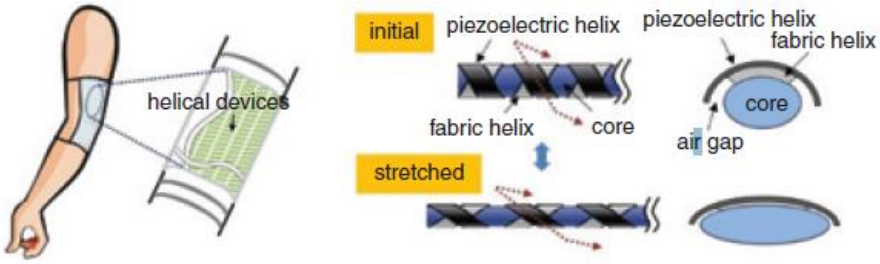


Figure 9. Schematic view of helical device. [10]

1.5 Design Selection

The helix design is accepted as the geometry to be studied as it is found to have the benefits of being flexible and being able to produce energy at very low frequencies; this result was verified experimentally by other researchers. Numerical modal analysis allows further development of this design and serves as the backbone of the study. The initial virtual design of the PZH element in this study is based heavily on the model from the experimental method and is used as a verification tool for comparing natural frequencies.

Table 1. Summary of various PZH designs

GEOMETRY	DESIGN	APPLICATION	EXCITATION
WAFER	Stacking PZT layers with protection	Large compression, frequency range <5Hz	External harmonic force (sine)
CANTILEVER	PZT mounted on cantilever beam with proof mass	Low frequency (unimorph), high frequency (bimorph), frequency range varies with design	Sine base excitation
DRUM	Ring fitted between two PZT plates	Variant of cymbal harvester	Cyclic loading
HELIX	Helical (PZT) structures around elastic core	Human body energy harvesting, frequency range <10Hz	External harmonic force (sine)
CYMBAL	PZT disk bonded to studded metal caps	Higher stress levels, frequency range ~100Hz	Cyclic loading

Table 2. Summary of various PZH designs (cont.)

GEOMETRY	FACTORS	POWER	BENEFITS
WAFER	Optimal load *R*, input amplitude, input freq.	Up to 100 mW	Low frequency, high durability
CANTILEVER	Optimal load *R*, resonate freq., geometry	μW range	Smaller devices
DRUM	Preload, optimal load *R*	Up to 10 mW	Reliable electrical/mechanical performance
HELIX	Excitation frequency, optimal load *R*	Up to 1 mW	Flexibility, high output, low frequency
CYMBAL	Type of PZT, optimal load *R*	Up to 30 mW	Less prone to cracking or buckling

2. Methodology

The research intended is fully quantitative; numerical analysis will be employed to evaluate the performance of the PZH design. The aforementioned methodology is summarized as shown in Fig. 12. However due to scope and time limitations, the study is only completed up to the data collection stage.

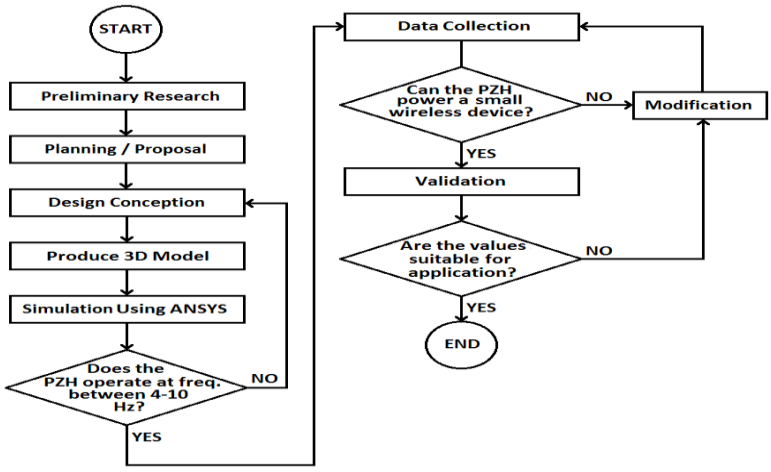


Figure 12. Estimated project flow chart

2.1 Project Overview

The aim of this project is purely numerical; experimental and analytical methods are not employed throughout the study. It is identified that future work involving experimental or analytical work may be required for further progress. The objective of this study is to conceive a design of a PZH, or a singular element of a PZH, whose natural frequencies are approximately 5 Hz and is coupled with the human body for energy harvesting. This frequency value is intended as human motion can be approximated as vibrations with such frequencies. Research is performed to identify the best design as each PZH has its own specifications and is suited to specific needs. Once the suitable frequency and load range are identified, the next step is to produce a 3D model using CAD software for simulation. Numerical modal analysis is then employed to determine the natural frequency of the system, or element where applicable. Should the natural frequency exceed the targeted range, redesign analysis are performed again. This process is continuously repeated until a desired shape is obtained. It is decided that the PZH is designed based on the helix structure. This design is proven to be able to operate at very low frequencies of fewer than 10 Hz [10] and is also shown to be elastic and flexible.

An initial design is conceived with further aid from literature encompassing such structures. The design is based on a singular element as previous researchers [10] have identified that the completed PZH is essentially an assembly of multiple elements and that power output increases linearly with the number of elements. The design of a singular element is simpler both in terms of the design as well as performing any future changes. Numerical modal analysis is then employed to evaluate its natural frequency to review its feasibility as a power source for a wireless device. Should the simulated frequency be less than satisfactory, modifications are made in attempt to further bring down (in most cases, the natural frequency of the element will be too high) the natural frequency of the PZH element.

2.2 Geometry Model

With all the considerations made, it is decided that the PZH will be based on the helical structure. A sample model is then prepared based on those identified in the literature. Fig. 13 shows a sample model created using Solidworks as the modeler.

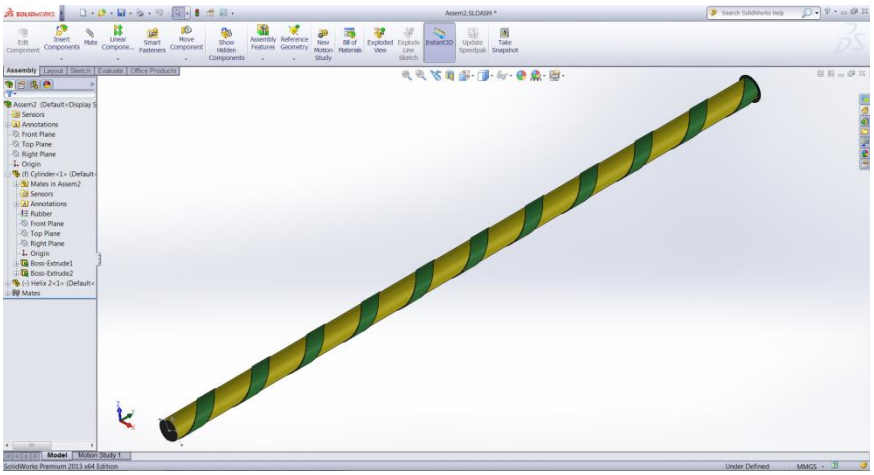


Figure 13. 3D model of assembly created using Solidworks.

The basic element of the PZH is essentially an elastic tubular core and a piezoelectric material wrapped in a single helix at 45 degrees from the longitudinal axis around the core. This basic element is to be assembled in a mesh or a weave to form an elastic device that can be worn by a person. The elasticity of the device allows piezoelectric conversion to take place from the deformation whenever the wearer produces a movement. This particular design assumes a rubber string of length 100 mm and diameter 3 mm as the core and polyvinylidene fluoride (PVDF) film of width 3 mm and thickness 100 μm as the piezoelectric material. The properties of both materials are listed in Table 3 below.

Table 3. Properties of rubber and PVDF.

Parameter	Rubber	PVDF
Elastic modulus (Nm^{-2})	6100000	3000000000 (in X)
Poisson's ratio	0.49	0.34 (in XY)
Shear modulus (Nm^{-2})	2900000	-
Mass density (kgm^{-3})	1000	1780
Tensile strength (Nm^{-2})	13787100	55000000 (in X)
Yield strength (Nm^{-2})	9237370	50000000
Thermal conductivity ($Wm^{-1}K^{-1}$)	0.14	0.2256
Specific heat ($Jkg^{-1}K^{-1}$)	-	1386

The above specifications are justified as researchers [10] have previously successfully conducted experimental trials using the aforementioned setup. A nominal 100 mm length of the core allows shorter analysis times as the design model is a lot simpler. The length of this elastic core can be varied to produce alternative results. In addition, other elastic materials may be considered. Rubber is used as the test material as its specifications are readily available for analysis. PVDF is used as the piezoelectric material as it has high strength, resistance to solvents and has a very low mass density, allowing the construction to be lightweight. Among other types of piezoelectric materials, PVDF can be easily acquired as thin film, further simplifying any potential manufacture processes should the study require experimentation.

To produce the design in Solidworks, a circle is first extruded to form a cylindrical tube. Following that, a thin film is sketched and wrapped around the cylinder to form the basic elemental assembly. Since performing everything mentioned results in only a single material property, the design will not be accurate. To form an assembly with two materials, two separate parts will be needed. As such, the helix wrap part of the assembly is produced by cutting (removing) the entire cylindrical tube, leaving only the helix behind. Both parts are then assembled together with another component of Solidworks using their own individual mechanical properties to form the PZH element.

3. Numerical Modal Analysis

Following the production of the geometric model, numerical modal analysis is employed with the aid of ANSYS software to determine the natural frequency of the system. Ideally, the model should have a natural frequency of approximately 5 Hz.

To initiate this process, the assembly file created using Solidworks must first be exported into a compatible file format, or more specifically the .IGES extension. The

model is then loaded using ANSYS Design Modeler and verified as errors with the design may occur when the model file is first imported into ANSYS. If no errors occur, it is then loaded into ANSYS Mechanical APDL to begin modal analysis. For this analysis, free boundary conditions are approximated on both ends as it will simplify simulation and make it easier to compare to researches based on experimental data. Figs. 14 to 17 show the results of the analysis using the fourth to seventh modes.

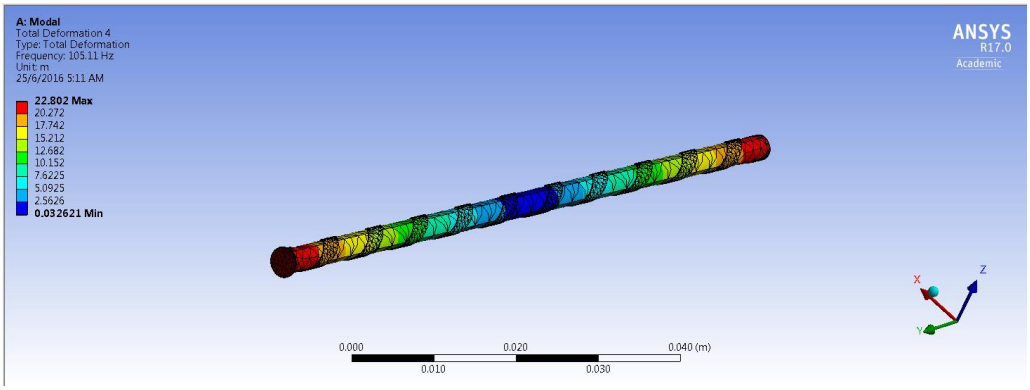


Figure 14. Mode shape at 105.11 Hz (4th mode).

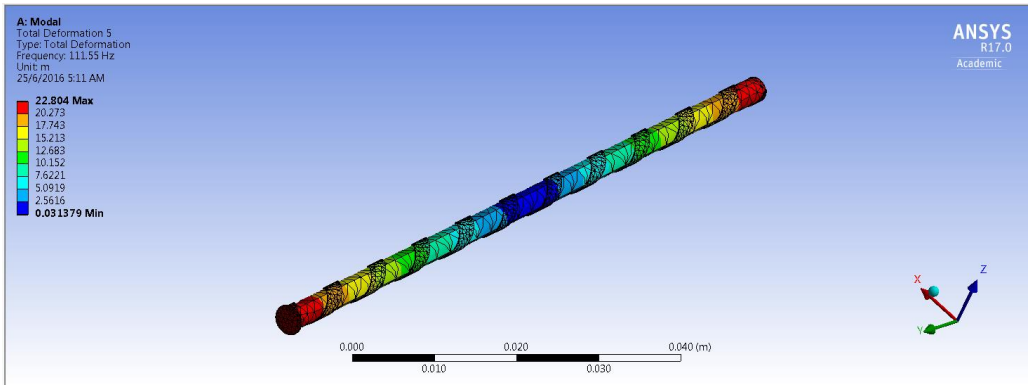


Figure 15. Mode shape at 111.55 Hz (5th mode)

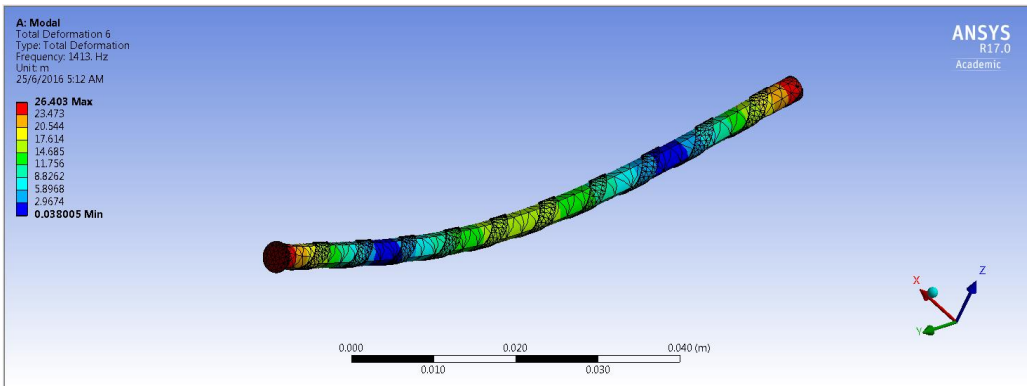


Figure 16. Mode shape at 1413.0 Hz (6th mode).

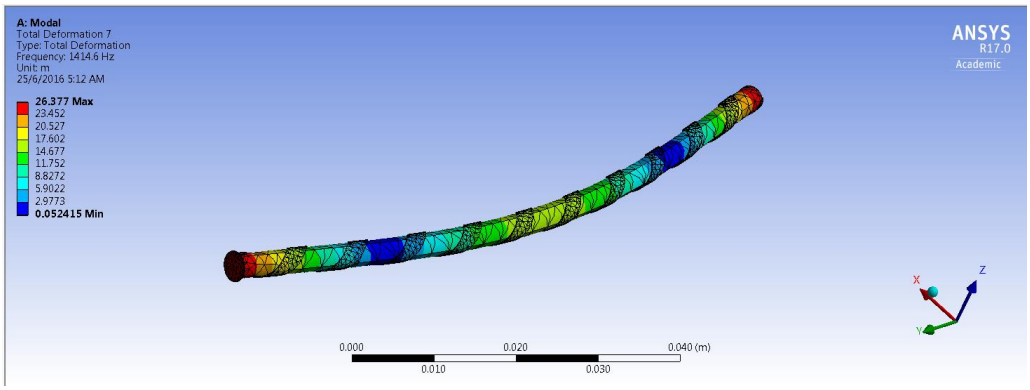


Figure 17. Mode shape at 1416.6 Hz (7th mode).

3.1 Initial Results

From the analysis, it can be identified that the lowest natural frequency of the system is approximately 105 Hz, which is far beyond the intended target of 5 Hz. Going beyond the fourth mode proves to be unhelpful as the frequencies only become higher beyond the fourth mode. The first three modes also prove to be unhelpful as those modes do not involve any deformation. In addition, their natural frequencies are often in the range of 0.01 Hz and lower and therefore do not reflect real world applications. Further improvement is required to bring down the natural frequency, either by changing the physical parameters or making a change to the overall design of the PZH.

3.2 Changing Helix Angle

Fig. 18 illustrates the change in frequency when the helix angle is changed to 30 degrees from the longitudinal axis. This mode shape results at the first mode and it is found to occur at 263.46 Hz, significantly higher than the initial set helix angle of 45 degrees. It is hypothesized that decreasing the helix angle increases the natural frequency of the element.

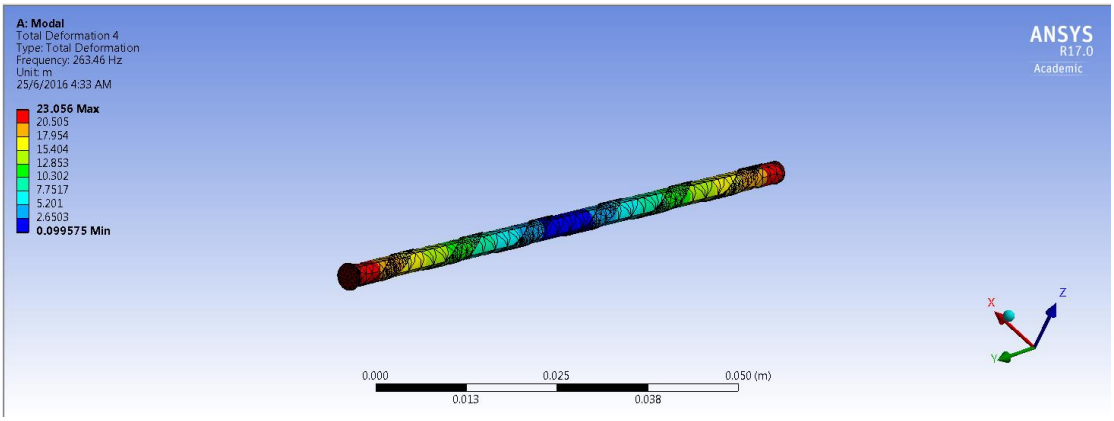


Figure 18. Mode shape at 263.46 Hz (4th mode, 30 degree helix).

Fig. 19 illustrates the change in natural frequency when the helix angle is changed to 60 degrees from the longitudinal axis. This mode shape results at the first mode and it is found to occur at 83.53 Hz, significantly better than the initial result. It is hypothesized that increasing the helix angle decreases the natural frequency of the element.

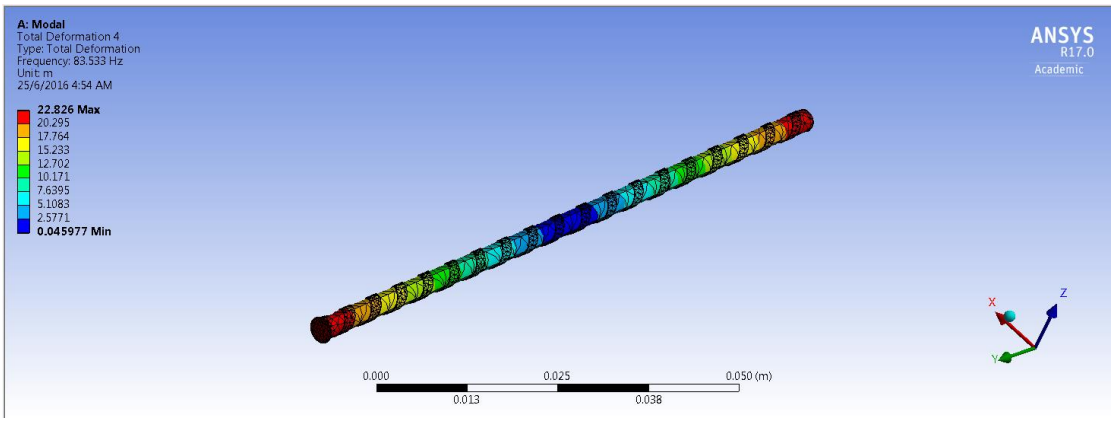


Figure 19. Mode shape at 83.53 Hz (4th mode, 60 degree helix).

There is a limitation of increasing the helix angle, mainly in CAD as the system cannot handle extremely large dimensions. Since the operation involves wrapping a sketch around a cylinder, a large angle would require a very large sketch to encompass the full length of the core. This is equally reflected in real world applications as a larger angle demands a much greater amount of PVDF film and would directly raise production costs.

4. Conclusion

Literature review has identified various types of PZHs to be considered, many of which have their own specialized uses. All of them have one thing in common; the energy generated by a PZH regardless of geometry is maximum at resonance; that is the PZH generates maximum energy when the input frequency matches the natural frequency of the system. Each design comes with their range of natural frequencies in which with numerical modal analysis, can be simulated and determined.

A conclusion was drawn to change the helix angle, believing that it affects the natural frequency of the element. Two new angles were proposed, one of which is 30 degrees from the longitudinal axis and the other at 60 degrees, both respectively below and above the initial set helix angle of 45 degrees. The smaller angle resulted in a much higher natural frequency, more than double the initial result at approximately 263.5 Hz whereas the larger angle resulted in a slightly reduced value at approximately 83.5 Hz. While not being the greatest result, this result does suggest that a larger helix angle generally results in a reduced natural frequency. There are limitations both in CAD and real world applications however; both relating to the area that can be sketched in the modeler, as well as the actual amount of PVDF film required for manufacture.

Using the information from numerical analysis, a prototype with the specifications as set in the study can be developed and tested experimentally to measure its power output. Another discrepancy with this study is that despite the fact that maximum energy generated by all vibration harvesters occurs only at resonance, it does not provide any indication that the PZH will be completely ineffective outside of this frequency range. This means that the output of the system can still be relatively high even if the system is not at resonance; however, additional efforts in the form experimental analysis are required to verify this claim. The obtained results can then be compared with those of other experimental researchers to determine any noticeable difference in output.

In addition to improving the natural frequency of the system, the power output of the system also needs to be identified to ensure that the system has some practical use in real world applications. For this, research on electronics and circuitry will have to be conducted. Since the scope of this study is purely numerical analysis, experimental and analytical methods are not performed and can be instead carried out following this study as a complement to determine potential uses of PZHs in the real world. Additionally, efforts can be made to identify raw power outputs of systems that are not necessarily at resonance as certain vibration energy harvesters are known to produce just as much power outside of resonance compared to other kinds of energy harvesters which operate solely at resonance.

Based on the research of others, it is also found that the helix structure serves as a high-potential foundation for PZHs of this type of applications as the other designs are simply better suited to cater industrial tier energy harvesting, that is harvesting energy in greater amounts. This is because helix designs are very suitable and compatible for the human body; they are flexible, they have the benefit of being elastic and durable, and their operational parameters, specifically their relatively low natural frequency and low loading requirements, are best for human body applications.

References

[1] Dagdeviren, C.; Yang, B.D.; Su, Y.; Tran, P.L.; Joe, P.; Anderson, E.; Xia, J.; Doraiswamy, V.; Dehdashti, B.; Feng, X.; *et al*. Conformal piezoelectric energy harvesting and storage from motions of the heart, lung, and diaphragm. *Proc*. *Natl*. *Acad*. *Sci*. *USA* 2014, *111*, 1927–1932.

[2] Roundy, S. and Wright, P. K., “A piezoelectric vibration based generator for wireless electronics,” Smart Materials and Structures, Vol. 13, No. 5, pp. 1131-1142, 2004.

[3] Kim, H.S., Kim, J.H., Kim, J.W., "A review of piezoelectric energy harvesting based on vibration," International Journal of Precision Engineering and Manufacturing, Vol. 12, No.6, pp. 1129-1141, 2011.

[4] Jiang, X.Z., Li, Y.C., Wang, J., Li, J.C., “Electromechanical modeling and experimental analysis of a compression-based piezoelectric vibration energy harvester,” International Journal of Smart and Nano Materials, Vol.5, No. 3, pp. 152-168, 2014.

[5] Jiang, X.Z., Li, Y.C., Li, J.C., Yao, J., “Journal of Renewable and Sustainable Energy, Vol. 6, 043110, 2014.

[6] Jiang, X.Z., Gu, X.Y., Wang, J., "Energy harvesting from large force vibrations using a piezoelectric wafer-stack harvester," International Journal of Applied Electromagnetics and mechanics, Vol. 46, pp. 979-990, 2014.
[7] Tressler, J.F., Howarth, T.R., Huang, D.H., "A comparison of the underwater acoustic performance of single crystal versus piezoelectric ceramic-based "cymbal" projectors," Journal of the Acoustical Society of America, Vol. 119, No. 2, pp. 879-889, 2008.
[8] Wang, S., Lam, K.H., Sun, C.L., Kwok, K.W., Lai, W.C., Guo, M.S., Zhao, X.Z., "Energy harvesting with piezoelectric drum transducer", Applied Physics Letters, Vol. 90, 113506, 2007.
[9] Li, X., Guo, M. and Dong, S., "A flex-compressive-mode piezoelectric transducer for mechanical vibration/strain energy harvesting," IEEE Transactions on Ultrasonics, Ferroelectrics and Frequency Control, Vol. 58, No. 4, pp. 698-703, 2011.
[10] Paradiso, J.A.; Starner, T. Energy scavenging for mobile and wireless electronics. *IEEE Pervas*. *Comput*. 2005, *4*, 18–27.

Experimental Analysis of Vibration of Chest Wall

Siti Sarah Bt Mohd. Ariff[1], Mohammad Hosseini[1], Narendiran Krishnasamy[2], Mohsen Nabi Poor[1], Satesh Narayana Namasivayam[1], Priya Madhavan[2], Wong Eng Hwa[2]

[1]*School of Engineering, Taylor's University, 47500, Subang Jaya, Selangor, Malaysia*
[2] *School of Medicine, Taylor's University, 47500, Subang Jaya, Selangor, Malaysia*

sitisarahmohdariff@sd.taylors.edu.my

Abstract
In the engineering field, machines are tested for health diagnosis through vibrational monitoring by studying the frequency content of said machines. By taking that same concept, it can be applied into the human health diagnosis by measuring the vibration of the human chest wall. This paper presents the experimental analysis of the human chest wall vibration on non-smokers, cigarette smokers, and electrical cigarette smokers. The aim of this study is to investigate the vibration measurements of the human chest wall of non-smokers, cigarette smokers, and electrical cigarette smokers in the hopes of benefiting future researchers in conducting human health diagnosis. The vibrational measurements are to be taken from 16 subjects (6 non-smokers, 5 cigarette smokers, and 5 electrical cigarette smokers) by using an accelerometer, a DAQ measurement hardware, a LabVIEW software for collecting data and a Matlab software for spectral analysis. The accelerometer will be secured by a trained doctor at two different locations of the chest wall; one directly above the left nipple and one directly below it. The raw signals will be presented in the time-domain, and will then be converted into the frequency domain through Fast Fourier Transform (FFT) algorithm. These spectral analyses include FFT analysis, Power Spectral Density (PSD) analysis, and Short-Time Fourier Transform analysis. The results for the measurements taken at above the left nipple showed no difference for all of the vibrational analyses, thus the author focused on the measurements taken from below the left nipple. It was found that the smokers show lower amplitude reading but higher frequency content based on the FFT and PSD analyses. It was noted that no difference can be seen through the STFT method. The vibration signals obtained from these subjects might give some insights to future researchers in conducting a human health diagnosis.

Keywords: Chest wall, vibration, human health diagnosis, FFT analysis, DAQ system.

1.0 Introduction

Vibration is known to be a dynamic phenomenon where it moves to-and-fro about equilibrium position. When taking vibration measurements, it can either be represented in the time domain or the frequency domain; the former shows the change in amplitude of vibration with time, whereas the latter describes it with the frequency spectrum [1]. These two domains are mathematically related via the Fourier Transform, which will be further discussed in Section 2.4.

In the engineering field, machine fault diagnosis and health monitoring is one of the main reasons vibration is measured. By conducting frequency analysis through measuring a machine's vibration, it can be tested to determine its lifespan as well as predicting any impending problems [1]. This technique involves taking the vibration measurement of a machine at good condition, and then monitoring it over time to study and observe any changes. These changes are usually an indication of possible problems, thus allowing preventive steps to be taken.

By taking that same principle, theoretically, it can be applied in the human health diagnosis whereby chest wall vibration measurements of smoking and non-smoking subjects are obtained. The frequency content in the smoking subjects might show some sort of an indicator of impending problems. The test subjects in the smoking category are then further divided into normal cigarette smokers and electrical cigarette smokers. The vibrational energy of these test subjects is to be studied to perform an educated human health diagnosis.

The human chest wall, which consists of structures such as the diaphragm, the ribcage and the abdomen, undergoes a dynamic motion during respiration [2]. This dynamic motion is referred to as vibrational energy at the human chest wall. Data on the chest wall vibration between different types of people have not yet been greatly quantified, especially between smoking and non-smoking subjects. This study of quantifying the human chest wall vibration between these subjects might offer some insights in the human health diagnosis.

Looking at it from a medical point of view, assessing the chest wall motion and its behaviour is a common medical practice. Medical students were taught to evaluate the chest wall expansion by placing their hands on the back of the patient; the thumb being on the midline section [3].

However, it is crucial to quantify these chest wall motions as a brilliant scholar, William Thomson Kelvin once said, "When you cannot express it in numbers, your knowledge is of a meager and unsatisfactory kind. You have scarcely, in your thoughts, advanced to the stage of science, whatever the matter may be" [4]. Therefore, the author will attempt to quantify these chest wall movements, specifically among smokers and non-smokers, by using a physical device.

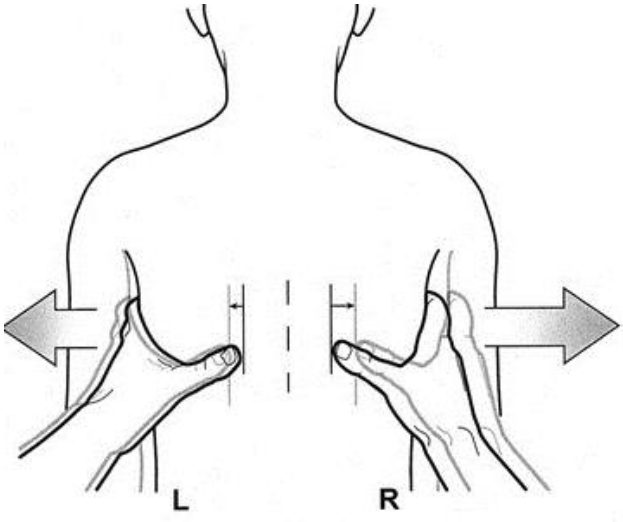


Figure 1: The Thumb Excursion Test Practiced in Medical School [3]

This physical device is called the DAQ system, which includes the accelerometer, the data acquisition (DAQ) measurement hardware, and the LabVIEW software installed on a Personal Computer (PC). In this case, the use of an accelerometer is to detect and take the reading of vibrational energy of the chest wall. It is generally known to convert a physical phenomenon (eg. vibration) into electrical signals [1]. These electrical signals will then be sent to the DAQ measurement hardware for signal conditioning and analog-to-digital conversion before they are sent to the PC for visualization of data.

The main objective of this study is to investigate the frequency content of the human chest wall vibration in non-smokers, cigarette smokers and electrical cigarette smokers, which might be beneficial for future researchers in conducting a human health diagnosis.

2.0 RESEARCH METHODOLOGY

2.1 Design of Experiment

The experiment includes the measuring of the chest wall vibration of smoking and non-smoking subjects; the smoking subjects will further consist of normal cigarette smokers and electrical cigarette smokers. There were 16 test subjects that volunteered in this experiment; 6 non-smokers, 5 cigarette smokers, and 5 electrical cigarette smokers. It should be taken into consideration that there was only one female test subject under the cigarette-smoking category. The other 15 test subjects were all males. All test subjects were aged between 22 – 27 years old. A short survey was conducted at the end of every experiment to find out about the test subject smoking habits and whether they have any other health issues, allowing the author to observe any correlation with the experimental results.



Figure 2: Taking of Measurements of a Test Subject in a Supine Position

The experiment was conducted at Clinical Skills Suite 2, which is located at Level 5, Block D, Taylor's University. The accelerometer was attached on the patient's chest with 3M medical tape, designed to be gentle on human skin as well as being secure enough for the sensor to take good measurements. It is worth noting that there were two different locations on the test subject's chest to take measurements from; one was directly below the left nipple and the other was above the left nipple. The placement of the accelerometer was done by a trained lecturer from School of Medicine.

As for the experimental equipment, the vibration measurement would use a DAQ system for measuring the signals. This DAQ system consists of mainly an accelerometer, DAQ hardware and computer software. The sensor used was a Bruel & Kjaer DeltaTron Accelerometer Type 4507 B with a frequency range of 0.3 Hz – 6 kHz as the sensor. The DAQ measurement hardware that will be used for this study is NI 9234 Module with 1-slot NI CompactDAQ Chassis with a maximum bandwidth of 23.04 kHz, which would be sufficient for the study of the human chest wall vibration. LabVIEW and Matlab will be used for data collection and data analysis respectively.

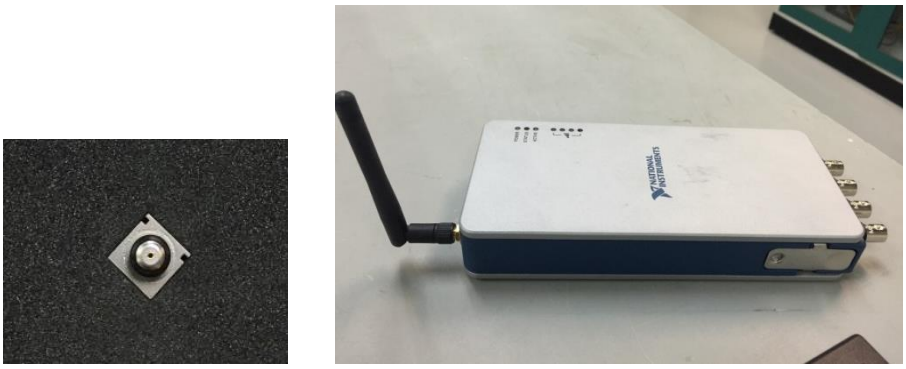


Figure 3: Bruel & Kjaer DeltaTron Accelerometer Type 4507 B and DAQ Measurement Hardware for this Experiment (picture taken by author)

This accelerometer was connected to the DAQ measurement hardware which is connected to the PC. During the collection of data, the patient will be in supine position in a relaxed state, while making no sudden movement as that might affect the data. Data collected from each patient will be stored into the PC.

2.2 Data Collection Parameters

The sampling frequency was determined by following the Nyquist Theorem which states that it should be at least 2.56 times greater than the highest frequency, f obtained in the measurement [5]. However, real world signals usually consist of frequency greater than the Nyquist frequency. Therefore, it is better to sample it at 5 to 10 times the highest frequency. If the sampling frequency is set less than 2f, the signal might be aliased. In other words, it might create false images of the signals at frequency below f, thus resulting in poor representation of the signal. By following the Nyquist Theorem, enough data is ensured to be collected in producing original signals, thus showing a better representation of data.

However, the author could not find information on what is the highest frequency given out by the chest wall during respiration. Therefore, literature reviews were conducted to find out what type of sampling rates used in experiments to measure the human breathing movement. Fekr and his team used a sampling rate of 50 Hz to measure respiration rate [6], Kikhia and his team used 10 Hz to measure body movement [7], and Dehkordi and his team used 500 Hz to record upper-body acceleration and the movement of chest and abdomen wall [8]. The author decided to use 500 Hz as a sampling rate to be safe, as too low of a sampling rate will cause aliasing. The signals were collected for at 15000 samples with a sampling frequency of 500 Hz.

2.3 Signal Processing

2.3.1 Pre-Processing Process

Before conducting the data analysis, a pre-processing stage was added. This pre-processing stage was necessary because it was seen that the time-domain signals were rather noisy, which might bury the desired frequency contents after signal processing. Therefore, a filter was needed to minimize or even eliminate this unwanted noise, thus achieving clearer results for the post-processing stage. A 2^{nd} order Butterworth low-pass filter was used with a cut-off frequency of 20 Hz.

2.3.2 Post-Processing & Analysis of Data

It is important to first familiarize oneself with the signal analysis and measurement workflow when taking the measurements, so that the author can perform the data collection and data analysis smoothly.

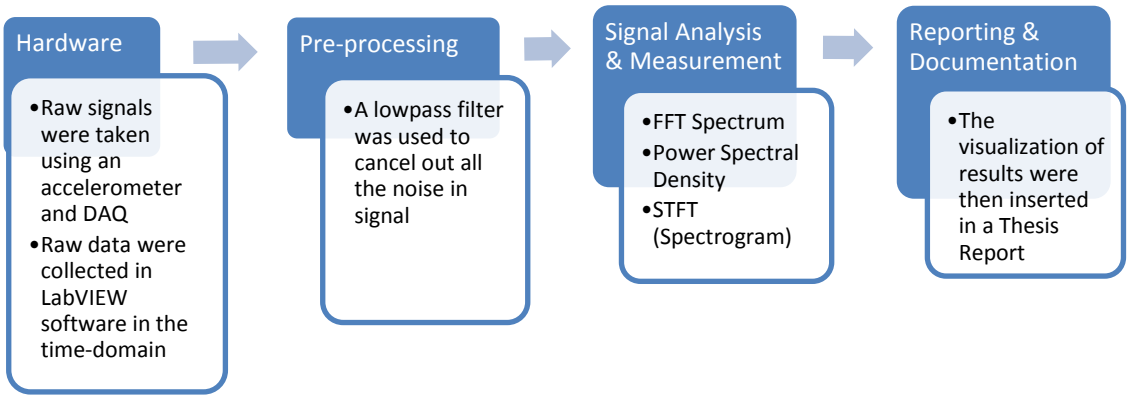


Figure 4: Signal Analysis & Measurement Workflow

After obtaining the results in LabVIEW, the data will be presented in the time domain, which shows the change in amplitude with time. However, the author will have to convert this data into the frequency domain, as it has been proven to give more information on the vibrational energy compared to the time domain [9]. This is known as spectral analysis. There are a few types of spectral analysis; however for this experiment, the author has chosen FFT spectrum analysis, PSD analysis, as well as STFT analysis. This conversion to the frequency domain graphs can be done by using Matlab software. To do this, the raw signals in time-domain collected in LabVIEW must first be imported into Matlab software in the form of excel files.

2.3.3 FFT

Signals in the time domain shows the amplitude of the signal at the moment of sampling. Fourier's theorem stated that the time domain waveform can consist of weighted sum of cosines and sines. This same waveform exists in the frequency domain as a pair of phase values and amplitude at each component frequency. The frequency spectrum provides more insights than the time signal domain [9], thus providing the author a higher understanding of the chest wall vibration.

It was found that the Fast Fourier Transform (FFT) method proved to be the most common type of analysis used [10]. FFT is an efficient and simple algorithm to calculate and compute Discrete Fourier Transform (DFT) [11]. To put it simply, FFT is most commonly used to convert time domain vibration signals into the frequency domain signals. It was also noted that the amplitude after FFT is performed would be the squared of the amplitude of the original signal.

Through FFT analysis technique, researchers are able to study the frequency pattern of a certain body or system that experiences some sort of vibration energy. In this study, the FFT function in Matlab was used to obtain this FFT spectrum, displaying

the frequency content of the signals along the x-axis. The frequency unit was hertz whereas the amplitude unit was G^2.

2.3.4 Power Spectral Density

As mentioned previously, the power in each frequency component of the signal after performing DFT/FFT can be obtained by squaring the amplitude or magnitude of that said frequency component [5]. Power spectral density (PSD) is used in measuring the power intensity of a signal in the frequency-domain. It is computed from the FFT spectrum of said signal. The units used for PSD is typically power per unit frequency. In this case, the unit is G^2/Hz since the measurement signal was in G, which equates to approximately 9.81 m/s^2. The frequency (Hz) value in the unit G^2/Hz represents the bandwidth rather than the frequency on the x-axis [12].

In this experiment, it was decided that this PSD spectral analysis should be conducted using Matlab, which might show some difference in pattern in the chest wall vibrational energy of the smokers and non-smokers. The number of FFT points and its window length were both set as 10,000 in Matlab as this showed a good frequency resolution. This particular number was obtained by the author by using the trial and error method to find good resolution. It was noted that the increment of window length and number of FFT points increase resolution.

2.3.5 STFT

STFT analysis converts the time domain signal into time and frequency localization, which gives information on the time and frequency of an event. The graph of STFT is known as a spectrogram. The magnitude of a signal is represented using a colour bar. There should be a compromise in choosing the window size of this analysis to make sure good representation of both time and frequency. Window size of 100 samples and number of FFT points of 2000 provided the best time and frequency resolution for this experiment.

3.0 RESULTS

There were three types of data analysis done on the vibrational signals; FFT analysis, PSD analysis and STFT analysis for both below and above the left nipple area. However, it was observed that the STFT or the spectrogram analysis does not show much difference between the three groups of people. Therefore, the other two analyses would be the focus in this discussion section.

Moreover, the vibrational measurements at above the left nipple area showed no difference between smokers and non-smokers, whereas there is a noticeable difference in the vibrational measurements at below the left nipple area. This is because more moving structures can be detected here such as the lungs, the heart, as well as the abdominal muscles which are moving while breathing. Due to this reason, the data for all spectral analysis on the vibrational measurements at above the left nipple area would be excluded here as well.

Based on the results, there was no noticeable difference between the normal cigarette smokers and the electrical cigarette smokers, which might be because the fact

that electrical cigarettes are fairly new in the market to have had a huge impact on the person's breathing pattern. Moreover, all of the electrical cigarette test subjects were cigarette smokers prior to switching to electrical cigarette smokers. For better representation of data, the author has combined the electrical cigarette smokers into one group, which is labelled as the smokers. Below are the results for PSD and FFT spectrum estimates for smokers and non-smokers that are obtained from Matlab interactive tool called Signal Processing Toolbox. It is noted that the results shown in the tables below do not include some exceptions by some test subjects. However, it will still be discussed below.

Table 1: FFT Spectrum Estimate for Smokers and Non-Smokers

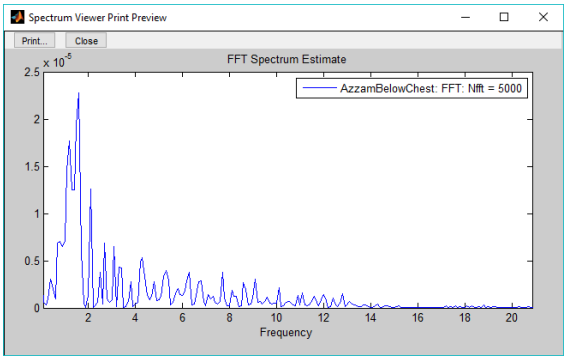
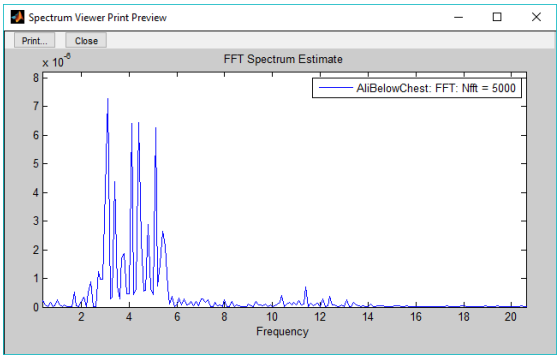
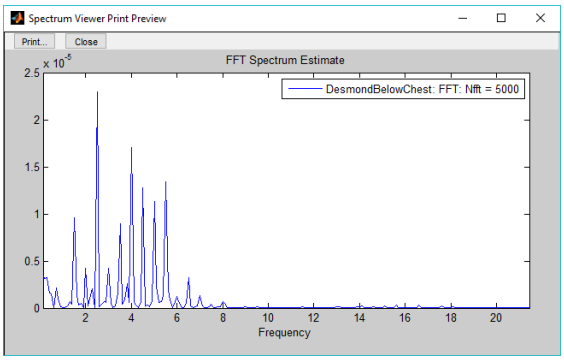
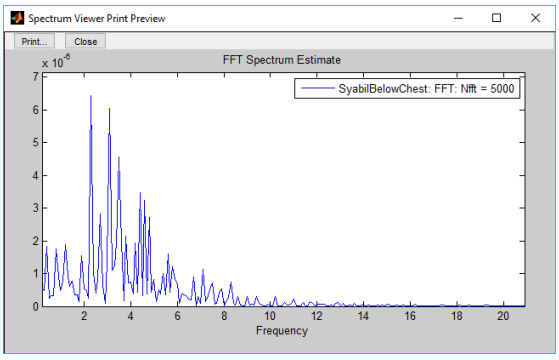
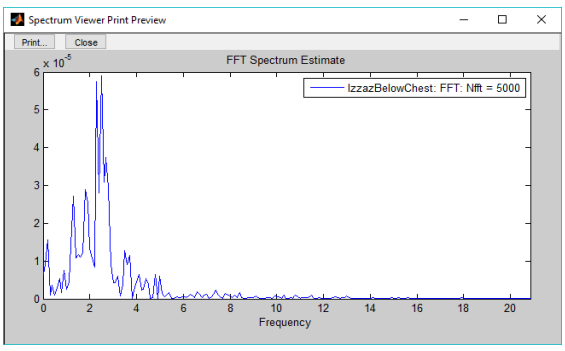
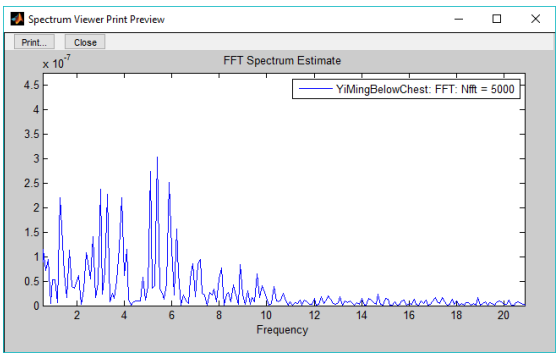
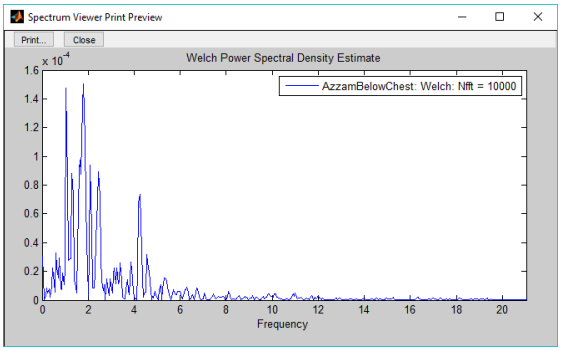
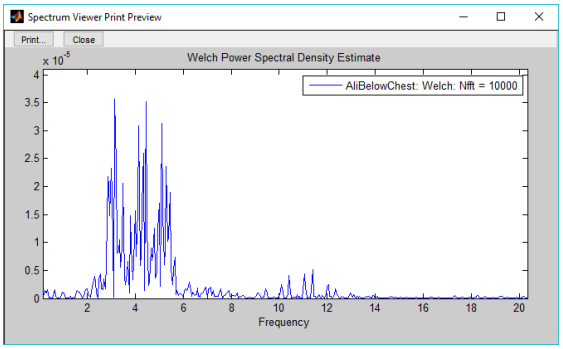
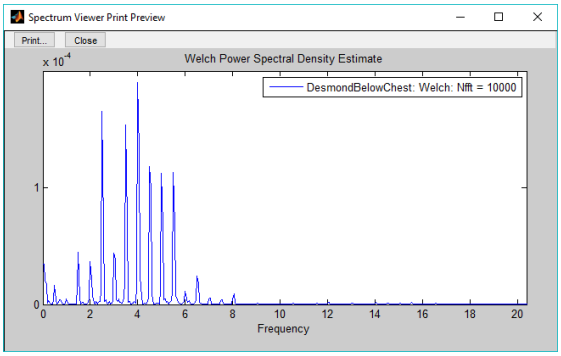
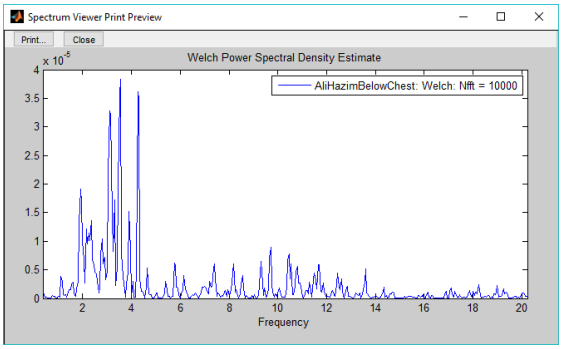
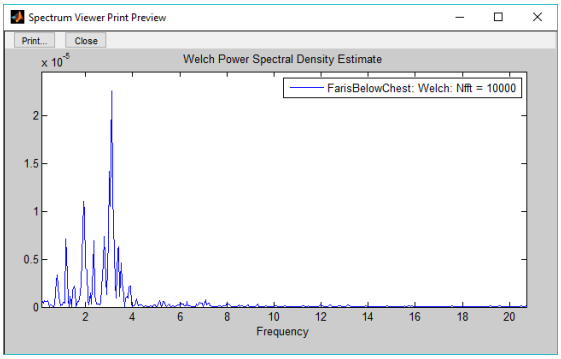
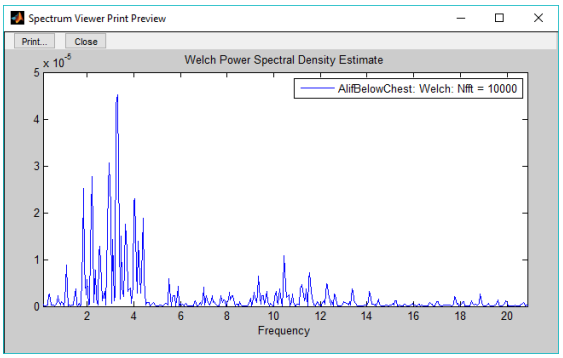
FFT Spectrum Estimate	
Non-Smokers	Smokers
	
	
	

Table 2: Power Spectral Density for Smokers and Non-Smokers

PSD Estimate	
Non-Smokers	Smokers
	
	
	

The first thing to note is that the all of the signals seem to be harmonic signals. In other words, the frequency components that were obtained in the graphs were multiples of the fundamental frequency. These frequency components are known to be harmonics. Considering that the signals are heartbeat signals, this would make sense as a heartbeat motion consists of a highly repeatable series of sine and cosine waveform. It is known that all harmonic signals are periodic as well.

As can be seen in the FFT spectrum estimate, the amplitude values for non-smokers are generally higher than the smokers. Referring to the PSD analysis, there is more noticeable frequency content after 10 Hz for the smokers when compared to non-smokers. However, it is noted that the higher frequency content for both smokers and non-smokers lie in between the range of 1 Hz – 6 Hz. Both of these analyses have shown

that non-smokers have higher amplitude but lower frequency, whereas the smokers have lower amplitude reading but higher frequency.

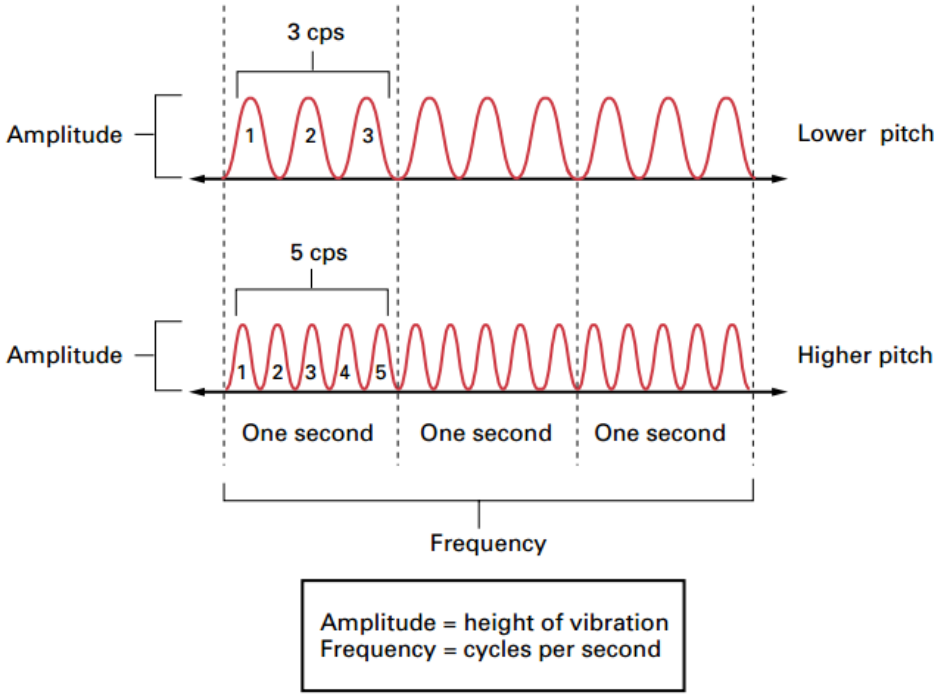


Figure 5: Percussion Pitch [13]

Referring to Figure 5, the relationship of frequency and amplitude of the human body is shown. Percussion is a method used to cause sound vibration on the human body by striking an object against another. The sound vibrations are produced by density of the body's underlying structures. The amplitude represents the height or depth of vibration, whereas the frequency represents the number of cycles per second. The concept of pitch can be described with frequency. The diagram shows that lower frequency produces lower pitch, whereas higher frequency produces higher pitch. It is said that a more solid structure has higher pitch (higher frequency) and a softer intensity (lower amplitude), whereas a more air-filled structure has lower pitch (lower frequency) and a louder intensity (higher amplitude) [13]. This would mean that the frequency content and the amplitude depend on the air content and the nature of the structures present at the location of percussion.

Since the above measurements were all taken below the left nipple area, the nature of the structures is a constant. This would suggest that the non-smokers have more air content, meaning to say more air is present in the chest wall area when compared to the smokers. Moreover, the higher frequency in the smokers would suggest a more rapid breathing.

Air goes into the mouth and nose, passing through the trachea. The trachea then splits into two branches of bronchus, which are then separated further into bronchiole, which further separates into the air sacs, known as the alveoli. Surrounding an alveolus, there are capillary tubes that carry pure blood and impure blood. The gas exchange between oxygen and carbon dioxide happens at the alveolus. The air that was breathed in carries oxygen that enters the lungs, and is then delivered to the bloodstream through

the alveoli; whereas carbon dioxide from the bloodstream is diffused into the alveoli, through the lungs, and is exhaled through the mouth and nose.

In a smoker, some lung tissue would be loss. Lung tissues referred here would be the air sac and tubular structures that carry the air to the air sacs (alveoli). The loss of these lung tissues will cause a block in the bronchiole, or may even cause the alveoli to lose its elastic recoiling capacity. Even though smokers can inhale well, the air may not reach the terminal air sacs due to the blockage at the bronchiole. When the air doesn't reach these terminal air sacs, there will be no gas exchange. Moreover, the elastic recoiling of the alveoli has to happen for gas exchange to happen. Consequently, there is more carbon dioxide present than oxygen. The brain detects this slack of oxygen, which in turn triggers the respiration action, thus increasing the breathing rate. Severe cases would cause the person to start panting.

As mentioned, the results in the table above do not include some exceptions. However, it is important to note these exceptions. Based on all the FFT spectrum results, 90% of the smokers showed amplitude readings less than 1×10^{-5} G^2, whereas 50% of non-smokers showed amplitude more than 1×10^{-5} G^2. However, this low percentage of non-smokers might be contributed to two things; the test subjects for non-smokers are much less than that of smokers, and that 2 out of 6 non-smokers have a BMI of more than 30, which by the standards equate to being obese [14]. The thicker layer of the chest wall due to the fat causes the sound transmission to be diminished, thus resulting in lower amplitude.

Based on all the PSD results, 90% of non-smokers showed no noticeable frequency contents above 10 Hz, whereas 80% of smokers showed noticeable frequency contents after this point. It is important to take note of the exceptions, as it may be correlated to any health issues. The other 10% exception of non-smokers showed a little bit of frequency content above 10 Hz, however it is very little. The other 20% of smokers showed little to no frequency content above 10 Hz, possibly due to the fact that these test subjects have only smoked for only 2 – 4 years.

4.0 CONCLUSION & FUTURE WORK

4.1 Conclusion

The measurement readings taken at above the left nipple area have not shown any significant difference, thus it can be concluded that a more accurate reading of the chest wall structure can be taken from below the left nipple area. Based on the FFT spectrum analysis, the amplitude of smokers was observed to be less than that of non-smokers. Based on the PSD analysis, most of the frequency contents with high amplitude are all concentrated between 1 Hz – 6 Hz for all test subjects. However, the smokers have frequency peaks more than 10 Hz whereas the non-smokers show almost no peaks at all after this point. The low amplitude and high frequency of the chest wall structure show would suggest that smokers breathe more rapidly than non-smokers in order to inhale more oxygen. The results of this experiment might be of use for future researchers in conducting a human health diagnosis.

4.2 Future Work

This study was limited to only smoking and non-smoking test subjects. Perhaps future work can study the vibration of the human chest wall of people with severe health issues or respiratory problems.

REFERENCE *(should not be numbered)*

[1] M. Serridge and T. R. Licht, *Accelerometers Piezoelectric and Vibration Preamplifiers. Theory and Application Handbook*. 1987.
[2] P. Seddon, "Options for Assessing and Measuring Chest Wall Motion.," *Paediatr. Respir. Rev.*, vol. 16, no. 1, pp. 3–10, 2015.
[3] R. M. Campbell, *VEPTR Expansion Thoracoplasty*. 2011.
[4] W. T. Kelvin, *Popular lectures and addresses*, no. v. 1. Macmillan & co., 1889.
[5] L. R. Van Bedaf, L. Heesink, and E. Geuze, "Pre-processing of Electromyography Startle Data : a Novel Semi-Automatic Method," no. September, pp. 2–3, 2014.
[6] A. R. Fekr, M. Janidarmian, K. Radecka, and Z. Zilic, "A Medical Cloud-Based Platform for Respiration Rate Measurement and Hierarchical Classification of Breath Disorders," no. case 1, pp. 11204–11224, 2014.
[7] B. Kikhia, M. Gomez, and L. L. Jimé, "Analyzing Body Movements within the Laban Effort Framework Using a Single Accelerometer," pp. 5725–5741, 2014.
[8] P. Dehkordi and K. Tavakolian, "Assessment of respiratory flow and efforts using upper ‐ body acceleration," pp. 653–661, 2014.
[9] S. Mohanta and U. C. Pati, "Monitoring and Analysis of Vibration Signal Based On Virtual Instrumentation," no. 1, pp. 3–8, 2013.
[10] P. A. Delgado-arredondo, A. Garcia-perez, D. Morinigo-sotelo, R. A. Osornio-rios, J. G. Avina-cervantes, H. Rostro-gonzalez, and R. D. J. Romero-troncoso, "Comparative Study of Time-Frequency Decomposition Techniques for Fault Detection in Induction Motors Using Vibration Analysis during Startup Transient," vol. 2015, 2015.
[11] S. Narwade, P. Kulkarni, and C. Y. Patil, "Fault Detection of Induction Motor Using Current and Vibration Monitoring," no. 4, 2013.
[12] F. Use, "Signal Processing Toolbox For Use with M ATLAB," *Analysis*, p. 800, 2001.
[13] J. Melorose, R. Perroy, and S. Careas, *Pocket Guide for Nursing Health Assessment*, vol. 1. 2015.
[14] National Institutes of Health and and B. I. National Heart, Lung, "Clinical guidelines on the identification, evaluation, and treatment of overweight and obesity in adults: The Evidence Report.," *NIH Publ.*, vol. 98–4083, no. Suppl 2, p. 51S–209S, 1998.

Numerical Analysis of the Shape of Dimple on the Aerodynamic Efficiency of NACA 0012 Airfoil

Zheng Pei Soh[1], Abdulkareem Shafiq Mahdi Al-Obaidi[1*]

[1]*School of Engineering, Taylor's University, Malaysia.*

[*]Abdulkareem.Mahdi@taylors.edu.my

Abstract
Aerodynamic efficiency can be improved by adding dimples, vortex generator, suction effect on boundary layer and more. Research show that adding dimples on the airfoil does improve the aerodynamic efficiency by delaying the separation of the flow. The purpose of this paper is to identify whether adding dimples on the surface of the standard NACA0012 airfoil will improve the aerodynamic efficiency, also to identify what is the impact on aerodynamic efficiency when the geometry of dimple changes. The main outcome of this research is to provide the best geometry of dimple which provides the highest aerodynamic efficiency. The geometry that considered in this study are round, square, triangle and ellipse. Besides the geometry of the dimple, different configurations of placing the dimple were also studied in this project. There are three different configurations that have been studied in this project, which is placing the dimple on the upper surface, lower surface as well as both upper and lower surface. In this study, the simulation is performed by using the Spalart-Allmaras turbulent model of the ANSYS's Fluent analysis system. The outcome of this study shows that, the best geometry for the dimple is ellipse. Ellipse's dimple increased the aerodynamic efficiency of the airfoil by 6.24 % at 5° Angle of Attack and 3% at 10° Angle of Attack. Besides that, the results also show that placing the dimple on the lower surface of the airfoil is the best configuration compared with placing the dimple on the top surface and both top and lower surfaces of the airfoil.

Keywords: Aerodynamic efficiency, NACA 0012 airfoil, dimple, lift, drag.

1. Introduction

The study which is related to aerodynamics has become one of the hot topics recently. According to "Science Direct" the number of journals or articles that related to aerodynamics has increased from 2095 in the year of 2010 to 4165 in the year of 2015. The study of aerodynamics is important, as it allows human to fly in an object (aircraft) which is heavier than the air. It is a study which emphasizing on the forces and the resulting motion of an object when it is moving through the air [1]. Everything

that moves through a medium is affected by aerodynamics [2]. According to National Aeronautics and Space Administration (NASA), the aerodynamic study on the flying objects is dealing with the 4 forces acting on it, which is lift, weight, drag and thrust forces. Since the main study of this project is focusing on the aerodynamics of an airfoil where the weight and thrust forces are not directly related, hence only the lift and drag forces will be taken into consideration in this paper. Lift force of on aircraft was mainly generated by the wings itself. The streamline design of the wings allow the air to flow faster at the upper surface of the wings which causes the pressure acting on the upper surface of the wings to be lower by comparing to the pressure acting on the lower surface of the wings, and hence the lift force is generated due to the pressure difference. The lift force is commonly expressed as the relation between the lift coefficient, density of air, velocity of the aircraft and the wing's surface area.

The drag force is a force that only can be minimised but not neglected. It is a force exerted as the object moving through a medium. The viscosity, density of the medium, the shape of the object and the roughness of the object's surface are the factors which cause the drag force. In a more simple word, it is the force which restricts the object from moving. At subsonic speeds, drag is divided into two components; parasite drag and induced drag in addition to induced drag due to angle of attack. It is also sharing the same relation to the factor as the lift force, the only different is the lift coefficient in the lift force equation is replaced by drag coefficient in the drag force equation.

NACA 0012 airfoil is chosen as the based model in this project. The reason being is that many studies were conducted by using the NACA 0012 airfoil, hence there are many available results or data which can be used for validation or comparing purposes. Airfoil is the element of a wing, and wings are the important part of an aircraft whose main function is to generate lift force. In other words, improving the aerodynamic efficiency of the airfoil will directly improve the aerodynamic efficiency of the wing. This is also one of the reasons why the study is only conducted on the airfoil instead of the wing. Aerodynamic efficiency is defined as the ratio of lift coefficient over drag coefficient: $Aerodynamic\ Efficiency = \frac{C_L}{C_D}$. Hence, the aerodynamic efficiency can be improved by either increasing the lift coefficient or decreasing the drag coefficient. Generally, improving the aerodynamic efficiency reduces the operating cost of a commercial aircraft [3].

Surface modification is one of the methods that the researchers are working on to improve the aerodynamic efficiency of the airfoil. The introducing dimple on the airfoil is a type of surface modification. When the air flowed through the dimpled airfoil, a small separation bubble will form, and this phenomenon will cause the flow to be accelerated and the boundary condition will undergo a transition from laminar to turbulent flow. Hence delayed the flow separation, reduce the wake formation and improved the aerodynamic efficiency [4]. These are also one of the reasons why golf ball is designed to fill with dimples. A study was conducted to compare the aerodynamic efficiency of the smooth ball and golf ball and the result shows that the tangential forces create drag on the golf ball, however, it is only contributing 5 % out of the total drag which is relatively small. Moreover, the pressure drag of the golf ball is way smaller than the smooth ball due to dimple which the turbulent boundary layer. Thus, introducing dimple will decrease the pressure drag which reduces the total drag

and hence increase in the aerodynamic efficiency [5]. Another study also conducted on the golf ball, and the results show that both lift and drag forces increased when dimples are added to the surface of the golf ball. However, the lift force generated are way greater than the drag force; in a nutshell, it increases the trajectory of the golf ball [6].

Introducing dimple on the airfoil is not a new method which could use to improve the aerodynamic efficiency, there are lots of studies conducted in this specific area. For example, there is a study which specifically focusing on the aerodynamic efficiency of the NACA 2412 airfoil with varies depths of dimple. The results show that increasing the depths of dimple will increase the boundary layer, and hence, increase the stalling angle, which allows the airplanes to reach a specific altitude with a shorter period of time [7]. There is also another study which studies the effect of the configuration of the dimple on the aerodynamic efficiency. Two types of dimple's configuration were studied in the project which done by Livya et al, the outward dimple and the inward dimple. It is proved that having the inwards dimple configuration are more benefits than the outward dimple configuration and adding dimple on the airfoil does increase the aerodynamic efficiency as well as increase the stalling angle [8]. Although, studies have proved that adding dimple on the smooth airfoil will increase the aerodynamic efficiency, however there is a gap which has not been done by any studies, which is the shape of the dimple. The majority of the studies was only conducted by using the semi-spherical shape's dimple, however there is no further investigation or study conducted which determine the effect of the shape of dimple on the aerodynamic efficiency.

The main objective of this study is to numerically determine the effect of the shape of the dimple on the aerodynamic efficiency. However, in this study the main concern is only to analyse the effect of the dimple, the result obtained is not necessary to be improving the aerodynamic efficiency, it might actually worsen the aerodynamic efficiency. Hence, the main finding of this project is to determine how much different can the shape of dimple affect the aerodynamic efficiency. A numerical study was conducted by using the ANSYS Fluent solver to achieve the objective of the project. The shapes of the dimple was fixed to be round, square, triangle and ellipse. The number of the dimples is fixed as 1, and the location of the dimple is fixed at 20 % of the chord which is close to the location of which the flow separation begin to occur [9]. The study will also be conducted for positive angles of attack (AOA), such as 0°, 5° and 10°. AOA is defined as the angle between the chord line of the airfoil and the direction of the air flow.

2. Numerical Set-up

ANSYS Workbench 15 is used to conduct the study. All of the simulations were computed by using the FLUENT solver which are commonly used to compute Computational Fluid Dynamic (CFD). In order to have more accurate setup, some simulations were computed beforehand. The results obtained are then validated by comparing with the results obtained from articles.

2.1 Validation cases

In order to plot the airfoil accurately, the coordinate data of the NACA 0012 airfoil with 1 m chord length was obtained, then the 2D drawing of the airfoil was generated in Design Modeler (default CAD software of the ANSYS). After the airfoil's drawing was generated the next step is to determine which type of meshing topologies are more suitable for the study. Since the validation cases are to validate the set-up by comparing the result with published article's results, hence the C-domain or C-topologies was selected which is the same meshing topology applied in the reference articles. The C-domain are approximately 12.5 chord lengths away from the airfoil [10]. **Figure 1** illustrates the 2D drawing constructed in Design Modeler.

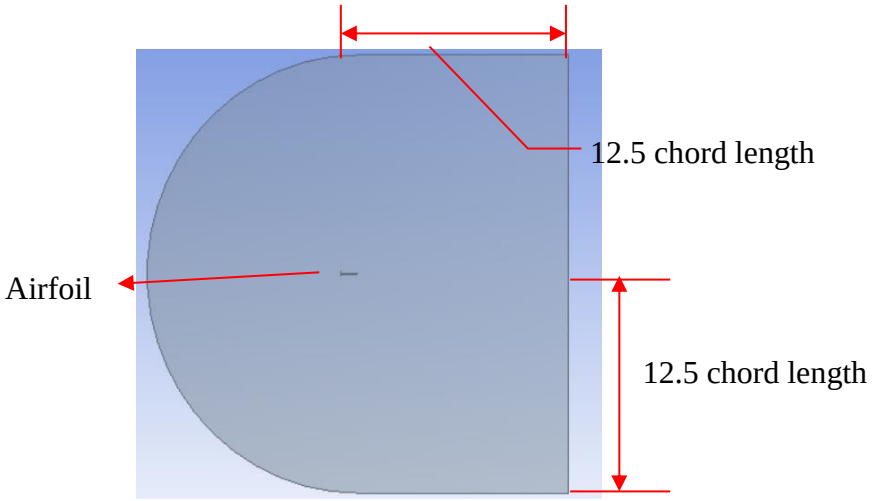


Figure 1. C-domain constructed in Design Modeler.

After the meshing topology was selected and created in Design Modeler, the C-domain was separated into four parts by using the "projection" function. This is to prepare for the "bias" setting in the meshing set-up. While in the meshing set up, the "bias: setting was used in order to create more meshing element as it comes closer to the airfoil. The more element around the airfoil, the more flow energy was captured and calculated by the system. **Figure 2** show the meshing created for the model.

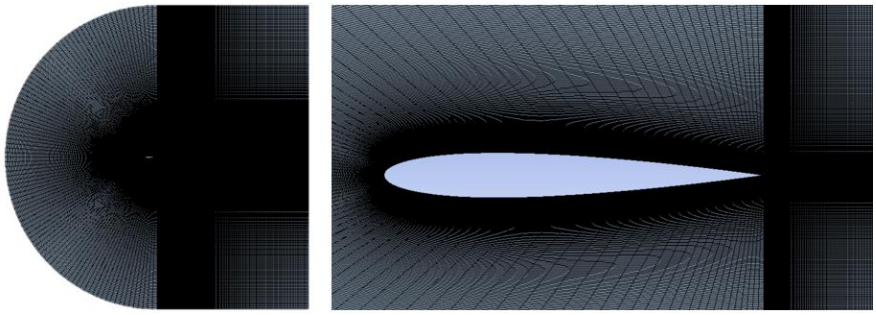


Figure 2. Meshing around the airfoil (left) and closed look on the airfoil (right)

It is important to check the meshing quality before continue to the following step, this is because meshing is one of the important factors which affects the accuracy of the results. According to one of the handbook or ANSYS guidebook created by ANSYS INC in 2013, low meshing quality will cause discretization errors, round-off errors, convergence difficulties, and nonscalable meshes which in overall will produce

non-reliable CFD results [11]. There are two factors that used to determine the meshing quality, there are the orthogonal quality and skewness. Skewness is calculated by using **Equation 1**. The smaller the skewness values, the lesser between the actual cell and the optimal cell. The skewness is in the range of 0 to 1, where 0 is the best and vice versa. It is acceptable for the skewness value which is less than 0.97. Beside skewness, the other factor which used to determine the meshing quality is the orthogonal quality. Which measure how far the meshing element from being a square in a scale of 0 to 1, where the orthogonal quality of 1 means that the meshing element is square in shape which is the most standard element shape. The minimum acceptable orthogonal quality is 0.15. Wall y plus is also another factor which can be used to determine the meshing quality, it must be below 30 in order to capture all the turbulent flow.

$$Skewness = \frac{Optomal\ cell\ size - actual\ cell\ size}{Optomal\ cell\ size} \tag{1}$$

After the meshing is done, the last step is to do the naming process before continue to the fluent set-up. In this process, the inlet, outlet, and airfoil (wall) will be named so that it would appear in the boundary condition tab in fluent. The naming was done according to the **Figure 3.**

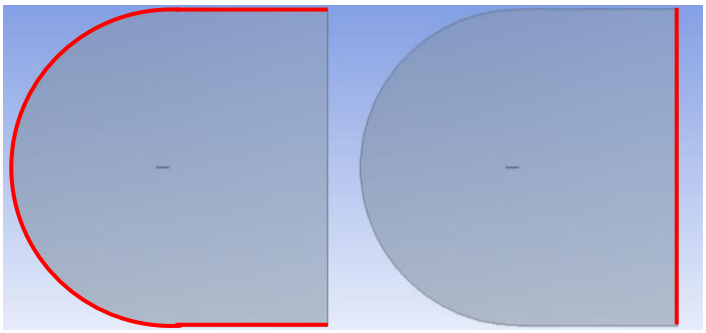


Figure 3. The red line on left figure are the inlet and red line on right figure are outlet.

The following step is the physical set-up which is done in the fluent software. The "double-decision" function was switched on, in order to obtain more accurate results. One of the studies shows that Spalart-Allmaras are of the best turbulent model which used to conduct the study on the aerodynamic of an airfoil[12]. The result shows that results obtained by using the Spalart-Allmaras model share the same trend as the experimental result, while on the other hand, the results obtained from K-epsilon turbulent model seems to be more inaccurate as the AOA increases. Hence, Spalart-Allmaras turbulent model was selected to conduct the simulation on this study. Every Reynolds-averaged Navier-Stokes Equation (RANS) models are formulated according to the general transport equations. Spalart-Allmaras is one of the RANS models which include an extra equation in the transport equation. The equation applied in Spalart-Allmaras are then become the equation which shown as **Equation 2.**

$$\frac{\partial \rho \tilde{\nu}}{\partial t} + \nabla \cdot \left(\rho \tilde{\nu} \boldsymbol{U} \right) = \nabla \cdot \left[\left(\mu + \rho \tilde{\nu} \right) \nabla \tilde{\nu} + C_{b2} \rho \frac{\partial \tilde{\nu}}{\partial x_k} \frac{\partial \tilde{\nu}}{\partial x_k} \right] + C_{b1} \rho \tilde{\nu} \tilde{\Omega} - C_{w1} \rho \left(\frac{\tilde{\nu}}{\kappa y} \right)^2 f_w \tag{2}$$

After the turbulent model was selected, the following step is to set-up the boundary condition. The results obtained can only be comparable with others researcher's results when both the studies are using the same Reynolds number. Reynold number is used measure the relative of inertia forces and viscous force, it can also be express as **Equation 3**.

$$Re = \frac{\rho v d}{\mu} \tag{3}$$

where,
Re (Reynold number) = $3x10^6$, ρ(density of the air) = 1.225 kg/$m^{3,}$ d (chord length) =1 m, and μ (the viscosity of the air) = $1.7894x10^{-5}$ kg/ms.

Hence, the velocity requires in order to achieve the same Reynolds number is 43.82 m/s. It will be troublesome the change the AOA of the airfoil as it would need to start all over again from the beginning by changing the geometry of the drawing. Since there is no distinction between the cases of a body moving through a stationary fluid and that of fluid moving with a constant velocity past a stationary body, changing the AOA of the airfoil can be just as simple as changing the direction of the flow acting to the airfoil. This can be done by resolving the velocity into x and y component by multiplying the velocity with sinθ for the velocity of y- component and cosθ for the velocity in the x-direction, where θ is the required AOA. The "simple" pressure-velocity coupling scheme was selected as it is also one of the common scheme which applied on studies which related to simulation of airflow over an airfoil [12,13]. In summary, all the set-up are summarised and as shown in **Table 1**.

Table 1. Summarised of fluent set-up.

Fluent set-up	
Model	Spalart-Allmaras
inlet	Velocity inlet with the velocity of 43.82 m/s
outlet	Pressure outlet with 0 gauge pressure (atmospheric pressure)
Solution Methods	SIMPLE
Solution Initialization	Standard Initialization, compute from inlet.

2.2 Actual cases (dimpled airfoil)

Since validation has done for the purpose to make sure that the set-up used is the correct setting, therefore the set-up for the actual cases will also be the same as what have been used in the validation cases. However, there are some minor changes in the meshing method for the actual cases due to the dimple which introduced on the airfoil. Hence, all the cases for actual study both smooth and dimpled airfoil were conducted by shifting the position of the airfoil to another position as shown in **Figure 4**. Method 1 is the method which used in the validation cases while method 2 is a new method which used in the study on the effect of the shape of the dimple on the aerodynamic efficiency of the airfoil.

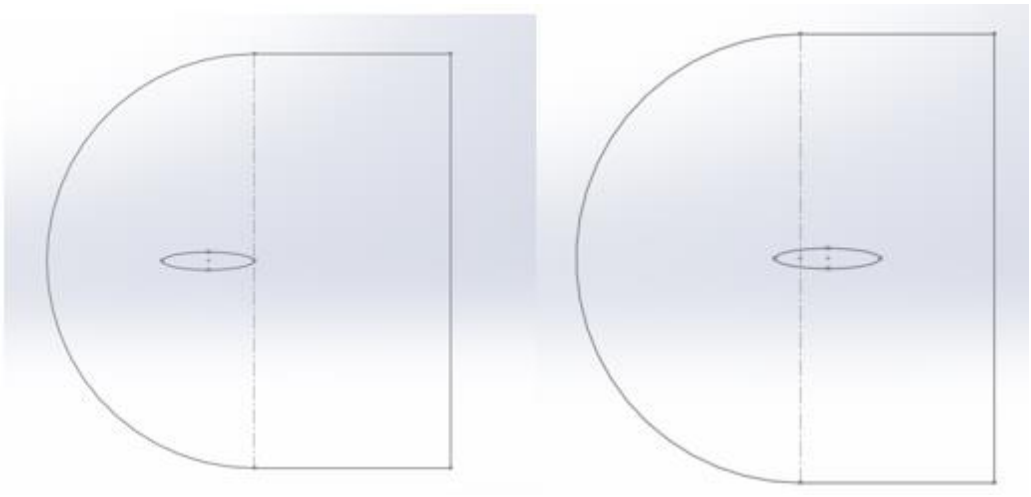


Figure 4. The (left) figure show is method 1, the (right) figure is the method 2.

The new method, method 2 is aligning the end of the C-shape (the construction line in Figure 5) at 0.15 of the chord length (just right before the location where the dimple is added), the reason being of why aligning the C shape at this location is to bring the asymmetric part of the dimpled airfoil in the square region of the C-domain. **Table 2** show the results obtained from two different meshing set-up on the round dimple's airfoil.

Table 2. Skewness and orthogonal quality of 2 different meshing set-up

		Average	Standard Deviation
orthogonal quality	Method 1	0.97	7.61E -02
	Method 2	0.99	2.03E -02
Skewness	Method 1	7.51E -02	0.13
	Method 2	4.94E -02	0.056

As mentioned in the previous section, the larger the orthogonal quality and the smaller the skewness the more accurate the result will be. According to table 2, method 2 will be a more suitable meshing set-up for the dimpled airfoil. **Figure 5** shows the differences between the two meshing method.

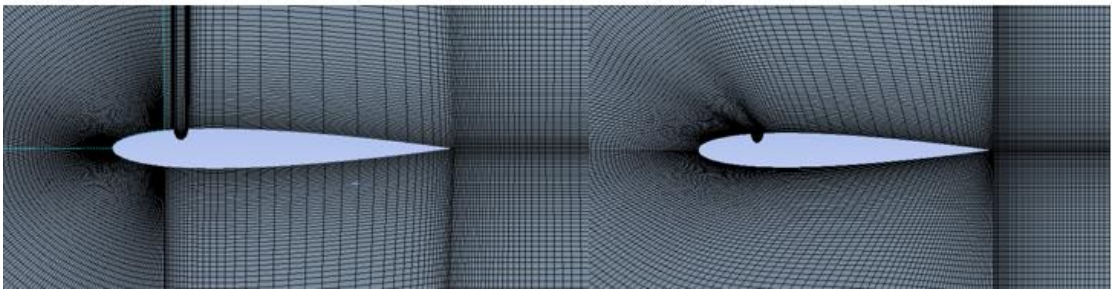


Figure 5. The meshing of method 2 (left) and method 1 (right)

Besides that, the Reynold number in the actual study will not be the same as the validation cases, which is $3x10^6$. There are odds that this study will be continued by carrying out the experimental analysis to validate the simulation results, therefore, the physical set-up for the actual cases is changed by according the limitation of the equipment available. The wind tunnel available in Taylor's University has the space limitation of 0.303 m height x 0.303 m width x 0.7 m length to fit the specimen [15]. Moreover, the power limitation of the motor is also limiting the speed of the airflow in the test section. Therefore, by taking into consideration of this two limitations, the actual case will be conducted on the airfoil which has the chord length of 0.1 m and the speed of the airflow has changed from 43.82 m/s to 10 m/s. In a nutshell, the dimpled airfoil simulation was conducted by using the new meshing method and the new physical set-up. Different shape of dimple was added on the smooth surface to determine its effect on the aerodynamic efficiency. Round shape, square shape, and triangle shape dimple are the same dimensions as shown in **Figure 6**. Whereas the ellipse shape will not be able to have the same dimension as the round. Therefore, the dimension of the ellipse was designed in such a way that it share the same sliced area as the round dimple. After some calculation, the width and depth of the ellipse dimple are 0.04 C and 0.03125 C. Besides the shape of the dimple, the configuration of the dimple was also studied in this project. All of the simulations were conducted on all the 4 shapes and 3 different configurations, which is adding the dimple on the top surface of the airfoil, on the bottom surface of the airfoil and lastly on both top and bottom surfaces of the airfoil. All dimples will be added at 20% of chord length as this is the location where the flow separation begins. The function of dimple is to delay the flow separation, hence the most suitable location to add the dimple will be located at 20% of the chord length away from the leading edge.

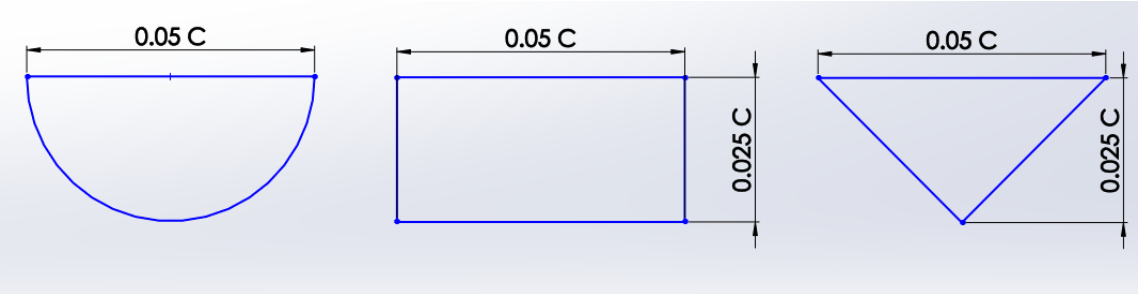


Figure 6. Dimension of the round, square, and triangle dimple.

3. Results and Discussions

The validation cases on the smooth airfoil were conducted for several AOA (0, 2, 4, 6, 8 and 10), and the results were validated by comparing to the results obtained from one the study which conducted by Eleni et al[16]. The result of comparison are shown in **Figure 7**.

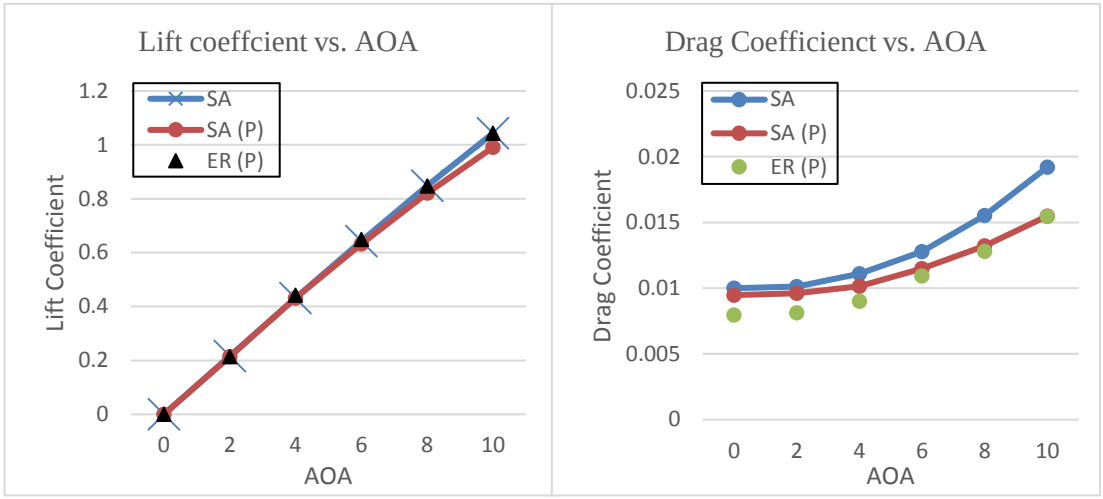


Figure 7. Comparison of both Lift and Drag coefficient vs. AOA.

where,
SA is Spalart-Allmaras model conducted in the current study
SA (P) is the results of Spalart-Allmaras model conducted by Eleni et al[16]
ER (P) is the experimental result that from Eleni used to compare the results[16]

According to Figure 8, there are almost negligible differences in the lift coefficient between the results obtained in the current study and Eleni's work[16]. There are obvious differences in the drag coefficient, however, some calculations have done on the percentage of differences, and the maximum percentage of differences obtained is 24.2% which is acceptable for the preliminary stage of design. As been told by project supervisor, according to the preliminary stage of design, a percentage of error is acceptable as long as it is below 30%.Both graphs show the same trend where the percentage of error increases as the AOA increases.

As mentioned in the previous section, the actual cases will be using the new method and set-up, hence simulations on the smooth airfoil were also conducted in order to compare the results with the dimpled airfoil. All the results were plotted and compared with the smooth airfoil. The acronyms used in **Figure 8 to 11** are explained in **Table 3**.

Table 3. Acronyms used in the following section.

Acronyms	Dimple's shape	Configuration of the dimple
RT,RB, RTB	Round	Top surface, Bottom surface, Top and Bottom surface
ST,SB,STB	Square	
TT,TB,TTB	Triangle	
ET,EB,ETB	Ellipse	

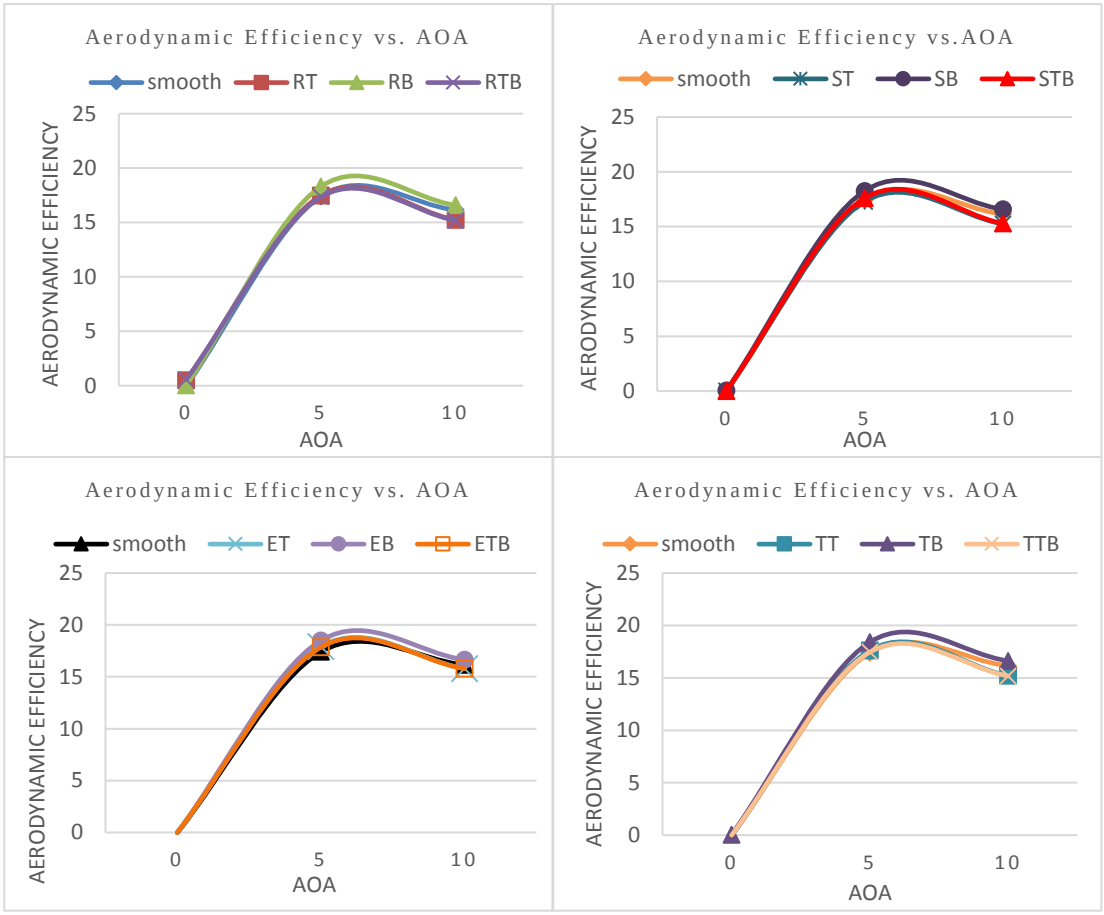


Figure 8. Aerodynamic efficiency vs. AOA for different shapes of dimple.

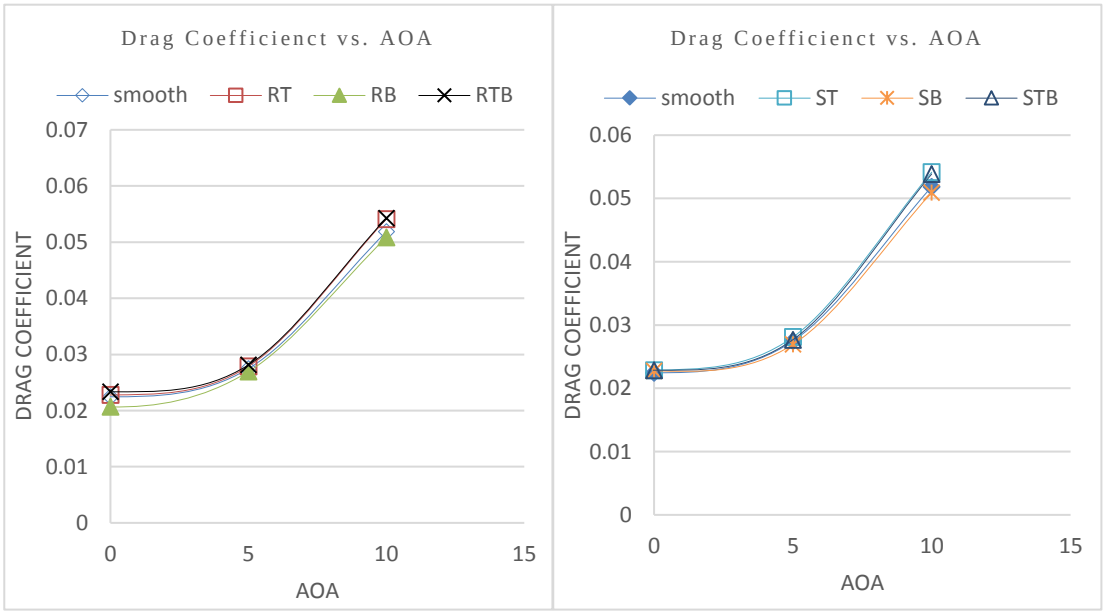


Figure 9. Drag coefficient vs. AOA for different shapes of dimple.

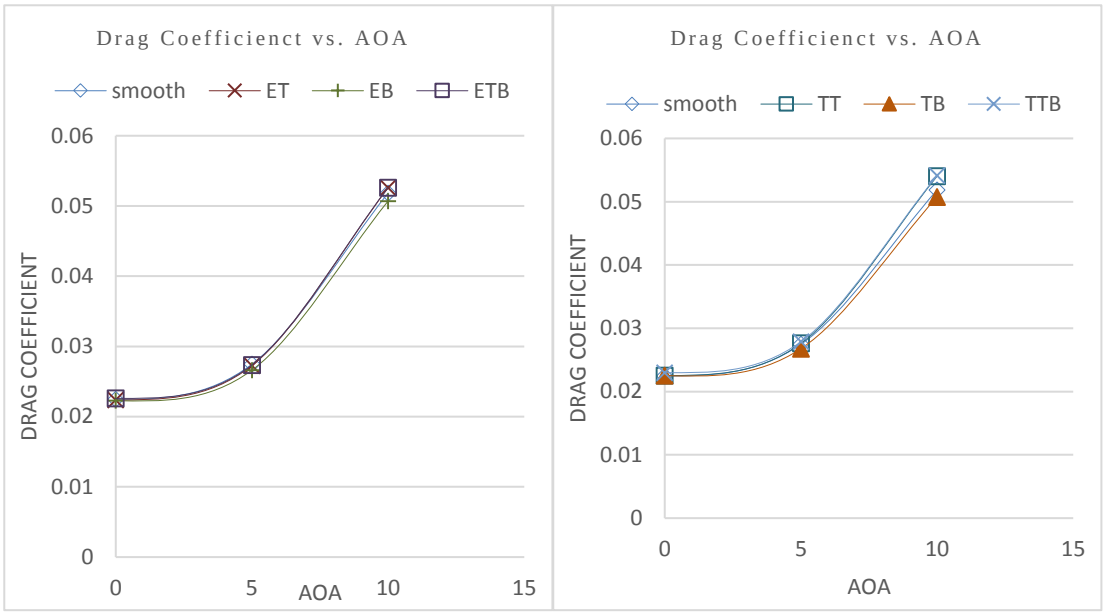


Figure10. Drag coefficient vs. AOA for different shapes of dimple.

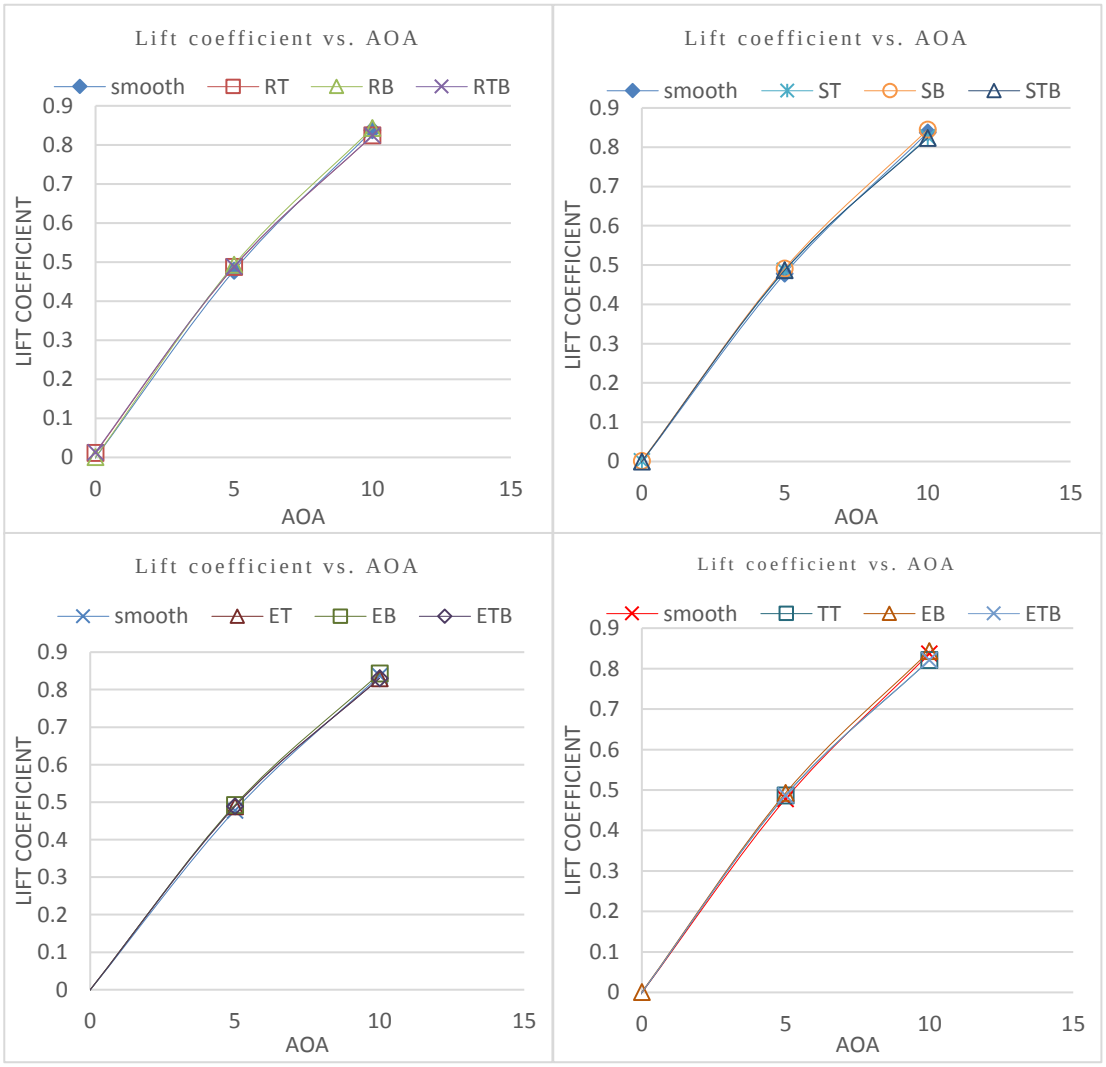


Figure 11. Lift coefficient vs. AOA for different shapes of dimple.

3.1 Effect of the configuration of the dimple

By referring to all those graphs plotted and shown in **Figures 8 to 11**, it can be concluded that adding dimple are not definitely increased the aerodynamic efficiency. Some of the models do show that the aerodynamic efficiency of the smooth airfoil is actually higher than the dimpled airfoil. However a trend was found from all of the data obtained, it seems that the configuration of dimple on the bottom surface of the airfoil are actually the best in terms of higher lift and lower drag coefficient as well as the higher aerodynamic efficiency, in all the 4 cases where the shape of the dimple are various. Although the difference in term of lift coefficient is not that clear or obvious, however there are a significant difference in terms of the drag coefficient which in a nutshell increases the aerodynamic efficiency of the airfoil. This is one of the new findings which has yet to seen in any other studies, most of the study was done with the dimple located on the top part of the surface only. The results obtained shows that, adding dimple on both top and bottom of the surface are very similar to the cases where the dimple is only added on the upper surface of the airfoil. Lift force is generated due to the pressure difference between the upper surface and the lower surface of the airfoil. As shown in **Figure 12**, the figure on the left show the velocity distribution contour of the flow when the dimple added on the bottom surface of the airfoil, and the figure on the right is the velocity distribution contour of the flow when the dimple added on the top surface of the airfoil. Turbulent flow will be generated inside of the dimple, and according to the **Figure 12**, it decreases the velocity of the flow, which in a nutshell increase the pressure at the location where the dimple is added. According to the Bernoulli's Principle, velocity is inversely proportional pressure, hence the surface where the dimple is added will have a higher pressure. There again explains the reason why adding dimple at the lower surface is better than adding dimple on the upper surface, which again justifies the results obtained in this study.

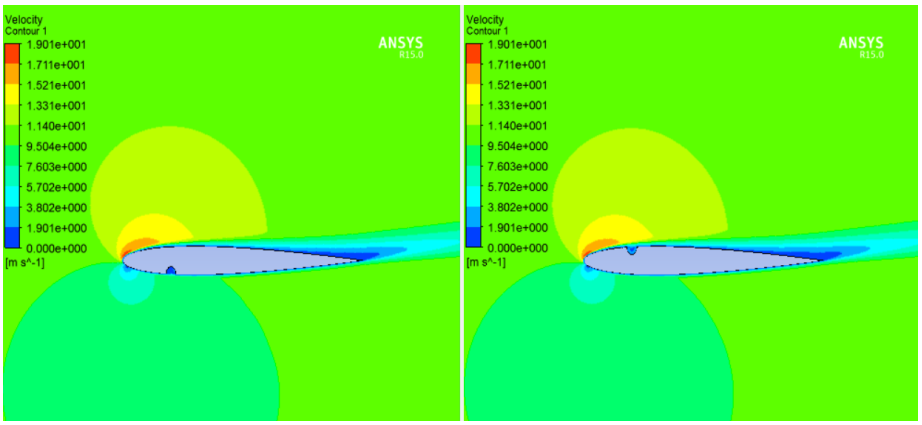


Figure 12.Velocity contour of the flow for both dimpled airfoil where the dimple is introduced at the bottom and the upper surface of the airfoil.

3. 2 Effect of the shape of dimple

Besides the location of the dimple, the main goal of this study is to determine which shape if dimple will bring the most effect on the aerodynamic efficiency. Some calculation has been done on the percentage of different between each of the model which has a dimple on the lower surface of the airfoil and the smooth airfoil. The results were tabulated as shown in **Table 4**.

Table 4. Percentage of different between each of the cases and smooth airfoil.

Type of airfoil	Aerodynamic Efficiency		Percentage of different by comparing with the smooth airfoil (%)	
	5 AOA	10 AOA	5 AOA	10 AOA
Smooth	17.40834	16.15208	-	-
Round dimpled	18.30901	16.58517	5.17	2.68
Square dimpled	18.25701	16.58350	4.88	2.67
Ellipse dimpled	18.49442	16.63623	**6.24**	**3.00**
Triangle dimpled	18.41197	16.61616	5.77	2.87

According to **Table 4**, the effect of dimple actually is more significant when it is at 5° AOA by comparing with 10° AOA. The most significant improvement of the aerodynamic efficiency from the smooth airfoil is the one with the ellipse dimple. In both AOA, the airfoil with ellipse dimple has the most significant improvement from the smooth airfoil in terms of aerodynamic efficiency. Even though the sliced area on both ellipse and round shape's dimple is the same, however there are significant different in the percentage of different with the smooth airfoil. This shows that, the width and depth of the dimple is one of the factor which will also affect the aerodynamic efficiency.

4. Conclusion and Future Work

The current study confirms that the most efficient or best dimple's shape is an ellipse. Introducing an ellipse dimple on the lower surface of the airfoil does improve the aerodynamic efficiency for all the AOA that have been studied in this paper. By comparing to the AOA that takes into consideration in this study, the effectiveness of the dimple is higher at low angle of attack for all of the shapes of dimple. However, further research could be carry on in order to justify the result obtained in this work. Experiments could be conducted to validate the simulation's results and also the observation obtained about the shape and location of the dimple. Moreover, more AOA and larger AOA should be conducted as the trend for the higher AOA might be different. Furthermore, some of the configuration of the dimple should be further research, such as the location to place the dimple, the size of the dimple as well as the effect of the number of dimples on the aerodynamic efficiency. Last but not least, the velocity used in this study are set to be 10 m/s, increasing velocity will affect the compressibility of the air, hence the result might be different if the same study was conducted by using different velocity.

References

[1] H. Nancy, "Beginner's Guide to Aerodynamics," 2015. [Online]. Available: https://www.grc.nasa.gov/www/k-12/airplane/bga.html. [Accessed: 17-May-2016].
[2] F. Wild, "What Is Aerodynamics?," May 2015.
[3] A. Hossain, N. Uddin, M. Mashud, and R. Mustak, "Experimental Study of Aerodynamic Characteristics Of Airfoils Using Different Shaped Dimples," pp. 13–17, 2015.
[4] D. Srivastav, "Flow Control over Airfoils using Different Shaped Dimples," vol. 33,

pp. 92–97, 2012.
[5] J. N. Libii, “Design of an experiment to test the effect of dimples on the magnitude of the drag force on a golf ball,” vol. 5, pp. 477–480, 2006.
[6] C.-H. Tai, J.-C. Leong, and C.-Y. Lin, “\n Effects of Golf Ball Dimple Configuration on Aerodynamics, Trajectory, and Acoustics\n ,” *J. Flow Vis. Image Process.*, vol. 14, pp. 183–200, 2007.
[7] E. C. Miller, “Effects on the Boundary Layer Caused by Inclusion of Dimples at Varying Depths,” *J. Aircr.*, vol. 49, pp. 969–972, 2012.
[8] E. Livya, G. Anitha, and P. Valli, “Aerodynamic Analysis of Dimple Effect on Aircraft Wing,” vol. 9, pp. 350–353, 2015.
[9] E. Colley, “Modelling Flow around a NACA 0012 foil,” *Report*, pp. 1–35, 2011.
[10] B. J Mullen, “FLUENT - Flow over an Airfoil - SimCafe,” 2015. [Online]. Available: https://confluence.cornell.edu/display/SIMULATION/FLUENT+-+Flow+over+an+Airfoil. [Accessed: 20-May-2016].
[11] A. INC, “Ask the Experts,” no. April, pp. 16–18, 2013.
[12] İ. Şahin and A. Acir, “Numerical and Experimental Investigations of Lift and Drag Performances of NACA 0015 Wind Turbine Airfoil,” *Int. J. Mater. Manuf.*, vol. 3, pp. 22–26, 2015.
[13] H. a Vaidya, “2D Analysis of Naca 4412 Airfoil,” vol. 2, pp. 1686–1691, 2013.
[14] R. H. C, M. N, and K. S, “Numerical Investigation of Flow Transition for Naca-4412 Airfoil Using Computational Fluid Dynamics,” *Int. J. Innov. Res. Sci. Eng. Technol.*, vol. 2, pp. 2778–2785, 2013.
[15] A.S.M Al-Obaidi and L.H. Yang, “Numerical and Experimental Assessment of Velocity with / without model inside Taylor ’ s Wind Tunnel Test Section,” , pp. 2, 2015.
[16] Douvi C. Eleni, T. I, Athanasios, and M. P.Dioissios, “Evaluation of the turbulence models for the simulation of the flow over a National Advisory Committee for Aeronautics (NACA) 0012 airfoil,” *J. Mech. Eng. Res.*, vol. 4, pp. 100–111, 2012.

eureca 2016 – Conference Paper
Paper Number 2ME26

Initial Look on Mechanical Power of a Kite-Based Airborne Wind Energy System in Malaysia for Microgeneration

Douglas Tong Kum Tien[1*], Tengku Mohamad Faris bin Tengku Salehudin[2]

[1]*School of Engineering, Taylor's University, Jalan Taylors, Subang Jaya, Malaysia*
[2]*School of Engineering, Taylor's University, Jalan Taylors, Subang Jaya, Malaysia*

[*]*DouglasKumTien.Tong@taylors.edu.my*

Abstract
Wind speeds in Malaysia is not great for energy harvesting. They are too intermittent and not very strong. This makes installation of traditional wind turbines not too feasible. However, using airborne wind energy system, (AWES) energy harvesting using wind might be possible. AWES can reach winds that are unreachable via normal means. Using the theory of rotational kinetic energy, an early look of power from wind was estimated in this paper. Arduino and an optical tachometer was used for the logging and measuring of data. Results shows that wind power generation from kite at the test site to be insignificant. The theoretical power however showed much better result. This is perhaps due to the fact of not-so-idealised situation during the experiment. Experimentation using better equipment at a better site by a multidisciplinary team is proposed as future work on this subject.

Keywords: Airborne Wind Energy System, kite power, low wind speed

1. Introduction

In the pursuit of clean and renewable energy, wind is increasingly becoming a popular field of study. From 1996 to 2012, the world's installed global capacity for wind generated power has increased from 6100 MW to 282430 MW [1], almost a 4630 % increase. This translates to roughly a three times increase of installed global capacity year-on-year for the past 16 years. Predominantly, these installations are found in Europe (38.67%) Asia (34.67%) and North America (23.92%).

When discussing wind energy, the first image that probably comes to mind are huge propellers propped onto massive white towers, spread out across an expansive flat grassy terrain, or at least somewhere along that line. These type of wind turbines are

classified as horizontal axis wind turbines or HAWT for short. These HAWTs typically about 100 m when measured from the hub height.

Deployed in installations known as wind farms, many countries harvest wind power as a source of alternative energy. These installations have shown various levels of success. For example, on the 20th December 2015, 45% of energy supplied to the state of Texas was from wind turbines [2]. Between 7th to 8th of May 2016, Germany's electricity price was so low, they were in the negative. In fact, they were basically paying users to use electricity [3]. That weekend, 87% of Germany's energy came from renewable sources. Lastly from the Land Down Under on the 16th of June 2016, Australia's energy needs were met by 8.5% via wind power, a record for them. And this was achieved without any addition to their wind power capacity for more than a year.

While various countries are reaping the benefit of wind energy, equatorial countries like Malaysia are less fortunate. According to a high altitude global wind energy density map drawn up by Archer and Caldeira [4], strong winds only grace those countries in the hemispheres as opposed to the ones lying on the equator. This is due to the formation of high altitude jet streams on the hemispherical sides of the globe. From that, it is clear that wind energy harvesting in Malaysia would not be as effective but this is not to mean that Malaysia could not reach a level of wind harvesting that is sufficient enough to be economical.

Research done by various researchers [1], [5] - [6] indicates that the average wind speeds found in Malaysia at a height of 10 m is less than 4.4 m/s. By that definition, Malaysia's wind can be categorised as a Class 1 wind, which is unsuitable for power generation, at least using typical wind turbines [7]. Despite that, there have been pilot projects to assess the suitability of using wind turbines as an alternative source of energy here in Malaysia. Such examples are like the ones and Terumbu Layang-Layang [8] and Perhentian Island [9]. However, according to Ho [7], these wind turbines were reported to be no longer operational.

Based on mentioned studies, a traditional wind farm does not show significant potential for long-term energy production through wind. If Malaysia are to harness the power of wind, a new approach may need to be evaluated. Such approach may lie in a new wind energy harvesting device called the airborne wind energy system (AWES).

One of the most basic form of AWES is a ground tethered wind turbine that flies or floats at high-altitude. The argument behind the concept of AWES is that the wind is stronger and more persistent at higher elevation. Such heights would be between 300 m to 1000 m [10]. A typical HAWT would usually stand at about 100 m measured from the hub height. Hence, if Malaysian wind is not suitable for HAWTs because the wind is too weak, there could be potential for power generation if the wind energy device could go higher.

Currently, the concept of AWES is popular in Europe and North America as many research groups, companies and start-ups are based there [10]. Hence, most work done on AWES has been primarily focused at locations where wind is much stronger than those found here in Malaysia. There has been no research done regarding the application of AWES for low wind speed countries or regions. Thus, the research

question stems from this gap in knowledge: How suitable are AWES for microgeneration under Malaysian wind condition?

Thus far, all research on AWES are focused on harnessing high-altitude jet streams. This is due to the fact interest in this new technology is promising in making wind generation for countries which uses wind turbines already even more economical. AWES use less material, lighter, less obtrusive and potentially have a higher power output than HAWTs. Thus far, no research on its application to make wind energy harvesting feasible for low wind speed countries have been done by any researcher. This technology has the potential to finally make wind power generation feasible for Malaysia. This research aims to demonstrate the effectiveness of such technology in Malaysia.

The objective of the experiment to assess the effectiveness of the AWES in terms of energy produced under Malaysian wind conditions for microgeneration.

2. Literature review

2.1.Airborne Wind Energy System Overview

The concept of AWES was introduced by Loyd in 1980 in his paper "Crosswind Kite Power" [11]. However, the idea did not garner any major interest until at least 10 years ago [10]. Since then, many groups had begun researching on the concept as a more promising alternative to the typical HAWT. Like during the early days of wind turbines, many groups also emerged with many new designs and concepts. Many designs like the Savonius and Darreus vertical axis wind turbines were explored before seemingly the tri-blade HAWTs took over as favourites. Right now, AWES seems to be in this phase of research, variety. Right now, there are probably a dozen different unique designs that are being developed, racing towards the mainstream. Generally, though, AWES can be seen as two major categories. They are:

1. Ground Generation AWES (GG-AWES)
2. Fly Generation AWES (FG-AWES)

The major distinction between these two is that GG-AWES has its generator placed on the ground while FG-AWES has its generator airborne.

GG-AWES generates electricity by relying on aerodynamic force generated by a kite or wing. Typically, a spool of tether is connected to a generator. Something like a drum will hold the spool. At the end of the tether, will be a kite or wing pulling the drum, rotating the generator. Once the drum runs out of tether, the generator will act as a motor and reel in the kite back. This process will use less energy than what was produced. The kite or wing will be having its angle of attack change during the reel-in and reel-out phase to either maximise or minimise lift [12]. Figure 1 shows a typical reel in and reel out phase of a GG-AWES.

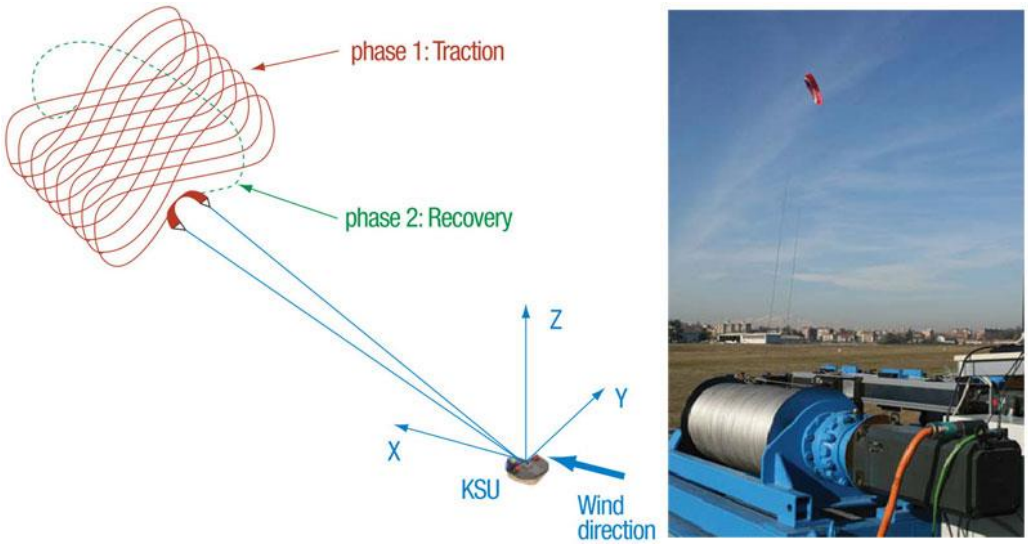


Figure 1: An example of a typical GG-AWES operation in generating electricity [13]

As for FG-AWES, there are two types, ones which utilises the crosswind flight and ones which doesn't. To distinguish between them, the former will be referred to as Type I and the later as Type II.

Type I uses a similar operating principle to the GG-AWES whereby a wing flies in a crosswind flight to generate electricity. Where it differs is in the position of the generator. Type I FG-AWES has its generator placed on the airborne part of the machine. This is typically a wind on an aircraft-like machine (see Figure 2). The tether attached on the ground does not produce electricity. It is merely just to anchor the kite. Wind passing through the rotors powers the on-board generators and it flies on a circular pathway shown in Figure 3.



Figure 2: Google's Makani Power energy kite [14]

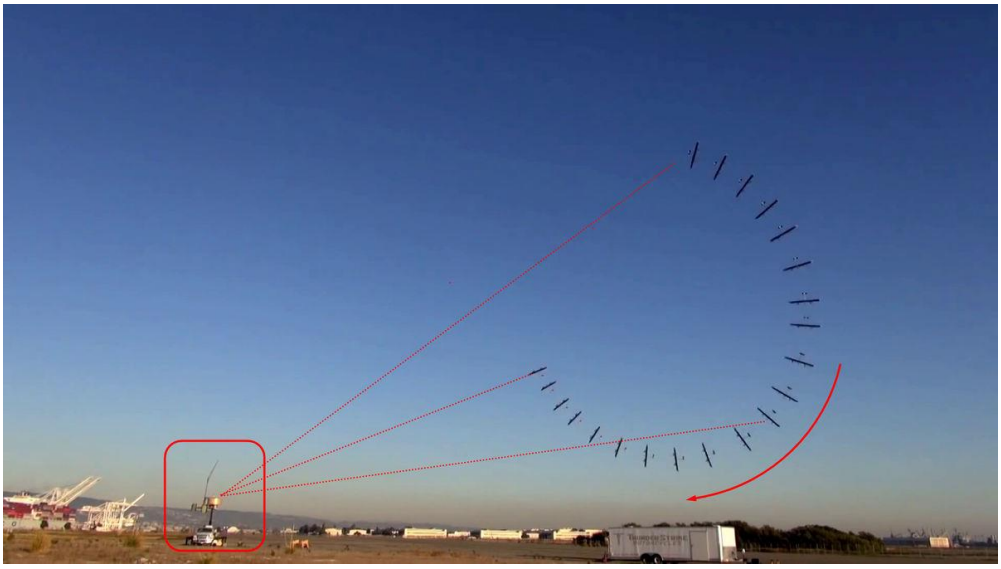


Figure 3: Type 1 FG-AWES typical operation path [15]

Type II FG-AWES are also referred to as the lighter-than-air system [12]. The generator is airborne from the use of light gasses, typically helium. Their operating principle is more similar to HAWTs. Such example of its design can be seen researched by MIT startup Altaeros Energies (see Figure 4).



Figure 4: Lighter-than-air AWES, BAT by Altaeros Energies

2.2.Malaysia's Electrical Power Consumption

For the purpose of this FYP, it is important to find a benchmark to compare electrical power produced by the AWES and electrical power typically used in a Malaysian household. According to Kubota et. al. the energy consumed of household

among their respondents was found to be 24.5 GJ yearly on average [16]. This means that on a daily basis, one household uses on average about 67 MJ worth of energy, which translates to about 18 kWh per day or 432 kW. The power consumption reported here is nearly half of what was reported by Ponniran et. al where they estimated a daily power usage of 824 kW [17].

From their methodology though, one might be more inclined to agree with estimates provided by Kubota et. al. While both relies on survey as their investigative tool, Kubota et. al. has a superior number of respondents; 366 vs. 50. Moreover, Kubota et. al. survey data not only includes appliances used by residence but also their usage duration. Ponniran et. al. did not mention this in their methodology or discussion but their data was presented in kW instead of kWh, which indicates that duration of usage might not have been considered. Kubota et. al. presents data in kWh and MJ to represent energy usage in their discussion. So a daily energy usage of 18 kWh is chosen as a benchmark for power consumption.

2.3.Malaysian Wind Characteristics

Malaysian winds are seasonal by nature and is effected by the southwest monsoon, northeast monsoon and two brief inter-monsoons [6]. Wind direction however is affected by the land and sea breeze [5]. The south-west monsoon occurs between late May to September while the north-east monsoon occurs between November and March [5].

Wind in Malaysia varies according to location [18] and for such cases, a wind map is required to see the characteristics of such variation. However, reliable wind map of Malaysia has not been created yet. A wind mapping study by the Sustainable Energy Development Authority (SEDA) is expected to be complete by 2016 [7].

Even without a proper wind map, many research work on Malaysian wind have been published over the last 10 years. Some of these research was criticised to be "grossly inaccurate" or too localised by Ho [7] but some do offer a glimpse on Malaysia's wind energy potential.

One of studies was done by Ibrahim et. al. [5] where they studied the wind characteristics of nine sites which are primarily situated at coastal areas. These 9 sites are Bintulu, Kota Kinabalu, Kuala Terengganu Airport, Kuching, Kudat, Mersing, Pulau Langkawi, Sandakan and Tawau. Wind speeds were gathered for a year through the Malaysian Meteorological Department (MMD) at a 10 m height. Wind data are interpolated to a height of up to 100 m for all locations using the Power Law equation. Weibull distribution is used to indicate the frequency of occurrences of specific wind speeds across all nine sites and Inverse Distance Weighted (IDW) interpolation method was utilised here to calculate unknown wind speed of the area surrounding the site.

It was discovered that Bintulu, Kuala Terengganu, Kuching, Mersing, Pulau Langkawi and Sandakan experiences faster wind during the northeast monsoon while Kota Kinabalu, Kudat and Tawau experiences faster wind speeds during the southwest monsoon. Figure 5 and Figure 6 shows where geographically these sites are. Referring

to the figures, it can be easily seen why the aforementioned sites experience highest wind speed on respective monsoon seasons. It is especially obvious for the sites during the northeast monsoon. All the five out of the six sites are directly exposed to the blowing wind.



Figure 5: Sites with faster wind speeds during northeast monsoon

Out of the nine sites chosen as location for their case study, Ibrahim et. Al deduced that Mersing has the highest potential for wind power generation from the Weibull distribution parameter calculated. It had less variation in wind speed with wind as strong as 3 m/s being more frequent at 60 m height. In fact, monthly wind mapping consistently shows the south part of Peninsular Malaysia to have more wind. Kudat comes second in their analysis. However, all sites seem to lie in the Class 1 wind, which is unsuitable for the deployment of HAWTs.



Figure 6: Sites with faster wind speeds during southeast monsoon

Another study by Masseran et. al. [18] evaluated the persistence level of wind speed for several wind stations in Peninsular Malaysia. Sites chosen for their study was Alor Setar, Bayan Lepas, Chuping, Ipoh, Cameron Highland, Kota Bahru, Kuantan, Malaca and Mersing. The objective of the study was to obtain a wind speed duration curve (WSDC) for their chosen site. By referring to WSDC, they can evaluate statistically, the percentage of time wind speeds exceeds 4 m/s, a minimum threshold for a typical HAWT would be able to operate. Again, they find Mersing to have the highest percentage albeit at only 18.2 %. Their data is based on wind speed data collected over a duration of three years.

Other studies [1], [5] - [6] also echoes the same result while using different methodology. Wind persistence and average wind speed are not suitable for the use of HAWTs in those locations case studies are done but again, as Ho mentioned in his paper, the examples used by many research does not cover the entirety of Malaysia. Case studies are too limited in its scope to completely doom wind energy as a viable source of alternative energy. Example of potential sites which have not been studied yet so far is are areas on the west side of the Titiwangsa Mountains which could experience strong wind during the southwest monsoon period.

2.4.Available Wind Power

The energy available in wind by itself is finite even if the creation of the phenomenon seems infinite. The power per unit area available in wind depends heavily on wind speed [17]. Power is defined by work done divided with time. For wind, work done (W_{wind}) can be expressed as Equation (1). The equation is exactly the same as kinetic energy where m is mass and U is velocity.

$$W_{wind} = \frac{1}{2}mU^2 \quad (1)$$

For wind mass flow rate is expressed as:

$$\frac{dm}{dt} = \rho AU \quad (2)$$

If the term mass in Equation (1) is replaced with mass flowrate in Equation (2), the resulting expression is as shown in Equation (3).

$$\frac{P_{wind}}{A} = \frac{1}{2}\rho U^3 \quad (3)$$

For Equations (2) and (3), A represents area that is being swept by the rotor of a wind turbine. P/A represents the power per unit area while U is the wind speed and ρ is the air density. As can be seen, wind velocity has a major influence on the power wind can generate. Assuming an air density of 1.225 $\frac{kg}{m^3}$, at 4 m/s, the theoretical power generation is 39.2 W per unit area. Double the wind speed to 8 m/s with the same density, the theoretical power generation climbed to 313.6 W per unit area. A 100 % increase on wind speed resulted in an 800 % increase in theoretical power output. This demonstrates how sensitive power output is to wind speed.

2.5.Betz Limit

Betz limit or Betz criterion is a fixed percentage which describes the maximum amount of energy that can be extracted from a fluid which is going through and idealised turbine [19]. Wind energy that goes through the rotor cannot be extracted with a 100 % efficiency. A 100 % efficiency turbine is impossible because it implies that the kinetic energy of in the wind is fully transferred to the turbine, which would result in zero velocity beyond the rotor. The derivation of the Betz limit assumes a rotor which does not possess a hub and has an infinite number of smooth rotor blades. In addition to that, the derivation only considers a free rotor within a hypothetical stream tube. Betz limit states that the maximum energy that can be extracted from a flowing limit is about 59.26 %.

This value of 59.26 % is excluding other factors such as turbulence and mechanical lost. So in the best of cases, a turbine will have a minimum loss of 40.74 %. Of course in practical application, percentage of loss is higher.

3. Methods

The experiment to find mechanical power follows the steps shown in Figure 7. Angular velocity and wind speed is measures simultaneously using the instruments described in subsection 3.4. A kite with a surface area of 0.5 m is flown to a start position of about 100 m and measurement of wind speed and rotational velocity is taken until it reaches 200 m. At that point, the kite is reeled back in to about 100 m and the measuring process is repeated until there are a set of three measurements of wind speed and rotational velocity from 100 m to 200 m.

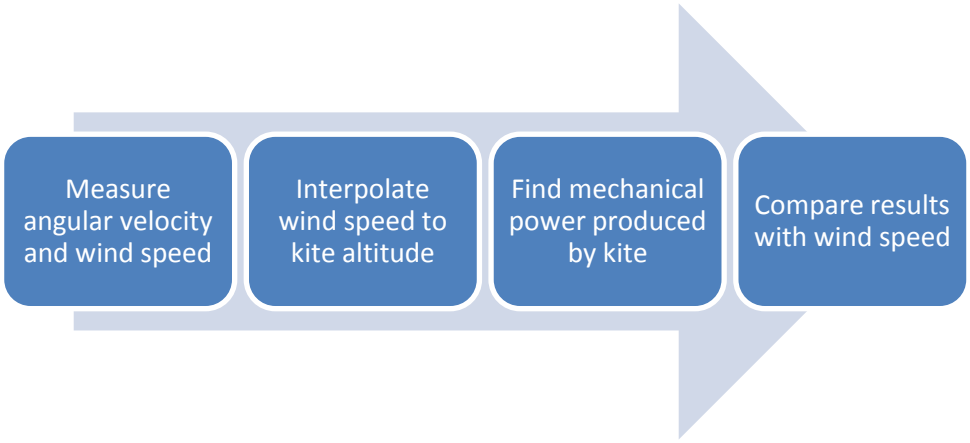


Figure 7. Experiment flowchart

3.1. Mechanical Power Measurement

There are numerous ways mechanical power can be measured. The most effective method is by using a dynamometer. Unfortunately, such instrument is not available as a resource. For this experiment, an alternative measuring device was manufactured based on how a dynamometer function. Detail on this device is further talked about in subsection 3.4.1

The power that is developed by the kite is measured through its ability to rotate a hollow metal shaft. A 200 m long thread is spooled onto a metal chrome shaft with ends slotted in a plastic enclosure. The untied end of the spooled thread is then attached onto a kite that will rotate the shaft. Refer to Figure 9 for an illustration.

Power that is being outputted by the kite can then be calculated through the concept of rotational kinetic energy. Firstly, for a rotating body, energy can be defined as Eq. (4), where I is a body's moment of inertia and ω is the rotational speed in radians per second.

$$KE_{rot} = \frac{1}{2} I\omega^2 \quad (4)$$

Power is defined as the rate work is being done. Hence by dividing time with the summation of rotational energy, average power can be computed. This equation of power is represented as Eq. (5). Δt is elapsed experiment data set time or how long was the measurement for ω is taken.

$$P_{ave} = \frac{\Sigma KE_{rot}}{\Delta t} \quad (5)$$

The resolution of measurement was taken at 1 reading per second. Hence, if say the data set resembles the one shown in Table 1, the calculation for average power would be like the one shown in Eq. (6). Note that elapsed time in Table 1 is cumulative.

$$P_{ave} = \frac{\mathrm{KE}_1 + KE_2 + KE_3 + KE_4}{T_4} \quad (6)$$

Table 1. Example of calculated data in experiment

Kinetic Energy (J)	Time elapsed (s)
KE_1	T_1
KE_2	T_2
KE_3	T_3
KE_4	T_4

For this experiment, the rotating body is a steel chrome pipe. So, the formula for *I* for a hollow pipe is given by Eq. (7).

$$I = \frac{1}{2}M(R_i^2 + R_o^2) \quad (7)$$

M is the mass of the pipe. R_i is the internal radius of the pipe and R_o is the external radius of the pipe.

3.2. Wind Speed Interpolation at High Altitude

Wind measurement is taken from 1 m above the ground. Wind speed at high altitude is determined through an empirical method: The power law equation. This method allows for a simple interpolation of wind speed. The power law equation is shown as Eq.(8).

$$\frac{U(z)}{U(z_r)} = \left(\frac{z}{z_r}\right)^{\alpha} \quad (8)$$

$U(z)$ represents the wind speed at a height, z. $U(z_r)$ is the wind velocity at the set reference height, z_r. Lastly, α is the power law exponent [20].

There a few methods to ascertain the value of α but in this experiment, it will be based on the correlation to surface roughness. Surface roughness in this circumstance is a description of the terrain. Artefacts like trees, building or a lack of them effects roughness. The equation to find α is given by Eq. (9).

$$\alpha = 0.096 \log_{10} z_0 + 0.016(\log_{10} z_0)^2 + 0.24 \quad (9)$$

z_0 in the above equation refers to surface roughness. The test area is by the ocean and has few trees with a few low buildings. According to Manwell et. al. [20], the value of z_0 can be taken as 0.2. This gives an α value of 0.18.

3.3.Site selection

Site selection is done based on two factors, current monsoon season and convenience. It is most ideal to go to a coast line near the north part of the peninsular at this time of year as it is on the southwest monsoon season but it is too far. So the best option is to go to Morib. It is relatively close and still facing the right side of the monsoon.

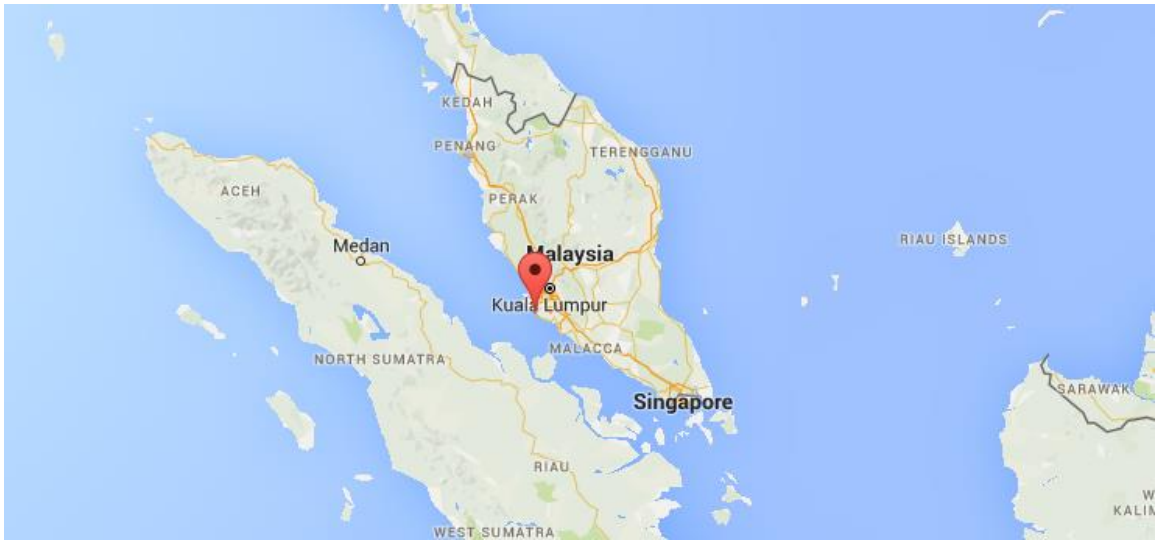


Figure 8: Position of Morib

3.4. Data Acquisition

3.4.1. Measuring rotational speed

Rotational speed is measured using an optical tachometer. Due to limited resources, the optical tachometer is self-made based on a schematic from the internet. The relatively simple sensor is fashioned using a pair of IR LED and receiver, two resistors and a variable resistor.

The basic principle of the sensor is similar to those used in other optical tachometer in the market. IR beams are emitted from a transmitter (the IR LED) towards a rotating body with a reflective marker or sticker placed on it. The reflective marker would reflect the IR

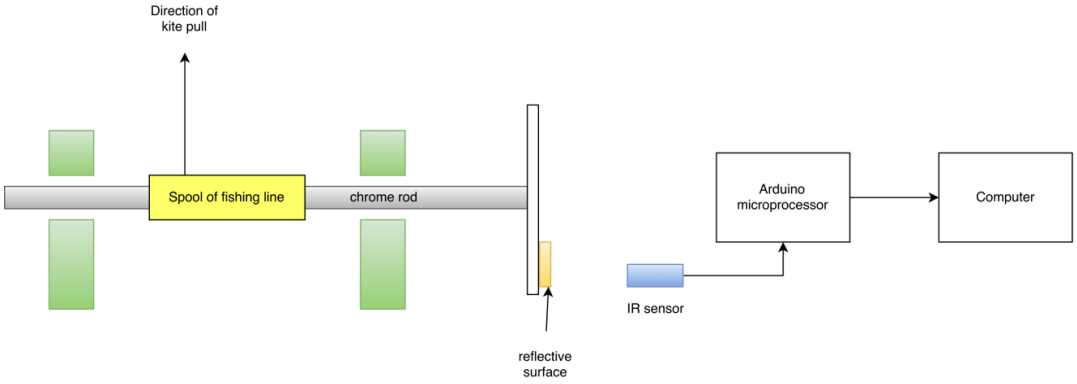


Figure 9: Experimental set-up

An Arduino microcontroller is used to gather angular velocity data from the sensor. The data is then saved as text using a serial port terminal application called CoolTerm. The software interfaces with the Arduino by being a serial monitor. Wind data is recorded manually by hand as it cannot interface with the Arduino unit.

3.4.2. Measuring wind speed

Wind speed is measured using an AP472 S1 vane probe by Delta Ohm. Because of a lack of data acquisition device to gather wind speed, a helper was employed to manually take down the wind speed. RPM data from kite is taken at 1 reading per second but it is not possible through human effort alone. Wind speed in between reading is considered constant.

4. Results and Discussion

Table 2 shows the average energy produced and average wind speed for the 3 data sets. From initial observation, the trend supports the notion that a higher average wind speed does correlate to higher energy output.

Table 2: Correlation between generated energy and wind speed

Set	$E_{average}$ (J/s)	E_{total} (J)	$V_{1\,m}$ (m/s)	$V_{10\,m}$ (m/s)	$V_{100\,m}$ (m/s)	$V_{200\,m}$ (m/s)
1	0.01	1.673	1.42	2.15	3.25	3.69
2	0.02	5.148	1.49	2.26	3.43	3.88
3	0.03	10.003	1.62	2.45	3.72	4.21

Power generated by wind is directly proportional to the cube of wind speed. Hence a little increase of wind can certainly effect energy produced. This seems to also be the case. A 4.7 % increase from 1.42 m/s to 1.49 m/s yields a 68% increase of energy output. A 6% increase from 1.49 m/s average wind speed to 1.62 m/s average wind speed yields a 48% increase in energy output.

Even so, focusing on actual yield shows what seems an insignificant amount of energy. However, it has to be noted that these yield are only representing energy gained from 5 minutes of power generation using a very small kite. It is worth noting here that each data set takes 5 minutes to complete and it takes another 5 minutes to reel the kite back in. if say the kite operates for a full day, it will have generated energy for 12 hours a day. This is equivalent to 720 minutes. Then, multiplying the E_{total} by 720/5 would give the daily energy yield of the kite. These estimations for power generation is tabulated in Table 3.

Table 3: Estimation for daily, monthly and yearly energy output based on experiment data alone

Set	$E_{total,1day}$ (J)	$E_{total,1month}$ (kJ)	$E_{total,1year}$ (MJ)
1	235.73	7.07	0.08
2	741.31	2.22	0.27
3	1440.43	20.74	2.49

Estimation from Table 3 is not enough. In fact, is it inaccurate because the frequency of the wind occurred during the experiment is not known. One of the more

important parameters looked into when determining potential energy output for wind power is the wind speed duration curve (WSDC). From a WSDC graph, the persistence of a particular wind speed can be statistically estimated. This is particularly useful for the purpose of this discussion as it expands the usefulness of the relatively small data set presented here.

To create a WSDC curve, a years' worth of wind speed data is required. This cannot be done in this study due to time constraint. Instead a WSDC curve created by Masseran et. al will be used here as reference. Figure 10 shown here is the WSDC graph taken from the paper they published [6].

The wind data here the WSDC is based on 10 wind stations. This literature does not mention the height where the wind speed was taken from but previous literatures [1], [5] cited that it is from a height of 10 m.

From data set 3, wind speed estimated at 10 m height is 2.45 m/s. Based on WSDC in Figure 10, such wind speeds occur around 48% of the time at Mersing in a three-year period. If that is the case, the adjusted energy generation yearly is as represented as Table 4.

Table 4: Adjusted yearly energy generation at Mersing using WSDC

Set	$E_{total,1year}$ (GJ)
1	0.000028
2	0.000095
3	0.000872

Value shown in Table 4 can be compared with the average household power consumption reported by Kubota et. al [16]. The reported yearly power consumption per household is 24.5 GJ. Based on the WSDC statistic and estimated power generated yearly, the power by the kite is very much quite low. It is not enough to even power fluorescent lamps, which accounts for 5 % of energy usage by a typical household [16].

There are many reasons that may attributed to this low output of energy. Some notable points are:

- Small kite area
- Possible low wind speed area
- Not flying in a crosswind motion
- Flying path is not optimised using automation
- Unsuitable kite design

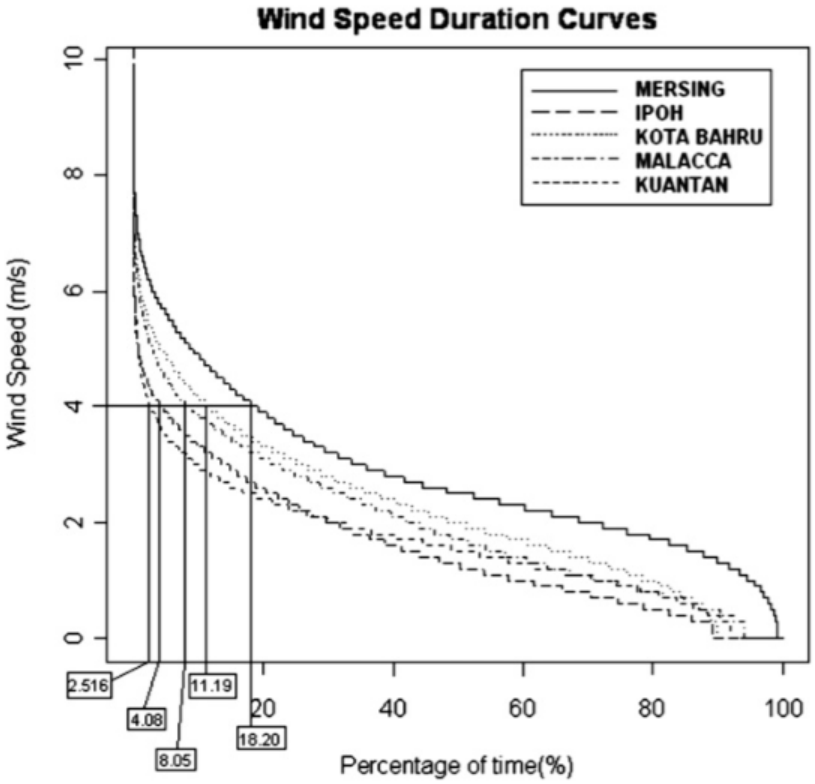


Figure 10: WSDC graph for Mersing, Ipoh, Kota Bahru Malacca and Kuantan based on three years' wind data [6]

The aerodynamic force developed by a kite is given as:

$$F_a = \frac{1}{2}\sqrt{C_D^2 + C_L^2 v_a^2 S} \quad (10)$$

Where C_D is the coefficient of drag of kite, C_L is the coefficient of lift of kite, v_a is apparent wind speed experienced by the kite and *S* is the area of the kite [21]. So a larger kite would give a larger force. The equation of power can be written as shown in Eq. (11). v_t is the speed of tether during the reel-out phase. So a kite with more surface area would give a better power output.

$$P = F_a v_t \quad (11)$$

Another reason for a low power output is due to the fact the wind passing through Morib passes Indonesia first. The experiment was done during the southeast monsoon period where wind comes from the southwest. Referring to Figure 8, Morib is positioned on the west side of the peninsular.

AWES in development in Europe and North America are very advanced. They employ autonomous control to optimise wind power generation. They also fly their kites in a crosswind motion as illustrated in Figure 1. The kite during the experiment on the other hand only fly in a straight path, catching the wind.

Even if the result of the experiment doesn't seem encouraging, it is interesting to see, theoretically how much can actually be achieved using a more suitable setup. Daily energy produced can then be estimated by assuming a 12-hour generation time. Using a kite of the same area, average power output for data set 1,2 and 3 are tabulated in Table 5.

Table 5: maximum theoretical power output of the same kite area

Set	$E_{total,1day}$ (J)	$E_{total,1month}$ (J)	$E_{total,1year}$ (J)
1	499,392	14,981,760	179,781,1120
2	547,776	6,433,280	197,199,360
3	669,600	20,088,000	241,056,000

Theoretically, now, the energy output yearly seems much more promising. The kite is supplementing about 1% of the total energy use. This number can be further increased by having a bigger area kite and flying at even higher altitude.

4.1.Errors

Error from this experiment may come from the reading of the instruments, mainly the tachometer and the weather vane. The error of the weather vane is can be considered minimal but the self-made tachometer may have more error. The tachometer was tested with a ready-made tachometer and shows consistent results.

From the analysis, error may be found in assumptions from wind extrapolation calculation and power estimation.

5. Conclusions

The work done here has shown the potential of AWES for the use of microgeneration in Malaysia. The experimental output from the kite was insignificant but the fact that the equipment and conditions not being ideal is a major contributing factor. Theoretically, using a small kite (about 0.5 m) shows that is able to get an average power of around 15.5 W, which is not a lot.

The research question this study was set up to do was to assess how suitable are AWES for microgeneration under Malaysian wind condition. From the given evidence, the answer is still difficult to assess. The test in the end was not conclusive enough since the result seems to skew towards unfeasibility. If the result showed promise under non-ideal condition, the answer to the research question would undoubtedly be a resounding yes but this report cannot give such endorsement.

The study however did achieve its objective, that is to assess the power generated from a kite. Although the research question was not answered conclusively, many points and useful knowledge can be taken away.

- Without a proper AWES setup and crosswind flight, power produced is limited

- Wind energy is heavily reliant on wind speed. A small increase in wind speed indeed showed at least 50 % increase in energy output based on experiment
- To achieve that strong wind, going higher in elevation is an option.

References

[1] S. M. Lawan, W. A. W. Z. Abidin, W. Y. Chai, A. Baharun and T. Masri, "The Status of Wind Resource Assessment (WRA) Techniques, Wind Energy Potential and Utilisation in Malaysia and Other Countries," *ARPN Journal of Engineering and Applied Science*, vol. 8, no. 12, pp. 1039-1053, December 2013.

[2] R. M. Julie , "Texas sets wind energy record as turbine produce 40 % of the state's electricity," 15 January 2015. [Online]. Available: http://inhabitat.com/texas-sets-wind-energy-record-as-turbines-produce-40-of-the-states-power/. [Accessed 17 June 2016].

[3] L. Cooke, "Germany generated so much renewable energy last weekend, electric prices went negative," 11 May 2016. [Online]. Available: http://inhabitat.com/germany-generated-so-much-renewable-energy-last-weekend-electric-prices-went-negative/. [Accessed 17 June 2016].

[4] C. L. Archer and K. Caldeira, "Global Assesment of High-Altitude Wind Power," *Energies*, vol. 2, no. 2, pp. 307-319, 2009.

[5] M. Z. Ibrahim, K. H. Yong, M. Ismail, A. Albani and M. Muzathik, "Wind Characteristics and GIS-Based Spatial Wind Mapping Study in Malaysia," *Journal of Sustainability Science and Management*, vol. 9, no. 2, pp. 1-20, 2014.

[6] N. Masseran, A. M. Razali, K. Ibrahim and W. Z. Wan Zin, "Evaluating the wind speed persistence for several wind stations in Peninsular Malaysia," *Journal of Energy*, vol. 37, pp. 649-656, 2012.

[7] L.-W. Ho, "Wind energy in Malaysia: Past, present and future," *Renewable and Sustainable Energy Review*, vol. 53, 279-295 January 2016.

[8] S. Kamarizzaman, A. M. Razali and M. Y. Othman, "Potensi Tenaga Angin di Terumbu Layang-Layang," *Journal of Industrial Technology*, vol. 5, no. 1, pp. 19-32, 1995.

[9] Z. Md Idrus, N. A. Hashim, S. N. Abdul Manan, M. A. Abdul Rahman, K. N. Abdul Maulud and O. Abdul Karim, "Potential of wind energy in sustainable development of resort island in Malaysia: A case study of Pulau Perhentian (Perhentian Island)," *Mathematical Methods, Computational Techniques, Non-Linear systems, Intelligent Systems*, pp. 431-435.

[10] A. Cherubini, A. Papini, R. Vertechy and M. Fontana, "Airborne Wind Energy Systems: A review of the technologies," *Renewable and Sustainable Energy Reviews*, vol. 51, pp. 1461-1476, 2015.

[11] M. L. Loyd, "Crosswind Kite Power," *Journal of Energy*, vol. 4, no. 3, pp. 106-111, 1980.

[12] M. Diehl, "Airborne Wind Energy: Basic Concepts and Physical Foundations," in *Airborne Wind Energy*, Springer-Verlag Berlin Heidelberg, 2013, pp. 1-22.

[13] B. Maccleary, "Advanced Controls enable Airborne WInd Power Generation," RTC Magazine, April 2011. [Online]. Available: http://www.rtcmagazine.com/articles/view/102112. [Accessed 23 June 2016].

[14] M. Barnard, "Google's Makani: From Regulatory to Technical to Wildlife Challenges," Clean Technica, 19 February 2014. [Online]. Available: http://cleantechnica.com/2014/02/19/googles-makani-regulatory-technical-wildlife-challenges/. [Accessed 23 June 2016].

[15] logx_tm, "Google が開発する空飛ぶ風力発電機「Makani」とは？," Gigazine, 18 March 2015. [Online]. Available: http://gigazine.net/news/20150318-makani-energy-kite/. [Accessed 23 June 2016].

[16] T. Kubota, S. Jeong, D. H. C. Toe and D. R. Ossen, "Energy Consumption and AIr-Conditioning Usage in Residential Buildings of Malaysia," *Journal of International Development and Cooperation*, vol. 17, no. 3, pp. 61-69, 2011.

[17] A. Ponniran, E. Sulaiman, S. A. Jumaat, M. Ishak, M. A. Chulan and S. Saiman, "A Study on Electric Energy Usage at the Residential Area," in *Energy & Environment Conference*, Kuching, Sarawak, 2007.

[18] N. Masseran, A. M. Razali and K. Ibrahim, "An analysis of wind power density derived from several wind speed density functions: The regional assessment on wind power in Malaysia," *Renewable and Sustainable Energy Reviews*, vol. 16, pp. 6476-6487, 2012.

[19] M. Ragheb and A. M. Ragheb, "WInd Turbines Theory - The Betz Equation and Optimal Rotor Tip Speed Ratio," in *Fundemental and Advanced Topics in Wind Power*, Rijeka, Croatia, InTech, 2011, pp. 19-38.

[20] J. F. Manwell, J. G. McGowan and A. L. Rogers, Wind Energy Explained - Theory, Design and Application (Second Edition), Chichester: John Wiley & Sons, Lts, 2009.

[21] R. Schmehl, M. Noom and R. v. d. Vlugt, "Traction Power Generation with Tethered Wings," in *Airborne Wind Energy*, pringer-Verlag Berlin Heidelberg, 2014, pp. 23-45.

[22] General Electric, "GE 2016 first quarter performance," 22 April 2016. [Online]. Available: http://www.ge.com/sites/default/files/ge_webcast_presentation_04222016_1_0.pdf. [Accessed 22 May 2016].

[23] Siemens, "Annual Report 2015," Siemens, Munich, 2015.

[24] K. Caldeira and C. L. Archer, "Global Assessment of High-Altitude Wind Power," *Energies*, vol. 2, no. 2, pp. 307-319, 2009.

[25] S. K. Najid, A. Zaharim, A. M. Razali, M. S. Zainol, K. Ibrahim and K. Sopian, "Analyzing the East Coast Malaysia Wind Speed data," *International Journal of Energy and Envieonment*, vol. 3, no. 2, p. 8, 2009.

[26] K. Sopian , A. Razali and M. Y. Othman, "Potensi tenaga angin di Terumbu Layang-Layang," *Journal of Ind technology*, vol. 5, no. 1, pp. 19-32, 1995.

[27] Y. K. Hwang, M. Z. Ibrahim, M. Ismail and A. Albani, "Wind Characteristic and GIS-BAsed Spatial Wind Mapping Study in Malaysia," vol. 9, no. 2, pp. 1-15, 2014.

eureca 2016 – Conference Paper
Paper Number 2ME27

To investigate the effects of coil geometry towards the electromagnetic induction of energy harvesting application

Thomson Chin Siong Hee[1*], Chung Kiat Thein[1]

[1]*School of Engineering, Taylor's University, Malaysia*

[*]thomsonheechinsiong@sd.taylors.edu.my

Abstract

Vibration-based electromagnetic energy harvester is receiving more interests as an energy conserving tool for wireless sensors and actuators. It harvests the mechanical energy that is available from vibration into electrical energy using electromagnetic induction. In the past few decades, various modifications are made currently in the similar field to optimize the power output of the designs. This paper described the related research works that are able to optimize the power output of the design and also to study the effects of different coil geometries to the power output of the design. The parameters that will be investigated are the number of coil turns, coil effective length, thickness of the magnets holder and the coil's shape and dimension. The project has also conducted analytical analysis to verify the simulation results from numerical analysis. The verification analysis shows that the average percentage of error between analytical and numerical analysis is 15.15 %. From the research, it is identified that higher number of coil turns will decrease the efficiency of electromagnetic induction due to resistance. Furthermore, it is identified that 11 mm coil effective length is the optimum effective length for the design as it has the highest improvement in performance. Although, longer effective length will generate more current output, it will also occupy more space for the design which eventually leads to a bigger design. Apart from that, the optimum thickness of magnets holder is set to be 2 mm through the simulationanalysis between the relationship between the thickness of magnets holder and induced current output conducted using Finite Element Analysi (FEA) software, Ansys Maxwell. Lastly, it is concluded that rectangular-shaped coil is the optimum coil shape for the project design setup as it generates the highest current output among the other coil shape.

Keywords: Electromagnetic, Coil, Geometries, Vibration, Ansys Maxwell

1. Introduction

With the rapid growing population of the world, the demand for energy that supplied to every device also increases rapidly. This has led to the challenge of insufficient energy supply also arises. However, engineers and scientist all around the world are working together to solve this challenge by focusing on the same topic, energy harvesting. In the recent years, energy harvesting has played an important role in the energy industrial or field. Energy harvesting is a process where minimal amount of energy is harvested from one or more energy sources to be stored or perform work. In the old days, this small amount of energies was not able to be captured due to the lack of advance technology that exists nowadays. Energy harvesting devices and tools are getting better and better in converting other forms of energy to electrical energy in terms of overall efficiency and effectiveness.

Energy harvesting applications come in many forms, some of the famous ones are photonic, thermal, and vibrational. Vibrational energy harvesting is where the where the motion of the vibrating objects generates electricity through either piezoelectricity or electromagnetic induction. Electromagnetic induction application that is used in the energy harvesting is based on Faraday's Law of electromagnetic induction [1]. A few of good examples that use electromagnetic induction to capture small trace of mechanical vibration to generate electrical energy to other devices to perform tasks are EnOcean ECO 200 and Perpetumm wireless sensor. However, based on the examples in the market, there is still room for improvement for these devices in term of power delivering efficiencies. Higher efficiencies of power output can be obtained from the same device with a different internal design of the device which will be the coil geometries. Coils are needed to cut the magnetic fluxes to generate electricity, hence, higher number of coils will generate more electricity. However, by increasing the number of coils does not necessarily increases the efficiency of the device. Furthermore, it will be not practical to have so many coils when the coils are already heavier than the device. Hence, the different arrangement of the coil which is the coil geometries strongly affects the output efficiency of the device within specific parameters to be investigated.

2. Research Methodology

This project comprises mainly of 3 parts which is verification, modelling using Finite Element Analysis (FEA) and simulation using Finite Element Analysis. Verification of results focuses on the accuracy and consistency of the simulation results from the theoretical results. Second part of the project is on the modelling of the energy harvesting device. Lastly, the simulation focuses on the analysis of simulation results obtained.

2.1 Modelling using Finite Element Analysis (FEA)

2.1.1 Design and Setup for Magnets and Steel Magnets Holder

For the setup of the energy harvesting device, there are total of 4 magnets in the design where 2 are on top and another 2 are at the bottom. The top ones has the same magnetic pole direction whereas the bottoms ones have opposite magnetic pole

direction from the top ones. The setup of the design is referred from S. Beeby's design for his micro electromagnetic generator [2]. The 3D and 2D illustrations of the design are shown in Fig.1 and Fig.2. The location of the magnets are designed in this way because it is necessary to guide the magnetic field back to the opposite side [3]. Apart from that, it also provide the highest induced current output according to Fleming's Right Hand Rule. Using this setup, the current will be induced in the same direction even though there are two different magnetic fields.

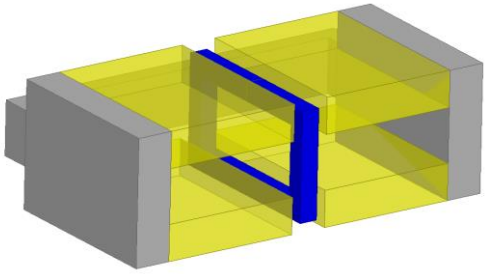


Figure 1: 3D model of the energy harvesting device with rectangular coil.

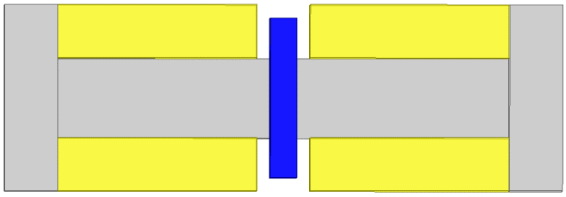


Figure 2: 2D model of the energy harvesing device with rectangular coil.

In order to minimize the magnetic flux lose into the air, steel magnet holder is located as shown. Referring to Arroyo et al., magnetic flux linkage will lose at high rate in the air at the side of the magnet if there is no ferromagnetic material to link the flux to create magnetic flux linkage [4]. Therefore, by minimizing the magnetic flux lose in the air, it is possible to obtain maximum induced current output from the electromagnetic induction energy harvesting device [5].

2.1.2 Design and Setup for the Coil

For this research project, there are 3 designed coil shapes for the simulations which are circular, polygon and rectangular coil as shown in Fig 3. Each design is modelled to be the same volume which is 28 mm^3.

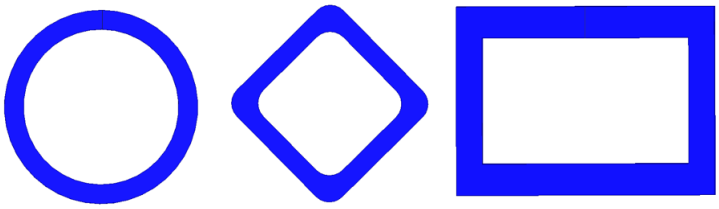


Figure 3: Circular, polygon and rectangular coil shape.

2.1.3 Material

For the magnets, the material used is Neodymium Iron (NdFe35) which is known as rare earth magnet and widely used as permanent magnets nowadays. The reason of using this material for the magnets is because it is most advance and widely commercialized magnet material. Apart from that, it is has also the most powerful magnetic properties [6]. The permanent magnet properties is shown in Table 1.

Table 1. Properties of magnet (NdFe35) obtained from Ansys Maxwell.

Relative Permeability	1.0997785406
Bulk Conductivity	625000 siemens/m
Magnetic Coercivity	-890000 A/m
Mass Density	7400 kg/m^3

Copper has high conductivity of electricity which makes it an ideal material for the coil. Due to the fact that energy harvesting devices harvest very little amount of electrical energy, electrical resistance is crucial in maximizing the power output. Furthermore, copper has been used in the electrical wiring industries for decades which makes it highly reliable and cheap. Therefore, copper is chose to be the material of the coil in this research project. The material properties of the copper is shown in Table 2.

Table 2. Properties of copper obtained from Ansys Maxwell.

Relative Permeability	0.999991
Bulk Conductivity	58000000 siemens/m
Mass Density	8933 kg/m^3

Steel 1010 is used as the material for magnet steel holder as it is a standard metal that is easily available and high tensile strength. The material properties of Steel 1010 is shown in Table 3.

Table 3. Properties of steel holder (Steel 1010) obtained from Ansys Maxwell.

Bulk Conductivity	2000000 siemens/m
Mass Density	7872 kg/m^3

2.2 Motion Setup

In most electromagnetic induction energy harvesting devices, the magnets are the vibrating or translating components of the system [7]. Steel magnet holder can be connected to a short beam that has high stiffness that increases the frequency of the oscillation. Higher frequency of oscillation is favorable in this research as it increase the number of times the coil cut through the magnetic flux. In the motion setup of the simulation, the velocity that the magnet is travelling is 6m/s with total distance travelled is 6 mm. The settings for the motion setup is shown in Table 4 and the travelling object in the simulation is the magnets and the magnets holders illustrated in Fig. 4.

Table 4. Motion Setup for the simulation project.

Moving vector	Z (Positive)
Motion Type	Translating
Initial Position	-3 mm
Translating Limit (Negative)	-3 mm
Translating Limit (Positive)	3 mm
Velocity	6 mm/s

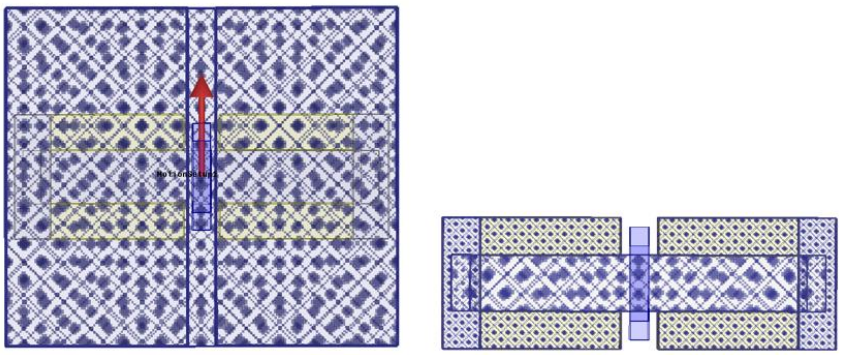


Figure 4. Magnet is set to be the moving object in the simulation.

2.3 Analysis Setup

The simulation is conducted in transient solution type because it is necessary to study the behavior of the induced current while translating. Therefore, the simulation is set with 0.1 s time step with stop time of 1 s. Hence, the simulation results will be presented in 0 s to 1 s with 0.1 s interval time.

3. Results and Discussions

3.1 Verification Analysis

3.1.1 Verification Method 1

Due to the microscale size of the electromagnetic induction energy harvesting device, the experimental analysis of the research project cannot be done and it is only possible in simulation and analytical analysis. Hence, to verify the results obtained from the simulation in FEA, analytical analysis is conducted to make verification on the simulation results. The verification is done by calculating the percentage error between the theoretical values and the simulation values. In the project, it is calculated that the average percentage error between theoretical values and simulation values is 15.15 % which is beyond the acceptable range of percentage error. However, with each set of data, it is shown that in Table 5, there is a consistency in the percentage error.

Resistance and the inductance in the coil is the main factor that deviates the accuracy of the simulation results and theoretical results by 15.15 %. In a rectangular shape coil, each four edges of the coil consists of bended wire where the inductance of the wire increases and leads to lower current induced.

Table 5. Percentage error between the analytical and simulation analysis.

Turns	Analytical Current Output (A)	Simulation Current Output (A)	Percentage Error (%)
100	0.065	0.055	15.72
200	0.131	0.110	15.72
300	0.196	0.170	13.16
400	0.261	0.220	15.72
500	0.326	0.277	15.10
600	0.392	0.332	15.20
700	0.457	0.387	15.28
800	0.522	0.443	15.14
900	0.587	0.498	15.20
1000	0.653	0.553	15.26

3.1.2 Verification Method 2

Another method of verifying the simulation results is by comparing the improvement of performance of each turns in analytical and simulation as shown in Table 6. It is observed from Fig. 5, that both analytical and simulation results show the same improvement pattern with each other. Therefore, it can be concluded that the simulation results are correct.

Table 6. Improvement in performance ratio for analytical and simulation analysis for each number of turns.

Number of turns	Analytical Current Output(mA)	Improvement Ratio	Simulation Current Output (mA)	Improvement Ratio
100	0.086	0	0.055	0
200	0.173	1.000	0.110	1.000
300	0.259	0.500	0.170	0.545
400	0.346	0.333	0.220	0.294
500	0.432	0.250	0.277	0.259
600	0.519	0.200	0.332	0.198
700	0.605	0.167	0.387	0.165
800	0.691	0.143	0.443	0.144
900	0.778	0.125	0.498	0.124
1000	0.864	0.111	0.553	0.110

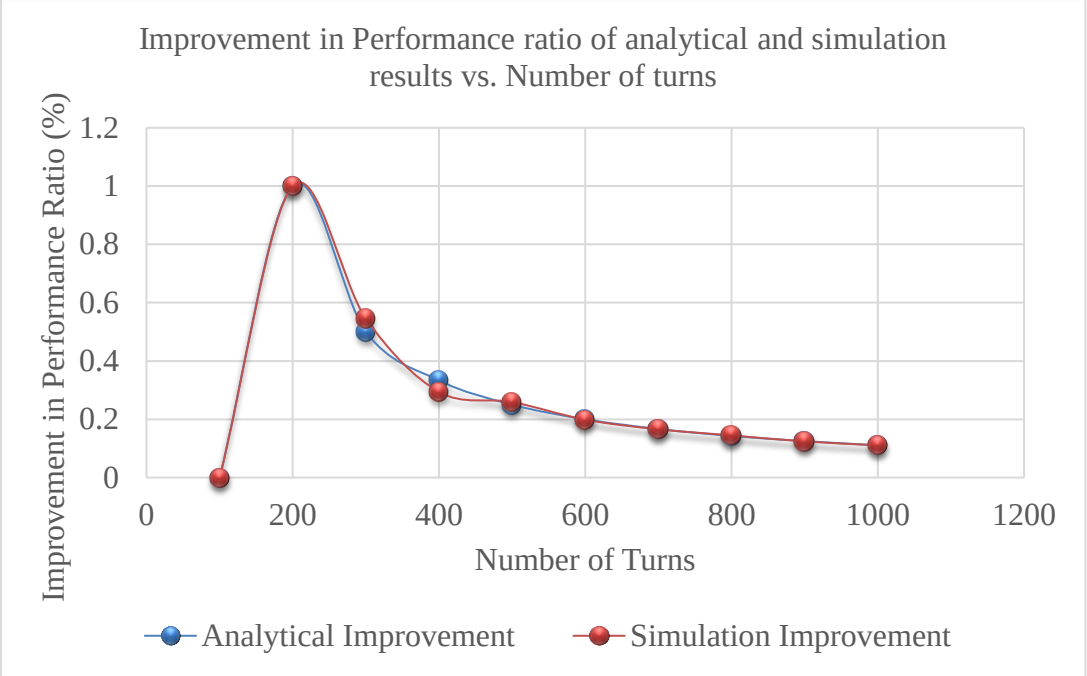


Figure 5. Improvement in performance ratio for analytical and simulation analysis for each number of turns.

3.2 Number of turns

To calculate the induced current of the coil, the mathematical equation is given as shown in Eq (1) [8].According to the Eq (1), number of turn of the coil affects the induced current output during the electromagnetic induction.

$$\boldsymbol{I = \frac{nBLv}{R}} \tag{1}$$

Where *I* is the induced current, *B* is the magnetic field strength, n is the number of turns, L is the coil effective length, *v* is the velocity of which the magnetic field is moving and *R* is the total resistance of the circuit. Analytical analysis and numerical analysis are done to observe the effects of number of turns of coil towards the current induced by electromagnetic induction. The simulation current outputs shown in the Table 7 are the maximum current output during 0.5 s. Current outputs are taken at 0.5 s of the transient simulation because it is the change in magnetic field is the greatest at 0.5 s.

From Figure 6, it is understood that the relationship between the numbers of turn of the coil is directly proportional to the induced current output of the coil. The greater the number of turns, the higher the induced current output. However, the simulation analysis shows that as the number of turn increases, the simulation results are getting further away from the analytical results. The deviation of simulation results from the analytical results means that the efficiency of the coil decreases when the number of turns increases. The reduction in efficiency of the coil is caused by the increased of the resistance due to the increased in coil length when number of coil turns increased [9]. From the simulation analysis results, it is concluded that increasing the number of coil turns is not the best method to increase the induced current output of the

coil. Hence, better methods are needed to be considered to optimize the induced current output of the electromagnetic induction energy harvesting device.

Table 7. Simulation and analytical current outputs according to number of turns.

Number of turns	Simulation Current Output (mA)	Analytical Current Output (mA)
100	0.055	0.0864
200	0.110	0.1728
300	0.170	0.2593
400	0.220	0.3457
500	0.277	0.4321
600	0.332	0.5185
700	0.387	0.6049
800	0.443	0.6913
900	0.498	0.7778
1000	0.553	0.8642

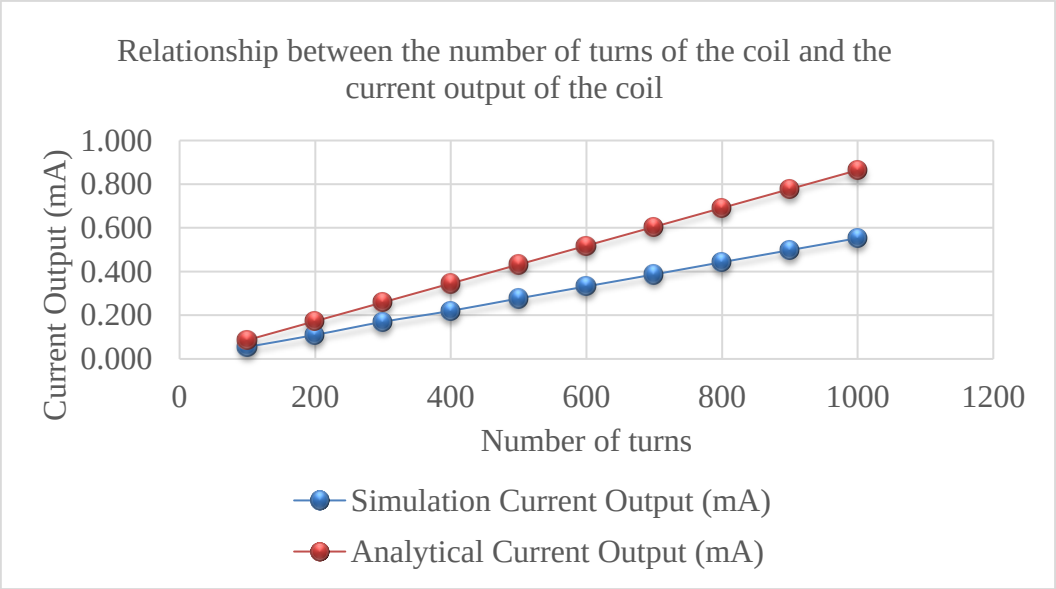


Figure 6. Relationship between the number of turns of the coil and the current output of the coil for simulation and analytical analysis.

3.3 Coil Effective Length

One of the few main factors that affects the outcome of the current output of the coil is the coil effective length. According to Eq (1), coil effective length is the coil length that is causing the change in magnetic flux which is also perpendicular to the direction of the magnetic field and the velocity [8]. The relationship of the coil length and the induced current is directly proportional in the equation 1. Thus, simulation analysis are done to understand the effects of coil effective length to optimize the energy harvesting device to provide highest possible power output.

In the simulation analysis, coil length is increased each time by 10% from the original length to observe the change in induced current output. Table 8. shows the percentage of improvement of the current output from the previous result with 10% of increment from the original length.

Table 8. Current output and percentage of improvement based non increment of coil effective length.

Percentage (%)	Coil Effective Length (mm)	Current Output (mA)	Percentage of Improvement (%)
0	10	0.553	0
10	11	0.594	7.41
20	12	0.618	4.04
30	13	0.636	2.91
40	14	0.642	0.94
50	15	0.646	0.62
60	16	0.648	0.31
70	17	0.649	0.15
80	18	0.649	0

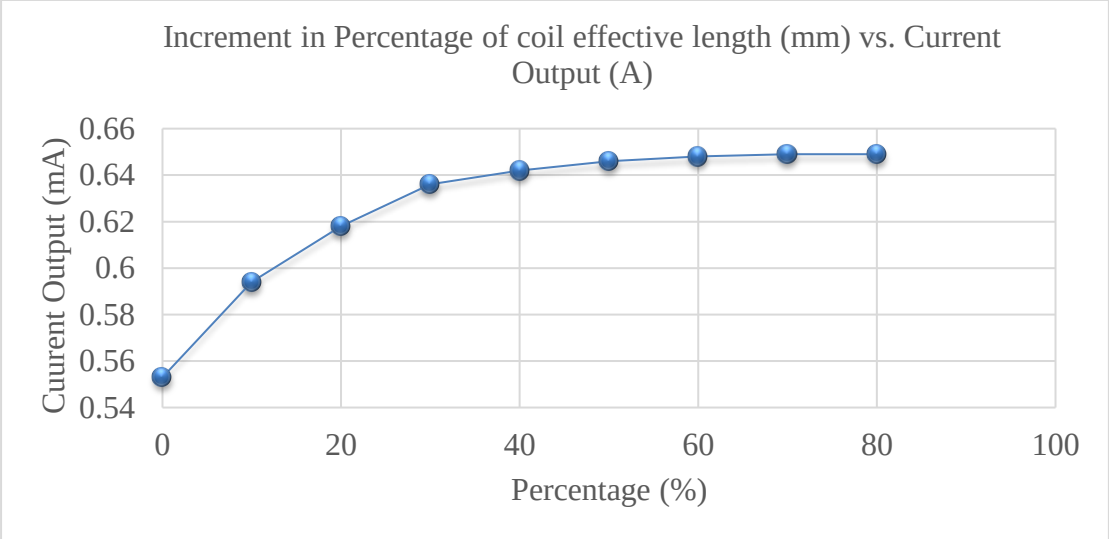


Figure 7. Increment in percentage of coil effective length against current output.

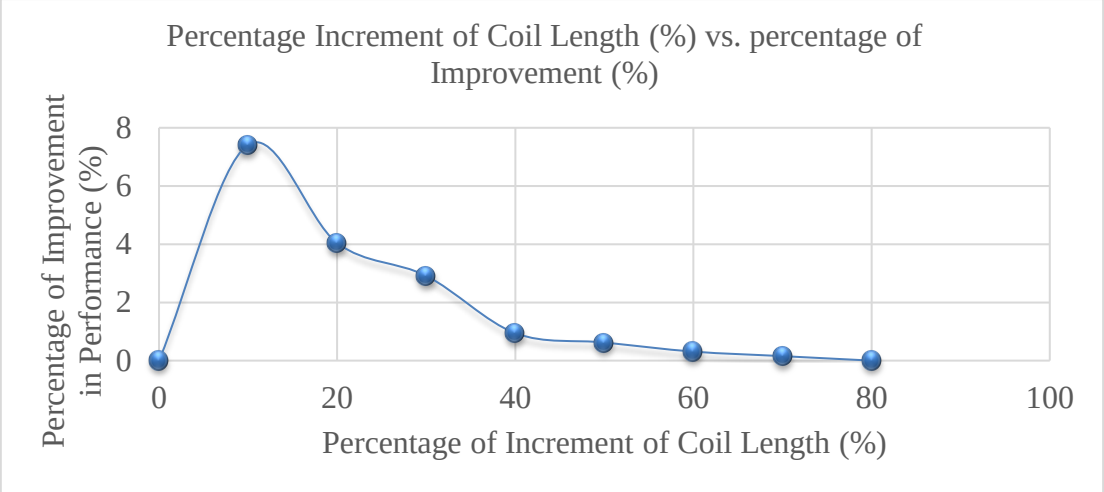


Figure 8. Percentage of increment if coil length against percentage of improvement.

Fig. 7 shows that the induced current output increases as the coil effective length increases, however, it is observed from Fig. 8 that with each increment of coil effective length, the percentage of improvement of the current output decreases and eventually became zero. This means that further increasing the coil effective length beyond 18 mm for this design will not increase the current output. Apart from that, referring from Fig. 8, the highest improvement of the current output is at 10% of increment of coil length which is 11 mm coil effective length.

In the design, every time the coil effective length is increased, the total volume of the design will also increase which will eventually occupy more space. When more space is occupied, it is harder to install the energy harvesting devices in a small space. Therefore, it is essential to balance between the demand of the current output and the space given. Coil effective length with highest percentage of increment in performance will be chosen to be the design of the project. Hence, coil effective length of 11 mm is chosen to be the coil effective length of the design for the project.

3.4 Thickness of Steel Holder

Apart from the number of turns and coil effective length that affects the final current output of the electromagnetic induction energy harvesting device, the thickness of the steel magnet holder also plays an important role in maximizing the current output. Magnet holder acts as a bridge for the magnetic flux to be guided back to the magnet to minimize the flux leakage [10]. When there is less flux leakage, there will be more magnetic flux linkage between the magnets [5]. Hence, enhanced the magnetic field strength of the system which generates more induced current in the coil. The wider the magnet holder is, the more induced current output there is, however as observed from Fig. 9, there is a turning point where the induced current output starts to decrease with expanding steel holder thickness. As shown in Table 9, the current output increases from 0.540 mA to 0.553 mA from 0.5 mm to 2 mm but decreases to 0.550 mA when the thickness is 3 mm. The induced current decreases as it reaches 3 mm because of the decrease in magnetic flux density. When the thickness of the steel holder increases, so does the volume. Therefore, the magnetic flux is spread further away from each other which resulting in the drop in magnetic flux density.

Table 9. Induced current output of the coil based on different thickness of magnet holder.

Thickness of the Steel Holder (mm)	Current Output (mA)
0.5	0.540
1	0.550
2	0.553
3	0.550

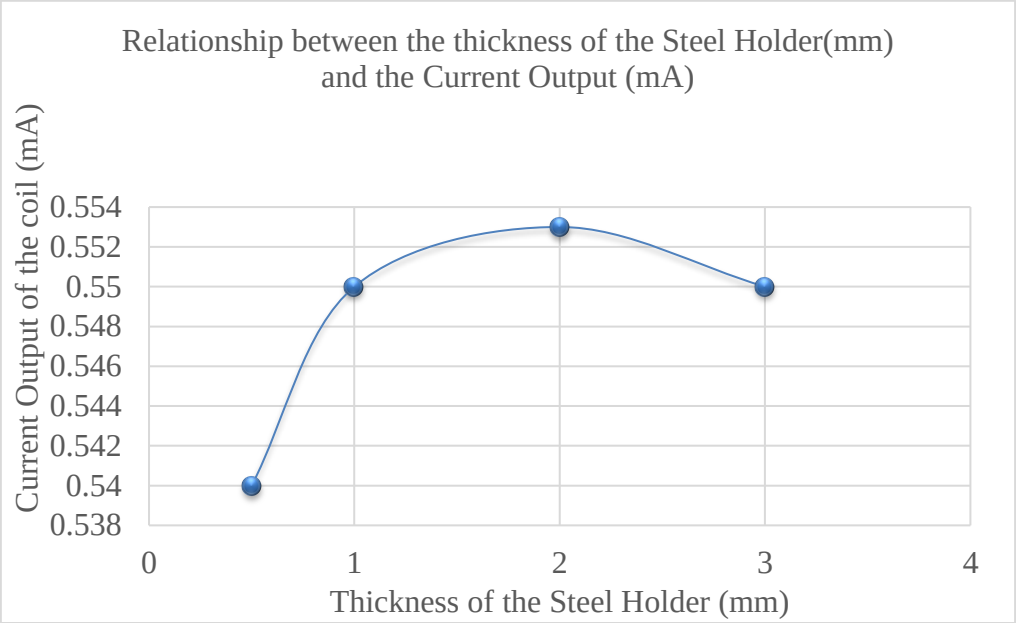


Figure 9. Relationship between the thickness of magnet holder and current output.

From Fig. 9, it is concluded that steel holder with thickness 2 mm will be used for the design of this project as it maximizes the induced current output of the device.

3.5 Different shape of coil

In this research project, the main purpose is to identify the effects of coil geometry towards the electromagnetic induction on energy harvesting applications. Hence, it is crucial to understand how the shape of the coil affects the induced current output of the energy harvesting device. Therefore, the project has conducted simulations on different shape of coil on the same simulation design setup. Three different shapes of coil are studied which are circular, polygon and rectangular shaped coil. All the results are tabulated in Table 10. Referring to the graph shown in Fig. 10, rectangular coil has the highest induced current output from 0.4s to 0.7s followed by polygon coil and lastly circular coil. Rectangular coil has the highest induced current output than the other 2 designs because it has the most coil effective length than the rest.

Table 10. Current output of different shaped coil with time interval of 0.1 second.

Time (s)	Rectangular Coil Current Output (mA)	Circular Coil Current Output (mA)	Polygon Coil Current Output (mA)
0.1	0.024	0.118	0.071
0.2	0.114	0.179	0.176
0.3	0.248	0.224	0.271
0.4	0.424	0.249	0.330
0.5	0.553	0.257	0.358
0.6	0.553	0.256	0.359
0.7	0.424	0.248	0.329
0.8	0.250	0.224	0.270
0.9	0.114	0.180	0.177
1	0.025	0.118	0.072

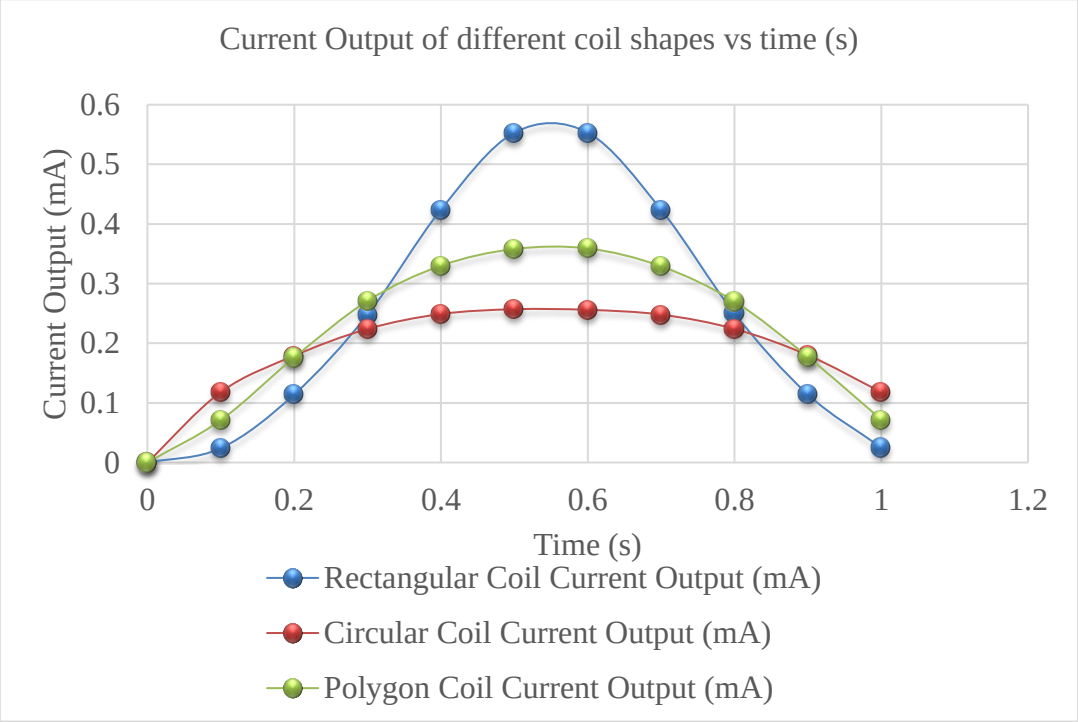


Figure 10. Current output of different coil shape against time.

4. Conclusion

In conclusion, the research project shows clear and understandable effects of different parameter on the coil geometry towards the electromagnetic induction on energy harvesting applications. In the research, analytical analysis is conducted to verify the results of simulation analysis where error of percentage of each set of data is calculated and improvement of performance of both analytical and simulation are calculated to verify the results of the simulation. The error of percentage between the analytical and simulation is calculated to be 15.15% which is acceptable despite the fact

that the analytical analysis ignore other factors such as inductance of the wire and flux leakage. In general, the simulation results are considered accurate and consistent compared to the analytical analysis. In the research, parameters such as number of turns of the coil, coil effective length and coil shape are studied and simulation analysis are conducted to decide the best design for the electromagnetic induction energy harvesting device. For the number of turns, the relationship between the number of turns of the coil and the induced current output is directly proportional but efficiency of the coil decreases when the number of coil turns increase. As for the coil effective length, the 11 mm coil effective length is chosen to be the best length for the coil as it has the highest increase in performance. Then, rectangular shaped coil is concluded to be the best coil shape compared to circular and polygon shaped coils producing the highest current 0.553 mA at 0.5s with 1000 number of coil turns.

References

[1] "Electromagnetic Induction : Magnetism and Electromagnetism - Electronics Textbook." [Online]. Available: http://www.allaboutcircuits.com/textbook/direct-current/chpt-14/electromagnetic-induction/. [Accessed: 01-Oct-2015].

[2] S. P. Beeby, R. N. Torah, M. J. Tudor, P. Glynne-Jones, T. O'Donnell, C. R. Saha, and S. Roy, "A micro electromagnetic generator for vibration energy harvesting," vol. 17, pp. 1257–1265, 2007.

[3] "An electromganetic, vibration-powered generator for intelligent sensor systems." [Online]. Available: http://eprints.soton.ac.uk/258862/1/S%26A.pdf. [Accessed: 07-Oct-2015].

[4] E. Arroyo, A. Badel, and F. Formosa, "Modeling and design of an electromagnetic vibration energy harvester and its dedicated energy extraction circuit," in *2012 IEEE International Instrumentation and Measurement Technology Conference Proceedings*, 2012, pp. 425–430.

[5] B. L. Ooi and J. M. Gilbert, "Design of wideband vibration-based electromagnetic generator by means of dual-resonator," *Sensors Actuators, A Phys.*, vol. 213, pp. 9–18, 2014.

[6] "Magnetic Materials & Assemblies from Eclipse Magnetics." [Online]. Available: http://www.eclipsemagnetics.com/row/magnet-materials-and-assemblies/. [Accessed: 07-Oct-2015].

[7] P. D. Mitcheson, T. C. Green, E. M. Yeatman, and A. S. Holmes, "Architectures for vibration-driven micropower generators," *J. Microelectromechanical Syst.*, vol. 13, no. 3, pp. 429–440, 2004.

[8] "Faraday Law of Electromagnetic Induction | Electrical4u." [Online]. Available: http://www.electrical4u.com/faraday-law-of-electromagnetic-induction/. [Accessed: 01-Oct-2015].

[9] T. O'Donnell, C. Saha, S. Beeby, and J. Tudor, "Scaling effects for electromagnetic vibrational power generators," *Microsyst. Technol.*, no. April, pp. 26–28, 2007.

[10] M. El-hami, P. Glynne-Jones, N. M. White, M. Hill, S. Beeby, E. James, a. D. Brown, and J. N. Ross, "Design and fabrication of a new vibration-based electromechanical power generator," *Sensors Actuators, A Phys.*, vol. 92, no. 1–3, pp. 335–342, 2001.

eureca 2016 – Conference Paper
Paper Number 2ME28

The Influence of Mixing Factors on the Flammability of R32 Refrigerant and Compressor Oil Mixture

Toh Khai Liang[1], Azadeh Ghadimi[1*], Lim Chin Hong[1], Phang Siew Wei[1], Chin Wai Meng[2]

[1]*School of Engineering, Taylor's University, Malaysia*
[2]*Daikin Research & Development Malaysia*

*Azadeh.Ghadimi@taylors.edu.my

Abstract
In the development of mitigating climate change and global warming, next generation refrigerants have been developed and are expected to replace the current standard refrigerants used in air-conditioning systems. R32 is introduced as one of the new class of zero Ozone Depletion Potential (ODP) and low Global Warming Potential (GWP) refrigerants. It has demonstrated significant performance improvements and environmental benefits in both industrialised and developing countries. In spite of its benefits, R32 refrigerant has been classified as a mildly flammable refrigerant. DAIKIN is keen to study on the flammability of R32 refrigerant and compressor oil mixture when it is leaked through an orifice. Influence of the mixing factors which are the upstream mass flow rate and mixture volume fraction on the downstream leakage velocity are studied. Medium relevance centre sizing meshes are selected based on its grid independency. Upstream mass flow rate exhibited a more significant effect on the average static pressure at the orifice outlet than the mixture's volume fraction. When the mass flow rate is increased by a quarter, the outlet average pressure is increased by 37%. The pressure shows only a 22% increase when the oil composition of the mixture is increased by a quarter. The volume fraction however has insignificant effect on the average outlet velocity. Critical flammable timeframe for the leaked mixture's concentration to lie within its flammability limits has also been predicted in the study. Time required for the leaked mixture to be flammable is the shortest when subjected to the highest upstream mass flow rate in the range specified by DAIKIN.

Keywords: R32, Mixing factors, VOF model, Flammability, Standard k- ε

1. Introduction

In response to the environmental concerns, the Montreal Protocol was adopted by countries around the world in 1989 [1] and subsequently the Kyoto Protocol in 1997 [2]. With effect of the protocols, there have been continuous efforts in protecting the

ozone layer and impeding the progression of global warming, these exercise are driven by an ongoing phase-out of chlorofluorocarbons (CFCs), hydrochlorofluorocarbons (HCFCs) and hydrofluorocarbons (HFCs) based refrigerants which deplete the ozone layer. Both developing and industrialised countries are deploying next generation refrigerants which have zero Ozone Depletion Potential (ODP) and low Global Warming Potential (GWP) than the predeceasing refrigerants [3].

R32 refrigerant, which is essentially Difluoromethane, has zero ODP and lower GWP of 675 compared to the commonly used R410A refrigerant which has a GWP of 2088 [4]. A reduction of 46,000 tons of carbon dioxide released per year is claimed by DAIKIN in the Japanese market which uses R32 instead of R410A refrigerant [3]. Panda et al. [5] reported that R32 refrigerant exhibits the best cooling and heating season performance improvement of 4% and 5% respectively when compared to R410A to be used as substitution for R22 refrigerant which is HCFC based. R32 is particularly suitable for applications that have used R410A or R22 refrigerants, primarily in split-air domestic air conditioning systems [4]. Furthermore, R32 refrigerants is readily available as it is a blend component of the R410A refrigerant.

As R32 refrigerant is gaining momentum, it is also important to evaluate the safety of R32 in terms of ignition potential as the safety risk might outweigh its potential environmental and performance benefits. Refrigerants are used in air conditioning systems which are in proximity to humans. A ruptured line or leaked refrigerant could create a local flammable concentration which will be combusted when it comes into contact with an ignition source [6]. Furthermore, flammability of R32 refrigerant is classified under the mildly flammable A2L class by American Society of Heating, Refrigerating and Air-Conditioning Engineers (ASHRAE) [7].

In conjunction with DAIKIN Malaysia's effort in studying the safety and ignition hazard of R32 refrigerants, an industrial-linked research has been established. The research centers on the possible hazards during the manufacturing stage of the refrigerants and air-conditioning systems. The pipes within an air-conditioner units must be sealed after injection of refrigerant by means of crimping which would induce a large amount of heat on the pressurised refrigerant inside the pipe network. More significantly, end parts of the pipe could also be sealed with weldments. Heat flux from welding introduces extreme temperatures by means of heat transfer into the refrigerant system [8].

At the instance when refrigerant leaked from the system comes into contact with an ignition source such as the open flame of welding gun, combustion might occur. An ignition source, fuel and oxidizer are essential elements for combustion [9]. With open flame in place as ignition source, leaked refrigerant as fuel and oxygen in the air as oxidizer, there is a risk of combustion occurrence. However, the Air-Conditioning and Refrigeration Equipment Manufacturers Association of Australia (AREMA) further constitutes that the concentration of the combustible R32 refrigerant-oil mixture must lie between the mixture's Lower Flammability Limit (LFL) and Upper Flammability Limit (UFL) [10] for the leaked mixture to be ignited. Therefore, the research focuses on determining the time required for the mixture's concentration to be flammable when subjected to different mixing factors by varying upstream mass flow rates and refrigerant-oil volume fractions. Period of time required for the downstream leaked mixture's concentration to lie within its flammability limits is identified as critical

flammable timeframe. Research outcome will contribute in DAIKIN's risk analysis on the ignition hazard of R32 refrigerant, where the critical flammable timeframe for the leaked mixture concentrations to lie within the respective flammability limits can be predicted.

2. Methodology

Theoretical analysis is implemented to obtain the density, LFL and UFL of the mixture. Subsequently, numerical analysis of R32 refrigerant-compressor oil mixture leakage through an orifice of a pipe into a 0.3 m^3cubic far field space is performed in ANSYS Fluent v15.0 solver. Physical dimensions such as pipe length, diameter, orifice size and cubic space are specified by DAIKIN. Critical flammable timeframe for the mixture to be within its LFL and UFL when it is leaked into the far field space can be predicted; in which the orifice outlet velocity and mass flow rate are to be obtained first from the numerical model results.

2.1 Theoretical Analysis

2.1.1 Properties of R32 Refrigerant and PVE Compressor Oil

Density and flammability limits (in volume % in air) of gaseous R32 refrigerant is taken from a technical information published by the AREMA [10]. The compressor oil used for R32 refrigerant is a non-hydrolytic lubricant generally known as polyvinylther (PVE) which is miscible with HFC refrigerants. Essentially, its chemical compound is vinyl acetate. Idemitsu Kosan Co. Ltd. developed a series of PVE oil and DAIKIN uses the Daphne Hermetic Oil FV50S which is a new development by Idemitsu with inclusion of anti-abrasion and antioxidants additives. Honeywell GasBook [11] is referred to obtain the density and flammability limits of the oil.

Table 1. Density and flammability limits of R32 refrigerant and PVE oil.

Properties	R32 refrigerant	PVE oil
Density (kg/m^3)	1100	926
Lower Flammability Limit (volume % in air)	13.3	2.6
Upper Flammability Limit (volume % in air)	29.3	13.4

2.1.2 Properties of R32 Refrigerant - PVE Compressor Oil Mixture

Equation (1) is used to determine the density of the two-phase R32 refrigerant and PVE oil mixture.

$$\rho_{mixture} = \frac{1}{\frac{x_{R32}}{\rho_{R32}} + \frac{x_{oil}}{\rho_{oil}}} \quad (1)$$

where x represents the volume fraction of the refrigerant and oil, ρ represents the density of the components.

The mixture's flammability limits are computed from the Le Chatelier's equations [12] in equation (2) and (3).

$$LFL_{mixture} = \frac{1}{\sum_{i=1}^{n} \frac{x_i}{LFL_i}} \quad (2)$$

$$UFL_{mixture} = \frac{1}{\sum_{i=1}^{n} \frac{x_i}{UFL_i}} \quad (3)$$

where LFL_i & UFL_i are the lower and upper flammability limits for component i in air, n is the number of combustible species.

DAIKIN has fixed the volume fractions to be 95% R32/5% oil (mixture of 95 R32 refrigerant with 5% of PVE oil), 96% R32/4% oil and 97% R32/3% oil. The density and flammability limits of the mixture vary based on different refrigerant-oil volume fractions.

Table 2. Density and flammability limits of refrigerant/oil mixture

Properties	Mixture Volume Fractions (% R32/% oil)		
	95/5	96/4	97/3
Density (kg/m^3)	1089.76	1091.79	1093.83
LFL (volume % in air)	11.03	11.42	11.84
UFL (volume % in air)	27.66	27.97	28.29

2.2 Governing Equations of Numerical Model and Turbulence Model

The flow of R32 refrigerant and PVE oil mixture in the pipe is treated as a homogeneous two-phase flow by assuming a steady state flow. Furthermore, the two-phase flow model is also based on the following idealisations:

- Local thermodynamic equilibrium is achieved between the two phases
- Pressure is uniform across any plane normal to the flow direction
- Sum of areas occupied by the two phases in any plane normal to flow direction is equal to the pipe cross section area

Hence, the flow is modelled as a multiphase flow with the Euler-Euler approach where the Volume of Fluid (VOF) model is used. The two phases share the same set of conservation equations in VOF model [13]. These governing equations for each of the phase are as follow shown in equation (4) and (5).

Conservation of Mass:

$$\frac{\partial}{\partial t}(\rho) + \nabla.(\rho U) = \sum_{n} S_n \quad (4)$$

where S_n represents the volumetric sources of n phases, U represents fluid velocity.

Conservation of Momentum:

$$\frac{\partial}{\partial t}(\rho U) + \nabla.(\rho U.U) = -\nabla.\pi + \rho g + F \quad (5)$$

where $\nabla.\pi$ represents the molecular contributions (pressure and viscous force), F represents external force.

Furthermore, turbulent flow of the mixture is simulated using the standard k- ε turbulence model. Standard k- ε models are widely used due to its simplicity, stability and excellent performance in industrial related flows [14]. Shah et al. [15] and Liang [16] employed this turbulence model for numerical analysis on flow through an orifice and numerical simulation of turbulent flows though structures respectively. The standard k- ε model has same conservation equations with VOF models. However, it has two extra governing equations which simplified the transport equations of turbulent kinetic energy, k in equation (6) and turbulent kinetic energy dissipation rate, ε in equation (7).

$$\frac{\partial}{\partial t}(\rho k) + \nabla.(\rho k U) = \nabla.\left(\frac{\mu_t}{\sigma_k}\nabla k\right) + 2\mu_t S_{ij}.S_{ij} - \rho\varepsilon \quad (6)$$

$$\frac{\partial}{\partial t}(\rho \varepsilon) + \nabla.(\rho \varepsilon U) = \nabla.\left(\frac{\mu_t}{\sigma_\varepsilon}\nabla \varepsilon\right) + C_{1\varepsilon}\frac{\varepsilon}{k}2\mu_t S_{ij}.S_{ij} - C_{2\varepsilon}\rho\frac{\varepsilon^2}{k} \quad (7)$$

where S_{ij} is the rate of deformation and adjustable constants from data fitting in which $\sigma_k = 1.00$, $\sigma_\varepsilon = 1.30$, $C_{1\varepsilon} = 1.44$, $C_{2\varepsilon} = 1.92$.

These governing equations are solved with default under-relaxation factors of pressure = 0.3, momentum = 0.7, turbulent kinetic energy = 0.8, turbulent kinetic energy dissipation rate = 0.8.

2.3 Meshing

Inlet (as shown as A) and outlet (as shown as B) surfaces selection is shown in the pipe geometry in Fig. 1. As per required by industrial partner, the length of the pipe is fixed to be 50 mm with an outer diameter of 6.35 mm. The orifice will be a 2 mm diameter surface downstream. Meshing at the near wall region and at the orifice in shown in Fig. 2.



Figure 1. Inlet and outlet surfaces of the pipe

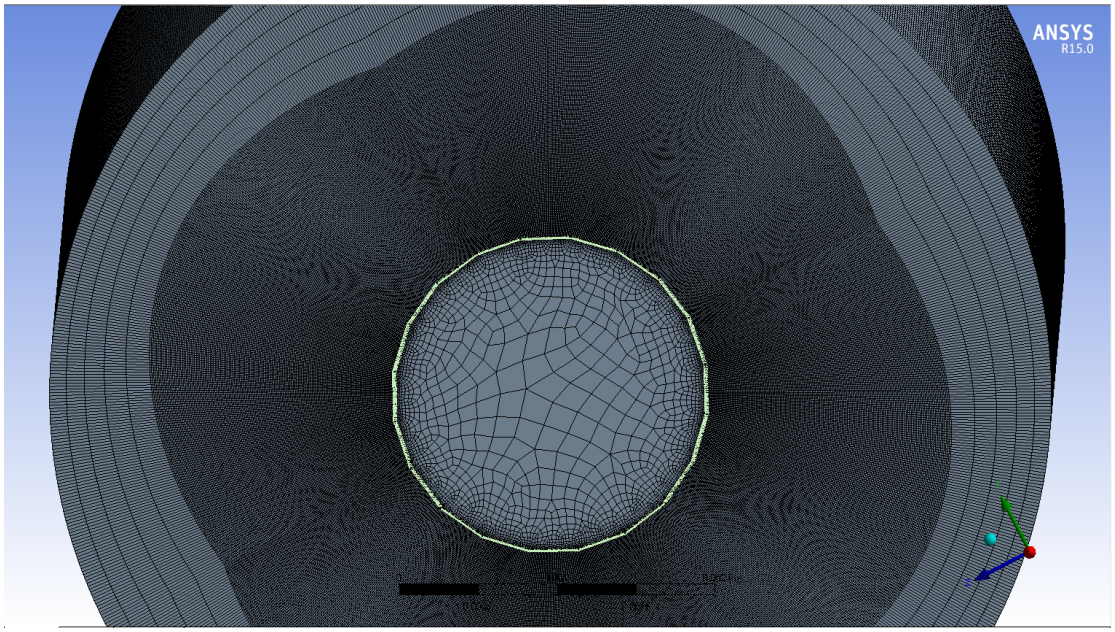


Figure 2. Near wall region and orifice meshing

A grid independence study was implemented (upstream mass flow rate of 200 g/min and 95% R32/5% oil) to determine the element size which is sufficiently fine where the solution changes by insignificant margin or does not change by further refinement of mesh. Mesh refinement were done by implementing different relevance centre sizing. From the study, it depicts that the finer the relevance centre, the larger the number of elements generated.

Table 3. Statistics of meshing with different relevance centre sizing

Properties	Relevance Centre Sizing		
	Fine	Medium	Coarse
Number of Elements	168695	104960	74660
Maximum Skewness	0.746	0.746	0.702
Minimum Orthogonal Quality	0.647	0.647	0.673

Average axial velocity and average static pressure for different relevance centre sizing are given in Fig. 3. There are no appreciable differences found in the velocity and pressure profiles for fine and medium meshes. However, there are significant margins of error between coarse and fine meshes. For fine mesh, hexahedral meshes have been used in all the simulations. It is ensured that at least one grid must be in the viscous sublayer (y^+<5) and other nodes in the turbulent and buffer zones [15].

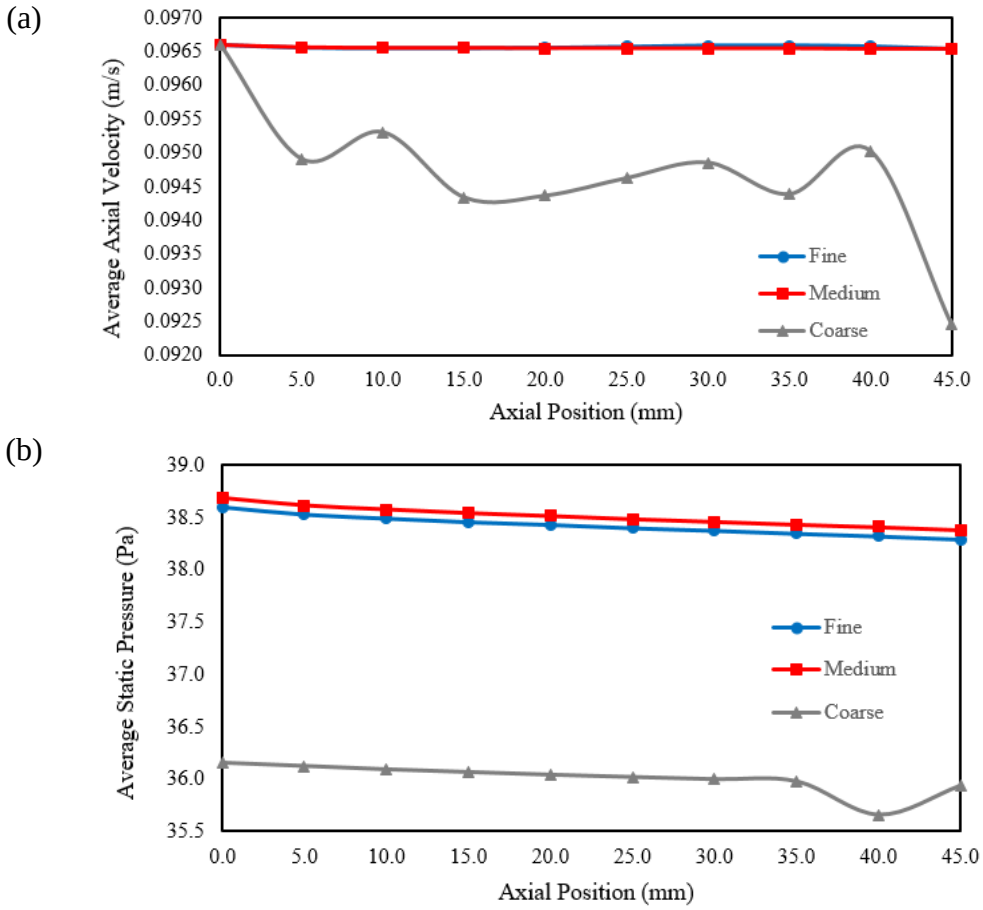


Figure 3. Effect of grid size on (a) average axial velocity and (b) average static pressure with different relevance centre sizing.

2.4 Boundary Conditions

The inlet of the flow is set as a velocity inlet. Although upstream mass flow rates are specified by DAIKIN, the inlet cannot be set as mass-flow inlet because VOF model requires the input of mass flow rates of each individual phase [17] which are not known. Hence, inlet velocity of the mixture is computed from the given mass flow rates. R32 refrigerant and PVE oil are set as primary and secondary phase of the flow respectively. The orifice is set as a far-field outlet because the leakage of the mixture will be dispersed into the atmosphere which have trivial pressurisation effect on the leakage. Hence, pressure-far-field is selected to mimic this scenario.

DAIKIN has specified upstream mass flow rates within the range of 50–200 g/min. Therefore, the inlet velocity of the simulations are computed from 50, 100, 150 and 200 g/min upstream mass flow rates. For each mass flow rate, the volume fraction of refrigerant/oil are varied: 95% R32/5% oil, 96% R32/4% oil and 97% R32/3% oil. No-slip condition for the boundary layers is imposed over walls [18]. Turbulent intensity is fixed at 5% for both inlet and orifice outlet. SIMPLE pressure-velocity coupling scheme is used as its improves the rate of solution convergence [19]. FLUENT solver stopped once the convergence criterion of 1E-6 is achieved.

3. Results & Discussion

Average pressure profiles subjected to different upstream mass flow rates are depicted in Fig. 4. As the mass flow rate is increased by a margin of 50 g/min, the average pressure at the orifice outlet increases accordingly. Numerical simulations are also performed with different refrigerant-oil volume fractions. An increasing amount of oil composition in the mixture also increases the average pressure proportionally. Since PVE oil is the secondary liquid phase of higher density and molecular weight than the vapour R32 refrigerant, therefore an increment of PVE oil presence in the mixture will result in larger pressure along the flow and at the orifice. For instance, in Fig. 4, when the mass flow rate of 95% R32 and 5% oil mixture is increased 25% from its previous value to 100 g/min, the average pressure at outlet increased by approximately 37%. On the other hand, as the oil composition of 100 g/min flow is increased from 4% to 5% (25% increment from previous value), it produced only an increment of about 22% in the average pressure. Hence, the effect on downstream pressure by increasing the upstream mass flow rate of mixture flowing into the pipe is more dominant than increasing the oil composition in the mixture.

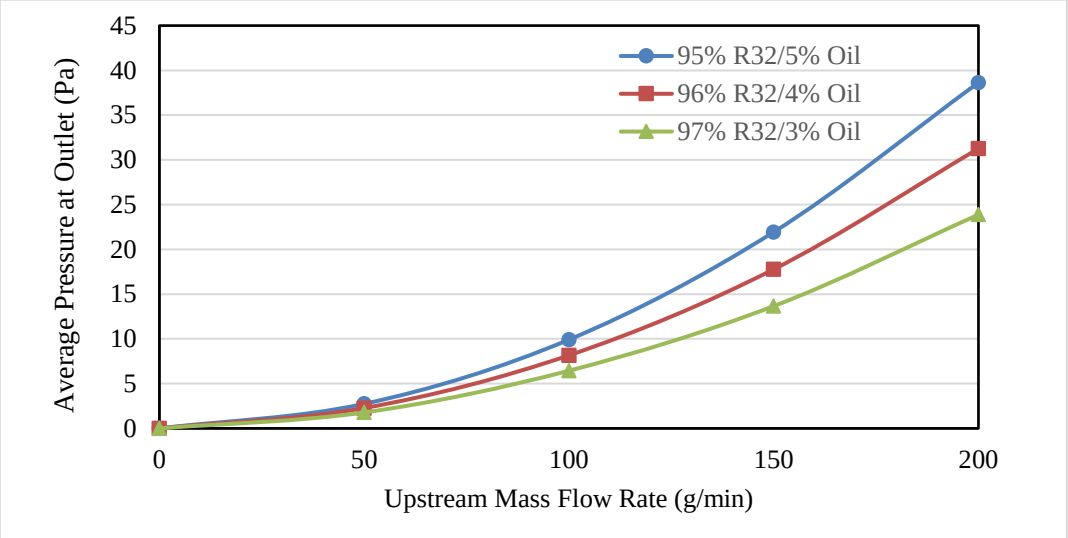


Figure 4. Graph of outlet average pressure against upstream mass flow rate

In addition to that, the effect of upstream mass flow rate on downstream flow property is further displayed evidently in Fig. 5. The average velocity at the orifice outlet is directly proportional to the mass flow rate. However, increment in oil composition shown insignificant effect on the downstream velocity as the lines of different refrigerant/oil mixture are stacked on top of one another in Figure 4-2 indicating trivial differences. This is because for the given range of mass flow rate between 50 – 200 g/min, the inlet velocity is low. For instance, at 200 g/min, the inlet velocity of the mixture is computed to be only 0.097 m/s. Since the molecular weight and molecular structure of PVE oil is larger than R32 refrigerant, therefore by increasing the volume percentage of PVE oil should cause the mass of the flow to be heavier and hence resulting in a drop in velocity. However, the flow velocity of mixture with 3%, 4% and 5% PVE oil is similar at the orifice outlet. This is due to the lubricating nature of PVE oil itself. Slowdown effect cause by its weight is at the same time compensated by its lubricating effect. Hence, when modifying the oil composition from 3-5%, the flow of mixture is reduced by the increase in weight but the additional PVE

oil also provides more lubrication for the flow in which it regains some of its velocity lost.

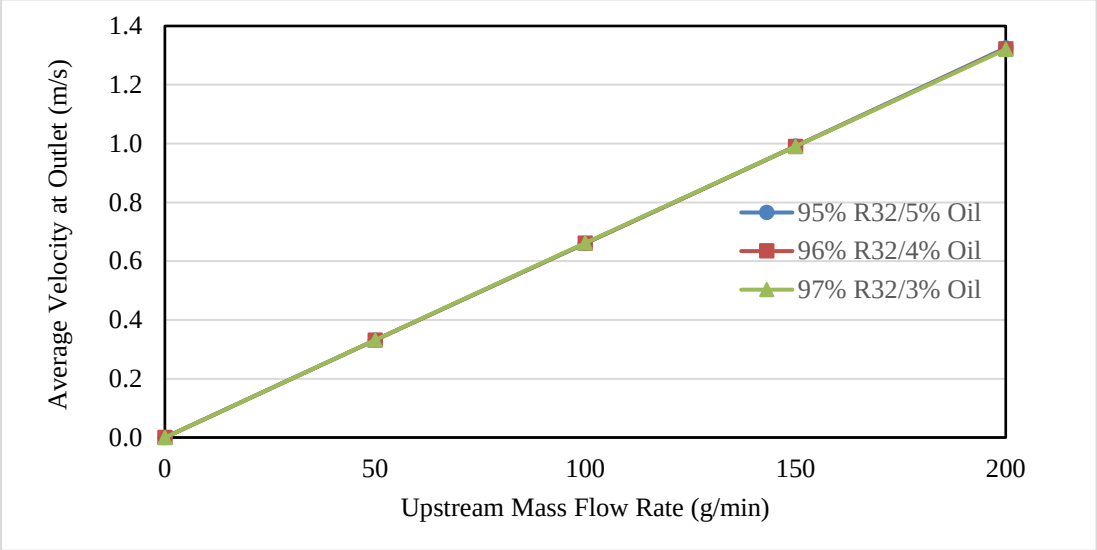


Figure 5. Graph of outlet average velocity against upstream mass flow rate

Subsequently, mass flow rates at the orifice outlet is obtained from the average velocities at the orifice based on the mass flow rate equation. Surface plot in Fig. 6 exhibits the influence of upstream mass flow rates and mixture volume fractions on the mass flow rate at the orifice. From the outcome obtained, there are only twelve data points. In order to generate the surface plot, MATLAB is utilised to interpolate the data between the available data points. A mesh grid is then generated. The distinct blue dots on the surface plot are the available data points. As shown by the gradient of the surface, the mass flow rate at the orifice is influenced by the upstream mass flow rate. Since the flow only has an inlet and an outlet, the increment of upstream mass flow rates will result in direct increment on the orifice mass flow rate which is located linearly downstream. Conversely, the flat surface of the plot indicates that for a fixed upstream mass flow rate, the effect of increasing oil composition on the orifice mass flow rate is insignificant. Since the effect of oil volume fraction on the outlet velocity is insignificant, therefore it also shows trivial influence on the outlet mass flow rates.

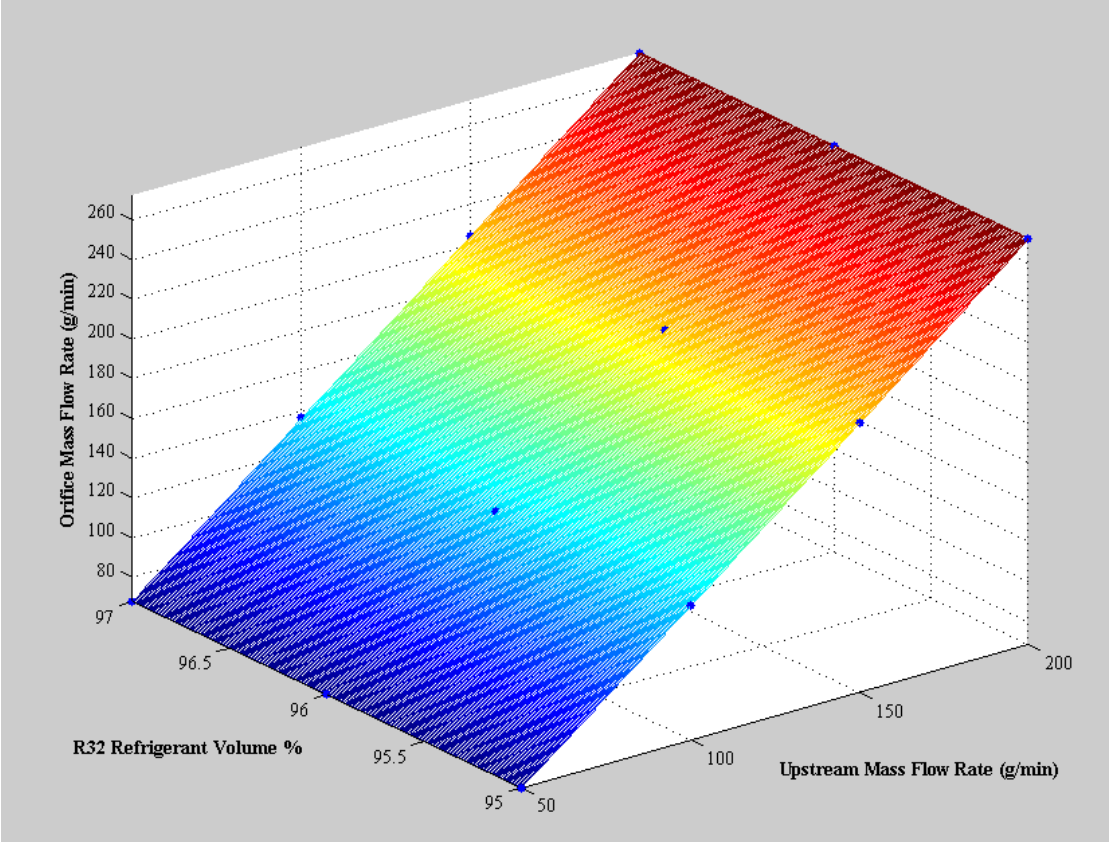


Figure 6. Surface plot of orifice mass flow rate against R32 refrigerant volume percentage and upstream mass flow rate

Mass of mixture combustible percentage in the 0.3 m^3 cubic space can be obtained from the product of the flammability limits and the spatial volume. Critical flammable timeframe can then be determined by taking the ratio of combustible mass at the flammability limits to the outlet mass flow rate of leaking mixture into the cubic space.

The critical flammable timeframe of the leaking mixture is predicted in Table 5. Time required for the mixture's concentration in air to attain its lower and upper flammability limits is only slightly affected (difference in hundred thousandths place) by different R32 refrigerant/PVE oil mixture's volume fraction. When the upstream mass flow rate is increased, the time required for the mixture percentage in air of the cubic space to be flammable is reduced. In other words, the time taken for combustion to occur from the ignition of the leaked mixture in the downstream space is shorter when the upstream mass flow rate is larger. For instance, the critical flammable timeframe for 200 g/min upstream mass flow rate of 95% R32/5% PVE oil is approximately between 12–30 minutes. That is to say if the leaking of mixture is stopped before the 12^{th} minute or is allowed to leak more than 30 minutes, ideally combustion will not occur. This is because the mixture is too lean to burn in the former case and it is too rich in combustible composition in air in the latter [9].

Table 4. Time required for leaked mixture's concentration to be within respective flammability limits with different mass flow rate and volume fraction

Upstream Mass Flow Rate (g/min)	Volume Fraction (% R32/% oil)	Time required to reach (minute)	
		LFL	UFL
50	95/5	47.67	119.56
	96/4	47.58	119.34
	97/3	47.45	119.01
100	95/5	23.92	60.01
	96/4	23.86	59.84
	97/3	23.77	59.63
150	95/5	15.94	39.97
	96/4	15.92	39.93
	97/3	15.89	39.85
200	95/5	11.92	29.89
	96/4	11.92	29.90
	97/3	11.92	29.89

4. Conclusion

From the grid independence test, medium relevance centre sizing mesh has exhibits grid independent solution. Hence, the number of elements generated by medium sizing meshes are sufficient for solution convergence. Based on the theoretical analysis and simulations, average velocity and average static pressure at orifice outlet displayed a proportional relationship with the upstream mass flow rates. Effect of R32 refrigerant and PVE oil volume fractions are less significant on the outlet velocities and pressures compared to that of upstream mass flow rate. Time required for the leaking mixture's concentration to lie within its lower and upper flammability limits have been predicted. Hence, the critical flammable timeframe is identified. Similarly, the effect of upstream mass flow rate is more notable than the mixture volume fractions on the critical flammable timeframe. Based on the range of upstream mass flow rate specified by DAIKIN, the flammability limits are breached earliest by the leaking mixture's concentration when the upstream mass flow rate is the largest, which is at 200 g/min. Therefore, among the two mixing factors of upstream mass flow rates and refrigerant-oil volume fractions, the former has a more significant influence on the flammability. The research can be carried on further by investigating the propagation of flame when the mixture is ignited in the downstream far-field space. Besides predicting the flammable timeframe of the leaked mixture, the distance of the flame propagation could also serve as an important safety indicator which represents a safe proximity when the mixture is ignited. Low GWP refrigerants is demanded by the current climate and R32 is most likely a suitable candidate. Hence, some flammability constraint of R32 refrigerant has begun to be accepted by countries with supporting researches from the industry and academics on the safety and hazards of R32 refrigerant.

Acknowledgements

This study has been conducted as an industrial linked final year research project with DAIKIN R&D Malaysia, on the ignition hazards and safety of R32 refrigerant.

The authors would like to thank DAIKIN R&D Malaysia Development Support Division for the support throughout the study.

References

[1] United Nations, "The Montreal protocol on substances that deplete the ozone layer.," Ozone Secretariat, United Nations Environmental Programme (UNEP), 1988.

[2] United Nations, "Kyoto Protocol to the United Nations Framework Convention on Climate Change," 1998.

[3] DAIKIN, "DAIKIN GROUP CSR Report," 2013.

[4] Linde-Gases, "R32 - Lower GWP HFC refrigerant for air conditionng aplications," pp. 1–3, 2013.

[5] M. Pande, Y. H. Hwang, J. Judge, and R. Radermacher, "An Experimental Evaluation of Flammable and Non-Flammable High Pressure HFC Replacements for R-22," in *Int. Refrigeration and Air Conditioning Conference*, pp. 21–26, 1996.

[6] A. Boussouf, "Hot Surface Ignition of R-32 and R-410A Refrigerant Mixtures With Lubricating Oil," *M. Sc. thesis, Univ. Maryl.*, 2014.

[7] ASHRAE STANDARDS COMMITTEE, "Designation and Safety Classifications of Refrigerants," 2000.

[8] J. Hu and H. L. Tsai, "Heat and mass transfer in gas metal arc welding. Part I: The arc," *Int. J. Heat Mass Transf.*, vol. 50, no. 5–6, pp. 833–846, 2007.

[9] D. Crowl and J. Louvar, "Fires and Explosions," in *Chemical Process Safety*, pp. 223–229, 2012.

[10] A. Air-conditioning and Refrigeration Equipment Manufacturers Association of Australia and C. Consumer Electronics Supplier Association, "R32 – COMMON QUESTIONS," 2014.

[11] Honeywell, "Flammable Gas Hazards," in *Honeywell GasBook*, 5th ed., Honeywell Analytics, pp. 18–19, 2013.

[12] C. V Mashuga and D. a Crowl, "Derivation of Le Chatelier's mixing rule for flammable limits," *Process Saf. Prog.*, vol. 19, no. 2, pp. 112–117, 2000.

[13] ANSYS Inc., "Fluent 12.0 User Guide." ANSYS Inc., 2009.

[14] W. Malalasekera and H. Versteeg, "An Introduction to Computational Fluid Dynamics: The Finite Volume Method," Pearson Education Ltd., pp. 67–75, 1995.

[15] M. S. Shah, J. B. Joshi, A. S. Kalsi, C. S. R. Prasad, and D. S. Shukla, "Analysis of flow through an orifice meter : CFD simulation," in *Chemical Engineering Science*, vol. 71, Elsevier, pp. 300–309, 2012.

[16] G. Liang, "Numerical Simulation of 3D , Complex , Turbulent Flows with Unsteady Coherent Structures : From Hydraulics to Cardiovascular Fluid Mechanics" Georgia Institute of Technology, 2004.

[17] ANSYS Inc., "ANSYS FLUENT 15.0 User's Guide," in *ANSYS FLUENT 15.0 User's Guide*, 2013.

[18] W. Li, X. Zhang, Z. Shuai, C. Jiang, and F. Li, “CFD Numerical Simulation of the Complex Turbulent Flow Field in an Axial-Flow Water Pump,” *Adv. Mech. Eng.*, vol. 2014, 2014.

[19] T. J. Craft and G. B. Building, “Pressure-Velocity Coupling,” in *Advance Modelling & Simulation: CFD*, The University of Manchester, pp. 9–12, 2008.

eureca 2016 – Conference Paper
Paper Number 2ME29

Further Development of Non-Contact Vibration Sensor for Rotating Machine

Wai Wai[1*], Lim Chin Hong[1]

[1]*School of Engineering, Taylor's University, Malaysia*

[*]*wai_6166@hotmail.com*

[1]*School of Engineering, Taylor's University, Malaysia*

Abstract

The objective of this project is to develop a non-contact vibration sensor to detect mechanical vibration of rotating machine. Many studies have proven that machine vibration analysis is an effective tools to detect machine health conditions for prognosis and predictive maintenance. Vibration analysis using contact type vibration sensors are used to maximize machine running time, improve machine reliability and safety. However, contact type sensors are not suitable in some applications such as on rotating machines or high electromagnetic wave environment. Therefore, this study is conducted to develop a non-contact vibration sensor to perform vibration analysis on electrical rotating machines like generators and motors. This study focuses on utilizing the ultrasonic technology to perform non-contact vibration measurement. The ultrasonic sensor able to detect object movement from a distance away by capturing the time between sending and receiving ultrasonic signals. HC-SR04 ultrasonic displacement sensor with Arduino Uno micro-controller are selected for this purpose. Experiments were conducted to identify the sensitivity, accuracy and limitation of this vibration sensing technique. It was found that the sensor can detect vibration frequency more than 1Hz, with minimum amplitude of 5mm from 3 metre away from the targets. The sensor also found that has optimum detecting range at 320mm with 5% of error percentage.

Keywords: Non-Contact, Vibration Analysis, Vibration Sensor, Ultrasonic Range Sensor

1 Introduction

Vibration is a physics phenomenon which object oscillates or reciprocates from equilibrium position. Vibration is quantified in tern of frequency (Hertz/Cycle per second). Human can sense the object is vibrating by physical contact or observe the object back-and forth movement. Sometimes vibration creates sounds that human can hear. However, in this project will be focus on the vibration creates by machine.

Machine vibration is the reciprocating movement of machines or machine components, especially machines that contain rotating element, it vibrates while operating. Most of the times machine vibration is unintended and undesirable as it causes mechanical loss and leads to damage the machine parts and components. Nevertheless, the vibration pattern of machines can be used for condition monitoring. (Naik et al. n.d.)Constant monitoring and analyzing machine vibration can predict the machine health conditions and mitigate potentiate irreversible breakdowns or failures.(Center n.d.) In addition, this machine health monitoring and fault diagnosis become more and more important especially in heavy industries. The rapid development of science and technology increase the large scale machine with higher operating speed and complicated structure design results in higher probability of various failure in practice. Such mechanical failures happen in heavy industries not just will cause enormous economic loss, but also will cause the loss of many people's lives.(Zhang 2013) Therefore, early fault diagnosis is important to ensure machine is reliable and safe to operate.

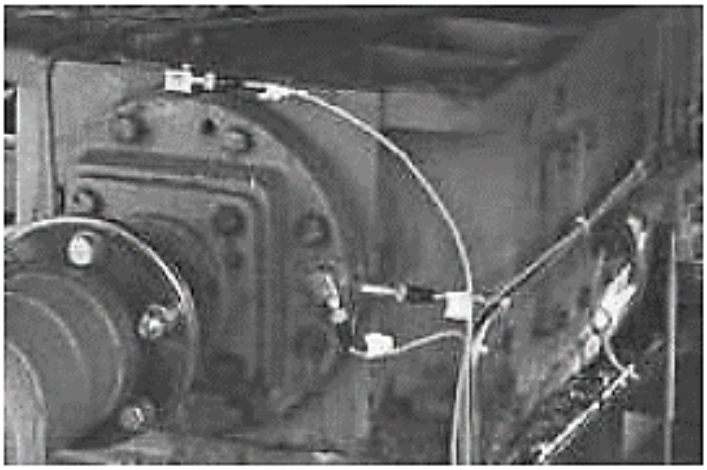


Figure 1. Accelerometer on a gear box*(Center n.d.)*

As mentioned, vibration analysis can detect these machinery problems and take an early machinery repairs to increase the lifespan of the machines, reduce machine down time and lead to higher machine reliability. In general industrial practice, accelerometer is the most common vibration sensing device to measure mechanical vibration and conduct vibration analysis. It is because the accelerometers can sense wide range of frequency, has high sensitivity and accuracy. However, the accelerometers have to make physical contact, usually mounted on the machine to retrieve vibration reading. The application of the accelerometer is shown in figure 1. In some cases, such as machines that contains high speed rotating element are very

challenging for an accelerometer to measure vibrations. Therefore, a non-contact vibration sensor is required to solve this problem.

In this project, an ultrasonic sensor is introduced to overcome current vibration sensing limitation. As mentioned above, ultrasonic is a sound waves that have frequency above the limits of human hearing, in excess of 20,000 cycle per second (hertz). The ultrasonic sensor can transmit and receive ultrasound waves, has a working principle similar to ultrasonic transducers such as radar and sonar systems. It generates a high-frequency sound waves out and waiting for the echo reflects, measuring the time taken between sending signal and receiving the echo to determine the distance to an object.



Figure 2. Ultrasonic Distance Sensor HC-SR04

The ultrasonic distance sensor (HC-SR04) is chosen for this project. It is one of the common ultrasonic range sensor available and compatible with Arduino microprocessor. It has the detection range up to 3000mm, 20Hz reading rate, 42 kHz frequency and resolution up to 3mm. This study will be focus on how to utilize the inexpensive ultrasonic range sensing technology to measure mechanical vibration and conduct vibration analysis. Besides, a test rig that able to vibrate at different frequency and amplitude will be set up to find out the sensitivity, accuracy and limitation of ultrasonic range sensor for vibration measurement on rotating machines. This ultrasonic vibration sensor will be tested on real life applications such as lathing machines or other rotating elements and compare to the existing conventional vibration sensors.

2 Research Methodology

2.1 Device and Setup

Ultrasonic Distance Sensor

Ultrasonic range sensor HC-SR04 was selected for this project. This ultrasonic range sensor HC-SR04 has a resolution up to 3mm, frequency up to 42 kHz and reading rate of 20Hz and range up to 4m.

The ultrasonic distance sensor HC-SR04 are worked with Arduino microprocessor to conduct this study. Arduino is one of the most common microcontroller board which enable users to control electric components such as LED's, servo and sensors. It is simple to learn, programme and able to run many applications. Arduino microprocessor is connected to a computer through a USB cable. Arduino software is required to install in computer. Arduino microprocessor reads the programming code from computer and received the distance reading from ultrasonic sensor and send back the reading to computer. The ultrasonic sensor is shown on figure 3 and specification is stated in table 1.

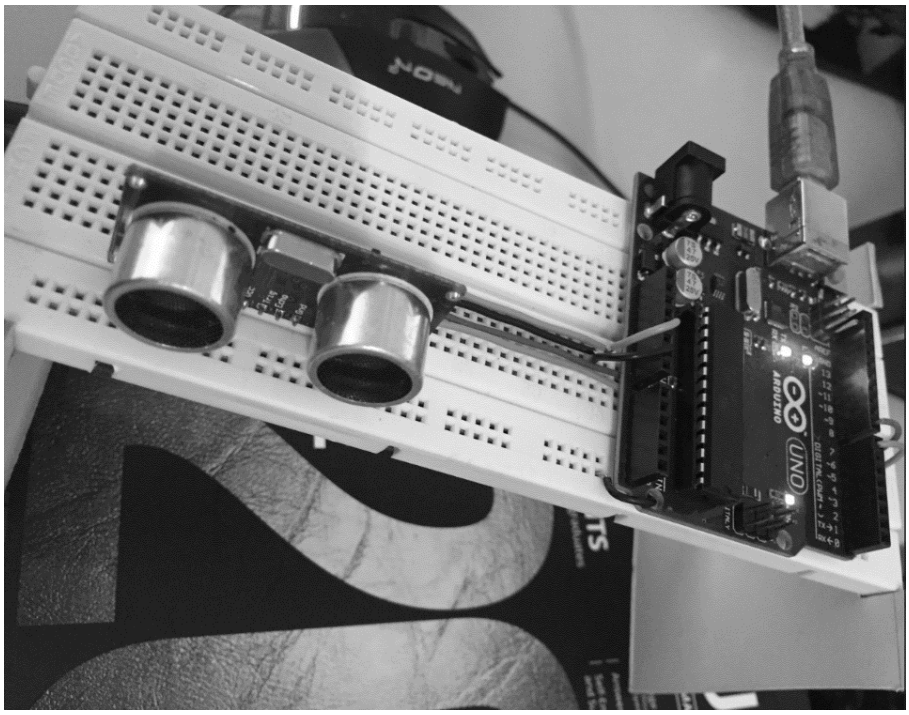


Figure 3. Ultrasonic Sensor Setup

The HC-SR04 ultrasonic distance sensor is initially built for detecting range by calculating the time interval between transmit signals and receiving echo. Since the ultrasonic distance sensor has high reading rate and frequency, the ultrasonic technology able to use on detecting mechanical vibration by sensing the position change of object.

Table 1: Specification of ultrasonic range sensor model MB1013

Ultrasonic Distance Sensor	Model HC-SR04
Reading Rate	20Hz
Frequency	42 kHz
Sensing Range	20mm- 4000mm
Operating Voltage	2.5V- 5.5V
Effectual Angle	<15°
Pulse Width	10uS
Resolution	0.3 cm
Sensor Output	Analog Voltage, RS232, TTL Serial

Besides, a test rig was built to test the ultrasonic sensor. The test rig is a device that able to program and vibrate in different frequency and amplitude. It is consists of a controller, servo motor, processor and black board. The servo is connected to the threaded shaft which enables the black board move back and forth in reciprocating movement. The ultrasonic sensor captured the movement of the black board to find out its limitation, sensitivity and accuracy.

Test Rig

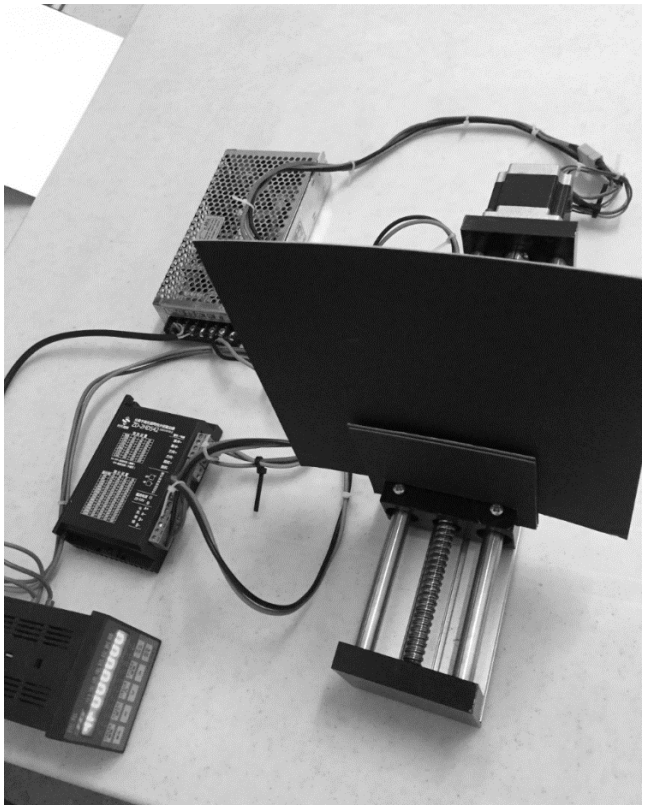


Figure 4. Test Rig

The test rig is a device that used for testing purpose for the ultrasonic sensor. It is consists of a controller, servo motor, processor, and black board. The test rig is programmable to turn the servo motor in different frequency and amplitude, rotating in clockwise and counter-clockwise. The servo is connected to the threaded shaft which enable the black board move back and forth in reciprocating movement. The ultrasonic sensor captured the movement of the black board to find out its limitation, sensitivity and accuracy.

2.2 Calibration and Testing

The ultrasonic vibration sensing device and test rig is setup as figure shown below. The ultrasonic sensor is tested under different frequency and amplitude to determine the specifications, sensitivity, the highest vibration frequency and lowest amplitude that the sensor able to record. The controllable test rig will be used as the target device to generate vibration for the ultrasonic vibration sensing device.

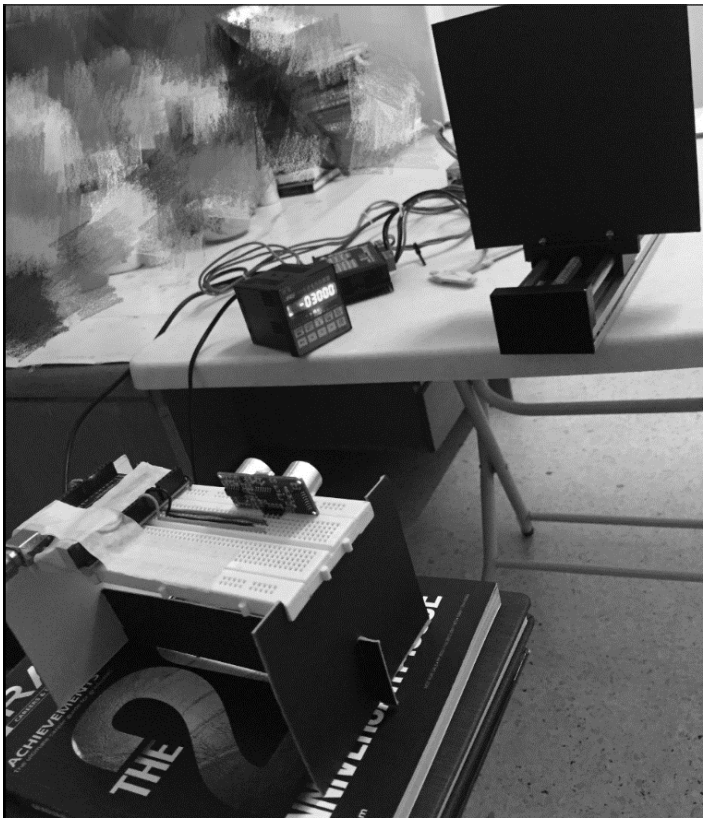


Figure 4. Experiment Setup

Experiment is conducted on the ultrasonic sensor to determine its capabilities, specifications and limitations. The test rig is placed a certain distance away from the sensor and programmed to vibrate at certain frequency and amplitude. The ultrasonic sensor captured the vibration of the black board and the result is compared to the initial value set in test rig. There are three parameters are tested on the ultrasonic sensor, which are amplitude, frequency and range.

Vibration Amplitude

Experiment is conducted to find out the limitation of the ultrasonic sensor on detecting maximum and minimum amplitude.

Vibration Frequency

Ultrasonic sensor send high frequency sound waves and evaluate the echo once detected an object. Therefore, there are gaps between each sound waves. When the moving object move in higher frequency, the result will be lesser accurate. Thus, experiment is conduction to determine the maximum frequency that the ultrasonic sensor able to capture.

Range/ Distance of Ultrasonic Sensor

As mentioned above, the test rig is set at certain distance away from ultrasonic sensor during experiment. The maximum and minimum detection range of the ultrasonic sensor test are conducted to determine the optimum working range without exceeding certain error percentage.

Accuracy Test

The result obtained from the ultrasonic sensor is compared to the initial value set at test rig. For example, the result of amplitude and frequency collected from sensor is the experimental value. The frequency and the amplitude of the test rig is actual value. The experimental value is compare to the actual value to find out the accuracy. Error percentage calculation is one of the most common and convenient method to determine the accuracy of the ultrasonic sensor.

2.3 Data Collection and Analysis

Ultrasonic sensor is considered as non-contact vibration displacement sensor. The ultrasonic sensor recorded the position of the vibrating device relative to time. Since the ultrasonic sensor send a high frequency reading rate (20Hz), in every seconds the sensor can detect object in 20 different position, thus the vibration pattern of the vibrating target device can be plotted. The result obtained from the ultrasonic sensor would be the distance between the sensor and object over time. Figure 3.8 shown the sample result collected by ultrasonic sensor when the test rig is moving at 30mm/s frequency. Graph is plotted instead of displaying in data for the ease of study and understanding.

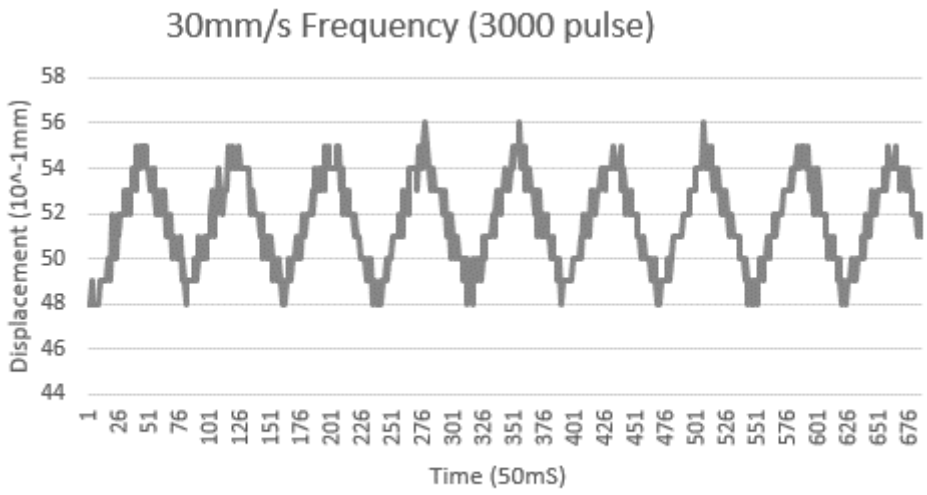


Figure 5. Graph of displacement versus time.

Such displacement graph can be interpret as vibration pattern. Using FFT (Fast Fourier Transform) method, the vibration displacement data can be converted into frequency spectrum pattern. Such frequency spectrum is the most common method to perform the vibration analysis.

Spectrum comparison is an effective method to detect the faults happened at the rotating element. (Kjaer n.d.)(Anderson et al. 2001)When the rotating element having faults such as shaft misalign, shaft bend or bearing defects, it will vibrates at different frequency and amplitude. Therefore, a comparison of two frequency spectra (reference spectrum and current spectrum) able to determine the conditions of rotating element. Figure 6 below shown a vibration spectrum comparison between healthy and faulty condition of rotating machines. It is clearly seen that the faulty rotating element shows significantly higher vibration amplitude than healthy condition rotating element.

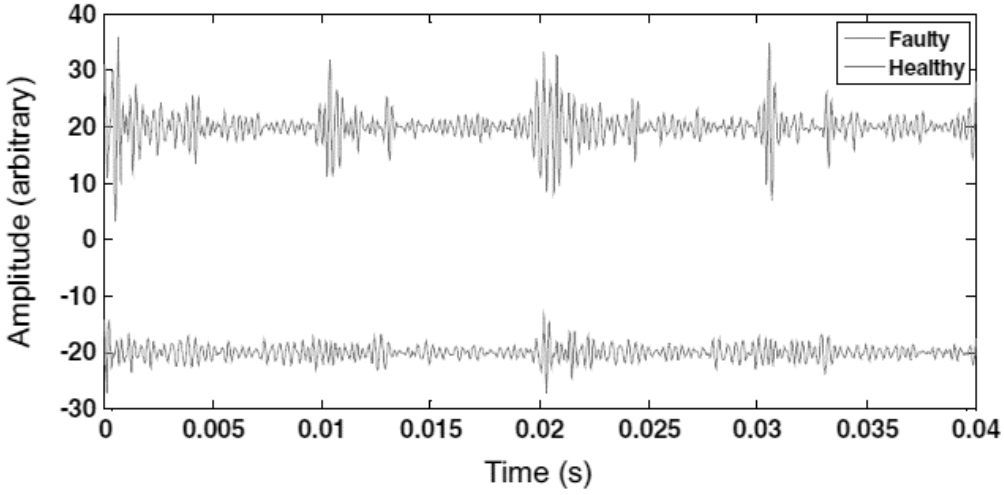


Figure 6. Spectrum comparison of faulty and healthy conditions of rotating machine*(Moosavian et al. 2016)*

3 Result and Discussion

3.1 Limitation of Measuring Angle

Based on the experiment conducted, the ultrasonic sensor has an optimum sensing angle at 30 degree (figure 4.1) (CytronMY). The ultrasonic sensor also have reading rate up to 20Hz (20 reading per second).

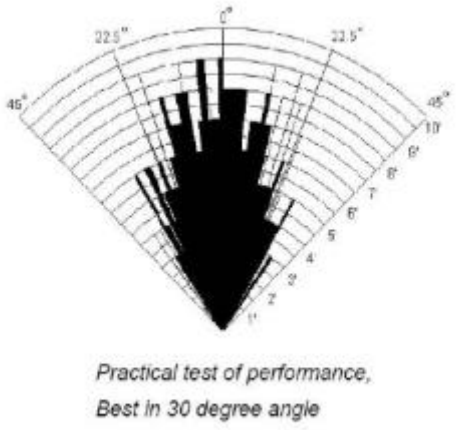


Figure 7. HC-SR04 measuring angle in practical test (CytronMY)

3.2 Limitation on Ultrasonic Sensor Range

The minimum detection range of the ultrasonic sensor is 50mm and maximum detection range is 4000mm. However, the accuracy of the sensor decreases if the distance between sensor and target device increases. Experiment is conducted to determine the optimum detection range for the ultrasonic sensor. The test rig is placed 100mm, 300mm, 500mm, 700mm and 900mm distance away from the sensor. The test rig is programmed to vibrate at same frequency and amplitude in this range test. The result from ultrasonic sensor is recorded and compare to the theoretical result which is the initial frequency and amplitude set on test rig. Error percentage is calculated and graph of error percentage versus distance is plotted.

The results is plotted as graph of displacement versus time for the ease of study and comparison. Based on the graph of displacement versus time below, the accuracy of the result showed decreasing significantly. In 700mm and 900mm graphs can see that the result collected by sensor is fluctuating compared to 100mm and 300mm graphs.

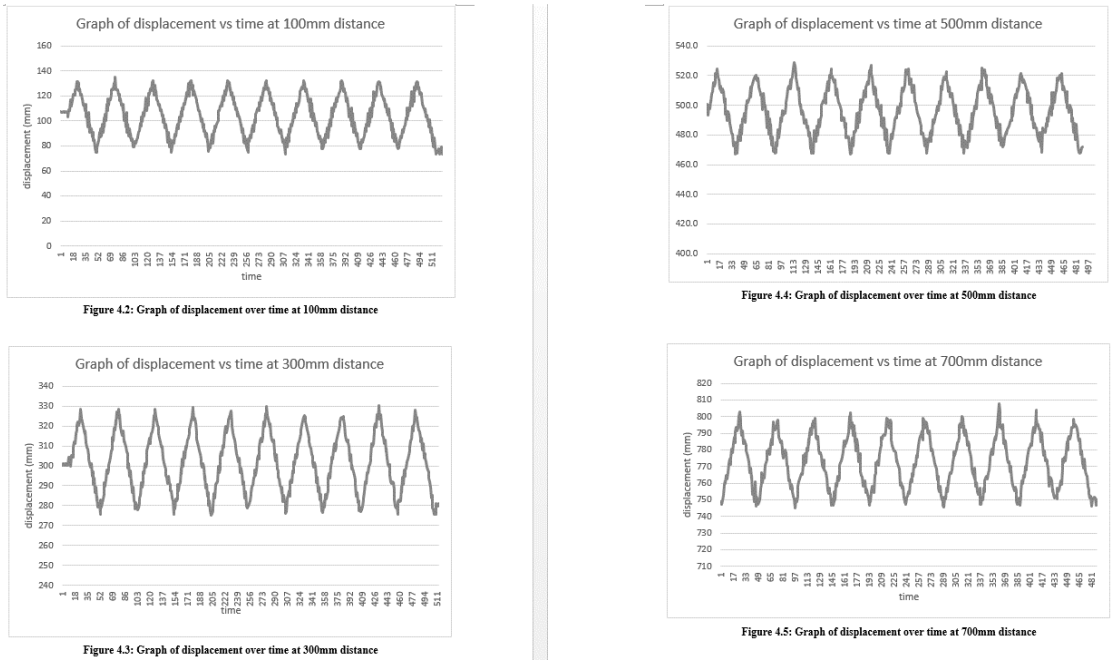


Figure 8. Result of range test.

Calculation Example

Result of displacement versus time at distance of 300mm is used to demonstrate as calculation example. Test rig is set to vibrate at 10mm/s frequency and 50mm amplitude. In each sin wave cycle, maximum point and minimum point are taken from the graph to calculate the range detected by the sensor. The result is averaged by 5 reading to achieve higher accuracy.

Table 2: Result of displacement versus time at 300mm distance

Maximum Point (mm)	Minimum Point (mm)	Range (mm)
328.70	275.77	52.93
328.69	278.87	49.82
328.60	275.77	52.92
327.60	275.20	52.40
329.28	275.26	54.05
	Average	54.42

$$Error\ Percentage\ (\%) = \frac{Experimental\ Value - Theoretical\ Value}{Theoretical\ Value} x100$$

$$= \frac{54.42mm\ - 50mm}{50mm} x100\%$$

Result

Table 3: Result of error percentage at different range/distance

Range	100mm	300mm	500mm	700mm	900mm
Error Percentage	4.2%	4.8%	8.6%	9.1%	11.2%

Graph of error percentage versus distance is plotted using the result in table above. Based on the graph below, it is observed that the error percentage is proportional to the distance. The error is higher as the distance between sensor and target device increases. If the optimum result requires error percentage less than 5 percent, the optimum detection range of the sensor is less than 320mm.

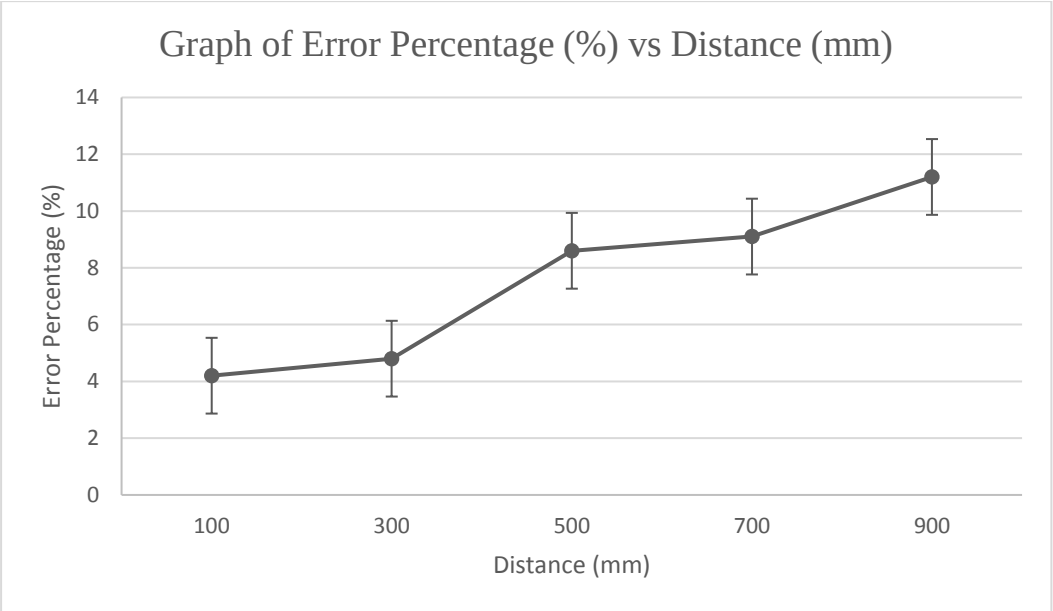


Figure 9. Relationship of error percentage to distance

3.3 Limitation on Vibration Frequency

Limitation of frequency is one of the most important criteria need to be tested on a vibration sensor. In real life applications, the non-contact vibration sensor need to have high frequency enough to detect the precise instantaneous location of the target device that vibrating at high speed to perform the vibration analysis.

In this research project experiment, the test rig is programmed to vibrate at certain frequency and the ultrasonic sensor record the results. The test rig is started at 0.166Hz and gradually increase until achieved its maximum frequency at 1.098Hz.

The results are presented in graph shown in figure to figure. It is observed that the accuracy of result decreases as the frequency of the test rig increases, especially the frequency had increased more than 0.814Hz.

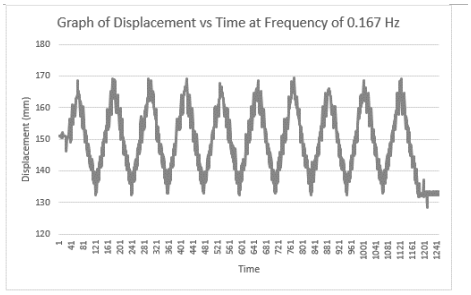


Figure 4.8 : Graph of displacement over time at frequency of 0.167Hz

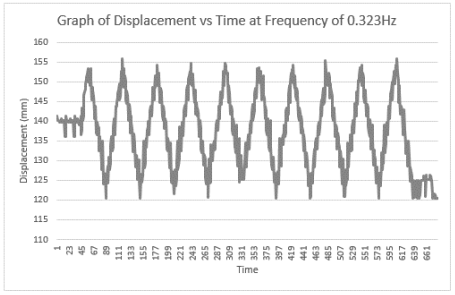


Figure 4.9: Graph of displacement over time at frequency of 0.323Hz

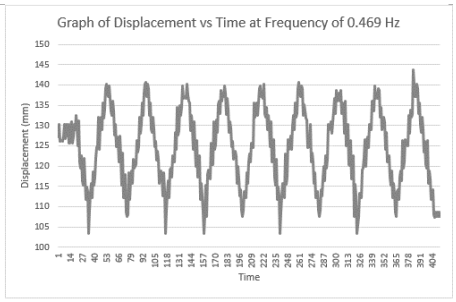


Figure 4.10: Graph of displacement over time at frequency of 0.469Hz

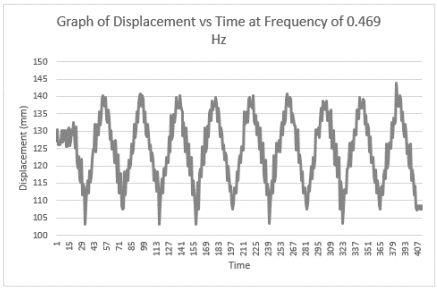


Figure 4.11: Graph of displacement over time at frequency of 0.469Hz

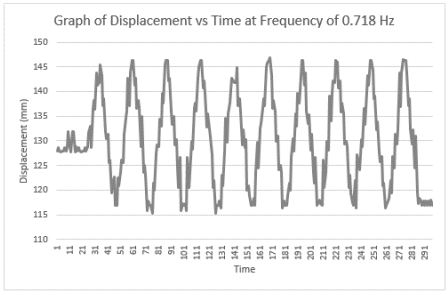


Figure 4.12: Graph of displacement over time at frequency of 0.718Hz

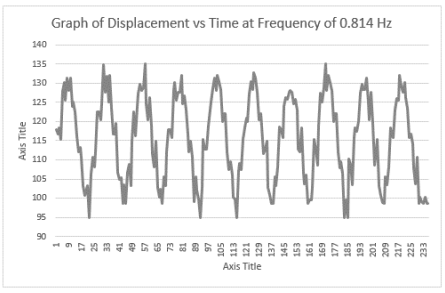


Figure 4.13: Graph of displacement over time at frequency of 0.814Hz

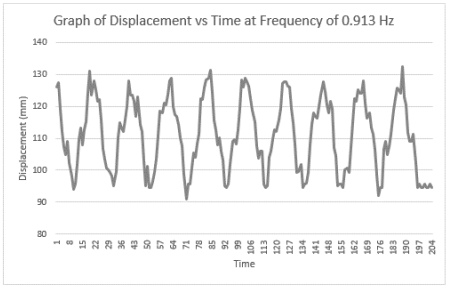


Figure 4.14: Graph of displacement over time at frequency of 0.913Hz

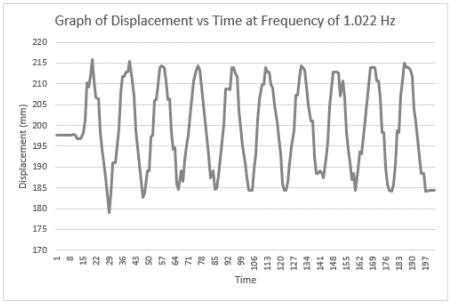


Figure 4.15: Graph of displacement over time at frequency of 1.022Hz

Figure 10. Result of frequency test.

Sample Calculation

Graph of displacement vs time at frequency of 1.66Hz is used to demonstrate as calculation example. The amplitude of vibration is set fixed at 30mm during the whole frequency test. Based on the graph of displacement vs time at frequency of 1.66Hz, 5 points between each cycle was taken and averaged for more precise reading. Since the ultrasonic sensor sends and receives 20 signals per second, therefore, the points recorded have to divide by 20 to obtain the time interval. Using the f=1/T formula, the experimental frequency value is able to calculated.

Result

Table 3. Experimental result of frequency at 0.166Hz

Frequency of 0.166Hz					
Points between each cycle	120	115	127	117	123
Average point per cycle		120.4			
Time Taken (seconds)		6.02			
Frequency (1/T, Hz)		0.167			

$$Error\ Percentage\ (\%) = \frac{Experimental\ Value - Theoretical\ Value}{Theoretical\ Value} x100$$

$$= \frac{0.167 - 0.166}{0.166} x100\%$$

$$= 0.6\%$$

Table 5. Error Percentage result under different frequency

Average point per cycle	120.4	60.8	41	31.8	26.6	23.6	20.08	18.2
Time Taken (seconds)	6.02	3.04	2.05	1.59	1.33	1.18	1.04	0.91
Frequency (Hz)	0.167	0.323	0.469	0.606	0.718	0.814	0.913	1.022
Actual frequency (Hz)	0.166	0.328	0.487	0.628	0.751	0.847	0.961	1.098
Error Percentage (%)	0.6	1.5	3.84	3.63	4.60	3.30	4.80	7.44

Graph of error percentage versus frequency is plotted using the result in table 4.4. Based on graph in figure 4.16, it is clearly seen that the error percentage is roughly proportional to the frequency of the target device. As the frequency of the test rig increases, the error percentage increases as well, the error percentage increase gradually between 0.167Hz to 0.814Hz. The error percentage increase significantly as the vibration frequency of the test rig increased more than 0.814Hz. The frequency of the target device has to be lower than 0.92Hz in order to achieve error percentage less than 5 percent.

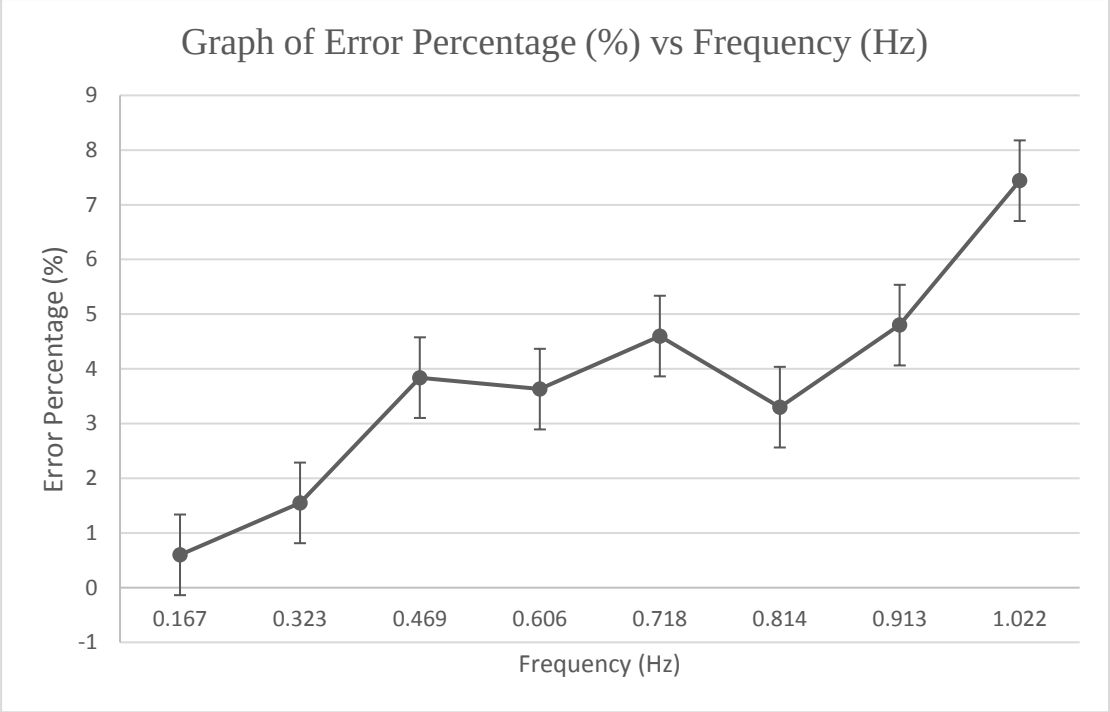


Figure 111. Relationship of error percentage to frequency

3.4 Limitation on Vibration Amplitude

Amplitude is the change from the equilibrium position to the peak position. It is one of the important measurement on conducting vibration analysis. The defected rotating parts not only will rotates at different frequency but also at different amplitude. It is important to find out the limitation of the ultrasonic sensor on detecting amplitude. The vibration result is better if the sensor able to detect smaller amplitude of vibration, giving a higher precision vibration analysis. In non-contact vibration displacement sensor, the limitation on the amplitude detected is actually depends on the resolution of the sensor. Higher resolution displacement sensor able to detect smaller position vibration, results in higher precision vibration reading. Although the ultrasonic sensor is stated that the theoretical resolution is 3mm, it is important to test it out in experiment to find out the performance in applications.

Experiment is conducted to find out the smallest amplitude that the ultrasonic displacement sensor able to detect. In this experiment, the test rig is placed within the optimum range which is 10-15cm away from the ultrasonic sensor. The frequency of the test rig is set fixed at 0.468 Hz through this whole amplitude test. The test rig is set to vibrate at 20mm amplitude and gradually decreased to 1mm. Total 6 different amplitude reading are taken , 20mm, 15mm, 10mm, 5mm, 3mm and 1mm.

The Figure 4.17 to figure 4.22 below showed the graph of displacement versus time at different amplitude. It is clearly seen that the accuracy of the result started to decrease as the amplitude of the vibration fell below 10mm. The result became vague and blurred as the amplitude dropped lower than 5mm. Displacement graph of 1mm amplitude showed in figure 4.22 is completely distorted and cannot be recognized. Therefore, the actual resolution of the ultrasonic sensor is around 3-5mm.

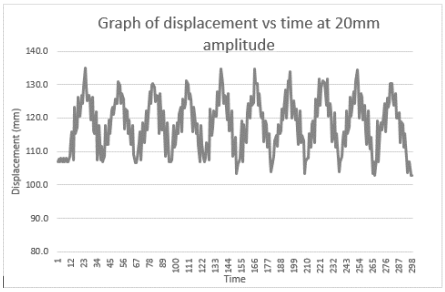


Figure 4.17: Graph of displacement vs time at amplitude of 20mm

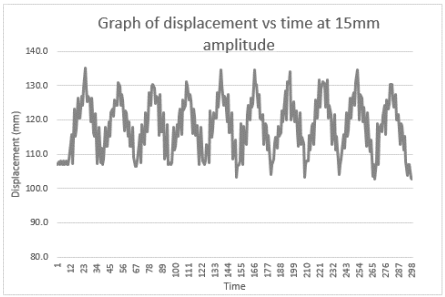


Figure 4.18 Graph of displacement vs time at amplitude of 15mm

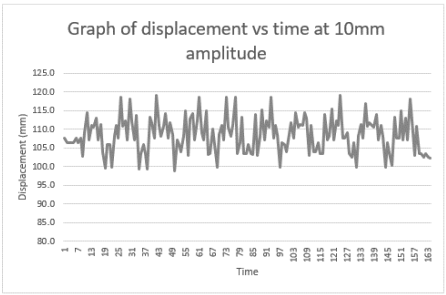


Figure 4.19: Graph of displacement vs time at amplitude of 10mm

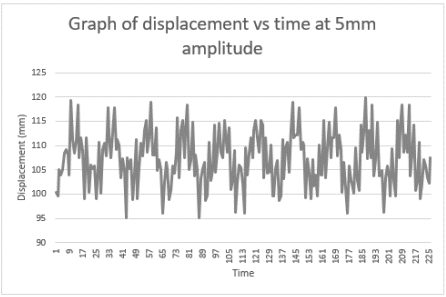


Figure 4.20: Graph of displacement vs time at amplitude of 5mm

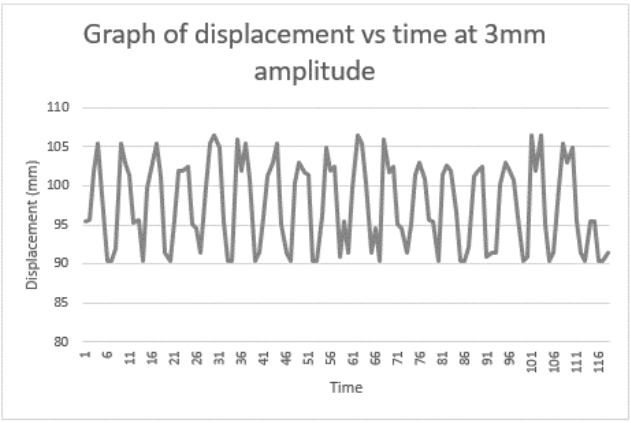


Figure 4.21: Graph of displacement vs time at amplitude of 3mm

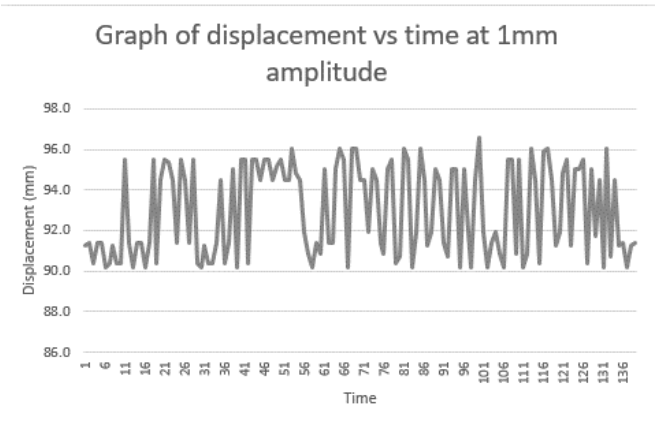


Figure 4.22: Graph of displacement vs time at amplitude of 1mm

Figure 12. Result of amplitude test

Sample Calculation

Result of displacement versus time at 20mm of amplitude is used to demonstrate the sample calculation. The result shown in table 4.5 is obtained from the graph in figure 4.17. The maximum point and minimum point of each cycle are taken to calculate each amplitude. 5 amplitude results are taken and averaged to obtain more accuracy result.

Table 6. Result of displacement vs time at 20mm of amplitude

Amplitude 20mm			
Maximum Point (mm)	Minimum Point (mm)	Peak to Peak (mm)	Amplitude (mm)
110.70	70.62	40.16	20.08
113.77	70.10	43.65	21.82
113.75	71.13	42.20	21.1
114.26	71.65	42.01	21
112.71	71.13	40.58	20.29
Average			20.86

From the table 4.5, the displacement detected by the ultrasonic sensor is 20.86 meanwhile the actual displacement of test rig is 20. Error Percentage have to be calculated to determine the accuracy of the ultrasonic sensor on detecting the amplitude of vibration by using the formula given below. The error percentage of the following data, 20mm, 15mm, 10mm, 5mm and 3mm are calculated and result is tabulated in table 4.6. Graph of error percentage versus amplitude is plotted using the result in table 4.6.

$$Error\ Percentage\ (\%) = \frac{Experimental\ Value - Theoretical\ Value}{Theoretical\ Value} x100$$

$$= \frac{20.86 - 20}{20} x100\%$$

$$= 4.3\%$$

Result

Table 7. Result of error percentage versus amplitude

Actual Amplitude (mm)	40	30	20	15	10	5	3
Amplitude result from experiment (mm)	41.42	32.13	22.83	18.78	14.3	9.6	-
Error Percentage (%)	4.3	7	14.15	23.7	43	92	-

Based on graph shown in figure 4.24, it is observed that the error percentage is inversely proportional to amplitude. As the amplitude of the vibration decrease, the error percentage increases. To obtain result that error percentage less than 20%, the amplitude of the vibration have to be more than 15mm. The error percentage in this amplitude section is quite high. It is because the resolution of the sensor was not high

enough, at 3mm, thus the vibration reading collected from the sensor fluctuating at 3mm, giving a high percentage error especially at lower amplitude.

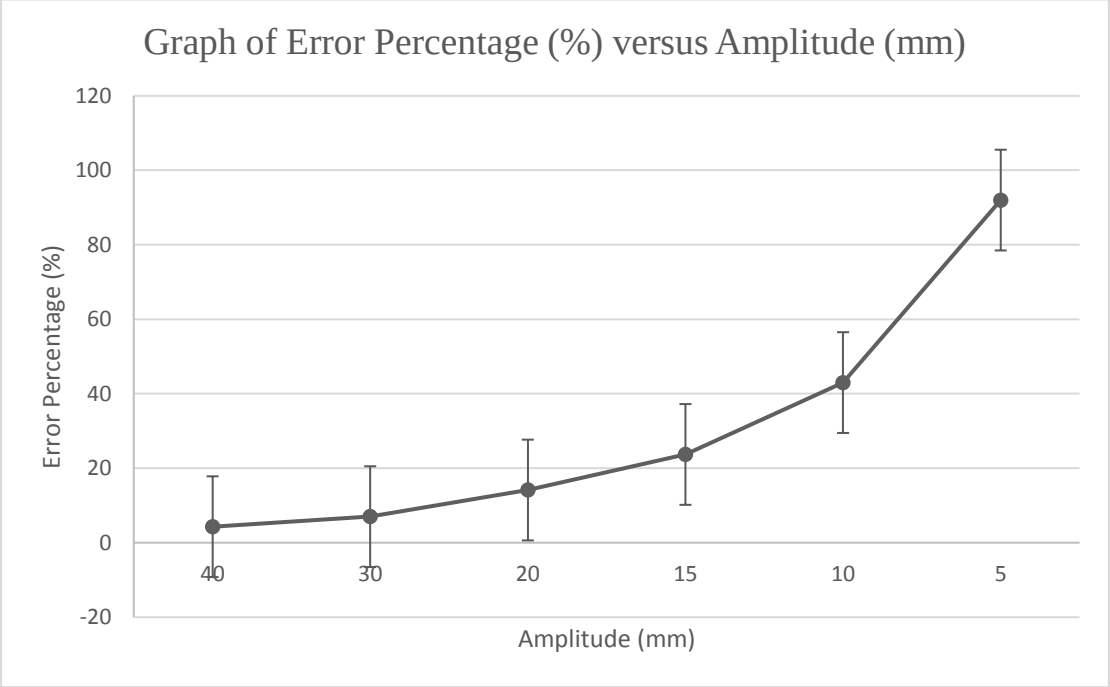


Figure 13. Relationship of error percentage to amplitude

4 Conclusion

Ultrasonic technology has been widely used in many field such as medical, automobiles and industries process control. In this research project, it is proven that the ultrasonic technology can be used as a new non-contact method to conduct vibration analysis. Ultrasonic sensor uses non-contact method, does not required to mount on the target device, therefore, it does not change the object mass or resonant characteristics while measuring vibration reading on machine. Therefore, the vibration measurement is more accuracy compare to contact method vibration sensors. The main objective of this research project is met by investigating the sensitivity, accuracy and limitation of the ultrasonic sensors. It has the maximum detection frequency of 1Hz, maximum amplitude of 3-5mm, and detection range of 320mm with 5% error percentage.

However, the difference between the ultrasonic sensor and existing conventional vibration sensors are too big. It is non-comparable as the resolution, frequency are far lower than the existing conventional vibration sensors. Those non-contact displacement sensors such as capacitive, eddy-current and laser displacement sensors have maximum frequency response up to 80 kHz, resolution as low at nanometers, able to locate the precise instantaneous location of the target device even vibrates at extremely high speed (Lion Precision, 2013). The resolution of ultrasonic sensor as low as millimeters greatly limits the capabilities on measuring vibration. Study of ultrasonic sensor on vibration analysis can be carried out as future work by replacing a higher resolution and frequency ultrasonic sensor.

Reference

[1] Anderson, B., Commercial, B. & Group, A., 2001. Practical Techniques for Utilizing Ultrasonic Technology To Complement Vibration Analysis. , 14(1), pp.4–7.

[2] Center, C.T., Industrial Vibration Analysis for Predictive Maintenance and Improved Machine Reliability. , (800), pp.1–5.

[3] Chaurasiya, H., 2012. Recent Trends of Measurement and Development of Vibration Sensors. , 9(4), pp.353–358.

[4] Kjaer, B.&, Machine-Condition Monitoring using Vibration Analysis. , pp.1–12.

[5] Liang, T.-C. & Lin, Y.-L., 2013. A fiber-optic sensor for the ground vibration detection. *Optics Communications*, 306, pp.190–197. Available at: http://www.sciencedirect.com/science/article/pii/S003040181300552X.

[6] Maekawa, A. et al., 2015. Development of noncontact measurement methods using multiple laser displacement sensors for bending and torsional vibration stresses in piping systems. *International Journal of Pressure Vessels and Piping*, pp.1–8. Available at: http://linkinghub.elsevier.com/retrieve/pii/S030801611500054X.

[7] Moosavian, A. et al., 2016. Piston scuffing fault and its identification in an IC engine by vibration analysis. *Applied Acoustics*, 102, pp.40–48. Available at: http://linkinghub.elsevier.com/retrieve/pii/S0003682X15002467.

[8] Naik, R.P., Thermal, N. & Corporation, P., Ultrasonic : A new method for condition monitoring.

[9] Neumann, M. et al., 2015. A laser-optical sensor system for blade vibration detection of high-speed compressors. *Mechanical Systems and Signal Processing*, 64-65, pp.337–346. Available at: http://linkinghub.elsevier.com/retrieve/pii/S0888327015002095.

[10] Pieraccini, M. et al., 2008. Interferometric radar vs. accelerometer for dynamic monitoring of large structures: An experimental comparison. *NDT & E International*, 41(4), pp.258–264. Available at: http://linkinghub.elsevier.com/retrieve/pii/S0963869507001454.

[11] Resolution, H., Voltage, L. & Range, U., 2014. HRLV - MaxSonar ® - EZ ™ Series. , pp.1–15.

[12] Rienstra, A. & Hall, J., 2002. Ultrasonic Detection. , 3(2), pp.1–4.

[13] Lion Precision, 2013. Vibration Measurement with Noncontact Displacement Sensor.

[14] Vargas, E. et al., 1997. Ultrasonic sensor for liquid-level inspection in bottles. *Sensors and Actuators a-Physical*, 61(1-3), pp.256–259. Available at: <Go to ISI>://WOS:A1997XX24400002.

[15] Wolf, J., Pirskawetz, S. & Zang, a., 2015. Detection of crack propagation in concrete with embedded ultrasonic sensors. *Engineering Fracture Mechanics*, 146, pp.161–171. Available at: http://linkinghub.elsevier.com/retrieve/pii/S0013794415004348.

[16] Zhang, Q., 2013. Vibration Sensor based Intelligent Fault Diagnosis System for Large Machine Unit in Petrochemical Industry. *Interface*, 2015(i), pp.1376–1381.

eureka 2016 – Conference Paper
Paper Number 2ME30

Design, Fabrication and Characterization of Two Axis Gimbal System for Dynamic Balance

Sundrrakannan A/L Arumugam, K. H. Cheah

School of Engineering, Taylor's University, Malaysia.

Sk_20@hotmail.my

Abstract
A good platform with maximum stability in the middle of air can be achieved by the help of counterweights. The platform will need a system that works with counterweights to react according to external factor and response accurately in order to regain stability. The angular motion of the platform cause by the disturbance torque leads to dynamic imbalance. This paper contain a two axes gimballed system. To achieve dynamic balance of the platform a gimbal is required. Gimbal isolates both the lifting force and aiming force by experiencing rotation about the bearing axes. This loops are then attached to each other through cross coupling units. Taking into consideration the Newton's third law of motion when two weights are distanced from each other, dynamic balance can be achieved with gimbal attached at the centre of gravity of the platform. The prototype is then tested by altering the centre of gravity of the platform to achieve dynamic balance. Numerous trials conducted and obtained result are compared to decide on the most preferable location of the centre of gravity and counterweight required to make the platform remain balanced at rest. The mass was placed in three different points and was altered to find its new centre of gravity. The rigid body new centre of gravity was not accessible to be pivoted as there is offset in the z-axis direction. Changing the mass point to two symmetrical location gives a better centre of gravity that fall in the rod without having any offset in z-axis direction

Keywords: Dynamic balance, Gimbal, Centre of gravity, Stabilization of platform

1. Introduction

To get a clear and good quality picture the photographer or the stand that holds the camera has to be stable and steady. Standing on ground or placing stand on the ground provides a very good stability for the pictures to be taken. A good platform with maximum stability in the middle of air can be achieved by the help of counterweights. The platform will need a system that works with counterweights to react according to external factor and response accurately in order to regain stability. Under different

circumstances such as vibration will cause the image to be blur. This is caused by the lens experiencing vibration as the shutter opens to snap. There have been few designs that has been with counterweights. Basically all the designs consist of the same components such as gimbal which is attached to handle that will hold the platform. The camera will be mounted on the platform and fixed to the bearings that was attached to the handle. The platform also will have counterweights to keep the platform stable while the handle is free to move with the help of bearing

The development of Steadicam started in 1973 by Garret Brown when he was first required to shot a scene on running and climbing stairs. So Garret brown was not satisfied with the unnatural shakiness and felt that the shakiness is a real distraction for the viewers. Watching a clip with shakiness for a certain period will actually lead to dizziness. Being able to run and take a shot without the video bouncing was Garret Brown's aim. The two main problems that was faced during handheld video graphing are the shocks and bounces. This shock and bounces are caused by two main factors that occurs during handheld video recording takes place. The first factor is the spatial vibration which is developed through the movement of the cameraman and next is the angular vibration which is the camera's movement during the shot. Isolating this two factors from each other will be able to take a better video.



Figure 1. Garret's brown Steadicam

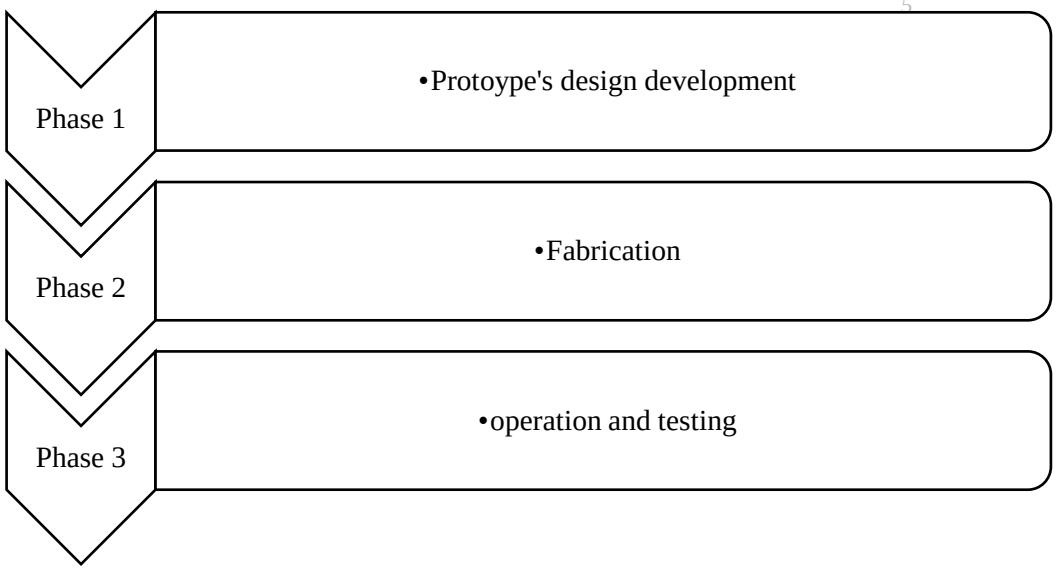
Physics laws was first researched regarding stability and it was narrowed down to few laws that affects stability of an object. Those are mass and inertia. But a heavy object is stable at rest but the problem occurs when it experiences motion. This problem was addressed by manipulating the centre of gravity of the object. To be able to stabilize an object at handheld one must be able to manipulate the centre of gravity of that certain object. The centre of gravity of an object is the point where all the mass are balanced out in all three dimension. Camera's centre of gravity is hard to be found as camera are not built symmetrical. Garret brown's idea was to move the centre of gravity of the camera so that the new centre of gravity will provide the opportunity to be manipulated. Taking this manipulation of centre of gravity into consideration a new design was proposed [1].

The design was mainly developed to achieve dynamic stability attaching a gimbal system at the new centre of gravity of the body. This two degree of freedom gimbal prototype is deduced by the basic assumption that rigid body is stagnant which means there is no mass unbalanced. Mass balancing can be done by creating inertia in

a symmetric condition. Two axes gimbal system was designed with 0° elevation or offset on the loops at rest. The rigid body which the mass is assumed to dynamically balance and the centre of gravity of the masses has been altered should remain symmetrical to their axes at rest. In another word the main importance research result will be derived from the consideration that the base platform and the gimbal are in dynamic balance through the cross coupling control system [2]. Therefore, this article is devoted to the presentation of a model of a two axes gimbal system in order to attain a new centre of gravity.

2. Methods and Material

Figure 2.



Methodology phases

Experimentation of the design will be done first to prove the reliability of the concept. The experiment involves a first prototype using PVC's. This has to be done firstly as fabrication using a prototyping
machines is costly so by proving the concept with PVC prototype. In addition this experiment will be involving in achieving a light weight platform

2.1 Design of prototype

The main conundrum that rose while making the prototype was getting a less friction and smooth working system at the gimbal part. The gimbal is the part which decides the efficiency of the system. Taylor's university engineering laboratory was fairly equipped with reasonable set of wood working tools as provided by the Taylor's university engineering laboratory. As for fabricating the prototype the material chosen was PVC pipes. A rectangle (T-Shaped) and cylindrical (I-Shaped) mount shaped counter weights was added to the top part of the thread while the other end was attached with mass proportional to the mass of the camera. As for this design the centre of gravity is being altered by adding counter weights at the top. Shifting of weight occurs as the centre of gravity is situated such that the weights exerts more force at the shorter

displacement. This concedes that the further the displacement from the centre of gravity the lesser the force exerted or lesser inertia is produced.

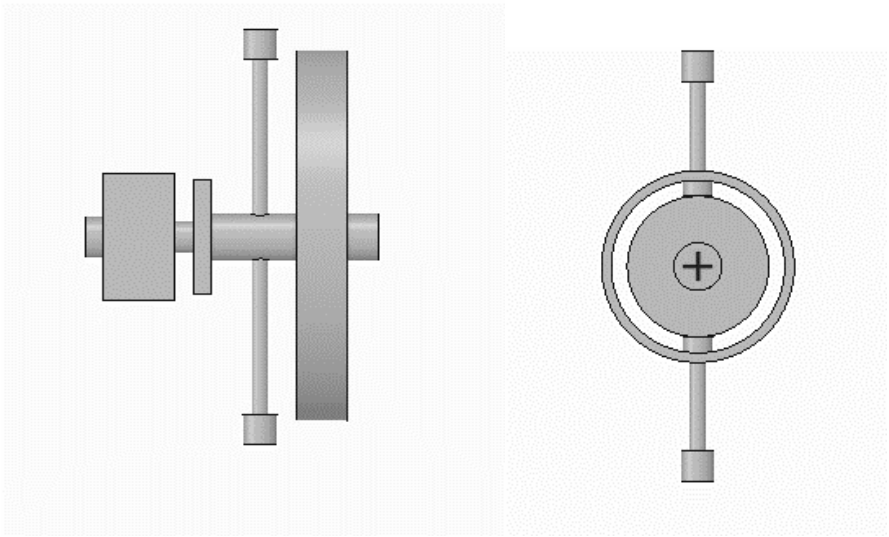


Figure 3. The side view and top view of initial design

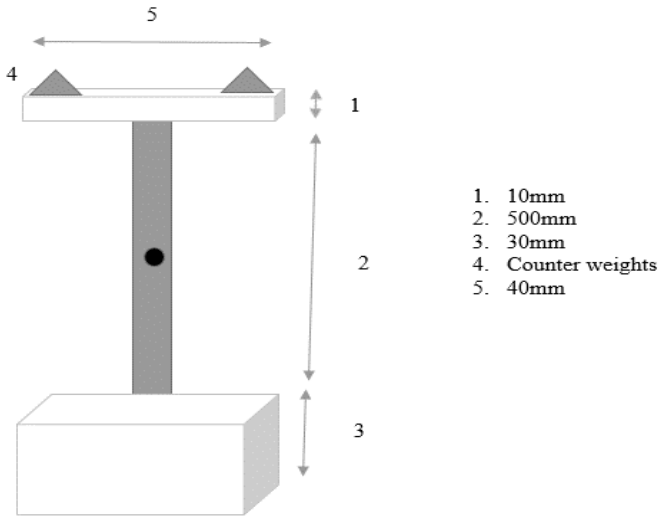


Figure 4. The geometrical representation of the platform

The shifting of weight plays an important role as it effects the stability of the system. When the center of gravity is an equal distance between two supports then each support bears equal weight. However, if one support is closer to the centre of gravity then it supports proportionally more weight than the other. Likewise, if the center of gravity is closer to one support than the other then the support closest to the center of gravity bears greater weight in proportion to the ratio of the distances. The counter weights are divide into two parts having equal mass as the camera mount. center of mass" and "center of gravity" are used synonymously in a uniform gravity field to represent the unique point in an object or system which can be used to describe the system's response to external forces and torques. The concept of the center of mass is that of an average of the masses factored by their distances from a reference point. The calculation was done based on Eq. (1), Eq. (2), Eq. (3) [3],

$$\frac{(m^1\,x^1)+(m^2\,x^2)}{(m^1+m^2)} = X \quad (1)$$

$$\frac{(m^2\,d)}{(m^1+m^2)} = X \quad (2)$$

$$\frac{(m^1\,x^1)+(m^2\,x^2)+(m^3\,x^3)}{(m^1+m^2+m^3)} = X \quad (3)$$

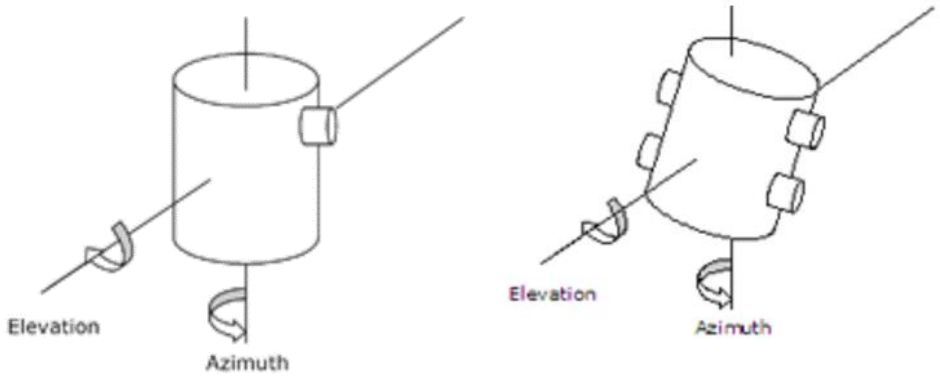


Figure 5. The overshooting of angular displacement as more point masses added

2.2 Gimbal

When a rigid body is being lifted it will experience angular motion, in another term it can be called swaying. This swaying occurs because of the lifting force is larger than the aiming force that is applied on the rigid body. This lifting force and aiming force both comes from the operator which in this case is the cameraman. When the camera man applies force to move or lift the camera he loses the aiming force on the camera as for humans are not exactly capable of constantly applying the same amount of force without any support. The longer the duration the more the force differs to move the camera. Thus the solution this problem can be handled by isolating both the lifting and forces. In order to isolate this two forces a gimbal system is required. Gimbal isolates the object from the rotation about the bearing axes. This gimbal is then attached to centre of the gravity of the rigid body and lifted. The rigid body will neglect the lifting force and remain stable without swaying. All the force that the operator applies to lift the rigid body is countered by the bearing by rotating. This gimbal is also works the same way as universal joint which allow movement in all direction. This gimbal system are mostly used for portable photography equipment, varying form singles axes gimbal heads to three axes gimbal heads [4, 5].

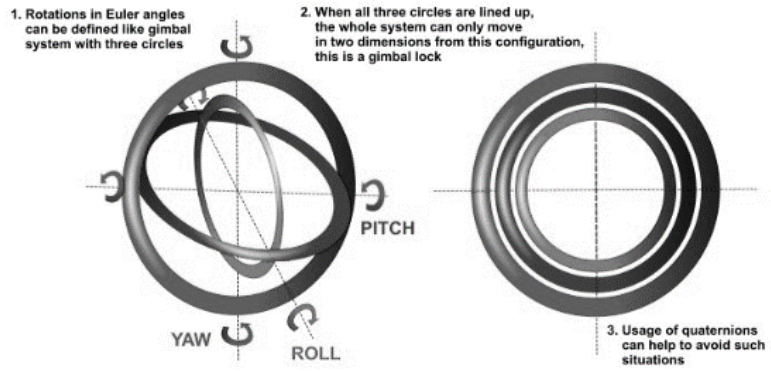


Figure 6. Rotation among the all the axes of gimbal

3

3. Fabrication

3.1 Gimbal

To design the gimbal, for the first part started with smallest ring using the 3/4"' PVC pipe was heated to 200°C and then using the help of g-clamp the 8mm outer diameter bearing was forced in to be fitted exactly. This enables the rod that pass through the middle of the bearing will be able to rotate 360° without any resistance. This gives some space for the PVC ring to be drilled for pivot points and attached with the middle ring using nut with bolt. All the nut and bolt are kept constant at 4mm to ensure that even weight addition occurs to the design. The inner ring needs two drilled points for pivots to be attached to middle ring. The middle ring using the $1\frac{1}{4}$"' PVC pipe needs four drilled point for pivot attachment as two points will be used to attach to the inner ring while the other two is required to be attached with the outer ring. All this points has to be in symmetry to ensure the whole system is in balance. This middle ring is to isolate the external force causing the movement in yaw direction. Nuts serves to lock the rings to one another without interfering the rotation of all the rings.

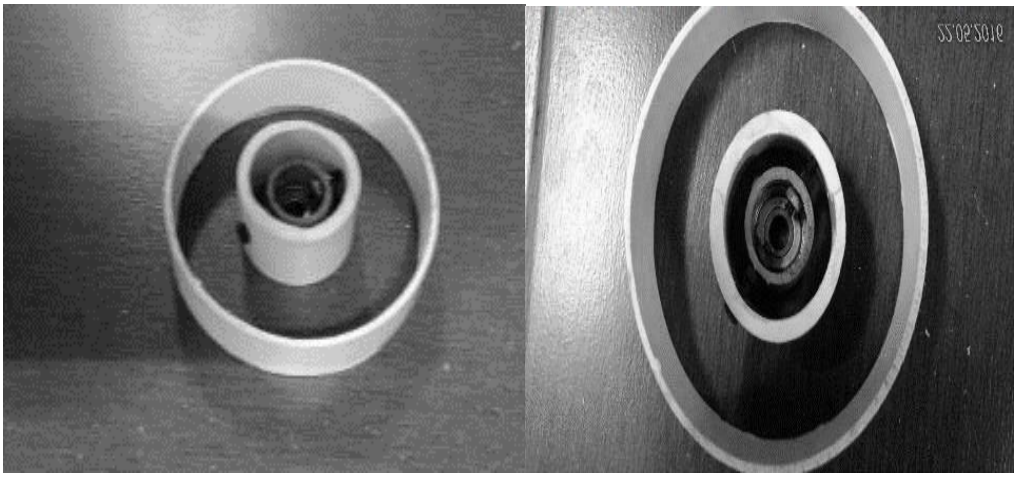


Figure 7. The inner loop with bearing and the middle loop

3.2 Platform

A 500mm threaded rod was mounted through the bearing inside the smallest loop. The nut is locked below and above the bearing to ensure the bearing stays in place without any ascending or descending of height during loading. The threaded rod is perfectly fitted through the bearing and locks the rod in place. Lock nuts hold the

bearing in place on the all thread rod, and can be screwed up or down to tweak the vertical height. Proper mount for the camera was not done as addition of weight were done during the testing**.** A rectangle and cylindrical mount shaped counter weights was added to the top part of the thread while the other end was attached with mass proportional to the mass of the camera.

4. Testing

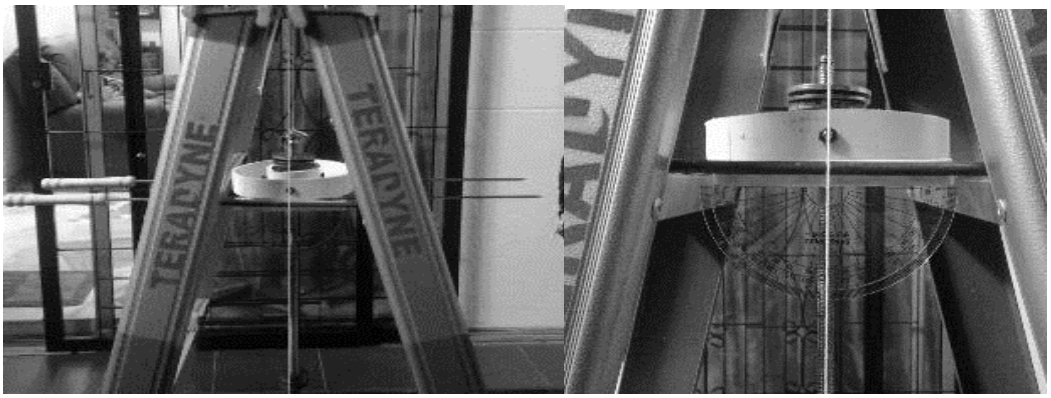


Figure 8. The platform is hanged for angular displacement testing

The data collected this project will be obtained experimentally to verify the functionality and obtaining a new centre of gravity for the prototype design. The prototype was suspended with no external torque or inertia acting on it. In order to obtain the correct ratio for the distance between the centre of gravity to the counter weight and camera mount. This ratio will be altered to prove that the distance between these points are affecting the dynamic balance of the platform. An analog water level was placed on the supporting platform to ensure the system is resting on flat surface and protector was placed to show the deviation of angle that the platform experience as the distance are altered. The testing is repeated with equivalent masses weighing 70g at both end of the rod while the distance from centre of gravity to the counter weight kept at 70mm and 60mm and the distance to the camera mount was 265mm to 180mm.

5.0 Result and Discussion

The outcome of the initial design proves that the system responses considering the distribution of weight and the distance between the individual masses. Cross coupling among two axes was used to react to the gimbals movement at the opposite direction to achieve stability. More specifically, when one loop is slewed the other axis responses by reacting and rotates countering the movement. Once the system comes to stop the distribution of mass will results the product of inertia to zero thus stabilizing the system.The distribution of mass is achieved by adding two weights in the opposite of the mass that causing the inertia resulting to dynamic unbalance. Having the counter weight placed in the opposite end of the thread that the camera was mounted will reduce the product of inertia to zero. But to achieve the dynamic balance the distance between the mass are placed is very crucial. The geometry of the camera and the counter weight also plays a role as each geometry has their own centre of gravity which when all this parts are attached together the overall structure will have its own new centre of gravity.

The counter weight are rested on a rectangular shaped aluminum plate which the centre of gravity was obtained based on Eq. (4) and Eq. (5). The centre of gravity of the rod was obtained using Eq. (6)

$$X_{COG} = \mathrm{B}/2 \quad (4)$$

$$y_{COG} = \mathrm{H}/2 + \mathrm{h} \quad (5)$$

$$I_{COG} = \frac{1}{4}m(a^2 + b^2) \quad (6)$$

The masses are now acting at three different points but attached to one rigid body. Splitting the mass two points at the counter weight was initially found that will help to reduce the weight used to counter the weight of camera as moment increases with displacement from its pivot point. But dividing the mass causes the centre of gravity of the rigid body to moves drastically from the preferable location. The centre of gravity is expected to fall somewhere in between the connecting rod so that attaching the gimbal would be possible. Splitting the masses causes the dynamic balance to move in both x-axis and z-axis direction. Obtaining the centre of gravity for regular solids through calculation is recommended but for an irregular solids experimental testing is much accurate.

5.1 Obtaining the centre of gravity for T-Shaped connecting rod

Table 1. Overshooting of angle with respect to relative distance from the center of gravity for T-Shaped connecting rod

Distance from C.O.G (mm)		Overshoot of angle in x-axis(degree°)	Overshoot angle in z-axis (degree°)
+70	-265	4	4
+70	-245	4	3
+70	-225	2	2
+70	-200	1	2
+70	-180	<1	2

Table 2. Overshooting of angle with respect to relative distance from the center of gravity for T-Shaped connecting rod

Distance from C.O.G (mm)		Overshoot of angle in x-axis (degree°)	Overshoot of angle in z-axis (degree°)
+60	-265	5	4
+60	-245	4	4
+60	-225	5	3
+60	-200	3	2
+60	-180	2	2

The data implies that the lesser the relative distance between the masses the lesser the overshoot of angle in z and x axes. The center of gravity of an object is calculated by taking the sum of its moments divided by the overall weight of the object. The moment is the product of the weight and its location as measured from a set point called the origin. As the distance of camera mount approaches the counter weight the platform results in less deviation. The largest distance between two masses are 335mm and smallest are 120mm. The counter weight distance is kept constant as the top part of this platform will be attached to a flying support. The system need clearance for the swaying of the platform and to return back to it dynamic balance once external force is exerted on it.

The distance of the camera mount was slowly decreased to find the point where the system approaches to zero deviation in any direction. From the table 1, the distance of 110mm apart gives the least deviation in both direction but there is still a deviation about 2° in the z-axis direction while the x-axis direction gives very slight overshooting. The T-shaped platform theoretical calculation states that the centre of gravity is situated at the centroid of the structure but experimental testing shows that the centre of gravity is slightly displaced in the z-axis from the theoretical centroid point. This situation was induced by the irregular shape of the platform. The counter weights mount is fabricated manually. During the fabrication the parts tend to undergo certain deformation in shape due to drilling and cutting through. The holes drilled at the both end has to be in symmetry and slight dents will cause the centre of mass to be displaced from its initial point. The rectangular plate is screwed to the rod with the help of nut and bolt and the same goes to the camera mount. This nuts and bolt mass are neglected in the theoretical calculation as the model is expected to be modelled using a rapid prototyping machine upon completion of designing and testing.

With the aid of rapid prototyping machine all the parts of the system are expected to have a precise measurements and the mass of each part are evenly distrusted as well. The parts are designed in way that there is no need for any assembly of parts and can be said that the whole platform is in one regular solid. Taking the platform as a whole makes the centre of gravity to be easily accessed. Analyzing the data found the system is having overshooting in z-direction which can be concluded that having just

two sides for counter weight is not enough to balance the system. The two sides counter weight seems sufficient for balancing in the x-axis direction but not for z-axis direction.

To solve this either another two sides more sides have to be added at the counter weights mount. This makes the system to have five point masses and calculating the centre of gravity is gets even complicated compared to initial three point masses. Due to time constraint for fabrication and testing addition of another two point mass is not approachable.

5.2 Obtaining the centre of gravity for I-Shaped connecting rod

Table 1. Overshooting of angle with respect to relative distance from the center of gravity for I-Shaped connecting rod

Distance from C.O.G (mm)		Overshoot of angle in x-axis(degree°)	Overshoot angle in z-axis (degree°)
+70	-265	4	4
+70	-245	4	3
+70	-225	2	2
+70	-200	1	1
+70	-180	<1	<1

Table 2. Overshooting of angle with respect to relative distance from the center of gravity for I-Shaped connecting rod

Distance from C.O.G (mm)		Overshoot of angle in x-axis (degree°)	Overshoot of angle in z-axis (degree°)
+60	-265	2	3
+60	-245	2	3
+60	-225	1	1
+60	-200	1	1
+60	-180	<1	<1

The largest distance between two masses are 335mm and smallest are 110mm. The counter weight distance is kept constant as the top part of this platform will be attached to a flying support. The distance of the camera mount was slowly decreased to find the point where the system approaches to zero deviation in any direction. From the table 3, the distance of 110mm apart gives the least deviation in both direction .The I-shaped platform theoretical calculation states that the centre of gravity is situated at the centroid of the structure but experimental testing shows that the centre

of gravity is slightly displaced in the z-axis from the theoretical centroid point. This situation was induced by the irregular shape of the platform. The counter weights mount is also fabricated manually and during fabrication the mount tends to also undergo deformation. This system has two point of masses compared to three point for the T-shaped platform. By having two point masses calculating the origin is simplified. Having a cylindrical counter weight mount, the mass are found to be acting at it centre so aligning centre of the mass of the camera mount will be much more efficient compared to aligning two mass point to one mass point.

In a nutshell, the I-shaped platform gives a much better prospect compared to the T-shaped platform. This whole system of stabilization are done with mechanical approach which limits the alteration of the design. Implying that the model has to base on mechanical approach to counter all the moments and inertia that it experiences choosing a design with just two point mass is preferable. Furthermore, Random error caused by human in fabrication also affects the overall system. This can be improved by performing the experiment several times with several more distances between masses in order to reduce this error.

5.3 Damping test

Vibration is key factor that directly affects the quality of taken of a camera. Once the camera experiences vibration the image take will be have dotted lines which are caused by the motion during the closing of shutter. In order to improve the quality of picture taken during flight or motion, isolation of vibration has to be done. Isolation of forces are done by the system by introducing the gimbal that response to external force. This gimbal makes sure that the external vibration that affects the camera are drastically reduced hence improving the quality of pic. The final prototype fabricated by RPM was tested for its capability of handling vibration. The platform is subject for high vibration disturbance so isolating this would eventually help us achieve the objective this study. The prototype was suspended with no external torque or inertia acting on it and random vibration was created by shaking the support slightly. The duration that the system takes to damp the movement experienced will be directly related to functionality of the gimbal system. Therefore this test is very crucial.

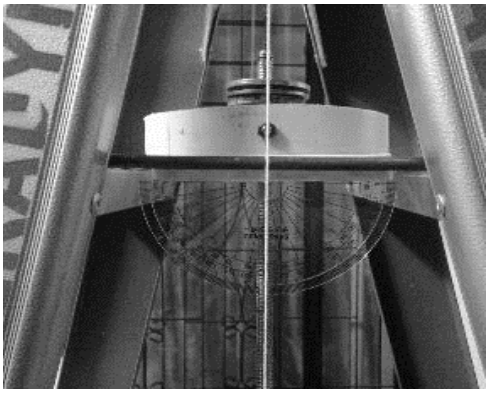


Figure 4.3. Platform is hanged for random vibration testing

Table 4.6. Time taken for the system to come to rest

Number of trials	Time take for system to come to rest (s)
1	7
2	8
3	7
4	7
5	8
average	7.4

The functionality of the gimbal is proved. The gimbal reacts to the external vibration and damps the movement of the system therefore we can say that system works but the time taken for the system to come to rest is averaged to roughly 7.4 secs which is quite long. This signifies that during flight the camera with roughly have disruption in the picture quality taken for seven second before the system counters this external force and brings back the camera to its stable position. This situation rises as there is no proper damping agents such as springs or rubbers are not incorporated with this design but since there will a flying support connected to this system in future that connection can be made out springs to enhance the damping.

5.4 Camera mounting

The camera used for this testing is the SJ 4000 model. This camera is also known as the Sports HD 1080P camera. The look of it resembles the normal GoPro camera but gives a much better performance compared to it. The body design comes in rectangle with physical dimension 30mm in height, 50 mm in length, and 41 mm in width.. The camera itself has certain anti shaking features incorporated within which therefore further increases the efficiency of the design. The counter weight used for the current design are set to be in circular shape as circles has their overall mass to be acting at one particular point and that point is at its origin. As we considering the exact same shapes for the bottom and top of the platform, this camera has to be set into a mount that comes in circular shape. Once the camera is fitted exactly to the mount we are altering the centre of gravity of camera as there is a new solid has been attached together which make the two parts to act as one body. The mount that the camera is attached is made using RPM machine as well.

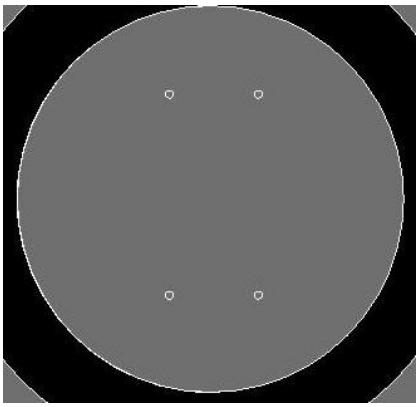


Figure 4.4. The platform is hanged for random vibration testing

Once the camera is attached on the mount it was placed on the table and random vibration was induced while the camera was on recording. This was done in order to ensure the safety of the camera during the flight as for the worst case scenario of system failure the camera

will experience a free fall from elevated location therefore providing a mount that damps vibration as well as protects the camera is essential

6. Conclusion

As a conclusion, a two axes gimbal system was proposed and fabricated utilizing the basic Newton's second law. The construction of the stabilization mechanism was induced through the idea of incorporating cross coupling and dynamic balancing. This project have proved that for the mechanical approach of stabilizing a platform having two point of masses gives a better efficiency compared to several point masses. An assessment between the system response among the I-Shaped and T-Shaped was done and the comparison result verified the design proposed. The test carried out was to study the relationship between the point masses and the relative distance among the masses to locate the centre of gravity of the prototype. Expanding the mathematical model of the platform assuming that the design have static mass balanced, the theoretical origin of the platform can be deduced. As for the I-Shaped platform the point masses has been limited to two and are designed to be in symmetrical which gives a much optimum mechanical approach dynamic balance.

For further future work, with the aid of rapid prototyping machine all the parts of the system are expected to have a precise measurements and the mass of each part are evenly distributed as well.

Acknowledgement

The authors would like to acknowledge Taylor's university for providing sufficient facilities to conduct the research of this project 2ME30.

References

[1] Jerry holway, Laurie Hayball, " The steadicam® operator Handbook" CRC Press 2013 , ISBN-9781136057977,volume 2, June 2013

[2] Ravindra S. (2008) Modeling and simulation of the dynamics of a large size stabilized gimbal platform assembly. Asian International Journal of Science and Technology in Production and Manufacturing, Vol. 1, No. 2, pp. 111-119.

[3] Hilkert J.M. (2008) Inertially stabilized platform technology. IEEE Control Systems Magazine, Vol. 28, pp. 26-46.

[4] Final report (1976) Analytic study of inside-out / coincident gimbal dynamics. The Bendix Corporation, Guidance System Division.

[5] Daniel R. (2008) Mass properties factors in achieving stable imagery from a gimbal mounted camera. Published in SPIE Airborne Intelligence, Surveillance, Reconnaissance (ISR) Systems and Applications V, Vol. 6946, doi:10.1117/12.778245.

eureka 2016 – Conference Paper
Paper Number EE_UG02

Home Automation System Using Verilog Hardware Description Language in Xilinx- Spartan3e and Altera- Cyclone II Field Programmable Gate Array Boards

Jaina Nica C. Bongulto[1*], Jayvee T. Medalla[2], Bernalyn M. Desate[2], Rionel Belen Caldo[1]

[1]*Computer Engineering Department*

[2]*Electrical Engineering Department*

Lyceum of the Philippines University-Laguna (LPU-L)

Corresponding E-mail: [*]jainanica12@gmail.com

Abstract

Home, which is often the place where people stay the longest or which serves as the endpoint after the long day of work outside is indeed a "happy home" when a system will be integrated to provide peace of mind for people living on it. In this study, the proponents designed a simulation and implementation of a structure that takes care of the homes' security, convenience, disaster detection and risks reduction. The security module contains the alarm system model that monitors intruders through doors, windows, garage and garden area. Convenience module, on the other hand, is designed to control the temperature and luminosity based ventilation and lighting systems' automatic switching mechanisms respectively. It also features convenient control for the home's garden water sprinkling system. Disaster detection and risks reduction includes early warnings for possible catastrophes like fire and heavy floods. This paper uses methodologies where users can manage devices by using Xilinx- Spartan3e and Altera- Cyclone II Field Programmable Gate Array boards. In this study, the proponents executed the system simulations through Verilog HDL using Xilinx ISE, Quartus II and ISim. The project outcomes agreed with the expectations, which can be seen through the systems' waveform behaviors and Register Transfer Level and Technology schematic diagrams.

Keywords: Verilog HDL; Xilinx- Spartan3e; ISim Simulation; Altera- Cyclone II; Register Transfer Level

1. Introduction

1.1 Background of the Study

Progress of technology started when famous laboratories like Bell Laboratories and many others developed such devices like vacuum tubes, transistors, integrated circuits, etc. which led to the formation of microelectronics that has a great aid to our new and advanced technologies in present times [1]. These technologies have been a big help in many importance aspects of human civilization. It develops faster and leads to the birth of microcontroller, integrated electronic computing device that acts like a computer on a chip [2]. Single chip that is very useful in performing very huge applications [3]. In this paper, the proponents explore the possibility of using the mentioned technology wonder to the place where we are living, homes.

Nowadays, the society has a great need for security considering that high crime rates are perceived. Burglars and trespassers are very common especially to places where people are expecting they are safe, usually homes [4]. Likewise, when talking about convenience especially after a whole day of tiring work, it is more beautiful to have a home that will give comfort and efficiency in one package [5]. Aside from security and convenience, it is also a great move to have a shelter that will offer an early detection of the possible disasters that will come around. Catastrophes like fire and heavy floods caused by extreme rains can damage the things that people mostly put importance to, worst case, can eliminate lives [6]. As what saying goes, "Prevention is better than cure".

In due course, the authors designed an integrated digital system that will provide virtual model for home security, convenience and disaster detection systems. In this paper, the programmers to provide simulations for the integrated system [7] used Verilog, which is one of the most common industry standard hardware description languages.

1.2 Statement of the Problem

With the high demands for useful and efficient home automation systems [8], the goal of this study is to create a house model that depicts an integrated system that will offer security and convenience to the homeowners. It also includes early detection of upcoming unwanted events with the inclusion of disaster monitoring and warning system. Talking about the home security, Crime is a significant concern in urban areas of the Philippines and typical criminal acts includes theft, carjacking, kidnappings and robberies. They are the incidents that are usually occurring at the expense of people's own homes [4]. Additionally, Philippines is one of the most disaster prone country in the world. Specifically, discussing about home disasters, it is also noted that fire and heavy floods are two of the most common catastrophes in the country [9].

Given the facts, this work will introduce design methodologies where users can control sensors and devices by using Field Programmable Gate Arrays (FPGAs). Nowadays, FPGA is used commercially and applied in different countries. Indeed, it is an advantage that undergraduate students will have background, proper skills and knowledge of FPGA before facing the professional world, which adopts and utilizes such technology. For educational purposes, different institutions have FPGA for their research papers and citations [10]. In this paper, the researchers executed the FPGA-

based system simulations through Verilog Hardware Description Language using Xilinx ISE and ISim.

1.3 Objectives of the Study

The prime objective of the project is to DESIGN, SIMULATE and IMPLEMENT an integrated circuit for home automation system that provides security, comfort, convenience, disaster-free home using Verilog Hardware Description Language with the aid of Xilinx- ISim, Xilinx- Spartan3e and Altera- Cyclone II Field Programmable Gate Array boards.

Specifically, this study aims to provide VIRTUAL MODELS and SIMULATIONS for the following situations:

- Security system that can be activated and deactivated through a 6- bit binary password. Combinations of possible binary passwords consists of one combination of correct password for activation that will power the sensors attached to the security module. Another password combination is dedicated for the security module's deactivation mode which will make the security sensors off
- Alarm systems at doors, windows, garden area and garage area when the magnetic and laser sensors interfaced to the mentioned house entrances are triggered
- Luminosity-based lighting system automatic switching mechanism and a temperature-based ventilation system automatic switching mechanism that are attached to the convenience module
- Automatic triggering of the fire alarm and water sprinkler mechanism whenever the smoke detector is activated
- Automatic triggering of the flood alarm whenever the flood sensor is activated

1.4 Scopes and Limitation

The integrated system was designed to control the door, window, garage area, fire alarm, flood alarm, luminosity and temperature. It is not designed to control any other devices. The entire system is dependent upon multiple sensors which act as input to the program. This is why Xilinx Spartan3e and Altera- Cyclone II FPGA boards are used because switches, input ports and output ports are incorporated within these boards. The proponents used sensors and alarms to achieve the objectives of this study however they did not focus anymore on the internal functionality of each sensor and just dwell on the relationship of the input and output signals simulated and implemented through Spartan3e- FPGA. Nevertheless, the authors still managed to list all the sensors used and their corresponding minimal specifications and schematic diagrams for the sake of complete documentation. Additionally, on the Altera- Cyclone II implementation of this project, the proponents did not incorporated any external devices like sensors, alarms and indicators to the board. Rather, the proponents utilized the embedded switches and indicators of the board to maximize the functions specified by the proposed digital system. The scope of the project is only controlling the device internally [8].

2. Methodology

Through setting a general initial hierarchical design for the integrated system, a model house is taken into account. After the setting, all virtual sensors and devices that will be used for the system's software and hardware simulations for the modules are also taken into consideration. The model sensor set includes magnetic, motion, sound, light and temperature, fire and flood detectors. The devices are the password checker, doors, windows, garage and garden areas, fire and flood alarm, fire sprinkler, garden water sprinkling system, ventilation and lighting system's automatic switching mechanisms. Verilog Hardware Description Language was used in synthesizing the integrated system, viewed through the Register Transfer Level diagrams [8].

2.1 Xilinx ISE, ISim and Quartus II

In this study, the researchers used Xilinx ISE and ISim for the Spartan3e- FPGA implementation of the proposed project. It was also used for logic coding, synthesis, viewing of register transfer level schematic diagrams, test bench coding and simulation of the proposed digital system. Xilinx ISE alongside with ISim is a software tool produced by Xilinx for synthesis and analysis of hardware description language systems, enabling the developer to synthesize their designs, perform timing analysis, examine RTL diagrams, simulate a design's reaction to different stimuli, and configures the target device with the programmer [12].

On the other hand, Altera- Quartus II is a software tool used by the proponents for the Cyclone II- FPGA implementation of the designed digital integrated circuit. Altera-Quartus II is applicable because it performs the ideal quality design of FPGA boards [13].

2.2 Conceptual Frameworks (Hierarchical Approach)

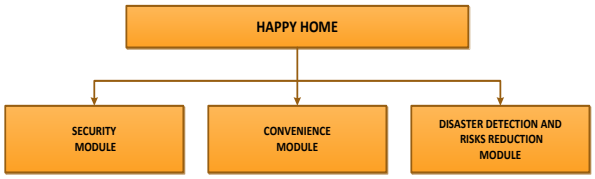


Figure 2. High Level- Hierarchical System of the Project

Figure 2 is the high level- hierarchical system representation of the project. In this paper, three sub- systems are synthesized into one integrated digital circuit. Under the mother module are the security, convenience and disaster detection and risks reduction modules.

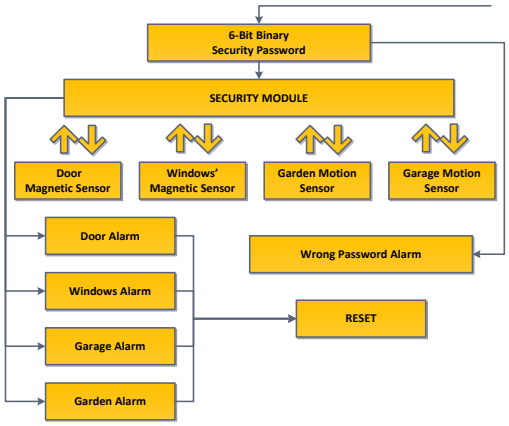


Figure 3. Low Level- Hierarchical System of the Security Module

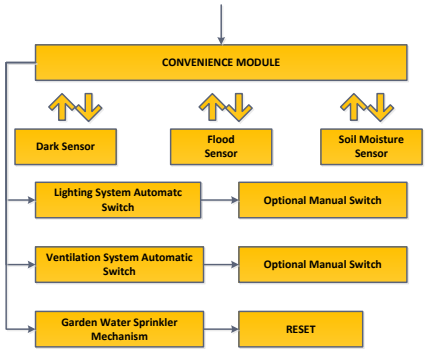


Figure 4. Low Level- Hierarchical System of the Convenience Module

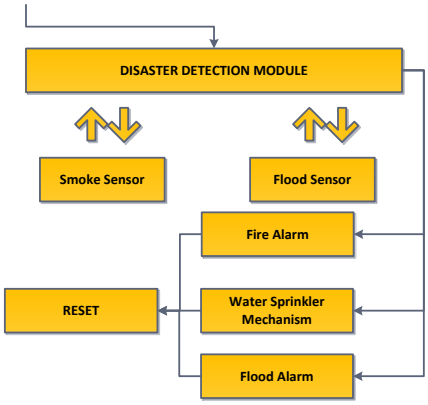


Figure 5. Low Level- Hierarchical System of the Disaster Detection and Risks Reduction Module

Figure 3, Figure 4 and Figure 5, which are the low- level hierarchical systems of each sub- modules of the project, shows the more detailed representations of the mentioned systems.

First, the security module features a six bit binary password that will activate and deactivate the whole security system. When the security system is activated through an allotted correct password combination, the magnetic sensors at the doors and windows and the motion sensor at the garage and garden area are also on. Whenever a trespasser will forcedly pass through the mentioned house entrances, the security alarms on each will trigger. For security module deactivation, there is another set of binary password combination that deactivates the whole system (no sensors working). In case

of the wrong password input, the programmers allotted sixty- two binary combinations that will outburst the wrong password alarm. All the alarms are interfaced with the Reset Alarm switch that will control their state (On/Off).

Then, the convenience module includes lighting, ventilation and garden water sprinkler automatic switching mechanisms. The lighting system is switched by the Light Dependent Resistor (LDR) that is plotted in a circuit attached to the input port of the FPGA board. Likewise with the ventilation system that is switched by the thermistor. Moreover, when the particular sound sensor for the garden water sprinkler switching mechanism is triggered, automatically, the water sprinkler mechanism will start to work.

Lastly, the disaster detection and risks reduction system will take care of the early detection of the fire and flood that occurs in homes. When the smoke detector senses smoke, the fire alarm and fire sprinkler will turn on. Likewise, when the flood sensor is triggered, the flood alarm will function.

2.3 Tabular, State Diagram and Real- Time Representations

Parts of the project flow are the tabular, state diagram and real- time representations of the systems that are incorporated with the whole project system. It became a prerequisite action for the proponents to be able to create a draft for the whole system's program coding.

2.3.1 Security Module

Security system of this study features a password checker for the activation and deactivation of it. When the input password is correct for activation and deactivation, all the sensors that are interfaced with the system are functioning and off respectively. On the other hand, when incorrect for both, the sensors are off and will stay off respectively.

Table 1 below is the tabular representation of the modes of the security module and their respective correct 6- bit binary input passwords.

Table 1. Security Module Mode and Correct Binary Passwords

SECURITY MODE	CORRECT 6- BIT BINARY PASSWORD
ACTIVATION	6'b010011
DEACTIVATION	6'b101100

Table 2 below, denotes the relationships between the security module modes and conditions. On the other hand, Table 3 shows the security sensors and alarms relationships. Attached also to the security module is the wrong password alarm that will outburst even without sensors detection, whenever a wrong input security password combination will be keyed- in to the checker for deactivation.

Table 2. Security Module Modes and Conditions

6- BIT BINARY PASSWORD	CONDITIONS	
6'b010011	Activation	Security Sensors = ON
	Deactivation	Security Sensors = ON
6'b101100	Activation	Security Sensors = OFF
	Deactivation	Security Sensors = OFF
Other Binary Combinations	Activation	Security Sensors = OFF
	Deactivation	Security Sensors = ON

Table 3 Security Sensors and Alarms Relationships

SECURITY SENSORS	BINARY CONDITION	ACTUAL CONDITION
DOOR MAGNETIC SENSOR	1'b0	Door Alarm = OFF
	1'b1	Door Alarm = ON
WINDOWS MAGNETIC SENSOR	1'b0	Windows Alarm = OFF
	1'b1	Windows Alarm = ON
GARDEN MOTION SENSOR	1'b0	Garden Alarm = OFF
	1'b1	Garden Alarm = ON
GARAGE MOTION SENSOR	1'b0	Garage Alarm = OFF
	1'b1	Garage Alarm = ON

2.3.2 Convenience Module

Attached to the convenience module is the reset alarm switch that will control the state of one of the convenience inputs which is the soil moisture sensor. On the other hand, the binary state of the all the convenience sensors namely, dark sensor, temperature sensor and soil moisture sensor dictates the actual condition of the output signals attached to the module. Table 4 below depicts the relationships between the input and output signals of the convenience module.

Table 4. Convenience Module's Input and Output Signals Relationship

CONVENIENCE SENSORS	BINARY CONDITION	ACTUAL CONDITION
Dark Sensor	1'b0	Automatic Lighting System Switch = OFF
	1'b1	Automatic Lighting System Switch = ON
Temperature Sensor	1'b0	Automatic Ventilation System Switch = OFF
	1'b1	Automatic Ventilation System Switch = ON
Soil Moisture Sensor	1'b0	Garden Water Sprinkler Mechanism = OFF
	1'b1	Garden Water Sprinkler Mechanism = OFF

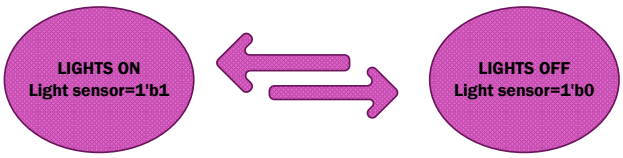


Figure 6. State Diagram Representation for the Convenience Module's Lighting System's Automatic Switching Mechanism

Figure 6 is the state diagram of the lighting system's automatic switching mechanism of the convenience module. The said mechanism includes a dark sensor that will dictate the state (on/off) of the bulbs in the house. In the Verilog program and simulation, the light sensor served as the input parameter and the brightness of the bulbs as the output. When the light sensor is equal to 1'b0, the light is in OFF state. Oppositely, when the light sensor is equal to 1'b1, the light is in ON state.

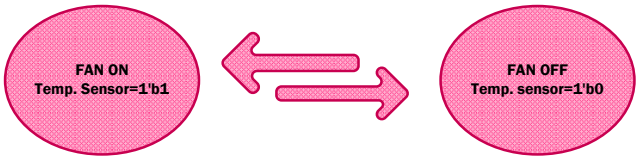


Figure 7 State Diagram Representation for the Convenience Module's Ventilation System's Automatic Switching Mechanism

The Figure 7 is the state diagram of the ventilation system's automatic switching mechanism of the convenience module. The mechanism includes a temperature sensor that will turn on and turn off the ventilation system of a particular house. In the Verilog program, the temperature sensor is the input parameter while the ventilation system is the output parameter. When the said sensor is at 1'b0, the ventilation system is in the OFF state. Oppositely, binary 1'b1 denotes an ON state of the ventilation system.

2.3.3 Disaster Detection and Risks Reduction Module

Attached to the disaster detection and risks reduction module are the detectors that will dictate the condition of their respective alarms and devices. Table 5 below shows the relationships between the detectors of this sub- module to their respective devices.

Table 5. DDRR Module's Input and Output Signals Relationships

DISASTER DETECTION SENSORS	BINARY CONDITION	ACTUAL CONDITION
Smoke Sensor	1'b0	Fire Alarm = OFF
		Water Sprinkler Mechanism = OFF
	1'b1	Fire Alarm = ON
		Water Sprinkler Mechanism = ON
Flood Sensor	1'b0	Flood Alarm = OFF
	1'b1	Flood Alarm = ON

The output signals attached to this sub- module are connected to main module's reset button which also controls the state of ther alarm and indicators.

2.4 RTL and Technology Schematic Diagrams

Figure 8, 9 and 10 are the low level register transfer, high level register transfer and technology schematic diagrams of the system respectively. In this work, input and output signals relationships are taken into consideration. Input 'clock' is used for the simulations' timing purposes. Input 'passwordC(5:0)' is a 6- bit password checker for the security system. When high, security system sensors are on, otherwise, off. Input 'doorSen' is the magnetic sensor at the door. When high, door alarm is on, otherwise, off. Input 'windowSen' is the magnetic sensor at the windows. When high, alarm at the windows is on, otherwise, off. Input 'garageSen' is the motion sensor at the garage area. When high, garage area alarm is on, otherwise, off. Input 'gardenSen' is the motion sensor at the garden area. When high, garden area alarm is on, otherwise, off. The 'activation' input depicts if the user is for activation of for deactivation phase. Additonally, the reset alarm switch is also intefaced will dictate the state of the output signals. On the other hand, input and output signals relationships are taken into consideration for the convenience module. Reset Alarm switch is also intefaced to

dictate the state of the output signal equivalent to the soil moisture sensor input signal. Lastly, the disaster detection and risks reduction system. Input 'floodsensor'is the sensor that will detect flood entering home premises. When high, flood alarm and the rescue signal sender are both on, otherwise, off. Input 'smokedetector' is the sensor that will detect smoke from house fires. When high, fire alarm and fire sprinkler are on, otherwise, off. All the sensors and devices used in the three sub- systems were sythesized into just one integrated digital circuit and readily subjected into one ISim simulation, Xilinx- Spartan3e and Altera- Cyclone II- FPGA boards implementation.



Figure 8 Low Level RTL Schematic Diagram of the 'Happy Home': Integrated Security, Convenience, Disaster Detection and Risks Reduction Systems

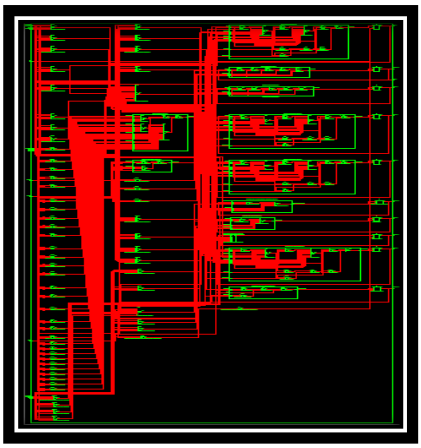


Figure 9 High Level RTL Schematic Diagram of the 'Happy Home': Integrated Security, Convenience, Disaster Detection and Risks Reduction Systems

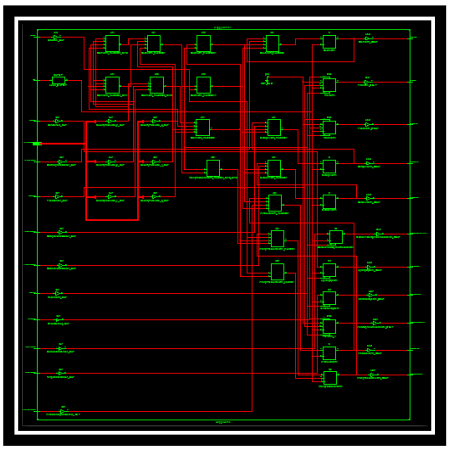


Figure 10. Technology Schematic Diagram of the 'Happy Home': Integrated Security, Convenience, Disaster Detection and Risks Reduction Systems

3. Experiments and Analysis of Results

This part contains the result and discussion of the system. This provides additional explanation, discussion and definition of the system and its parts, which is conceptualized below, Figure 11

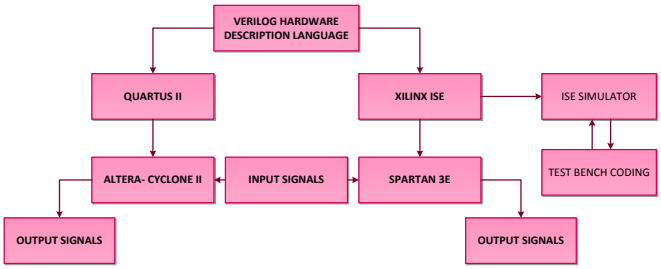


Figure 11. Summary of the System to be tested

Figure 11 is the main concept of the summarize system which illustrates how the parts of the system are interconnected and explains the relationship of each parts to one another. The Verilog HDL is a high level programming language used by the proponents to describe the behavior of the system [14]. With this, the proponents integrates the used of software which are the Quartus II and Xilinx ISE to come up in the said system. The Altera-Cyclone II used for the command (such as switch and indicators) for able to manipulate the sensors externally in order to analyze the relationship between the input and output signals simulated and implemented through Spartan3e- FPGA.

3.1 Project Tests

In this study, the original plan of the proponents was to test the proposed digital design of an integrated circuit for home automation system through simulating and implementing the Verilog HDL codes to Xilinx ISE- ISim and Spartan3e FPGA board only. On the process of Spartan3e implementation, for the sake of meeting the project's objectives, the researchers oversaw the disadvantages of directly incorporating the external devices needed to the FPGA board. Some of the external devices, specifically the sensors having a high output voltage than limiting requirement for the board (3.3

Volts to 5 Volts), affected the stability of the Field Programmable Gate Array board. The Spartan3e- FPGA suddenly became unstable and inaccurate. The logic flow of the Verilog HDL codes were seen accordingly when it comes to ISim simulations but not when it comes to hardware implantation. In due course, the proponents decided to pursue the contingency plan of maximizing the unfortunate events that had come.

According to their contingency plan, the proponents will now test their designed digital system through the following:

- Simulation using Xilinx ISE- ISim and Implementation using Xilinx- Spartan3e FPGA board with Stable Condition
- Implementation using Xilinx- Spartan3e FPGA board with Erratic Condition
- Implementation using Altera- Cyclone II FPGA board

3.2 Tests for Functionality, Reliability and Accuracy

Table 6. Posible Conditions for Functionality, Reliability and Accuracy Testing

No	ACTIVATION	CONDITIONS
1	ON	SECURITY PASSWORD = CORRECT FOR ACTIVATION && Reset Alarm = OFF && Door Magnetic Sensor = OFF
2	ON	SECURITY PASSWORD = CORRECT FOR ACTIVATION && Reset Alarm = OFF && Door Magnetic Sensor = ON
3	ON	SECURITY PASSWORD = CORRECT FOR ACTIVATION && Reset Alarm = OFF && Windows Magnetic Sensor = OFF
4	ON	SECURITY PASSWORD = CORRECT FOR ACTIVATION && Reset Alarm = OFF && Windows Magnetic Sensor = ON
5	ON	SECURITY PASSWORD = CORRECT FOR ACTIVATION && Reset Alarm = OFF && Garage Motion Sensor = OFF
6	ON	SECURITY PASSWORD = CORRECT FOR ACTIVATION && Reset Alarm = OFF && Garage Motion Sensor = ON
7	ON	SECURITY PASSWORD = CORRECT FOR ACTIVATION && Reset Alarm = OFF && Garden Motion Sensor = OFF
8	ON	SECURITY PASSWORD = CORRECT FOR ACTIVATION && Reset Alarm = OFF && Garden Motion Sensor = ON
9	ON	SECURITY PASSWORD = CORRECT FOR ACTIVATION && Reset Alarm = OFF && Door Magnetic Sensor = OFF && Windows Magnetic Sensor = OFF && Garage Motion Sensor = OFF && Garden Motion Sensor = OFF
10	ON	SECURITY PASSWORD = CORRECT FOR ACTIVATION && Reset Alarm = OFF && Door Magnetic Sensor = ON && Windows Magnetic Sensor = ON && Garage Motion Sensor = ON && Garden Motion Sensor = ON
11	ON	SECURITY PASSWORD = WRONG FOR ACTIVATION Reset Alarm = OFF && Door Magnetic Sensor = ON/ OFF && Windows Magnetic Sensor = ON/OFF && Garage Motion Sensor = ON/OFF && Garden Motion Sensor = ON/OFF
12	OFF	SECURITY PASSWORD = CORRECT FOR ACTIVATION && Reset Alarm = OFF && Door Magnetic Sensor = ON && Windows Magnetic Sensor = ON && Garage Motion Sensor = ON && Garden Motion Sensor = ON
13	OFF	SECURITY PASSWORD = CORRECT FOR ACTIVATION && Reset Alarm = OFF && Door Magnetic Sensor = OFF && Windows Magnetic Sensor = OFF && Garage Motion Sensor = OFF && Garden Motion Sensor = OFF

14	OFF	SECURITY PASSWORD = CORRECT FOR DEACTIVATION && Reset Alarm = OFF && Door Magnetic Sensor = ON/ OFF && Windows Magnetic Sensor = ON/ OFF && Garage Motion Sensor = ON/ OFF && Garden Motion Sensor = ON/ OFF
15	OFF	SECURITY PASSWORD = WRONG PASSWORD FOR DEACTIVATION && Reset Alarm = OFF && Door Magnetic Sensor = ON/ OFF && Windows Magnetic Sensor = ON/ OFF && Garage Motion Sensor = ON/ OFF && Garden Motion Sensor = ON/ OFF
16		Dark Sensor = ON
17		Dark Sensor = OFF
18		Temperature Sensor = ON
19		Temperature Sensor = OFF
20		Soil Moisture Sensor = ON && Reset Alarm = OFF
21		Soil Moisture Sensor = OFF && Reset Alarm = OFF
22		Smoke Sensor = OFF && Reset Alarm = OFF
23		Smoke Sensor = ON && Reset Alarm = OFF
24		Flood Sensor = OFF && Reset Alarm = OFF
25		Flood Sensor = ON && Reset Alarm = OFF
26		Reset Alarm = ON

Table 6 is the summation of tests done that has been tested for its functionality, reliability and accuracy. For the test of functionality, they listed numerous conditions that the designed system can be into. The proponents came up with 26 possible conditions. The functionality will be tested according to the set conditions:

On the other hand, the researchers tested for the reliability of the project design by testing it for 30 trials (15 trials for ISim simulation and 15 trials for 15 trials for hardware implementation). After the trails, the proponents set hypothesis to be met:

- 1st Hypothesis:
  SUCCESS Remark && SUCCESS Remark = SUCCESS
- 2nd Hypothesis
  SUCCESS Remark && FAILED Remark = FAILED
- 3rd Hypothesis:
  FAILED Remark && SUCCESS Remark = FAILED
- 4th Hypothesis:
  FAILED Remark && FAILED Remark = FAILED

Lastly, the test of accuracy depends on both test for functionality and reliability. The said test will be measured by using the set formula below:

Accuracy (%) = (Number of SUCCESS Remarks/ Total Number of Trials for each Condition) 100

The second project test that the proponents did is through Xilinx- Spartan3e FPGA board implementation. The input and output signals represented by set of digital sensors, alarms and indicators are incorporated at the input and output signal ports of the said FPGA board.

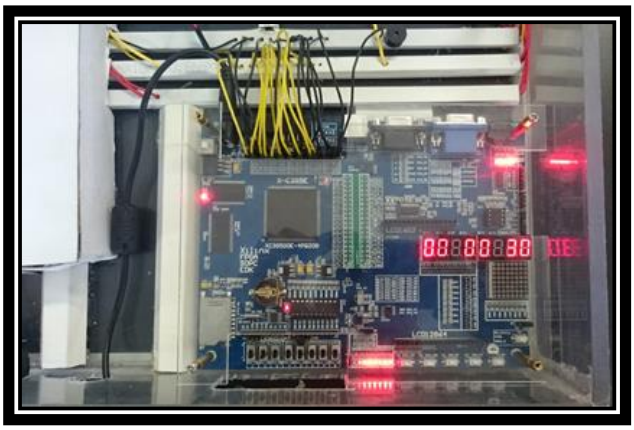


Figure 12. Spartan3e- FPGA Implementation

Figure 12 which is the real- time representation of the configurations for the Xilinx- Spartan3e FPGA implementation. It also depicts the actual connections of the input and output devices to the FPGA board.

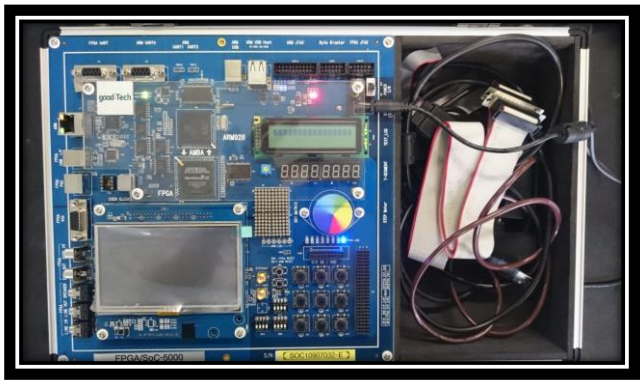


Figure 13. Altera- Cyclone II Implementation

On the other hand, Figure 13 is the real- time representation of the configurations for the Altera- Cyclone II FPGA implementation, which is the third project test for the proposed digital system. It also depicts the actual connections of the input and output devices to the FPGA board.

3.4 Xilinx ISE- ISim Simulations and Spartan3e FPGA Board with Stable Condition Implementation

The first project test that the proponents did is the software- hardware tandem of Xilinx ISE- ISim simulations and Spartan3e FPGA board with stable condition implementation. The percentage accuracy is:

% Accuracy (Over- all) = (26/ 26) 100
% Accuracy (Over- all) = 100%

3.5 Spartan3e FPGA Board with Erratic Condition Implementation

The second project test that the proponents did is the Spartan3e FPGA board with erratic condition implementation. The percentage accuracy is:

% Accuracy (Over- all) = (14/ 26) 100

% Accuracy (Over- all) = 53.85%

3.6 Altera- Cyclone II FPGA Implementation

The third project test that the proponents did is the Altera- Cyclone II FPGA implementation. The percentage accuracy is:

% Accuracy (Over- all) = (15/ 15) 100
% Accuracy (Over- all) = 100%

3.7 Column Chart

Figure 14 below shows the column chart representing the over- all percentage accuracy of all the project tests done.

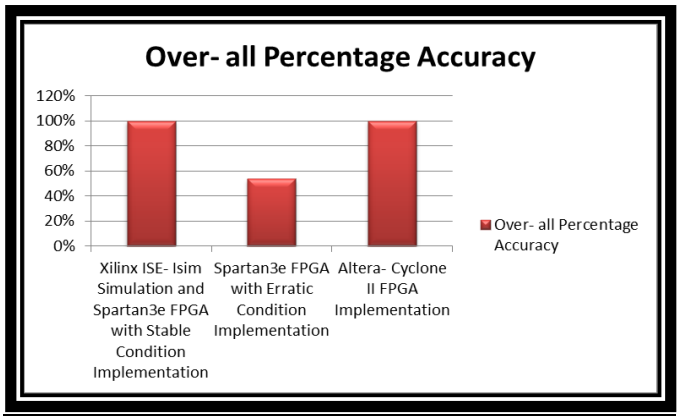


Figure 14. Column Chart of the Over- all Percentage Accuracy

4. Conclusion and Recommendations

The goal of the research was achieved by the use of Verilog Hardware Description Language coded in Xilinx ISE and Altera Quartus II. Then the codes were simulated in Xilinx ISim and implemented using Xilinx- Spartan3e (stable and erratic condition) and Altera- Cyclone II Field Programmable Gate Array boards. Verilog HDL really helped the proponents, in order to implement the programming aspect of the project. It provides instructive waveforms which are very valuable in understanding the concept of the research. With this, the researchers realized that Xilinx ISE and Quartus II tool can be verified as learnable tools for simulation and a great integrated development environment. It was also realized that it is easier to design, synthesis, and simulate different digital system circuits using the said software tools. We simply have to be very careful in programming, considering that we are designing and realizing the hardware circuitry. All Verilog output waveforms simulated and displayed by the tools show that the Home automation System is operating accordingly. Thus, the 'Happy Home' was successfully completed and feasible for implementation. In implementation, the researchers made a miniature of a house with structural cabling incorporated with different sensors. These sensors served as an input to the FPGA board. The digital output by the sensors fed to the FPGA board generates an output through the use of different output mechanism like buzzers, LED indicator, and DC motors. In addition, the code that was programmed in the board was operating accordingly. Hence, the implementation of the Home Automation System was successful and now possible for IC wafer fabrication. Additionally, it was also concluded that FPGA boards are

sensitive when it comes to accepting and relating to outside voltage parameters. They are so vulnerable to outside devices so the users must have a double time on reading the specification sheets of any programmable boards.

The proponents are recommending forwarding this project design to a company that manufactures Application Specific Integrated Circuit (ASIC). It is also recommended for the researchers to explore the possibility on trying to implement the designed digital codes to other available Field Programmable Gate Array boards. For the future researchers to acquire a new Spartan3e FPGA board so they can experience and share the wonder of this very promising advanced technology. It is also recommended that when they already acquire a new one, they must be careful on incorporating external devices to it specifically when that device output a high voltage level. The recent proponents suggest for them to use relay mechanisms before the implementation of any. For the College of Engineering and Computer Studies of LPU-Laguna to encourage more students to pursue research project like this. FPGA-concerned researches here in the Philippines are very limited due to the constraints of availability of some materials, nevertheless, these kind of research endeavors are now very timely, marketable and internationally accepted.

References

[1] [Online] http: http://www.pbs.org/transistor/album1/ (accessed August 10, 2014)
[2] [Online] http://en.wikipedia.org/wiki/Programmable_read-only_memory (accessed July 8, 2014)
[3] [Online] http://www.brighthubengineering.com/commercial-electrical-applications/71447-where-integrated-circuits-are-used/ (accessed August 10, 2014)
[4] [Online]https://www.osac.gov/pages/ContentReportDetails.aspx?cid=13574 (accessed August 10, 2014)
[5] [Online] http://reslife.rpi.edu/update.do?artcenterkey=759 (accessed August 10, 2014)
[6] [Online] http://www.disasterium.com/10-worst-natural-disasters-of-all-time/ (accessed August 10, 2014)
[7] Grzegorz Budzyń, "Programmable Logic Design, Chapter 2: VHDL vs. Verilog," Master programmes in English, Wroclaw University of Technology
[8] Komol Arafat. Gani, Farzana. Yasmin, A B M Najmul. Karim, Iqbalur. Rahman , "Home Automation System Design Using Verilog Hardware Descriptive Language," 2nd International Conference on Recent Trends in Computer and Information Engineering (ICRTCIE'2013) Dec. 20-21, 2013 Bali (Indonesia), North South University
[9] [Online] http://www.adpc.net/pdr-sea/cbdo-dr/chapter1.html (accessed August 10, 2014)
[10][Online] http://www.asti.dost.gov.ph/index.php/press-room-mainmenu-27/1-latest/57-fpga-based-design-using-vhdl-training (accessed July 8, 2014)
[11]Prof. Stephen A. Edwards, "The Verilog Language, COMS W4995-02," Fall 2002, Columbia University, Department of Computer Science
[12][Online] http://en.wikipedia.org/wiki/Xilinx_ISE (accessed August 1, 2014)
[13][Online] https://www.element14.com/community/docs/DOC-40098/l/altera-introduction-to-the-quartus-ii-software (accessed June 21, 2016)

[14][Online] http://ece.niu.edu.tw/~chu/download/fpga/verilog.pdf (accessed June 21, 2016)

eureca 2016 – Conference Paper
Paper Number EE_UG05

Microcontroller-Based Body Mass Index Calculator and Monitoring System with Classifier Using Fuzzy Logic Algorithm

Zaira P.Caranay[1*], Chexel D. Agustin[2], Christian G. Lizardo[2], Kristine Jade F. Magpantay[2], Rio A. Aguilar[2], Rionel Belen Caldo[1]

[1]*Computer Engineering Department*

[2]*Electronics Engineering Department*

Lyceum of the Philippines University-Laguna (LPU-L)

Corresponding e-mail: [*]zairacaranay1@gmail.com

Abstract

Body Mass Index (BMI) is a human body measurement of weight and height that defines the body fats. It is the commonly accepted index for classifying the health status whether a person is normal, underweight and obese. It shows a relationship with clinical risks factors for cardiovascular disease (Freedman et al., 1999). According to the Bogalusa Heart Study, around 60% of 5 - 10 year old kids who were overweight had clinical danger element for cardiovascular illness including hyperlipidemia, lifted insulin and hypertension, and 20% had two or more hazard variables. In this paper, BMI of a person will be monitored and managed through calculation and analysis. The Microcontroller-Based Body Mass Index Calculator and Monitoring System with Classifier Using Fuzzy Logic Algorithm is a device that records the height and the weight of a person as well as the BMI. It also analyses the body status whether the person is underweight, normal, overweight and obese. It endorses the use of sensor technology specifically an ultrasonic sensor with a cord data transmission which can be use in order to obtain the height of a person and load cell for obtaining the weight. The system operates through input variables of height, weight, and personal information that will be simulated by the algorithm of the fuzzy logic and will be programmed into the C# language in Visual Studio. The fuzzy logic serves as the brain that analysed the calculated BMI and the body status. The proposed system also consists of printer that will print the data and the obtained body measurements. It also has the capability of recording the data gathered into the database that is used to monitor the body status of the person. Generation of charts with respect to age gender and department can also be done by the system. The proposed model is tested through the use of T-Test method in order to analysed the acceptability error of the device and test its performance compared to the traditional way of measuring BMI in the clinic.

Keywords: SMART Farm; Data Logging; Monitoring; Arduino; VB.Net; LCD; DHT11, VH400, DS7911

1. Introduction

This section covers the novelty of the study, statement of the problem and the general objectives. It will discussed what, when, where and how they will implement the system.

1.1 Background of the Study

The number ascertained from a man's weight and tallness is called Body Mass Index. It shows the status of a man's muscle to fat quotients and is an option for direct measures of it. Knowing your BMI gives you a thought of how sound your weight is. Moreover, Body Mass Index is an economical and simple tool strategy for monitoring of weight classes because the calculation requires only height and weight and can be used in assessing whether a person is malnourished/ underweight, overweight, obese or normal. Present BMI calculators are based on the BMI-for-age chart that contains the height, the weight, and the age brackets in determining the approximate BMI value and its classification. Since people nowadays were getting involved and attached with the fast advancement of technology, there are already computer- generated BMI measuring applications that can be found online which are made accessible for a more convenient way of knowing one's body fat status. This requires the height and the weight of the user, and some asks for age and gender too. These applications are programmed to do the calculations of BMI. The most common way of obtaining a person's BMI is by using the English formula which states that the BMI is equal to the square of the individual's weight in pounds everywhere throughout the square of the same individual's stature measured in inches, then, increasing the answer by 703. The other one is through the metric arrangement of isolating the individual's weight, measured in kilograms everywhere throughout the square of individual's stature in meters. Mathematically, these are respectively expressed as:

$$\text{BMI} = \frac{\text{weight (lb)}}{\text{height (in}^2\text{)}} \times 703 \qquad \textit{Equation 1}$$

$$\text{BMI} = \frac{\text{weight (kg)}}{\text{height (m}^2\text{)}} \qquad \textit{Equation 2}$$

Aside from the height and weight of a person as parameters in getting BMI, their age and gender are also factors of the BMI result. Standard weight status class that are the same for all ages and for both men and ladies will be used for adults aged 20 and above. According to Center for Disease Control and prevention, woman have a tendency to have more muscle to fat ratio ratios than men and more established individuals, overall, have a tendency to have more muscle to fat quotients than more youthful grown-ups. Exceedingly arranged contenders may similarly have high BMI in light of expanded quality rather than expanded body vastness.

Overweight and obesity are characterized as unusual or intemperate fat collection that may harm wellbeing [1]. As per the World Health Organization, with the BMI more than or equivalent to 25 is overweight, and a BMI more prominent than or equivalent to 30 is fat. Those individuals who are experiencing obesity are inclined of building up certain sorts of malignancy, coronary illness, stroke and diabetes among other wellbeing issues [2]. Centers for Disease Control and Prevention expressed that for grown-ups 20 years of age or more, more than 66% (68.8 percent) of grown-ups are thought to be overweight or fat and for youngsters and youthful, around 1 in 3 young

men (33 percent) are thought to be overweight or large, contrasted and 30.4 percent of young ladies [3]. In 2008, those grown-ups age 20 and more seasoned who were overweight is around 1.4 billion. Of these, more than 200 million men and about 300 million ladies were corpulent. More than 40 million kids less than 5 years old were overweight or large in 2012.These two are the main dangers for worldwide passing. Around 3.4 million grown-ups kick the bucket every year as a due to being overweight or corpulent. [4]. In the Philippines, 22.3% of Filipino grown-ups were overweight, and 6.1% were corpulent base on the overview of the Food and Nutrition Research Institute (FNRI) in 2011. The FNRI-DOST additionally expressed that the issue of weight was expanding in a disturbing rate in the Philippines where 7 out of 10 ladies and 1 out of 10 men were influenced [5]. People don't take it into consideration of measuring their BMI for they might not know the purpose of doing so or they do not care at all what does their BMI indicates. Scientifically, setting aside the importance of measuring BMI may have a risk of developing health problems.

Since there is a variation in getting the BMI of a person, the so- called fuzzy rule- based system could be used to synthesize the methods from a various logic by creating a computer program of rules. The fuzzy logic provides development of algorithms based on the input of the person thus seeks application of mathematics to diffuse concepts.

1.2 Statement of the Problem

Body weight regulation has been a critical general wellbeing issue as of recent years. As indicated by the statistic, corpulence issue has turned into a scourge that causes costly expenses to the general wellbeing administrations. Corpulence is comprehended as both a cause and in the meantime an impact of mental and in addition behavioral issues. Viewing the issue from the proponent's point of view, setting aside the importance of measuring BMI may have a risk of developing health problems. People don't take into consideration of measuring their BMI for they might not know the purpose of doing so or they do not care at all what does BMI indicates might be one of the factors that causes obesity.

1.3 Objectives of the Study

The general objective of the study is to design and simulate Microcontroller-Based Body Mass Index Calculator and Monitoring System with Classifier Using Fuzzy Logic Algorithm.

Specific Objectives:

1. To measure height and weight of the user.
2. To give numeric value of BMI that correlates the body fats of the person.
3. To explore the functionality of Fuzzy logic in classifying the BMI.
4. To develop a low-cost and efficient device using microcontroller for clinical use.
5. To create a system that will update and save the data for monitoring purposes.
6. To test and assess the accuracy and statistical acceptability of error of the system.

2 Methodology

2.1 Fuzzy Logic Approach

The theory which is introduced by Zadeh (1965) known as fuzzy set as an expansion of the traditional thought of set considering that a component can have a place halfway, yet not totally, to a class. Zadeh's numerical thought is anything but difficult to apply to the universe of biomedical since ideas here are not precisely characterized.

The Fuzzy Logic is a numerical device for managing uncertainty and gives a system to manage imprecision and non-straight data presented by Lotfi Zadeh in 1965. It provides inference or deduction structure which is similar to human reasoning capabilities. It utilizes theory of probability in measuring the chance with which a given occasion is relied upon to happen and clarify what will happen if the normal occasion will happen. Etymological builds, for example, some, low, medium, regularly, few are being spoken to by the fuzzy theory instrument. The theory of fuzzy logic is based upon the possibility of relative assessed enlistment similar to the components of mentation and mental methods. In Fuzzy Logic, indeterminate or uncertain information are displayed with the utilization of fluffy sets, Fig. 1, so frequently experienced in real life.

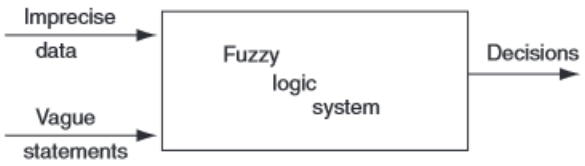


Figure 1: A fuzzy logic system which acknowledge uncertain information and unclear articulations, for example, low, medium, and high and gives choice.

2.2 Proposed System

The proposed system will use fuzzy logic approach in getting the BMI classification of a person. The value of the BMI will be calculated and manipulated by a microcontroller through the inputs weight and height which will be obtain through the use of ultrasonic sensor and load cells. Since there is a variation in the classification of the BMI of a person with respect to age, the calculated BMI and the age of the user will served as the input of the fuzzy logic. The fuzzy logic provides development of algorithms based on the input of the person thus seeks application of mathematics to diffuse concepts. The fuzzy logic will decide whether a person is underweight, normal, overweight or obese base on the input BMI and age. The results will be stored in a database for statistical purposes and will be printed through thermal printer together with the recommendation.

2.3 Block Diagram

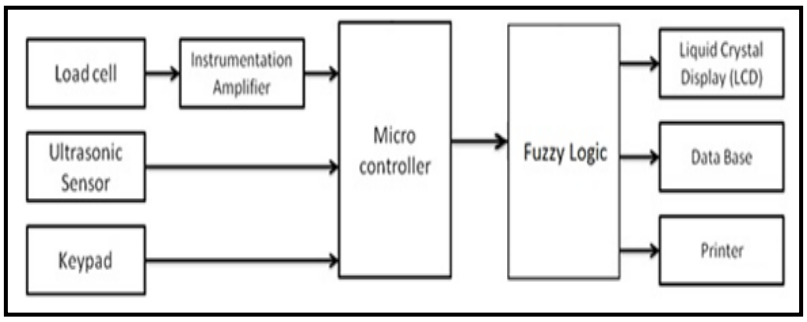


Figure 2: Block diagram of the proposed System

The initial procedure is to start the machine, the system will ask for the information of the user which includes the name, age, gender and location. The microcontroller Arduino will receive the data from the inputted user's information and the data from the load cells and the ultrasonic sensor. The ultrasonic sensor and load cell will measure the height and weight of the person. Then the microcontroller will process the data gathered and will be stored in the database. The results from the microcontroller will be displayed in the LCD display in order to view the measured BMI and status of the person. The fuzzy logic will serve as the brain that will analyzed the calculated BMI and the body status. If the calculated BMI result of less than 18.5 it will fall under the category of Underweight. Result that ranges from 18.5- 24.9 is considered Normal while 25- 29.9 BMI is Overweight. 30 and above is considered to be Obese. The calculation of the BMI would still be dependent on the formula whether it is English or Metric which is depending on the parameters that the height and weight measuring device will provide. The information will be stored in the data base. The results can be displayed in LCD display and/or on the monitor of the computer to print the result.

2.4 Schematic Diagram

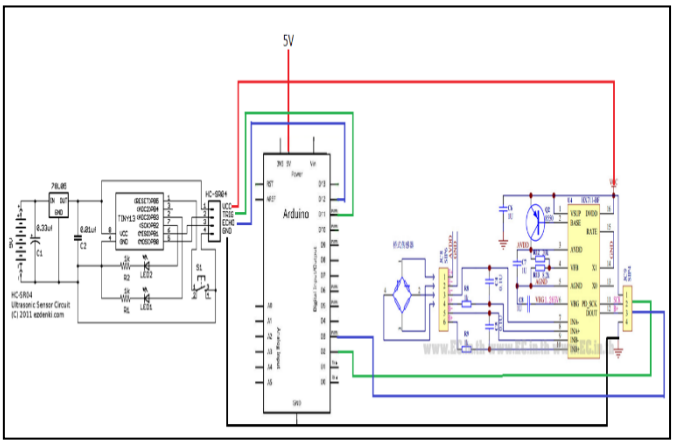


Figure 3: Schematic diagram of the proposed

2.5 IPO Chart

The IPO Chart of the proposed project is described in the figure below:

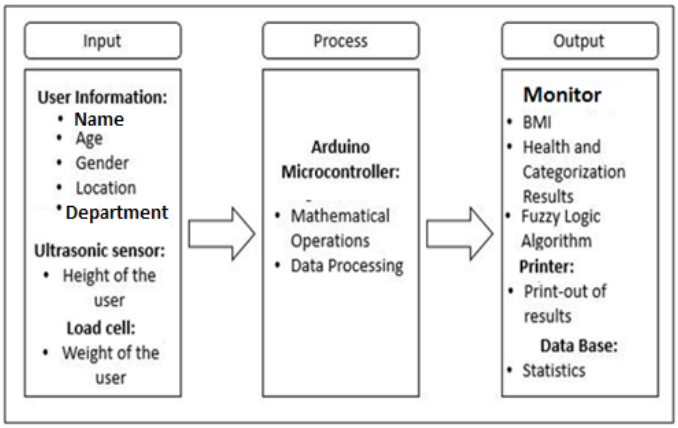


Figure 4. IPO Chart of the proposed project

Through related literatures and past studies, the project was conceptualized to develop and implement a system that will automatically calculate the Body Mass Index (BMI) of a person using microcontroller and sensors with a database that will record and monitor the results. The proponents gathered information and concepts in relation to calculation of the BMI using microcontrollers, load cell and sensors. Aside from the components used for the hardware, knowledge about Visual Basic and Matlab is essential to the proponents. The system will be a digital weighing scale, so programming will be needed in order to develop and design a system for measuring height and weight and calculating the BMI. With all the research, knowledge and concepts concerning Body Mass Index Calculation system, the proponents have conceptualized their own system which will include calculating and monitoring the body mass index of a person.

2.6 System Requirements

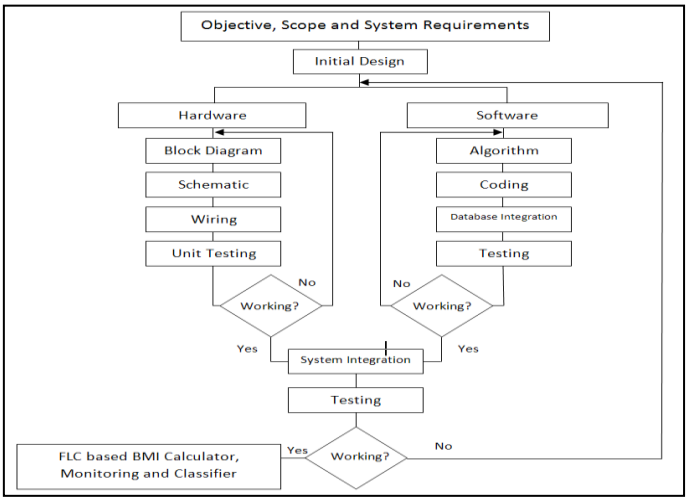


Figure 5. Requirements of the system

2.7 Flowchart

Below is the flow chart developed to guide in the development of the proposed system.

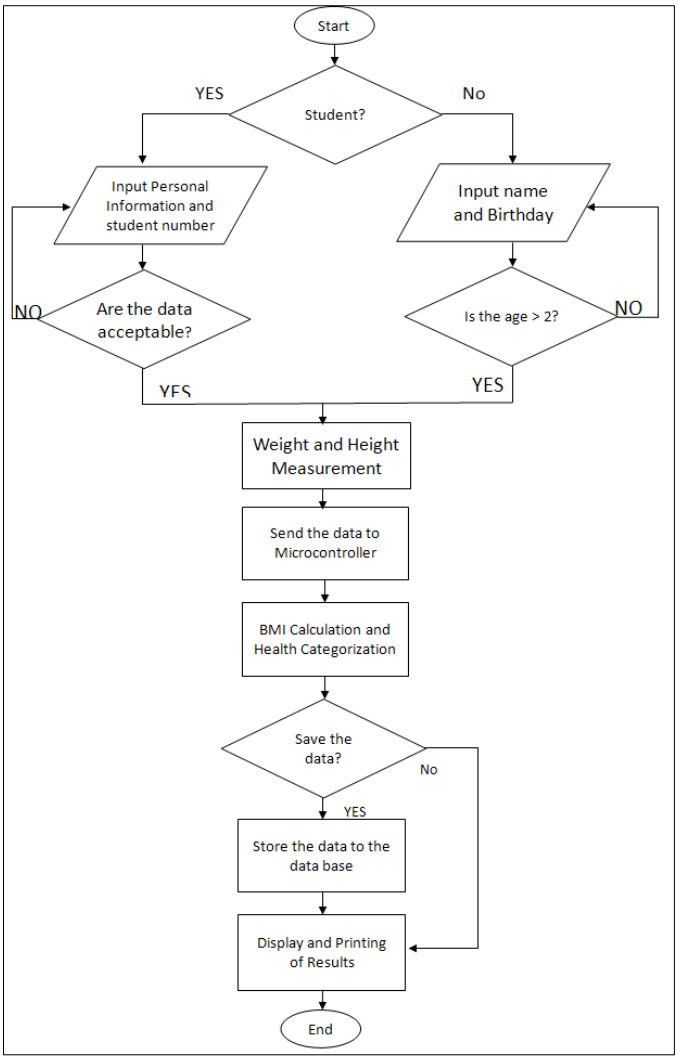


Figure 6. Flowchart of the system

3. Results and Discussion

3.1 Project Descriptions

In this paper, a BMI calculator was designed through fuzzy logic approach which can be helpful for health risk assessment of the user. The device can also be useful in management and controlling of health status of a person. If the user is obese, the system will suggest or recommended what the user should do in order to make his/her BMI normal, same as when the user is underweight. The Fuzzy Logic Controlled Body Mass Index Calculator for Health Risks Assessment can give accurate flexible and fast response compare to other algorithm since it uses fuzzy logic approach. In addition, the propose system is designed to have a statistical tool which will output multiple graphs about the BMI of a person vs age, gender and location.

3.2 Properties of the Project

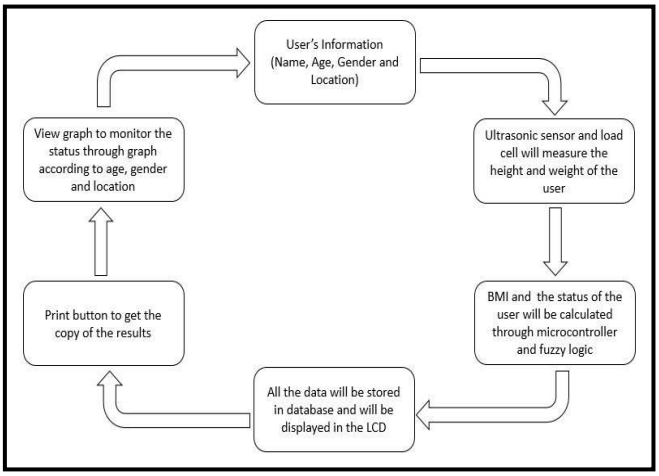


Figure 7. Paradigm of the of the System

The paradigm of the system that is shown in Fig. 7 shows the procedure on how the Body Mass Index Calculation, Monitoring and Management system works. The first thing to do is to input the user or patient's information which contains the person's name, age, gender, and his/her location. Using the load cell and the height sensor, the height and weight of the person can be measured. Then using the measured height and weight, the body mass index will be calculated as well as the status of the user or patient through the use of microcontroller and fuzzy logic. All the gathered and computed data will now be stored in the database which will be displayed in the LCD display.

An added feature in the system is that the user will now be able to print and provide a copy of the result of the BMI and its status. Besides the printer, the system is also capable of providing a graph, monitoring the status of the results according to age, gender and location.

3.3 Tools and Methodologies of the System

In this section, the methods and procedures in developing the system are stated. It includes the hardware and software used and the methods in assessing the functionality of the system.

- Ultrasonic Sensor- used for measuring height

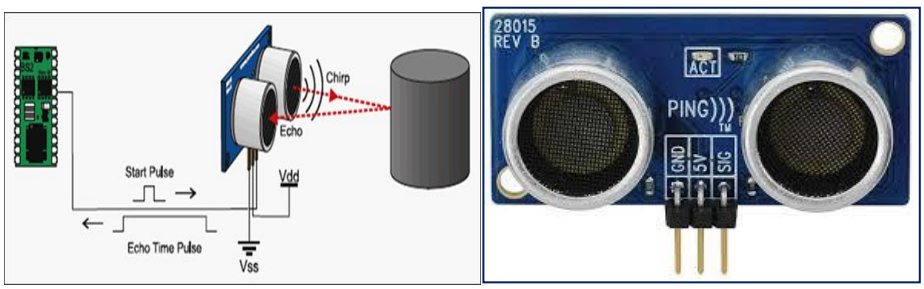


Figure 8: Ultrasonic senor's operations

An ultrasonic sensor can be used as a proximity sensor, which allows transmission and reception of sound waves. It emits an acoustic waves in with frequency greater than upper limit of human hearing also known as audible range (20

Hertz to 20 Kilohertz). It determines the distance between the location of the sensor and the object or person depending on the time passed amongst emanating and getting the sound waves. The time snuck past amongst discharging and enduring is regarding the unit of the article from the sensor.

- Load Cell- used for measuring weight

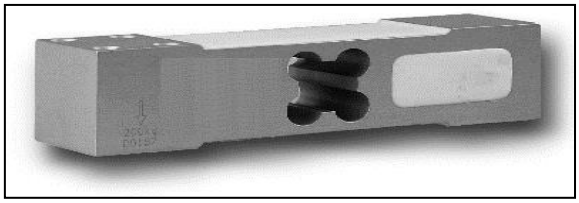


Figure 9: Load cell

Load cell is a sensor or a transducer which changes over a heap or constrain following up on it into an electrical sign. This electrical sign relies on upon the kind of burden cell and hardware utilized. It can be a voltage, current or recurrence variety. It is a weight estimation gadget essential for electronic scales that show weights in digits.

- HX711 Amplifier- amplifies voltage coming from load cell

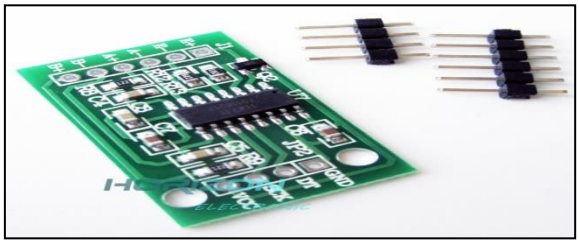


Figure 10: Instrumentation Amplifier

HX 711 amplifier permits to effortlessly read load cells to quantify weight. By associating the amplifier to your microcontroller you will have the capacity to peruse the adjustments in the resistance of the heap cell and with some alignment you'll have the capacity to get extremely precise weight estimations. This amplifier can be used in making own modern scale, process control or basic nearness discovery. Load cells utilize a four wire wheatstonebridge to interface with the HX711.

- Arduino Uno Microcontroller - fetch the datafom the sensors and the one who calculate the BMI numeric value.

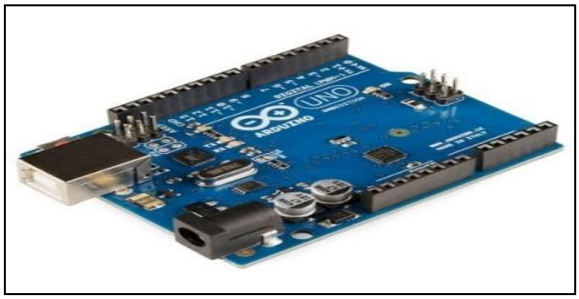


Figure 11: Microcontroller

According to W. Durfee, University of Minnesota, "The Arduino microcontroller is an easy to use yet powerful single board computer that has gained

considerable traction in the hobby and professional market." The microcontroller serves as the control unit of the system.

- Printer

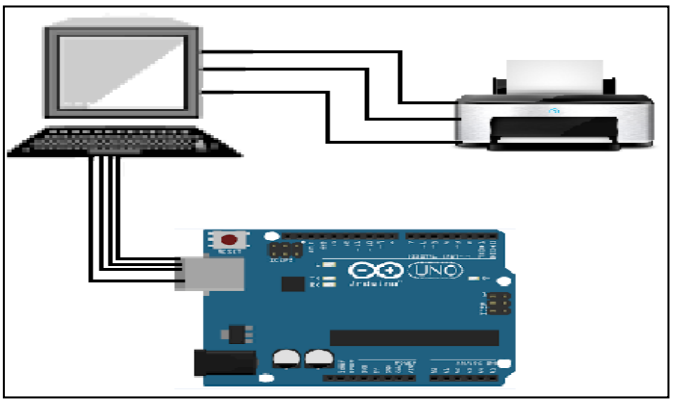


Figure 12: Microcontroller

The data will be displayed in the monitor and will be stored in the database for monitoring purposes. Hardcopy of the data and results gathered from the user will be printed.

- Fuzzy logic

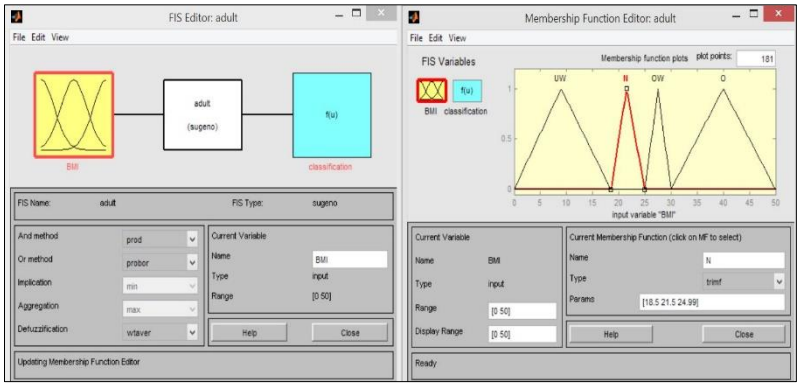


Figure 13: FIS editor for BMI classification

Fuzzy Logic Algorithm will be installed in the Arduino Uno for calculating or for determining the Body Mass Index of the user. The figures shown are the FIS editors and Membership functions of BMI-age-gender cutoffs. These figures show the range of the BMI and their classifications from 2 years old to 20 years old and above.

- Visual Studio C# Programming Language

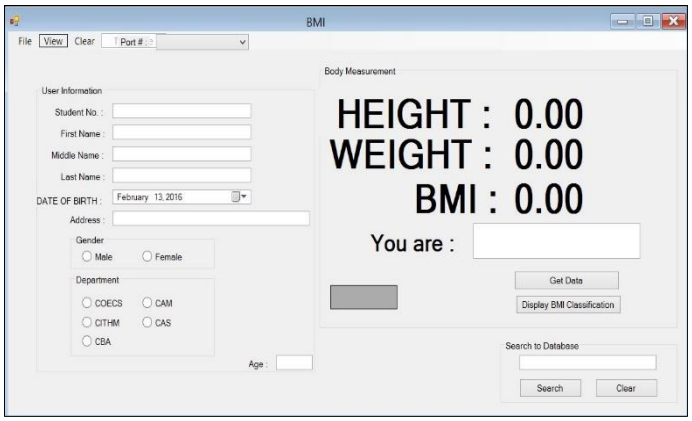
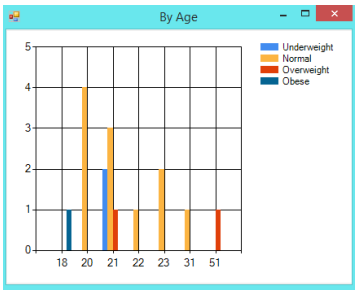
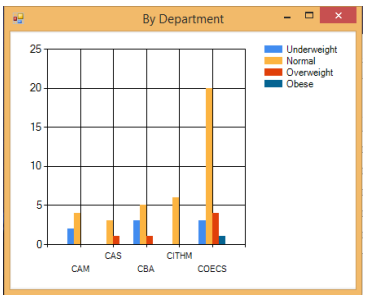


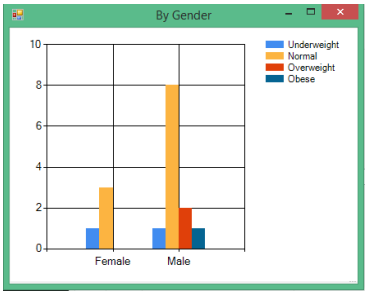
Figure 14: Graphical User Interface of the System using C# Programming Language

The programming language C# in Visual Studio was used in the system's Graphical User Interface. This serves as the window of the user to see the measured height and weight together with the numeric value of the BMI and its classification.

- Chart Generation

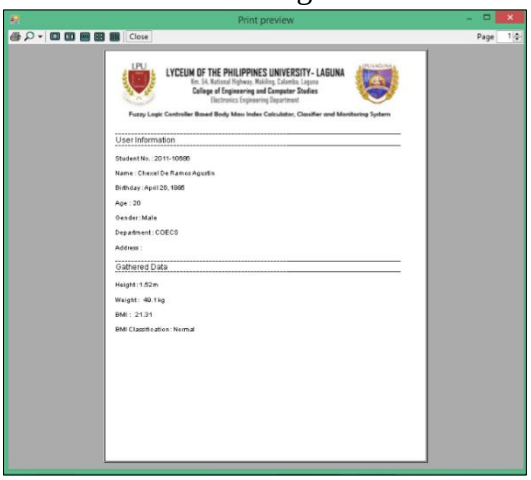






The system is capable of producing chats based on the data that are store in the data base. These charts defines the number of user that are underweight, normal, overweight or obese with respect to age, gender and location.

- Printing Results



4. Data and Results

Experimental values were obtained by getting the mean of each sample and compare it to the actual value through the use of statistical method, called T-test. The calculation of P value of each test is calculated through the use of Microsoft Excel.

Table 1. Measure of relationship between means of the actual value and means of experimental value for height measurement

Height Sensor		
# of samples	Actual value	Experimental value
1	1.61	1.59
2	1.55	1.52
3	1.57	1.55
4	1.58	1.58
5	1.62	1.62
6	1.73	1.71
7	1.54	1.53
8	1.55	1.55
9	1.58	1.58
10	1.53	1.51
11	1.54	1.54
12	1.52	1.5
13	1.46	1.46
14	1.5	1.48
15	1.55	1.54
16	1.67	1.67
17	1.55	1.54
18	1.56	1.55
19	1.58	1.57
20	1.62	1.59

*****Criteria: if $P \geq 0.05$ then accept the null hypothesis

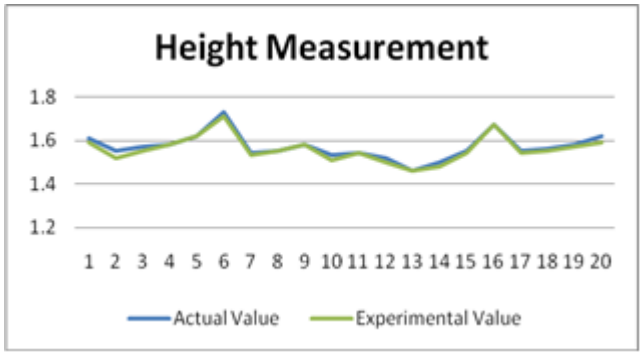


Figure 15: Line Graph for Actual and Experimental Value for Height Measurement

Table 2: Statistical Acceptability of Error of Ultrasonic Sensor Using T-Test

	Variable 1	*Variable 2*
Mean	1.5705	1.559
Variance	0.003531316	0.003546316
Observations	20	20
Hypothesized Mean Difference	0	
Df	38	
t Stat	0.611320363	
P(T<=t) one-tail	0.272313752	
t Critical one-tail	1.68595446	

Table 2 presents that the P-value is greater than the t-value which is 0.05 and since the P-value serves as the evidence that null hypothesis is true, therefore the null hypothesis is accepted. The error and difference between two methods are insignificant and are purely due to the random errors only. Based on the T-Test, the proponents can say that the proposed system is accurate.

Table 3: Measure of relationship between means of the actual value and means of experimental value for height measurement

Weight Sensor		
# of samples	Actual value	Experimental value
1	77.8	77.73
2	42.3	42.48
3	47	47.2
4	59.5	59.53
5	62.2	62.3
6	60.3	60.37
7	58.5	58.73
8	47.4	47.6
9	49.3	49.23
10	58	58.1
11	50	50.17
12	49.5	49.6
13	44.3	44.63
14	52.1	52.47
15	47.6	47.76
16	63.6	63.8

17	47.55	47.83
18	49	48.8
19	55.5	55.3
20	46.1	45.77

*Criteria: if P≥0.05 then accept the null hypothesis

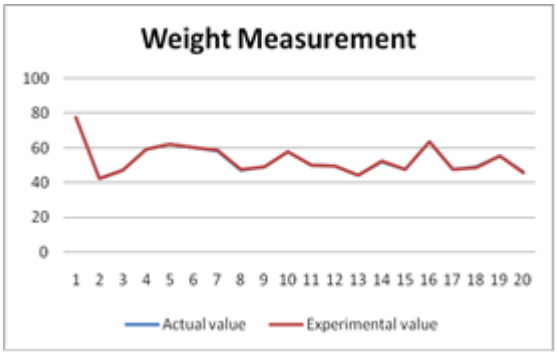


Figure 16. Line Graph for Actual and Experimental Value for Weight Measurement

Table 4: Statistical Acceptability of Error of Load Cell Using T-Test

	Variable 1	*Variable 2*
Mean	53.3775	53.47
Variance	72.73644	72.26657895
Observations	20	20
Hypothesized Mean Difference	0	
Df	38	
t Stat	-0.03435	
P(T<=t) one-tail	0.486388	
t Critical one-tail	1.685954	

Table 4 presents that the P-value is equal to 0.486388 and is far greater than the t-value which is 0.05. This implies that null hypothesis is accepted and the difference of the actual value from the experimental value is due to random errors only and will not affect the accuracy and functionality of the system. The results suggested that the proposed design is accurate.

5. Conclusion

After conducting some experiments and analysis, the proponents gathered enough data which are vital in answering the problems and defining if the established information supports the objectives of the study. The development of Microcontroller-Based Body Mass Index Calculator with Classifier Using Fuzzy Logic Algorithm is focused in the study. This paper proposes a different approach for calculating and classifying Body Mass Index by using microcontroller and Fuzzy Logic. To comply for the objectives of the study, the proponents arrive in the following conclusions: The proponents were able to get the height and weight of the user through the use of ultrasonic sensor and load cell. Arduino Uno was used as microcontroller that fetched all the data coming from the sensors and calculate the numeric value of Body Mass Index. The BMI value together with the age of the user are processed through the algorithm of Fuzzy Logic and will decide whether the person is Underweight, Overweight or Obese. Visual Studio, C# programming language makes the GUI of the system. All the data were stored in the data base through MySQL. Using the T-Test

method, the proponents were able to determine the acceptability of error the device and found out that the error are insignificant and are only due to the random errors. Thus the statistical method suggested that the error will not affect the accuracy and functionality of the system. The indicators were also tested if the microcontroller could be able to operate properly and all the trials were successful. Accuracy and precision of the proposed system were determined based on the several test that the proponents have conducted. For the accuracy of ultrasonic sensor and load cell, the percentage of error ranges from 0% to 1.97% and 0% to 0.87% respectively.

References

[1] WHO, 2000, Obesity: preventing and managing the global epidemic. WHO Technical Report Series No.894. World Health Organization, Geneva.

[2] Antecol H. and Bedard K., (2006), "Why do immigrants converge to American health status level?", Demography, vol.43(2), pp.337-360.

[3] CDC Pediatric Growth Charts. Using the BMI-for-Age Growth ChartsRetrieved (October2014)fromhttp://www.cdc.gov/nccdphp/dnpa/growthcharts/training/modules/module1

[4] Nutritionist-Dietitians' Association of the Philippines (2014). Healthier You Facts: OBESITY Retrieved (October 2014) from http://www.ndap.org.ph/obesity

[5] (Orlistat) Xenical Philippines (2014). BMI For Filipinos Retrieved (October 2014) from http://www.newyou.com.ph/bmi-for-filipinos

[6] Department of Health and Human Services Center for disease control and prevention – Body Mass Index: Consideration for Practitioners from http://www.medindia.net/ patients/patient info/body-mass-index-limitations.htm

eureca 2016 – Conference Paper
Paper Number EE_UG08

Implementation of Enhanced Aluminum–Copper Based Solid Oxide Fuel Cell (SOFC) for Warning Light

Jonel Jozef B. Catapang[1*], John Marlo C. Agbuya[2], Ma. Jonalyn B. Babasa[2], John Eric B. Precilla[2], Rionel Belen Caldo[1]

[1]*Computer Engineering Department*

[2]*Electrical Engineering Department*

Lyceum of the Philippines University-Laguna (LPU-L)

Corresponding e-mail: [*]jonelcatapang@gmail.com

Abstract

The purpose of this research is to develop a Solid Oxide Fuel Cell (SOFC) using a different set of materials integrating it on a small scale system designed by the proponents. A fuel cell can be easily compared to an ordinary battery for which they both provide electricity; however, it continuously generates electricity providing sufficient presence of its fuel. The proponents used copper and aluminum for the plates of the fuel cell module, and cement as the electrolyte. This study simultaneously explores the possibility of constructing a SOFC with different set materials, promotes green energy and the integration of different modules to create an application innovatively.

Keywords: aluminum,battery, cement, copper, fuel cell, green energy, SOFC

1. Introduction

1.1 Background of the Study

In the last decades, air pollution became a common problem of countries all over the world. To address this problem, several researchers then proposed of means of reducing the pollution and prevent it if possible. The use of green energy was introduced; some are putting resources into wind vitality and sun based vitality, and in addition other renewable vitality, to minimize smoldering of fossil energizes, which causes overwhelming air contamination. In this instance, the proponents came up with an idea to create a system which will draw in the H_2S pollutant as the main fuel source and be converted into electrical energy through the use of a solid oxide fuel cell, which will be constructed out of easily available materials. The study aims to verify if the construction of Solid Oxide Fuel Cell for small scale system using Al and Cu is feasible,

and at the same time, the safety in the premises of the Mt. Makiling Mud Spring will be improve.

1.2 Problem Statement

The Mt. Makiling is an inactive volcano and is also a place for mountaineering. Tourists usually explore easy trail of mud spring where volcanic gasses like Hydrogen Sulfide (H_2S) is coming out from the spring which is unsafe to human when too much was inhaled. Also, the mud spring is a dangerous area for the tourist to wander around especially at night.

In regards of this, the proponents carry out the study to address the following problems:

- Will the use of aluminum and copper as electrodes along with conductive concrete as electrolyte are possible for SOFC?
- Is SOFC feasible for small scale system?
- How will the SOFC be implemented to the Mt. Makiling Mud Spring?
- Will the SOFC be able to generate a usable voltage?
- How to integrate a booster module and a dark sensor module to the SOFC?

1.3 Objectives

The general objective is to construct Solid Oxide Fuel Cell using easily available materials Copper and Aluminum to generate electrical energy by feeding volcanic gases including H_2S coming from Mt. Makiling Mud Spring.

Specifically, it aims:

- To fabricate the Anode electrode using Copper and the Cathode electrode using Aluminum and incorporate conductive concrete which will serve as the electrolyte for the device
- To generate an output voltage at least ranging from 0.7 V to 5V
- To store the generated electricity to a 5 V super capacitor
- To integrate booster module for amplification of generated voltage and a dark sensor module
- To integrate LED warning light for safety precaution during night

2. Methodology

2.1 Conceptual Framework

The study aims to design and construct a planar SOFC with alternative components and will be tested in the vicinity of Mt. Makiling Mud Spring. The proponents adapted the research process into a flow chart and IPO chart will be presented as a graphical presentation which may perhaps said the readers for better understanding of the study. Also the sequence of the system is represented in a block diagram.

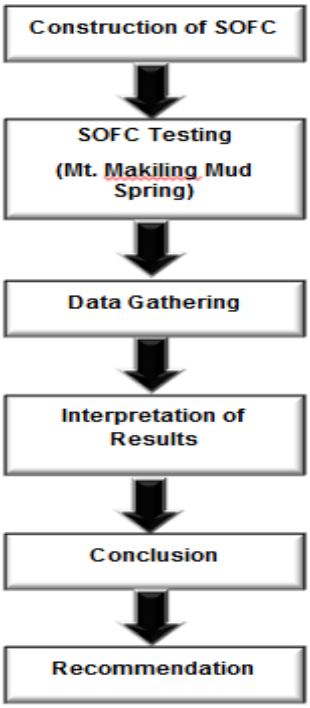


Figure 1. Method of Research

2.2 System Block Diagram

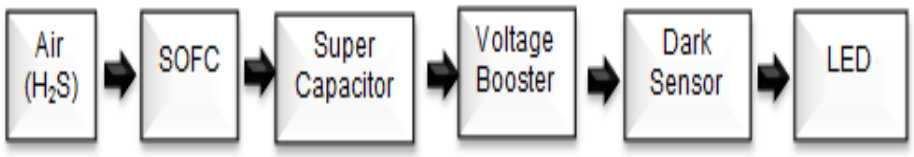


Figure 2. System Sequence

As figure 2 shows, the system will start when the SOFC accumulate sufficient amount H_2S and then convert it into electricity. The generated voltage will be stored into supercapacitor then it will be amplified through a voltage booster. Next stage, through a dark sensor, if the illuminance level of the environment drops 10 lux or below (night darkness), the sensor will allow the current to flow otherwise the circuit is in 'open' state. When the dark sensor triggers, the LED will also be triggered.

2.3 Flow Chart

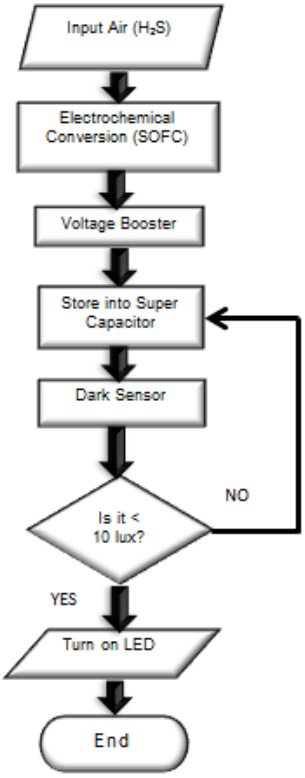


Figure 3. Flow Chart

2.4 IPO Chart

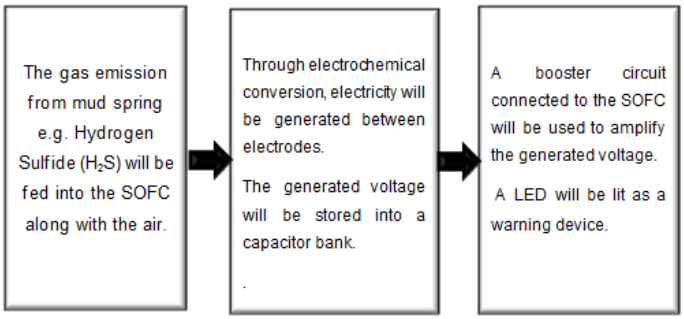


Figure 4. IPO Chart

As shown in Figure 4, the input of the system will be the volcanic gas e.g. Hydrogen Sulfide (H_2S). H_2S will be fed into the SOFC which then will be process and undergo electrochemical conversion; hence there will be a potential difference between the electrodes. The generated voltage will be amplified by a booster circuit after being stored in a capacitor bank. And the amplified voltage will be used to light a LED which will serve as a warning device for hikers and other people venturing dangerous zone in Mt. Makiling Mud Spring.

3. Designs and Considerations

The proponents conducted this study predominantly intended to attain a set of objectives ministering to solve the stated problems. The study tails developmental scheme and was tested through experimental method. Set of experiments were conducted to fully understand the operating principle of the system. Data will be

presented in tables, figures and through theoretical computations. Also the results will be used to determine whether the study is feasible or not. The study followed the stages shown in the block diagram below.

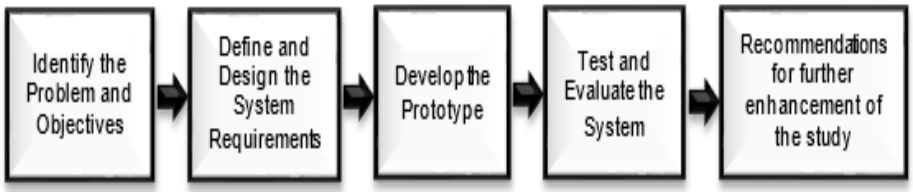


Figure 5. Research Process Block Diagram

Figure 5 shows the research process that the proponents used as the guide of developing a system regarding this study. It is the sequential steps depicting every content of this study.

3.1 System Design

The proponents designed and implemented the prototype to fit and workable in a small scale system. The designed system is presented through a schematic diagram below.

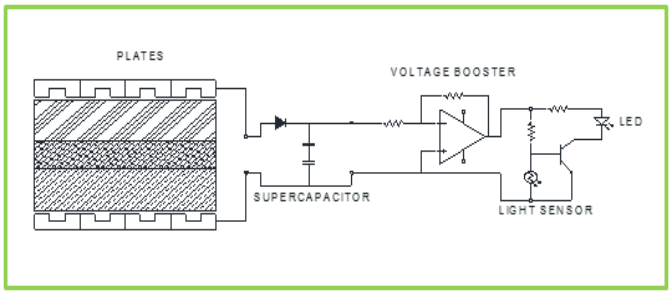


Figure 6. Schematic Diagram of the System

Figure 6 shows the schematic diagram of the system. The prototype will harness volcanic gasses from the Mud Spring, then by electrochemical conversion the plates will generate an electrical potential which will then be stored in a supercapacitor. The generated voltage will be boosted into 5 volts DC and be use to lit the warning LEDs which are triggered on and off by a photo resistor.

3.2. Prototype Components

3.2.1. Plates

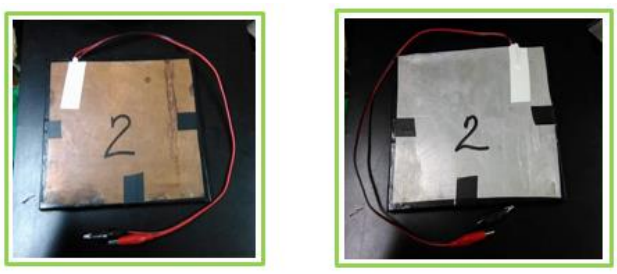


Figure 7. SOFC Metal Plates

The SOFC is composed of terminal plate's usually two different metals acting as anode and cathode part of the fuel cell. The proponents made use of alternative

materials instead of using the commercially available ones. For the anode part, the proponent used copper plates while for the cathode part aluminum plates were used. These materials were chosen primarily because of having a relatively high electron conductivity and thermal conductivity which are essential traits needed by the plates of a SOFC [1].

3.2.2. Electrolyte

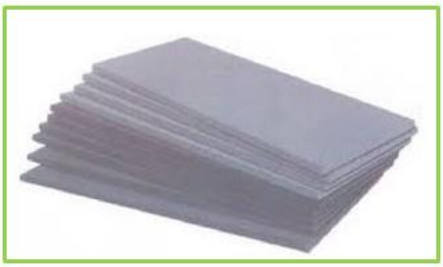


Figure 8. Conductive Concrete

In SOFC, electrolyte is usually a dense layer of ceramic found between the plates. Electrolyte must be a material capable of handling compression stress and strong enough to shoulder the weights of the plates especially in stacks. Also, electrolyte requires good ionic conductivity and electronic conductivity must be kept low to prevent misfortunes from spillage current. In the development of the prototype, the proponents used a conductive concrete as the substitute electrolyte considering it had characteristics impart to that of the conventional material [2].

3.2.3. Supercapacitor



Figure 9. Supercapacitor

A supercapacitor also known as ultracapacitor is fundamentally a capacitor with a much higher capacitance value compare to an ordinary capacitor. Most supercapacitors were made using either an electric double- layer capacitance or an electrochemical pseudocapacitance or it could be the combination of both. Supercapacitor can store energy up to 10 times more than the value that an ordinary capacitor capable of storing. It is usually used in applications which requires prompt charge/ discharge cycles without breaking or malfunctioning. The proponents, based on design, used two supercapacitor rated 500F- 2.7V and are connected in series resulting to a 5.4V storage capacity. The supercapacitors are used to store the generated voltage coming from the plates, storing it until the energy will be fed into the load [3].

3.2.4. Voltage Booster



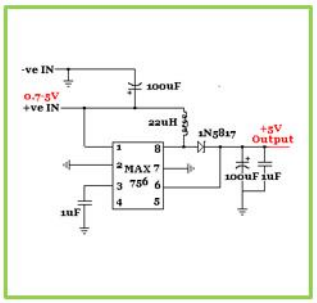


Figure 10. Voltage Booster Figure 11. Voltage Booster Schematic

A voltage booster or converter is a circuit used to amplify or attenuate electrical energy from one value to another. It can also be in DC/ DC, AC/ AC, DC/ AC and AC/ DC. The conversion of the energy were done primarily to match the power input of the devices or base on its application. The researchers used a voltage booster circuit requiring a minimum input of 0.7 V then amplify it into 5V before being fed into the load side of the system. The output voltage is regulated and maintained at 5V [4].

3.2.5. Photoresistor



Figure 12. Photoresistor

A photoresistor is a light sensitive device where the resistance decreases as the incident light intensity is increasing. The proponents used a light sensor that creates a yield signal showing the power of light by measuring the brilliant vitality that exists in an exceptionally limit scope of frequencies essentially called "light", and which ranges in recurrence from "Infra-red" to "Unmistakable" up to "Bright" light range. The sensor will trigger the LED when the illuminance of the environments drops to the design's preset [5].

3.2.6. LED



Fig. 13 Light- Emitting Diode

A semi-conductor device such as light-emitting diode (LED) is capable of radiating light when its threshold voltage are met and current flows in it.In this study, the proponents used LEDs as the primary load and will serve as a warning lights. The LEDs are mounted in a warning signage telling hikers and campers passing through the Mud Spring to take caution while on site. The LEDs will be activated when the environment drops into a particular illuminance set by the sensor [6].

4. Results and Discussions

The research was done methodically as shown in the block diagram in the previous chapter (Figure 5). The results gathered will attest the workability of the system which will then be used as the primary basis of the study's feasibility. The proponents used three variations in experimentation for comparable results. The gathered results are tabulated and presented below.

Table 1: Single Module

Module No.	Time of exposure	Voltage Measurement Before Exposure (V)	Voltage Measurement After Exposure (V)	Charge Rate Before Exposure (mV/sec)	Charge Rate After Exposure (mV/sec)
1	30 mins	1.364	1.366	0	0.0909
2	30 mins	1.302	1.310	0	0.1333
3	30 mins	1.359	1.366	0	0.0513



Figure 14. Single Module Test

At first test, the three modules' electric potential were measured individually before being exposed into the volcanic gasses. After 30 minutes of exposure, there is barely an increase of potential difference across the plates, however the charge rate increased from 0 mV/sec up to 0.1333 mV/sec.

Table 2: Two Module in Series

Module No.	Time of exposure	Voltage Measurement Before Exposure (V)	Voltage Measurement After Exposure (V)	Charge Rate Before Exposure (mV/sec)	Charge Rate After Exposure (mV/sec)
1 & 2	30 mins	2.264	2.270	0	0.0417
2 & 3	30 mins	2.890	2.896	0	0.0392
1 & 3	30 mins	2.720	2.726	0	0.0339



Figure 15. Two Modules in Series Test

In the second test, two modules were connected in series. The voltages across the plates were measured before and after being exposed into the gasses. The total voltage in series is simply the algebraic sum of the voltages of modules connected in series. As seen in the results of the first test, two modules in series were also not capable of charging the supercapacitor before being exposed into the gasses. After 30 minutes of exposure, the plates were now capable of charging the supercapacitor.

Table 3: Three Module in Series

Module No.	Time of exposure	Voltage Measurement Before Exposure (V)	Voltage Measurement After Exposure (V)	Charge Rate Before Exposure (mV/sec)	Charge Rate After Exposure (mV/sec)
1, 2 & 3	30 mins	4.05	4.12	0	0.0294



Figure 16. Three Modules in Series Test

At the final test, three modules were connected in series. The total voltage coming from the plates is equal to 4.05V, approximately the algebraic sum of each potential difference of the plates. In this test, the plates were exposed for an hour. Yet again, the measured voltage after exposure just barely increased and the charge before exposure is equal to zero. From this, the proponents concluded that before exposure the plates were not capable of charging the supercapacitor because SOFC requires a relatively high temperature for it to function normally.

5. Conclusions

The main objective of the study was to determine whether the prototype is feasible or not. Hence, the proponents did a breakdown of the entire study and see if it achieve the objectives set prior to the development of the prototype. After developing the prototype and subjected it into different tests and conditions, the proponents came up with the following results and conclusions regarding the study.

- Using aluminum and copper as electrodes along with conductive concrete as electrolyte for construction of SOFC was possible and is significantly more economical compared to the used of conventional materials.
- The SOFC developed by the proponents was able to operate in the designed small scale system, thus the proponents concluded that the SOFC is feasible for electronic applications or any other systems alike with the set up.
- The implementation of the system was set in Mt. Makiling Mud Spring. The fuel cell fed on through the volcanic gasses coming from the Mud Spring and used it as the fuel powering up the system.
- The prototype was able to generate at least 0.7 V and the proponents successfully integrated the use of supercapacitor to store the generated voltage.
- The proponents effectively implemented the use of a booster circuit which amplify the generated voltage into 5V and use it as the input source of the LEDs. The LEDs were being controlled by a phototransistor, activating them at the preset illuminance. The LEDs were used as warning lights for safety precaution around the selected area.

Seeing the results produced by the study, the proponents therefore concluded that the system is feasible and prompted to generate better results with few adjustments.

6. Recommendations

For further enhancement of the study, the proponents were prompted to formulate the following recommendations which could help the future researchers having the same or related topic.

For construction of the SOFC

- The plates should be porous enough to boost ionic conductivity and they should have a relatively high electron conductivity.
- The electrolyte should be relatively thin in thickness but strong enough to handle the mechanical stress it will be subjected to. Also electrolyte should have a good ionic conductivity and low electronic conductivity to reduce leakage currents.
- The terminals of the plates should be designed and placed or soldered well for more efficient transmission of energy and for measuring purposes.

For experimentation and data gathering

- Select a site or location which can provide an abundant source of gasses or fuel aimed to use.
- For better and accurate results, SOFC should be subjected directly into the fuel and the system should maintain a relatively high working temperature. A SOFC is more efficient at high temperature.
- Addition of test variations may be implemented for more comparable data and conclusive results.

Acknowledgments

The proponents would like to express their gratitude to those people who made this study a realization. The proponents wish to acknowledge the adviser of the study, Engr. Anthony Jefferson Atienza, for giving the idea of researching about renewable energy and specifically, introducing the solid oxide fuel cell technology. He supported

the research study from the beginning until the end. Also, the proponents want to give thanks to Engr. Rio Aguilar for giving valuable ideas regarding electronic components and modules that are integrated in the study. Furthermost, the proponents offer this feat to GOD, for this study will not be possible nor a successful one without His guidance.

References

[1] http://education.seattlepi.com/reaction-aluminum-copper-electrolysis-5549.html
[2] http://ecst.ecsdl.org/content/3/42/13.abstract
[3] http://batteryuniversity.com/learn/articlewhats_the_role_of_the_supercapacitor
[4] http://www.instructables.com/id/Adjustable-Voltage-Step-up-07- 55V-to-27-55V/
[5] http://www.resistorguide.com/photoresistor/
[6] http://electronics.howstuffworks.com/led.htm

eureca 2016 – Conference Paper
Paper Number EE_UG09

Remote – Switching Application System for Intelligent Home: A Comparative Analysis of Telephone Line and Mobile Telephony

Lenard C. Dorado[1*], Alyanna Rozel T. Cruz[2], Sarah Dyan S. Garraton[2], Alexis M. Malolos[2], Jonalyn G. Ebron[1], Rionel Belen Caldo[1]

[1]*Computer Engineering Department*

[2]*Electronics Engineering Department*

Lyceum of the Philippines University-Laguna (LPU-L)

Corresponding e-mail: *lenarddorado@gmail.com

Abstract

Remote-switching controlling is one of the functions of home automation that provide better quality of life to people especially to the elderly and disabled. It incorporates brought together control of lighting, HVAC (warming, ventilation, and aerating and cooling), machines, security locks of entryways and entryways and different frameworks, to give enhanced accommodation, solace, vitality productivity and security [3]. It uses different technologies such as Infrared (IR), Bluetooth, Mobile telephony, Radio Frequency (RF), Internet, Dual Tone Multi Frequency (DTMF) and so forth. In this paper the proponents used two different technologies in order to provide a comparative analysis between telephone system and mobile telephony. Both systems use Arduino Mega 2560 as its microcontroller. The proponents conduct tests by having three modes of operation: telephone to telephone, mobile phone to telephone, and mobile phone to GSM. Both methods for controlling the gadget/s can be worked with the same procedure for the phone and cellular telephone has the same capacity. They just vary on how they contrast in transmitting the information. While in GSM module framework, the gadget/s can be controlled by utilizing SMS or messaging the GSM module to kill or on the gadget/s. The programming language used in this system is Cpp language. The proponents aim to evaluate the results of systems experimentation in Functionality, Reliability, and Efficiency. These experiments helped the proponents to determine which is the best mode and a system of communication.

Keywords: Remote switching controlling, Home automation, Arduino, Telephone System, Mobile

1. Introduction

1.1 Background of the Study

Oftentimes, individuals tends to forget or unplug electronic devices and/or appliances due to either lack of time or simply forgetting to turn them off, which sometimes causes a fire or conflagration. Because of this, intelligent home is developed and now becomes a trend in modern house concept.

According to Smart Homes Association, the best meaning of intelligent/smart home is the incorporation of innovation and administrations through home systems administration for a superior nature of living [1]. This concept started at the beginning of the 20th century. Smart home solace, security, vitality proficiency (low working expenses) and accommodation at all times to the home owners, whether someone's home or not. This term is commonly used to define homes or residences that have electronic/electrical appliances and devices that can be remotely controlled by a time schedule, from any part of the room or house, from any location in the world [2]. This technology was created and innovated by the researchers as time passed by to give people a better life. Now, this technology is known as home automation.

Home automation refers to controlling of appliances, providing security and monitoring the house through a simple, yet powerful controller. It can provide better quality of life to people, especially to the elderly and disabled. It consists brought together control of lighting, HVAC (warming, ventilation, and cooling), machines, security locks of entryways and entryways and different frameworks, to give enhanced accommodation, solace, vitality productivity and security [3].

Remote-switching/controlling is one function of home automation. It uses different technologies such as Infrared (IR), Bluetooth, Mobile telephony, Radio Frequency (RF), Internet, Dual Tone Multi Frequency (DTMF) and so forth. However, these technologies have its own problems and issues in developing a remote – switching control system. Infrared radiation has limited operation commonly used in remote controls. It is a point – to – point operation [17]. Bluetooth can be used for a limited range and its energy usage is quite low. Radio frequency (RF) does not need line – of – sight to transmit data and can be used for long range communication. On the contrary, interference can occur during the transmission of data. RF can be used for Wi – Fi, WiMax, Near Field Communication (NFC), Radio Frequency Identification (RFID) and other system that uses RF signals [19]. Just like what the other researchers used, there is also the Internet. The internet can be used also as a medium to send data, information or commands not just for browsing. The problem with this type of technology is that it has security issues. There are vulnerability threats.

On the other hand, Dual Tone Multi Frequency or DTMF is widely used in telecommunication systems. It is a technique for teaching a phone exchanging arrangement of the phone number being dialed, or to issue summons in exchanging frameworks or related telephony gear [9]. DTMF has empowered the long separation motioning of dialed numbers in the voice recurrence range over phone lines. It dispensed with the need of telecom administrator between the guest and the advanced mechanized dialing on the phone exchanging focuses [10]. It is a tone dialing/signaling that is commonly used in telephony and each key on the telephone has an assigned

frequency. This tone is composed of two sine waves, the higher and lower frequency, of the assigned frequency. This individual frequency is assigned to design the frequency filters easily and to pass easily the telephone lines in which the maximum bandwidth will be extended from 300 Hz to 3.5 kHz. It is not designed for transferring data, but for controlling signals only. It will be possible to signal at a rate of around 10 beeps or 5 bytes per second with the use of standard decoders [11].

Also, mobile telephony is another wireless technology, which is primarily used in communications. It can connect one user to another user from around the globe effortlessly [12]. One of the protocols of mobile telephony is the Global System for Mobile communication (GSM) [13]. This technology can also be used for the remote switching application system. GSM is an open, computerized cell innovation that is utilized to transmit versatile voice and information services [14]. GSM SMS, short term for Short Messaging Service, is the process of exchanging short messages from and back to a mobile phone, fax machine and/or IP address over mobile or telephone network. Though cellular or mobile phones can make a phone call, GSM SMS is for text only. Messages should not contain any images or graphics and should have alpha - numeric characters not greater than 160. When the message is sent, Short Message Service Center (SMSC) will receive the message and will be sent it to the appropriate mobile device user [15]. If the mobile phone of the user is turned off, the recipient of the message will still receive the message as soon as he/she turned on his/her mobile phone.

The proponents of the study aim to compare the two modes of operation, the wired and wireless operation, in three phases as a remote – switching application system for intelligent home to switch on/off the home electronic devices and appliances using telephone and mobile telephony. Telephone line will be used as the medium of wired operation using DTMF technology and mobile telephony as the medium of wireless operation using GSM SMS technology. The proponents of this study chose to use DTMF because it is simpler, cheaper and can operate on longer distance range and GSM because it is more convenient, more secure, safer and can also operate on longer distance range unlike other technologies available [16][14].

1.2 Objectives

The focal objective of the study is to provide a comparative analysis of telephone system and mobile telephony in a remote switching application system.

This study aims to:

1. develop a remote switching system using DTMF signalling via telephone line and GSM SMS technology
2. switch electronic/electrical devices and/or appliances using DTMF signalling and GSM SMS technology
3. test the reliability, functionality and efficiency of the remote switching in three phases:
    a. Cellphone(transmitter) to GSM module(receiver) using SMS
    b. Telephone(transmitter) to Telephone(receiver) using DTMF
    c. Cellphone(transmitter) to Telephone(receiver) using DTMF

4. compare the modes of operation for the remote switching system

2. Methodology

2.1 Proposed System and Block Diagram

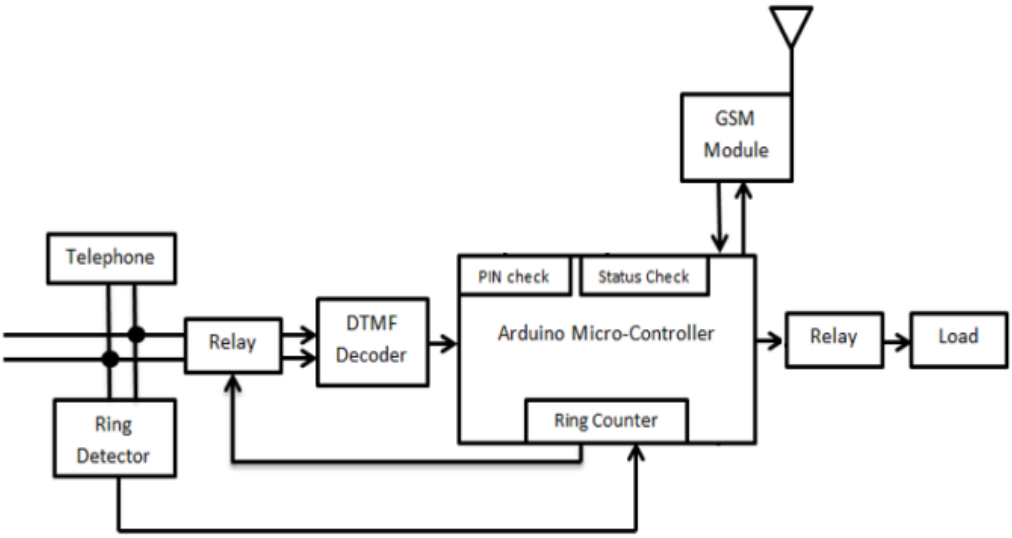


Figure 1. Block diagram of the remote switching system

Figure 1 illustrates the high-level block diagram of the remote switching system. In order to remotely switch the devices/appliances, there is a need for a remote controller which is in the form of a telephone or a mobile phone. This will enable the user to control the system from a distance place using DTMF signalling and sending an SMS message. For the DTMF signalling, the ring detector block intercepts the ringing signal coming from the telephone exchange as the call is received by the telephone. This block indicates the ringing of the telephone and will be fed to the microcontroller. The Arduino microcontroller will perform the counting of the ring/s. The relay, which is connected to the telephone will be triggered depending on the number of pre-configured rings. The triggering of the relay will bring the line in an off-hook condition. The line will now be connected to the remote controller and the line is now open to the transmission of the DTMF tones. The DTMF tones are fed to the DTMF decoder. These tones are analog signals which will be converted into digital form by the DTMF decoder. The output of this block will be fed to Arduino microcontroller for processing. This system has a main controller. It will perform the counting of the rings, checking of the PIN input, checking of the device/appliance status and the driving of the relay circuit. Using GSM, a SMS message which contains the PIN and the command from the user will be received by the GSM module and it will be fed up to the Arduino microcontroller for further processing. The GSM module can receive and send SMS message. The system is also composed of a latch circuit which is needed to determine the status of the loads connected to the relay circuit.

2.2 IPO Chart

Presented in the figure below is the IPO chart of the system.

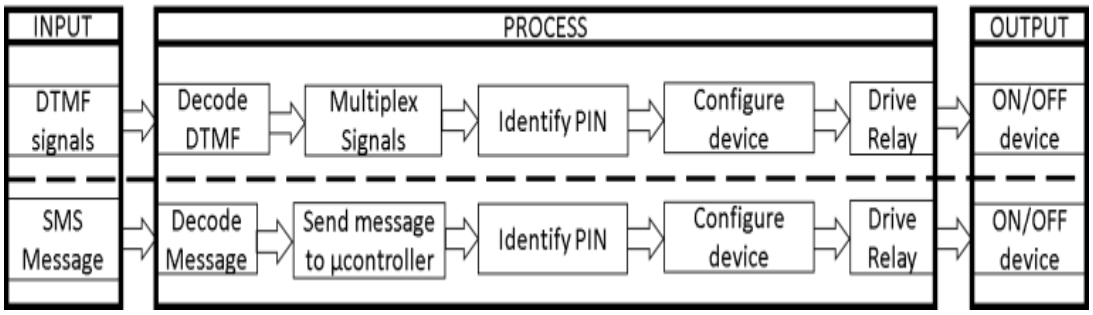


Figure 2. IPO chart of switching control system

The process of the system will be dependent on the type of electronic message that is going to be inputted. If the user chooses to control the devices by calling, the input to the system will be the DTMF signals, and if the user chooses to control the devices by through the GSM module the input will be an SMS message.

The DTMF pertains to the signals which will serve as the instruction parameter and the controlling signal of the system. These signals are produced from the dialled keypad and will be sent to the switching control system through the telephone lines. These inputs are received by the system with help of the DTMF decoder interfaced through the telephone lines. DTMF is received as analog signals, the purpose of the DTMF decoder is to convert these signals to digital form for compatible use in digital circuits. The outputs of the decoding process are in BCD form. Multiplexing will be required to convert these BCD outputs in a more suitable form for the utilization in the succeeding processes of the system. After the conversion of the digital signals, the next step is to process these digital signals so as to comply with the system requirements and specifications. The microcontroller will process these signals to confirm the PIN which is pre-configured by the developer. After the successful validation of the PIN, the process will go to the next stage, which is the selection of the device or appliance to be switched. The final process will involve driving of the designated relay pre-configured by developer of the system. As an output the device or appliance will switch to either of state or on state depending on the selected instruction of the user.

When the user opts to control the system through the GSM module, the user has to send an SMS message to the system. This message contains the PIN preconfigured by the developer of the system. Also, this message has the instruction for the selected device to be switched. This message will be received by the GSM module and will be sent to the microcontroller for processing. Depending on the message received and decoded by the GSM module, the commands will be done by the microcontroller as instructed. As an output the device or appliance will switch to either off state or on state depending on the selected instruction of the user.

2.3 Pseudocode

- Using DTMF

1. Start
2. Call home telephone
3. Detect ringing signal
4. Count ringing signal

5. Does it ring once? If not, go to step 2. Otherwise,
6. Connect to line
7. Input pin
8. Is the pin correct? If no, go to step 7. Otherwise,
9. Input device code
10. Is selected device on? If no, go to step 11. Otherwise,
11. Is switching key pressed? If no, go to step 14. Otherwise,
12. Drive relay
13. Switch on/off device
14. End

- Using GSM

1. Start
2. Send SMS message to GSM module
3. Decode message
4. Send decoded message to µcontroller
5. Is the PIN correct? If not, go to step 8. If yes,
6. Drive relay
7. Switch on/off
8. Send SMS to user
9. End

2.4 Flowchart

Below is the flow chart developed to guide in the development of the proposed system.

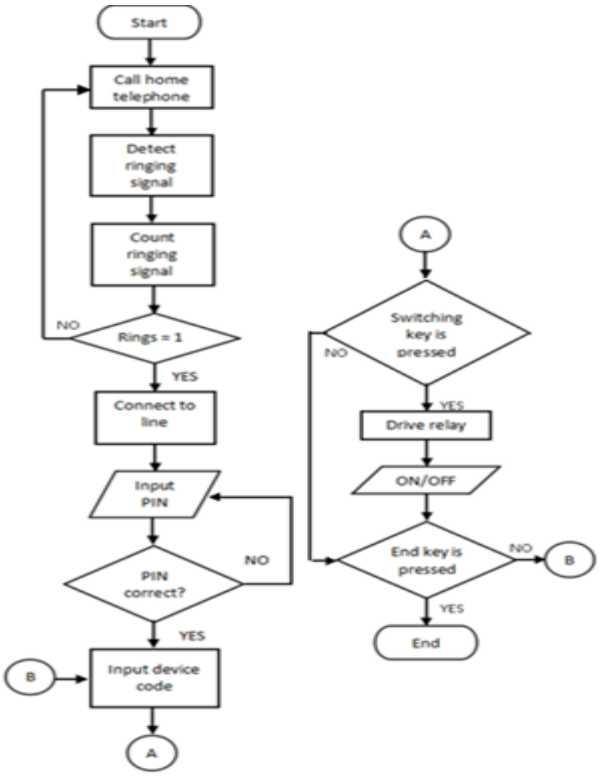


Figure 3. Process flowchart of the remote – switching system using DTMF signalling

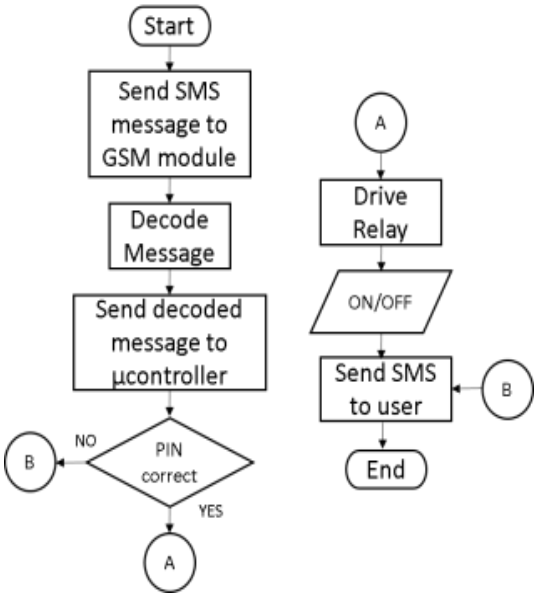


Figure 4. Process flowchart of the remote – switching system using GSM

Using DTMF signalling, the process of remote switching system will start from calling the telephone situated at home. After receiving the call from the remote section, the ringing signal is detected by the ring detector circuit. The numbers of rings are counted by the ring counter integrated to the ring detector circuit and after a ring the remote section will automatically connect the line. The user will send the 4 - digit PIN using the touch pad of the phone. If the PIN is invalid, the user will input again the PIN until it has been validated. The user will now input the device code. After selecting the device, the user has an option to switch on/off the device using the switching key. If the switching key is pressed and the device is in the ON state, the device will switch to the OFF state, otherwise, the other way around.

Using GSM SMS technology, the process of switching system will start from sending a SMS message to the GSM module. The GSM module will decode the SMS message sent by the user. The decoded message will be sent to the microcontroller. If the PIN from the SMS message is invalid, a message is sent to the user saying that the PIN input is invalid. If the PIN is correct the process of remote switching will proceed. The microcontroller will now switch on or off the device chosen depending on the command of the user. After the device has been switched on or off, an SMS message containing the current status of the device will be sent to the user.

3. Results and Discussions

3.1. Project Description

The study entitled “Remote – Switching Application System for Intelligent Home: A Comparative Analysis of Telephone Line and Mobile Telephony” is a study comparing two transmission modes that are used to switch on and off a device/s. The system is composed of two subsystems: the DTMF decoder system and the GSM module system. The two subsystem were controlled by the Arduino Mega 2560 microcontroller. In DTMF decoder system, the device/s can be controlled through telephone – to – telephone and mobile phone – to – telephone. Both way of controlling

the device/s can be operated with the same process since the telephone and mobile phone has the same function. They only differ on how they differ in transmitting the data. While in GSM module system, the device/s can be controlled by using SMS or texting the GSM module to turn off/on the device/s. The programming language used in this system is Cpp language.

3.2. Properties of the Project

The proponents deliberated and concluded the entire concept and design of the systems as it is developed. They premeditated and established the functionality of each system, all the details on how it will operate and the components to be used on each system's preferences and features. These are all in compliance to the gathered information from the previous research studies and literatures.

The key feature of the system is its versatility as it is designed to be controlled by two different means; DTMF signalling and GSM SMS. To integrate the two different subsystems of the remote control system and to provide processing functions, Arduino Mega 2560 microcontroller was chosen by the proponents. It has been chosen over Arduino UNO microcontroller since the system needs to have more input/outputs pins to be interface with the subsystems of the remote-switching system. An Arduino compatible GSM shield is needed for the SMS-based remote-switching control. There are a number of GSM shields and modules available in the market and are ready to be interfaced with a number of microcontrollers and programmable integrated circuits, but not all are compatible with Arduino microcontrollers. The logic high of Arduino microcontrollers is 5V, therefore a GSM shield that works with the same specification is preferable to prevent damages to the GSM module/shield and for it to perform the necessary functions properly. The proponents chose e-Gizmo GSM/GPRS shield which satisfies the requirements of the designed system.

Using the remote-switching control system via DTMF signaling, there is a need for a ring detector circuit to notify the system that a call is present. The telephone ringing voltage is typically about 90-100 Vrms which is not advisable to be interfaced with a microcontroller, therefore a device which provides electrical isolation and is capable receiving such large amount of voltage is required to properly interface it to the microcontroller. An optocoupler is chosen to provide the ring detection of the telephone ringing signal.

Since the DTMF remote-switching control system receives commands through the DTMF tones generated by the user, a DTMF receiver/decoder is required to provide the decoding of these DTMF tones and provide an output to be fed to the microcontroller.

It necessary to put the line in an off-hook condition to be able to send the DTMF tones through the telephone line therefore an off-hook circuit is required. To mimic the lifting of the cradle of the telephone set, a relay module will be used to provide a loop and put the line in an off-hook condition and hold the line. Also these relays will be used to switch ON/OFF the devices by putting/cutting the current from the power grid.

3.3 Experiments

The testing of the system is divided into three phases designated for each modes of operation. Twenty-two (22) trials, 18 trials and 18 trials were conducted for mobile to GSM module operation, mobile phone to telephone and telephone to telephone respectively.

For the SMS-based application of the system, a mobile phone is used to send messages to the GSM module. The message contains the 4-digit PIN and the command as illustrated in Figure 19. The proponents observed the response of the system and the results are tabulated as shown in Table 4.

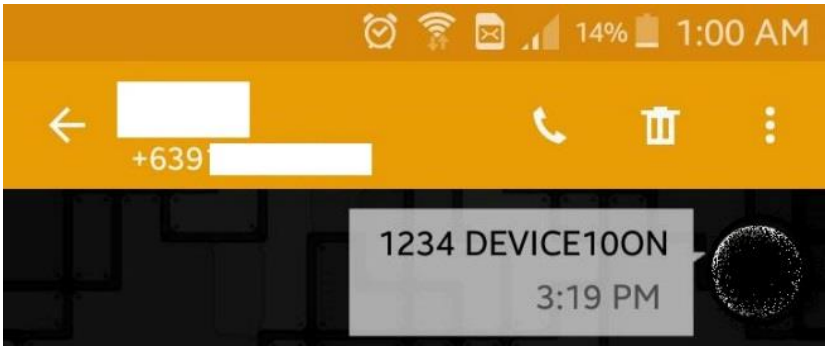


Figure 5. SMS message sample

Table 4. Results of the test using mobile phone to GSM module operation mode

Trial	SMS Command	Device Number										REMARKS
		1	2	3	4	5	6	7	8	9	10	
1	DEVICE1ON											CORRECT
2	DEVICE1OFF											CORRECT
3	DEVICE2ON											CORRECT
4	DEVICE2OFF											CORRECT
5	DEVICE3ON											CORRECT
6	DEVICE3OFF											CORRECT
7	DEVICE4ON											CORRECT
8	DEVICE4OFF											CORRECT
9	DEVICE5ON											CORRECT
10	DEVICEOFF											CORRECT
11	DEVIC 6ON											CORRECT
12	DEVICE6OFF											CORRECT
13	DEVICE7ON											CORRECT
14	DEVICE7OFF											CORRECT
15	DEVICE8ON											CORRECT
16	DEVIC 8OFF											CORRECT
17	DEVICE9ON											CORRECT
18	DEVICE9OFF											CORRECT
19	DEVICE10ON											CORRECT
20	DEVICE10OFF											CORRECT
21	ONALL											CORRECT
22	OFFALL											CORRECT

LEGEND(Device Response) Device Turns ON Device Turns OFF

The system is also tested using the DTMF signaling in the two remaining modes of operation. This includes the mobile phone to telephone operation and the telephone to telephone operation. To test the system using the said modes, the user inputs first the 4-digit PIN predefined in the program of the system and then the user presses # after each number desired number of device to be switched on and * after each number desired to be switched off. Shown in Figure 20 is the screenshot of the mobile phone used for the test. The same operation is done with the telephone to telephone operation

mode except that the remote device is a telephone. Table 5 and 6 are the tabulated results of the test for the operation using DTMF signaling in two modes namely; mobile phone to telephone and telephone to telephone respectively.

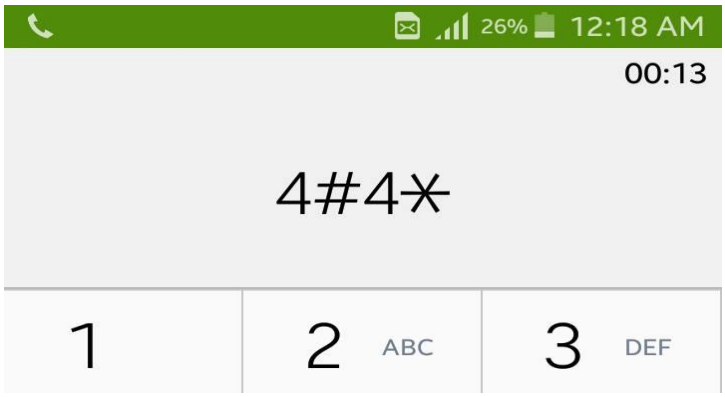


Figure 20. Screenshot of the mobile phone used for the test using DTMF signaling

Table 5. Results of the test using mobile phone to telephone operation mode

Trial	Keys Pressed	Device Number										REMARKS
		1	2	3	4	5	6	7	8	9	10	
1	1#	■										CORRECT
2	1*	■										CORRECT
3	2#		■									CORRECT
4	2*		■									CORRECT
5	3#			■								CORRECT
6	3*			■								CORRECT
7	4#				■							CORRECT
8	4*				■							CORRECT
9	5#					■						CORRECT
10	5*					■						CORRECT
11	6#						■					CORRECT
12	6*						■					CORRECT
13	7#							■				CORRECT
14	7*							■				CORRECT
15	8#								■			CORRECT
16	8*								■			CORRECT
17	9#									■		CORRECT
18	9*									■		CORRECT

LEGEND(Device Response) Device Turns ON ■ Device Turns OFF ■

Table 6. Results of the test using telephone to telephone operation mode

Trial	Keys Pressed	Device Number										REMARKS
		1	2	3	4	5	6	7	8	9	10	
1	1#											CORRECT
2	1*											CORRECT
3	2#											CORRECT
4	2*											CORRECT
5	3#											CORRECT
6	3*											CORRECT
7	4#											CORRECT
8	4*											CORRECT
9	5#											CORRECT
10	5*											CORRECT
11	6#											CORRECT
12	6*											CORRECT
13	7#											CORRECT
14	7*											CORRECT
15	8#											CORRECT
16	8*											CORRECT
17	9#											CORRECT
18	9*											CORRECT
LEGEND(Device Response)		Device Turns ON					Device Turns OFF					

Tables 4, 5 and 6 show the results of the test conducted to evaluate the functionality of the system.

4. Conclusion

A remote switching application using two modes of transmission was developed in this study. This system has two subsystems which compares two modes of operation in three ways of switching on and off a device/s. The first system is composed of DTMF decoder which will be used to get the desired outcome for the wired transmission and the other system is composed of GSM module which will be used to get the desired outcome for the wireless transmission. It was compared based on how efficient, reliable and fast the system responds to the command/s of the user. The test of functionality depends on the response of the system with respect to its function. Since its function is to control the device/s, the test will be based if the system will control the device/s or not. The statistical treatment that was used by the proponents is the percentage error for each mode. The reliability of the system will be based to the response time of each mode of operation. The delay for each mode is observed by the time it takes for one operation of a device to complete whether turning on or turning the device. The statistical treatment that was used in this test is the percentage relative standard deviation for each samples. The efficiency of the system will be evaluated based on the outcomes on the test of reliability. The mode with the fastest response will be the basis for comparison of the efficiency of the remaining modes of operation.

Based on the results of the series of test conducted by the proponents, the three ways of controlling the device/s are capable of switching on and off each device, therefore, the system is fully functional. The response time for each mode is graphically represented and each response varies and from the graph, a little difference from one response from the other can be observed. Though the response of each system varies, the system is still considered reliable. From the average response time of each mode, the average speed of response of each mode is gained and is then graphically

represented. Through this, the difference on each mode can be observed instantly and can be inferred that the telephone to telephone operation is the most efficient among the other two modes based on the response time of the system.

Acknowledgement

The proponents would like to acknowledge the assistance of Engr. Rionel Caldo for sharing his knowledge and wisdom. To our beloved parents for their moral and financial support. Also, to the Lyceum of the Philippines University - Laguna for the resources which are helpful in the entire research. Most of all, to our Almighty God for the blessings, strength, knowledge and wisdom that He gave to us to make this possible.

References

[1] Rosslin John Robles and Tai-hoon Kim, "Applications, Systems and Methods in Smart Home Technology: A Review", International Journal of Advanced Science and Technology, vol. 15,pp.37-46 February 2010.
[2] (2015) Smart Home USA website. [Online]. Available:http://www.smarthomeusa.com/smarthome/.
[3] Michael Cahlin (2015) The High – Tech House website. [Online]. Available: http://thehightechhouse.weebly.com/.
[4] Maureen Kaine – Krolak, and Mark E. Novak, "An Introduction to Infrared technology:Applications in the Home, Classroom, Workplace and Beyond".
[5] (2015) Engineers Garage website. [Online]. Available: http://www.engineersgarage.com/articles/bluetooth-technology.
[6] (2015) The Free Dictionary by Farlex website. [Online]. Available: http://www.thefreedictionary.com/radio+frequency.
[7] (2015) Webopedia website. [Online]. Available: http://www.webopedia.com/TERM/I/Internet.html.
[8] (2015) Enkivillage website.[Online]. Available: http://www.enkivillage.com/advantages-anddisadvantages-ofinternet.html.
[9] Frank Durda IV. (2015) Dual Tone Multi-Frequency (Touch-Tone) Reference. [Online]. Available:http://nemesis.lonestar.org/ reference/telecom/signaling/dtmf.html.
[10] (2015) Engineers Garage website. [Online]. Available: http://www.engineersgarage.com/tutorials/dtmf-dual-tone- multiple-frequency .
[11] hw.cz website. [Online]. Available: http://hw-server.com/dtmf-basics.
[12] (2015) The Advantages and Disadvantages of Mobile Phone Technology website. [Online]. Available: http://www.c-gps.org/the-advantages-and-disadvantages-of-mobile-phone-technology/.
[13] Whatis.com website. [Online]. Available: http://whatis.techtarget.com/reference/Fast-Guide-to-MobileTelephony.
[14] Mobile world website. [Online]. Available: http://www.mobileworld.org/gsm_about_04.html.
[15] Webopedia website. [Online]. Available: [a] http://www.webopedia.com/TERM/S/short_message_service.html.
[16] T.L.V.V.Hemanth, P.Sasi kiran and A.Suresh," Industrial Application of DTMF Communication in Robotics", International Journal of Innovative Research and Development, vol. 2, pp. 928-938, April 2013.

[17] Maureen Kaine-Krolak and Mark E. Novak. (2015) An Introduction toInfrared Technology: Applications in the Home, Classroom, Workplace, and Beyond[Online]. Available: http://trace.wisc.edu/docs/ir_intro/ir_intro.htm.

[18] (2015) Link Labs website. [Online]. Available: http://www.link-labs.com/applications-of-home-automation/.

[19] (2015) Radio-Electronics.com website. [Online]. Available:http://www.radioelectronics.com/info/rftechnology-design/.

[20] Manhal J. Alhelaly, "Appliances Control Using Mobile Phone (DTMF)", Thesis, University of Omer Al-Mukhtar, June 2010.

[21] Answers website. [Online]. Available: http://www.answers.com/Q/What_is_DTMF_How_DTMF_is_used_What_are_the_advantages_of_DTMF

[22] Yahoo Answers website. [Online]. Available: https://ph.answers.yahoo.com/question/index?qid=20090825040434AAPblEA.

[23] Tho Nguyen and Linda G. Bushnell, "Feasibility Study of DTMF Communications for Robots", UWEE Tech. 2004-0013, University of Washington, April 6, 2004.

[24] Teach - ICT .com website. [Online]. Available: http://www.teach-ict.com/gcse_new/communication/comm_methods /miniweb/pg9.htm.

[25] IT103: Communication. [Online]. Available: http://saaammieee .blogspot.com/2010/02/text-messaging-advantages-and.html

DATA MANAGEMENT SYSTEM OF AN FLC-BASED TEMPERATURE MONITORING FOR AIR CONDITIONING SYSTEM

Lenard C. Dorado*, Harold Jay A. Bernardo, Billy James A. Gandeza, Nelmar A. Mendoza, Van Allen T. Rivera, Rionel Belen Caldo

Computer Engineering Department, Lyceum of the Philippines – Laguna

Corresponding e-mail: *lenarddorado@gmail.com

Abstract
A Data Management System of an FLC-Based Temperature Monitoring for Air Conditioning Units that allows the user to monitor the temperature condition of a room was designed and developed in this study. This study is divided in two parts; the software and the hardware. In hardware, the proponents use a microcontroller and a temperature sensor. On the other hand, in software, parts include all the programming languages like Arduino IDE, MatLab Fuzzy Logic Toolbox and Visual Basic. Net. Moreover, the proponents used the Sugeno-style of fuzzy inference system and triangular membership functions. The element to be considered for monitoring includes the temperature and humidity for air parameters. The parameters for the temperature is categorized as Very Cold (VC), Cold (C), Normal (N), Hot (H) and Very Hot (VH) while for the parameters of the humidity are categorized as Very Good (VG), Good (G), Fair (F), Poor (P) and Very Poor (VP). On the other hand, the output parameters are categorized as a Highly Acceptable (HA), Acceptable (A), Just Acceptable (JA), Not Acceptable (NA) and Highly Not Acceptable (HNA). The proponents will validate and verify the results using the MatLab Fuzzy Logic Toolbox and this study will be simulated purely mathematical.

Keywords: Temperature Sensor, Arduino, Fuzzy logic, Sugeno Style, MatLab Fuzzy Logic Toolbox.

1. Introduction

Fuzzy logic essentially utilizes a rational and choice system which does not have certain limits like human rational. The reasoning of approximation is the main focus of fuzzy logic rather than precise and fixed. In the system of Fuzzy Logic Control (FLC), comprehensive model of knowledge is not a requirement unlike the other control

systems. On the other hand, FLC system is a simple to develop that can be easily executed in a standard computer [1] [2].

Air conditioning systems are one of the important parts of almost every establishment. But they contribute to the large part of the total energy consumption. Based on some studies, the majority of energy use in buildings is associated with the Heating, Ventilation, and Air-Conditioning systems, that contribute a total of 50% energy consumption [3]. Therefore, it indicates that the consumption of air conditioning system sets a major demand on the nation's electrical power consumption wherein most of the units are operating in heavy load. When the user uses the air conditioning system, a lot of energy is wasted that will cause to an energy shortage because heating and cooling devices have the maximum power intake. [4]

According to ASHRAE Standard 55-2010, the recommended indoor temperature is typically ranges from 20 ºC to 26 ºC and the recommended level of indoor humidity is ranges from 30% to 60% in air conditioned establishments. When the temperature and humidity exceed the normal, comfortable indoor environment, it can cause to the negatively impact air quality and harmful to health. [5]

The main purpose of this system is to reduce the temperature oscillations and to monitor the humidity of the room by using the MatLab Fuzzy Logic Toolbox. This proposed design work of data management system of an FLC based temperature monitoring for air conditioning units is the application of fuzzy logic control system consisting different input variables. In order to assure the functionality of the system, it is essential to precisely and correctly detect the temperature and the humidity of a certain room to assure human comfort. The measurement basis for the temperature is Celsius (℃) and for the humidity measurement unit of air conditioning system is a percentage (%). Moreover, the sensors of the systems have the combination of the temperature and humidity sensing capability. In which, the temperature and the humidity information response through sensors and the receiver will store the data into the database. The fuzzy logic control mechanism would acquire the data in the database and compare the temperature and humidity parameters requested by the user and calculate the membership function.

In this study, the proponents will use the theories and principles of fuzzy logic in order to monitor the temperature and humidity based on the parameters. The element to be considered for monitoring includes the temperature and humidity for air parameters. The parameters for the temperature are categorized as Very Cold (VC), Cold (C), Normal (N), Hot (H) and Very Hot (VH) while for the parameters of the humidity is categorized as Very Good (VG), Good (G), Fair (F), Poor (P) and Very Poor (VP). On the other hand, the output parameters are categorized as a Highly Acceptable (HA), Acceptable (A), Just Acceptable (JA), Not Acceptable (NA) and Highly Not Acceptable (HNA).

The proponents preferred to use the Sugeno-style of fuzzy inference system. In terms of the input and output parameters, the proponents will use the triangular membership function. The proponents will validate and verify the results using the MatLab Fuzzy Logic Toolbox and this study will be simulated purely mathematical.

1.1. Objectives

The general objective of the study is to design and develop a system that is capable of monitoring the temperature of the air conditioning system.

Further objectives are specified as follows:

A. To set the normal temperature that is highly recommended for humans in the room/laboratories.
B. To perform test procedures to determine whether the prototype is operating in its optimum operating condition.
C. To determine the parameters of the temperature monitoring system will meet the standard requirements using Fuzzy – Logic MatLab Toolbox Kit.

2. Methodology

2.1. MATLAB Programing Platform

MATLAB is one application that has a high-performance language for technical computing. It can be used for computing, visualizing, and programming an easy-to-use environment where the user can solve the problems easily, fast and legible. It is an intelligent framework whose fundamental information component is an exhibit that doesn't require dimensioning. It is good at solving matrix, vectors or even a fraction to make the results simpler and accurate.

- **Fuzzy Logic Toolbox**

The fuzzy logic toolbox is capable of analyzing, designing and simulating the systems providing the functions, apps, and a Simulink block based on fuzzy logic. The function of the toolbox is to guide everyone through the procedures of designing fuzzy inference systems. Functions are provided for many common methods, including fuzzy clustering and adaptive Neuro-fuzzy learning.

The toolbox lets you model complex system behaviors using simple logic rules, and then implements these rules in a fuzzy inference system. You can use it as a stand-alone fuzzy inference engine. Alternatively, you can use fuzzy inference blocks in Simulink and simulate the fuzzy systems within a comprehensive model of the entire dynamic system.

2.2 Block Diagram

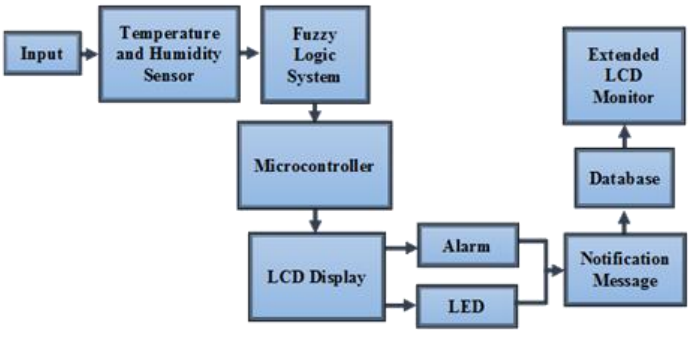


Figure 1. System Block Diagram

The Figure 1 depicts the process or the flow of the entire system. Using MatLab Fuzzy logic Toolbox, inputs that are from the temperature and humidity sensor are initialized in the fuzzy inference system to formulate a fuzzy logic rules. Then, the input will be sent to the Microcontroller, which is the brain of the system. Then the output of the system will be displayed in an LCD display with corresponding alarm, notification message and LEDs will be turned on with the corresponding temperature and humidity.

2.3 IPO Chart

Table 1 Conceptual Framework Diagram

INPUT	PROCESS	OUTPUT
➢ Hardware knowledge in Arduino Microcontroller and DHT11 Temperature and Humidity Sensor. ➢ Software knowledge in Arduino IDE, MATLAB Fuzzy Logic Toolbox and Visual Basic.Net	➢ Planning ➢ Brainstorming ➢ Analysis of the Study ➢ Design and development of the Study ➢ Testing ➢ Improvement of the system.	Temperature Monitoring System

In order for the study to meet the requirements, the proponents had to have enough knowledge regarding with the Arduino Microcontroller and DHT11 for hardware and Arduino IDE, Visual Basic.Net and MatLab Fuzzy Logic Toolbox for the Software.

In the process of the system, planning is the first step to know the flow of the system. In terms of gathering and collecting data, brainstorming is one of the easiest way in order to have enough and valid data. Having also the brainstorming, the proponents were able to research about the study and analyzed every detail that can be used in the study. Then, it will follow by the designing and developing of the hardware and software part of the system. After that, several tests will be conducted in order to test the accuracy, reliability and especially the functionality of the system. By finishing all the requirements, the output of the study is equivalent to the outcome of the input and process of the study that were able to come up and create a Temperature Monitoring system.

3. Results and Discussion

3.1 Project Description

Data Management System of an FLC-Based Temperature Monitoring for Air Conditioning Units that will assess the environmental factors like temperature and humidity that will provide comfortable environment levels in terms of cooling and optimized electricity consumption. This system will monitor and control the temperature of a room. Once the system detects that the temperature reaches the given range, the system will trigger and will send a notification pop-up message to the control panel and will display on a monitor or LCD. With the use of Fuzzy logic the systems were able to determine its range of limitation and calculation of where it will notify the

status of the temperature and humidity. The system will use Visual Basic.Net programming language as the GUI (Graphical User Interface) of the system.

3.2 Tools and Methodologies of the System

3.2.1 Software

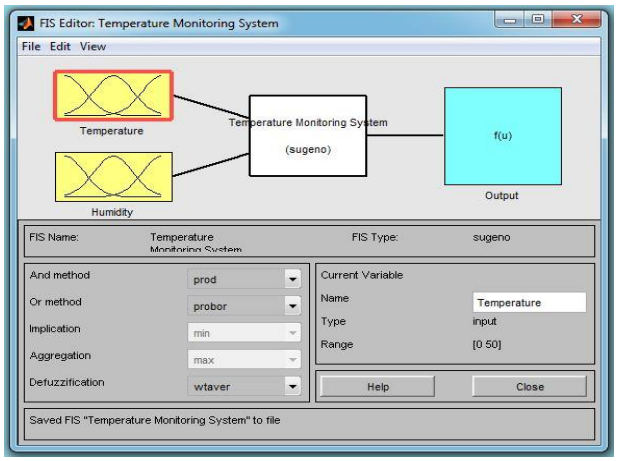


Figure 2. FIS Editor

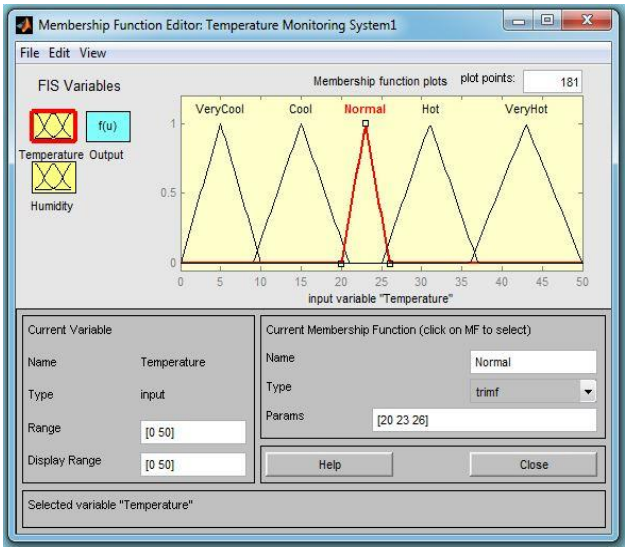


Figure 3. Temperature Parameters

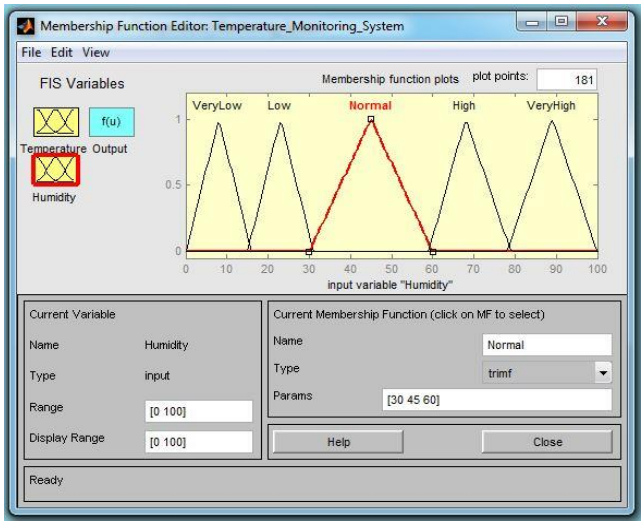


Figure 4. Relative Humidity Parameters

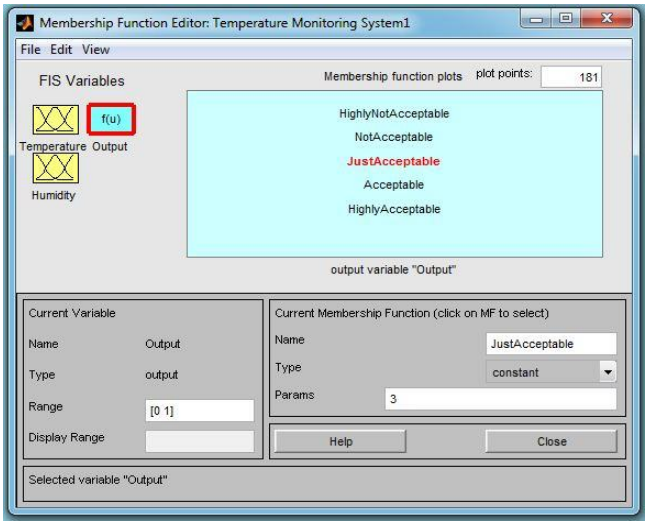


Figure 5. Membership Function Editor (Crisp Output)

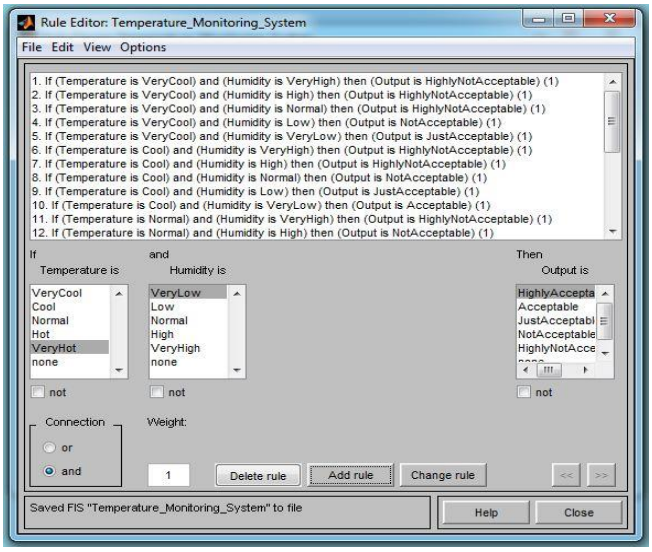


Figure 6. Fuzzy Rule Editor

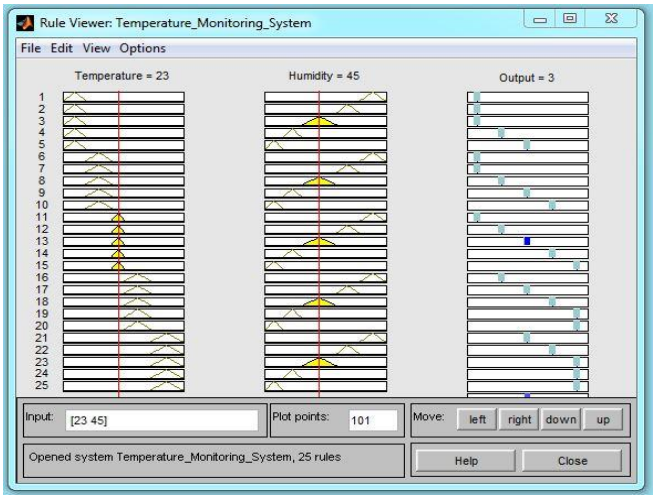


Figure 7. Fuzzy Rule Viewer

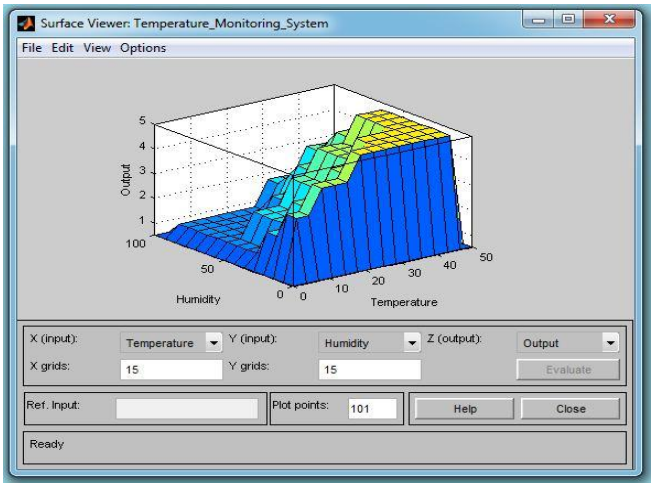


Figure 8. FIS Surface View

In Figure 2 depicts the FIS Editor which consists of the inputs and the output. Inputs include the temperature and relative humidity which is illustrated in Figure 3 and Figure 4. For the temperature, it is classified into five linguistic classes: Very Cool (0-10^{o}C), Cool (9 ^{o}C – 21 ^{o}C), and Normal (20 ^{o}C – 26 ^{o}C), Hot (25 ^{o}C - 37 ^{o}C) and Very Hot (36 ^{o}C - 50 ^{o}C). On the other hand, relative humidity is also classified into five linguistic classes: Very Low (0% - 16%), Low (15% - 31%), Normal (30% - 60%), High (59% - 79%) and Very High (78% - 100%). In Figure 5, the crisp output is shown in the membership function editor and it is the output or the crisp output for the fuzzy logic system which is classified into five linguistic classes; Highly Acceptable, Acceptable, Just Acceptable, Not Acceptable and Highly Not Acceptable. Figure 6 illustrates the fuzzy rule editor for the temperature monitoring system. On the other hand, the graphical illustration of the rules is shown in the Figure 7. The graphical illustration of the rules is elicited in Figure 8 which also includes the surface view of the temperature monitoring system with temperature parameters in the x-axis, relative humidity in y-axis and output in z-axis.

3.2.2 Hardware

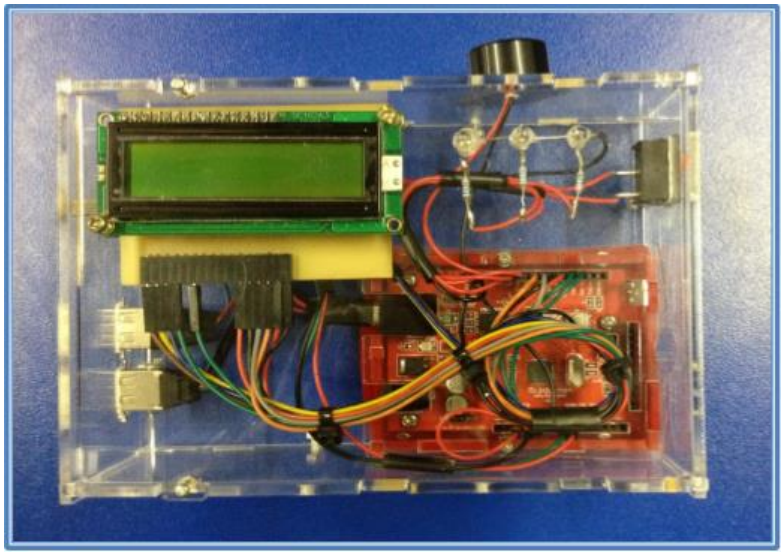


Figure 9. The Prototype

Figure 9 shows the hardware or the prototype of the system. The hardware is designed to monitor the temperature and the humidity through the use of the Arduino microcontroller and the temperature and humidity sensor. Once the system detects that the temperature reaches the set point of a parameters, the system will trigger and will send a notification message and will display in a monitor or LCD. Furthermore, a LED lights is used as an indicator whether the temperature is cold, hot or in normal temperature. When the temperature is higher than the normal temperature then RED Led lights will turn on, otherwise a BLUE Led lights will turn on when it is below the normal temperature and basically when the temperature n is in normal temperature then a YELLOW Led lights will turn on. Moreover, with the application of fuzzy logic, the systems were able to determine its range of limitation and calculation of the temperature and relative humidity.

4. Experiments and Analysis of Results

In Table 6 shows the findings in Testing 1 of temperature monitoring system from 10:00am to 1:30pm with 20-30 approximate numbers of people. The testing was held in laboratory room Computer Laboratory 4 in Lyceum of the Philippines University-Laguna. Each color represents different room position to maximize the reliability of the results. Moreover, the membership function retains the condition as "Normal" with the temperature ranges from 21 ºC to 23 ºC and a value of relative humidity ranges from 39 % to 42 %. Linguistic classification based on crisp output retains the reading of "Just Acceptable" on the entire testing.

Table 2. Tabulated Data of Testing 1 at the Computer Laboratory 4 of LPU-Laguna

Date	Time	Temperature	Humidity	Membership Function	Crisp Output	Linguistic Classicication
9/22/2015	10:00:19 AM	22	41	Normal	2.941	Just Acceptable
9/22/2015	10:05:19 AM	22	41	Normal	2.941	Just Acceptable
9/22/2015	10:10:19 AM	22	40	Normal	2.977	Just Acceptable
9/22/2015	10:15:19 AM	22	40	Normal	2.977	Just Acceptable
9/22/2015	10:20:19 AM	22	40	Normal	2.977	Just Acceptable
9/22/2015	10:25:19 AM	22	40	Normal	2.977	Just Acceptable
9/22/2015	10:30:19 AM	22	40	Normal	2.977	Just Acceptable
9/22/2015	10:31:19 AM	22	40	Normal	2.977	Just Acceptable
9/22/2015	10:35:19 AM	22	40	Normal	2.977	Just Acceptable
9/22/2015	10:40:19 AM	22	40	Normal	2.977	Just Acceptable
9/22/2015	10:45:19 AM	22	40	Normal	2.977	Just Acceptable
9/22/2015	10:50:19 AM	22	41	Normal	2.941	Just Acceptable
9/22/2015	10:55:19 AM	23	40	Normal	2.946	Just Acceptable
9/22/2015	11:00:19 AM	23	40	Normal	2.946	Just Acceptable
9/22/2015	11:01:19 AM	23	40	Normal	2.946	Just Acceptable
9/22/2015	11:05:19 AM	23	40	Normal	2.946	Just Acceptable
9/22/2015	11:10:19 AM	22	41	Normal	2.941	Just Acceptable
9/22/2015	11:15:19 AM	23	40	Normal	2.946	Just Acceptable
9/22/2015	11:20:19 AM	23	40	Normal	2.946	Just Acceptable
9/22/2015	11:25:19 AM	23	40	Normal	2.946	Just Acceptable
9/22/2015	11:30:19 AM	23	39	Normal	2.982	Just Acceptable
9/22/2015	11:35:19 AM	23	39	Normal	2.982	Just Acceptable
9/22/2015	11:40:19 AM	23	39	Normal	2.982	Just Acceptable
9/22/2015	11:45:19 AM	23	39	Normal	2.982	Just Acceptable
9/22/2015	11:50:19 AM	23	39	Normal	2.982	Just Acceptable
9/22/2015	12:00:08 PM	22	40	Normal	2.977	Just Acceptable
9/22/2015	12:05:08 PM	22	40	Normal	2.977	Just Acceptable
9/22/2015	12:10:09 PM	22	40	Normal	2.977	Just Acceptable
9/22/2015	12:15:08 PM	22	41	Normal	2.941	Just Acceptable
9/22/2015	12:20:08 PM	22	41	Normal	2.941	Just Acceptable
9/22/2015	12:25:09 PM	22	42	Normal	2.903	Just Acceptable
9/22/2015	12:30:08 PM	22	42	Normal	2.903	Just Acceptable
9/22/2015	12:35:08 PM	22	41	Normal	2.941	Just Acceptable
9/22/2015	12:40:08 PM	22	41	Normal	2.941	Just Acceptable
9/22/2015	12:45:08 PM	22	41	Normal	2.941	Just Acceptable
9/22/2015	12:46:08 PM	22	41	Normal	2.941	Just Acceptable
9/22/2015	12:50:15 PM	22	40	Normal	2.977	Just Acceptable
9/22/2015	12:55:15 PM	22	41	Normal	2.941	Just Acceptable
9/22/2015	1:00:15 PM	22	41	Normal	2.941	Just Acceptable
9/22/2015	1:05:15 PM	22	41	Normal	2.941	Just Acceptable
9/22/2015	1:10:15 PM	22	41	Normal	2.941	Just Acceptable
9/22/2015	1:15:45 PM	22	41	Normal	2.941	Just Acceptable
9/22/2015	1:20:15 PM	22	41	Normal	2.977	Just Acceptable
9/22/2015	1:25:15 PM	21	40	Normal	3.007	Just Acceptable
9/22/2015	1:30:15 PM	21	41	Normal	2.968	Just Acceptable

Table 3. Tabulated Data of Testing 2
at the Computer Laboratory 4 of LPU-Laguna

DATE	TIME	INPUT PARAMETERS		CRISP OUTPUT	LINGUISTIC CLASSIFICATION
		Temperature	Humidity		
9/29/2015	10:00:19 AM	25	55	2	Not Acceptable
9/29/2015	10:05:19 AM	23	49	3	Just Acceptable
9/29/2015	10:10:19 AM	22	47	3	Just Acceptable
9/29/2015	10:15:19 AM	22	45	3	Just Acceptable
9/29/2015	10:20:19 AM	21	43	3	Just Acceptable
9/29/2015	10:25:19 AM	21	42	3	Just Acceptable
9/29/2015	10:30:53 AM	20	42	3	Just Acceptable
9/29/2015	10:31:13 AM	20	42	3	Just Acceptable
9/29/2015	10:35:13 AM	19	42	3	Just Acceptable
9/29/2015	10:40:13 AM	19	42	3	Just Acceptable
9/29/2015	10:45:13 AM	19	42	3	Just Acceptable
9/29/2015	10:50:13 AM	19	42	3	Just Acceptable
9/29/2015	10:55:13 AM	19	42	3	Just Acceptable
9/29/2015	11:00:13 AM	19	42	3	Just Acceptable
9/29/2015	11:02:46 AM	19	41	3	Just Acceptable
9/29/2015	11:05:06 AM	19	41	3	Just Acceptable
9/29/2015	11:10:06 AM	19	42	3	Just Acceptable
9/29/2015	11:15:06 AM	19	42	3	Just Acceptable
9/29/2015	11:20:06 AM	19	41	3	Just Acceptable
9/29/2015	11:25:06 AM	19	41	3	Just Acceptable
9/29/2015	11:30:06 AM	19	41	3	Just Acceptable
9/29/2015	11:33:11 AM	19	41	3	Just Acceptable
9/29/2015	11:35:11 AM	19	41	3	Just Acceptable
9/29/2015	11:40:11 AM	18	43	3	Just Acceptable
9/29/2015	11:45:11 AM	18	43	3	Just Acceptable
9/29/2015	11:50:11 AM	18	43	3	Just Acceptable
9/29/2015	11:55:11 AM	18	43	3	Just Acceptable
9/29/2015	12:00:11 PM	18	43	3	Just Acceptable
9/29/2015	12:01:11 PM	18	43	3	Just Acceptable
9/29/2015	12:07:35 PM	18	43	3	Just Acceptable
9/29/2015	12:10:15 PM	19	42	3	Just Acceptable
9/29/2015	12:15:15 PM	19	42	3	Just Acceptable
9/29/2015	12:20:15 PM	19	42	3	Just Acceptable
9/29/2015	12:25:15 PM	20	42	3	Just Acceptable
9/29/2015	12:30:15 PM	20	42	3	Just Acceptable
9/29/2015	12:31:15 PM	20	42	3	Just Acceptable
9/29/2015	12:35:15 PM	20	42	3	Just Acceptable
9/29/2015	12:40:15 PM	20	42	3	Just Acceptable
9/29/2015	12:45:11 PM	20	42	3	Just Acceptable
9/29/2015	12:50:11 PM	20	42	3	Just Acceptable
9/29/2015	12:55:11 PM	20	42	3	Just Acceptable
9/29/2015	1:00:11 PM	20	42	3	Just Acceptable
9/29/2015	1:01:11 PM	19	42	3	Just Acceptable
9/29/2015	1:05:11 PM	20	42	3	Just Acceptable
9/29/2015	1:10:11 PM	20	42	3	Just Acceptable
9/29/2015	1:15:11 PM	20	42	3	Just Acceptable
9/29/2015	1:20:58 PM	20	42	3	Just Acceptable
9/29/2015	1:25:18 PM	19	42	3	Just Acceptable
9/29/2015	1:30:18 PM	20	43	3	Just Acceptable

In table 3, the testing was held on the same time in same room CL4 with less number of people as compared to testing. The reading of membership function based on the value of temperature is said to be "Cold" because the number of people is considered as factor on detecting the value of temperature. Furthermore, the temperature reading ranges from 18 ºC - 25 ºC while the humidity ranges from 41% – 55% considering all the linguistic classification is labeled as "Just Acceptable".

5. Conclusion

Upon doing the research, the proponents came up with the parameters with Very Hot, Hot, Normal, Cold and Very Cold with the help of ASHRAE standard. Those parameters are used for MatLab Fuzzy Logic toolbox for determining the temperature condition. The proponents also are able to verify that the number of people or the volume of the object in a specific room can be a huge factor on detecting the temperature and humidity. The position of the sensor is quite sensitive for the detection of temperature because of air conditioning unit's location. Also they were able to realize that the relative humidity is more visible on the outside part of the room, specifically on the windows because of sudden change in temperature. The system is proved to be reliable and accurate based on the several test conducted by the proponents. After the development of software and hardware components of the system. The proponents have the opportunity to test the system's functionality and accuracy. After dealing with series of testing, the system's functionality is proven capable monitoring temperature in a specific room.

6. Recommendations

The proponents recommend to the future researchers the followings:

1. Future researchers can use a larger scale of rules and membership functions.
2. In this study the proponents use the Sugeno style of FIS; future researchers can use the Mamdani Inference method instead.
3. Use other computational intelligence and implement it using a microcontroller.

7. Acknowledgements

This study woould not be possible without the various individuals who helped us. The proponents acknowledge Engr. Rionel Caldo, as their thesis adviser. The proponents also would like to thank their parents and family for giving the unconditional support both in terms of financial and emotional. Lastly, Jesus Christ, who is the source of knowledge and strength and guiding the proponents to assure the success of this study. The researcher would like to extend their deepest gratitude.

References

[1] Basu, Srismrita (2012). Realization of Fuzzy Logic Temperature Controller. Retrieved May 03, 2015, from www.ijetae.com/files/Volume2Is sue6/ IJETAE_0612_2

[2] Kumar, V., Kumar, S., & Kansal, H. (January 2014). Fuzzy Logic Controller Based Operating Room Air Condition Control System. Retrieved April 30, 2015,

from www.ijireeice.comy/upload/2014/.../IJIREEICE1A_a_vikas_ fuzzy_logic.pdf
[3] Das, T.K, & Das, Y. (2013). Design of a Room Temperature and Humidity Controller Using Fuzzy Logic. Retrieved May 03, 2015, from ajer.org/ papers/v2 (11)/J02118697.pdf
[4] Aftab, Muhammad (2013). Engineering Wireless Sensor Networks for Smart Air-conditioning Units. Retrieved May 03, 2015, from web.mit.edu/parmstr/Public/aaRe prints/.../Thesis_Muhammad_ Aftab.pdf
[5] Dash, S.K., Mohanty, G., & Mohanty, A. (December 2012). Intelligent Air Conditioning System using Fuzzy Logic. Retrieved April 30, 2015, from http://www.ijser.org/researchpaper%5CIntelligent-Air-Conditioning-System-using-Fuzzy-Logic.pdf
[6] Ali, Dr. Issam Mohammed (2012). Developing of a Fuzzy Logic Controller for Air Conditioning System. Retrieved April 30, 2015, from http://www.iasj.net/iasj?func= fulltext&aId=67701
[7] Burroughs, H. E. & Hansen, S. J. (2011). Managing Indoor Air Quality. United States of America, The Fairmont Press, Inc. Retrieved August 23, 2015 from https://books.google.com.ph/books?isbn=1105847977
[8] Yuan, Y., Pan, D., Wang, D., Xu, X., Peng, Y., Peng, X. & Wan, P.J. (2012). Thermal Inertia: Towards an Energy Conservation Room Management System. Retrieved May 10, 2015, from www4.comp.polyu.edu.hk/~ csdwang/Publication/greenroom_long.pdf
[9] Wellem, T. & Setiawan, B. (September 2012). Microcontroller- based Room Temperature Monitoring System. Retrieved April 28, 2015, from http://citeseerx.ist.psu.edu/viewdoc/download?doi=10.1.1.258.9540&rep=rep1&type=pdf
[10] Caldo, Rionel B. (2015). FLC-Based Indoor Air Quality Assessment for ASHRAE Standard Conformance. Retrieved February 2015, from link.springer.com/ content/pdf/10.1007%2F978-3-662-47200-2_75.pdf

Design and Development of an FLC - Based Ground Grid Integrity Testing Equipment for Sotero H. Laurel (SHL) Bldg. Of Lyceum of the Philippines University – Laguna (LPLU – L)

John Kenneth C. Filler[1*], Bryan M. Dimayuga[2], Kevin Martin E. Jaron[2], Alexander T. Montero[2], Mark Kenneth Z. Peros[2], Rionel Belen Caldo[1]

[1]Electrical Engineering Department
[1]Computer Engineering Department
Lyceum of the Philippines University – Laguna (LPU-L)

Corresponding e-mail: * Gspfiller@gmail.com

Abstract
This study provides a distinctive approach in assessing the integrity of a grounding system for it uses an advanced technique by constructing an equipment that is capable of determining the integrity of the grounding system of an institutional building. In this study, the proponents make use of the concepts of fuzzy logic in the assessment of the ground grid integrity test of LPU-L SHL bldg. It can be classify as Highly Acceptable (HA), Considerably Acceptable (CA), Just Acceptable (JA), Poor (P) and Critical (C). The input parameters include grounding conductor (conductivity), earth resistivity (Ω-oC) and grounding electrode (Ω -mm). The parameters in the model are acquired through the use of standards prescribed by the Philippine Electrical Code (PEC) and the Institute of Electrical and Electronics Engineering (IEEE). This study aims to provide a mathematical model to assess the integrity of the grounding system of the SHL bldg., design a fuzzy-based system, simulate and verify the effectiveness of the results. The proponents preferred to use the triangular membership functions and Sugeno-style of fuzzy inference systems.

Keywords: fuzzy logic; ground grid integrity; Sugeno-style; Matlab Fuzzy Logic Toolbox

1. Introduction

The effectiveness of Electrical system design and wiring of an institutional building depends on the reliability of its components. This includes proper functions of protective devices (such as fuses, circuit breakers and contactors for motors), proper insulation of conductors and also its grounding system. There are drawbacks and issues in electrical safety. This includes but not limited to electrical ground faults, short circuit

currents, lightning and other transients often do occur in an institutional building. In this regard, issues of electrical safety when servicing electrical equipment has acquired growing importance. By establishing the new principles and methods of protection, taking into account advances in science and practice of electrical safety are only some of the ways to improve electrical safety conditions [1].

A properly designed, installed and maintained grounding system is very important for a safe and effective electrical system in an institution. The most important reason for effective grounding is to protect people. Second, is to include protection of structures and equipment for unintentional contact with energized lines. This also ensures the maximum safety for electrical system faults [1].

It is important to keep in mind that the requirements contained in the Institute of Electronics and Electrical Engineers (IEEE) codes or any codes that can be used as a standard for electrical system design constitute minimum electrical installation requirements. These minimum requirements cannot ensure that the equipment will perform satisfactorily. For this reason, electrical practitioners often require additional grounding components. One of these consists of a copper conductor that is directly connected to earth and installed in the perimeter of the building. The steel building columns and some non – current carrying metallic frame of electrical equipment or some electrical part of the system are connected to this copper conductor to complete the grounding system [2].

There are many factors in determining the overall integrity of the grounding system. The voltage drop, resistance and the continuity and the earth resistance can significantly impact the overall resistance of the grounding system. The moisture content, mineral content, soil type, soil contaminants and any other related factors determine the overall resistivity of the earth. To properly design a grounding system, the earth resistivity must be measured and also must be in a good condition to establish a low resistive grounding [1].

The testing and evaluation of the integrity of the grounding system to determine its actual condition is the first step in the process to correct problems. The study is focused on creation of a new approach towards establishing condition monitoring for grounding integrity. Considerable benefits such as time and labor reduction for the grounding devices investigation with increase of accuracy of failures location can be achieved by using this proposed technique.

Lyceum of the Philippines University – Laguna (LPU-L) itself consists of high voltage apparatus, switchgear equipment and any other equipment that involves electricity. It is necessary to hand over normal and safe operating condition to all people inside the institution. In due course, it is important for LPU-L to provide an effective and reliable grounding system. One reason for increased risk during electrical fault or short circuit condition is due to ineffective integrity of the grounding devices.

In this study, the proponents will use the concepts and principles of fuzzy logic in simulation of the ground grid integrity test. The factors and parameters to be considered for classifying the integrity of the grounding system include the grounding conductor (conductivity), earth resistance (Ω-^{o}C) and the grounding electrode (Ω -mm).

The parameters will be categorized as Very Good (VG), Good (G), Satisfactory (S), Poor (P) and Critical (C). The proponents will use triangular membership functions for its input and output parameters and it would employ the Sugeno style of fuzzy inference system. The proponents would verify the results using Matlab Fuzzy Logic Toolbox and it will be compared to derived formulas in Excel. This study will be simulated purely mathematical.

1.3. Objectives of the Study

The prime objective of this study is to design and develop an equipment that is capable of determining the integrity of the electrical grounding system of Lyceum of the Philippines – Laguna, Sotero H. Laurel Culinary Arts Building and clearly identifies the weak points and discontinuities.

Specifically, this study aims to:

a) Understand the importance of a grounding system and how it affects the electrical system of an institutional building,
b) Design and develop an equipment that will measure the grounding conductor resistance, grounding electrode resistance and earth resistance
c) Asses using Fuzzy – Logic MatLab Toolbox Kit that the installation and the parameters of the grounding system will meet the basic requirement of the National Electrical Code, Philippine Electrical Code and IEEE Code.

2. Review of Related Literature

The proponents gathered several references that provided them with different ideas, thoughts and knowledge for developing the ground grid integrity test. By these studies, the proponents managed to come up with a concrete knowledge of developing new ideas that will contribute well to the study.

Table 1. Tabular Charts of Related Studies

Title	Description	Hardware	Software Used	Test Method Used
Ground Grid Integrity	This article tackles about the testing of the integrity of the ground grid through resistance test and how it is being done.	Grid Tester that is capable of injecting high current	N/A	Resistance Test
Importance of High Speed Fault Clearing	This paper describes the impact of having a high speed fault clearing of protective devices.	N/A	N/A	N/A
Fuzzy Logic Control of Water Quality Monitoring and Surveillance for Aquatic Life Preservation in Taal Lake	This paper shows how the fuzzy logic can be used in assessing the quality of water in Taal Lake Batangas. The proposed system was implemented using MatLab Fuzzy Logic Toolbox and Excel VB Macro Program.	N/A	N/A	N/A
Substation Grounding	This paper describes the appropriate design of substation grounding.	N/A	N/A	N/A
Investigating Grounding Grid Integrity Based on the Current Injection Method	This paper shows a method that can be used in testing the ground grid integrity through injecting high amount of current.	Current injection generator through the use of Op-Amp (OPA549)	N/A	Current Injection Method
Analysis of a Steel Grounding System	In this paper, a thorough analysis of the performance of a large grounding system made of steel instead of copper conductors buried in a low soil resistivity was discussed.	Steel Conductors	N/A	Fall-of-Potential Method
Application of Electromagnetic Field Theory to Measure Correct Grounding System Impedance	This paper shows a technique in measuring the ground impedances that minimizes the effects of inductive coupling, conductive coupling and power line grounding.	N/A	HIFREQ	Fall-of-Potential Method
Mathematical Modeling for Assessing Integrity of Power Systems Grounding Devices	This paper introduces a new technique to monitor the operating conditions of a grounding device of high voltage equipment and systems without any diggings and forced tripping through evaluation of the magnetic field distribution along the current-carrying horizontal element when it has been deteriorated.	N/A	N/A	Mathematical Modeling through the use of the use of the principles of Biot-Savart Law
Substation Ground Grid Continuity D.C High Current Test Method	This paper introduces a method of testing the ground grid through the use DC high current test method by injecting a 300 amperes DC through the ground grid and measuring the voltage drop.	N/A	Current Injection Generator	DC high Current Test
Ground Grid Integrity testing Using MEGGER Model GTS-300 as Implemented by the National Grid Corporation of the Philippines-Calamba	This paper describes the theory of operation and process of testing the transmission substation ground grid owned and operated by NGCP through the use of MEGGER Model GTS-300	MEGGER Model GTS-300	N/A	Injection of a substantial amount of current

2.1. Synthesis

Based on the review of related literature, it can be summarized that ground grid integrity test is vital in maintaining the effectiveness and reliability of the grounding system. The principles behind the operation of grounding system and how it affects the overall performance of an electrical system were discussed. In order to maintain an effective grounding system, an assessment of its integrity should be done to ensure that it can still operate properly especially upon the occurrence of a fault or short circuit.

Therefore, testing and assessing the ground grid integrity was made possible through several ways. This can be seen above in which different techniques was employed. Injecting AC inputs were usually done in testing the integrity of the grounding system. Technology has a big impact in the modernization of ground grid integrity testing methods. Advanced electronics, programmable equipment and computer simulation techniques became a trend in today's era as they have more precise measurements and results rather than the usual methods which require much data inputs.

Table 1 below tabulates the comparison of related literature on the basis of the following parameters: a.) Description of the study, b.) Hardware, c.) Software Used. D.) Test of Method Used.

It can be seen that the test of the grounding integrity is usually done in a substation. For this reason, the proponents decided to conduct the test in an institutional building since it is not yet been established in a structure outside the substation. In addition, the proponents will design an equipment that will test the grounding for the given research area using point-to-point method. It is also proved that this is the first time to test the integrity of the grounding system of an institutional building. Also, the proponents decided to use MatLab Fuzzy Logic Toolbox Kit for the Assessment of the integrity of the grounding system.

3. Fuzzy Rule Based System

There are fuzzy rules constructed to assess the integrity of the grounding system such as Highly Acceptable (HA), Considerably Acceptable (CA), Just Acceptable (JA), Poor (P) and Critical (C).

A hierarchical structure was constructed for the simulation of the grounding system, *Refer to figure 3.1.* The second level characterizes the grounding conductor integrity, earth resistance and the grounding electrode to obtain an acceptable grounding system for monitoring and surveillance purposes. The last hierarchical level characterizes the integrity of the grounding system. The following are the sample rules stored at three different hierarchical levels of structure:

If the Grounding Conductor Resistance is<poor> and the Earth Resistance is<very good> the Grounding Electrode Resistance is<good>
Then the Ground Grid Integrity is<JA>

If the Grounding Conductor Resistance is<good> and the Earth Resistance is<very good> the Grounding Electrode Resistance is<very good>
Then the Ground Grid Integrity is<CA>

If the Grounding Conductor Resistance is<critical> and the Earth Resistance is<poor> the Grounding Electrode Resistance is<good>
Then the Ground Grid Integrity is<P>

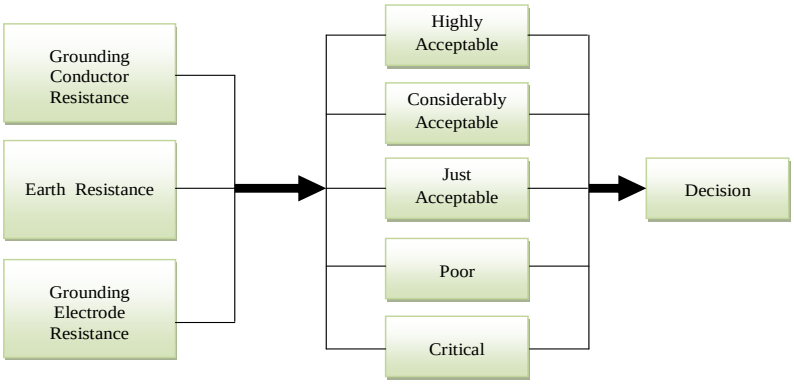


Figure 1. Hierarchical Structure for the simulation of the integrity of the grounding system.

The proponents have used the basic process of designing the fuzzy logic for the assessment of the integrity of the grounding system as shown in Figure 2. The process consists of five steps. For the first process involving the formulation of the problem the inputs to the fuzzy controller are the Grounding Conductor Resistance, Earth Resistance and the Grounding Electrode Resistance. The variable is scored and sent to the ground grid integrity assessment. The preceding step is by selecting the fuzzy inference rule. This method relies on by trial and error. The inference rule is selected based on the degree of match. The input values are averaged to fit linguistic terms. The proponents used triangular function in defining membership function. In this step involves determining the position and the shapes of the membership function as the factors in determining the performance of the fuzzy logic. The next is by performing fuzzy inference based on inference method. In this method the efficiency of the final control surface is determined by the inference and deffuzzification methods. Lastly is by selecting a deffuzification method to assess the integrity of the grounding system. In this case, deffuzification is done by calculating the center of gravity and the output is produced through averaging technique.

In this study the proponents used Sugeno style over Mamdami method because of only those constant values will vary unlike in Mamdami method the membership functions will also varied. Therefore Mamdami method will be more complicated than the Sugeno Style.

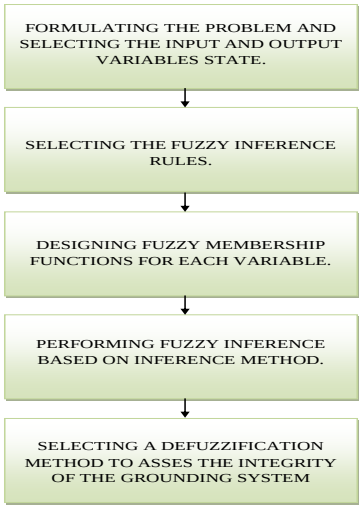


Figure 2. Design of Fuzzy Logic for the Assessment of the Ground Grid Integrity

4. Research Process

In chase of a successful upshot of this study, developmental method was employed by the proponents as their basis of their procedures which predominantly intend to achieve the set of objectives to solve the stated problems. Aforementioned to the system's advancement, this study also comprise of the design of the system, where planning, problem definition and setting up of the objectives were involved.

The study also comprises of the testing and valuation of the system as the proponents used experimental method in testing the system's operation. Set of experiments were conducted to tabulate successful and abortive results. To depict the system development life cycle, the proponents have used flowcharts and block diagrams to clearly understand the process.

The design of the entire system goes behind the procedures below:

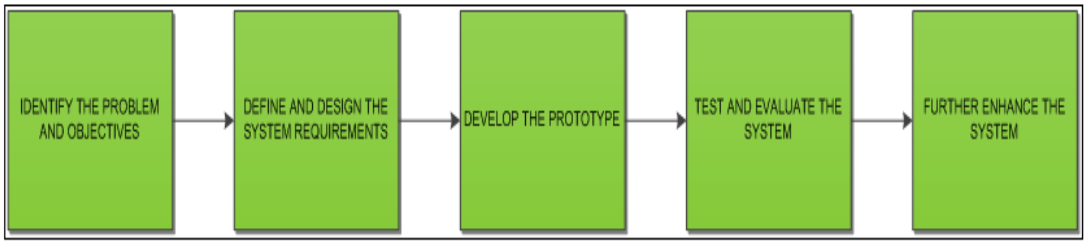
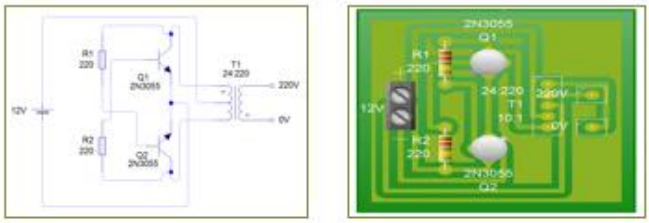


Figure 3. Research Process Block Diagram

Figure 3 shows the sequential process of the system. It depicts the system's developmental process which serves as a guide by the proponents in putting up the project.

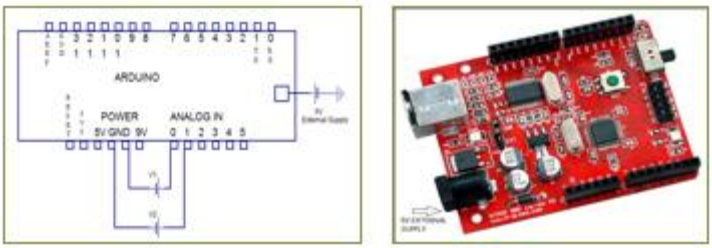
4.1 Prototype Components

- **Power Inverter**



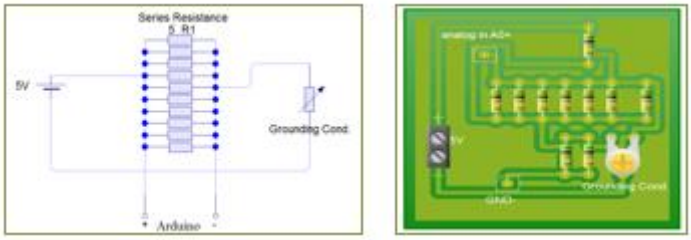
Power inverter is an electrical device that converts direct current (DC) to alternating current (AC). The circuit main components comprise of a 12V/12Ah dc source which will serve as the main power source of the system, two 2N3055 NPN transistors that act as the switching part and connected in a push-pull configuration which will generate a square wave that will be fed in the step up transformer to amplify the voltage.

- **Arduino Microcontroller**



Arduino Microcontroller is an open-source physical computing platform based on a simple microcontroller board, and a development environment for writing software for the board. It will serve as the brain of the system for it manipulates and executes the algorithm and converts the measured analog input into its equivalent digital output**.**

- **Voltage Divider Circuit**



The voltage divider circuit will serve as the circuit for measuring the resistance of the given parameters using voltage divider theorem and the equations below:

$$V_{Arduino} = \frac{R_1}{R_1 + R_{parameter}} \, x \, E_{source} \qquad Eq.\ 1$$

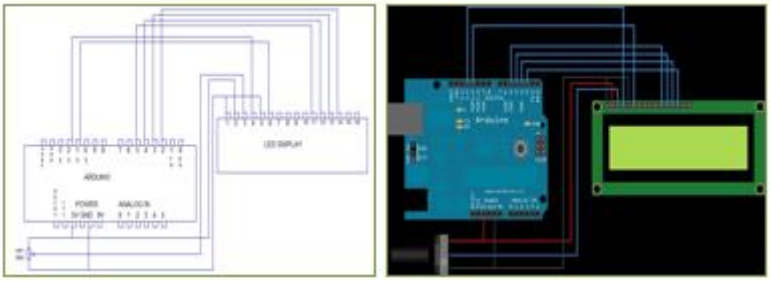
$$(V_{Arduino})(R_1 + R_{parameter}) = R_1 E_{source}$$

$$V_{Arduino} R_1 + V_{Arduino} R_{parameter} = R_1 E_{source}$$

$$V_{Arduino} R_{parameter} = R_1 E_{source} + V_{Arduino} R_1$$

$$R_{parameter} = \frac{R_1 E_{source} + V_{Arduino} R_1}{V_{Arduino}} \qquad Eq.\ 2$$

- **LED Display**



The LED display will be the output indicator of the system. The digital output coming from the arduino microcontroller will be displayed and viewed in the LED display.

- **MatLab Fuzzy Logic Toolbox**

The linguistic variables are commonly used instead of numerical variables in fuzzy logic system. Fuzzification is the process of converting a numerical variable (real number or crisp variables) into a linguistic variable (fuzzy number or fuzzy variable). The perception, experience and the general knowledge of the system behavior serve as the derivation that will act as the control rules that relate the fuzzy output to the fuzzy inputs. In this study, the proponents make use of the averaging technique in deriving its membership functions. The rule table for the designed fuzzy logic system for ground grid integrity assessment is given in Table 2

Table 2. Fuzzy Associative Memory (FAM) Matrix for Ground Grid Integrity Assessment

Count	Weight	Grounding Conductor	Earth resistivity	Grounding Electrode	Ground Grid Integrity (Classified Value)	Ground Grid integrity (Linguistic Class)
0	w1	5	5	5	5.00	HA
1	w2	5	5	4	4.68	CA
2	w3	5	5	3	4.36	CA
3	w4	5	5	2	4.05	CA
4	w5	5	5	1	3.73	JA
5	w6	5	4	5	4.77	CA
6	w7	5	4	4	4.45	CA
7	w8	5	4	3	4.14	CA
8	w9	5	4	2	3.82	JA
9	w10	5	4	1	3.50	JA
10	w11	5	3	5	4.55	CA

From the combination of the input parameters such as grounding conductor, earth resistance and grounding electrode, 125 fuzzy rule bases were able to formulate. The triangular figures of the associated function of this arrangement presume that for any particular input there is only one dominant fuzzy subset. The linguistic variables are converted into a numerical variable.

Creating, editing and observing the fuzzy inference system makes use of five primary Graphical User Interfaces (GUIs). It comprise of Fuzzy Inference System (FIS) Editor, Membership Function Editor, Rule Editor, Rule Viewer and Surface Viewer. If changes were made to the FIS of one of the toolbox, the effect can be seen in other GUIs since it is dynamically connected with each other. In addition to these five primary GUIs, the toolbox includes the graphical ANFIS Editor GUI, which is used for building and analyzing Sugeno-types adaptive neural fuzzy inference systems [3].

The method used in this study for Matlab Fuzzy Logic Toolbox simulation is the Sugeno or Takagi-Sugeno-Kang of fuzzy inference that was introduced in 1985 and it is similar to Mamdani method in many respects. The first two parts of the fuzzy inference process, fuzzifying the inputs and applying the fuzzy operator are exactly the same. Sugeno output membership functions are either linear or constant unlike the Mamdami. In this paper, the proponents think about the use of constants as output membership functions [3].

5. Experiments and Analysis Of Results

The experimentation was done methodically as discussed in the block diagram in the previous chapter (*Figure 3*). The results obtained from the experimentation will prove the system's effectiveness and consistency.

5.1 Earth Resistance Measurement

The earth resistance of a single spike, of diameter and length buried to earth with a soil resistivity can be calculated as follows:

$$R_g = \frac{\rho}{2\pi L}\left[\ln\left(\frac{8L}{d}\right) - 1\right] \qquad Eq.\ 3$$

Where: **ρ** Soil resistivity of the soil in ohm – meter (Ωm)
L Buried length of the rod in meter (m)
d diameter of the rod in meter (m)

The proponents conducted a parallel test of measuring earth resistance by using a 10 centimeter (0.1 meter) in length, 3.5 square millimeters (2.11×10^{-3} meter in diameter) copper rod supposing that the rod is the actual grounding rod buried.

$$R_g = \frac{\rho}{2\pi L}\left[\ln\left(\frac{8L}{d}\right) - 1\right] \qquad Eq.\ 4$$

$$R_g = \frac{120\Omega m}{2\pi(0.1m)}\left[\ln\left(\frac{8(0.1m)}{0.00211m}\right) - 1\right]$$

$$R_g = \frac{120\Omega m}{2\pi(0.1m)}[\ln(378.966) - 1]$$

$$R_g = 190.985\Omega[\ln(378.966) - 1]$$

$$R_g = 190.985\Omega[5.937 - 1]$$

$$R_g = 190.985\Omega[4.937]$$

$$R_g = 942.978\Omega$$

Table 3. Tabulated Results

No. of trials	Measured value	Theoretical value	Percentage error
Trial 1	843. 33 ohms	942.978 ohms	10.567%
Trial 2	1019 ohms	942.978 ohms	8.062%
Trial 3	848.33 ohms	942.978 ohms	10.037%
Trial 4	848.33 ohms	942.978 ohms	10.037%
Trial 5	726.43 ohms	942.978 ohms	22.964%

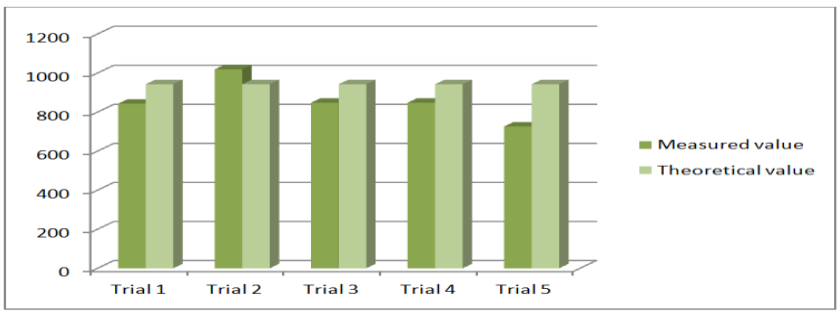


Figure 4. Graphical Representation of Results

5.2 Grounding Conductor and Electrode Measurement

The value of the grounding conductor resistance can be obtained using the formula formulated George Simon Ohm known as the Laws of Resistance:

$$R_c = \frac{\rho L}{A} \qquad \textit{Eq. 5}$$

Where: **ρ** Conductor resistivity in ohm – meter (Ωm)
L Length of the conductor in meter (m)
A Area of the conductor in square meter (m^2)

The proponents made a computation parallel for the test procedure conducted to measure the resistance of the grounding conductor to prove and to assure the accuracy of the equipment for the measurement of the grounding conductor resistance using a 3 meter copper conductor with a 5.18868 x 10^{-7} m^2 area.

$$R_c = \frac{\rho L}{A}$$

$$R_c = \frac{(1.68\ x\ 10^{-8}\Omega m)(3m)}{5.18868\ x\ 10^{-7}\ m^2}$$

$$R_c = 0.0971\Omega$$

In addition to test the accuracy of the equipment, the proponents also conducted a test using a carbon type resistor with a value of 150 ohms ±5% tolerance.

Table 4.Tabulated Results

No. of trials	Measured value	Theoretical value	Percentage error
Trial 1	0.06 ohms	0.0971 ohms	38.14%
Trial 2	0.13 ohms	0.0971 ohms	34.02%
Trial 3	0.17ohms	0.0971 ohms	38.14%
Trial 4	0.13 ohms	0.0971 ohms	75.26%
Trial 5	0.05ohms	0.0971 ohms	48.45%

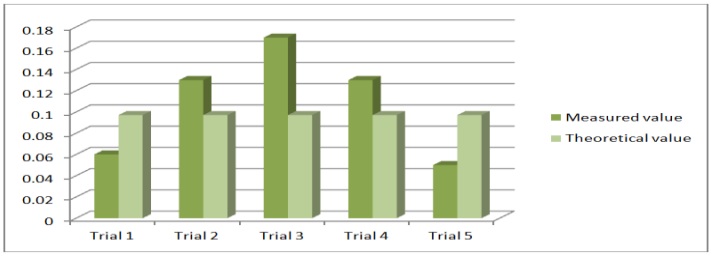


Figure 5. Graphical Representation of Results

Table 5. Tabulated Results

No. of trials	Measured value	Theoretical value	Percentage error
Trial 1	150.15 ohms	150 ohms	0.1%
Trial 2	145.59 ohms	150 ohms	2.94%
Trial 3	155ohms	150 ohms	3.33%
Trial 4	137.22 ohms	150 ohms	8.52%
Trial 5	150.10 ohms	150 ohms	0.067%

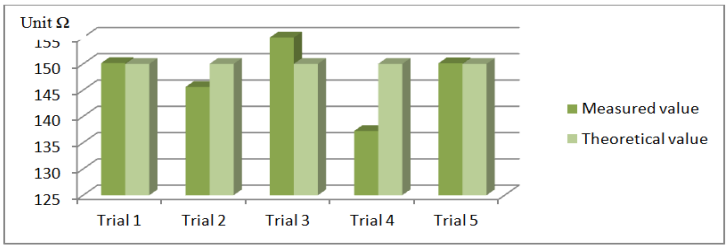


Figure 6. Graphical Representation of Results

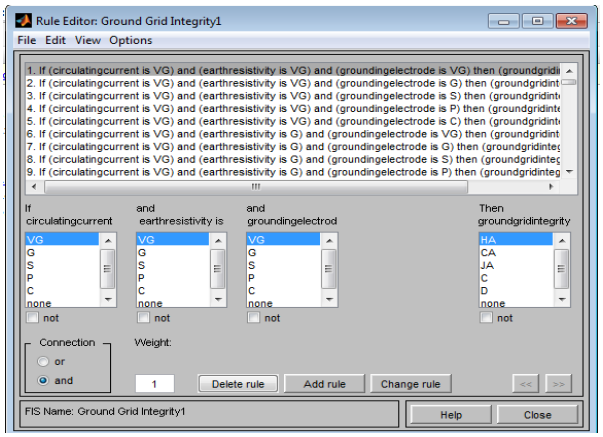


Figure 7 *Rule Editor for Ground Grid Integrity Assessment*

The proponents have used the rule editor (Figure 7) and rule viewer (Figure 8) for ground grid integrity testing using Matlab fuzzy logic toolbox. It is where the FAM matrix of 125 rules is plugged in. The proponents conducted 10 tests to determine the reliability of the fuzzy system for each linguistic classification. Table 6 shows the simulation results, which classifies the integrity of the grounding system as Highy Acceptable, Considerably Acceptable, Just Acceptable, Poor or Critical. Based from the results obtained, it could be analyzed that there is a perfect correlation between fuzzy system for, PEC and IEEE standards for ground grid integrity test as shown in Table 7.

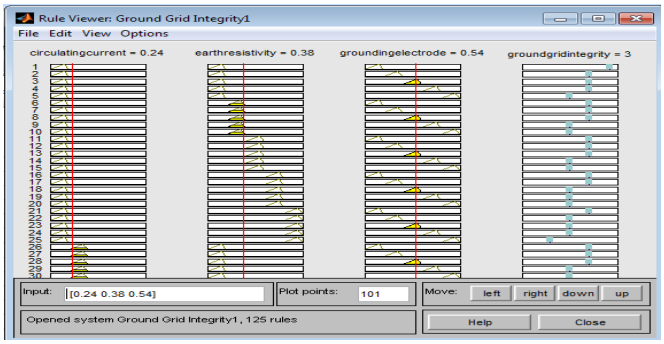


Figure 8. Rule Viewer for Ground Grid Integrity Assessment

Table 6. Testing Results using MatLab Fuzzy Logic Toolbox

Trials	Board Predictive Assessment Input Parameters		Input Values (Normalized)	Crisp Output (Matlab Fuzzy Logic Toolbox)	Linguistic Classification
1	Ground Grid Integrity	Grounding Conductor	0.24	3	Just Acceptable
		Earth Resistivity	0.38		
		Grounding Electrode	0.54		
2	Ground Grid Integrity	Grounding Conductor	0.36	4	Considerably Acceptable
		Earth Resistivity	0.54		
		Grounding Electrode	0.19		
3	Ground Grid Integrity	Grounding Conductor	0.11	3	Just Acceptable
		Earth Resistivity	0.78		
		Grounding Electrode	0.88		
4	Ground Grid Integrity	Grounding Conductor	0.57	2	Poor
		Earth Resistivity	0.66		
		Grounding Electrode	0.92		
5	Ground Grid Integrity	Grounding Conductor	0.16	4	Considerably Acceptable
		Earth Resistivity	0.19		
		Grounding Electrode	0.35		
6	Ground Grid Integrity	Grounding Conductor	0.87	1	Critical
		Earth Resistivity	0.72		
		Grounding Electrode	0.69		
7	Ground Grid Integrity	Grounding Conductor	0.52	3	Just Acceptable
		Earth Resistivity	0.08		
		Grounding Electrode	0.75		
8	Ground Grid Integrity	Grounding Conductor	0.17	5	Highly Acceptable
		Earth Resistivity	0.19		
		Grounding Electrode	0.19		
9	Ground Grid Integrity	Grounding Conductor	0.38	3	Just Acceptable
		Earth Resistivity	0.78		
		Grounding Electrode	0.27		
10	Ground Grid Integrity	Grounding Conductor	0.32	2	Poor
		Earth Resistivity	0.76		
		Grounding Electrode	0.67		

Table 7. Verification of Fuzzy based results with PEC/IEEE Standards

Trials	Parameters		Actual Input Values	PEC standards	IEEE standards	PEC/IEEE standards	Linguistic classification (fuzzy system for ground)		Linguistic classification (fuzzy system for ground)		%	
1	Grounding Conductor	Voltage Drop	0.011 V/ft	N/A	0.03 V/ft	4 - Good	VG	Good	HA	CA	20	45.45
		Resistance	1.22mΩ/ft	955.34 μΩ/ft - 2.626mΩ/ft	N/A	4 - Good					30	
		Watts-Loss	353mW/ft	342mW/ft - 942.08 mW/ft	N/A	4 - Good					20	
		Continuity	short	short	short	5 - Very Good					30	
	Earth Resistance	Soil Resistance	3.88Ω	N/A	5Ω	3 - Satisfactory	S		JA		40	22.73
		Soil Temperature	M	N/A	N/A	4 - Good					40	
		Moisture Content	38%	N/A	N/A	2 - Poor					20	
	Grounding Electrode	Depth	369mm	750 mm	N/A	3 - Satisfactory	G		CA		28.57	31.82
		Electrode Resistance	7.42Ω	25Ω	N/A	4 - Good					42.86	
		Spacing	1850mm	1800 mm	N/A	5 - Very Good					28.57	
2	Grounding Conductor	Voltage Drop	0.053 V/ft	N/A	0.03 V/ft	2 - Poor	VG		HA		20	45.45
		Resistance	0.983mΩ/ft	955.34 μΩ/ft	N/A	4 - Good					30	
		Watts-Loss	236mW/ft	942.08 mW/ft	N/A	5 - Very Good					20	
		Continuity	short	short	short	5 - Very Good					30	
	Earth Resistance	Soil Resistance	0.9Ω	N/A	5Ω	5 - Very Good	G		CA		40	22.73
		Soil Temperature	M	N/A	N/A	4 - Good					40	
		Moisture Content	8%	N/A	N/A	1 - Critical					20	
	Grounding Electrode	Depth	203mm	750 mm	N/A	2 - Poor	S		JA		28.57	31.82
		Electrode Resistance	18.6Ω	25Ω	N/A	3 - Satisfactory					42.86	
		Spacing	1389mm	1800 mm	N/A	4 - Good					28.57	

6. Conclusions

The contribution of this study is a tangible procedure in deter-mining the effectiveness of the integrity of the grounding system. Developed in this thesis is an FLC based equipment that is capable of determining the integrity of the grounding system of LPU-L SHL bldg. The proponents had developed the ground grid integrity test-ing equipment by injecting a substantial amount of direct current into the grounding system and measuring its important parameters. The equipment has the capability to assess and classify the condi-tion of the grounding system and if it can still operate properly in normal and anomalous conditions especially upon the occurrence of a fault.

The assessment of the grounding system was done through the use of the concepts of fuzzy logic. Averaging technique was em-ployed in deriving its membership functions. From the combina-tion of the input parameters such as grounding conductor re-sistance, earth resistance and grounding electrode resistance, 125 fuzzy rule bases were able to formulate. The triangular figures of the associated function of this arrangement presume that for any particular input there is only one dominant fuzzy subset. The lin-guistic variables are converted into a numerical

variable. The pro-ponents think about the use of constants as output membership functions.

It has been verified experimentally from theoretical studies and actual data analysis as supported by the data above to prove the effectiveness of the results. It can be seen that ground grid integrity test is working as it should be, considering that it established a perfect correlation between theoretical and the actual values that had been obtained.

The proponents were able to establish a distinctive approach towards the unsophisticated way of assessing the integrity of the grounding system that will present a cheaper and quicker method which will also apply most likely to the improvement and devel-opment of maintaining an effective and reliable grounding system.

7. Acknowledgement

The authors acknowledge Jesus Christ, who is the source of wisdom and knowledge in the study of fuzzy-based system for ground grid integrity assessment for LPU – L, SHL Bldg. Also the proponents would like to thank Engr. Jose Lumbera, OIC of High Voltage Equipment Testing and Diagnostics Department of Nation-al Grid Corporation of the Philippines, Engr. Dennis Asaldo of Lyceum of the Philippines – Laguna and Engr. Andres Dela Cueva of College of Engineering and Computer Studies for giving them an ample time to share his knowledge and expertise regarding the ground grid integrity testing.

References

[1] W. Keith Switzer, “Practical Guide to Electrical Grounding,” ERICO, Inc., 1999
[2] Truman C. Surbrook and Jonathan R. Althouse, “Interpreting the National Electrical Code 8th Edition”, 2008.
[3] Rionel B. Caldo, “Fuzzy Logic Derivation and Simulation of a Three-Variable Solar Water Heater Using Matlab Fuzzy Logic Toolbox,” Proceed-ings of the November 2013 IEEE International Conference.
[4] Allan H. Robbins and Wilhelm C. Miller, “Circuit Analysis: Theory and Practice, 3rd edition”, Thomson/Delmar Learning, 2003.
[5] Philippine Electrical Code, Institute of Integrated Electrical Engineers of the Philippines, 2009.
[6] 81 – 2012 – IEEE Guide for Measuring Earth Resistivity, Ground Imped-ance, and Earth Surface Potentials of a Grounding System.
[7] [Online]. http://en.wikipedia.org/wiki/Copper_loss [Accessed: August 1, 2014].
[8] B.L. Theraja and A.K. Theraja, “ABC of Electrical Engineering”, S.Chand and Company LTD., 2012.
[9] [Online]. http://ecmweb.com/content/achieving-acceptable-ground-poor-soil [Accessed: August 1, 2014].

eureca 2016 – Conference Paper
Paper Number EE_UG12

An Artificial Intelligence System of Monitoring and Security Using Optical Character Recognition for Vehicular Plate Number in Lyceum of the Philippines University - Laguna

Onine M. Mico, Angelino P. Flores, Veryll John Sumague, Rionel Belen Caldo*

Computer Engineering Department Lyceum of the Philippines University-Laguna (LPU-L), Laguna, Philippines

Corresponding e-mail: *rionel14_caldo@yahoo.com

Abstract
This paper describes a project for the design and implementation of Automatic License Plate Recognition using the algorithm of Optical Character Recognition in Matlab. ALPR plays an important role in terms of Security and surveillance which also provides cumulative application access control, traffic control and detection of stolen vehicles. Since the project is OCR driven, it is divided into different stages of image manipulation to provide an accurate output of processed license plate number. Visual Basic .Net is used as the face of the system for the signal and notification controls of authorization and is linked to OCR in Matlab. The use of ALPR requires a specific horizontal and vertical alignment for precise recognition of plate number. ALPR, generally, is used in public works and highways, in this project, the proposed system will be implemented in private sectors, specifically in an Educational Institution.

1. Introduction

The security is one the main proportions to make the life inside of an institution sustainable and well functional. Our country's schools and colleges are confronted with continuous dangers, for example, viciousness, drugs, bullying, crimes, normal catastrophes and even terrorism. [1]. In order to reduce the risk of the phenomenon, the security of the institutions must be well maintained. Most of the educational institutions around the Philippines have parking lots for students and teachers that provide a convenient place to park and enter or leave campus. Most of which have security cameras installed to help secure the premises. Putting cameras before the Main doors will notify the school security guard to the suspicious conduct around the autos and helps the policemen to seek after suspects if anything is stolen or vandalized.

1.1 Background of the Study

In this study, an integrated ALPR will be used in a system using the algorithm of Optical Character Recognition with the help of designed interface in Visual Basic .NET for the increased of security in LPU – The LPU-L have security cameras installed in some designated areas but Main Gates does not have any and Main Gates that are not monitored digitally can increase the risk of danger for students and faculty. And for some instances, visitors or outsiders with personal vehicles can enter the school premises without the permission of the guards on duty. This means that the security of the institution is below average.

A properly secured institution or area is consist of materials intended for security purposes to attain a sustainable environment. Such materials includes Surveillance camera, which are common nowadays for it increases the security of a certain area and its common function is to record videos for crime prevention, traffic monitoring and many more. For example, major expressways have an advanced security materials installed in every toll plaza to monitor vehicles. This includes the automatic acquisition of vehicles' plate number through the use of surveillance cameras in case some disturbances occurs.

1.2 Statement of the Problem

The LPU-L since it was established and began to operate is still managing in manual labor type classification. Partial areas of the campus have accomplished increasing the security but the Main Gates is still without a proper security system and thus increasing the risk of danger of the institutions and its people.

1.3 Objectives of the Study

The prime goal of this study is to make and create a plate number recognition using the MATLAB Image Processing toolbox and Optical Character Recognition with Visual Basic .NET interface for the Main Gates of LPU-L. This study aims to:

a.) To develop an intelligent system that can provide security and safety by acquiring the plate number of vehicles coming in and out of the campus
b.) To develop a Visual Basic System Interface for the control of monitoring procedure and data procurement process
c.) To test the performance and reliability of the prototype and the system.

2. Methodology

2.1 Visual Basic .Net

Visual Basic was presented as the primary programming dialect that backings programmable graphical client interfaces (GUI) utilizing the dialect supplied objects. An object oriented language that comprises of two basic parts. First, which includes set of objects, it is the part of visual and which includes the high level programming language, this is the language part. These two components were joined to make an alternate application which is generally seen inside the desktop [2].

2.2 Matlab

MATLAB used for technical computing, is one application that has a high-performance language. It can be used for computing, visualizing, and a user friendly environment programming tool where the user can solve the problems easily, fast and legibly. It is also a communicating system whose basic data element is an array which doesn't required any dimensioning on the system. It is good in solving matrix, vectors or even a fraction to make the results simpler and accurate [3].

2.3 Optical Character Recognition

An acknowledgment of printed or composed content in a certain object that is being scanned by the medium such as cameras, IP camera and any other capturing devices. It will analyze the image captured and translate the picture into character codes, for example, ASCII it is usually used in processing of data. On the process, captured image will be broke down for light and dim areas or spot with a specific end goal to recognize each alphabetic letter or numeric digit. Once the character is recognized, the value will be converted into ASCII code and give the equivalent value.

2.4 Arduino

A pre-gathered Arduino board incorporates a microcontroller, which is modified utilizing Arduino programming language and the Arduino advancement environment. Fundamentally, this stage gives an approach to fabricate and program electronic segments. Arduino programming language is a disentangled from of C/C++ programming language in view of what Arduino calls "outlines," which utilize essential programming structures, variables and capacities. These are then changed over into a C++ program.



Figure 1. Arduino Controller

Figure 1 is the main component of the system where the data is being processed. Arduino served as a controller and identify whether the inputted plate number is a regular or a visitor on the institution.

2.5 Proposed Design

The system aims to prove the possibility of integration and implementation of ALPR in LPU – Laguna to increase the institutions' safety and security. The system used the Matlab for the algorithm of Optical Character recognition intended for vehicle's plate number and Visual Basic .NET for the interface providing signal and notification controls.

2.6 Block Diagram

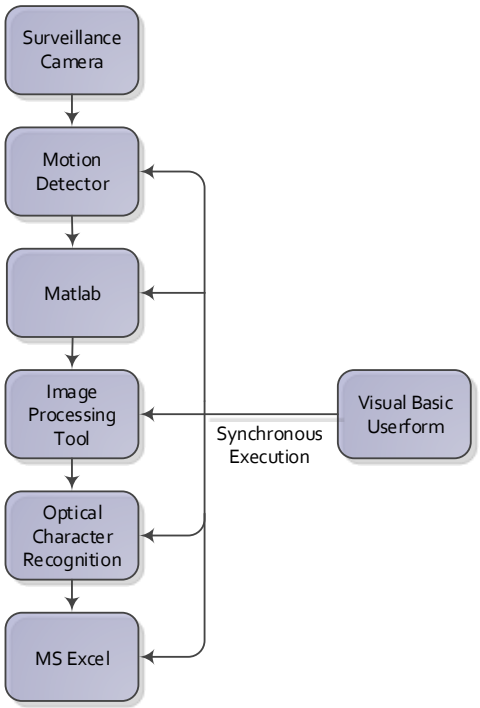


Figure 2. Simplified Block Diagram

Figure 2 is a improved block diagram of the system application. Since the system is for security purposes, the interface in built with username and password. The interface is designed with a homepage/home screen and the main controls is built in another form wherein the main functions of the system is provided. When the plate number is entered, the system will search the database if the input is regular in the institution or a visitor. The system will notify the user when the plate number is a visitor and will be prompted to be added on the database of not.

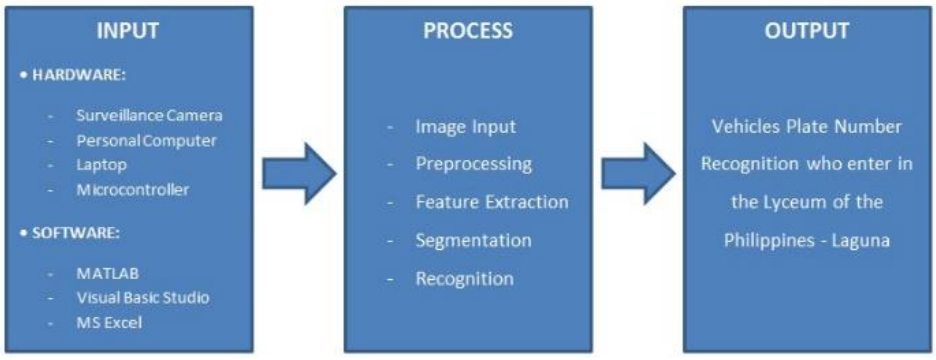


Figure 3. Flow of the System

Figure 3 which demonstrate the flow of the system and its application has been stated. The system will capture a vehicle plate number and serve as a data, this data will be process with the help of MATLAB Image Processing Tools and undergo a different steps in order to obtain the desired information. After the process and manipulation the system will produce an output and save it to the MS Excel application for security and future use.

A database linked to the visual basic interface will be provided for the saving of the plate numbers. Included in the database is the list of vehicles' plate numbers allowed and recognized by the administration of LPU – Laguna.

2.7 Pseudocode

1. Start
2. ALPR Structure
3. User Log-In
    - Input value for security purposes
4. Verification of Account
5. Choose Recognition
6. Input plate number
7. Choose incoming or outgoing
8. If incoming, the system will notify if regular or visitor
9. If regular, time logged in will be recorded
10. If visitor, the user is prompt to add to pending list or not
11. If outgoing, time logged out will be recorded
12. End

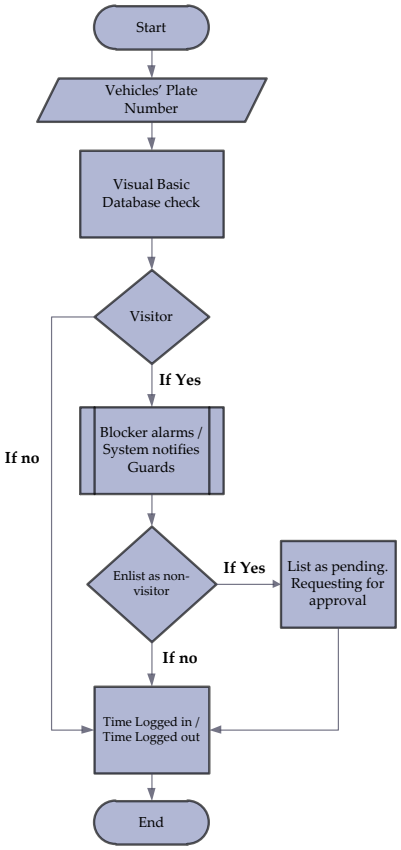


Figure 4. Flow Chart of the System

3. Result and Discussion

3.1 Project Description

This system is made using Matlab and OCR integration and Visual Basic .NET to provide an efficient security system for LPU – Laguna also to increase its safety. The system is run through an integrated algorithm of OCR designed in MatLab and is linked to the designed interface dedicated for signal and notification controls.

3.2 Tools and Methodologies of the System

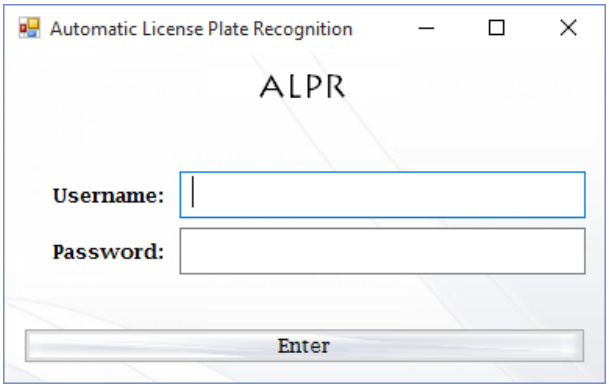


Figure 5. System Log-in

This system ID is for the administrator and authorized personnel of the institution.

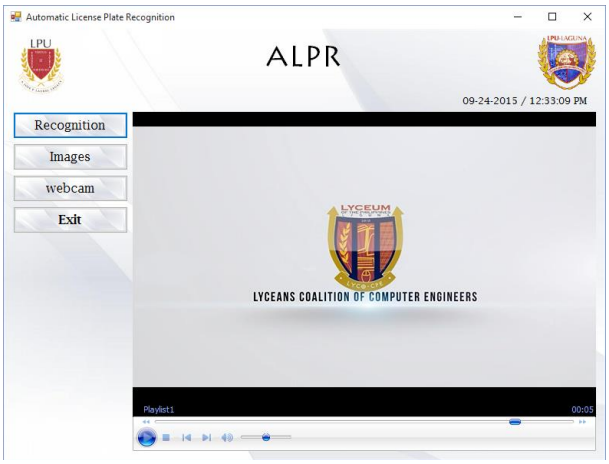


Figure 6. System Home Page

This is the homepage of the designed interface wherein the recognition, images and exit tab is available.

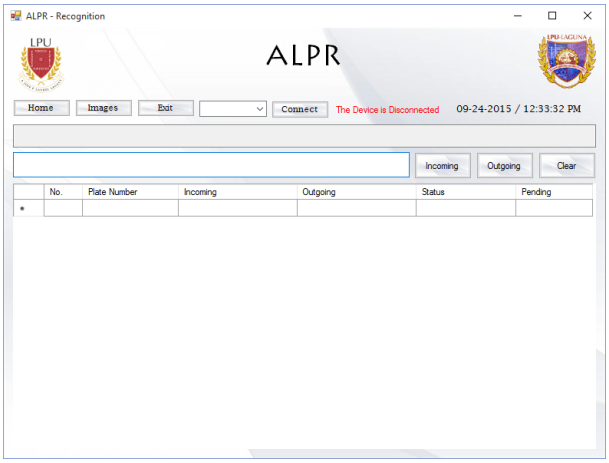


Figure 7. Recognition page

This is the operation form of the system. The connect button is dedicated for the connection of Arduino for signaling indicators which is required in order to fully operate the system. If the Arduino is not connected, the buttons for operation is disabled.

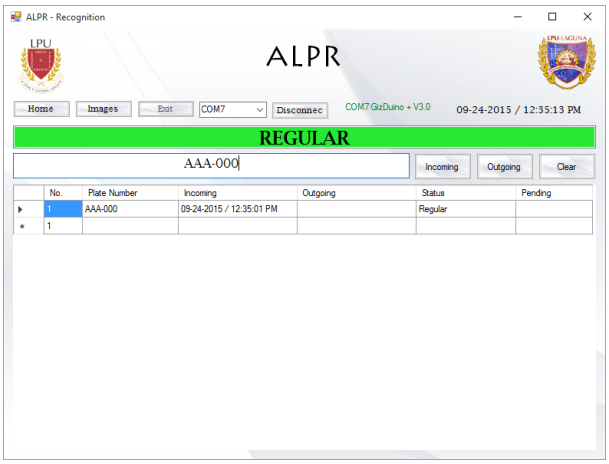


Figure. 8. Regular Notification - Incoming

When the inputted Plate Number is regular or is registered to the Administrations' records, the form will notify "Regular" and will also signal the Arduino to flash the Green Traffic Light. The time logged in will be recorded in the "Incoming" column.

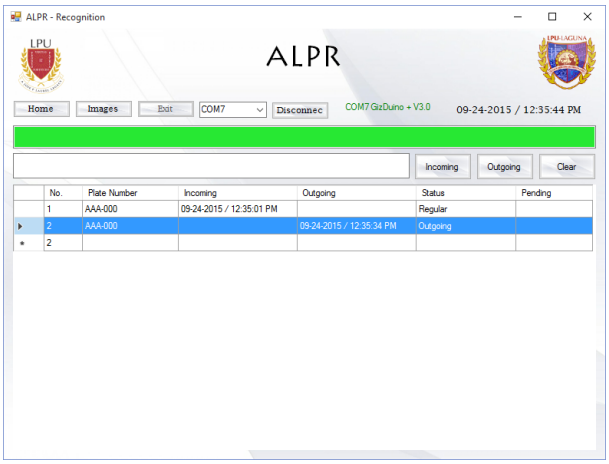


Figure 9. Outgoing

The time logged out will be recorded in the "Outgoing" column when the vehicle is leaving the school premises.



Figure 10. Prompt - Pending

When the inputted Plate Number is not on the records of the Administration, the form will notify "Visitor" and will also signal the Arduino to flash the Red Traffic Light. The time logged in will be recorded in the "Incoming" column in the vehicle is entering the premises.

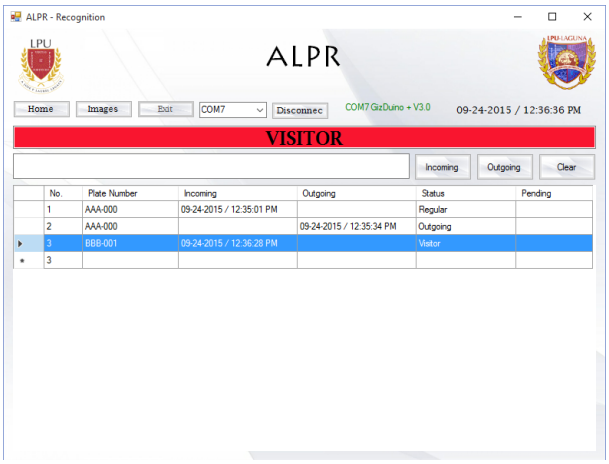


Figure 11. Visitor Notification - Incoming

If the owner of the inputted plate number does not want to enlist as regular, the status will be recorded as "Visitor" and also the time logged in.

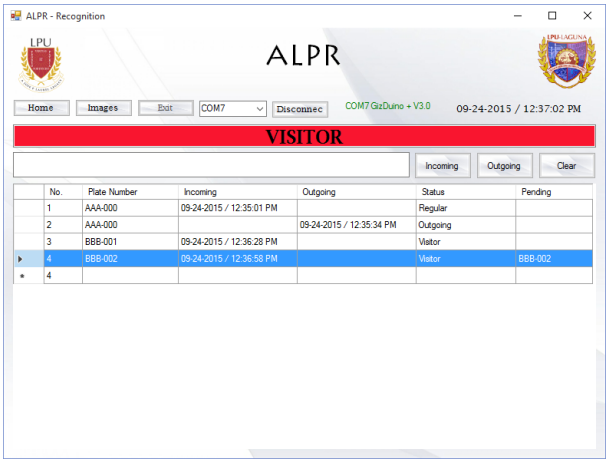


Figure 12. Visitor Notification – Incoming Pending

If the owner of the inputted plate number wants to enlist as regular, the status will be recorded as "Visitor" and also the time logged in and the inputted plate number will also be recorded in the Pending column aligned in the time recorded.

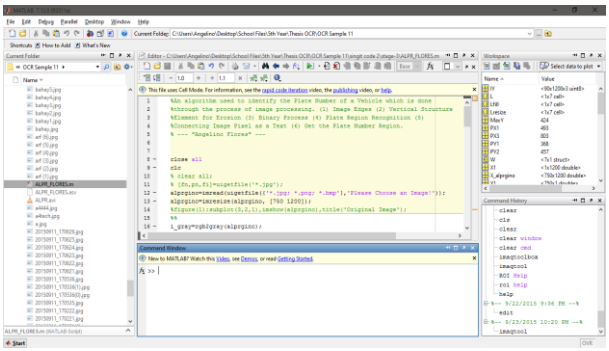


Figure 13. Matlab User Interface

This figure shows the entire software application used in processing the image taken by the camera. This is the algorithm that identifies and analyzed the supplied image and output the region of the plate number.

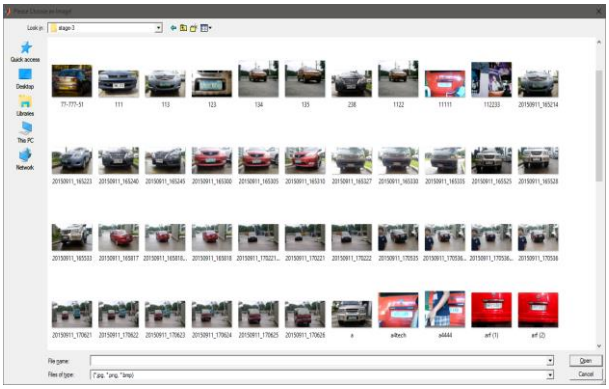


Figure 14. Matlab Image Directory

This is where the captured image stores, the images are compiled and run by the Matlab in this directory. It is very important to specify your target image directory to avoid the error and malfunction as well as the disruption of the whole process.

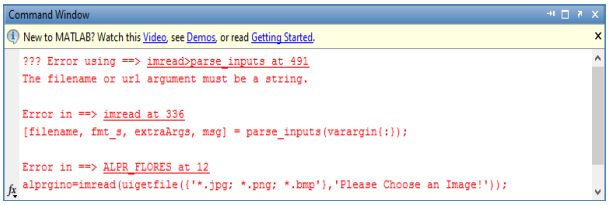


Figure 15. Matlab Error Notification

Error message when cancelling the selection panel of an image to be processed.

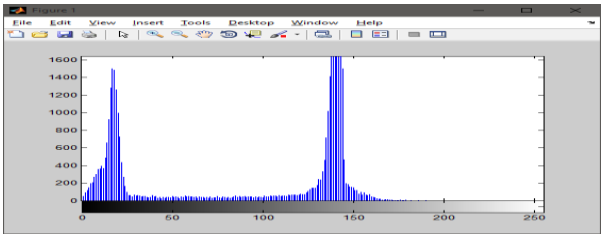


Figure 16. Image Histogram

A sample of RGB Image Histogram where the system is considering in order to get the most number of pixel in the image in order to identify the plate number region of a vehicle.



Figure 17. Image Filtering

A stage where the RGB Image is converted to a Grayscale Image as part of the pre-processing of the system.



Figure 18. Image Binarization

The input image was converted to a binary by thresholding, getting the image edges and eroded, then the morphological images has been made to identify the plate region of a vehicle.



Figure 19. Plate Number Region

After the pre-processing, thresholding, and binarization of an image the extraction of plate number region from the RGB image was the next step.

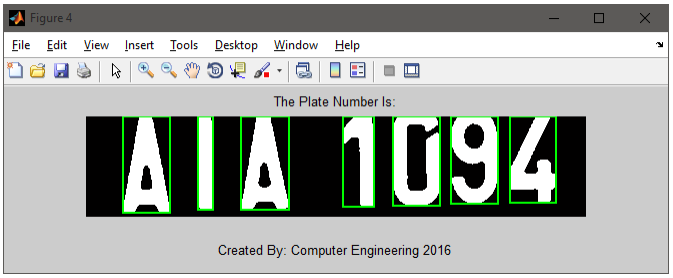


Figure 20. Output Plate Number

This is the final process of the system wherein the plate number region was converted into grayscale, threshold and the final step was the graythresh. In order to identify the character easily bounding box was used.

4. Conclusion

The system was made and developed by the proponents to record the incoming and outgoing vehicle who passes the vehicular gate of the institution.

The system is working in a proper camera placement within the required distance to capture the front view of the vehicle. The lighting, vehicular position, camera placement and plate number positioning have a big effect on detecting the plate region of a vehicle. These are the reason why the proponents set a stop box mark where the vehicle should touch to clearly identify by the camera.

The detection of the system was successfully done with a proper set-up of camera's range from the target image. The background or environment is a big dilemma of the system therefore the camera is enclosed to the vehicle and as much as possible no other images will be captured just the parts of the front view of the vehicle. The plate number can be detected even on the sideways view as long as the target region is at the centered of the image.

5. Recommendation

The system is in a good working condition considering the factors that may affect the process of detection. The proponents suggest that in order to get more accurate and reliable image and plate numbers consider a high definition type of camera or capturing devices. Image capturing and video recording must be at least minimum of 16 megapixel. The blocker is one of the best equipment that can be used instead of stop marking box that the proponents used.

To further maximize the efficiency of this project the next researcher must spend a lot of time in doing research, reading more related literatures and conceptualizing the possible limitations of this project. One recommendation for the next researchers is that action camera is a best medium for this kind of project, take the whole region of the front vehicle and make sure that the background is lessen. Another improvement that can be done for the system is building a templates depend on the characters that supports the plate numbers. The scope and limitation of the proponents can be widen and improved considering the different position of a vehicle towards the medium.

This project will benefit not only the institution but also the security guards who uses the manual inputting of data in order to monitor the incoming and outgoing vehicles. This system can make their job easily and fast without standing over the heat of the sun.

Acknowledgements

Before anything else, the proponents would like to thank our Almighty God for giving us the knowledge, wisdom, strength, protection, and guidance all throughout the development of this project. To our parents who won't stop supporting us until the end and in our loving professors who shows their support and guidance, without them this project would not be possible. The proponents would like to extend their gratitude to De La Salle University - Canlubang students under the advisee of Engr. Rionel B. Caldo, MsECE for sharing their knowledge regarding image processing in Matlab..

References

[1] [Online].Available:http://discoverysoftware.com/five_tips_to_improving_school_safety_and_security/ [Accessed: May 11, 2015].
[2] [Online].Available:http://searchwindevelopment.techtarget.com/definition/Visual-Basic-NET [Accessed: May 10, 2015]
[3] [Online].Available:http://cimss.ssec.wisc.edu/wxwise/class/aos340/spr00/whatismatlab.htm/ [Accessed: May 10, 2015]
[4] [Online].Available:https://www.techopedia.com/definition/27874/arduino
[5] Sharma et al, (2014) "Automatic License Plate Recognition using optical character recognition and template matching on yellow color license plate."
[6] Ozbay et. al, (2007) "Automatic Vehicle Identification by Plate Recognition"
[8] Kranthi et. al, (2011) "Automatic Number Plate Recognition"
[9] Ganapathy et. al, (2006) "Optical Character Recognition Program for Images of Printed Text Using a Neural Network"
[10] Dojcinovic et. al, (2012) "Neural Network Based Optical Character Recognition System"
[11] Farhad et. al, (2014) "An Efficient Optical Character Recognition Algorithm using Artificial Neural Network by Curvature Properties of Characters"
[12] Cho et. al, (2014) "Recognition of Severely Distorted License Plate Numbers"
[13] Beibut et. al, (2013) "Effective Algorithms and Methods for Automatic Number Plate Recognition"
[14] H.R. Ain Moghassemi and A.Broumandnia (2005), "Iranian License Plate Recognition Using Connected Component and Clustering Techniques"
[15] Chen et. al, (2012) "Android-Based Patrol Robot Featuring Automatic License Plate Recognition"
[16] [Online].Available:http://www.zonetrigger.com/WZThelp/ [Accessed: May 10, 2015]
[17] [Online].Available:bwlabel.(1994~2015).Retrieved from MATHWORKS:http://www.mathworks.com/help/images/ref/bwlabel.html
[18] [Online].Available: RegionProps. (1994~2015).Retrieved from MATHWORKS: http://www.mathworks.com/help/ I mages/ref/regionprops.html
[19] [Online]. Available: Edge Detection. (1994 ~ 2015)

Retrieved from MATHWORKS:http://www.mathworks .com/help/images/ref/edge.html

[20] [Online].Available: Morphological Images. (1994~2015) Retrieved from MATHWORKS:http://www.mathworks.com /help/images/morphology-fundamentals-dilation-and-erosion.html

[21] [Online].Available: bwareaopen. (1994~2015). Retrieved from MATHWORKDS:http://www.mathworks.com/help/ima ges/ref/bwareaopen.html

Implementation of an FLC Based Indoor Air Quality Monitoring System with Ventilation Control Mechanism

Jonel Jozef Catapang [1*], Irra Edralyn Manalo[2], Paul Jonathan Dimaano[2,] Jed Daryl Louise Lingat[2], Denmor Colinares[2], Maricar Mirano [2] , Rionel B. Caldo[1]

[1] *Computer Engineering Department*

[2] *Electronics Engineering Department*

Lyceum of the Philippines University – Laguna (LPU-L)

Corresponding e-mail: [*]*Jonel_catapang@gmail.com*

Abstract

Indoor air pollution is a serious health problem in most rural countries because of solid fuels usage. This paper presents a new approach to monitor and normalize indoor air quality (IAQ) by utilizing Sugeno style of fuzzy interference system. The work of this FLC-based IAQ monitoring system is not merely to sense the existence of the odourless unobservable pollutant but also to normalize the IAQ by controlling the ventilation system according to the level of carbon dioxide present in the room and the room temperature and relative humidity level. Matlab's Fuzzy Logic Toolbox was used to define the fuzzy sets which would be used to control the ventilation system to normalize the air quality.

Keywords: Indoor air pollution, Sugeno style fuzzy interference, Matlab, Arduino Microcontroller

1. Introduction

1.1 Background of the Study

The quality of air in the surrounding is essential to maintain good health and safe environment. While it is very important to focus on the outdoor problems of air quality, it must be realized that air pollution is an indoor problem as well. In fact, the air we breathe inside our house is more polluted than we think it is. As indicated by Environmental Protection Agency (EPA), indoor air contamination can be two to five times more dirtied contrasted with the air contamination outside, in some cases it is 100 times more contaminated than the level of contamination outside.

We humans exhale carbon dioxide through our lungs. Carbon dioxide is the waste generated as we use up oxygen [1]. Since we spend most of our time inside our home, the concentration of carbon dioxide indoors is higher compared to the concentration outside [2]. Carbon dioxide poisoning victims die because of hypercapnia. Hypercapnia results when there is too much carbon dioxide in our blood [3].

The World Health Organization has indicated in their official website [4] that out of 4.3 million people who die yearly because of diseases triggered by household air pollutions, six percent die from lung cancer, 12 percent from Pneumonia, 22 percent from Chronic Obstructive Pulmonary Disease, 26 percent from Ischemic Heart Disease and 34 percent from stroke.

To find out if the air we breathe is clean and unpolluted, this paper therefore proposes to create an indoor air quality system that can monitor and control the condition of air in enclosed areas. The system uses the concepts and principles of fuzzy logic algorithm. A set of command for the control is formed through fuzzy logic rules to assess the state of the air. During a range of time, the system will continuously detect the state of the air with a list of parameters (air and gaseous parameters). If the air quality failed a number of tests, the system will output warning to call the attention of the occupants in an LCD display or when the test is in completion. The study will also include the use of Matlab Fuzzy Logic Toolbox for the input and output construction, sensors, and Arduino microcontroller for the control operation.

1.2 Objectives of the Study

The general objective of this study is to develop and improve an indoor air quality monitoring system with ventilation control mechanism by implementing fuzzy logic technique that will normalize the air quality. Specifically, the study aims to:

1. To describe the fuzziness in indoor air quality
2. To develop a program using fuzzy logic that will process the data from the sensors
3. To be able to detect and measure the level of indoor air quality and provide ventilation control mechanism

2. Methodology

This paper made use of different models to illustrate the system's design. The system's architecture was presented using block diagram while the process of the system was demonstrated using IPO Chart, Pseudo Code and Flow Chart.

- Fuzzy Logic

A Fuzzy rationale is a type of numerous esteemed rationale in which reality estimations of variables might be any genuine number somewhere around 0 and 1. By qualification, in Boolean rationale, the variables truth qualities are 0 or 1. Fluffy rationale has been stretched out to handle the considered incomplete truth, where reality quality may go between totally genuine and totally false [10].

The proponents utilized the use of fuzzy logic because of its flexibility when it comes to decision making. Fuzzy logic is also easy to understand for people with average technical knowledge. Another edge of fuzzy logic is its implementation of fuzzy rules; the proponents have a wide range of options on how the system will respond to a certain situation.

Fuzzy logic's ability to define a unique fuzzy rules makes it suitable for the goal of the paper.

2.1 System Design

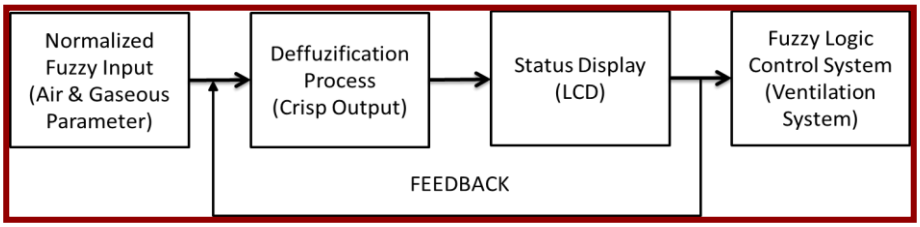


Figure 1. High-Level Block Diagram of an FLC-Based Indoor Air Quality Assessment

The normalized fuzzy input module refers to the two input variables, air and gaseous parameters. An air parameter involves the temperature and relative dampness of the air. Vaporous parameter alludes to the level of Carbon Dioxide present noticeable all around. The inputs will be fuzzified through predefined fuzzy sets. The data will then be defuzzified to give crisp outputs of Normal, Critical, or Dangerous. These crisp outputs will control the power level which will be fed up to the ventilation system. The proponents utilized the use of the Sugeno style of fuzzy interference system.

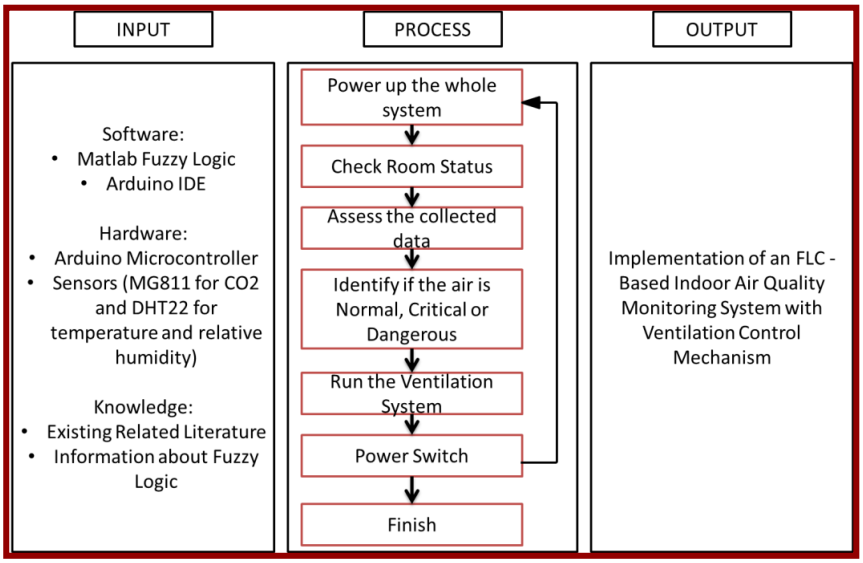


Figure 2. IPO Chart of the System

1. Sensors determine room status
2. System assesses the gathered data
3. Categorize the quality of the indoor air
4. The ventilation system is on standby mode when the air quality is normal
5. Run the ventilation when the air quality gets critical/dangerous
6. Stop the ventilation system when the air quality is back to normal

Figure 3. Pseudo Code of the System

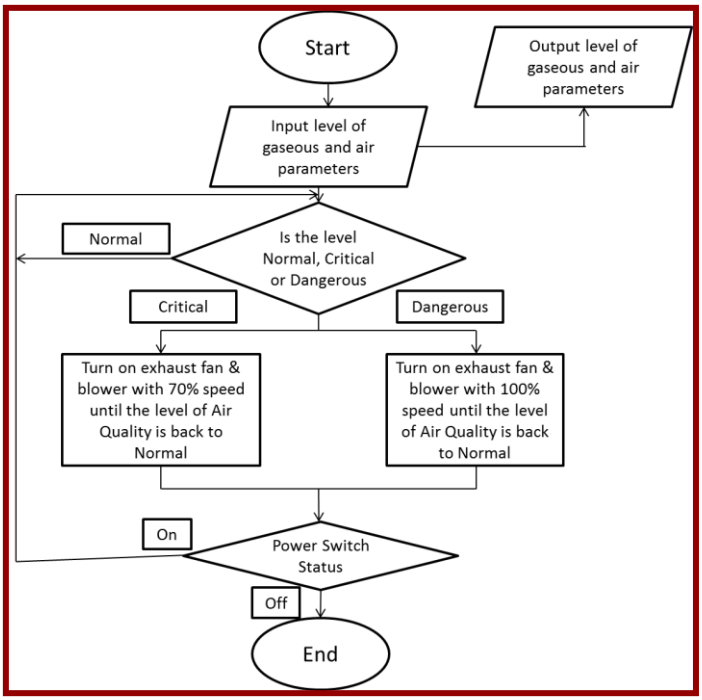


Figure 4. Flowchart of the System

Figure 4 shows the flow of the indoor air quality monitoring system with ventilation control mechanism. The sensors will detect the presence of the indoor air pollutant (carbon dioxide) and determine the room temperature and its relative humidity. The level of the parameters will be the input of the system. Based on the rules established by the proponents, the fuzzy logic will decide what to do. As shown on the flowchart, when one or both parameters gets dangerous or critical, the system will control the speed of the fan to 70% of its full speed or turn on the fan to its maximum power depending on the fuzzy rules set by the proponents. However, when the value of the parameter is back to normal, the system will let the system read data from the sensors and wait until the reading became dangerous or critical again. The system will continue to monitor and normalize the indoor air as long as it is supplied by power.

2.2 Proposed Design

In order to monitor the level of indoor air pollution present in a room, the proposed design will be using different sensors for the air and gaseous parameters. The

input value for each sensor will be classified as Good Hot (GH), Good Cold (GC), Fair Hot (FH), Fair Cold (FC), Poor Hot (PH) or Poor Cold (PC).

After determining the level of indoor air quality, the input values will be assessed using fuzzy logic and decide what crisp outputs to produce, one for air parameters and another for gaseous parameters. These crisp outputs are categorized as Normal, Critical, or Dangerous.

Using Arduino microcontroller with implemented fuzzy rules, the speed of the blower (for air parameters) and exhaust fan (for gaseous parameter) are controlled depending on the crisp outputs. If the output is Normal, the speed of either fan is 0%, for Critical, 70% and for Dangerous, 100% speed.

Table 1. Classification of Input Values for each Parameter

	Parameters		
Input Level	Temperature (°C)	Relative Humidity (%)	Carbon Dioxide (ppm)
Good 1 (hot)	23<T<=26	40<H<=45	CO2<=500ppm
Good 2 (cold)	22<T<=23	45<H<=50	
Fair 1 (hot)	26<T<=29.5	35<H<=40	500<CO2<800ppm
Fair 2 (cold)	21<T<=22	55<H<=65	
Poor 1 (hot)	29.5 <T	0<H<=35	CO2>=800ppm
Poor 2 (cold)	21 >=T	65<H<=100	

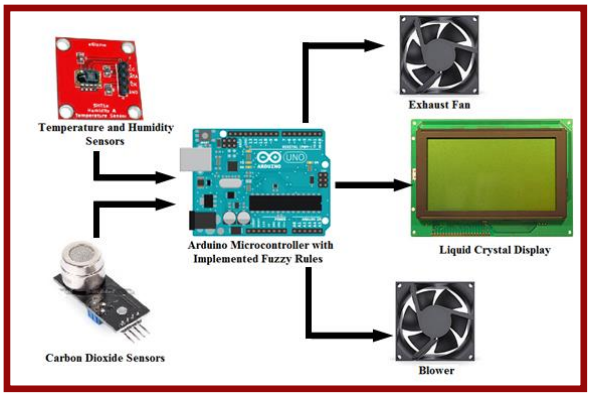


Figure 5. System Model

This project makes use of sensors to detect the level of the air parameters and the gaseous parameters present in the room. The IAQ needs to be assessed in order to know if its level is still safe or not, and Fuzzy Logic was chosen by the proponents to do this task. The speed of the fan must be controlled depending on the level of the IAQ and Arduino microcontroller is utilized to control the speed of the fan. Also, to show the current level of the Indoor Air Quality, an LCD Display is used in the system.

3. Results and Discussion

Table 2. Data Gathered for Controlled Environment

	Input			Output	
Trial	Temperature (°C)	Relative Humidity (%)	Carbon Dioxide (ppm)	Fuzzy Logic Crisp Output	Output (Fan Speed)
1	27.4	63.1	787	0	0%
2	27.4	63.1	438	0	0%
3	27.4	63	575	0	0%
4	27.4	63	<400	0	0%
5	27.4	62.9	<400	0	0%
6	27.4	62.9	618	0	0%
7	27.4	62.9	477	0	0%
8	27.4	62.9	561	0	0%
9	27.4	63	479	0	0%
10	27.4	63	667	0	0%
11	27.4	63.1	<400	0	0%
12	27.4	63.1	652	0	0%
13	27.4	63.1	<400	0	0%
14	27.4	62.7	590	0	0%
15	27.4	62.7	485	0	0%
16	27.4	62.8	499	0	0%
17	27.4	62.9	<400	0	0%
18	27.4	62.9	624	0	0%
19	27.4	63.1	<400	0	0%
20	27.4	63.2	611	0	0%
21	27.4	63.2	569	0	0%
22	27.4	63.2	468	0	0%
23	27.4	63.2	<400	0	0%
24	27.4	63.2	581	0	0%
25	27.4	63.1	<400	0	0%
26	27.4	63.2	<400	0	0%
27	27.4	63.2	563	0	0%
28	27.4	63.2	454	0	0%
29	27.4	63.1	650	0	0%
30	27.4	63.1	676	0	0%

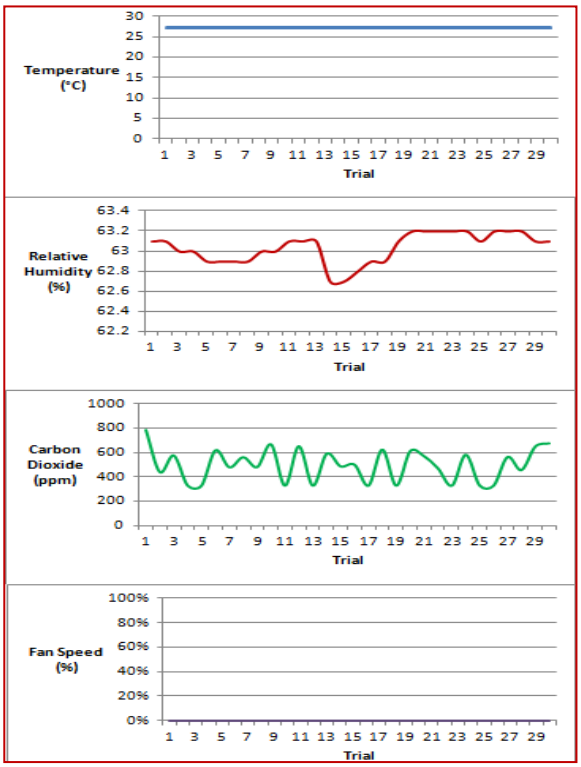


Figure 6. Graphical Representation of the Data Gathered for Controlled Environment

Figure 6 shows the graphical representation of the data obtained by the system within the room environment when the proponents did not increase the factors that can contribute to the varying of the temperature, relative humidity, and carbon dioxide. The graph shows that all the input parameters are in either fair or good level.

Table 3. Data Gathered for Uncontrolled Environment

	Input			Output	
Trial	Temperature (°C)	Relative Humidity (%)	Carbon Dioxide (ppm)	Fuzzy Logic Crisp Output	Output (Fan Speed)
1	26.8	64.1	591	0	0%
2	26.8	65	618	0	0%
3	26.9	64.2	614	0	0%
4	26.9	64.4	603	0	0%
5	27	64.6	615	0	0%
6	27.1	65	612	0	0%
7	27.2	67.5	604	0.5	70%
8	27.2	67.6	613	0.5	70%
9	27.5	67	596	0.5	70%
10	27.6	66.8	593	0.5	70%
11	27.7	66.7	611	0.5	70%
12	27.9	76	699	0.5	70%
13	28	76.2	697	0.5	70%
14	28.1	75.9	691	0.5	70%
15	28.4	75.5	726	0.5	70%
16	28.7	75.6	719	0.5	70%
17	28.8	75.7	711	0.5	70%
18	29	76.2	801	1	100%
19	29.5	74.4	840	1	100%
20	30.7	71	837	1	100%
21	30.5	68.8	830	1	100%
22	30.2	66.4	820	1	100%
23	29.9	66.5	813	1	100%
24	29.7	65.4	813	1	100%
25	29.5	65	704	0.5	70%
26	29.4	64.9	633	0.5	70%
27	29.3	64.8	626	0.5	70%
28	28.9	64.9	632	0	0%
29	28.8	64.5	602	0	0%
30	28.7	64	605	0	0%

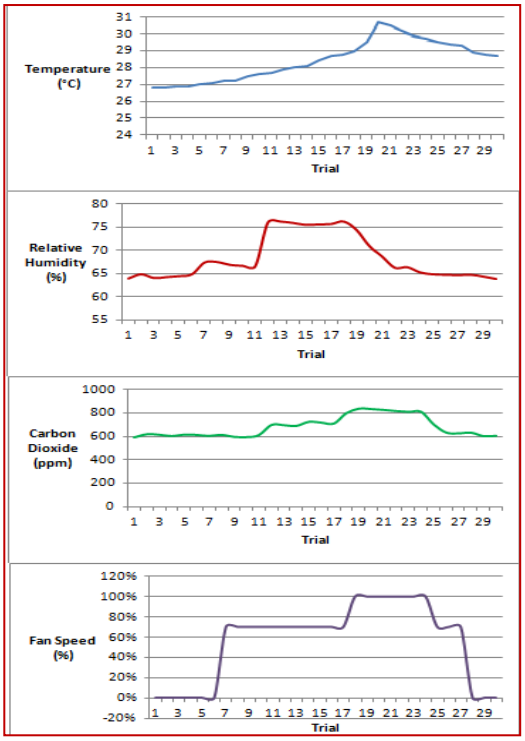


Figure 7. Graphical Representation of the Data Gathered for Uncontrolled Environment

Figure 7, on the other hand, shows the graphical representation of the data obtained by the system within the room environment under unusual conditions as the proponents increased the factors that can contribute to the change of temperature, relative humidity, and carbon dioxide. The graph shows the increase in the speed of the ventilation fans as the level of the parameters increase.

7. Conclusions

Developed in this study is an FLC-based monitoring system of indoor air quality with ventilation control mechanism. The successfulness of the project study has been demonstrated experimentally from the simulations and actual data analysis conducted by the proponents. The system is working properly as supported by the data in chapter 4. When the sensor detected a certain value, the Arduino microcontroller using the fuzzy rules will decide what to do. When the Arduino microcontroller determined that one or all of the parameters is good or fair, the ventilating fans will not run. But if one of the three parameters is critical, the speed of the ventilating fans will be 70 percent of the maximum, and if two or all the parameters are critical, the speed of the fan will be 100 percent.

The system was able to perceive, assess, and categorize the presence of the parameters, and intelligently execute an action within a short range of time immediately after level classification has been done. We can therefore say that the application of Fuzzy Logic Technology enabled the researchers to attain the set objectives in this paper.

Though the system responded accordingly to the design requirements, in terms of size, the capacity of the system to detect problems in the air quality is limited to smaller rooms because only one sensor was utilized. For enclosed areas with dimensions slightly larger than the room used during the experiment, two or more systems must be installed. Also, the presence of other parameters aside from the temperature, relative humidity, and carbon dioxide cannot be treated by the system.

For the continuity of operation, as stated in the scope and limitations of the study, power lost will discontinue the operation of the device because the control system is driven by electricity.

7. Recommendations

The proponents recommend the use of a backup battery in case of power failure so as to have the system to be functioning continually despite the circumstances. Also, consideration of outdoor air quality that may affect indoors shall be done in future studies to see if such factor can affect health issues as well.

Acknowledgment

The proponents of this research would like to thank God, first of all, for the wisdom that He had given to them. Without that wisdom, this paper will not be accomplished well.

They would also like to express their sincere gratitude to their adviser, Engr. Rionel Caldo for sharing all his knowledge about research making and for all the patience while guiding them during the whole process.

Besides from their adviser, the proponents are also grateful for their parents and siblings for the continuous support that they are giving to them.

The researchers would like to thank Lyceum of the Philippines University - Laguna for providing important resources like the library and the internet access which are really helpful in doing the entire research.

References

[1] The Effects of Too Much Carbon Dioxide in the Blood. (2013 , August 16). Retrieved from http://www.livestrong.com/article/218049-the-effects-of-too-much-carbon-dioxide-in-the-blood/

[2] INDOOR ENVIRONMENTAL QUALITY. (2013, June 18). Retrieved from http://www.cdc.gov/niosh/topics/indoorenv/buildingventilation.html

[3] Sanders, A.. How Does Carbon Dioxide Poisoning Kill a Human?. Retrieved from http://www.ehow.com/how-does_4695252_carbon-dioxide-poisoning-kill-human_.html

[4] Household air pollution and health. (2014, March). Retrieved from http://www.who.int/mediacentre/factsheets/fs292/en/

eureca 2016 – Conference Paper
Paper Number EE_UG16

Realization of Fuzzy Logic Controller for DC-DC Buck Converter in an FPGA

Joseph T. Seranilla*, Rionel B. Caldo

Computer Engineering Department, Lyceum of the Philippines University – Laguna

Corresponding email: * jhayseranilla06@yahoo.com

Abstract
The concepts of fuzzy logic for dc-dc buck converter circuit were used in this study. The parameters in the model were acquired through Analog to Digital Converter (ADC) circuit. The error and change in error are the input parameters and the duty cycle is the output of the fuzzy controller. The Pulse Width Modulation (PWM) signal switched the dc-dc buck converter. The proponent had used triangular membership functions, Mamdani and Sugeno-style of fuzzy inference systems in this proposed. The membership functions were classified as Negatively Big (NB), Negatively Small (NS), Zero Area (ZO), Positively Small (PS) and Positively Big (PB). This study aims to design a fuzzy-based system, simulate and verify the effectiveness of the fuzzy results. It is purely simulated using Matlab Fuzzy Logic Toolbox and verified with Microsoft Excel derivation termed as Caldo's Membership Function Template (CMFT). The fuzzy logic controller for DC-DC buck converter was successfully realized in Spartan 3E Field Programmable Gate Array (FPGA) using VHDL programming language in Xilinx ISE platform.

Keywords: dc-dc buck converter, fuzzy logic, Caldo's Membership Function Template (CMFT), Matlab toolbox, Sugeno-style, Spartan 3E, FPGA, Xilinx ISE, VHDL

1. Introduction

There are four classifications of non-linear control namely: 1) ac-ac converters, 2) ac-dc converters, 3) dc-ac converters, and 4) and dc-dc converters (Ofoli, 2005). An electrical circuit that transfers a dc voltage source to another load is known as direct current – direct current (Dc-dc) converter. This type of converter is a power converter, which acts as a transformer that converts power from one form to another. In other context, this converter is termed as dc voltage converter, as it considers stepping dc voltage source up or down depending on the needs and requirements of the design (Web-1). The dc-dc converter is handy and affordable tool. It is considered to be the heart of the power supply, as it affects the overall performance of the power supply system. The converter accepts dc and produces a controlled dc output (Jaber, 2011). The dc to dc converter will regulate dc input voltage and will produce the required output voltage, which is higher or lower than the input battery voltage. There are

different types of dc-dc converters. Among its typical type is the Buck or step down converter and the Boost or step up converter. Buck converters produce an average output voltage lower than the input source voltage. On the contrary, boost converters produce an average output voltage higher than the input source voltage. In conclusion, when the output voltage set point is less than the input voltage, it is called a Buck converter. On the other hand, when the output voltage set point is higher than the input voltage, then it is a Boost converter (Web-1). In dc-dc converter systems, various traditional methods based on feedback control theory were adopted. However, these methods require complex and tedious computations. Moreover, finding the cost-effective reliable controller is a must for researchers and designers (Ismail et.al, 2010). One of the most commonly used control method is the Proportional Integral (PI) or Proportional Integral Derivative (PID) controller. It is widely used for variety of control systems. This application includes, but not limited to, aerospace, process control, manufacturing, robotics, automation and many more (Chander, 2010). Accordingly, in this type of control method, researchers are finding difficulty in providing good performance both in dynamic and in steady-state responses. This is because the parameters are fixed during operation (Xiao, 2004).

Fortunately, computational intelligence is now available as an alternative and efficient control method, as it reduces the processing time of the controller. There are many variations of intelligent systems. In this study, the proponent preferred to use the concepts and principles of fuzzy logic. Fuzzy Logic Controller (FLC) converts linguistics based on the knowledge of the experts into an automatic control strategy by forming fuzzy rules or rule bases (So, 1994). FLC's operation is not purely concern on the accuracy of the model, but on the effectiveness of the formulated rules. This operation tends to simplify the design for dc-dc converter applications (Caldo et.al, 2013). In 2006, Liping Guo investigated the issues in the design and in the implementation of digital controllers for buck and boost converters using linear and nonlinear control methods in his dissertation (Guo, 2006). On the literatures, Guo cited that the fuzzy logic technology is becoming a trend in today's era of advanced microcomputer technology, from control theory to artificial intelligence (Feng, 2003). This is because fuzzy technology features broad, yet explicit and understandable tool that would replicate and interpret human language without requiring precise and complex mathematical models (So, 2005). Professor Zadeh is the father of fuzzy logic and he articulated that we do not require precise input, yet we are capable of obtaining highly adaptive control (Web-3).

Accordingly, FLC does not require precise mathematical model and it has excellent immunity to external disturbances. However, FLC requires considerable amount of computational power because of its complex and heuristic decision making processes (Taeed, 2010). FLC has drawback in high speed processing applications. The solutions using microcontrollers of general purpose and Digital Signal Processor (DSP) present a slow speed of processing because the fuzzy control is implemented by a software program (Ramos, 2000). Also, DSP is costly and may not be justifiable in certain applications (Taeed, 2010). Another solution, here proposed, is the implementation of the fuzzy control in Field Programmable Gate Array (FPGA) board. FPGAs were predominantly used for implementing simple digital circuits (Compton, 2002). Recently, even undergraduate students are capable of constructing complex digital devices on FPGA chips (Sklyarov, 2005). In FPGA, the development system works on personal computers and it presents high processing speed (Ramos, 2000).

Moreover, advanced researches are being performed intensively in system-on-chip and network-on-chip applications (Sklyarov, 2011). In Philippine setting with no wafer fabrication facility, FPGA-related researches are needed. It will contribute to the growing knowledge of FPGA applications in the Philippines (Marquez, 2011). Fuzzy logic can be chosen as an alternative design method to nonlinear controllers. In fact, FLC can be inexpensively implemented with FPGA-based controller (Rubaai, 2004). In this work, the proponent will integrate fuzzy logic in DC-DC buck conversion using FPGA. The fuzzy logic will represent the software part and the FPGA forms part the hardware of the system.

FPGAs were predominantly used for implementing simple digital circuits (Compton, 2002). Recently, even undergraduate students are capable of constructing complex digital devices on FPGA chips (Sklyarov, 2005). In FPGA, the development system works on personal computers and it presents high processing speed (Ramos, 2000). Moreover, advanced researches are being performed intensively in system-on-chip and network-on-chip applications (Sklyarov, 2011). In Philippine setting with no wafer fabrication facility, FPGA-related researches are needed. It will contribute to the growing knowledge of FPGA applications in the Philippines (Marquez, 2011). Fuzzy logic can be chosen as an alternative design method to nonlinear controllers. In fact, FLC can be inexpensively implemented with FPGA-based controller (Rubaai, 2004). In this work, the proponent will integrate fuzzy logic in DC-DC buck conversion using FPGA. The fuzzy logic will represent the software part and the FPGA forms part the hardware of the system.

1.2 Buck Converter

Intuitively, the name 'buck converter' evolves from the fact that the input voltage is bucked/chopped or attenuated (Yusoff, 2010). The buck converter, as emphasized on previous section, converts the unregulated source voltage *Vin* into a lower (step down) output voltage *Vout*. The ratio of the ON time (*tON*) when the switch is closed to the entire switching period (T) is defined as the duty cycle D = *tON / T* (Lee, 1993). When the switch is open, the diode conducts. The capacitor supplies energy to the load and the inductor current flows through the capacitor and the diode (Mohan et.al, 1995). The output voltage is controlled by changing the duty cycle. During steady state, the ratio of output voltage over input voltage is D, which is given by (1).

$$Vout/Vin = D \qquad \textit{equation 1}$$

1.3 Objectives of the Study

The prime objective of this study is to design and simulate a fuzzy logic controller for dc-dc buck converter in an FPGA. Specifically, this study aims to: a) present the derivation of fuzzy control rules for the buck converter circuit, b) develop a mathematical model of fuzzy logic controller for variable output voltage dc-dc buck (*of 3.3V down to 2V input voltage levels to 1.5 voltage output*), c) develop a modelling variable dc output voltage using MATLAB fuzzy logic toolbox for buck converter, d) simulate and verify the performance of the fuzzy system in an FPGA.

2. Methodology

This research aims to develop a fuzzy-based DC-DC buck converter in an FPGA. The system will require a voltage input from the ADC and it will be converted to its 8-bit equivalent. If the length is 8-bit, it proceeds to normalization process. The two input variables: voltage error (e) and change in error (de) will be normalized. These inputs will be described fuzzily and will be defuzzified using Mamdani and Sugeno style of fuzzy inference systems. The crisp output will be produced using averaging technique. The FPGA conversion and white LED driving system is the main focus of the study. The white LED, being the load, is the one being controlled by the FPGA. The output variable of fuzzy controller is the duty cycle of Pulse Width Modulation (PWM) output. This fuzzy output is converted to a control signal that would come from the FPGA. The FPGA will be responsible for controlling white LED with consideration to the obtained duty ratio.

The functionality of FPGA conversion system is to take digital control signals from the fuzzy logic controller. It will recognize the duty cycle and will display the output to the white LEDs. The interface between the two will be implemented in VHDL code.

The proponent will design the fuzzy logic controller of dc-dc buck converter circuit using MATLAB Fuzzy Logic Toolbox software. The proponent will do assumptions, derivations and computations to make the necessary algorithms for the FPGA. In order to confirm that the mathematical model will give a stable output frequency, simulation on MATLAB will be made. Then, it will be translated for hardware modeling. Afterwards, a VHDL code will be developed on a Xilinx platform. After creating VHDL source codes, it is to be simulated through ModelSim. This simulation is important as it helps the proponent verify his source codes, as to whether it will or will not give the desired results. Should it pass the verification process, then it is ready to be implemented into the FPGA board and drive white LEDs. The source code will take into consideration the frequency, duty cycle and output voltage of the dc-dc buck converter. Most importantly, the test and evaluation of the performance of the fuzzy control system will be initiated.

3. Design Considerations

In pursuit of successful outcomes of the study, the proponent implemented procedures using the developmental method. Primarily, this method aims to achieve the set of objectives to solve the stated problems. Prior to the system's development, this study covers designing of the system. This is where the problem definition, planning and setting up of the objectives were established.
The study also encompasses the testing and evaluation of the system as the proponent used experimental method in the testing of the system's functionality. The proponent conducted set of experiments to tabulate successful and failed results from series of tests.

3.1 Proposed Design

In order to control the DC output voltage of buck converter and to ensure good variable output voltage, the fuzzy logic controller for closed loop control of DC-DC converter is proposed in this project. The proposed system consists of dc-dc buck converter to maintain dc voltage.

The system requires voltage input from the user after the ADC conversion process. It will be interpreted in an 8-bit digital input and it will be processed using fuzzy logic system to produce an 8-bit voltage output. The stepping down of the voltage input is simulated using Modelsim. The implementation for buck converter in FPGA is purely mathematical.

The fuzzy logic controller is the main focus of the whole system and it will be implemented using the Spartan-3E family of Field-Programmable Gate Array (FPGA) board. This FPGA family has the following features: very low cost, high-performance logic solution for high-volume, consumer-oriented applications, proven advanced 90-nanometer process technology, multi-voltage, multi-standard SelectIO™ interface pins and up to 376 I/O pins or 156 differential signal pairs (Web-4). The buck circuit and the ADC circuit are the hardware devices in the system that will be interfaced to the controller. The FLC will administer the whole system's operation including the output of the buck circuit in order to drive the specified buck load. The fuzzy logic controller will produce a duty cycle as its crisp output. The ADC circuit will serve as the feedback and monitoring circuit for the system. The buck load will attest to the driving power of the resulting output voltage of the buck circuit and will serve as the input to the feedback system (Liu et.al, 2005).

During system operation, given a specified input voltage for the buck circuit, the output voltage of the buck will decreased due to the clock signal provided by the PWM module obtained from the duty cycle (*measured in percentage*). The clock signal is necessary to drive the power transistor of the buck circuit. The output voltage of the buck will be able to drive the specified buck load. The buck load consists of a specified load and a load resistor. The buck load will have an equivalent load voltage (resistor voltage) that will provide the ADC circuit input. The ADC circuit output will be delivered to the PWM generator in order to provide the necessary clock signal that will satisfy the required output voltage needed to drive the load. This operation goes on whenever the input voltage of the buck circuit varies. This maintains the output efficiency of the system. There are two (2) input parameters necessary to step down the voltage input to desired voltage output. Duty cycle is the output parameter of the FLC and it will be fed back to the controller until the desired voltage is satisfied for a specific dc-dc converter circuit.

The last phase of fuzzy logic systems' operation is vital. This method is known as defuzzification. To get the crisp output, a popular method known as the center-of-gravity formula is used. This is given by (2).

$$\text{Center of Gravity} = \frac{\sum_{i=1}^{n} o_i \cdot \mu_i}{\sum_{i=1}^{n} \mu_i}$$

equation 2

The ADC conversion is necessary to convert the analog values to digital fuzzy inputs. The fuzzy sets will be deffuzified and it will give a crisp output that will be fed to the DC-DC converter system. The cycle continues until the desired output voltage is achieved.

As for the step-by-step process to be followed in programming FLC for DC-DC buck converter using DevCpp. The proponent considers the following. First, the user has to define the pre-processor commands and initialize constant values. The next step is to construct the main body of the program. This includes the declaration of global/local variables, the function/s to be used and the process executions to be undertaken. Then, build the Fuzzy Logic System operation by *looping*, *switch* and *if-else* statements. Compute for the degrees of membership by Triangular membership function and compute for the crisp output. Finally, display weight values of FAM Matrix entries and the crisp output. The fuzzy controller for a DC-DC converter has two inputs. The first input is the error in the output voltage e[k] = Ref - ADC[k], where ADC[k] is the converted digital value of the k^{th} sample, and Ref is the digital value corresponding to the desired output voltage (*in this work, 1.5 V*). The second input, ce[k] = e[k]-e[k-1], is the difference between the error of the k^{th} sample and the error of the $(k-1)^{th}$ sample. The two inputs are normalized and will be fed into the fuzzy controller. The output of the fuzzy controller is the duty cycle d[k]. It is measured in percentage. The values are normalized in -1 to 1 range and it can be tuned to obtain satisfactory response (Guo, 2006).

3.2 Fuzzy Rule Based System

A set of rules is constructed for classifying dc-dc converter as Positively Big (PB), Positively Small (PS), Zero Area (ZO), Negatively Small (NS) and Negatively Big (NB) (Caldo et.al, 2012). The AND operator was used and represented in rule bases. Hierarchical structure for dc-dc buck converter classification resulting in set of rules can be constructed. Voltage error (ve) and change in error (de) will be judged in the first hierarchical level of knowledge base. The last hierarchical level will characterize the duty ratio with respect to dc-dc buck converter. Following are the sample rules stored at two different hierarchical levels of the knowledge base:

- If *Voltage Error* is <NB> and *Change in error* is <NB> Then *Duty Cycle of PWM Output* is <NS>
- If *Voltage Error* is <NB> and *Change in error* is <NS> Then *Duty Cycle of PWM Output* is <ZO>
- If *Voltage Error* is <NB> and *Change in error* is <ZO> Then *Duty Cycle of PWM Output* is <PS>

3.3 Fuzzy Logic Controller for the Proposed System

In this study, the input parameters are voltage. The error e(k) and change in error Δe(k) are inputs to the FLC system, which were normalized. The error is computed by comparing equation (3). From the computed error e(k) and previous error [E previous(k)], the change in error is computed as elicited in equation (4).

$$e(k) = Vref(k) - Vo(k) \quad \textit{equation 3}$$

$$\Delta e(k) = e(k) - [E\ previous(k)] \quad \textit{equation 4}$$

Five linguistic variables are used for the input variable e(k) and Δe(k). They are NB, NS, ZO, PS and PB. There are many types of membership functions. This includes triangular-shaped, trapezoidal-shaped, Gaussian, sigmoid, pi-shaped, bell-shaped and so forth. For simplicity, the triangular membership function will be used in this study

for easy and reduced calculations. In this work, only five membership functions are to be used for two inputs: error and change in error. The input fuzzy membership functions are shown in Figures 1 and 2. The triangular membership functions for data inputs voltage error and change in error is normalized in the range of -1 to 1. The proponent chooses such range to have a more centralized set of normalized data, with zero being the central point (Web-2).

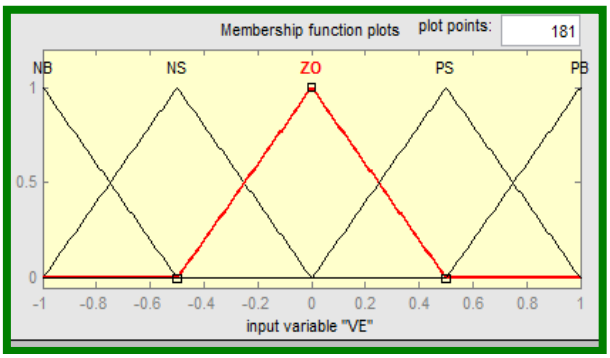


Figure 1: Error (input)

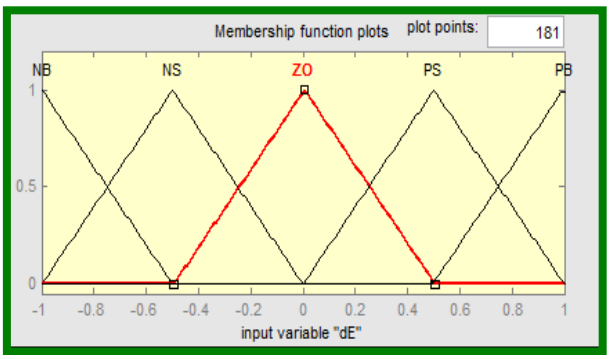


Figure 2: Change in error (input)

The rule table for the FLC-based buck converter is given in Table 1. The element in weight 1 means that, *"If error is NB and change in error is NB then output is NS"* while the element in weight 2 means that, *"If error is NB and change in error is NS then output is ZO"*. Also, the element in weight 24 means that, *"If error is PB and change in error is PS then output is NB"* while the element in weight 25 means that, *"If error is PB and change in error is PB then output is NS"*.

Table 1: Fuzzy rules for buck converter

WEIGHTS	LINGUISTIC INPUTS	LINGUISTIC OUTPUT	INPUT		OUTPUT
			1st	2nd	
w1	If (e) is <NB> and (de) is <NB>	Then duty cycle of PWM output is <NS>	NB	NB	**NS**
w2	If (e) is <NB> and (de) is <NS>	Then duty cycle of PWM output is <ZO>	NB	NS	**ZO**
w3	If (e) is <NB> and (de) is <ZO>	Then duty cycle of PWM output is <PS>	NB	ZO	**PS**
w4	If (e) is <NB> and (de) is <PS>	Then duty cycle of PWM output is <PB>	NB	PS	**PB**
w5	If (e) is <NB> and (de) is <PB>	Then duty cycle of PWM output is <PS>	NB	PB	**PS**
w6	If (e) is <NS> and (de) is <NB>	Then duty cycle of PWM output is <ZO>	NS	NB	**ZO**
w7	If (e) is <NS> and (de) is <NS>	Then duty cycle of PWM output is <PS>	NS	NS	**PS**
w8	If (e) is <NS> and (de) is <ZO>	Then duty cycle of PWM output is <PB>	NS	ZO	**PB**
w9	If (e) is <NS> and (de) is <PS>	Then duty cycle of PWM output is <PS>	NS	PS	**PS**
w10	If (e) is <NS> and (de) is <PB>	Then duty cycle of PWM output is <ZO>	NS	PB	**ZO**
w11	If (e) is <ZO> and (de) is <NB>	Then duty cycle of PWM output is <PS>	ZO	NB	**PS**
w12	If (e) is <ZO> and (de) is <NS>	Then duty cycle of PWM output is <PB>	ZO	NS	**PB**
w13	If (e) is <ZO> and (de) is <ZO>	Then duty cycle of PWM output is <PS>	ZO	ZO	**PS**
w14	If (e) is <ZO> and (de) is <PS>	Then duty cycle of PWM output is <ZO>	ZO	PS	**ZO**
w15	If (e) is <ZO> and (de) is <PB>	Then duty cycle of PWM output is <NS>	ZO	PB	**NS**
w16	If (e) is <PS> and (de) is <NB>	Then duty cycle of PWM output is <PB>	PS	NB	**PB**
w17	If (e) is <PS> and (de) is <NS>	Then duty cycle of PWM output is <PS>	PS	NS	**PS**
w18	If (e) is <PS> and (de) is <ZO>	Then duty cycle of PWM output is <ZO>	PS	ZO	**ZO**
w19	If (e) is <PS> and (de) is <PS>	Then duty cycle of PWM output is <NS>	PS	PS	**NS**
w20	If (e) is <PS> and (de) is <PB>	Then duty cycle of PWM output is <NB>	PS	PB	**NB**
w21	If (e) is <PB> and (de) is <NB>	Then duty cycle of PWM output is <PS>	PB	NB	**PS**
w22	If (e) is <PB> and (de) is <NS>	Then duty cycle of PWM output is <ZO>	PB	NS	**ZO**
w23	If (e) is <PB> and (de) is <ZO>	Then duty cycle of PWM output is <NS>	PB	ZO	**NS**
w24	If (e) is <PB> and (de) is <PS>	Then duty cycle of PWM output is <NB>	PB	PS	**NB**
w25	If (e) is <PB> and (de) is <PB>	Then duty cycle of PWM output is <NS>	PB	PB	**NS**

From the tabulated table for buck converter, the fuzzy rule base is formulated into 25 rules. The reverse process of fuzzification is called defuzzification. In this method, the linguistic variables are being converted into its equivalent numerical values. As the weighted sum method is considered to be the best well-known defuzzification method, it is utilized in the present model. The defuzzified output is the duty cycle dc(k), which can also be classified as PB, PS, ZO, NS and NB.

3.4 Matlab Fuzzy Logic Toolbox

Primarily, there are five (5) graphical user interface (GUI) tools for building, editing and observing fuzzy inference systems in the toolbox. This includes, Fuzzy Inference System (FIS) editor as shown in Figure 3, Membership Function Editor (Figures 1 and 2), Rule Editor (Figure 4), Rule Viewer (Figure 5) and Surface Viewer (Figure 6). These GUIs are dynamically linked with each other, and if changes were made to the FIS of one of the toolbox, the effect can be seen in other GUIs.

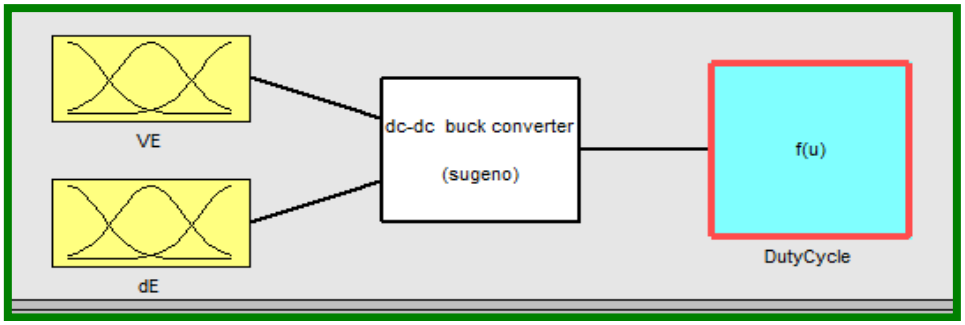


Figure 3: FIS editor for buck

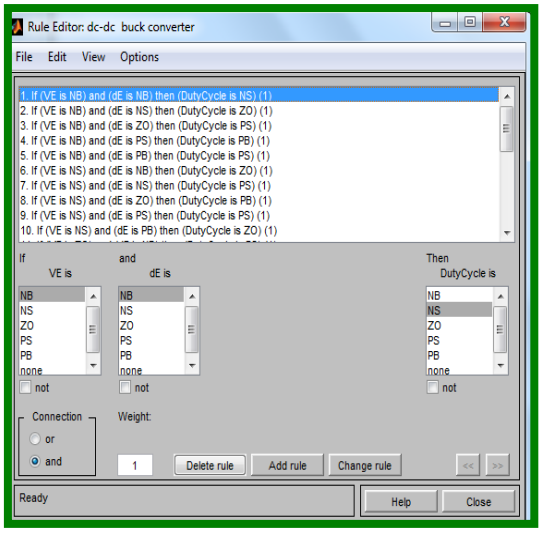


Figure 4: Rule editor for buck

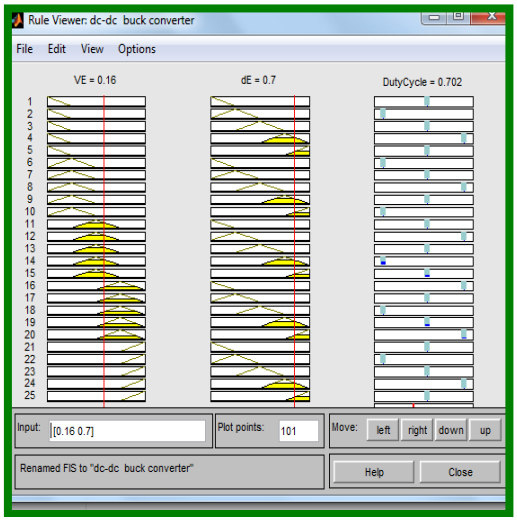


Figure 5: Rule viewer for buck

Figure 4 is the rule editor for the buck converter. It is where the FAM matrix of 25 rules is plugged in. On the other hand, the graphical illustration of the rules for buck simulation purposes is elicited in Figure 5. This is where the user can manually input values for VE and dE and obtain the duty cycle. The surface view of the buck converter with voltage error as the x-axis, change in error as the y-axis and duty cycle as the z-axis is shown in Figure 6.

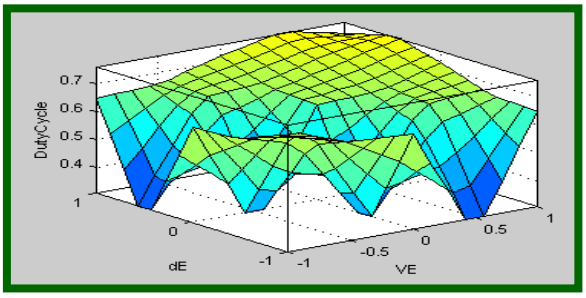


Figure 6: Surface viewer for buck

3.5 Implement the System

Finally, the FLC for buck converter, which is purely mathematical (VHDL coded) is implemented in Spartan-3E FPGA. Figure 7 on the next page shows the RTL schematic of buck converter circuit when *'fuzzyfinal2'* was set as top module. It could be observed that there are five unit modules (u0, u1, u2, u3 and u4). The number of bits for input and output parameters is allocated including the interconnection of each submodules. The *'samplecorrector'* module fetches the input voltage from the ADC circuit and it will be converted from 8-bit to 12-bit. The *'errorgen'* module will then generate the voltage error and the *'normalizer'* module will normalize the error, so as to fit the membership functions assigned by the proponent. The normalized output is processed in *'fuzzyfinal'* module. This module produces the quotient in 24-bit. The *'buck'* module is responsible for fetching the duty cycle in 12-bit. It produces the voltage output in 24-bit and it will be sent back to *'errorgen'*. The cycle continues until the system is able to achieve the desired output voltage.

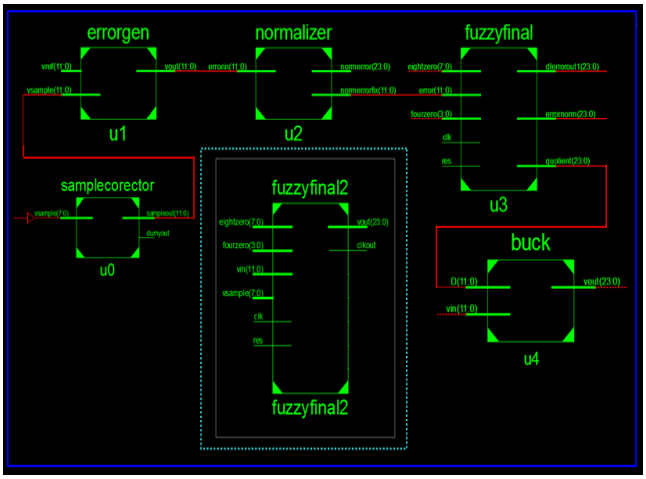


Figure 7: RTL schematic of buck converter circuit

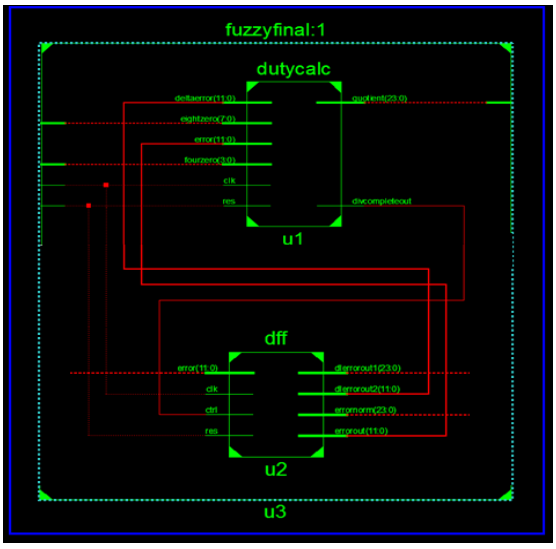


Figure 8: RTL schematic of buck converter circuit

(Top module: fuzzyfinal2) (Top module: fuzzyfinal)

Figure 8 shows the *'fuzzfinal'* module, which applies to buck converter. This module is responsible for calculating the crisp output (duty cycle) obtained from the quotient of cgout and wtotal. The parameter 'cgout' is the numerator and 'wtotal' is the denominator. The numerator is obtained by adding the product of each constant and its equivalent weights. On the other hand, the denominator is the summation of the 25 weights.

4. Experiments and Analysis of Results

The experimentation is done systematically. First, the ADC gives an 8-bit digital input voltage and it was converted to 4-bit integer part and 8-bit fractional part to achieve accuracy. The program automatically computes for the voltage error and the change in error in 12-bit binary format. The FLC computes for the 10 triangular membership functions and generates the 25 weights. Finally, it gives a duty cycle that will step down (buck) the input voltage. It will be expressed in percentage for PWM module. Then, a feedback will be sent so as to monitor if the required output voltage has been achieved, if not, the FLC controller will continuously adjust the PWM module of the FPGA until the required output voltage is attained. In identifying the exact error that occurred in an approximation, the true value (V) is subtracted from the approximate value ($V_{approximate}$) obtained for different trials. This is commonly known as the absolute error formula, which is given by (5).

$$\text{Absolute Error} = V_{absolute} = | V - V_{approximate}| \qquad \textit{equation 5}$$

Relative error compares the size of the error to the size of the object being measured (Web-5). In this test, the proponent expressed its relative error in percent. It is known as the Percentage Relative Error, given by (6).

$$\text{Percentage Relative Error} = (\text{Absolute Error} / \text{True Value}) * 100 \qquad \textit{equation 6}$$

In simulating the DC-DC buck converter system, the proponent conducted 14 trials for different voltage inputs of range 2 to 3.3 in stepping down the input voltage to desired voltage output of 1.5 as shown in Table 2. This simulation is made for two different metrologies: Fuzzy Logic Matlab Toolbox and Excel Fuzzy Derivation termed as Caldo's Membership Function Template (CMFT). The proponent derived the Sugeno-style and Mamdani FIS fuzzy logic algorithms for dc-dc buck converter using Microsoft Excel and named it as CMFT (Caldo et.al, 2013). The results obtained using Matlab Fuzzy Logic Toolbox was compared with the results obtained using CMFT. The comparison between these two methods for obtained PWM duty cycle is tabulated. It was realized that there was a perfect correlation between the crisp outputs obtained for both methods. This means that there is perfect correlation of the variables being compared, regardless of input range. In general, Microsoft Excel and Matlab Fuzzy Logic Toolbox, of different programming platforms and of different methodologies, are correlated with each other and can both be powerfully used in dc-dc buck converter simulation.

Table 2: Complete simulation results for dc-dc buck converter

Matlab Fuzzy Logic Toolbox Simulation Results (DC-DC Buck Converter)								
Vin	Vref	No. of Iterations	Vout - Vref	VE[pre]-VE[now]	normalized inputs		Crisp Output	Vin*D
			Voltage Error	Change in Error	VE	dE	Duty Cycle	Vout
2	1.5	1	2	2	0.55	0.55	0.729	1.46
2.1	1.5	1	2.1	2.1	0.59	0.59	0.735	1.54
2.2	1.5	1	2.2	2.2	0.62	0.62	0.738	1.62
2.2	1.5	2	0.12	2.08	-0.1	0.58	0.666	1.47
2.3	1.5	1	2.3	2.3	0.66	0.66	0.742	1.71
2.3	1.5	2	0.21	2.09	-0.07	0.58	0.667	1.53
2.4	1.5	1	2.4	0.744	0.69	0.69	0.744	1.79
2.4	1.5	2	2.11	0.669	-0.04	0.59	0.669	1.61
2.5	1.5	1	2.5	2.5	0.72	0.72	0.745	1.86
2.5	1.5	2	0.36	2.14	-0.01	0.6	0.672	1.68
2.6	1.5	1	2.6	2.6	0.76	0.76	0.745	1.94
2.6	1.5	2	0.44	2.16	0.01	0.61	0.674	1.75
2.6	1.5	3	0.25	0.19	-0.05	-0.07	0.565	1.47
2.7	1.5	1	2.7	2.7	0.79	0.79	0.744	2.01
2.7	1.5	2	0.51	2.19	0.04	0.62	0.679	1.83
2.7	1.5	3	0.33	0.18	-0.02	-0.08	0.575	1.55
2.7	1.5	4	0.05	0.28	-0.12	-0.04	0.537	1.45
2.8	1.5	1	2.8	2.8	0.83	0.83	0.742	2.08
2.8	1.5	2	0.58	2.22	0.06	0.63	0.682	1.91
2.8	1.5	3	0.41	0.17	0	-0.08	0.586	1.64
2.8	1.5	4	0.14	0.27	-0.09	-0.04	0.558	1.56
2.8	1.5	5	0.06	0.08	-0.12	-0.11	0.508	1.42
2.9	1.5	1	2.9	2.9	0.86	0.86	0.74	2.15
2.9	1.5	2	0.65	2.25	0.09	0.64	0.687	1.99
2.9	1.5	3	0.49	0.16	0.03	-0.08	0.59	1.71
2.9	1.5	4	0.21	0.28	-0.07	-0.04	0.571	1.66
2.9	1.5	5	0.16	0.05	-0.08	-0.12	0.521	1.51
3	1.5	1	3	3	0.9	0.9	0.736	2.21
3	1.5	2	0.71	2.29	0.11	0.65	0.691	2.07
3	1.5	3	0.57	0.14	0.06	-0.09	0.588	1.76
3	1.5	4	0.26	0.31	-0.05	-0.03	0.591	1.77
3	1.5	5	0.27	-0.01	-0.04	-0.14	0.524	1.57
3	1.5	6	0.07	0.2	-0.11	-0.07	0.531	1.59
3	1.5	7	-1.41	1.48	-0.62	0.37	0.5	1.5
3.1	1.5	1	3.1	3.1	0.93	0.93	0.732	2.27
3.1	1.5	2	0.77	2.33	0.13	0.67	0.695	2.15
3.1	1.5	3	0.65	0.12	0.09	-0.1	0.586	1.82
3.1	1.5	4	0.32	0.33	-0.03	-0.02	0.612	1.9
3.1	1.5	5	0.4	-0.08	0	-0.17	0.514	1.59
3.1	1.5	6	0.09	0.31	-0.11	-0.03	0.549	1.7
3.1	1.5	7	-1.4	1.49	-0.62	0.38	0.504	1.56
3.2	1.5	1	3.2	3.2	0.97	0.97	0.726	2.32
3.2	1.5	2	0.82	2.38	0.14	0.68	0.697	2.23
3.2	1.5	3	0.73	0.09	0.11	-0.11	0.583	1.87
3.2	1.5	4	0.37	0.36	-0.01	-0.01	0.634	2.03
3.2	1.5	5	0.53	-0.16	0.04	-0.19	0.511	1.64
3.2	1.5	6	0.14	0.39	-0.09	0	0.578	1.85
3.2	1.5	7	-1.35	1.49	-0.6	0.38	0.512	1.64
3.2	1.5	8	-1.56	0.21	-0.68	-0.07	0.43	1.38
3.2	1.5	9	-1.82	0.26	-0.77	-0.05	0.485	1.55
3.3	1.5	1	3.3	3.3	1	1	0.72	2.38
3.3	1.5	2	0.88	2.42	0.17	0.7	0.703	2.32
3.3	1.5	3	0.82	0.06	0.14	-0.12	0.583	1.92
3.3	1.5	4	0.42	0.4	0.01	0	0.65	2.15
3.3	1.5	5	0.65	-0.23	0.09	-0.22	0.507	1.67
3.3	1.5	6	0.17	0.48	-0.08	0.03	0.59	1.95
3.3	1.5	7	-1.35	1.52	-0.6	0.39	0.517	1.71
3.3	1.5	8	-1.59	0.24	-0.69	-0.06	0.432	1.43
3.3	1.5	9	-1.87	0.28	-0.78	-0.04	0.489	1.61

5. Conclusion

Developed in this research is a simulation model of buck converter using three programming platforms: Matlab Fuzzy Logic Toolbox, DevCpp and Excel VB Macro. The proponent had developed the fuzzy logic controller by fine tuning and trial and error method using the Mamdani and Sugeno style of fuzzy inference systems, the FAM Matrix for buck converter used by (Yusoff et.al, 2010)in the paper, *'Comparative Study of Fuzzy Logic Controller and Proportional Integral Derivative Controller on DC-DC Buck Converter'*, and the Output Membership Functions used by (Safarinejadian et.al, 2012) on their paper entitled, *'Hybrid Fuzzy Logic Controllers for Buck Converter'*. The FPGA-based hardware model of buck converter in one fuzzy logic controller to control duty cycle of Pulse Width Modulation (PWM) signal generator is VHDL coded and tested for accuracy and reliability. It has been verified experimentally from the simulations and actual data analysis presented that the FPGA-based FLC controller is working properly, considering that it established perfect correlation with three programming platforms used in the study. The novelty of this research is the use of three different programming platforms for simulation, fine tuning, monitoring and controlling purposes.

6. Recommendation and Future Directives

This research aims to provide a study of integration of a FLC controller in the FPGA platform, which is to be used in a DC-DC buck converter. If further researchers would want to provide improvement of the present research, the proponent has a few points of recommendations that might help. The proponent makes use of five (5)

classifications to interpret the 25 linguistic rules using triangular membership functions. Future researchers could go for higher classifications to generate larger number of rules. Also, they can use other type of membership functions such as trapezoidal and gaussian both for the input and output parameters. The performance of fuzzy control system was tested and evaluated in terms of accuracy and reliability. The system could be tested for load and line regulations. Also, the settling time could further be improved as its performance indicator. The implementation of buck converter in FPGA is purely mathematical. It is recommended to implement it in a hardware model using actual buck converter circuit. If greater efficiency is needed, the proponent recommends implementing the FPGA-based FLC controller on a boost and buck-boost converter. Also, the buck circuit design is limited to an input voltage range of 2V - 3.3V. Another recommendation, in response to the design limitations, would be to implement a design that would allow buck circuit higher than 3.3V. In addition, future researchers could consider using other computational intelligence metrologies such as neural networks, fuzzy-neural and genetic algorithms.

References

[1] Caldo R.B. and Dadios E. (2012). Fuzzy Logic Control of Water Quality Monitoring and Surveillance for Aquatic Life Preservation in Taal Lake. *Proceedings of the 2012 IEEE International Conference,* Cebu, Philippines.

[2] Caldo R.B. and Yap R.Y. (2013). Design, Development and Implementation of a Fuzzy Logic Controller for DC-DC Buck and Boost Converter in an FPGA. *Proceedings of the 2013 International Conference on Control Automation and Information Sciences (ICCAIS),* Nha Trang, Vietnam,25-28 November 2013

[3] Caldo R.B. and Yap R.Y. (2013). Simulation of Fuzzy Logic Controller for DC-DC Buck and Boost Converter in Three Programming Platforms. *Proceedings of the 2013 Asia Pacific Industrial Engineering and Management System (APIEMS),* Cebu, Philippines, 3-6 December 2013.

[4] Chander S., Agarwal P. and Gupta I. (2010). FPGA-based PID Controller for DC-DC Converter. *Proceedings of the 2010 IEEE International Conference.*

[5] Compton K. and Hauck S. (2002). Reconfigurable Computing: A Survey of Systems and Software. *ACM Computing Surveys,* vol. 34, no. 2, June 2002, pp. 171–210.

[6] Feng G., Zhang W. and Liu Y. (2003). An Adaptive Current Mode Fuzzy logic Controller for DC-DC Converters. *Proceedings of the 2003 IEEE International Conference.*

[7] Guo L. (2006). Design and implementation of digital controllers for buck and boost converters using linear and nonlinear control methods. Ph.D. dissertation, Auburn University, Auburn, Alabama, August 7, 2006.

[8] Ismail N., Musirin I., Baharom R. and Johari D. (2010). Fuzzy Logic Controller on DC/DC Boost Converter. *Proceedings of the 2010 IEEE International Conference on Power and Energy*, Kuala Lumpur, Malaysia, Nov 29 – Dec 1, 2010

[9] Jaber F.S. (2011). Development of a dc-dc buck boost converter using fuzzy logic control. M.S. thesis, Universiti Tun Hussein Onn, Malaysia, May 2011.

[10] Lee Y. S. (1993). *Computer-Aided Analysis and Design of Switch-Mode Power Supplies*. Marcel Dekker, Inc., New York, Basel, Hong Kong.

[11] Liu Y. and Sen P. C. (2005). Digital Control of Switching Power Converters. *Proceedings of the 2005, IEEE Conference on Control Applications*, Toronto, Canada, August 28-31, 2005.

[12] Mohan N., Undeland T. M. and Robbins W. P. (1995). *"Power Electronics: Converters, Applications, and Design"*.John Wiley & Sons, Inc.
[13] Ofoli A. and Rubaai A. (2005). Real-Time Implementation of a Fuzzy Logic Controller for DC-DC Switching Converters. *Proceedings of the 2005 IEEE International Conference.*
[14] Ramos R., Roset X. and Mhuel A. (2000). Implementation of Fuzzy Logic Controller for DC/DC Converters Using Field Programmable Gate Array (FPGA). *Proceedings of the 2000 IEEE International Conference.*
[15] Rubaai A. and Chouikha M. (2004). Design and Analysis of Fuzzy Controllers for DC-DC Converters. *Proceedings of the 2004 IEEE International Conference.*
[16] Safarinejadian B. and Jafartabar F. (2012). Hybrid Fuzzy Logic Controllers for Buck Converter. *Proceedings of the 2012 International Conference on Artificial Intelligence and Image Processing (ICAIIP'2012),* Dubai (UAE), October 6-7, 2012.
[17] Sklyarov V. and Skliarova I. (2005). Teaching Reconfigurable Systems: Methods, Tools, Tutorials and Projects. *IEEE Trans. on Education*, vol.48, no. 2, May 2005, pp. 290-300.
[18] Sklyarov V., Skliarova I. and Sudnitson A. (2011). FPGA-based systems in information and communication. *Proceedings of the 2011 IEEE International Conference.*
[19] So W. C., Tse C. K. and Lee Y. S. (1994). A Fuzzy Controller for DC-DC Converter. *Proceedings of the 1994 IEEE International Conference.*
[20] So W., Tse C. and Lee Y. (2005). Development of a Fuzzy Logic Controller for DC/DC Converters: Design, Computer Simulation, and Experimental Evaluation. *Proceedings of the 2005 IEEE International Conference.*
[21] Taeed F., Salam Z. and Ayob, S.M. (2010). Implementation of Single Input Fuzzy Logic Controller for Boost DC to DC Power Converter. *Proceedings of the 2010 IEEE International Conference on Power and Energy,* Kuala Lumpur, Malaysia, November 29 – December 1, 2010.
[22] Xiao W. and Dunford W. (2004). Fuzzy Logic Auto-Tuning Applied on DC-DC Converter. *Proceedings of the 30th Annual Conference of the IEEE Industrial Electronics Society,* Busan, Korea, November 2-6, 2004.
[23] Yusoff M.J, Ismail N., Musirin I., Hashim N. and Johari D. (2010). Comparative Study of Fuzzy Logic Controller and Proportional Integral Derivative Controller on DC-DC Buck Converter. *Proceedings of the 4th International Power Engineering and Organization Conference (PEOCO2010*), Shah Alam, Selangor, Malaysia, June 23-24, 2010.
[24] http://dcdcconverter.org/, consulted 23 July 2015.
[25] http://www.benetzkorn.com/2011/11/data-normalization-and-standardization/, consulted 23 July 2015.
[26] http:// www.seattlerobotics.org/encoder/mar98/fuz/flindex.html/, consulted 23 July 2015.
[27] http://www.xilinx.com/support/documentation/data_sheets/ds312.pdf, consulted 23 July 2015.
[28] http://www.math.tutorvista.com/number-system/percentage-relative-error.html, consulted 23 July 2015.

eureca 2016 – Conference Paper
Paper Number EE_UG17

Water Quality Assessment Using Back Propagation Network for Aquatic Life Preservation in Taal Lake

Joseph T. Seranilla*, Rionel Belen Caldo

Computer Engineering Department, Lyceum of the Philippines University – Laguna

Corresponding email: *jhayseranilla06@yahoo.com

Abstract
Artificial Neural Network (ANN) being a program-based computational intelligence technique is acquiring knowledge through training and learning. Considering that this tool is suited to environmental problems involving control and operation of multiple parameters, the proponent combines the concepts and principles of fuzzy logic and ANN and then uses them in assessing the quality of water in Taal Lake of Batangas City. Through the use of the sample raw of data of relative levels coming from the environmental quality standards of surface water and standard values, the parameters in the model are acquired. The goal of the study is to train and test an ANN system and compare the results with the use of fuzzy logic.

Keywords: artificial neural network; fuzzy logic; water quality; Taal Lake; environmental assessment

1. Introduction

A standout amongst the most essential elements of water quality assessment is measuring and observing its physical, chemical and biological parameters. At present, different studies concentrated on the measures of these critical water quality evaluation parameters. However, the operations of those measurements and assessments usually depend on the human operation with experience. At the appropriate time, the nature of characterizing such evaluation for particular use included significant instabilities [1].

The greater part of the accessible strategies and instruments which intend to screen water quality parameters continuously is costly and require broad investigation. In the Philippines, it is important to lead examines that would address aquatic life concerns. Adjusted to this, the proponent might want to propose the use of Artificial Neural Network (ANN), which is showed in Figure 3, to help in providing less expensive tool to assess water quality. This endeavor is a continued study of water quality assessment in Taal Lake. The latter was entitled, *Fuzzy Logic Control of Water Quality Monitoring and Surveillance for Aquatic Life Preservation in Taal Lake*.

The water ecological quality evaluation including the single-element assessment and the coordinated assessment is characterized as the quantitative or qualitative assessment process for water quality base on the utilization and consumption of water as noted by the water quality examination and the observing data [2].

There are diverse strategies to discover rules, patterns and their relationships in a set of data. Artificial neural network (ANN) is a program-based computational intelligence technique, which is firstly introduced to understand the simulation of human brain via mathematical model [3]. Recently, ANN has been broadly used in different environmental models and processes. The ANN models have the ability to correctly represent complex and non-linear behaviors of poorly understood processes. It makes a system or model highly suited to the assessment of the fuzzy systems [4].

Recently, the ANN technology has been used to assess the quality of water environment because of the unique self-learning, self-composed, nonlinear approximation capability and good fault tolerance. Along these lines, the research of the water ecological quality evaluation has been done in light of the neural system in this paper [5].



Figure 1. Taal Lake [photo courtesy of Balikas]

1.1 Objectives of the Study

Applying ANN in water quality assessment in Taal Lake is the main goal of this research. Specifically, this study aims to: a) train and test critical water quality parameters (inputs) of Taal Lake, b) develop a neuro-based water quality monitoring system in Taal Lake, c) test and assess the performance of the ANN system, and d) compare the results of using ANN versus Fuzzy Logic

This paper comprises of the following major segments. In segment 2, the proponent describes the detailed assessment model. Segment 3 exhibits the evaluation occasion and the outcomes. Segment 4 finishes up the paper.

2. Integrated Assessment Model for Water Environmental Quality

2.1. Neural Network

Since 1990, neural network had become a frontal subject with fast development in the fields of engineering and information technology [6]. Because of its limited application, comprehensive consideration is vital in neural network in terms of filling the demands of engineering and characterizing their models.

Back-propagation (BP) neural network, as considered to be a simple structure, requiring fast and easy calculations for mu lti-input/multi-output parameters is a good choice in the application of integrated assessment for water environmental quality.

2.2. Integrated Assessment Model

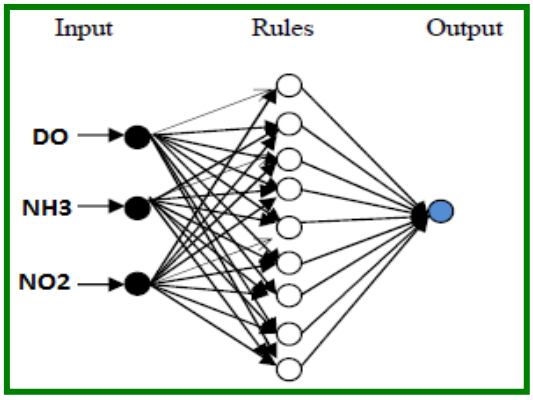


Figure 2. The flow chart of ANN

The flowchart of the ANN as shown in Figure 2 has three layers: the input layer, the hidden layer and the output layer. It can be noted that the number of input layer is the same as the input variables (DO, NH_3 and NO_2). The number of units in the hidden layer cannot be less than the number of training cases. The output layer, on the other hand, is dividing the output of the associated previous layer by each unit in the output layer. [7].

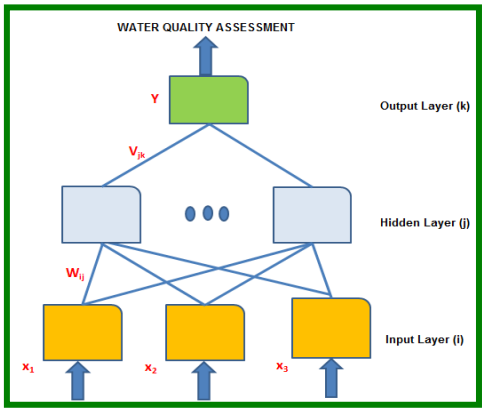


Figure 3. The model of integrated assessment which is based on BP neural network

As shown in Figure 3, the model of integrated assessment has been up and described with three layers: input, hidden, and output which is in line with BP neural network. To make the model clearly describe, the set of X defined as the input layer while the Y as the output node. [5]

Figure 4 below is a further description of the process of the BP neural networks algorithm [8]. It can be observed that the error value being calculated between the values of the output and the target should be less than the allocated tolerance error. If this condition was met for all predefined parameters, it only suggests that the requirements of BP neural networks were achieved.

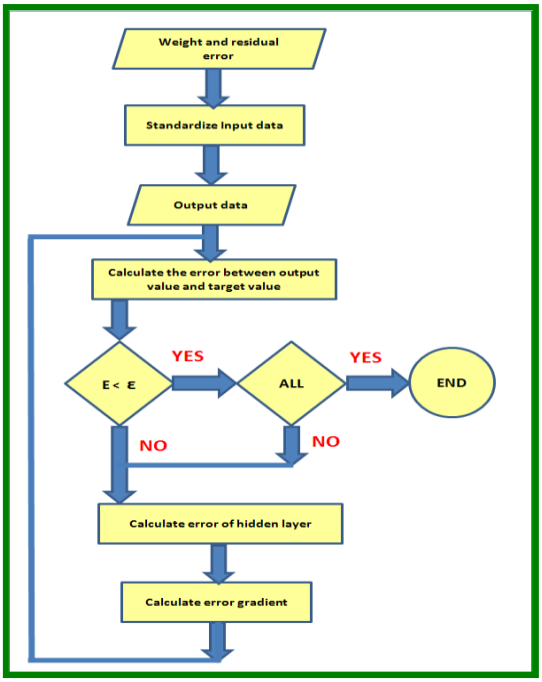


Figure 4. Flowchart of BP neural networks algorithm

2.3. Fuzzy Logic Interface Systems

Fuzzy method is obtained from capability of human. This method develops membership functions based on human understanding. [9].

In the beginning, the proponents distinguished water quality specialists. The proponents with the specialists had gathered applicable field information for capability purposes. Considering the accessible information to be utilized for investigation is inadequate, the proponents created information on the scope of qualified information. Using poll and interview, the view of specialists about the semantic portrayal of lake water quality for checking and reconnaissance was acquired. The parameters distinguished for characterizing water quality by the specialists are: Ammonia (NH3), Nitrite (NO2) and Dissolved Oxygen (DO) as shown in Figure 5.

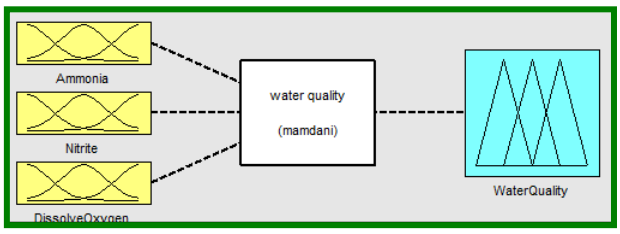


Figure 5. Fuzzy Inference System

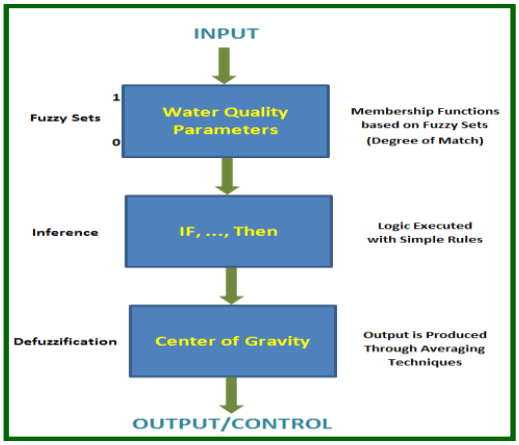


Figure 6. Fuzzy Logic Control Process

In outline, a fuzzy choice is the output of measuring the proof and its significance in the same way that people decide. Fluffy logic reflects human-like deduction where the human can derive a deduce an imprecise conclusion from an accumulation of uncertain premises [10].

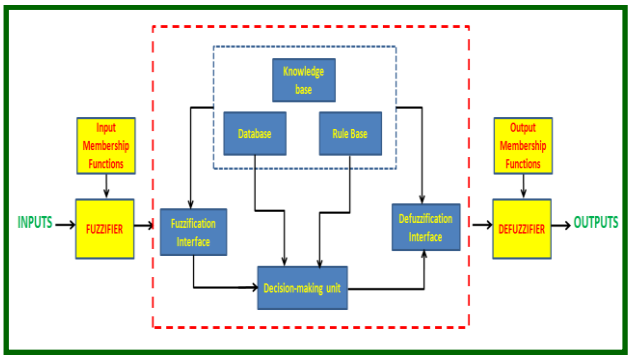


Figure 7. Fuzzy Inference System (FIS) Configuration

The proponents make used of Mamdani method for the accompanying convincing reasons: a) it is unconstrained, b) it is normally utilized and generally acknowledged and c) it is suited to framework requiring human mediation.

2.3.1 Input/Output Membership Functions

In this study, there are three inputs into the water quality fuzzy controller, namely, ammonia, nitrite and dissolve oxygen. In line with this, there are three membership functions used to describe each critical water parameters. Every capacity is marked Very Poor, Poor, Fair, Good, and Very Good, and is appeared in Figure 8. The membership functions are indistinguishably named for better investigation. The yield of surveying the nature of water chooses whether the water quality is Highly Not Acceptable (HNA), Not Acceptable (NA), Just Acceptable (JA), Acceptable (A) or Highly Acceptable (HA). As shown in figure 9, binary value represents the functions. 1 as the highest and 0 as the lowest.

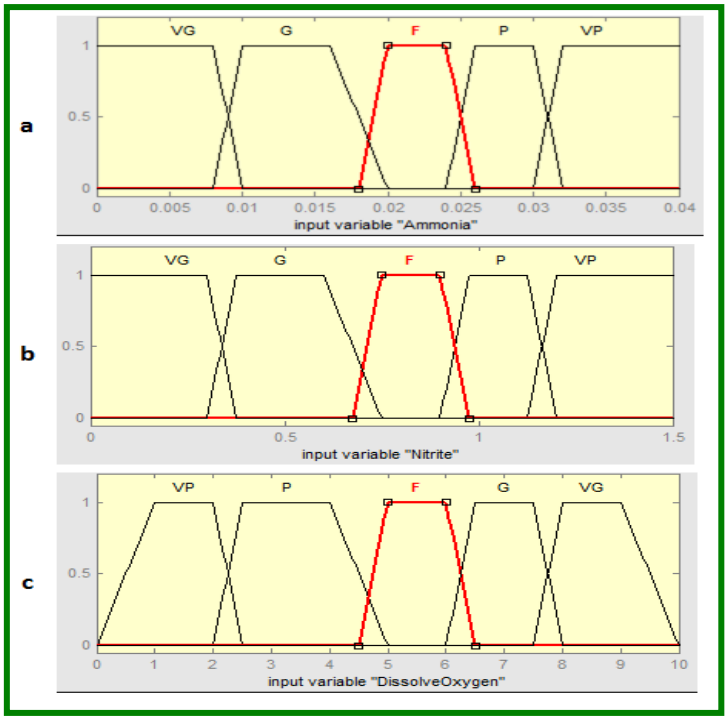


Figure 8. Membership Functions for Critical Water Parameters: a) Ammonia; b) Nitrite; c) Dissolved Oxygen

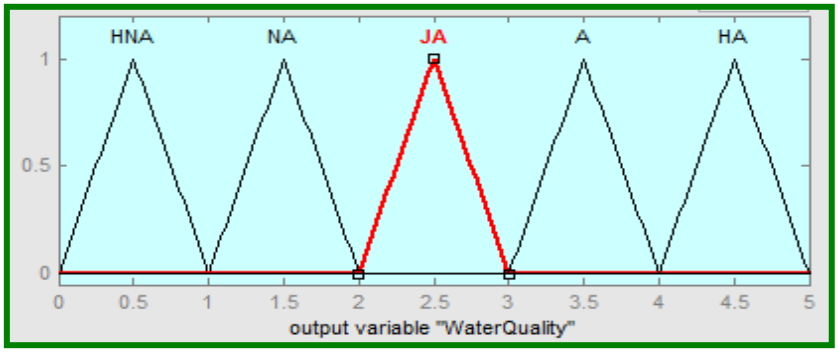


Figure 9. Membership Function for Water Quality Assessment

2.4. Fuzzy Logic Interface Systems Vs Neural Network

The proponents decided to compare the Fuzzy Logic and Neural Network to test if they can provide same results. After the test, the proponents realized that the Fuzzy Logic and Neural Network tools are perfectly correlated with each another. Fuzzy logic can make decisions based on the given data while Neural Network tries to incorporate human way of thinking to solve problems without employing the use of heavy mathematics. These two methods can be used to solve vague problems, but they have different ways of solving this. In fuzzy logic the proponents are to make the rules while the neural network it requires learning process and training data.

3. Application and Analysis

3.1 Results of Artificial Neural Network (ANN) Methodology

Taal Lake is playing an important role in the scenery of Batangas. Thus, surveillance and monitoring of the lake is vital. However, such process involves a great deal of uncertainty. This study overlooks modeling of both statistical uncertainties in the field data and cognitive uncertainties based on the knowledge of experts. The Bureau of Fisheries and Aquatic Resources (BFAR) water quality experts have identified three critical parameters for lake water monitoring and surveillance — Ammonia (NH_3), Nitrite (NO_2) and Dissolved Oxygen (DO) as the index of assessment. Moreover, the sample data can be chosen according to the value of quality standards for surface water environment of each factor. The criterion and actual values can be seen in Table 1.

Table 1. Criterion of water quality (mg/L)

LEVEL	Input sample data (index)			Expected Output Data
	Dissolved Oxygen (≤)	Ammonia (≤)	Nitrite (≤)	
Very Poor (VP)/Highly Not Accepted (HNA)	1	0.032	1.2	1
Poor (P)/Not Accepted (NA)	2.5	0.026	0.9757	2
Fair (F)/Just Accepted (JA)	5	0.02	0.75	3
Good (G)/Accepted (A)	6.5	0.01	0.375	4
Very Good (VG)/Highly Accepted (HA)	8	0.004	0.15	5

The proponent generated 500 data as graphed in Figure 12 on the appendix (between the ranges of observed concentrations) with respect to predefined membership functions. The data inputs are randomly generated using Excel VB Macro. Seventy percent of samples were taken as Training and the remaining 30% are equally divided to Validation and Testing samples. With the sample data, the neuron number of the hidden layer is computed as 20 on Matlab 7.8 platform. The parameter weights to layer 1 from input 1 are represented with iw, the parameter weights to layer represented with lw.

iw = [-3.0277 1.3518 -2.0476; 4.2428 12.7529 -3.8578; 3.7746 5.6496 -4.7984; 7.846 -1.6727 6.0917; -18.2952 -12.2876 -20.3376; 8.3877 12.7676 0.62908; 2.1226 2.0895 -1.6739; 1.7001 -0.075467 -2.2871; -5.4515 -4.0776 -3.0302; 1.071 -1.3144 -1.4624; 0.55854 1.8782 0.5698; -7.0699 0.15136 4.1373; 0.029231 3.96 0.43209; -1.1507 -0.2775 -2.1476; -1.123 -1.5986 1.6258; -1.0942 -5.2725 -2.4207; 6.0732 -6.0756 -0.31664; -2.3257 -3.1581 3.2215; -3.2313 7.6749 1.5084; -1.5373 0.46874 1.7096]

lw = [0.28496 -0.024812 0.19686 0.23538 -0.043372 0.072431 -0.46899 0.73332 -0.036061 0.33651 -0.48341 -0.060198 0.094049 -0.16447 1.3975 0.083104 -0.051576 -0.82858 0.17181 1.2014]

Figure 10 below shows the relationship of training error and epochs. It is observable that at about 39 epochs, the training error stabilized. The average error tolerance is computed to be 0.001.

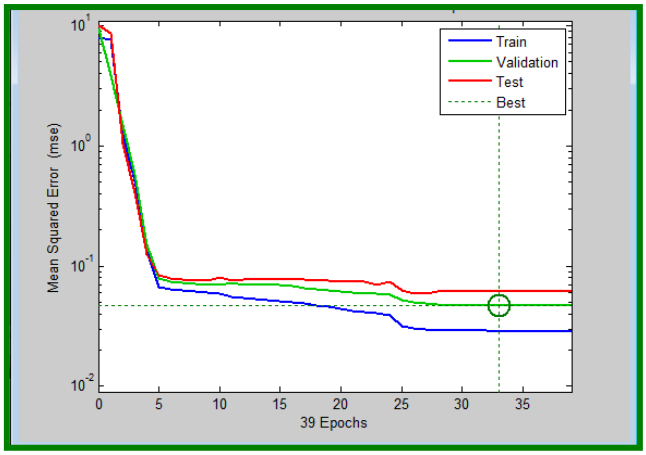


Figure 10. The training error of ANN

In addition to above results, the figure below shows "very high correlation" between the target and the expected output values. It considers both individual and general samples. Refer to Table 2 for the correlation coefficient table.

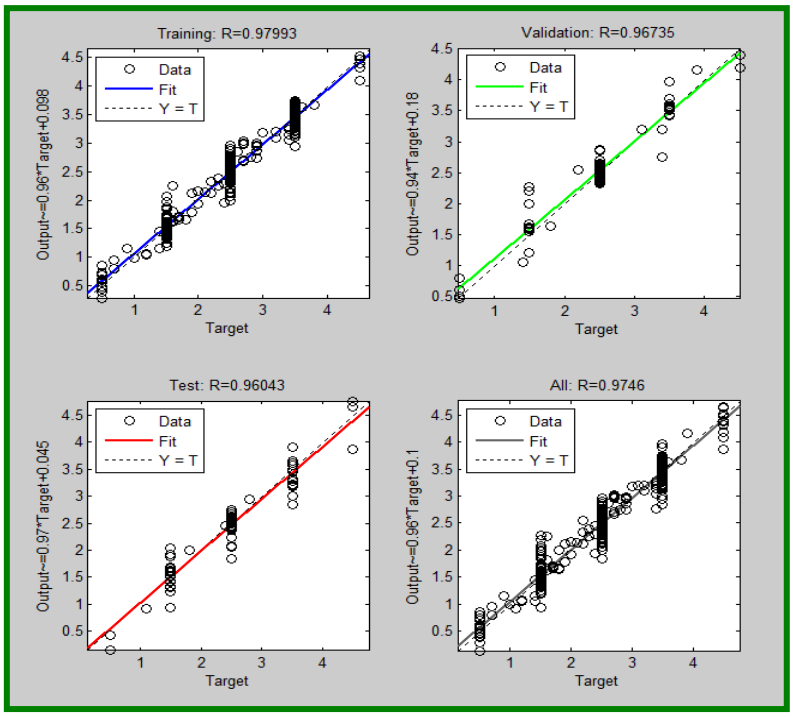


Figure 11. The training regression analysis of ANN

Table 2. Correlation Coefficient Table

Correlation Coefficient	Remarks
0.00 TO +/- 0.20	Negligible correlation
+/- 0.21 TO +/- 0.40	low correlation
+/- 0.41 TO +/- 0.50	substantial correlation
+/- 0.51 TO +/- 0.80	marked correlation
+/- 0.81 TO +/- 1.00	high to very high correlation

3.2 Network Testing and Performance

Network testing and performance require additional or new set of input/output pairs called as test set. The test set is used in assessing the performance of the network after the training has been completed. It is a must that the test set is different from the training set [11].

Testing the criterion data in Table 3 gives correlated results as follows. The error is tolerable considering the classified range for each assessment.

Table 3. Criterion vs Test Data Results

Data Count	INPUTS			RESULTS				
	NH3	NO2	DO	Target (Fuzzy-Based)	Output (Neuro-Based)	CLASSIFIED RANGE	ERROR	Water Quality Assessment
1	0.032	1.2	1	1	0.8751	0 to 1	0.1249	Very Poor (VP)/Highly Not Accepted (HNA)
2	0.026	0.9757	2.5	2	1.612	1.1 to 2	0.388	Poor (P)/Not Accepted (NA)
3	0.02	0.75	5	3	2.628	2.1 to 3	0.372	Fair (F)/Just Accepted (JA)
4	0.01	0.375	6.5	4	3.471	3.1 to 4	0.529	Good (G)/Accepted (A)
5	0.004	0.15	8	5	4.5273	4.1 to 5	0.4727	Very Good (VG)/Highly Accepted (HA)

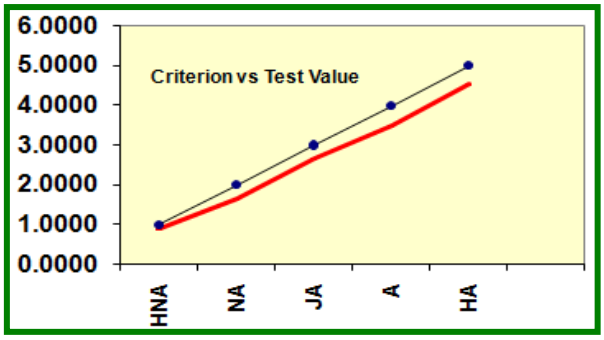


Figure 12. Criterion vs Test (ANN Method)

Taking [0.03 0.62 7.06] as the testing data of the ANN system, we will get a result of 2.6538.This is to say that, the quality of water in Taal Lake is Just Acceptable (between the range 2.1 to 3).

Table 4. Measure of Correlation Between Fuzzy Logic and Neural Networks of Water Quality Assessment

Water Quality Correlation Values between Fuzzy Logic and Neural Networks						
TRIALS (based on data generated)	Water Quality Parameters	Data Values	Crisp Output (Fuzzy Logic)	Crisp Output (Neural Networks)	True Error	%Relative Approximate Error
Week 1, Day 1	NH3	0.03	2.5	2.6538	-0.1538	-6.152
	NO2	0.62				
	DO	7.06				
Week 1, Day 2	NH3	0.03	2.5	2.6885	-0.1885	-7.54
	NO2	0.62				
	DO	5.33				
Week 2, Day 1	NH3	0.02	2.5	2.4834	0.0166	0.664
	NO2	1.07				
	DO	5.8				
Week 2, Day 2	NH3	0.04	1.5	1.41	0.09	6
	NO2	0.49				
	DO	2.9				
Week 3, Day 1	NH3	0.04	1.5	1.4455	0.0545	3.633333333
	NO2	0.95				
	DO	3.02				
Week 3, Day 2	NH3	0.01	3.9	3.6871	0.2129	5.458974359
	NO2	0.31				
	DO	7.75				
Week 4, Day 1	NH3	0.03	2.5	2.3719	0.1281	5.124
	NO2	1.18				
	DO	8.63				
Week 4, Day 2	NH3	0.04	2.5	2.3422	0.1578	6.312
	NO2	0.88				
	DO	7.61				
Week 5, Day 1	NH3	0.01	4.5	4.1779	0.3221	7.157777778
	NO2	0.12				
	DO	8.14				
Week 5, Day 2	NH3	0.02	3.2	3.1223	0.0777	2.428125
	NO2	0.69				
	DO	7.09				

3.3 Fuzzy Logic Toolbox versus ANN Toolbox

MATLAB 7.8.0 (R2009a) incorporates into its accumulation of toolboxes a thorough API for creating fuzzy logic and neural networks. Alongside console-based programming offices, MATLAB 7. 8 incorporates an easy to-use GUI that embodies all capacities accessible in the Fuzzy Logic and Neural Networks Toolboxes. The proponents liked to utilize these toolboxes in this study [12].

The outcomes got utilizing Matlab Fuzzy Logic Toolbox was contrasted and the outcomes got utilizing Matlab Neural Network Toolbox. The comparison between these two methods is shown in Figure 14. It was understood that there was a very high relationship between the two methods. This legitimizes the unwavering quality and precision of the outcomes when a few trials (30 generated data) are made. The true error and the relative approximate error give an acceptable value (considering the range of expected output). This implies that regardless of the method utilized, the client and/or the specialist will in any case get the same accurate values for water quality assessment.

4. Conclusions

Based on BP neural network, the model of integrated assessment for water environmental quality has been successfully proposed and in addition connected to the detail instance assessment. The study showed that the ANN model is simple, available, stable and effective. This paper had introduced the algorithms of Fuzzy Logic and ANN. Its concepts and principles are used in water quality assessment. The result proponent gets is credible. The assessment is reliable due to very high correlation between Fuzzy Logic and ANN results. The combination of Fuzzy Logic and ANN approach is therefore can be applied in the assessment of water quality of Taal Lake.

The paper presents a technique employing artificial neural networks for automatic assessment of water quality. The paper is relevant and important as per the needs of the developing world. Also, it presents a cheaper approach to the assessment of water quality in Taal Lake, which will also apply most likely to the assessment of any other vital bodies of water in the country.

References

[1] Caldo Rionel. Fuzzy Logic Control of Water Quality Monitoring and Surveillance for Aquatic Life Preservation in Taal Lake. The Second IEEE CIS Distinguished Lecture Series (2011)
[2] FF Liu, C Q Chen, SH L Tang, "Comprehensive Assessment of Water Environmental Quality Based on Improved Multiple Objective Decision," Environmental Monitoring in China, Vol. 25, no. 5, pp. 4-7, May 2009.
[3] Ilker, B. T.,Cenk K. and Mustafa S. Predicting the strength development of cements produced with different pozzolans by neural network and fuzzy logic [J]. Materials and Design,29(2008):1986-1991.
[4] Yugyung Lee, Alok Khemka, Jin-Wook Yoo et al. Assessment of diffusion coefficient from mucoadhesive barrier devices using artificial neural networks [J]. International Journal of Pharmaceutics, 351(2008):119-126.
[5] Wang Jian, Feng Yu, Zhang He, Hu Tingting. The Research Assessment Method for Water Environmental Quality Based on Neural Network. Third International Conference on Intelligent Networks and Intelligent Systems (2010).
[6] S Q Ding, L H Guo, "Artificial Neural Network," Harbin: Harbin Engineering University Press, pp. 12-20, March 2008.
[7] Ma Huiqun, Liu Ling. Water Quality Assessment using Artificial Neural Network. International Conference on Computer Science and Software Engineering (2008).
[8] Changjun Zhu, Xiujuan Zhao. Evaluation of Water Quality based on artificial neural network using VB. International Symposium on Information Science and Engineering (2008)
[9] Fuzzy Logic with Engineering Applications, Timothy J. Ross Professor and Regents' Lecturer, University of New Mexico, McGraw-Hill, Inc. 1995
[10] Fuzzy Logic and Control Software and Hardware Applications, Mohammad Jamshidi, Nader Vadiee, Timothy J. Ross, University of New Mexico, 1993, page 220 Chapter 10. Fuzzy Logic for Personnel Detection
[11] The Promise of Neural Networks, J.G. Taylor, Centre of Nueral Networks, King's College, Deparment of Mathematics, Strand London UK
[12] Neural Network Toolbox, MATLAB 7.8.0 (R2009a)
[13] http://www.scribd.com/thomagt/d/20792004-NFTOOL,
[14] http://www.scribd.com/thomagt/d/20791915-comparator-using-ANN-in-NNtool

Preliminary Study on EEG Extraction for Meditation

Jen-Looi Tee[1]*, Wai-Yie Leong[1]
[1]*Taylor's University, Malaysia*

*teejenlooi@sd.taylors.edu.my

Abstract
EEG is a convenient method to study the functional state of the brain and brain-body-mind connection. The mental activity characteristics of meditation is poorly defined in literature. This study investigates the EEG signal during meditation, a mental activity described as being in a state of calmness and focused attention. The objective is to study and extract features present in EEG signal during meditation. The approach taken to extract EEG features associated with meditation is done through time series analysis, using the normalized signal amplitude mean as the primary feature. EEG signal is recorded at point F3 and F4, during meditation and post meditation. A significant difference in signal amplitude mean between these two states of the mind was observed. The normalized amplitude mean of 0.00525 is proposed as a cut off, where normalized amplitude mean below 0.00525 is shown to be associated with meditation activity.

Keywords: EEG, Feature Extraction, Time Series Analysis, Amplitude Mean, Meditation.

1. Introduction

The human brain is a bio-chemical and a bio-electrical organ. The brain functions and communicates through neurotransmission, a phenomenon where signals are transmitted from one neuron to another via neurotransmitters. Neurotransmitters in the form of chemical messengers can be either stimulating or inhibiting. As chemical messengers (either exciting or inhibiting) binds to the receiving end of a neuron, the sum of stimulation, if it passes a specific threshold, would trigger the receiving neuron to fire off an electrical nerve impulse called an action potential which travels along the neuron. Upon reaching the end of the neuron, the electrical impulse triggers a release of neurotransmitters, and the process repeats itself on the next neuron. If the released neurotransmitters have an excitatory effect, it causes post-synaptic potentials at the excited receivers. Compared to an action potential, a post-synaptic potential has a larger field and duration is generally accepted as the source of EEG signal [1]. Neurons form an intricate network, and interaction among neurons gives rise to a dynamic ionic electrical fluctuation, commonly called 'brain waves', in the brain. 'Brain waves' are not truly waves produced by the brain, but are thus called due to the observed rhythmic changes in neural activity that takes the form of sinusoidal waves [2]. These rhythmic

wave forms appeared to reflect certain mental functions of the brain. Through careful observation, it is possible to identify specific patterns associated with different functional state of the brain and thus use the specific patterns, also known as EEG features, as classifiers of mental functions.

The research objective here is to investigate EEG features present during specific events or conditions, which are also called event related potentials (ERP). ERP associated with specific events can in turn be used as a classifier. The specific activity being studied in this research is meditation (a mental activity of calm, focused attention).

This article was written with the following sections: section 2 - a literature review on EEG development and measurement procedures, section 3 - methodology of this study, section 4 - results and discussion, and section 5 - conclusion.

2. Literature Review

Richard Caton first successfully recorded electrical activity with a mirror galvanometer and having non-polarisable electrodes firmly affixed onto the exposed brains of monkeys and rabbits [3]. Caton reported in 1875 that the pattern in electrical currents recorded appeared to have a relation to the functional state of the brain. In 1877, Caton reported observation of electrical variations mapped to states of wakefulness, sleep, anesthesia and death.

Electroencephalogram (EEG), the recording of 'brain waves', is a term coined in 1924 by German psychiatrist Hans Berger [4], who was the first to successfully describe changes in EEG recording associated with epilepsy. Many more application of EEG, clinical or otherwise, has been successfully employed since.

Evolution in EEG equipment and measurement procedure has resulted in modern EEG measurements to be non-invasive. The measurement procedure is performed by placing gold plated low impedance electrode on a person's scalp using a bit of adhesive conductive paste [5]. An EEG recording device has at least two electrodes, one placed at the reference point, often the ear mastoid, and the other electrode at a point of interest. Multiple electrode can be simultaneously placed at different point of interest. The EEG device compares the tiny fluctuating voltage at the measurement electrode with the reference electrode and registers the difference between them. It is common for EEG device to sample the measurements at a rate of 128Hz, 256Hz or higher, and changes in the difference between electrodes are recorded as a time series data set.

As each neuron produces only the slightest electrical current, it takes a collective of neurons in close proximity to fire at the same time for a change in voltage to be detected by the EEG device. Furthermore, the source (cerebral cortex) of the desired signal is located beneath layers of meninges (Pia, Aracnoid, Dura), skull, and scalp tissue. The electromagnetic signal must travel through these layers and are subjected to signal attenuation. As a result, temporal resolution of EEG is poor, with little or no difference detected by electrodes placed side-by-side each other. A standard electrode placement, the 10-20 electrode placement system shown in Fig. 1, was adopted by the International Federation in Electroencephalography and Clinical Neurophysiology in 1958 [6].

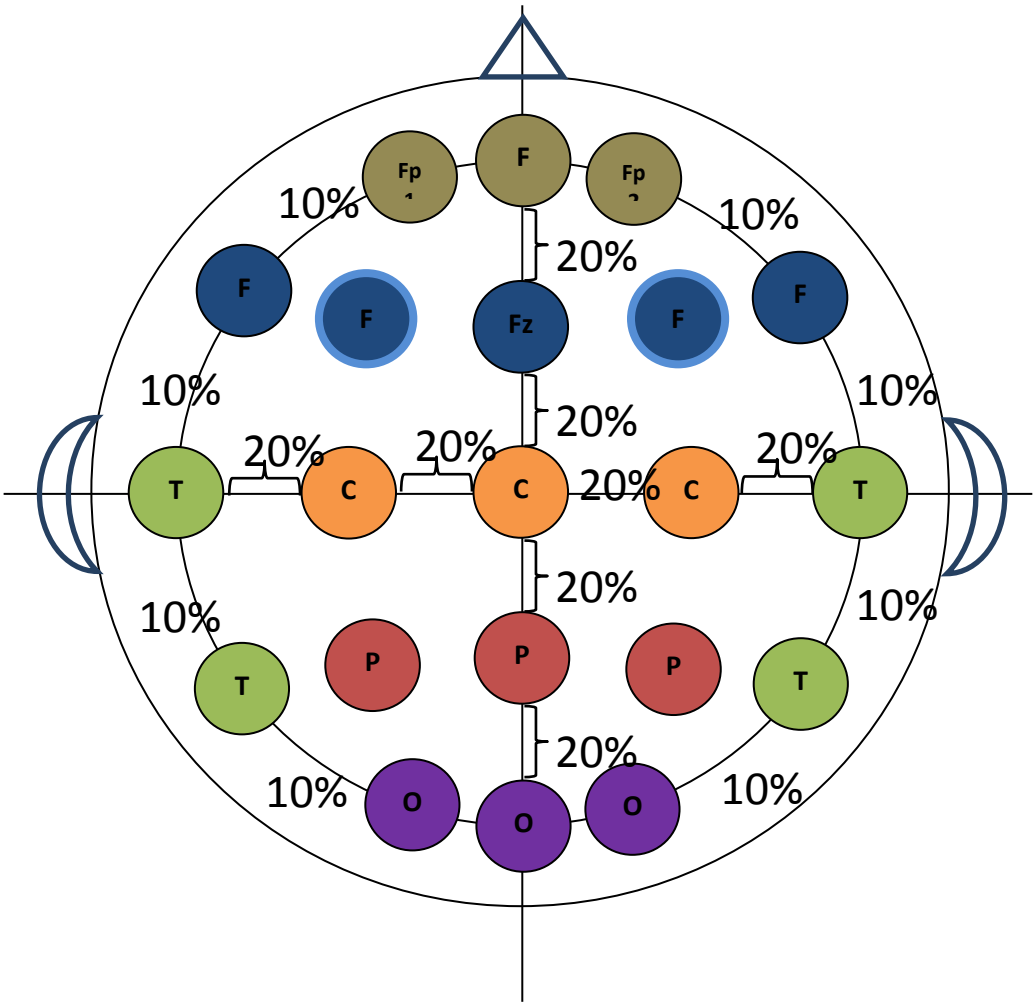


Figure 1. Top view of subject's scalp showing a simplified 10-20 standard electrode placement system for EEG electrode.

An advanced EEG recording device with the appropriate measurement procedures are required to reliably capture the desired signal, coupled with signal processing (Filtering and Feature Extraction) steps to produce results that can be mapped to various functional state of the brain.

One of the most commonly used methods for EEG signal processing is the EEG signal power spectrum, where the EEG signal is processed using the Fourier Transform, where the convoluted sinusoidal waves are broken down into their individual components for further analysis and classification. Fourier transform changes the data from the time domain to the frequency domain. The frequency of the transformed signal is separated into five categories, as shown in Fig 2. The categories are Delta band, which ranges from 0.5 - 4 Hz; Theta band, which ranges from 4 - 7 Hz; Alpha band, which ranges from 7 - 14 Hz; Beta band, which ranges from 14 - 30 Hz; and Gamma band, which includes frequencies higher than 30 Hz. Research on EEG signal has typically focused upon signals within the 0.5 - 30 Hz. This universal classification system has also developed into a framework for more advanced EEG research.

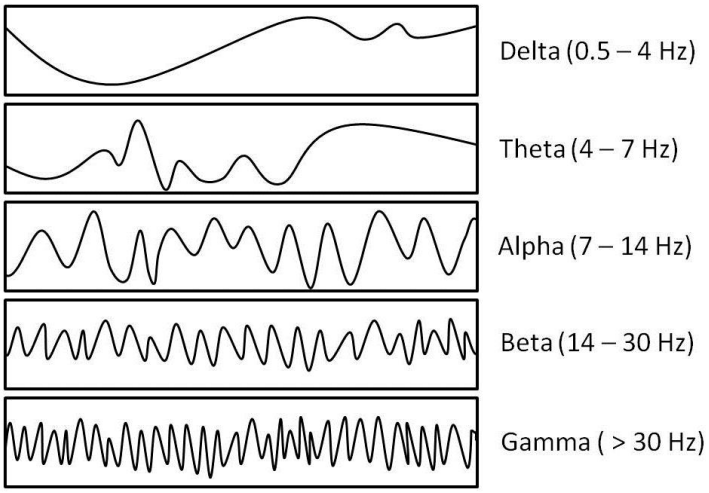


Figure 2. Categories of brain wave frequencies and respective labels.

3. Methodology

This study is based on an experimental setup. Equipment requirement for this study centralizes around the Electroencephalogram. The device used is manufactured by CamNTech, named the CamNTech Actiwave Multichannel Recorder, a class 2a (EU) medical device. It includes the EEG recording device, electrode leads, conductive adhesive paste (for interface between electrode and subject's scalp surface), and a docking interface which links the EEG recorder to a PC. The device comes with a user guide and the operational procedures were clearly described within the Actiwave User Guide [5].

One criterion in signal recording (sampling) lies with satisfying the Nyquist criterion. The Nyquist principle states that the sampling rate of the signal, *fs*, must exceed twice the maximum frequency, *B* (band-limit), for the signal to be reconstructed from the sample.

$$f_s > 2B \tag{1}$$

This is a criteria that must be met in order to avoid signal aliasing, where two different sine waves can give the same samples if one of the sine wave has a frequency higher than half of the sampling frequency, rendering the actual (high frequency) data undetectable. Given that $x(t)$ is the original signal, and the Fourier transform of $x(t)$ is $X(f)$:

$$X(f) = \int_{-\infty}^{\infty} x(t) e^{-i2\pi ft}\, \mathrm{d}t \tag{2}$$

The Poisson summation formula shows that:

$$X_s(f) = \sum_{k=-\infty}^{\infty} X(f - kf_s) \tag{3}$$

For $f > f_s/2$, the higher frequency component cannot be distinguished from a lower frequency component.

The Actiwave device sample signals at a rate of at least 128Hz, and capable of scaling upwards to over 1024Hz . Since most EEG signal of interest lies between 0.5Hz - 30Hz range, which has been widely accepted and segregated into Delta waves (0.5Hz - 4Hz), Theta waves (4Hz - 7Hz), Alpha waves (7Hz - 14Hz), Beta waves (14 - 30Hz), these signals lie well within the measurement range of this measurement devices.

Studies by [7]–[10] have observed increase in EEG theta band frequencies associated with meditation. The primary definition of meditation in this study is reliant upon the observation of increased theta band frequencies during meditation process.

Theta Healing® [11], a meditation practice founded by Stibal, who authored a book titled under the same name, stated that the Theta Healing® technique is a meditation process, when performed accordingly to the instructions, stimulates the brain to produce observable signals in the EEG theta band frequencies. The sampling frame for this study is drawn from Theta Healing® practitioners from Malaysia, Singapore, and Australia. Data collection were conducted at Theta Healing® seminars, at the respective venue, with permission and prior mutual agreement. Data collection takes place in the late afternoon, after the conclusion of regular seminar activities.

Subjects were tasked with performing Focused Attention Meditation guided by an audio recording [12] according to the standard practice of Theta Healing®. The subject was briefed with the procedure, and remain seated comfortably during the entire measurement. EEG electrodes was placed on the F3 and F4 according to the EEG 10-20 standard placements of electrodes (corresponding to the brain's frontal lobe) of subject. The F3 and F4 points are selected based on previous studies [13-17], where F3 and F4 were some of the points where increase in theta band frequencies during meditation are more observable.

EEG measurements of these two points will be recorded during meditation and after the mediation process stops. The audio recording guides participants through approximately eleven minute visualization meditation process. At the end of the audio recording, subject is instructed to stop meditation activity. The EEG recording continues for another three minutes, recording post meditation signal. EEG data were then extracted and evaluated. The collected data goes through a data processing flow as shown in Fig. 3.

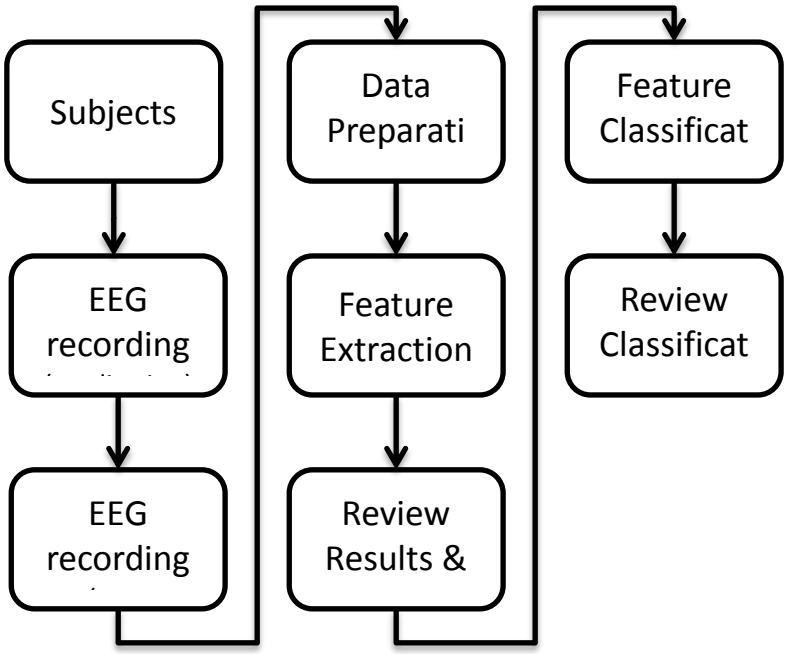


Figure 3. Process Flow Diagram.

4. Results and Discussion

EEG signal from nine subjects are recorded. Each subject yielded results from two channels (F3 and F4). Data from each channel were sampled twice, each sample segment is eight seconds in duration. A total of 36 meditation data and 33 post meditation data were recorded. Figure 4 shows an example of an EEG recording.

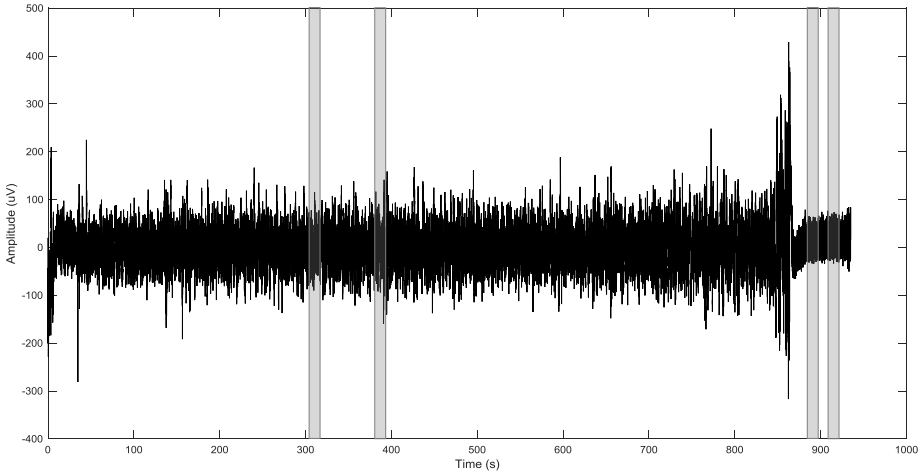


Fig 4. EEG recording of F3 point of subject who began meditation at 0 second mark and stopped at 850 second mark.

Two 8 seconds segment of meditation data (highlighted in Figure 4) were extracted from between 100 - 700 seconds frame, with an example shown in Figure 5. Two 8 seconds segment of post meditation data (highlighted in Figure 4) were extracted from between 850 - 950 seconds frame, with an example shown in Figure 6.

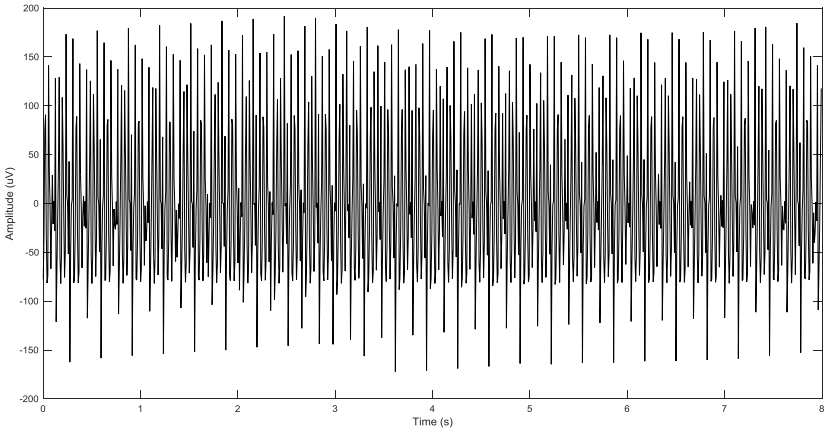


Fig 5. Sample data of 8 second segment extracted from meditation period (F3 point)

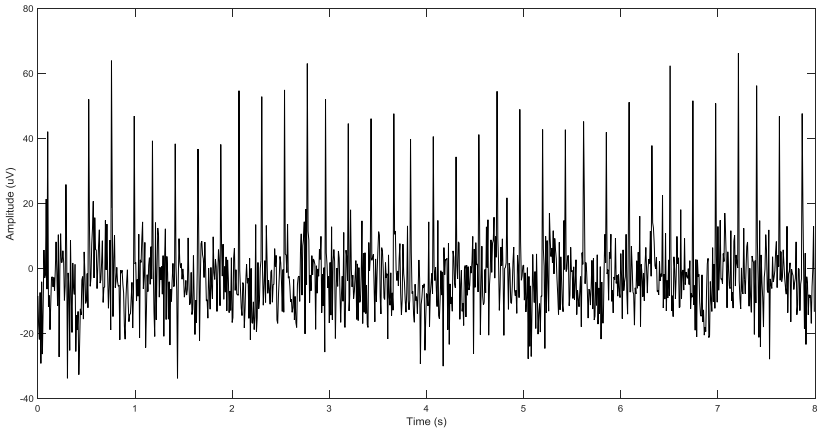


Fig 6. Sample data of 8 seconds segment extracted from post meditation period (F3 point)

A segmented meditation signal, as shown in Fig. 5 depicted a relatively rhytimic brain activity with balanced positive and negative voltage spikes. Where as in Fig. 6, the post meditation signal shows voltage spikes that are much more lopsided on the positive voltage end.

The time domain signal were normalized and the amplitude mean, median, standard deviation, maximum, minumum, and range were quantified and compared. Among these statistical data collected, the amplitude mean data presented the most significant difference.

In Fig 7. we observe that normalized amplitude mean of meditation signal is generally lower by one to two order of magnitude.

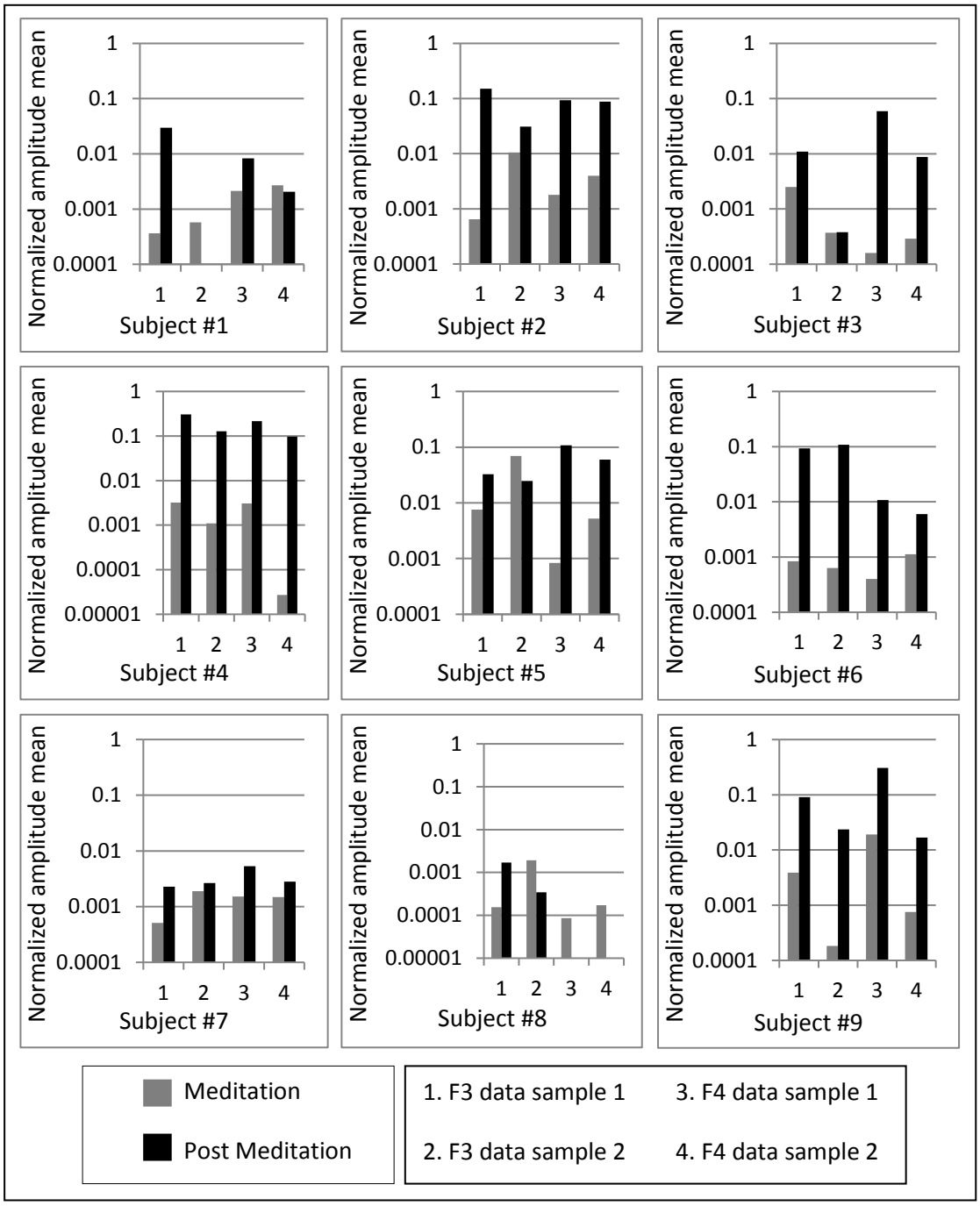


Figure 7. Meditation and post meditation signal amplitude mean of individual subjects.

By taking the average of the amplitude mean of each subject, the average meditation signal's amplitude mean is significantly lower as seen in Table 1.

Table 1. Signal amplitude mean and standard deviation comparison between meditation and post meditation.

Signal Amplitude Mean		Standard Deviation	
Meditation	Post Meditation	Meditation	Post Meditation
4.20E-03	6.24E-02	1.17E-02	8.11E-02

There are some post meditation data, specifically subject #7 and #8 in Fig 7., observed to have low amplitude mean, similar to meditation data. It is likely these practitioners are still in meditation (state of calm focused attention) during post meditation, and these data collected during post meditation still reflected a physical state of meditation, possibly causing a negative impact on the accuracy of this study. The larger standard deviation in the post meditation data also supports the likelihood of this observation.

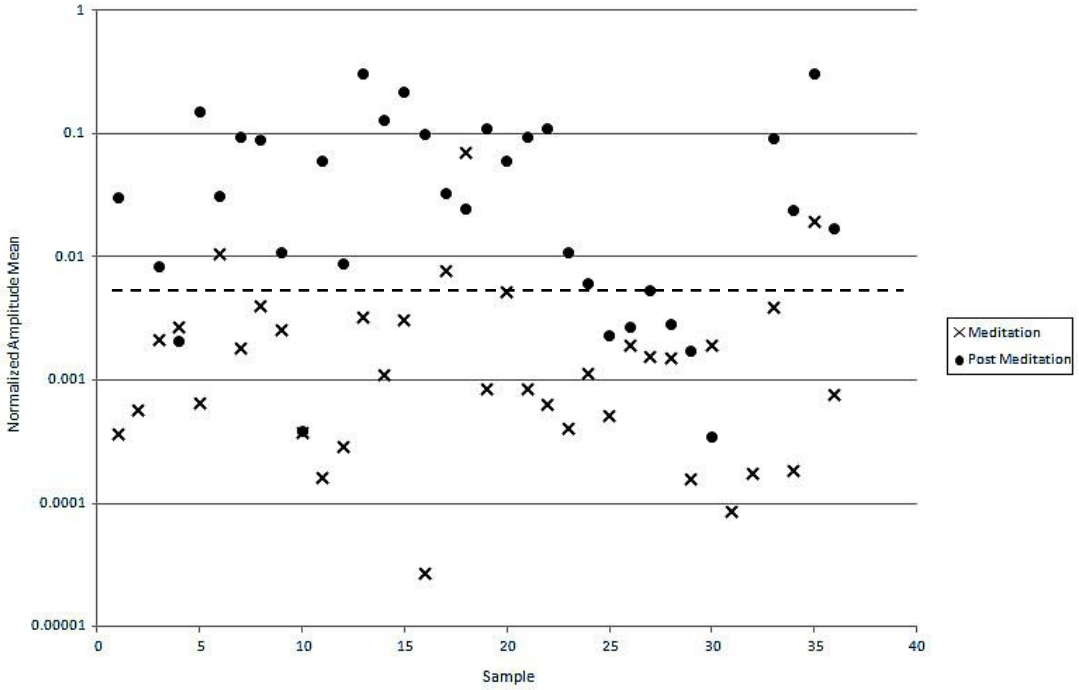


Figure 7. Signal amplitude mean of meditation signal and post meditation signal of all nine subjects.

From Fig. 7, a normalized amplitude mean of 0.00525 is proposed as a cut off. When the amplitude mean (of a normalized EEG signal) is centered around zero with a deviation less than 0.00525, the subject's functional state of mind is associated with the mental activity of meditation. A 84.06% accuracy is achieved in classifying meditation activity using this system. Accuracy was calculated as follows

$$Accuracy = \frac{(True\ Positive + True\ Negative)}{(Positve + Negative)} = \frac{(32+26)}{(36+33)} = 84.06\% \quad (4)$$

Matthews Correlation Coefficient was calculated as follows

$$MCC = \frac{(TP)(TN) - (FP)(FN)}{\sqrt{(TP+FP)(TP+FN)(TN+FP)(TN+FN)}} \quad (5)$$

with TP referring to True Positive (meditation classified as meditation), TN referring to True Negative (post meditation classified as post meditation), FP referring to False Positive (post meditation classified as meditation), and FN referring to False Negative (meditation classified as post meditation).

At 84.06%, this is the highest accuracy achieved using cut off at 0.00525, seen in Fig. 9. Also seen in Fig 9. is the Matthews Correlation Coefficient agreeing to 0.00525 as the best cut off option for this binary classifier.

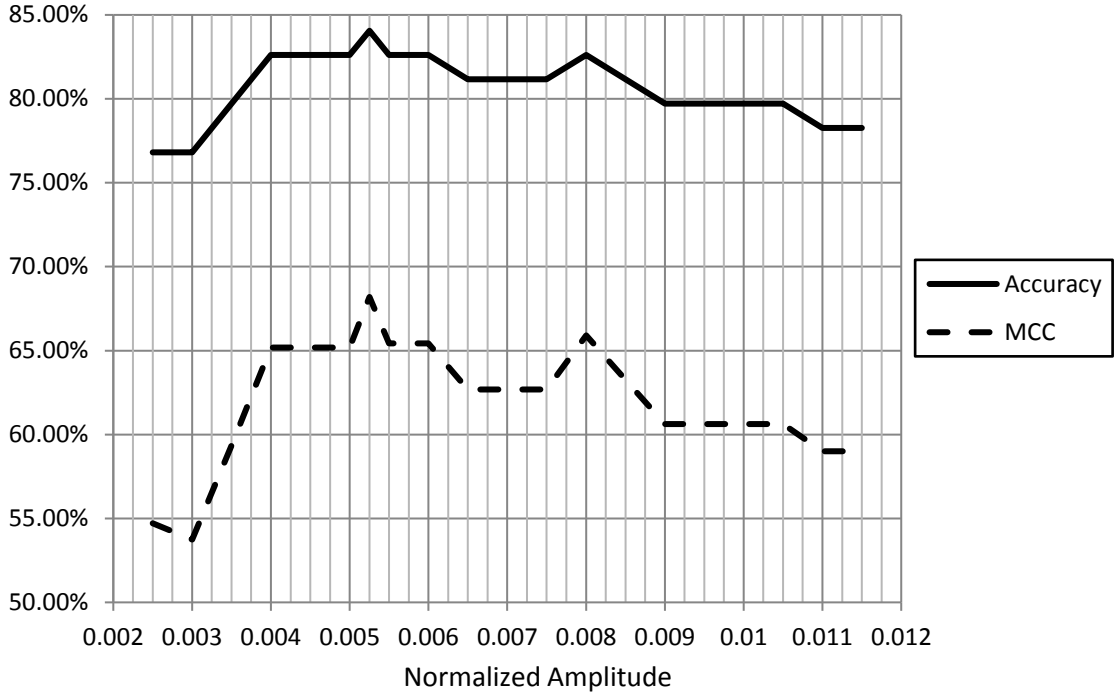


Figure 9. Classifier Accuracy and Matthew Correlation Coefficient when using varying normalized amplitude as classifier cut off.

5. Conclusion

There is very little literature and research available in the study of EEG other than in clinically (disease/disorder) related situations. The finding in this research, as intended, successfully offers an additional feature - the amplitude mean, to be used as a feature for classification in the study of meditation EEG.

A 84.06% accuracy is achieved in classifying meditation activity by using the normalized amplitude mean with a cut off set at 0.08 as a yes-no criteria. The classifier's accuracy leaves room for improvement. In order to improve upon this issue, it is suggested for further studies to have a larger sample size. It is also suggested to improve upon the data collection process, so as to maximize the distinction between the meditation state and post meditation state.

Reference

[1] A. J. Rowan and E. Tolunsky, *Primer of EEG*. Philadelphia: Butterworth Heinemann, 2003.

[2] M. Teplan, "Fundamentals of EEG measurement," *Meas. Sci. Rev.*, vol. 2, pp. 1–11, 2002.

[3] T. F. Collura, "History and evolution of electroencephalographic instruments and techniques.," *Journal of clinical neurophysiology : official publication of the American Electroencephalographic Society*, vol. 10. pp. 476–504, 1993.

[4] L. F. Haas, "Hans Berger (1873-1941), Richard Caton (1842-1926), and electroencephalography," *J. Neurol. Neurosurg. Psychiatry*, vol. 74, no. 1, p. 9, 2003.

[5] G. Ungless, "The Activewave User Guide." CamNTech Ltd., Cambridgeshire, UK, 2014.

[6] H. H. Jasper, "The ten-twenty electrode system of the International Federation," *Electroencephalogr. Clin. Neurophysiol.*, vol. 10, no. 2, pp. 371–375, 1958.

[7] K. Rubia, "The neurobiology of Meditation and its clinical effectiveness in psychiatric disorders," *Biol. Psychol.*, vol. 82, no. 1, pp. 1–11, 2009.

[8] B. R. Cahn and J. Polich, "Meditation states and traits: EEG, ERP, and neuroimaging studies.," *Psychol. Bull.*, vol. 132, no. 2, pp. 180–211, 2006.

[9] Y.-Y. Tang, Y. Ma, Y. Fan, H. Feng, J. Wang, S. Feng, Q. Lu, B. Hu, Y. Lin, J. Li, Y. Zhang, Y. Wang, L. Zhou, and M. Fan, "Central and autonomic nervous system interaction is altered by short-term meditation.," *Proc. Natl. Acad. Sci. U. S. A.*, vol. 106, no. 22, pp. 8865–70, 2009.

[10] S. W. Xue, Y. Y. Tang, R. Tang, and M. I. Posner, "Short-term meditation induces changes in brain resting EEG theta networks," *Brain Cogn.*, vol. 87, no. 1, pp. 1–6, 2014.

[11] V. Stibal, *Theta Healing (TM)*, 6th Ed. Carlsbad, California: Hay House, Inc., 2013.

[12] V. Stibal, "Abundance Meditation (CD)." Theta Healing Institute of Knowledge, Idaho Falls, Idaho, 2007.

[13] B. R. Cahn, A. Delorme, and J. Polich, "Occipital gamma activation during Vipassana meditation," *Cogn. Process.*, vol. 11, no. 1, pp. 39–56, 2010.

[14] W. P. Wong, D. a. Camfield, W. Woods, J. Sarris, and a. Pipingas, "Spectral power and functional connectivity changes during mindfulness meditation with eyes open: A magnetoencephalography (MEG) study in long-term meditators," *Int. J. Psychophysiol.*, 2015.

[15] W.Y.Leong, C. M. THAN, Features of Sleep Apnea Recognition and Analysis, *International Journal on Smart Sensing and Intelligent System*, VOL. 7, NO. 2, MAR 2014.

[16] W.Y.Leong, Andrew Ng, An EEG-Based Approach For Left-Handedness Detection, *Journal of Biomedical Signal Processing and Control*, *Elsevier* , Vol. 10, March 2014, Pages 92–101.

[17] R.S.Tung, W.Y.Leong, Processing Obstructive Sleep Apnea Syndrome (OSAS) Data, Journal of Biomedical Science and Engineering, 2012

eureca 2016 – Conference Paper
Paper Number PG02

Cryogenic Liquefaction of Air as an Energy Storage for Cold Storage Application

Yvonne H.L Lim[1*], Mushtak Al-Atabi[1], Richard A. Williams[2]

[1]*Taylor's University*

[2]*Heriot-Watt University*

[*]Corresponding author: yvonnehl.lim@gmail.com

Abstract

Cold is essential in 21st century living. Air conditioning, storage and transportation of food, data centre cooling, the storage of medical and blood-based products all require refrigeration and cooling. The demand for cold is projected to increase as the world population increases and becomes increasingly global. The liquid air energy and cold storage system utilises solar energy to produce liquid air as a form of energy storage. The expansion of air to generate electricity produces cold energy. The cold energy can be stored and utilised for various cold applications. The study aims to determine the eutectic-water-salt solution phase change material's suitability as a cold storage system for the liquid air energy storage system using computational fluid dynamics, CFD and by experimental means. An economic analysis utilising present value calculations and levelised cost is used to determine the economic viability of the proposed system for food storage systems. It is found that magnesium nitrate eutectic-water salt solution is the best option as a cold storage system for the liquid air system based on the numerical and experimental studies and economic analysis.

Keywords: Liquid air energy storage, cold storage systems, phase change material, economic analysis

1. Introduction

The demand for cold application worldwide has increased over the years, specifically in the 21st century and is expected to continue to increase. Cold energy is required in the cold chain, from the production of food to the consumers; storing medicine, space cooling, data center cooling and in the industrial cooling systems. It is estimated that 200 million tonnes of food each year is wasted due to the lack of a cold chain; and 2 million vaccine prevented deaths due to the lack of cold storage and

refrigeration of these vaccines [1], [2]. It is estimated that 71% of data centres power consumption is due to the cooling requirements of the data centre [3].

With the event of climate change, home air conditioning alone accounts for 8% of electricity usage in the United States, and the European Commission has projected that the building cooling demand in the European region to further increase by 70% in the next 10 years. The demand for cold energy has been increasing exponentially since the start of the 21st century and is projected to continue to increase to meet the demand of growing population and an increasingly global community. It is estimated that by 2060, the demand for space cooling worldwide would exceed the demand for heat according to the Netherlands Environmental Assessment Agency [1]. The increase of space cooling requirement also increases the energy consumption proportionally and may lead to concerns in energy security.

Cold is essential for modern day living and it is paramount to ensure that cold is produced sustainably. This study focuses on the integration of cold capture in liquid air energy storage system and utilisation of captured cold in cold storage for food. The cold capture system used is eutectic-water salt solution phase change material. A numerical and experimental study was carried out to determine the most suitable cold storage material for the cold storage using the rate of cold charge and discharge, the effective NTU. An economic analysis of using the system was also carried out for the utilisation of food storage system.

2. Background

Renewable energy use worldwide has been increasing due to the demands of an industrialized and globalized country. However, renewable sources are generated at locations away from where the electricity demand is and often at off-peak hours. Energy storage systems are necessary to curb this waste of energy. Current energy storage systems include pumped hydro, compressed air energy storage, batteries, supercapacitors and thermal energy storage systems. There are challenges that restrict the use of these energy storage system. Pumped hydro and compressed air energy storage systems are geographically constraint. Batteries and supercapacitors have relatively short lifespan. There has been a recent increase in interest towards liquid air as an energy storage system. Liquid air energy storage system is a type of cold thermal energy storage. It isn't location constricted and have a relatively long lifespan of 25 to 50 years [4]–[6].

Liquid air can be produced using renewable energy when the renewable energy produced is greater than the demand, this allows for energy to be stored in the form of liquid air instead of being wasted; or off peak electrical energy. The liquefied air can then be expanded used in power recovery cycles to run turbines which in turn generate electricity when required. The expansion of liquid air also generates cold energy, this cold energy can be captured and stored in phase change materials and used instead of conventional refrigeration systems.

Phase change materials use its latent storage capabilities to store thermal energy. Phase change materials (PCMs) are usually used in the storage of heat, ie heat from solar power; there are not many applications of PCMs for cold energy, especially at subzero temperatures. PCMs for cold energy are usually used for air-conditioning, and the making of ice [7], [8]. The ideal phase change material has large fusion heat, high thermal conductivity, excellent cyclic stability, proper phase change temperature, chemically stable and is easily manufactured and has low cost [7]. Fusion heat is essential for the PCM to store cold energy per unit mass, large fusion heat allows for more energy to be stored in a small unit mass. Thermal conductivity is important to conduct thermal energy throughout the material. Cyclic stability is the stability of the PCM over charging and discharging period, a longer cyclic stability allows the PCM to be used over a longer period of time. Chemical stability is important aspect of PCM to ensure that it does not react chemically with the heat transfer fluid or the containing medium. PCMs are categorised to three different categories, eutectic water-salt solution, non-eutectic water salt solution, and composite PCMs.

Eutectic water-salt solution have been selected considering safety, health and environmental condition. Eutectic water-salt solution PCMs have relatively less hazardous properties compared to the commercialized eutectic water-salt solution for sub-zero applications [9]. The PCMs, calcium chloride, potassium carbonate and magnesium nitrate water-salt solutions for this study were chosen based on their eutectic point closest to the temperature of regasification (-60°C) and cold refrigeration application (-10 - 0°C) and a high fusion heat by mass.

CFD has been used in the study of PCMs as latent heat storage material. Computational fluid dynamics is used in the study of PCM in various different applications, among which is the study of PCM in heat exchangers, cooling electronic systems, as well as heating, ventilation and air-conditioning [10]. There have been many applications of CFD in PCM research, however, many of the studies that have been carried out are on PCM latent heat storage for heating purpose. The storage of cold energy have been carried out, however not on subzero cold energy as required in this research.

Table 1. Summary numerical investigation of PCM using CFD

System studied	**Solver and schemes used**	**Findings**	**Assumptions and validation**	**Ref**
Heat storage – Storage efficiency with and without foil in the solidification process of KNO3-NaNO3 PCM in solar power generation using direct steam technology controlled by pure conduction	FLUENT 6.3	The use of aluminium foil accelerates the heat transfer rates.	The influence of natural convection was neglected. Theoretical model validation.	[11]

Heat storage – The effect of temperature difference on thermal energy by studying the heat transfer and fluid flow in a plate fin for rapid heat absorbed/released techniques	ANSYS FLUENT SIMPLE	Correlation between liquid fraction and thermal storage time; and transient heat flux and melting period.	Liquid PCM and air are compressible inside the plate-fin thermal energy storage/release systems. Experimental validation from literature.	[12]
Heat storage – The effect of internal tube position in the melting process of n-octadecane as PCM in concentric and eccentric double pipe heat exchanger	ANSYS FLUENT SIMPLE and PRESTO	Melting rate of both HEX was the same in early stage but the melting rate in the concentric model decreased towards end of melting process due to conduction between hot tube and cold solid PCM.	Experimental validation.	[13]
Cold storage – The effect of grid resolution of accuracy of a simulated shell and tube HEX with PCM in shell side to analyse transient heat transfer during phase change process.	ANSYS CFX	CFD melting results is longer than experimental results due to the neglect of natural convection process.	Natural convection was not taken into account. Experimental validation	[14]
Cold storage – The reduction of internal building temperature fluctuations and increased time delay between internal and external conditions when using PCM in clay brick for building applications	ANSYS FLUENT SIMPLE and second-order upwind	Time delay increased by 3 hours and the temperature swing reduced by half.	Internal heat gains not taken into account. Experimental validation.	[15]
Heat storage – The effect of heat source temperature and velocity of heat transfer fluid on the on thermal energy storage tank design.	Commercial CFD code.	Increase in heat transfer rate due to increase in velocity. The CFD and experimental results are in close agreement.	Environmental conditions are not taken into account in the CFD simulation. Experimental validation.	[16]

gives a summary of studies in which CFD was used in the study of PCM.

There have been many applications of CFD in PCM research, however, many of the studies that have been carried out are on PCM latent heat storage for heating purpose. The storage of cold energy have been carried out, however not on subzero cold energy as required in this research.

Table 1. Summary numerical investigation of PCM using CFD

System studied	**Solver and schemes used**	**Findings**	**Assumptions and validation**	**Ref**
Heat storage – Storage efficiency with and without foil in the solidification process of KNO_3-	FLUENT 6.3	The use of aluminium foil accelerates the heat transfer rates.	The influence of natural convection was neglected.	[11]

$NaNO_3$ PCM in solar power generation using direct steam technology controlled by pure conduction			Theoretical model validation.	
Heat storage – The effect of temperature difference on thermal energy by studying the heat transfer and fluid flow in a plate fin for rapid heat absorbed/released techniques	ANSYS FLUENT SIMPLE	Correlation between liquid fraction and thermal storage time; and transient heat flux and melting period.	Liquid PCM and air are compressible inside the plate-fin thermal energy storage/release systems. Experimental validation from literature.	[12]
Heat storage – The effect of internal tube position in the melting process of n-octadecane as PCM in concentric and eccentric double pipe heat exchanger	ANSYS FLUENT SIMPLE and PRESTO	Melting rate of both HEX was the same in early stage but the melting rate in the concentric model decreased towards end of melting process due to conduction between hot tube and cold solid PCM.	Experimental validation.	[13]
Cold storage – The effect of grid resolution of accuracy of a simulated shell and tube HEX with PCM in shell side to analyse transient heat transfer during phase change process.	ANSYS CFX	CFD melting results is longer than experimental results due to the neglect of natural convection process.	Natural convection was not taken into account. Experimental validation	[14]
Cold storage – The reduction of internal building temperature fluctuations and increased time delay between internal and external conditions when using PCM in clay brick for building applications	ANSYS FLUENT SIMPLE and second-order upwind	Time delay increased by 3 hours and the temperature swing reduced by half.	Internal heat gains not taken into account. Experimental validation.	[15]
Heat storage – The effect of heat source temperature and velocity of heat transfer fluid on the on thermal energy storage tank design.	Commercial CFD code.	Increase in heat transfer rate due to increase in velocity. The CFD and experimental results are in close agreement.	Environmental conditions are not taken into account in the CFD simulation. Experimental validation.	[16]

3. Methodology

The study utilizes numerical study of computational fluid dynamics, and process simulation from previous studies [17]; for cold charging of PCM and the experimental study was carried out to study the cold discharge of the PCM. A lifecycle cost analysis was carried out to determine the feasibility and economic benefits of utilizing a liquid air energy storage system with integrated cold storage.

3.1 Cold storage

The study on cold storage has been carried out using CFD and experimental. The capturing of cold was done using CFD as the cold capture experimentally involves extremely cold liquid nitrogen and complex experimental set-up. Both are required to give an overall view of the system.

The numerical study is used to model the capture of cold using computational fluid mechanics. Computational fluid dynamics, or CFD for short has been used widely in research. CFD studies are used to model flow and heat transfer simulations before carrying out experimental studies or where experimental studies are expensive. In this study, freezing and melting phase change is modelled by ANSYS FLUENT using its Solidification/Melting model. The software uses enthalpy-porosity formulation to model this phase change. The liquid-solid mushy zones are modelled as a porous zone with porosity equal to the liquid fraction. Liquid fraction is the fraction of the cell volume that exists in liquid phase. The liquid fraction is computed by the software based on the enthalpy balance for each iterations [18].

UniSim Design Suite under steady-state conditions was carried out by Lim et al [17] to determine the energy consumption and the energy generation from the process and well as the cold generated from the system. The energy consumption and generation data will be used in the lifecycle cost analysis and the cold generated was used for the CFD simulation.

CFD is used to model the phase change of water in an enclosed space with liquid nitrogen flowing through via a copper tube as described by Tan et al [19]. Figure 1 shows the test section used in the simulation. The tube wall was set to be a cooling heat source. The material of the pipe used is copper, the heat transfer model used is convection with a free stream temperature of 77K. The heat transfer coefficient used is 1,000 W/m^{2}K (heat transfer coefficient for air).

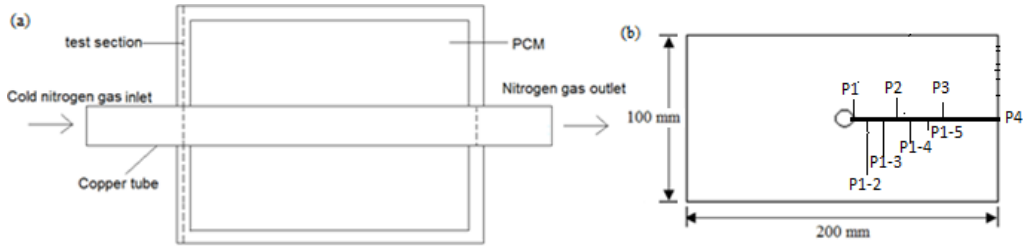


Figure 1: Test section (a) side view; (b) front view

The solver was set to model transient flow using the SIMPLE and power law discretization methods. The effect of the use of different PCMs were tested using the same parameters. As mentioned, the PCMs were enclosed in the test section, and the cooling power was supplied from the tube opening in the geometry. The simulation was carried out as transient process for a simulation time of 1800s with a timestep of 0.1s.

Meshing was carried out using the MESH component in ANSYS FLUENT. Grid independence was carried out using the mesh refine function in ANSYS Fluent. This was done by running simulations of 60s simulation times with increasingly larger number of grids. This was stopped when the compared results obtained had a p-value of less than 0.005.

8 points are tested in the simulation. These points are P1 (0 mm, 0mm), P1-2 (20 mm, 0 mm), P1-3 (30 mm, 0 mm), P2 (33.3 mm, 0 mm), P1-4 (40 mm, 0 mm), P1-5 (50 mm, 0 mm), P3 (66.6 mm, 0mm), and P4 (100 mm, 0mm). Initial 4 points (P1, P2, P3, P4) were used, however, after the first set of simulation, it was found that the freezing region only occurred before P2. Hence, an additional 4 points (P1-2, P1-3, P1-4, P1-5) were tested. These points are shown in Figure 1. The properties of the PCMs are listed in Table 2 and Table 2 are utilized in the specification of material in the simulation.

Table 2. Properties of PCM

PCM	Melting Temperature (K)			Latent heat (J/g)	Density (kg/m^3)	Heat capacity (J/kg.K)	Thermal conductivity (W/m.K)	Viscosity (kg/ms)	Ref
	Onset	End	Actual						
29.8 wt% $CaCl_2/H_2O$ solution	229.49	242.02	240.51	13.25	1,258	3,100.0	0.52	5.032 x 10^{-3}	[7], [9], [20],
39.6 wt% K_2CO_3/H_2O solution	237.02	251.07	249.17	26.18	1,400	3,000.0	0.52	6.300 x 10^{-3}	[7], [9], [20]
34.5 wt% $Mg(NO_3)_2$/ H_2O solution	242.31	249.40	247.08	185.70	1,330	3,665.1	0.52	2.310 x 10^{-3}	[7], [9], [21], [22]

Experimental study was carried out to study the release of captured cold. The phase change material was cooled initially using solid carbon dioxide. The PCM was considered ready to use when the temperature achieve the temperature of the solid carbon dioxide which is -60°C or 213K. The PCM is left to discharge its energy and temperature reading was measured at an interval of 5 min with a T-type thermocouple until all the PCM melted.

The experimental results will be used to calculate the effective number of heat transfer units in a heat exchanger, or effective NTU for short. It is defined as the ratio of the actual heat released, which would be calculated from the experiment; and the theoretical heat released which is obtained from DSC analysis from 213K to the melting point. The effective NTU was used to evaluate the performance of the system. It is calculated using Equation 1.

$$\varepsilon_{NTU} = \frac{Q_{Actual}}{Q_{Theoretical}} = \frac{m_{HTF} C_{p,HTF} (T_{w,f} - T_{w,i})}{Q_{Theoretical}} \quad (1)$$

Where
ε is the effective NTU;

Q_{Actual} is the actual cold released by the cold storage system;
m_{HTF} is the mass of heat transfer fluid;
$Cp_{,HTF}$ is the specific heat capacity of heat transfer fluid which in this case is water;
$Tw_{,f}$ is the final temperature of heat transfer fluid;
$Tw_{,i}$ is the initial temperature of heat transfer fluid.

3.2 Lifecycle cost analysis

Lifecycle cost analysis of the system takes into account the full cost of the system throughout the lifetime of the system. This includes the total capital cost and operating and maintenance cost. The total cost would then be converted to the present value using a discount rate of 9%, the acceptable rate for liquefaction systems [23]. The area to be cooled is a 25 m^2 (5 m by 5 m) floor space. The four walls of the room have cooling coils running through them where air that is regassified circulates and cools the room. The system includes 21 m^2 solar panels with a rating of 3 kW for sunlight intensity of 1000 W/m^2. The liquid air system runs for 24 hours and uses 0.39 kW to generate 1 kg of liquid air and releases 0.20 kW of power when 1 kg of liquid air is expanded; and would run over the span of 25 years.

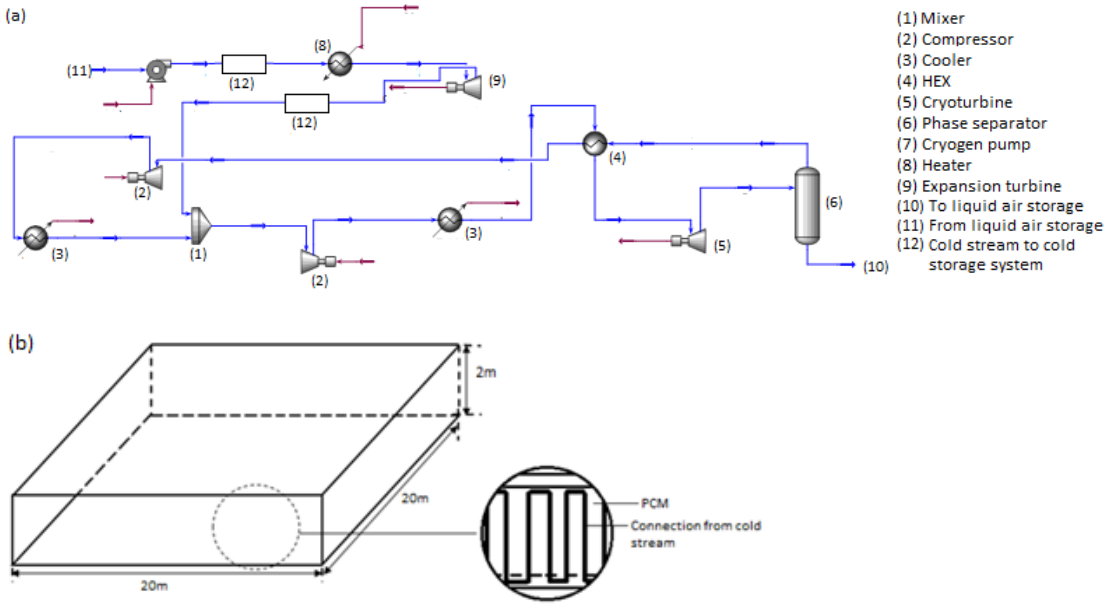


Figure 2. Liquid air system (a) Overall process cycle; (b) Cold storage system

The costing for the system in this study was done by considering the cost of individual components obtained from suppliers. The individual components have been chosen based on the parameters required to produce and generate power from liquid air and is estimated to be USD 28,381. Total capital cost is the total cost of building the system which is a one off cost that is incurred at the beginning of the system lifecycle and is listed in Table 3.

Table 3. Total capital cost

Type of cost	Percentage of equipment cost	Cost (USD)
Equipment cost	-	28,381

Cost of engineering	25%	7,095.25
Contractor fee	5%	1,419.05
Contingency cost	5%	1,419.05
	Total capital cost, T_{Cap} (USD)	38,314.40

The cost of electricity in Malaysia for medium size industry tariff for off-peak usage is considered to be USD 0.0498 [24]. The maintenance cost is the cost incurred to provide maintenance for the system, this is taken to be 5% of the equipment cost [25]. The lifecycle cost analysis then takes the base date, this current year; as the date to which all cash flows are discounted. This is considered the present value of the system.

The total sum of the operation and maintenance for the lifetime of the system is the sum of the present value of the electricity and maintenance over the lifetime of the system.

$$C_{O\&M,PV} = C_{E,PV} + C_{M,PV} \quad (2)$$

$$C_{E,PV} = \sum_{i=1}^{n} \frac{C_{E,i}}{(1+r)^i} \quad (3)$$

$$C_{M,PV} = \sum_{i=1}^{n} \frac{C_{M,i}}{(1+r)^i} \quad (4)$$

Where

$C_{E,I}$ is the cost of electricity for the particular year i.

$C_{M,i}$ is the cost of maintenance for year i.

i is the year from the beginning of the lifecycle of the system to the end of the 25 years.

The total cost of the system is then the annualised total capital cost and the annualised cost of operation and maintenance over 25 years.

$$C_{Total} = C_{Cap} + C_{O\&M,PV} \quad (5)$$

Levelised cost of the system, LCOS is the net present value of a unit cost of electricity over the lifetime of the generating asset. It is the total cost of the system over the total operating hours of the system. It is also described as the cost per kWh storage capacity.

$$LCOS = \frac{Total\ cost\ of\ system}{Total\ hours\ of\ operation}\ (\$\ per\ kWh) \quad (6)$$

An average cooling system for a cold storage room of the given size costs $26,859. This is calculated based on the price of a cold storage room of that size and cooling capacity, converted to present value. The cost ratio of the liquid air energy storage system with cold storage and the average conventional cooling system enables one to compare the cost of the proposed system.

4.0 Results and Discussion

4.1 Cold storage

The spread of cold (the temperature drop) extends to over 75% of the PCM body, however the temperature drop of 50% of the cold spread is less than 60 K. The rate of cooling is shown in Figure 3 for 8 points in the test section.

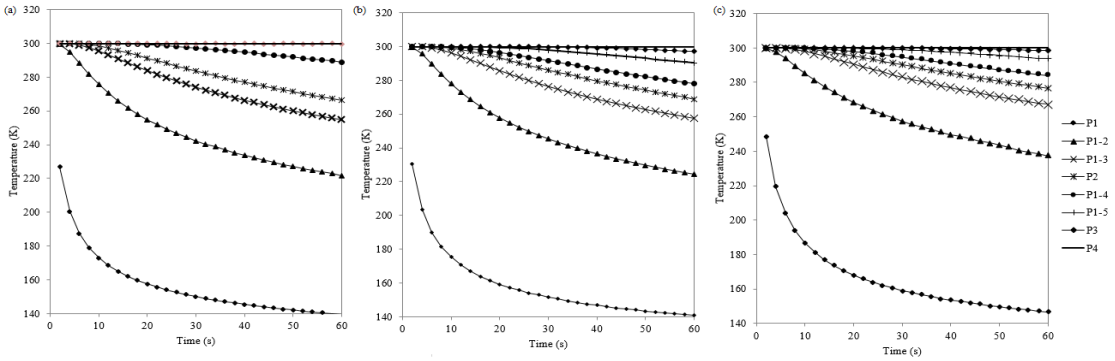


Figure 3. Rate of temperature decrease for PCM: (a) $CaCl_2$; (b) K_2CO_3; (c) $Mg(NO_3)_2$

The magnitude of the rate of temperature decrease, dT/dt decreases with time for all three PCMs at P1. dT/dt for $CaCl_2$ and K_2CO_3 at P1-2 also decreases with time but increases for $Mg(NO_3)_2$ before decreasing. The rate of temperature decrease with respect to distance from the cooling source remains relatively constant for $CaCl_2$ and K_2CO_3 PCM solutions. $Mg(NO_3)_2$ solution has the highest rate of decrease of the three PCMs at P1 and the lowest rate of decrease at P1-2. This gives a difference of 9.81 K/min. This corresponds to the melting point and latent heat of fusion of the $Mg(NO_3)_2$ solution as seen in Table 2. The initial temperature drop is fast due to its melting point and the spread of cold through the PCM is lowest due to the high latent heat of fusion. This allows $Mg(NO_3)_2$ to store more cold per unit mass of solution.

Figure 4 shows the rate of solidification of the PCM. The rate of solidification of $CaCl_2$ and K_2CO_3 is the same at P1. Both PCM freezes almost immediately. The rate of solidification for P1 for $Mg(NO_3)_2$ slower at 25%/min. At P1-3 all three PCMs hardly froze. At P1-2, the rate of solidification is 5.5%/min, 6.3%/min and 7.1%/min for $CaCl_2$, K_2CO_3 and $Mg(NO_3)_2$ respectively. The onset of solidification at P1-2 began after 30 minutes, 24 minutes and 40 minutes for $CaCl_2$, K_2CO_3 and $Mg(NO_3)_2$.

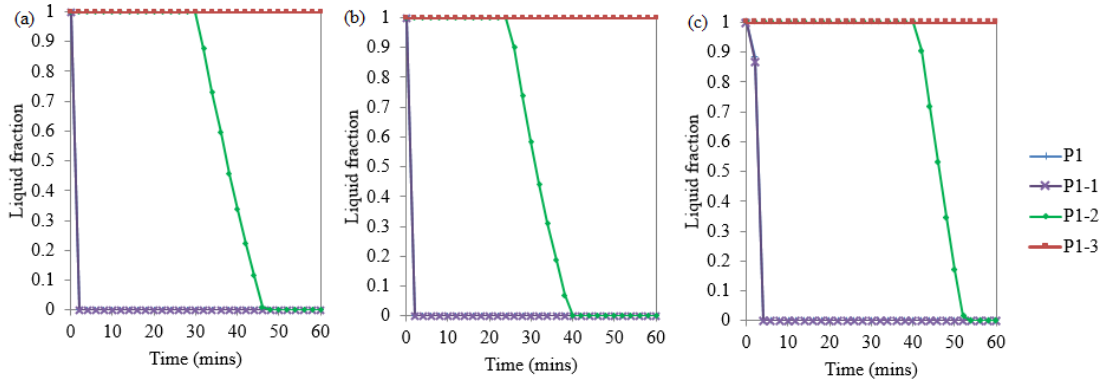


Figure 4. Rate of solidification of PCM: (a) $CaCl_2$; (b) K_2CO_3; (c) $Mg(NO_3)_2$

The total area of total solidification for the PCMs are 3.66%, 4.20% and 3.19% of the total area of the test section for $CaCl_2$, K_2CO_3 and $Mg(NO_3)_2$. This shows that the PCM solution is able to absorb cold energy from the surrounding at a higher rate than the other two PCMs. The total area for total solidification and partial solidification

for $Mg(NO_3)_2$ is the lowest of all PCMs at 3.19% and 1.33%, showing that $Mg(NO_3)_2$ solution is able to store more cold. This concludes that the $Mg(NO_3)_2$ solution is a suitable cold storage as it would be able to store a larger amount of cold at a higher rate than the other two PCMs that have been studied.

Computational fluid dynamics is a useful tool in analysis of heat transfer as it allows the analysis to be carried out without manufacturing elaborate equipment. The CFD simulations give a visual representation of data and allows for quick modifications to the set-up without manufacturing. However various assumptions in the simulation simplifies the complexity of real life systems and neglect certain physical properties.

4.2 Experimental study

Figure 5 displays the cold discharge curves for calcium chloride, potassium carbonate and magnesium nitrate solutions with the melting temperatures of each PCM. The initial discharge of cold is rapid and it slows down around the melting onset and then rapidly increases as the melting is completed.

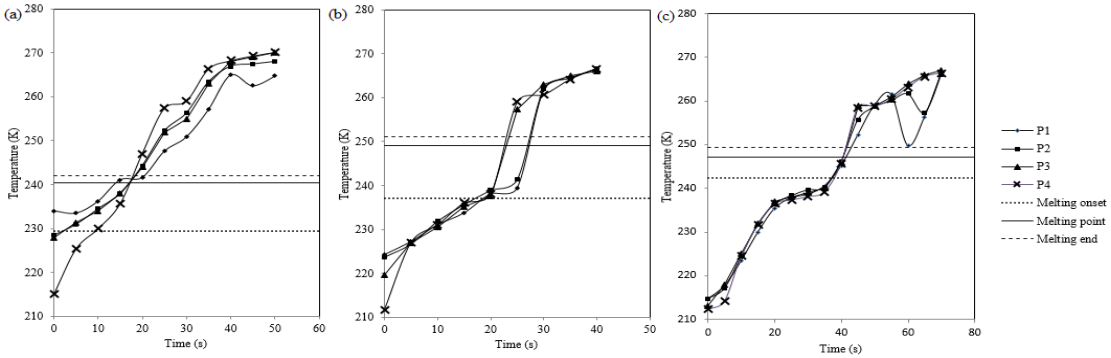


Figure 5. Experimental temperature vs time curve for (a) $CaCl_2$; (b) K_2CO_3; (b) $Mg(NO_3)_2$

It is assumed that all the cold energy from the expansion of liquid air is absorbed by the phase change material and the cold released during the PCM discharging process to the HTF is equivalent to the process of heat transfer in a heat exchanger. Hence Equation 1 is used as a measure of the effectiveness of the heat transfer.

Table 4. Theoretical heat transfer of PCM

PCM	$Q_{Theoretical}$ (latent heat) (J/g)	ε_{NTU}
$CaCl_2$	25.09	0.5146
K_2CO_3	51.60	0.5053
$Mg(NO_3)_2$	165.28	0.4880

The highest effective NTU by the experimental analysis shows that calcium chloride has the highest effective NTU, making it the most efficient phase change material to be used as storage material among the three. However the effective NTU of $CaCl_2$ is merely 0.0093 more than that of K_2CO_3 and 0.0266 more than $Mg(NO_3)_2$.

Converting the effective NTU into percentage, all three PCMs are approximately 50% effective, considering for heat transfer applications, 50% effective NTU is reasonable. Therefore all three PCMs have reasonable effective NTU.

Considering all factors, the PCM magnesium nitrate is considered the most suitable PCM for liquid air energy storage with integrated cold storage system.

4.2 Lifecycle cost analysis

The economic viability of the energy storage system can be determined by the levelised cost of the system, LCOS. The LCOS shows the cost per kWh of electricity produced by the system. The hours of autonomy of the system is also calculated to determine the duration that the system is able to function "off-grid". The cost index is used to compare the liquid air energy storage system as compared to conventional systems for food refrigeration.

The cost of the system is considered along with the generation of electricity due to the expansion of liquid air. The total cost of the system along with the solar panels is calculated to be $36,342. The cost ratio of the system compared to the conventional refrigeration room is 1.35, which translates to $9,483 additional cost. The LCOS of the system is $0.1659/kWh. The cost of electricity generated is however still higher than the off peak cost of electricity from the grid ($0.0498/kWh). In terms of hours of autonomy, the cold storage is able to operate for 29.3 hours without any electrical energy source from one cycle. This is beneficial in rural areas where electricity supply may not be reliable. The operation of cold storage without electricity supply allows for food and medicines to be stored even when there is no electricity. All these factors combined indicates that the cold storage system integrated with liquid air energy and cold storage system has the economic potential to replace the conventional system as a cooling system.

5.0 Addressing the Grand Challenges for Engineering

The realization of an integrated liquid air energy and cold storage system would assist in addressing two of the 14 Grand Challenges for engineering, making solar energy affordable and to improve and restore urban infrastructure. The integration of the system into existing infrastructure would reduce the dependence upon grid energy for cold applications. The use of solar energy for liquefaction would help make solar energy economical as shown in the economic analysis. Cold energy is in high demand globally. Cold energy is required to cool data centres, store and transport food, store vaccines, medicines and blood for blood banks, air conditioning etc [2]. The incorporation of liquid air energy storage as well as cold capture in building is able to supply part of the cold energy needed to address part of the cold demand. This would reduce the reliance on the supply of cold to be from grid energy, thus reduces the

demand for electricity from the grid, restoring and improving urban infrastructure, which is one of the 14 Grand Challenges for engineering.

6. Conclusion

The demand for cold energy is constantly increasing due to the modern lifestyle and event of climate change. Food security, medicines, space cooling, data centre cooling is only part of the need for cold energy. Cold is also highly polluting producing large amounts of carbon dioxide and contributing to the depletion of the ozone layer due to the HFC leaks from refrigeration system. Hence the need for a clean alternative for generation of cold is required.

Liquid air energy and cold storage utilises the solar energy to generate both electricity and cold energy. Three eutectic water-salt solutions were studied, 29.8wt% calcium chloride/H_2O solution, 39.6wt% potassium carbonate/H_2O solution and 34.5wt% magnesium nitrate/H_2O solution as potential PCM storage material of liquid air system. Based on the CFD as well as experimental results, 34.5wt% magnesium nitrate/H_2O solution is the most suitable for cold storage application. It has a latent heat of 185.69 J/g, it is able to store 185.69 J of cold per gram of solution. The melting/freezing point of the solution is 247.08 K, this temperature falls within the temperature range of various cold applications. The CFD analysis shows the rate of cooling and solidification of the PCM and it is found that the rate of cooling and solidification of the magnesium nitrate/water solution PCM is favourable as a cold storage medium. The effective NTU analysis shows that the calculated value of effective NTU for the solution is 48.8% which is slightly less than the 50% effective NTU threshold set.

The economic analysis of the system is also carried out and it is found that as compared to conventional systems over a period of 25 years, the cost ratio of the system is 1.35 and the LCOS is higher as compared to the cost of electricity generation from the grid. However, it runs solely on solar power and has a 29 hour autonomy period, making it essentially self-sufficient which is useful in rural areas where electricity is scarce and an economically viable option. Further study can be done to further reduce the cost of the liquid air system as well as studying the use of the system in different applications.

Acknowledgment

The research is funded by the by the Ministry of Education Malaysia, Fundamental Research Grant Scheme (Grant no: 320201-TK61-321-C31) and supported by Taylor’s University through its PhD Scholarship Programme.

References

[1] G. (Birmingham E. I. Harper, “Doing cold smarter,” Birmingham, 2015.
[2] L. Kitinoja, “Exploring the Potential for Cold Chain Development in Emerging

and Rapidly Industrialising Economies through Liquid Air Refrigeration Technologies," Birmingham, 2014.

[3] B. N. Rasmussen, "Calculating Total Cooling Requirements for Data Centers," 2007.

[4] I. Hadjipaschalis, A. Poullikkas, and V. Efthimiou, "Overview of current and future energy storage technologies for electric power applications," *Renew. Sustain. Energy Rev.*, vol. 13, no. 6–7, pp. 1513–1522, Aug. 2009.

[5] G. Zotter, W. Hermeling, and W. Sanz, "Thermodynamic analysis of a novel cryogenic Rankine cycle," in *ASME Turbo Expo*, 2012, pp. 1–10.

[6] H. Chen, T. N. Cong, W. Yang, C. Tan, Y. Li, and Y. Ding, "Progress in electrical energy storage system: A critical review," *Prog. Nat. Sci.*, vol. 19, no. 3, pp. 291–312, Mar. 2009.

[7] G. Li, Y. Hwang, R. Radermacher, and H.-H. Chun, "Review of cold storage materials for subzero applications," *Energy*, vol. 51, pp. 1–17, Mar. 2013.

[8] E. Oró, a. de Gracia, a. Castell, M. M. Farid, and L. F. Cabeza, "Review on phase change materials (PCMs) for cold thermal energy storage applications," *Appl. Energy*, vol. 99, pp. 513–533, Nov. 2012.

[9] Y. J. Tan, M. Al-atabi, V. A. Doshi, and A. Kumar, "Capturing Cold Energy from Regasification of," in *5th EURECA Conference*, 2015, no. 2, pp. 1–15.

[10] A. A. Al-Abidi, S. Bin Mat, K. Sopian, M. Y. Sulaiman, and A. T. Mohammed, "CFD applications for latent heat thermal energy storage: A review," *Renew. Sustain. Energy Rev.*, vol. 20, no. April, pp. 353–363, 2013.

[11] C. Guo and W. Zhang, "Numerical simulation and parametric study on new type of high temperature latent heat thermal storage system," *Energy Convers. Manag.*, vol. 49, 2008.

[12] W. B. Ye, D. S. Zhu, and N. Wang, "Numerical simulation on phase-change thermal storage/release in a plate-fin unit," *Appl. Therm. Eng.*, vol. 31, no. 17–18, pp. 3871–3884, 2011.

[13] A. Darzi, F. M, and K. Sedighi, "Numerical study of melting in a concentric and eccentric horizontal annulus," *Appl. Math. Model.*, vol. 36, pp. 4080–4086, 2012.

[14] N. H. S. Tay, F. Bruno, and M. Belusko, "Experimental validation of a CFD model for tubes in a phase change thermal energy storage system," *Int. J. Heat Mass Transf.*, vol. 55, no. 4, pp. 574–585, 2012.

[15] T. Silva, R. Vicente, N. Soares, and V. Ferreira, "Experimental testing and numerical modelling of masonry wall solution with PCM incorporation: A passive construction solution," *Energy Build.*, vol. 49, pp. 235–245, 2012.

[16] T. Ali, R. A. Bakar, B. A. Sup, M. F. Zainudin, and G. L. Ming, "Study on thermal-fluid effect of thermal energy storage tank design in solar energy applications," *Energy Procedia*, vol. 68, pp. 3–11, 2015.

[17] Y. H. L. Lim, M. Al-atabi, and R. A. Williams, "Cryogenic Liquefaction of Air as an Energy Storage : Numerical Study of Liquefaction and Power Recovery Process," in *4th EURECA Conference*, 2015, pp. 1–12.

[18] F. Inc., "Modeling Solidification and Melting," in *Fluent User's Guide*, Cannonsberg, PA, 2001, pp. 21–1 – 21–14.

[19] H. Tan, Y. Li, H. Tuo, M. Zhou, and B. Tian, "Experimental study on liquid/solid phase change for cold energy storage of Liquefied Natural Gas (LNG) refrigerated vehicle," *Energy*, vol. 35, no. 5, pp. 1927–1935, 2010.

[20] Å. Melinder, "Thermophysical Properties of Aqueous Solutions Used as Secondary Working Fluids," 2007.

[21] S. Mahiuddin and K. Ismail, "Temperature and concentration dependence of

viscosity of Mg(NO3)2-H2O systems," *Can. J. Chem.*, vol. 60, pp. 2883–2888, 1982.

[22] (NeoChim), "Magnesium nitrate solution information," Dimitrovgrad, Bulgaria, 2004.

[23] M. Akhurst, A. Atkins, R. Uk, R. Bruges, S. Cooper, S. Consulting, T. Evison, M. Group, N. Goode, G. Thornton, S. Nelmes, H. P. Storage, N. Owen, D. Sanders, C. Advisory, S. Saunders, D. Ing, and A. Schlotmann, "Liquid Air in the energy and transport systems: Opportunities for the industry and innovation in the UK," 2013.

[24] (TnB), "Malaysian Industry Energy Tariffs," 2014. [Online]. Available: http://www.tnb.com.my/business/for-industrial/pricing-tariff.html. [Accessed: 30-Aug-2014].

[25] R. K. Sinnott, *Chemical Engineering Volume 6: Chemical Engineering Design*, 4th ed. Jordan-Hill, Oxford: Elsevier, 2005.

A Numerical Study of the Effect of a Perforation on Natural Frequencies of Guitar Soundboards

M.K. Lee[1*], M. Hosseini Fouladi, N.N. Satesh

School of Engineering, Taylor's University,

No.1 Jalan Taylor's, 47500, Subang Jaya, Selangor, Malaysia

*leemk996@gmail.com

Abstract

The effects of size of perforations on the natural frequencies of rectangular and circular plates have been studied by numerous researchers. The present work focuses these concepts on an irregular shaped plate such as the guitar soundboard. A plate is considered as irregular if its shape is neither rectangular nor circular. However, as the shape of the soundboard is irregular, a satisfactory analytical solution has yet to be found. Therefore, a numerical study using the finite element method is used to determine the effect of a perforation upon the natural frequencies of the soundboard. CATIA was used to model the soundboard and ANSYS was used in the analysis. Results of the analysis show that the variation of natural frequencies with mode numbers can be represented by a linear relationship for each sound hole of constant radius. These results also show that size of sound holes have negligible effect on the natural frequencies.

Keywords: Soundboard, perforation, natural frequencies, mode numbers

1. Introduction

Perforations or cut-outs are commonly found in many mechanical, civil, aerospace, missiles and marine structures. Their main function is to reduce the weight of these huge structures or simply to allow access to mechanical components and electrical systems for maintenance purposes. They are also used for ventilation purposes and in some cases for modifying the resonant frequencies of the structures.

Perforated plates are widely used in nuclear power plant equipment, heat exchangers as well as in pressure vessels.

Various methods have been used to investigate the effects of perforations on the natural frequencies of plates. Aksu and Ali [1] investigated the dynamic characteristics of rectangular plates with one to two cut-outs using finite difference formulation and verified their findings from experimental data. Ali and Atwal [2] considered simply-supported rectangular plates with rectangular cut-outs using the Raleigh-Ritz method. Natural frequencies of rectangular plates with an arbitrarily located rectangular cut-out were determined using the Rayleigh quotient by Lee *et. al* [3]. The least-squares method was used by Hegarty and Ariman [4] to investigate the free vibration of a simply-supported and clamped rectangular plate with a central circular hole. Cho *et.al* [5] used the assumed mode method and Lagrange's equation of motion to determine the natural frequencies of rectangular plates by subtracting the energy of openings from the energy of the plate.

The effects of variously shaped holes on the free vibration of rectangular plates were investigated by Huang and Sakiyama [6]. Variously shaped perforations considered were rectangular, circular, elliptic and oval in nature. Experimental analysis using holographic interferometry and finite element analysis were used by Monahan *et.al* [7] to investigate a clamped plate with different sizes of cut-outs. The stiffness of trapezoidal sheets perforated by different arrays of holes was carried out by Kathagea *et.al* [8]. Natural frequencies and mode shapes obtained from digital speckle interferometry by Romero *et.al* [9] were compared to those obtained from approximate analytical solution by the Rayleigh-Ritz method using orthogonal polynomials.

Mali and Singru [10], [11] introduced the concept of negative masses for perforations and obtained the fundamental frequency of a rectangular plate with four circular perforations arranged in a rectangular pattern. Lam *et.al* [12] obtained a deflection function for an originally complex domain of a rectangular plate with cut-outs and non-homogeneity by dividing the domain into appropriate rectangular segments. Lam and Hung [13] used this method in combination with orthogonal polynomials generated by the Gram-Schmidt process to investigate plates with cracks and cut-outs.

The objective of the current work is the study of the effects of perforations on the natural frequencies of an irregular shaped plate in the form of a guitar soundboard. The perforation is in the form of a sound hole. Various sizes of sound holes are used in this study. The effects on the natural frequencies caused by sound holes of various sizes are investigated over the first fifteen modes. The numerical study involving modal analysis is performed using ANSYS. Results of this study could be used in conjunction with the acoustic component of ANSYS for future studies in attempts to improve the acoustic power of the guitar.

2. Methodology

2.1 Modelling

A Torre's model of a guitar soundboard is adopted for this study. It was modelled using CATIA with dimensions consistent with that of a Torre's model. This model is shown in Fig. 1a and saved with a file extension of .stp. This file is then imported into ANSYS for modal analysis. The contour of the Torre's model is constructed using a 9-centre method proposed by Boullosa [14] and is as shown in Fig. 1a. Fig. 1b shows the position of the normal-sized sound hole of radius 41.9 mm.

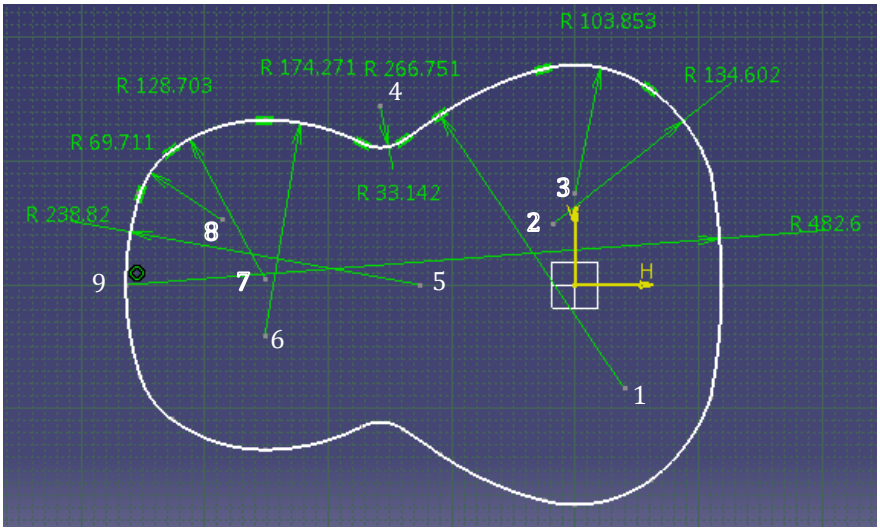


Figure 1a. Contour dimensions of Torre's soundboard using 9-centre method [14].

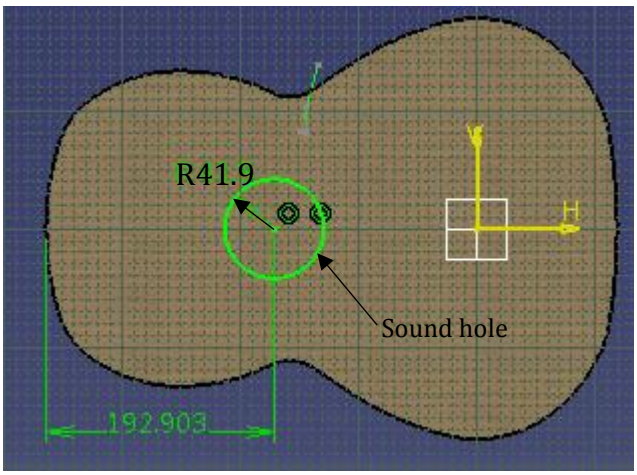


Figure 1b. Dimensions and position of sound hole

2.2 Modal Analysis

The modal analysis module from ANSYS was used for this study and the soundboard was imported for analysis. Properties of the material used are summarised in Table 1.

(a) Material properties used are as follows:

Table 1. Plate Specifications of Soundboard

Material	White Spruce
Young's modulus, E (Pa)	1.0E10
Poisson's ratio, ν	0.42
Density, ρ (kg-m^{-3})	430
Thickness, h (mm)	2.0

(b) Type and Properties of Element used in the analysis:

Element type: Solid186 (hexahedral)
Properties of Element:
This element has mid-side nodes and is used for three-dimensional modelling of solid structures and allows for quadratic displacements. It has 20 nodes and three degrees of freedom at each node: translations in the nodal *x*, *y*, and *z* directions. It also allows for plasticity, stress stiffening, large deflections and large strains. KEYOPT(2) = 0 specifies uniform reduced integration technology, KEYOPT(3) = 0 ensures that the element is a non-layered structural solid, and KEYOPT(6) = 0 specifies pure displacement formulation.

(c) Analysis Criteria:

Number of modes to evaluate = 15
Boundary Condition: The soundboard is clamped around its outer contour.
Mesh type used for mesh convergence study: Coarse, Medium, Fine.

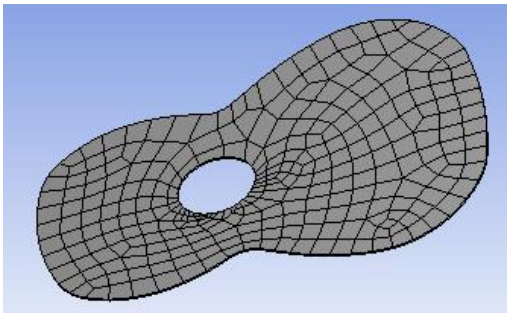


Figure 2a. Coarse Mesh
(Number of nodes: 2257
Number of elements: 291)

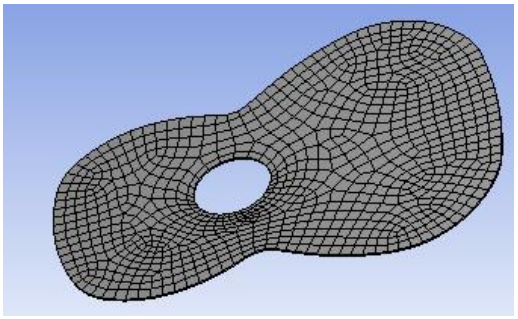


Figure 2b. Medium Mesh
(Number of nodes: 6454
Number of elements: 872)

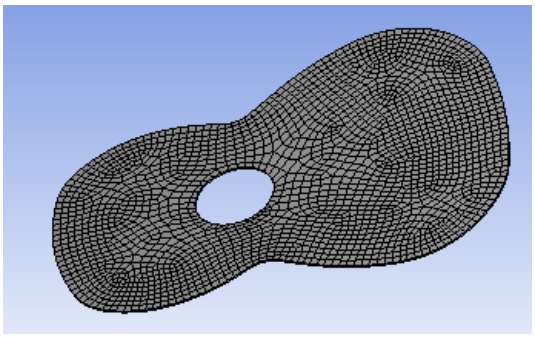


Figure 2c. Fine Mesh
(Number of nodes = 14819; Number of elements = 2042;
Element Quality = 0.432; Parallel Deviation = 7.030^0; Aspect Ratio = 4.425)

Figure 2. Relative Mesh size for soundboard with a sound hole of 41.9 mm radius.

3. Results

Numerical results from ANSYS for mesh independent tests for soundboards with no hole, normal-sized hole of radius R41.9mm, medium-sized hole of radius R49.0mm and for a large-sized hole of radius 53.0mm are shown in Tables 2, 3, 4 and 5 respectively.

Table 2. Frequency convergence (no hole)

Boundary Condition: CLAMPED Soundboard (no hole)			
Meshing Mode No.	Coarse *f* (Hz)	Medium *f* (Hz)	Fine *f* (Hz)
1	181.54	173.24	171.29
2	256.71	246.05	243.29
3	374.64	359.64	356.55
4	384.78	367.81	363.36
5	551.93	526.93	522.48
6	584.9	555.52	547.92
7	649.49	618.25	610.74
8	658.99	628.81	620.97
9	780.69	742.9	736.4
10	851.88	809.45	800.61
11	994.5	931.99	919.62
12	1004	946.32	935.04
13	1047.5	989.75	978.61
14	1097	1040.6	1028.5
15	1113.2	1046.9	1032.9
	Coarse	Medium	Fine
Nodes	1518	5110	13747
Elements	195	691	1902

Table 3. Frequency convergence, normal-sized hole (R41.9mm)

Boundary Condition: CLAMPED Soundboard (R41.9mm)			
Meshing Mode No.	Coarse f (Hz)	Medium f (Hz)	Fine f (Hz)
1	179.54	173.91	172.18
2	265.55	254.88	251.99
3	354.66	344.81	342.03
4	379.97	366.55	362.81
5	540.73	516.98	510.85
6	575.18	555.28	550.32
7	623.2	602.46	596.24
8	652.14	627.95	621.66
9	720.82	699.13	693.51
10	793.94	764.69	757.41
11	966.61	931.12	920.7
12	973.77	931.69	922.58
13	1018.3	982.61	973.35
14	1049.3	1013.2	1004.2
15	1081.5	1037.7	1024
	Coarse	Medium	Fine
Nodes	2257	6454	14819
Elements	291	872	2042

Table 4. Frequency convergence, medium-sized hole (R49.0mm)

Boundary Condition: CLAMPED Soundboard_(R49.0mm)			
Meshing Mode No.	Coarse f (Hz)	Medium f (Hz)	Fine f (Hz)
1	179.21	174.41	172.29
2	272.16	263.34	259.16
3	352.64	342.38	339.12
4	377.78	366.51	362.09
5	532.93	515.64	507.4
6	600.51	580.13	572.91
7	616.43	596.47	589.03
8	652.12	631.36	623.58
9	729.24	704.79	696.21
10	798.93	771.61	761.84
11	964.38	930.15	917.65
12	966.79	931.52	919.96
13	1015.8	979.87	966.46
14	1042.5	1007.8	996.45
15	1098.9	1052.6	1036.2
	Coarse	Medium	Fine
Nodes	2231	6196	14323
Elements	286	833	1969

Table 5. Frequency convergence, large-sized hole (R53.0mm)

Boundary Condition: CLAMPED Soundboard_(R53.0mm)			
Meshing Mode No.	Coarse f(Hz)	Medium f(Hz)	Fine f(Hz)
1	179.1	173.78	172.27
2	277.9	266.36	263.36
3	353.12	341.54	339.11
4	377.45	365.21	361.71
5	536.03	515.72	509.45
6	608.59	590.03	584.65
7	620.98	592.87	587.44
8	659.9	632.97	626.86
9	743.69	707.66	702.15
10	806.4	776.84	769.25
11	964.44	924.19	915.25
12	973.92	928.94	919.85
13	1028.4	976.53	966.4
14	1047.9	1002.4	993.62
15	1108.5	1055.4	1042.5
	Coarse	Medium	Fine
Nodes	2188	6600	14272
Elements	279	890	1961

Numerical results from ANSYS for variation of frequency with mode number for various sizes of sound holes are shown in Table 6. Radii of the holes are in millimetres.

Table 6. Natural Frequency (Hz) versus Mode Number for Various Hole Size

Boundary Condition: CLAMPED/Meshing: Fine Hole Size (mm)							
Mode No.	R41.9	R45.0	R47.0	R49.0	R51.0	R53.0	R0
1	172.18	169.95	172.21	172.29	172.19	172.27	171.29
2	251.99	255.44	256.9	259.16	261.17	263.36	243.29
3	342.03	342.11	339.49	339.12	338.86	339.11	356.55
4	362.81	357.38	362.2	362.09	361.72	361.71	363.36
5	510.85	510.71	507.04	507.4	507.87	509.45	522.48
6	550.32	558.55	565.83	572.91	579.93	584.65	547.92
7	596.24	585.84	590.97	589.03	586.63	587.44	610.74
8	621.66	614.81	622.62	623.58	624.66	626.86	620.97
9	693.51	696.99	694.24	696.21	698.8	702.15	736.4
10	757.41	758.87	759.24	761.84	764.81	769.25	800.61
11	920.7	908.17	918.4	917.65	915.97	915.25	919.62
12	922.58	912.42	920.34	919.96	919.51	919.85	935.04
13	973.35	969.74	967.18	966.46	965.82	966.4	978.61
14	1004.2	992.89	998.2	996.45	994.72	993.62	1028.5
15	1024	1017.2	1032.7	1036.2	1039.3	1042.5	1032.9

The effects of normal-sized hole (R41.9mm), medium-sized hole (R49.0mm) and large-sized hole (R53.0mm) on the natural frequencies of the soundboard are shown in Fig. 3.

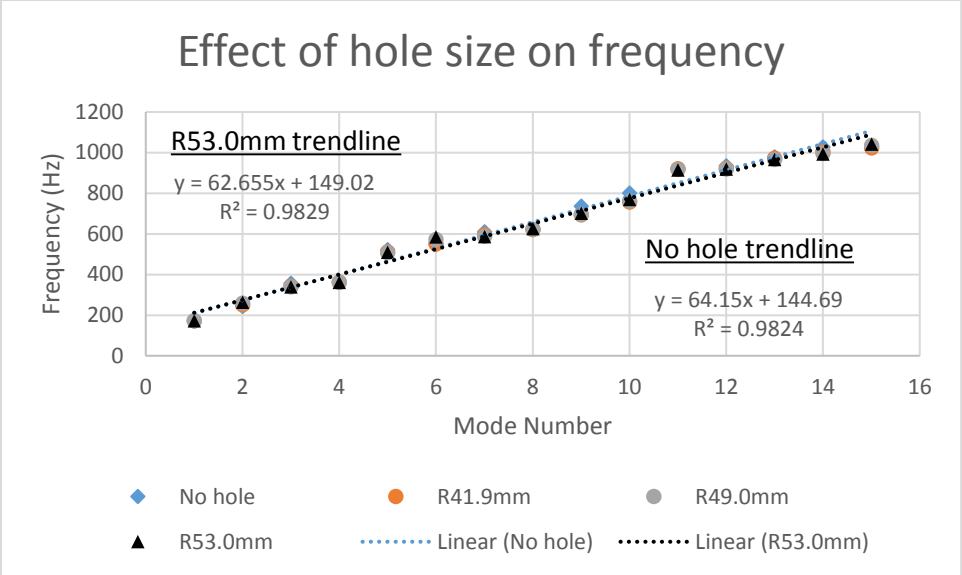


Figure 3. Variation of Frequency with Mode Number for normal-sized, medium-sized and large-sized hole sizes.

4. Discussion

Data from mesh independent tests shown in Tables 2, 3, 4 and 5 for soundboards with no-hole, R41.9mm small-sized hole, R49.0mm medium-sized hole and R53.0mm large-sized hole indicate that the natural frequencies converge to more accurate values as mesh sizes are refined. The relatively smaller difference in magnitude of the frequencies between the medium and fine meshes as compared to those between coarse and medium meshes indicate that the natural frequencies have converged to more accurate values. This indicates that the final values of the natural frequencies are independent of mesh size. For the fine mesh, the average value of the element quality of 0.432 indicate that the cell quality is good. The average values of the parallel deviation and aspect ratio of the element are 7.030^0 and 4.425 respectively.

The effects of holes of different sizes on the natural frequencies of the soundboard are studied using soundboards perforated by a normal-sized hole (R41.9mm), a medium-sized hole (R49.0mm) and a large-sized hole (R53.0mm). Fig.3 indicates that the effect of sound holes of different sizes on the natural frequencies can be quantified by a linear relation between the natural frequencies and mode number. The R-squared values of approximately 98.2 to 98.3% for the no-hole and large-sized hole soundboards also indicate that the numerical values of the natural frequencies are very close to the predicted values of the regression model. Similar effects are also observed for the normal- and medium-sized hole soundboards from Fig. 3.

Fig. 3 also indicates that the data points for the normal-sized and the medium-sized hole soundboards follow almost similar trend lines to those of the no-hole and

large-hole soundboards. These results leads to the conclusion that the sizes of the sound holes in this investigation has negligible effects on the natural frequencies of the soundboard.

5. Conclusion

The properties of the element SOLID186 are appropriate for this analysis. Mesh independence has been established and the natural frequencies of the soundboard have converged to accurate values.

The sizes of the sound holes used in this investigation are found to have no or negligible effects on the natural frequencies of the soundboard.

References

[1] G. Aksu and R. Ali, "Determination of dynamic characteristics of rectangular plates with cutouts using a finite difference formulation," *J. Sound Vib.*, vol. 44, no. 1, pp. 147–158, 1976.

[2] A. Ali and S. J. Atwal, "Prediction of natural frequencies of vibration of rectangular plates with rectangular cutouts," *Comput. Struct.*, vol. 12, no. 6, pp. 819–823, 1980.

[3] H. P. Lee, S. P. Lim, and S. T. Chow, "Prediction of natural frequencies of rectangular plates with rectangular cutouts," *Comput. Struct.*, vol. 36, pp. 861–869, 1990.

[4] R. F. Hegarty and Y. Ariman, "Elasto-dynamic analysis of rectangular plates with circular holes," *Int. J. Solids Struct.*, vol. 11, no. 7–8, pp. 895–906, 1975.

[5] D. S. Cho, N. Vladimir, and T. M. Choi, "Approximate natural vibration analysis of rectangular plates with openings using assumed mode method," *Int. J. Nav. Archit. Ocean Eng.*, vol. 5, no. 3, pp. 478–491, 2013.

[6] M. Huang and T. Sakiyama, "Free vibration analysis of rectangular plates with variously shaped holes," *J. Sound Vib.*, vol. 226, no. 4, pp. 769–786, 1999.

[7] J. Monahan, P. J. Nemergut, and G. E. Maddux, "Natural frequencies and mode shapes of plates with interior cutouts," *Shock Vib. Bull.*, vol. 41, no. 7, pp. 37–49, 1970.

[8] K. Kathagea, T. H. Misiekb, and H. Saal, "Stiffness and buckling load of perforated sheeting," *Thin-Walled Struct.*, vol. 44, no. 12, pp. 1223–1230, 2006.

[9] G. G. Romero, E. E. Alans, C. C. Martnez, L. G. Nallim, M. W. Toledo, and L. Ivarez, "Vibration analysis of perforated plates using time-average digital speckle pattern interferometry," *Exp. Mech.*, vol. 50, no. 7, pp. 1013–1021, 2010.

[10] K. D. Mali and P. M. Singru, "Determination of the fundamental frequency of perforated plate with rectangular pattern of circular holes by negative mass approach for the perforation," *Int. J. Adv. Mater. Manuf. Charact.*, vol. 1, no. 1, pp. 105–109, 2012.

[11] K. Mali and P. M. Singru, "Determination of the fundamental frequency of perforated rectangular plates:Concentrated negative mass approach for the perforation," *Adv. Acoust. Vib.*, pp. 1–6, 2013.

[12] K. Y. Lam, K. C. Hung, and S. T. Chow, "Vibration analysis of plates with cutouts by the modified Rayleigh-Ritz method," *Appl. Acoust.*, vol. 28, no. 1, pp. 49–60, 1989.

[13] K. Y. Lam and K. C. Hung, "Orthogonal polynomials and subsectioning method for vibration of plates," *Comput. Struct.*, vol. 34, no. 6, pp. 827–834, 1990.
[14] R. R. Boullosa, "A note on a geometric method for the guitar's contour," *Savart J.*, pp. 1 – 4, 2013.

eureca 2016 – Conference Paper
Paper PG04

Extraction of Tremor Feature From ECG Signals

Chow Shee Onn[1,*], Leong Wai Yie[2]
[1]*School of Engineering, Taylor's University, Malaysia*
[2]*School of Engineering, Taylor's University, Malaysia*

[*]chowshee@yahoo.com

Abstract
This paper studies the algorithms that can be used for detecting unusual feature in electrocardiograms (ECG). Medical doctor relies heavily on ECG for the diagnosis of heart disease. The shape of the ECG curve contains very important data and information about heart condition. The ECG signal was produced from the electrical conduction of heart muscle when the heart is pulsating when pumping blood throughout the body. Information extracted from ECG will be used to study numerous malign or even life-threatening cardiac disease. A variety of algorithm based on various methods had been developed to study the heart-disease. Attention is paid on focusing the measurement of QT interval in ECG signal. Wiener filter will be used to filter off noise and unwanted interference from the original ECG signal. The property of the filtered signal is studied and assessed using a variety of methods like statistics and wavelet. Wavelet is applied on the filtered signal to extract special feature associated with the recorded ECG signal. The final result shows that special feature appears on the filtered signal indicating that certain anomaly is present in the ECG signal. Comparison of the Haar wavelet transform with the Daubechies method shows similar feature but different wavelet. Daubechies wavelet transform marks the T wave offset early while the Haar shows the feature later.

Keywords : Wavelet transform, ECG feature extraction, algorithm, QT interval.

1. Introduction

The analysis and identification of the shape of ECG signal is important for the diagnosis of cardiac disorders. The ECG signal pattern show the amplitude and relative intervals of the different waves (P, QRS and T wave). Automatic ECG feature extraction methods are important as manual beat-by-beat measurement of ECG points is not practical in clinical practice.

QT interval is one of the most important ECG feature. The prolonged time-interval for QT means malign cardiac arrhythmias and can lead to sudden cardiac death.

Study had shown that certain drug can prolong the QT interval, causing adverse effect on the heart [1]. Many algorithms for ECG feature extraction had been developed. Further study is being carried out on the proper formalisation of QT interval.

This paper will discuss and present the commonly used methods for measuring QT interval. Besides conventional, semi-automated and automated measurement methods will also be discussed. This paper will also explore for a novel algorithm to filter off noise from a signal so as to extract feature of tremor from ECG (Electrocardiography) signal. Investigation will be carried out on the pattern of ECG (Electrocardiography) signal. Attention will be paid to find a novel algorithm to filter off noise so as to study the ECG (Electrocardiography) signal.

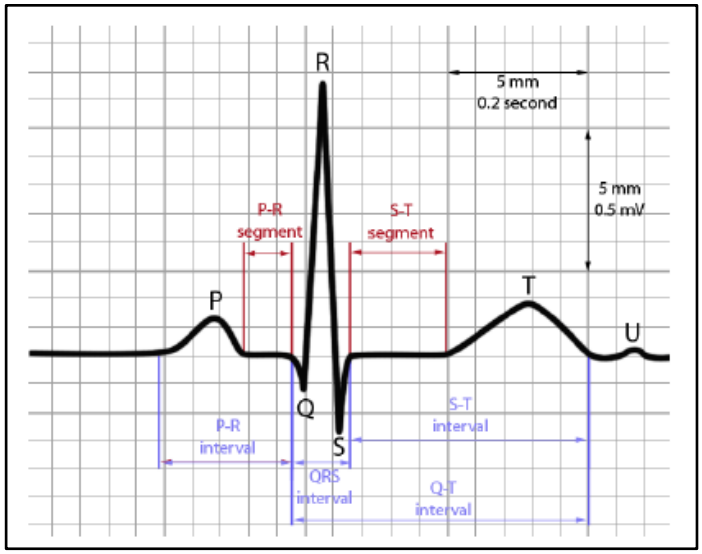


Figure 1. Typical ECG pattern [2]

Table 1 : Physiological duration of the characteristic components of an ECG pattern [3]

Wave or interval	Guide value for the physiological duration in s
P wave	0.05 – 0.10
PQ interval	0.13 – 0.20
Q wave	< 0.05
QRS complex	0.05 – 0.10
S wave	< 0.04
QT interval	0.18 – 0.52

2. Literature Review

In the study of signal processing, many filters of different configurations and designs were used to filter and reduce the effect of noise from signals obtained from particular sources. The Wiener filter is used to generate a desired random process by using the method of linear time-invariant (LTI) of filtering of an observed noisy signal, assuming known stationary signal and noise spectra.

The filter algorithm is trying to minimize the mean square error between the random signal and the desired signal.

2.1 Noise Filtering Using Wiener Filter

The main purpose of designing a Wiener filter is to compute a statistical unknown signal using a known signal as input. The filtering of the known signal will produce output as an estimate. The input signal may consist of unknown signal of interest that has been corrupted by the addition of noise [4]. The concept of the Weiner filter is based on a statistical approach like the Minimum Mean-Square Error (MMSE). It can filter out the noise from the corrupted signal to provide the signal of interest [5].

When designing a Wiener filter, one is assumed to have the knowledge of the spectral properties of the original signal and its noise [6]. The property of the filter is linear time-invariant which can produce an output very close to the original signal. It is frequently used in the process of convolution and deconvolution. The characteristics of Wiener filters are :

a) The signal and the noise are stationary linear stochastic processes with known spectral characteristics or known autocorrelation and cross-correlation.
b) The filter can be constructed physically and tested to achieve the desired output.
c) The performance criterion for the filter is Minimum Mean-Square Error (MMSE).

2.2 Application of Wiener Filter

The Wiener Filters are used widely in the field of digital communication, control systems, image processing and signal processing. The filter can be used in image processing and signal processing to remove unwanted noise from picture and signal. It is used as a pre-processor to remove noise from an audio signal, especially speech, before speech processing.

The wide application of Wiener filter can be grouped into the four areas as shown.

- Noise reduction
- Signal detection
- System detection and identification
- Deconvolution

2.3 Wiener filter

The Wiener filter [7] is used to produce an estimate of a desired output signal by linear time-invariant (LTI) filtering of an observed noisy signal, assuming known stationary signal and noise spectra. The function for the Wiener filter is to minimize the mean square error between the estimated random signal and the desired signal.

3. Theory and Research Methodology

The Wiener filter has 3 possible solution cases. The first is noncausal solution where a noncausal filter is analysed that requires an infinite amount of both past and future data. The second is a causal solution where a causal filter is used. The third is

the finite impulse response (FIR) where a finite amount of past data is used [8]. The first case is simple to solve but is not realistic for real-time applications. Wiener filter main usage is solving the second case where the causality requirement is in effect.
Noncausal solution

$$G(s) = \frac{S_{x,s}(s)}{S_x(s)} e^{\alpha s} \quad (1)$$

Where *S* are spectra. Provided that *g(t)* is optimal, then the minimum mean-square error equation reduces to

$$E(e^2) = R_s(0) - \int_{-\infty}^{\infty} g(\tau) R_{x,s}(\tau + \alpha) d\tau \quad (2)$$

and the solution g(t) is the inverse two-sided Laplace Transform of G(S).
Causal solution

$$G(s) = \frac{H(s)}{S_x^+(s)} \quad (3)$$

Finite impulse response of Wiener filter for discrete series

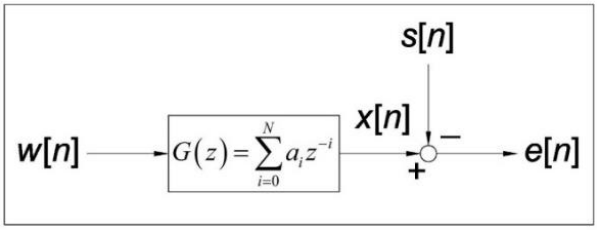


Figure 2. Block diagram of noise filtering.

Figure 2 shows the block diagram of the FIR Wiener filter for discrete series. An input signal *w*[*n*] is convolved with the Wiener filter *g*[*n*] and the result is compared to a reference signal *s*[*n*] to obtain the filtering error *e*[*n*].

In order to derive the coefficients of the Wiener filter, consider the signal *w*[*n*] being fed to a Wiener filter of order *N* and with coefficients $\{a_i\}$, where *i=0, 1, 2,….N*. The output of the filter is denoted *x*[*n*] which is given by the expression

$$x[n] = \sum_{i=0}^{N} a_i w[n-i] \quad (4)$$

The residual error is denoted by *e*[*n*] and is defined as *e*[*n*]=*x*[*n*]-*s*[*n*]. The Wiener filter is designed so as to minimize the mean square error. This can be stated as follows :

$$a_i = arg_{min} E\{e^2[n]\} \quad (5)$$

where $E\{\ \}$ denotes the expectation operator. The mean square error (MSE) may be written as :

$$E\{e^2[n]\} = E\{(x[n] - s[n])^2\}$$

$$= E\{x^2[n]\} + E\{s^2[n]\} - 2E\{x[n]s[n]\} \quad (6)$$

To find the vector $[a_0,\ldots,a_N]$ which minimizes the expression above, calculate its derivative with respect to a_i

$$\frac{\partial}{\partial a_i} E\{e^2[n]\} = 2\sum_{j=0}^{N} R_w[j-i]a_j - 2R_{sw}[j] \qquad i=0,\ldots,N \quad (7)$$

Letting the derivative be equal to zero results in

$$\sum_{j=0}^{N} R_w[j-1]\, a_j = R_{sw}[i] \qquad i=0,\ldots,N \quad (8)$$

which can be rewritten in matrix form **Ta**=**v**

$$\begin{bmatrix} R_w[0] & R_w[1] & \ldots & R_w[N] \\ R_w[1] & R_w[0] & \ldots & R_w[N-1] \\ \vdots & \vdots & \ddots & \vdots \\ R_w[N] & R_w[N-1] & \ldots & R_w[0] \end{bmatrix} \begin{bmatrix} a_0 \\ a_1 \\ \vdots \\ a_N \end{bmatrix} = \begin{bmatrix} R_{sw}[0] \\ R_{sw}[1] \\ \vdots \\ R_{sw}[N] \end{bmatrix} \quad (9)$$

These equations are known as the Wiener-Hopf equations. The matrix **T** appearing in the equation is a symmetrical Toeplitz matrix. Under suitable conditions on **R**, these matrices are known to be positive definite and therefore non-singular yielding a unique solution to the determination of the Wiener filter coefficient vector, $\mathbf{a}=\mathbf{T}^{-1}\mathbf{v}$. Furthermore, there exists an efficient algorithm to solve such Wiener-Hopf equations known as the Levinson-Durbin algorithm so an explicit inversion of **T** is not required.

4. Experimental Setup

The experiment was setup to extract feature of tremor from ECG signal. Figure 3 shows the steps and methodology involved in carrying out the study on the signal. At first mathematical equations are formulated to conduct the filtering of noise. Data of ECG signal is collected in which the Wiener algorithm is applied to filter off the noise. Auto-correlation and Cross-correlation is applied in the process. To extract the ECG features from tremor, Haar wavelets and Daubechies wavelets were applied to the process.

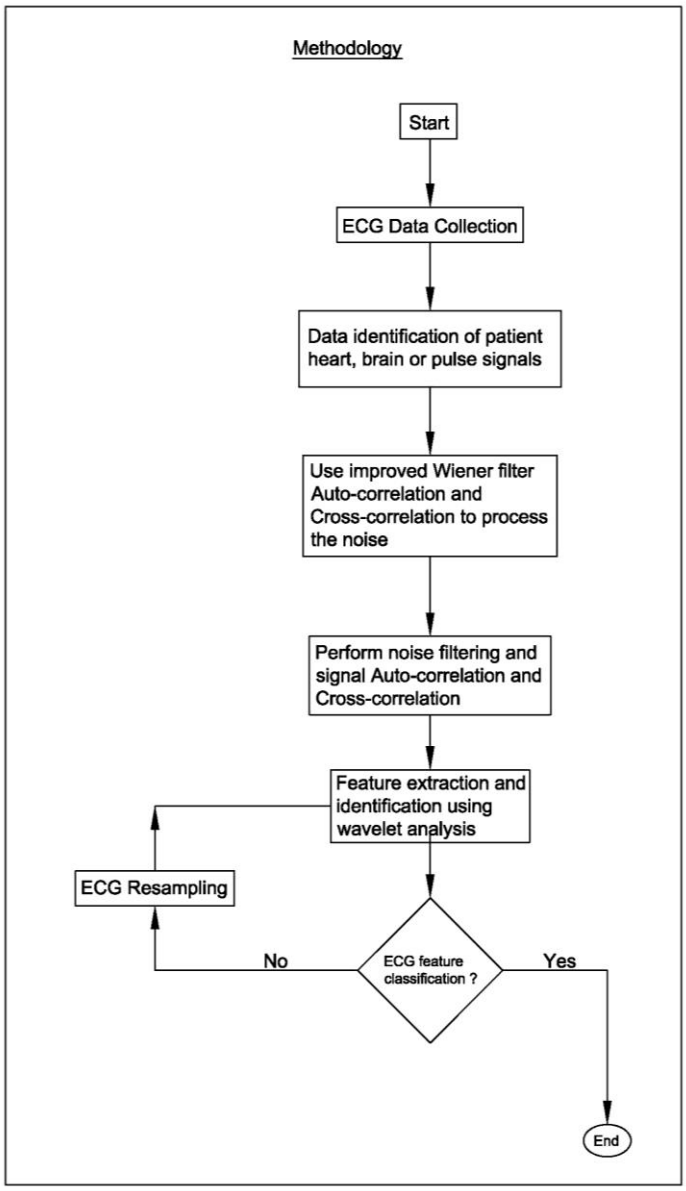


Figure 3. Flowchart of ECG feature extraction

In this experiment, the recordings of 16 subjects with Parkinson's disease (PD) were investigated. Parkinson's disease shows the symptom of progressive loss of dopamine neurons in the substantia nigra of the midbrain and is associated with tremor, bradykinesia and rigidity. Regular or harmonic tremor is a phenomenon seen in Parkinson's disease. The frequency for the tremor is shifted to a lower range typically of 4-6 Hz [8]. The amplitude for the tremor increases, the shape of the oscillation will change. Initially these changes are intermitten, becoming more obvious as the disease progresses.

This database shown 16 index finger with tremor velocity. These subjects received chronic high frequency electrical deep brain stimulation (DBS) either uni- or bi-laterally within one of three targets:

- Vim = the ventro-intermediate nucleus of the thalamus (n=3),
- GPi = the internal Globus pallidus (n=7), or

- STN = the subthalamic nucleus (n=6).

In this surgical operation, an electrode is implanted into subcortical structures (Vim, Gpi or STN) for long-term stimulation at frequencies greater than 100 Hz.

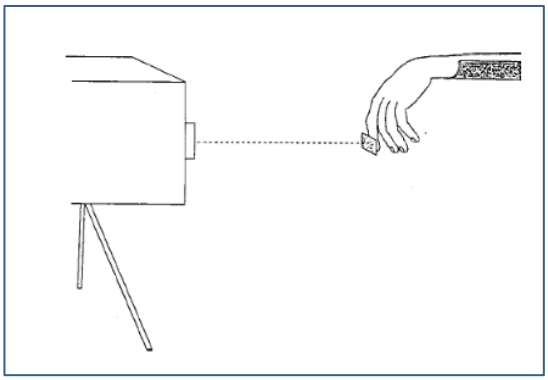


Figure 4. Velocity laser recording of rest tremor

5. Results and Discussions

The figure 5a show the ECG signal extracted from Parkinson patient. The signal contains information on the abnormalities hidden in the human heart. It also contains noise and interference created from the measuring equipment.

Wiener filter and wavelet of figure 5b shows the signal with the noise removed using the filter. The Wiener filter was applied on the original signal to remove those unwanted noise and interference. The final output was plotted out to compare with the original signal. Wavelet is more flexible as it can provide more scope and level for analysis. The special feature could be extracted using Wavelet, the results are highlighted using the square box.

The original and raw ECG signal is fed into FIR Wiener filter to obtain the filtered result. Software will provide the algorithm to calculate the new waveform.

Figure 5c shows the wavelet analysis on original signal. It indicates that special feature exist in the ECG signal as evidenced in the wavelet plot. Figure 5d shows the histogram and cumulative histogram for the original ECG signal

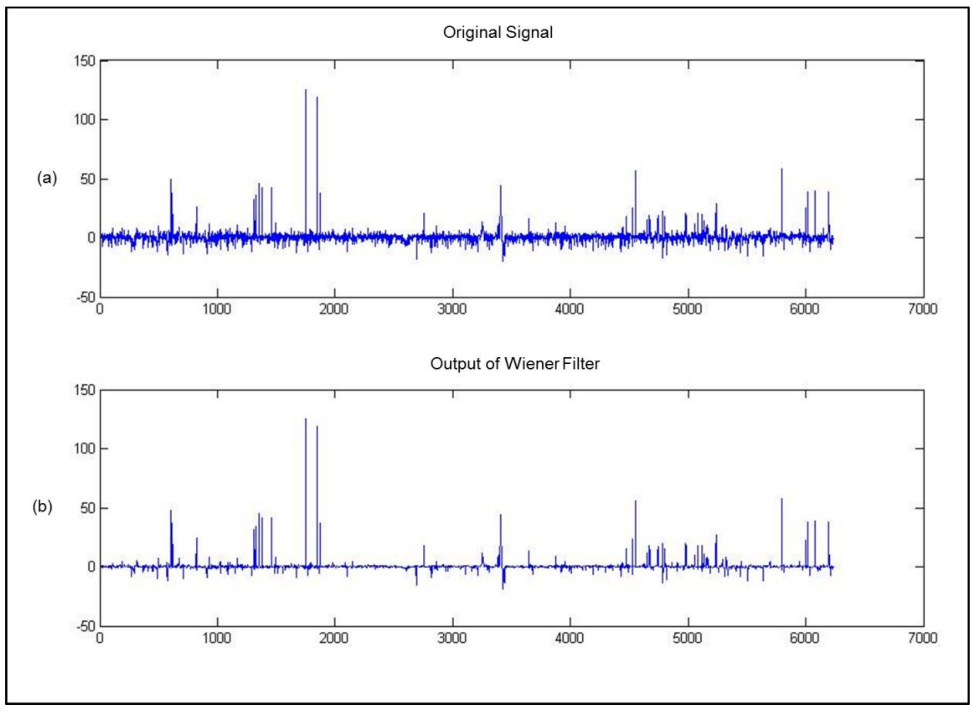


Figure 5(a) : Original signal, (b) Filtered signal.

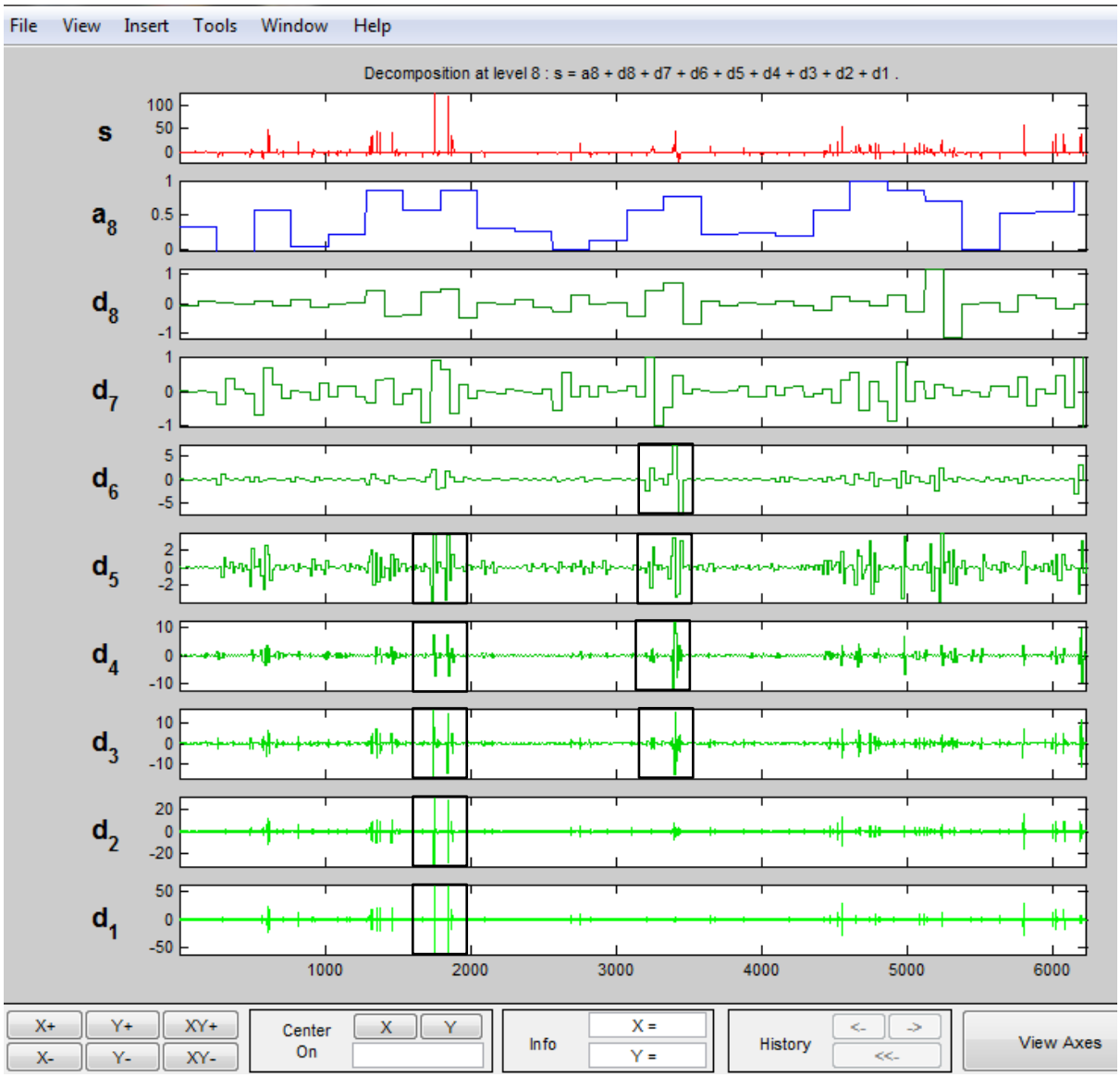


Figure 5c : Haar wavelet analysis on original signal as shown in Figure 5a.

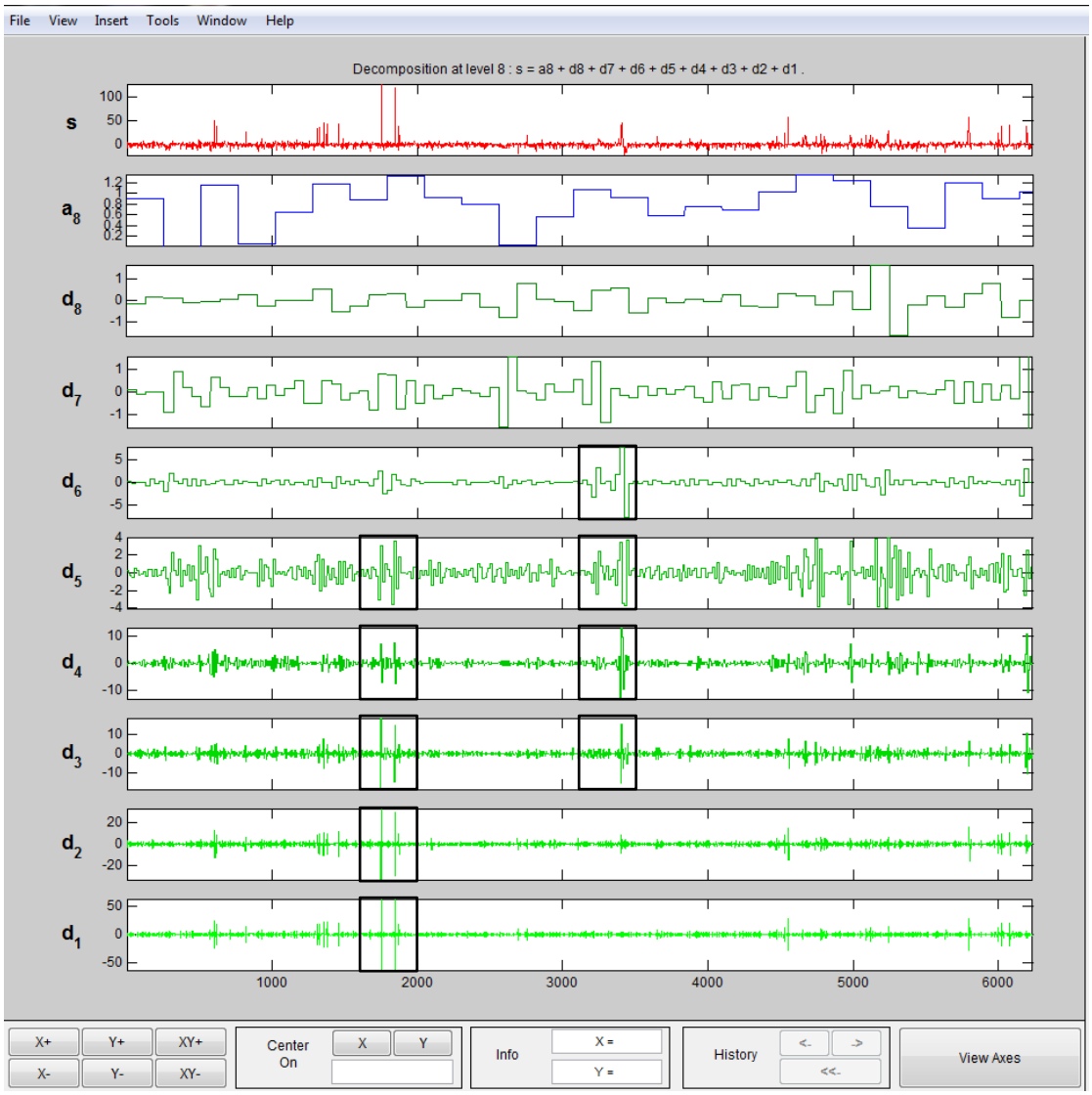


Figure 5d : Daubechies wavelet analysis on original signal as shown in Figure 5a.

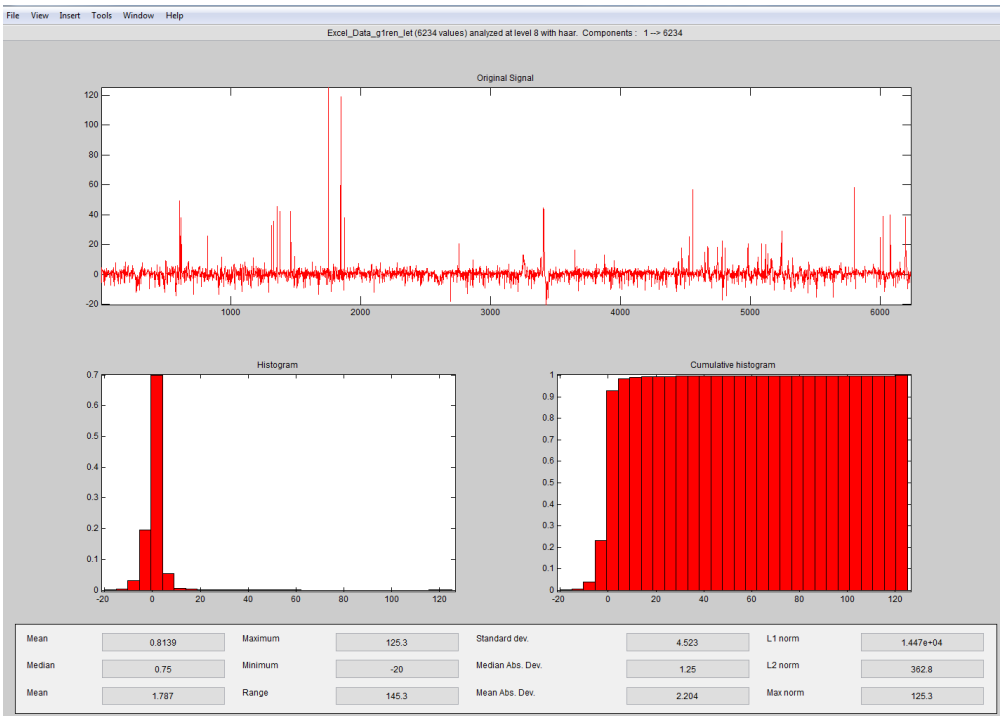


Figure 5e : Histogram and Cumulative Histogram for Original Signal.

Table 2. Mean, Variance and Standard Deviation for the ECG Signal

Signal Filename	Mean	Variance	Standard Deviation
g1ren	0.81388	20.45624	4.52286

The above mentioned wavelet transform method has the disadvantage that the detection of the characteristic points in the ECG is dependent on the firstly determined R peak because the latter is used for the calculation of all other values. The precise and exact R peak detection is therefore essential since an error affects all further points. Despite the influence of the R peak point, the multi-resolution wavelet transform and the decomposition of the signal allow a close approximation of the ECG signal given that for every single feature appropriate details can be selected which make noticeable one particular feature.

Comparison of the Haar wavelet transform with the Daubechies method shows similar feature but different wavelet. Daubechies wavelet transform marks the T wave offset early while the Haar shows the feature later.

The remaining discrepancy in the mark of the determined T wave offset between automated algorithms and expert annotations is exemplified in the two different existing versions for the algorithm developed by Hayn [9]. When they modified their algorithm to increase the agreement with the evaluation by physicians and therefore the performance of their algorithm, the reduction of agreement with other algorithms resulted. This ambiguity illustrates the need of further research on this regard.

6. Conclusion

Many different algorithms based on diverse methods have been developed for the automated ECG feature extraction. They are efficient and characterised by a high performance and show results that fulfil the requirements for sensitivity and error ranges satisfactorily. Today, automated ECG feature extraction algorithms are standard in clinical practice and support physicians in the evaluation of ECG curves and medical diagnosis. A significant factor in this context is the saving of time which becomes more important in consideration of current changes in health care systems. Another advantage of automated algorithms is the elimination of operator-dependence which makes measurements more reproducible.

Nevertheless, the precise detection of ECG features is still not resolved or completed. The development of an algorithm that is able to take into account the amount of information contained in the ECG waveform is meaningful but challenging. The extensive ability of humans in pattern recognition and matching cannot be reproduced by a computer so far. Moreover, the ECG shapes show a wide variability because the anatomy, physiology and functionality of the heart are different from human to human. Patterns differing to a great extend can still be physiological instead of indicating an underlying heart disease.

Still, there is no gold-standard or algorithm that would give precise and always reliable results as illustrated in the study carried out by Baumert et al where it turned out that none of the tested algorithms was able to detect a QT variability after the infusion of a QT prolonging drug. Moreover, these results pointed out the requirement of a high qualitative, noise free ECG recording because noise affects the performance of extraction algorithms. Especially for the QT duration the clear detection of the T wave offset which is however often masked by noise is crucial because a prolongation of only a few milliseconds (in an interval of a total length of up to 500ms or more) can indicate a cardiac disorder. This fact points out the requirement of precise and exact measurements.

Acknowledgement

The author would like to express his appreciation to his supervisor, co-supervisor and all supporting staff for the helps and guidance provided throughout the entire research project.

Reference

[1] James H. McClellan, Ronald W. Schafer and Mark A. Yoder. (2003). *Signal Processing First* (1st ed.). Pearson.
[2] Alan V. Oppenheim, Ronald W. Schafer. (2010). *Discrete-Time Signal Processing* (3rd ed.). Pearson.
[3] Monson Hayes. (2011). *Schaum's Outline of Digital Signal Processing* (2nd ed.). McGraw-Hill.
[4] Hwei Hsu. (2013). *Schaum's Outline of Signals and Systems* (3rd ed.). McGraw-Hill.
[5] Alan V. Oppenheim, Alan S. Willsky, S. Hamid. (1996). *Signals and Systems* (2nd ed.). Prentice Hall.

[6] John G. Proakis, Dimitris K Manolakis. (April, 7, 2006.). *Digital Signal Processing, Principles, Algorithms and Applications* (4th ed.). Prentice Hall.
[7] Steven W. Smith. (1997). *The Scientist & Engineer's Guide to Digital Signal Processing* (1st ed.). California Technical Pub.
[8] Richard G Lyons. (2011). *Understanding Digital Signal Processing* (3rd ed.). Pearson.
[9] Hayn, D., Kollman, A. and Schreier, G. 2006. *Automated QT Interval Measurement from Multilead ECG Signals. Computers in Cardiology*. 2006, 33:381-384.

Acoustic Absorption Phenomena of Fibro-Granular Composites

Hasina Mamtaz[1*], Mohammad Hosseini Fouladi[2], Mushtak Al-Atabi[3], Satesh Narayana Namasivayam[4]

Taylor's University, School of Engineering, Subang Jaya, Selangor 47500, DE Malaysia.

[*]*hasina_ctg@yahoo.com*

Abstract

The current study was conducted to enhance the acoustic absorption performance of fibrous materials. The industrially prepared fiber has thinner diameter compared to the fresh fiber. This reduction in the diameter of industrial fibers is observed due to various chemical treatments, at the cost of the removal of moisture contents. In previous studies the acoustic absorption performance of single fibrous material showed lower acoustic absorption at low frequency region. Current research is initiated to improve this shortcoming by combining the granular materials with fibrous materials. This new composite of fiber and grain is named as fibro-granular composite. The acoustic absorption performance of this composite which is the combination of coir fiber and rice husk, is illuminated in this paper in terms of the simple Delany-Bazley and rigid frame Johnson-Champoux-Allard model. The calculated value of the sound absorption coefficient of coir fiber-rice husk composite is compared to the simple coir fiber composite in order to validate the analytical results. The comparison shows the better acoustic absorption performance of fibro granular composite at low frequency due to higher flow resistivity. The probable cause of this phenomenon is due to the incorporation of rice husk grains as a compensation for the removal of moisture contents. The effective amount of the fiber diameter reduction, which has significant effect in the enhancement of low frequency sound absorption, has not been addressed yet. The study aimed to introduce this new concept of fiber diameter reduction amount in the formulation of the analytical approaches. The analysis of the variability of the fiber diameter after the industrial processing is investigated in this paper in terms of rigid frame Johnson-Champoux-Allard model. Finally the elimination of three major environmental problems which are noise pollution, environmental pollution and waste elimination is highlighted in this study.

Keywords: Fiber, Grain, Fiber diameter, Acoustic absorption.

1. Introduction

An increasing demand for producing natural acoustic materials is the outcome of the raising concern of noise and environment pollution. These materials have drawn considerable interests in noise reduction for building construction, automotive interior noise, room interior surface and household applications. In the last few years the green technology has been studied to replace the agricultural waste with the traditional fibers for noise absorption purpose due to their biodegradability, lightweight, cost effective, nontoxic and nonabrasive quality. Coir fibers are highly abundant across all parts of the world. It is an important agricultural waste in Malaysia. The individual fiber cell is hollow and the presence of the hollow cavity in fibers decreases its bulk density and makes coir fiber light and delicate to serve as an acoustic and thermal insulator [1].

In order to achieve the better fiber quality, the pre-treatment of fresh natural fiber is needed for commercial use in parallel with synthetic fiber. Among various pre-treatment techniques, alkaline treatment or mercerization is a common method of producing high quality industrial fibers. It complements the fibers with anti-fungus quality and thinner diameter at the cost of the removal of some acoustic absorption substances like oil, wax, pectin and hemicellulose and other impurities with which the fiber's surface is covered [2]. Shahani F et al. [3] reported that finer fiber with reduced diameter enhances the sound absorption performance of nonwoven fabric material by reducing the possible connectivity of pores.

Rice is a commonly cultivated crop in almost all parts of the world. Two widely abundant agricultural residual wastes, which exist due to the cultivation of rice crop are- rice husk and rice straw. The potential of these two products are reported to be used as important resources of renewable energy. But unfortunately this energy gets wasted by open burning while disposed for the next crop, which leads to the environment pollution by carbon emission. Rice husk has highly moisture resistible, incombustible and anti-fungal material qualities. It is a great resource as a raw biomass material for producing composite materials. In order to improve the mechanical properties of natural fiber composites, rice husk waste is found to be an effective filler in fiber- matrix composite [4]. Rice husk waste has been investigated as an efficient acoustic absorber at low frequency region. It has been reported that dried rice husk together with polyurethane binder showed significant value of sound absorption coefficient at low frequency region compared to wood shaved materials. The absorption peak was found at a frequency of 250 Hz for 25% rice husk-polyurethane composite with a value of 0.889 [5].

Thus far, numerous researchers have approached distinct models to predict acoustic performance of natural fibers and their composites. Many of them have shown outstanding achievements in revealing the potential usage of natural fibers in sound absorption technology. Delany M and Bazley E [6] introduced a simplified model of sound propagation in porous media by using only parameter- flow resistivity. This is an intrinsic property of porous material which determines the acoustical behaviour of the material. Their method is still considered as good and fast approximation to the solution. Based on flow resistivity Delany and Bazley estimated the surface acoustic impedance, to obtain the sound absorption coefficient of a single layer, homogenous porous material. However it is observed that the Delany-Bazley model is unable to predict the frame resonance information in the overall absorption pattern.

In 1994, a rigid frame method was introduced by Johnson-Allard to predict the acoustic characteristics of porous materials. In this model the frame was considered as motionless. This model involves five non-acoustical parameters- flow-resistivity, porosity, tortuosity, viscous characteristics length and thermal characteristics length. [7].

Mahzan S et al.[8] studied the effectiveness of coir fiber-recycled rubber composite as a promising sound absorbing material. The effect of second hand rubber and polyurethane resin as a binder was investigated in two composite structures at various compositions to investigate the possible substitution of traditional and metal fiber. The result showed higher absorption coefficient for mid to high frequency range which is 0.8-0.85 for 25% polyurethane together with coir fiber and rubber grain composite. It was found that the lower content of binder influence the density and porosity value of the material.

The purpose of this study is to investigate the absorption phenomena of fibro-granular composite in order to enhance the acoustic absorption performance of fibrous materials. This new composite is the combination of natural fiber and bio-granulates of arbitrary grain sizes. A new factor, fiber diameter reduction(d_{red}) is incorporated in the formulation in order to determine the effective amount of fiber diameter reduction, for the best value of acoustic absorption coefficient. l

2. Analytical Models

2.1 Delany-Bazley- Model

The theoretical explanation of the absorption phenomena of various porous materials was stated by many authors by proposing various models. The aim of almost all the models was to estimate the materials acoustical parameters such as characteristic impedance, surface acoustic impedance and wave propagation constant. In order to estimate the characteristic impedance Z_f and wave propagation constant γ_f, Delany M and Bazley E [6] has developed an empirical formula of a homogenous and isotropic fibrous materials and normalized them into a dimensionless group. Since this method depends only on the flow resistivity parameter of the material, their model is considered to be a simple model and easy for fast approximation. This model can be used for large frequency range and availability of the flow resistivity of the material. However, the implementation of the model is restricted to a certain range of flow resistivity (σ), which is $1000 \leq \sigma \leq 50000$ MKS rayl m^{-1} and porosity close to 1.

According to Delany M and Bazley E [6], the empirical relations for characteristic impedance Z_c, propagation constant K and surface acoustic impedance Z can be stated below as in terms of flow resistivity σ [9]

$$Z_c = \rho 0\, c_0\, [1 + 0.057 b^{-0.754} - i(0.087 b^{-0.732})] \quad (1)$$

$$k = \frac{2\pi f}{Co} [0.189\, b^{-0.595} + \mathrm{i}(1 + 0.0978 b^{-0.7})] \quad (2)$$

$$Z = Z_c \coth(k.d) \quad (3)$$

Where ρ_0 is the air density, c_0 is the speed of sound in air, f = Sound wave frequency, d is the thickness of porous layer, $b = \frac{\rho_0 f}{\sigma}$ = dimensionless parameter. This model is applicable only for $0.01 \leq b \leq 1.0$;

2.2 Johnson-Champoux-Allard Model

In the rigid frame Johnson-Champoux-Allard Model, the solid phase of the frame remains motionless. In this model five non-acoustical parameters- flow-resistivity (σ), porosity (φ), tortuosity($\propto_\infty$), viscous characteristics length (Λ), and thermal characteristics length (Λ') are involved in the expression of the effective density $\rho(\omega)$ and the bulk modulus $K(\omega)$ of the rigid framed porous materials. The effective density $\rho(\omega)$ [10] and bulk modulus $K(\omega)$ [11, 12] are stated in Eqs. (4) and (5),

$$\rho(\omega) = \alpha_\infty \rho_o \left[1 + \frac{\sigma\phi}{j\omega\rho_o\alpha_\infty}\sqrt{1 + \frac{4\,\alpha_\infty^2 \eta \rho_o \omega}{\sigma^2 \Lambda^2 \omega^2}}\right] \quad (4)$$

$$K(\omega) = \frac{\gamma P_o}{\gamma - (\gamma-1)\left[1 - j\frac{8\eta}{\Lambda'^2 N_p \rho_o \omega}\sqrt{1 + j\frac{\Lambda'^2 N_p \rho_o \omega}{16k}}\right]^{-1}} \quad (5)$$

Where,
γ= Ratio of the specific heat capacities of air, P_0= Atmospheric pressure, N_p= Prandtl number of the air and ω= Angular frequency.

The expression for characteristic impedance $Z_c(\omega)$, the complex wave number $k_c(\omega)$, surface acoustic impedamnce Z can be estimated by the following Eqs. (6), (7) and (8) respectively [12, 13]:

$$Z_c(\omega) = \frac{1}{\phi}\sqrt{\rho(\omega).K(\omega)} \quad (6)$$

$$k_c(\omega) = \omega\sqrt{\rho(\omega)/K(\omega)} \quad (7)$$

$$Z = Z_c(\omega).\coth(k_c(\omega)) \quad (8)$$

On the basis of above mentioned models, surface acoustic impedance (Z) can be estimated by using Eq. (8), the sound absorption coefficient (α) at a normal incidence of the porous layer while backed with a rigid wall can be calculated as:

$$\alpha = 1 - \left|\frac{Z - Z_0}{Z + Z_0}\right|^2 \quad (9)$$

Where, $Z_0 = \rho_0 c_0$ =Impedance of the air.

3. Methodology

Based on research, the study illustrated the methodology flow chart in order to introduce the concept of the amount of fiber diameter reduction in the above formulations. This concept will be useful for the assessment of the effective amount of fiber diameter reduction which will have a significant role for the enhancement of acoustic absorption. The study reported that the removal of fiber moisture content can be compensated by introducing the filler/granular materials. Figure. 1. shows the methodology flow chart of the current study.

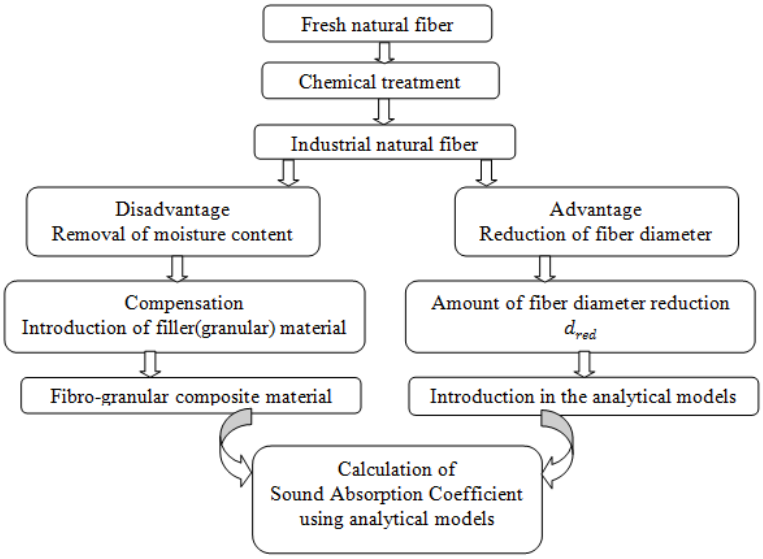


Figure 1. Methodology Flow-Chart

Stacy E [14] stated that sound absorption is the measure of the propagation of sound energy that falls on a given surface and is not reflected. Hence the effectiveness of any porous material depends on the value of its sound absorption coefficient which is close to one, with an absorption plane on a large frequency range. In order to predict the sound absorption coefficient of any fibro-granular composite materials, the study investigated composite structure of coir fiber and rice husk materials for acoustic absorption purpose. Data collected from relevant published studies [15-17] to predict the value of sound absorption coefficient by using new parameter. Matlab^{R} 7.0 editor does the job for running the plot of sound absorption coefficient in the frequency range between 0-5kHz.

4. Results and discussion

Flow resistivity of fibrous material [18] and loose granular material [19]can be estimated from the following empirical Eqs. (10) and (11) having bulk density. Bulk density of a porous material can be defined by the mass per unit volume.

$$\sigma_f = 490 \frac{\rho_{bulk}^{1.61}}{d_{fiber}} \tag{10}$$

$$\sigma_g = \frac{400(1-\varphi_g)^2(1+\varphi_g)^5\mu}{\varphi_g D^2} \tag{11}$$

The measured values of parameters $\sigma, \varphi, \propto_\infty$, Λ and Λ' for coir fiber(C.F) [16] and the new fibro-granular composite which is coir fiber-rice husk (C.F+R.H) [15-17] are furnished in Table.1.

Table 1. The comparison study of the five parameters of C.F and C.F+R.H at 45mm thickness.

Material	Sample weight (gm)	σ (Nsm^{-4})	φ	$\propto_\infty$	Λ (μm)	Λ' (μm)
C.F	56.3	6298	0.70	1.19	20	40
C.F+R.H	72.27	6754	0.76	1.15	26.32	52.64

Figure. 2. represents the comparison study of the acoustic absorption of 45mm thickness of coir fiber-rice husk fibro-granular composite material in terms of the Delany-Bazley and Johnson-Champoux-Allard model.

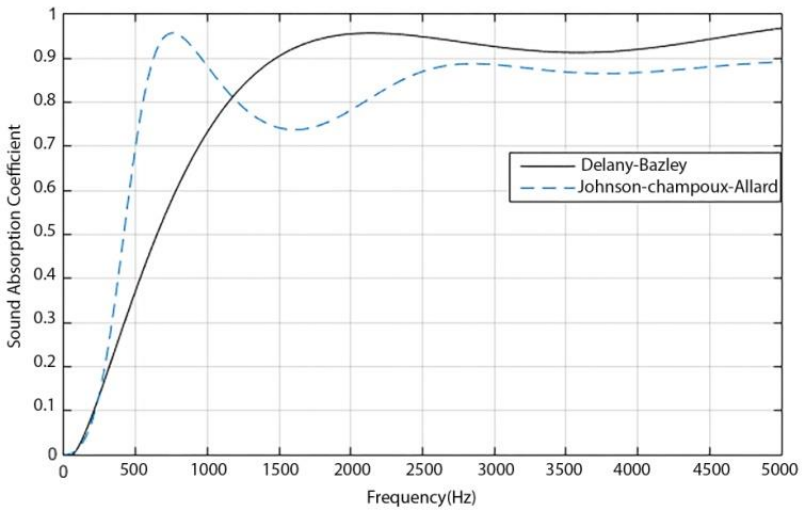


Figure 2. Acoustic absorption coefficient of coir fiber and rice husk, fibro-granular composite of thickness 45mm and mass 72.27mg.

The comparison analyses of the acoustic absorption performance of coir fiber-rice husk fibro-granular composite with simple coir fiber composite[16] is illustrated in terms of Delany-Bazley and Johnson-champoux-Allard models. Figures. 3. and 4. represent the comparison study of both composites in terms of Delany-Bazley and Johnson-champoux-Allard models respectively.

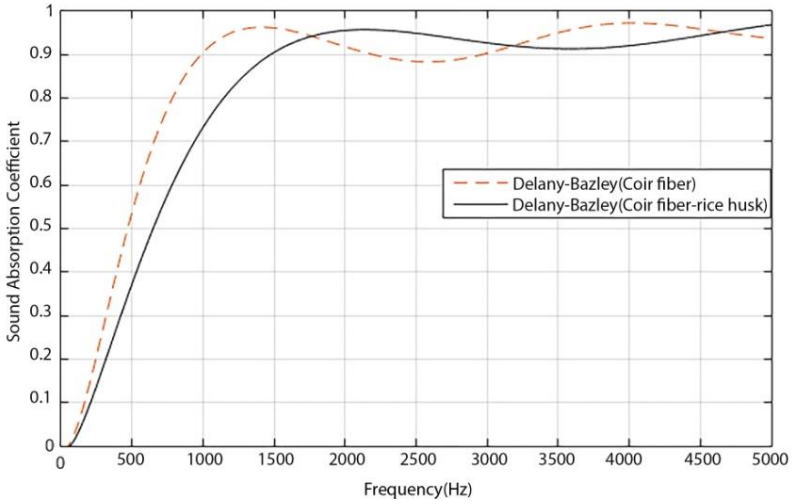


Figure 3: Comparison analysis of acoustic absorption coefficients of coir fiber-rice husk, fibro-granular and simple fibrous composites in terms of Delany-Bazley model.

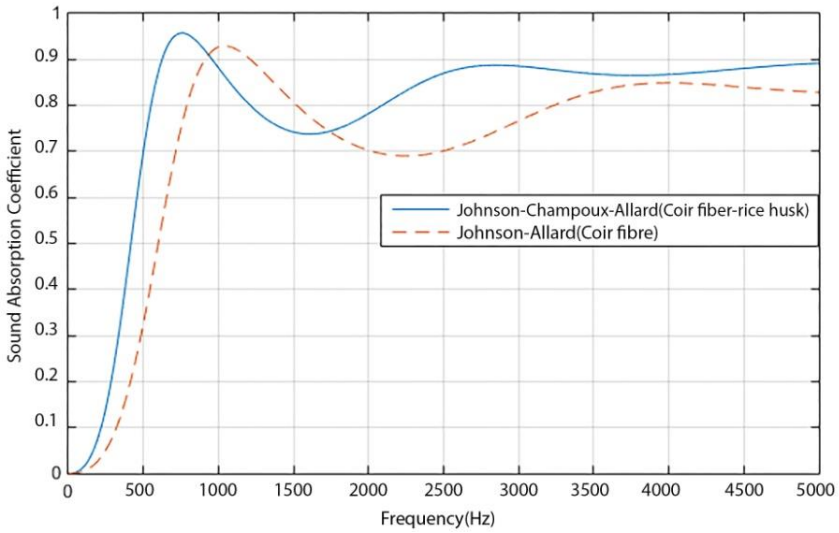


Figure 4: Comparison analysis of acoustic absorption coefficients of coir fiber-rice husk, fibro-granular and simple fibrous composites in terms of Johnson-Champoux-Allard model.

The comparison study of the acoustic absorption performance of C.F+R.H composite is furnished in Figure 2, in terms of Delany-Bazley and Johnson-Champoux-Allard model. For Johnson-Champoux-Allard model, the C.F+R.H composite shows the better acoustic absorption performance at low frequency region with resonance peak, whereas for Delany-Bazley it is almost same at overall frequency band. The reason can be described in two ways. Firstly, Delany-Bazley model is an easy and fast approximation method, which is derived from the empirical equation. It estimates the combined acoustical behaviour of the composite for overall frequency band without any position of the resonance. Secondly, Delany-Bazley is an one parameter dependent model, which is flow resistivity. On the other hand there are five parameters involved in Johnson-Champoux-Allard model. Which make it possible to predict the accurate resonance including the complete absorption pattern.

Figure 3 illustrates that, the difference between the acoustic absorption of both composites is not that significant for Delany-Bazley model. The average value of the sound absorption coefficient for C.F and C.F+R.H composite was found 0.83 and 0.9 respectively, at over all frequency band. In this model, fibro-granular composite shows better acoustic absorption performance at mid frequency region compared to simple fibrous composite.

Figure 4 demonstrates that, for the Johnson-Champoux-Allard model, fibro-granular composite shows better acoustic absorption performance at all frequency ranges compared to simple fibrous composite. The peak was found at 757Hz and the value of sound absorption coefficient of fibro-granular composite is 0.96.

The comparison studies in Figure 3 and 4 are for the validation of the theoretical outcome of the current study of fibro-granular composite with the relevant study of simple fibrous composite material. The current paper reported that the acoustic absorption performance of the fibro-granular composite is much better than the simple fibrous and granular composite at low frequency region. The phenomenon can be described by the fact that the introduction of granular materials in the fibrous composite causes the reduction in porosity, increase in flow resistivity and two characteristics lengths, which promotes the acoustic absorption.

Considering the binders as a part of fiber, Fouladi MH [20] introduced the expression of the diameter of industrially prepared coir fiber mixed with binder (d_{mix}) to be used in the Allard model. Following this concept and considering the binders as a part of fiber, a new parameter (d_{red}) is introduced in the Eq. (12) below-

$$d_{mix} = (d_{fiber} - d_{red}) + d_{fiber}\,\varphi \quad (12)$$

Where,

d_{fiber}= Diameter of fresh fiber ,d_{red} = Reduction of fiber diameter after pre-treatment, $d_{fiber}\varphi$ =Compensation due to binder mix and $(d_{fiber} - d_{red})$ = Diameter of industrially prepared coir fiber.

In the numerical simulation of Nor MJM et al. [21], the gradual increase of the sound absorption coefficient was found with the decrease of fiber diameter at low frequency region. Karthikeyan A and Balamurugan K [2] reported that the increase in alkaline concentration results in the decrease of fiber diameter and fiber strength as well at certain extent. They confirmed that the 6% of alkali treated coir fiber-epoxy resin composite caused the reduction of fresh coir fiber diameter from 274μm to 231 μm with better mechanical strength compared to untreated composites. Figure. 5. represents the sound absorption performance of C.F+R.H composite at different fiber diameters due to different alkaline concentration.

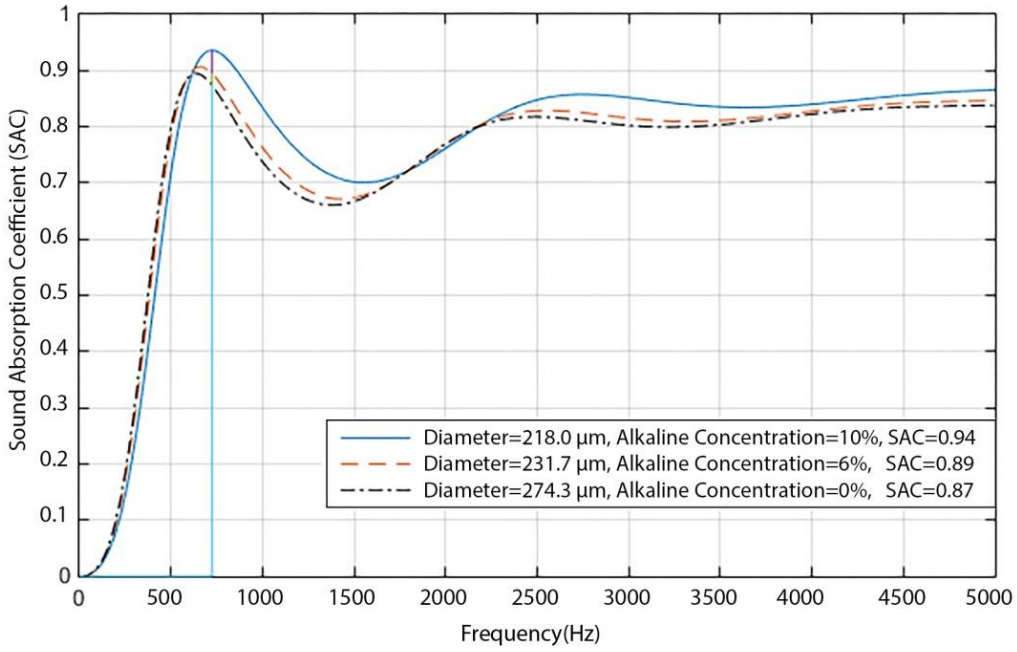


Figure 5: Acoustic absorption coefficients of 45mm coir fiber-rice husk, fibro-granular composites at different fiber diameters in terms of Johnson-Champoux-Allard model**.**

The result displayed in Figure.5. shows that the absorption coefficient changes with the variation of fiber size. The peak of absorption coefficient is shifted to lower frequency region, which is 724Hz, with the reduction of fiber diameter. Increase in alkaline concentration causes the decrease in fiber strength. Therefore, it is important to know the effective amount of akaline concentration in order to avoid the fiber fracture. From the above observations, it is clearly evident that for 6% alkaline concentration, d_{red}= 43 μm is the effective amount, which helps for the enhancement of the low frequency acoustic absorption of coir fiber. This parameter might help to measure the chemical concentration during the pretreatment of fibers to be remained with their better mechanical strength and life expectancy as well.

5. Conclusion

The study was conducted to investigate the absorption behaviour of a new fibro-granular composite through the formulation of two suitable analytical approaches. The peak value of SAC of coir fiber-rice husk fibro granular composite was found to be 0.96 at 757Hz and for coir fiber it was found to be 0.93 at 1041Hz. The result demonstrates that, fibro-granular composite is superior to simple fibrous composite as sound absorbent material. This is because in a fibro-granular composite, each component helps in optimizing the acoustic properties of the other component, in order to absorb the sound at the desired frequency, so as to acquire the highest overall sound absorption. An optimum amount of pores can be formed by adding granular materials. The introduction of granular materials such as rice husk, rubber, plastic granules etc. in fibrous composite materials contributes to higher flow resistivity which enhances the acoustic absorption performance at the low frequency region. However, high flow resistivity and low porosity phenomenon confines the application of this new materials in building construction, room interior surface and household elements for sound absorption.

Reduction of fiber diameter has great influence for the enhancement of low frequency acoustic absorption. The study reports that it requires 6% alkaline concentration for 43 μm of coir fiber diameter reduction in order to achieve the value of sound absorption coefficient is 0.89 at 724Hz.

The study confirms that the industrial manufacturing of the acoustic absorbers from waste residues will contribute to a promising new fibro-granular composite material, thereby confronting the volatile price of the traditional acoustic absorbers.

References

[1] Waifielate, A.A., Abiola, B.O.(2008). *Mechanical Property Evaluation of Coconut Fibre*, Master of Science Thesis, Blekinge Institute of Technology , Karlskrona, Sweden.

[2] Karthikeyan, A. and Balamurugan, K.(2012). Effect of alkali treatment and fiber length on impact behavior of coir fiber reinforced epoxy composites, *Journal of Scientific & Industrial Research*, 71(9), 627-631.

[3] Shahani, F., Soltani, P. and Zarrebini, M.(2014). The Analysis of Acoustic Characteristics and Sound Absorption Coefficient of Needle Punched Nonwoven Fabrics, *Journal of Engineered Fabrics & Fibers (JEFF),* 9(2), 85-92.

[4] Satapathy, A., Jha, A.K., Mantry, S., Singh, S. and Patnaik, A. (2010). Processing and characterization of jute-epoxy composites reinforced with SiC derived from rice husk, *Journal of Reinforced Plastics and Composites,* 29(18), 2869-2878.

[5] Mahzan, S., Zaidi, A., Mujahid, A., Ghazali, M.I., Yahya, M.N. and Ismail, M. (2009). Investigation on sound absorption of rice-husk reinforced composite, *Proceedings of Malaysian Technical Universities Conference on Engineering and Technology(MUCEET)* (pp. 19-22), MS Garden, Kuantan, Pahang, Malaysia.

[6] Delany, M. and Bazley, E. (1970). Acoustical properties of fibrous absorbent materials, *Applied Acoustics,* 3(2), 105-116.

[7] Allard, J.F. and Daigle, G. (1994).Propagation of sound in porous media: Modeling sound absorbing materials, *The Journal of the Acoustical Society of America,* 95(5), 2785-2785.

[8] Mahzan, S., Ahmad Zaidi, M.A, Arsat, N, Hatta, M.N.M, Ghazali M.I. and Rasool Mohideen, S. (2010). Study on sound absorption properties of coconut coir fibre reinforced composite with added recycled rubber, *International Journal of Integrated Engineering* , 2(1), 29-34.

[9] Dunn, I. and Davern, W. (1986). Calculation of acoustic impedance of multi-layer absorbers, *Applied Acoustics,* 19(5), 321-334.

[10] Johnson, D.L, Koplik, J. and Dashen, R. (1987). Theory of dynamic permeability and tortuosity in fluid-saturated porous media, *Journal of fluid mechanics*, 176(3), 379-402.

[11] Champoux, Y. and Allard, J.F. (1991). Dynamic tortuosity and bulk modulus in air-saturated porous media, *Journal of Applied Physics*, 70(4), 1975-1979.

[12] Allard, J.F. (1993). *Propagation of sound in Porous media, Modelling sound absorbing materials,* New York and London: Elsevier Application Science, 284, 1-351,

[13] Kino, N., Ueno, T., Suzuki, Y. and Makino, H. (2009). Investigation of non-acoustical parameters of compressed melamine foam materials, *Applied Acoustics*, 70(4), 595-604.

[14] Stacy, E. (1959). Sound insulation in buildings. *The Journal of the Royal Society for the Promotion of Health*, 79(6), 789-797.

[15] Abdullah M., Husain Z. and Pong S.Y. (2003). Analysis of cold flow fluidization test results for various biomass fuels. *Biomass and Bioenergy*, 24(6), 487-494.

[16] Fouladi, M.H., Ayub, M. and Nor M.J.M. (2011). Analysis of coir fiber acoustical characteristics, *Applied Acoustics*, 72(1), 35-42.

[17] Sakamoto S., Takauchi Y., Yanagimoto K. and Watanabe S. (2011). Study for Sound Absorbing Materials of Biomass Tubule etc. *Journal of Environment and Engineering* , 6(2), 352-364.

[18] Ballagh K. (1996). Acoustical properties of wool. *Applied Acoustics*, 48(2), 101-120.

[19] Voronina N,Horoshenkov K. (2003) A new empirical model for the acoustic properties of loose granular media. *Applied Acoustics*, 64(4), 415-432.

[20] Fouladi, M.H., Nor, M.J.M, Ayub, M. and Leman, Z.A. (2010). Utilization of coir fiber in multilayer acoustic absorption panel, *Applied Acoustics*, 71(3), 241-249.

[21] Nor, M.J.M., Ayub, M., Zulkifli, R., Amin, N. and Fouladi, M,H. (2010). Effect of different factors on the acoustic absorption of coir fiber, *Journal of Applied Sciences*, 10(22), 2887-2892.

eureca 2016 – Conference Paper
Paper Number EE_UG13

An Arduino-Based Voting System with Security Using Arduino IDE

Avigail Anne T. Sanchez[1*], Charles Erick C. Ligpitan[1], Kurt C. Cuaresma[1],
Allen B. Flores[1], Rionel Belen Caldo[1]

[1]*Computer Engineering Department, Lyceum of the Philippines University- Laguna*

Corresponding e-mail: [*]*avigailannesanchez@gmail.com*

Abstract
School election is an annual event in all schools, many of the student leaders are being busy with their campaign and platforms. As a student of an institution it is necessary and required to vote. Student's need to find a leader that can lead them on the right path and give to them the service that they need. Every student has the right to vote and most of the schools are using manual voting which consumes too much time and effort to view the results and to write the name of the candidates. Manual voting is not secured, transparent and accurate and human error can occur. The basis of this project is to create a low cost and friendly user voting system by the use of Arduino and Arduino IDE. This project consists of Arduino microcontroller, LCD, push buttons and laptop. The system will permit only the poll organizer to control the system after entering the correct password. The system will requires single character commands to allow voter to cast the vote. The Arduino will let the voter cast the vote on input of character "A" in the serial monitor screen. This will allow only a single vote to be casted in a single prompt. This will avoid the voter to make multiple fake votes. This voting system allows the user to vote by just pushing the push button and their vote will easily appear in the LCD screen to assure that their vote is counted. The admin can check the number of votes in the Arduino serial monitor for the verification of the election.

Keywords: Voting, Election, Arduino, Security, Dev C++, Arduino IDE, Serial Monitor

1. Introduction

1.1 Background of the Study

The advancement of technology nowadays submerged itself toward education. Technology has a great advantage in our daily life is has reached its maximum of providing a sustainable technology towards quality of education. Universities, colleges and schools around the world embraces the rapid growth of technology.

In an election we all know that voting is very important. A voting system is one of the example of an embedded applications. The voting system can be difficult to use depending on the number of voters involved. An Arduino microcontroller can be used to make a voting system that would be appropriate for small elections such as in schools or colleges. This project was designed to ensure and guaranteed the security and safety of the election. The whole voting process will be completed using Arduino uno and arduino ide. We all are all familiar with other types of voting machines, but in this project, we have choose to use the Arduino microcontroller to make a voting system.

Voting machines is a combination of electronic equipment, software, firmware and documentation that is use to display election results and information in the election. The first voting machines is mechanical but through the increasing knowledge and capabilities of human kind they innovate and integrate things for a better life ,the most frequently use voting system is electronic voting machines. The feature of this system is the use of Serial Monitor in Arduino IDE is used to complete the polling operation and the LCD will display the result of the voting.

An Arduino is used for building electronics projects. Arduino is a microcontroller that is consisting a physical programmable circuit board and software or IDE (Integrated Development Environment) that runs on your computer it is used to write and upload computer code to the physical board. It is popular with those people that is starting with electronics. It does not need a separate piece of hardware unlike most of the programmable circuit boards. Arduino IDE is just like a simplified version of DEV C++, to use it easier to learn to program.

1.2 Statement of the Problem

Manual voting is time consuming, it requires an accurate hand count of votes while determining an appropriate winner after an extensive vote certification process. The results of manual elections come into question due to several factors regarding human error or corrupt election practices. The problem of the study comprises the following:

- How are we going to implement a voting system using Arduino microcontroller?
- How can we make sure the security of the system by the use of Arduino microcontroller?
- How can we satisfy the necessity of the user in an easy to use voting system?

1.3 Objectives of the Study

General Objective

- To give the user a reliable and stable voting system which is organize and easy to use using Arduino Microcontroller.

Specific Objectives:

- To have a voting system that is secured and protected by the admin and that they will have the control in the voting process.
- To assure the user that voting system that they are using is user- friendly and manageable.
- To have a voting system that can be use in a small scale election.

1.4 Significance of the Study

This research project will be a significant endeavor in promoting an electronic Voting system that can be a useful tool in a small scale election. This research will also be a beneficial for a school, classroom and small organizational election. Furthermore, this research can be used as a future reference for the researchers on the subject of microcontroller and voting system.

1.5 Scope and Limitation of the Study

Every research project has its limitation and constraint. This research paper focuses only on a voting system by the use of Arduino microcontroller. The components that been used are Arduino Microcontroller, 16x2 LCD, push buttons, connecting wires and laptop. This research aims to develop a user- friendly and reliable voting system by the use of Arduino Microcontroller.

The voting system would be a great fit for a small scale elections such as in classroom, schools and small organizations. This system is limited only to a number of five candidates. It was intended to guarantee the security of the election for having a password and giving the complete authority to the operator to control the election.

2. Review of Related Literature

Voting system is the new program to have the easiest process of election. By the means that it is new, many people have a problem on using it and why is it important to use. The procedures of a voting system include counting of votes, casting of votes and deciding the winners of the election. As the political scientist said, voting system is the easiest way on conducting an election. In voting system, it can determine who is selected, the people that voted and the candidates the runs for the election. Basically, the one that wins the election applies the policies that have been discussed. Since that voting wisely matters, voting system valuable as well for the process on clean voting experience. Different examples of voting system takes place in any election. [1]

The voting was first occurred in Rome in 139BC by a simple method means of written paper ballots [2]. The existing process was enhanced and used by Australian in 1858. This new process use sets of ballots that the government provides. The ballots consist with list of candidates and voters need to show their designated area marked by their pen, stamps and specified markers [3]. Voters now will have a privacy to place

their votes, and then the paper ballots was returned, sealed, and kept in high security until the day of tally.

According to Kimball and Kropf (2005) the paper ballots and the design has a direct effects on the results negatively, which some votes remain unrecorded. In the means of Arduino voting system the vote of the user will be record surely directly in the data base also the user's vote will be flash in LCD screen. The work collects from the baseline usability data for many habitual voting systems. Everett, Byme, and Greene (2006) make a study of three types of paper ballots: the bubble ballots, arrow ballots, and open-response ballots. They make more study at lever machine to apply it in paper ballots; in 2007 the punch card was added in the system. The general outcome, the bubble ballots were seem to be the voting system that is more effective in having a great number of users.

Online voting system have some issues like the voters don't have a receipt or proof of voting, others have slow internet connection, some issues are it so dangerous, it can be hacked by hackers, and it is user-friendly when disabled persons will vote on online. The survey provided a personal views of the use of the o\online voting system it also tackles the security reasons and the requirements of the voting system [7].

In the study of e-Voting Security Study an extensive survey of e-voting technology has been provided [9]. In this study the author provides a survey of current projects both in academic and commercial in addition to the academics area in the survey, the views and opinions regarding the issues is understood. The project identifies the threats, sources of occurrence and some probable approaches of occurrence in the voting systems. It also has the security objectives and necessities of a useful electronic voting system [8].

A student council election on schools is an activity wherein students choose the specified candidates, which will characterize each position in the council. By this method, each student where under go in several procedures to process the votes. [10]

Electronic voting system (EVS) is a term used in different types of voting elections using electronic components in tallying. It is the most widely used instrument on processing the votes in an election. [11] Nowadays in the 21st generation computer is the most thing that we used, using computer will help the students in many ways. The computer become the way to know the latest information about the innovating technology. Over the past years the computer is evolving, it is faster and capable to do many things. The council promote the use of computer in teaching and learning, it helps to deliver information among the students. The evolution of computer also comes with the evolution of internet. Many people nowadays are fond of using the internet some of them are using online voting system, the advantage of using online voting is that the ballot is controlled by the site and the voters in rural areas can votes without going to the city and it is time-friendly because it has no hassle to come to the precinct.

Voting through online is more advantage than using electronic methods from to paper balloting at a controlled site. It may reassure contributing in the balloting procedure by those voters who are discouraged by the inconvenience of having to attend at a physical location. There are many factors that can affect people not to vote or elect candidates [11].

2.1 Synthesis of Literatures

Voting System is very useful for election in school, organization and most especially in a whole country. Many researchers has their own idea and proposed system in making voting system. For the political scientist voting systems are translated into seats into legislature. The reason why the voting systems are important is that it determine who is elected and which voters are represented. Those elected candidate directly affects what kinds of policies are passed and who benefits or suffers from those that are elected. By the used of voting system the voting process will be easy and it would not consume too much time in counting the votes and declaring the winner for the election. The growing use of technology in our daily lives is creating new demands for the benefits of the society. Through this voting system we can increase the accuracy, reliability and fast result of the election.

2.2 Conceptual Framework

Table 1. IPO Chart of Arduino Voting System

INPUT	PROCESS	OUTPUT
"A"	The program will start and the user can input their vote.	Display the name of the candidates
Pushbutton 1		Name of the candidate 1
Pushbutton 2		Name of the candidate 2
Pushbutton 3	The Arduino will get the vote depending on the push button that has been push	Name of the candidate 3
Pushbutton 4		Name of the candidate 4
Pushbutton 5		Name of the candidate 5
"S"	The program will display the result	Display the result in LCD

In the table 1 above, the IPO chart of the program shows that the "A" is for the security of the admin to control and make sure that the user has voted just one time so letter "A" must be inputted first to start the program and the letter "S" must be inputted if the admin want to check if the result in LCD screen is tally to the serial monitor screen and lastly it is show that every candidate has a corresponding push button so that if the user push it the vote will be count on it. After every vote it will be process by the Arduino so it will automatically display in the LCD screen.

3. Methodology

3.1 Arduino Uno

Arduino Uno it is recognize as a microcontroller board which is created based on the ATmega328P. This microcontroller has 14 digital input and output pins. It has a 16 MHz quartz crystal, a USB connection, a power jack, an ICSP header and a reset button. It is very useful and convenient for it contains everything that is necessary to support the Arduino microcontroller. This microcontroller will work by just simply connecting it to a computer or laptop with a USB cable.

3.2 System Block Diagram

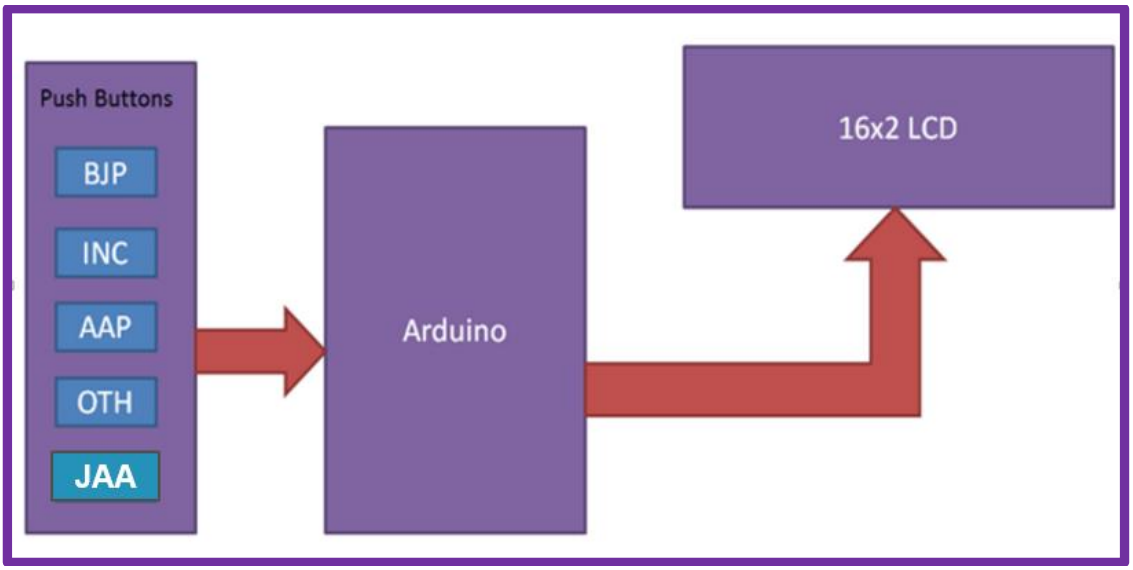


Figure 1. Block Diagram of the System

In the figure 1 above it is clearly shown that the input will be from the push button which will be use by the user to be able to vote. There are five push buttons that was used to distinguish the name of the candidate that they will vote. After pushing the button of the user's desired candidate the Arduino microcontroller will process the vote and after that the candidate that was selected by the user will appear in the LCD screen and also it will be counted in the poll monitor screen.

3.3 System Flowchart

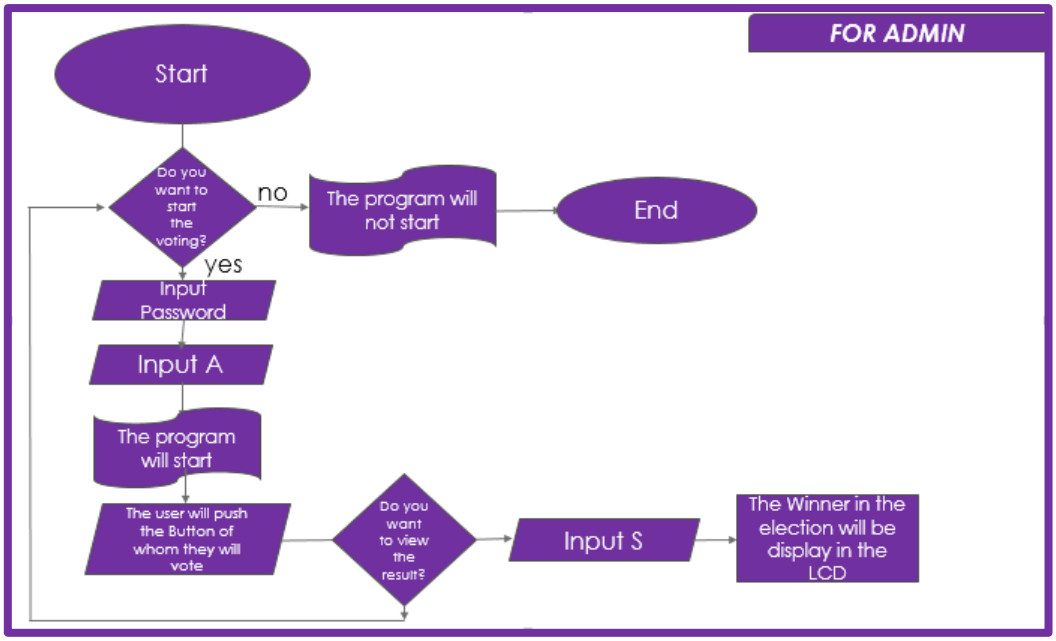


Figure 2. Flowchart of the system for the admin of the program

In figure 2 it is shown that the admin has the overall control in the whole process of the voting and after the admin has inputted the desired password the voting process will begin. If the user will start to vote, the admin will input the letter "A" in the serial monitor screen and after that the program will allow the user to vote their chosen candidate. The admin of the system will input the letter "A" in the serial monitor screen in each voter that will vote so that a single vote will be counted. The letter "A" that must be inputted first in the serial monitor will be the go signal in the system to accept the vote from each voter and if the admin are not yet inputting the letter "A" the vote will not be accepted by the system to aasure the security that only one vote can be accepted by each voter. If the election is done the admin will input the letter "S" to view in the serial monitor the result of the election and also the winner of the election will be displayed in the LCD screen.

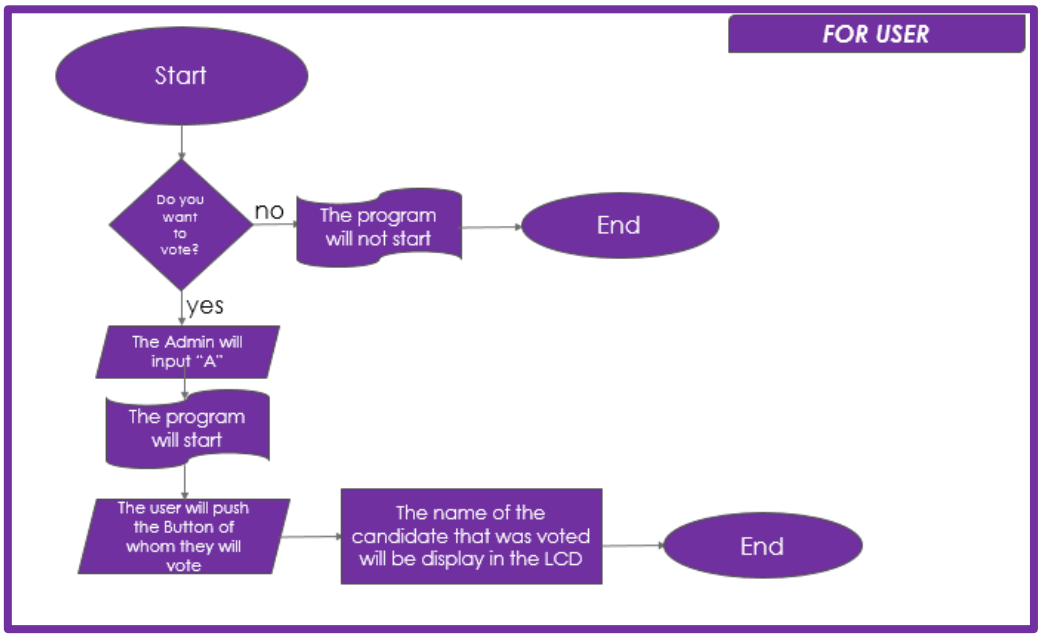


Figure 3. Flowchart of the system for the user of the program

In figure 3 it is shown that the user will only push the pushbutton for them to vote. The candidate in the election has one assigned push button so that the user will not hesitate in which button they will push for their desired candidate and after they push the button their vote will appear in the LCD 16x2 screen. Each voter can vote in the system just once.

4. Result and Discussion

In the proposed program that the researchers made it is designed and implemented to be a user-friendly and accessible. It is also designed to consider the user's need and requirement for a manageable and accessible voting system. In this paper the researchers put some ways to show different analyses like figures and connections on how the Arduino will be used.

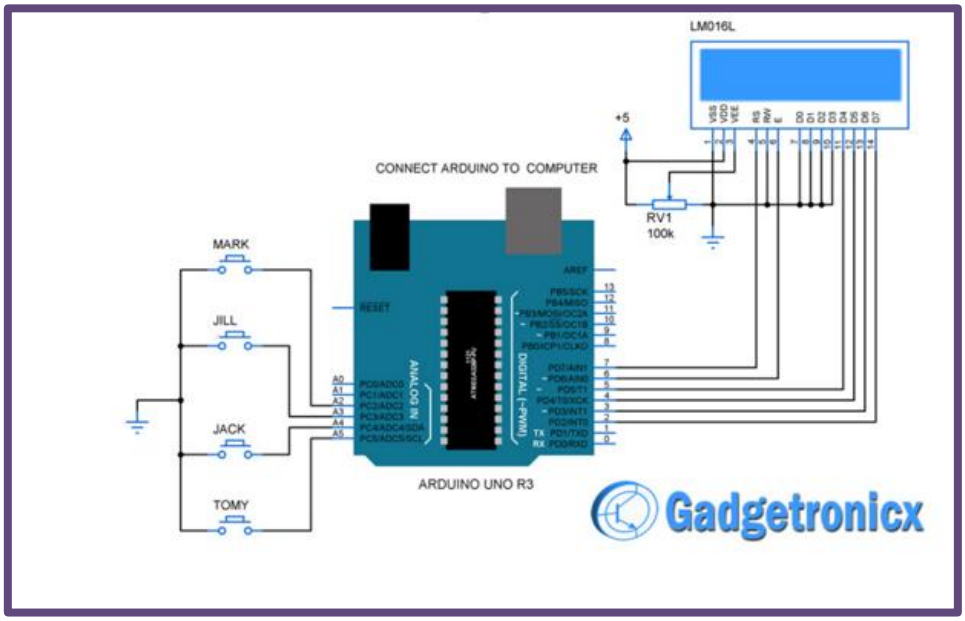


Figure 4. Schematic Diagram of the Arduino Voting System

In the figure 4 above it shows the schematic diagram of the voting system. It shows here the connection of the pushbutton to the Arduino and to the LCD screen. The Arduino Microcontroller will be connected to the laptop or P4C to compile the codes and to make it work. The whole process of voting is already programmed in the arduino microcontroller.



Figure 5. The LCD Display the Name of the Candidates

In the figure 5 it is show that the LCD 16x2 display the result of the election. The result appeared in the LCD cscreen so that the user will easily check if their votes is already counted. In here it is see that the vote will appear below the the name of the candidate they voted.

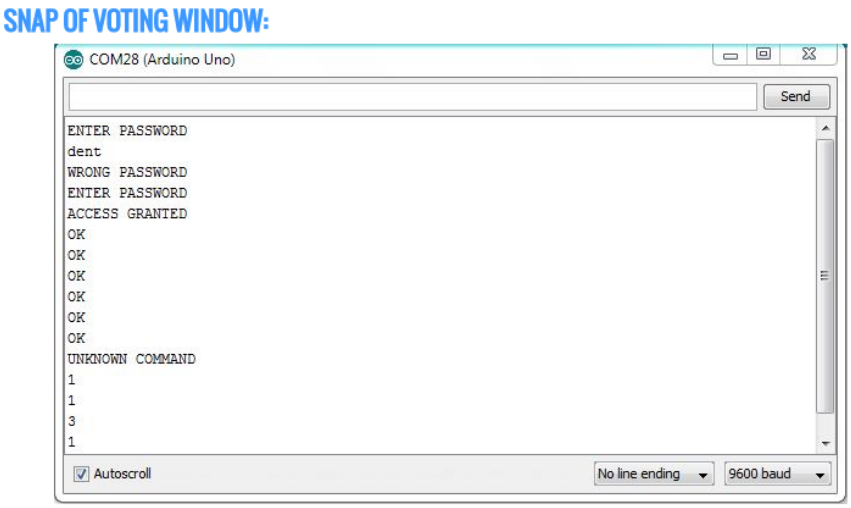


Figure 6. The Serial Monitor display the Result of the Voting

In the figure 6 it is clearly shown the serial monitor screen of the system. In which it is seen that the security of the election is assured. The admin of the voting system will be the one to control the whole voting to assure that there is just one vote for each voters. It displays how many votes did the voting.



Figure 7. The prototype of the Arduino Voting System

In figure 7 it shows the prototype of the Arduino-Based Voting System. The name of the candidate is display on its case and if the user will vote they will just push the desired candidate that they want to vote.

Table 2. Reliability Percentage of the System

Trial	Total No. Voter	Arduino-based Voting System					Total no. of Votes	Percentage of the Reliability of the system
No.	No.	Binay	Roxas	Poe	Santiago	Duterte	No.	%
1	10	3	2	1	3	1	10	100%
2	30	2	3	4	6	15	30	100%
3	15	1	2	3	4	5	15	100%
4	20	5	5	2	3	5	20	100%
5	25	3	7	3	8	4	25	100%

In the table 2 above it shows that the reliability of the system is 100% the proponent has test several trials to prove the reliability of the Arduino-based Voting System. The total number of voter is indicated their and when the researchers sum it up with the total number of votes it is the same. With the several test that the researchers have made it is prove that the system is reliable and stable.

5. Conclusion

Through the development and continues advancement of the technology voting system are now being made. In the entire course of this project, based from the results

and discussion that is presented, the researchers concluded that the objectives of the project is successfully achieved. The System that the proponent made is working stable and reliable based on the table 2 in the results and discussion. The researchers have made the system secured and protected. The admin has a password to control the poll by just inputting it for the program to start. For the voter to start voting the admin must input letter "A" and to show the result in the serial monitor the admin must input letter "S". The system is easy to use and user-friendly the user will just push the push button and the voting process is all done. This voting system can give the result immediately by displaying it in the serial monitor screen. When the admin input the letter "S" the tally of the voting will be displayed. The researchers have successfully produced, manageable, useful, secured, reliable and user-friendly arduino voting system that can be used in small-scale election such as in classroom our party list voting.

6. Recommendation

The paper only focuses in a voting system using arduino microcontroller, LCD and Serial monitor. From the findings during this project, the researchers give the following recommendation to the future researchers: For the program, since every year we are conducting an election the researchers recommend to use the program that we have for simple and faster result of the election. Also this is a good advantage to use Arduino microcontroller in making a more digitalize and upgraded voting system that can be use in a huge election.

Acknowledgment

The authors of this paper would like to give their deepest thanks and gratitude above all to God for the guidance, strength, knowledge, wisdom and patience in every day. They would also like to give their gratitude to Engr. Rionel Caldo their professor who support them and guide them to finish this research paper. Lastly, the researchers would like to give thanks to their family, friends and loved ones who support and inspire them in every day. This research paper would not be possible without the help and support of everyone.

References

[1] Amy, D. J. (April 8, 2005). What are Voting Systems and Why are They Important?

[2] Voting: What Is; What Could Be, (2001, July). Available: http://www.vote.caltech.edu/Reports/

[3] D.A. Kumar, T.U.S Begum, "A Novel design of Electronic Voting System Using Fingerprint," International Journal of Innovative Technology & Creative Engineering, vol.1, no.1, pp.12-19, January 2011.

[4] Everett, S. P. (n.d.). The Usability of Electronic Voting Machines and How Votes Can Be Changed Without Detection. http://chil.rice.edu/.

[5] Greene, K. K. (n.d.). A Comparison of Usability Between VotingMethods.usenix.org/legacy/event/evt06/tech/full_papers/greene/greene_html/.

[6] "Electronic Voting," Ronald L. Rivest, Technical Report, Laboratory for Computer Science, Massachusetts Institute of Technology.

[7] "e-Voting Security Study," E-Democracy Consultation, U. K. Cabinet Office, http://www.edemocracy.gov

[8] By: Shiexy, (August 2010) Voting System. Studymode.com retrieved from www. Studymode.com/essays/voting-system-381603.htm

[9] 2012, 07 E voting system. Studymode.com. Retrieved from www. Studymode.com/essay/E-votingsystem-1047789.html

[10] By: marangel26(2011,05). Psu bayambang campus Votingsystem.studymode.comRetrieved frim www. Studymode,com/essay/psu-bayambang-campus-voting-system-708937.html

[11] Canada, E. (June 13,2014). Establishing a Legal Framework for E-voting in Canada. E-voting in an Uncontrolled Environment (Internet Voting)